www.jresm.org

Research on Engineering Structures and Materials

Volume 11
Issue 4
August 2025

P-ISSN: 2148-9807 E-ISSN: 2149-4088

The International Journal of **Research on Engineering Structures and Materials (RESM**) is a peer-reviewed open access journal (p-ISSN: 2148-9807; o-ISSN: 2149-4088) published by MIM Research Group. It is published in February, April, June, August, October, and December.

The main objective of RESM is to provide an International academic platform for researchers to share scientific results related to all aspects of mechanical, civil, and material engineering areas.

RESM aims the publication of original research articles, reviews, short communications technical reports, and letters to the editor on the latest developments in the related fields.

All expenditures for the publication of the manuscripts are most kindly reimbursed by *MIM Research Group*. Thus, authors do not need to pay for publishing their studies in the journal.

The scope of the journal covers (but not limited to) behavior of structures, machines and mechanical systems, vibration, impact loadings and structural dynamics, mechanics of materials (elasticity, plasticity, fracture mechanics), material science (structure and properties of concrete, metals, ceramics, composites, plastics, wood, etc.,), nano-materials performances of new and existing buildings and other structural systems, design of buildings and other structural systems, seismic behavior of buildings and other structural systems, repair and strengthening of structural systems, case studies and failure of structural systems, safety and reliability in structural and material engineering, use of new and innovative materials and techniques in energy systems and mechanical aspects of biological systems (biomechanics and biomimetics).

The topics covered in JRESM include:

- Structural Engineering
- Mechanical Engineering
- Material Engineering
- Earthquake Engineering
- Nano-technology
- Energy Systems (Focus on Renewable)
- Biomechanics and Biomimetics
- Environment (Material and Engineering System Related Issues)
- Computer Engineering and Data Science (Material and Engineering System-Related Issues)

Abstracting and Indexing
Please visit http://www.jresm.org for more information.

Graphics and Design

Mehmet Yılmaz myilmaz@jresm.net

RESEARCH on ENGINEERING STRUCTURES & MATERIALS

Research Group

RESEARCH on ENGINEERING STRUCTURES & MATERIALS

Editorial Board

Editor in Chief		
Hayri Baytan Özmen	Usak University	Türkiye
Editors		
Antonio F. Miguel	University of Evora	Portugal
Michele Barbato	University of California Davis	USA
Mehmet Palancı	Arel University	Türkiye
Francesco D'Annibale	University of L'Aquila	Italy
Chitaranjan Pany	Vikram Sarabhai Space Centre	India
Badrinarayan Rath	Wollega University	Ethiopia
Taymaz Tabari	Jagiellonian University	Poland
Tamer Saracyakupoglu	İstanbul Gelisim University	Türkiye
Ivan Banović	University of Split	Croatia
Rayah Nasr Al-Dala'ien	Al-Balqa Applied University	Jordan
Balasubramanian Ramesh	Dhanalakshmi Srinivasan University	India
Abbasali Sadeghi	Islamic Azad University	Iran
Srinivasan Anandhan	National Institute of Technology Karnataka	India
Huatian Zhao	Imperial College London	UK
Blessen Skariah Thomas	National Institute of Technology Calicut	India
Majid Pouraminian	Islamic Azad University	Iran
Blessen Skariah Thomas	National Institute of Technology Calicut	India
Ibrahim Alshaikh	University of Science and Technology	Yemen
Seyed Reza Samaei	Islamic Azad University Science And Research Branch	Iran
Uzair Aslam Bhatti	Hainan University	China
Tian Su	Shandong University of Technology	China

Editorial Office

Publishing Manager		
Mehmet Yılmaz	MIM Research Group	Türkiye
Production Editor		
Damla Yalçıner Çal	MIM Research Group	Türkiye
Language Editors		
Gaye Kuru	Uşak University	Türkiye
Mete Çal	MIM Research Group	Türkiye

Editorial Board Members		
Farid Abed-Meraim	Arts et Metiers ParisTech	France
P. Anbazhagan	Indian Institute of Science	India
Raffaele Barretta	University of Naples Federico II	Italy
R.S. Beniwal	Council of Scientific and Industrial Research	India
Antonio Caggiano	University of Buenos Aires	Argentina
Noel Challamel	University of South Brittany	France
Abdulkadir Çevik	Gaziantep University	Türkiye
J. Paulo Davim	University of Aveiro	Portugal
Hom Nath Dhakal	University of Portsmouth	UK
Ali Faghidian	Islamic Azad University	Iran
S. Amir M. Ghannadpour	Shahid Beheshti University	Iran
Ali Goodarzi	Harvard University	USA
Jian Jiang	National Institute of Standards and Technology	USA
Ramazan Karakuzu	Dokuz Eylül University	Türkiye
Arkadiusz Kwiecien	Cracow University of Technology	Poland
Stefano Lenci	Universita Politecnica delle Marche	Italy
Silva Lozančić	University of Osijek	Croatia
Fabio Mazza	University of Calabria	Italia
Yuan Meini	North University of China	China
Stergios A. Mitoulis	University of Surrey	UK
Vinayagam Mohanavel	Anna University	India
Ehsan Noroozinejad Farsangi	Kerman Graduate University of Technology	Iran
Alaa M. Rashad	Shaqra University	Saudi Arabia
Mohammad Mehdi Rashidi	University of Tongji	China
Pier Paolo Rossi	University of Catania	Italy
Neritan Shkodrani	Polythecnic University of Tirana	Albania
Y.B. Yang	National Taiwan University	Taiwan

Advisory Board Members

A. Abdelbary	Alexandria University	Egypt
A. Karthik	SRM Institute of Science and Technology	India
Abbasali Sadeghi	Islamic Azad University	Iran
Abdelhalim Bensaada	University of Yahia Fares of Medea	Algeria
Abdellah Douadi	Ferhat Abbas University of Setif 1	Algeria
Abdel-Nasser Sharkawy	Faculty of Engineering, South Valley University	Egypt
Abdul Haseeb Wani	Presidency University, Bengaluru	India
Abid Ustaoglu	Bartın University	Türkiye
Abrham Gebre	Addis Ababa University	Ethiopia
Ahmed Maamoun	McMaster University	Canada
Aicha Rouabeh	University of Bouira	Algeria
Alaa M. Rashad	Housing & Building National Research Center (HBRC)	Egypt
Aleksandar Ašonja	University Business Academy	Serbia
Ameer Baiee	University of Babylon	Iraq
Amirreza Sadeghi	University of Birjand	Iran
Andi Yusra	Universitas Teuku Umar	Indonesian
Andriy Huts	Rzeszow University of Technology	Poland
Anthony N. Papathanassiou	National and Kapodistrian University of Athens	Greece
Arash Rahimi	University of Perugia	Italy
Arun KK	Kumaraguru College of Technology Coimbatore	India
ARUNKUMAR K	Mangalam College of Engineering	India
Ary A. Hoyos-Montilla	Construction School at Universidad Nacional de Colombia	Colombia
Ashhad Imam	National Institute of Technology Jamshedpur	India
Ayoub Souileh	University Mohammed V	Morocco
Azad A. Mohammed	University of Sulaimani	Iraq
Azzura Ismail	Universiti Tun Hussein Onn Malaysia	Malaysia
B.P.R.V.S. Priyatham	GMR Institute of Technology	India
Badrinarayan Rath	Wollega University	Ethiopia
Bengi Gözmen Şanlı	Mersin University	Türkiye
Berrin ikizler	Ege University	Türkiye
Bilge Demir	Karabuk University	Türkiye
Cagri Yardimci	Usak University	Türkiye
Canan Kandilli	Usak University	Türkiye
Caroline S. Sobhy	Fayoum University	Egypt
Catur Harsito	Universitas Sebelas Maret	Indonesia
Chau-Khun Ma	Universiti Teknologi	Malaysia
Christopher Fapohunda	Federal University Oye-Ekiti	Nigeria
Damilola Oyejobi	University of Botswana	Botswana
Daniel Cruze	Mohamed Sathak A J College of Engineering	India
Deep Tripathi	University of Sherbrooke	Canada
Dr Abhilash P P	Indian Institute of Technology (BHU)	India
E.R. Teixeira	University of Minho	Portugal
Ebrahim Sharifi Teshnizi	Ferdowsi University of Mashhad,	Iran
Edwin Klu	Virginia Tech	USA
Elavenil S	Vellore Institute of Technology	India
Emin Erdem	Pamukkale University	Türkiye
Ercan Isik	Bitlis Eren University	Türkiye
Eric M. Lui	Syracuse University	USA
Erion Bukaci	Polytechnic University of Tirana	Albania
Erion Bukaci	Polytechnic University of Tirana	Albania
Essam H. Mohamed	South Valley University	Egypt
Fatih Ahmet Senel	Süleyman Demirel University	Türkiye
Fokruddin Ahmad	Washington State University	USA

Advisory Board Members

Gaurav Dhadse	G. H. Raisoni Institute of Engineering and Business Management Jalgaon Maharashtra	India
Ghasan Fahim Huseien	Universiti Teknologi Malaysia	Malaysia
Gökhan Gece	Bursa Teknik University	Türkiye
Gururaj Hatti	KLS VDIT	India
Gustavo Bosel Wally	Federal University of Rio Grande do Sul	Brazil
Güneş Harman	Yalova University	Türkiye
Gür Emre Güraksın	Afyon Kocatepe University	Türkiye
Haithem Boumediri	Université Constantine 1	Algeria
Hakan Sarikaya	Uşak University	Türkiye
Halit Cetiner	Isparta University	Türkiye
Hamid Saberi	University of Eyvanekey	Iran
Hamoon Fathi	Islamic Azad University	Iran
Hasan ULUS	Selcuk University	Türkiye
Hasibullah Azizi	Andhra University	India
Hayri B. Ozmen	Usak University	Türkiye
HILTON AHMAD	Universiti Tun Hussein Onn Malaysia	Malaysia
Hossein Jarrahi	University of Birjand	Iran
Hossein Kabir	University of Illinois	USA
Hüsnügül YILMAZ ATAY	Izmir Katip Celebi University	Türkiye
Irina Volokitina	Karaganda Industrial University	Kazakhstan
J. Eswari	National Institute of Technology	India
J. Paulo Davim	University of Aveiro	Portugal
J. Paulo Davim	University of Aveiro	Portugal
Javad Vaziri	University of Semnan	Iran
Jayalalitha Subbaiah	SASTRA Deemed University	India
Jesús Castro	Universitat Politecnica de Catalunya	Spain
Kabiru Mustapha	Kwara State University	Nigeria
Kamel Chaoui	Badji Mokhtar University	Algeria
Kaplan Kaplan	Kocaeli University	Türkiye
Kourosh Mehdizadeh	Islamic Azad University	Iran
Lavanya Prabha	SRM Easwari Engineering College	India
Lawrence Zahemen Tuleun	University of Ilorin	Nigeria
Leonid Dvorkin	National University of Water and Environmental Engineering	Ukraine
Lomesh Mahajan	Dr. Babasaheb Ambedkar Technological University	India
Luiz Rocha	Federal University of Rio Grande do Sul	Brazil
Lyamine Briki	University of Batna2	Algeria
M. Jafaryar	Babol Noshirvani University of Technology	Iran
Madhulika Sinha	National Institute of Technology	India
Maheswaran Muthiah	Kalasalingam Academy of Research and Education	India
Majid M.A. Kadhim	University of Babylon	Iraq
Majid Pouraminian	Islamic Azad University	Iran
Matthew Martianus Henry	Bina Nusantara University	Indonesia
Md. Golam Kibria	Rajshahi University of Engineering & Technology	Bangladesh
Md. Zia ul haq	Panjab University	India
Mehdi Khorasani	Isfahan University of Technology	Iran
Mehdi Panji	Islamic Azad University	Iran
Mehmet Kaya	Bozok University	Türkiye
Melika Mahmoodabadi	Islamic Azad University	Iran
Mevlüt Gürbüz	Ondokuz Mayıs University	Türkiye
Mihir Mishra	Texas A&M University	USA
Mohammad Lesani	University of Tehran	Iran
Mohammad. I Al Biajawi	Universiti Malaysia Pahang Al-Sultan Abdullah	Malaysia

Advisory Board Members

Mohammad Afrazi	Tarbiat Modares University	Iran
Mohammad Hossein Razmkhah	Semnan University	Iran
Mohammad Naeim Moradi	Amirkabir University of Technology	Iran
Mohammadreza Baghoolizadeh	Shahrekord University	Iran
Mohammed Jalal Al-Ezzi	University of Bilad Al-Rafidain	Iraq
Mohd Nasim	IPS Academy, Indore	India
Mohd Syahrul Hisyam Mohd Sani	Universiti Teknologi MARA (UiTM)	Malaysia
Mohsen Hajizamani	Graduate University of Advanced Technology	Iran
Moslem Paidar	Islamic Azad University	Iran
Motahhareh Nezafat Tabalvandani	Islamic Azad University	Iran
Mounika Ganta	Vignana Bharathi Institute of Technology	India
Mukaila Anifowose	Federal Polytechnic Offa	Nigeria
Murtala Namakka	Universiti Malaysia Sarawak	India
Mutluhan Akin	Nevşehir Hacı Bektaş Veli University	Türkiye
N. Arunachelam	Mepco Schlenk Engineering College	India
N.L.N. Kiran Kumar	Sri Venkateswara University	India
N.Venkata Sairam Kumar Namepalli	R.V.R & J.C College of Engineering	India
Nabil Bella	Tahri Mohamed University of Bechar	Algeria
Nahida Nazim Musayeva	Azerbaijan National Academy of Sciences	Azerbaijan
Naveen S	National Institute of Technology, Raipur	India
Nazime Seda Şaşmaz Karacan	Usak University	Türkiye
Neeraj SN	Visvesvaraya Technological University	India
Nermin Demirkol	Kocaeli University	Türkiye
Nhlanhla Nyembe	University of the Witwatersrand	South Africa
Nilesh Masne	GESCOEMSR	India
Ninu Praseetha N S		India
Ola Mazen Makki	University of Al-Qadisiyah	Iraq
Oladimeji Olatunji Ojo	Federal University of Technology Akure	Nigeria
Oleg V. Devitsky	Federal Research Centre Southern Scientific Centre of the Russian Academy of Sciences	Russia
Oleksii Hrechanyi	Zaporizhzhia National University,	Ukraine
Orhan Gülcan	General Electric Aerospace	Türkiye
Oritonda Muribwathoho	Cape Peninsula University of Technology	South Africa
P. Manoj Kumar	KPR Institute of Engineering and Technology	India
P. Marimuthu	SASTRA Deemed to be University	India
Parmo Parmo	UIN Sunan Ampel Surabaya	Indonesia
Partheeban Pachaivannan	Chennai Institute of Technology	India
Qasim M. Shakir	University of Kufa	Iraq
Qiang Ou	Chongqing University, Chongqing	China
Ramnarayan Sahu	Rajeev Gandhi Technical University	India
Rayeh Nasr Al-Dala'ien	Universiti Tenaga Nasional	Malaysia
Revathi Srinivasan	Mepco Schlenk Engineering College	India
Roberto Nascimbene	School of Advanced Studies IUSS Pavia	Italy
ROYAL MADAN	Chandigarh University	India
S. Ali Faghidian	Islamic Azad University	Iran
S. Ali Faghidian	Islamic Azad University	Iran
S. Gholizadeh	Urmia University	Iran
Saeid Foroughi	Selçuk University	Türkiye

Advisory Board Members

Sai Krishna Pinnamaneni	University of Texas at Arlington	USA
Saifulnizan Jamian	Universiti Tun Hussein Onn Malaysia	Malaysia
Saman Saadatfar	Islamic Azad University	Iran
Saman Mansouri	UNISTRAPG	Italy
Samuel Awe	Automotive Components Floby AB	India
Sangeetha Palanivelu	SSN College of Engineering	India
Sarmila Sahoo	Heritage Institute of Technology Kolkata	India
Sasikumar Palanisamy	Kumaraguru College of Technology	India
Sastri M V S S	Vasavi College of Engineering	India
Saumen Mandal	National Institute of Technology Karnataka	India
Selcuk Selimli	University of Karabük	Turkey
Serdar Gungor	Bilecik Şeyh Edebali University	Türkiye
Serkan Elcin	Pamukkale University	Türkiye
Seymur Bashirzade	Azerbaijan University	Azerbaijan
Shahazadi Begum	Baba Institute of Technology and Sciences	India
Shahrul Niza Mokhatar	Universiti Tun Hussein Onn Malaysia	Malaysia
Shaise K. John	College of Engineering Trivandrum	India
Shashi Prakash Dwivedi	G. L. Bajaj Institute of Technology & Management	India
Shoulong Zhang	Harbour Engineering Research Institute Co. Ltd.	China
Siti Aisyah Nurjannah	Universitas Sriwijaya	Indonesia
Somayyeh Pourbakhshian	Islamic Azad University	Iran
Srinivasan Anandhan	National Institute of Technology Karnataka	India
Sumanth Ratna Kandavalli	New York University	USA
Sunday Chukwuemeka	Ceramics Research and Production Dept. (CRPD)	Nigeria
Suriyaprakash Rajadesingu	SRM Institute of Science and Technology	India
Talha Taskanat	Erciyes University	Türkiye
Tasnia Ahmed	Military Institute of Science and Technology (MIST)	Bangladesh
Toufik Sebbagh	University of Skikda	Algeria
Upendra K. Mallela	Aerospace Vertical, Largy Services Limited	India
Utsav Koshti	Nirma University	India
Venkatesh Chava	CVR College of Engineering, India	India
Victor Rizov	University of Architecture	Bulgaria
Vijayasarathy Rathanasalam	ATRIA Institute of Technology	India
Vinicius Pepe	University Ritter dos Reis	Brazil
Waleed A Abbas	University of Technology	Iraq
Xiaojian Wang	Xinjiang University	China
Yamini Sreevalli I	Vellore Institute of Technology	India
Yuliang Chen	Guangxi University of Science and Technology	China
Yuvaperiyasamy M	Saveetha School of Engineering	India
Yuvaraj K	K.S.Rangasamy College of Technology	India
Zafer Kaya	Dumlupınar University	Türkiye
ZAINORIZUAN MOHD JAINI	Universiti Tun Hussein Onn Malaysia	Malaysia
Zainab Tolu Giwa	Kwara State University	India
Zeynep Ekincioğlu Küzeci	Kırşehir Ahi Evran University	Türkiye
Ziyauddin Seikh	Aliah University	India

In This Issue

Research Article
1389 **C. Poornima, T. V. Vineeth Kumar**
Characterizing polylactic acid/basalt fiber composite: Synthesis, characterization, and mechanical property evaluation

Research Article
1399 **Eknath Nivrutti Aitavade, Hanmant Virbhadra Shete, Prashant S. Jadhav**
Investigations in wear and friction behavior of blends of Laxmitaru-FAME with nanoparticles as additives

Research Article
1413 **Suvidha, Sumesh Jain, C. Arvind Kumar**
Studies on durability, thermal and morphological property with partial replacement of single use waste plastic and complete recycled aggregate in eco-friendly self-compacting concrete

Research Article
1427 **Uday M, H R Vitala, Dileep B P, Bharath V, Udaya Devadiga, V Auradi**
Mechanical and wear characterization of nitrided Al-5%Ti-B metal matrix composite reinforced with Al_2O_3 particles

Research Article
1441 **Samir Chouarfia, Lakhdar Sedira, Kamel Meftah, Wahid Kaddouri**
A multiphase membrane element with rotational DOFs for the elastic analysis of date palm fibre reinforced PVC composite

Research Article
1469 **Arun B R, Srishaila J M, Md Khalid S, Veerabhadrappa Algur, Kavyashree K,Tanu HM**
Prediction of machine learning application in the development of novel sustainable self-compacting geopolymer concrete

Review Article
1491 **Panga Bhavana, N. K. Karthikeyan, S. Elavenil**
Integrating self-sensing nano composite and fiber optic sensors technologies for advancing structural monitoring: A mini review

Technical Note
1509 **Manjunatha K, Girish D P, Vasanth Kumar B S, Yashaswini T, Dinesh M H, Dilip Kumar K, Poornima K, Madeva Nagaral, Nagaraj Namdev, V Auradi**
Influence of forging on the hardness and tensile properties of Al7075/TiC composites

Research Article
1523 **Brijesh Singh, Shamsher Bahadur Singh, Sudhirkumar V. Barai, P N Ojha, Rohit Kumar**
Mechanical properties and fracture behavior of concrete made with sintered fly ash lightweight coarse aggregate and electric arc furnace slag as fine aggregate

Research Article
1545 **M. Suneel, G. V. Rama Rao**
Effect of Nano-TiO2 at macro and micro level of concrete by partial substitution of cement

Research Article
1561 **Chakrasali Chandrakumar, Irappa Sogalad, Arun Kumar Shettigar, Akash Korgal, Madeva Nagaral**
Exploring welding parameter effects on friction stir weld joints in aluminum 8006 alloy using response surface methodology

Research Article
1579 **Zhino A. Shawais, Khamees N. Abdulhaleem, Hussein Hamada**
Flexural behavior of the reinforced t-beam containing hybrid recycled-aggregate self-compacting concrete

Research Article
1595 **Amina Benguelil, Brahim Elkhalil Hachi, Mohamed Haboussi**
Analytical modeling of fracture energy with cohesion effects based on experimental investigations

Research Article
1615 **Abdellah Douadi, Riad Babba, Kamel Hebbache, Mourad Boutlikht, Nour El Houda Khitas, Abderraouf Messai, Redha Hammouche**
Evaluation of CFRP confinement performance and predictive accuracy of design codes and stress-strain models for concrete

Technical Note
1633 **Abdel-Nasser Sharkawy**
The effect of increasing hidden layers on the performance of the deep neural network: Modelling, investigation, and evaluation

Research Article
1653 **Mustafa Hayri Kesikoglu**
Comparative analysis of R/SWIR, NIR/SWIR, and NDSI classification methods for determination of snow cover change on Erciyes Mountain, Türkiye using Landsat satellite images

Research Article
1667 **Khadija Benhaddou, Ayoub Souileh, Latifa Ouadif, Achraf Mabrouk, Sabihi Abdelhak, Khadija Baba, Mustapha Rharouss**
Valorization of marine dredged sediments from Jebha Port as a sustainable alternative to dune sand in concrete manufacturing

Research Article
1683 **Gunnam Sanijya, Bala Murugan R, Samatha Chowdary P**
Sustainable stabilization of native subgrade soil for low-volume roads using copper slag and cementitious materials

Research Article
1703 **Ravi Prasad Penda, I V Ramana Reddy**
Mechanical performance of slurry-infiltrated fibrous concrete with varying ratios of scrap tire steel fibers and commercial steel fibers

Research Article
1721 **Yasser Oueld El Haj El Ghali, Abou-Bakr Cherki, Chouaib Benqlilou, Mohammed Khalil El Kouifat**
Physico-chemical characterization of fine gray clay with micrometric particle size

Research Article
1733 **Fakhriza, Muhd Haiyum, Nawawi Juhan, Jenne Syarif, Nurlaili, Ariefin, Bukhari Kasim, Indra Mawardi, Iskandar Hasanuddin, Muhammad, Faisal Abnisa**
Exploring the physical, mechanical, and thermal properties of oil palm trunk and ramie fiber hybrid bio composites as building insulation materials

Research Article
1749 **Zahraa Mohammed Kamil Al-Mayali, Mahmoud Ziada**
Enhancement of mechanical properties and sulfuric acid resistance in slag-based geopolymer mortars via metakaolin incorporation

Research Article
1767 **Sameh Fuqaha, Ahmad Zaki, Guntur Nugroho**
Optimizing indoor air quality in sustainable homes: A simulation-based evaluation of VOC emissions from bamboo-based materials

Research Article
1787 **Gouthami Patnaik Palter, Kanaka Durga Sambhana, Venkata Giridhar Poosarla, Potharaju Malasani**
Influence of calcium sources on strength and self-healing characteristics of bacterial concrete

Review Article
1817 **Othmane Karrame, Mohammed Aqil, Mohammed Ammari, Laïla Ben Allal**
Artificial intelligence-assisted optimization of concrete mixes to enhance the durability of civil engineering structures in marine environments

Research Article
1833 **K. Pushpa, S. Jayakumar, N. Pannirselvam**
Comparing mechanical properties of concrete with recycled aggregates using different mixing methods

Research Article
1847 **Ahmed Messaoud Djebar, Mohamed Mouli, Karim Belmokretar, Ramdane Chihaoui, Yassine Senhadji, Ahmed Soufiane Benosman, Mehdi Seghiri**
Impact of industrial waste fillers in self-compacting mortars: A comparative analysis of mechanical performance

Research Article
1863 **Fatimah Fahem Al-Khafaji**
Enhancing the performance of cold bitumen emulsion mixtures with coir and glass fibres: Experimental and numerical analysis

Free access to tables of content, abstracts and full text of papers for web visitors.

Copyright © 2023

Research on Engineering Structures & Materials
MIM Research Group Publications
P-ISSN: 2148-9807
E-ISSN: 2149-4088
http://www.jresm.org

ABSTRACTING / INDEXING

The international journal of Research on Engineering Structures and Materials (RESM) is currently Abstracted/Indexed by Asos Indeks, CiteFactor, Cosmos, CrossRef, Directory of Research Journal Indexing, Engineering Journals (ProQuest), EZB Electronic Journal Library, Global Impact Factor, Google Scholar, International Institute of Organized Research (I2OR), International Scientific Indexing (ISI), Materials Science & Engineering Database (ProQuest), Open Academic Journals Index, Publication Forum, Research BibleScientific Indexing Service, Root Indexing, Scopus, Ulakbim TR Index (Tubitak), Universal Impact Factor and under evaluation by many other respected indexes.

Check web site for current indexing info, www.jresm.org

Research on Engineering Structures & Materials
www.jresm.org
Research Group

Research Article

Characterizing polylactic acid/basalt fiber composite: Synthesis, characterization, and mechanical property evaluation

C. Poornima [a], T. V. Vineeth Kumar *[,b]

Department of Mechanical Engineering, Siddaganga Institute of Technology, Karnataka, India

Article Info

Article History:

Received 12 May 2024
Accepted 31 Oct 2024

Keywords:

Polymers;
Basalt fiber;
Polylactic acid;
Maleic anhydride;
Injection molding

Abstract

This investigation focused on enhancing the mechanical properties of polylactic acid (PLA) through the incorporation of basalt fibers and a maleic anhydride coupling agent. Basalt fibers, renowned for their high tensile strength and modulus, were selected as a potential reinforcement to augment PLA's mechanical performance. To optimize interfacial bonding between the hydrophilic PLA matrix and hydrophobic basalt fibers, maleic anhydride was employed as a coupling agent. The results indicate that the inclusion of 3 wt.% maleic anhydride and 10-20 wt.% basalt fibers significantly improved the composite's tensile strength by 40% and flexural strength by 51%. These findings underscore the potential of basalt fiber-reinforced PLA as a high-performance, sustainable material for diverse applications.

© 2025 MIM Research Group. All rights reserved.

1. Introduction

In recent years, there has been a notable surge in the quest for environmentally friendly and sustainable alternatives to conventional petroleum-based composites. Polylactic acid (PLA), a biodegradable and renewable thermoplastic polymer, has garnered significant attention due to its advantageous mechanical properties and minimal carbon footprint. Researchers are actively exploring ways to enhance PLA's mechanical performance by incorporating various types of fibers.

The studies on PLA/basalt fiber highlights the potential of basalt fiber reinforced composites as sustainable alternatives to synthetic fiber-based composites. While natural fibers offer environmental benefits, their mechanical properties often limit their applications. By combining basalt fibers with PLA, researchers have developed composites with promising tensile and flexural strengths. This work explores various fabrication techniques and mechanical characterization studies on basalt/PLA composites, underscoring their potential as eco-friendly replacements for traditional composites [1]. Previous research also highlighted the challenge of poor interfacial adhesion between basalt fiber and epoxy resin, limiting the widespread application of this promising green material. In a recent study, Wu et al. [2] addressed this issue by developing a novel surface modification technique involving citric acid modified β-cyclodextrin and polyethyleneimine. Their approach resulted in a substantial 76.9% increase in interfacial adhesion strength compared to unmodified fibers. The authors attributed this enhancement to the unique structure of β-cyclodextrin, which, in combination with PEI, created a multifunctional interphase that improved stress transfer, energy dissipation, and crack deflection. This research contributes significantly to the development of high-performance, environmentally friendly basalt fiber composites and offers a potential pathway for industrial-scale production due to the simplicity and sustainability of the modification process. Xue et al. [3] developed ternary PLA composites

*Corresponding author: vineethkumartv@sit.ac.in
[a]orcid.org/0000-0002-8561-9544; [b]orcid.org/0000-0002-4028-3813
DOI: http://dx.doi.org/10.17515/resm2024.279me0512rs

reinforced with short basalt fiber (SBF), incorporating PBAT and nano-silica. These composites exhibited substantial enhancements in tensile modulus (103%) and crystallinity (185.5%) compared to pure PLA, without compromising structural integrity. The inclusion of PBAT, nano-silica, and SBF also improved thermal stability, expanding the potential of PLA for high-temperature applications.

The recyclability of PLA and PLA-based natural fiber-reinforced composites (NFRCs) through conical twin screw extrusion was studied by Finnerty et al. [4]. PLA exhibited discoloration and an increased glass transition temperature by 15°C after six recycling cycles. While the impact strength of both BF and HNT-reinforced NFRCs remained relatively stable, tensile properties showed variations. BF-reinforced composites experienced a significant 30% decrease in tensile strength after three recycling cycles due to fiber length reduction and poor interfacial adhesion. In contrast, HNT-reinforced composites maintained tensile strength within 50-60MPa for up to three cycles but declined by 12% thereafter. The study highlights the potential of recycling PLA-based composites while identifying challenges related to fiber length, interfacial adhesion, and PLA degradation. Further research is needed to optimize recycling parameters and improve composite performance. Cao et al. [5] investigated the enhancement of PLA mechanical properties through carbon fiber (CF) reinforcement. The addition of CF significantly improved the thermal stability and crystallinity of PLA, as evidenced by TGA and DSC analysis. The melt flow rate decreased from 27.6 g/10 min to 12.1 g/10 min with CF incorporation. Notably, tensile strength increased by 42.49% to 91.58 MPa in PLA/CF composites compared to pure PLA. XRD analysis indicated a refined crystalline structure in PLA/CF. SEM observations revealed a transition from brittle to ductile fracture behavior with CF reinforcement. These findings demonstrate the potential of CF as an effective reinforcement for enhancing the overall performance of FFF-produced PLA materials.

Polylactic acid, a biodegradable polymer, has gained significant attention as a sustainable alternative to petroleum-based composites. To enhance PLA's mechanical performance, researchers have explored the incorporation of reinforcing fibers, including basalt fibers. Previous studies have primarily focused on improving interfacial adhesion, exploring diverse processing techniques, and incorporating additional components to optimize composite properties. While advancements have been made in terms of mechanical properties, thermal stability, and corrosion resistance, challenges related to interfacial adhesion, recyclability, and the impact of processing conditions on composite properties persist [6, 7].

This study aims to expand upon the existing body of research by comprehensively investigating the synthesis, properties, and mechanical behavior of PLA/basalt fiber composites. Previous studies have explored the potential of basalt fibers as reinforcement for PLA, but this research delves deeper into understanding the factors influencing the overall performance of these composites. By building upon successful processing techniques used for other polymer-based composites, we seek to optimize the integration of basalt fibers into the PLA matrix and assess the resulting mechanical properties. This research article focuses on the use of maleic anhydride (MAH) as a compatibilizer to improve the interfacial adhesion between basalt fibers and PLA in composites. While compatibilizer-free basalt/PLA composites may have been considered, the study's primary goal is to investigate the effectiveness of MAH in enhancing the mechanical properties and performance of these composites. Without a compatibilizer, the incompatibility between basalt fibers and PLA could have led to poor interfacial bonding, phase separation, and reduced mechanical strength. By using MAH, the study aims to address these potential issues and optimize the properties of the basalt/PLA composites.

2. Materials

Compostable bio-based PLA, known as luminy LX175, is purchased from Banka Bioloo Limited, located in Hyderabad. Basalt chopped fiber is procured from Nickunj Eximp Entp P Ltd, Mumbai. The nominal diameter and length of the basalt fiber are determined to be 13 micrometers and 6 millimeters, respectively. The properties of basalt fiber and PLA are presented in Table 1.

Table 1. Properties of basalt fibre and PLA

Properties	Basalt fiber	Polylactic acid
Density, g/cm^3	2.65	1.24
Nominal length, mm	6	-
Nominal Diameter, µm	13	-
Tensile Strength, MPa	2365	45
Elasticity modulus, GPa	93.4	93.4
% Elongation at Break	2.9	5
Melting Point, ^{0}C	1500	150

3. Methods

3.1 Sample Preparation

Basalt fibers, constituting 10% and 20% by weight, are combined with a 3% by weight maleic anhydride coupling agent and PLA pellets. This mixture undergoes processing in a twin-screw extruder equipped with a 40 mm diameter, co-rotating screw operating at 80 revolutions per minute as shown in Figure 1. Extrusion temperatures range from 140°C to 170°C. The interlocked screws generate shear pressures that facilitate thorough mixing and dispersion of the fibers within the PLA matrix. The coupling agent improves the interfacial adhesion between the PLA matrix and basalt fibers.

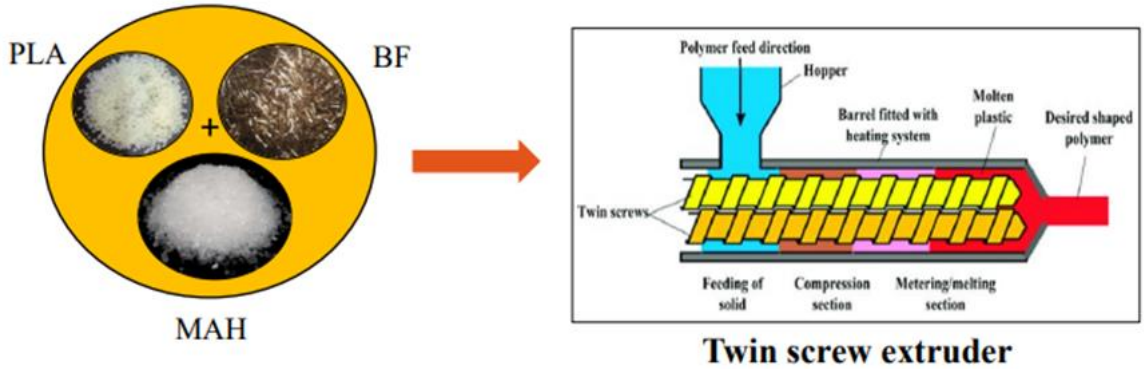

Fig. 1. Composite sample preparation

The resulting composite strands, containing 10% and 20% basalt fibers, are transformed into pellets through palletization and subsequently annealed at 100°C for one hour. These pellets are then processed using an NP100/200 injection molding machine featuring a 40 mm screw diameter and an L/D ratio of 19.6. The machine's heated barrel melts the pellets, which are then molded into desired shapes and cooled to solidify. Table 2 presents the primary injection molding parameters.

Table 2. Injection molding parameters

Parameters	Value
Clamping tonnage, ton	60
Injection speed, MPa	50
Injection pressure, bar	80
Refilling speed, rpm	50
Back pressure, bar	4
Shot weight, grams	50
Temperature profile along the barrel (from hopper to nozzle), ^{0}C	140-145-150-155

3.2 Mechanical Testing

Flexural properties, including strength and modulus, were evaluated according to ASTM D790 via a three-point bending test. A crosshead speed of 2 mm/min was maintained during testing. The flexural modulus was calculated from the resulting load-displacement data. The experimental set up is as shown in Figure 2.

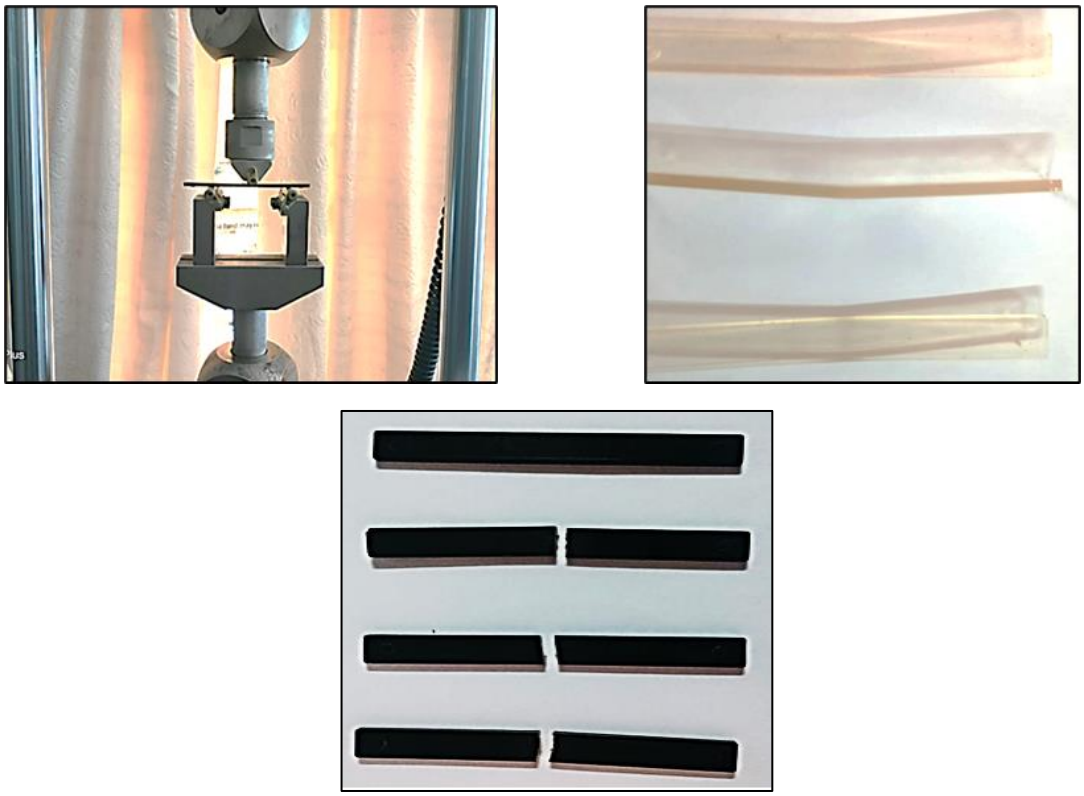

Fig. 2. Flexural testing

Tensile properties were determined according to ASTM D638 using a universal testing machine. A constant crosshead speed of 1.5 mm/min was applied, and load-displacement data was collected. Elastic modulus was calculated from the initial linear region of the resulting stress-strain curve. The experimental set up is as shown in Figure 3.

Fig. 3. Tensile testing

Hardness was assessed using the Yuzuki Rubber Hardness Test. A steel ball or diamond cone indented the material's surface, and the indentation depth was converted to a Rockwell hardness number. The experimental set up is as shown in Figure 4.

Fig. 4. Hardness testing test rig

3.3 Scanning Electron Microscopy

SEM was used to evaluate the basalt fiber-reinforced PLA composites' fracture surfaces. The composites were cryogenically fractured, then coated with a conductive substance to prepare the samples. The microstructure of the entire composite as well as the fiber-matrix adhesion and fiber dispersion were revealed by SEM imaging.

4. Results and Discussions

4.1 Mechanical Properties

The influence of basalt fiber reinforcement on the mechanical properties of PLA composites was investigated. Maleic anhydride (MAH) was incorporated as a coupling agent to enhance interfacial adhesion between the basalt fibers and the PLA matrix. The mechanical properties of the composites containing 10 and 20 weight percent basalt fibers were assessed through tensile, flexural, and hardness tests. Table 3 presents the tensile strength (σ_1), Young's modulus (E_1), flexural strength (σ_2), flexural modulus (E_2), and hardness values obtained from these tests.

Table 3: Mechanical properties of basalt fiber/polylactic acid composite

Materials	Tensile			Flexural		Hardness
	σ_1 [MPa]	E_1 [MPa]	ε [%]	σ_2 [MPa]	E_2 [MPa]	HRC Value
PLA	46.369	1825	5.169	84.987	3576	70
PLA/10wt.% basalt fiber	50.224	1978	4.89	89.768	4923	72
PLA/20wt.% basalt fiber	66.025	2905	3.224	127.685	5206	74

The tensile strength, flexural strength, and hardness of PLA composites increased with increasing basalt fiber content. Figure 5 illustrates the comparison of these properties for PLA and its composites. The addition of 20 wt.% basalt fibers resulted in enhancements of 24%, 29%, and 2.7% for tensile strength, flexural strength, and hardness, respectively. These findings underscore the positive influence of basalt fiber reinforcement on the mechanical properties of the PLA matrix. Hardness, a key indicator of a material's resistance to indentation, was evaluated for the basalt fiber reinforced PLA composite using a Yuzuki Rubber Hardness Tester with the Shore D scale. This measurement provides valuable insights into the composite's overall mechanical properties.

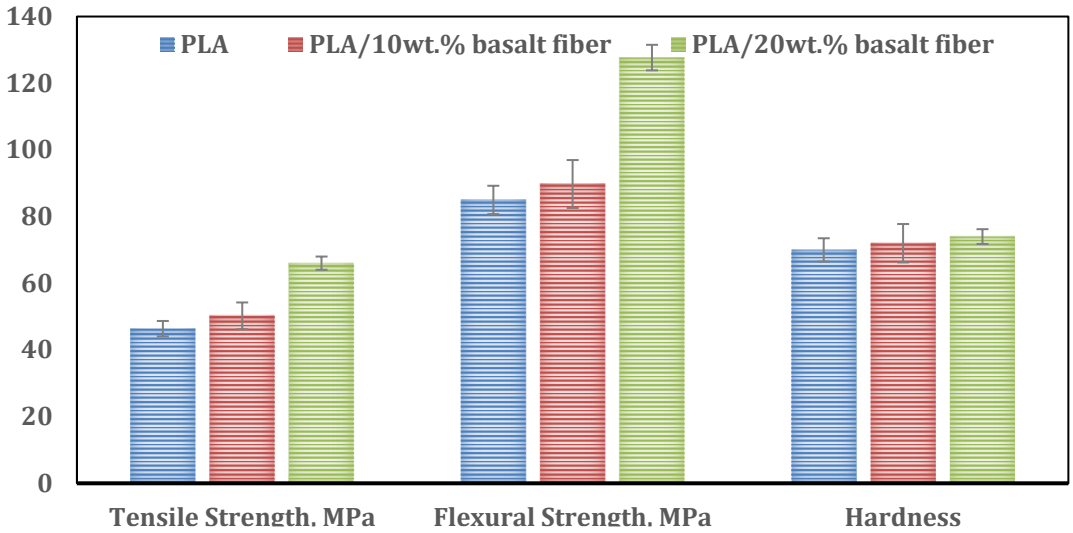

Fig. 5. Comparison of tensile strength, flexural strength and hardness of PLA composites

The stress–strain curves of the PLA/ basalt fiber composites with different basalt fiber content are shown in Figure 6. For all samples, the curves were linear at low strain, followed by plastic deformation in the region of 1.5% strain. At higher strains, the composites yielded up to a breaking strain of 5% for the PLA. The curves clearly show that the tensile strength of the composites increased markedly with increasing basalt fiber. The elongation at break, indicating a material's ductility, decreased with increasing basalt fiber content in the PLA composites. While neat PLA exhibited an elongation at break of 5.169%, this value reduced to 4.89% and 3.224% for composites containing 10 wt.% and 20 wt.% basalt fibers, respectively. This trend signifies a trade-off between enhanced strength and reduced ductility upon basalt fiber incorporation.

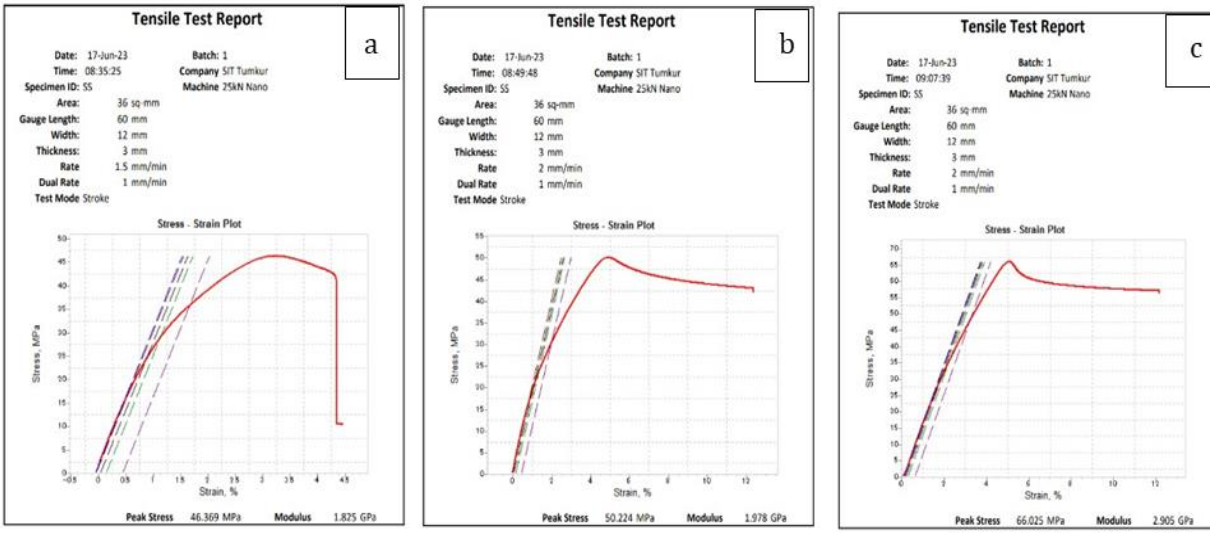

Fig. 6. Stress - Strain curve for PLA (a) PLA (b) PLA/Basalt fiber composite 10 wt. % (c) PLA/Basalt fiber composite 20 wt. %

Figure 7 illustrates the tensile and flexural moduli of the PLA composites. The addition of basalt fibers significantly enhanced the Young's modulus, indicative of increased stiffness and resistance to deformation under tensile load. Pure PLA exhibited Young's modulus of 1825 MPa. This value increased to 1978 MPa and 2905 MPa for composites containing 10 wt.% and 20 wt.% basalt fibers, respectively, representing improvements of 8.3% and 59.5%.

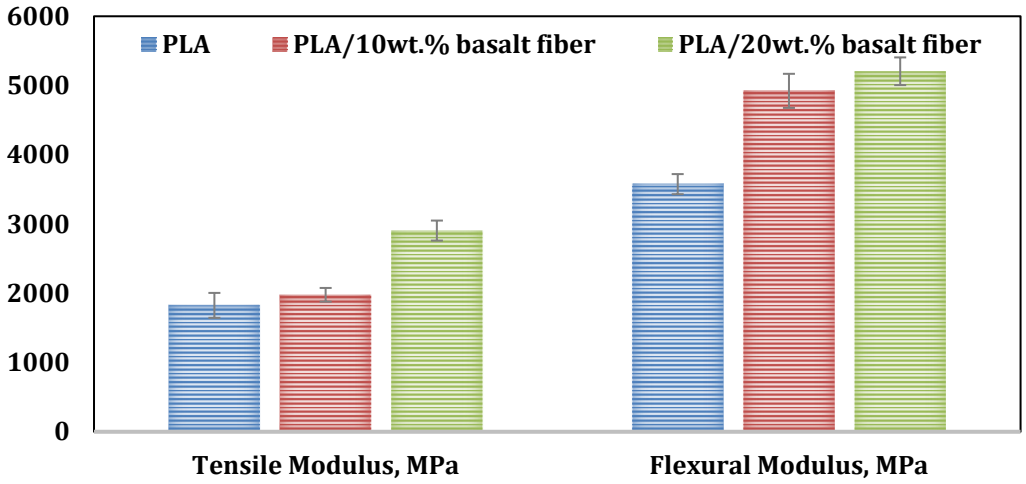

Fig. 7. Comparison of tensile and flexural modulus of PLA composites

Flexural modulus, a measure of a material's stiffness under bending, also increased with basalt fiber addition. While the PLA/10 wt.% composite showed a notable improvement in flexural modulus compared to both pure PLA and the PLA/20 wt.% composite, the latter also exhibited an increase over the neat PLA. The addition of MAH as a compatibilizer to 20 wt.% basalt fiber reinforced PLA composites resulted in improved flexural strength to 127MPa compared to 105MPa as reported by Aslan et al. (2018) [8]. The enhanced tensile strength of the PLA/basalt fiber composites can be attributed to the basalt fiber's stiffness and the presence of immobilized or partially immobilized polymer phases. The following factors contribute to the increase in mechanical properties,

- Physical Interactions: Basalt fibres reinforce PLA by transferring load, with their orientation, length, and volume fraction impacting the composite's properties [1, 9,10]
- Chemical Interactions: Strong interfacial adhesion between basalt fibres and PLA, enhanced by coupling agents or surface treatments, is crucial for optimal composite performance. Polymer matrix compatibility also affects interaction strength [11-14]

4.2 Morphological Analysis

The SEM investigation employed a high-resolution scanning electron microscope to analyze the samples. To improve image quality and mitigate charging effects, a thin layer of conductive material was sputter-coated onto the samples. SEM micrographs of the basalt fiber reinforced PLA composites were captured at 100µm and 200µm magnifications. Uniform dispersion of basalt fibers within the PLA matrix was observed, along with strong adhesion at the fiber-matrix interface, indicating the effectiveness of the maleic anhydride coupling agent. No fiber pull-out or surface irregularities were evident on the basalt fibers for both compositions (Figure 8 and 9). At 200µm magnification, individual basalt fibers were more clearly visible. Their random orientation within the composite was confirmed, with minimal voids or gaps observed. This suggests well-bonded interfacial regions.

A well-bonded interfacial region in polymers enhances mechanical strength and adhesion, improves thermal and electrical properties, and reduces defect formation. This results in better overall performance and durability of the material [15]. In the 20wt.% BF/PLA composite (Figure 9), the basalt fibers were evenly distributed throughout the PLA matrix, and strong adhesion was maintained at the fiber-matrix interface. No fiber pull-out or breakage was observed, and the basalt fiber surfaces appeared smooth with well-bonded interfacial regions. Tensile testing revealed stretched fibers within the composite. No grouping or aggregation of basalt fibers was observed, and their random orientation was confirmed. The above morphological observations are found to incline with SEM results reported by Aslan et al. (2018) [8]. Few voids or gaps were present, indicating well-bonded interfacial regions. The coarse surfaces observed in Figures 8 and 9 suggest a brittle fracture mechanism.

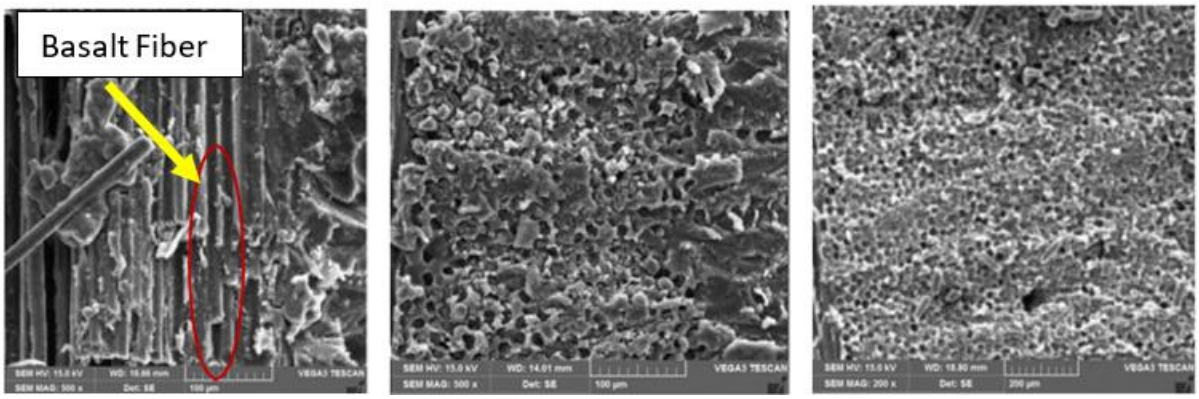

Fig. 8. SEM Observation of 10wt.% BF/PLA

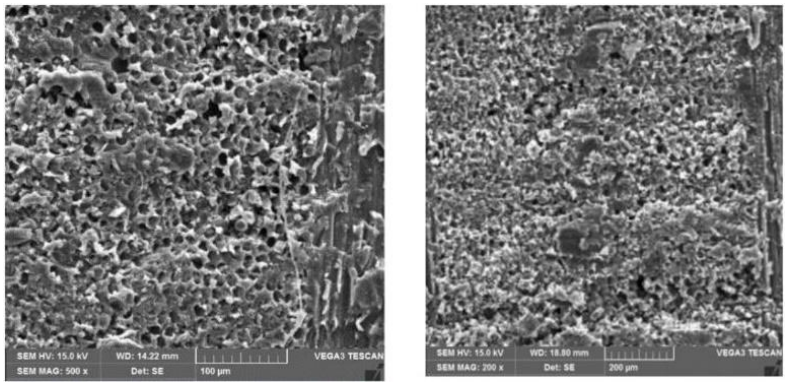

Fig. 9. SEM Observation of 20% Basalt fiber/PLA

5. Conclusion

In summary, the integration of basalt fibers in various proportions has notably bolstered both the tensile and flexural characteristics of PLA composites. Incorporating 10 wt. % basalt fibers yielded an 8.3% upsurge in tensile strength to 50.224 MPa and a 5.6% increase in flexural strength to 89.768 MPa. Elevating the basalt fiber content to 20 wt. % resulted in a significant enhancement of both tensile and flexural strength to 66.025 MPa and 91.797 MPa, respectively. These results underscore the effectiveness of basalt fibers in enhancing the mechanical properties of PLA composites, making them suitable for applications requiring heightened stiffness and strength.

Moreover, the observed enhancements in elastic modulus (E) indicate heightened stiffness and structural integrity of the composites, offering valuable insights for the development of bio-based materials with superior performance characteristics. Specifically, PLA/basalt fiber composites exhibit considerable potential for use in automotive components, where superior strength and rigidity are imperative.

These materials hold promise for the fabrication of structural automotive components such as body panels, interior trims, and reinforcing elements, owing to their enhanced mechanical properties and structural integrity. The increased tensile and flexural strength of these composites contribute to heightened durability and load-bearing capacity, thereby enhancing performance and safety in automotive applications.

Furthermore, the observed improvements in elastic modulus (E) offer benefits in terms of enhanced handling and greater deformation resistance, particularly advantageous for automotive parts. In summary, the study underscores the potential of basalt fiber-reinforced PLA composites in automotive applications, presenting opportunities for the development of lightweight, high-performance components that can contribute to fuel efficiency, weight reduction, and compliance with rigorous safety and performance standards in the automotive industry.

References

[1] Mohanty S, Singh JIP, Dhawan V, Singh S, Belaadi A. A review on basalt/PLA composite and its chemical and mechanical properties. 2024. p. 020016. https://doi.org/10.1063/5.0192257

[2] Wu Q, et al. Synergistic interactions of citric acid grafted β-cyclodextrin and polyethyleneimine for improving interfacial properties of basalt fiber/epoxy composites. Compos Sci Technol. 2024;251:110575. https://doi.org/10.1016/j.compscitech.2024.110575

[3] Xue G, Liang H, Pu Y, Wang D, Wang Y. Enhancing thermal stability and tensile performance of short basalt fiber-reinforced PLA composites with PBAT and nano-silica. Compos Commun. 2024 Jun;48:101894. https://doi.org/10.1016/j.coco.2024.101894

[4] Finnerty J, et al. Effect of mechanical recycling on the mechanical properties of PLA-based natural fiber-reinforced composites. J Compos Sci. 2023 Apr;7(4):141. https://doi.org/10.3390/jcs7040141

[5] Cao M, et al. Preparation and characterization for the thermal stability and mechanical property of PLA and PLA/CF samples built by FFF approach. Materials. 2023 Jul;16(14):5023. https://doi.org/10.3390/ma16145023

[6] Khandelwal S, Rhee KY. Recent advances in basalt-fiber-reinforced composites: Tailoring the fiber-matrix interface. Compos B Eng. 2020 Jul;192:108011. https://doi.org/10.1016/j.compositesb.2020.108011

[7] Ramezani Dana H, Ebrahimi F. Synthesis, properties, and applications of polylactic acid-based polymers. Polym Eng Sci. 2023 Jan;63(1):22-43. https://doi.org/10.1002/pen.26193

[8] Aslan M, Kaya M, Güler O, Alver Ü. Effect of fibre content on the mechanical properties of basalt fibre reinforced polylactic acid (PLA) composites. 2018 Jan.

[9] Coughlin N, et al. Development and mechanical properties of basalt fiber-reinforced acrylonitrile butadiene styrene for in-space manufacturing applications. J Compos Sci. 2019 Sep;3(3):89. https://doi.org/10.3390/jcs3030089

[10] Ilyas R, et al. Natural fiber-reinforced polylactic acid, polylactic acid blends and their composites for advanced applications. Polymers (Basel). 2022 Jan;14(1):202. https://doi.org/10.3390/polym14010202

[11] Seghini MC, et al. Interfacial adhesion of basalt fibre reinforced polymer composites. 2019 [cited 2024 Nov 5]. Available from: https://hal.science/hal-03008706

[12] Jia H, et al. Highly enhancing the interfacial and mechanical properties of basalt fiber/poly(phthalazinone ether nitrile ketone) composite by thermoplastic sizing agents with different structures. Polymers (Basel). 2022 Jul;14(14):2947. https://doi.org/10.3390/polym14142947

[13] Huang S, Fu Q, Yan L, Kasal B. Characterization of interfacial properties between fibre and polymer matrix in composite materials - a critical review. J Mater Res Technol. 2021 Jul;13:1441-1484. https://doi.org/10.1016/j.jmrt.2021.05.076

[14] Hou X, Yao S, Wang Z, Fang C, Li T. Enhancement of the mechanical properties of polylactic acid/basalt fiber composites via in-situ assembling silica nanospheres on the interface. J Mater Sci Technol. 2021 Sep;84:182-190. https://doi.org/10.1016/j.jmst.2021.02.001

[15] Poornima C, Shivanna MU, Sathyanarayana S. Influence of basalt fiber and maleic anhydride on the mechanical and thermal properties of polypropylene. Polym Compos. 2023 Jan;44(1):57-68. https://doi.org/10.1002/pc.27026

Blank Page

Research on Engineering Structures & Materials
www.jresm.org
Research Group

Research Article

Investigations in wear and friction behavior of blends of Laxmitaru-FAME with nanoparticles as additives

Eknath Nivrutti Aitavade [*,1,a], Hanmant Virbhadra Shete [2,b], Prashant S. Jadhav [3,c]

[1]*Department of Mechanical Engineering, Keystone School of Engineering, Pune, India*
[2]*Department of Mechanical Engineering, Ashokrao Mane Group of Institutions, Kolhapur, India*
[3]*Department of Mechanical Engineering, Rajarambapu Institute of Technology, Sakharale, India*

Article Info

Article History:

Received 05 June 2024
Accepted 07 Nov 2024

Keywords:

Laxmitaru-FAME;
Nanoparticles;
Friction;
Wear;
Bio-diesel

Abstract

Blending of biofuels with petro-diesels has become indispensable for environmental conservation, offering considerably enhanced tribological qualities that contribute in power saving along with extension in the lifespan of compression-ignition (CI) engines. The objective of this work is to investigate the tribological features of nanoadditivated Laxmitaru- fatty acid methyl ester (FAME) blends in petro-diesel, by means of a 4-ball tribometer following American Society for Testing and Materials (ASTM) D 4172 standard. The experiments involved B-10 (10 percent biodiesel mixed with petro diesel), B-20 and B-30 variants along with neat petro-diesel. Nano Silicon dioxide (SiO_2) was added in varying concentrations of 0.20%, 0.50%, 0.75%, and 1% by weight with Laxmitaru-FAME. The results revealed 75 % decrease in coefficient of friction (COF) and 55% reduction in wear compared to neat diesel (B0). Wear patterns of the experimental spheres were analysed by means of scanning electron microscopy (SEM), which indicated the material insertion and consequential mending on interface by nanoparticles due to highly stable dispersions.

© 2025 MIM Research Group. All rights reserved.

1. Introduction

The continued dependence on fossil fuels remains significant, despite their release of harmful gases into the atmosphere. These toxic emissions pose serious risks, particularly by damaging the ozone layer, which protects the Earth from harmful ultraviolet (UV) radiation. Human-induced air pollution has led to deteriorating air quality, especially in cities. Alarmingly, nine out of ten people globally struggle to access clean air. In regions where pollution levels exceed safe limits, there is a heightened risk of illness. The accumulation of these pollutants threatens the environment and human health, contributing to climate change, rising temperatures, melting glaciers, and escalating sea levels. This urgent situation calls for a global shift from conventional fuels to renewable energy sources, which offer a promising solution to reducing pollution and fostering a healthier environment [1]. Biofuels exhibit superior lubricating properties than petro-diesel. When biofuel is improved by nano additivation, it further enhances lubricity beyond that of neat biodiesel. This enhancement prolongs the lifespan of engine parts, specifically diesel injection system along with diesel pumps, that rely on diesel for lubrication. Maintaining adequate lubricity in engine fuel is essential for extending the durability of engine parts and safeguarding surfaces from wear during relative motion. Enhanced lubrication ability correspondingly lessens power loss via lessening motion resistance amid engine parts. In contrast, traditional diesel fuel exhibits poor lubricating characteristics compared to biofuels, highlighting the importance of exploring alternative fuels to meet increasing necessities [2, 3]. While numerous biofuels reveal favorable lubricity performance,

*Corresponding author: eknath.aitavade@keystonesoe.in, enaait70@gmail.com
[a]orcid.org/0000-0001-9963-7674; [b]orcid.org/0000-0001-5758-472X; [c]orcid.org/0000-0002-3102-6460
DOI: http://dx.doi.org/10.17515/resm2024.308ma0607rs

some exhibit unacceptable abrasion attributes due to rust and interface damage, posing potential harm to engines and limiting their utility. This underscores the need for tribological investigations into various biodiesels and the utilization of novel nanoparticles for addressing the lacunas [3]. Additionally, few overlooked biofuels warrant investigation in this regard. Several researchers have utilized various nanoparticles to enhance the tribological properties of lubricant oils, yielding highly beneficial outcomes. Ensuring the proper dispersion and precise mass/volume ratios of nanoparticles are crucial when incorporating them. Ultrasonication is employed to verify effective dispersion [2,4-16]. The following Table 1 shows the summary.

Table 1. Use of different Nanoparticles by various researchers

Nanoparticle Type	Size (nm)	Weight% (wt.%)	Improvement/Characteristics Observed
La_2O_3 [2]	20–1000	1%	Exhibits optimal adhesive wear at high loads and abrasive wear at high speeds
Al_2O_3 [4,30]	20-30	3%	Thermal conductivity increased by 31%, Better combustion in engine
CeO_2 [5]	10-50	0.6%(1:3 ratio)	Demonstrates minimal wear and low friction
Copper oxide(CuO) [6,7,19,26,28]	20-50	0.5-1%	Enhanced tribological performance due to strength and shape retention
Magnesium-doped zinc oxide (ZMO)[8]	10-100	2.5	Small particle size provides superior tribological properties
Activated carbon nanoparticle from bamboo [9]	50	0.01-0.05%	Maximal enhancement in lubrication efficiency with respect to friction coefficient and wear reduction.
Silicon dioxide (SiO_2)[10,12,19,27,30]	10-100	0.5-3%	Improves tribological characteristics due to stability, large surface area, and effective dispersion
Carbon nanotubes (CNTs)[11]	10-50	0.1-5%	Reduces wear by 73% and increases load capacity by 20%
Unstructured carbon, graphite, graphene[13,14]	10-100, 20-100, 1-100	1.0%	Provides optimal friction and wear performance
Halloysite nanotubes (HNT)[15]	30-70	1.5%	Enhances friction and wear properties compared to non-additive oil
Titanium oxide-TiO_2 and Zinc oxide-ZnO[21]	20-50	30ppm	Enhancement in engine performance

Subsequent research reviewed FAME production using numerous kernels, identifying Algae, Castor, Laxmitaru (*Simarouba glauca*) and many more promising sources. The cultivation of Laxmitaru was originated at the National Bureau of Plant Genetic Resources in Orissa, India. Unattended Laxmitaru-FAME (Simarouba glauca Methyl Ester) was tested in a CI engine. Laxmitaru-FAME exhibited lower brake thermal efficiency compared to diesel. Emission analysis revealed significant reductions in HC and smoke emissions (22% and 33% for B50 blend; 40% and 27% for B100) but increased NOx emissions (8% for B100; 5% for B50). Laxmitaru-FAME blends' brake thermal efficiencies were marginally inferior compared to petro-diesel. Assessments showed comparable performance between Laxmitaru-FAME-diesel blends and standard diesel [17]. Research was carried out to explore the potential use of Laxmitaru crude oil in biodiesel production. Simarouba glauca seed oil was identified as a viable feedstock for biodiesel synthesis. When tested, its performance and emission characteristics were found to be favorable compared to conventional diesel, meeting the requirements of ASTM D6751, BIS, and European standards. [18]. Literature reveals that a B-20 Laxmitaru-FAME blend narrowly matches petro-diesel. While the mechanical efficiency of diesel slightly surpasses Laxmitaru-FAME blends, B0 and B20 perform similarly. Laxmitaru-FAME at 20% exhibited slightly superior brake thermal efficiency to petro-diesel. Exhaust emission temperatures for all FAMEs were higher than petro-diesel, with B20

showing lower average variations in CO and HC but higher NOx emissions. Despite this, B20 is deemed the most suitable biodiesel blend, with potential for reducing NOx emissions through advanced technologies. Combustion characteristics of Laxmitaru-FAME B20 blends closely resembled diesel, positioning Laxmitaru-FAME as a viable alternative to conventional diesel. Neat biodiesel, known as B100, is rarely used due to its tendency to clog injectors. More commonly available biodiesel blends include B20 (20% biodiesel, 80% petroleum diesel) and B5 (5% biodiesel, 95% petroleum diesel). B20 is approved for use in heavy-duty diesel trucks, and modern diesel engines like Ford Power Stroke, GM Duramax, and Dodge Cummins can run B20 without voiding warranties. Since 2011, Ford Super Duty trucks even feature a "B20" badge on the Power Stroke fender. B20 has been found to offer optimal engine performance, requiring no engine modifications and showing Brake Thermal Efficiency (BTE) and Brake Specific Fuel Consumption (BSFC) similar to neat diesel (B0)[1,19,20]. Another study investigated the combustion, efficiency, and emissions of a single-cylinder diesel engine using three fuel blends: biodiesel-diesel (B20), biodiesel with chemically and biologically synthesized nanoparticles (B20A30C30), and biodiesel with conventional particles (B100). A homogeneous fuel mixture was created using titanium oxide (TiO_2) and zinc oxide (ZnO) nanoparticles, enhancing combustion due to their high surface area. The engine with nanoparticles (B20A30C30) showed 16% higher brake thermal efficiency, with significant reductions in nitrogen oxides (32%), carbon monoxide (62%), hydrocarbons (48%), and smoke emissions (40%) [21]. Further study used Zinc oxide nanoparticles mixed with Tungsten phosphoric acid (TPA) as a catalyst for biodiesel production from waste cooking oil. An optimal methanol-to-oil ratio of 1:6, at 60-65°C with 4 wt.% catalyst, resulted in a 94% ester conversion. The biodiesel properties largely met ASTM standards, and blends (B10, B20, B100) showed better engine performance and lower carbon emissions compared to diesel [22]. Hence it is evident that B20 is the most suitable blend. Another research investigates friction and wear issues related to Simarouba glauca biodiesel (SGB) in automotive engines using a pin-on-disc tribotester. Different fuels were tested, including SGB100 biodiesel and various blends (SGB15, SGB30, SGB50) under controlled conditions. The results revealed that SGB had the lower coefficient of friction and wear scar, indicating better performance than diesel, along with reduced metal loss. This suggests that Simarouba glauca biodiesel blends can enhance tribological properties compared to conventional diesel fuels. [23]

Rising oil prices, dwindling crude oil reserves, and environmental concerns regarding lubricating oil pollution have underscored the need for alternative lubricants. Biolubricant oils offer eco-friendly alternatives to mineral oils, boasting inherent characteristics such as increased lubricity, higher viscosity index, eminent flash points, along with reduced evaporation. These natural oils can be utilized in both lubrication regimes due to their long fatty acid chains and the presence of polar groups in vegetable oil compositions [16,24]. Thus, wear and friction studies of Laxmitaru-FAME are imperative to assess its suitability in practice. Present study involves investigational study of the friction and wear of petro-diesel, Laxmitaru-FAME and petro-diesel mixtures with nanoparticle additives using a 4-ball tribotester utilizing Silicon dioxide (SiO_2) nanoparticles. From literature survey it is found that SiO_2 nanoparticles are very meagrely employed. Its non-poisonous nature, blandness, pollution-freeness, elemental strength, suspension, large surface area, small dimension, efficient dispersion, low cost, fluidity with good load-viscosity characteristics are the factors of its qualification in this research. Consequently, advances in the nano-additives in order to enhance the utilization array of the lube-oils are required. The intension is also to check the capability of nano SiO_2 to maintain its sole properties at elevated loads as numerous nanomaterials fail to do so. This will broaden the application scope of lubricants using SiO_2 additives [19, 25,27].

2. Materials

The biofuel was extracted from Simarouba glauca oil through transesterification method. In transesterification the chemical reaction with Laxmitaru oil is carried out utilizing alcohol and alcohol-esters as well as glycerol gets generated. The triglyceride gets transformed by sequential removing the alkyl forming a diglyceride, a monoglyceride and in conclusion a glycerol. This intends to enhance flowability of biofuel. In addition, triglycerides gums and waxes are segregated. FAMEs are popular amid the fatty acid esters. Figure 1 demonstrates chemical balance and Figures 3 and 4 reveal the blend variants. The fatty acid contents of Laxmitaru biofuel from gas chromatography reveals that the percentage of Oleic acid is highest.

While ethanol is favored for transesterification because of its environment-friendly characteristics and lower toxicity, methanol is frequently chosen owing to cost-effectiveness with respect to other options. Consequently, FAMEs are more prevalent than Fatty acid alkyl esters (FAAE). Tables 2-4 reveal the important attributes of Laxmitaru-FAME along with mixture details. The diesel fuel was taken from Bharat Petroleum Corporation Ltd Kolhapur Petrol Pump. It had following major attributes: Acidity Inorganic-Nil, Acidity total mg of KOH/g- 0.20, Ash percent by mass -0.01, Carbon residue (Ramsbottom) on 10 percent residue, % mass - 0.30, Cetane Number - 46, Cetane Index - 48, Flash Point-a. Abel, °C 35, b. Pensky Martens, °C- 66 (1), Kinematic Viscosity, cSt at 40° C- 4.9 mm^2/s, Total Contamination, mg / kg-24, Density at 15°C kg/cu.m-822, Total Sulphur, mg/kg, 336, Water Content, mg/kg, 169, Total Sediment, mg per 100 ml- 1.5, Oxygen content, % vol. - 0.5.

The SiO_2 nanoparticles were purchased from Sigma-Aldrich dealer in Kolhapur. According to specifications by supplier, SiO_2 nanoparticles are almost sphere-shaped, normal dimension 20 nm, mass 2.2-2.6 g/cm^3 and 99.5 % pure. The SEM image of SiO_2 nanoparticles is shown in Figure 2. The important physicochemical attributes of FAME of test oil are Density [ASTM D1448]- 0.876 gm/cm^3; HCV [ASTM D6751]- 37.5 MJ/Kg; Kinematic Viscosity [D445]- 5.38 mm^2/s at 40°C; Flash point [ASTM D93]- 138°C [19].

Table 2. The important attributes of mixtures

Mixture	Higher Calorific Value J/Kg	Viscosity mm^2/s	Density gm/cm^3
B-10	39.8×10^6	5.1	0.827
B-20	38.9×10^6	5.23	0.830
B-30	38.5×10^6	5.33	0.838
B-100	37.5×10^6	5.38	0.876
Diesel	45.6×10^6	4.9	0.822

Table 3. The important attributes of mixtures

Sr. No.	Details	Quantity
1.	Neat Petro- diesel:-(B-0)	50 ml
2.	Petro-diesel and 10% biodiesel:(B-10)	
3.	Petro-diesel and 20% biodiesel:(B-20)	
4.	Petro-diesel and 30% biodiesel:(B-30)	

Table 4. The important attributes of mixtures

Sr. No.	Mixture Particulars	Quantity
1.	Neat petro-diesel-(B-0)	01
2.	Neat-petro-diesel + Neat Simarouba glauca Methyl Ester (B-10, B-20 and B-30) variants.	03
3.	Neat petro-diesel + Modified Simarouba glauca Methyl Ester with nano-SiO2 (0.2, 0.5, 0.75 and 1 % Weight) and B-10, B-20 and B-30 variants.	12

3. Methods

3.1 Generation of Additivated Simarouba Glauca Methyl Ester

The dispersion of nano-SiO_2 additives was carried out in Simarouba glauca Methyl Ester with amount of 0.2, 0.5, 0.75 and 1% on weight basis. Ultrasonication was done for 15 minutes by Model-LMUC-3, Make- LABMAN. The dispersion steadiness was ascertained for 7 days. Overall, sixteen variants are made in order for test [19]. Literature suggests that many researchers have used

concentrations in the range of 0.2 to 1% with uniform increments. The optimal concentrations are also found within the same range. Hence the similar range of 0.2, 0.25, 0.75 and 1 wt.% is chosen for present study [4-15, 26].

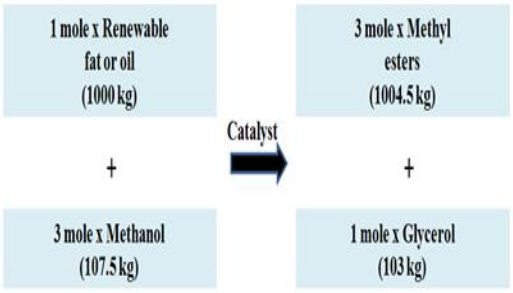

Fig. 1. Chemical reaction for biodiesel production [19]

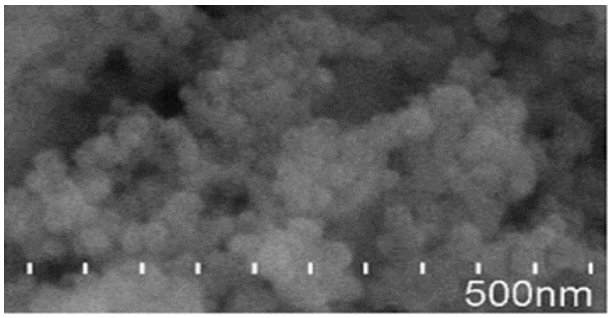

Fig. 2. The SEM image of SiO_2 nanoparticles

3.2 Making of Blends of Laxmitaru-FAME and Additivated Laxmitaru-FAME with Petro-Diesel

Mixtures of Simarouba glauca Methyl Ester and nano additivated Simarouba glauca Methyl Ester in petro-diesel were made taking 10%, 20% and 30% amounts (B10, B20 and B30) by volume. It is known that B20 has manifested better performance characteristics, yet, B30 blend is also investigated in this research [1,18,19]. This is because of the fact that the Simarouba glauca biodiesel is quite novel and literature survey also depicts that very less tribological research has been carried out on the same. Hence its tribological behaviour is still not completely known. Consequently, it was decided to work on B30 blends also as it is possible that Simarouba glauca might give better performance for B30 blend also. In order to ascertain this likelihood experimentation has been carried out on B30 blends also. The higher blends more than 30% have following issues so maximum B30 blends were chosen. They face lack of legal encouragement and pricing. Higher blend has a solvent effect which can dissolve engine deposits. The discharge of these deposits may block filters and necessitate recurrent filter replacement. Also, they contain less energy than petroleum diesel. It also decreases engine life. It thickens at cold temperatures and also has high viscosity in general. Consequently, these exhibit distinctive storage issues, increase nitrogen oxide emissions, although it greatly reduces other toxic emissions.

3.3 Tribological Experiments

Tribological assessments were conducted using a 4-ball-tribometer, with Figure 5 illustrating the specifics about the experimental configuration. The machine and all its important parts are indicated. Prior to each test, all testing equipment underwent thorough cleaning. Neat petro-diesel besides other 15 variants, enumerated in Table 3 and Table 4, got evaluated in the 4-ball-tribometer. Testing procedures adhered to ASTM-D-4172 guidelines. Test balls made of chrome alloy steel AISI standard E52100, with a diameter of 12.7 mm, Grade 25 EP (Extra Polish-0.02-micron Ra), and hardness ranging from 64-66 HRC, were employed. Comparative analysis of test results was conducted. Acetone was employed for washing the steel balls after every experimental iteration. Wear rates were determined based on the mean Wear Scar Diameter measured on the 3 fixed balls. The Figure 6 shows the macro image of the wear scar obtained on one of the sample lower balls. The the SEMs are taken in the same order for all the balls and they all show similar wear. Also Figure 7 shows the three balls fixed inside the cup. Four ball tester kinematic details are depicted in Figure 8. Friction coefficients were continuously monitored throughout every experiment. Assessment parameters for all samples aligned with ASTM-D-4172 specifications, detailed as follows:

- Load during Testing: 392±2N
- Duration of Testing: 3600 seconds
- Rotational Speed: 1200 +/- 60 revolutions per minute
- Temperature-: 75°C +/- 2°C

Fig. 3. Samples of Diesel blends with Simarouba glauca Methyl Ester (B10, B20, B30) [19]

Fig. 4. Simarouba glauca Methyl Ester with SiO_2 nanoparticles samples prepared for experimentation [19]

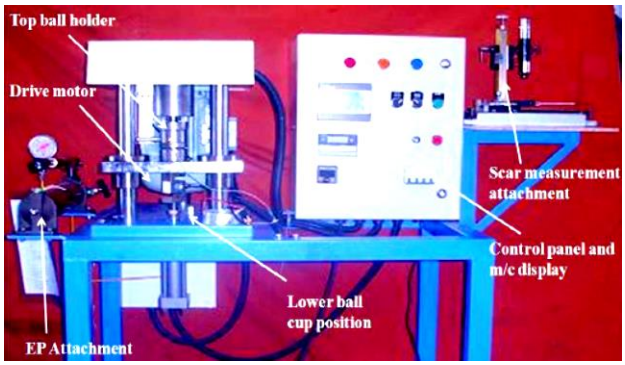

Fig. 5. Experimental Set up: Four Ball Tester (ASTM D4172)

Fig. 6. Macro Image of Wear Scar

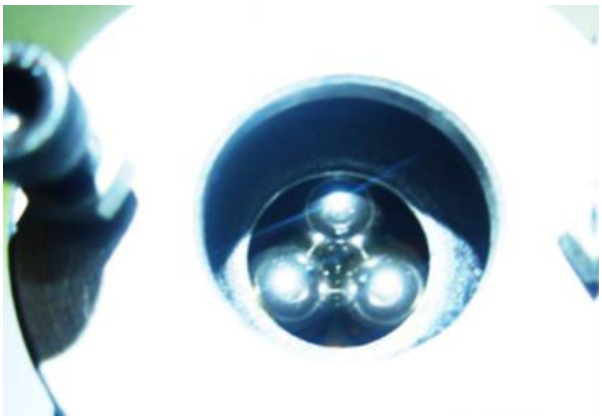

Fig. 7. Balls fixed inside the cup

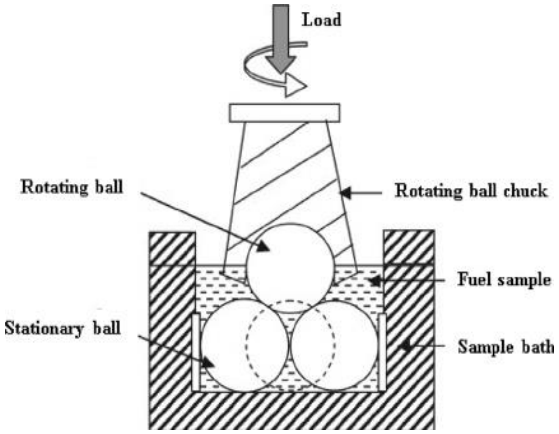

Fig. 8. Four ball tester kinematic details [3]

The Average COF is estimated using a torque meter by the machine. The torque meter measures this resistance to rotation, which is directly related to the frictional force between the balls. Throughout the test, the torque values are recorded at regular intervals. The data acquisition system linked to the 4 Ball Tester processes this data and calculates the instantaneous COF. The average COF is determined by calculating the mean of these recorded COF values over the test duration.

The ball's worn surface is assessed by SEM for particular maximum and minimum wear of balls. This is used further for deciding the mode of wear prevalent then. [19,27,28]. Every experimental test was repeated for three times to minimize possible error in data recorded. The uncertainties in

values of different quantities were estimated. The overall uncertainty level was found to be within ±2%. Similar trends were found in each iteration.

4. Results and Discussion

4.1 Friction Analysis

Following results were observed after experimentation on different sixteen combinations of diesel, Simarouba glauca Methyl Ester and nanoparticles. Figures 9-13 indicate the outcome of the diverse percentage permutation of Diesel, Simarouba glauca Methyl Ester and SiO_2 Nanoparticles with Wt. % of 0.2, 0.5, 0.75, and 1% respectively on COF. The reduction in COF in the presence SiO_2 nanoparticles can be credited towards their ball-bearing effect at interface. There is a combination of polishing and rolling phenomena. Due to asperity polishing bulk COF drops as a result of good surface finish. The sudden changes in the friction graph are observed in Figure 9 (diesel +30% SGME) and Figure 12 (diesel +20% SGME). In Figure 9 this is due to the fact that four ball test has transition between lubrication regimes, such as boundary lubrication to mixed/hydrodynamic lubrication. Changes in these regimes and polishing effect of nanoparticles results in low friction levels. Also, the rise in the friction in Figure 12 may be due to Local surface damage resulting in temperature rise during the test affecting lubricant viscosity and wear rate. As temperature increases, lubricant viscosity decreases, reducing its ability to form a stable film. And transition to boundary lubrication takes place which has led to sudden higher friction [29]

Conversely high amount of nanoparticles caused increase in COF due to local surface damage, which may be due to ill distributed tribo sintering. The Figures 14-17 show the effect of different percentage combination of Diesel, Simarouba glauca Methyl Ester and SiO_2 Nanoparticles with Wt. % of 0.2, 0.5, 0.75, and 1% respectively on average COF. From these the lowest COF is observed for 30% Simarouba glauca Methyl Ester and 0.2 wt.% SiO_2 nanoparticles i.e., 0.0198. This is the combined effect of less agglomeration of nanoparticles and the 30 % of Simarouba glauca Methyl Ester having high viscosity [7,10,13,16,19]. As observed in the Figure 23 for average COF, Blend variants and the nanoparticles % for SiO_2 nanoparticles there is a consistent decrease in the COF as the biodiesel % goes on increasing in the blends. But there is no such characteristic seen for increase in the nanoparticle percentage. 0.2% combination-B30 shows the lowest COF in the family of biodiesel blends. This is attributed to polishing effect of hard SiO_2 nanoparticles. For neat biodiesel B100 – 0.2% combination shows the lowest COF. For B20 blend increase in nanoparticle % shows adverse effect on COF, by increasing its value. It is possibly due to elevated hardness of SiO_2 nanoparticles and their agglomeration tendency leading to the abrasive wear. Also, the similar trend is seen for B100 variant i.e., increase in COF. Increase in COF is observed for 1% SiO_2 nanoparticles with the growing Simarouba glauca Methyl Ester %. i.e., B:30 blend. From the friction plots it is evident that the lubrication regime typically falls within the boundary lubrication and mixed lubrication regions.

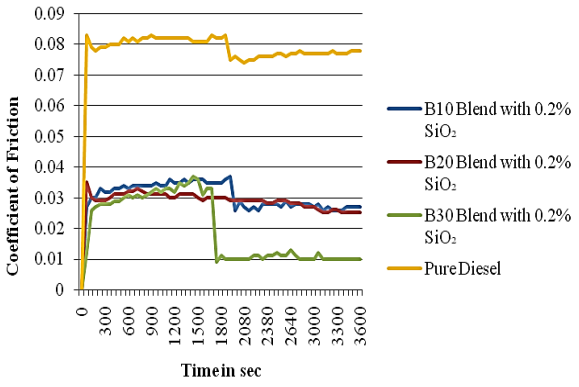

Fig. 9. Influence of 0.2% of SiO_2 nanoparticles in Laxmitaru-FAME in petro-diesel blend on COF

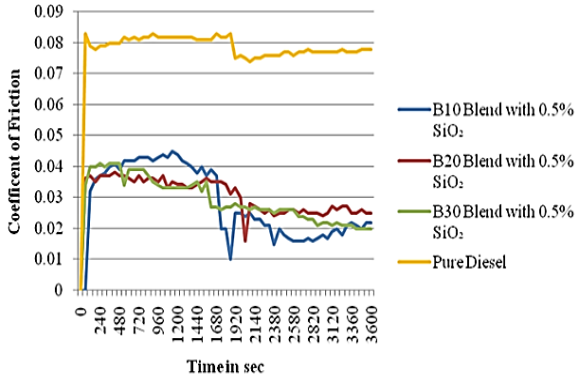

Fig. 10. Influence of 0.5% of SiO_2 nanoparticles in in Laxmitaru-FAME in petro-diesel blend on COF

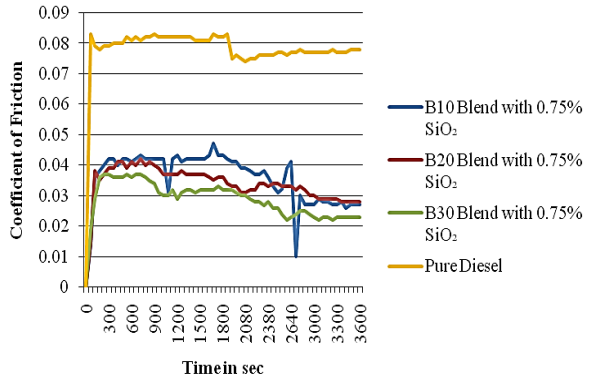

Fig. 11. Influence of 0.75% of SiO_2 nanoparticles in in Laxmitaru-FAME in petro-diesel blends on COF

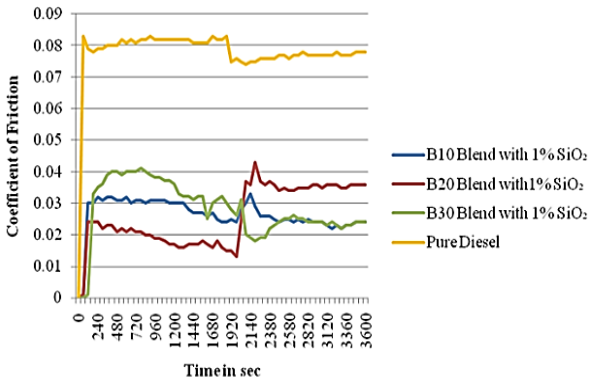

Fig. 12. Influence of 1% of SiO_2 nanoparticles in in Laxmitaru-FAME in petro-diesel blends on COF

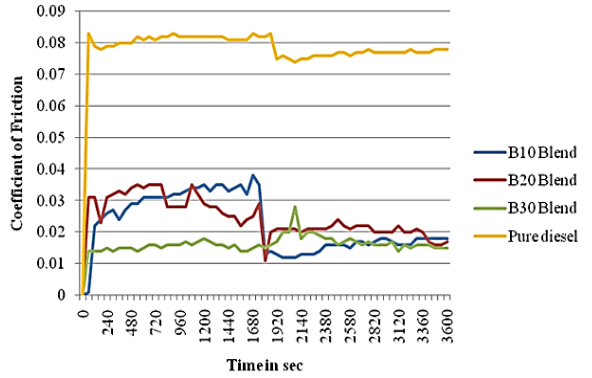

Fig. 13. Influence of % of Simarouba glauca Methyl Ester in blends on friction

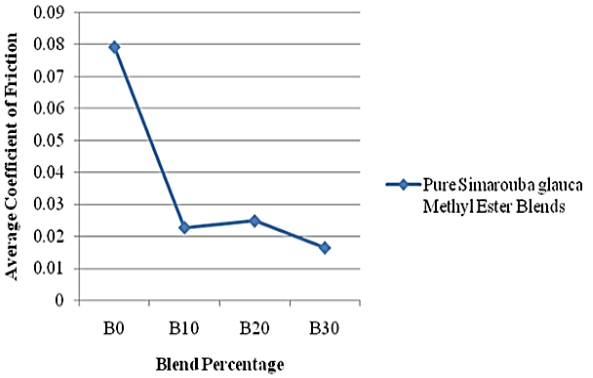

Fig. 14. Influence of % of Simarouba glauca Methyl Ester in blends on average friction

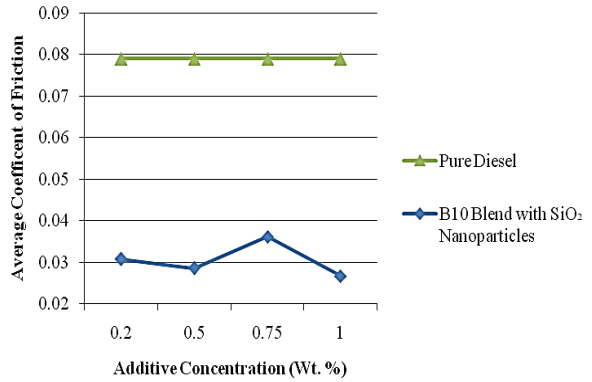

Fig. 15. Influence of % of SiO_2 nanoparticles in Simarouba glauca Methyl Ester for B10 blends on average friction

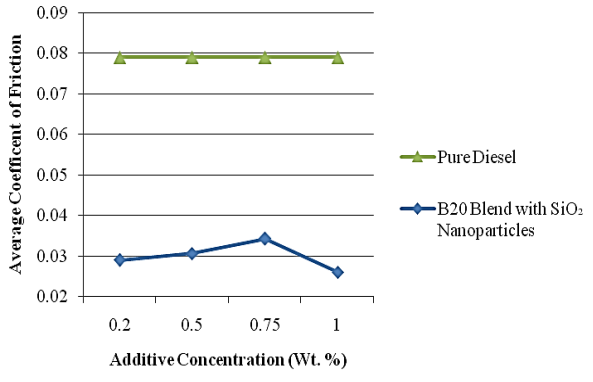

Fig. 16. Influence of % of SiO_2 nanoparticles in Simarouba glauca Methyl Ester for B20 blends on average friction

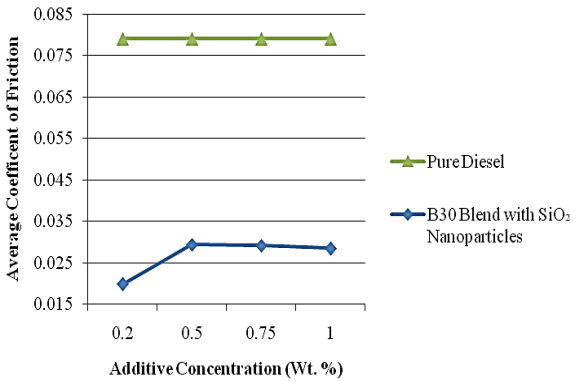

Fig. 17. Influence of % of SiO_2 nanoparticles in Simarouba glauca Methyl Ester for B30 blends on average friction

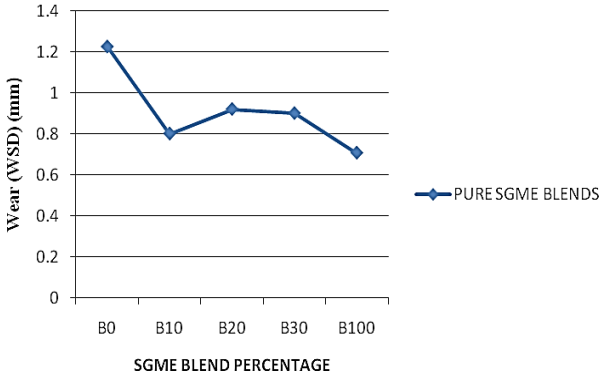

Fig. 18. Influence of % of Simarouba glauca Methyl Ester in blends on wear

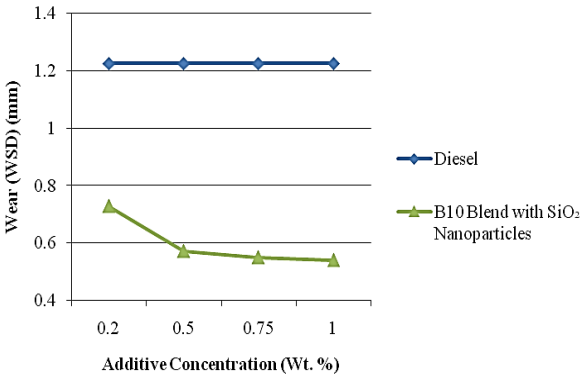

Fig. 19. Influence of % of SiO_2 nanoparticles in Simarouba glauca Methyl Ester for B10 blends on WSD

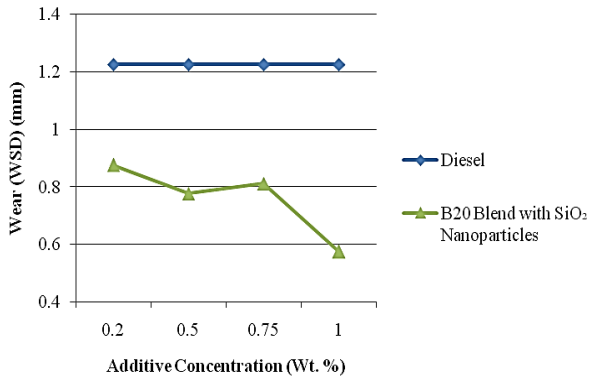

Fig. 20. Influence of % of SiO_2 nanoparticles in Simarouba glauca Methyl Ester for B20 blends on WSD

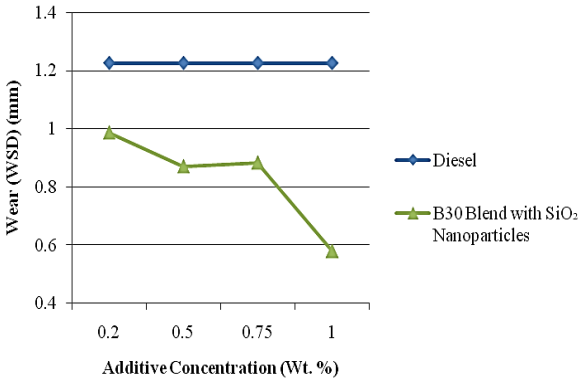

Fig. 21. Influence of % of SiO_2 nanoparticles in Simarouba glauca Methyl Ester for B30 blends on WSD

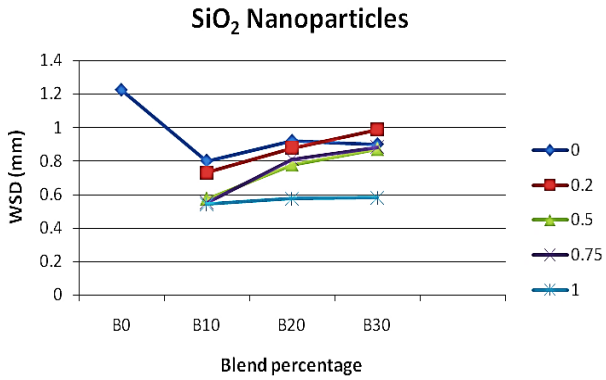

Fig. 22. Influence of % of Simarouba glauca Methyl Ester and SiO_2 nanoparticles in blends on WSD

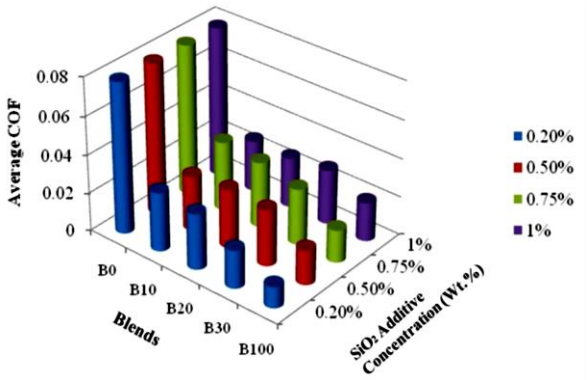

Fig. 23. General summing up of Change in Average COF for all permutations of SiO_2 nanoparticles

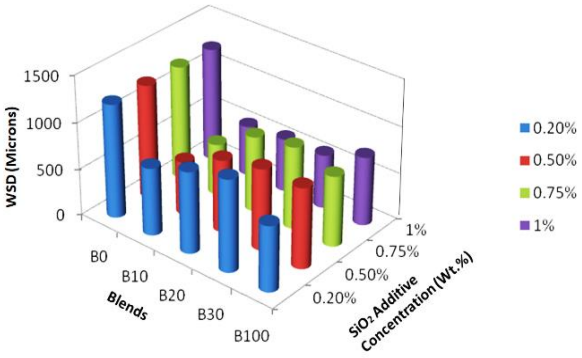

Fig. 24. General summing up of Change in WSD for all permutations of SiO_2 nanoparticles

4.2 Wear Analysis

The change of WSD (Wear Scar Diameter) as per various permutations of SG (Simarouba glauca) oil and nanoparticles as shown in Figures 18-22 and 24 indicate that the rise in the amount of Simarouba glauca Methyl Ester leads to improvement in the results. Also, these charts show that if additive concentration is increased the WSD of blended oil also improves. Additivated samples show combination of abrasive and adhesive wears and mending. As seen in the Figure 22 and 24 for WSD, blend variants and the nanoparticles % for SiO_2 nanoparticles there is a consistent decrease in the WSD as the nanoparticles % goes on increasing in the blends for B10,B20,B30. For neat biodiesel B100-0.20% combination shows the lowest WSD. For B100 increase in nanoparticle % shows adverse effect on WSD, by increasing its value in case of 0.5% of nanoparticles. This may be due to hardness and surface deterioration by SiO_2 nanoparticles. Also, the similar trend is seen for B20and B30 variants i.e., increase in WSD for 0.75% nanoparticle amount. Increment in WSD is seen in entire % of SiO_2 nanoparticles through the increment in biodiesel percentage.

Hard SiO_2 nanoparticles at the interface abrade the surface due to uneven tribo sintering as seen in Figure 25. The surface is rougher. This leads to high wear and results in maximum WSD. Conversely for same SiO_2 wear of steel ball for B10 and 1% wt. SiO_2 nanoparticles blend was observed to be lowest and 55% lower than that for neat diesel (B0) proving its advantage for this percentage. This can be attributed to more even dispersion of nanoparticles at B10 biodiesel giving highly uniform wear [7,13,16,19].

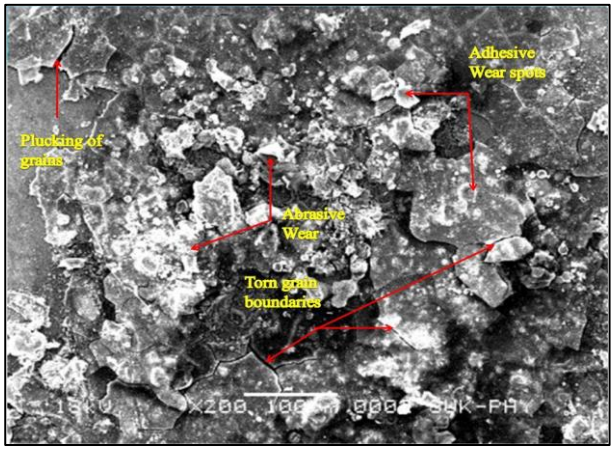

Fig. 25. SEM image showing the wear scar resulting from the use of neat diesel fuel without blending and nanoparticles (Maximum Wear Scar Diameter - 1.226 mm)

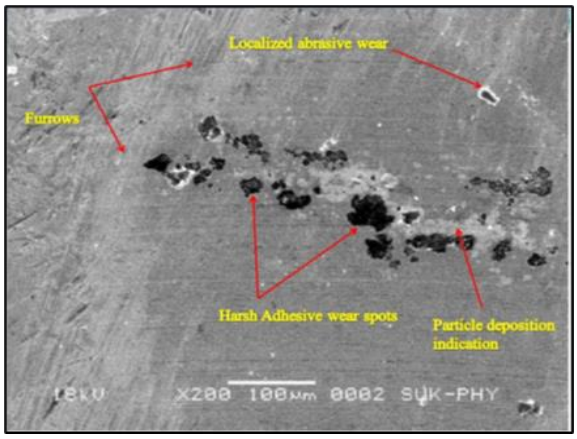

Fig. 26. SEM images displaying the wear scar from a diesel blend containing 30% Simarouba glauca Methyl Ester and 0.2 wt. % SiO_2 nanoparticles (Maximum Wear Scar Diameter - 0.988mm)

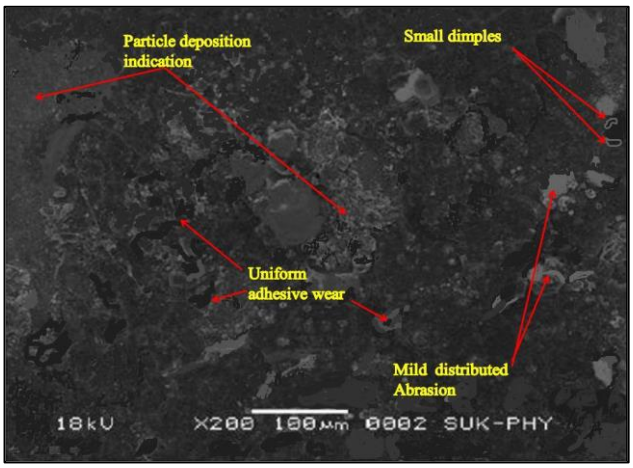

Fig. 27. SEM image depicting the wear scar resulting from a diesel blend containing 10% Simarouba glauca Methyl Ester and 1% by weight of SiO_2 nanoparticles (Minimum Wear Scar Diameter - 0.541 mm)

4.3 Worn Surface Micrographic Analysis

Worn-out surfaces of the balls were characterized using SEM. Figures 25, 26 and 27 show the SEM images of worn-out surface of balls for different bio diesel blends. The micrographs show material fiber fracture. Material fiber typically refers to the alignment or orientation of the material's grain structure or fibers within a material. Minimum WSD is observed for B10 blend having 1 % wt. of SiO_2 nanoparticles. It shows that the SiO_2 nanoparticles have more dispersiveness and load carrying capacity. Micrograph showed by Figure 27 indicates Ra improvement by mending. Figure 25 shows grain boundary crack initiation and propagation. This type of fracture takes place due to creep phenomena in which grains are stronger and grain boundaries are weaker. In such cases crack initiation is delayed but once initiated it propagates faster. This may be due to local temperature rise leading to adhesive and abrasive wear permutation. Very rough surface with grain separations is seen. This may be attributed to local overheating and interface fatigue. The Figure 26 displays micrograph for 30% Simarouba glauca Methyl Ester and 0.2 wt. % SiO_2 nanoparticles. Maximum Wear Scar Diameter of 0.988mm is obtained for this case which is very much unfavorable. Highly heterogeneous wear combination is observed like localized abrasive wear, furrows and harsh adhesive wear. This may be due to instantaneous localized crests due to SiO_2 promoting the localized adhesion. The Figure 27 for nano-SiO_2 additive makes uniformly spread wear all through the grains and grain boundaries in contrast with Figures 25 and 26. This may be credited to the material insertion by nanoparticles. This mending and polishing are seen in Figure 27. This noteworthy enhancement in the anti-wear property of SiO_2 additives is due to highly stable dispersions maintaining nonstop nanoparticles flow for mending on interface.

5. Conclusions

- There is a consistent decrease in the COF as the biodiesel percentage goes on increasing in the blends. But there is no such characteristic seen for increase in the nanoparticle percentage. B30-0.2% combination shows the lowest COF in the family of biodiesel blends. This is attributed to polishing effect of hard SiO_2 nanoparticles. This also enhances surface finish at the interface.
- For neat biodiesel B100 – 0.2% combination shows the lowest COF. For B20 blend increase in nanoparticle % shows adverse effect on COF, by increasing its value. It is possibly due to elevated hardness of SiO_2 nanoparticles and their agglomeration tendency leading to the abrasive wear. This can be overcome by using additional surfactant. Also, appropriate vegetable excerpt will be smart substitute which may perform as a basic agent in addition to coating agent. Also, the similar trend is seen for B100 variant i.e., increase in COF. Increase in COF is observed for 1% SiO_2 nanoparticles with the growing Laxmitaru-FAME %. i.e., B:30 blend.

- There is a consistent decrease in the WSD, as the nanoparticles % goes on increasing in the blends for B10, B20 and B30. For neat biodiesel B100-0.20% combination shows the lowest WSD. For B100 increase in nanoparticle percentage shows adverse effect on WSD, by increasing its value in case of 0.5% of nanoparticles. This may be due to hardness and surface deterioration by SiO_2 nanoparticles. Also, the similar trend is seen for B20and B30 variants i.e., increase in WSD for 0.75% nanoparticle amount. Increment in WSD is seen in entire % of SiO_2 nanoparticles through the increment in biodiesel percentage.
- The results revealed 75 % decrease in COF and 55% reduction in WSD compared to neat diesel (B0).
- Overall, it is perceived that SiO_2 performs meritoriously from friction and wear point of view. It justifies as a low-cost option to mitigate engine friction and wear.

References

[1] Bitire SO, Jen TC. Performance and emission analysis of a CI engine fueled with parsley biodiesel–diesel blend. Materials for Renewable and Sustainable Energy. 2022 Jul 22;11(2):143–53. https://doi.org/10.1007/s40243-022-00213-4

[2] Xu Y, Peng Y, Zheng X, Dearn KD, Xu H, Hu X. Synthesis and tribological studies of nanoparticle additives for pyrolysis bio-oil formulated as a diesel fuel. Energy. 2015 Mar 31;83:80–8. https://doi.org/10.1016/j.energy.2015.01.117

[3] Fazal MA, Haseeb ASMA, Masjuki HH. Investigation of friction and wear characteristics of palm biodiesel. Energy Conversion and Management. 2013 Jan 2;67:251–6. https://doi.org/10.1016/j.enconman.2012.12.002

[4] Chiam HW, Azmi WH, Usri NA, Mamat R, Adam NM. Thermal conductivity and viscosity of Al_2O_3 nanofluids for different based ratio of water and ethylene glycol mixture. Experimental Thermal and Fluid Science . 2016 Sep 19;81:420–9. https://doi.org/10.1016/j.expthermflusci.2016.09.013

[5] Zhao Z, Ma Y, Wan H, Ye Y, Chen L, Zhou H, et al. Preparation and tribological behaviors of polyamide-imide/polytetrafluoroethylene lubricating coatings reinforced by in-situ synthesized CeO_2 nanoparticles. Polymer Testing. 2021 Jan 30;96:107100. https://doi.org/10.1016/j.polymertesting.2021.107100

[6] Sofiah AGN, Samykano M, Shahabuddin S, Pandey AK, Kadirgama K, Said Z, et al. Copper (II) oxide nanoparticles as additives in RBD palm olein: Experimental analysis and mathematical modelling. Journal of Molecular Liquids . 2022 Jul 22;363:119892. https://doi.org/10.1016/j.molliq.2022.119892

[7] Jatti VS, Singh TP. Copper oxide nano-particles as friction-reduction and anti-wear additives in lubricating oil. Journal of Mechanical Science and Technology. 2015 Feb 1;29(2):793–8. https://doi.org/10.1007/s12206-015-0141-y

[8] Kalyani N, Jaiswal V, Rastogi RB, Kumar D. The investigation of different particle size magnesium-doped zinc oxide (Zn0.92Mg0.08O) nanoparticles on the lubrication behavior of paraffin oil. Applied Nanoscience . 2015 Jun 27;7(6):275–81. https://doi.org/10.1007/s13204-015-0471-1

[9] Talib N, Jamaluddin N nor A, Sheng NTK, Kiow NLW, Abdullah H, Ahmad S, et al. Tribological study of activated carbon nanoparticle in nonedible nanofluid for machining application. Evergreen . 2021 Jun 1;8(2):454–60. https://doi.org/10.5109/4480728

[10] Rastogi PM, Kumar R, Kumar N. Effect of SiO_2 nanoparticles on the tribological characteristics of jatropha oil. Materials Today Proceedings. 2020 Oct 20;46:10109–12. https://doi.org/10.1016/j.matpr.2020.09.377

[11] Senatore A, Hong H, D'Urso V, Younes H. Tribological behavior of novel CNTS-Based lubricant grease in Steady-State and fretting sliding conditions. Lubricants. 2021 Oct 29;9(11):107. https://doi.org/10.3390/lubricants9110107

[12] Mande AC, Mandlik SN, Nimbalkar SR. Experimental analysis of tribological properties of lubricating oil using nanoparticle additives. Int J Adv Res Innov Ideas Educ. 2016;2(1):637-45

[13] Cristea G, Radulescu AV, Georgescu C, Radulescu I, Deleanu L. Influence of additive concentration in soybean oil on rheological and tribological behavior. International Conference of Aerospace Sciences (AEROSPATIAL), Bucharest, Romania. INCAS Bull. 2018;10(4):35-43.

[14] Cristea GC, Georgescu C, Dima D, Deleanu L. Influence of graphene as additive in soybean oil. IOP Conference Series Materials Science and Engineering. 2018 Nov 29;444(2):022012. https://doi.org/10.1088/1757-899x/444/2/022012

[15] Suresha B, Hemanth G, Rakesh A, Adarsh KM. Tribological behaviour of pongamia oil as lubricant with and without halloysite nanotubes using four-ball tester. AIP Conference Proceedings . 2019 Jan 1; https://doi.org/10.1063/1.5117954

[16] Kegl T, Kovač Kralj A, Kegl B, Kegl M. Nanomaterials as fuel additives in diesel engines: A review of current state, opportunities, and challenges. Prog Energy Combust Sci. 2021;83
[17] Devan PK, Mahalakshmi NV. Utilization of unattended methyl ester of paradise oil as fuel in diesel engine. Fuel . 2009 May 13;88(10):1828–33. https://doi.org/10.1016/j.fuel.2009.04.025
[18] Jeyalakshmi P. Characterization of Simarouba glauca seed oil biodiesel. Journal of Thermal Analysis and Calorimetry . 2019 Jan 2;136(1):267–80. https://doi.org/10.1007/s10973-018-7985-1
[19] Aitavade EN, Kamate SC. Experimental analysis of tribological properties of simarouba glauca biodiesel with nanoparticles. In: IGI Global eBooks . 2021. p. 1388–402. https://doi.org/10.4018/978-1-7998-8591-7.ch057
[20] The conversion of used cooking oils into biodiesel. *Biofuels International*. 2021. https://biofuels-news.com/news/the-conversion-of-used-cooking-oils-into-biodiesel/
[21] Anish M, Bency P, Jayaprabakar J, Joy N, Jayaprakash V, Susmi SKS, et al. An evaluation of biosynthesized nanoparticles in biodiesel as an enhancement of a VCR diesel engine. Fuel. 2022 Jul 28;328:125299. https://doi.org/10.1016/j.fuel.2022.125299
[22] Jayaraman J, Dawn SS, Appavu P, Mariadhas A, Joy N, Alshgari RA, et al. Production of biodiesel from waste cooking oil utilizing zinc oxide nanoparticles combined with tungsto phosphoric acid as a catalyst and its performance on a CI engine. Fuel. 2022 Aug 4;329:125411. https://doi.org/10.1016/j.fuel.2022.125411
[23] Singh Y, Singh NK, Sharma A, Singla A. Sustainability of chemically modified Simarouba glauca for tribological applications and chemical structure analysis at different loads. Biomass Conversion and Biorefinery . 2022 Dec 23;14(13):14239–49. https://doi.org/10.1007/s13399-022-03682-9
[24] Zhang X, Li C, Zhou Z, Liu B, Zhang Y, Yang M, et al. Vegetable Oil-Based Nanolubricants in Machining: From physicochemical properties to Application. Chinese Journal of Mechanical Engineering . 2023 Jun 30;36(1). https://doi.org/10.1186/s10033-023-00895-5
[25] Şencan AÇ, Şirin Ş, Saraç ENS, Erdoğan B, Koçak MR. Evaluation of machining characteristics of SiO_2 doped vegetable based nanofluids with Taguchi approach in turning of AISI 304 steel. Tribology International . 2023 Nov 23;191:109122. https://doi.org/10.1016/j.triboint.2023.109122
[26] Aitavade EN, Kamate SC. Tribological characterization of Simarouba glauca methyl ester (SGME) using oxide nanoadditives. Journal of the Institution of Engineers (India) Series D. 2022 Jan 31; https://doi.org/10.1007/s40033-021-00305-x
[27] Aitavade EN, Kamate SC. Influence of blend and oxide nanoparticle additive parameters on tribological attributes of Simarouba glauca biodiesel (SGME). Materials Today Proceedings. 2021 Jan 1;44:2147–52. https://doi.org/10.1016/j.matpr.2020.12.277
[28] Aitavade E, Kamate S. Experimental Investigation of Tribological Characteristics of Blends of SGME Modified with Copper Oxide Nanoadditivation. Trends in Sciences. 2022 Mar 3;19(6):3047. https://doi.org/10.48048/tis.2022.3047
[29] Akchurin A, Bosman R, Lugt PM, Van Drogen M. On a Model for the Prediction of the Friction Coefficient in Mixed Lubrication Based on a Load-Sharing Concept with Measured Surface Roughness. Tribology Letters . 2015 May 30;59(1). https://doi.org/10.1007/s11249-015-0536-z
[30] Adzmi MA, Abdullah A, Naqiuddin A. Combustion characteristics of biodiesel blended with Al_2O_3 and SiO_2 nanoparticles. In AIP Conference Proceedings 2019 Jan 11 (Vol. 2059, No. 1). AIP Publishing. https://doi.org/10.1063/1.5085995

Blank Page

Research on Engineering Structures & Materials
www.jresm.org
Research Group

Research Article

Studies on durability, thermal and morphological property with partial replacement of single use waste plastic and complete recycled aggregate in eco-friendly self-compacting concrete

Suvidha [1,a], Sumesh Jain [1,b], C. Arvind Kumar [*,2,c]

[1]*Department of Civil Engineering, Om Sterling global University, Hisar, Haryana, India*
[2]*Department of Civil Engineering, Matrusri Engineering College, Hyderabad, Telangana, India*

Article Info

Article history:

Received 09 June 2024
Accepted 17 Oct 2024

Keywords:

Self compacting concrete;
High density polyethylene;
Polypropylene;
Durability;
Scanned electron microscope;
Fourier transform infrared spectroscopy

Abstract

This study focuses on creating an eco-friendly self-compacting concrete (EF-SCC) by recycling waste materials like plastic and construction debris. The researchers collected High-Density Polyethylene (HDPE) and Polypropylene (PP) plastics, cleaned and shredded them, then used them to partially replace fine sand at different levels, from 5% up to 20%. They also replaced all the traditional coarse rock aggregate with recycled materials from construction waste. The concrete's flow and ease of pouring (workability) were tested, and it was found that mixes with recycled aggregates flowed faster, with the best result being a 6-second flow time when using 10% HDPE. Durability tests were done by exposing the concrete to acid and sulphate attacks over several weeks, showing that the recycled concrete with plastics held up well, with only minor weight loss after 56 days in acid. Thermal tests showed that adding plastic lowered the concrete's heat conductivity by 30-35%, making it better at insulating. Microscopic analysis showed that the plastic was well integrated with the cement mixture, and chemical tests confirmed there were no harmful reactions between the plastic and the cement. Overall, the study suggests that EF-SCC made with recycled aggregates and plastic waste can keep key properties needed for construction, making it a promising, sustainable building material.

© 2025 MIM Research Group. All rights reserved.

1. Introduction

India is the only country after the USA and European Union to produce the world's largest polymers, and it even creates waste plastic, according to the National Circular Economy Roadmap (NCER). India alone produces 3,500,000 metric tons of waste plastic, of which only 30% is recycled according to The Economics Times India 2023. Therefore, waste plastic generation in India can be utilized in the preparation of concrete with partial replacement of Fine Aggregate (FA) [3, 9 and 42], Coarse Aggregate (CA) [36], or Cement (C) which protects from depleting natural resources and protect the environment.

Substantial work is carried out on ordinary concrete, with the replacement of plastic waste [8], High Density Polyethylene (HDPE) [9], Polyethylene Terephthalate (PET) [10-18], E-Plastic [26], polypropylene (PP) [19-24], and Poly Vinyl Chloride (PVC) [25]. The waste plastic was also used as a replacement for cementitious materials [22], as FA [10-13, 15, 17, 18], and CA [14, 21, 23] as plastic fibers in concrete [24]. Most researchers have worked on partial replacement of FA/CA from 0% to 100%. Among the waste plastic used worldwide, PP and PET are widely recommended to be used as CA in concrete. Most of the

*Corresponding author: arvind.cholker@matrusri.edu.in
[a]orcid.org/0009-0009-5993-9948; [b]orcid.org/0009-0009-3818-3977; [c] orcid.org/0000-0003-3980-9088
DOI: http://dx.doi.org/10.17515/resm2024.315ma0609rs

work is carried out on the fresh properties (workability), hardened properties (mechanical properties), durability properties (Acid attack, sulfate attack, RCPT), and thermal properties (temperature variation, thermal conductivity) of concrete. The slump value (workability) of concrete was increased by being replaced partially by PP and PET as plastic waste conventional concrete [10, 14, 21]. The FA, the PET material can improve the workability property, i.e., slump cone test in concrete; this is because the plastic material has low workability and is frictionless [10-11]. It was found that waste plastic (PET), which is round and smooth in shape when replaced with FA in concrete, helps to improve the workability property of ordinary concrete [14]. The partially replacing PP with brick and stone CA, they found that the slump value (workability) of concrete was increased with the percentage increase in PP content regardless of water/cement (W/C) ratios [21].

Nevertheless, an opposite study was observed when PET was partially replaced with concrete. Its workability decreased with PET material increase [13, 15, 18, and 28]. The same material (PET) was used when its rheology was changed; the workability was reduced [13]. When PET was replaced by 20% with FA, it was observed that its workability, and slump value, were reduced by 25% [15]. The slump value (workability) of concrete with PET material in concrete was decreased because of its irregular shape and size. The use of PET material to replace FA in concrete observed the same pattern of reduction in workability because of the surface area of PET material [18 and 28]. The plastics used to replace FA or CA have a more specific gravity (SG) when compared with virgin plastic. Nevertheless, the waste plastics SG is lower than the natural fine and coarse aggregates [14 and 21]. Consequently, plastic waste has negligible weight compared to conventional material and, when replaced with concrete, can reduce the weight on soil strata [14 and 21]. The replacement of PET FA with brick aggregate found that 10% replacement reduced concrete density by 50%. The heat treatment to PET materials, and when replaced in concrete with FA, a linear reduction in the density was observed [14 and 29]. With a maximum percentage of 15%, the dead weight was reduced by 5.6%. It was also found a linear reduction in density when replaced with PP in concrete. The optimum reduction percentage of 7.4% and 8.4% was observed with a 30% replacement of PP waste plastic with brick and stone aggregate in concrete [21]. The waste plastic material utilized to prepare self-compacting concrete to consider was lightweight concrete [40-41]

Some of the researchers on the replacement of Waste Foundry Sand (WFS) with fine aggregate showed interesting facts and figures for M60 grade SCC. The replacement can be till 30% without any changes in the virgin properties of SCC. The waste generated from the foundry is considered one of the meaningful utilization techniques. It was even observed that treated WFS can reduce the density of concrete and make SCC a lightweight, sustainable, and green material [43]. The usage of waste PET plastic as fiber with the substitute of fine aggregate showed that the entire replacements (0.25, 0.5, 0.75, 1.0, and 1.25) % showed a decrement in compressive strength after 28 days of curing [44]. He also observed that the coefficient of correlation between the porosity and compressive strength is inversely weak relation. The use of fly ash with PET bottles to ameliorate the flexural and compressive strength of SCC was analyzed by [6, 34, 35, and 45]. The test results showed that the increase of PET fibers decreased the flowability of SCC. It was observed that fly ash with PET fiber reduced in its compressive strength but increased its flexural properties.

When replaced with FA or CA in concrete, the above waste plastic materials have many advantages and must be cross verified using statistical tools. The Response Surface Methodology (RSM) is a specific approach within the broader Design of Experiments (DOE) framework, used to model and analyze the effects of multiple factors on responses with fewer experiments. This method is usually applied in concrete technology (CT) to predict the mix proportions and the strength properties of various grades of concrete [2, 27-29].

With the increasing demand in infrastructure and construction industries and models with solid/perfect performance, ANN [32-33] and RSM increasingly handle various civil engineering projects, primarily in material science engineering. ANN has been widely used in many engineering disciplines to counter the drawbacks of empirical formulas and approaches to assess or predict the model with non-linear multivariate interrelationships between concrete's mechanical properties [30].

The present study aims to evaluate the workability, durability, thermal and morphological properties of Eco Friendly –Self Compacting Concrete (EF-SCC) with partial (5%, 10%, 15%, and 20%) replacement of HDPE and PP material and complete replacement of recycled coarse aggregate (RCA).

2. Materials and Methods

The concrete mix in this study used 43-grade Ordinary Portland Cement, following the IS 8112:1989 standard. Fine sand from river sources was used as the fine aggregate and was screened through a 4.75 mm sieve to meet the IS 2386 (Part-1):1963 specifications. To improve the concrete's performance and keep it workable for longer, a superplasticizer called Conplast was added. This additive makes the concrete easier to pour without needing vibration, and it's both chloride-free and low in alkali, helping ensure a durable and high-quality mix.

Table 1. Physical Properties

Properties	Cement	Fine Aggregate (FA)	Coarse Aggregate (CA)	Recycled Aggregate (RA)	HDPE	PP
Specific gravity	3.15	2.61	2.75	2.45	0.864	1.225
Water absorption (%)	12%	2.64	0.85	0.92	0.38	0.27
Fineness modulus	-	2.45	8.35	6.25	3.12	5.36
Maximum particle size (mm)	50 µm	4.75	20	20	3.75	27.50
Density	1.44 g/cm^3	2400-2900 kg/m^3	1200-1450 kg/m^3	1750 kg/m^3	0.90-0.94 g/cm^3	0.90 to 0.91 g/cm^3

In this study, local High-Density Polyethylene (HDPE) and Polypropylene (PP) were chosen for their similar strength profiles. HDPE has a tensile strength ranging from 31.37 MPa to 42 MPa, while PP falls between 27.5 MPa and 39.9 MPa. Their flexural strengths differ more, with HDPE ranging from 10 to 50 MPa and PP from 10 to 20 MPa, making both suitable for enhancing the strength properties of concrete. The recycled aggregates were collected from broken concrete test cubes; they were soaked in water for 24 hours to help remove the old cement paste, then thoroughly dried in either sunlight or an oven. Full details of their physical characteristics are listed in Table 1.

Table 2. M40 grade Eco-Friendly Self-Compacting Concrete (EF-SCC) mix proportion

Nomenclature	W/C=0.40					
	Cement (kg/m3)	CA (kg/m3)	FA (kg/m3)	100% RA (Kg)	HDPE	PP
HDPE5	273.5	776.52	60.52	776.52	3.21	-
HDPE10			54.10		6.42	-
HDPE15			44.47		9.63	-
HDPE20			31.63		12.84	-
PP5			60.52			3.21
PP10			54.10			6.42
PP15			44.47			9.63
PP20			31.63			12.84

2.1 Methods

To understand how HDPE and PP perform in concrete, various tests were done to measure their physical properties, which are shown in Table 1. Concrete mixes were made with a water-to-cement ratio of 0.40, designed for M40 grade Eco-Friendly Self-Compacting Concrete (EF-SCC) according to the standards in IS 456:2000 and IS 10262:2019 (mix details are in Table 2). The testing included a V-funnel test for workability, acid and sulfate resistance tests at 28, 56, and 90 days (using 100x100x100 mm samples), a thermal conductivity test on samples sized 180 mm in diameter and 20 mm thick, and detailed analyses with Scanning Electron Microscopy (SEM) and Fourier Transform Infrared Spectroscopy (FTIR) to study the concrete's structure and composition.

3. Results and Discussion

The current article focuses on the use of recycled coarse aggregate and waste plastic in the construction sector to improve the study of the long-term characteristics of EF-SCC. The greatest amount of plastic trash should be used in the development of various infrastructure projects to reduce the increase of plastic garbage at dumping yards, therefore protecting the environment. Similarly, recycled aggregate from building and demolition debris will be considered best practice in the construction business.

3.1 Workability

The workability test was performed on freshly mixed concrete of various compositions to know the flowability of the concrete (EFNARC) 2002). The findings show whether concrete workable is if it's a self-compacting concrete compacted with the help of its self-weight. The below results are taken when 100% replacement of RCA was used instead of natural coarse aggregate with various percentage replacements of HDPE and PP.

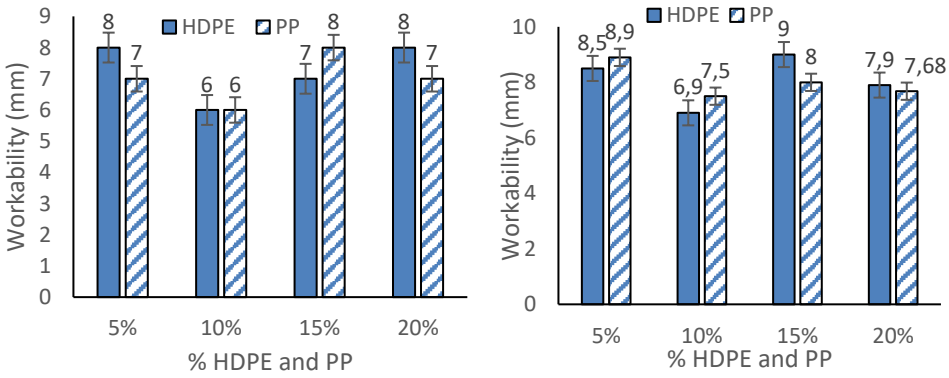

(a) (b)

Fig. 1. V funnel test (a) 100% Recycled Aggregate (RA) (b) 100% Natural Aggregate (NA)

3.1.2 V-Funnel test

The V-funnel test is used to check how easily the concrete can flow and fill spaces, especially for concrete with aggregate sizes up to 20 mm, based on EFNARC 2002 standards. In this test, 12 liters of concrete are poured into a V-shaped funnel. When the lid is opened, the time it takes for all the concrete to flow out is measured, giving an indication of its flowability. It is observed that the RA took less time to empty the funnel than the NA. The RA with 10% of HDPE and PP both recorded 6secs to empty the funnel, whereas RA with the same percentage showed 6.9secs and 7.5secs respectively as shown in Fig 1. The RA showed with 5% HDPE showed 8secs but as the percentage of HDPE was increased to 10% it was reduced by 2secs. The optimum percentage of HDPE with RA is 10% and it is the same case with PP also. This was the same case with measuring the workability of SCC to find the errors with different materials [22-23]

With NA in EF-SCC, the HDPE material at all the percentage replacements showed better results when compared with PP as shown in Fig 1b. The last time recorded was 10% of HDPE followed by 7.9secs, 8.5secs & 9secs at 20%, 5%, and 15% partial replacement respectively. When PP material was partially replaced with FA in EF-SCC it showed a slight increase in time when compared with HDPE. The optimum percentage of PP materials was the same as that of HDPE i.e., 10% of FA. The time recorded at various percentages of PP material in EF-SCC is 8.9secs, 7.5secs, 8secs, 7.6secs at 5%, 10%, 15% & 20% partial replacement respectively. The same pattern of even recorded by other authors to find the mixed proportion of EF-SCC [22-24]

3.2 Durability

3.2.1 Acid Attack

The acid attack was performed on both RA and NA with different percentages of waste plastic. The test is conducted according to ASTM C, 262-2001 for EF-SCC with NA/HDPE-PP & RA/HDPE-PP. The percentage of weight loss increased with an increase in days. It was observed that the NA showed less loss in weight because of its alkalinity present [46] in it as shown in fig 2. The pattern for both RA and NA was the same at all ages with both HDPE and PP material.

The maximum weight loss was observed by RA with HDPE at 56 days i.e., 5.4%. Similarly, with NA the maximum weight was with the same material i.e., HDPE at 56 days i.e., 5.1%.

The weight loss is nearly less those 5% after 28 days of acid attack in both RA and NA with both HDPE and PP material. This weight loss is negligible and can be considered to be utilized in the construction industry.

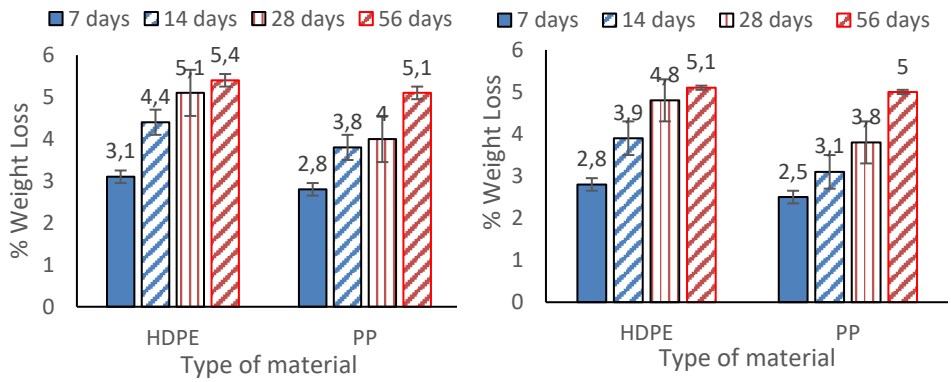

(a) (b)

Fig. 2. Acid attack (a) RA and (b) NA

3.2.2 Sulphate Attack

A sulfate attack test, as per ASTM C 1012-2012, was performed on concrete with HDPE and PP. In M40 EF-SCC mixes, both materials exhibited low weight loss at 28 days. For PP, weight loss continued to decrease until day 28, but both HDPE and PP showed a slight increase by day 56, regardless of using recycled or natural aggregates (see Fig 3). The greatest weight loss occurred at 7 days, reaching 9.1% for HDPE and 8.7% for PP. Across all testing periods, weight loss for both materials stayed under 10%.

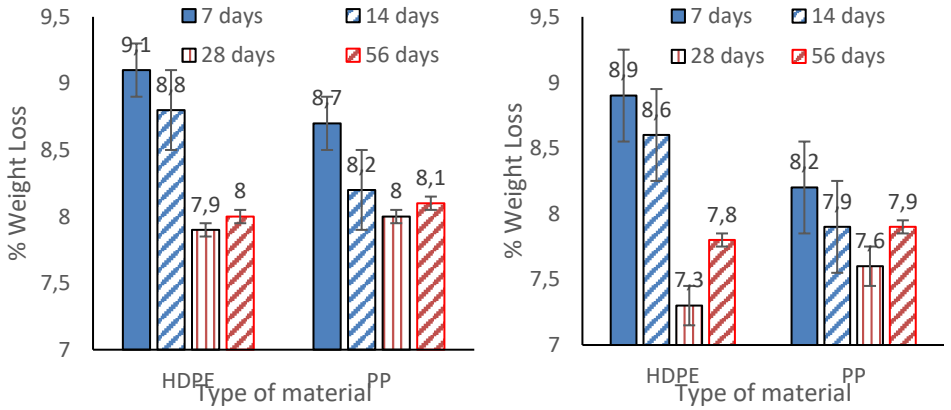

(a) (b)

Fig. 3. Sulphate attack (a) recycled aggregate and (b) natural aggregate

The sulfate attack test showed an opposite pattern of the graph when compared with the acid attack. This is because the EF-SCC is placed in sulphuric acid which dissolves all the carbonated & hydroxides ($Ca(OH)_2$, $CaO•SiO_2•nH_2O$) present in cement paste which causes strength and weight loss.

3.3 Thermal Conductivity

Thermal conductivity testing was done on all samples according to IS 3346:1980. Each sample was sized at 180 mm in diameter and 20 mm in thickness to allow heat to pass in only one direction. To ensure accuracy, two samples were prepared and tested for each mix, so heat flowed exclusively through the specimens. The thermal conductivity (k) was then determined using a specific calculation method.

$$K = \frac{Q}{2A}\left(\frac{L}{Th-Tc}\right) \quad (1)$$

Where K= Thermal Conductivity in W/m.K; Q= amount of heat transferred through the material in Joules/second or Watts; A= is the area of the surface in square meters; Th-Tc= difference in temperature in Kelvin.

The thermal conductivity (K) was less than 1 w/mk for all the specimens after 7days of curing in both HDPE and PP material with complete RA in EF-SCC. As the percentage of waste plastic was increased from 5% to 20% the K value was linearly reduced. This is the main purpose of HDPE and PP material to improve the thermal properties of building envelopes. If HDPE and PP material is used in the construction of houses, it can regulate the heat flow and can control the room temperature. The least K value is 0.69 w/mk at 7 days for HDPE material. The value of K increased after 7 days of curing till 14 days and then it slowly reduced till 28 days of curing as shown in Fig 4. The value of K after 28 days of curing is most important to analyze the heat flow in buildings as it achieves full strength. It was observed that PP material (0.71 w/mk) showed optimum reduction in the value of K when compared with HDPE (0.76 w/mk) at 20% partial replacement. When NA was used with HDPE and PP material it was observed that the thermal conductivity K was more than 1 w/mk for 5% of both HDPE and PP material at all ages. The maximum value of K was observed in 5% of HDPE material at 14days of curing. There was a drastic reduction in K value at 14 days of testing for more than 5% of HDPE material as shown in Fig 5. The lowest value of K was recorded after 28 days of curing with 20% of PP material i.e., 0.8 w/mk. The PP material showed better thermal conductivity than HDPE material at all ages. At 7 days only for 5% the HDPE material showed 1.3 w/mk whereas PP material showed 0.89 w/mk.

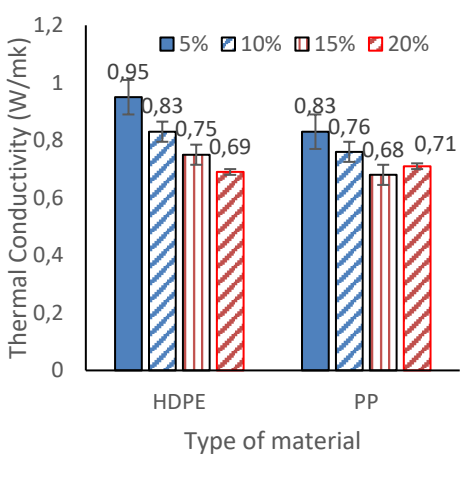

(a)

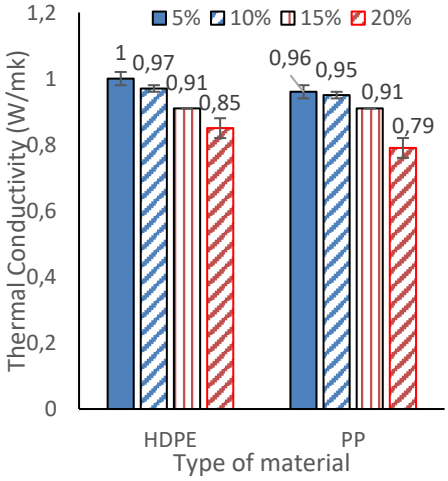

(b)

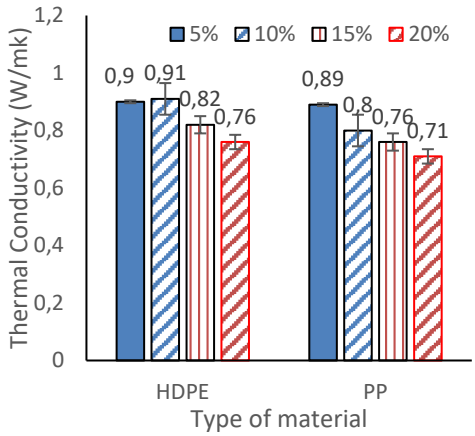

(c)

Fig. 4. Thermal conductivity with RA in EF-SCC for a) 7days b) 14days c) 28days

The least value of K in both the material was 0.74 w/mk and 0.79 w/mk as shown in fig 5. At 14 days only HDPE material showed **a** drastic reduction in K value when compared with PP material. At 28 days the linear relation to that of RA pattern was observed in NA material also. It is recommended to use the RA with HDPE and PP material to improve the thermal performance of buildings**.** A correlation between all the percentages of HDPE and PP for NCA sing excel sheet is given in Table 3. It was observed that at 7 days the correlation is 0.935 which is in good relation for both the materials but as the days of curing increased the correlation has reduced by 36% to 0.57 and then increased to 0.952, because initially in starting days of curing the cements heat of hydration is rapid and them it slowly reduces. When RCA was used in concrete and it was tested for thermal conductivity, it was observed that the correlation at 7 days and 14 days was 0.918 and 0.948 respectively, but the relation was reduced to 0.845 at 28days. This can be because of the RCA material in concrete which consist of cement paste around the material of RCA.

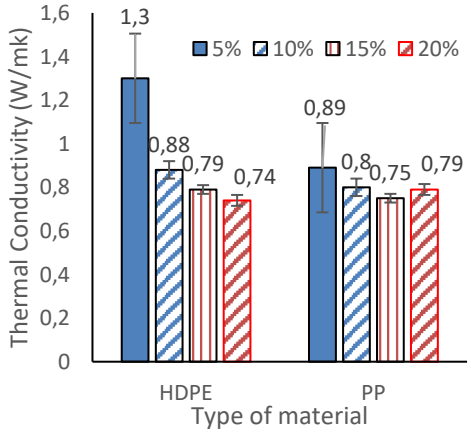

(a)

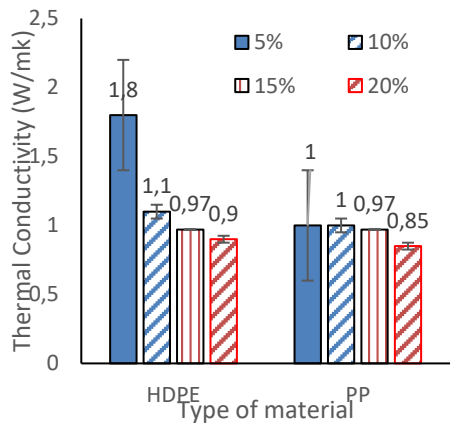

(b)

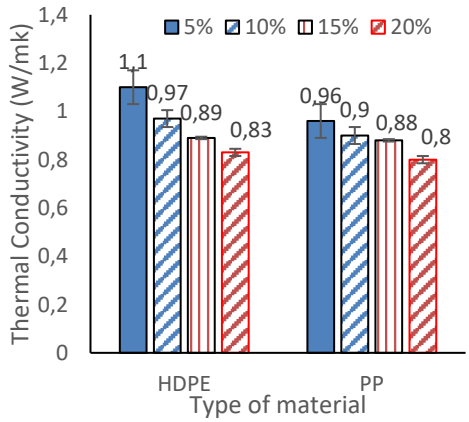

(c)

Fig. 5. Thermal conductivity of NA in EF-SCC for a) 7days b) 14 days c) 28days

Table 3. Correlation between HDPE and PP material

Days / Material	7	14	28
	Natural Coarse Aggregate (NCA)		
HDPE PP	0.9352	0.575	0.9528
	Recycled Coarse Aggregate (RCA)		
HDPE PP	0.918	0.948	0.845

3.3 Morphological Analyses

The Fig 6 displayed below is from an examination of the wetting and spreading coefficient, which suffers from numerous unknown and many causes. Primarily the surface tension and interfacial tension lead to many errors if the temperature variation is not so accurate, secondly, the temperature with high melting points degrades the polymers & nanoparticles changing their surface properties, and even in high viscous polymers it has different crystallization and melting temperatures. Therefore, it is most important to analyze the morphological properties of HDPE and PP material and to interpretation of this material characterization.

The SEM images show the dispersion of HDPE and PP materials in M40 grade SCC. The majority of PP materials form in spherical droplets with an average radius of 4.3 +/- 1mm which is suspended as a matrix of polyolefin. Closer magnification of HDPE and PP revealed that it looks like a continuous microstructure. It is observed that it has two phases which are recognized by the different textures of fractured surfaces, as the HDPE material is more ductile and exhibits a corrugated texture because of localized yielding, similarly, PP material is very fragile and has a smooth surface and it is also visible in its appearance. Differentiating between both PP and HDPE material allows noticing droplets of PET which are embedded in the PP phase. It is also observed that the surface energy of PET when

processing of high reactivity of ester linkage [26]. Future the morphological study observed that the HDPE and PP are in good agreement with the EF-SCC.

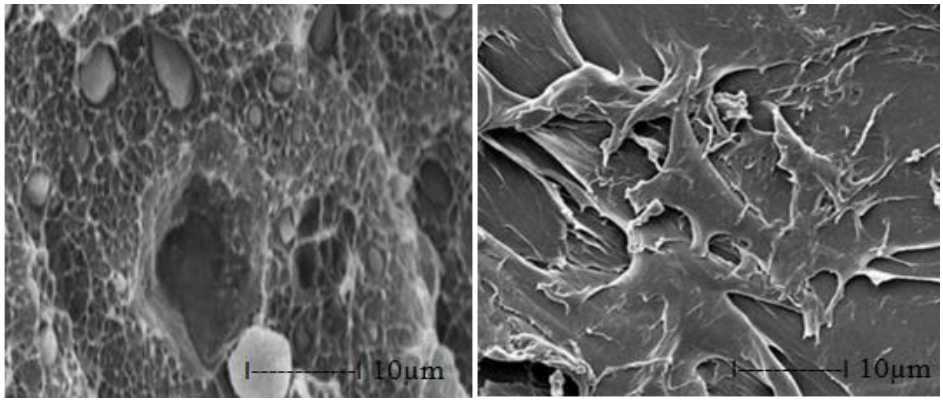

Fig. 6. SEM images (7.5% replacement) of a) HDPE b) PP. (The scan is 10µm)

3.4 Fourier-Transform Infrared Spectroscopy (FTIR)

FTIR analysis was carried out on all mixes with the highest amounts of HDPE and PP, following ASTM E168 and ASTM E1252 standards. This analysis helps identify significant chemical bonds in the materials. In the conventional concrete samples, a broad peak at 3445 cm^{-1} was detected, suggesting the presence of water bonds. There were also weaker peaks at 777.86 cm^{-1} and 693.43 cm^{-1}, indicating bending vibrations associated with the C-O bond.

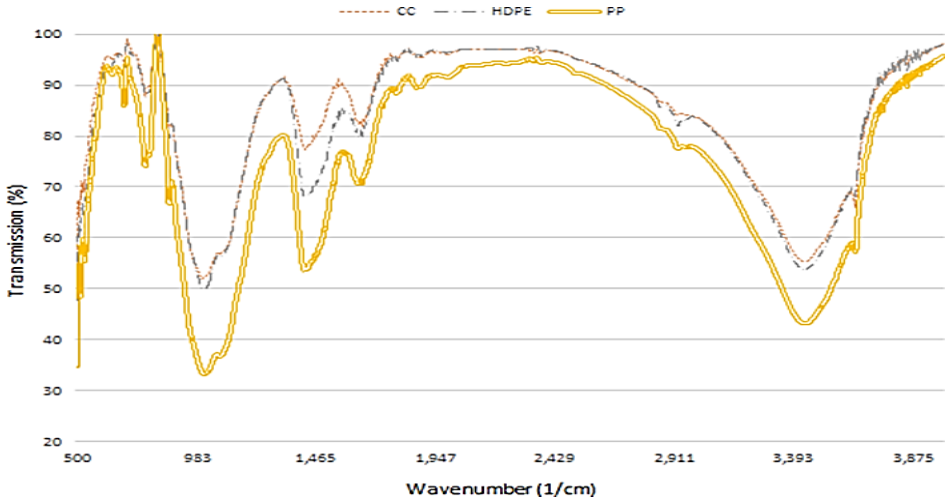

Fig. 7. FTIR analysis of conventional concrete, HDPE, and PP material

The broad peak at 1000 cm^{-1} indicates stretching of the Si-O-Si bond. In the HS24 sample, Si-H stretching is observed at 526.58 cm^{-1}, corresponding to the CO2 transmittance spectrum. A peak at 1016.04 cm^{-1} confirms the presence of the Si-O-Si bond, while the alkaline groups CH2 and CH3 are noted at 1427.19 cm^{-1}. The C=C stretching in aromatic groups appears at 1641.02 cm^{-1}, and a peak at 3443.94 cm^{-1} indicates the presence of OH and Si-OH bonds. Additionally, multiple stretching vibrations of OH can be seen at 3854.49 cm^{-1}. These same trends were also observed in the cement mixed with HDPE.

A new absorption bond is not noticed for cement mortar with HDPE and PP, which indicates that partial replacement of waste plastic does not alter the chemical bond of cement mortar significantly. Whereas a weak bond of OCH3 was noticed at 534.5 & 515.7 respectively. The above results state that the reduction in strength and heat evolution in concrete is due to the interaction between sand and cement interface or chemical effects or due to the mechanical properties but not due to the alternate reaction of waste plastic with cement or sand Phases.

4. Conclusion

The above materials HDPE and PP for different mechanical, durability, and thermal properties were evaluated.

- The workability of the EF-SCC is good compared to conventional concrete. When recycled coarse aggregate (RCA) was completely replaced with natural coarse aggregate (NCA) its workability in V funnel test slightly less.
- Both the materials HDPE and PP took 6sec to empty the v funnel with RCA in concrete which is the lowest of all the mixes. With NCA the difference with HDPE and PP material was approximately 0.4secs in each mix.
- The percentage weight loss when measured for concrete cubes of EF-SCC in acid attack, showed continues increase in its weight loss at all ages for both RCA and NCA.
- The sulphate attack test for RCA material with both HDPE and PP material showed same pattern. The difference in percentage weight loss at different ages was continuously decreasing till 28 days but at 56 days the percentage weight loss was again increased. The same pattern was even observed with NCA, but as much as RCA.
- The acid attack was observed less in PP compared to HDPE but as for sulphate attack the PP material has more impact.
- As the curing days increased to 28days the K value was less for PP material rather than HDPE material i.e., 0.71w/mk. But for NA concrete K value at 28 days is 1.1. Thermal conductivity observed at 14 days of curing is good at 100% RA concrete as well as 100% NA concrete.
- As the above results show the 100% RA can be used in EF-SCC which gives approximate equal values to NA in EF-SCC.
- The SEM images of the morphological study observed that the HDPE and PP are in good agreement with the EF-SCC.
- The FTIR results state that the reduction in strength and heat evolution in concrete is due to the interaction between sand and cement interface or chemical effects or due to the mechanical properties but not due to the alternate reaction of waste plastic with cement or sand Phases.

5. Further Studies

It is recommended to conduct microstructural properties, different thermal properties, and use of different waste plastics in different types, and different grades of concrete.

References

[1] Ghaly AM, Gill MS. Compression and deformation performance of concrete containing post-consumer plastics. J Mater Civ Eng. 2004;16(4):289-96. https://doi.org/10.1061/(ASCE)0899-1561(2004)16:4(289)

[2] Naik TR, Singh SS, Huber CO, Brodersen BS. Use of post-consumer waste plastics in cement-based composites. Cem Concr Res. 1996;26(10):1489-92. https://doi.org/10.1016/0008-8846(96)00135-4
[3] Choi YW, Moon DJ, Kim YJ, Lachemi M. Characteristics of mortar and concrete containing fine aggregate manufactured from recycled waste polyethylene terephthalate bottles. Constr Build Mater. 2009;23(8):2829-35. https://doi.org/10.1016/j.conbuildmat.2009.02.036
[4] Choi YW, Moon DJ, Chung JS, Cho SK. Effects of waste PET bottles aggregate on the properties of concrete. Cem Concr Res. 2005;35(4):776-81. https://doi.org/10.1016/j.cemconres.2004.05.014
[5] Marzouk OY, Dheilly RM, Queneudec M. Valorization of post-consumer waste plastic in cementitious concrete composites. Waste Manag. 2007;27(2):310-8. https://doi.org/10.1016/j.wasman.2006.03.012
[6] Albano C, Camacho N, Hernández M, Matheus A, Gutiérrez A. Influence of content and particle size of waste PET bottles on concrete behavior at different w/c ratios. Waste Manag. 2009;29(10):2707-16. https://doi.org/10.1016/j.wasman.2009.05.007
[7] Islam MJ, Meherier MS, Islam AKMR. Effects of waste PET as coarse aggregate on the fresh and harden properties of concrete. Constr Build Mater. 2016;125:946-51. https://doi.org/10.1016/j.conbuildmat.2016.08.128
[8] Batayneh M, Marie I, Asi I. Use of selected waste materials in concrete mixes. Waste Manag. 2007;27(12):1870-6. https://doi.org/10.1016/j.wasman.2006.07.026
[9] da Luz Garcia M, Oliveira MR, Silva TN, Castro ACM. Performance of mortars with PET. J Mater Cycles Waste Manag. 2021;23(2):699-706. https://doi.org/10.1007/s10163-020-01160-w
[10] Frigione M. Recycling of PET bottles as fine aggregate in concrete. Waste Manag. 2010;30(6):1101-6. https://doi.org/10.1016/j.wasman.2010.01.030
[11] Umasabor RI, Daniel SC. The effect of using polyethylene terephthalate as an additive on the flexural and compressive strength of concrete. Heliyon. 2020;6(8). https://doi.org/10.1016/j.heliyon.2020.e04700
[12] Kim SB, Yi NH, Kim HY, Kim JHJ, Song YC. Material and structural performance evaluation of recycled PET fiber reinforced concrete. Cem Concr Compos. 2010;32(3):232-40. https://doi.org/10.1016/j.cemconcomp.2009.11.002
[13] Kayali O, Haque MN, Zhu B. Some characteristics of high strength fiber reinforced lightweight aggregate concrete. Cem Concr Compos. 2003;25(2):207-13. https://doi.org/10.1016/S0958-9465(02)00016-1
[14] Islam MJ, Shahjalal M. Effect of polypropylene plastic on concrete properties as a partial replacement of stone and brick aggregate. Case Stud Constr Mater. 2021;15. https://doi.org/10.1016/j.cscm.2021.e00627
[15] Sjah J, Chandra J, Rastandi JI. The effect of usage of crushed polypropylene plastic waste in mechanical properties of concrete. Int J Civ Eng Technol. 2018;9(7):1495-505.
[16] Ozbakkaloglu T, Gu L, Gholampour A. Short-term mechanical properties of concrete containing recycled polypropylene coarse aggregates under ambient and elevated temperature. J Mater Civ Eng. 2017;29(10). https://doi.org/10.1061/(ASCE)MT.1943-5533.0002046
[17] Yang S, Yue X, Liu X, Tong Y. Properties of self-compacting lightweight concrete containing recycled plastic particles. Constr Build Mater. 2015;84:444-53. https://doi.org/10.1016/j.conbuildmat.2015.03.038
[18] Kou SC, Lee G, Poon CS, Lai WL. Properties of lightweight aggregate concrete prepared with PVC granules derived from scraped PVC pipes. Waste Manag. 2009;29(2):621-8. https://doi.org/10.1016/j.wasman.2008.06.014
[19] Senthil Kumar K, Baskar K. Recycling of E-plastic waste as a construction material in developing countries. J Mater Cycles Waste Manag. 2015;17(4):718-24. https://doi.org/10.1007/s10163-014-0303-5

[20] Yin S, Tuladhar R, Sheehan M, Combe M, Collister T. A life cycle assessment of recycled polypropylene fibre in concrete footpaths. J Clean Prod. 2016;112:2231-42. https://doi.org/10.1016/j.jclepro.2015.09.073
[21] Dawood AO, Al-Khazraji H, Falih RS. Physical and mechanical properties of concrete containing PET wastes as a partial replacement for fine aggregates. Case Stud Constr Mater. 2021;14. https://doi.org/10.1016/j.cscm.2020.e00482
[22] Saikia N, de Brito J. Mechanical properties and abrasion behaviour of concrete containing shredded PET bottle waste as a partial substitution of natural aggregate. Constr Build Mater. 2014;52:236-44. https://doi.org/10.1016/j.conbuildmat.2013.11.049
[23] Yerramala S. Properties of concrete with eggshell powder as cement replacement. Indian Concr J. 2014;88:94-105.
[24] Ofuyatan MO, Adeniyi AG, Ijie D, Ighalo JO, Oluwafemi J. Development of high-performance self-compacting concrete using eggshell powder and blast furnace slag as partial cement replacement. Constr Build Mater. 2020;256:119403. https://doi.org/10.1016/j.conbuildmat.2020.119403
[25] Ofuyatan MO, Edeki SO. Dataset on predictive compressive strength model for self-compacting concrete. Data Brief. 2018;17:801-6. https://doi.org/10.1016/j.dib.2018.02.008
[26] Ofuyatan MO, Edeki SO. Dataset on the durability behavior of palm oil fuel ash self compacting concrete. Data Brief. 2018;19:853-8. https://doi.org/10.1016/j.dib.2018.05.121
[27] Rantung D, Supit SWM, Nicolaas S. Effects of different size of fly ash as cement replacement on self-compacting concrete properties. J Sustain Eng Proc Ser. 2019;1(2):180-6. https://doi.org/10.35793/joseps.v1i2.25
[28] Iqbal S, Ali A, Holschemacher K, Ribakov Y, Bier TA. Effect of fly ash on properties of self-compacting high strength lightweight concrete. Period Polytech Civ Eng. 2017;61:81-7. https://doi.org/10.3311/PPci.8171
[29] Guo Z, Jiang T, Zhang J, Kong X, Chen C, Lehman DE. Mechanical and durability properties of sustainable self-compacting concrete with recycled concrete aggregate and fly ash. Constr Build Mater. 2020;231:117115. https://doi.org/10.1016/j.conbuildmat.2019.117115
[30] Ardalan RB, Joshaghani A, Hooton RD. Workability retention and compressive strength of self-compacting concrete incorporating pumice powder and silica fume. Constr Build Mater. 2017;134:116-22. https://doi.org/10.1016/j.conbuildmat.2016.12.090
[31] Cheng E, Sun X. Effects of wood-surface roughness, adhesive viscosity and processing pressure on adhesion strength of protein adhesive. J Adhes Sci Technol. 2006;20(9):997-1017. https://doi.org/10.1163/156856106777657779
[32] Adeniyi AG, Igwegbe CA, Ighalo JO. ANN Modelling of the adsorption of herbicides and pesticides based on sorbate-sorbent interphase. Chem Africa. 2021;4(2):443-9. https://doi.org/10.1007/s42250-020-00220-w
[33] Ighalo JO, Adelodun AA, Adeniyi AG, Igwegbe CA. Modelling the effect of sorbate-sorbent interphase on the adsorption of pesticides and herbicides by historical data design. Iranica J Energy Environ. 2020;11:253-9. https://doi.org/10.5829/IJEE.2020.11.04.02
[34] Azhdarpour AM, Nikoudel MR, Taheri M. The effect of using polyethylene terephthalate particles on physical and strength-related properties of concrete: A laboratory evaluation. Constr Build Mater. 2016;109:55-62. https://doi.org/10.1016/j.conbuildmat.2016.01.056
[35] Pirzada RA, Kalra T, Laherwal FA. Experimental study on use of waste plastic as coarse aggregate in concrete with admixture superplasticizer polycarboxylate ether. Int Res J Eng Technol. 2018;5(03):558-63.

[36] Manjunath BTA. Partial replacement of E-plastic waste as coarse-aggregate in concrete. Procedia Environ Sci. 2016;35:731-9. https://doi.org/10.1016/j.proenv.2016.07.079
[37] Bulut HA, Şahin R. A study on mechanical properties of polymer concrete containing electronic plastic waste. Compos Struct. 2017;178:50-62. https://doi.org/10.1016/j.compstruct.2017.06.058
[38] Sadrmomtazi A, Dolati-Milehsara S, Lotfi-Omran O, Sadeghi-Nik A. The combined effects of waste Polyethylene Terephthalate (PET) particles and pozzolanic materials on the properties of self-compacting concrete. J Clean Prod. 2016;112:2363-73. https://doi.org/10.1016/j.jclepro.2015.09.107
[39] Záleská M, Pavlíková M, Pokorný J, Jankovský O, Pavlík Z, Černý R. Structural, mechanical and hygrothermal properties of lightweight concrete based on the application of waste plastics. Constr Build Mater. 2018;180:1-11. https://doi.org/10.1016/j.conbuildmat.2018.05.250
[40] Al-Hadithi AI, Hilal NN. The possibility of enhancing some properties of self-compacting concrete by adding waste plastic fibers. J Build Eng. 2016;8:20-8. https://doi.org/10.1016/j.jobe.2016.06.011
[41] Kou SC, Lee G, Poon CS, Lai WL. Properties of lightweight aggregate concrete prepared with PVC granules derived from scraped PVC pipes. Waste Manag. 2009;29:621-8. https://doi.org/10.1016/j.wasman.2008.06.014
[42] Wang R, Meyer C. Performance of cement mortar made with recycled high impact polystyrene. Cem Concr Compos. 2012;34:975-81. https://doi.org/10.1016/j.cemconcomp.2012.06.014
[43] Thorneycroft J, Orr J, Savoikar P, Ball RJ. Performance of structural concrete with recycled plastic waste as a partial replacement for sand. Constr Build Mater. 2018;161:63-9. https://doi.org/10.1016/j.conbuildmat.2017.11.127
[44] Arulrajah A, Yaghoubi E, Wong Y, Horpibulsuk S. Recycled plastic granules and demolition wastes as construction materials: Resilient moduli and strength characteristics. Constr Build Mater. 2017;147:639-47. https://doi.org/10.1016/j.conbuildmat.2017.04.178
[45] Kalantarov AI, Prosanov IV, Kadomtseva YV, Vinogradova OV. Using waste polyethylene as a substitute for sand in the production of polymer concrete. Inorg Mater Appl Res. 2021;12:182-6.
[46] Jana Renuka, Konda Rajasekhar. Studies on Effect of Sulphuric Acid Attack on Concrete Made with Colloidal Silica as Replacement and Addition to Cement. Ecological engineering & environmental technology, 2024, 25(6), 331–343

Blank Page

Research on Engineering Structures & Materials
www.jresm.org
Research Group

Research Article

Mechanical and wear characterization of nitrided Al-5%Ti-B metal matrix composite reinforced with Al_2O_3 particles

Uday M [1,a], H R Vitala [1,b], Dileep B P [2,c], Bharath V [3,d], Udaya Devadiga [4,e], V Auradi [*,5,f]

[1]*Dept. of Mechanical Eng., SJB Institute of Technology, India & Visvesvaraya Technological University, India*
[2]*Dept. of Mechanical Eng., Amrita School of Engineering, Amrita Vishwa Vidyapeetham, India*
[3]*Dept. of Mechanical Eng., RNS Institute of Technology, Visvesvaraya Technological University, India*
[4]*Dept. of Mechanical Eng., Nitte (Deemed to be University) NMAM Institute of Technology, India*
[5]*Dept. of Mechanical Eng., Siddaganga Institute of Technology, India*

Article Info

Article history:

Received 12 June 2024
Accepted 27 Oct 2024

Keywords:

Al-5%Ti-B alloy;
Al_2O_3 particles;
Stir casting;
Nitriding;
Ultimate strength;
Wear

Abstract

The mechanical behavior and wear characteristics of nitrided Al-5%Ti-B alloy reinforced with Al_2O_3 have been investigated in this paper. The integration of Al_2O_3reinforcement into the Al-5%Ti-B alloy matrix offers promising opportunities for enhancing the mechanical and wear resistance properties of the composite material. Through a comprehensive experimental approach, various mechanical properties like tensile strength and hardness are evaluated alongside wear behavior under different conditions. The study also investigated how the nitriding treatment influenced both characteristics of microstructures and mechanical properties of the composite material. The results indicate significant improvements in mechanical properties and wear resistance following the incorporation of Al_2O_3 reinforcement and nitriding treatment. Microstructural analysis using techniques such as scanning electron microscopy and X-ray diffraction provided insights into the structural changes induced by the reinforcement and nitriding processes. The findings of this study contribute to the understanding of the synergistic effects between reinforcement, alloy composition, and surface treatments in enhancing the mechanical and wear properties of metal matrix composites, thereby offering potential applications in various engineering fields.

© 2025 MIM Research Group. All rights reserved.

1. Introduction

Metal matrix composites (i.e. MMCs) have emerged as promising materials for a wide variety range of engineering applications due to their superior mechanical properties and tailored functionalities [1, 2]. Among MMCs, aluminum-based alloys have attracted extensive interest due to their lightweight nature, corrosion resistance, and high strength-to-weight ratio [3, 4]. In recent years, there has been a focus on improving the tribological and mechanical characteristics of Al-based MMCs by integrating reinforcement materials and implementing surface treatments. Aluminum matrix composites have emerged as a focal point of research and development, owing to their remarkable attributes which outshine those of traditional monolithic aluminum alloys. [5, 6].

In this context, the combination of Al-5%Ti-B alloy with Al_2O_3 reinforcement presents an intriguing avenue for improving the mechanical and tribological characteristics of aluminum-based composites. Incorporating Al_2O_3, a ceramic material known for its exceptional hardness, thermal stability, and resistance to wear, into the matrix of the Al-5%Ti-B alloy presents an

*Corresponding author: vsauradi@sit.ac.in
[a] orcid.org/0000-0002-9995-9558; [b] orcid.org/0000-0002-6805-836X; [c] orcid.org/0000-0002-2423-4245;
[d] orcid.org/0000-0001-6765-4728; [e] orcid.org/0000-0002-9565-9726; [f] orcid.org/0000-0001-6549-6340
DOI: http://dx.doi.org/10.17515/resm2024.317me0612rs

opportunity to elevate the overall performance of the composite material [7, 8]. Additionally, the introduction of nitriding treatment further augments the surface properties and microstructural characteristics of the composite, potentially leading to enhanced mechanical strength and wear resistance.

The rationale behind investigating nitrided Al-5%Ti-B alloy reinforced with Al_2O_3 lies in the quest for materials advancement with enhanced properties to meet the demanding requirements of modern engineering applications. By comprehensively studying the wear and mechanical characteristics of this composite system, valuable insights can be gained into its performance under several loading conditions, providing crucial information for potential applications in sectors such as aerospace, automotive, and manufacturing.

2. Material Synthesis

2.1 Raw Materials

Aluminum-based MMCs are commonly used due to its lightweight, good thermal conductivity, and high strength-to-weight ratio. Adding elements like titanium and boron to aluminum can further improve its mechanical properties. Al-5%Ti-B alloy, often referred to as a master alloy, is a specialized material commonly used in the aluminum alloy industry. This alloy holds significant importance in the manufacturing of aluminum alloys tailored to possess distinct properties and characteristics. Kori et al. [9] conducted detailed experiments aimed at elucidating the mechanism involved in the reaction between molten aluminum and salts during the production of Al-Ti-B master alloys.

Al-5%Ti-B is primarily known for its grain refinement capabilities. The addition of Al-5%Ti-B allows for better control over the microstructure of the aluminum. In the casting process, Al-5%Ti-B can help reduce the formation of defects like shrinkage cavities and porosity. This is particularly important in industries where high-quality cast aluminum components are required, such as the automotive and aerospace sectors. With Al-5%Ti-B it can lead to increased tensile strength, elongation, and overall mechanical performance in aluminum alloys. This makes it valuable for manufacturing components where high-strength aluminum is necessary.

2.2 Reinforcement

Reinforcement particles can interact physically or electrochemically with the matrix, which is important for enhancing oxidization. Additionally, the relationship of the reinforcement and matrix can also accelerate oxidization. The oxidization at the particle and matrix interface can lead to high diffusion along the enormous interfacial regions in Metal Matrix Composites (MMCs), resulting in enhanced corrosion resistance. The particles such as Al2O3, SiC, B4C, etc., when reinforced in aluminum can improve the mechanical and tribological properties while reducing ductility. Nevertheless, there has been a moderate degree of sparse reporting on the optimization of weight percentages of reinforcements (Al_2O_3 and SiC) and heat treatment aimed at enhancing the mechanical and tribological properties of MMCs. Over the past few decades, numerous research reports have emphasized the tribological and mechanical attributes of MMCs. Arun et al. [10] studied the influence of Al_2O_3 and Gr on the tribological and mechanical behavior of Al-MMC. They used various weight percentages of Al_2O_3 (5, 10 and 15%) and a constant weight percentage of graphite (5%) to produce composites by a stir casting process. From the results, they concluded that the composites' hardness increased with the increase in weight percentage of Al_2O_3 particles.

Vedrtnam and Kumar [11] have investigated the behavior of wear on aluminum reinforced with silicon carbide and copper. From the work, it shows that the most influential parameter on wear rate of the composite was weight percentage of the reinforcements. Load and sliding

speed were second and third, respectively in the order of dominance while sliding distance had the least effect.

2.3 Material Processing

Stir casting is a widely used technique for the fabrication of MMCs such as Al-Ti-B alloy reinforced with Al_2O_3 particles. This technique entails integrating reinforcing materials, such as ceramic particles, into a molten metal matrix via mechanical agitation during solidification. The process typically begins with the melting of the base metal alloy, followed by the addition of the reinforcement particles into the molten metal [12, 13]. Mechanical stirring is then applied at a speed of 250 rpm to disperse the reinforcement particles uniformly throughout the matrix as shown in figure 1. The major benefits of this process are applicability to mass production. The stir casting process costs very low (up to 1/10th) for mass production of MMCs when compared to powder metallurgical process. To achieve proper filler distribution within the matrix during the stir casting process, it is essential that the temperature of the melt exceeds that of the Aluminum because of these factors, stir casting emerges as the predominant and viable technique for manufacturing MMCs [14, 15].

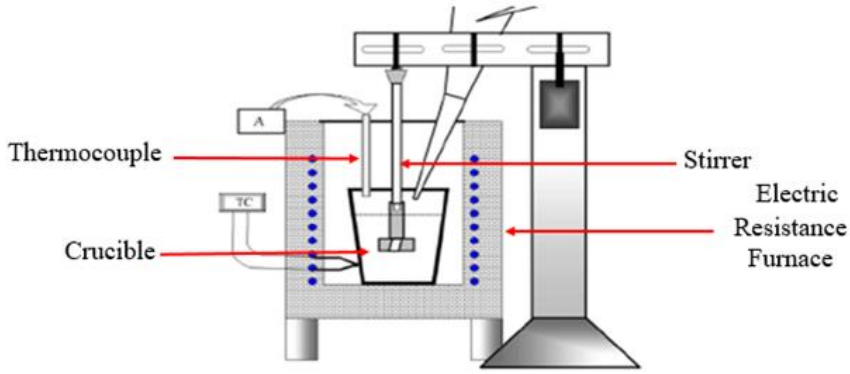

Fig. 1. The schematic diagram of the furnace used for composite ingot preparation

2.4 Gas Nitriding

Gas nitriding is a thermo-chemical process aimed at enhancing the surface properties of materials, typically steel, through nitrogen enrichment. Gas nitriding process was carried out at Vescon Engineering, Bengaluru. In this particular instance, theAl-5%Ti-B alloy with Al_2O_3 material in varying percentages has undergone gas nitriding treatment for 72 hours at 520°C.The treatment was conducted to bolster the material's hardness and wear resistance. After the 72-hour treatment period, the chamber was allowed to cool to room temperature, and samples were later removed for analysis. While the primary focus of gas nitriding is on diffusing nitrogen into the surface layers of steel, it's worth noting that if aluminum is present in the system, it could potentially react with ammonia gas under specific conditions to form aluminum nitride (AlN). However, the primary goal of the gas nitriding process remains the enrichment of the alloy surface with nitrogen to optimize its mechanical properties [16, 17].

$$3NH_3 + 2Al \rightarrow AlN + 3H_2 \quad (1)$$

This reaction represents the formation of aluminum nitride (AlN) from ammonia and aluminum, which is consistent with the presence of aluminum and ammonia gas. The alloying elements (Al, Ti, B) may form solid solutions or intermetallic compounds with nitrogen. The formation of aluminum nitride (AlN) on aluminum and aluminum alloys can indeed be

enhanced by microstructure refining and micro-alloying. This enhancement is attributed to several factors, and grain boundary diffusion of nitrogen in AlN is one of them [18,19,20].

3. Experimental Details

Figure 2 (a) is SEM micrograph of alumina particles and energy-dispersive X-ray spectroscopy (EDXS) serves as a tool for identifying the elemental composition of materials in a nitrided (Al-5%Ti-B) alloy specimen reinforced with Al2O3 as shown in figure 2 (b). The distinct nitrogen peak in the spectrum confirms the presence of nitrogen among other elements.

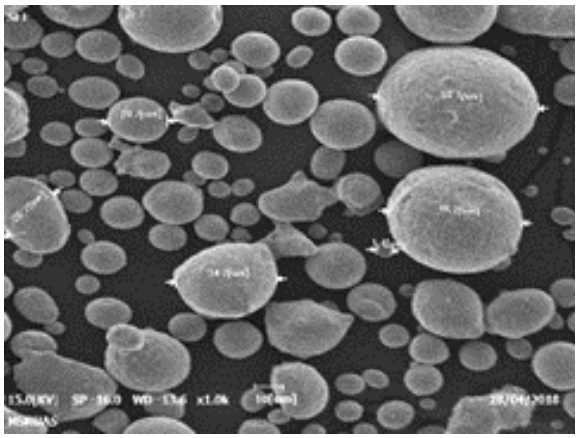

(a)

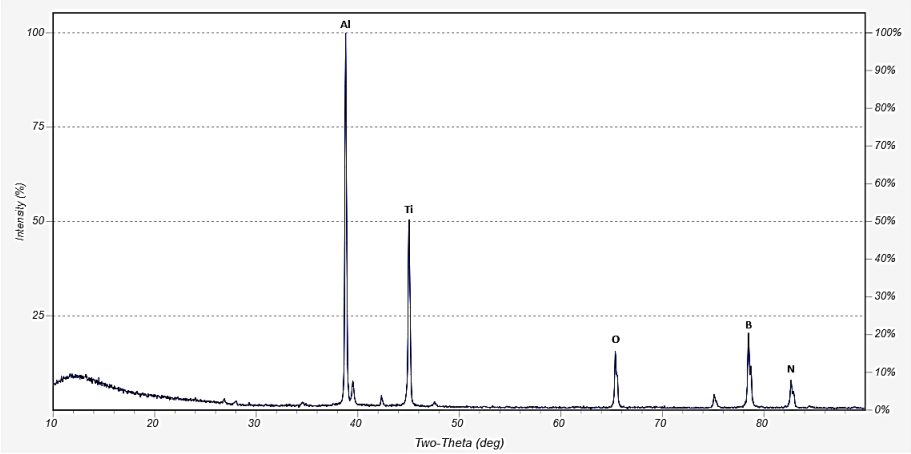

(b)

Fig. 2. (a) SEM micrograph of Al_2O_3 particles (b) XRD result of nitrided Al-Ti-B composition reinforced with Al_2O_3

The scanning electron microscope (SEM) as shown in figure 3 facilitates microanalysis and the examination of the dispersion of reinforcement particles within the matrix material. At a magnification of 100x,250x and 500x SEM enables the observation of distribution characteristics, surface texture, and particle orientation within the material's reinforcement distribution. Meanwhile, grain size is scrutinized at 500x magnification, providing insights into the alloy's microstructure and mechanical properties.

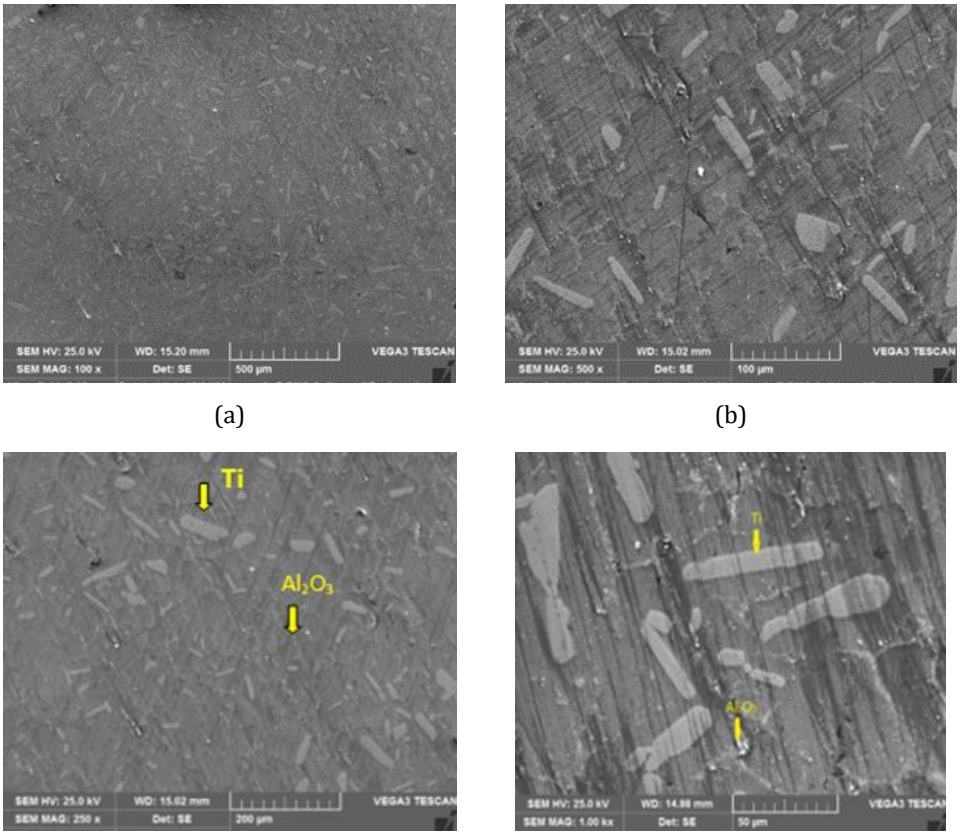

Fig. 3. SEM result of (a-b) Al-5%Ti-B composition (c-d) Al-5%Ti-B composition reinforced with Al_2O_3

4. Results and Discussions

4.1 Tensile Test

The process begins with the preparation of composite ingots, which are subsequently chopped into smaller pieces to facilitate re-melting. Re-melting occurs within an atmospheric controlled electrical resistant furnace, using graphite crucible to hold the chopped ingots. Al–5Ti–1B rods were cut and weighed accurately and added to the molten material at 75^{o}C, until they reach a molten state. Once molten, the reinforcement material Al_2O_3 is added and is gently stirred by stirrer for approximately 5-10 minute to achieve uniformity. The Tensile specimen is prepared as per the ASTM standards as shown in figure 4(a). One set the tensile specimen underwent gas nitriding treatment for 72 hours at 520°C as shown in figure 4 (b). The composite samples underwent tensile testing utilizing a computerized PC2000 tensiometer from Kudale Instruments (P) Ltd. Initial specimen preparation was conducted following the guidelines outlined in the ASTM E8M standard.

Fig. 4. (a) Non-Nitrated Tensile specimen and (b) Nitrated Tensile specimen as per ASTM standard with 0%, 2%, 4% and 6% of reinforced Al_2O_3

The tensile test results in the figures 5 indicate a noticeable increase in the ultimate true stress of the composites incorporating Al_2O_3 particles. Specifically, as shown in figure 5, it clearly indicates that the 6% Al_2O_3 sample exhibited the highest tensile strength, whereas the 0% Al_2O_3 sample displayed the lowest. This improvement in tensile strength for the sample can be attributed to the enhanced bonding between the matrix and the hybrid reinforcements. The same composition is nitrided and tested for tensile strength it is observed that there is improvement in its tensile property as well. Nitriding introduces nitrogen into the surface of the material, creating a hard, wear-resistant layer of nitrides. This layer increases the surface hardness and resistance to deformation, contributing to overall tensile strength.

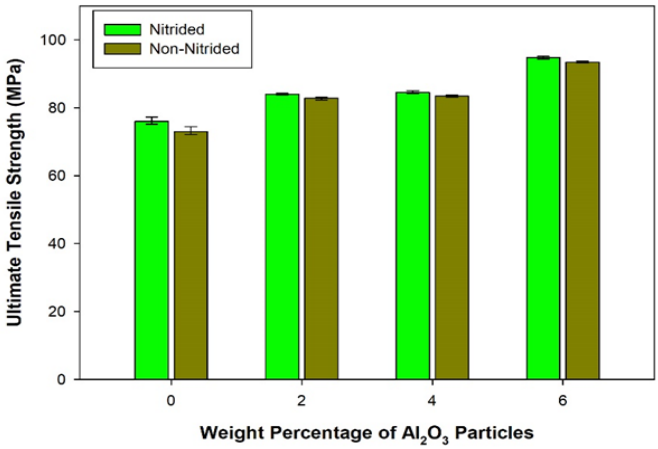

Fig. 5. Nitrated and Non- Nitrated Tensile strength of (Al-5%Ti-B) materials with 0%, 2%, 4% and 6% of reinforced Al_2O_3

4.2 Hardness test

Microhardness examination was conducted on the Micro-Vickers hardness testing machine by Mitutoyo in accordance with ASTM requirements to determine the hardness values in the (Al-5%Ti-B) with Al_2O_3 composite. The indentation made by applying the test force to a specimen using a quadrangular shaped pyramid diamond indenter whose face-to-face angle is 136°. The intention of this experiment was to evaluate the impacts of nitriding and the rise in weight

percentage (wt.%)of aluminum oxide on the lightweight aluminum alloy matrix, as hardness serves as an indicator of a product's resistance to plastic deformation.

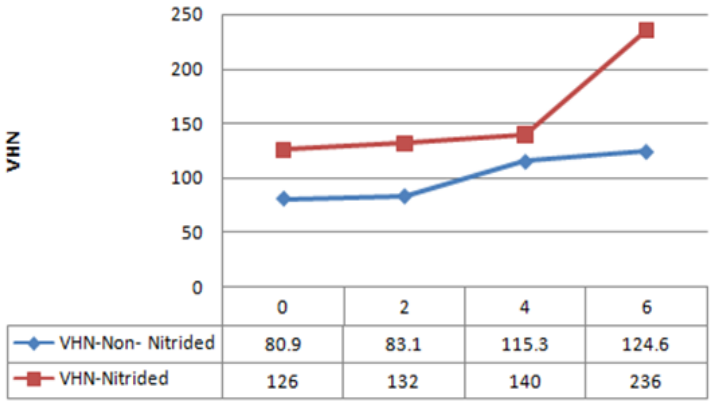

	0	2	4	6
VHN-Non- Nitrided	80.9	83.1	115.3	124.6
VHN-Nitrided	126	132	140	236

Fig. 6. Nitrided and Non- Nitrided Vicker's hardness of (Al-5%Ti-B) materials with 0%, 2%, 4% and 6% of reinforced Al_2O_3

The examination aimed to observe the influence of addition of aluminum oxide and nitriding on the hardness values to Al-5%Ti-B alloy. Figure 6 display the variation in hardness values with the wt.% of 0,2,4 and 6 aluminum oxide. It was noted that the hardness values increased with the increase in aluminum oxide content. This observation can be endorsed to the ceramic nature of aluminum oxide particulates, which are inherently harder compared to the aluminum matrix alloy. Now since the same composition is nitrated and tested for hardness, it results in an increase in the resistance to deformation and, consequently, an increase in hardness.

4.3 Wear Test

Al-5%Ti-B samples as per ASTM G99 with varying weight percentage of Al_2O_3 are made ready for dry sliding type of wear test. The test is performed on 10mm diameter and 30mm length cylindrical specimens with the help of pin on disc wear testing equipment. The test was conducted at 10N, 20N and 30N with the sliding speed of 500rpm for duration of 15min.

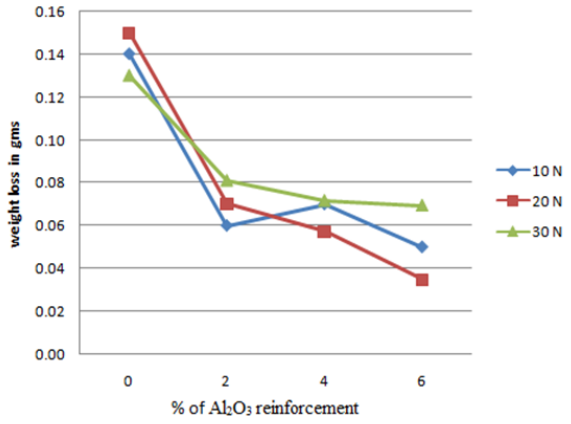

(a)

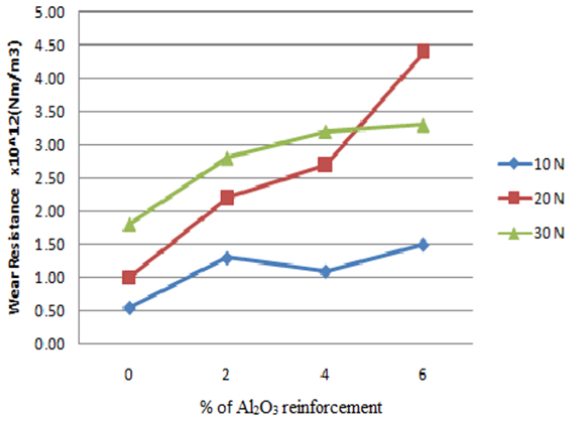

(b)

Fig. 7.(a) Wear loss and 7and (b) Wear Resistance of non Nitrided (Al-5%Ti-B) materials with 0%, 2%, 4% and 6% of reinforced Al_2O_3

Figure 7(a) and 8(a) shows wear loss of non-nitrided and nitridedAl-5%Ti-B material is of about 0.15gms and 0.13gm without inclusion of Al_2O_3 reinforcement. But with increasing in percentage of Al2O3 the composites have shown a greater wear resistance as compared to (Al-5%Ti-B). Effect of varying load on wear resistance of non-nitrided and nitrided (Al-5%Ti-B) alloy and its composites is presented in figure 7(b)and 8(b) respectively. The graph shown in the figures consists of three curves representing the behavior of material for varying loads of 10N, 20N and 30N for a track radius of 60mm with time of 15min and speed 500rpm.For the case of alloy without reinforcements the wear resistance of non-nitrided and nitrided is found to be 0.55and 0.61x10^12 Nm/m^3 respectively for 10N and 1.8 and 1.61x10^12 Nm/m^3 respectively for 30N. The wear resistance tends to increase with the increase in load from 10 N to 30 N. The increase in wear resistance is quite minimal with the increase in load. For the case of (Al-5%Ti-B) with 2% Al_2O_3 reinforcement wear resistance of non-nitrided and nitrided is found to be 1.3 and 1.5x10^12Nm/m3 respectively for 10N and 2.8 and 2.81x10^12 Nm/m3 respectively for 30N.

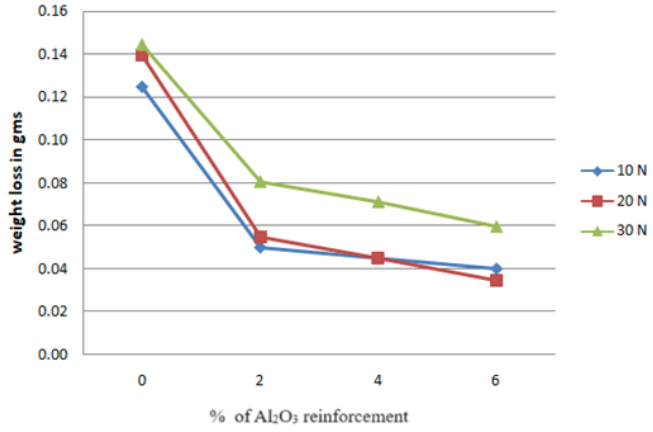

(a)

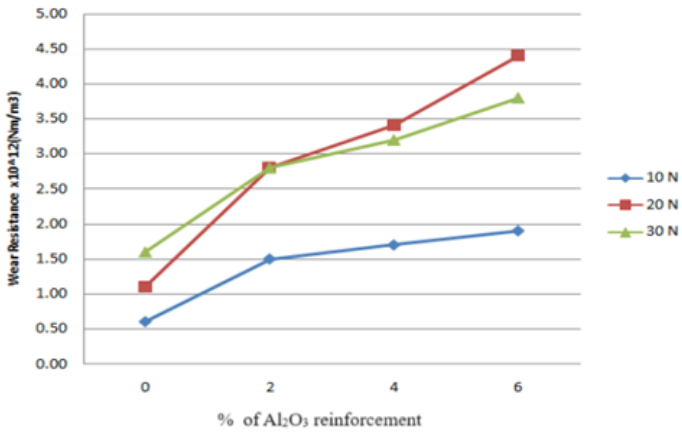

(b)

Fig. 8. (a)Wear loss and 7(b) Wear Resistance of nitride (Al-5%Ti-B) materials with 0%, 2%, 4% and 6% of reinforced Al_2O_3

For the case of Al-5%Ti-Bwith 4% Al_2O_3 reinforcement wear resistance of non-nitrided and nitrided is found to be 1.10and 1.70x10^12Nm/m^3 respectively for 10N and 3.2 and 3.33 x10^12 Nm/m^3 respectively for 30N and for the case of Al-5%Ti-Bwith 6% Al_2O_3 reinforcement wear resistance of non-nitrided and nitrided is found to be 1.5 and 1.9x10^12Nm/m3 respectively for 10N and 3.30 and 3.80x10^12 Nm/m^3 respectively for 30N. The wear resistance tends to increase with the increase in load from 10 N to 30 N. The wear resistance typically experiences a gradual increase with higher loads for all materials, whether alloys or composites. The SEM micrographs illustrate distinct wear characteristics between the nitrided and non-nitride samples of varying % Al2O3 reinforced composite materials under dry sliding conditions. Figure 9(a), the non-nitrided sample displays noticeable rough patches on the wear surface, indicating significant material removal or deformation. Conversely, Figure 9(b) depicts the nitrided composite sample with a smoother surface and fewer instances of delamination [21-24].

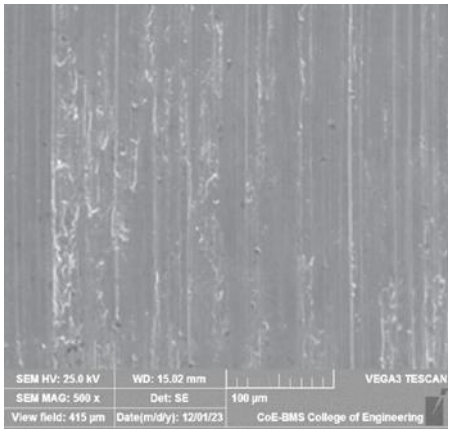

(a-1)

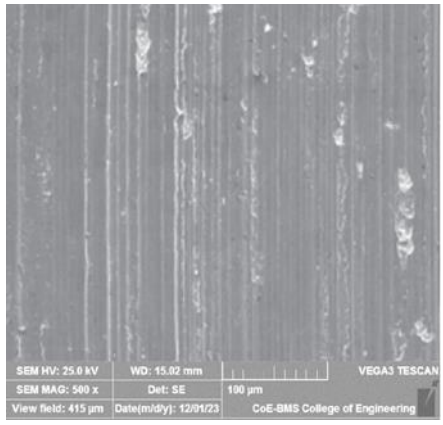

(a-2)

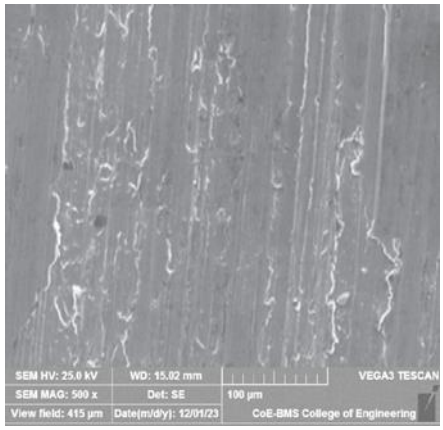

(a-3)

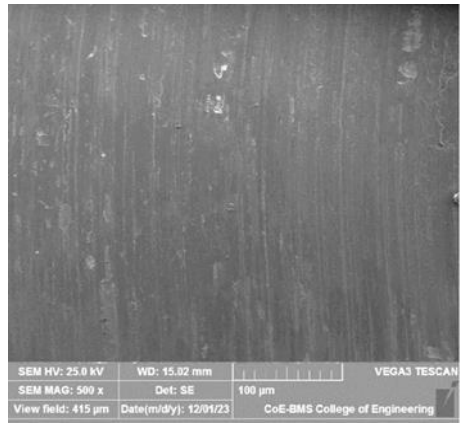

(a-4)

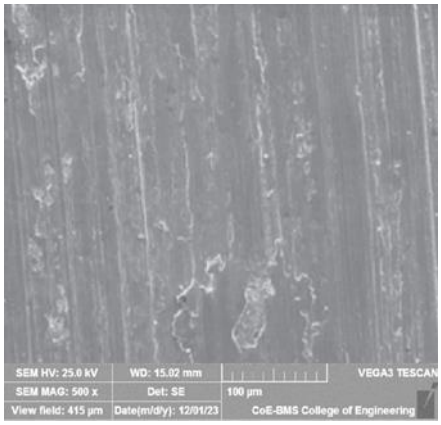

(b-1)

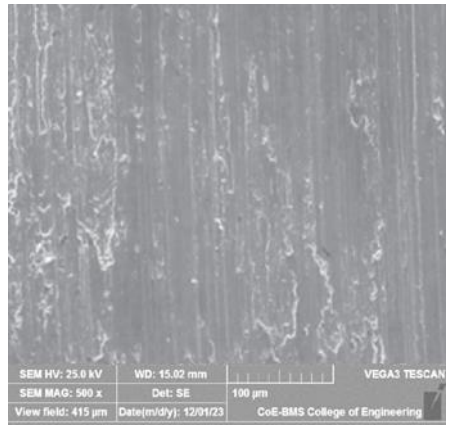

(b-2)

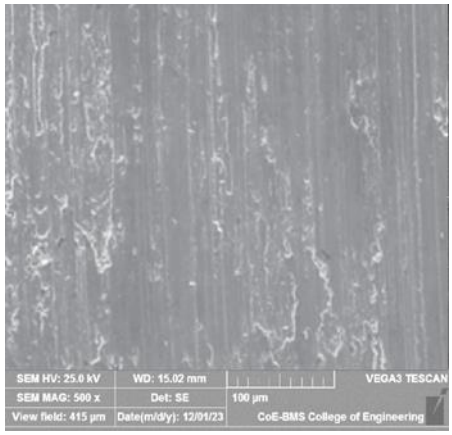

(b-3)

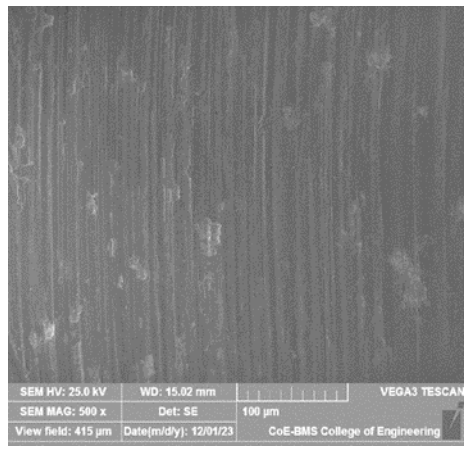

(b-4)

Fig. 9. (a) Non Nitrided (b) Nitrided SEM showing wear surface of Al-5%Ti-B composition reinforced with varying percentage (0,2,4and6%) of Al_2O_3

This smoother surface suggests reduced wear severity compared to the non-nitrided sample, highlighting the beneficial role of the nitrided layer in enhancing wear resistance. Additionally, the presence of reinforcement particles in the nitrided composite further contributes to its improved wear resistance.

5. Conclusion

The study on the mechanical and wear characterization of nitrided Al-5%Ti-B metal matrix composite reinforced with Al2O3 has provided valuable insights into the behavior and performance of this composite material. These Al-5%Ti-B with Al2O3 composites were synthesized by the liquid metallurgy technique i.e., stir casting method. Al-5%Ti-B with 2, 4 and 6 varying weight percentages of alumina particles were successfully synthesized by the stir casting method. The comprehensive analysis of mechanical properties and wear behavior, several key findings have been elucidated. The incorporation of Al2O3 reinforcement particles into the Al-5%Ti-B matrix has led to improved mechanical properties such as increased strength and hardness. It was noted that the hardness values increased with the increase in aluminum oxide content. This improvement can be credited to the reinforcing influence of the ceramic phase embedded within the metal matrix. The Al-5%Ti-B - alumina composites with nitriding exhibited more hardness and ultimate tensile strength as compared to the normal alumina particles reinforced composites.

Nitriding treatment has demonstrated a significant impact on the wear behavior of the composite material. The combination of nitriding treatment and Al2O3 reinforcement has shown synergistic effects in enhancing the wear resistance of the composite material. The nitrided layer, in conjunction with the reinforcing particles, has contributed to mitigating wear mechanisms such as abrasion, adhesion, and delamination, thereby improving the overall durability of the composite material. The results of this research carry practical significance for utilizing Al-5%Ti-B metal matrix composites reinforced with Al2O3 in industries where wear resistance holds paramount importance, including automotive, aerospace, and machinery sectors. The augmented mechanical attributes and wear resistance exhibited by the composite material render it a highly promising choice for components exposed to rigorous operational environments. The combined effect of nitriding process on the surface of the wear specimens and addition of the alumina particles resulted in the higher wear resistance as compared to the normal composites.

References

[1] Bharath V, Nagaral M, Auradi V. Preparation of 6061Al-Al2O3 metal matrix composite by stir casting and evaluation of mechanical properties. International Journal of Metallurgical and Materials Science and Engineering, 2012; 2 (3): 22-31.

[2] Nagaral M, Auradi V, Kori SA. Microstructure and mechanical properties of Al6061-Graphite composites fabricated by stir casting process. Applied Mechanics and Materials, 2015;766: 308-314. https://doi.org/10.4028/www.scientific.net/AMM.766-767.308

[3] Siddesh M, Shivakumar BP, Shashidhar S, Nagaral M. Dry sliding wear behavior of mica, fly ash and red mud particles reinforced Al7075 alloy hybrid metal matrix composites, Indian Journal of Science and Technology, 2021; 14 (4): 310-318. https://doi.org/10.17485/IJST/v14i4.2081

[4] Veeresh Kumar GB, Gude VC, Mandadi SV, Jayarami R, Madeva N, Naresh K. Effects of addition of Titanium Diboride and Graphite Particulate Reinforcements on physical, mechanical and tribological properties of Al6061 Alloy based Hybrid Metal Matrix Composites, Advances in Materials and Processing Technologies, 2022;8 (2): 2259-2276. https://doi.org/10.1080/2374068X.2021.1904370

[5] Gopal Krishna UB, Vasudeva B, Virupaxi A, Nagaral M. Effect of percentage variation on wear behaviour of tungsten carbide and cobalt reinforced Al7075 matrix composites

synthesized by melt stirring method, Journal of Bio-and Tribo-Corrosion, 2021; 7 (3): 89. https://doi.org/10.1007/s40735-021-00528-1
[6] Sallahauddin A, Nagaral M, Reddappa HN, Auradi V. Effect of B4C particulates addition on wear properties of Al7025 alloy composites. American Journal of Materials Science, 2015;5(3C): 53-57.
[7] Zeeshan A, Muthuraman V, Rathnakumar P, Gurusamy P, Nagaral M. Investigation on the tribological properties of copper alloy reinforced with Gr/ZrO2 particulates by stir casting route. Materials Today: Proceedings, 2020;33: 3449-3453. https://doi.org/10.1016/j.matpr.2020.05.351
[8] Bharath V, Auradi V, Nagaral M, Satish BP. Influence of alumina percentage on microstructure, mechanical and wear behavior of 2014 aluminium alumina metal matrix composites, Jurnal Tribologi, 2020;25 (1): 29-44
[9] Kori SA, Murty BS, Chakraborty. Preparation and Characterization of Al-B and B-Rich Al-Ti-B master alloys for the grain refinement of Al-7Si alloy. AFS Trans,2001; 1-20.
[10] Arun PA, Alwarsamy T, Rajmohan T, Prabhu R. The influence of alumina on mechanical and tribological characteristics ofgraphite particle reinforced hybrid Al-MMC. Journal of Mechanical Science and Technology,2014; 28(11): 4737-4744. https://doi.org/10.1007/s12206-014-1040-3
[11] Vedrtnam A, Kumar A. Fabrication and wear characterization of silicon carbide and copper reinforced aluminium matrix composite. Materials Discovery, 2017;9: 16-22. https://doi.org/10.1016/j.md.2018.01.002
[12] Pankaj RJ, Nagaral M, Shivakumar R, Jayasheel IH. Impact of boron carbide and graphite dual particulates addition on wear behavior of A356 alloy metal matrix composites, Journal of Metals, Materials and Minerals, 2020;30 (4): 106-112. https://doi.org/10.55713/jmmm.v30i4.642
[13] Rashmi PS, Mahesh TS, Zeeshan A, Veeresha G, Nagaral M. Studies on mechanical behaviour and tensile fractography of boron carbide particles reinforced Al8081 alloy advanced metal composites, Materials Today: Proceedings, 2022;52: 2115-2120. https://doi.org/10.1016/j.matpr.2021.12.397
[14] Emamya M, Razaghian A, Lashgari HR, Abbasi R. The effect of Al-5Ti-1B on the microstructure, hardness and tensile properties of Al2O3 and SiC-containing metal-matrix composites, Materials Science and Engineering A, 2008; 485: 210-217. https://doi.org/10.1016/j.msea.2007.07.090
[15] Xie H, Fouad, Dileep BP, Kumar RS, Kannan S. Fabrication of high-performance LaFeO3/CuCo2O4 nanocomposite for X-band stealth application Colloids and Surfaces A: Physicochemical and Engineering Aspects, 2023; 677:132414 https://doi.org/10.1016/j.colsurfa.2023.132414
[16] Bhujang MG, Bhujang MS, Hanyalu RV. Effect of Nitriding on Wear Behavior of Graphite Reinforced Aluminum Alloy Composites. Journal of Surface Engineered Materials and Advanced Technology, 2011; 1(2).
[17] Venkataraman V, Madeva N. Mechanical characterization and wear behavior of aerospace alloy AA2124 and micro B4C reinforced metal composites, Journal of Metals, Materials and Minerals, 2020; 30 (4): 97-105. https://doi.org/10.55713/jmmm.v30i4.641
[18] Balaraj V, Nagaraj K, Nagaral M, Auradi V. Microstructural evolution and mechanical characterization of micro Al2O3 particles reinforced Al6061 alloy metal composites, Materials Today: Proceedings, 2021; 47: 5959-5965. https://doi.org/10.1016/j.matpr.2021.04.500
[19] Varadraj KR, Kumar S, Vitala HR, Ravishankar MK, Dileep BP. Effect of Chromium on Mechanical and Corrosion Behaviour of Ferrous Metal Matrix Composites by Using Powder Metallurgy Route, Lecture Notes in Mechanical Engineering, 2023: 225-234. https://doi.org/10.1007/978-981-19-4140-5_19

[20] Nagaraj N, Mahendra KV, Nagaral M, Subbaraya MK, Chandrasekhar GL, A review on processing and properties of aluminum based metal matrix composites. Brazilian Journal of Development, 2024;10(5): e69389-e69389. https://doi.org/10.34117/bjdv10n5-009

[21] Shoufa L, Moslem P, Sadok M, Olatunji OO, Ibrahim M, Ibrahim E. Development of AA6061/316 stainless steel surface composites via friction stir processing: effect of tool rotational speed. Materials Characterization, 2022; 192: 112215. https://doi.org/10.1016/j.matchar.2022.112215

[22] Shoufa L, Moslem P, Olatunji OO, Michaela SP, Sadok M, Azlan MZ, Qiaorong Z, Jinpeng W. Friction stir processing of hybridized AZ31B magnesium alloy-based composites by adding CeO2 and ZrO2 powders: mechanical, wear, and corrosion behaviors. Journal of Materials Research and Technology. 2023; 24:1949-1972. https://doi.org/10.1016/j.jmrt.2023.03.028

[23] Shaohai L, Moslem P, Shoufa L, Sadok M, Suresh Kumar P, Mohanvel V. Importance of pin number on mechanical properties and wear performance during manufacturing of AA6061/316 surface composite via FSP. Materials Letters, 2022; 326:132919. https://doi.org/10.1016/j.matlet.2022.132919

[24] Liang H, Moslem P, Azlan MZ, Mohamad RA, Sherzod A, Michaela S. Effect of processing environment during friction stir processing of AZ31/(ZrO2+CuO)p surface composite on the mechanical and tribological performance. Journal of Materials Research and Technology. 2024; 28:1891-1899. https://doi.org/10.1016/j.jmrt.2023.11.222

Research on Engineering Structures & Materials
www.jresm.org
Research Group

Research Article

A multiphase membrane element with rotational DOFs for the elastic analysis of date palm fibre reinforced PVC composite

Samir Chouarfia [1,a], Lakhdar Sedira [*,1,b], Kamel Meftah [2,3,c], Wahid Kaddouri [3,d]

[1]*Laboratory of Mechanical Engineering (LGM), University of Biskra, Algeria*
[2]*Laboratoire de Génie Énergétique et Matériaux, University of Biskra, Algeria*
[3]*Laboratoire de Mécanique des Structures & Matériaux, University of Batna 2, Algeria*

Article Info

Article History:

Received 07 July 2024

Accepted 30 Sep 2024

Keywords:

Multiphase finite element;
Plane fibre rotation;
Representative volume element;
Date palm fibre PVC composite

Abstract

The main contribution of this work is the development of a new multiphase 4-node quadrilateral membrane finite element (PFR4M) for the analysis of elastic properties of polymer-based composites. Based on Plane Fibre Rotation (PFR) concept, the present element is formulated and implemented in Standard Abaqus software using two internal subroutines. The scope of application is extended to a wide range of materials which exhibit significant contrast between the mechanical properties of components. For this purpose, a date palm fibre reinforced PVC composite is prepared and characterized to provide microstructural imaging that serves as heterogeneous domain and used in numerical validation. The effects of the mesh size and the weight fractions of fibre on the performance of the multiphase element are analyzed. Statistical study is carried out to assess the size of the Representative Volume Element (RVE) of the composites. The present element is compared with two classical finite elements and the mean field model of Mori-Tanaka (MT). The obtained results show excellent convergence towards the effective property for all the considered configurations. An improved accuracy with respect to the classical 4-node element is achieved, which demonstrates the effectiveness of the present element in solving these homogenization problems.

© 2025 MIM Research Group. All rights reserved.

1. Introduction

Plant fibre composites are a viable and approved increasing substitute to traditional materials due to their sustainability, low cost and adequate strength. Currently they gain a wide range of applications in sectors where the environment impact and high strength-to-weight ratio are required. Several works have been carried out on the development and characterization of composites based on the bamboo [1], the date palm fibres [2] and the hemp [3] among others.

The theory of structured composites, where the fibres are aligned, is widely treated in the literature. A recent research review [4] has focused on overall mechanical behaviors of multilayer plates and shells, such as static, free vibration and buckling analysis of composite panels. On the other hand, composites reinforced with random fibres need more competitive modelling techniques, computational tools, and experimental methods to better understand and investigate their mechanical behaviors. Predicting of effective properties of such materials has given rise to several homogenization methods. The Mean Field (MF) Methods [5] are used firstly to substitute the interaction between components with average interactions from the entire material.

*Correspondingauthor: l.sedira@univ-biskra.dz

[a]orcid.org/0009-0005-6074-2676; [b]orcid.org/0000-0003-1735-2195; [c]orcid.org/0000-0002-5671-602X; [d]orcid.org/0000-0002-2654-815X

DOI: http://dx.doi.org/10.17515/resm2024.342ma0707rs

Considering either extreme assumptions or Eshelby's inclusion problem, different methods are presented by Voigt [6] and Reuss [7], Hashin and Shtrikman[8], Mori-Tanaka [9] to estimate rigorous bounds and effective properties of composites. Unfortunately, most of MF models could not consider the appropriate inclusion morphologies, and their real arrangements in the structure to reach this goal.

Nowadays, the multi-scale methods appeared as good numerical tools for analysis of mechanical behaviour of composites with multiple interacting between phases or materials. For instance, the Pixel Finite Element Method (PFEM) uses a small square (in 2D) or cubic (in 3D) elements to discretize a digital image of the material, each element represents a specific properties of components [17]. Mishnaevsky[18] proposed the voxel mesh generation method to model the progression of deformation and damage in composites with random and graded microstructures. Although this approach is easier, it has a high computational cost since more complex 3D images are considered. However, the modelling of the entire material needs a sample that can be either considered perfectly periodic or heterogeneous. The properties therefore will be derived from a unit cell [19] or otherwise from a Representative Volume Element (RVE).

Recently, a Finite Element based Multiphase Method (MPFE) is developed as an advanced numerical technique where each phase or material is typically assigned specific properties and behavior, and the interactions between phases are taken into account. In some context of structural and composite analyses, it can be assumed that the properties of each phase are related to individual integration points within the elements. However, the mesh of microstructure is independent of the phase arrangement of the material, and simulating deformation in a complicated microstructure can be done with simple FE-meshes [20].

Numerous works have been published on the application of this technique for *bio*-composites. Sukiman *et al*. [21] were interested in using the MPFE technique on analysis of short fibre-reinforced composite with random orientation and long fibres. El-Moumen *et al*. [22] used this method with real images of polypropylene bio-composite reinforced with aggregates of shells of argan nut to predict the effective Young's modulus. Djebara *et al*. [23] applied the same approach to estimate the effective properties of polymer-clay nano-composites. It should be noted that, most of research are based on low-order approximation, where the four-node quadrilateral or eight-node curvilinear elements, with either 2×2 or 3×3 Gauss integration schemes, are employed for mesh generation in the multiphase FE technique. Generally, structural refined meshes are used in the previous published works to assess the mechanical or physical properties of composites [24]. However, it is known that the accuracy of the finite element computation is closely related, at the same time, on the quality of mesh and the order of the finite element. Regarding the heterogeneous material, Kanit *et al*. [25] provided in their work a comparison between a regular mesh with multiphase elements and free mesh with tetrahedral elements to study microstructures with a generation of Voronoi mosaic reinforcement. The authors find that the mean stresses and deformations obtained by both types of meshes are identical; the only difference exists in the local field assessment.

In order to improve the kinematics' approximation of lower-order finite elements and to provide better prediction of the mechanical behavior of homogeneous materials in terms of computational time and accuracy, several 2D and 3D solid finite elements based respectively on Plane Fibre Rotation (PFR) [15,26] and Space Fibre Rotation (SFR) concept [27] are developed. This concept considers additional quadratic displacement terms caused by virtual rotations of a nodal space/plane fibre within the element [15,28]. However, numerical research is rarely devoted to developing enhanced finite element techniques intended to the analysis of composites with random distribution of fibres. Recurring issue in recent years has been the use of an element that contains inclusions with discontinuous material properties within its boundaries will have a weakly discontinuous displacement field along the interface boundaries [29]. Therefore, Hiriyur *et al*. [29] proposed an XFEM model that used nodal enrichment functions within the framework of the partition of unity method to improve the finite element approximations over a structured mesh. On the other hand, Cunha *et al*. [30] developed a FEM-based numerical model to simulate the crack behavior of the steel fibre reinforced concrete. The approach considers a combination of 3D solid

and projected 3D truss elements, to evaluate the stiffness matrices of the concrete and the short discrete embedded fibres domains. The corresponding local degrees of freedom for each truss are projected on those of 3D solid element. This approach is subsequently extended by Ayad and Kebir[12] to 2D Projected Fibre concept PF, that helps to assess the effective properties of hemp-polypropylene composite [3]. At first, the authors have developed a Projected Fibre Triangular element PFT that considers a combination of 2-node beam finite element and 3-node constant triangular element to evaluate the elastic properties of a reinforced hemp fibre polypropylene composite. Tiar *et al*. [13] extended the PF approach within the scope of the geometrical nonlinear analysis of microstructure. Therefore, a four-node quadrilateral membrane element named PFQ4, Projected Fibre 4-node Quadrilateral element, is developed. Zouari *et al*. [14] have combined PF and PFR approaches to develop two 4-nodequadrilateral elements baptized PFQ4R* and PFQ4R, Projected Fibre 4-node Quadrilateral element with Rotational variables. The short fibre is embedded as 2-node truss and Timoshenko plane beam elements, in each element, respectively.

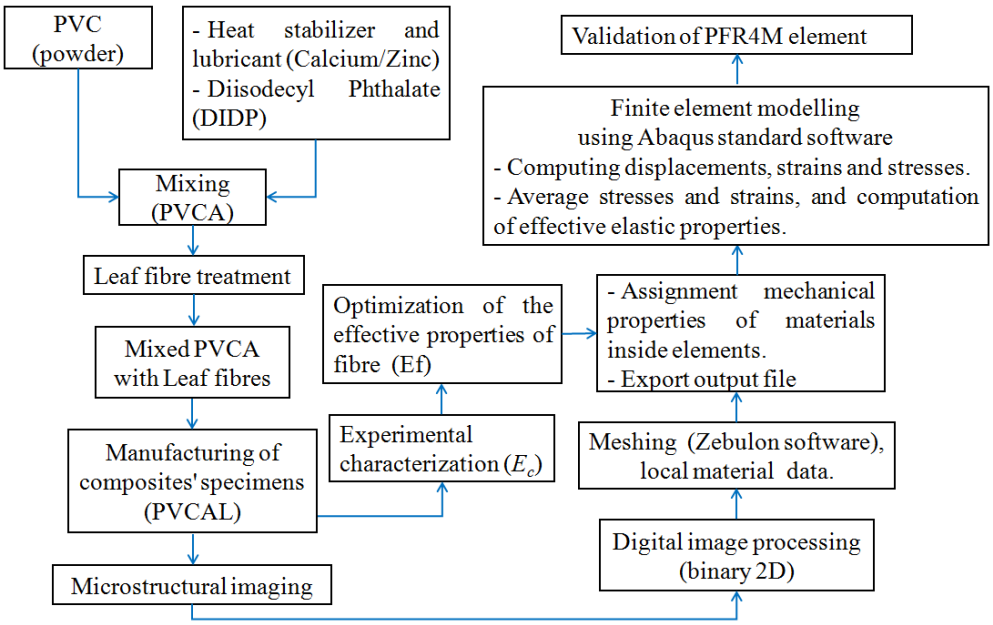

Fig. 1. Overall procedure of the experimental and numerical work

Due to the additional terms offered by the kinematic based on PFR and confirmed by Ayad [15], Zouari *et al*. [16], while adopting the multiphase approach, a new multiphase 4-node quadrilateral element is developed and implemented using the Abaqus Standard with the User Element subroutine UEL (see documentation in [31]). The displacement variational formulation is adopted to formulate the element stiffness matrix and force vector. The stiffness matrix is computed via an integration scheme of 2×2 Gauss points. A set of numerical tests are performed and compared with MT method [9,11] and classical finite elements [10]. Furthermore, since the micro-structural analysis is affected by geometric and the reel disposition of fibres in the pre-treated image, a date palm fibre reinforced PVC composite was developed, and a tensile test is performed.

The main purpose of the present study is to validate the performance and accuracy of the new multiphase element (PFR4M) in the prediction of elastic properties of the date palm fibre reinforced PVC composites. Experimental and numerical approaches are depicted in Fig. 1. The present paper is structured as follows. Section 2 is devoted to the numerical formulation of the finite membrane element including its stiffness matrix and the force vector. The section 3 deals with the MPFE method where the digital processing of the microstructure images, meshing and application of boundary conditions are detailed. The elaboration process of a date palm fibre reinforced PVC composite and experimental analysis of its elastic properties are detailed in Section 4. The next section deals with some numerical experimentation required for adjusting the elastic property of the fibre. The performance of PFR4M element is discussed

in Section 6, where effects of mesh, RVE sizes and the weight fraction on the effective mechanical properties are analyzed. Finally, this paper ends with a general conclusion.

2. Finite Element Formulation

2.1. Variational Formulation

Considering a linear elastic body problem in a state of small strains that occupies the domain Ω and its boundary$\partial\Omega$, as shown in Fig. 2. The equilibrium equation in the mixed configuration for a body subjected to body forces$\underline{f}^{v}$ is then given by:

$$Div\left(\underline{\underline{\sigma}}\right) + \underline{f}^{v} = 0 \tag{1}$$

Where, $\underline{\underline{\sigma}}$ is the mechanical stress tensor. In order to complete the boundary value problem, the displacement boundary conditions on$\partial\Omega_u$and the traction boundary conditions on $\partial\Omega_t$must be satisfied:

$$\begin{cases} u_i = U_i & on\ \partial\Omega_u \\ \sigma_{ij} n_j = T_i & on\ \partial\Omega_t \end{cases} \tag{2}$$

wheren_i is thei^{th} component of the normal *N* to the surface of the body in the initial configuration, as shown in Fig. 2.

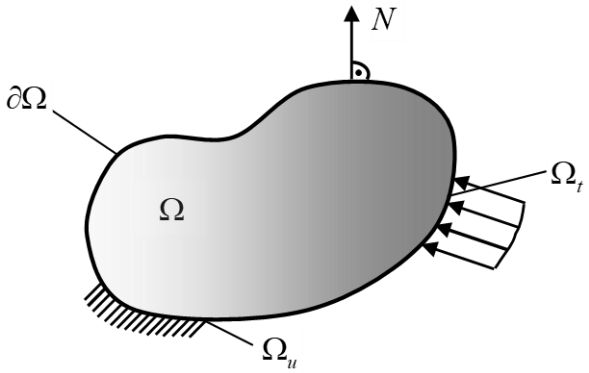

Fig. 2. Equilibrium of an elastic domain

The weak form $\delta\Pi$ of the equilibrium equation (Eq. (1)) is obtained by introducing the admissible test function $\delta\underline{u}$verifying$\delta\underline{u} = 0$ on $\partial\Omega_u$and integrating by parts, using the divergence theorem. The following weak form is obtained:

$$\partial\Pi = \int_{\Omega} \sigma_{ij}\delta\varepsilon_{ij}\, d\Omega - \left[\int_{\Omega} f_i^{v}\delta u_i d\Omega + \int_{\delta\Omega_t} T_i\delta u_i dS\right] = \delta W_{int} - \delta W_{ext} = 0 \tag{3}$$

where δW_{int} and $\delta W_{ext}$are respectively the internal and external mechanical virtual works.

The virtual gradient field $\delta\underline{\underline{\varepsilon}}$ is related to $\delta\underline{u}$ by the following expression:

$$\delta\underline{\underline{\varepsilon}} = \frac{1}{2}\left(\underline{\underline{grad}}(\delta\underline{u}) + \underline{\underline{grad}}^{T}(\delta\underline{u})\right) \tag{4}$$

From Eq. (3), the weak form can be rewritten as follows:

$$\partial\Pi = \int_{\Omega} \{\delta\varepsilon\}^{T}\{\sigma\}\, d\Omega - \left[\int_{\Omega} f_i^{v}\delta u_i d\Omega + \int_{\delta\Omega_t} T_i\delta u_i dS\right] = \delta W_{int} - \delta W_{ext} = 0 \tag{5}$$

where {σ} and {ε} are respectively the Cartesian stress and strain vectors given by:

$$\{\sigma\} = \{\sigma_{xx} \quad \sigma_{yy} \quad \sigma_{zz} \quad \tau_{xy} \quad \tau_{xz} \quad \tau_{yz}\}^T \tag{6}$$

$$\{\varepsilon\} = \{\varepsilon_{xx} \quad \varepsilon_{yy} \quad \varepsilon_{zz} \quad \gamma_{xy} \quad \gamma_{xz} \quad \gamma_{yz}\}^T \tag{7}$$

with $\gamma_{xy} = 2\varepsilon_{xy}, \gamma_{xz} = 2\varepsilon_{xz}$ and $\gamma_{yz} = 2\varepsilon_{yz}$

2.2. Principle of the PFR model

The Plane Fibre Rotation Concept is an in-plane adaptation of the advanced Space Fibre Rotation concept proposed by Ayad *et al*. [15]. The authors consider additional quadratic terms in the displacement field that allows a curvature at particle *p* within the element. These terms are linked to out-plane virtual rotation of the nodal fibre $\underline{ip}$, see Fig.3a. This fibre rotation represented by the vector $\underline{\theta}$ around the node *i*, generates an additional vector $\theta_i \underline{k} \wedge \underline{ip}$. This term can be considered in bilinear displacement field to formulate the PFR4M as:

$$\underline{u}(\xi,\eta) = \sum_{i=1}^{4} N_i(\xi,\eta)\left(\underline{u_i} + \theta_i \underline{k} \wedge \underline{ip}\right) \tag{8}$$

where N_i are the shape functions associated to the classical bilinear element. ξ, η are the curvilinear local coordinates. u_i, v_i and θ_i are the nodal displacements: two displacement and rotation. $\underline{ip}$ is defined as:

$$\{ip\}^T = \langle x - x_i \quad y - y_i \rangle \tag{9}$$

x and *y* are the global coordinates given as:

$$x = \sum_{i=1}^{4} N_i(\xi,\eta) x_i \quad ; \quad y = \sum_{i=1}^{4} N_i(\xi,\eta) y_i \tag{10}$$

by substituting Eqs. (9)-(10) in Eq. (8), the two in-plane components of the displacement field u and v can be written as:

$$\begin{Bmatrix} u(\xi,\eta) \\ v(\xi,\eta) \end{Bmatrix} = \sum_{i=1}^{4} N_i(\xi,\eta) \begin{Bmatrix} u_i - (y - y_i)\theta_i \\ v_i + (x - x_i)\theta_i \end{Bmatrix} \tag{11}$$

The displacement vector can be rewritten in matrix form as:

$$\{u\} = [N]\{u_n^e\}; \ [N] = \begin{bmatrix} N_u \\ N_v \end{bmatrix} \tag{12}$$

Where,

$$\begin{bmatrix} N_u \\ N_v \end{bmatrix} = \begin{bmatrix} \cdots N_i & 0 & -N_i(y - y_i) \\ 0 & N_i & N_i(x - x_i) \end{bmatrix} \cdots, i = 1,4 \tag{13}$$

and $\{u_n^e\} = \{\cdots u_i \quad v_i \quad \theta_i \quad \cdots \quad i = 1,4\}^T$ is the nodal degrees of freedom vector of PFR4M element containing three DOF's per node, Fig. 3b.

The virtual displacement vector $\delta\underline{u}$ can also be written as follows:

$$\{\delta u\} = [N]\{\delta u_n^e\} \tag{14}$$

The strain tensor of any point *p* is classically defined in the global coordinate system by:

$$[\varepsilon] = \begin{bmatrix} \varepsilon_{xx} & \varepsilon_{xy} \\ \varepsilon_{xy} & \varepsilon_{yy} \end{bmatrix}, \varepsilon_{xx} = u_{,x}; \varepsilon_{yy} = v_{,y}; \varepsilon_{xy} = \frac{1}{2}(u_{,y} + v_{,x}) \tag{15}$$

Using strain components of Eq. (7) and the interpolation of the displacement vector (Eq. (12)), the matrix relationship between the stain vector $\{\varepsilon\}$ and the nodal degrees of freedom vector $\{u_n^e\}$ can be written as:

$$\{\varepsilon\} = [B]\{u_n^e\}; \underbrace{[B]}_{3\times 12} = \begin{bmatrix} [N_{u,x}] \\ [N_{v,y}] \\ [N_{v,x} + N_{u,y}] \end{bmatrix} \tag{16}$$

Where,

$$\begin{matrix} [N_{\alpha,x}] = j_{11}[N_{\alpha,\xi}] + j_{12}[N_{\alpha,\eta}] \\ [N_{\alpha,y}] = j_{21}[N_{\alpha,\xi}] + j_{22}[N_{\alpha,\eta}] \end{matrix}; \alpha = u, v \tag{17}$$

and j_{lk} are the inverse Jacobian matrix components defined by:

$$[j] = \begin{bmatrix} x_{,\xi} & y_{,\xi} \\ x_{,\eta} & y_{,\eta} \end{bmatrix}^{-1} \tag{18}$$

Therefore, for linear elastic problems, the substitution of the virtual displacement vector (Eq. (14)) and the relationship between virtual strain and stress (Hooke's law), in the weak form of the equilibrium Eq. (5) allows to reduce the problem to the following algebraic system:

$$[k^e]\{u^e\} = \{F^e\} \tag{19}$$

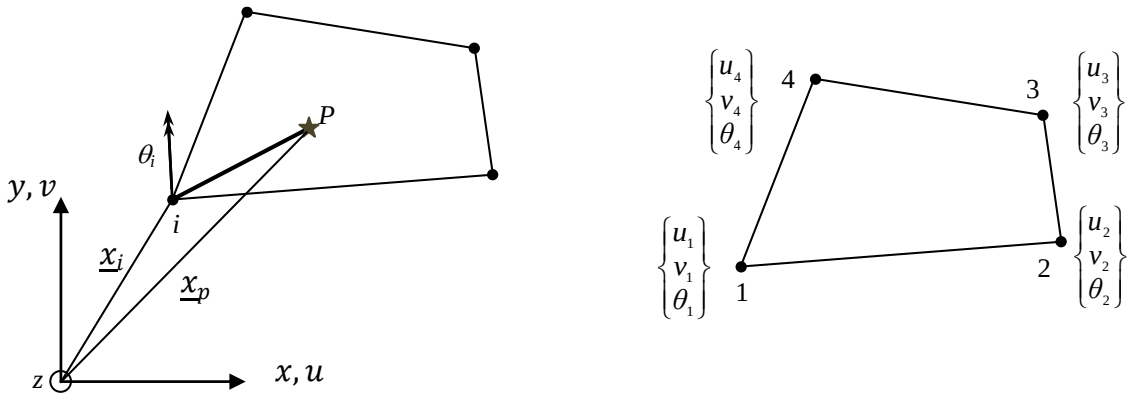

Fig. 3. (a) Plane fibre rotation concept. (b) 4-node quadrilateral FE-based on out-plane fibre

Where,

$$[k^e] = \int_{-1}^{1}\int_{-1}^{1} [B]^T[C][B]\, det\, J\, h\, d\xi\, d\eta = \sum_{i=1}^{n_{ip}}\sum_{j=1}^{n_{ip}} \omega_i\, \omega_j\, h\, [B]^T_{\xi_i,\eta_j}[C]_{\xi_i,\eta_j}[B]_{\xi_i,\eta_j}\, det\, J \tag{20}$$

and

$$[F^e] = \int_{V^e} [N]^T\{f_v\}\, dV^e + \int_{V^e} [N]^T\{T\}\, dS^e \tag{21}$$

[k^e] is the (12×12)-sized element stiffness matrix and {F^e} is the (12×1)-sized element external force vector.

where [C] is the elasticity matrix relating the stress and strain vectors, which computed either in fibre or matrix, det J is the Jacobi determinant, h is the thickness of element, ω_i and n_{ip} are the weight and the number of point Gauss quadrature rule, respectively. In fact, the longitudinal Young's modulus E and the Poisson's ratio νcan be assumed at least as linear function $P(x,y)$. Both can take the following form:

$$P(x,y) = \sum_{i=1}^{n_{ip}} N_i(\xi,\eta)\, P_i \tag{22}$$

At elementary computing level, the elastic properties of both matrix and reinforcement are collocated point by point in the integral (Eq. (20)) and take only constant values at points of Gauss quadrature rule. Fig. 4 shows the inter-phase treatment and the geometric localization of two or more material phases relative to integration points within PFR4M element. For the isotropic elastic case, the elasticity matrix is written as:

$$[C] = \frac{E_{Ph}}{1-\nu_{Ph}^2}\begin{bmatrix} 1 & \nu_{Ph} & 0 \\ \nu_{Ph} & 1 & 0 \\ 0 & 0 & \dfrac{(1-\nu_{Ph})}{2} \end{bmatrix}, Ph = matrix\ or\ fibre \tag{23}$$

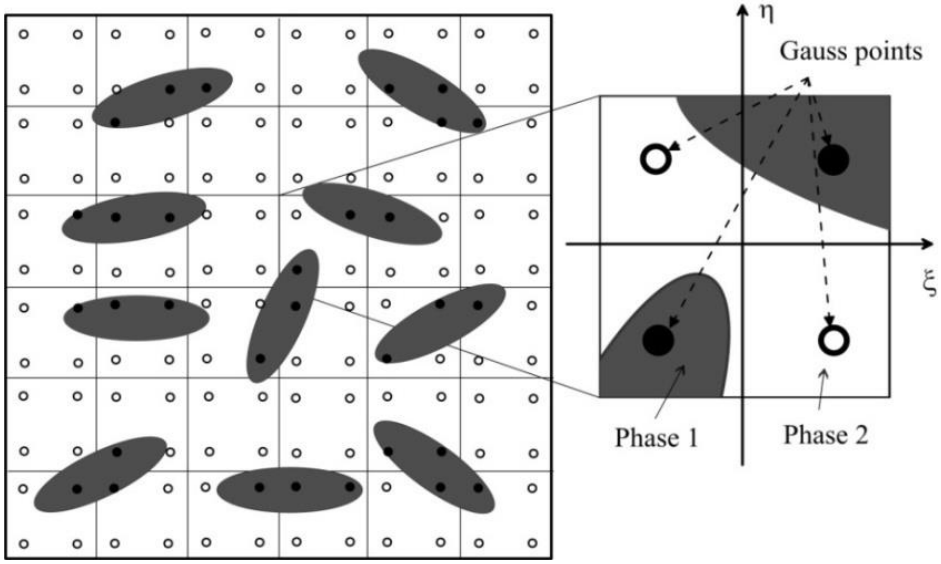

Fig. 4. Localization of material phases in PFR4M element

3. Multiphase Mesh Technique

In this section, the main focus is on describing the meshing technique employed for numerical modelling, called multiphase element method (MPFE). This technique was developed by Lippmann *et al*. [32] and has also been used by several authors [33,34] El-Moumen et al [35], among others, have applied this method to estimate the mechanical properties of polymer composites based on the aggregates of argan shell. The method consists of superimposing a finite element grid (Fig. 5a), defined by its integration points (as shown in Fig. 4), onto the binary 2D image of the microstructure (Fig. 5b). Each integration point is assigned properties according to the grayscale shade of the phase it intersects, as illustrated in Fig. 4. As a result, a single element may have multiple properties associated with its integration points, hence the term multiphase finite element. The obtained meshed microstructure with a 200x200 finite element grid is presented in Fig. 5c. For this purpose, an advanced Zmesh module of Zebulon finite element code [10] was used

in digital image analyzing. A FORTRAN routine was also developed to extract properties related to both materials in each integration points in all elements of mesh, an output file is then exported to the User-defined External Databases Subroutine UEXTERNALDB [31] to assign the elastic properties for each integration points and calculate the stiffness matrices, see Fig. 55. Furthermore, a post-processing is performed to deduce the local mechanical behavior in the whole microstructure, see Fig. 5d.

Boundary conditions

For the determination of the effective properties (Longitudinal Young's modulus and Poisson ratio), a uniaxial tensile test in the x-direction is applied with the boundary conditions shown in Fig. 6, as follow:

- Side *OA*: 0 displacement in the *x* direction and 0 tangential stress in the *y* direction;
- Side *OB*: 0 displacement in the *y* direction and 0 tangential stress in the *x* direction;
- Side *BC*: δ displacement in the *x* direction and 0 tangential stress in the *y* direction.

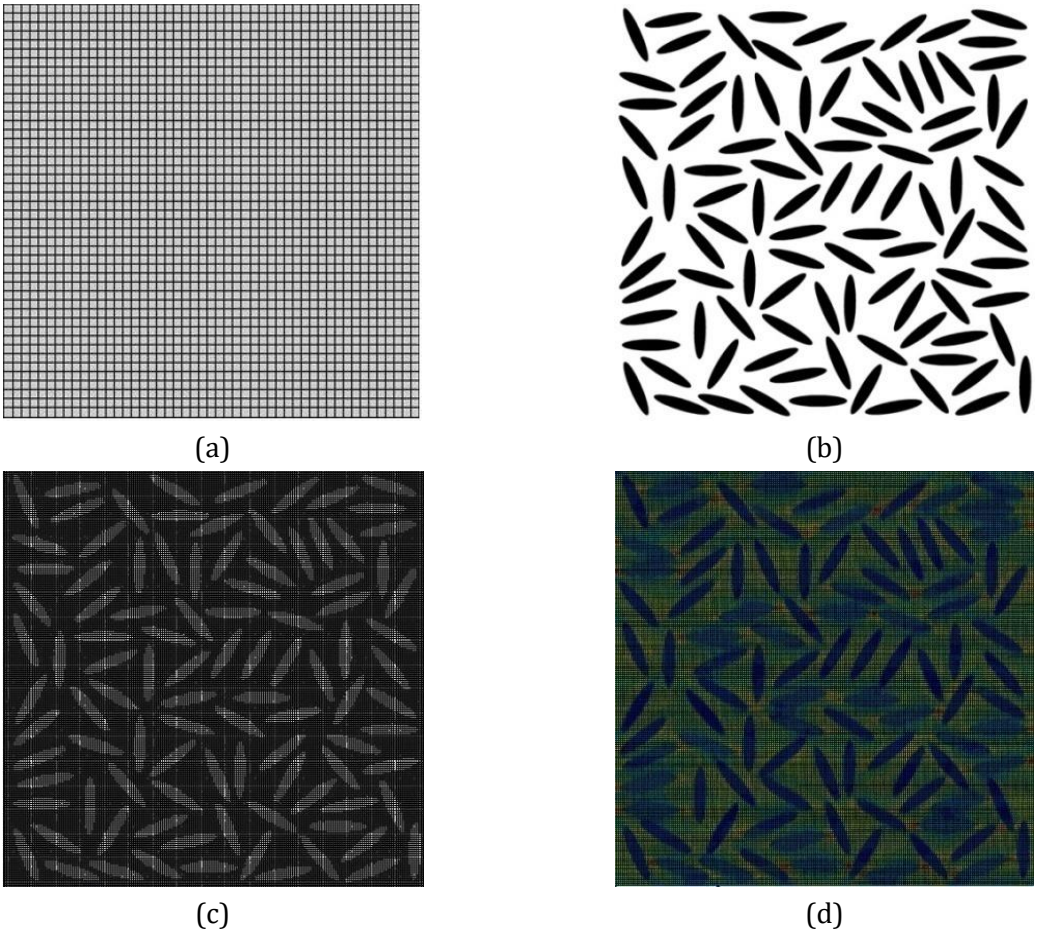

(a) (b) (c) (d)

Fig. 5. Multi-phase mesh technique. (a) finite element regular mesh (grid), (b) bicolour image of REV (grid), (c) meshed microstructure, (d) post-processing (local mechanical behaviour)

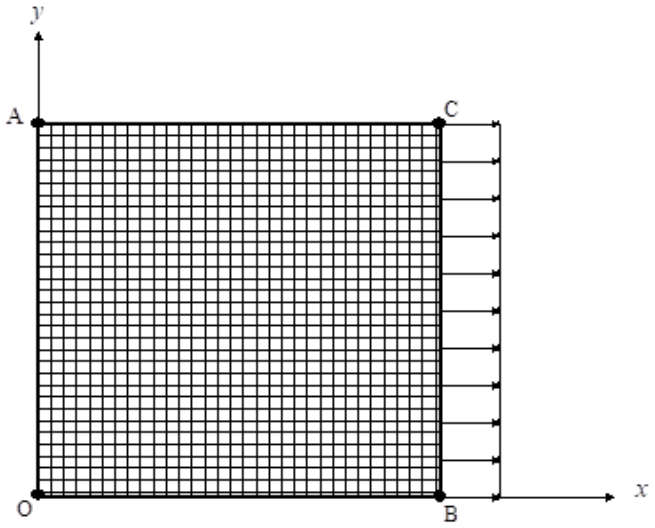

Fig. 6. Illustration of the applied boundary conditions

4. Material and Mechanical Test

4.1 Composite Preparation

The new numerical approach is intended to be approved on simulation of elastic behavior of real materials with random fibre distribution and high heterogeneity ratio. For this purpose, a date palm fibre reinforced PVC composite material (PVCAL) is prepared and considered in the present study. First, a powder of pure PVC (PVC SE 1200) is mixed with heat stabilizers and lubricant Calcium/Zinc to increase the processing output of extrusion and to protect the PVC matrix from thermal degradation. The Di-IsoDecyl Phthalate DIDP is also added as processing aids in rigid PVC to increase flexibility and lifetime. On the other hand, the fibre of Leaf is vegetal pruning residues of date palms. These wastes are extracted from a natural texture as round yarn of length L_f (3-8 mm) and diameter D_f (0.2-0.7 mm). The final mixture- additives, denoted PVCA is mixed with Leaf fibres and extruded using a Plasti-Corder PLE 330 single screw extruder Fig. 7a. The extrusion is carried out with a rotation speed of 30 rpm and heated zones about 175 °C as an average temperature. In second step, the PVCAL compounds are poured into a rectangular mould, heated to a temperature of 175°C and pressed progressively until 200 bars. The sheets reinforced composites of 4 mm of thickness are removed from the mould when the cooling process achieves a temperature of 45°C. See Fig. 7b. Finally, CNC cutting is used to shape dumbbell samples of PVCAL.

4.2 Tensile Testing

Tensile testing was carried out on a testing machine INSTRON5969, fitted with a 5 kN load cell. The load was applied by moving the crosshead of the machine at a specific deformation of 1%/min according to ASTM D 3039 standards.

(a) (b)

Fig. 7. Preparation of PVCAL material (a) compounding. (b) moulded PVCAL composite plates

The test is performed until the material breaks, except some specimens of the pure PVCA matrix. All data will be stored and processed by the Bluehill software supplied with the machine; Fig. 8

illustrates the results of stress/strain curves of five samples, pure PVCA and PVCA with date palm fibres for four weight fractions 10%, 15%, 20% and 25%.

The longitudinal Young's moduli defined as mean values and average standard deviation are depicted in Table 1. According to the obtained results, it is observed that with the increase in the weight fraction of the fibres, the Young's modulus of the composite considerably improves. These results will be considered as a reference for the numerical validation.

5. Numerical Experimentation

5.1 Mechanical Properties of Fibre

Mechanical behavior of the date palm fibre has already been studied and presented by Djebloun and Hecini[35] among others. Although the vegetal fibres are considered as orthotropic materials [36], the authors revealed the only longitudinal Young's modulus which varies between 4160 and 4300 MPa, while the Poisson's ratio is in the range of most plant fibres 0.115 - 0.136. Regarding our protocol, the Leaf fibres have undergone alkaline treatment during the preliminary cleaning process and may be affected by the absorption of the plasticizer when mixed with the PVC matrix. In addition, the composite is experienced a high aggressive processing technique, cutting, extrusion friction, compression moulding etc. Given the latest constraints, the calculation of the properties of the fibre becomes a task which must be carried out in situ the final composite material. Therefore, a set of experimental results of the Young's moduli of the homogeneous materials are involved in an optimization problem (Eq. (24)). A numerical study is performed to assess an average value of the longitudinal Young's modulus (E_f) of the Leaf fibre that fulfils almost experimental results. It is about minimizing the residual between the experimental values and the fitted value E_c^{MT} provided by the MT-3D model, for E_f values ranging from 0 to 6000 MPa.

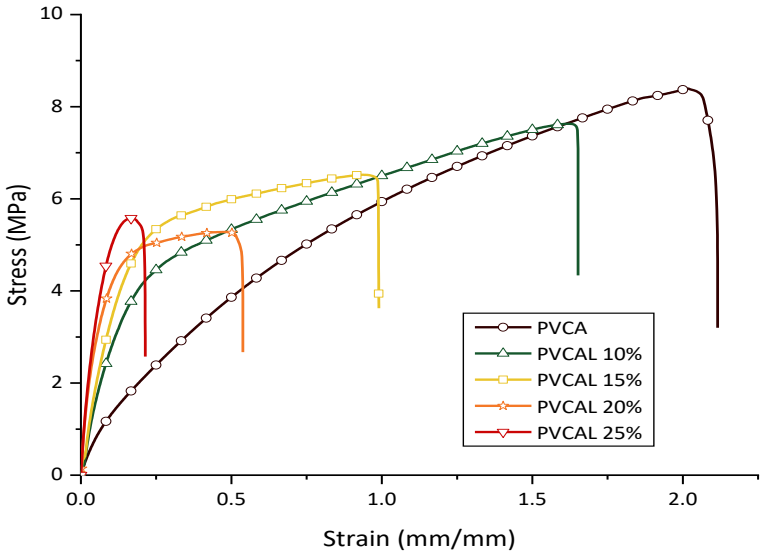

Fig. 8. Tensile test of PVCAL composite with different weight fractions of fibres

The optimization problem is given as bellows:

$$E_C^{MT}(E_f) \approx E_C^{exp} \quad , \quad E_f \in [0\ , 6000] \tag{24}$$

where E_C^{MT}: Longitudinal Young's modulus function of composite obtained from the homogenized elastic stiffness tensor of the MT-3D model, Eq. (25) and E_C^{exp}: Individual experimental data of Young's modulus of composite.

The complete elastic stiffness tensor for the composite is given by Benveniste[11] as:

$$C = C^m + v_f\langle (C^f - C^m)A^f\rangle\left(v_m I + v_f\langle A^f\rangle\right)^{-1} \quad (25)$$

A^f is the the dilute mechanical strain concentration tensors of fibre [37]. Its average value$\langle A^f\rangle$ is computed by 3D integration scheme using 15×15×15 Gauss points and a unit orientation distribution function. The following properties are considered: E_m = 10.52, ν_m = 0.48, ν_f= 0.125, ζ = 10. Fig. 9 represents the curves of the longitudinal Young's moduli of composites ($E_C^{MT(3D)}$) as a function of the Young's modulus of fibre (E_f). The curves are plotted for four volume fractions of composite reinforcement.

Table 1. Longitudinal Young's modulus of PVCAL composite materials

	PVCAL composite materials				
Weight fractions of fibre W_f (%)	0.00	10.00	15.00	20.00	25.00
Volume fractions of fibre V_f (%)	0.00	14.80	22.25	28.88	35.05
Longitudinal Young's modulus (MPa)	10.521 ±1.374	19.402 ±1.886	27.547 ±3.608	39.187 ±5.798	59.997 ±11.800

It can be noted that, all curves go up and asymptotically reaching towards fixed values. The resolution of the system of equations (Eq. (24)) showed a value of 3492.54 MPa of the fibre Young's modulus that minimizes and stabilizes the deviation between the theoretical simulation and the experimental data. This reveals that the over-rigidity of the fibre from this value has no effect on elastic property of the composite. That raises again the ability of the approach to address this relationship unlike to mixture homogenization law in fibre-reinforced composites, where a linear variation is expected. On the other hand, the experimental Young's moduli of composites are fulfilled within this range, 3000 to 6000 MPa, except the composite reinforced with W_f = 25% of fibres. Despite this single numerical deviation regarding the experimentation, that can be explained by the drawback of the analytical model for the high-volume fraction of fibre, $V_f \approx$ 35.05%, a longitudinal Young modulus of 3492.54 MPa is considered as an optimal solution throughout.

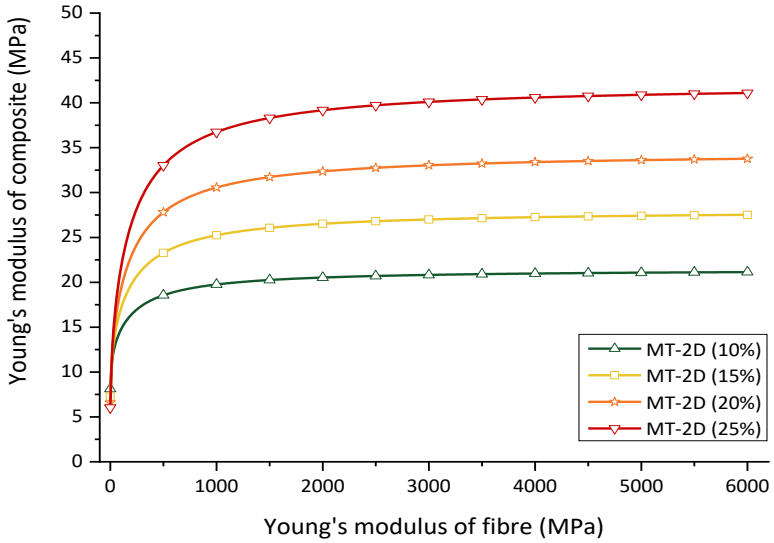

Fig. 9. Elastic longitudinal modulus of PVCAL composites versus the material property of fibres

5.2 Digital Processing of The Microstructure

Based on color shade, numerical image analyses are performed to define the arrangement of different phases of the microstructure for different weight fractions, see Fig. 10a. Numerical images are captured with sufficient resolution, until 3888 pixels, and converted into a simple binary image depicted in Fig. 10b. The final image has two colors, black and white, that define the two phases. In this work, the color black represents the matrix, and the fibres are white.

Errors and parasitic noise in a microstructure image are eliminated by more realistic processing of the microstructure image using thresholding and filtering image processing tools. A full description of the analysis of the real microstructure is provided by El-Moumen *et al*. [22]. The main image transformation operations can be summarized as follows:

- Threshold: to reduce the image to two colors black and white and to transform greyscale images into 8-bit binary images using a threshold, pixel values ranging from 0 to 255.
- Noise filter: to remove noise from an image.
- Generic filters: it removes and develops lighter white or darker black areas of the image by using dilate and erode.

The final image is used to provide numerical cartography of the processed microstructure. Data collected by Zebulon software is useful for generating numerical information which would allow for mapping and identification of the stiffness of the microstructure. The mechanical properties of fibres and matrix pixels at the interface of the regular mesh grid, can be distinguish by superposition of the integration points of each element on the material area. Fig. 4 shows the location of point's integration in quadrilateral four nodes element, when numerical integration scheme of 2×2 points is used. In this work, the multi-phase quadrilateral element PFR4M, developed in Section 2, has been applied with regular mesh for numerical simulations.

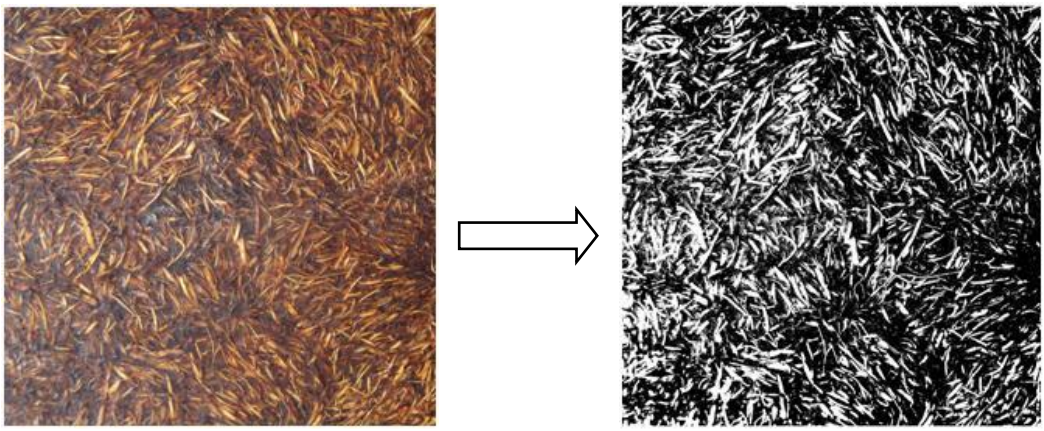

(a) (b)

Fig. 10. Numerical image processing of PVCAL composite (a) high resolution image of RVE, (b) greyscale image

6. Numerical Validation

The multiphase finite PFR4M element was implemented in the FE code Abaqus Standard via the user element subroutine UEL [31], (see Appendix) . The performance of the proposed model is analyzed trough the convergence test. Furthermore, the effect of reinforcement volume fraction and the size of the RVE on the elastic properties of PVCAL composite have been examined. The results obtained by the PFR4M element were compared with: experimental results, the classic four-node linear C2d4, the eight-node quadratic C2d8 multiphase elements [10], and the mean field model of Mori-Tanaka [9].

6.1 Effects of Mesh and Weight Fraction on Convergence Tests

Square random composite plates of PVCAL simply supported at one edge and subjected to unit pressure load at the opposite edge is analyzed with the proposed multiphase element. The analysis deals with a simulation of the tensile experimental test of the PVCAL material. Different weight fractions, 10%, 15%, 20% and 25% are analyzed considering plane stress hypothesis. The digital image processing for low fraction is conducted and rescaled using a size of 3888×3888 pixels, so that the pixel colour ratio relative to corresponding volume fraction of each microstructure can be achieved. However, the graphic treatment of crowded microstructures (W_f= 20% and 25%) is partially respected, the task was carried out meticulously without harming the real appearance of the microstructures. See Fig. 11.

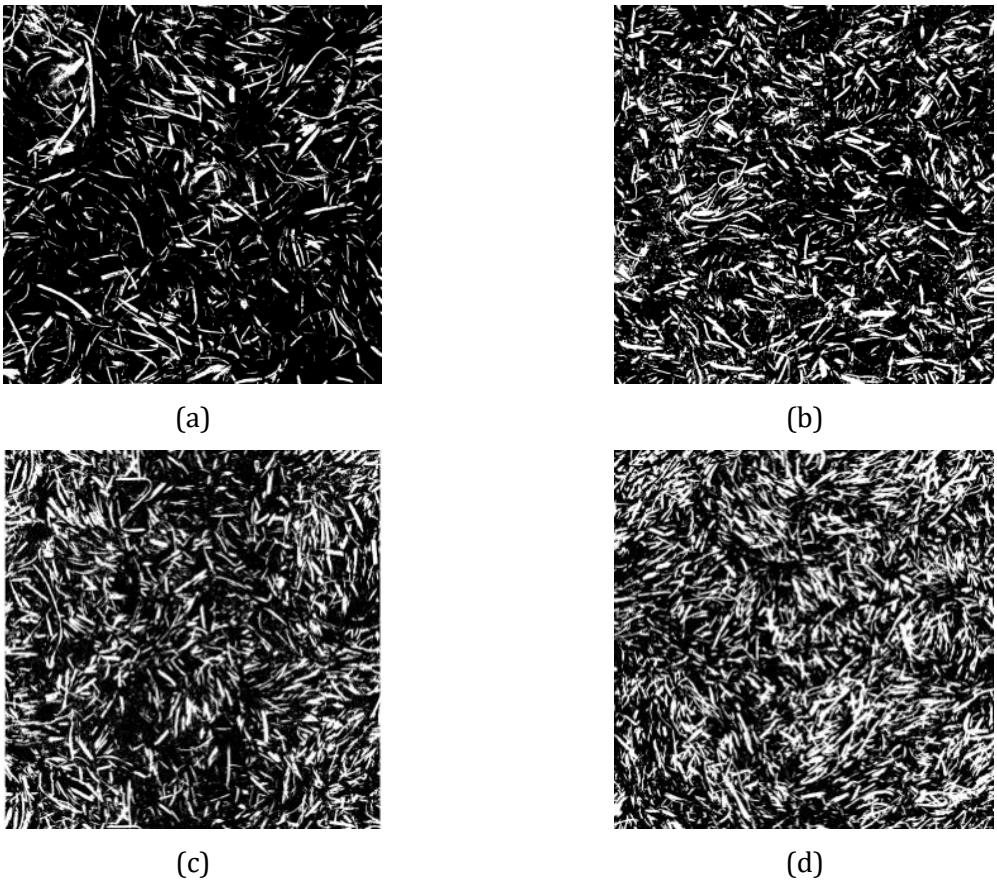

(a) (b)

(c) (d)

Fig. 11. Digitalized images for different weight fractions of fibre (a) W_f = 10%, (b) W_f = 15%, (c) W_f = 20%, (d) W_f = 25%

Numerical analysis is performed by increasing the number of elements from a course to very refined meshes, 2500 to 160000 elements. Mean values of longitudinal Young's modulus and Poisson ratio, computed and confronted to those obtained by C2d4 and C2d8 multiphase elements [10] are presented in Fig. 12 and Fig. 13. Fig. 12 and Fig. 13 show a great dependence between the convergence of results and the quality of the mesh and consequently by the number of DOF's. Young's moduli decrease with increasing number of elements. A monotonic convergence to both experimental and Mori-Tanaka results is observed. This property is not achieved for coarse mesh and requires at least 90000 elements for both PFR4M and C2d8 and more than 160000 elements for C2d4. On the other hand, the Poisson ratio results show ascending curves which increase versus the mesh refinement and converge towards slightly underestimate values. It is worth to note a good accuracy and agreement between the present element and C2d8. A discrepancy between these two elements and the standard linear element C2d4 cannot be ignored; this confirms again the improved performance of the present element, due to the additional higher order terms in displacement field, which already proved in previous work for isotropic materials [16,28].The

effect of the weight fraction on mechanical properties can be conducted through the numerical results using a refined mesh, see Table 2 and Table 3.

Regarding the Poisson' ratio and according to the analytical results, the Fig. 14b shows a slight slope and independence versus the weight fraction. However, numerical curves obtained by two multiphase elements depict lower values that are gradually decreased.

Table 2. Longitudinal Young's modulus as a function of the number of elements for different weight fractions.

		Mean values for the longitudinal Young's modulus (MPa)								
		Mesh						MT (3D)	MT (2D)	Exp.
Wf (%)	Element	50×50	100×100	150×150	200×200	300×300	400×400			
10	C2d4	41.752	35.480	31.712	28.841	26.186	24.896	20.912	25.260	19.402 ±1.887
	PFR4M	29.160	27.447	26.156	24.696	23.421	22.696			
	C2d8	31.837	27.176	25.703	24.247	22.956	22.013			
15	C2d4	114.819	77.821	58.102	49.260	40.018	35.244	27.148	34.617	27.547 ±3.608
	PFR4M	58.864	48.027	41.105	37.368	32.883	30.318			
	C2d8	64.571	47.663	39.854	35.120	30.757	28.396			
20	C2d4	143.098	99.109	75.481	60.442	47.233	42.003	33.239	44.468	39.187 ±5.798
	PFR4M	79.142	61.551	52.297	44.783	38.004	35.013			
	C2d8	92.690	59.091	47.064	41.340	35.760	32.899			
25	C2d4	332.472	212.228	147.733	104.825	72.250	59.153	40.377	55.199	59.997 ±11.800
	PFR4M	171.081	121.563	93.286	73.251	56.371	48.917			
	C2d8	182.445	106.017	76.110	60.856	49.822	44.628			

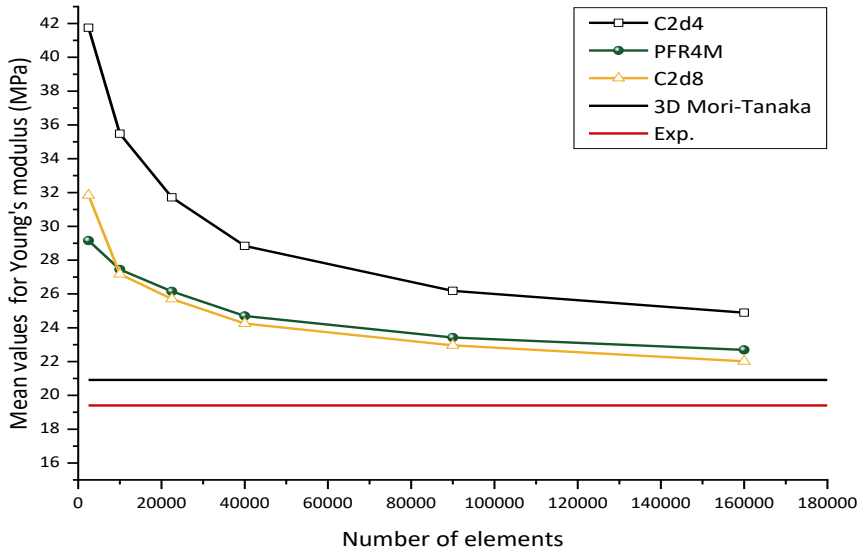

(a)

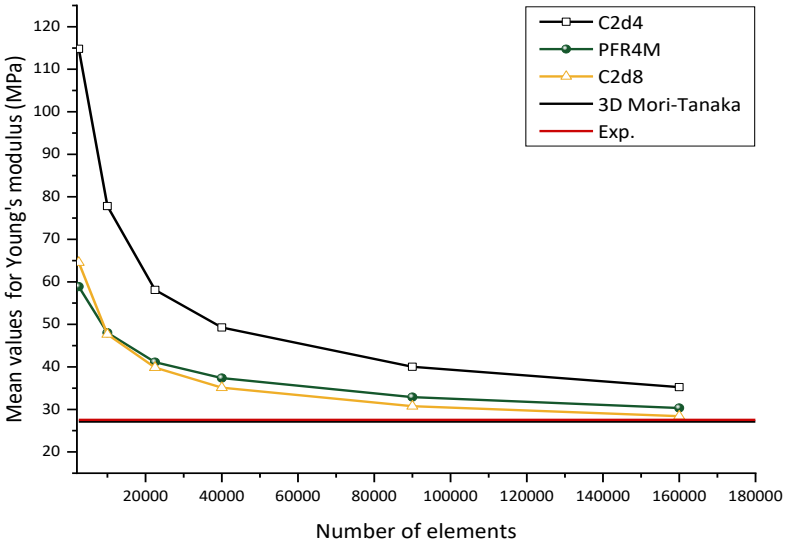

(b)

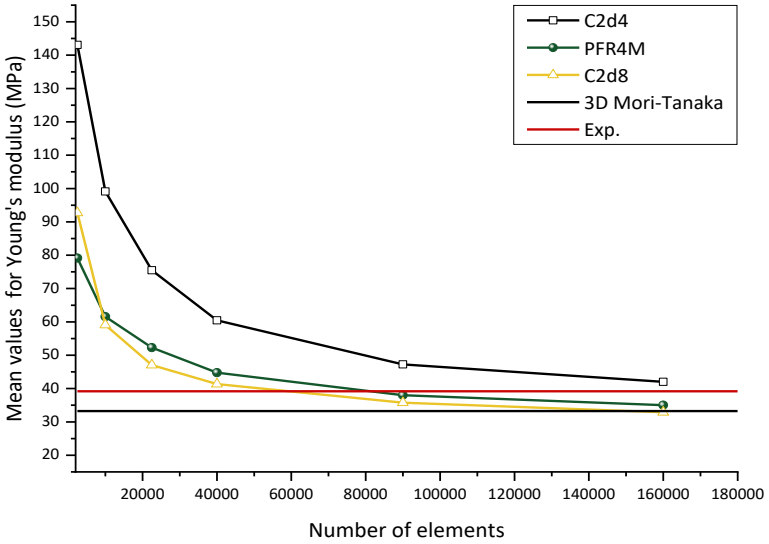

(c)

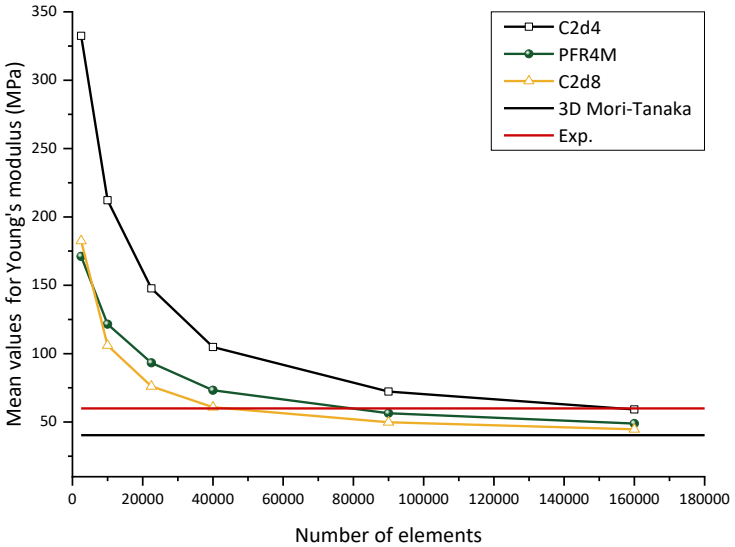

(d)

Fig. 12. Effect of mesh size on the longitudinal Young's modulus of PVCAL: convergence test (a) W_f = 10%, (b) W_f = 15%, (c) W_f = 20%, (d) W_f = 25%

These curves are like an inverse trigonometric function arctangent with negative slope and inflection point at W_f = 17%. This can be explained by the descendant relationship between the Poisson ratio and the aspect ratio of fibres considered in Mori-Tanaka model, included in Eshelby tensor. One can deduce that the increase of the volume fraction in RVE images implies the adhesion of the neighboring pixels and reveals therefore a different aspect ratio of fibres, inadequately.

Table 3. Poisson's ratio as a function of the number of elements for different weight fractions.

		Mean values of Poisson ratio							
		Mesh						MT (3D)	MT (2D)
Wf (%)	Element	50×50	100×100	150×150	200×200	300×300	400×400		
10	C2d4	0.312	0.350	0.372	0.388	0.401	0.410	0.468	0.416
	PFR4M	0.403	0.415	0.418	0.426	0.427	0.431		
	C2d8	0.373	0.395	0.409	0.414	0.422	0.427		
15	C2d4	0.302	0.325	0.353	0.373	0.392	0.405	0.463	0.402
	PFR4M	0.391	0.395	0.416	0.424	0.428	0.433		
	C2d8	0.328	0.379	0.398	0.408	0.420	0.427		
20	C2d4	0.192	0.248	0.256	0.280	0.303	0.317	0.458	0.394
	PFR4M	0.293	0.331	0.327	0.344	0.349	0.354		
	C2d8	0.246	0.287	0.307	0.321	0.336	0.343		
25	C2d4	0.213	0.254	0.270	0.291	0.307	0.322	0.454	0.388
	PFR4M	0.291	0.321	0.331	0.341	0.348	0.359		
	C2d8	0.255	0.292	0.313	0.325	0.344	0.354		

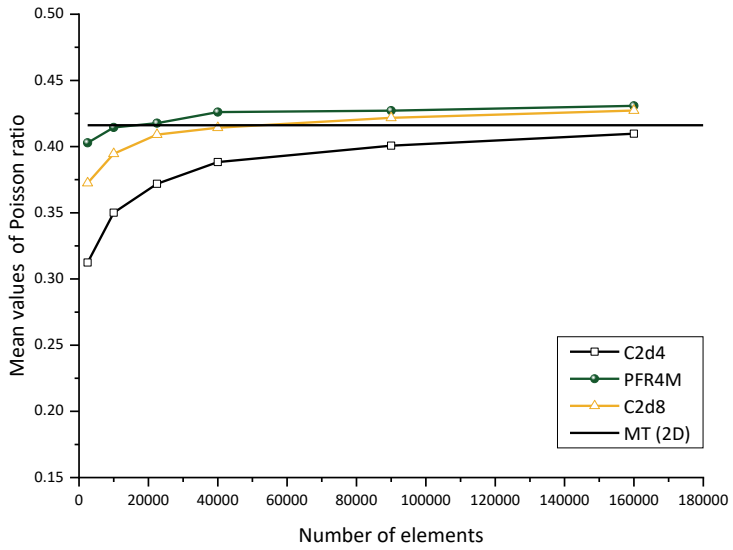

(a)

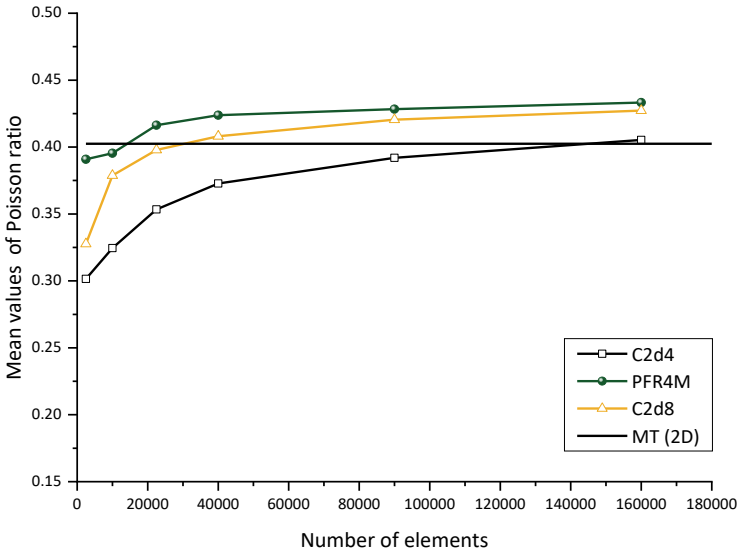

(b)

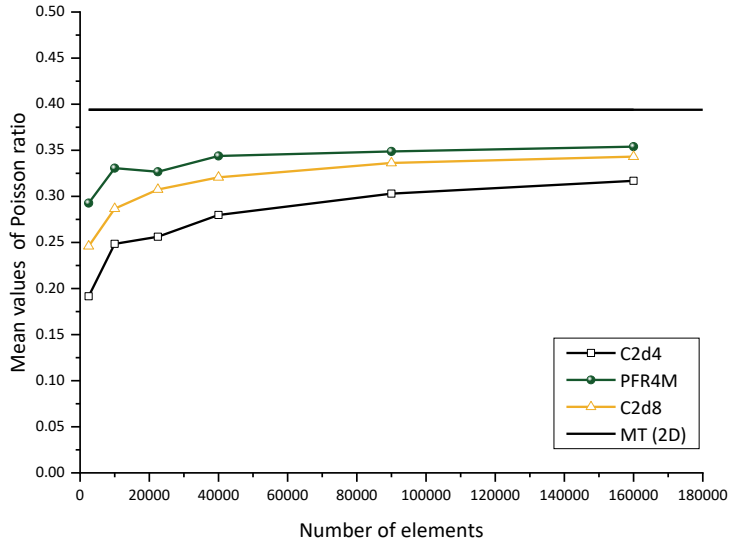

(c)

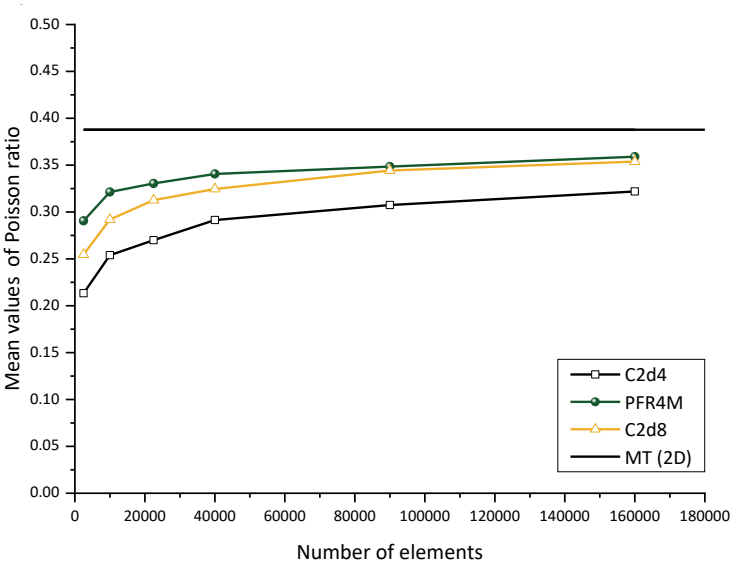

(d)

Fig. 13. Effect of mesh size on Poisson ratio of PVCAL: convergence test (a) W_f = 10%, (b) W_f = 15%, (c) W_f = 20%, (d) W_f = 25%

Fig. 14 presents the longitudinal Young's modulus and Poisson's ratio for all examined volume fractions, comparing the obtained results with both experimental data and the Mori-Tanaka model. It can be seen form Fig. 14a, that the longitudinal Young's modulus is strongly affected by the increase of the weight fraction and present a linear proportional relationship, at least in the analyzed range. In case of low volume fractions, the results of the longitudinal Young's modulus obtained by PFR4M and C2d8 are close to those of the experimental and Mori-Tanaka models. However, the present element provides better accuracy than the linear C2d4 element. This can be explained by the quadratic interpolation of displacement field of the PFR4M, which leads as well as the C2d8, to a linear strain rather than constant. On the other hand, the superiority of C2d8 is not only due to the large number of the interpolation nodes, but also to the extra integration points required in exact integration scheme, i.e. 3×3 points.

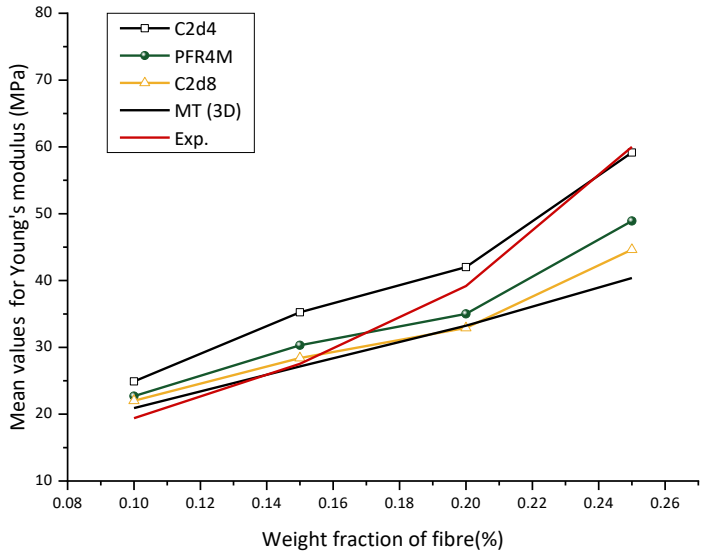

(a)

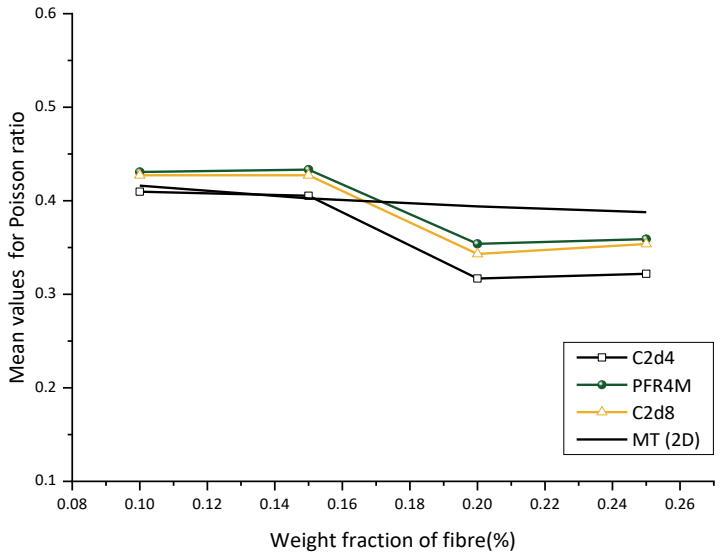

(b)

Fig. 14. Mechanical properties versus weight fraction. (a) Longitudinal Young's modulus. (b) Poisson ratio

An abundance of integration points in the C2d8 element reflects a better shift in the discontinuous mechanical properties of constituent materials in the same multiphase element. At higher volume

fractions, this performance is confirmed again except for W_f = 25% where a large standard deviation in experimental test is noticed. Furthermore, the performance of the PFR4M element is confirmed against the C2d4 element. This exception can be explained by a real large overlapping area of fibre which cannot be considered in the numerical assessment of the local stiffness regardless the type of multiphase element. By contrast, the overlapping in RVE has been avoided in the analytical mean field method. It should be noted that the image of the experimental specimen often does not lead to a good representative surface element at large fractions [22].

6.2 Statistical Analysis of RVE Size

This section presents a statistical analysis employed to determine the representative volume element (RVE) size for date palm fibre-reinforced PVC composites. The study assesses the elastic properties (Young's modulus and Poisson's ratio) of the composites using a combination of variance-based method and Monte Carlo simulations, with five microstructural realizations for each RVE size and across different weight fractions of fibre reinforcement. The variance (Eq. (26)) in elastic properties is computed for each configuration to ensure that the RVE size captures the material's mechanical behavior reliably and efficiently. The study is conducted over five different weight fractions of fibre reinforcement, including 5%, 10%, 15%, 20%, and 25% by weight, to investigate how the RVE size and elastic properties vary with fibre content. For each fibre weight fraction, the RVE size is varied, and the following steps are carried out:

- Multiple RVEs of increasing sizes (from 20×20 to 3500×3500 pixels) are created to represent different regions of the composite microstructure. For instance, different RVE sizes in the middle of the microstructure for low weight fraction of fibre (W_f = 10%), are shown in Fig. 15.
- For each RVE size and fibre weight fraction, five different realizations of the microstructure are generated. These realizations account for the random orientation and plane distribution of the fibres. Realizations for all weight fractions of VER of size 1000×1000 pixels are depicted in Fig. 16.

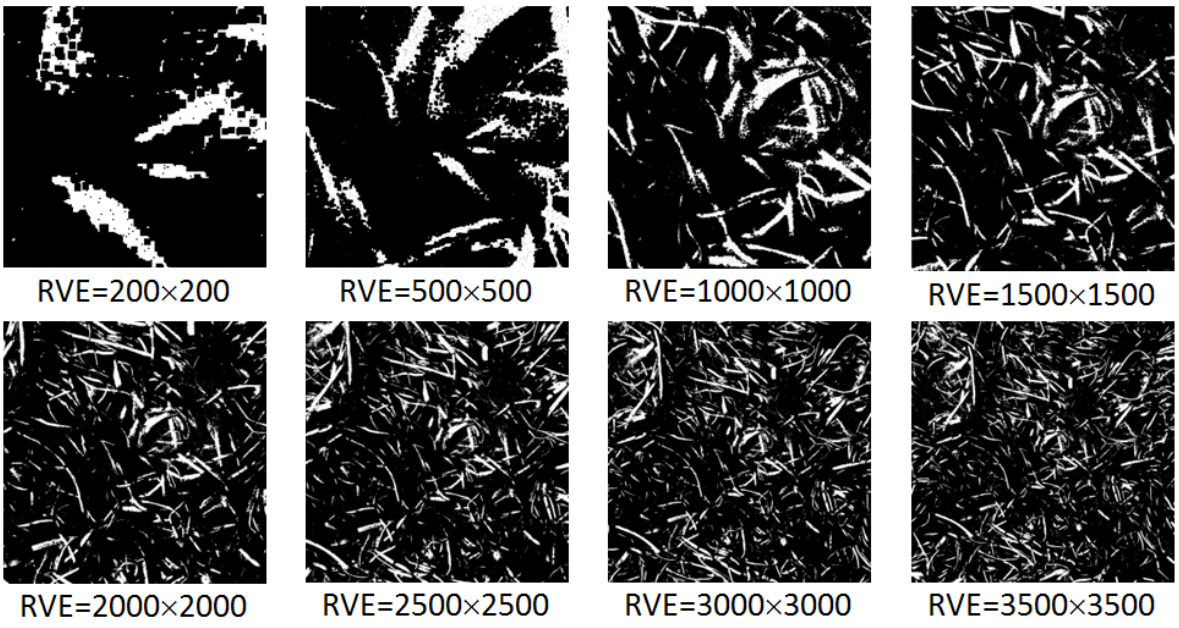

Fig. 15.Different RVE sizes of microstructure (Pixels), W_f=10%, RVE in the middle

- Using finite element analysis (FEA), the Young's modulus and Poisson's ratio are computed for each realization at each RVE size and each weight fraction.
- For each RVE size and weight fraction, the variance of the elastic properties is computed across the five realizations. The variance is given by:

$$\sigma^2 = \frac{1}{N}\sum_{i=1}^{N}(P_i - \bar{P})^2, \qquad N = 5 \tag{26}$$

Where P_i is the individual elastic property in the i realization and $\overline{P}$ is the mean value.

The elastic properties of the treated materials are shown in Fig. 17 and Fig. 18. An oscillating discrepancy between the numerical and experimental results can be observed where the size of RVE is less than 2500×2500. A fluctuation is shown in the mean values of Young's modulus and a slight bias is observed through the Poisson's ratio curves of C2d4, PFR4M elements. This can be explained by the large contrast between the elastic properties of matrix and reinforcement E_f/ E_m = 332 that could lead to a significant deviation in arithmetic average results for almost realizations of small RVE' size. On the other hand, at very low weight fractions, fluctuations in the computed effective properties are relatively small and increase suddenly with increasing weight fraction. This is because the reinforcements are widely spaced and their distribution is relatively uniform and the fibre interactions are minimal. The matrix material dominates the overall behavior of the composite, and local variations in reinforcement distribution do not have strong impact.

However, it can also be noted that the confidence intervals decrease with increasing the RVE's size and tend towards small values. On the other hand, regarding the Young's moduli, PFR4M element gives closer results to the MT-3D than C2d4, whereas its performance about the computing the Poisson ratios is confirmed only for height weight fraction if the MT-2D is considered. However, all results are generally bounded by experimental and analytical models and the standard deviations remain lower than 5% for RVE Sizes greater than 3000×3000 pixels. This such confidence level means that five realizations are sufficient to estimate accurately this elastic property.

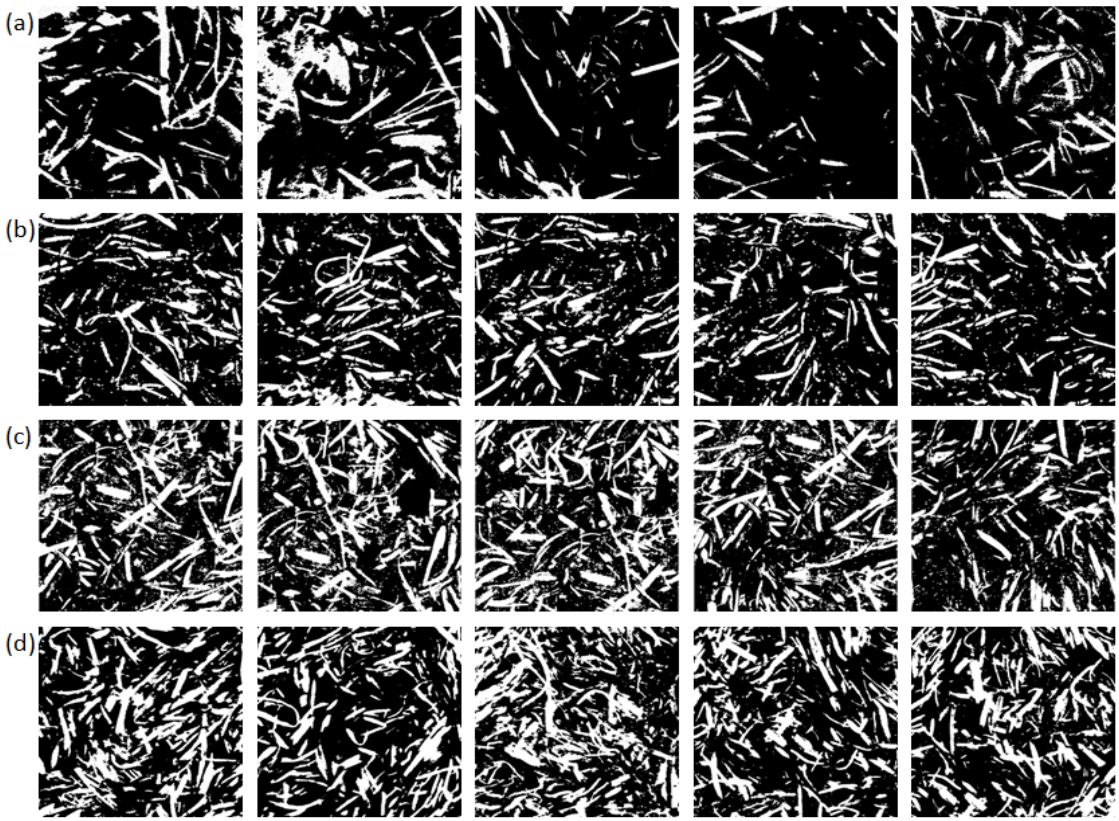

Fig. 16.Realizations of microstructure for RVE' size 1000×1000 pixels, and weight fractions of fibres: (a) W_f = 10%, (b) W_f = 15%, (c) W_f = 20%, and (d) W_f = 25%

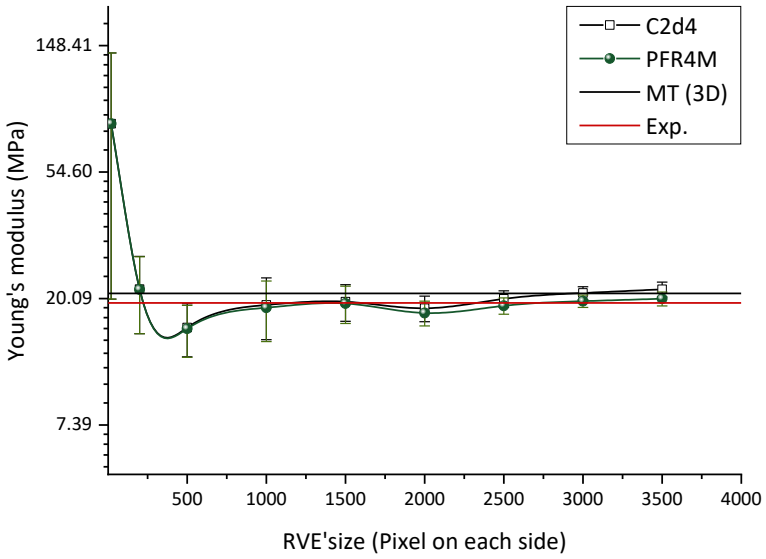
C2d4
PFR4M
MT (3D)
Exp.
148.41
54.60
20.09
7.39
Young's modulus (MPa)
500
1000
1500
2000
2500
3000
3500
4000
RVE'size (Pixel on each side)

(a)

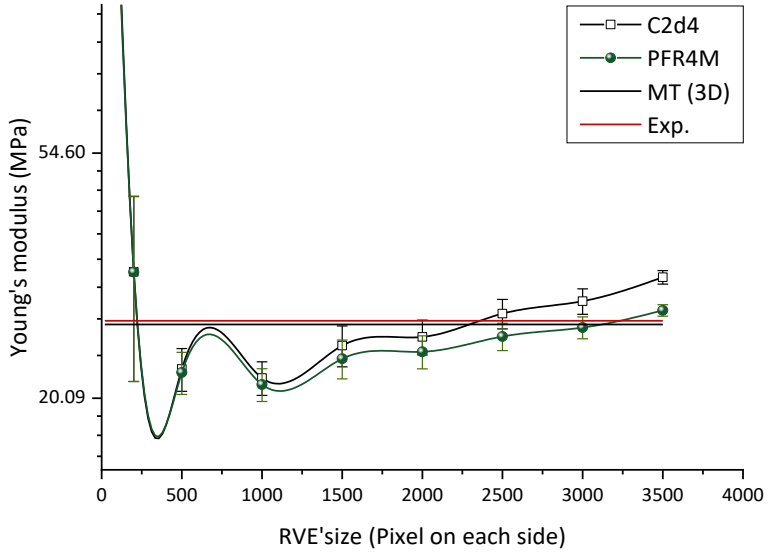
C2d4
PFR4M
MT (3D)
Exp.
54.60
20.09
Young's modulus (MPa)
0
500
1000
1500
2000
2500
3000
3500
4000
RVE'size (Pixel on each side)

(b)

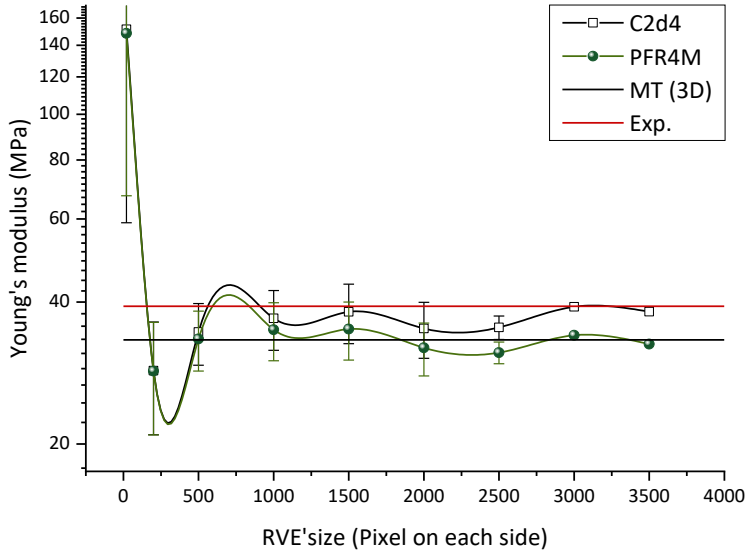
C2d4
PFR4M
MT (3D)
Exp.
160
140
120
100
80
60
40
20
Young's modulus (MPa)
0
500
1000
1500
2000
2500
3000
3500
4000
RVE'size (Pixel on each side)

(c)

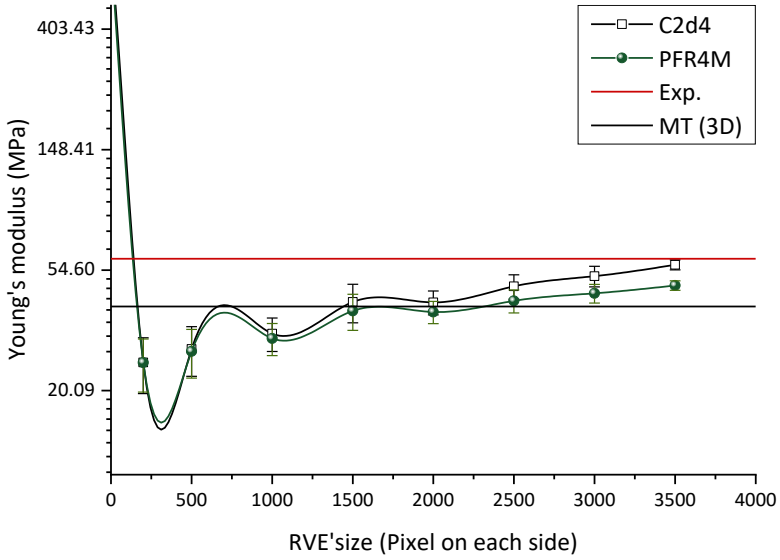

(d)

Fig. 17.Mean values of the longitudinal Young's modulus versus the RVE size (a) W_f = 10%, (b) W_f = 15%, (c) W_f = 20%, (d) W_f = 25%

This agrees well with recommendation reported by Kanit et al. [38] and confirmed by the low variance values, assumed that the composite's properties can be determined either by a small number of realizations on bigger volumes or by many realizations for low volumes. The main characteristic of an RVE is the minimum sample size that allows for the determination of the effective property of the composite. To ensure this, the RVE must satisfy two conditions. The first is the condition of ergodicity, which means that the average properties of a medium no longer change as the sample size increases. This variation is represented on the *x*-axis in Figures 17 and 18. The second is the condition of stationarity, which is reflected by the consistency of the average property across different samples of the same size. This is represented by the variance values in Figures 17 and 18. The application of this principle to the results from the different samples, presented in Figures 17 and 18, clearly shows that from a size of 2500x2500 pixels, the averages of the effective properties stabilize with very low variances. This allows concluding that the RVE size in this case is approximately 2500×2500 pixels. The proposed element shows excellent convergence towards the effective property for all the considered configurations, clearly demonstrating its effectiveness in solving these homogenization problems.

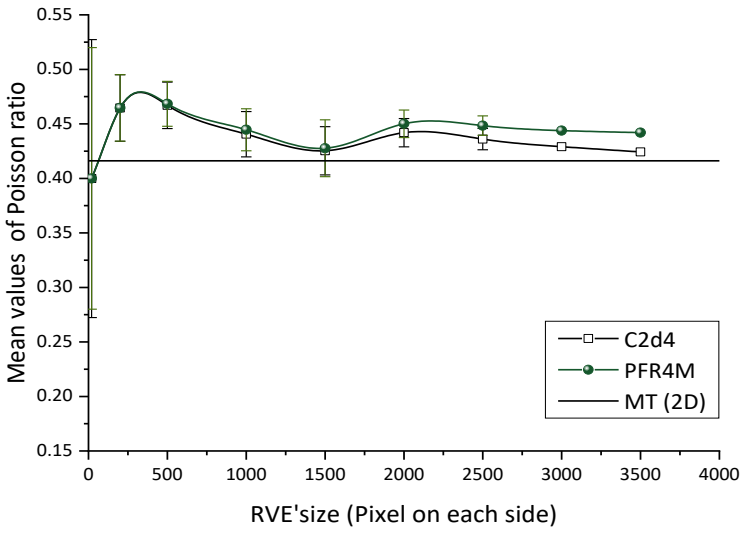

(a)

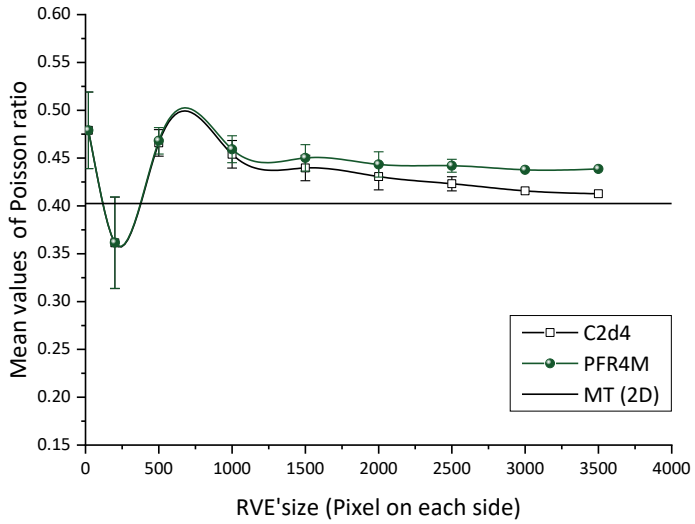

(b)

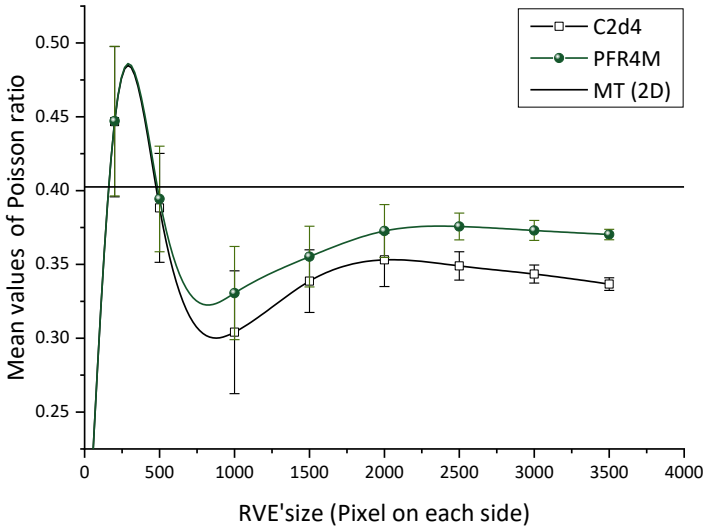

(c)

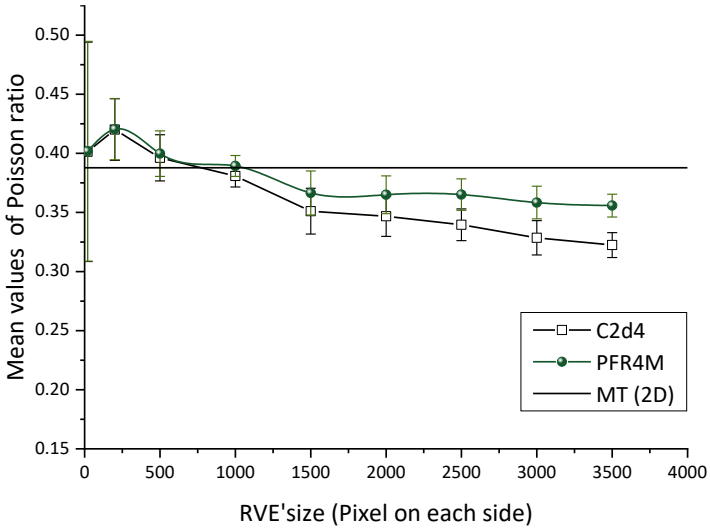

(d)

Fig. 18.Mean values of the Poisson ratio versus the RVE size (a) W_f = 10%, (b) W_f = 15%, (c) W_f = 20%, (d) W_f = 25%

7. Conclusion

New 4-node multiphase finite quadrilateral element is developed and implemented in Abaqus software to assess the elastic properties of date palm fibre reinforced PVC composite. The performance tests of the proposed element were performed through a set of numerical tests that revealed: an excellent convergence to the effective elastic properties was achieved by a mesh of the microstructure greater than or equal to 300×300 elements. The effectiveness of the PFR4M modelling was like the 8-node quadratic element and comparable to the MT -2D mean field homogenization model. The convergence's rate is an improvement over the 4-node classical finite element C2d4 [10] which is used in most previous studies, for instance in the virtual microstructure treated by Bourih et al. [39], among others. The additional degree of freedom per node relatively increases the problem size, nevertheless the use of this type of element remains essential in the assembly with beam and shell structures, according to Zouari et al. [16]. On the other hand, it is found that the large contrast between the mechanical properties of the matrix and the vegetal reinforcement significantly affects the findings of effective properties, factor that brings about fluctuations at small RVE size. From a size of 2500×2500 pixels, the averages of the effective properties stabilize with very low variances. Furthermore, as the weight fraction of reinforcement increases, the interactions between fibres increase. This leads to phenomena like clustering and overlapping of fibres which affect local properties. Ultimately, the kinematic potential of the present element related to its rotational degree of freedom gives opportunity, in future investigation to analyse the bending behaviour of composite materials with random reinforcements.

Nomenclature

Materials

PVC	Polyclorer vinyl chloride
PVCA	Polyclorer vinyl chloride with additives
PVCAL	Date palm fibre reinforced PVCA composite
ζ	Fibre aspect ratio

Equivalent-continuum model and composite

$<A_f>$	Dilute mechanical strain concentration tensor of fibre
C_f	Elastic stiffness tensor of fibre
C_m	Elastic stiffness tensor of matrix
E	Young's modulus
I	Identity tensor

Finite elements (FE)

C2d4	Classical 4-node linear element (Zebulon 8.4 software) [10]
C2d8	Classical 8-node quadratic element (Zebulon 8.4 software) [10]
DOF	Degree of freedom
Exp.	Experimental result.
MT	Mori-Tanaka Method [9,11].
MT-2D	Mori-Tanaka homogenization 2D model used to predict the elastic behavior (in -plane random orientation of fibres)
MT-3D	Mori-Tanaka homogenization 3D model used to predict the elastic behavior (Spatial random orientation of fibres).
MF	Mean Field methods [5]
PF	Projected fibre concept [12]
PFQ4	Projected fibre element based on combination of C2d4 and two-node truss element [13]
PFQ4R	Projected fibre element based on combination of 4-node PFR4 and 2-node Timoshenko plane beam.
PFQ4R*	Projected fibre element based on combination of 4-node PFR4 and 2-node Timoshenko plane beam [14]
PFR	Plane fibre rotation concept [15]
PFR4	4-node quadrilateral element based on plane fibre rotation concept [16]
PFR4M	Multiphase 4-node quadrilateral element based on plane fibre rotation
PFT	Projected fibre element based on combination of 3-node triangular element and 2-node truss element [12]
SFR	Space Fibre Rotational concept [15]
PFT	Projected fibre element based on combination of 3-node triangular element and 2-node truss element

Acknowledgments

This work was supported and funded by the Directorate General for Scientific Research and Technological Development (DGRSDT). The authors would like to thank the plastics laboratory technical staff of Biskra cable industry for its help in the formulation and material design.

References

[1] Sreadha AR, Pany C. Review on fabrication of bamboo composite materials reinforced concrete. J Sci Technol 2020;5:258–79. https://doi.org/doi.org/10.46243/jst.2020.v5.i3.pp258-279

[2] Benchouia HE, Boussehel H, Guerira B, Sedira L, Tedeschi C, Becha HE, et al. An experimental evaluation of a hybrid bio-composite based on date palm petiole fibers, expanded polystyrene waste, and gypsum plaster as a sustainable insulating building material. Constr Build Mater 2024;422:135735.

[3] Elouaer A. Contribution à la compréhension et à la modélisation du comportement mécanique de matériaux composites à renfort en fibres végétales. PhD, University of Reims Champagne-Ardenne, 2011.

[4] Sreadha AR, Pany C. Static, free vibration and buckling analysis of composite panels; a review. Adv J Grad Res 2021;9:21–45.

[5] Eshelby JD. The determination of the elastic field of an ellipsoidal inclusion, and related problems. Proc R Soc London Ser A Math Phys Sci 1957;241:376–396. https://doi.org/10.1098/rspa.1957.0133.

[6] Voigt W. Ueber die Beziehung zwischen den beiden Elasticitätsconstanten isotroper Körper. Ann Phys 1889;274:573–587. https://doi.org/10.1002/andp.18892741206.

[7] Reuss A. Berechnung der fließgrenze von mischkristallen auf grund der plastizitätsbedingung für einkristalle. ZAMM-Journal Appl Math Mech Für Angew Math Und Mech 1929;9:49–58. https://doi.org/10.1002/zamm.19290090104.

[8] Hashin Z, Shtrikman S. A variational approach to the theory of the elastic behaviour of multiphase materials. J Mech Phys Solids 1963;11(2):127–140. https://doi.org/10.1016/0022-5096(63)90060-7.

[9] Mori T, Tanaka K. Average stress in matrix and average elastic energy of materials with misfitting inclusions. Acta Metall 1973;21:571–574. https://doi.org/10.1016/0001-6160(73)90064-3.

[10] Z-set User commands handbook, Version 9.1

[11] Benveniste Y. A new approach to the application of Mori-Tanaka's theory in composite materials. Mech Mater 1987;6:147–157. https://doi.org/10.1016/0167-6636(87)90005-6.

[12] Kebir H, Ayad R. A specific finite element procedure for the analysis of elastic behaviour of short fibre reinforced composites. The Projected Fibre approach. Compos Struct 2014;118:580–588. https://doi.org/10.1016/j.compstruct.2014.07.046.

[13] Tiar A, Zouari W, Kebir H, Ayad R. A nonlinear finite element formulation for large deflection analysis of 2D composite structures. Compos Struct 2016;153:262–270. https://doi.org/10.1016/j.compstruct.2016.05.102.

[14] Zouari W, Kebir H, Assarar M, Ghomari T, Ayad R. Numerical modelling of 2D composite solids accounting for local fibre bending stiffness. Compos Struct 2020;244:112289. https://doi.org/10.1016/j.compstruct.2020.112289.

[15] Ayad R. Contribution to the numerical modeling of solids and structures and the non-newtonian fluids forming process. 2002.

[16] Zouari W, Hammadi F, Ayad R. Quadrilateral membrane finite elements with rotational DOFs for the analysis of geometrically linear and nonlinear plane problems. Comput Struct 2016;173:139–149. https://doi.org/10.1016/j.compstruc.2016.06.004.

[17] Herrera-Solaz V, Patriarca L, Foletti S, Segurado J, Niffenegger M. Microstructure-based modelling and Digital Image Correlation measurement of strain fields in austenitic stainless steel 316L during tension loading. Mater Sci Eng A 2019;751:99–106.

[18] Mishnaevsky Jr LL. Automatic voxel-based generation of 3D microstructural FE models and its application to the damage analysis of composites. Mater Sci Eng A 2005;407:11–23. https://doi.org/10.1016/j.msea.2005.06.047.

[19] Pany C, Li G. Application of periodic structure theory with finite element approach. Front Mech Eng 2023;9:1192657.

[20] Mishnaevsky Jr L, Lippmann N, Schmauder S. Computational design of multiphase materials at the mesolevel. ASME Int. Mech. Eng. Congr. Expo. Novemb. , 2001, p. 11–16.

[21] Sukiman MS, Kanit T, N'Guyen F, Imad A, Moumen A El, Erchiqui F. Effective thermal and mechanical properties of randomly oriented short and long fiber composites. Mech Mater 2017;107:56–70. https://doi.org/10.1016/j.mechmat.2017.02.002.

[22] El Moumen A, Imad A, Kanit T, Hilali E, El Minor H. A multiscale approach and microstructure design of the elastic composite behavior reinforced with natural particles. Compos Part B Eng 2014;66:247–254. https://doi.org/10.1016/j.compositesb.2014.05.008.

[23] Djebara Y, El Moumen A, Kanit T, Madani S, Imad A. Modeling of the effect of particles size, particles distribution and particles number on mechanical properties of polymer-clay nano-composites: Numerical homogenization versus experimental results. Compos Part B Eng 2016;86:135–142. https://doi.org/10.1016/j.compositesb.2015.09.034.

[24] Benhizia A, Kanit T, Outtas T, Madani S, Imad A. Computation of effective behavior of isotropic transverse composite in nonlinear problems. Mech Res Commun 2014;59:6–13. https://doi.org/10.1016/j.mechrescom.2014.03.005.

[25] Kanit T, Forest S, Galliet I, Mounoury V, Jeulin D. Determination of the size of the representative volume element for random composites: statistical and numerical approach. Int J Solids Struct 2003;40:3647–3679. https://doi.org/10.1016/S0020-7683(03)00143-4.

[26] Ayadi A, Meftah K, Sedira L. Elastoplastic analysis of plane structures using improved membrane finite element with rotational DOFs: Elastoplastic analysis of plane structures. Frat Ed Integrità Strutt 2020;14:148–162. https://doi.org/10.3221/IGF-ESIS.52.13.

[27] Meftah K, Zouari W, Sedira L, Ayad R. Geometric non-linear hexahedral elements with rotational DOFs. Comput Mech 2016;57:37–53. https://doi.org/10.1007/s00466-015-1220-8.

[28] Meftah K, Sedira L. A four-node tetrahedral finite element based on space fiber rotation concept. Acta Univ Sapientiae, Electr Mech Eng 2019;11:67–78. https://doi.org/10.2478/auseme-2019-0006.

[29] Hiriyur B, Waisman H, Deodatis G. Uncertainty quantification in homogenization of heterogeneous microstructures modeled by XFEM. Int J Numer Methods Eng 2011;88:257–78. https://doi.org/10.1002/nme.3174.

[30] Cunha VMCF, Barros JAO, Sena-Cruz JM. A finite element model with discrete embedded elements for fibre reinforced composites. Comput Struct 2012;94:22–33. https://doi.org/10.1016/j.compstruc.2011.12.005.

[31] Abaqus Version 6.9. Analysis User's Manual, volume VI : User Subroutines and Parametric Studies. Dassault Systèmes Simulia Corp; 2009.

[32] Lippmann N, Steinkopff T, Schmauder S, Gumbsch P. 3D-finite-element-modelling of microstructures with the method of multiphase elements. Comput Mater Sci 1997;9:28–35. https://doi.org/10.1016/S0927-0256(97)00055-4.

[33] Kaddouri W, El Moumen A, Kanit T, Madani S, Imad A. On the effect of inclusion shape on effective thermal conductivity of heterogeneous materials. Mech Mater 2016;92:28–41. https://doi.org/10.1016/j.mechmat.2015.08.010.

[34] Masmoudi M, Kaddouri W, Kanit T, Madani S, Ramtani S, Imad A. Modeling of the effect of the void shape on effective ultimate tensile strength of porous materials: Numerical homogenization versus experimental results. Int J Mech Sci 2017;130:497–507. https://doi.org/10.1016/j.ijmecsci.2017.06.011.

[35] Djebloun Y, Hecini M. Phisycal and Thermomechanical Characteristics of Epoxy Biocomposites Laminates Reinforced by Mat of Date Palm Tree Fibers. J Compos Adv Mater Des Compos Des Matériaux Avancés 2022;32. https://doi.org/10.18280/rcma.320603.

[36] Christophe B. Fibres naturelles de renfort pour matériaux composites. Éditions Tech l'Ingénieur 2013;249.

[37] Odegard GM, Gates TS, Wise KE, Park C, Siochi EJ. Constitutive modeling of nanotube–reinforced polymer composites. Compos Sci Technol 2003;63:1671–1687. https://doi.org/10.1016/S0266-3538(03)00063-0.

[38] Kanit T, N'Guyen F, Forest S, Jeulin D, Reed M, Singleton S. Apparent and effective physical properties of heterogeneous materials: Representativity of samples of two materials from food industry. Comput Methods Appl Mech Eng 2006;195:3960–3982. https://doi.org/10.1016/j.cma.2005.07.022.

[39] Bourih A, Bourih K, Kaddouri W, Masmoudi M, Madani S. Modeling of the Pore Shape Effect on the Effective Young's Modulus of Lotus-Type Porous Materials by a Numerical Homogenization Technique. Adv Mater Res 2022;1171:73–86.

Appendix

Flow char of interface between ABAQUS, UEL and Zmech module

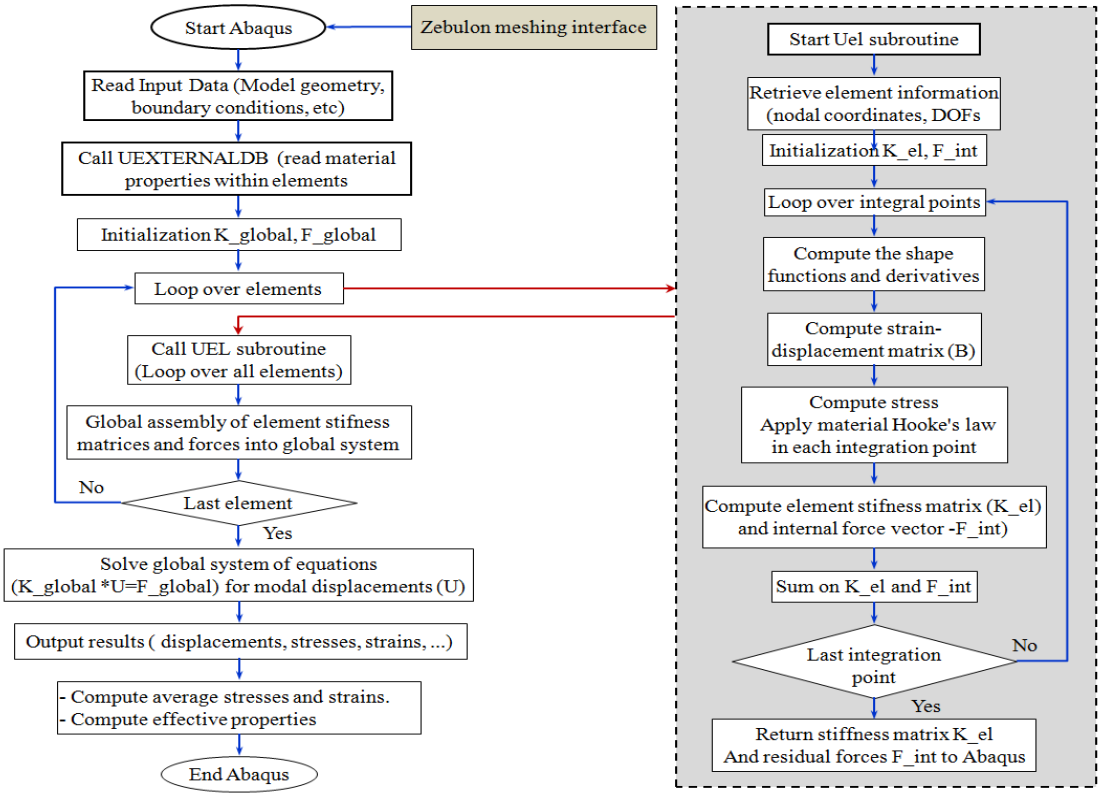

Blank Page

Research on Engineering Structures & Materials
www.jresm.org
Research Group

Research Article

Prediction of machine learning application in the development of novel sustainable self-compacting geopolymer concrete

Arun B R [1,a], Srishaila J M [2,b], Md Khalid S [*,3,c], Veerabhadrappa Algur [4,d], Kavyashree K [5,e], Tanu HM [3,f]

[1]*Department of Civil Engineering, Dr.AIT, Bangalore, 560072, Karnataka, India*
[2]*Department of Civil Engineering, SJMIT, Chitradurga, 577501, Karnataka, India*
[3]*Department of Civil Engineering, Ballari Institute of Technology and Management, Ballari, 583104, Karnataka, India*
[4]*Department of Mechanical Engineering, RYMCE, Ballari,583104, Karnataka, India*
[5]*Department of Civil Engineering, GPT, Mulbagal, 563131, Karnataka, India*

Article Info

Article History:

Received 16 July 2024
Accepted 21 Nov 2024

Keywords:

Self-compacting geopolymer concrete;
Scanning electron microscope;
Manufactured sand;
Metakaolin;
Ground-granulated blast furnace slag;
Molarity

Abstract

This work conducted experimental research into the flow and mechanical characteristics of self-compacting geopolymer concrete (SCGC) made from ecologically beneficial byproducts of industry such as ground granulated blast furnace slag (GGBFS) and metakaolin (MK). Through trial and error, the mix's proportion of self-compacting geopolymer concrete (SCGC) was determined. The mass fraction of GGBFS with metakaolin was varied by 0%, 10%, 20%, and 30% by mass for all molarities, including 8M, 10M, and 12M. The superplasticizer (S.P.) dose of 1.5% and the fluid-to-binder (F/B) ratio of 0.37 by mass were held constant for each mix percentage, with the extra water content being changed correspondingly. Workability properties were assessed in addition to mechanical properties, which comprised compressive strength, split tensile strength, flexural strength, shear strength, and impact strength. The application of machine learning algorithms to forecast the compressive strength of SCGC is the focus of this study. Specifically, Random Forest (RF), Gradient Boost, and Extreme Gradient Boost (XGB) are utilized. Different success measures, like Root mean squared error (RMSE), mean squared error (MSE), mean absolute error (MAE), and R-squared (R^2), are used to judge these methods. The Gradient Boost model outperforms the others, achieving an R^2 score of 0.934 on training data and 0.929 on test data, showcasing its precision and accuracy. The success of the Gradient Boost model can be attributed to its incorporation of randomness and ensemble diversity, making it a powerful tool for predicting compressive strength in various scenarios.

© 2025 MIM Research Group. All rights reserved.

1. Introduction

The constant winds of change are ever-present in the field of environmental sustainability and design, where carbon dioxide emissions monitoring is used as a comparison metric. The speed with which this change is occurring within our sphere of influence is particularly disturbing. The dominant ideologies that have guided the development of our economy and manufacturing have recently shown signals of extreme unsustain ableness. Our modern world has been shaped in fundamental and widespread ways through the ecological reverberations caused by the unstoppable rise of population and the relentless advance of urbanization. Understanding this

*Corresponding author: khalid.s@bitm.edu.in
[a]orcid.org/0000-0003-3455-8910;[b]orcid.org/0000-0001-6161-9542; [c]orcid.org/0000-0002-4728-099X; [d]orcid.org/0000-0001-6094-6197; [e]orcid.org/0009-0006-0112-3370; [f]orcid.org/0000-0001-9760-9469.
DOI: http://dx.doi.org/10.17515/resm2024.354ma0716rs

complex transition requires analyzing its constituent parts, with due consideration provided to both past data and anticipated future tendencies. Ordinary concrete is a composite miracle in the world of building supplies, consisting of just 12% cement, 8% mixing water, and 80% aggregate. This means that every year, in addition to the astonishing 1.6 billion tons of cement produced worldwide [1], the concrete industry consumes almost 10 billion tons of sand and rock, along with a billion tons of mixing water. The concrete industry is the undisputed giant, using a massive 12.6 billion tons of raw materials every year, making it the world's top natural resource consumer [2]. Cement, the immovable foundation of conventional concrete, is seeing a surge in demand as a result of rising concrete demand. With the unstoppable storm of population growth and the relentless gears of industrialization, the shadow of pollution resulting from cement manufacture grows larger by the year. Unfortunately, cement production is expected to increase from its current 7% of global CO_2 emissions to 17% in the future. At the crossroads of a rapidly expanding sector of construction and a need for environmental stability, a search for harmony begins. Because of this, the cement industry must go beyond its existing narrative, which is centered on increasing cement replacement levels and expanding the use of industrial by-products as SCMs. People are calling for a big change to get rid of cement and instead synthesize new materials that are better for the environment and use less energy [3]. The invention of geopolymer concrete marked a new era in the industry, one that eliminated dealing with the massive fuel costs associated with traditional high-temperature kilns. When compared to the emissions created by one ton of Portland cement, the 0.18 tons of CO_2 produced by the burning of carbon fuel per ton of Geopolymeric cement is a significant improvement. With the development of self-compact geopolymer technology, a novel, non-conventional, cement-free binder has emerged, a wonder that self-compacts without segregation, flowing seamlessly into every corner, undisturbed by obstructive barriers, and embracing formwork with remarkable ease [4].

Metakaolin is widely recognized as a key raw material in the synthesis of geopolymers due to the substantial contributions it makes to our understanding of the material because of the high concentrations of SiO_2 and Al_2O_3 it contains[5]–[7]. In a chemical synergy, calcium hydroxide and metakaolin combine forces to generate hydrated calcium aluminates and silico aluminates, resulting in a significant enhancement of binding strength. Metakaolin boasts an extensive surface area of 12,000 m^2/g, far surpassing that of regular cement [2]. But the fact remains metakaolin's demand places limits on the field of strength creation [8]. When playing with fly ash and GGBFS [9], its high aluminum concentration makes it the silicon-reduction expert. Although cement's demand is unrelenting, it may not be necessary to call for the expansion of current cement plants if available fly ash, GGBFS, and metakaolin are used efficiently [10]. These developments have strengthened the construction industry to the point where it can achieve complete sustainability [11]. And in this complicated web, the investigation's principal aim becomes clear. Still, the primary focus of this study is on the enhancement and functionality of GGBFS-Metakaolin-based self-compacting geopolymer concrete (SCGC). Here, GGBFS plays the role of reference mix, setting the context for the introduction of metakaolin at 0%, 10%, 20%, and 30% of the total mass of GGBFS, respectively. The primary objective of this research is to investigate the relationship between workability and strength, specifically highlighting the complex correlations that arise from the extensive domain of machine learning techniques and compressive strength. A continuous investigation is being conducted to thoroughly examine the complex aspects of microstructural properties, a field that is both mysterious and complicated featuring elaborate structures and intricate patterns.

In the world of materials, scientists like Daniel L.Y. Kong [12] have discovered some interesting connections between different substances, like fly ash and metakaolin, and their strength when exposed to high temperatures. They use special tools to look closely at the materials. They found that fly-ash-based geopolymer materials have tiny pathways that help moisture escape when heated, which keeps the material strong. But metakaolin-based geopolymer materials don't have these pathways and can become weaker. In the present study, Siddique et al.[13] investigate the mysterious phenomenon of water absorption in geopolymer concrete. A complex novel emerges, whereby the amounts of water absorption fluctuate within the mysterious range of 5.8–7.1%. In this context, the central character is the 12M mix, an individual distinguished by its notable

attributes of low water absorption and a substantial volume of permeable voids. The performance shown on the platform of material science demonstrates a profound correlation, whereby the combination of minimal water absorption and permeable void volume results in the emergence of remarkable compressive strength. The author, Jiale Shen et al. [14], discusses machine learning algorithms like gradient boost (GB), random forest (RF), and extreme gradient boost (XGB). Their main interest was in the compressive strength of geopolymers made from building and demolition waste (CDWG). The results are appealing, and the accuracy of the predictions goes beyond $R^2 > 0.9$, striking great heights. Among the maestros, GB and XGB rise to the top, making RF look weak in comparison.

1.1 Research Significance

The novel approach to the study of self-compacting concrete using metakaolin has been extensively carried out and the various machine learning algorithms and strength parameters have been extensively discussed in detail. These new findings point the way toward material optimization and sustainable construction materials. Machine learning in geopolymer concrete is emerging research that will improve the understanding, design, and optimization of geopolymer concrete properties. Geopolymer concrete, a more sustainable alternative to traditional Portland cement concrete, is made using industrial by-products such as slag and metakaolin. Various Machine learning (ML) methods can significantly enhance the performance prediction, mix design optimization, and quality control of this material. The new things that have been conducted in this current research are the prediction of experimental results with random forest, gradient boost, extreme gradient boost, evaluation, mean absolute error, mean square error, root mean square error, and R Square.

2. Materials

The binder materials employed in the experimental work are GGBFS and Metakaolin. GGBFS is rich in calcium oxide whereas metakaolin is rich in alumina & silica. Hence the use of these two binders will result in long strength gain and early-stage reactivity ensuring balanced strength development. Other materials like fly ash, Rice husk ash, and sugarcane bagasse ash can also be used, but GGBS and Metakaolin show higher reactivity, especially in cold conditions, where fly ash and other binders can take longer to react. Concrete with GGBS & metakaolin tends to have low thermal shrinkage and creep compared to other materials. This property is essential for large-scale construction.

2.1. Ground-Granulated Blast Furnace Slag (GGBFS)

Silica and calcium oxide make up GGBFS, a granular, non-metallic substance crushed to less than 45 microns [15]. The physical and chemical characteristics of GGBS are shown in Table 1. The chemical composition test results of GGBFS are in accordance with the specifications.

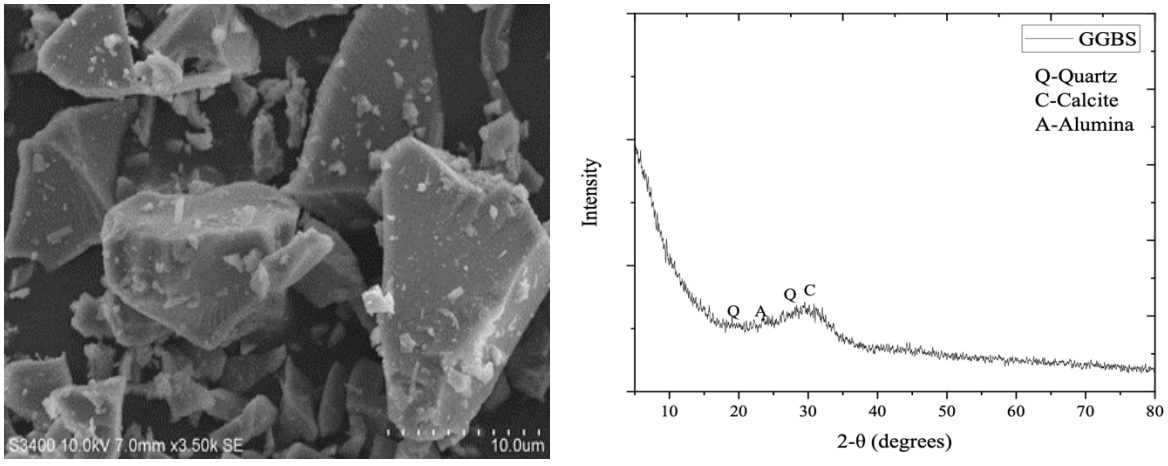

(a) (b)

Fig. 1. (a) SEM image of GGBFS; (b) XRD Diffraction patterns of GGBFS

The morphology of the GGBFS SEM micrographs Fig 1 (a) is approximately angular, brittle, and elongated. The GGBFS XRD reveals the presence of a notable amorphous phase composed of alumina, calcite, and quartz Fig 1 (b). From Fig.1(a) SEM image it is noticed that the GGBS material is angular in shape with irregularly shaped particles present in it.

2.2. Metakaolin

Metakaolin is a pure, amorphous, extremely reactive pozzolana aluminium silicate that forms stable hydrates with lime in water and gives mortar hydraulic characteristics. The physical and chemical characteristics of Metakaolin are in Table 1. Powder-based Metakaolin Fig 2 (a) SEM micrographs are amorphous. Metakaolin XRD Fig 2 (b) reveals MK humps and peaks from 20° to 35°, indicating an amorphous phase with quartz, mullite, muscovite, and anatase peaks. From Fig.2(a) SEM image, it is seen that metakaolin shows platy in nature.

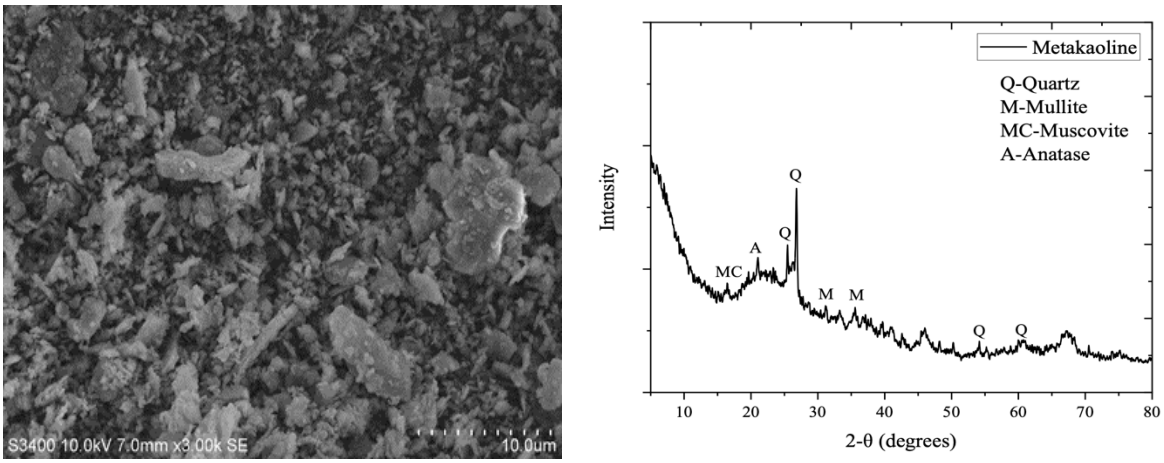

(a) (b)

Fig. 2. (a) SEM image of metakaolin; (b) XRD diffraction of metakaolin

Table 1. Physical and chemical properties of GGBFS and metakaolin

Parameters	GGBFS	Metakaolin
	Physical Properties	
Color	Light grey	White
Specific Gravity	2.7	2.01
Surface Area	450 m^2/kg	1200 m^2/kg
	Chemical Properties	
SiO_2	33.77%	52%
CaO	33.77%	---
Al_2O_3	13.24%	42.2%
MgO	8.46%	---
Fe_2O_3	0.05%	0.7%
Mno	0.65%	---
Sulphide Sulphur	2.23%	---
Total chlorides	0.01%	---

2.3. Alkaline Activators Preparation

This study employed an alkaline solution of NaOH and Na_2SiO_3. Sodium silicate aids in binder dissolution. Sodium hydroxide pellets in water create a solution at the right concentration. The molar content of sodium hydroxide solution varies. Before mixing with sodium silicate, this solution undergoes treatment for 24 hours. After mixing, the polymerization process reacts and produces heat, so leave it for 20 minutes before using. The entire research used a ratio of sodium silicate solution to sodium hydroxide is 2.5. Sodium hydroxide pellets have 99% purity and 2.13

specific gravity. The Sodium silicate consists of 14.43% Na_2O, 29.55% of SiO_2, 56.11% of water with 74 Pa.sec viscosity specific gravity of 1.55 and pH is 12.

2.4. Super Plasticizer (S.P)

Master Glenium SKY 823 has a pH of >6, a relative density of 1.08 + 0.01 at 250 °C, and a chloride ion concentration of <0.2%.

2.5. Aggregates

Using M-SAND as a fine aggregate, this study found 2.59 specific gravity, 2.2% water absorption, and grade "Zone II". The coarse aggregate employed in this study has 2.67 specific gravity, 0.65% water absorption, 15.23% combination index, and 28.98% crushing value. The test sample meets IS: 383-2011 standard [16].

2.6. Mix Proportions

In the current study, metakaolin was employed to substitute twelve GGBFS blends at mass proportions of 0%, 10%, 20%, and 30% with 8M,10M, and 12M of sodium hydroxide solution. For SCGC workability, the superplasticizer was held at 12% for all molarities and the binder was adjusted with extra water according to molarities by mass to gain the required workability of SCGC. Table 2 shows the GGBS/metakaolin-based SCGC Mix Proportion details

Table 2. Mix proportion of GGBFS/Metakaolin-based SCGC

Mixes	Binder Components (%)	GGBFS (Kg/m^3)	Metakaolin (Kg/m^3)	M-Sand (Kg/m^3)	Coarse Aggregate (Kg/m^3)	NaOH+ water (Kg/m^3)	Na_2SiO_3 (Kg/m^3)	Molarity (M)	Extra Water (%)
M1	GGBFS 100% & MK 0%	434.68	0	695	1044	64.75	161.875	8M	6
M2	GGBFS 90% & MK 10%	391.21	43.47	695	1044	64.75	161.875	8M	8
M3	GGBFS 80% & MK 20%	347.74	86.94	695	1044	64.75	161.875	8M	10.5
M4	GGBFS 70% & MK 30%	304.28	130.4	695	1044	64.75	161.875	8M	12.5
M5	GGBFS 100% & MK 0%	434.68	0	695	1044	66.18	165.45	10M	6.5
M6	GGBFS 90% & MK 10%	391.21	43.47	695	1044	66.18	165.45	10M	9
M7	GGBFS 80% & MK 20%	347.74	86.94	695	1044	66.18	165.45	10M	11
M8	GGBFS 70% & MK 30%	304.28	130.4	695	1044	66.18	165.45	10M	13
M9	GGBFS 100% & MK 0%	434.68	0	695	1044	67.5	168.77	12M	7
M10	GGBFS 90% & MK 10%	391.21	43.47	695	1044	67.5	168.77	12M	10.5
M11	GGBFS 80% & MK 20%	347.74	86.94	695	1044	67.5	168.77	12M	12
M12	GGBFS 70% & MK 30%	304.28	130.4	695	1044	67.5	168.77	12M	14

2.7. Preparation of Concrete, Casting/Curing

Before making the new SCGC, GGBFS, metakaolin, and manufactured sand were blended in the right amounts. The coarse aggregate was then added to the mixer in a specific proportion in a saturated dry surface (SSD) state and mechanically mixed for 2.5 min. After the dry mix, a well-shacked liquid combination (F/B) with the alkaline solution, superplasticizer, and additional water was pumped into the mixer for at least 3 minutes to combine it. Extra water has been added to the mix based on trial and error to maintain the flowability of the developed self-compacting geopolymer concrete. The addition of extra water was necessary to achieve the

desired workability of the self-compacting geopolymer concrete. Without sufficient water, the concrete would have been too dry and difficult to work with. The freshly formed concrete was evaluated for significant working characteristics to categorize self-compacting concrete. Also, slump flow, V-funnel, and L-box tests were assessed for workability properties. Hardened properties for specimens were produced following new SCGC testing. After vigorous hand mixing, the new concrete was poured into moulds without compaction into cubes, cylinders, prisms, etc., filling all moulds spaces with their weight. Scraping the specimens top removed surplus material and flattened them. Three samples were cast and evaluated for each combination in the experiment. After casting, samples, and moulds were oven-baked at 700 °C for 24 hours. After this oven-drying cycle, the study samples were taken from the moulds and kept at room temperature until test day.

3. Fresh Properties and Test Results of SCGC

The fresh characteristics of SCGC mixes were assessed using three SCC parameters according to EFNARC guidelines [16]. They are filling, passing, and segregation resistance. The current research assessed these features for all molarities utilizing Slump Flow, V-Funnel, and L-Box. Table 3 displays the workability test results.

Table 3. Workability test results for SCGC

Mixes	M1	M2	M3	M4	M5	M6	M7	M8	M9	M10	M11	M12	Range of workability values for SCC
Slump Flow (mm)	685	660	655	655	675	655	650	640	660	650	650	635	650-800 mm
V-Funnel (sec)	10.9	11.5	12	13	11	12	12.5	13.5	12	12.21	13	14	6-12 Sec
L-Box (H2/H1)	0.89	0.85	0.84	0.82	0.87	0.83	0.83	0.82	0.85	0.82	0.8	0.79	0.8-1.0

As shown in Fig 1 (a), GGBFS particles are flaky and elongated and have a large surface area, while metakaolin particles are amorphous and have a large surface area (Fig 2 (a) and Table 1), making it difficult to achieve the EFNARC-required flow. The slump flow is lowered for 10%,20%and 30% metakaolin replacement by 3.6% to 4.3%, 2.9% to 5.1%, and 1.5% to 3.7% compared to the control mix (GGBFS 100) for 8M, 10M, and 12M. Slump flow percentage decreases by 3.6% for reference mix M1 from 8M to 12M, 1.5%, 0.7%, and 3.05% for mixes M2, M3, and M4. The V-funnel test evaluates the filling capability of SCGC, showing an increase in flow time with metakaolin percentage. At 12M, all values slightly exceeded the specified limit. Substituting 10%,20% and 30% metakaolin for the control mix increases V-funnel flow time by 5.5% to 19.26%, 9% to 22.72%, and 1.75% to 16.66%, respectively.

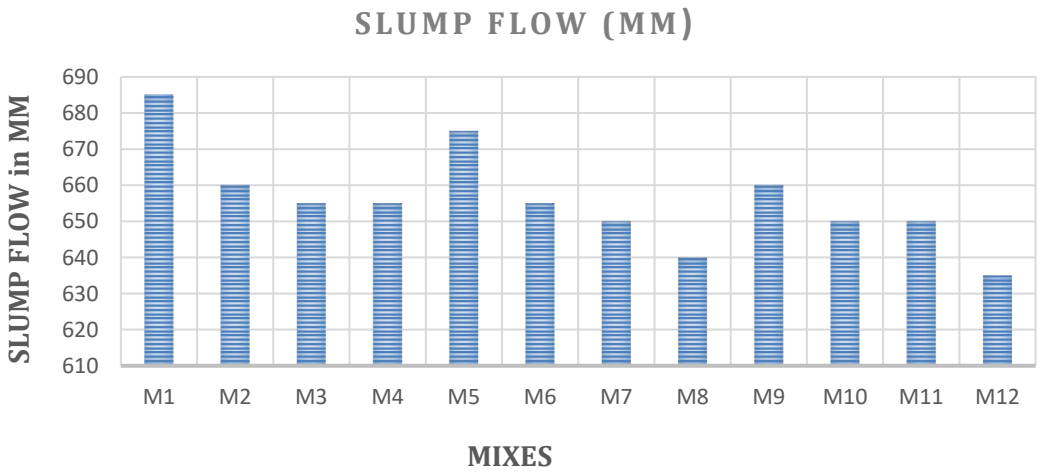

Fig. 3. Slump flow value for all the mixes

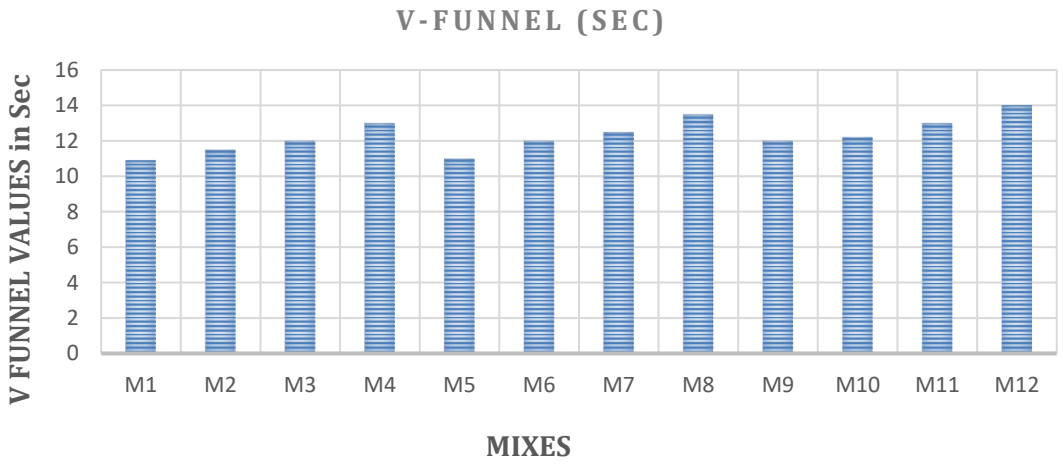

Fig 4. V Funnel value for all the mixes

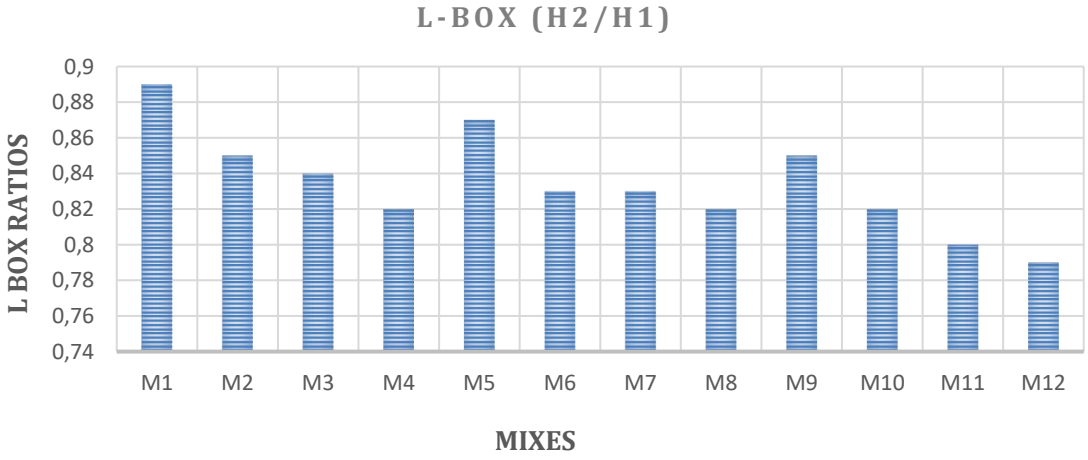

Fig 5. L Box ratios for all the mixes

The V-funnel flow time for reference mix M1 increased by 10% from 8M to 12M, while for mixes M2, M3, and M4, it increased by 6.17%, 8.33%, and 7.7%, respectively. The blocking ratio of L-box decreases with increased metakaolin content and sodium hydroxide concentration, similar to slump flow and V-Funnel test results. However, replacements of metakaolin with 10%, 20%, and 30% decrease the blocking ratio by 4.50% to 7.86%, 4.6% to 5.7%, and 3.5% to 7.0%, respectively. The percentage decrease from 8M to 12M for replacing GGBFS with metakaolin by 0%, 10%, 20%, and 30% is 4.5%, 3.52%, 4.76%, and 3.65%, respectively.

4. Hardened Properties of Self-Compacting Geopolymer Concrete

4.1. Compressive Strength Tests

This experiment evaluated the compressive strength of a cube sample 100mm in a digital 2000KN compression testing machine (CTM) following IS 516-1959 [17] guidelines. The study found that increasing the percentage of metakaolin in the sample resulted in a decrease in strength. However, as the molarity increased, the strength also increased [3].

The percentage decrease in strength by replacing GGBFS with 10%, 20%, and 30% of metakaolin when compared to the control mix GGBFS 100 at the end of 90 days was around 2.10% 4.21% 12.63% for 8M, 7.54%,11.32%,16.03% for 10M and 8.20%,11.47%,6.40% for 12M of sodium hydroxide solution. The percentage increase in strength from 8M to 10M and from 10M to 12M at the end of 90days was 11.57% and 15.09% for the M1 series, 5.37% and 14.28% for the M2 series, 3.23% and 14.89% for the M3 series, and 9.87% and 14.60% for the M4 series. Table 4

shows compressive strength test results and Fig 6 shows compressive strength values for various mixes.

Table 4. Compressive strength test results in MPa

Mix Id	3 days	7 days	28 days	56 days	90 days	Molarity
M1	41	42	45	46	47.5	8
M2	40.5	41.5	44	45	46.5	
M3	39	40	42.5	44	45.5	
M4	38	38.5	40	40.5	41.5	
M5	46	47.5	50	51.5	53	10
M6	43	44	47	47.5	49	
M7	41.5	42	44.5	46	47	
M8	40	41	43	44	44.5	
M9	49	50	56.5	59	61	12
M10	47.5	48	53.5	55	56	
M11	45	46	52	53	54	
M12	44	44.5	49	50	51	

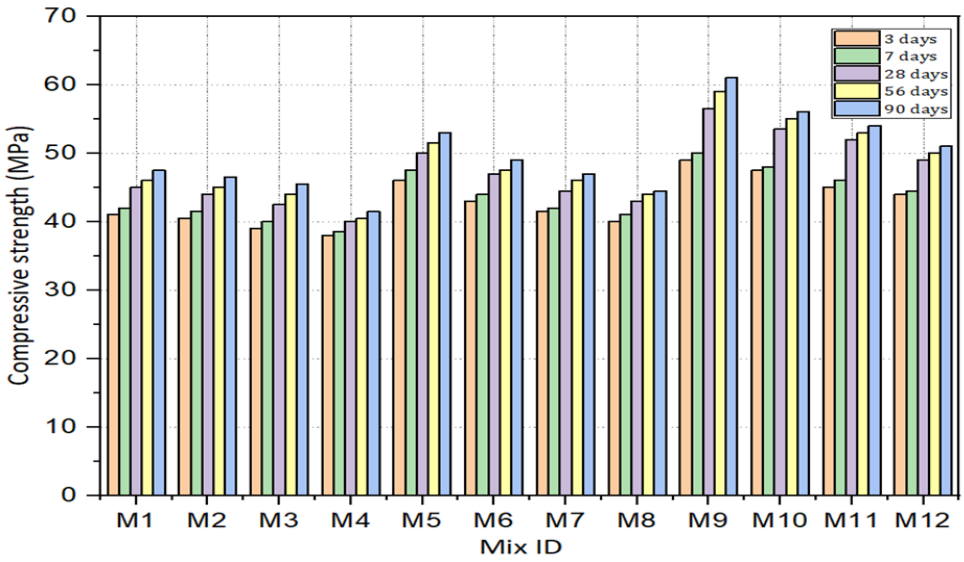

Fig 6. Compressive strength test results

4.2. Split Tensile Strength Tests

The experiment was conducted in a CTM on a 150 mm diameter and 300 mm height cylinder specimen according to IS 516-1959 [17]. The tensile strength decreased with increased metakaolin content and increased with increased molarity compared to the control mix.

Table 5. split strength test results in MPa

Mix Id	7 Days	28 Days	56 Days	Molarity
M1	4.25	4.67	4.73	8
M2	3.96	4.2	4.38	
M3	3.82	3.96	4.1	
M4	3.53	3.67	3.82	
M5	4.7	4.85	5	10
M6	4.37	4.5	4.9	
M7	4.2	4.35	4.5	
M8	3.9	4.2	4.25	
M9	5.2	5.5	5.55	12
M10	4.8	4.95	4.98	
M11	4.6	4.7	4.74	
M12	4.3	4.5	4.63	

The percentage decrease in strength by replacing GGBFS with 10%, 20%, and 30 % of metakaolin when compared to the control mix GGBFS 100 at the end of 56 days was around 7.39%, 13.32%,19.23% for 8M, 2%,10%,7.64% for 10M and 10.27%,17.08%,19.87% for 12M. After 56 days, the M1 series increased by 5.70% and 11% from 8M to 10M and 10M to 12M, the M2 series by 11.87% and 1.63%, the M3 series 9.75% and 5.33%, and the M4 series 8.94%. Table 5 shows split strength test results and Fig 7 shows split tensile strength values for various mixes.

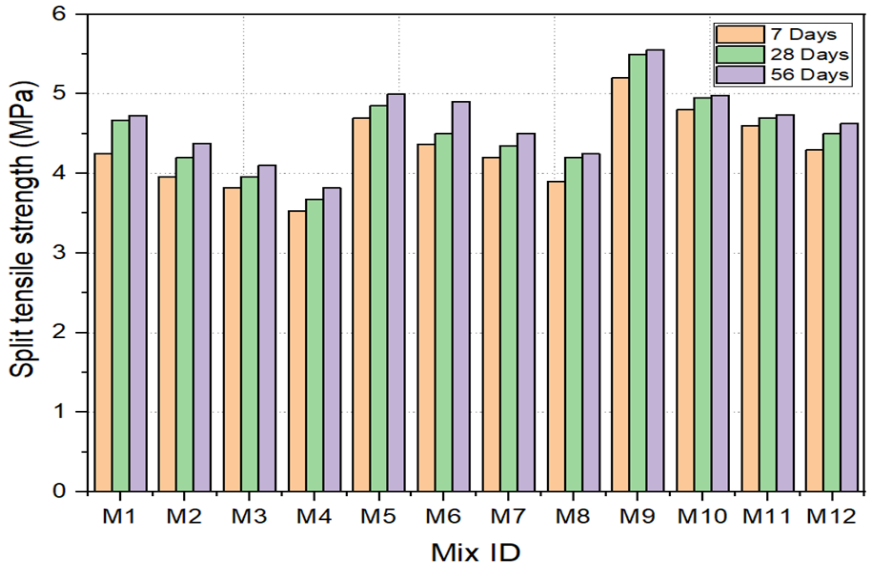

Fig 7. Split tensile strength test results

4.3. Flexural Strength Tests

The 100×100×500 mm sample was tested in a flexural testing machine. Increasing metakaolin concentration lowers flexural strength, whereas increases with greater molarity. At 56 days, the percentage drop in strength for 10%,20% & 30% replacement of GGBFS when compared to control mix GGBFS100 was around 1.65%,2.68%,6.40% for 8M, 1.1%,3%,4% for 10M and 19.20%, 22.24%,21.28% for 12.

Table 6. Flexural strength test results in MPa

Mix Id	7 Days	28 Days	56 Days	Molarity
M1	4.62	4.68	4.85	8
M2	4.57	4.59	4.77	
M3	4.51	4.65	4.72	
M4	4.37	4.49	4.54	
M5	4.35	4.92	5	10
M6	4.7	4.85	4.95	
M7	4.61	4.77	4.85	
M8	4.4	4.72	4.8	
M9	5.1	5.45	6.25	12
M10	4.82	4.92	5.05	
M11	4.75	4.81	4.86	
M12	4.6	4.72	4.92	

M1 series strength increases from 8M to 10M and 10M to 12M at 56 days are 3.09% and 25%, M2 series is 3.77% and 2.02%, M3 series is 2.75% and 0.2%, and M4 series is 5.72% and 2.5%. Table 6 shows flexural strength test results and Fig 8 shows flexural strength values for various mixes.

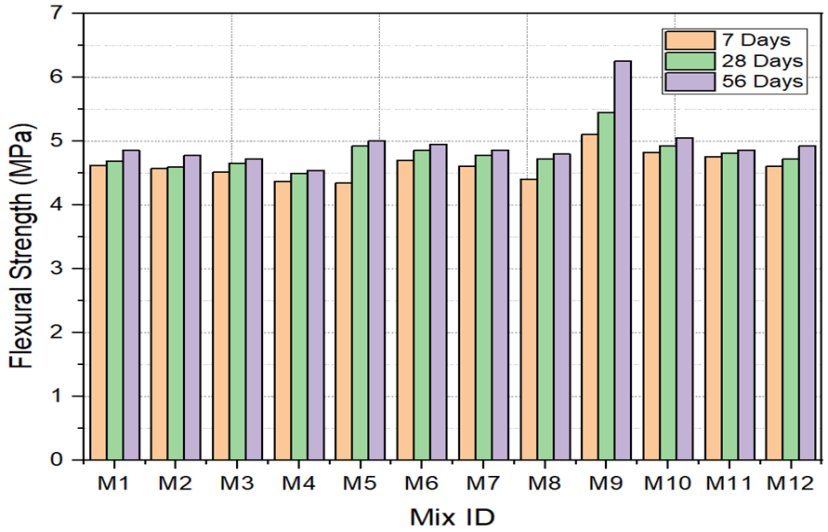

Fig 8. Flexural strength test results

4.4. Shear Strength Tests

Bairagi and Modhera [18] and Baruah and Talukdar [19] recommended applying shear strength tests on an L-shaped shear test specimen on self-compacting geopolymer concrete in the absence of a code. Inserting a 90× 60 ×150 mm steel block into 150 mm side-cube moulds before pouring concrete generated the samples. Shear test specimen details are in Fig 9. In a CTM system, the sample was loaded till failure.

Fig. 9. Details of the shear test

Table 7. Shear strength test results in MPa

Mix Id	7 Days	28 Days	56 Days	Molarity
M1	4.44	4.6	4.65	8
M2	3.89	4.05	4.15	
M3	3.22	3.35	3.47	
M4	2.95	3	3.1	
M5	4.5	4.65	4.7	10
M6	3.97	4.1	4.2	
M7	3.28	3.4	3.51	
M8	3.02	3.07	3.14	
M9	4.62	4.7	4.74	12
M10	4.2	4.25	4.3	
M11	3.35	3.43	3.54	
M12	3.1	3.15	3.2	

Replacement of GGBFS with metakaolin for 8M, 10M, and 12M lowers strength by 10.75,25.37%, and 33.33% for 8M,10.63%,25.31% and 33.19% for 10M, and 9.28%,25.31% and 32.48% for 12M compared to control mix M1(GGBFS100) after 90 days. The M1 series has a 1.07% and 0.85% strength increase from 8M to 10M and 10M to 12M after 90 days, whereas the M2 series has 1.20% and 2.38%, the M3 series 1.15% and 0.85%, and the M4 series 1.29% and 1.91%. IS 456-2000 [20] suggests M20 grade (conventional) concrete has a maximum shear strength of 2.5 MPa. Regardless of molarity, all mixtures, including the reference mix, exceeded 2. 5MPa.In recent studies, it was also observed that geopolymer concrete gave remarkable and positive results for bonding and interface [27]. Table 7 shows shear strength test results and Fig 10 shows shear strength values for various mixes.

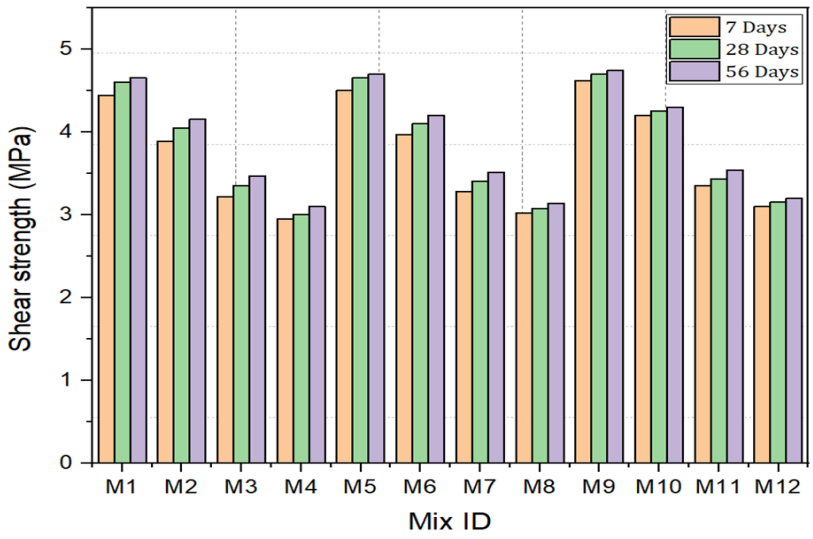

Fig. 10. Shear strength test results

4.5. Impact Strength

Self-compacting geopolymer concrete impact strengths were measured using Schruder's impact test equipment. This is exactly 150 mm-diameter, 60 mm-thick samples were selected. Fig 11 (a) & (b) show a 45.4 N hammer (ball) from 457 mm being lowered in Schruder's impact evaluation system. Observe the number of blows needed for the first and final breakdown. The final crack indicates that the specimen has structurally failed under the impact loads. Cracks in the sample sufficiently under impact loads at least three of four concrete portions on the base plate are the ultimate failure.

(a) (b)

Fig 11. (a) Impact test setup; (b) failure of impact specimen

Table 8. Impact Energy of GGBS/Metakaolin-based SCGC

Mix	Molarity	28 Days		56 Days		90Days	
		First crack	Final crack	First crack	Final crack	First crack	Final crack
M1	8M	1515	1597	1618	1722	1743	1805
M2		1452	1494	1514	1556	1597	1639
M3		1348	1411	1411	1452	1514	1556
M4		1183	1245	1245	1286	1328	1390
M5	10M	1618	1701	1763	1846	1867	1950
M6		1556	1639	1618	1680	1701	1763
M7		1494	1577	1556	1618	1639	1722
M8		1411	1514	1473	1535	1514	1556
M9	12M	1660	1763	1888	1950	2012	2157
M10		1597	1660	1701	1763	1805	1867
M11		1535	1597	1618	1680	1701	1763
M12		1452	1514	1535	1597	1618	1680

Based on ACI Committee 544's [21] procedure, Table 8 displays specimen impact strengths and ultimate failure. GGBFS is replaced with metakaolin for 10%, 20%, and 30% and evaluated for all molarities at 28, 56, and 90 days. As the metakaolin content increases, compressive strength increases but the impact resistance decreases. This is due to the denser, more brittle matrix formed by the metakaolin, which reduces the material's ability to absorb and distribute impact energy, leading to cracks under impact loads. The energy absorption capacity of SCGC increased with molarity regardless of the mix, and a 10% substitution of GGBFS with metakaolin improved energy absorption for all testing days. The percentage improvement in strength at ultimate failure from 8M to 10M and 10M to 12M with 10% metakaolin substitution of GGBFS at 90 days is 7.56% and 5.89%.

5. Microstructure Studies

The SEM images from Fig 12 (a)-(b) & (e) -(f) for 8 molarity and Fig 12 (c)-(d) & (g) – (h) for 12 molarity of hardened geopolymer concrete samples after 3 days and 28 days compressive strength tests made with GGBFS100 mix (GGBFS100%) and GM70 mix (GGBFS 70% and metakaolin 30%) demonstrate binder composition and molarity microstructure. Early-stage hydration of calcium aluminates produces needle-shaped prismatic crystals referred to as Ettringite [Fig. 12 (a)]. At 28 days, this Ettringite vanished and became a solid concrete structure [Fig. 12(b)]. All SEM image of SCGC having 12 M of Na (OH) solution show a thick GGBFS composite microstructure with slag grains and few microfractures. High-pozzolanic GGBFS particles produce a denser matrix, resulting in better strength after 28 days. GGBFS composite SEM images (b), (d), (f), and (h) reveal good matrix-GGBFS particle interfacial bonding at 28 days. GGBFS substituted with metakaolin did not show Ettringite. The SEM images from (e) to (h) indicate a strong, compact microstructure as metakaolin expanded due to its huge surface area. As seen in SEM images (e) and (f), metakaolin concentration increases in C-S-H crystals after 3 days. Higher curing times diminish C-S-H crystals by increasing their strength. Due to the large surface area of GGBFS and metakaolin, extra water was provided to ensure flow, resulting in the increase of small pores and micro-cracks as seen in SEM images from (e) and (h), which may explain the decrease in strength with increased metakaolin content. Higher amounts of NaOH break up metakaolinite particles and make the bond between monomers more reactive, which makes the geopolymer's intermolecular bonding stronger. SEM images (c), (d), (g), and (h) of SCGC having 12 M of Na (OH) solution have a more compact and denser microstructure than (a), (b), (e), and (f). Samuel Demie et al. [22] used a field emission scanning microscope (FESEM) to analyze SP dosage. They found dense ITZ development between aggregate and binder matrix at high SP dosages and vice versa, resulting in high compressive strength.

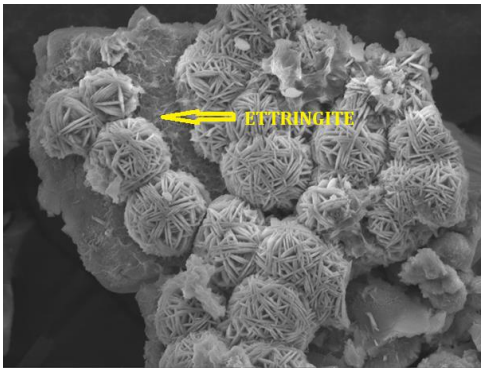

(a) GGBFS100 for 3 days (8M)

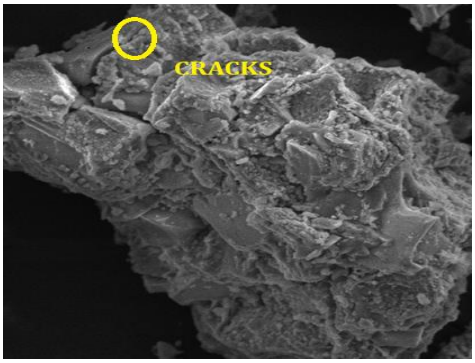

(b) GGBFS100 for 28 days (8M)

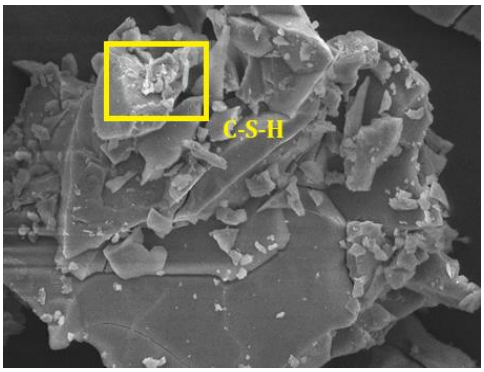

(c) GGBFS100 for 3 days (12M)

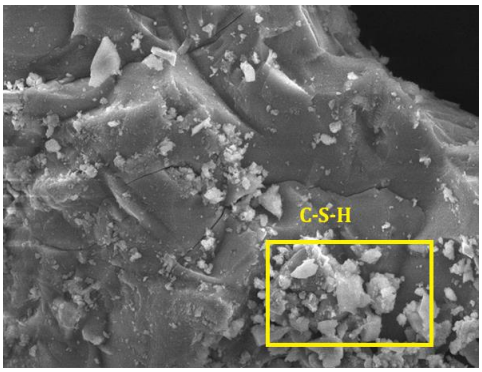

(d) GGBFS100 for 28 days (12M)

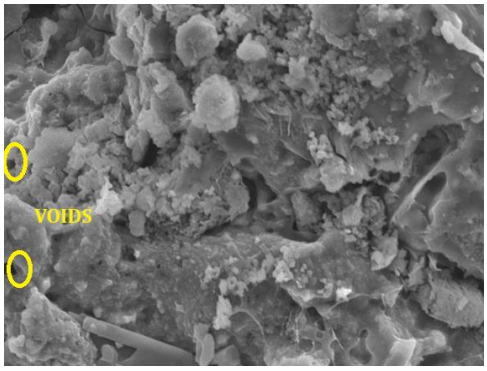

(e) GGBFS70+MK30 for 3 days (8M)

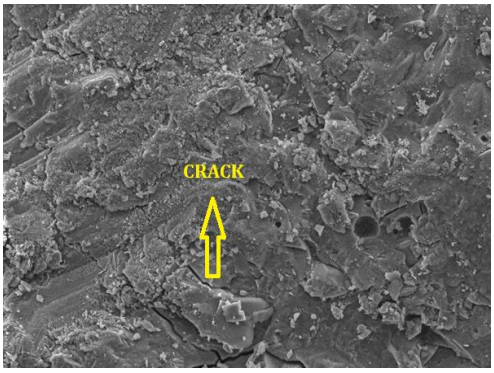

(f) GGBFS70+MK30 for 28 days

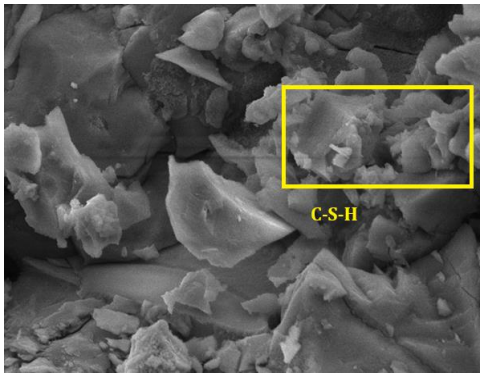

(g) GGBFS70+MK30 for 3 days

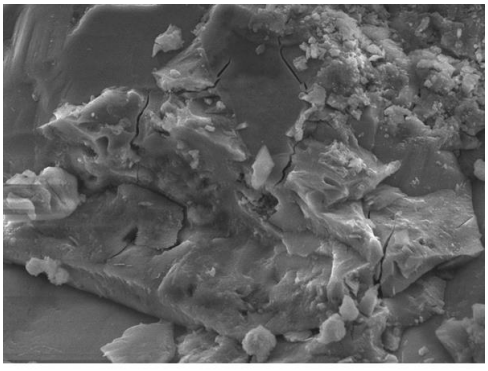

h) GGBFS70+MK30 for 28Days

Fig. 12. SEM images of GGBFS/Metakaolin based SCGC w.r.t Different binder composition and molarity

6. Application of Machine Learning (ML) Methods

6.1 Random Forest

The Random Forest Regressor is a potent machine-learning algorithm employed for regression tasks. Its core mechanism involves the amalgamation of multiple decision trees to improve the robustness and accuracy of predictions. Each decision tree taught by a Random Forest (RF) Regressor uses a unique, randomly selected section of the training data, some of which may be repeated. This procedure is commonly referred to as bootstrap aggregating or bagging. The amalgamation of these decision trees through ensemble averaging serves the dual purpose of introducing randomness and mitigating overfitting, ultimately resulting in reduced variance and an overall improvement in the model's predictive accuracy [23]. The algorithm is mentioned below.

Training data D = $\{(x_i, y_i)\}_{i=1}^{n}$, number of trees T, number of features m to randomly select to each split.

1. For each tree t (from 1 to T)

- Randomly sample n data points from D with replacement (bootstrapping).
- Use the bootstrapped dataset to train the t-th decision tree.
- At each split in the tree:
  - Randomly select mmm features from the total features.
  - Find the best split using one of the selected features.
- Grow the tree until a stopping condition is met (e.g., max depth, minimum samples per leaf).

2. Store the trained decision tree $f_t(x)$

3. Prediction

If there are T decision trees in the forest, the prediction $\hat{y}$ For a new input x is the average of the predictions from all trees:

$$\hat{y} = \frac{1}{T}\sum_{t=1}^{T} f_t(x) \tag{1}$$

Where; T is the total number of trees, $f_t(x)$ is the prediction from the t-th tree for input x.

6.2 Gradient Boost

Gradient Boosting is an ensemble machine learning technique that builds predictive models by merging multiple weak learners, typically decision trees, sequentially. It begins with a simple model and progressively adds more trees, each designed to correct the errors of the preceding ones. Gradient Boosting minimizes the loss function gradient, adjusting model parameters to improve predictions. It's highly effective for regression and classification tasks, providing robust and accurate results. Regularization techniques like learning rate control the overfitting [24]. The formula for the calculation of the predicted values and the residual errors at each iteration is mentioned below: Predicted Value (F) at iteration m:

$$F_m(x) = F_{(m-1)}(x) + learning\ rate * h_m(x) \tag{2}$$

$F_m(x)$ represents the predicted value after adding the m-th tree. $F_{\{m-1\}}$ (x) represents the anticipated or projected value derived from the preceding iteration. learning rate is a hyperparameter that quantifies the individual tree contributions (usually < 1). $h_m(x)$ is the prediction made by the m-th decision tree. Residual Error (R) at iteration m:

$$R_m(x) = y - F_m(x) \tag{3}$$

$R_m(x)$ represents the residual error, which is the key distinction between the actual target value (y) and the predicted value at the m-th iteration ($F_m(x)$).

6.3 Extreme Gradient Boost

XGB is a well-known machine learning ensemble algorithm known for its exceptional performance in regression and classification tasks. It enhances the traditional gradient boosting technique by incorporating regularization, parallel processing, and handling missing data effectively. XGB constructs a set of decision trees in an iterative fashion, optimizing them to minimize a defined loss function. It employs gradient descent and a second-order gradient for faster convergence. The algorithm's distinctive features include pruning to prevent overfitting and automatic handling of missing values [24]. The algorithm is mentioned below. Training data $D = \{(x_i, y_i)\}_{i=1}^{n}$, number of boosting rounts T, learning rate η, loss function $l(y, \hat{y})$, regularization parameters γ and λ.

1. Initialize the model:

- Set initial predictions $\hat{y}_i{}^0$= mean (y)

2. For each boosting round t (from 1 to T)

- Compute residuals for each observation:

$$r^t{}_i = -\frac{\partial l(y_i - \hat{y}_i{}^{t-1})}{\partial \hat{y}_i{}^{t-1}} \tag{4}$$

- Train a decision tree $f_t(x)$ to fit the residuals $r_i{}^t$
- Calculate the leaf weights $w_j$for the tree $f_t(x)$ using:

$$w_j = -\frac{\sum_{i\epsilon leaf\ j} r_i^t}{\sum_{i\epsilon leaf\ j} h_i^t + \lambda} \tag{5}$$

- Where h_i^t is the second derivative of the loss function. Update predictions:

$$\hat{y}_i^t = \hat{y}_i^{t-1} + \eta f_t(x_i) \tag{6}$$

3. Add regularization term:

$$\mathcal{L} = \sum_{i=1}^{n} l\left(y_i \hat{y}_i{}^t\right) + \sum_{k=1}^{t} \gamma\left(f_k\right) \tag{7}$$

For a given dataset with n observations, the objective function $\mathcal{L}$ to be minimized is:

$$\mathcal{L} = \sum_{i=1}^{n} l\left(y_i \hat{y}_i{}^t\right) + \sum_{k=1}^{t} \mathcal{L}\left(f_k\right) \tag{8}$$

Where; $l\left(y_i \hat{y}_i{}^t\right)$is the loss function, typically Mean Squared Error for regression;

$$l\left(y_i \hat{y}_i{}^t\right) = \left(y_i - \hat{y}_i{}^t\right)^2 \tag{9}$$

$\mathcal{L}(f_k))$ is the regularization term that penalizes the complexity of each tree, f_k defined as;

$$\mathcal{L}(f_k) = \Upsilon T + \frac{1}{2}\lambda \sum_{j=1}^{T} w_j{}^2 \tag{10}$$

Where; T is the number of leaves in the tree, W_j represents the weight of leaf j.

6.4 Evaluation

The evaluation of regression models in machine learning encompasses the use of many measures to assess their performance in predicting continuous numeric values. In this work, we have used four evaluative metrics namely, Mean Absolute Error (MAE), Mean Squared Error (MSE), Root Mean Squared Error (RMSE), R-squared (R^2) Score [23].

6.4.1 Mean Absolute Error (MAE)

The Mean Absolute Error (MAE) is a metric that quantifies the average absolute difference between the anticipated values and the actual target values. It provides a straightforward understanding of prediction errors [21].

$$MAE = \left(\frac{1}{n}\sum(predicted - actual)\right) \tag{11}$$

6.4.2 Mean Squared Error (MSE)

MSE calculates the average squared difference between predicted and actual values. It amplifies the impact of larger errors and is widely used in regression evaluations.

$$MSE = \left(\frac{1}{n}\right)\left(\sum(predicted - actual)^2\right) \tag{12}$$

6.4.3 Root Mean Squared Error (RMSE)

RMSE provides an interpretable metric in the same units as the target variable and is calculated as the square root of MSE. Large errors are penalized more severely than MAE.

$$RMSE = \sqrt{MSE} \tag{13}$$

6.2.4 R-squared (R^2) Score

R^2 measures the proportion of the dispersion in the target variable that is predictable from the independent variables. It ranges from 0 to 1, where 1 indicates a perfect fit and 0 implies that the model doesn't explain any variance [25].

$$R^2 = 1 - \left(\frac{MSE(model)}{MSE(mean)}\right) \tag{14}$$

7. Results and Discussion

In this work, the ML models are implemented on the experimental dataset to predict the compressive strength. Implementing ML models using optimization strategies improves accuracy [26,28]. Table 9 lists hyperparameters and evaluation matrix findings.

Table 9: Optimization parameters and performance of ML algorithms

ML Model	R^2 training	R^2 test	MAE	MSE	RMSE	Optimized parameters
RF	0.909	0.822	1.122	2.486	1.576	n_estimator=100
XGB	0.935	0.845	0.575	1.851	1.360	Random state=42
GB	0.934	0.929	0.593	1.852	1.361	Learning rate=0.35

The optimized parameter(n_estimator=100) involves generating 100 independent trees, contributing to improving the prediction accuracy. A higher value generally enhances the performances of models. Random state 42 ensures reproducibility, and learning rate=0.35 controls step size, balancing model accuracy, and overfitting. Cross-fold validation is utilized with value K=10 for all the ML models as another optimization approach. The results of the individual models are discussed in detail below:

7.1 Random Forest

Fig 13 (a) depicts the correlation seen between the experimental values and the predicted values obtained from the RF model. The scatter plot visually represents the training data with red data points and the test data with blue data points. The solid black line represents the optimal fit of the model, while the red and blue dotted lines represent the training and test datasets,

respectively. The RF model was implemented, yielding an R^2 score of 0.909 on training data and 0.822 on test data.

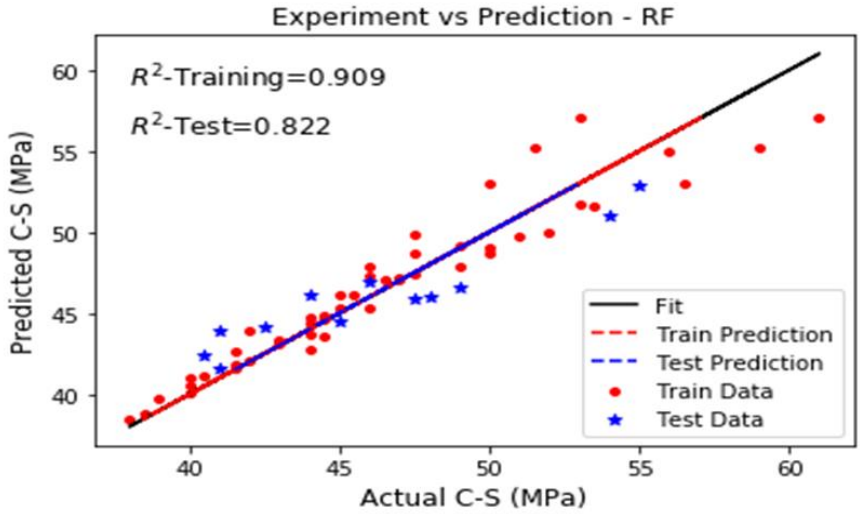

(a)

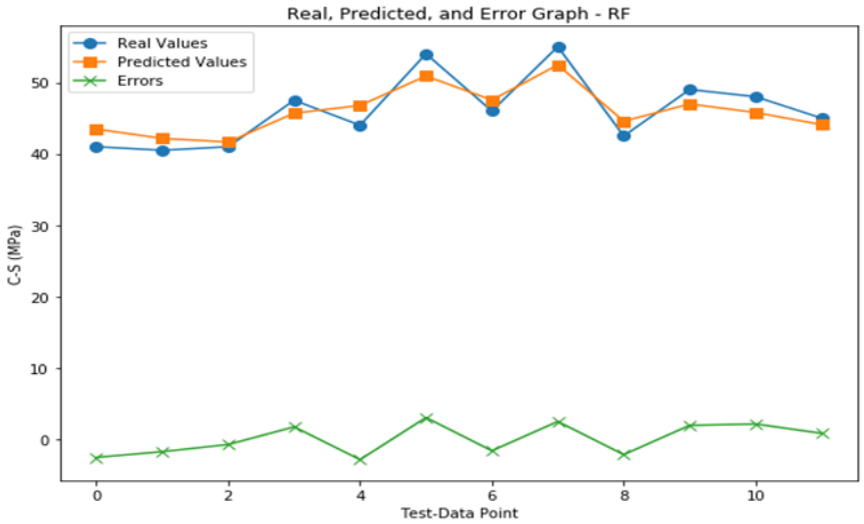

(b)

Fig. 13. (a) Correlation between the actual and predicted RF model results and b) Error graph- RF

Fig 13 (b) illustrates a similarity between the observed data points and the predicted ones by the RF model. This is evident from the small discrepancies visible in the line graph, indicating a close alignment between the actual and expected data.

7.2 Extreme Gradient Boost

Fig 14 (a) and (b) present a comparison of the predicted and observed outcomes generated by the XGB model. The RF model's predictions on both the training and test data sets were surpassed by the XGB model's implementation (R^2 = 0.935 and R^2 = 0.845, respectively).

The better accuracy observed in XGB compared to RF appears to be the result of gradient boosting. This technique combines the predictions of multiple decision trees sequentially, enabling it to capture intricate relationships in the data and improve accuracy. RF, on the other hand, builds multiple decision trees independently and averages their predictions, which can be more successful for certain complex datasets.

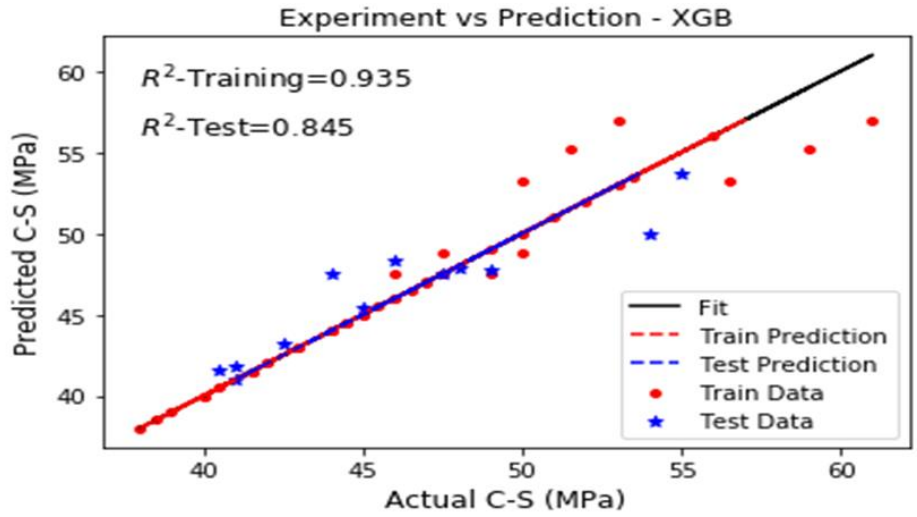

(a)

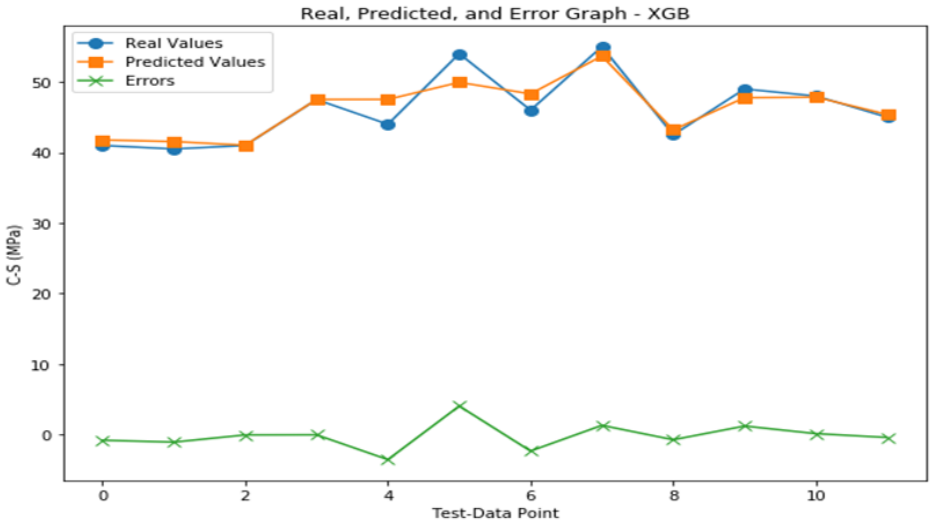

(b)

Fig. 14. (a) Correlation between the actual and predicted XGB model results and (b) Error graph- XGB

7.3 Gradient Boost

Fig 15 (a) and (b) provide an analysis in comparison to the observed and anticipated outputs of the GB model. Fig 15 (a) presents the correlation between the experimental outcomes and the predictions derived by the GB model. The GB model has been put into action successfully with an impressive 0.934 R^2 score on the training data and a commendable 0.929 on the test dataset. The outcome of the GB model demonstrates a higher level of precision compared to the outputs of the RF and XGB models.

The error graph- GB demonstrates a strong correspondence between the observed data points and the anticipated data points, as evidenced by the low discrepancy observed in the line graph. The GB model has demonstrated superior accuracy in comparison to alternative models, with the fewest errors. The reasons for achieving the highest accuracy in the GB model are because of the model's mechanism, such as randomness and ensemble diversity, which can greatly contribute to improved performance.

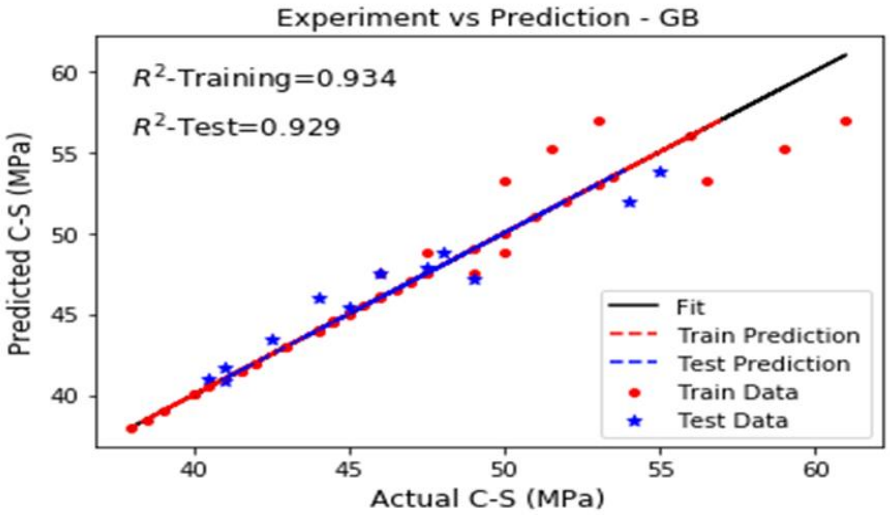

(a)

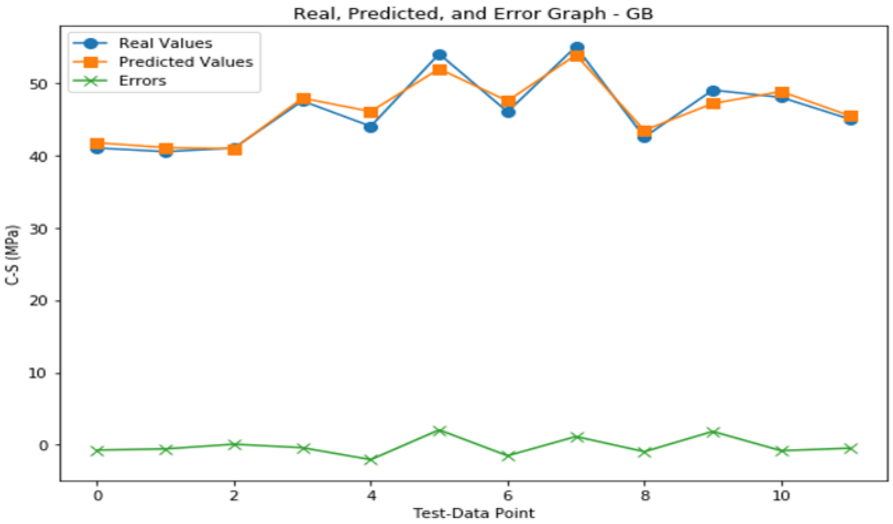

(b)

Fig 15(a): Correlation between the actual and predicted GB model results and (b) Error graph- GB

Firstly, the outcome of this randomness has the potential to various accuracy scores when the models are trained multiple times. However, this presents an opportunity for improvement and discovering even better results. If the GB model's random initialization aligns favorably, it has the potential to produce even better accuracy. Secondly, the GB model offers the exciting opportunity to combine with a diverse set of base models, such as decision trees with different characteristics or other learners, to form a powerful ensemble. If the GB ensemble is well-designed, it has the potential to outperform XGB.

8. Conclusion

- Workability parameters such as slump flow and L-Box values exhibited a decrease as molarity increased due to the higher solute concentration leading to stronger intermolecular forces, reducing flowability and causing slower movement through the funnel, while V-funnel values demonstrated an increase So, as molarity increases, the activator solution will be thicker and moves more slowly, which will cause higher V-funnel values. The values were marginally greater than the specified limits of EFNARC at 10M and 12M for only the 30% replacement of GGBS with metakaolin.

- The slump flow decreases by 3.6% to 4.3%, 2.9% to 5.1%, and 1.5% to 3.7% with 10% and 30% metakaolin replacement for 8M, 10M, and 12M, while the V-funnel flow time rises by 5.5% to 19.26%, 9% to 22.72%, and 1.75% to 16.66%. The slump flow & V funnel values show low workability as metakaolin content increases. Similarly, the L-box test also shows a decline in the blocking ratio, decreasing by 4.50% to 7.86% with higher metakaolin and sodium hydroxide concentrations. This is due to metakaolin's higher pozzolanic nature leading to higher water demand.
- The percentage increase in strength from 8M to 10M and from 10M to 12M at the end of 90days was 11.57% and 15.09% for the M1 series, 5.37% and 14.28% for the M2 series, 3.23% and 14.89% for the M3 series, and 9.87% and 14.60% for the M4 series. The compression strength is enhanced with increasing molarity, irrespective of the mixture. As the molarity increases the strength of SCGC increases due to the higher concentration of sodium hydroxide solution leading to higher alumina-silicate gel and densified matrix in the mix employed. The same trend is observed in the split tensile, flexural, and shear strength of concrete. Irrespective of molarity, all mixtures, including the reference mix, the shear strength exceeded 2.5MPa.
- Irrespective of the binder proportions and molarities, GGBS/Metakaolin-based oven-cured SCGC generally gains strength with age. The GGBS and Metakaolin-based SCGC produce a three-dimensional aluminosilicate network that binds the particles together, which gives a higher strength gain in the mixes developed with respect to age, type of curing, and age of curing.
- The compressive strength of SCGC exhibited a decrease across all ages as the volume of metakaolin added to GGBS increased from 0% to 30% due to metakaolin appearing more compact, uniform, and homogeneous, with fewer unreacted particles & has experienced partial alkali activation.
- An increase in molarity and the passage of time both result in a more compact matrix and fewer micro-cracks in GGBS composites, which translates to greater strength. However, when metakaolin was used in place of GGBS, more water was needed to achieve flow; this led to a rise in unreacted CSH crystals, microscopic gaps, and micro-cracks, resulting in a less compact structure and a decrease in strength.
- As the percentage of metakaolin in the material increased, the impact resistance decreased, and vice versa for GGBS. Energy absorption by SCGC increased with increasing molarity, and 10% metakaolin substitution of GGBS resulted in the highest energy absorption capacity across all test days. The denser microstructure formed by metakaolin can reduce the material's ability to absorb energy upon impact. Additionally, metakaolin's higher silica content can increase the overall brittleness of the geopolymer concrete, limiting its capacity for deformation under impact loading.
- The gradient boost model exhibited superior performance due to its superior accuracy, regularization, and ability to handle noisy data, making it ideal for optimizing mixes in terms of mechanical properties compared to other machine learning models on the test dataset, achieving an R^2 of 0.929, MAE of 0.593, RMSE of 1.361, and MSE of 1.852 when predicting the compressive strength of GGBS.
- R^2 training, R^2 test, MAE, MSE, and RMSE are helpful for assessing the model's accuracy, error distribution, and ability to generalize, providing a comprehensive understanding of model performances.
- The successful implementation of machine learning models has delivered impressive results in accurately predicting compressive strength on our experimental dataset. These models show great potential for applications in fields like construction and materials science, with promising predictive accuracies.
- The results demonstrate that machine learning models with hyperparameter tuning are highly effective in achieving enhanced prediction accuracy even on small datasets.

9. Future Scope of The Present Research

- The study can be extended further by employing natural fibers in self-compacting geopolymer concrete.

- This study can be extended to know the effect of temperature of SCGC with varying temperatures (elevated temperature study)
- A durability study can be employed for the above mixes to study the effect of early and long-term acid/salt exposure.
- Further, the sustainability analysis can be conducted for the above mix proportions.
- Cost analysis of Self-compacting geopolymer concrete can be studied.

References

[1] Md Khalid S, Shobha MS. Ternary blended geopolymer concrete: a review. In: IOP Conference Series: Earth and Environmental Science. 2021;822:1-8. https://doi.org/10.1088/1755-1315/822/1/012043
[2] Khalid SM, Shobha MS. Effect of ternary blends on mechanical strength, durability and microstructural properties of geopolymer concrete. Iran J Sci Technol Trans Civ Eng. 2023. https://doi.org/10.1007/s40996-023-01241-4
[3] HM T, Unnikrishnan S. Utilization of industrial and agricultural waste materials for the development of geopolymer concrete: a review. Mater Today Proc. 2022;65:1290-1297. https://doi.org/10.1016/j.matpr.2022.04.192
[4] Khalid S, Reshma T, Shobha M, Priyanka G, Siriki VS. Analysis of strength and durability properties of ternary blended geopolymer concrete. Mater Today Proc. 2021;54:259-263. https://doi.org/10.1016/j.matpr.2021.08.307
[5] Zhang Z, Yao X, Huajun Z, Yue C. Role of water in the synthesis of calcined kaolin-based geopolymer. Appl Clay Sci. 2009;43:218-223. https://doi.org/10.1016/j.clay.2008.09.003
[6] Kamseu E, Rizzuti A, Leonelli C, Perera D. Enhanced thermal stability in K2O-metakaolin-based geopolymer concretes by Al2O3 and SiO2 fillers addition. J Mater Sci. 2010;45(7):1715-1724. https://doi.org/10.1007/s10853-009-4108-1
[7] Fang Y, Li H, Wang Z, Zhang K, Cui P, Dong B. The effect of metakaolin on the hardening process of alkali-activated slag by using electrochemical impedance spectroscopy. Earth Environ Sci. 2019. https://doi.org/10.1088/1755-1315/300/5/052011
[8] Justice JM, Kennison LH, Mohr BJ, Beckwith SL, McCormick LE, Wiggins B, et al. Comparison of two metakaolins and a silica fume used as supplementary cementitious materials. In: Proceedings of the Seventh International Symposium on Utilization of High-Strength/High-Performance Concrete, ACI SP-228. Washington DC: American Concrete Institute; 2005. p. 213-226.
[9] Phair JW, van Deventer JSJ, Smith JD. Effect of Al source and alkali activation on Pb and Cu immobilization in fly-ash based 'geopolymers'. Appl Geochem. 2004;19(3):423-434. https://doi.org/10.1016/S0883-2927(03)00151-3
[10] Malhotra VM, Mehta PK. High-performance, high-volume fly ash concrete: materials, mixture proportioning, properties, construction practice, and case histories. Aug 2002.
[11] HM T, Unnikrishnan S. Mechanical strength and microstructure of GGBS-SCBA based geopolymer concrete. J Mater Res Technol. 2024;7816-7831. https://doi.org/10.1016/j.jmrt.2023.05.051
[12] Kong DLY, Sanjayan JG, Sagoe-Crentsil K. Comparative performance of geopolymers made with metakaolin and fly ash after exposure to elevated temperatures. Cem Concr Res. 2007;37(12):1583-1589. https://doi.org/10.1016/j.cemconres.2007.08.021
[13] Siddique R. Utilization of industrial by-products in concrete. Procedia Eng. 2014;95:335-347. https://doi.org/10.1016/j.proeng.2014.12.192
[14] Shen J, et al. Prediction of compressive strength of alkali-activated construction demolition waste geopolymers using ensemble machine learning. Constr Build Mater. 2022;360:129600. https://doi.org/10.1016/j.conbuildmat.2022.129600
[15]IS 383 (1970): Specification for coarse and fine aggregates from natural sources for concrete, Bureau of Indian Standards, Manak Bhavan, 9, Bhadur Shah Zafar Marg, New Delhi, 110002.
[16] EFNARC Guidelines for SCC. Available from: https://wwwp.feb.unesp.br/pbastos/c.especiais/Efnarc.pdf.
[17]IS 516 (1959): Method of tests for strength of concrete, Bureau of Indian Standards, Manak Bhavan, 9, Bhadur Shah Zafar Marg, New Delhi, 110002.
[18] Bairagi NK, Modhera CD. Shear strength of fiber-reinforced concrete. ICI J. 2001;47-53.
[19] Baruah P, Talukdar S. A comparative study of compressive, flexural, tensile and shear strength of concrete with fibers of different origins. 2007;81:17-24.
[20]IS-456 (2000), Plain and Reinforced Concrete—Code of Practice, Bureau of Indian Standards, Manak Bhavan, 9, Bhadur Shah Zafar Marg, New Delhi, 110002.
[21] ACI PRC-544.4-18: Guide to design with fiber-reinforced concrete. Sep 29, 2023. Available from: https://www.concrete.org/store/productdetail.aspx?ItemID=544418&Language=English&Units=US_AND_METRIC.

[22] Demie S, Nuruddin MF, Shafiq N. Effects of micro-structure characteristics of interfacial transition zone on the compressive strength of self-compacting geopolymer concrete. Constr Build Mater. 2013;41:91-98. https://doi.org/10.1016/j.conbuildmat.2012.11.067
[23] Hulipalled P, Algur V, Lokesha V, Saumya S, Satyanarayan. Interpretable ensemble machine learning framework to predict wear rate of modified ZA-27 alloy. Tribol Int. 2023;188:108783. https://doi.org/10.1016/j.triboint.2023.108783
[24] Hulipalled P, Algur V, Veera L, Saumya S. Intelligent retrieval of wear rate prediction for hypereutectoid steel. Multiscale Multidiscip Model Exp Des. 2023;6:1-13. https://doi.org/10.1007/s41939-023-00172-x
[25] Hulipalled P, Algur V, Veera L. An approach of data science for the prediction of wear behaviour of hypereutectoid steel. J Bio Tribo Corros. 2022;8. https://doi.org/10.1007/s40735-022-00668-y
[26] Algur V, Hulipalled P, Veera L, Nagaral M, Auradi V. Machine learning algorithms to predict wear behavior of modified ZA-27 alloy under varying operating parameters. J Bio Tribo Corros. 2022;8. https://doi.org/10.1007/s40735-021-00610-8
[27] Sumanth Kumar B, Sen A, Rama SD. Shear strength sustainable construction materials. Select Proceedings of ASCM 2019. 2019;68:105-117. https://doi.org/10.1007/978-981-15-3361-7_8
[28] Wang Q, Ahmad W, Ahmad A, Aslam F, Mohamed A, Vatin NI. Application of soft computing techniques to predict the strength of geopolymer composites. Polymers. 2022;14:1074. https://doi.org/10.3390/polym14061074

Research on Engineering Structures & Materials
www.jresm.org
Research Group

Review Article

Integrating self-sensing nano composite and fiber optic sensors technologies for advancing structural monitoring: A mini review

Panga Bhavana [a], N. K. Karthikeyan [b], S. Elavenil [*,c]

Vellore Institute of Technology, Chennai-campus, School of Civil Engineering, Chennai, India

Article Info

Article History:

Received 22 July 2024

Accepted 12 Sep 2024

Keywords:

Concrete structure;
Structural health monitoring;
Advanced sensing technologies;
Fiber optic sensors;
Self-sensing nano composites;
Multifunctional sensors

Abstract

Concrete structures are susceptible to various damages due to ageing and natural hazards. The growing research focus in civil engineering systems is Structural Health Monitoring (SHM). Meanwhile, advanced sensing technologies play an eventual role in SHM, enhancing safety and maintenance by providing real-time data on concrete structures. This review represents the characteristics of advancing sensing technology, such as self-sensing sensors based on nanomaterials and fiber optic sensors. Further, the investigation has been performed to comprehend the evolving field of sensing technology related to several aspects, such as the principal mechanism, practical application, and challenges pertain to SHM. The advantages and limitations of integrating self-sensing multifunctional sensors with nanotechnology as an alternative to fiber optic sensors is discussed. In addition, the analogy of these two sensors is detailed to understand the efficiency of advanced sensing technology using nanotechnology. Both types of sensors exhibit the capability to monitor the changes in the structures. Self-sensing technology provides a straightforward solution, thus leading to cost-effective and simplified structural integrity compared to complex and fragile fiber optic sensors. Self-sensing multifunctional sensors offers an efficient integrated approach while fiber optic sensors provide comprehensive solution for structural monitoring. Particularly, self-sensing sensors offers direct data collection and large-scale applications for extensive projects due to their ease of installation. Therefore, the highly advanced self-sensing sensors with Level 5 technology will eventually be an ideal choice over FOS for SHM.

© 2025 MIM Research Group. All rights reserved.

1. Introduction

Concrete is an extremely versatile and composite material, that has been used globally for buildings, bridges, highway pavements, dams, tunnels, railway roads, sewers, and other infrastructure for over 200 years because of its durability, strength, and affordability [1]. Despite this, due to a lack of advanced technologies in concrete and limited maintenance of infrastructures [2,3], the concrete is subjected to extreme conditions, including chemical and physical effects, changes in the environmental conditions due to concrete shrinkage, stress, and pressure due to overloads leads to cracking, freeze-thaw cycle, corrosion, abrasions, and deterioration [4–7]. Thus, SHM would be of great scientific importance in detecting early signs of deterioration to extend the life of structures and reduce maintenance costs in existing structures [8]. Furthermore, it greatly adapts to the challenges of a dynamic building environment. An innovative approach to SHM involves real-time and continuous monitoring of structures to assess the performance, condition, and integrity of civil infrastructures [9,10]. The SHM collects data about the structural behavior and

[*]Corresponding author: elavenil.s@vit.ac.in
[a]orcid.org/0009-0004-5252-9915; [b]orcid.org/0000-0002-7963-7009; [c]orcid.org/0000-0003-4964-829X
DOI: http://dx.doi.org/10.17515/resm2024.362ma0722rv

identifies irregularities to allow insights that makes the decision [11]. A major component involved in SHM is advanced sensing technology that is based on various types of sensors. However, employing advanced sensing technology such as fiber optic sensors (FOS) [12] and self-sensing multifunctional sensors (SSMS) [13] for SHM has become comprehensive research interest. Due to these recent advancements in SHM, non-destructive techniques (NDT) of foretelling structural damage have significantly reduced [14].

The FOS play a crucial role in SHM due to their durability, accuracy, and ability to provide real-time data on various parameters of structures [15]. In SHM, the FOS involves in monitoring the changes in properties of structural elements by utilizing optical fibers with the interaction of light frequency and strain within the structure [16]. Such FOS is highly sensitive to detect small structural changes due to environmental conditions. Therefore, multiple sensors are required to be multiplexed along a single optical fiber to reduce the complexity and cost during installation. Moreover, it gives the possibility of monitoring using remote control for structures where the data can be transmitted over long distances. In the context of SHM, fiber-optic sensors are applied to monitor the strain and stress, temperature, crack detection, vibration, pressure, and load distributions in critical areas of structures [17,18], that extends the lifespan of infrastructures. It ultimately leads to improved infrastructure resilience by reducing unnecessary manual inspections and repair.

Noticeably, Intrinsic self-sensing sensors or SSMS are cement-based sensors which could be an alternative to fiber optic sensors but with different mechanism which is competitive and challenging in SHM to analyze the integrity and condition of the structures. SSMS are placed directly in different forms such as embedded, coating, sandwich, and bulk form into the structural material [19] to measure various parameters, such as strain, humidity, and temperature, without any external sensors [20]. The principle of self-sensing sensors is typically based on piezoelectric [21] and capacitive sensors. These self-sensing sensors are built directly into the structure without external attachments and highly sensitive to small changes in the behavior of the structure, respond quickly, and allow for immediate assessment of structural health. It has limited measurement range compared to some other external sensors. Additionally, developing and embedding SSMS can be expensive depending on the sensing material and challenging, respectively [22]. This mini state-of-the-art discusses the complete characteristics of FOS and SSMS with their features for dominant SHM application.

2. Characteristic of Advanced Sensing Technologies

2.1 Fiber optic sensors

In the field of civil engineering, the integration of FOS has emerged as an advanced technology for monitoring the structural integrity and complexity of various structures [23]. FOS are becoming more popular for SHM because they have a high level of sensitivity, accuracy, and can measure parameters like as strain, temperature, and vibration without significant signal loss. Due to their resilience to electromagnetic interference and lightweight characteristics, they are well-suited for integration into different structures without affecting their qualities. FOS possess durability, resilience under challenging conditions, and the ability to facilitate multiplexing, allowing for the simultaneous monitoring of several sensors using a single fiber. In addition, their ability to sense and gather data from multiple locations allows for continuous monitoring of a whole structure, providing real-time information. The extended longevity and little upkeep of FOS also contribute to its cost-effectiveness in the context of extensive, vital infrastructures. FOS is adopted for condition assessment of concrete piers which is subjected to impact load [24] as well as in static and dynamic monitoring of large structures [25]. Typically, FOS are classified in varieties as shown in Figure 1, including Fabry-Perot type interferometers (FP-I), Fiber Bragg grating (FBG), microbend, wavelengths, and Brillouin [16,17,26] with special coatings and strain mechanisms which are useful in detecting various parameters such as stress, pressure, length, crack width, temperature, and chemical changes. The aforementioned advanced sensor technology provides engineers and researchers with real-time data, allowing them to comprehensively understand how structures behave under different conditions. For instance, Figure 2 shows the overview of FOS with deep learning techniques for SHM. However, the installation of these sensors poses many

challenges, especially ensuring their proper integration into structural components. To overwhelm such setback, it is associated with fiber escape, strain relief conduits, and wireless telemetry solutions to improve the reliability and efficiency of installation [27,28]. The FOS is unsusceptible to radio and electromagnetic interference owing to its dielectric material [29]. Among FOSs, the use of FBG sensor and Stimulated Brillouin Scattering (SBS) sensors has become prevalent in measuring temperature and strain with exceptional sensitivity and accuracy [30]. Besides the change in wavelength of FBG, the change in strain and temperature can be determined using the Equation (1) and modelled by using equation (2) – (5) [31–35].

$$\frac{\Delta\lambda_B}{\lambda_B} = P_e\varepsilon_{zz} + \left(P_e\ (\alpha_s - \ \alpha_f\right) + \zeta)\ \Delta T \tag{1}$$

Where P_e is coefficient of strain optic α_s is thermal expansion of material; α_f thermal expansion of optic fibre; ε_{zz} is axial strain; ζ is coefficient of thermo-optic;

$$\Delta\lambda_B = K_\varepsilon\varepsilon + \ K_T\Delta T + \ K_pP \tag{2}$$

$$K_\varepsilon = [1 - 0.5n_{eff}\ \left(\rho12 - \ \nu(\rho11 - \ \rho12)\right)]\lambda_B \tag{3}$$

Where;

$$K_T = [\alpha + \ \xi]\lambda_B \tag{2}$$

$$K_P = [-\frac{1-2\nu}{E} + \frac{n^2}{2E}\ (1-2\nu)(2\rho12 + \ \rho11)]\lambda_B \tag{3}$$

But the FBG sensors that is attached to the structures using adhesives, failing to which errors due to temperature [36]. Also, Moyo et al. compared the static and tensile test results of concrete beam and steel bar, respectively. The investigation exhibit that the FBG can be effectively used for strain measurement because the system having an accuracy of 5με and sensitivity of 1με [32]. Whereas, FBGs are particularly suitable for distributed sensing, while SBS sensors enable distributed sensing capabilities [37].

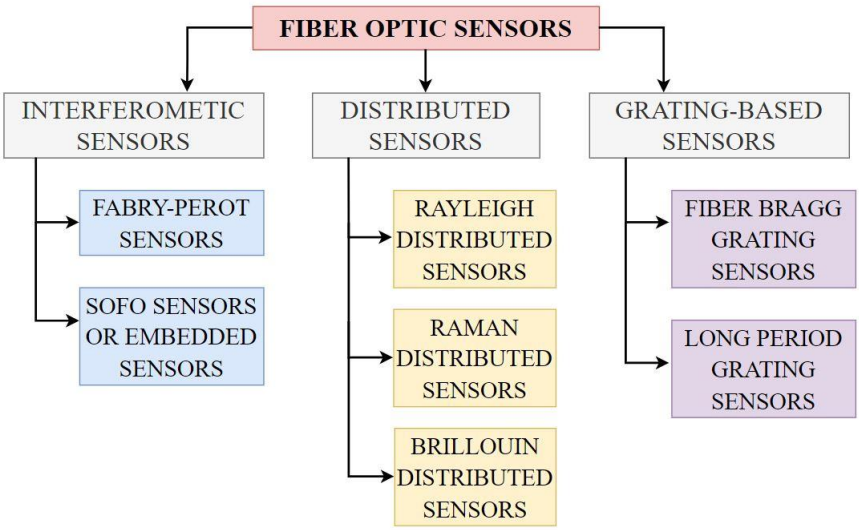

Fig. 1. Classification of fiber optic sensors

The distributed FOS enables the automatic interpretation of crack measurement using machine learning techniques [38]. Such FOS technologies offer reliable and precise solutions to various technical challenges making them invaluable tools for monitoring and data collection in a wide range of civil engineering applications like infrastructure monitoring [39] and marine structures [40]. Consequently, a significant innovation in the field of smart optical fiber (SOF) is the development of FOS pre-embedded in concrete (PEC) as shown in Figure 3 a) and 3 b). The particular sensors are specifically designed to analyse the temperature characteristics of various cementitious matrix materials and pre-stressed bars. Despite the practical challenges associated with the sensitivity and fragility of FOS [25], the implementation of PEC sensors represents a significant leap forward in the quest for enhanced structural monitoring and safety within the construction industry [41,42].

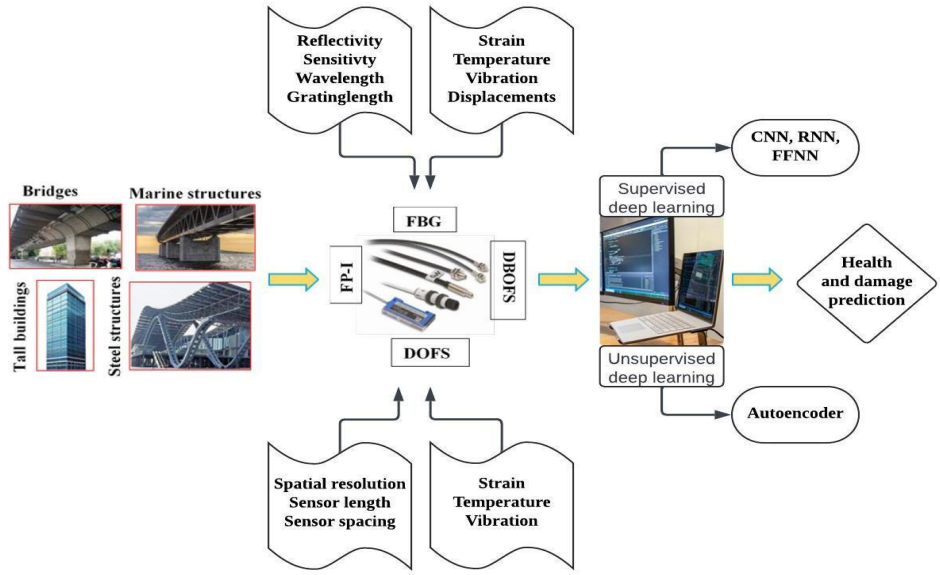

Fig. 2. Overview of FOS with deep learning technique for SHM

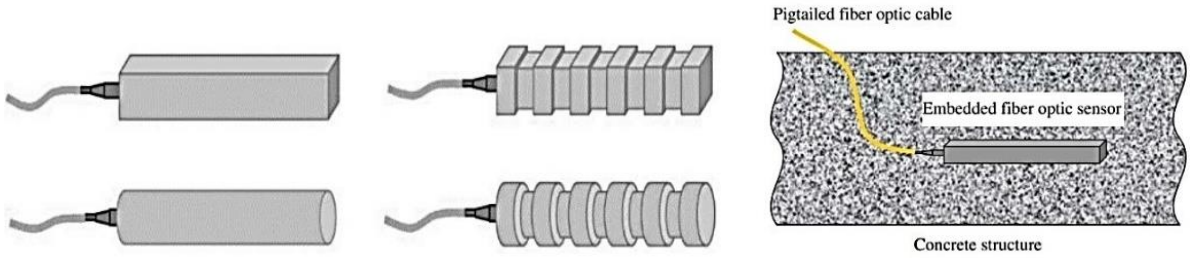

(a) (b)

Fig. 3. (a) Shapes of PEC sensors [42], (b) Embedded FOS in concrete structure [41]

In addition, the FOS has led to the discovery and use of plastic optical fibers (POF) in crack and monitoring applications due to its traditional fragility. The POFs exhibit light intensity changes at the initial crack growth stage, making them suitable for early detection. The experimental results using crack simulation samples and concrete beams exhibit that the sensitivity of POF in crack monitoring decreases as the angle between POF and crack increases [43]. Moreover, lens based POF is used to monitor the rebar corrosion due to impressed current [44]. Eventually, the advances towards POF is by highlighting the adaptability and flexibility of FOS technology associated with structural health monitoring [43,44]. Besides the crack and corrosion monitoring, the real-time analysis of temperature and strain of the pavement slabs are monitored using distributed FOS. It has the capability of providing a comprehensive analysis of longitudinal temperature distributions, heat flux transfer from top to bottom, and strain patterns in both vertical and longitudinal orientations.

The immediate insights derived from these results aid in assessing potential deformation patterns within the pavement slab, contributing to game changer of structural assessments and maintenance [45,46]. Additionally, FOS continue to evolve and offers a recent advancement capability for SHM. For instance, the recent insights such as smaller, flexible FOS enabling integration into diverse structure; improved spatial resolution for detecting minute changes over long distances; and wireless communication enhancing the real-time data transmission. In addition, FOS integrated with AI and IoT analytics for predicting and assessing the damages in the structure.

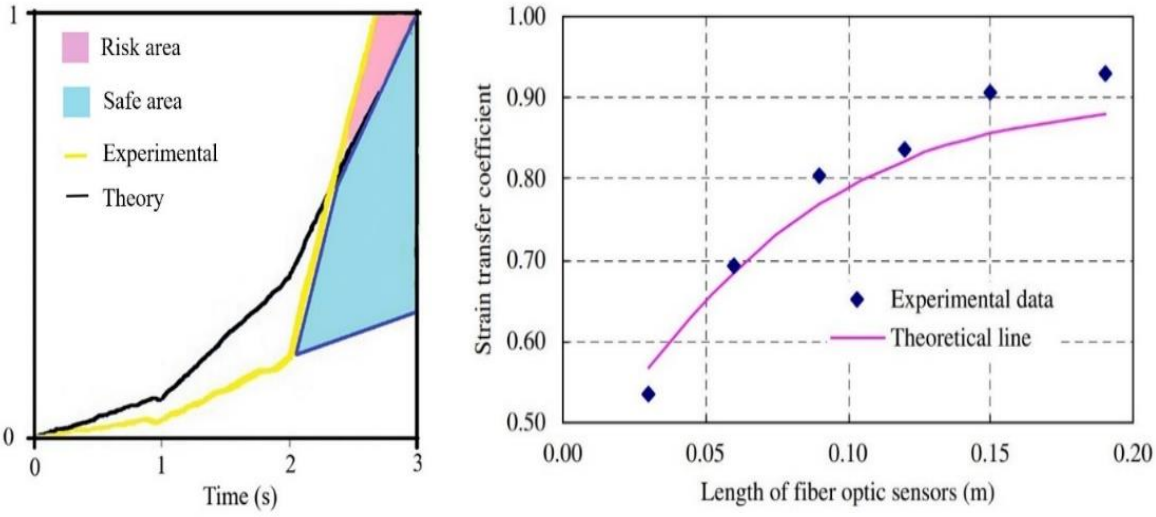

Fig. 4. Graphical representations of experimental and theoretical results for SHM using FOS [16,41]

The FOSs can assess various parameters, including strain, temperature, refractive index, chloride ion concentration, and pH value for all type of reinforced concrete. The Figure 4 represents the graphical interpretation of experimental and theoretical results obtained using FOS, where the structural integrity is determined between two curves. The FOS has the advantage in offering real-time information on structural deformation and stress, which can improve safety by detecting potential problems before they occur. In this regard, the real-time data obtained using linear regression curve between the corrosion penetration and deformation measured using optical fiber is depicted in the Figure 5 for an elementary observation. Furthermore, the continuous monitoring supported by FOS technology contributes to the development of predictive maintenance strategies, minimizing the risk of structural failure, and optimizing the lifespan of critical infrastructure.

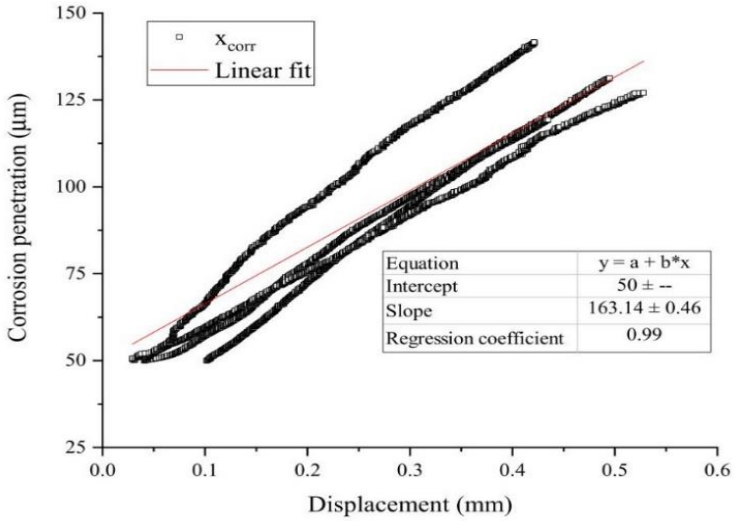

Fig. 5. Linear regression curve for the real-time data using optical fiber [44]

It is used to monitor the shrinkage and creeps of the concrete, loads on cable bridges, rebar corrosion and crack detection, rail tracks, underground mines, water pipelines for leakages, masonry structures, steel and concrete bridges. The implementation of optical fiber in various forms for SHM of different civil structures and elements is shown in the Figure 6. However, there are still certain shortcomings in FOS such as expensive interrogation system, need for specialist expertise and several repeaters for signal boosting. Moreover, to understand the working principal of FOS, it is necessary to know the basics of light propagation in fiber optical cables where the entire process is based on the principle of total internal reflection. This phenomenon is particularly noticeable when the shell material has a lower refractive index than the core material. The proper application of these principles is essential for the successful design and deployment of fiber optic sensing systems. Nonetheless, the FOS is commonly employed for SHM, the operative service and durability of sensors is quite a disadvantage and requires an alternative with multifunctional properties.

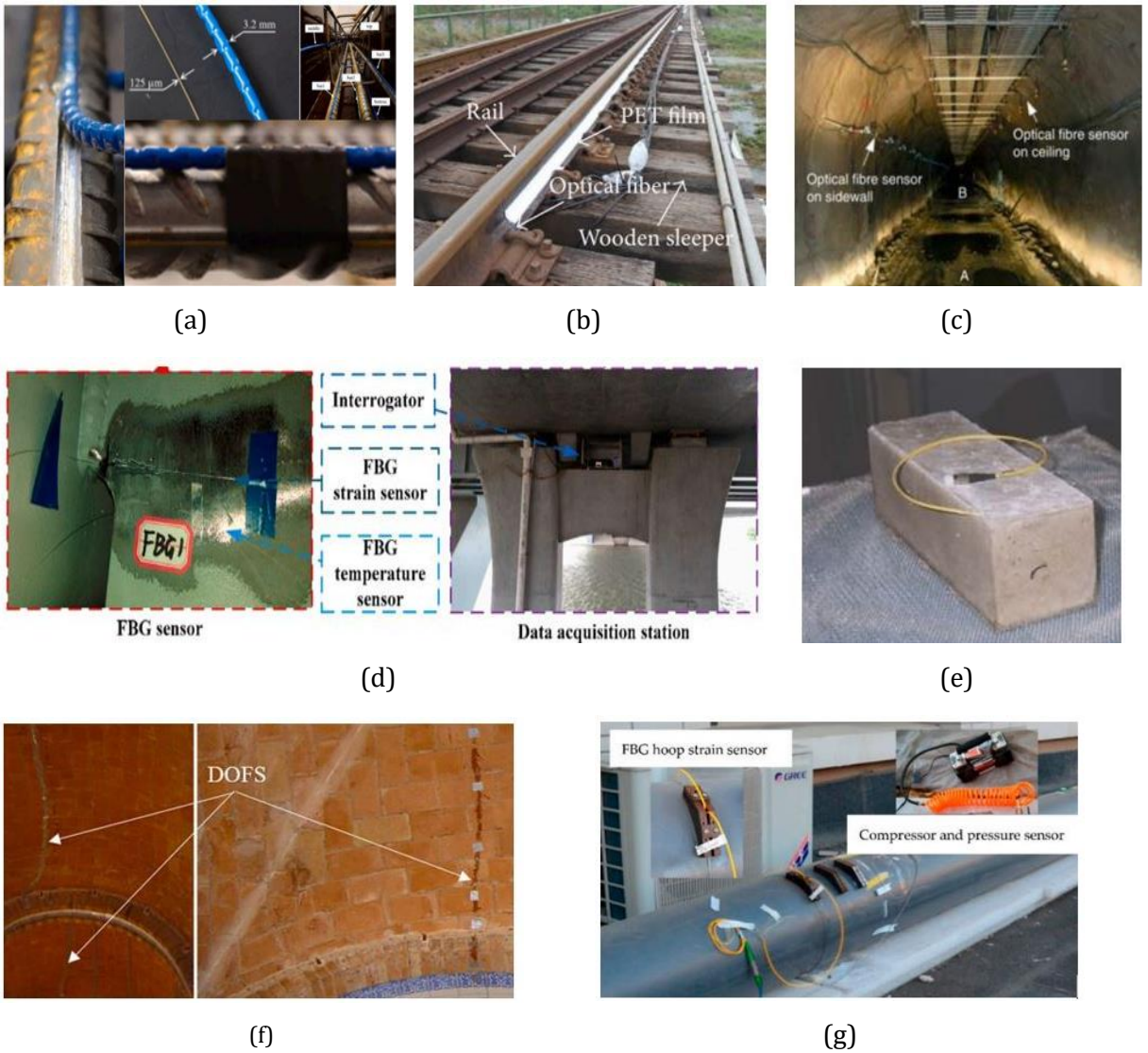

Fig. 6. Implementation of FOS is various forms for system of civil SHM a) Crack detection in rebar [47] b) Monitoring rail tracks [48] c) Strain monitoring in underground mining tunnel [49] d) Monitoring steel bridge crossing in china [50] e) Embedded sensors in concrete element for SHM [41] f) Crack detection in masonry walls [51] g) Monitoring leakage in the water pipeline [52]

2.2 Nano Self-Sensing Composites/Multifunctional Sensor

The cement matrix is not a conductive material without sensing parameters. Therefore, a conductive filler is dispersed effectively into the cementitious matrix to develop SSMS composite [53–57]. The structure of SSMS composites is depicted in Figure 7 a). This technique is based on the principle of the piezo resistivity effect, where the nano functional filler creates a conductive network resulting in conductivity [58–60]. While incorporating nano conductive fillers, the electrical resistivity of composites will reduce to 1 ohm cm. The conductivity network formed by the effective electron hopping and percolation path attributes to the sensitive particles inside the cement matrix, which is called as percolation threshold (Φ_c). Figure 7 b) depicts the formation of conductive networks in the matrix. The different conduction theories for SSMS composites includes, percolation theory [61], the tunneling effect [62], electric field emission [63], and effective medium theory [64]. The behavior of SSMS depends on the nature of electrical conductivity in the matrix as a function of filler concentration (Φ), during the process of percolation. There are different zones of conductive mechanisms during the formation of conductive networks. In the zone A ($\Phi < \Phi_c$) mechanism, the conductive filler or nanofiller percentage is less compared to the percolation threshold. Here, the cement matrix will tend to have high resistivity due to the more movement of electrons which resist creating a conductive network. It is also called an insulation zone showing ionic conduction. In zone B ($\Phi = \Phi_c$), percolation indicates that the conductive filler amount is equal to the percolation threshold. Therefore, the distance between the fillers will be reduced and the conductive link will start resulting in tunnelling conduction. In zone C ($\Phi > \Phi_c$), the filler concentration will be greater than the percolation threshold and the mechanism itself stabilizes the sensing property inside the matrix.

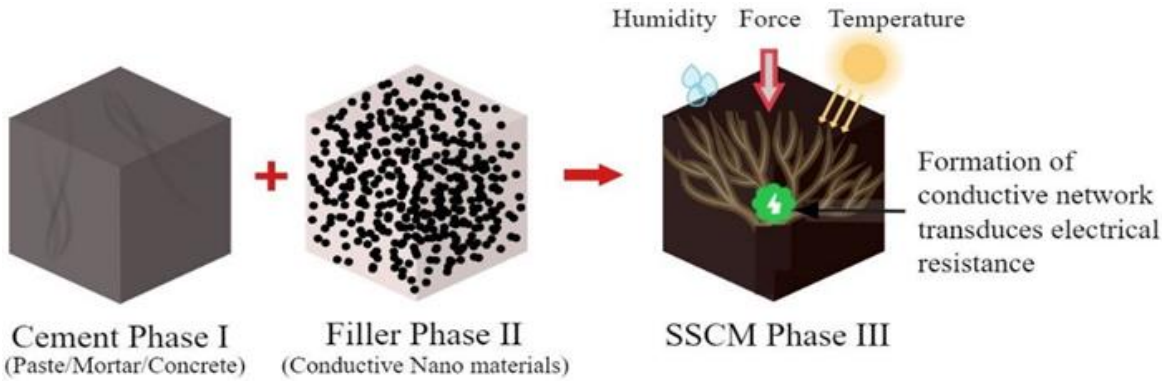

(a)

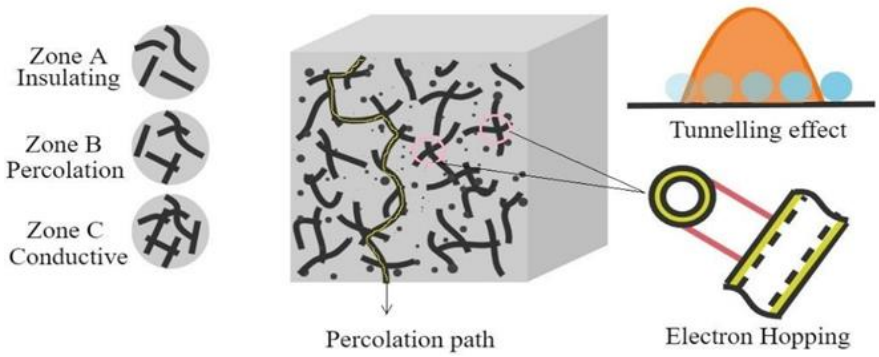

(b)

Fig. 7. a) 3-phase structure of self-sensing [65], b) Formation of conductive network in matrix [65]

When these sensing composites are exposed to the natural ecological process or external forces or loads [53,61], the network inside the matrix is distributed leading to FCR (fractional change in resistivity). By principally adopting this method, electrical property could be measured to

determine the cracks, damage, stress, strain, temperature, and humidity in various loading conditions like static or cyclic. This also depends on the contact between the fillers in the composites due to piezo resistivity [59]. The principle of SSMS behaves like a human brain as a nervous system like human action [66]. The cement-based sensors were compared with 10mm foil strain sensor for cyclic compression load by converting to electrical resistivity resulting in less error margin.

The SSMS composite influenced with conductive nanomaterial influence multifunctional properties that are used effectively in the different civil engineering application for SHM. Cement-based sensors are exceptionally efficient for SHM owing to their material compatibility with concrete, which guarantees precise and dependable readings of strain, cracks, and deformation. Their self-sensing capabilities, utilizing variations in electrical resistivity to identify stress and fractures, facilitate the early diagnosis of structural problems. These sensors, embedded directly in concrete, provide durability, long-term stability, and resilience to hostile environments, rendering them suitable for continuous monitoring. Cement-based sensors are cost-effective and easily integrated during construction, offering both local and distributed sensing capabilities to monitor extensive areas or crucial locations. Their adaptability, along with prospective improvements through smart materials, renders them a sustainable and efficient choice for long-term infrastructure monitoring. Concurrently, SSMS composites is also defined as nanocomposites with special properties like sensor application which is used in advanced industries [67]. Moreover, it is appropriately used in many applications to monitor the effects of the reinforced concrete beams [68], stress-strain behavior of concrete using cement sensor by short analysis time [69], beam-column sub-assemblage using embedded SSMS [70], to transform roads into smart pavements by weigh-in-motion (WIM) characterization [71,72], and to detect the traffic of vehicle speed and human motion [73,74]. Moreover, SSMS is used in rail infrastructures for low-cost monitoring, railway sleepers, and aircraft structures for self-diagnostic functionalities [75–77]. In addition, the self-sensing sensors are used to evaluate the temperature and moisture variations of concrete structure [20].

The renaissance of SSMS composites is developed with essential sensing properties such as electrical resistivity, piezo resistivity (FCR, hysteresis, linearity, repeatability, and signal to noise ratio), electrical sensitivity (stress, strain, and force sensitivity), and conductivity. Simultaneously, developing hydrophobic SSMS composites is crucial for maintaining the durability of cement-based composites [78,79]. The schematic illustration of measuring electrical resistivity and piezo resistivity is depicted in the Figure 8 a) and 8 b). In order to measure the multifunctional sensing ability, the following relevant formulae are used, as stated in the equation (6) – (15).

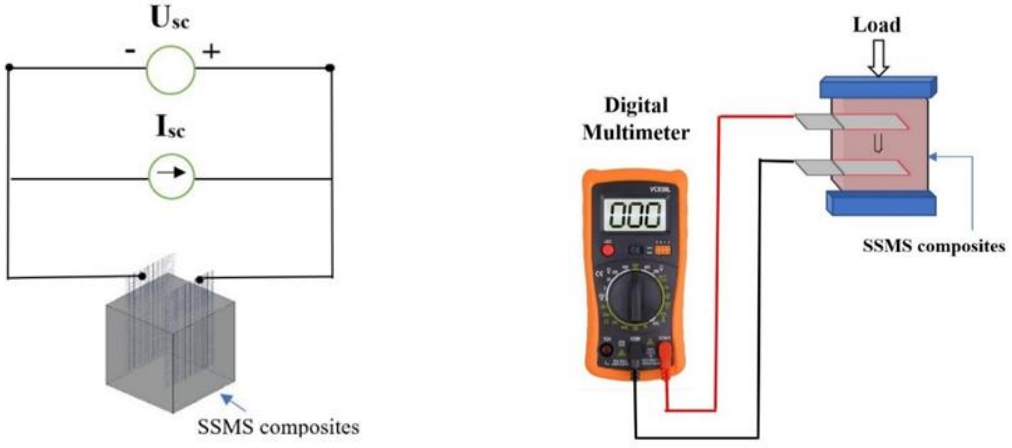

(a) (b)

Fig. 8 a) Electrical resistivity measurement, b) piezoresistivity measurement

2.2.1 Electrical Resistivity (ρ)

$$\rho = \frac{U_{sc} \cdot R_r \cdot A}{U_r \cdot L} \Omega.cm \quad (6)$$

where U_{sc} = voltage of the sensor composite (v), U_r = voltage of the resistor (v), R_r = resistance of the resistor (Ω), L = distance between electrodes (cm), and A = area of electrodes (cm^2).

2.2.2 Piezo Resistivity

$$FCR = \frac{\frac{V_{sc} \cdot R_r}{V_r} - R_i}{R_i} \quad (7)$$

Where V_{sc} = voltage over the sensor composite (v), R_r = resistance of the resistor (Ω), R_i = initial electrical resistance of the sensor composite (Ω), V_r = voltage of the resistor (v);

$$Hysteresis\ (H) = \frac{\Delta\, FCR_{max}}{FCR_f} \quad (8)$$

$$Repeatability\ (L) = 1 - \frac{\Delta\, FCR_{max-i}}{FCR_f} \quad (9)$$

$$Linearity\ (E) = \frac{\Delta Max}{\Delta \rho_{FS}} \quad (10)$$

$$Signal\ to\ noise\ ratio\ (SNR) = 10log_{10}\left(\frac{P_s}{P_n}\right) = 10log_{10}\left(\frac{A_s^2}{A_n^2}\right) \quad (11$$

Where $\Delta\, FCR_{max}$ = maximum variation of FCR, FCR_f = change in electrical resistance under loading, $\Delta\, FCR_{max-i}$ = maximum change in FCR, $\Delta\rho_{FS}$ = full scale FCR output value, P_s = signal power, P_n = noise power, A_s = amplitude of signal, A_n= amplitude of noise, and ΔMax = maximum deviation between the piezoresistive.

2.2.3 Electrical Sensitivity

$$Strain\ sensitivity\ co: \frac{\Delta R/R_i}{\varepsilon} = \frac{FCR}{\varepsilon} \quad (12)$$

$$Stress\ sensitivity\ coefficient: \quad \frac{\Delta R/R_i}{\sigma} = \frac{FCR}{\sigma} \quad (13)$$

$$Force\ sensitivity\ coefficient: \quad \frac{\Delta R/R_i}{F} = \frac{FCR}{F} \quad (14)$$

Where ΔR = variation in electrical resistance (Ω), ε = strain due to load, σ = stress/load, R_i = initial electrical resistance of SSMS (Ω), ε = strain due to load, σ = stress/load.

2.2.4 Conductivity

$$\delta = \delta_f \left(\frac{\varphi - \varphi_c}{1 - \varphi_c}\right)^{\gamma} \quad (15)$$

Where, δ_f = filler conductivity, γ = universal exponent, φ = filler concentration, and φ_c = percolation threshold.

The dominant sensing parameters are crucial in self-sensing composites for structural health monitoring application. The Table 1 depicts the various improved parameters to attain smart composites. Whereas, the challenges faced during installation, visualization, and identifying the crack patterns and failures are greatly reduced. The integration of nanomaterials into the SSMS enables it to exhibit versatile characteristics, which can be effectively utilized in a range of applications. These include monitoring high-speed rail infrastructures, detecting traffic, and implementing smart pavements through weigh-in-motion (WIM) sensing. Further, SHM is utilized

in several applications, including railway sleepers, vibrations, structure deformations, dynamic load behavior, aviation structures, self-cleaning, stress-strain behavior of concrete, corrosion of steel in concrete structures, and monitoring the operation of large-scale sub-assemblages such as RC beams and beam-columns. This enables the use of SSMS in SHM to achieve intelligent and sustainable infrastructures, with a focus on high accuracy and convenient installation. Figures 9 depict the utilization and implementation of SSMS in various structural contexts to monitor the condition and detect any damage. The high precision self-sensing sensors paves the way for various field applications as an alternate to FOS to attain smart infrastructure.

Table 1. Improved parameters of self-sensing multifunctional sensor

Type of composites	Stress Sensitivity (% / MPa)	Strain Sensitivity	Linearity (%)	Repeatability (%)	Hysteresis (%)	Ref. / Year
Paste	1.35	227	4.17	4.05	3.61	[77]/2007
Mortar	2.69	7.4	-	-	-	[80]/2015
Mortar	$2.86*10^{-3}$	30.28	-	-	-	[81]/2017
Mortar	3.12	521	-	-	-	[82]/2018
Mortar	-	155	-	0.95	-	[83)/2020
Mortar	-	-	15.47	28.12	-	[84]/2021
Mortar	-	155.5	0.961	-	-	[85]/2021
Mortar	2.714	-	11.795	13.178	-	[86]/2021
Paste	-	74.90	0.67	-	1.14	[87]/2021
Paste	1.27	408	15.51	11.92	25.86	[88]/2022
Paste	-	30.10	-	0.994	-	[89]/2022
Paste	1.39	463	10.84	10.05	19.32	[90]/2022
Paste	0.49	86.03	-	-	-	[91]/2022
Paste	-	142	0.891	0.750	0.382	[92]/2022

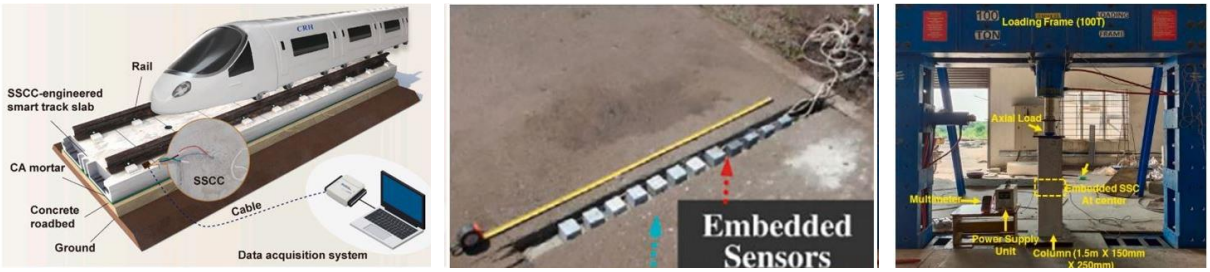

(a) (b) (c)

(d) (e)

Fig. 9. a) High speed rail monitoring [77] b) Traffic monitoring [93] c) Measuring deflection of column using SSMS [94] d) vibration sensing of RC beam [95] e) Application of SSMS in structures [65]

3. Analogy between FOS and SSMS

In contrast to FOS with SSMS technology for SHM, both technologies have their own advantages and limitations. Besides, FOS, developed by the Fiber Bragg grating and Fiber-Perot interferometer, provides versatile and advanced techniques for collecting real-time data on various parameters; automated technology perception is more capable, particularly in certain situations. In SSMS sensing technology, such as smart materials with built-in sensing capabilities directly emerge into structural elements. This inherent characteristic exhibits the process of monitoring, reduces complexity in integrating, and mitigates both fragility and sensitivity. Furthermore, SSMS technology is often integrated with the structural components in order that monitoring can be distributed and continuous without additional instrumentation.

Table 2. Comparative study between different FOS and SSMS composite

Sensors	Type	Material	Working principle	Type of damage detected	Advantages	Limitations
Fiber Optics Sensor	Optical	Optic fiber	Light refractivity	Multiple	Effective for damage detection for entire length of fiber, Free from Electromagnetic Influence	Fragile, hence proper care to be taken while installation
FBG Sensor	Optical	Optic Fiber	Light refractivity	Multiple	Effective for damage detection for entire length of fiber, Free from Electromagnetic Influence	Fragile, hence proper care to be taken while installation
Carbon based graphene sensor	Wired, electrical	Carbon nano material	Change in electronic energy band	Multiple	Lightweight and highly sensitive	In certain applications it is used for particularly for one damage parameter
Cement based sensor	Wired, electrical	Cement with nano material	Change in fractional change in resistivity	Multiple	Parent element which is easy to embed into concrete	In certain applications it is used for particularly for one damage parameter

In practice, SSMS sensing technology can provide a more straightforward solution, particularly when the structural material is capable of sensing. Therefore, it can lead to cost savings and simplified monitoring, compared to the more complex installation processes and potential issues with FOS. Moreover, SSMS sensing technologies provide a more direct and immediate assessment of structural conditions because they are intrinsically embedded within the structural material, providing real-time feedback without any external sensors. However, it's important to choose between FOS and SSMS sensing technology depending on the requirements of the application. FOS is applied for various parameters, such as temperature, strain, pressure, and environmental changes. Their adaptability and versatility make them convenient for a broad range of applications. Additionally, SSMS sensing technologies can be more advantageous in the SHM applications. The comparative study for different FOS and SSMS sensors used for SHM is shown in Table 2. Concisely, both FOS and SSMS composites exhibit the capability to monitor the changes in their surroundings. Meanwhile, they contribute valuable insights into SHM and environmental conditions through their different physical principles.

4. Conclusion and Future Study

This mini-review gives the retrospective discussion on the characteristics of advanced sensing technologies, such as self-sensing cement sensors developed using nanomaterials and commercially available fiber sensors. The investigation has been performed to perceive the evolving field of sensing technology related to several aspects, such as the principal mechanism, practical application, and challenges pertain to SHM. Eventually, this mini-review guides an understanding of AST for SHM with FOS and SSMS composites with their principles and parameters. The priority of either FOS or SSMS composites in SHM may depend on the specific projects. However, sensitivity and measurement accuracy are the crucial parameter for adopting both FOS and SSMS for detecting the changes during structural integrity. Whereas, selecting right FOS involves balancing the accuracy, reliability, and range on the specific requirement for SHM. While the SSMS technologies offer an efficient integrated approach over the intended service life of the structure with stability, durability, and compatibility with cement. Particularly, SSMS offers simplified data acquisition and higher scalability for extensive projects due to their ease of installation. Notably, FOS only provides a comprehensive solution for monitoring various parameters. Ultimately, the choice between the technologies should also be guided by an understanding of the project's requirements with consideration of factors such as accuracy, sensitivity, cost, and structural environment. Nevertheless, the development of SSMS composites is challenging with complicated nanomaterial that is to be optimized. In this regard, SSMS composites with higher evolution (level 5) technology in SHM will be an ideal choice for early detection of potential issues during structural integrity. Hence the SSMS composites is recommended over FOS in multiple contexts for SHM. The future direction and challenges in the evolution of SSMS is outlined as follows:

- Extensive investigation is necessary to achieve self-healing property in SSMS composites for structural integrity.
- The parameters of SSMS composites could be optimized by decoupling algorithm with circuit measurement method or micro-mechanic modeling.
- In-depth investigation is required to study the synergistic effect of SSMS composites.
- The trend of correlating SSMS composites with concrete structures could be extended beyond the SHM to military vigilance.

Abbreviations

FBG – Fiber bragg grating
FCR – Fractional change in resistivity
FOS – Fiber optic sensor
POF – Plastic optical fibers
SHM – Structural health monitoring
SSMS – Self-sensing multifunctional sensor

Acknowledgement

Authors would like to thank Vellore Institute of Technology for providing facilities for carry this research and thank Dean-School of Civil Engineering.

References

[1] Gagg CR. Cement and concrete as an engineering material: An historic appraisal and case study analysis. Eng Fail Anal. 2014;40:114-40. https://doi.org/10.1016/j.engfailanal.2014.02.004
[2] Gardner D, Lark R, Jefferson T, Davies R. A survey on problems encountered in current concrete construction and the potential benefits of self-healing cementitious materials. Case Stud Constr Mater. 2018;8(October 2017):238-47. https://doi.org/10.1016/j.cscm.2018.02.002
[3] Van Damme H. Concrete material science: Past, present, and future innovations. Cem Concr Res. 2018;112(May):5-24. https://doi.org/10.1016/j.cemconres.2018.05.002
[4] Madraszewski S, Stephan D. The decisive role of the abrasion stress in concrete corrosion during acid attack - Comparison of resistance of different concrete types. Constr Build Mater. 2023;408(May):133736. https://doi.org/10.1016/j.conbuildmat.2023.133736

[5] Afroz S, Nguyen QD, Zhang Y, Kim T, Castel A. Cracking of limestone calcined clay blended concrete and mortar under restrained shrinkage. Constr Build Mater. 2023;386(May):131599. https://doi.org/10.1016/j.conbuildmat.2023.131599
[6] Gan L, Liu Y, Zhang Z, Liu J, Jin H, Sun Y. Dynamic mechanical properties of concrete with freeze-thaw damage under different low-temperature conditions. J Build Eng. 2023;80(August):107986. https://doi.org/10.1016/j.jobe.2023.107986
[7] Pandiyan T, Solaiyan E. Effect of zinc industrial waste on the mechanical and microstssructural properties of the ternary blended concrete. Glob Nest J. 2024;26(3):05555.
[8] Yi TH, Li HN. Innovative structural health monitoring technologies. Measurement\. 2016;88:343-4. https://doi.org/10.1016/j.measurement.2016.05.038
[9] Salehi H, Burgueño R, Chakrabartty S, Lajnef N, Alavi AH. A comprehensive review of self-powered sensors in civil infrastructure: State-of-the-art and future research trends. Eng Struct. 2021;234(December 2020):111963. https://doi.org/10.1016/j.engstruct.2021.111963
[10] Yu X, Fu Y, Li J, Mao J, Hoang T, Hao W. Recent advances in wireless sensor networks for structural health monitoring of civil infrastructure. J Infrastruct Intell Resil [Internet]. 2023. https://doi.org/10.1016/j.carbpol.2021.118159
[11] Jayawickrema UMN, Herath HMCM, Hettiarachchi NK, Sooriyaarachchi HP, Epaarachchi JA. Fibre-optic sensor and deep learning-based structural health monitoring systems for civil structures: A review. Measurement. 2022;199(May):111543. https://doi.org/10.1016/j.measurement.2022.111543
[12] Ansari F. Fiber optic sensors for structural health monitoring of civil infrastructure systems. In: Karbhari VM, Ansari FBTSHM of CIS, editors. Woodhead Publishing Series in Civil and Structural Engineering [Internet]. Woodhead Publishing; 2009. p. 260-82. https://doi.org/10.1533/9781845696825.1.260
[13] Wang Y, Sun S, Zhang L. Self-sensing cementitious composites incorporating hybrid NGPs/CNTs/NCBs for structural health monitoring. Sensors Actuators A Phys. 2023;357(March):114365. https://doi.org/10.1016/j.sna.2023.114365
[14] Pallarés FJ, Betti M, Bartoli G, Pallarés L. Structural health monitoring (SHM) and Nondestructive testing (NDT) of slender masonry structures: A practical review. Constr Build Mater. 2021;297:123768. https://doi.org/10.1016/j.conbuildmat.2021.123768
[15] Floris I, Adam JM, Calderón PA, Sales S. Fiber Optic Shape Sensors: A comprehensive review. Opt Lasers Eng. 2021;139(December 2020):106508. https://doi.org/10.1016/j.optlaseng.2020.106508
[16] Das S, Saha P. A review of some advanced sensors used for health diagnosis of civil engineering structures. Measurement. 2018 Dec 1;129:68-90. https://doi.org/10.1016/j.measurement.2018.07.008
[17] Taheri S. A review on five key sensors for monitoring of concrete structures. Constr Build Mater. 2019;204:492-509. https://doi.org/10.1016/j.conbuildmat.2019.01.172
[18] Fan L, Bao Y. Review of fiber optic sensors for corrosion monitoring in reinforced concrete. Cem Concr Compos. 2021;120(March):104029. https://doi.org/10.1016/j.cemconcomp.2021.104029
[19] Han B, Ding S, Yu X. Intrinsic self-sensing concrete and structures: A review. Meas J Int Meas Confed. 2015;59:110-28. https://doi.org/10.1016/j.measurement.2014.09.048
[20] Adresi M, Pakhirehzan F. Evaluating the performance of Self-Sensing concrete sensors under temperature and moisture variations- a review. Constr Build Mater. 2023;404(August):132923. https://doi.org/10.1016/j.conbuildmat.2023.132923
[21] Gomasa R, Talakokula V, Kalyana Rama Jyosyula S, Bansal T. A review on health monitoring of concrete structures using embedded piezoelectric sensor. Constr Build Mater. 2023;405(August):133179. https://doi.org/10.1016/j.conbuildmat.2023.133179
[22] Siahkouhi M, Razaqpur G, Hoult NA, Hajmohammadian Baghban M, Jing G. Utilization of carbon nanotubes (CNTs) in concrete for structural health monitoring (SHM) purposes: A review. Constr Build Mater. 2021;309(June):125137. https://doi.org/10.1016/j.conbuildmat.2021.125137
[23] Bremer K, Wollweber M, Weigand F, Rahlves M, Kuhne M, Helbig R, et al. Fibre Optic Sensors for the Structural Health Monitoring of Building Structures. Procedia Technol. 2016;26:524-9. https://doi.org/10.1016/j.protcy.2016.08.065
[24] Xie J, Yang H, Jing Z, Zhang Y, Hong W, Hu X. Condition assessment of concrete piers subjected to impact load using fiber optic sensing. Case Stud Constr Mater. 2022;17(October):e01597 Contents. https://doi.org/10.1016/j.cscm.2022.e01597
[25] Antunes P, Lima H, Varum H, André P. Optical fiber sensors for static and dynamic health monitoring of civil engineering infrastructures: Abode wall case study. Meas J Int Meas Confed. 2012;45(7):1695-705. https://doi.org/10.1016/j.measurement.2012.04.018
[26] Han T, Wu G, Lu Y. Crack monitoring using short-gauged Brillouin fiber optic sensor. Meas J Int Meas Confed. 2021;179(January):109461. https://doi.org/10.1016/j.measurement.2021.109461
[27] Clark P, Boriniski J, Gunther M, Poland S. Modern fibre optic sensors. Smart Mater Bull. 2001;2001(6):8-11. https://doi.org/10.1016/S1471-3918(01)80170-2

[28] Fernando GF. Fibre optic sensor systems for monitoring composite structures. Reinf Plast. 2005;49(11):41-9. https://doi.org/10.1016/S0034-3617(05)70836-5
[29] Ansari F. State-of-the-art in the applications of fiber-optic sensors to cementitious composites. Cem Concr Compos. 1997;19(1):3-19. https://doi.org/10.1016/S0958-9465(96)00038-8
[30] Jo HJ, Park DY, Kim KW, Ahn TJ. Real-time monitoring of concrete curing using fiber Bragg grating sensors: Strain and temperature measurement. Sensors Actuators A Phys. 2023;362(July):114650. https://doi.org/10.1016/j.sna.2023.114650
[31] Majumder M, Gangopadhyay TK, Chakraborty AK, Dasgupta K, Bhattacharya DK. Fibre Bragg gratings in structural health monitoring-Present status and applications. Sensors Actuators, A Phys. 2008;147(1):150-64. https://doi.org/10.1016/j.sna.2008.04.008
[32] Moyo P, Brownjohn JMW, Suresh R, Tjin SC. Development of fiber Bragg grating sensors for monitoring civil infrastructure. Eng Struct. 2005;27(12 SPEC. ISS.):1828-34. https://doi.org/10.1016/j.engstruct.2005.04.023
[33] Takeda S ichi, Sato M, Ogasawara T. Simultaneous measurement of strain and temperature using a tilted fiber Bragg grating. Sensors Actuators A Phys. 2002;101:107-16. https://doi.org/10.1016/S0924-4247(02)00188-7
[34] Poloso T. Fibre Bragg grating optical sensing technology. Smart Mater Bull. 2001;(September):7-10. https://doi.org/10.1016/S1471-3918(01)80151-9
[35] Matveenko V, Kosheleva N, Serovaev G. Measurement of strain and temperature by fiber-optic sensors embedded into samples manufactured by additive technology. Procedia Struct Integr. 2022;42:307-14. https://doi.org/10.1016/j.prostr.2022.12.038
[36] Kister G, Winter D, Badcock RA, Gebremichael YM, Boyle WJO, Meggitt BT, et al. Structural health monitoring of a composite bridge using Bragg grating sensors. Part 1: Evaluation of adhesives and pro tection systems for the optical sensors. Eng Struct. 2007;29(3):440-8. https://doi.org/10.1016/j.engstruct.2006.05.012
[37] Villalba S, Casas JR. Application of optical fiber distributed sensing to health monitoring of concrete structures. Mech Syst Signal Process. 2013;39(1-2):441-51. https://doi.org/10.1016/j.ymssp.2012.01.027
[38] Liu Y, Bao Y. Automatic interpretation of strain distributions measured from distributed fiber optic sensors for crack monitoring. Measurement. 2023;211:112629. https://doi.org/10.1016/j.measurement.2023.112629
[39] Wijaya H, Rajeev P, Gad E. Distributed optical fibre sensor for infrastructure monitoring: Field applications. Opt Fiber Technol. 2021;64(May):102577. https://doi.org/10.1016/j.yofte.2021.102577
[40] Mieloszyk M, Majewska K, Ostachowicz W. Application of embedded fibre Bragg grating sensors for structural health monitoring of complex composite structures for marine applications. Mar Struct. 2021;76(November 2020):1-17. https://doi.org/10.1016/j.marstruc.2020.102903
[41] Yang J, Yuan L. Package and installation of embeddable fiber optic sensors. Opt Lasers Eng. 2009;47(10):1085-90. https://doi.org/10.1016/j.optlaseng.2009.05.002
[42] Yuan LB, Jin W, Zhou LM, Lau KT. The temperature characteristic of fiber-optic pre-embedded concrete bar sensor. Sensors Actuators, A Phys. 2001;93(3):206-13. https://doi.org/10.1016/S0924-4247(01)00657-4
[43] Zhao J, Bao T, Chen R. Crack monitoring capability of plastic optical fibers for concrete structures. Opt Fiber Technol. 2015;24:70-6. https://doi.org/10.1016/j.yofte.2015.05.008
[44] Ramani V, Kuang KSC. Monitoring of rebar corrosion in concrete structures using a lens-based plastic optical fiber (LPOF) sensor. Constr Build Mater. 2021;276:122129. https://doi.org/10.1016/j.conbuildmat.2020.122129
[45] Liao W, Zhuang Y, Zeng C, Deng W, Huang J, Ma H. Fiber optic sensors enabled monitoring of thermal curling of concrete pavement slab: Temperature, strain and inclination. Measurement. 2020;165:108203. https://doi.org/10.1016/j.measurement.2020.108203
[46] Lokesh R, Pandian MS, Karthikeyan NK, Hema N. Performance of different post tensioning slab system and its environmental constraints. AIP Conf Proc [Internet]. 2023 Sep 13;2764(1):50008. https://doi.org/10.1063/5.0144285
[47] Berrocal CG, Fernandez I, Bado MF, Casas JR, Rempling R. Assessment and visualization of performance indicators of reinforced concrete beams by distributed optical fibre sensing. Struct Heal Monit. 2021;20(6):3309-26. https://doi.org/10.1177/1475921720984431
[48] Yoon HJ, Song KY, Choi C, Na HS, Kim JS. Real-Time Distributed Strain Monitoring of a Railway Bridge during Train Passage by Using a Distributed Optical Fiber Sensor Based on Brillouin Optical Correlation Domain Analysis. J Sensors [Internet]. 2016 Jan 1;2016(1):9137531. https://doi.org/10.1155/2016/9137531

[49] Naruse H, Uehara H, Deguchi T, Fujihashi K, Onishi M, Espinoza R, et al. Application of a distributed fibre optic strain sensing system to monitoring changes in the state of an underground mine. Meas Sci Technol [Internet]. 2007;18(10):3202. https://doi.org/10.1088/0957-0233/18/10/S23
[50] Ye XW, Su YH, Xi P Sen. Statistical analysis of stress signals from bridge monitoring by FBG system. Sensors (Switzerland). 2018;18(2):491. https://doi.org/10.3390/s18020491
[51] Barrias A, Rodriguez G, Casas JR, Villalba S. Application of distributed optical fiber sensors for the health monitoring of two real structures in Barcelona. Struct Infrastruct Eng [Internet]. 2018 Jul 3;14(7):967-85. https://doi.org/10.1080/15732479.2018.1438479
[52] Jia Z, Ren L, Li H, Sun W. Pipeline leak localization based on FBG hoop strain sensors combined with BP neural network. Appl Sci. 2018;8(2):146. https://doi.org/10.3390/app8020146
[53] Han J, Pan J, Cai J, Li X. A review on carbon-based self-sensing cementitious composites. Constr Build Mater. 2020 Dec 30;265:120764. https://doi.org/10.1016/j.conbuildmat.2020.120764
[54] Li L, Wei H, Hao Y, Li Y, Cheng W, Ismail YA, et al. Carbon nanotube (CNT) reinforced cementitious composites for structural self-sensing purpose: A review. Constr Build Mater. 2023;392(November 2022):131384. https://doi.org/10.1016/j.conbuildmat.2023.131384
[55] Henrique Nalon G, Lopes Ribeiro JC, Gonçalves Pedroti L, Marcio da Silva R, Nery Duarte de Araújo E, Emilio Soares de Lima G. Smart laying mortars for masonry structures: effects of lime/cement ratio and carbon nanomaterials content on self-sensing behavior. Cem Concr Compos. 2024;145(March 2023):105351. https://doi.org/10.1016/j.cemconcomp.2023.105351
[56] Le HV, Nguyen VM, Pham TN, Tang VL, Pham XN, Nguyen DL, et al. Self-sensing characteristics of smart high-performance cementitious composites containing multiwall carbon nanotubes, steel fibers, and steel slag aggregates under compression. Sensors Actuators A Phys. 2024;365(December 2023):114920. https://doi.org/10.1016/j.sna.2023.114920
[57] Karthikeyan NK, Elavenil S. Enhancing the interface of cement-paste composite by dispersing sustainable nano-carbon pyrolytic char with silica fume: a sustainable and effective approach. Glob Nest J. 2024;26(4):05662. https://doi.org/10.30955/gnj.005662
[58] Dong W, Li W, Wang K, Guo Y, Sheng D, Shah SP. Piezoresistivity enhancement of functional carbon black filled cement-based sensor using polypropylene fibre. Powder Technol. 2020;373:184-94. https://doi.org/10.1016/j.powtec.2020.06.029
[59] Dong W, Li W, Wang K, Vessalas K, Zhang S. Mechanical strength and self-sensing capacity of smart cementitious composite containing conductive rubber crumbs. J Intell Mater Syst Struct [Internet]. 2020 May 5;31(10):1325-40. 8 https://doi.org/10.1177/1045389X20916788
[60] Karthikeyan NK, Elavenil S. Dispersion effect of nano-structure pyrolytic carbon on mechanical , electrical , and microstructural characteristics of cement mortar composite. Int J Smart Nano Mater [Internet]. 2024;00(00):1-45.
[61] Bueche F. Electrical resistivity of conducting particles in an insulating matrix. J Appl Phys [Internet]. 2003 Nov 10;43(11):4837-8. https://doi.org/10.1063/1.1661034
[62] Simmons JG. Generalized Formula for the Electric Tunnel Effect between Similar Electrodes Separated by a Thin Insulating Film. J Appl Phys [Internet]. 2004 Jun 9;34(6):1793-803. https://doi.org/10.1063/1.1702682
[63] van Beek LKH, van Pul BICF. Internal field emission in carbon black-loaded natural rubber vulcanizates. J Appl Polym Sci [Internet]. 1962 Nov 1;6(24):651-5. https://doi.org/10.1002/app.1962.070062408
[64] D S McLachlan. An equation for the conductivity of binary mixtures with anisotropic grain structures. J Phys C Solid State Phys [Internet]. 1987;20(7):865. https://doi.org/10.1088/0022-3719/20/7/004
[65] Kanagasundaram K, Solaiyan E. Smart cement-sensor composite_ The evolution of nanomaterial in developing sensor for structural integrity. Struct Concr. 2023;24(5):1-41. https://doi.org/10.1002/suco.202201145
[66] Dong W, Li W, Vessalas K, He X, Sun Z, Sheng D. Piezoresistivity deterioration of smart graphene nanoplate/cement-based sensors subjected to sulphuric acid attack. Compos Commun. 2021;23(August 2020):100563. https://doi.org/10.1016/j.coco.2020.100563
[67] Davim JP, Charitidis CA, editors. Nanocomposites [Internet]. Materials, Manufacturing and Engineering. De Gruyter.
[68] Ding S, Dong S, Ashour A, Han B. Development of sensing concrete: Principles, properties and its applications. J Appl Phys [Internet]. 2019 Dec 23;126(24):241101. https://doi.org/10.1063/1.5128242
[69] Wang L, Aslani F. Structural performance of reinforced concrete beams with 3D printed cement-based sensor embedded and self-sensing cementitious composites. Eng Struct. 2023;275(November 2022):115266. https://doi.org/10.1016/j.engstruct.2022.115266
[70] Pan HH, Guan JC. Stress and strain behavior monitoring of concrete through electromechanical impedance using piezoelectric cement sensor and PZT sensor. Constr Build Mater. 2022;324(February):126685. https://doi.org/10.1016/j.conbuildmat.2022.126685

[71] Rao RK, Sindu BS, Sasmal S. Real-time monitoring of structures under extreme loading using smart composite-based embeddable sensors. J Intell Mater Syst Struct [Internet]. 2022 Nov 8;34(9):1073-96. https://doi.org/10.1177/1045389X221128586
[72] Birgin HB, Laflamme S, D'alessandro A, Garcia-Macias E, Ubertini F. A weigh-in-motion characterization algorithm for smart pavements based on conductive cementitious materials. Sensors (Switzerland). 2020;20(3):659. https://doi.org/10.3390/s20030659
[73] Abedi M, Fangueiro R, Gomes Correia A. A review of intrinsic self-sensing cementitious composites and prospects for their application in transport infrastructures. Constr Build Mater. 2021 Dec 6;310:125139. https://doi.org/10.1016/j.conbuildmat.2021.125139
[74] Dong W, Li W, Guo Y, Sun Z, Qu F, Liang R, et al. Application of intrinsic cement-based sensor for traffic detections of human motion and vehicle speed. Constr Build Mater. 2022;355(July):129130. https://doi.org/10.1016/j.conbuildmat.2022.129130
[75] Vertuccio L, Guadagno L, Spinelli G, Lamberti P, Tucci V, Russo S. Piezoresistive properties of resin reinforced with carbon nanotubes for health-monitoring of aircraft primary structures. Compos Part B Eng. 2016;107:192-202. https://doi.org/10.1016/j.compositesb.2016.09.061
[76] Jing G, Siahkouhi M, Riley Edwards J, Dersch MS, Hoult NA. Smart railway sleepers - a review of recent developments, challenges, and future prospects. Constr Build Mater. 2021;271:121533. https://doi.org/10.1016/j.conbuildmat.2020.121533
[77] Ding S, Xiang Y, Ni YQ, Thakur V kumar, Wang X, Han B. In-situ synthesizing carbon nanotubes on cement to develop self-sensing cementitious composites for smart high-speed rail infrastructures. Nano Today. 2022;43:101438. https://doi.org/10.1016/j.nantod.2022.101438
[78] Karthikeyan NK, Elavenil S. Developing Integral Hydrophobic Cement Mortar Composite Using Sustainable Carbon Nanomaterial: Wettability and Surface Energy. Iran J Sci Technol - Trans Civ Eng. 2024. https://doi.org/10.1007/s40996-024-01603-6
[79] Joseph Gnanaraj S, Vasugi K. A comprehensive review of hydrophobic concrete: surface and bulk modifications for enhancing corrosion resistance. Eng Res Express. 2024;6(3):032101. https://doi.org/10.1088/2631-8695/ad5d55
[80] Han B, Ou J. Embedded piezoresistive cement-based stress/strain sensor. Sensors Actuators A Phys [Internet]. 2007;138(2):294-8. https://doi.org/10.1016/j.sna.2007.05.011
[81] Han B, Zhang L, Sun S, Yu X, Dong X, Wu T, et al. Electrostatic self-assembled carbon nanotube/nano carbon black composite fillers reinforced cement-based materials with multifunctionality. Compos Part A Appl Sci Manuf [Internet]. 2015;79:103-15. https://doi.org/10.1016/j.compositesa.2015.09.016
[82] Monteiro AO, Cachim PB, Costa PMFJ. Self-sensing piezoresistive cement composite loaded with carbon black particles. Cem Concr Compos [Internet]. 2017;81:59-65. https://doi.org/10.1016/j.cemconcomp.2017.04.009
[83] Zhang L, Ding S, Li L, Dong S, Wang D, Yu X, et al. Effect of characteristics of assembly unit of CNT/NCB composite fillers on properties of smart cement-based materials. Compos Part A Appl Sci Manuf. 2018;109(June):303-20. https://doi.org/10.1016/j.compositesa.2018.03.020
[84] Nalon GH, Ribeiro JCL, Araújo END de, Pedroti LG, Carvalho JMF de, Santos RF, et al. Effects of different kinds of carbon black nanoparticles on the piezoresistive and mechanical properties of cement-based composites. J Build Eng [Internet]. 2020;32:101724. https://doi.org/10.1016/j.jobe.2020.101724
[85] Wang L, Aslani F. Development of self-sensing cementitious composites incorporating CNF and hybrid CNF/CF. Constr Build Mater [Internet]. 2021;273:121659. https://doi.org/10.1016/j.conbuildmat.2020.121659
[86] Dong W, Guo Y, Sun Z, Tao Z, Li W. Development of piezoresistive cement-based sensor using recycled waste glass cullets coated with carbon nanotubes. J Clean Prod [Internet]. 2021;314:127968. https://doi.org/10.1016/j.jclepro.2021.127968
[87] Wang L, Aslani F. Piezoresistivity performance of cementitious composites containing activated carbon powder, nano zinc oxide and carbon fibre. Constr Build Mater. 2021;278:122375. https://doi.org/10.1016/j.conbuildmat.2021.122375
[88] D'Alessandro A, Tiecco M, Meoni A, Ubertini F. Improved strain sensing properties of cement-based sensors through enhanced carbon nanotube dispersion. Cem Concr Compos [Internet]. 2021;115:103842. https://doi.org/10.1016/j.cemconcomp.2020.103842
[89] Liu L, Xu J, Yin T, Wang Y, Chu H. Improving electrical and piezoresistive properties of cement-based composites by combined addition of nano carbon black and nickel nanofiber. J Build Eng [Internet]. 2022;51:104312. https://doi.org/10.1016/j.jobe.2022.104312
[90] Wang Y, Fu Y, Meng Z, Wan B, Han B. Experimental study and piezoresistive mechanism of electrostatic self-assembly of carbon nanotubes-carbon black/epoxy nanocomposites for structural health monitoring. J Mater Sci [Internet]. 2022;57(26):12416-37. https://doi.org/10.1007/s10853-022-07402-6

[91] Wang Y, Zhang L. Development of self-sensing cementitious composite incorporating hybrid graphene nanoplates and carbon nanotubes for structural health monitoring. Sensors Actuators A Phys [Internet]. 2022;336:113367. https://doi.org/10.1016/j.sna.2022.113367
[92] Dong W, Li W, Sun Z, Ibrahim I, Sheng D. Intrinsic graphene/cement-based sensors with piezoresistivity and superhydrophobicity capacities for smart concrete infrastructure. Autom Constr. 2022;133:103983. https://doi.org/10.1016/j.autcon.2021.103983
[93] Han B, Zhang K, Yu X, Kwon E, Ou J. Nickel particle-based self-sensing pavement for vehicle detection. Meas J Int Meas Confed. 2011;44(9):1645-50. https://doi.org/10.1016/j.measurement.2011.06.014
[94] A. D, D. S, Pichumani M. Electro-mechanical investigations of steel fiber reinforced self-sensing cement composite and their implications for real-time structural health monitoring. J Build Eng [Internet]. 2022;51:104343. https://doi.org/10.1016/j.jobe.2022.104343
[95] Rao RK, Sasmal S. Smart nano-engineered cementitious composite sensors for vibration-based health monitoring of large structures. Sensors Actuators A Phys [Internet]. 2020;311:112088. https://doi.org/10.1016/j.sna.2020.112088

Blank Page

Research on Engineering Structures & Materials
www.jresm.org
Research Group

Technical Note

Influence of forging on the hardness and tensile properties of Al7075/TiC composites

Manjunatha K [1,a], Girish D P [1,b], Vasanth Kumar B S [1,c], Yashaswini T [2,d], Dinesh M H [1,e], Dilip Kumar K [3,f], Poornima K [4,g], Madeva Nagaral [5,h], Nagaraj Namdev [6,i], V Auradi [7,j]

[1]*Department of Mechanical Engineering, Government Engineering College, India*
[2]*Vidya Vikas Institute of Engineering and Technology, India*
[3]*Dept. of Mechanical Eng., Nitte (Deemed to be University), NMAM Institute of Tech. (NMAMIT), Nitte, India*
[4]*Proudhadevaraya Institute of Technology, India*
[5]*Aircraft Research and Design Centre, Hindustan Aeronautics Limited, India*
[6]*Department of Mechanical Engineering, APS Polytechnic, Bangalore-560082, Karnataka, India*
[7]*Department of Mechanical Engineering, Siddaganga Institute of Technology, India*

Article Info

Article history:

Received 24 July 2024
Accepted 29 Oct 2024

Keywords:

Al7075 alloy;
TiC;
Stir casting;
Hot forging;
Mechanical properties

Abstract

This study offers a thorough examination of the mechanical characteristics shown by as-cast and hot-forged Al7075-TiC alloy composites. Optical micrographs are used to verify the different characteristics of these composites. The process of hot forging has been shown to improve the dispersion and orientation of TiC particles inside the matrix, hence preserving the structural integrity of the interface between the matrix and the reinforcement. The observed relationship between the augmentation of TiC reinforcement and the diminishment of the mean grain size is described to the mechanisms of nucleation and dynamic re-crystallization. It is worth mentioning that hot-forged composites routinely demonstrate refined microstructures, which in turn lead to enhanced mechanical characteristics. The process of stir casting followed by hot forging of Al7075-TiC composites has improved mechanical properties, indicating their potential appropriateness for high-performance applications.

© 2025 MIM Research Group. All rights reserved.

1. Introduction

Aluminum and its alloys are highly sought-after materials in engineering fields like aerospace, automotive, marine, and construction. This is because aluminum and its alloys have great mechanical properties like ductility, formability, malleability, and strength. Researchers are looking into ways to improve their mechanical properties and meet changing engineering needs through secondary processing to make them work better. Metal Matrix Composites (MMCs) were made when researchers looked into how to add reinforcing elements to the aluminum matrix [1, 2]. When added to aluminum alloys, titanium carbide (TiC) has stood out because it increases both mechanical strength and ductility. This reinforcement also makes the tribological properties better, lowering the coefficients of sliding resistance and friction. Using techniques like powder metallurgy and liquid metallurgy, TiC-reinforced MMCs with different microstructures can be made. This makes it possible to study their engineering uses in depth [3, 4]. This study focuses on making a composite out of an aluminum alloy 7075 matrix that is only strengthened by TiC

*Corresponding author: mechpoornima@gmail.com
[a] orcid.org/0000-0002-9011-1315; [b] orcid.org/0000-0001-7561-921X; [c] orcid.org/0009-0000-3069-5323; [d] orcid.org/0009-0008-0243-4271; [e] orcid.org/0000-0002-2394-1511; [f] orcid.org/0000-0002-9997-0749; [g] orcid.org/0009-0006-9419-1603; [h] orcid.org/0000-0002-8248-7603; [i] orcid.org/0000-0003-4097-9631; [j] orcid.org/0000-0001-6549-6340
DOI: http://dx.doi.org/10.17515/resm2024.364ma0724tn

particles. This will be done through liquid metallurgy and hot forging, which will also improve the mechanical properties of the composite. Characterization methods like microscopy give information about the microstructure, morphology, and phase composition, which is very important for understanding processing properties. To figure out if a composite is suitable, its hardness, tensile strength, tribological properties, and thermal properties are all looked at. Aluminum is the most commonly used matrix material for MMCs, as it offers several desirable attributes, including low density, excellent thermal and electrical conductivity, precipitation hardening capability, corrosion resistance, and high damping capacity. Moreover, it offers an extensive range of mechanical properties, depending on its chemical composition. Al-based MMCs are usually strengthened with ceramic particulates, such as Al2O3, SiC, B, AlB2, TiB2, BN, SiO2, AlN, and others. Various fabrication methods, predominantly based on casting or powder metallurgy, are available for creating nano-size (or micro-size) particle/metal composites [8, 9]. However, achieving uniform dispersion of particles in liquid metal can be challenging. Furthermore, micro-level porosity, a common casting defect, can pose difficulties in creating micro-level geometries [10].

The mechanical properties and microstructure of MMCs have been improved by methods like forging and extruding. Because it can be bent without breaking, forging is an especially good way to make things. This method improves the load-bearing capacity of MMCs by realigning the grain structures and strategically placing reinforcements. Forging also makes it easier to make parts because it cuts down on waste and costs and lets you change the way a material works [5-12]. Wang and Chen [13] provide their results in their detailed review, which delves into the mechanical properties of aluminum matrix composites. The authors go into extensive length about various production procedures, microstructural characteristics, and mechanical behaviors associated with the usage of these composites. This study emphasizes the importance of secondary processing techniques, such as forging and extrusion, in the process of tailoring mechanical properties to specific application requirements. By evaluating a wide range of studies, the authors give a complete assessment of the criteria influencing the enhancement of strength, ductility, and other mechanical characteristics in secondary processed aluminum composites. As a result, they can convey information in a clear and succinct way.

This review is an excellent resource for academics and engineers who want to maximize the mechanical performance of aluminum-based materials. Zhan and Zhang [14] investigate how equal channel angular pressing (ECAP) affects the microstructure and mechanical properties of SiC particle-reinforced aluminum composites. According to the study's findings, secondary processing by ECAP results in considerable improvements in mechanical properties. These advantages include enhanced strength and hardness. An analysis of the material's microstructure reveals a refined grain structure as well as SiC particles that are equally distributed throughout the aluminum matrix. This research demonstrates the use of ECAP as a secondary processing method for altering the properties of aluminum composites. Furthermore, it provides insights into the mechanisms responsible for the observed improvements in mechanical behavior. Jia and his colleagues [15] investigated the influence of the forging process on TiC-reinforced aluminum composites in their study. The researchers are examining the microstructural changes generated by the forging process and linking those changes with improvements in the material's mechanical properties. According to the researchers, forging enhances the dispersion of TiC particles, resulting in better tensile strength and hardness, as demonstrated by a number of mechanical tests and in-depth micrograph studies.

This research sheds light on the complex connection between secondary processing and microstructural development, providing critical insights into the fabrication of high-performance aluminum composites. Zhang and his colleagues investigate [16] the effect of

in situ equal channel angular pressing (ECAP) on Al-TiB2 composites. According to the study's findings, secondary processing with ECAP results in finer microstructures, greater particle dispersion, and enhanced mechanical properties. The microstructural changes generated by ECAP boost the tensile strength and hardness of the composites significantly. By investigating the relationship between microstructure and mechanical behavior, this research demonstrates the potential of secondary processing approaches for changing the properties of aluminum-based composites. This association was investigated in the research. The mechanical properties of aluminum matrix composites reinforced with Al2O3 particles are the major focus of Li and colleagues' study [17]. The study introduces a novel extrusion process with the goal of increasing the mechanical properties of these composites. The authors show that further processing, in this instance extrusion, improves the material's hardness, ductility, and strength. An analysis of the material's microstructure indicates that it has a refined grain structure and uniformly dispersed Al2O3 particles. This research highlights the relevance of secondary processing techniques for modifying the mechanical properties of aluminum composites to meet the needs of a specific application. Huang et al. [18] explore the mechanical characteristics of Al-SiC composites produced via semi-solid stirring and extrusion. The research shows how secondary processing may improve the mechanical properties of these composites. The authors show enhanced strength and hardness by examining the microstructural changes caused by semi-solid stirring and extrusion. The study underlines the importance of secondary processing in enhancing the characteristics of aluminum-based composites for high-performance engineering applications. Tao and colleagues [19] investigate the effects of extrusion on Al-TiB2 composites in situ. The research focuses on the effect of secondary processing on the microstructure and mechanical characteristics of composites. The researchers demonstrate a link between improved particle dispersion and increased tensile strength and hardness using extensive microstructural and mechanical investigation [20, 21]. This study adds to our understanding of the relationship between secondary processing and the mechanical behavior of aluminum composites. In the past few years, people have become more interested in MMCs, which has led to more research into secondary processing methods like forging. This method is good for industries that need high-performance materials because it can improve mechanical properties and microstructure. For practical applications, it is important to have a deep understanding of how MMC behaves during secondary processing, especially forging. Forging is a good way to make MMC because it lets you fine-tune the microstructure and mechanical properties by controlling things like temperature and rate of deformation. Because of this, MMCs are perfect for a wide range of uses, from high-stress parts to parts that don't wear out easily. The objective of the current study is to manufacture aluminum alloy composites reinforced with TiC using liquid metallurgy and forging techniques, and afterwards assess their mechanical characteristics.

2. Materials and Methods

The matrix was made of an aluminum alloy made of 7075 aluminums. This alloy has a high ratio of strength to density, which makes them a popular choice for a wide range of uses. For this study, powdered particles of titanium carbide (TiC) were chosen to be used as reinforcement. The TiC particles (30-40 microns) were made by M/s Metallizing Jodhpur, Rajasthan. In 3 wt.% steps, a maximum weight percentage of 9 wt.% was used for TiC to make sure that everything was the same. TiC was chosen as the reinforcement material because it has unique properties that could help improve the properties of the composite. Fig. 1 and Fig. 2 show scanning electron micrographs and energy-dispersive X-ray spectroscopy (EDAX) patterns of TiC particles.

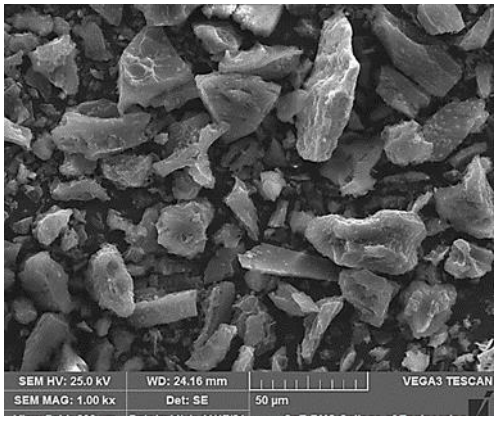

Fig. 1. SEM of TiC particles

At 770°C, an electrical resistance furnace was used to melt the aluminum 7075 alloy. To make a controlled vortex in the molten aluminum alloy, a mechanical stirrer covered with ceramic was used. In this changing environment, heated, already-mixed TiC particles were added slowly while the mixture was constantly stirred. Before adding the TiC particles, they were heated in a muffle furnace at 200°C for one hour to make sure they were evenly spread out. From 0 to 9 wt.%, the weight fraction of titanium carbide (TiC) particles was changed in a planned way by 3 wt.%. TiC was always used as a reinforcement in all composite recipes. The method of preparation was used to make sure that the TiC reinforcement particles were spread out evenly in the aluminum matrix. To get rid of any trapped gases, degassing tablets, which are easy to find on the market, were added to the molten mixture.

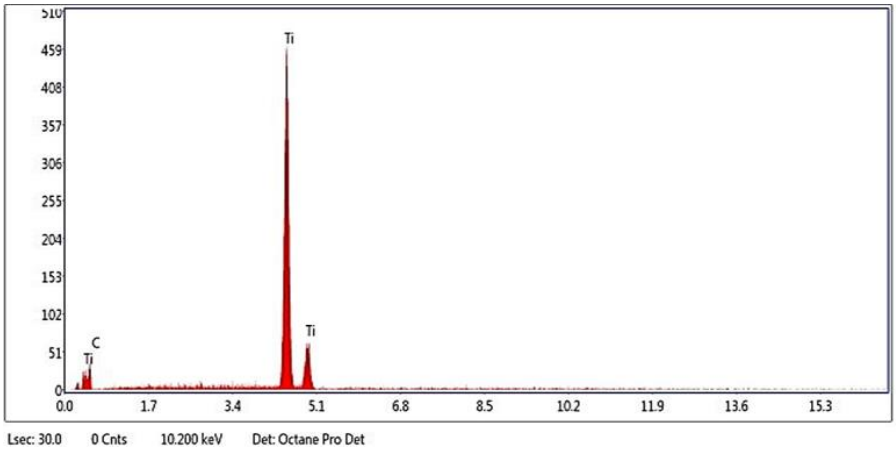

Fig. 2. EDS of TiC particles

The treated molten mixture was then poured into 200 mm long and 80 mm wide metal molds that had been heated. This picture shows what the material looks like after the casting and processing steps. The height and diameter of both the cast matrix alloys and the cast composites were machined to be 80 mm. The 80 mm diameter was for the cast matrix alloys. The muffle furnace was heated to 550 degrees Celsius, and billets that had been machined were put inside. At M/s Fitwel forgings Pvt. Ltd. in Tumkur, Karnataka,

India, heated billets were forged in an open die using a one-ton hydraulic hammer. Before the casting process, the cylinder-shaped billets were heated for 30 minutes at 580+3°C to get them ready. The machined billets that had been heated were then forged according to the process parameters with deformation ratio of 6:1. The microhardness tests were done with a Vickers microhardness tester, a 100-gram load, and a 10-second dwell time. In line with ASTM A370 standards, tensile tests were done with a TUE-C-400 universal testing machine.

3. Results and Discussion

3.1 Microstructural Analysis

Fig. 3 (a-d) shows optical micrographs that show the microstructure of Al7075 alloy composites that have been made stronger with TiC particles. The micrographs show that very small pieces of TiC are spread out across the matrix alloy. Even though the cast micrographs show that there are some clusters of TiC particles, the hot-forged Al7075-TiC composite shows that the synthesized TiC particles are more evenly spread out and can be moved to different places. After the hot forging process, the TiC particles are aligned in the direction that the metal is flowing, which is an important thing to notice.

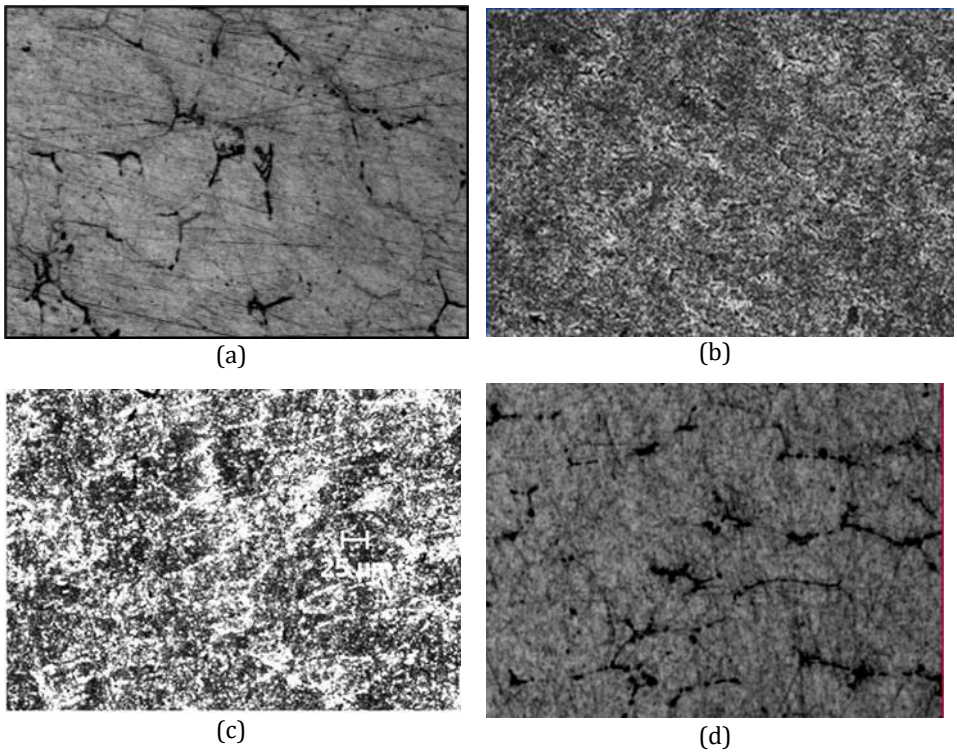

Fig. 3. Optical Micrographs of (a) As-cast Al7075 alloy (b) Forged Al7075 alloy (c) Al7075-9 wt.% TiC Composites(d) Forged Al7075-9 wt.% TiC Composites

Even after hot forging, there is no evidence that the link between the matrix alloy and the TiC reinforcement has lost its structural integrity. Figure shows some micrographs that show this to be true. When looked at through a microscope, the titanium carbide (TiC) particles that are made are said to be between 25 and 50 micrometers in size. After seeing the particles in question, this conclusion was made. Hot forging helps spread out TiC

particles that have clumped together. This reduces the number of places where there are no particles at all. Figure 1.1 shows that the porosity is getting smaller, which is the most important thing. At the same time, the microstructure is getting denser and smoother.

3.2 Grain Size Analysis

Fig. 4 shows the size distribution of the grains in composites made of Al7075 alloy and TiC particles. These composites were made using the stir-casting and hot-forging methods, respectively. When the number of synthetic reinforcements in the matrix alloy goes up, there is a clear pattern that shows the grain size of the composites that are made drops by a large amount. This is true whether you look at the as-cast or hot-forged state. When hot-forged composites are compared to their as-cast counterparts, it is clear that the grain refinement is higher in all of the cases that were looked at. No matter what happens, this is always true. Figure shows that the average grain size of the Al7075-TiC composite decreases by 51% when it is as-cast, and then it decreases by 55% when it is hot forged. This is a very important find. Compared to the grain size of the matrix alloy in its as-cast state, the average grain size reduction for the Al7075-TiC composite in its as-cast state is 49% and in its hot-forged state it is 59%. This is because when the matrix alloy is hot-forged, the average grain size is cut by 59%.

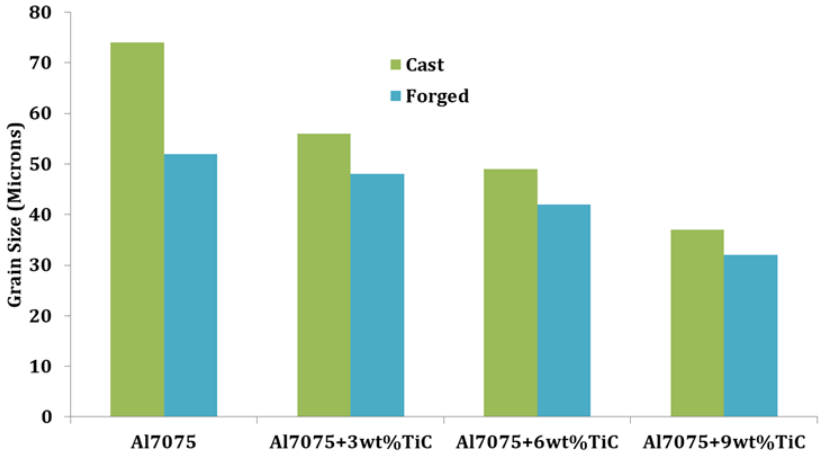

Fig. 4. Variation of grain size with TiC reinforcement for cast and forged composites

Adding ceramic particles to the molten aluminum alloy is what caused the granules to get smaller. During the phase of solidification, these ceramic particles act as places where new crystals can form. Also, micrographs show that the microstructure of cast composites is not as refined as the microstructure of hot-forged composites, which is more refined. The use of thermo-mechanical processing, which causes a lot of plastic deformation and a big drop in particle size, could be to blame for the observed refinement. The micrograph displays a fine and homogeneous dispersion of reinforced particles within the matrix alloy. Following the forging process, TiC particles are orientated in the direction of the metal flow during hot forging.

3.3 Micro-Hardness

Fig. 5 shows the differences in hardness that happen when TiC reinforcement is added to cast and forged composites. When stiff reinforcements are added to a matrix alloy that is normally soft and flexible, the matrix material's hardness increases by a lot. This is what happens when composites made of Al7075 are stir-cast and then hot-forged after being

strengthened with TiC. When stiff reinforcing materials are added to a matrix alloy, the total hardness of the alloy goes up [22, 23]. There are a number of important reasons that led to this change. Most of the time, thermal mismatch is caused by a big difference between the matrix alloy without reinforcement and the reinforced phase in the coefficient of thermal expansion. Both the matrix alloy and the reinforced phase have this difference [24, 25].

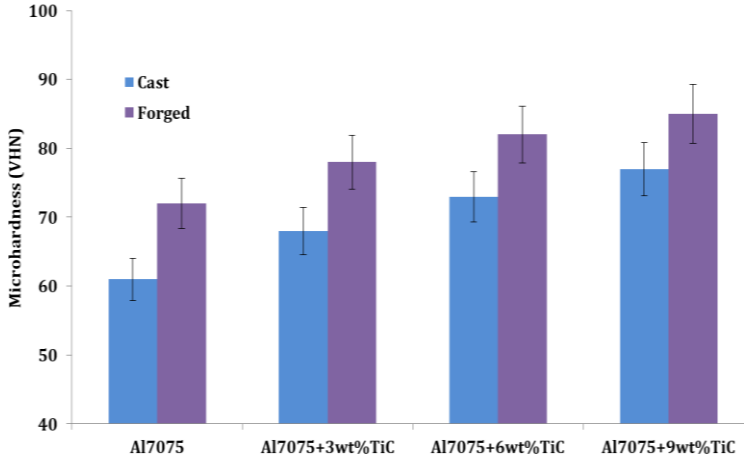

Fig. 5. Variation of hardness with TiC reinforcement for cast and forged

The different rates of expansion of the different materials contribute to the development of residual stresses, which lead to a hardening of the composite in the end. Also, the increased hardness that may be seen in these composites may be due to the uniform dispersion and microscopic particle size of the reinforcement, as well as the successful integration of the unreinforced alloy with the reinforcement [26, 27]. The increased hardness of the material is due to how the composite parts fit together and how the reinforcing particles are now more evenly spread out. When the pictures from optical and scanning electron microscopy (SEM) are looked at in great detail, it is clear that the composite material's porosity has been greatly reduced. This can be blamed on the in-situ processing method that was used.

This research shows that both the average and absolute values of hardness are higher for secondary processed composites than for primary processed composites. There are two main things that cause these things to happen. In composites that are processed a second time, the amount of grain refinement is much higher, which makes the material much harder. During the next steps, any tiny flaws that may have been caused by the way the first casting was done are often fixed. This makes the material more uniform and structurally strong. The improvement in hardness, which came from a higher resistance to plastic deformation, might be related to the fact that the average grain size got smaller as the product was being made. Because of this drop, the number of dislocations is successfully brought down. After hot forging, the hardness of stir-cast Al7075 composites that had TiC added to them went up. This could be due to a number of different things. Because of how these processes work together, the composites have better mechanical properties that make them good for applications that need to be more durable [28].

3.4 Ultimate Tensile Strength

Fig. 6 shows a comparison study of UTS. This analysis shows how the tensile strength of Al7075 alloy composites that have gone through primary processing is different from those that have gone through secondary processing. After the TiC particles made these composites stronger, they were heated up and put through a process called "hot forging." This evaluation shows that the tensile strength of composites is much higher than that of unreinforced versions of the same material during both the first and second stages of processing. Also, it has been shown that adding TiC reinforcement significantly increases the ultimate tensile strength (UTS). When the Al7075-10wt% TiC composites were first processed, their properties got better by 65%. When they were then processed again, their properties got better by 88%. Most of the reason why the composite material has a higher ultimate tensile strength is because rigid TiC particles are mixed into the matrix [29, 30]. This is because the mechanical properties of the composite material are better. The above-mentioned reinforcing process has led to the emergence of a number of factors that, when taken together, are to blame for the increase in UTS that has been seen.

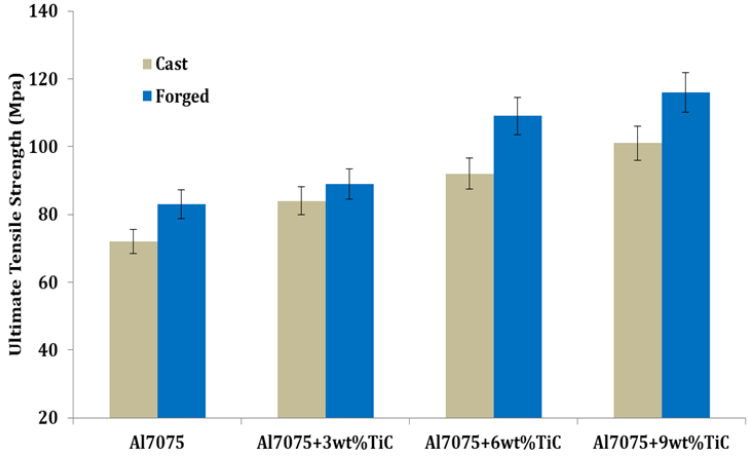

Fig. 6. Variation of UTS with TiC reinforcement for cast and forged composites

3.5 Ductility

Fig.7 shows the ductility of the composites. Most of the loss of ductility that happens when the reinforcement concentration goes up is due to the presence of hard TiC particles in the Al7075 composite. These particles encourage the formation of brittle phases within the matrix. Experiments have shown this to be true. Al7075 composites that have been hot-forged after being strengthened with TiC particles and going through the process described above can show the effect mentioned above. The presence of intrinsically fragile phases, as well as any secondary or intermetallic phases that may be present, makes spots in the material more likely to start cracking early, which makes the material as a whole less flexible [31]. On the other hand, using secondary processing has an effect that is the exact opposite of the first. It makes the material more flexible. During the hot forging process, a lot of grain refinement and re-crystallization takes place. This is why this happens. The process described above helps to strengthen the bond between the matrix and the reinforcement at the interface. This, in turn, makes the material more flexible. The increased interfacial contacts play a big role in spreading out stress and stopping cracks from spreading, which improves the material's ability to bend without breaking [32]. When compared to the ductility of the main processed base alloy, the ductility of the

Al7075-9wt%TiC composite in its secondary processed state is 18% lower, and the ductility of the base alloy in its primary processed state is 9% lower.

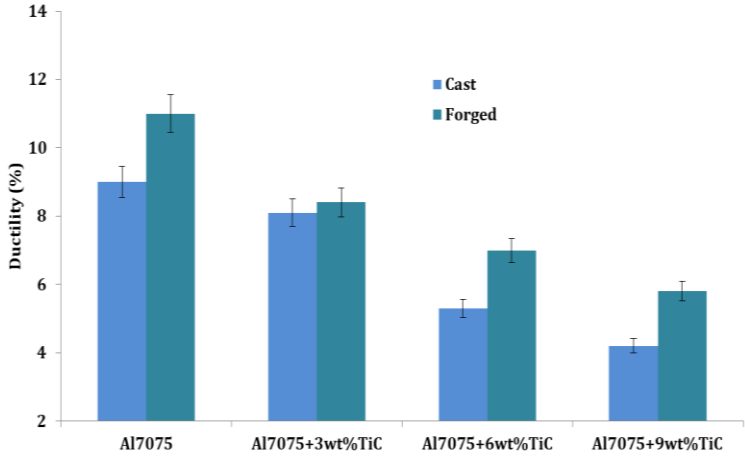

Fig. 7. Variation of ductility with TiC reinforcement for cast and forged composites

3.6 Fractured Surface Analysis

Fig.8 (a-d) shows scanning electron micrographs of the broken surfaces of tensile specimens made from Al7075 alloy composites that have been through both primary and secondary processing. These composites have been forged in a hot environment and have TiC particles embedded in them to make them stronger. The pictures we talked about before give us a lot of information about how the materials break, which helps us understand the underlying mechanisms that determine how the materials fail. After looking at the micrographs, especially Fig.8, in more detail, it becomes clear that the sample has shallow dimples and trim bands. These things point to the fact that there was plastic deformation right before the building fell down. Fig.8 shows that both primary and secondary treated Al7075 alloy and Al7075-TiC composites show clear signs of particle breaking. The fact that the above-mentioned discovery was made shows how strong and long-lasting the bond between the matrix alloy and the TiC reinforcement is. This bond is a side effect of the way the composite material is made and the benefits of the strategy for reinforcing integration [33, 34]. Al7075 alloy shows ductile fracture in nature.

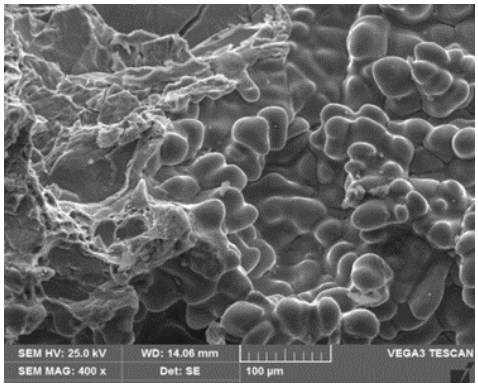

(a)

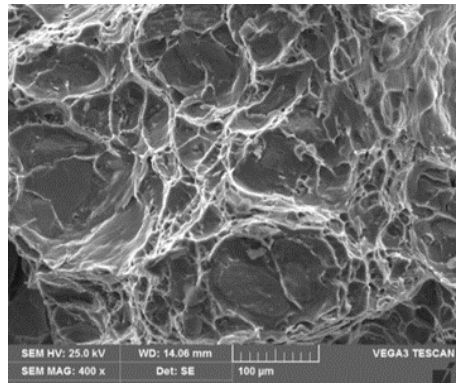

(b)

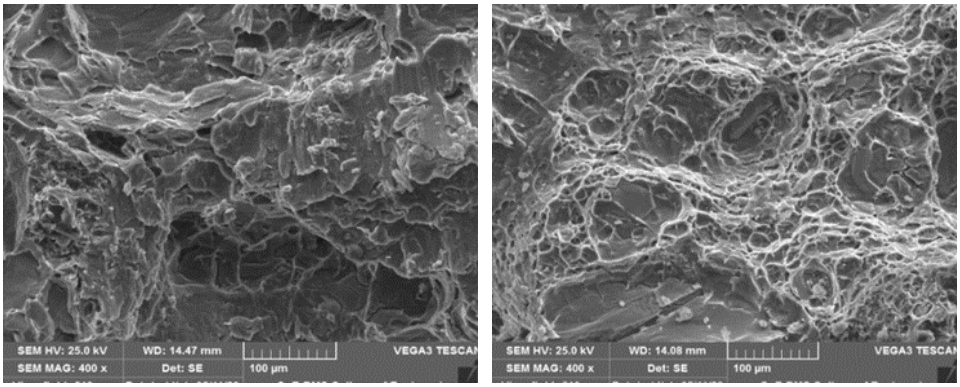

(c) (d)

Fig. 8. Fractured SEM Micrographs of (a) As-cast Al7075 alloy (b) Forged Al7075 alloy (c) Al7075-9 wt.% TiC Composites(d) Forged Al7075-9 wt.% TiC Composites

The hot forging makes the Al7075 alloy fracture as ductile and brittle in nature. Also, interfacial fractures can be seen in certain places, as shown in Fig.8. Based on what was seen, one could figure out that the composite material breaks in a complicated way. This process involves the formation of voids and their subsequent filling, as well as the breaking of TiC particles that are embedded in the matrix alloy. The complicated interactions between the different ways that composites can break show how complicated the failure mechanisms [35, 36]. When the way the matrix alloy and composites break is compared to how the matrix alloy breaks, it is clear that there is a big difference between the two. The very even distribution of larger voids in the matrix alloy, which is one of the things that makes it unique, suggests that it breaks in a ductile way. On the other hand, there is evidence that there are fewer voids in the composites, which suggests that they break in a way that is ductile at the microscopic level but brittle at the macroscopic level [37, 38]. The addition of stiff TiC reinforcement makes the composite stronger, but it also makes it more likely to show brittle fracture characteristics because it has a higher tendency to do so. The brittle fracture behaviour is observed in the case of Al7075 alloy with TiC reinforced composites. The presence of TiC particles makes the soft matrix as brittle by reducing the ductility [39, 40].

4. Conclusion

Al7075 alloy with 3, 6 and 9 wt.% of TiC particles composites were developed by conventional stir process. An influence of combined effect of TiC particles weight percentages and hot forging effect on grain size, micro-Vickers hardness and ultimate tensile strength were investigated. The optical micrographs corroborate the microstructural investigation of as-cast and hot-forged Al7075-TiC alloy composites, which demonstrate unique properties. Micrographs of optical microscope indicated the distribution of titanium carbide particles in the Al7075 alloy composites. Hot forging improves particle dispersion and alignment while keeping matrix-reinforcement links intact. Hot forging disperses agglomerated TiC particles and hence reduces porosity. Because of nucleation and dynamic recrystallization, increasing TiC reinforcement corresponds with lower average grain sizes. Hot-forged composites have consistently refined microstructures, resulting in better characteristics. The use of thermo-mechanical processing, which causes a lot of plastic deformation and a big drop in particle size, could be to blame for the observed refinement. The hot forging of as cast Al7075 and 3, 6 and 9 wt.% of TiC composites impacted in the reduction of grain size. As the weight percentage

of TiC content increased from 3 to 9 wt.% in the matrix, the micro hardness of prepared composites was enhanced. The hardness of as cast Al7075 alloy was 60 VHN, with the 9 wt.% of TiC particles and hot forging combined effect it was 85 VHN. An improvement of 41.66% was obtained with the addition of 9 wt. % of TiC and hot forging. Further, an ultimate strength of Al7075 alloy increased with hot forging and reinforcement of TiC particles. The ultimate strength of as cast Al7075 alloy was 72 MPa, with an incorporation of 9 wt. % of TiC and hot forging, it was 118 MPa. An improvement of 63.88% was obtained with hot forging and TiC particles inclusion. The Al7075-TiC composites with hot forging exhibited superior hardness and tensile properties as compared to the as cast alloy and composites. Various fracture mechanisms were observed in the Al7075-TiC composites. Al7075 alloy represented ductile mode of fracture, while Al7075 with TiC composites were exhibited brittle and ductile mode fracture surface behaviors.

References

[1] Pankaj RJ, Sridhar BR, Nagaral M, Jayasheel IH. Evaluation of mechanical properties of B4C and graphite particulates reinforced A356 alloy hybrid composites. Materials Today: Proceedings, 2017;4 (9):9972-9976. https://doi.org/10.1016/j.matpr.2017.06.304

[2] Satish BB, Samuel D, Bharath V, Madeva N, Aravinda T, Vijee K, Virupaxi A. Development and mechanical characterization of Al6061-Al2O3-Graphene hybrid metal matrix composites. Journal of Composites Science, 2021;5 (6):155. https://doi.org/10.3390/jcs5060155

[3] Veeresh Kumar GB, Gude V, Mandadi SV, Jayarami KR, Nagaral M, Naresh K. Effects of addition of titanium diboride and graphite particulate reinforcements on physical, mechanical and tribological properties of Al6061 Alloy based hybrid metal matrix composites. Advances in Materials and Processing Technologies, 2022; 8 (2):2259-2276. https://doi.org/10.1080/2374068X.2021.1904370

[4] Jayasheel IH, Prasad TB, Nagaral M, Pankaj J, Auradi V. Microstructure and dry sliding wear behaviour of Al2219-TiC composites. Materials Today: Proceedings, 2017; 4 (10):11004-11009. https://doi.org/10.1016/j.matpr.2017.08.058

[5] Ashby MF, Shercliff HR, Cebon D. Materials: Engineering, Science, Processing and Design. Butterworth-Heinemann, 2019.

[6] Gu D, Shen YL, Jiang QC, Peng XJ, Li XL. Fatigue behaviors and microstructure of TiCp/Al composites at elevated temperatures. Journal of Alloys and Compounds, 2017; 695:2237-2244.

[7] Suryanarayana C. Mechanical alloying and milling. Progress in Materials Science, 2001;46(1-2):1-184. https://doi.org/10.1016/S0079-6425(99)00010-9

[8] Jiang F, Wei D, Zhang D, Sun S. Tribological behavior of TiC reinforced Al composites at elevated temperature. Wear, 2014; 315(1-2):118-125.

[9] Polmear IJ. Light Alloys: From Traditional Alloys to Nanocrystals. 3rd ed. Oxford: Elsevier Butterworth-Heinemann, 2006.

[10] Lu L, Shen Y, Chen X, Qian L, Lu K. Ultrahigh strength and high electrical conductivity in copper." Science, 2004;304(5669):422-426. https://doi.org/10.1126/science.1092905

[11] Patil JA, Bhate N. Effect of spray parameters on microstructure and hardness of in situ Al6061-10% TiC composite coatings. Surface and Coatings Technology, 2012;207:483-490.

[12] Bhagat RB, Mohan TP. In-situ cast composites: a review. Journal of Minerals & Materials Characterization & Engineering, 2006; 5(2):145-154.

[13] Wang Y, Chen D. Mechanical properties of aluminum matrix composites: A review. Journal of Materials Science & Technology, 2019;35(12):2703-2718.

[14] Zhan J, Zhang Y. Microstructure and mechanical properties of SiCp/Al composites processed by equal channel angular pressing. Materials Science and Engineering: A, 2018; 737: 93-100.
[15] Jia H. Effect of forging process on microstructure and mechanical properties of TiC/Al composites. Materials Science and Engineering: A, 2020;770:138541.
[16] Zhang Y. Microstructure and mechanical properties of in situ Al-TiB2 composites processed by equal channel angular pressing. Journal of Alloys and Compounds, 2019; 770:444-450.
[17] Li C. Enhanced mechanical properties of aluminum matrix composites reinforced with Al2O3 particles through a novel extrusion process. Materials Science and Engineering: A, 2018;713:180-189.
[18] Huang H. Mechanical properties of Al-SiC composites fabricated by semi-solid stirring and extrusion. Journal of Alloys and Compounds, 2020; 826: 154171.
[19] Tao X. Effects of extrusion on microstructure and mechanical properties of in situ Al-TiB2 composites. Materials Science and Engineering: A, 2018; 736:106-115.
[20] Gopal Krishna UB, Vasudeva B, Virupaxi A, Nagaral N. Effect of percentage variation on wear behaviour of tungsten carbide and cobalt reinforced Al7075 matrix composites synthesized by melt stirring method. Journal of Bio-and Tribo-Corrosion, 2021;7 (3):89. https://doi.org/10.1007/s40735-021-00528-1
[21] Vasanth Kumar HS, Kempaiah UN, Madeva N, Revanna K. Investigations on mechanical behaviour of micro B4C particles reinforced Al6061 alloy metal composites. Indian Journal of Science and Technology, 2021;14 (22):1855-1863. https://doi.org/10.17485/IJST/v14i22.736
[22] Zeeshan A, Muthuraman V, Rathnakumar P, Gurusamy P, Madeva N. Studies on mechanical properties of 3 wt% of 40 and 90 µm size B4C particulates reinforced A356 alloy composites. Materials Today: Proceedings, 2022; 52:494-499. https://doi.org/10.1016/j.matpr.2021.09.260
[23] Raj Kumar, Deshpande RG, Gopinath B, Jayasheel H, Madeva N, Auradi V. Mechanical fractography and worn surface analysis of nanographite and ZrO2-reinforced Al7075 alloy aerospace metal composites. Journal of Failure Analysis and Prevention, 2021;21:525-536. https://doi.org/10.1007/s11668-020-01092-5
[24] Nagaraj N, Mahendra KV, Madeva N. Microstructure and evaluation of mechanical properties of Al-7Si-fly ash composites, Materials Today: Proceedings, 2018;5 (1):3109-3116. https://doi.org/10.1016/j.matpr.2018.01.116
[25] Krishna D, Prashanth L, Madeva N, Rakesh M, Hanumantharayagouda MB. Microstructure and mechanical behavior of B4C particulates reinforced ZA27 alloy composites. Materials Today: Proceedings, 2017;4,8: 7546-7553. https://doi.org/10.1016/j.matpr.2017.07.086
[26] Manjunatha TH, Yadavalli B, Madeva N, Venkataramana V, Jayasheel IH. Investigations on mechanical behavior of Al7075-nano B4C composites, IOP Conference Series: Materials Science and Engineering, 2018; 376 (1):012091. https://doi.org/10.1088/1757-899X/376/1/012091
[27] Anjan Kumar BH, Chaithra PC, Ragavendra C, Chandrasekhar SB, Latha SB, Madeva N, Suresh R. Synthesis and mechanical characterization of Si3N4 reinforced copper-tin matrix composites, Journal of the Mechanical Behavior of Materials, 2021;30 (1):199-206. https://doi.org/10.1515/jmbm-2021-0020
[28] Pankaj RJ, Madeva N, Shivakumar R, Jayasheel IH. Impact of boron carbide and graphite dual particulates addition on wear behavior of A356 alloy metal matrix composites, Journal of Metals, Materials and Minerals, 2020;30 (4):106-112. https://doi.org/10.55713/jmmm.v30i4.642
[29] Rashmi PS, Mahesh TS, Zeeshan A, Veeresha G, Madeva N. Studies on mechanical behaviour and tensile fractography of boron carbide particles reinforced Al8081 alloy

advanced metal composites, Materials Today: Proceedings, 2022;52:2115-2120. https://doi.org/10.1016/j.matpr.2021.12.397

[30] Anjan Babu VA, Saravanan R, Raviprakash M, Madeva N, Nithin K. Microstructural characterization and wear behavior of 12 wt% of boron carbide reinforced Al2030 alloy composites. Materials Today: Proceedings, 2022; 52: 439-444. https://doi.org/10.1016/j.matpr.2021.09.098

[31] Rashmi PS, Hemanth RT, Madeva N, Nithin K, Auradi V. Effect of B4C particles addition on the mechanical, tensile fracture and wear behavior of Al7075 alloy composites. Journal of Bio-and Tribo-Corrosion, 2024;10 (2). https://doi.org/10.1007/s40735-024-00841-5

[32] Pathalinga GP, Chittappa HC, Nagaral M, Auradi V. Influence of B4C Reinforcement Particles with Varying Sizes on the Tensile Failure and Fractography of LM29 Alloy Composites, Journal of Failure Analysis and Prevention, 2020;20 (6):2078-2086. https://doi.org/10.1007/s11668-020-01021-6

[33] Madeva N, Auradi V, Kori SA, Veena S. Mechanical characterization and wear behavior of nano TiO2 particulates reinforced Al7075 alloy composites. Mechanics of Advanced Composite Structures, 2020;7(1):71-78.

[34] Bharath V, Santhrusht SA, Nagaral M, Virupaxi A, Kori SA. Characterization and Mechanical Properties of 2014 Aluminum Alloy Reinforced with Al2O3p Composite Produced by Two-Stage Stir Casting Route. Journal of The Institution of Engineers (India): Series C, 2018;100;277-282. https://doi.org/10.1007/s40032-018-0442-x

[35] Ananthakrishna S, Madeva N, Chandrashekar A, Meshel QA, Ravikiran KB, Nithin K, Virupaxi A, Saiful I, Ranga RC, Abdul R, Mohammad AK, Channa KN. Influence of graphite particles on the mechanical and wear characterization of Al6082 alloy composites. ACS Omega, 2023;8(30):26828-26836. https://doi.org/10.1021/acsomega.3c01313

[36] Subhashchandra SG, Mahadev S, Madeva N, Shashidhar S, Auradi V. Microstructural evolution and mechanical behavior of 90 micron sized B4C particulates reinforced Al2219 alloy composites. Materials Today: Proceedings, 2021;45:7138-7142. https://doi.org/10.1016/j.matpr.2021.02.026

[37] Raksha MS, Madeva N, Satish BB, Chandrashekar A, Mohammad SK, Mohammed OAW, Saiful I, Vivek B, Rohini KP, Mohammad AK, Abdul R. Impact of boron carbide particles and weight percentage on the mechanical and wear characterization of Al2011 alloy metal composites. ACS Omega, 2023;8(26):23763-23771. https://doi.org/10.1021/acsomega.3c02065

[38] Shashidhar S, Vijaya Kumar P, Shantharaja M, Nagaral M, Shivananda BK. Processing, microstructure and tensile behavior of nano B4C particulates reinforced Al2219 alloy composites. Materials Today: Proceedings, 2018;5(11):25158-25164. https://doi.org/10.1016/j.matpr.2018.10.317

[39] Shantharaj P, Prashanth AS, Madeva N, Bharath V, Auradi V, Dharshan K. Microstructure, tensile and compression behavior of B4C particles reinforced Al7075 matrix composites. Materials Today: Proceedings, 2022;52:1135-1139. https://doi.org/10.1016/j.matpr.2021.11.008

[40] Chandrasekhar GL, Vijayakumar Y, Nagaral M, Rajesh A, Manjunath K, Kaviti RVP, Auradi V. Synthesis and tensile behavior of Al7475-nano B4C particles reinforced composites at elevated temperatures. Materials Physics and Mechanics, 2024;52(3):44-57.

Blank Page

Research on Engineering Structures & Materials
www.jresm.org
Research Group

Research Article

Mechanical properties and fracture behavior of concrete made with sintered fly ash lightweight coarse aggregate and electric arc furnace slag as fine aggregate

Brijesh Singh [*,1,a], Shamsher Bahadur Singh [2,b], Sudhirkumar V. Barai [2,c], P N Ojha [3,d], Rohit Kumar [3,e]

[1]*Birla Institute of Technology & Sciences Pilani, Pilani & Group Manager at National Council for Cement and Building Materials, Ballabgarh, India*
[2]*Department of Civil Engineering, Birla Institute of Technology and Sciences Pilani, Pilani, India*
[3]*National Council for Cement and Building Materials, Ballabgarh, India*

Article Info

Article history:

Received 14 Aug 2024
Accepted 29 Sep 2024

Keywords:

Sintered fly ash lightweight coarse aggregate;
Electric arc furnace slag;
Lightweight concrete;
Modulus of elasticity;
Stress-strain;
Fracture behavior

Abstract

The present work evaluates mechanical properties and fracture behaviour of concrete made with combination of sintered flyash lightweight coarse aggregate (SFA) and electric arc furnace (EAF) slag as fine aggregate. The mechanical properties and fracture performance of concrete has been evaluated at w/b of 0.6 and 0.4 for three concrete mix combinations namely (a) lightweight concrete with SFA and natural fine aggregate (b) lightweight concrete with SFA and electric arc furnace slag as fine aggregate (c) normal concrete with granite aggregate and electric arc furnace slag. The concrete mixes prepared are evaluated for compressive, flexural strength, split tensile strength, elastic modulus and stress strain curve behaviour. Fracture behaviour has been investigated on notched beams of size 100*100*500 mm under three-point bend test as per RILEM procedure for both normal weight and lightweight concrete. The plot of Load vs CMOD (Crack Mouth Opening Displacement) and Load vs displacement were used for evaluating the fracture behaviour of both types of concrete using various standards and RILEM recommendations. Fracture performance has been compared in terms of parameters such as modulus of elasticity, fracture energy, initial load compliance, stress-intensity factor, energy release rate, and characteristic length.

© 2025 MIM Research Group. All rights reserved.

1. Introduction

The natural aggregates use in conventional reinforced concrete construction creates environmental problems and are energy intensive, which is crucial to consider for sustainable building and a circular economy. There has been need of huge number of aggregates by construction industry and natural sources are getting depleted over period of time. Fly ash and electric arc furnace slag are among major industrial bi-product generated in India. In last one and half decade, there is a serious focus towards adoption of industrial wastes in suitable ways thereby achieving sustainability and circular economy. Increase in use of renewable sources and other alternatives from industrial bi-products is a need of an hour to counter huge requirement of concrete as material in construction. Sintered fly ash lightweight concrete day by day is getting attention in construction industry because of its lower dead load, superior durability performance, enhanced thermal and sound insulation along with better fire resistance [1-2]. The structural grade

*Corresponding author: brijeshsehwagiitr96@gmail.com
[a] orcid.org/0000-0002-6512-1968; [b]orcid.org/0000-0001-6847-0701; [c]orcid.org/0000-0001-5100-0607; [d]0000-0003-1754-4488; [e]orcid.org/0009-0000-6167-375X
DOI: http://dx.doi.org/10.17515/resm2024.396me0814rs

lightweight concrete density generally varies from 1100 to 1900 kg/m^3 with minimum compressive strength of 17 MPa [3]. The sintered fly ash lightweight coarse aggregate (SFA) is mainly produced from fly ash as raw material through sintering process [1-2]. Lightweight concrete has been known to be better in mechanical, durability and thermal properties but one set back or limitation of lightweight concrete is its brittle behavior and lower resistance to crack formation under load. This brittle property of concrete limits its flexural capacity and can be hazardous in earthquakes [3-7]. Due to the brittle behavior, concrete structures undergo cracking under flexural loads and has possibility to fail suddenly without showing signs of distress. The mechanical performance and fracture behavior of normal weight concrete has been examined and researched deeply in the recent decades resulting in in-depth understanding of its fracture phenomenon [3-7]. Fracture performance of normal and ultra-high-performance concrete at different strain rate has been examined in past. The aggregate in concrete system is about 65-70% of the total volume and plays a critical role in deciding the physical properties and mechanical behavior of concrete both in its fresh and hardened state. The interactions among the aggregate and the cement paste impacts many of the concrete properties in hardened state such as strength, stiffness and fracture toughness. The study indicated that fracture parameters are sensitive to strain rates and not much effect of strain rate has been evident on softening fracture energy. The fracture behavior of lightweight concrete is reported to be comparable to normal concrete however in normal concrete, dense and strong aggregates resist the crack propagation, whereas crack propagation path can be different in lightweight concrete depending upon quality of interfacial transition zone [5-7]. The type of aggregate and its shape as well as surface texture has been highlighted to be having little impact on the facture energy of normal strength concrete compared to high strength concrete [7]. The fracture resistance of normal concrete depends on factors such as compressive strength; water/binder ratio; size, shape and content of the aggregate. In case of normal strength concrete both the toughness and the fracture energy of concrete have been reported to increase with the increase in compressive strength, size of aggregate size and quantity of aggregate.

There are several fracture models available for non-linear analysis of concrete structures such as the Hillerborg et al. model on fictitious crack theory [6], Jenq and Shah [7] model considering two parameter approach and Bazant et al. model on crack band [8]. The brittleness and ductility estimation of concrete can be quantified through its fracture properties [9-11]. To determine the concrete's fracture properties, RILEM [12-13] recommends testing of notched beams via a three-point bend tests. Among different fracture parameters, fracture energy is one important indicator for comparing or analyzing the concrete cracking resistance and toughness. RILEM definition of fracture energy is the quantum of energy needed to develop a crack with unit area. Apart from fracture energy, other indicators of fracture behavior are stress based intensity factor, rate of energy release, initial load compliance and characteristic length. Trivedi et al. [15] investigated three different approaches for fracture behavior study of concrete such as Bi-linear approximation, RILEM procedure and energy release rate and found similar results indicating that either of three approaches are suitable. Experimental investigation by Murthy et al. [16] on tension softening for nano engineered concrete and fracture energy highlighted that ratio of notch to depth significantly influence fracture energy determination under RILEM method. Gil et al. [17] examined the effects of addition of silica fume as supplement cementitious material in normal weight concrete and investigated how various aggregate sizes influence fracture parameters also an optimized dose of silica fume for fracture toughness and peak strength was determined. Study conducted by Siregar et al. [18] highlights that degree of brittleness of high strength concrete gets affected by w/b and aggregate size wherein aggregate strength mainly influences peak fracture energy. EAF slag is a co-product of metallurgical processes of steel manufacturing

and produced from EAF of primary steel producers generating low carbon steel which does not have problem of heavy metals or free lime due to low basicity. This type of slags can be better suited for the construction industry as fine aggregate. EAF are responsible for over 40% production of steel globally [19]. The older plants have been using basic oxygen furnace (BOF) routes for making steel from recycled scrap metal in order to be more sustainable and economical. Steel production using electric arc furnaces in Europe generates slag over 10 million tons every year, and this amount will further increase in the future. Past studies with EAF slag as aggregates from steel making has shown improved mechanical characteristics and high specific density (generally more than 3.2) primarily because of its elevated levels of ferrous oxide. However, carbon steel slag production in past from basic oxygen furnace (BOF) has shown some dimensional instability because of hydration of magnesia and free lime [20-22]. EAF slag aggregates from steel making process has shown water absorption coefficient varies from 0.2% - 10 % [21]. In past decade [23-24], studies have focused on durability and mechanical properties of concrete containing EAF slag for normal concrete. The previous studies have reported feasibility of producing structural concrete utilizing EAF slag as coarse aggregate by fully replacing natural aggregates in normal concrete. Improvements in compressive strength, tensile strength, and elastic modulus have been reported with the use of EAF slag as coarse aggregate. [23-27]. The utilization of EAF slag is also environment friendly and has lower environmental emissions compared to natural aggregate [26-29]. However, the studies with SFA and EAF slag as fine aggregate for lightweight concrete production and subsequent evaluation of mechanical and fracture performance is not reported in literature.

1.1 Research Significance

The literature survey indicates that there are numerous studies conducted on total replacement of aggregate from natural origin with EAF slag as coarse aggregate in normal weight concrete. The comparison of fracture energy and related mechanical parameters of plain lightweight concrete with SFA in comparison to normal weight concrete with natural coarse aggregate is scanty. However, no study could be found in literature pertaining to concrete's fracture behavior and mechanical properties made with combination of SFA and EAF slag as fine aggregate. In the present study, concrete's mechanical characteristics and fracture behavior of concrete has been evaluated at water to binder ratio of 0.6 and 0.4 for three concrete mix combinations namely (a) lightweight concrete with SFA and natural fine aggregate (b) lightweight concrete with SFA and EAF slag as fine aggregate (c) normal concrete with natural granite aggregate and EAF slag.

2. Materials

This research explores the production of normal weight concrete, OPC cement (43 Grade) conforming to IS:269 [29], coarse (Figure-1b) and fine aggregates (Figure-1a), silica fume, superplasticizer and water are used. For production of lightweight concrete, OPC cement (43 Grade), natural fine aggregate and SFA, silica fume, superplasticizer and water are used. For production of lightweight concrete with EAF slag as fine aggregate, OPC cement (43 Grade), SFA and EAF slag as fine aggregate, silica fume, superplasticizer and water are used. In the study, crushed fine aggregate and EAF as fine aggregate conforms with Zone II of IS 383:2016 [30] and coarse aggregate having 20 mm as maximum nominal size also conforms with IS 383:2016. Table 1 displays the physical characteristics of both fine and coarse aggregate. Figure 1 (a) and (b) displays the fine and coarse aggregate, respectively. The mechanical properties of SFA used as coarse aggregate are given in Table-2 and chemical composition of SFA, cement OPC 43 grade, silica fume and EAF slag fine aggregate is given in Table-3.

(a) (b)

Fig. 1. (a) Fine aggregate (stone dust) and (b) Coarse aggregate (granite)

(a) (b)

Fig.2 . (a) Sintered fly ash lightweight aggregate, Fraction: 4-8 mm and (b) Sintered fly ash lightweight aggregate, fraction: 8-16 mm

(a) (b)

Fig. 3. (a) Electric Arc Furnace (EAF) Slag Fine Aggregates and (b) processing of Electric Arc Furnace (EAF) steel slag

The SFA is brown in color as shown in Figure-2 and has black core. The EAF slag as fine aggregate sample is shown in Figure-3 (a). The processing of EAF slag is displayed in Figure-3 (b). The microstructure of SFA is shown in Figure-4. The samples of SFA (two fractions 8-16 mm and 4-8 mm) have been utilized as coarse aggregate. For preparation of concrete mixes for lightweight concrete, the fine aggregate (crushed stone) used in study conforms to IS: 383-2016. For lightweight concrete; as per IS 383:2016, zone-II crushed fine aggregate [30] was used. The polycarboxylic ether based chemical admixture (Auramix 300 PC) conforming to Indian Standard IS:9103[31] was used for all concrete mixes.

Table 1. Aggregates properties

Property		Granite		Sintered Fly ash Lightweight Aggregate		Fine Aggregate	
		20 mm	10 mm	8-16 mm	4-8 mm	Natural Stone dust	EAF Slag
Specific gravity		2.81	2.82	1.49	1.47	2.65	3.39
Water absorption (%)		0.3	0.3	17.93	17.50	0.59	1.16
Sieve Analysis Cumulative Percentage Passing (%)	20mm	98	100	100	100	100	100.00
	10	2	68	30	100	100	100.00
	4.75	0	2	0	13	99	99.00
	2.36	0	0	0	2	89	89.00
	1.18	0	0	0	0	64	61.00
	600 µ	0	0	0	0	43	36.00
	300 µ	0	0	0	0	26	20.00
	150 µ	0	0	0	0	14	11.00
	Pan	0	0	00	0	0	0.00

Table 2. Mechanical properties of sintered fly ash lightweight aggregate used in study

Fraction	LWA designation	Specific gravity	Water absorption at 24 hours (%)	Loose bulk density (kg/m^3)	Crushing Strength (N/mm^2)	10 % Fines (Ton)
4-8 mm	LWA-I	1.47	17.50	813	8.80	-
8-16 mm	LWA-II	1.49	17.93	849	7.70	3.60

Table 3. Chemical composition of sintered fly ash lightweight aggregate and OPC cement

Component	CaO (%)	SiO_2 (%)	Al_2O_3 (%)	Fe_2O_3 (%)	SO_3 (%)	MgO (%)	Na_2O Equivalent (%)	Loss of Ignition
Sintered fly ash lightweight aggregate	2.45	62.50	25.85	4.19	0.29	0.53	0.77	1.48
Cement OPC 43 grade	59.60	21.22	7.19	4.25	2.50	1.90	1.05	1.94
Silica fume	-	95.02	-	0.80	-	-	-	1.16

Fig. 4. Microstructure of sintered fly ash lightweight aggregate (10 µm and 1.5x)

3. Concrete Mix Design

3.1. Concrete Mix Design

3.1.1 Normal Concrete Mix Design

The w/b for concrete mix preparation was 0.6 and 0.4 for producing normal weight concrete (NWAC) mixes using granite as coarse aggregate. The slump was maintained in 75 -100 mm range. The mix design for normal weight concrete was done as per procedure given in IS: 10262-2019 [32]. Table 4 provides the concrete mix details.

3.1.2 Lightweight Concrete Mix Design with Natural Fine Aggregates and with EAF Slag as Fine Aggregates

The w/b ratio used for concrete mix preparation was 0.6 and 0.4 for producing lightweight concrete (LWAC) mixes using SFA with natural fine aggregates and with EAF slag as fine aggregates. The sintered fly ash lightweight aggregate, due to its porous nature, exhibits comparatively higher water absorption than natural aggregates. The use of lightweight coarse aggregates in dry condition with water correction equal to water absorption of aggregate leads to segregation of mix in fresh state and increase in net free water to cement ratio leading to reduction in strength of concrete. Other than this, the direct correction of water absorption fails to consider the impact of cement paste and in actual scenario it is cement paste and not water alone which dictates the water absorption potential of lightweight aggregates. This issue can be resolved by use of lightweight aggregate in dry state condition with proper correction in water absorption taking into account the effect of cement paste for given w/b of concrete mix. The mix design for lightweight concrete with SFA was done in accordance with procedure given in Indian Standard IS: 10262-2019 [32] and curve was developed for water absorption correction of aggregate. The sintered fly ash lightweight aggregate used in present study is highly porous and its water absorption is about 18 percent. In the present study, the combined aggregate grading given in IS: 9142-2018 [33] has been adopted. The absorption potential of sintered fly ash lightweight aggregate has been determined in the study wherein moisture content of lightweight aggregates was known. Initially the moisture content and initial weight of the aggregate were recorded. The mortar pastes of w/b 0.7 was prepared and placed in container. Twenty-five aggregates were first placed in a cement paste present in the container for the period of 5, 15, 30, 45 and 60 minutes to decide optimum absorption period (soaking period). After the specified period of absorption, the lightweight aggregates were removed from the paste and the excess paste attached to the outer surface of aggregates was separated with help of nylon brush. The removal time of excess paste was kept not more than one minutes in order to not absorb the water trapped in the aggregates particles which takes part in further hydration of cement paste. Thereafter, weight of aggregates was measured. After this the aggregates were placed inside an oven for period of 48 hours at a temperature of 105°C. Finally, dry weight of aggregate was determined and aggregate absorption values were determined. The total absorption by the lightweight coarse aggregate in terms of percentage is calculated as difference of mass of aggregate after 45 minutes of soaking and initial mass of aggregate before soaking divided by initial mass of aggregate before soaking multiplied by 100. The total water absorption by the lightweight coarse aggregate in terms of percentage is calculated as difference of mass of aggregate after 45 minutes of soaking and the oven-dried aggregate's mass divided by oven-dried aggregate's mass multiplied by 100. The difference between the percentage of total absorption by the lightweight coarse aggregates and total water absorption by the lightweight coarse aggregate is termed as total paste absorption potential of lightweight coarse aggregate. The water absorption values at water to cement ratio of 0.70 for absorption period of 5, 15, 30, 45 and 60 minutes were 12.84. 13.84, 14.36, 14.86, 14.90, respectively. Based on this study, 45 minutes absorption period for sintered fly ash

lightweight aggregate has been considered in this study as the absorption capacity of the aggregates beyond this period was almost negligible.

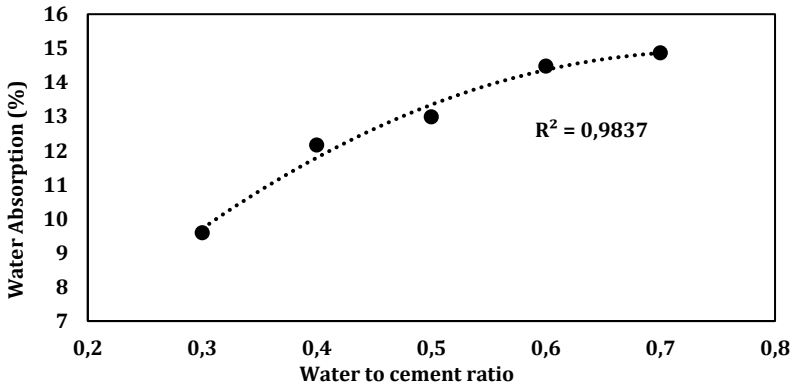

Fig. 5. Relationship between water absorption of sintered fly ash lightweight aggregate with water to cement ratio for 45 minutes absorption period

Thereafter, this exercise was repeated for mortar paste of w/b ratio of 0.3, 0.4, 0.5 and 0.6. Thereafter, correlation was developed between sintered fly ash lightweight aggregate water absorption potential and different w/b ratios. The correlation developed is presented in Figure-5 for absorption period of 45 minutes. The correlation developed is to be used in water absorption correction of sintered fly ash lightweight aggregate utilized as coarse aggregate in concrete mix. The mix design details of both normal and lightweight concrete is given in Table-4. In table-4, NC denotes normal concrete, LC denotes lightweight concrete with (SFA) and natural fine aggregate and LCEAF denotes lightweight concrete with SFA and EAF as fine aggregates (100 % replacement with natural fine aggregate). A 60 kg batch of concrete has been prepared for each concrete mix. Firstly, in the pan mixer the fraction of lightweight coarse aggregates, fine aggregates and cement was mixed to obtain homogenous mix and thereafter 80 percent water was added and mixing was performed for a duration of 2-3 minutes [34]. Subsequently, the leftover 20 percent water and the admixture were introduced, and the mixing process was extended for another 2 to 3 minutes.

Table 4. Concrete mix design for normal and lightweight concrete

Mix ID	w/b	Cementitious Content [Cement + Silica Fume] (kg/m³)	Water Content (kg/m³)	Chemical Admixture % by weight of cement	Fine Aggregate (kg/m³)	Coarse Aggregate (kg/m³)	
						10 mm	20 mm
NC-0.6	0.60	285 (271+14)	170 (After Correction 175)	0.60	765	492	738
LC-0.6	0.60	285 (271+14)	170 (After Correction 258)	0.70	785	245	370
LCEAF-0.6	0.60	285 (271+14)	170 (After Correction 262)	0.50	788	241	368
NC-0.4	0.40	425 (382+43)	170 (After Correction 175)	1.00	580	515	775
LC-0.4	0.40	425 (383+42)	170 (After Correction 239)	0.90	733	229	345
LCEAF-0.4	0.40	425 (383+42)	170 (After Correction 243)	0.80	735	230	346

It is to be noted that the initial mixing period is critical for sintered fly ash lightweight aggregate due to its absorption characteristics. Adjustment was done to mixing water to accommodate water absorption of the aggregates. The mounds were cleaned properly and concrete cube was compacted on vibration table wherein each of three layers were properly compacted. After 24 hours, the concrete cubes were taken out of the molds. The environmental conditions of laboratory were 27±2°C temperature and 65% or more relative humidity. The concrete cube specimen was tested in surface dried saturated condition as per IS: 516 (part-1/sec-1) [35]. The concrete developed has a slump in between 75-100 mm.

4. Details of Specimen

The concrete specimens of various size were prepared for different tests discussed hereunder as per the standards and literature. The 28-day cube compressive strength was determined as per procedure given in IS:516 on cube size of 150 mm x 150 mm x 150 mm. The concrete cylinders of size 150 mm diameter and 300 mm height are cast for evaluating stress strain behavior of concrete, modulus of elasticity and split tensile strength of concrete as per IS: 516. For fracture study at 28-day age as per literature and RILEM procedure, the three-point bend tests were performed on beam of 100 mm cross section and 500 mm length with 35mm notch (Figure-6 and 7). Table 5 gives details of specimens and Figure 5 displays the cast samples with molds.

Table 5. Details of specimen and tests performed

Sl.	Type of Sample	Sample size (mm)	Parameter evaluated
1.	Cube	150 mm	28-day age compression test
2.	Cylinder	150 Diameter x 300 height	Split Tensile Strength, Modulus of Elasticity, Stress-Strain at 28-day age
3.	Beam	100 mm cross section and 500 mm length	Three-point bend test for flexural strength and fracture study

Fig. 6. Concrete cubes, cylinders, and beams in molds

Fig. 7. Notched beam sample

5. Experimental Method

The method adopted for determining compressive strength, stress strain behavior, split tensile strength, modulus of elasticity and fracture parameters are discussed in this section.

5.1. Compressive Strength, Stress Strain Behavior, Modulus of Elasticity and Split Tensile Strength

The 28-day cube compressive strength, split tensile strength, modulus of elasticity and stress strain behavior was determined as per IS: 516. These tests were carried out on a compression testing machine of capacity 3000 KN. The test setup for stress strain behaviour and modulus of elasticity of concrete is given in Figure 8.

Fig. 8. Test setup for stress strain behavior and modulus of elasticity of concrete of concrete

5.2. Study on Fracture Behavior Using Three-Point Bending Test

The three point bend test was performed on notched beams of size 100 x 100 x 500 mm for both normal weight and lightweight concrete. The plot of Load vs CMOD (Crack Mouth Opening Displacement) and Load vs deflection were utilised for determination of fracture behaviour of both types of concrete using various standards and RILEM recommendations. Fracture performance was evaluated by determining modulus of elasticity, fracture energy, initial load compliance, stress intensity factor, energy release rate and characteristic length. In Figure-9, the three point bend test diagram and in Figure 10 the test set up in laboratory has been shown.

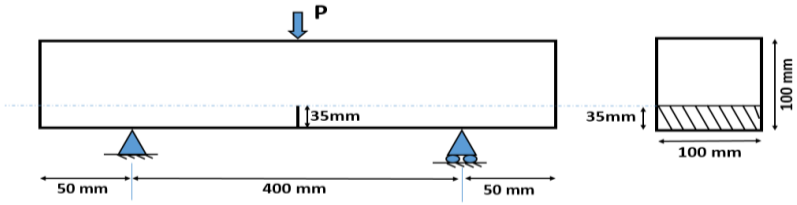

Fig. 9. Three-point bend test diagram

The beam of 100 mm cross section and 500 mm length with 35mm notch [13, 36] was created in middle of beam and clear span was kept as 400 mm. The load on beam specimen was given through a displacement mode operated machine of 30T capacity. The mid-point beam delfection was recoded using CMOD and Linear Variable Displacement Transducer (LVDT) (Figure-10a). The clip gauge using two nos. steel type knife edges were placed at the bottom beam's bottom for CMOD measurement as represented in Figure 10(b). 18 nos. concrete beams were evaluated for fracture performance study and out of which for each mix given in Table 4, the three beams were tested.

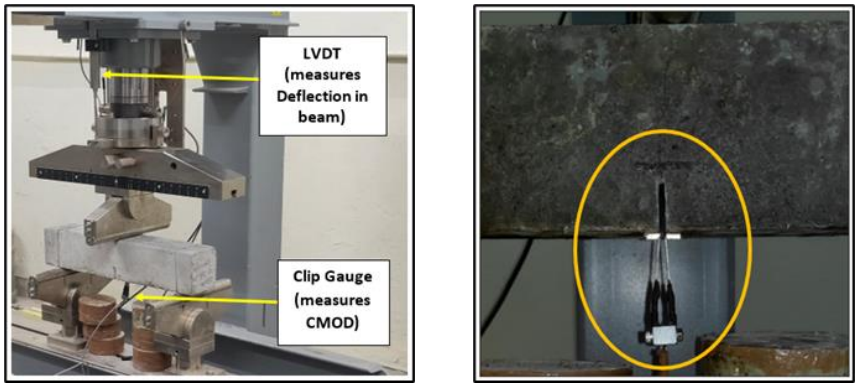

(a) (b)

Fig. 10 (a) Typical setup for three-point bend test and (b) CMOD measurement using clip gauge

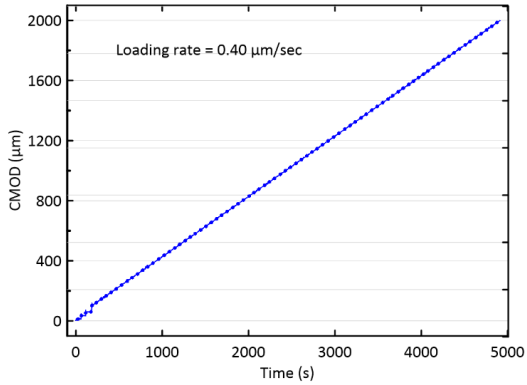

Fig. 11. Crack Mouth Opening Displacement (CMOD) vs time plot for the test

Figure 11 illustrates the plot of CMOD vs time.. The test was conducted in displacement operated mode in machine and loading rate for CMOD was maintained at 0.40µm/s. The experiment continued to point of failure of beam or to point where CMOD was 1000 µm.

6. Test Results and Discussions

Properties of fresh concrete, including workability and air content, were assessed for each of the six concrete mixes. Workability was measured in terms of slump at various intervals—specifically at 0, 30, 60, 90, and 120 minutes after the mix preparation. The results of are provided in Table 6.

The concrete mixes were formulated to attain initial slump of 75 to 100 mm using suitable dosages of commercially available PCE based chemical admixture. Concrete mixes incorporating EAF slag as sand instead of natural fine aggregate showed similar trend and rate of slump loss as compared to their equivalent normal concrete mixes and mixes of lightweight concrete with natural fine aggregate and SFA. The reason for such behavior may be attributed to similar grading and zone of EAF slag as sand and conventional fine aggregate (crushed sand), as both are of zone II grading as per IS 383: 2016. All the six mixes showed almost similar and comparable air content (around 2.3 to 2.9%). All the mixes were observed to be homogenous and no signs of bleeding and segregation were observed.

Table 6. Workability and air content of concrete mixes

Mix ID	w/b	Workability of concrete (slump in mm) 0 Min	30 Min	60 Min	90 Min	120 Min	Air Content, %
NC-0.6	0.60	100	80	65	45	25	2.5
LC-0.6	0.60	90	70	50	40	20	2.3
LCEAF-0.6	0.60	80	60	40	30	20	2.5
NC-0.4	0.40	100	70	55	30	25	2.7
LC-0.4	0.40	90	70	55	35	20	2.6
LCEAF-0.4	0.40	85	70	55	30	20	2.9

6.1. Mechanical Properties and Stress Strain Behavior

This section presents the mechanical properties of concrete as determined by IS: 516, including its modulus of elasticity, split tensile strength, compressive strength, and stress-strain behavior. Table 7 gives the test findings. Figure 12 displays the fracture specimen following the split tensile test.

Table 7. Compressive strength, elastic modulus and split tensile strength of concrete

w/b	Type	28-day in (MPa) Cube Strength	Split Tensile Strength	Modulus of elasticity
0.60	NC-0.6	28.33	2.28	28270
0.60	LC-0.6	25.00	2.22	18860
0.60	LCEAF-0.6	26.50	2.15	19094
0.40	NC-0.4	47.55	4.17	32852
0.40	LC-0.4	37.87	3.09	20940
0.40	LCEAF-0.4	38.50	2.64	22423

Table 7 gives results of the 28-day cube compressive strength, elastic modulus and split tensile strength of (a) lightweight concrete with natural fine aggregate and SFA as coarse aggregates, (b) lightweight concrete with SFA as coarse aggregate and EAF as fine aggregate and (c) normal concrete with natural granite and fine aggregate. The split tensile strength and compressive strength for all the above concrete mixes with w/b of 0.6 are comparable in case of both normal and lightweight concrete with natural and EAF slag as fine aggregate.

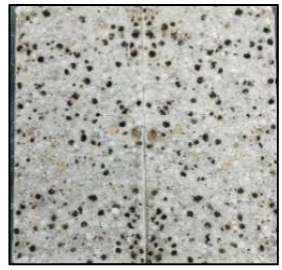

Fig.12. Fractured lightweight concrete specimen after split tensile test

The split tensile strength, compressive strength and elastic modulus for normal concrete mix with w/b 0.4 are more than both lightweight concrete with SFA and natural fine aggregate as well as lightweight concrete with SFA and EAF slag as fine aggregate. The modulus of elasticity of SFA based concrete for both types of fine aggregate i.e. natural sand

and EAF slag as sand are around 30-40% lower compared to normal weight concrete. However, modulus of elasticity, split tensile strength and compressive strength are comparable for both lightweight concrete with SFA, natural fine aggregates and lightweight concrete with SFA and EAF slag as fine aggregate. From the results it is seen that split tensile to compressive strength ratio lies in between 5-10% for lightweight concrete. Whereas in conventional concrete this ratio lies between 5- 10%. This indicates that the tensile strength of normal concrete and lightweight concrete is nearly same [37-39]. The observation of splitted surface of specimen indicates that the fracture path gets transferred via aggregates in lightweight concrete (Figure-12).

In case of lightweight concrete, it can be inferred that the bonding within the cement paste matrix and sintered fly ash lightweight aggregate are higher than the aggregate's strength. Because of lower crushing strength in sintered fly ash lightweight aggregates compared to natural aggregate, the lightweight concrete could not give similar split tensile strength for similar w/b ratio. The important parameter of any concrete is its elastic modulus and its depends upon the moduli of both aggregates and paste matrix. In lightweight concrete, the elastic modulus of aggregate is the weakest link and it leads to overall reduction of elastic modulus of lightweight concrete. In the lightweight concrete, the elastic modulus of aggregate and paste are closer to each other compared to normal weight concrete leading to uniform stress distribution, simultaneously reducing concentration of stress and destruction occurs at the weakest link which is aggregate in case of lightweight aggregate. Figure 13 illustrates the stress-strain responses of each concrete mix at various w/b ratios.

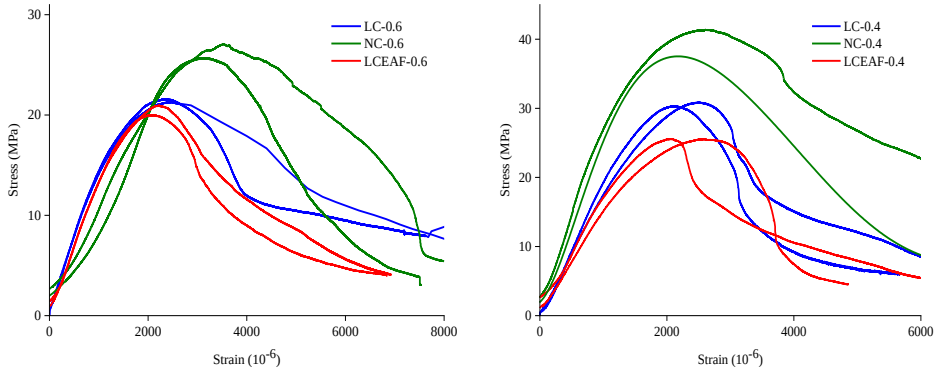

Fig. 13. Stress-**s**train curve

In comparison to normal weight concrete, which shows linear behavior up to 35-50% of maximum load, the stress strain plot of lightweight concrete depicts linear behavior up to 70-80% of maximum load for each lightweight concrete with SFA and natural fine aggregate as well as lightweight concrete with EAF slag as fine aggregate and sintered fly ash lightweight coarse aggregates. The study conducted in past [40] has shown the linear behavior up to 90-95% of peak load for lightweight concrete. The high level of linearity observed compared to the present study can be explained by the small maximum size of the lightweight aggregate used in the concrete mix. The size of aggregate used by Domagala et al. was 4-8 mm whereas in present study the size range of lightweight aggregate used is 4-16 mm. The surface characteristics of lightweight aggregate and its porous nature as well as internal curing in lightweight concrete system makes superior interfacial transition zone as well monolithic product leading to prolonging the rising branch of curve representing concrete stress strain.

The failure of lightweight concrete happens in brittle manner once fracture initiates due to inferior aggregate interlocking mechanism wherein crack passes through the aggregates

compared to normal concrete where fracture initiates at the interface of aggregate and mortar [41]. The past studies [41] has shown that fracture in lightweight aggregate is bound to happen through the aggregate but in case of sintered fly ash lightweight aggregate-based concrete, the fracture is happening around the aggregate. In general, the lightweight concrete stress strain behavior can be categorized into three parts. The first part is linear portion which is up to 70-80% of maximum load associated to strain of approximately 90-95% where macro crack initiates in the central portion of cylindrical specimen. The second part is the portion of stress strain curve where stress increases steadily and strain increases at faster rate. In this part the concrete continues to crack and cracks formed are more than normal concrete because of lower strength of porous lightweight aggregate. The third part of curve indicates the point beyond the peak stress, where stress decreases at faster rate and reaches to almost half of the peak load indicating brittle and shear type of failure in case of lightweight concrete. Thereafter, the stress gradually decreases with increasing strain because of the cracks getting capacity through the residual stress and frictional resistance mainly.

6.2 Load-CMOD and Load-Deflection Behavior of Lightweight Concrete and Normal Concrete

This section presents the plot of load vs deflection and load vs CMOD behavior of normal concrete (NC), lightweight concrete with SFA and natural fine aggregate (LC) and lightweight concrete with SFA and EAF as fine aggregate (LCEAF) for w/b ratio of 0.4, 0.6 in Figure 14. These graphs implemented for the assessment of fracture indicator to the point of failure. The failure point is addressed by sudden change in deflection that happens without a load increment in Load-Deflection curve or sudden change in CMOD that happens without a load increment in Load-CMOD curve.

The plot load vs deflection and load vs CMOD curves are comparable for both lightweight concrete with SFA and natural fine aggregate and lightweight concrete with SFA and EAF slag as fine aggregate. The non-linear ascending and descending branches in flexural curves of lightweight concrete with SFA including difference in results and pattern can be correlated with the non-linearity in tensile mode stress-strain behavior and formation of the process zone of fracture in front of the initial notch. In case of lightweight concrete, larger fracture process zone gets formed before the peak because of weaker aggregate to paste bond.

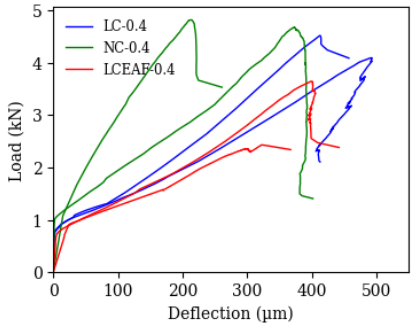

(a) Load Vs deflection plot

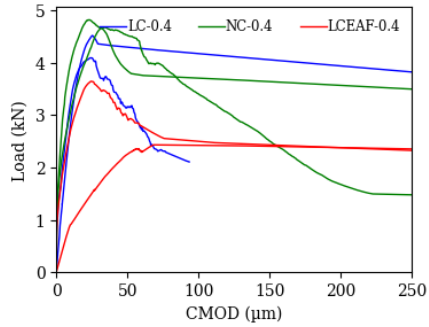

(b) Load Vs CMOD plot

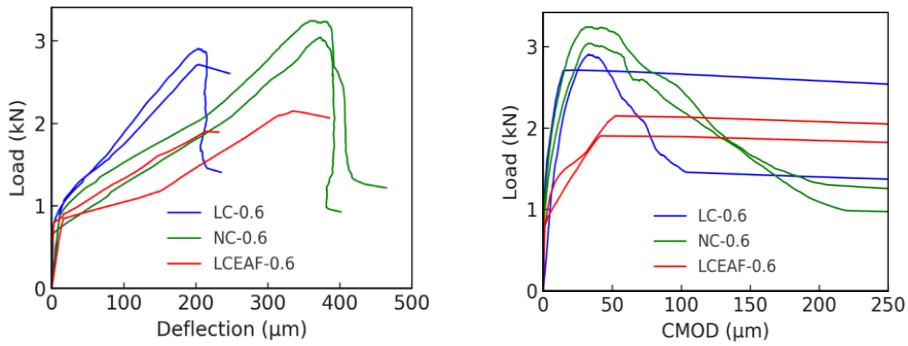

(a) Load Vs deflection plot (b) Load Vs CMOD plot

Fig. 14. Load Vs deflection plot & Load Vs CMOD plot for w/b of 0.4 and 0.6

The exact reason behind the flat flexural curves in lightweight concrete in comparison to normal weight concrete is not fully understood and one of the reasons can be tortuous crack path in lightweight concrete in comparison to normal concrete.

6.3 Fracture Energy

Fracture energy is referred to as the quantum of energy needed to create a crack with unit area, it is denoted by G_f. It is a critical parameter that is used to examine and assess concrete crack resistance, brittleness and toughness. Fracture energy is calculated by the formula from RILEM 50 [12, 43] given below;

$$G_f(N/m) = (W_o + mg\delta_o)/A_{lig} \quad (1)$$

Where W_o = Area below load and deflection plot as shown in Figure 15, m = Beam mass between the support, g = The gravitational acceleration, i.e., 9.81 m/s^2, δ_o = Failure deflection of specimen and A_{lig} = Ligament area.

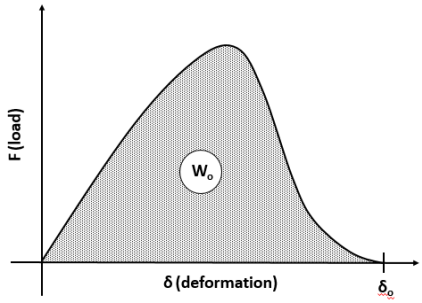

Fig. 15 Area within load and mid-point deflection plot of beam [32]

The comparison of fracture energy of the normal concrete (NC), lightweight concrete with SFA and natural fine aggregate (LC) and lightweight concrete with SFA and EAF as fine aggregate for both w/b 0.4 and 0.6 is presented in Figure 16. It has been suggested by Mazloom et al. [42] that the correction in fracture energy related parameters can yield accurate results where the peak loads of geometrically similar beams which defines the initial fracture energy with respect to corresponding peak loads are adjusted considering the effect of the specimen weight. In present case correction has not been considered as here only the relative comparison is made for fracture parameters of various concrete systems with different types of aggregates.

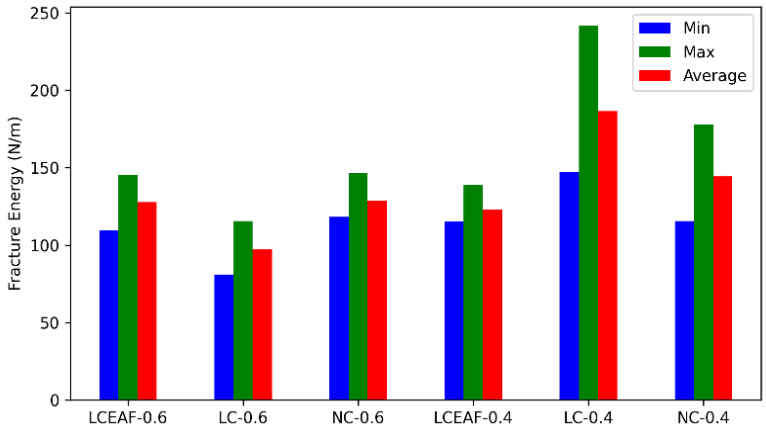

Fig. 16 Fracture energy for w/b ratio of 0.6 and 0.40

Normal concrete and lightweight concrete exhibit comparable fracture energy. For w/b ratio of 0.6, the average fracture energy for all the six concrete mixes varies from 100 to 125 N/m. For w/b ratio of 0.4, the average fracture energy for all the six concrete mixes varies from 125 to 180 N/m. The average fracture energy is comparable for both lightweight concrete with SFA and natural fine aggregate and lightweight concrete with SFA and EAF slag as fine aggregates. The past studies [14-15] has shown that fracture in lightweight aggregates is bound to happen through the aggregate but in case of sintered fly ash lightweight aggregate-based concrete, the fracture is happening around the aggregate. The reason behind this theory can be attributed to development of large stress at interface of lightweight aggregate and cement matrix due to incompatibility of modulus of elasticity of both aggregate and cement matrix. Additionally, some crack resistance is also provided by the hard-outer shell of sintered fly ash lightweight aggregate.

6.4 Modulus of Elasticity and Initial Compliance

Initial compliance represented by Ci, is defined as the reciprocal of gradient of initial linear segment of load versus CMOD curve. Equation (2), as given by [12], is used to get the MOE for the concrete beams with midpoint notch using the Ci.

$$E\ (MPa) = 6S\ \frac{\alpha V_1(\alpha)}{C_i d b^2} \tag{2}$$

Where $\alpha = a/d$, a= initial notch depth, d= beam depth. The computation of the gradient of the load-CMOD curve's initial straight segment is displayed in Figure 13. Equation (3) provided by Tada et al. [25] is used to determine V1(α) as follows:

$$V_1(\alpha) = 0.76 - 2.28\alpha + 3.87\alpha^2 - 2.04\alpha^3 + \frac{0.66}{(1-\alpha)^2} \tag{3}$$

The Table 8 presents the value of MOE as obtained from initial compliance by using equation 2. It can be observed that Load-CMOD compliance method for MOE gives higher result than the actual as concrete exhibits greater strength. The MOE by this method is not accurate and reliable, therefore actual MOE is used for calculation of subsequent parameters in the study.

Table 8. Elastic Modulus and initial compliance of concrete

w/ b ratio	Cube compressive strength (MPa)	Initial compliance Ci (10-9 m/N)	Modulus of elasticity, GPa [cmod test]	Modulus of elasticity (GPa) [As per Arora et al. For NWC [26] / IS: 9142-2018 for LWC [24]]
NC-0.6	28.33	6.67	24.0	28.27
LC-0.6	25.00	4.54	35.3	18.86
LCEAF-0.6	26.02	9.09	17.7	19.09
NC-0.4	47.55	4.48	35.8	32.85
LC-0.4	37.87	3.92	40.9	20.94
LCEAF-0.4	36.51	6.06	26.5	22.42

The compliance method suggested by RILEM is complicated, difficult, and sensitive to various test parameters. It requires a high degree of measurement sensitivity in mechanical bend tests, in the order of {10-^{9}} meters. Compliance is a function of the initial slope, which can vary slightly based on individual graph analyses. Even a little deviation in measuring the initial level slope in Load-CMOD curve significantly affects the MOE. Figure 17 represents best representative curve for calculating the starting gradient of the Load-CMOD curve for different w/b ratios of the mix. From this study, it is evident that this method for determining MOE should not be preferred and is limited to use for comparative analysis only. Other well-known standard empirical methods should be used for MOE calculations.

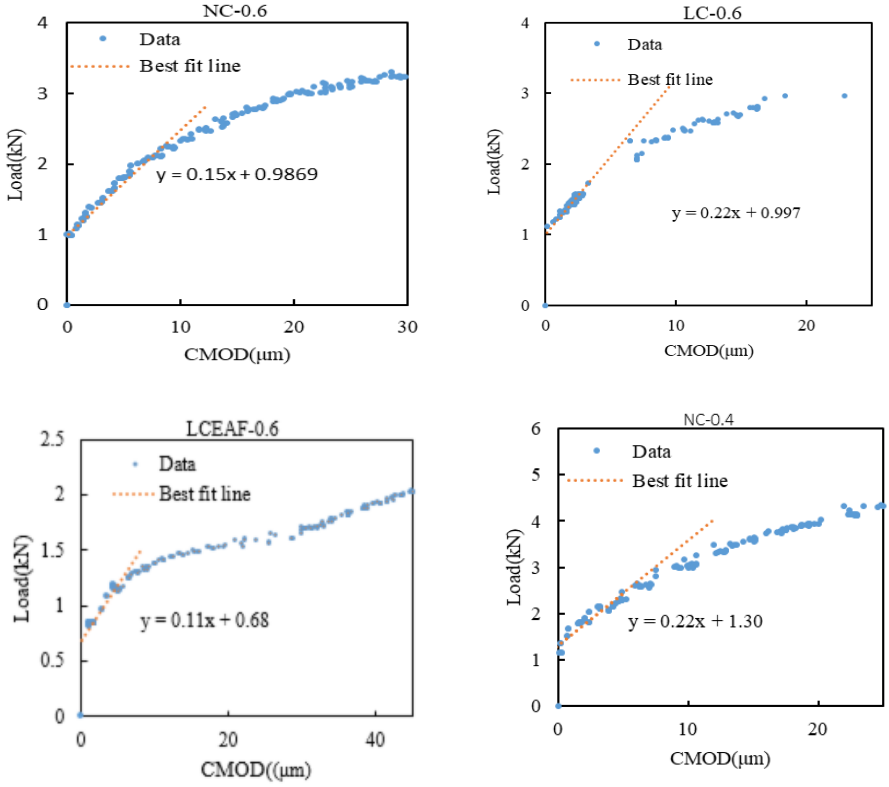

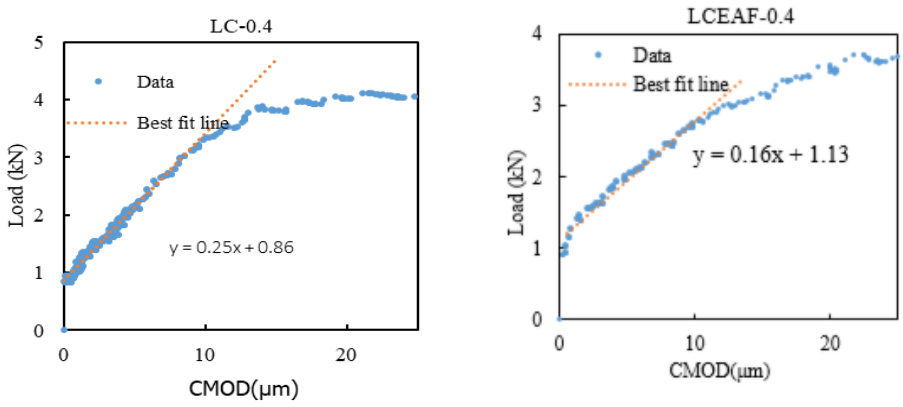

Fig. 17. Initial compliance calculation from Load-CMOD curves

6.5 Stress Intensity Factor (K_{Ic})

It is defined as stress measurement adjacent to the crack and computed using equation-4 [12]. It represents the state of stress and crack propagation rate in the neighborhood of the crack or notch tip. The specimen with higher (K_{IC}) shows higher stress is distributed in the vicinity of the crack representing less brittle the material.

$$K_{IC}\,(MPa\sqrt{m}) = 3(P_{Nmax} + 0.5W)\frac{S\sqrt{\pi a}}{2d^2 b}f(\alpha) \quad (4)$$

Where P_{Nmax} = Peak load beam with midpoint notch in N, W = Total weight of the beam between the supports, S = Span of the beam in m, α = a/d = 0.35, f(α) = Geometric adjustment concerning the bending load. For calculation of f(α) Finite Element Method is required for varying property of material, size and notch depth [27]. But in the present study equation (5) is used for comparative analysis because of simplicity and wide acceptance of this:

$$f(\alpha) = \frac{1.99 - \alpha(1-\alpha)(2.15 - 3.9\alpha + 2.7\alpha^2)}{\sqrt{\pi}(1+2\alpha)(1-\alpha)^{3/2}} \quad (5)$$

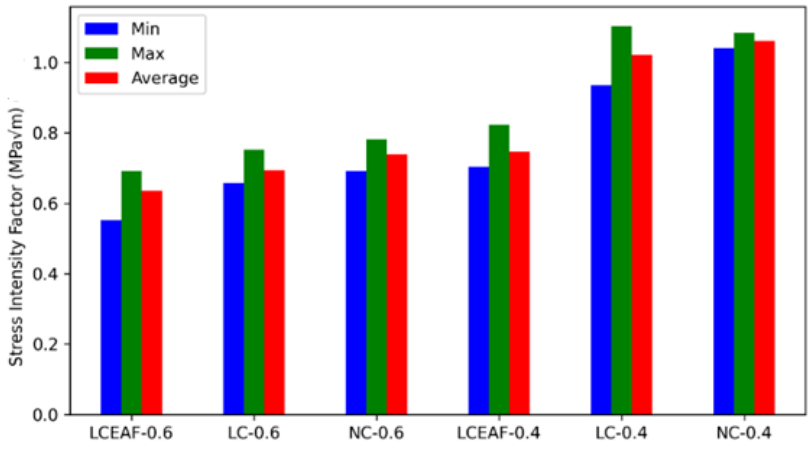

Fig. 18. Stress intensity factor

Figure 18 shows the test results of stress intensity factor. The graph shows that the average stress intensity factor of both normal concrete and lightweight concrete are comparable. The average stress intensity factor is comparable for both lightweight concrete with SFA and natural fine aggregate and lightweight concrete with SFA and EAF slag as fine aggregate. The reduction in w/b ratio leads to increase in the K_{IC} for both normal weight concrete and lightweight concrete. It is also seen that K_{IC} increases with increase in compressive strength of the concrete because formation of initial cracks depends upon the tensile strength of the beam. The stress intensity factor for w/b ratio in case of LCEAF samples are less dominant in comparison to lightweight concrete with natural fine aggregate and normal concrete with natural coarse and fine aggregates.

6.6 Critical Energy Release Rate (G_{IC})

It is defined as rate of change of energy when new fracture surface is created. It quantifies the energy change associated with crack growth. It is important parameter to predict fracture toughness and crack growth behavior. The equation given by RILEM [12, 27] and mentioned below in eq. (6) is adopted for calculation of G_{IC}:

$$G_{IC}(N/m) = \frac{{K_{IC}}^2}{E} \tag{6}$$

Figure 19 shows that the energy release rate in case of lightweight concrete is higher as compared to normal weight concrete for both w/b ratios. It indicates that in the lightweight concrete the strain energy release with formation of new crack will be higher in comparison to normal weight concrete which was evident in stress strain behavior also where a greater number of crack formation occurs at peak stress. The average energy release rate is comparable in case of w/b ratio 0.6 and 0.4 for both lightweight concrete with SFA and natural fine aggregate and lightweight concrete with SFA and EAF slag as fine aggregate.

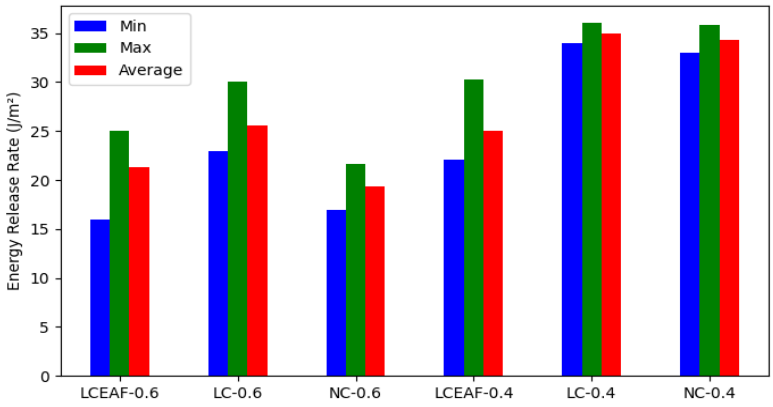

Fig. 19. Energy release rate

6.7 Characteristic Length of Concrete

Characteristic length is inherent property of material which indicates smallest possible width of a zone where damage occurs in a non-local continuum model [26]. It indicates the smallest possible spacing of fracture in discrete fracture model. It is calculated to understand and compare the brittleness of two different materials. The lesser the characteristic length, the lesser the spacing of fracture due to easier crack propagation and more brittle the material. It helps to predict how materials will behave when they start to

break. The following formula (7) from [27] can be used to compute it. Here f_{st} is split tensile strength, G_f is fracture energy and E is elastic modulus.

$$L_{ch}(mm) = \frac{EG_f}{{f_{st}}^2} \quad (7)$$

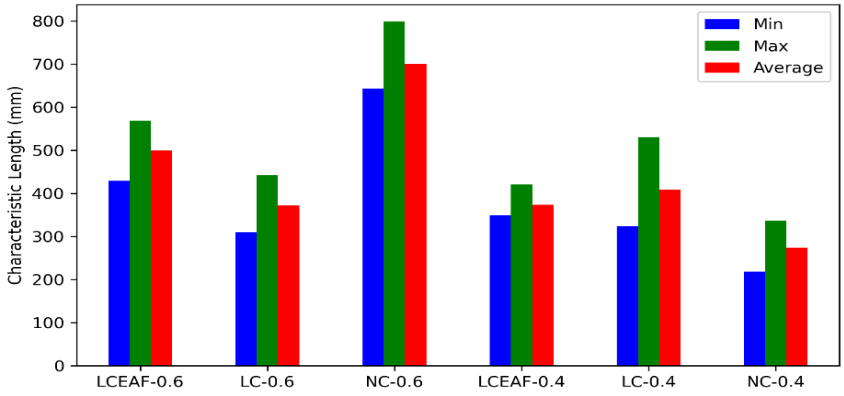

Fig. 20. Characteristic length

The characteristic length of lightweight concrete is shorter than normal concrete for w/b ratio 0.6. However, the difference in characteristic length of lightweight concrete is less in comparison to normal concrete for w/b ratio 0.4. For w/b ratio of 0.6, the average characteristic length for all the six concrete mixes varies from 380 to 700 mm. For w/b ratio of 0.4, the average characteristic length for all the six concrete mixes varies from 290 to 400 mm. The average characteristic length is comparable for both lightweight concrete with SFA and natural fine aggregates and lightweight concrete with SFA and EAF slag as fine aggregate.

7. Conclusions

From the experimental study on mechanical behavior of normal weight and lightweight concrete in terms of compressive strength, split tensile strength, modulus of elasticity, stress strain behavior and fracture parameters using three different concrete systems namely (a) normal concrete (NC), (b) lightweight concrete with SFA and natural fine aggregates (LC) and (c) lightweight concrete with SFA and electric arc furnace slag as fine aggregate (LCEAF); following conclusions are drawn:

- Split tensile strength tests revealed that lightweight concrete exhibits a split tensile to compressive strength ratio between 5% and 7%, while this ratio ranges from 5% to 10% for normal weight concrete. The elastic modulus in case of lightweight concrete is about 60-70% of elastic modulus of normal weight concrete.
- As compared to normal weight concrete, which shows linear behavior up to 35-50% of maximum load, the stress strain plot of lightweight concrete depicts linear behavior up to 70-80% of peak load for lightweight concrete. The fracture in case of lightweight aggregate with sintered fly ash lightweight aggregate-based concrete is happening around the aggregate due to internal curing and prolonged hydration happening because of porous nature of sintered fly ash lightweight aggregate.
- The comparison of load-CMOD and Load Deflection behavior of lightweight concrete and normal concrete for both w/b 0.4 and 0.6 indicates that ascending portion of Load–Deflection and load-CMOD plot of concrete with SFA slightly steeper and linear than normal weight concrete. The non-linear ascending and

descending branches in flexural curves of lightweight concrete with SFA can be correlated with the non-linearity in tensile mode stress-strain behavior and formation of the process zone of fracture in front of the initial notch.

- The fracture energy of both normal concrete and lightweight concrete are comparable. For w/b ratio of 0.6, the average fracture energy for all the six concrete mixes varies from 100 to 125 N/m. For w/b ratio of 0.4, the average fracture energy for all the six concrete mixes varies from 125 to 180 N/m. In case of sintered fly ash lightweight aggregate-based concrete, the fracture is happening around the aggregate. The reason behind this phenomenon can be attributed to development of large stress at interface of lightweight aggregate-paste matrix due to incompatibility of elastic modulus of both aggregate-paste matrices.
- The average stress intensity factor is comparable for both lightweight concrete with SFA and natural fine aggregate and lightweight concrete with SFA and EAF slag as fine aggregate. As the w/b ratio decreases the KIC for both lightweight concrete and normal weight concrete increases. It is also seen that KIC increases with increase in concrete's compressive strength because formation of initial cracks depends upon the tensile strength of the beam.
- The lightweight concrete shows higher energy release rate in comparison to normal weight concrete for both w/b ratios. It indicates that in the lightweight concrete the strain energy release with formation of new crack will be higher than normal weight concrete which was evident in stress strain behavior also where a greater number of crack formation occurs at peak stress.
- The characteristic length of lightweight concrete is smaller than normal concrete for w/b ratio 0.6. However, the difference in characteristic length of lightweight concrete is smaller in comparison to normal concrete for w/b ratio 0.4.
- The mechanical and fracture behavior of lightweight concrete is different from normal concrete in terms of elastic modulus, stress strain characteristics, crack propagation process zone and characteristics length and needs to be considered appropriately in design of concrete depending upon type of application. However, mechanical and fracture behavior of lightweight concrete with SFA and natural fine aggregates and lightweight concrete with SFA and EAF slag as fine aggregate is comparable.

References

[1] Singh B, Singh SB, Barai SV. Performance of concrete made using sintered fly ash lightweight aggregate-A review. Indian Concrete Journal. 2023;97(7):41-59.
[2] Ojha PN, Singh B, Behera AK. Sintered fly ash lightweight aggregate-Its properties and performance in structural concrete. Indian Concrete Journal. 2021;95(6):20-30.
[3] Mazloom M, Mirzamohammadi S. Fracture of fibre-reinforced cementitious composites after exposure to elevated temperatures. Magazine of Concrete Research. 2020;73:701-713. https://doi.org/10.1680/jmacr.19.00401
[4] Mazloom M, Saffari A, Mehrvand M. Compressive, shear and torsional strength of beams made of self-compacting concrete. Computers and Concrete. 2015;15:935-950. https://doi.org/10.12989/cac.2015.15.6.935
[5] Mazloom M, Mirzamohammadia S. Computing the fracture energy of fiber reinforced cementitious composites using response surface methodology. Advances in Computational Design. 2021;6(3):225-239.
[6] Hillerborg A, Modeer M, Peterson PE. Analysis of crack formation and crack growth in concrete by means of fracture mechanics and finite elements. Cement and Concrete Research. 1976;6(6):773-782. https://doi.org/10.1016/0008-8846(76)90007-7

[7] Jenq YS, Shah SP. Two parameter fracture model for concrete. Journal of Engineering Mechanics. 1983;111(10):1227-1241. https://doi.org/10.1061/(ASCE)0733-9399(1985)111:10(1227)
[8] Bazant ZP, Oh BH. Crack band theory for fracture of concrete. Materials and Structures. 1983;16(3):155-178. https://doi.org/10.1007/BF02486267
[9] Zhang MH, Gjorv OE. Mechanical properties of high strength lightweight concrete. ACI Materials Journal. 1991;88(3):240-247. https://doi.org/10.14359/1839
[10] Patel V, Singh B, Arora VV. Study on fracture behaviour of high strength concrete including effect of steel fiber. Indian Concrete Journal. 2020;94(4):1-9.
[11] Ojha PN, Singh B, Singh A, Patel V, Arora VV. Experimental study on creep and shrinkage behaviour of high strength concrete. Indian Concrete Journal. 2021;95(2):30-42.
[12] RILEM TC-50 FMC. Determination of the fracture energy of mortar and concrete by means of three-point bend tests on notched beams. Materials and Structures. 1985;18:106-290. https://doi.org/10.1007/BF02472918
[13] Shah SP. Determination of fracture parameters (KIcs and CTODc) of plain concrete using three-point bend tests. Materials and Structures. 1990;23:457-460. https://doi.org/10.1007/BF02472029
[14] Sahoo S, Lakavath C, Suriya SS. Experimental and analytical studies on fracture behavior of fiber-reinforced structural lightweight aggregate concrete. Journal of Materials in Civil Engineering. 2021;33(5). https://doi.org/10.1061/(ASCE)MT.1943-5533.0003680
[15] Trivedi N, Singh RK, Jayant C. A comparative study on three approaches to investigate size independent fracture energy of concrete. Engineering Fracture Mechanics. 2015;138:49-62. https://doi.org/10.1016/j.engfracmech.2015.03.021
[16] Murthy AR, Ganesh P, Kumar SS, Iyer NR. Fracture energy and tension softening relation for nano-modified concrete. Structural Engineering and Mechanics. 2000;54(6):1201-1216. https://doi.org/10.12989/sem.2015.54.6.1201
[17] Gil DM, Golewski GL. Effect of silica fume and siliceous fly ash addition on the fracture toughness of plain concrete in mode I. In: IOP Conference Series: Materials Science and Engineering. Institute of Physics Publishing; 2018. https://doi.org/10.1088/1757-899X/416/1/012065
[18] Siregar APN, Rafiq MI, Mulheron M. Experimental investigation of the effects of aggregate size distribution on the fracture behaviour of high strength concrete. Construction and Building Materials. 2017;150:252-259. https://doi.org/10.1016/j.conbuildmat.2017.05.142
[19] IISI Steel Statistical Yearbook. Brussels, Belgium: International Iron and Steel Institute; 2004. Available from: http://www.worldsteel.org/
[20] Pellegrino C, Gaddo V. Mechanical and durability characteristics of concrete containing EAF slag as aggregate. Cement and Concrete Composites. 2009;31:663-671. https://doi.org/10.1016/j.cemconcomp.2009.05.006
[21] Abu-Eishah S, El-dieb A, Bedir M. Performance of concrete mixtures made with electric arc furnace (EAF) steel slag aggregate produced in the Arabian Gulf region. Construction and Building Materials. 2012;34:249-256. https://doi.org/10.1016/j.conbuildmat.2012.02.012
[22] Motz H, Geiseler J. Products of steel slags-an opportunity to save natural resources. Waste Management. 2001;21:285-293. https://doi.org/10.1016/S0956-053X(00)00102-1
[23] Pellegrino C, Cavagnis P, Faleschini F, Brunelli K. Properties of concretes with black/oxidizing electric arc furnace slag aggregate. Cement and Concrete Composites. 2013;37:232-240. https://doi.org/10.1016/j.cemconcomp.2012.09.001

[24] Faleschini F, De Marzi P, Pellegrino P. Recycled concrete containing EAF slag: environmental assessment through LCA. European Journal of Environmental and Civil Engineering. 2014;18. https://doi.org/10.1080/19648189.2014.922505
[25] Arribas I, Santamaria A, Ruiz E, Ortega-Lopez V, Manso JM. Electric arc furnace slag and its use in hydraulic concrete. Construction and Building Materials. 2015;90:68-79. https://doi.org/10.1016/j.conbuildmat.2015.05.003
[26] Adegoloye G, Beaucour LA, Ortola S, Noumowe A. Concretes made of EAF slag and AOD slag aggregates from stainless steel process: mechanical properties and durability. Construction and Building Materials. 2015;76:313-321. https://doi.org/10.1016/j.conbuildmat.2014.12.007
[27] Manso JM, Polanco JA, Losanez M, Gonzalez JJ. Durability of concrete made with EAF slag as aggregate. Cement and Concrete Composites. 2006;28:528-534. https://doi.org/10.1016/j.cemconcomp.2006.02.008
[28] Akinmusuru JO. Potential beneficial uses of steel slag wastes for civil engineering purpose. Resources Conservation and Recycling. 1991;5:73-80. https://doi.org/10.1016/0921-3449(91)90041-L
[29] Bureau of Indian Standards. Ordinary Portland Cement-Specification IS 269. 2015.
[30] Bureau of Indian Standards. Coarse and Fine Aggregate for Concrete-Specification IS 383. 2016.
[31] Bureau of Indian Standards. Concrete Admixtures-Specification IS 9103-1999. 1999.
[32] Bureau of Indian Standards. Concrete Mix Proportioning-Guidelines IS 10262. 2019.
[33] Bureau of Indian Standards. Artificial Lightweight Aggregate for Concrete-Specification Part 2: Sintered Fly Ash Coarse Aggregate IS 9142 (Part-2). 2018.
[34] Nadesan MS, Dinakar P. Mix design and properties of fly ash waste lightweight aggregates in structural lightweight concrete. Case Studies in Construction Materials. 2017;7:336-347. https://doi.org/10.1016/j.cscm.2017.09.005
[35] Bureau of Indian Standards. Hardened Concrete-Methods of Test Part-1, Testing of Strength of Hardened Concrete, Section-1: Compressive, Flexural and Split Tensile Strength IS 516 (Part 1/Sec 1). 2021.
[36] Karamloo M, Mazloom M. An efficient algorithm for scaling problem of notched beam specimens with various notch to depth ratios. Computers and Concrete. 2018;22:39-51.
[37] Arora VV, Singh B, Jain S. Experimental studies on short term mechanical properties of high strength concrete. Indian Concrete Journal. 2016;90(10):65-75.
[38] Arora VV, Singh B, Patel V, Trivedi A. Evaluation of modulus of elasticity for normal and high strength concrete with granite and calc-granulite aggregate. Structural Concrete. 2021;22(S1). https://doi.org/10.1002/suco.202000023
[39] Ojha PN, Singh P, Singh B, Singh A, Mittal P. Fracture behavior of plain and fiber-reinforced high strength concrete containing high strength steel fiber. Research on Engineering Structures and Materials. 2022.
[40] Domagała L. Modification of properties of structural lightweight concrete with steel fibres. Journal of Civil Engineering and Management. 2011;17(1):36-44. https://doi.org/10.3846/13923730.2011.553923
[41] Liu X, Wu T, Liu Y. Stress-strain relationship for plain and fibre-reinforced lightweight aggregate concrete. Construction and Building Materials. 2019. https://doi.org/10.1016/j.conbuildmat.2019.07.135
[42] Mazloom M, Salehi H. The relationship between fracture toughness and compressive strength of self-compacting lightweight concrete. IOP Conference Series: Materials Science and Engineering. 2018; 431. https://doi.org/10.1088/1757-899X/431/6/062007
[43] Bazant Z P, Planas J. Fracture and Size Effect in Concrete and Other Quasibrittle Materials. Florida, CRC Press, First Published 1998.

Research on Engineering Structures & Materials
www.jresm.org
Research Group

Research Article

Effect of Nano-TiO_2 at macro and micro level of concrete by partial substitution of cement

M. Suneel [*,1,2,a], G. V. Rama Rao [1,b]

[1]*Department of Civil Engineering, Andhra University College of Engineering, Visakhapatnam, India*
[2]*Department of Civil Engineering, S.R.K.R. Engineering College, Bhimavaram, India*

Article Info

Article History:

Received 17 Aug 20204
Accepted 04 Oct 2024

Keywords:

Nano-TiO_2;
Workability;
Strength;
Variations;
Macro level;
Micro level

Abstract

At macro level the strength of the concrete will decline due to several reasons like high water-cement ratio, improper compaction and improper curing. At micro level concrete strength will reduce due to poor pore structure. Since the cement acts a binding agent upon reacting with water, the fineness of the cement influences the strength. Higher water cement ratio leads to higher porosity. Fine particles of very high specific surface area may affect the pores of concrete leading to strength enhancement rather than decline. In this study is aimed to study the effects of partial substitution of nano-TiO_2 for cement into concrete, on mechanical strength and microstructure. Fresh and hard macro level properties are investigated for M40 and M60 with cement replacement 0% to 2% by nano-TiO_2. SEM images were examined for studying dispersion of particles and XRD for products of hydration at micro level. It is found that at 1% of nano-TiO_2 strength for M40 and M60 were higher with other percentages replacements.

© 2025 MIM Research Group. All rights reserved.

1. Introduction

Most highly used man-made material is concrete heterogeneous rigid at macro and porous at micro with varied sizes of pores effecting mechanical properties significantly. Many key attributes, including strength and permeability, are directly or indirectly related to the characteristics of these pores [1,2]. It is studied that mechanical and durability properties are highly affected by pore structure of concrete [3]. Using very fine particles could fill voids or pores of concrete, the mechanical properties would improve. Addition of nano particles of higher surface energy into cement concrete, acts as nucleus and grow to form conglomeration for hydrated products of cement. Dispersion of the nano particles leads to form strong microstructure by the conglomeration, when quantity of nano particles is small for higher dispersion [4]. Some nano fillers can react with hydration products in cementitious materials, acting as nano-cores. This enables unique structures around the fillers that differ from those in traditional cement. These distinct areas significantly influence the overall behavior of the cementitious composites. [5].

Cement mortars with nano-FeO_3 and nano-SiO_2 had reduced $Ca(OH)_2$ and pores being filled up when compared with plain cement mortars. Furthermore, nano particles strengthened concrete at paste phase and paste and aggregates phase [4]. The mechanical strengths in compression and flexural of concrete with nano-TiO_2 are higher than concrete with nano SiO_2, which is mainly dispersion of particles having lower specific surface area of nano-TiO_2(240m^2/g) than nano-SiO_2(640m^2/g) [6].

Nano clays, Nano carbon tubes, mineral oxides like alumina, silica, metallic oxides like iron, titanium, zinc, zirconium etc are the various nano materials used in building materials. Presently

*Corresponding author: suneel.m@srkrec.ac.in
[a]orcid.org/0000-0003-3828-6203; [b]orcid.org/ 0000-0002-3443-8890
DOI: http://dx.doi.org/10.17515/resm2024.402ma0817rs

usage of nano-TiO_2 has gained lot of interest as construction materials because of low in cost, high chemical activity and stable [7-9]. The workability of concrete is affected when nano particles are added in high quantity due to their lager specific surface area [10]. The raise in water quantity is noticed for concrete mixtures due to lower size and larger surface area in absorbing water in high [11, 12].

Incorporation of nano-TiO_2 to concrete was carried out first from the available research was by Li in Harbin Institute of Technology, China [13]. Nano-TiO_2 particles are non-pozzolanic materials which do not react, but they are refill the pore structures. Nano-TiO_2 accelerates hydration of cement, significant peak during heat of hydration takes place early with improved potential, reduced occurrence and lower setting time duration compared to the conventional specimen providing additional nucleation sites and raise in water demand. [14]. Nano-TiO_2 being fine in particle size the strength of concrete is enhanced by accelerating hydration and pore filling. Drying Shrinkage minimized with addition of nano-TiO_2 and hydrophilicity of paste is increased [15]. Addition of nano-TiO_2 modified the microstructural mechanisms filling pores by producing homogeneous dense needle shaped calcium silicate hydrated gel hydration products with sustained deposition on improving properties of concrete [16].

In the early stages of hydration, porosity increases due to the formation of voids. However, as hydration continues, the growth of hydrates fills these voids, leading to a subsequent reduction in porosity. Significant changes in porosity observed over time, reflecting the transition from initial expansion to eventual densification as the cement paste matures [17]. During the hydration crystallization of $Ca(OH)_2$ reduced at aggregate and cement paste interface enhancing the structure and mechanical properties. Increase in nano-TiO_2 quantity in concrete limits the space required for gel growth and reduces $Ca(OH)_2$ in cement matrix.[18,19]. The performance of concrete can be optimized by the nano-TiO_2 photocatalytic activity decomposition of gaseous pollutants [20]. The surface hardness of concrete that possess 1% nano-TiO_2 exhibited significant betterment than nano-silica and polypropylene. Hydrophilicity of nano-TiO_2 provides zero contact and reflectance in high level with 5% content in concrete mixtures [21]. Nanofillers migrate with water into interfacial zone of aggregates and cement mortar by the nano-core effect enhances bond strength. Beyond the substitution of 1% of nano fillers to cement in concrete the bond strength between aggregates and cement mortars turns to decline [22].

The suitability of nano-TiO_2 as cementitious materials is identified in XRD diffraction with smooth hump establishing amorphous phase. Rutile and anatase phases are noticed in the peaks of XRD diffraction. [23]. Nano-TiO_2 renders cementitious composites through its excellent properties and by optimizing hydration, which improves strength and reduces shrinkage. This allows for tailored performance, lower production costs, and longer-lasting infrastructure. Future advancements promise even more efficient and multifunctional applications in construction [24].

The quality of concrete mainly influenced by materials properties, preparation and workmanship. Due to various reasons the quality of concrete pertaining to strength is declined. The inclusion of nano-TiO_2 into concrete has been done extensively and observed considerable improvement in the strength of concrete. The longevity of concrete will also enhance on improved strength by partial substitution of nano-TiO_2. In addition to the enhancement of strength and longevity, the maintenance cost of concrete structures with nano TiO_2 can be less than conventional concrete.

In this paper, experimental study on concrete with partial substitution of cement by nano-TiO_2 varying partially with an interval of 0.5%, up to 2% for two grades M40 and M60, is presented. Two grades of concretes from Table no. 2 of IS 456, M40 and M60 were selected, and their mix designs are done following IS 10262:2009 guidelines. Workability and strength properties at macro and SEM and XRD analysis at micro level, with and without substitution of Nano Titanium Dioxide for both M40 and M60 grade concretes are investigated.

2. Materials

Nano TiO_2, ordinary Portland cement (OPC 53 grade), fine aggregate (river sand), coarse aggregate (natural crushed aggregates), water and super plasticizer are used for preparing of both M40 and M60 grade concretes to observe the effect of nano-TiO_2 by cement partial replacement.

2.1. Cement

In the present experimental investigation for lower pore size in cement paste phase OPC 53 grade Ordinary Portland cement is utilized throughout the work. In accordance with IS: 12269-1987 cement procured is tested for the basic physical properties and are shown in Table 1.

Table 1. Basic physical properties of OPC 53

Property	Standard Consistency	Setting time		Specific gravity	Compressive strength at 28 days
		Initial	Final		
Test results	32%	130 minutes	270 minutes	3..15	57.30 N/mm^2

2.2 Nano-TiO_2

Nano-TiO_2 is purchased at a cost of INR 375/- per kilogram from local paint shop. In general, it is mixed in paints as a pigment. From the literature is found that particles ranging from 50 – 200nm and density about 3.9 g/cm^3. Titanium hardness improves the strength and durability of cement concrete.

2.3 Fine Aggregate

Godavari river sand clear from clay, slit and organic impurities is procured from local supplier. The laboratory tested physical properties are shown in the Table 2.

Table 2. Laboratory tested physical properties of fine aggregate

Property	Specific gravity	Unit weight (kg/m^3)		Fineness Modulus	Zone
Test results	2.58	1620 (loose)	1750 (dense)	2.74	II

2.4 Coarse Aggregate

Maximum size of 20mm with 67% and 10 mm with 33% of total coarse aggregate mass are used throughout the research work. Test results for physical properties are tabulated in Table 3.

Table 3: Laboratory tested physical properties of coarse aggregate

Property	Specific gravity	Unit weight (kg/m^3)	Fineness Modulus
Test results	2.72	1400 (loose)	2.74

2.5 Water

Potable fresh water available in the laboratory, which was clean without any organic substances is used in preparing the wet mix of concrete.

2.6 Super Plasticizer (Fosroc Conplast SP430)

Concrete with lower water-cement ratio yields poor workability like low slump and low compaction factor values. But, to achieve high strength water-cement ratio has kept low for all the variations. So, for the same water-cement ratio using chemical admixtures like Conplast SP430 is

used better slump and compaction factor values have yielded. Since the superplasticizer releases water-logged between cement grains during mixing, the same water-cement ratio adopted to keep its effect similar.

3. Experimental Investigation

In the experimental study mix proportions were obtained as per IS 10262: 2009 mix guidelines for both M40 and M60 grade concrete having water-cement ratios 0.40 and 0.38 respectively. Primarily trial concrete mixes without superplasticizer yielded low slump stiff concrete and low compaction factor values. Based on trials superplasticizer added 0.8% of mass of cement for better workability. Mix proportions for both M40 and M60 concrete grades are shown in Table 4.

Table 4. M40 and M60 grades mix proportions

Constituents	Cement	Fine aggregate	Coarse aggregate	w/c ratio
For M40	1	1.825	3.420	0.40
For M60	1	1.516	2.966	0.38

The effect of nano-TiO_2 on concrete workability and strength were studied experimentally by partial substitution of cement with nano-TiO_2 content varying from 0% to 2% for both grades of concretes. Test methods executed on concretes in fresh state as per IS codes, listed in Table 5 for assessing workability. After casting the specimens for each mix of each grade, left for a period of 24 hours and then extracted out of moulds to place in curing tanks. Specimens were tested for carrying strength developed after the curing periods of 3, 7 and 28 days. Test methods performed on concretes in fresh and hardened state are listed in Table 5 for assessing compressive strength, split tensile strength and flexural strength.

Table 5. Test methods for assessing properties of concrete

Property	Test Method	Specimen Shape	Specimen Size, mm	Guidelines
Slump	Slump cone test	-	-	IS 1199 : 1959
Compaction Factor	Compaction apparatus test	-	-	IS 1199 : 1959
Compressive strength	Compression test	Cube	100x100x100	IS 516 : 1959
Split tensile strength	Split tensile test	Cylinder	100x 200	IS 5816 : 1999
Flexural strength	Flexural test	Beams	500x100x100	IS 516 : 1959
Microstructure	SEM	powder	75µ Passing	Nishka Labs,HYD
Hydrate Products	XRD	Powder	75µ Passing	Nishka Labs,HYD

4. Results and Discussions

4.1 Workability Properties of Concretes M40 and M60

In the fresh state of concrete workability was assessed by performing tests slump cone and compaction factor apparatus, the test results were tabulated in Table 6. The influence of nano-TiO_2 on concrete strengths like compressive, split tensile and flexural are graphically represented with obtained values at 3, 7 and 28 days of curing for both grades M40 and M60 in chart 1 to 6.

Table 6. Test results for assessing workability

S. No	% TiO_2	Slump (mm)		Compaction Factor	
		For M40	For M60	For M40	For M60
1	0	44	37	0.882	0.868
2	0.5	35	33	0.854	0.844
3	1.0	32	27	0.846	0.842
4	1.5	26	24	0.842	0.838
5	2.0	21	18	0.821	0.826

4.2 Strength Properties of Concretes M40 and M60

The influence of nano-TiO_2 on strength development is examined at macro level and micro level. Investigation results at macro level strength properties like compressive, split tensile and flexural strengths are presented from chart no1 to 3 for M40 grade concrete and from chart no. 4 to 6 for M60 grade concrete. Micro level study is presented by SEM and XRD analysis by figures 8, 9 and 10.

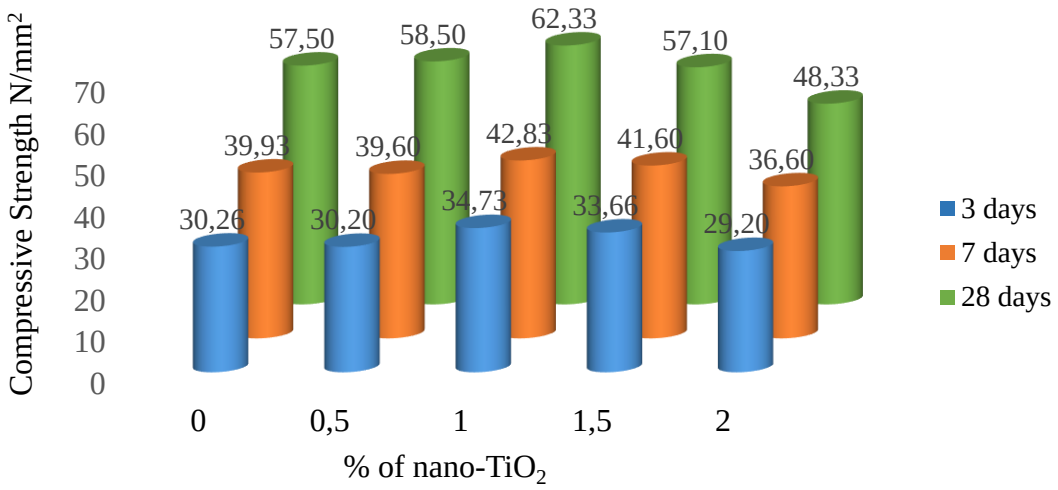

Fig. 1. Compressive strength for concrete M40 grade

From the Figure 1, it can be noticed that as days of curing increased 3 days to 28 days the strength is increased as in the case of conventional concrete. As the partial replacement increasing from 0.5 to 1.0% the compressive strength is increased and thereafter declined. It can be observed that nano-TiO2 as 1% partial substitution for cement has exhibited higher strength than all other percentages of substitutions for all curing periods. The maximum compressive strengths obtained are 34.33N/mm2 at 3days, 42.83N/mm2 at 7 days and 62.33N/mm2 at 1% of nano TiO2.

From the Figure 2, it can be identified that increase in period of curing 3 days to 28 days there is increase in split tensile strength similarly as in the case of conventional concrete. It can be noticed that nano-TiO2 as 1% partial substitution for cement has shown more split tensile strength than all other percentages of replacements for all curing periods. As the partial replacement increasing from 0.5 to 1.0% the split tensile strength is increased and thereafter decreased. The maximum split tensile strengths obtained are 2.29N/mm2 at 3days, 3.29N/mm2 at 7 days and 3.67N/mm2 at 1% of nano-TiO2.

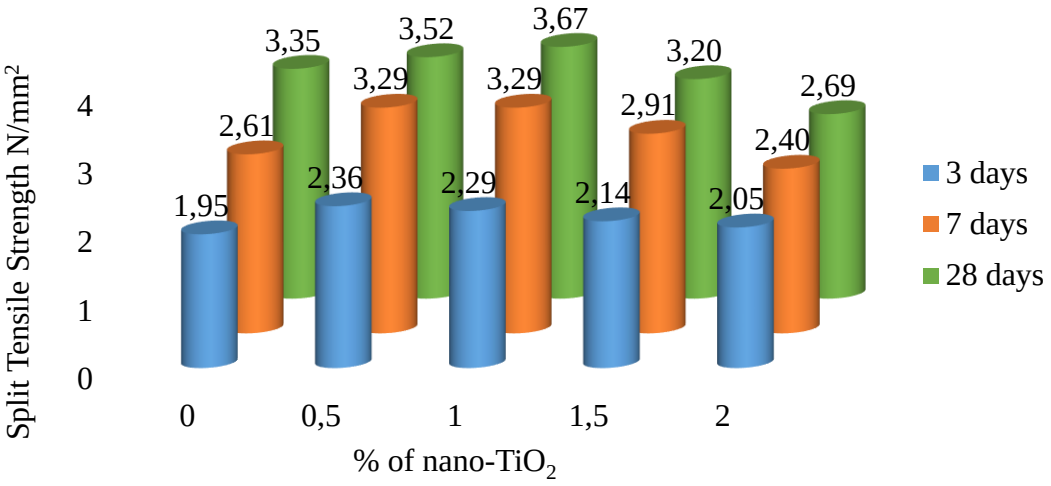

Fig. 2. Split tensile strength for concrete M40 grade

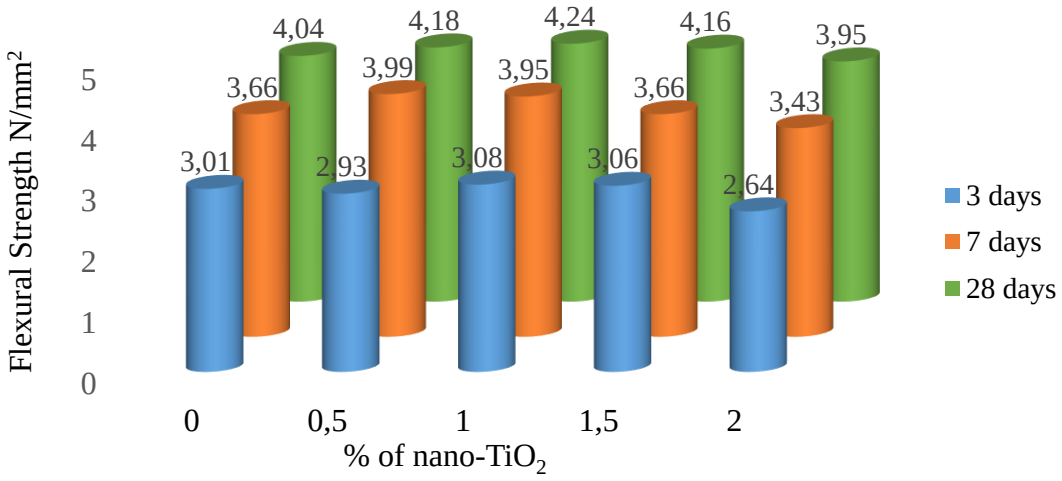

Fig. 3. Flexural strength for concrete M40 grade

From the Figure 3, it can be observed that period of curing 3 days to 28 days shows increase in flexural tensile strength similarly as in the case of conventional concrete. As the partial replacement increasing from 0.5 to 1.0% the flexural tensile strength is increased and thereafter declined. Also, it can be noticed that nano-TiO_2 as 1% partial substitution for cement has exhibited higher flexural strength than all other percentages of replacements for all curing periods. The maximum flexural strengths obtained are 3.08 N/mm² at 3 days, 3.95N/mm² at 7 days and 4.24N/mm² at 1% of nano-TiO_2.

From the Figure 4, it can be noticed that as days of curing increased 3 days to 28 days the compressive strength is also increased as in the case of conventional concrete. As the partial replacement increasing from 0.5 to 1.0% the compressive strength is increased and thereafter decreased. It can be observed that 1% of nano-TiO_2 as partial substitution for cement has exhibited maximum strength values than all other percentages of replacements for all curing periods. The maximum compressive strength values obtained are 46N/mm² at 3days, 62N/mm² at 7 days and 74.66N/mm² at 1% of nano-TiO_2.

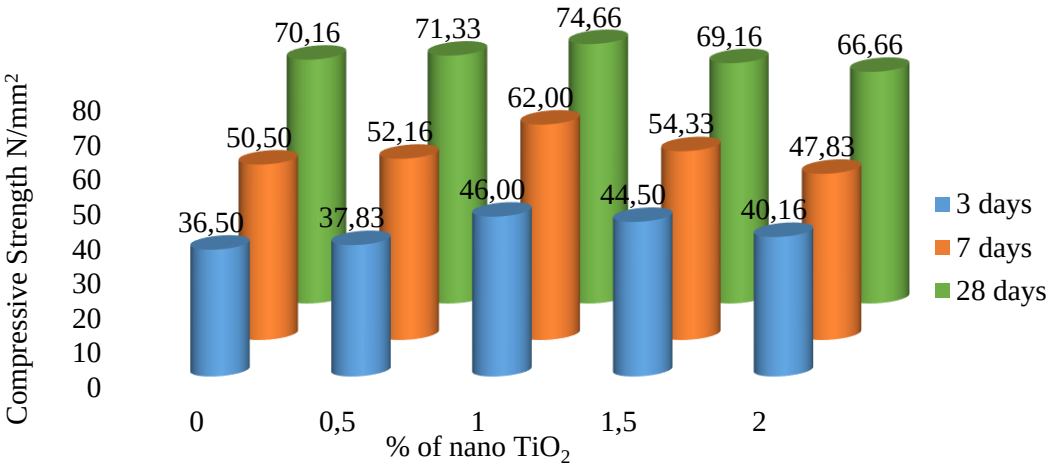

Fig. 4. Compressive strength for concrete M60 grade

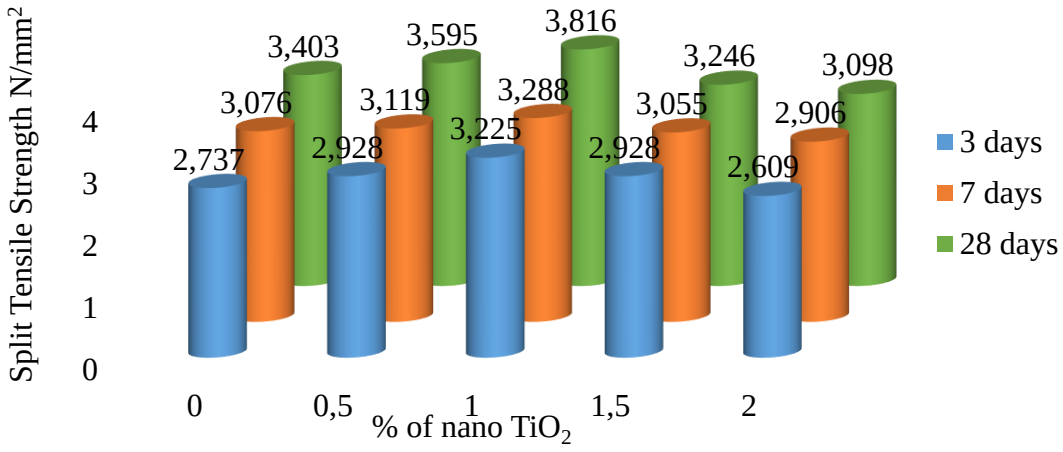

Fig. 5. Split tensile strength for concrete M60 grade

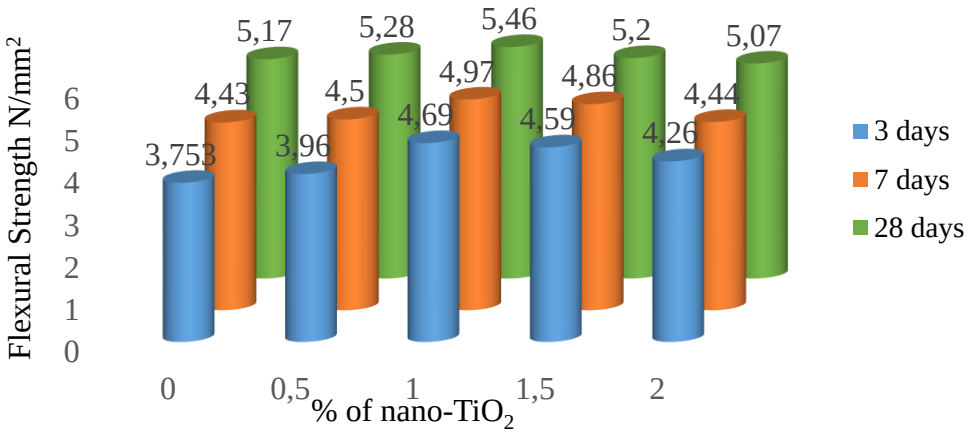

Fig. 6. Flexural strength for concrete M60 grade

From the Figure 5, it can be identified that increase in period of curing 3 days to 28 days there is increase in split tensile strength similarly as in the case of conventional concrete. It can be noticed that 1% of nano-TiO2 as partial substitution for cement has shown higher split tensile strength than all other percentages of replacements for all curing periods. As the partial replacement increasing from 0.5 to 1.0% the split tensile strength is increased and thereafter decreased. The maximum split tensile strengths obtained are 3.225N/mm2 at 3days, 3.288N/mm^2 at 7 days and 3.816N/mm^2 at 1% of nano-TiO_2.

From the Figure 6, it can be observed that period of curing 3 days to 28 days shows increase in flexural tensile strength similarly as in the case of conventional concrete. As the partial replacement increasing from 0.5 to 1.0% the flexural strength is increased and thereafter declined. Also, it can be noticed that nano-TiO_2 as 1% partial substitution for cement has exhibited higher split tensile strength than all other percentages of replacements for all curing periods. The maximum flexural strengths obtained are 4.69 N/mm2 at 3 days, 4.97N/mm^2 at 7 days and 5.46N/mm^2 at 1% of nano-TiO_2.

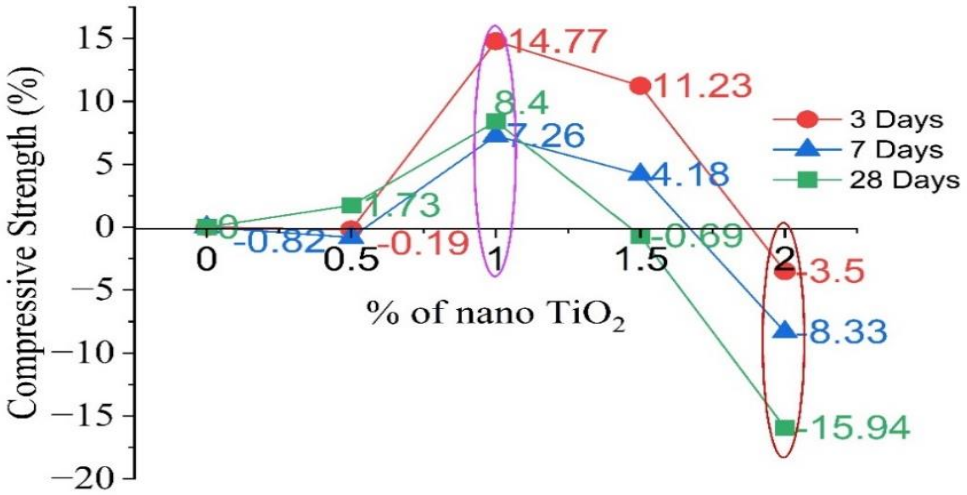

Figure 7: Compressive strength variation with % Nano-TiO_2 for M40 grade concrete

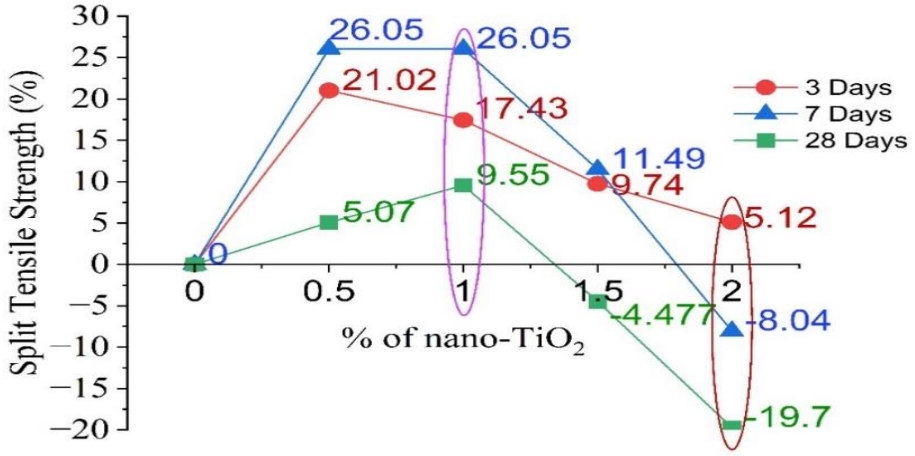

Fig. 8. Split tensile strength variation with % Nano TiO_2 for M40 grade concrete

From the Figure 7 with reference to compressive strength of conventional concrete, the variations with the increase in nano-TiO_2 content can be observed percentage wise. At 1% of nano-TiO_2 in all the curing periods strength obtained are higher comparing with other percentages of replacement, vice-versa at 2% of nano-TiO_2. The strength at 1% are 7.26% 8.4% and 14.77% higher than

concrete of 0% nano-TiO_2.The decline of compressive strength at 2% can be clearly assessed from this chart.

From the Figure 8 with reference to conventional concrete split tensile strength, the variations with the increase in nano-TiO_2 content can be observed. At 0.5% and 1% of nano-TiO_2 in all the curing periods strength obtained are higher comparing with other percentages of replacement, vice-versa at 2% of nano-TiO_2. From this chart the decrease in split tensile strength at 2% can be clearly observed.

From the Figure 9 with reference to conventional concrete flexural strength, the variations with the increase in nano-TiO_2 content can be observed. At 1% of nano-TiO_2 in all the curing periods strength obtained are higher comparing with other percentages of replacement, vice-versa at 2% of nano-TiO_2. From this chart the decrease in flexural strength at 2% can be clearly observed.

From the Figure 10 with reference to compressive strength of conventional M60 grade concrete, the variations with the increase in nano-TiO_2 content can be observed percentage wise. At 1% of nano-TiO_2 in all the curing periods strength obtained are higher comparing with other percentages of replacement, vice-versa at 2% of nano-TiO_2. The strength at 1% are 6.41% 22.77% and 26.02% higher than concrete with 0% nano-TiO_2.The decline of compressive strength at 2% can be clearly assessed from this chart.

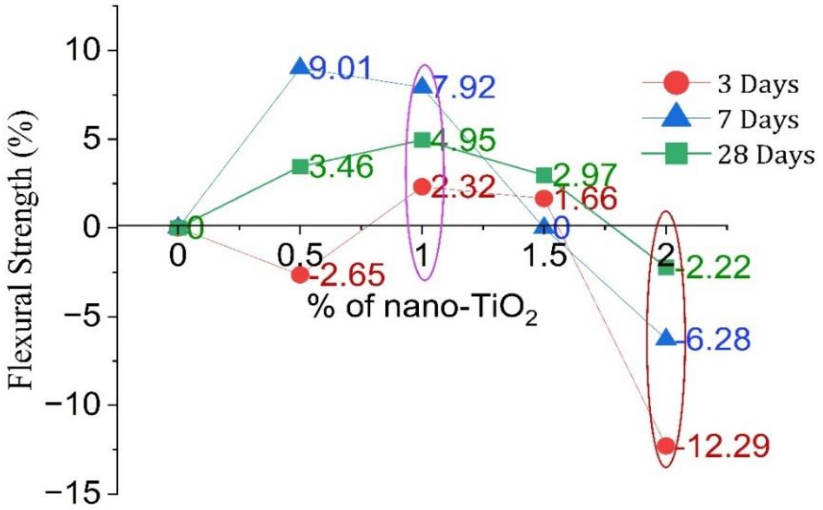

Fig. 9. Flexural strength variation with % Nano-TiO_2 for M40 grade concrete

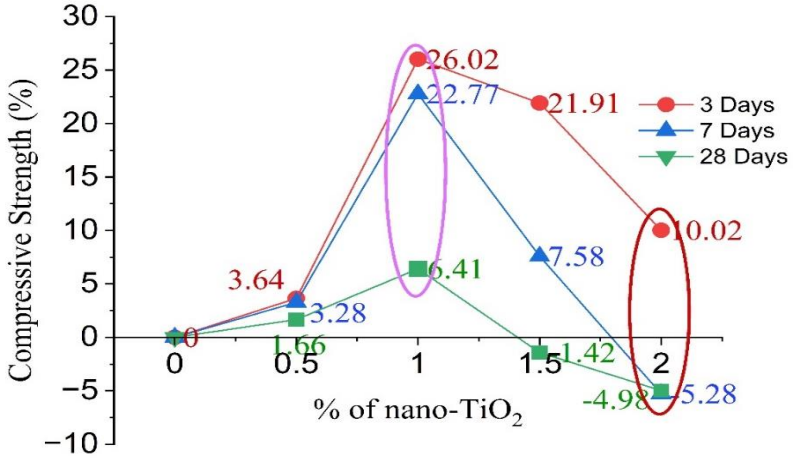

Fig. 10. Compressive strength variation with % Nano-TiO_2 for M60 grade concrete

From the Figure 11 with reference to M60 grade conventional concrete the split tensile strength, variations with the increase in nano-TiO_2 content can be observed. At 1% of nano-TiO_2 in all the curing periods strength obtained are higher comparing with other percentages of replacement, vice-versa at 2% of nano-TiO_2. From this chart the decrease in split tensile strength at 2% can be clearly observed.

From the Figure 12 with reference to M60 grade conventional concrete flexural strength, the variations with the increase in nano-TiO_2 content can be observed. At 1% of nano-TiO_2 in all the curing periods strength obtained are higher comparing with other percentages of replacement, vice-versa at 2% of nano-TiO_2. From this chart the decrease in flexural strength at 2% can be clearly observed.

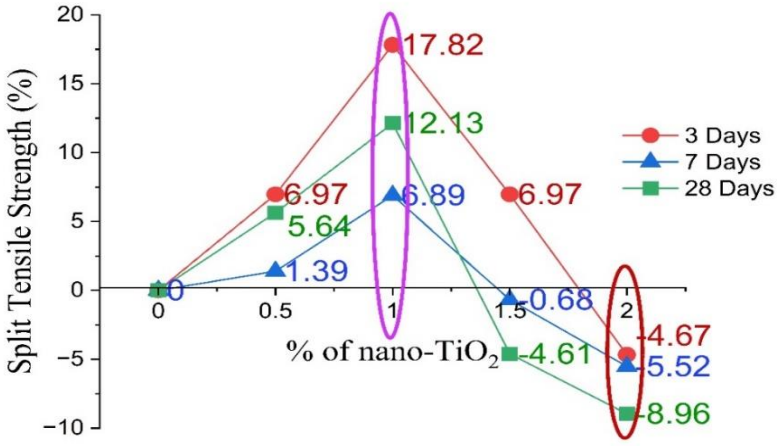

Fig. 11. Split tensile strength variation with % Nano-TiO_2 for M60 grade concrete

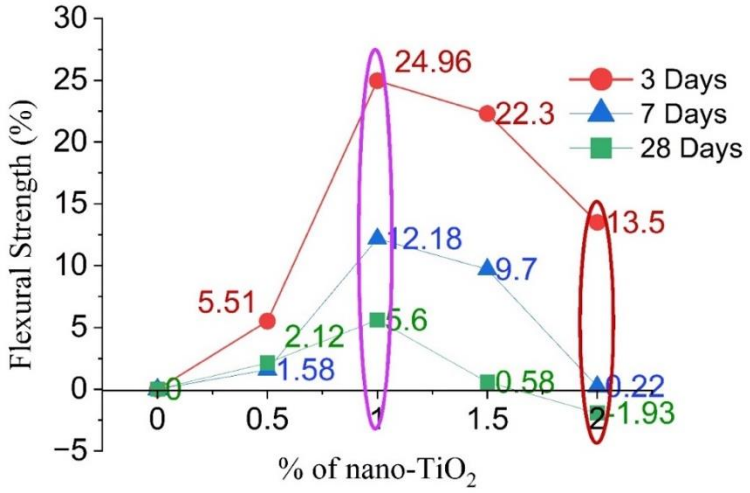

Fig.12. Flexural strength variation with % Nano-TiO_2 for M60 grade concrete

4.3 Micro-Structural Analysis Through SEM and XRD

In general, nanoparticles can provide better void filling and other favorable filler effects due to their extremely small particle size when compared to conventional concrete OPC cementing substances; the filler impacts produce an OPC concrete microstructure with enhanced density and reduced pore size [20]. An SEM test was performed on M40 and M60 grade concrete specimens with different nano-TiO_2 as 0%, 1%, 1.5%, and 2% by dry weight of cement to examine the effect of nano-TiO_2 on the microstructure of specimens.

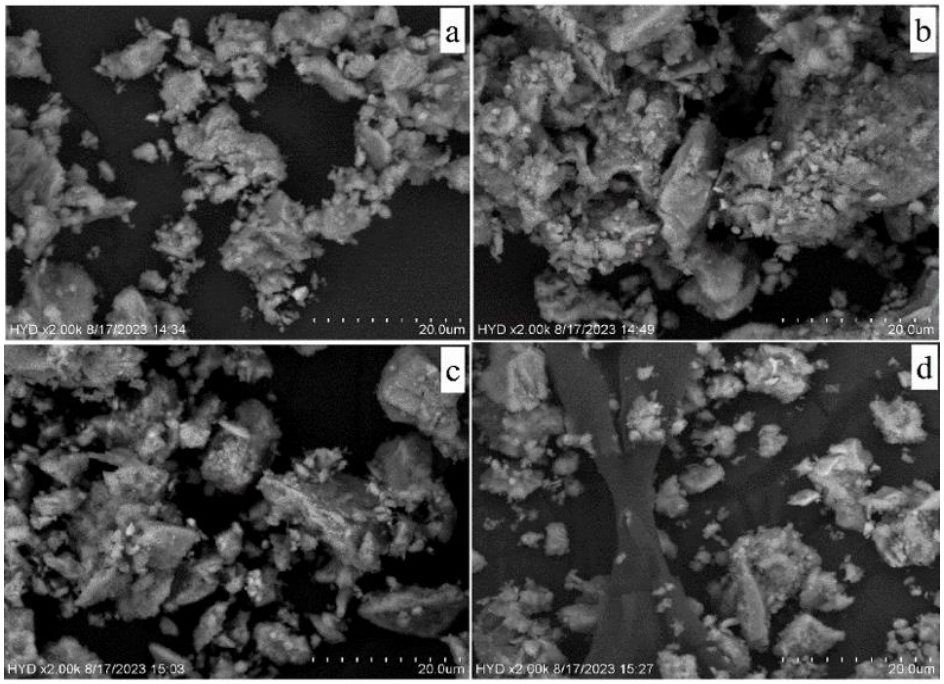

Fig. 13. SEM images of M40 concrete blended with nano-TiO_2

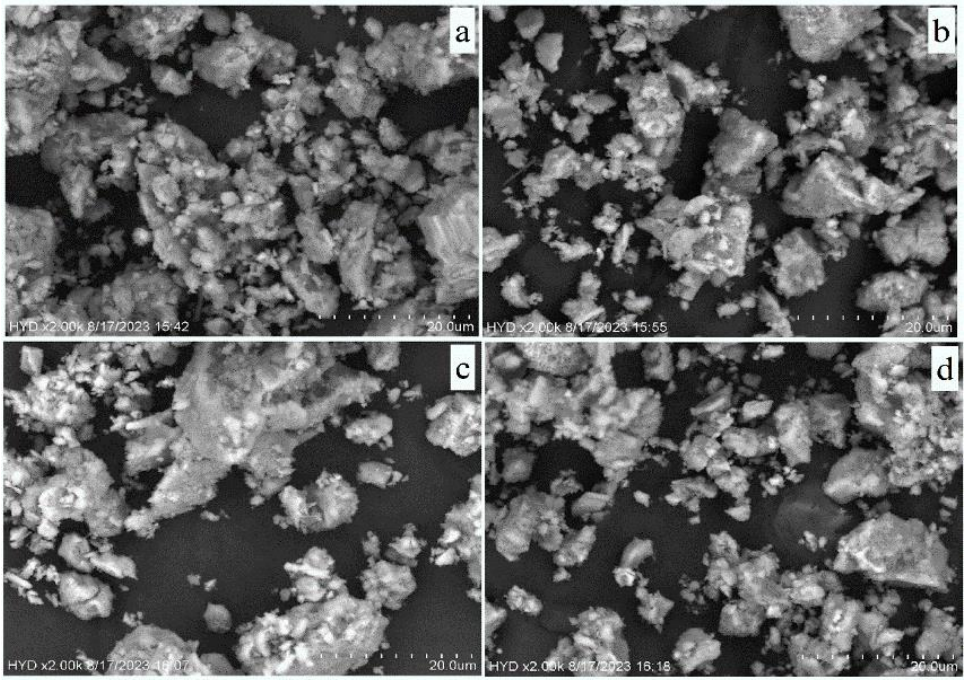

Fig. 14. SEM images of M60 concrete blended with nano-TiO_2

Figures 13 and 14 depict M40 and M60 grade concrete results, respectively. Figure 14 depicts a nano-TiO_2 microstructure with more reacting particles and a denser structure. As a result, employing nano-TiO_2 reduced the size and quantity of unreacted particles. Some researchers found a similar good effect of nanoparticles on lowering voids ratio [20, 25]. Nano-TiO_2 indeed improves the microstructure by enhancing hydration and filling pores, leading to longer longevity strong concrete. The needle-shaped calcium silicate hydrate (C-S-H) that forms contribute to a denser matrix, which not only increases strength but also reduces drying shrinkage. This hydrophilic behavior aids in moisture retention and enhances overall performance. Overall, the incorporation of nano-TiO_2 is a promising way to optimize concrete properties.

Electron beam-induced contamination can significantly hinder nanoparticle measurements, making them either erroneous or completely impossible. The challenges posed by contamination can significantly affect the analysis of particle size and morphology. In scanning electron microscopy (SEM), the secondary electron (SE) images often suffer from contamination obstructing fine details, making particle identification difficult. This is especially problematic if the contamination is unevenly distributed or if it significantly alters the surface characteristics of the particles [26].

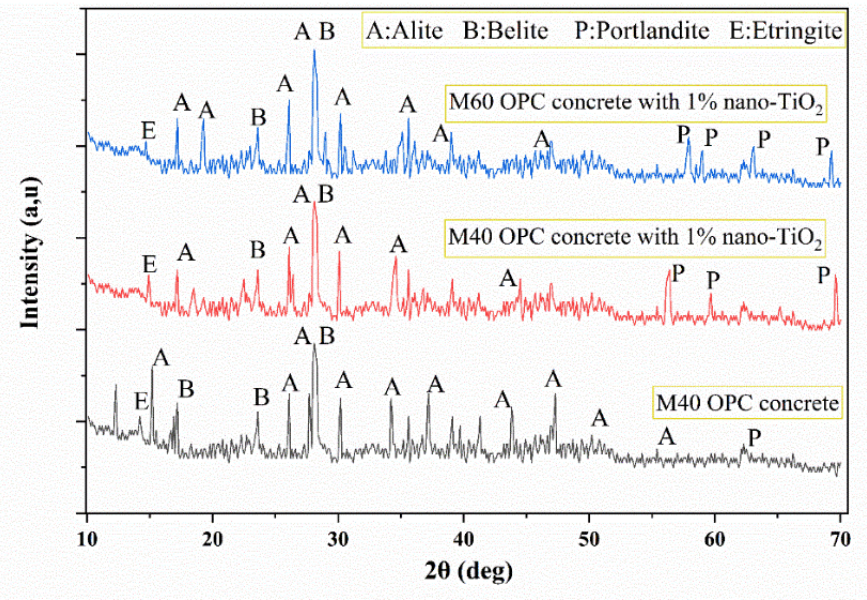

Fig.15. XRD traces of different concrete samples (a) M40 OPC concrete (b) M40 OPC concrete with 1.0% nano-TiO_2 (c) M60 OPC concrete with 1.0% nano-TiO_2

Figure 15 depicts an XRD examination of concrete with nano-TiO_2 after 28 days of curing to evaluate structural evolution. Major specimen phases have been identified as Ettringite, Portlandite, Alite, and Belite. Peak height changes and the creation of additional peaks were observed after 28 days. The intensity of the Alite and Belite phases diminished, and a new peak of portlandite was discovered. With the inclusion of nano-TiO_2, no additional new crystalline form was identified. The results showed that $Ca(OH)_2$ crystals (portlandite), which are required for the production of C-S-H gel, emerge in concrete containing nanoparticles but not in samples without nanoparticles, suggesting the synergistic effect of nanoparticles on the creation of subsequent C-S-H gel.

5. Conclusions

Workability declination in *both* concretes M40 and M60 with the increase in nano TiO_2. Slump and compaction factors values decreased with increase in nano-TiO_2 content *because* of its high specific surface area which increase water demand. Maximum compressive strengths for both M40 and M60 concretes are obtained at 1% nano TiO_2 at rate of 8.40% and 6.41% compared to conventional concrete. Using very fine particles reduces space required for CSH gel development thereby resulted in decrease in compressive strength after 1% nano-TiO_2 content. Similar trend is observed in split tensile and flexural strengths, maximum values are yielded at 1% nano-TiO_2 content with an increase of 9.55% and 12.41% than that of regular concrete for grades of concrete M40 and M60.

In general concrete is treated as brittle material, strong in compression and weak in tension, upon substitution of nano-TiO_2 the test results revealed, that spilt tensile strength of concrete much higher than concrete without nano-TiO_2. SEM images *show* the dispersion as the nano-TiO_2 content increase which resulted decrease in strength beyond 1% nano-TiO_2 content. XRD analysis provides evidence on formation of portlandite and $Ca(OH)_2$ at 1% of Nano-TiO_2 for achieving maximum strengths for both M40 and M60 concrete grades . Based on this experimental work results nano-TiO_2 of 1% can be concluded as preferable content at which maximum strength values are found.

Using concrete with nano-TiO_2 not only improves strength and longevity but also incorporates self-cleaning properties due to its photocatalytic nature. This means that structures can remain cleaner for longer periods, significantly reducing maintenance costs and effort.

In terms of sustainability, these factors contribute to a lower overall environmental impact. A longer-longevity structure needs lesser repairs and replacements, which in turn conserves resources and reduces waste. Additionally, the self-cleaning aspect can help maintain aesthetic qualities without the need for harsh chemicals, further supporting eco-friendly practices. Overall, integrating materials like nano-TiO_2 into concrete is a promising step toward more sustainable construction.

Acknowledgement

The authors acknowledge that this study is supported by Department of Civil Engineering, Andhra University College of Engineering, Visakhapatnam for guiding and Department of Civil Engineering, SRKR Engineering College, Bhimavaram for providing Lab facilities.

References

[1] Bágel L, Zˇivica V. Relationship between pore structure and permeability of hardened cement mortars: on the choice of effective pore structure parameter. Cement and Concrete Research 27.8 (1997): 1225-1235. https://doi.org/10.1016/S0008-8846(97)00111-7

[2] Tanaka, Kyoji, and Kiyofumi Kurumisawa. Development of technique for observing pores in hardened cement paste. Cement and Concrete Research 32.9 (2002): 1435-1441. https://doi.org/10.1016/S0008-8846(02)00806-2

[3] Poon, C. S., Y. L. Wong, and L. Lam. The influence of different curing conditions on the pore structure and related properties of fly-ash cement pastes and mortars. Construction and Building Materials 11.7-8 (1997): 383-393. https://doi.org/10.1016/S0950-0618(97)00061-5

[4] Hui Li, Hui-gang Xiao, Jie Yuan, Jinping Ou, Microstructure of cement mortar with nano-particles. Composites Part B: Engineering 35.2 (2004): 185-189. https://doi.org/10.1016/S1359-8368(03)00052-0

[5] B. Han, L. Zhang, S. Zeng, S. Dong, X. Yu, R. Yang, J. Ou, Nano-core effect in nano-engineered cementitious composites. Composites Part A: Applied Science and Manufacturing 95 (2017) 100-109. https://doi.org/10.1016/j.compositesa.2017.01.008

[6] Zhang, Mao-hua, and Hui Li. Pore structure and chloride permeability of concrete containing nano-particles for pavement. Construction and Building Materials 25.2 (2011): 608-616. https://doi.org/10.1016/j.conbuildmat.2010.07.032

[7] Yuranova, T., Sarria, V., Jardim, W., Rengifo, J., Pulgarin, C., Trabesinger, G., & Kiwi, J. Photocatalytic discoloration of organic compounds on outdoor building cement panels modified by photoactive coatings. Journal of Photochemistry and Photobiology A: Chemistry 188.2-3 (2007): 334-341. https://doi.org/10.1016/j.jphotochem.2006.12.032

[8] Piewnuan, C., Wootthikanokkhan, J., Ngaotrakanwiwat, P., Meeyoo, V., & Chiarakorn, S. Preparation of TiO2/(TiO2-V2O5)/polypyrrole nanocomposites and a study on catalytic activities of the hybrid materials under UV/Visible light and in the dark. Superlattices and Microstructures 75 (2014): 105-117. https://doi.org/10.1016/j.spmi.2014.07.026

[9] Yasmina, M., Mourad, K., Mohammed, S. H., & Khaoula, C. Treatment heterogeneous photocatalysis; factors influencing the photocatalytic degradation by TiO2. Energy Procedia 50 (2014): 559-566. https://doi.org/10.1016/j.egypro.2014.06.068

[10] Ltifi, M., Guefrech, A., Mounanga, P., & Khelidj, A. Experimental study of the effect of addition of nano-silica on the behaviour of cement mortars. Procedia Engineering 10 (2011): 900-905. https://doi.org/10.1016/j.proeng.2011.04.148

[11] Zapata, L. E., Portela, G., Suárez, O. M., & Carrasquillo, O. Rheological performance and compressive strength of superplasticized cementitious mixtures with micro/nano-SiO2 additions. Construction and Building Materials 41 (2013): 708-716. https://doi.org/10.1016/j.conbuildmat.2012.12.025

[12] Mukharjee, B. B., & Barai, S. V. Influence of nano-silica on the properties of recycled aggregate concrete. Construction and Building Materials 55 (2014): 29-37. https://doi.org/10.1016/j.conbuildmat.2014.01.003

[13] Li, H., Zhang, M.H., Ou, J.P., 2006. Abrasion resistance of concrete containing nanoparticles for pavement. Wear 260 (11-12), 1262-1266. https://doi.org/10.1016/j.wear.2005.08.006

[14] Chen, J., Kou, S.C., Poon, C.S. Hydration and properties of nano-TiO2 blended cement composites. Cement and Concrete Composites. 2012 May 1;34(5):642-9. https://doi.org/10.1016/j.cemconcomp.2012.02.009
[15] A.K. Bandyopadhyay. Nano Materials, New age international, New Delhi, India, (2010).
[16] Feng, D., Xie, N., Gong, C., Leng, Z., Xiao, H., Li, H., Shi, X., 2013. Portland cement paste modified by TiO2 nanoparticles: a microstructure perspective. Ind. Eng. Chem. Res. 52 (33), 11575-11582. https://doi.org/10.1021/ie4011595
[17] Peiran Li, Wengui Li, Kejin Wang, Hanbing Zhao, Surendra P. Shah, Hydration and microstructure of cement paste mixed with seawater - An advanced investigation by SEM-EDS method. Construction and Building Materials 392 (2023) 131925. https://doi.org/10.1016/j.conbuildmat.2023.131925
[18] Ren, J., Lai, Y., Gao, J., 2018. Exploring the influence of SiO2 and TiO2 nanoparticles on the mechanical properties of concrete. Constr. Build. Mater. 30 (175), 277-285. https://doi.org/10.1016/j.conbuildmat.2018.04.181
[19] Jalal, M., Fathi, M., Farzad, M., 2013. Effects of fly ash and TiO2 nanoparticles on rheological, mechanical, microstructural and thermal properties of high strength self compacting concrete. Mech. Mater. 15 (61), 11-27. https://doi.org/10.1016/j.mechmat.2013.01.010
[20] Meng, T., Yu, Y., Qian, X., Zhan, S., Qian, K., 2012. Effect of nano-TiO2 on the mechanical properties of cement mortar. Constr. Build. Mater. 1 (29), 241-245. https://doi.org/10.1016/j.conbuildmat.2011.10.047
[21] Sanalkumar, K.U., Yang, E.H., 2021. Self-cleaning performance of nano-TiO2 modified metakaolin-based geopolymers. Cem. Concr. Compos. 1, (115) 103847. https://doi.org/10.1016/j.cemconcomp.2020.103847
[22] Xinyue Wanga, Sufen Dongb, Ashraf Ashourc, Wei Zhanga, Baoguo Hana, Effect and mechanisms of nanomaterials on interface between aggregates and cement mortars. Construction and Building Materials 240 (2020) 117942. https://doi.org/10.1016/j.conbuildmat.2019.117942
[23] Daniyal, M., Akhtar, S., Azam, A., 2019. Effect of nano-TiO2 on the properties of cementitious composites under different exposure environments. J. Mater. Res. Technol. 8 (6), 6158-6172. https://doi.org/10.1016/j.jmrt.2019.10.010
[24] Z. Li, S. Ding, X. Yu, B. Han, J. Ou, Multifunctional cementitious composites modified with nano-titanium dioxide: a review, Composites Part A: Applied Science and Manufacturing 111 (2018):115-137 https://doi.org/10.1016/j.compositesa.2018.05.019
[25] Pathak, S. S., & Vesmawala, G. R. (2022). Effect of nano TiO2 on mechanical properties and microstructure of concrete. Materials Today: Proceedings, 65, 1915-1921. https://doi.org/10.1016/j.matpr.2022.05.161
[26] András E. Vladára, Vasile-Dan Hodoroabab, Characterization of nanoparticles by scanning electron microscopy. Characterization of Nanoparticles Measurement Processes for Nanoparticles Micro and Nano Technologies (2020), Pages 7-27. https://doi.org/10.1016/B978-0-12-814182-3.00002-X
[27] Li, H., Xiao, H.G., Yuan, J., Ou, J., 2004. Microstructure of cement mortar with nanoparticles. Compos. B Eng. 35 (2), 185-189. Li, W., Huang, Z., Zu, T., Shi, C., Duan, W.H., Shah, S.P., 2016. https://doi.org/10.1016/S1359-8368(03)00052-0
[28] Duan, P., Yan, C., Luo, W., Zhou, W., 2016. Effects of adding nano-TiO2 on compressive strength, drying shrinkage, carbonation and microstructure of fluidized bed fly ash based geopolymer paste. Constr. Build. Mater. 1 (106), 115-125. https://doi.org/10.1016/j.conbuildmat.2015.12.095
[29] Chunping, G., Qiannan, W., Jintao, L., Wei, S., 2018. The effect of nano TiO2 on the durability of ultra-high-performance concrete with and without a flexural load. Ceram-Silikáty. 1 (62), 374-381. https://doi.org/10.13168/cs.2018.0033
[30] Joshaghani, A., Balapour, M., Mashhadian, M., Ozbakkaloglu, T., 2020. Effects of nanoTiO2, nano-Al2O3, and nano-Fe2O3 on rheology, mechanical and durability properties of self-consolidating concrete (SCC): An experimental study. Constr. Build. Mater. 10, (245) 118444. https://doi.org/10.1016/j.conbuildmat.2020.118444
[31] Meng, J., Zhong, J., Xiao, H., Ou, J., 2021. Interfacial design of nano-TiO2 modified fly ash-cement based low carbon composites. Constr. Build. Mater. 8, (270) 121470.Moro, C., Francioso, V., Schrager, M., Velay-Lizancos, M., 2020. TiO2 nanoparticles influence on the environmental performance of natural and recycled mortars: A life cycle assessment. Environ. Impact Assess. Rev. 1, (84) 106430. https://doi.org/10.1016/j.eiar.2020.106430
[32]Zhang, R., Cheng, X., Hou, P., Ye, Z., 2015. Influences of nano-TiO2 on the properties of cement-based materials: Hydration and drying shrinkage. Constr. Build. Mater. 15 (81), 35-41. https://doi.org/10.1016/j.conbuildmat.2015.02.003

[33] Ren, Z., Liu, Y., Yuan, L., Luan, C., Wang, J., Cheng, X., Zhou, Z., 2021. Optimizing the content of nano-SiO2, nano-TiO2 and nano-CaCO3 in Portland cement paste by response surface methodology. J. Build. Eng. 1, (35) 102073. https://doi.org/10.1016/j.jobe.2020.102073
[34] Sorathiya, J., Shah, S., Kacha, S.M., 2017. Effect on addition of nano "titanium dioxide"(TiO2) on compressive strength of cementitious concrete. Kalpa Publications in Civil Engineering. 22 (1), 219-225.
[35] M.S. Shetty. Concrete Technology, S.Chand Publishing, New Delhi, 2012.
[36] IS: 12269:1987, Ordinary Portland cement 53-grade-specifications.
[37] IS: 10262-2009, Concrete mix proportioning - Guidelines.
[38] IS: 516-1959; Methods of tests for strength of concrete (eleventh reprint, April 1985) Bureau of Indian standards, New Delhi.
[39] IS: 383-1970: Specifications for coarse and fine aggregates for natural sources of concrete (second revision), Bureau of Indian standards, New Delhi.
[40] D.Harinarayana, CEO of NISHKA Research Pvt, Ltd., Hyderabad. (www.nishkalabs.com)

Blank Page

Research on Engineering Structures & Materials
www.jresm.org
MIM Research Group

Research Article

Exploring welding parameter effects on friction stir weld joints in aluminum 8006 alloy using response surface methodology

Chakrasali Chandrakumar [*,1,a], Irappa Sogalad [2,b], Arun Kumar Shettigar [3,c], Akash Korgal [3,d], Madeva Nagaral [4,e]

[1]*Dept. of Mechanical Eng., Proudhadevaraya Institute of Technology, Hospet, Karnataka, India*
[2]*Dept. of Mechanical Eng., University BDT College of Engineering, Davanagere, Karnataka, India*
[3]*Dept. of Mechanical Eng., National Institute of Technology, Surathkal, Karnataka, India*
[4]*Aircraft Research and Design Centre, Hindustan Aeronautics Limited, Bangalore, Karnataka, India*

Article Info

Article History:

Received 29 Aug 2024

Accepted 18 Nov 2024

Keywords:

Friction stir welding;
Microhardness;
Impact toughness;
Response surface methodology;
Central composite design

Abstract

This study aims to develop mathematical models that can predict the characteristics related to mechanics, such as microhardness and impact resistance, of Aluminum that has been friction stir-welded 8006 alloy joints with 95% confidence. The four process parameters tool tilt angle, welding speed, tool pin shape, and rotating speed were systematically varied across three levels. Following a response surface and central composite design approach that is face-centered, the influence of different factors on the mechanical properties of aluminum 8006 alloy joints was assessed. The highest impact toughness of 58 joules was observed in joints specially prepared by a cylindrical threaded pin profile tool with a 1° tilt angle operating at 800 RPM and a feed rate of 20 mm/min and test was conducted at room temperature. Additionally, it was investigated how process factors affected impact toughness by ANOVA and the results revealed that the tool pin geometry is identified as the most significant process variable on impact toughness, contributing 52.52%, thereafter the tool tilt angles (15.53%), rotating speed (8.80%), and welding speeds (5.84%). The findings showed that, for impact toughness, the tool tilt angle and pin shape were more important than welding speed and tool rotation speed, but the tool pin profile and the welding speed showed governance over rotational speed and angle of tilt in case of hardness. The joints achieved a maximum hardness of 166 VHN at stir zone of the welded specimen made from a threadless taper pin tool for the speed of 1200 rpm, the tool was tilted at 2 degrees while welding at a speed of 40 mm/min. Finally, the effects of process parameters on the microstructure of friction stir welded Aluminum 8006 alloys were addressed and discussed.

© 2025 MIM Research Group. All rights reserved.

1. Introduction

Exploring for lightweight materials, particularly Aluminum 8006 alloy is a promising material because of its unique combination of mechanical properties like, corrosion resistance, and lightweight nature makes an extensive variety of applications such as automotive body panels, food packaging, heat exchangers, electrical conductors, and structural components. FSW is a groundbreaking welding method that was initially developed in 1991 by Wayne Thomas of the United Kingdom's "The Welding Institute" (TWI). It is a method of solid-state welding that connects

*Corresponding author: chakrasali@pdit.ac.in
[a]orcid.org/0009-0004-0618-6915; [b]orcid.org/0000-0002-4475-3579; [c]orcid.org/0000-0003-0273-7746;
[d]orcid.org/0000-0002-6237-3983; [e]orcid.org/0000-0002-8248-7603
DOI: http://dx.doi.org/10.17515/resm2024.424ma0829rs
Res. Eng. Struct. Mat. Vol. 11 Iss. 4 (2025) 1561-1578

several metal parts without melting. Wahid et al. [1] examined the performance of butt joints produced through friction stir welding of AA8011 alloy and identified that welding speed is the utmost important aspect, followed by diameter of shoulder diameter and the tool's rotating speed. Within the stir zone, the microstructure revealed tiny, equiaxed granules that had rapidly recrystallized and it exhibited a better microhardness compared to the original metal. Davidson et al. [2] They investigated how the mechanical characteristics of AA8011 alloy were affected by the friction stir welding process variables. Their findings revealed that the joint achieved a peak tensile strength of 82 MPa when produced with an axial force of 2.15 kN, the welding process employed a tool rotation speed of 1400 RPM and a feed rate of 45 mm/min. Additionally, they observed the presence of finer grains, a defect-free joint, and improved tensile strength and hardness in the stir zone. Raghuraj et al. [3] investigated the highest micro-hardness value and ultimate tensile strength which utilized a tool rotation speed of 1400 RPM, and a feed rate of 25 mm/min, and a dwell time of 7 seconds. They also observed that the rotation of the tool pin transferred material from the advancing side to the retreating side, with temperature variations being more pronounced. The influence was more significant on the retreating side than on the advancing side. Navneet et al. [4] found the highest value of 84.44 MPa tensile strength and 64.95 percent efficiency as that of base metal. Taguchi analysis was employed to optimize the tensile strength testing parameters, which were 1,500 rpm speed, 1° tilt angle, and 50 mm/min feed. The sample with outstanding tensile strength, equiaxed grain's structure, maximum temperature of 389 °C, and reaching its peak on the advancing side, nugget zone, a hardness value of 36.4 HV was found. Palani et al. [5] used a hybrid fuzzy-based response surface methodology was employed to determine the optimal process parameters for friction stir welding. The optimal parameters were found to be a rotating speed of 2050 rpm, a 90° angle of tool tilt, and a transverse speed of 40 mm/min. Additionally, the study revealed that welding speed was the primary factor affecting the toughness of the joints. In contrast, the study revealed that tool tilt angle and welding speed were the most significant contributors to Vickers microhardness. Ito et al. [6] evaluated the Vickers hardness of 7075-O raised while the 7075-T6 joints' Vickers hardness dropped in the stir zone. In contrast to the O joints, whose Vickers hardness increased even more after 5 months of natural age, the T6 joints' stir zones hardened to a point where they were almost as hard as the base material. Gao et al. [7] studied the microstructure and hardness of an aluminum 6082 alloy friction stir welded joint. The distribution of hardness followed a 'W' shape, with a base material hardness value of 103 HV, a heat-affected zone (HAZ) hardness value of 72 HV, and a nugget zone hardness value of 84 HV. The Grain microstructure and particles from the second phase were studied in different parts of the joint by Wan et al. [8]. The top joint region near the ultimate welding nugget zone has the highest microhardness of 89.4 HV. Due to significant plastic deformation, this region is known as the thermomechanical impacted zone. Essa et al. [9] investigated weld joints that showed better quality than the base metal's hardness, indicating that the hardening phase was reprecipitated in the weld zone. Average joint hardness values increased with decreasing rotational speed, and the results revealed that the microhardness profile was greatly impacted by the speed of rotation. The effect of traverse speed on hardness was small. Tariq et al. [10] examined the impact of process variables on the strength of the materials, the grain size and second phase particle size are increased with increasing the tool rotating speed. Density had minimal impact on the hardness of particles in the second phase. Bi-layered aluminum weldments' micro hardness reduced with increasing grain size according to the Hall-Petch equation. Sudhir Kumar et al. [11] explored that the weld joints were of higher quality than the base metal's hardness, which was potentially explained by the reprecipitation of the strengthening phase within the weld zone. The impact of the speed of the weld on hardness was small. Sadashiva et al. [12] explored the impact strength of the composite materials that shows the divergent behavior concerning both weld speed and feed rate during FSW and is caused by the inadequate thermal energy produced during welding at high speeds and feed rates. In general, the strength of the composites shows a substantial 60% improvement compared to the original AA2024 alloy in its cast state. Devaiah et al. [13] identified that the speed of the rotation of the tool has the greatest impact on the strength of welded joints, accounting for 53.02% of the overall effect. The tool tilt angle contributes 36.91%, while the traverse speed only contributes 6.14%. The optimal process conditions were determined to be a rotational speed of 1120 RPM, a feed rate of 70 mm/min, and a tool tilt angle of 20 degrees. Gurmeet et al. [14]

examined the joint strength of friction stir welded aluminum 6082-T6 alloy. Analysis of the tungsten inert gas welding technique showed that the welded joints displayed better mechanical qualities than the welded joints prepared from the TIG approach and included equiaxed granules that are fine. Conversely, large granules were seen in the TIG welded joints. Umasankar et al. [15] observed the generation of temperature is affected by the tool's rotational speed, with faster rotational speed resulting in increased temperature. They observed that 1100 rpm was the optimal rotational speed for achieving maximal impact strength and that friction pressure and contact length affected the weld joint strength. It was also apparent from the scanning electron microscope images that the dimples impacted the ductility quality of the welded components. Akbari et. al [16] discovered that the most important factor influencing the Si particle size, UTS, and force of composites was transverse speed. The Si particle size and B4C particle dispersion quality in the aluminum matrix of the parent material were strongly impacted by FSP variables. Asadi et.al [17] investigated that FSW annealing refines stir zone particle size and lowers microhardness. In fracture, stir zone structural integrity affects absorbed energy. The safe window for defect-free joints increased for each pin shape and rotation speed. Pin profile impacts fracture energy more than hardness and grain size. A neural network found that 309 mm/min traversal speed, 495 rev/min rotational speed, and threaded cylinder pin shape were the best compromise process parameters. Akbari et. al [18] explored input-output relationships using response surface methodology (RSM). The hybrid multi-objective optimization found the ideal probe diameter, shoulder diameter, and probe height of 5.1 mm, 17.63 mm, and 3.86 mm. The investigation found that shoulder diameter, probe diameter, and probe height most affected temperature force and failure load. Ahmadi et. al [19] experimentally conducted that the high rotating speed to welding speed ratios produce coarser and larger grains and validate welded samples' weak or strong performance. Welding speed improves Vickers microhardness and ultimate tensile strength, whereas rotational speed decreases both. The square-pin weld with 80mm/min welding and 1600 RPM rotating speeds had the highest DIC-aided fracture toughness.

Kesharawani Rahul et. al [20] studied the effect of tool design on the quality of friction stir welds (FSW), it has been observed that the use of a threaded cylindrical tool pin in friction stir welding (FSW) achieved a defect-free, uniform mixing of powder particles with the aluminum matrix and high-quality of joints. Optical micrographs, along with EDS analysis, also reveal an oxygen weight percentage of 11.35% in the stir zone (SZ) and the effective incorporation of powder particles, was confirmed in SEM images. Rahul et. al [21, 22] explored the influence of pin profiles on friction stir welded aluminum 6061-T6 alloy with Al_2O_3 particle reinforcement join. The results reported that the threaded pin profiles were enhanced the material mixing and improved the flow in the plasticized state, compared to flat pins, where the plasticized material tends to adhere to the tool pin surface and microstructural shows that the powder particles are more uniformly distributed in the stir zone (SZ) when using threaded pins, whereas agglomeration occurs with flat pins. The EBSD studies indicate that the average grain size in the SZ is finer for threaded pins (3.74 μm) compared to flat pins (5.64 μm). Additionally, the fraction of high-angle grain boundaries is higher for threaded pins, suggesting enhanced material refinement and improved weld quality. Imad et. al [23] was reported the comparison of size of reinforced particles in Al6061-matrix composites. The result shows that the significant microstructural refinement of SiC and Zn particle-reinforced Al-matrix composites, with grain sizes of 4.79 μm and 4.18 μm, respectively and also the composites exhibit improved micro hardness 130 HV for Zn, 112 HV for SiC_P. However, the higher mechanical properties, with UTS values of 224 MPa (SiC) and 236 MPa (Zn), and YS values of 155 MPa (SiC) and 172 MPa (Zn), outperforming the unreinforced AA6061-T6. However, elongation is decreased to 35% compared to 52% for the base alloy. Jha et. al [24] demonstrated the efficiency of the friction stir lap welding (FSLW) technique in creating excellent dissimilar AA6061/AA7075 joints. They found that, the defect-free interfaces were produced under these optimized parameters of 850 RPM rotational speed, and 55 mm/min of feed rate. Microstructural examination result also shows the significant grain refinement and shear textures in the stir region due to continuous dynamic recrystallization (CDRX). In spite of that some thermal softening of material reduced the micro hardness, while the SZ exhibits improved strength, ductility, and strain-hardening properties.

Considering the literature review, it is evident that numerous researchers have employed various statistical and optimization methods to identify the ideal procedure for using friction stir welding to evaluate the connection quality between various aluminum alloys. To date, a limited amount of research has explicitly focused on the friction stir processing (FSP) of the AA8006 aluminum alloy. However, there is a notable absence of systematic investigations into the microstructural and mechanical properties, including hardness and impact toughness, of AA8006 when subjected to FSW. This study hopes to fill this gap by investigating the impact of FSW on AA8006 alloy, offering novel insights into its weldability and performance attributes.

Therefore, the primary objectives of this work are to determine the optimal process parameters such as tool tilt angle, rotating speed, welding speed, and tool pin shape to achieve defect-free, strong weld joint and to establish an empirical relationship for impact toughness by using central composite design of response surface methodology (RSM). Furthermore, the study explored the impact of welding parameters on the hardness and microstructural changes in AA8006 aluminum alloy resulting from friction stir welding.

2. Experimental Procedures

This section provides a detailed explanation of the welding parameters, experimental setup, and research methodology.

2.1. Materials and Selection of Tool

This work uses the stir casting process to fabricate a base plate made of As-cast aluminum 8006 alloy. The chemical composition used to produce aluminum 8006 alloy material is shown in Table 1. After fabrication, an EDM wire electro-discharge machine is used to cut two plates to the required dimensions of 80x60x6 mm. A friction stir welding approach is used to join the plates, using three different tool pin profiles of H13 high-speed steel. The pictorial representation of three tool pin profiles and the detailed dimensions of the tools are shown in Fig. 1

Table 1. Chemical constituent of aluminum 8006 alloy

Elements	Actual Value
Zinc, Zn	0.1%
Magnesium, Mg	0.1%
Manganese, Mn	0.60%
Silicon, Si	0 .30%
Iron, Fe	1.6%
Copper, Cu	0.1%
Aluminium, Al	97.2%

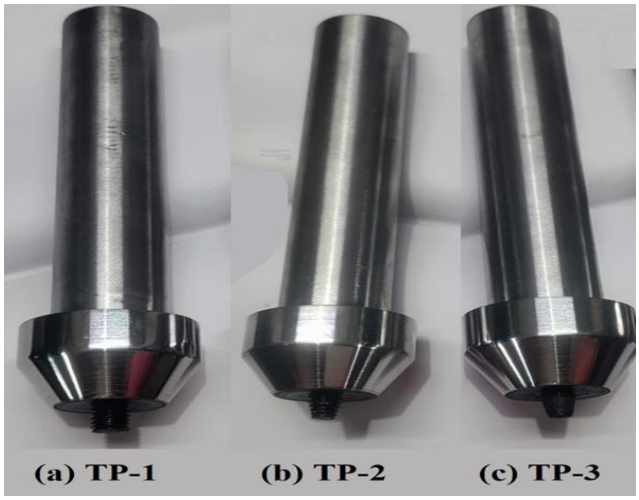

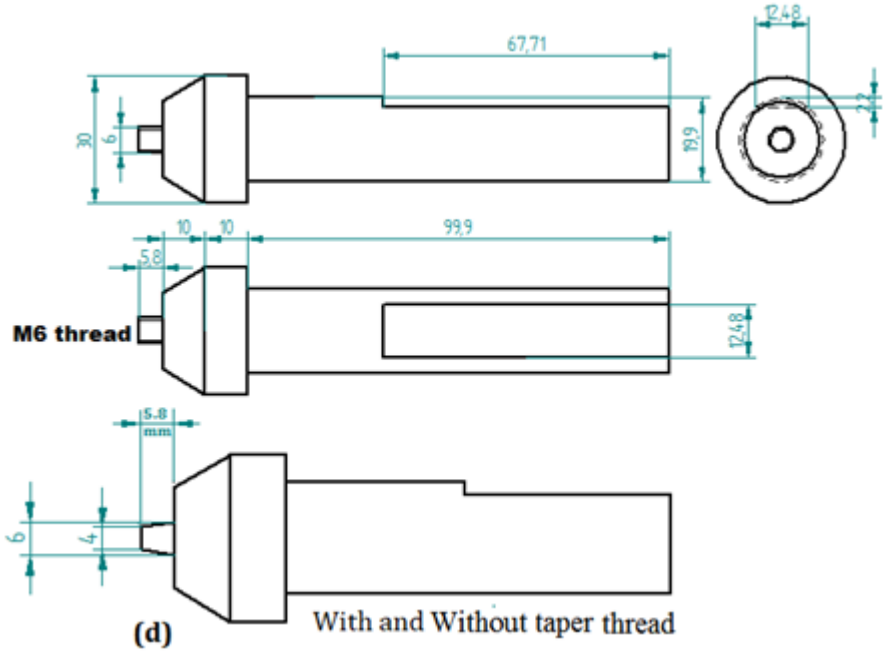

Fig. 1. Tool pin profiles: (a) TP-1: Threaded straight pin tool profile, (b) TP-2: Threaded taper pin tool profile, (c) TP3- Threadless taper pin tool profile, (d) Dimension of Tools

2.2. Selection of Parameters

This research has employed 4 welding parameters: traverse speed, tool speed rotation, tool pin profile, and tool tilt angle. The selection process parameters are crucial because rotational speed controls heat generation, while traverse speed ensures the right balancing of heat input to form uniform microstructure and sound welds. The tool tilt angle helps in material blending and void reduction, whereas the tool pin profile influences material flow and mixing within the weld zone.

Table 2. Selected levels and variables of the process

Parameter	Symbol	Units	Levels		
			-1	0	+1
Traverse Speed	TS	mm/min	20	30	40
Rotational Speed	RS	rpm	800	1000	1200
Tool pin profile	TP	N/A	TP-1	TP-2	TP-3
Tool tilt Angle	TA	º	1°	1.5°	2°

2.3 Friction Stir Welding Technique

A computer-controlled FSW machine was used for the joint fabrication. The cast iron plate is utilized as a backing plate. Every one of the welds is 120 mm long. The workpiece was systematically labeled after every experiment. Before welding the surface of aluminum 8006 alloy plates is cleaned thoroughly to remove contaminants and ensure a pristine welding environment. Then the plates were rigidly fixed in the FSW machine using precise fixtures and clamps to maintain alignment as shown in Fig. 2.

After that, the required process parameters are entered into the computer to control the friction stir welding operation. During the FSW operation, the generation of heat due to friction between the rotating tool and material leads to the metal being in a solid-state condition. The tool then stirs the softened material, creating a seamless bond.

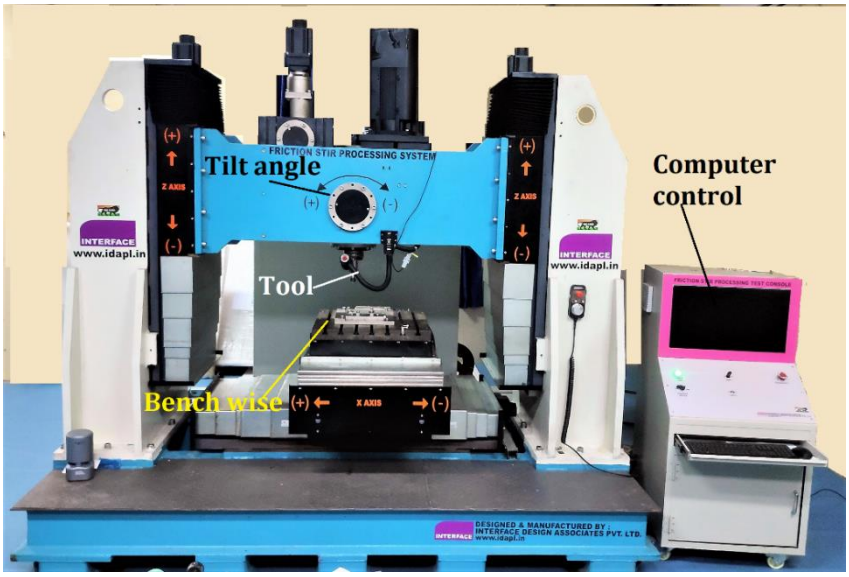

Fig. 2. Computerized friction stir welding machine setup

2.4 Preparation of FSW Specimen

The specimens for Charpy impact toughness and Vickers microhardness were prepared in a direction perpendicular to the weld. According to ASTM E23-04 standard, the impact test specimens were extracted from the welded plate to the required dimensions with the help of wire EDM, and the dimensions of prepared Charpy impact samples were revealed in Fig. 3. The notch measured 10 mm in length, 2 mm in depth, and a 45° angle. Subsequently, the specimens underwent meticulous polishing to eliminate surface flaws and ensure a fine surface finish. The specimen preparation procedure was carefully executed to ensure the precision and consistency of the impact test results.

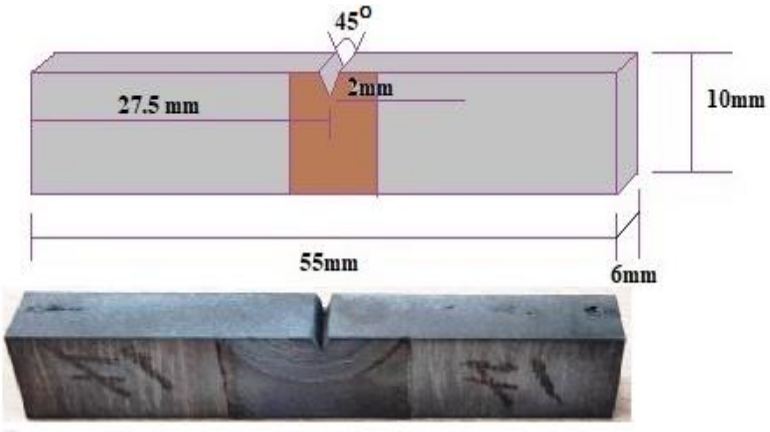

Fig. 3. Specimen dimensions for impact test

3. Statistical Analysis

The statistical analysis of friction stir welded aluminum 8006 alloy involves a systematic study of factors which as traverse rate, tool pin shape, angle of tilt, and rotation speed. ANOVA and regression analysis are used to assess the influence of these parameters on the quality of welding and mechanical characteristics.

Statistical analysis not only evaluates the consistency and reliability of FSW joints but also guides the formulation of predictive models, enabling precise control over the welding process for optimal results. To determine the optimal combination of these factors, an experimental setup is used that combines response surface methodology (RSM) with a face-centered central composite design

(CCD). Table 2 provides a detailed report of the process variables employed in the experiments, with their respective values. The central composite design uses the full factorial method, which includes three distinctive levels for each parameter.

3.1 ANOVA for Charpy Impact Toughness

ANOVA is performed on the Charpy impact strength of friction stir welding of AA8006 alloy using various welding parameters. The ANOVA evaluates the significance of these factors and their contribution to the impact strength of FSW joints. An ANOVA is used to determine the factors that have a statistically significant effect on the toughness of the welded joint by comparing the means of impact strength for various parameter values. This study helps in interpreting the most relevant variables and allows the optimization of friction stir welding (FSW) conditions to achieve enhanced Charpy impact strength in AA8006 alloy. ANOVA results reveal significant findings: the high Model F-value of 62.78 indicates the model's overall significance, confirming its relevance in explaining the impact toughness variations. Additionally, the significant Lack of Fit, indicated by the F-value of 9.08, highlights the importance of the model fit precision, highlighting the need for further adjustment in the areas where the model lacks accuracy.

Table 3. Experimental DOE with output response

Expt. No.	Input parameters				Output response	
	Rotational Speed in (RPM)	Traverse Feed (mm/min)	Angle of Tilt in (Degree)	Tool pin profile	Impact Toughness (Joule)	MHV at Nugget zone
1	800	20	1°	1	58	118
2	1200	20	1°	1	46	125
3	800	40	1°	1	44	121
4	1200	40	1°	1	42	131
5	800	20	2°	1	40	124
6	1200	20	2°	1	36	134
7	800	40	2°	1	34	130
8	1200	40	2°	1	31	142
9	800	20	1°	3	36	137
10	1200	20	1°	3	24	140
11	800	40	1°	3	28	142
12	1200	40	1°	3	18	146
13	800	20	2°	3	25	148
14	1200	20	2°	3	15	150
15	800	40	2°	3	19	152
16	1200	40	2°	3	12	166
17	800	30	1.5°	2	43	141
18	1200	30	1.5°	2	35	149
19	1000	20	1.5°	2	33	137
20	1000	40	1.5°	2	30	140
21	1000	30	1°	2	39	138
22	1000	30	2°	2	32	145
23	1000	30	1.5°	1	47	138
24	1000	30	1.5°	3	32	153
25	1000	30	1.5°	2	40	145
26	1000	30	1.5°	2	39	145
27	1000	30	1.5°	2	40	146
28	1000	30	1.5°	2	41	147
29	1000	30	1.5°	2	40	146
30	1000	30	1.5°	2	39	145
31	1000	30	1.5°	2	39	145

The ANOVA analysis of impact toughness in friction stir welded AA8006 alloy provides insights into the individual contributions of parameters on the toughness of the joint. The coefficient of determination (R^2) at 98.21% specifies that 98.21% of the variability in impact toughness is explained by the chosen parameters, affirming the model's strong fit and reliability. Furthermore, the modified R^2, closely aligning with the projected R^2 at 96.65%, indicates that the model is appropriately constructed without unnecessary variables, ensuring its accuracy.

Statistical analysis not only evaluates the consistency and reliability of FSW joints but also guides the formulation of predictive models, enabling precise control over the welding process for optimal results. To determine the optimal combination of these factors, an experimental setup is used that combines response surface methodology (RSM) with a face-centered central composite design (CCD). Table 2 provides a detailed report of the process variables employed in the experiments, with their respective values. The central composite design uses the full factorial method, which includes three distinctive levels for each parameter. The high accuracy, shown by the proportion of signal to noise over 4 (specifically, 33.594 in this instance), underscores the model's dependability in detecting significant trends amongst the background noise in the data.

Table 4. ANOVA Summary for Impact Strength

Source of Variation	SS	DOF	MS	F (F value)	P (P value)	% of contribution
Model	3037.54	14	216.97	62.78	< 0.0001	
RS	272.22	1	272.22	78.76	< 0.0001	8.80
TS	180.50	1	180.50	52.22	< 0.0001	5.84
TA	480.50	1	480.50	139.02	< 0.0001	15.53
TP	1624.50	1	1624.50	470.02	< 0.0001	52.52
RS*TS	20.25	1	20.25	5.86	0.0278	0.65
RS*TA	12.25	1	12.25	3.54	0.0781	0.34
RS*TP	16.00	1	16.00	4.63	0.0470	0.52
TS*TA	12.25	1	12.25	3.54	0.0781	0.34
TS*TP	4.00	1	4.00	1.16	0.2980	0.13
TA*TP	16.00	1	16.00	4.63	0.0470	0.52
RS*RS	1.73	1	1.73	0.5000	0.4897	0.056
TS*TS	115.94	1	115.94	33.55	< 0.0001	3.75
TA*TA	18.70	1	18.70	5.41	0.0335	0.60
TP*TP	4.49	1	4.49	1.30	0.2709	0.15
Residual	55.30	16	3.46			1.79
Lack of Fit	51.87	10	5.19	9.08	0.0069	significant
Pure Error	3.43	6	0.5714			
Cor Total	3092.84	30				
R^2: 98.21%	Adjusted R^2: 96.65%	Predicted R^2: 90.18%				

3.2 Mathematical Regression Model

A formula in mathematics was created to ascertain the connection between welding speed, rotating speed, tool pin profile, and tool inclination angle. By analyzing experimental data, regression coefficients for a mathematical model featuring second-order polynomials were identified. To quantify the impact toughness of friction, stir-welded aluminum 8006 alloys, regression equation (1) was formulated, which can be expressed as follows:

$$IT = 70.0 - 0.0730\,RS + 2.926\,TS + 7.0\,TA - 12.64\,TP - 0.0672\,TS*TS - 10.87\,TA*TA + 1.28\,TP*TP + 0.1500\,TS*TA + 1.750\,TA*TP \quad (1)$$

Using design expert (version 22.0.8) software, the regression model coefficients for impact toughness were determined with a 95% level of confidence. Impact toughness, or IT, is the dependent variable in the regression formula that quantifies the impact of each process variable.

The RS, TS, TA, and TP variables are the coefficients in this equation, which include linear, square, and interaction terms. The terms with positive coefficient indicate the most significant influence variable on impact toughness whereas the negative coefficient term says that the less influence on impact energy of welded joint. The above equation (1) reveals that the welding speed and angle of tool tilt are the high-impact variables, where the rotational speed and profiles of the tool pin eradicate the material toughness. The square and interaction terms have negligible effect on the impact toughness of the FSWed joint.

4 Results and Discussion

4.1 Categorization of Charpy Impact Toughness of FSWed Plates

The Charpy impact toughness test was conducted to predict how different process factors affect the impact energy of the specimen. The average impact toughness value of the samples of 31 experimental are presented in Table 3. The outcomes show that the FSWed fabricated by a straight threaded pin tool with 800 rpm rotational speed, 20mm/min traverse speed, and 1° the angle of the tool tilt gives a maximum impact strength value of 58 joules because the threaded profile aids in optimal material flow, leading to improved bonding structural integrity with a fine-grained, defect-free microstructure and energy absorption in the weld zone. Nevertheless, the threadless taper pin tool yielded the lowest impact strength measurement of 12 joules when operated at 1200 rpm, 40 mm/min traverse speed, and 2° tilt angle. This is because the threadless taper pin geometry of the tool renders the stirring and mixing processes ineffective and higher rotational speeds result in uneven and coarser microstructure due to excessive heat generation and rapid traverse [25, 26].

The ANOVA results show that the tool pin profile has a significant impact on hardness value compared to other process parameters as represented in Table 4. The percentage of contribution of the tool pin profile has the highest value of 52.52% to the overall effect. The tool tilt angle contributes 15.53% of its total, and the rotating speed and traverse speed provide contributions of just 8.80% and 5.84% respectively of its total contribution.

4.1.1 3-Dimensional Surface Plot for The Impact Toughness

The three-dimensional surface plot (from Stat-ease software) of impact toughness provides a visual representation of the intricate relationship between various parameters in friction stir welded Aluminum 8006 alloy. This plot visually translates complex data into a comprehensible form, enabling a clear understanding of how factors such as rotation speed, traverse rate, and tool profile influence impact toughness. The surface plot provides important insights into maximizing welding conditions for improved impact toughness and overall material performance by visualizing these interconnections.

Fig. 4(a) illustrates the three-dimensional surface plot of impact toughness vs rotational speed and traverse speed. As a result of the findings, the impact energy was found to decrease when the rotational speed and welding feed were elevated. The impact energy peaked at a traverse speed of 30 mm/min and a rotational speed of 800 RPM. During welding, excess heat and rapid cooling occur at the welding portion with maximum speed and feed rate, leading to low bonding strength. The interaction between the tool tilt angle and traverse speed 3-D surface plot with impact strength is shown in Fig. 4(b). The surface plot illustrates a clear trend that the impact toughness decreases as the tool tilt angle and traverse speed increase in friction stir welded AA8006 alloy. An increase in the angle of tilt results in alterations in the welding dynamic forces, impacting the grain structure and the material flow in the welding process. Also, the higher traverse speeds affect reduced heat input, disturbing the metallurgical bonding and resulting in decreased impact toughness. Fig. 4(c) shows the interaction between the tool's rotating speed and angle of tilt against impact toughness. Results reveal that 800rpm speed and 1° angle of tilt give maximum impact strength and for maximum value, both parameters negatively influence the material's ability to absorb impact energy. Fig. 4(d) demonstrates that the tool pin geometry and rotational speed were the primary

factors influencing impact toughness. The surface plot indicates that the highest impact toughness is achieved with the threaded straight pin tool produced with a welded joint, at the minimum speed.

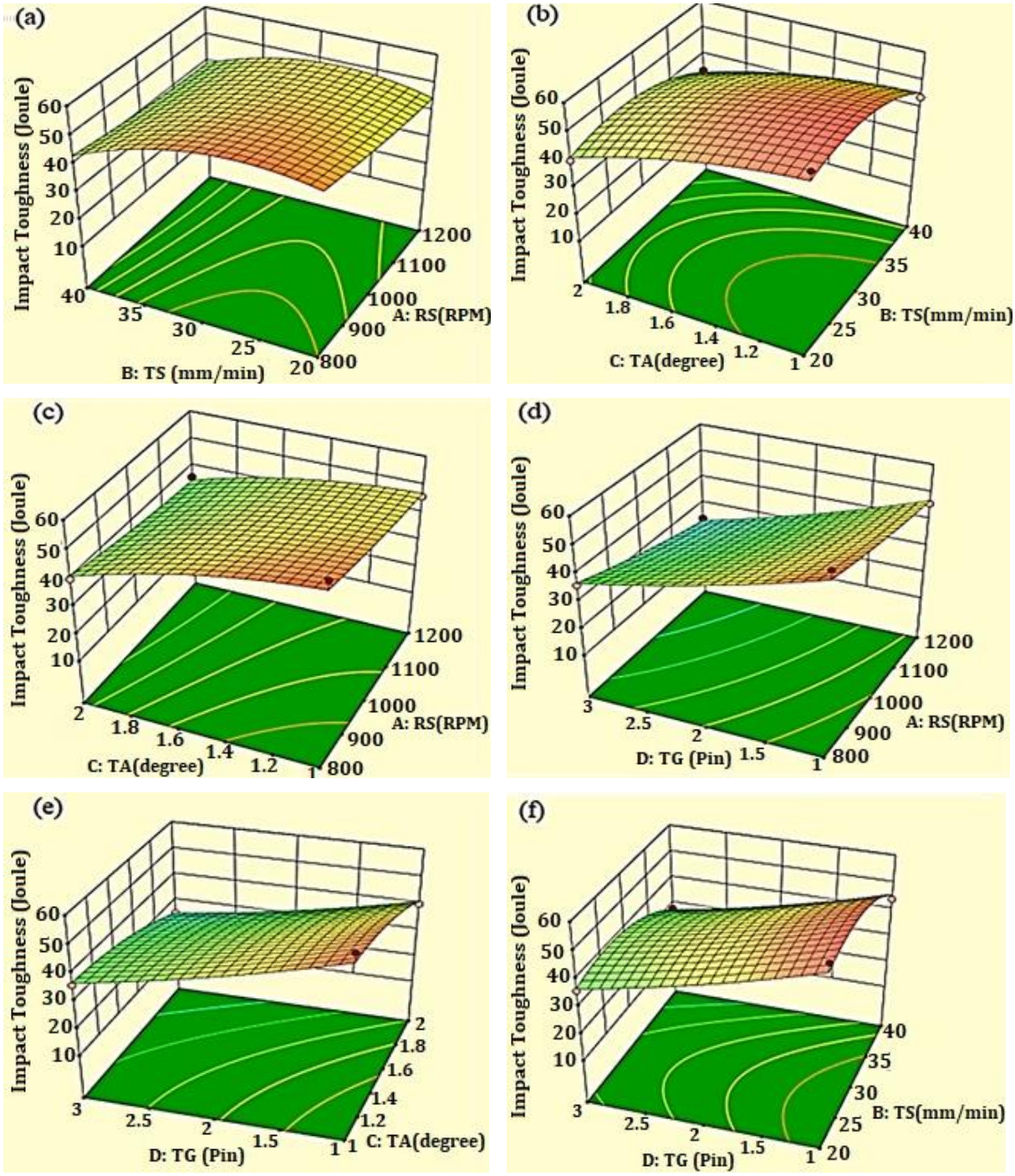

Fig. 4. Three-dimensional Surface plot of IT vs a) Traverse speed and tilt angle, b) rotational speed and speed, c) rotational speed and tool tilt angle, d) tool pin geometry and rotational speed, and e) tool pin geometry and tilt angle

The descending trend on the surface plot also indicates that increasing the rotational speed and weld with TP-2 and TP-3 tools, suggests that specific combinations of these factors compromise the mechanical properties of friction stir welded aluminum 8006 alloy. The impact toughness of the weld decreased with increasing speed in comparison to other tools' distinct pin geometries. Fig. 4(e) illustrates the influence of the tool pin design and tilt angle on toughness. For a tilt angle of 1°, the straight pip tool exhibits maximal impact toughness, which diminishes as the tool tilt angle increases. Fig. 4(f) displays the correlation between tool pin shape and traverse speed on impact energy. The results concluded the impact toughness is higher when the traverse speed increases

gradually up to 30 and with further increases in traverse speed the impact energy decreases. Insufficient heat input is unable to be provided to the weld zone is affected by the increase in welding speed. The straight thread pin will mix up the material properly and form a fine-grain structure.

4.2 Characterization of Vickers Microhardness of FSWed Plates

In the present study, according to ASTM E384, the Vickers microhardness of friction stir welded aluminum 8006 alloys has been conducted. It measures material hardness at a microscopic level to evaluate weld quality, and hardness distribution in the joint and also identifies the influence of process parameters on the materials. The Vickers digital microhardness testing machine was used. This test is based on the principle of measuring the diagonal lengths of an indentation made by a diamond-shaped indent.

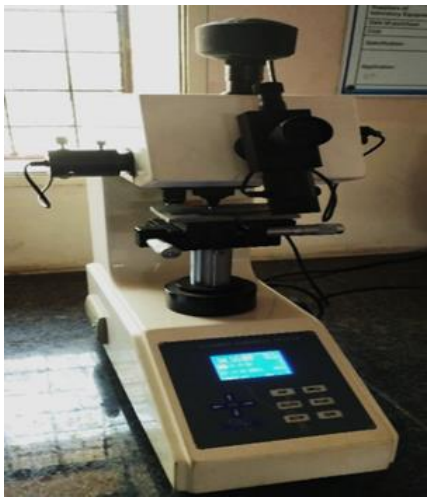

Fig. 5. Vickers Microhardness testing machine

Before the testing, the specimens were polished and finished to get a clear mirror image using a fine 800-grade emery paper and to avoid errors during the experiments. The specimen's microhardness was measured at several locations on plates positioned 2mm apart, ranging from the center of the weld to the margins of the plate. The welding center acted as the stir zone, which refers to the area subjected to heat and mechanical force from the tooltip. This area is often referred to as the zone affected by thermomechanical factors. The zone impacted by heat was located next to the welded region, where it was exposed to heat generated by the FSW process. The extreme area was an unaffected zone that was the utmost edge of the plates. By applying a 500gf load for a specific dwell time of 15 sec at room temperature, the indenter creates an impression on the material surface. The hardness values are recorded from the digital display of the Vickers microhardness testing machine (model: HVS-1000DN) as presented in Fig. 5. The recorded microhardness values are presented in Table 3.

Fig. 6 shows the contour plot (from Origin2023b SR1 student version) of the microhardness profile of 31 friction stir welded AA8006 alloy specimens under several process parameters. The different regions are identified from the welded region. The central part of the welded region as indicated in the red line shown in Fig. 6 is referred to as the Nugget Zone (NZ). In this region, the instant heat is generated by the stirring action of the tool due to which material undergoes plastic deformation. This is the origin distance from which other regions are referenced at equidistance on either side of the welded region. The zone that is impacted by both mechanical and thermal effects but less intense which was present in surrounding the NZ known as the TMAZ, and it is located 2 mm onward on either side of NZ indicated by green lines. The heat-affected zone (HAZ), considered to be at a distance of 4mm from TMAZ, is the region affected by the heating of the base material as shown in blue lines. The next to the remaining portion of the HAZ zone is called the base metal (BM) zone where the material will not experience the heating effect as illustrated in blue color. It indicates from the contour plot that NZ has a high hardness value in all the specimens tested because the metal faces thrust and rotational friction forces from the shoulder, alongside shear

stress and rotational friction from the tool pin. Under plastic deformation, frictional heat, and swirl action, broken grains must undergo dynamic recovery and recrystallization [27].

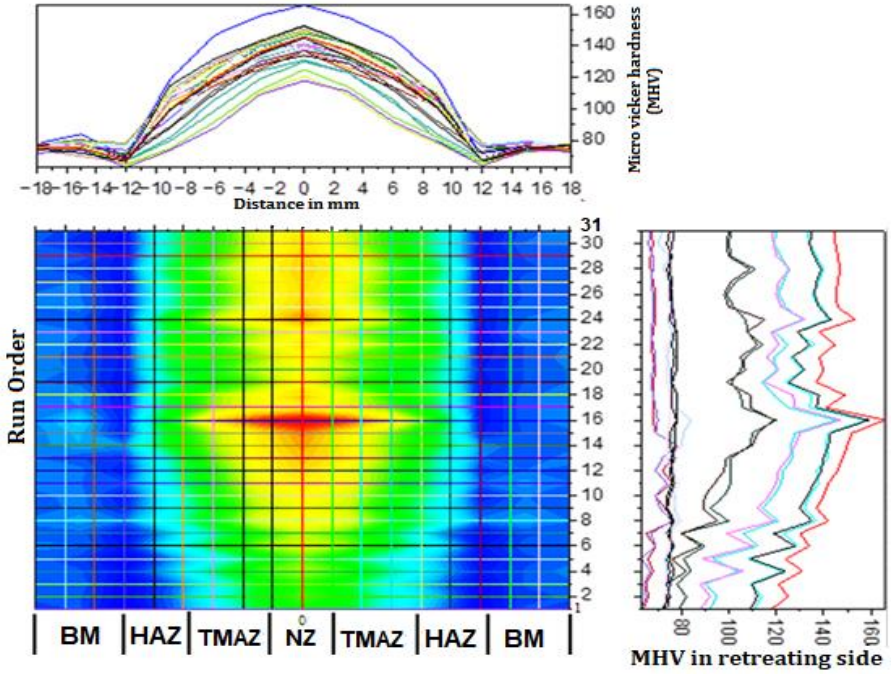

Fig. 6. Contour plot representation of microhardness distribution for 31 test specimens at different regions

In NZ, the increase of recrystallization grains is not of great importance. Thus, it is evident that the NZ microstructure has a homogeneous grain size distribution with small, equiaxed grains that are smaller than those in the base metal (BM) as shown in Fig. 8. The highest hardness value is obtained when the rotating speed of the tool increases as indicated by Fig.7. The run order 16 test specimens had a maximum hardness value of 166 VHN. Regardless of rotational speed, welding speed, tilt angle, and tool profile, all experimental runs consistently showed that the hardness of the nugget zone (NZ) in friction stir welded aluminum 8006 alloys is significantly greater than that of the base metal, as indicated at the top of the contour plot. This occurs because, in the process of friction stir welding, the material undergoes substantial plastic deformation and suffers high strain rates as a result of the stirring action of the revolving tool.

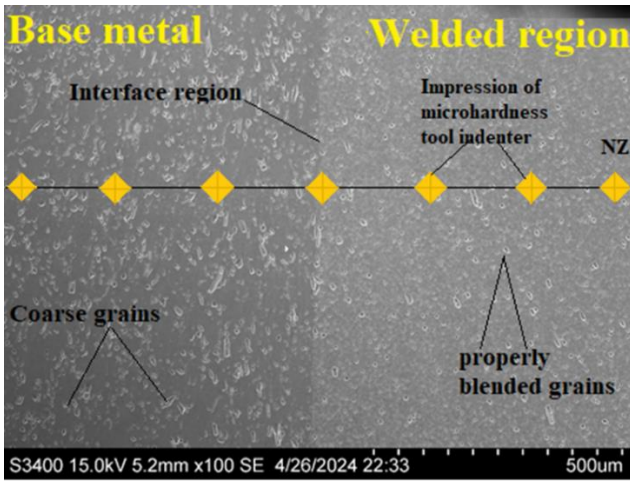

Fig. 7. SEM microstructure of top surface of FSW specimen

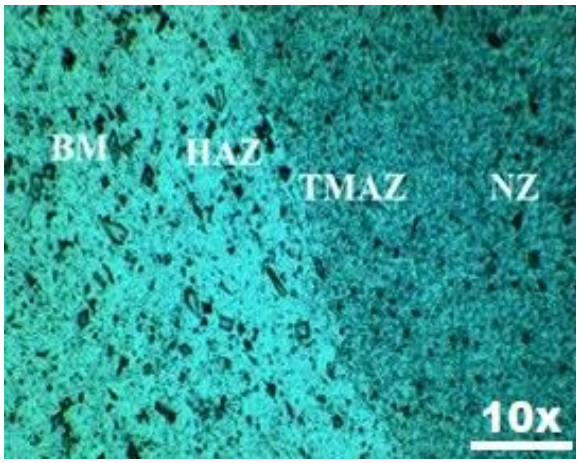

Fig. 8. Microstructure of various zones in FSWed metal

Sl. No	Run order	Process Parameters	Microscopic Image analyzer with Magnification
01	1	1200rpm, 40mm/min,1°, TP-3	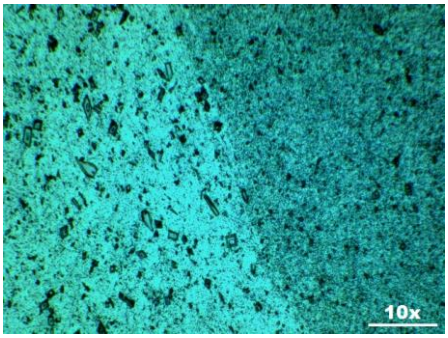
02	5	800rpm, 20mm/min, 2°, TP-1	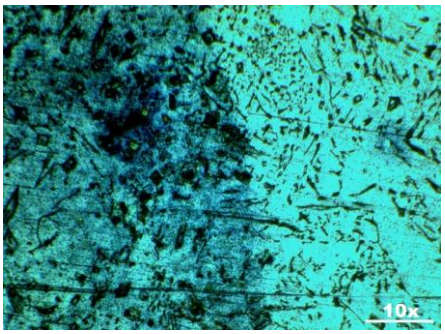
03	9	1200rpm, 40mm/min, 2°, TP-1	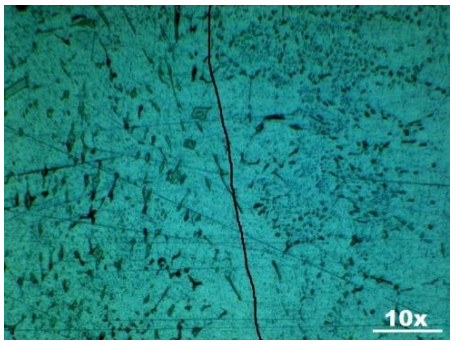
04	15	1000rpm, 30mm/min, 2°, TP-2	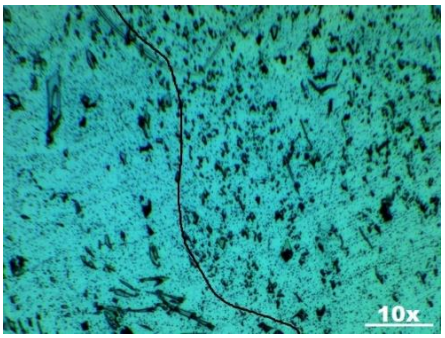
05	25	1200rpm, 40mm/min, 2°, TP-3	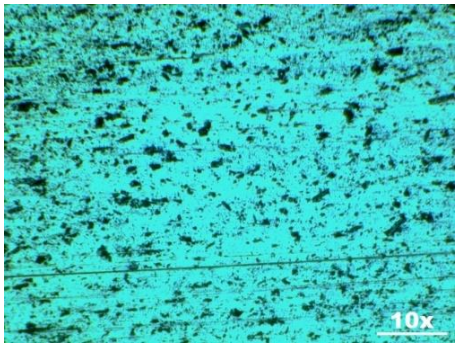

Fig. 9. Image analyzer microstructure of different FS welded specimens

In the metallographic investigation of aluminum 8006 alloys, Keller's Reagent was frequently employed as the etchant. The solution was formulated by combining 5 mL of Nitric Acid (HNO_3), 3 mL of Hydrochloric Acid (HCl), 2.0 mL of Hydrofluoric Acid (HF), and 190 mL of distilled water. The acids were incrementally introduced to the water while maintaining constant agitation to guarantee thorough mixing. The polished aluminum specimen was subsequently etched by immersing it in Keller's Mixture or spreading the solution with a brush for 10 to 30 seconds, contingent upon the desired etch depth. After etching, the sample was washed with distilled water and ethanol to arrest the chemical process and avoid over-etching. Ultimately, it was dried using warm air before microscopic analysis. This technique clarified the edges of grains, and flaws within the microstructure of the aluminum 8006 alloy as shown in Fig. 9.

The material undergoes recrystallization as it passes through the plastic stage. As demonstrated in microstructure Fig. 8, recrystallization causes new, smaller grains to develop in the base metal, replacing the earlier, bigger grains. The nugget zone experiences an increase in hardness because of the presence of these extremely small recrystallized grains. Higher material hardness is produced by the greater grain boundaries that smaller grains usually have, which prevent dislocation movement [28]. TMAZ is the name of the area next to NZ. Because the material flow generated plastic shear stress, the material in the nugget zone deforms plastically; recrystallization does not take place in the TMAZ. Moreover, heat from the stir zone has a minor impact on the substance. For this reason, the grains in this area elongated in the direction of the highest shear stress. The top section's granules are extended downward. The heat-cycle-influenced zone that does not undergo plastic deformation known as the HAZ, is the next section of the TMAZ. The structure is similar to base material because the grains are coarser. when the base metal experiences neither a heat cycle nor mechanical deformation [29].

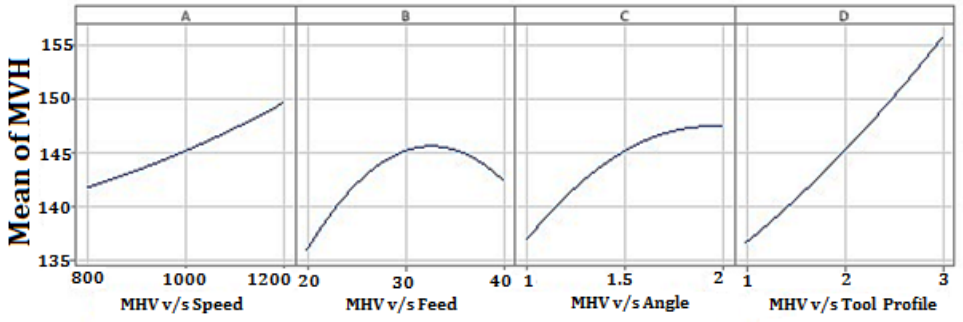

(a) Main effective plot for MHV

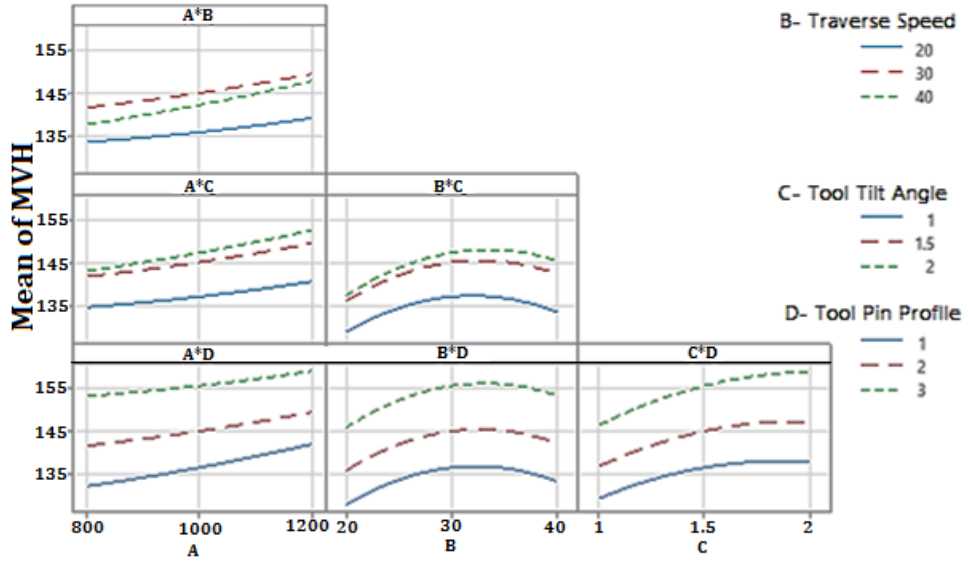

(b) Interaction plot for MHV

Fig. 10. (a)Main effective plot, (b) Interaction plot for MHV

The right side of the contour plot in Fig. 6 also reveals how the hardness values were changed concerning the run order of the experiments towards the retreating side. At the NZ, the threadless taper pin tool in experimental run number 16 has a maximum hardness value and a decreasing hardness value as it shifts from the nugget zone (NZ) toward the base material's boundary. The tool has a 1200 rpm rotating speed, a 40 mm/min traversal speed, and a 2° tilt angle. Similarly, excluding run order 16, all run order values' hardness gradually decreased irrespective of process parameters. Figure 10 shows the main and interaction plots (from the Minitab 21.1.0.0 version) for the microhardness value. A threadless taper pin profile tool's hardness rises in tandem with its traverse speed, rotating speed, and angle of tilt. But behind 30 mm/min traverse speed, the hardness value decreases gradually, as represented in Figure 10(a). The effect of the interaction of process variables on MHV is illustrated in Figure 10(b), which shows that the traverse speed to the angle of tilt has the minimum effect on the material's microhardness as compared with other variables.

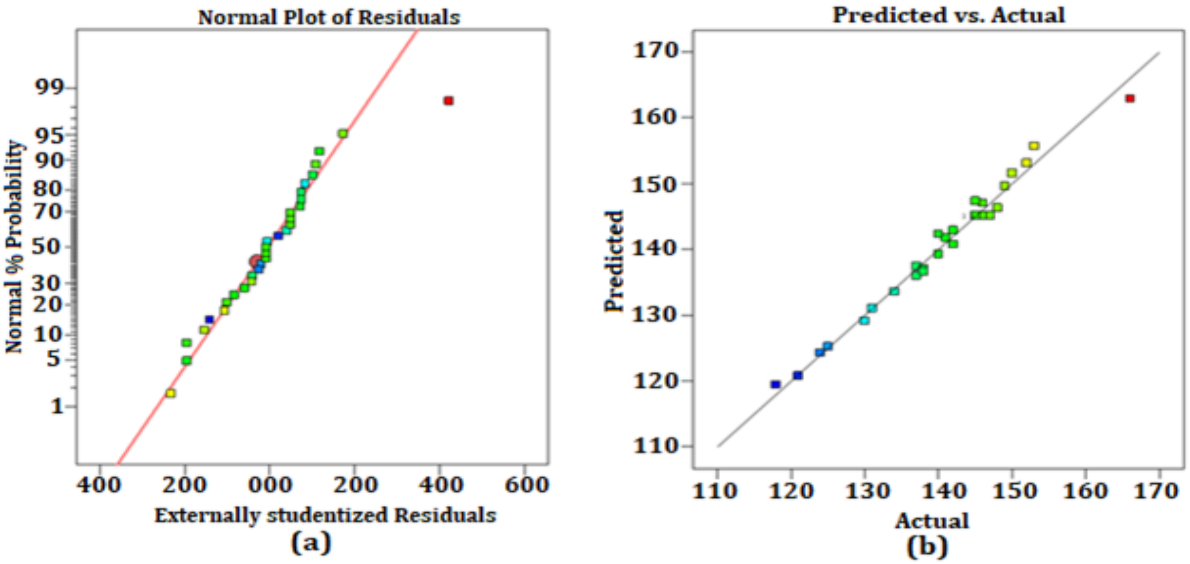

Fig. 11. Response of (a) residual vs normal % probability, (b) Predicted vs Actual

The response plot of normal % probability versus externally studentized residuals is shown in Figure 11(a). The externally standardized residuals' normal probability plot shows that the errors are generally distributed as they align closely with the straight line. The microhardness values, as indicated by Fig. 11(b), illustrate that the projected model has high accuracy since the predicted and actual values fall within extremely small deviations from their respective straight lines.

4.3 Optimization

The Response Surface Methodology's goal is to identify the ideal factor values that maximize response. Table 5 provides a summary of the optimization's outcomes.

Table 5. Optimized process parameters, their levels, and response

Process Parameters	Impact Toughness	Microhardness value
Rotating speed	800 rpm	1200 rpm
welding speed	20 mm/min	40 mm/min
The angle of tilt	1°	3°
Profile of tool pin	Threaded straight-pin tool	Threadless taper pin tool
Output response value	58 Joules	166 MHV

5. Conclusions

The mechanical attributes, like impact toughness and microhardness, were examined utilizing a central composite design and response surface approach after aluminum 8006 alloy was joined using FSW. The mechanical properties of the welded joints were evaluated using empirical equations. The following conclusions were drawn from the study's findings:

- A robust mathematical model for predicting mechanical characteristics, specifically impact toughness in friction stir-welded aluminum 8006 alloys, was established using a central composite design of response surface methodology.
- The mathematical model successfully improved the impact toughness of the material by identifying the best combination of process conditions, including tool pin profile, rotational speed, welding speed, and tool tilt angle.
- The tool pin shape was found to be a major influencing factor on the impact strength of the FS-welded joints. Threaded straight cylindrical threaded pin profile tool demonstrated the highest impact toughness as compared to other tool pin profiles.
- The maximum impact toughness of 58 joules was achieved with a straight cylindrical threaded pin profile tool, a rotation speed of 800 rpm, a welding speed of 20 mm/min, and a tool tilt angle of 1°.
- ANOVA results identified that the profile of the tool pin has the highest significant influence on the impact strength of welded joints, contributing 52.52% to the overall effect. The tool tilt angle accounts for 15.53%, but the rotating speed and traverse speed provide just 8.80% and 5.84% respectively.
- The hardness of the FSW aluminum 8006 alloy joints varies by location. The hardness value reduces as the tool proceeds from the nugget zone to the edge of the base material. However, the highest hardness is observed in the nugget zone, as the weld zone experiences an increase in hardness, which may also lead to increased brittleness. The optimal parameters for these observations were a tilt angle of 2°, a rotational speed of 1200 rpm, and a welding speed of 40 mm/min.
- The hardness development in friction stir welding samples relatively improved Vickers microhardness of 166 VHN as compared to a base material, and other methods at the stir zone for straight cylindrical threaded pin tool.
- The contour plots indicate that microhardness values were the highest value at the stir zone and as it moves towards base metal the microhardness decreases gradually and forms a 'W' shape structure.
- Microstructure from image analyzer represents that higher value process parameters form very fine grain structures as compared to lower-level parameter values.

Acknowledgment

We heartily express our gratitude to the RYMEC, Ballari for their assistance and resources that contributed significantly to the success of this study.

References

1] Wahid MA, Sharma N, Goel P, et al. Friction stir welding of AA 8011: mechanical and microstructure behavior. Trends in Manufacturing Processes: Select Proceedings of ICFTMM 2018, 2020; 129-138. https://doi.org/10.1007/978-981-32-9099-0_14

[2] Davidson BS, Neelakrishnan S. Influence of friction stir welding parameters on tensile properties of AA8011 aluminum alloy plate. Journal of Computational and Theoretical Nanoscience, 2018; 15: 93-98. https://doi.org/10.1166/jctn.2018.7060

[3] Panwar R, Chandna P. An experimental investigation of Al-Li alloy 8090 joint fabricated with friction stir welding (FSW) process by Taguchi-based DOE, for predicting thermal behavior, mechanical and metallurgical characteristics. Ilkogretim Online; 20.

[4] Khanna N, Bharati M, Sharma P, et al. Design-of-experiments application in the friction stir welding of aluminium alloy AA 8011-h14 for structural application. Multidiscipline Modeling in Materials and Structures, 2020; 16: 606-622. https://doi.org/10.1108/MMMS-07-2019-0130

[5] Palani K, Elanchezhian C, Ramnath BV, et al. Hybrid Fuzzy based response surface optimization of welding parameters on Vickers microhardness and impact strength of FSWed AA8011-H24 aluminum alloy joints. Materials Today: Proceedings, 2020; 23: 573-582. https://doi.org/10.1016/j.matpr.2019.05.412

[6] Ito T, Goloborodko A, Motohashi Y, et al. Metallurgical factors affection Vickers hardness of friction stir welded joint of 7075 aluminum alloy. Keikinzoku, 2010; 60: 275-281. https://doi.org/10.2464/jilm.60.275

[7] Gao KY, Li B, Ding YS, et al. Investigations on the Hardness Distribution and Microstructure of Friction-Stir-Welded 6082 Aluminum Alloy. In: Materials Science Forum. Trans Tech Publ, 2020, pp. 116-122. https://doi.org/10.4028/www.scientific.net/MSF.993.116
[8] Wan L, Huang Y, Lv Z, et al. Effect of self-support friction stir welding on microstructure and microhardness of 6082-T6 aluminum alloy joint. Materials & Design 2014; 55: 197-203. https://doi.org/10.1016/j.matdes.2013.09.073
[9] Essa GMF, Zakria HM, Mahmoud TS, et al. Microstructure examination and microhardness of friction stir welded joint of (AA7020-O) after PWHT. HBRC journal, 2018; 14: 22-28. https://doi.org/10.1016/j.hbrcj.2015.05.002
[10] Tariq M, Khan I, Hussain G, et al. Microstructure and micro-hardness analysis of friction stir welded bi-layered laminated aluminum sheets. International Journal of Lightweight Materials and Manufacture, 2019; 2: 123-130. https://doi.org/10.1016/j.ijlmm.2019.04.010
[11] Kumar S, Kumar P. Study the effect of parameters of friction stir welding on the impact strength of aluminium 6063. International Journal of Current Engineering and Technology, 2016; 6: 993-998.
[12] Sadashiva M, Shivanand HK. Characteristic investigation on impact strength of aluminium based hybrid composite plates weld by FSW. International Journal Engineering and Technology, 2018; 7: 120-127. https://doi.org/10.14419/ijet.v7i3.12.15891
[13] Devaiah D, Kishore K, Laxminarayana P. Study the process parametric influence on impact strength of friction stir welding of dissimilar aluminum alloys (aa5083 and aa6061) using Taguchi technique, International Advance Research Journal Science Engineering Technology, 2016; 3: 15303-15310.
[14] Singh G, Kang AS, Singh K, et al. Experimental comparison of friction stir welding process and TIG welding process for 6082-T6 Aluminium alloy. materials today: proceedings, 2017; 4: 3590-3600. https://doi.org/10.1016/j.matpr.2017.02.251
[15] Das U, Toppo V. Effect of tool rotational speed on temperature and impact strength of friction stir welded joint of two dissimilar aluminum alloys. Materials Today: Proceedings, 2018; 5: 6170-6175. https://doi.org/10.1016/j.matpr.2017.12.223
[16] Akbari M, Asadi P, Aliha MRM, Et Al. Modeling and optimization of process parameters of the piston alloy-based composite produced by FSP using response surface methodology. Surface Review and Letters, 2023; 30: 2350041. https://doi.org/10.1142/S0218625X23500415
[17] Asadi P, Aliha Mrm, Akbari M, Et Al. Multivariate optimization of mechanical and microstructural properties of welded joints by FSW method. Engineering Failure Analysis, 2022; 140: 106528. https://doi.org/10.1016/j.engfailanal.2022.106528
[18] Akbari M, Rahimi Asiabaraki H. Modeling and optimization of tool parameters in friction stir lap joining of aluminum using RSM And NSGA II. Welding International, 2023; 37: 21-33. https://doi.org/10.1080/09507116.2022.2164530
[19] Ahmadi M, Pahlavani M, Rahmatabadi D, Et Al. An exhaustive evaluation of fracture toughness, microstructure, and mechanical characteristics of friction stir welded al6061 alloy and parameter model fitting using response surface methodology. Journal of Materials Engineering and Performance, 2022; 1-19. https://doi.org/10.1007/s11665-021-06461-1
[20] Kesharwani R, Jha KK, Anshari MdAA, Imam M, Sarkar C. Comparison of microstructure, texture, and mechanical properties of the SQ and thread pin profile FSW joint of AA6061-T6 with Al2O3 particle reinforcement. Materials Today Communications, 2022 Dec; 33: 104785. https://doi.org/10.1016/j.mtcomm.2022.104785
[21] Kesharwani R, Jha KK, Imam M, Sarkar C, Barsoum I. Comparison of microstructural, texture and mechanical properties of SiC and Zn particle reinforced FSW 6061-T6 aluminium alloy. Journal of Materials Research and Technology, 2023; 26: 3301-21. https://doi.org/10.1016/j.jmrt.2023.08.161
[22] Rahul Kesharwani, Jha KK, Imam M, Sarkar C. Multiphysics computational modelling and experimental analysis of friction stir welding of aluminium alloy metal matrix composites (AAMMCs). Engineering Failure Analysis, 2024; 108893-3. https://doi.org/10.1016/j.engfailanal.2024.108893
[23] Rahul Kesharwani, Kishor Kumar Jha, Imam M, Sarkar C, Barsoum I. Correlation of microstructure, texture, and mechanical properties of friction stir welded Joints of AA7075-T6 plates using a flat tool pin profile. Heliyon, 2024; e25449-9. https://doi.org/10.1016/j.heliyon.2024.e25449
[24] Jha KK, Rahul Kesharwani, Imam M. Investigation on microstructural evolution and local mechanical performance of friction stir lap welded AA6061-T6/ AA7075-T6 joints. Engineering Failure Analysis, 2024; 160: 108258-8. https://doi.org/10.1016/j.engfailanal.2024.108258
[25] Venugopal V, Singh VP, Kuriachen B, et al. Effect of Process Parameters and Tool Pin Profiles on Microstructural Evolution and Mechanical Properties of Friction Stir Welded AA5052. Arabian Journal for Science and Engineering. Epub ahead of print, 2024. DOI: 10.1007/s13369-024-09714-y. https://doi.org/10.1007/s13369-024-09714-y
[26] Sabari SS, Malarvizhi S, Balasubramanian V. The effect of pin profiles on the microstructure and mechanical properties of underwater friction stir welded AA2519-T87 aluminium alloy. International

Journal of Mechanical and Materials Engineering, 2016; 11: 5. https://doi.org/10.1186/s40712-016-0058-y

[27] D'Souza AD, Rao SS, Herbert MA. Evaluation of Microstructure, Hardness and Mechanical Properties of Friction Stir Welded Al-Ce-Si-Mg Aluminium Alloy. Metals and Materials International, 2020; 26: 1394-1403. https://doi.org/10.1007/s12540-019-00372-6

[28] Prabhu S, Shettigar AK, Rao K, et al. Influence of welding process parameters on microstructure and mechanical properties of friction stir welded aluminium matrix composite. Materials Science Forum, 2017; 880: 50-53. https://doi.org/10.4028/www.scientific.net/MSF.880.50

[29] Kumar A, Veeresh Nayak C, Herbert MA, et al. Microstructure and hardness of friction stir welded aluminium-copper matrix-based composite reinforced with 10 wt-% SiCp. Materials Research Innovations, 2014; 18: S6-84. https://doi.org/10.1179/1432891714Z.0000000001016

Research on Engineering Structures & Materials
www.jresm.org

Research Article

Flexural behavior of the reinforced t-beam containing hybrid recycled-aggregate self-compacting concrete

Zhino A. Shawais [1,a], Khamees N. Abdulhaleem [1,b], Hussein Hamada [*,2,c]

[1]*Civil Engineering Department, University of Kirkuk, Kirkuk, Iraq*
[2]*Al-Qalam University College, Kirkuk 36001, Iraq*

Article Info

Article History:

Received 04 Sep 2024
Accepted 06 Oct 2024

Keywords:

Flexural behavior;
T-Beam;
Hybrid concrete;
Recycled aggregate;
Self-compacting concrete

Abstract

Self-compacting concrete (SCC) flows under its weight and resists segregation, distinguishing it from conventional concrete. Recycled concrete aggregate (RCA) offers a sustainable alternative to natural aggregates, reducing resource depletion and enhancing environmental properties. This study experimentally investigates the flexural behavior of nine T-beams composed of hybrid SCC with varying reinforcement ratios (ρ1= 0.45%, ρ2= 1.05%, ρ3= 1.85%) and different RCA proportions (0%, 50%, 100%) in the web zone. At the same time, the flange was cast using only SCC. Four-point load tests were conducted to assess the impact of RCA replacement and reinforcement on the beams' performance. Results indicate that RCA replacement reduces the drop in loading capacity with increased reinforcement, improving both stiffness and bearing capacity. Additionally, higher RCA content shifted the failure mode from flexural to shear, particularly in beams with higher reinforcement ratios, demonstrating RCA use's economic and environmental benefits.

© 2025 MIM Research Group. All rights reserved.

1. Introduction

Self-compacting concrete (SCC) was first developed in Japan in 1988 to enhance concrete performance and increase durability [1]. This type of concrete offers various economic, social, and environmental benefits, including faster construction and reduced noise [2]. SCC is characterized by its ability to flow under its weight, allowing it to fill densely reinforced areas without segregation and without the need for vibrators [3-5]. Xiao [6] noted that incorporating recycled concrete aggregates (RCA) into concrete production presents an innovative solution to the global challenges of depleting natural resources. Sun et al. [7] evaluated the potential of using waste concrete recycling materials (WCRM) in SCC production. They replaced fine and coarse aggregates at varying levels while maintaining a constant water-binder ratio of 0.4. Their findings indicated that WCRM can reduce the strength and workability of SCC. Additionally, Xiao et al. [8] investigated the long-term effects of RCA on strength, shrinkage, and durability. They concluded that the long-term performance of RAC can improve over time.

Currently, there is a global trend towards developing innovative types of concrete to reduce pollution as well as reduce construction costs [9-11]. Therefore, sustainable and recyclable materials should be prioritized across various construction applications. One of the most practical and eco-friendly solutions is to repurpose concrete from the rubble of buildings demolished due to age or natural disasters. This approach provides an alternative to natural aggregates, helping to conserve natural resources commonly used in the construction industry [12]. Additionally, the use of industrial [13] and agricultural waste [14] further contributes to reducing resource depletion.

*Corresponding author: enghu76@gmail.com
[a]orcid.org/0009-0002-2178-6930; [b]orcid.org/0000-0001-9049-227X, [c]orcid.org/0000-0001-9911-8639
DOI: http://dx.doi.org/10.17515/resm2024.428me0904rs

To produce economical and environmentally friendly concrete that meets specifications, materials with specific properties tailored to their position within the structural member can be used [4, 15, 16]. To enhance the efficiency of concrete, including reducing its weight and production cost, hybrid concrete (HC) can be utilized [17]. In structural members subjected to flexural loading, two behavior zones exist: one under tension and one under compression. Since reinforcing steel strengthens the tension zone, hybrid concrete containing recycled aggregate can be effectively employed in this region [18]. T-beams, commonly used in bridge decks and to support concrete slabs on simple walls, are ideal for large spans, making them suitable for industrial and commercial structures. They are also frequently used as precast members. One key advantage of T-beams is their large compression area, which increases the load-bearing capacity of the structural member [19].

Fahmy and Idriss [20] examined the flexural behavior of reinforced concrete T-beams made from hybrid concrete, incorporating recycled aggregate concrete (RAC) with both normal and high-strength concrete. Their results indicated that using RAC as a filler in the core of T-beam webs is a promising construction technique. It can effectively predict the development, propagation, and width of shear and flexural cracks. Hason et al. [17] evaluated the flexural ductility indices of T-beams made from natural aggregate (NA) and recycled aggregate (RA). They found that replacing NA with RA slightly reduced the flexural capacity and led to a decrease in the ductility indices of RA T-beams compared to reference beams.

Ali and Malik [21] conducted both experimental and theoretical investigations into the flexural and shear behavior of reinforced concrete T-beams made with hybrid concrete. Their findings highlighted the significant impact of using steel fibers in the web concrete and high-strength concrete in the flange, which resulted in increased maximum load and first cracking load. Fang et al. [22] studied the shear behavior of hybrid T-beams composed of lightweight and normal-weight concrete. They developed an equation to predict the interfacial shear transfer strength of these hybrid T-beams. Marzoq and Borhan [23] investigated the structural response of hybrid reinforced concrete T-beams made from reactive powder concrete (RPC) and normal concrete (NC) under bending moments. Testing four beams with different concrete types for the flange and web, they concluded that the type of concrete significantly influences T-beam behavior. You et al. [18] conducted an experimental study on self-compacting, simply supported hybrid fiber-reinforced concrete T-beams under four-point loading. Their results showed that hybrid fibers significantly enhanced the ultimate load and altered the failure mode.

Khattar and Khadir [19] studied the flexural behavior of T-beams cast from self-compacting concrete (SCC) with recycled coarse aggregate (RCA) partially replacing natural coarse aggregate at ratios of 0%, 50%, and 75%. They found that increasing the RCA replacement to 50% reduced the first cracking load by 15.5%, without affecting the ultimate load. At a 75% RCA replacement, both the first cracking load and ultimate load decreased by 31% and 10%, respectively, while deflection and crack width increased. Doubling the main reinforcement ratio led to a 20% increase in the first cracking load and a 46% increase in the ultimate load, with corresponding decreases in deflection and crack width.

Given the limited research on the structural behavior of hybrid concrete T-beams incorporating self-compacting concrete (SCC), this study focuses on the flexural performance of such beams made with SCC using either natural coarse aggregate (NCA) or recycled coarse aggregate (RCA). The coarse aggregate in the web zone was replaced by 0%, 50%, and 100%, resulting in three groups of T-beams. Each group was further tested with three different main reinforcement diameters (8mm, 12mm, 16mm) to assess their impact on the beams' flexural behavior. This research aims to deepen the understanding of reinforced concrete with RCA and serves as a valuable reference for both future studies and practical engineering applications involving RAC.

2. Experimental Program

This study presents the details of the experimental program, including a brief description of the material properties and quantities used in the concrete mixtures. It also outlines the specimens utilized to investigate the flexural behavior of reinforced concrete T-beams. The production

method of self-compacting concrete (SCC) and the tests conducted on both its fresh and hardened states are briefly reviewed. Additionally, the testing procedures for the T-beams and the mechanisms used to evaluate their behavior are thoroughly explained.

Three different concrete mixtures were prepared, each with varying proportions of recycled coarse aggregate (0%, 50%, and 100%) replacing natural coarse aggregate (NCA). For each mixture, three concrete beams were cast with main reinforcement steel of varying diameters (8mm, 12mm, and 16mm) in the tension zone. The three mixtures were used for casting the web zone, while the mixture containing only NCA was applied to the flange zone of the concrete T-beams.

2.1. Materials Description

2.1.1 Cement

Ordinary Portland cement was used in this study, with a fineness modulus of 295 m2/kg and a specific gravity of 3.15 which is locally manufactured and complies with the approved standards and specifications [24].

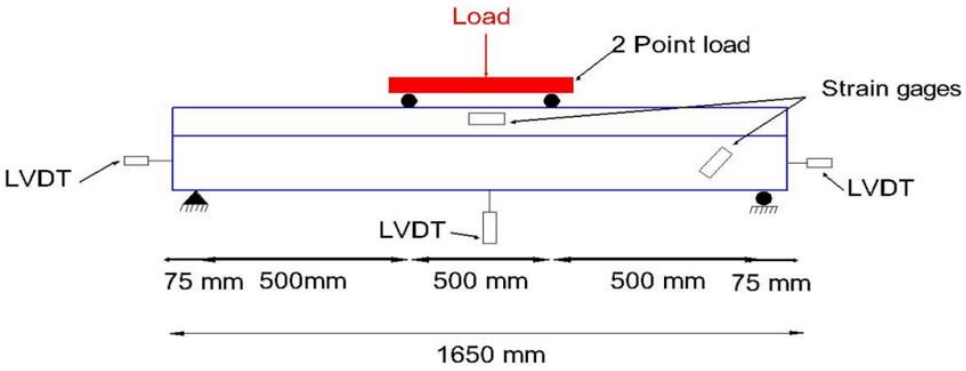

Fig. 1. Illustration of the dimensions and details of the T-beam specimens

2.1.2 Fly Ash

About 7% of the world's carbon dioxide emissions come from the production process of ordinary Portland cement (OPC) [25], so fly ash (class F) with a specific gravity of 2.2 was used as a binder and filler to reduce the amount of cement used and produce SCC that complies with the specifications.

2.1.3 Silica Fume

Since silica fume contains a high percentage of silicate oxide, it is added to concrete to increase its compressive strength through its reaction with calcium hydroxide. The chemical components and their proportions for cement, fly ash, and silica fume are listed in Table 1.

Table 1. The chemical components of the cement, fly ash, and silica fume

Oxide (%)	Cement	Fly ash	Silica fume
CaO	62.6	5.11	0.4
Al_2O_3	5.03	20.73	0.7
SiO_2	20.77	55.67	93.2
MgO	2.3	2.65	0.1
Fe_2O_3	3.1	12.96	1.5
K_2O +Na_2O	1.08	2.54	1.4
SO_3	2.16	0.34	0.1
Specific gravity	3.15	2.2	2.1

2.1.4 Fine and Normal Coarse Aggregates

The fine and natural coarse aggregates (NCA) used in the study were locally sourced, river-rounded aggregates that conformed to the specifications outlined in [26]. The fineness modulus of the fine aggregate was 2.34, with a maximum coarse aggregate size of 16 mm. The water absorption rates for the fine and coarse aggregates were 2.1% and 0.57%, respectively, while their specific gravities were 2.58 and 2.65. Detailed sieve analyses for both fine and coarse aggregates are presented in Tables 2 and 3, respectively.

2.1.5 Recycled Coarse Aggregate (RCA)

The main objective of the present study is to replace the NCA with RCA. The source of the RCA is the rubble of the concrete roof of a demolished house whose age is more than 25 years. The concrete blocks were brought to the laboratory and crushed, after which sieve, analysis was conducted to obtain aggregates with acceptable gradation. To ensure obtaining RCA with gradation identical to the NCA, the recycled aggregate of each size was stored in special bags. Then, the aggregates were used in the required weights according to the gradation ratio as inserted in Table (3). The specific gravity of the RCA was 2.45, while its water absorption rate was 5.7%. The physical properties of RCA as shown in Table 4.

Table 2. Sieve analysis of fine aggregate

Sieve No.	Passing%	ASTM Standard Limits [26].
3/8 in (9.5 mm)	100	100
No.4 (4.75mm)	98	90-100
No.8 (2.36mm)	92	75-100
No.16 (1.18mm)	81	55-90
No.30 (0.6mm)	58	35-59
No.50 (0.3mm)	26	8-30
No.100 (0.15mm)	7	0-10
Sieve No.	Passing %	ASTM Standard Limits [26].

Table 3. Sieve analysis of NCA and RCA

Sieve Size (mm)	Percentage of Passing		ASTM Standard Limits [26]
	NCA	RCA	
20	100	100	100
14	94	94	90 -100
10	62	62	50 - 85
5	0	0	0 - 10

Table 4. Physical properties of RCA

Dry Specific gravity	2.27
SSD Specific gravity	2.4
Apparent Specific gravity	2.45
Loose bulk density	1481 kg/m3
Rodded bulk density	1594 kg/m3
Water absorption	5.7 %

2.1.6 Super-Plasticizer

To ensure that SCC according to the specifications, a superplasticizer (SP) was added to the concrete mixtures at a rate of 1.5 % to improve its flowability and fluidity. Viscocrete GS-180, which was produced by Sika for additives, was used. This superplasticizer helps to reduce the amount of water in the mixture and increase its viscosity.

2.1.7 Steel Reinforcement

To study the effect of changing the area of reinforcement on the behavior of concrete T-beams, three different diameters of steel were used for the main reinforcement (longitudinal direction) in the tension zone. Reinforcement bars with diameters (8mm, 12mm, and 16mm) were used, with reinforcement ratios (0.45%, 1.05%, and 1.85%), respectively. On the other hand, reinforcement bars with a diameter (8 mm) were used for the shear reinforcement (stirrups) of all concrete beams to resist the shear stresses. The physical properties of the reinforcing bars used in the present study are listed in Table 5.

Table 5. Physical properties of the steel reinforcing bar

Bar diameter (mm)	Yield strength Fy (MPa)	Ultimate stress Fu (MPa)
8	388	552
12	544	645
16	568	652

2.2 Mixing Proportions

The design of SCC mixes is different from that of conventional concrete. Trial and error are used to determine the proportions of concrete mix materials using EFNARC limitations [27]. Three basic criteria must be satisfied to produce an SCC that meets the specifications: including the ability to flow without vibrating and its resistance to segregation. Consequently, the fresh properties of concrete used in the present study are determined through basic tests, including slump flow test, V-funnel test, and L-box test. These tests are subject to EFNARC specifications and guidelines [27]. According to these tests, the proportions of materials for concrete mixes were determined. The NCA was replaced by RCA in three proportions (0%, 50%, and 100%). The water-to-binder ratio (w/b) and superplasticizer content for all concrete mixtures were 0.4 and 1.5%, respectively. We maintained a consistent water-cement ratio for all concrete mixtures. When adjusting the RCA content from 0% to 50% and then to 100%, was added extra water based on the RCA's absorption rate to preserve the water-binder ratio across the three mixtures. This additional water ensures the RCA reaches a saturated surface-dry (SSD) condition without affecting the absorption rate of the SCC mix. The quantities of materials used in the concrete mixes for the present study are listed in Table 6.

Table 6. The concrete design mixes used in the present study

Materials	Mix Code		
	SCC-RC00	SCC-RC50	SCC-RC100
Cement (kg/m^3)	370	370	370
Fly Ash (kg/m^3)	80	80	80
Silica Fume (kg/m^3)	50	50	50
Water (l/m^3)	200	200	200
Water/Cement (w/c)	0.54	0.54	0.54
Water/Binder (w/b)	0.4	0.4	0.4
Superplasticizer (%)	1.5	1.5	1.5
Fine Aggregate (kg/m^3)	800	800	800
NCA (kg/m^3)	850	425	0
RCA (kg/m^3)	0	393	786

2.3 T-Beam Designation

The T-beam specimens were designed with appropriate dimensions to simulate real structural members, providing an accurate representation of their behavior under applied loads. In the laboratory, the T-beams measured 1650 mm in total length and 250 mm in total depth. The flange was 60 mm thick and 200 mm wide. The web of the T-beam was 100 mm wide with a clear height of 190 mm, as illustrated in Figure 1. Flexural behavior was analyzed by applying two-point loads

after dividing the clear span into three equal parts, ensuring a shear-to-span ratio of 2. The clear span between supports was 1500 mm for each specimen. After manufacturing the molds with the specified dimensions, they were painted before pouring the concrete to ensure easy demolding and smooth specimen surfaces. The main reinforcement bars and shear reinforcement were prepared according to the specified dimensions for each specimen. Additionally, the concrete mix components were weighed and prepared with precision, following the quantity schedule, before the pouring process. A concrete cover of 15 mm was maintained from all directions for all T-beams.

2.4 Specimen Preparation

To investigate the flexural behavior of T-beam specimens, the experimental program involves preparing and casting nine distinct T-beam specimens made from hybrid self-compacting concrete (SCC). The study examines the impact of varying the main reinforcement area on flexural behavior by using three different diameters for the tension zone: 8 mm, 12 mm, and 16 mm, represented as 2Ø8, 2Ø12, and 2Ø16, respectively. For each reinforcement type, three concrete mixtures were utilized: SCC-RC00, SCC-RC50, and SCC-RC100.

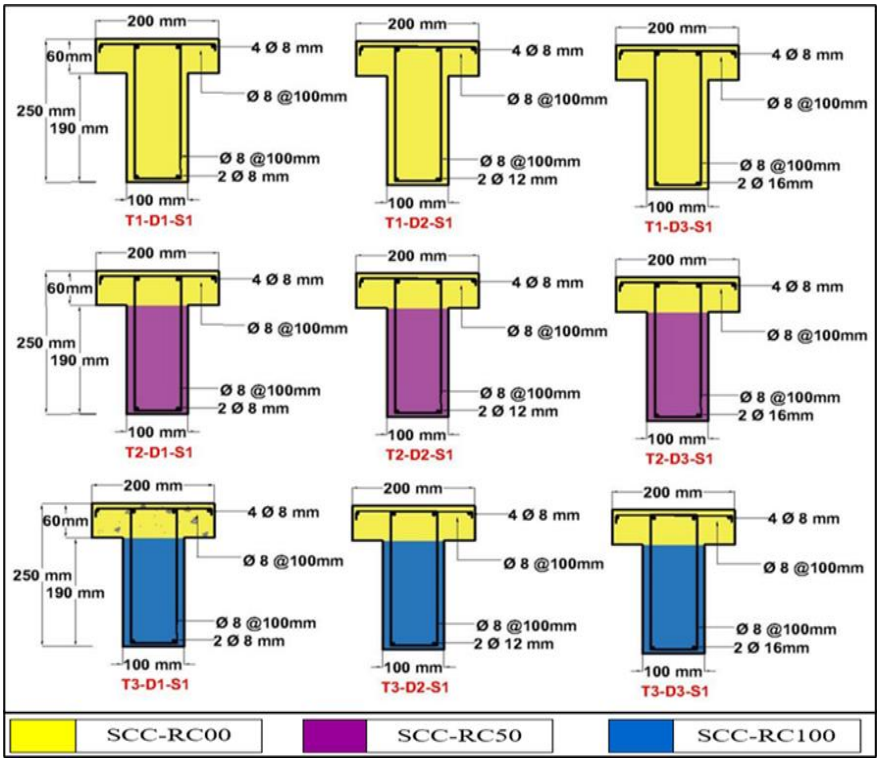

Fig. 2. The details illustration of the T-beam specimens used in the present study

Table 7. Classification of the T-beam specimens

T-beam code	Concrete type in T-beam web.	Concrete type in T-beam flange.	Main reinforcement
T1-D1	SCC-RC00 [1]	SCC-RC00 [1]	2Ø8
T1-D2			2Ø12
T1-D3			2Ø16
T2-D1	SCC-RC50 [2]		2Ø8
T2-D2			2Ø12
T2-D3			2Ø16
T3-D1	SCC-RC100 [3]		2Ø8
T3-D2			2Ø12
T3-D3			2Ø16

1: SCC mixture 0% RCA, 2: SCC mixture 50% RCA, 3: SCC mixture 100% RCA.

The first mixture, SCC-RC00, consists of pure SCC without any replacement of natural coarse aggregate (NCA). In the second mixture, SCC-RC50, 50% of the NCA was replaced with recycled concrete aggregate (RCA) in the web, while the flange was cast using SCC-RC00. The third mixture, SCC-RC100, involved a complete replacement of NCA with RCA, applied to all three reinforcement types. To maintain consistent flexural behavior across all T-beams, the spacing of the shear reinforcement (stirrups) was kept constant at Ø8@100 mm. The T-beam specimens are classified and grouped as shown in Table 7. Figure 2 illustrates the details of the reinforcements and the types of concrete used for casting the flange and web of the T-beams.

2.5 Mixture Preparation and Casting

The preparation method for self-consolidating concrete (SCC) differs from that of conventional concrete. The materials listed in Table 7 are used to calculate the quantities required for one batch. First, the coarse and fine aggregates are mixed with additional water for two minutes to achieve a saturated surface dry (SSD) condition. Next, the binder materials cement, fly ash, and silica fume are added along with half the water volume, and this mixture is blended for another two minutes. The remaining water is combined with the superplasticizer and incorporated into the mixture. Mixing continues for five minutes to ensure uniformity.

Once the mixing is complete, immediate fresh tests are conducted on the SCC mixture to assess its properties. Three tests are performed: the slump flow test, V-funnel test, and L-box test. The T-beam models are then cast according to the specified details, along with three cubes and three cylinders for each concrete batch, without the use of a vibrator. Only the web zone of each T-beam specimen is cast initially. After 24 hours, the flange zone is cast using SCC containing only normal coarse aggregate (NCA). Following another 24 hours, the specimens are removed and immersed in water for curing for 28 days before testing.

2.6 Testing Procedures

Since the concrete used is self-compacting, it was necessary to conduct fresh tests for each concrete mixture in its fresh state. Also, the compressive strength and tensile strength of the concrete in its hardened state will be found. On the other hand, the flexural test of reinforced concrete T-beams will be conducted to know the flexural behavior.

2.6.1 Fresh Properties Testing

The fresh properties of the mixtures used in this study were assessed according to EFNARC specifications. To evaluate flowability and viscosity, the slump flow test was conducted. The V-funnel test was employed to determine the filling ability of the self-compacting concrete (SCC). Additionally, the L-box test was used to assess the concrete's resistance to segregation.

In the slump test, the time taken for the concrete to reach the circumference of a circle with a diameter of 500 mm is recorded after lifting the cone. The final diameter of the circular area resulting from the spread of the concrete, known as the slump diameter, is also measured. Following this, the V-shaped funnel flow test is conducted, where the time taken for the mixture to completely empty the funnel is recorded. Finally, the L-box test measures the vertical distances at the start (h1) and end (h2) of the basin after the concrete flow ceases, allowing for the calculation of the h2/h1 ratio.

2.6.2 Hardened Properties Testing

The compressive strength and tensile strength of concrete used in the present study will be determined by mechanical tests at 28 days of age. A 2000 kN universal testing machine will be used. The compressive strength of each concrete mixture will be determined using cubic specimens of size 100*100*100 mm. The cubic specimens were loaded at a rate of 0.3 MPa/s according to British Standard (B.S) [28]. Also, the splitting test will be conducted for cylindrical specimens of size 100*200 mm, according to ASTM [29]. The cylindrical specimens are loaded at a rate of 1.5 kN/s. To obtain reasonable results, the average strength value of three identical specimens will be found.

2.6.3 Flexural Testing

After 28 days of curing in water, the specimens will be removed, and their surfaces will be thoroughly cleaned. They will then be painted white to enhance the visibility of cracks and their progression during loading. A strain gauge will be affixed horizontally above the expected failure line (the beam's midpoint) to measure the concrete strain under flexural behavior. Additionally, another strain gauge will be attached along the line connecting the support and loading location at a 45-degree angle on both sides of the T-beam to assess the shear behavior during loading.

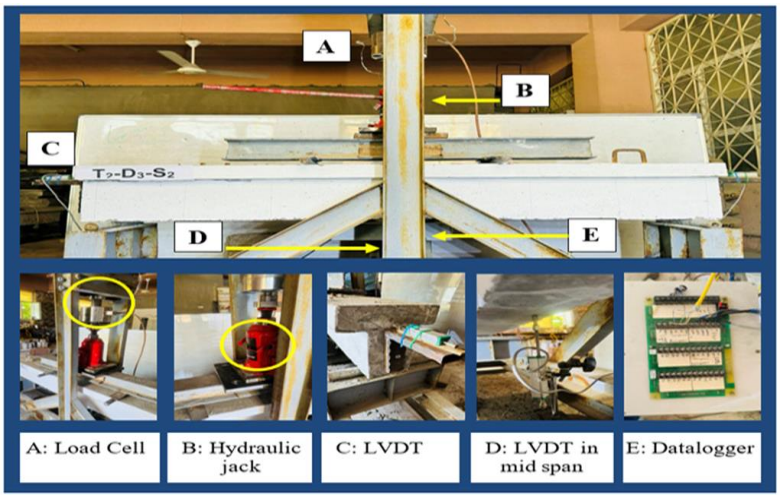

Fig. 3. Illustrations of the concrete T-beam testing procedure

To measure deflection under loading, a linear variable displacement transducer (LVDT) will be installed at the mid-span of the beam from the bottom, with an accuracy of approximately 75/4000 mm. Two additional LVDTs, each with an accuracy of about 25/4000 mm, will be positioned on both sides of the specimen (in the web zone) to measure horizontal displacement (slip) from each side of the T-beam. These instruments will be connected to an 80-rpm data logger, which in turn will be linked to a laptop. The specimens will be subjected to loading using a 200 kN load cell. For each loading stage, the loads and corresponding deflections on the beam surface will be recorded, along with observations of cracks until the test concludes. Loading will cease when the deflection reaches 30 mm for all T-beam specimens. The data on loads and deflection results will be automatically saved on the computer. After completing the test, photographs of the specimen, crack patterns, and the final failure form will be taken. Figure 3 illustrates the steps involved in performing the load test on the T-beam specimens.

3. Results and Discussion

3.1 Fresh Properties of SCC

The fresh properties of the SCC mixtures were evaluated through three tests to ensure compliance with EFNARC specifications. A slump flow test measured the concrete's flowability, a V-funnel test assessed its flow time, and an L-box test examined its resistance to segregation.

Table 8. Results of fresh properties of SCC mixtures

Mix Code	RCA %	Slump Test		V-funnel	L-Box
		T_{500} (sec.)	Dia (mm)	sec.	(h_2/h_1)
SCC-RC00	0%	2.34	760	6.72	0.94
SCC-RC50	50%	2.84	744	8.55	0.91
SCC-RC100	100%	3.32	720	10.53	0.88
EFNARC limitations [4].		2-5	600-800	≤12	0.8-1.0

According to EFNARC, the slump flow time (T500) should range between 2 and 5 seconds, with the flow diameter ideally between 600 and 800 mm. The V-funnel flow time should not exceed 12

seconds, and the L-box ratio (h2/h1) should fall between 0.8 and 1. The test results of the mixtures used in this study, shown in Table 8, were consistent with EFNARC standards. The T500 for all mixtures was under 5 seconds, while the slump flow diameters ranged from 720 to 760 mm. V-funnel flow times ranged between 6.72 and 10.53 seconds, and the L-box ratio (h2/h1) was between 0.88 and 0.94. Overall, all mixtures adhered to EFNARC specifications.

3.2 Hardened Properties of SCC Mixtures

The compressive and tensile strengths of the concrete used in this study are presented in Table 9. These values represent the average of three specimens for each concrete mixture. The results indicate that compressive and tensile strengths gradually decreased as the percentage of RCA replacement increased, compared to the mixture containing only NCA. Specifically, compressive strength decreased by 9% and 25%, and tensile strength by 28% and 39%, respectively, for 50% and 100% RCA replacement, as detailed in Table 9. This reduction in strength can be attributed to the lower quality of RCA compared to NCA, as the RCA was sourced from construction rubble specifically, the demolition of a house roof over 25 years old. Additionally, the brittleness of the aggregate was likely exacerbated by the crushing process used to obtain coarse aggregates of the required size and specification.

Table 9. Results of Hardened properties of SCC mixtures

Mix Code	RCA %	Compressive strength (MPa)	Tensile strength (MPa)
SCC-RC00	0	67.0	5.93
SCC-RC50	50	61.1	4.26
SCC-RC100	100	50.4	3.63

3.3 Flexural Behavior of T-Beam

The flexural test results for T-beams reveal their general behavior under flexural loading, summarized as follows: In the early stages, initial cracks appear in the lower portion of the mid-span tensile zone. The load at which these cracks first form is known as the first cracking load (Pcr). As the load increases, these cracks widen and spread until the yield load (Py) is reached, marking the onset of reinforcement steel yielding. Beyond this point, deflection rises rapidly while load capacity slows, reaching the ultimate load (Pu). Afterward, the load capacity decreases as deflection continues to increase, eventually leading to beam failure. Table 10 presents the test results, showing the load values along with corresponding deflections for the T-beams.

Table 10. Flexural test results for concrete T-beams used in the present study

T-beam code	First cracking point		Yielding point		Ultimate point		Ductility index Δu/Δy	stiffness (KN/mm) Py/Δy	Failure mode*
	Load (Pcr) (kN)	Deflection (Δcr) (mm)	Load (Py) (kN)	Deflection (Δy) (mm)	Load (Pu) (kN)	Deflection (Δu) (mm)			
T1-D1	16.6	1.51	37.4	5.19	54.1	30	5.78	7.21	F
T1-D2	29.4	1.89	126.1	13.75	143.2	30	2.18	9.17	F+S
T1-D3	30.9	2.09	181.9	14.71	198.9	30	2.04	12.37	F+S
T2-D1	16.4	1.08	37.7	5.76	44.1	30	5.21	6.55	F
T2-D2	19.9	1.66	132.5	13.61	135.2	30	2.20	9.74	F+S
T2-D3	28.8	2.01	173.1	13.11	185.3	30	2.29	13.20	F+S
T3-D1	15.3	1.66	24.8	5.06	42.5	30	5.93	4.90	F
T3-D2	17.6	1.24	120.9	11.49	129.1	30	2.61	10.52	S
T3-D3	19.2	1.43	174.3	10.53	174.4	15.89	1.51	16.55	S

∗ F: Flexural failure, S: Shear failure.

3.3.1 Load Capacity

Table 10 presents the load-capacity stages of concrete T-beams with varying replacement ratios of RCA (0%, 50%, and 100%) and three different reinforcement ratios (0.45%, 1.05%, and 1.85%).

The first cracking load was observed to increase as the RCA replacement ratio rose, regardless of the reinforcement ratio. This suggests a reduction in the stiffness of the T-beam with higher RCA content, as illustrated in Figure 4. Overall, the yielding load of the T-beam increases with a larger reinforcement area but decreases as the RCA replacement ratio increases. For concrete with NCA, the yielding load increased by 237% and 386%, corresponding to reinforcement ratio increases of 233% and 311%, respectively. When 50% of the NCA was replaced with RCA, the yielding load increased by 252% and 360% for the same reinforcement increases. Replacing all the NCA with RCA resulted in even higher increases in yielding load, by 388% and 603%, for the same reinforcement ratio increments.

Conversely, when using 8 mm diameter reinforcing bars, the ultimate load decreased by 19% and 22% for RCA replacement ratios of 50% and 100%, respectively. With 12 mm diameter bars, the decrease in ultimate load was 6% and 10% for the same replacement ratios. For 16 mm diameter bars, the reductions were 7% and 12%, respectively, for 50% and 100% RCA replacement. In conclusion, the reduction in load capacity of concrete T-beams decreases as the RCA replacement ratio increases, especially with higher reinforcement ratios. This indicates that using RCA in the web of concrete not only improves load capacity but also offers economic and environmental benefits compared to NCA.

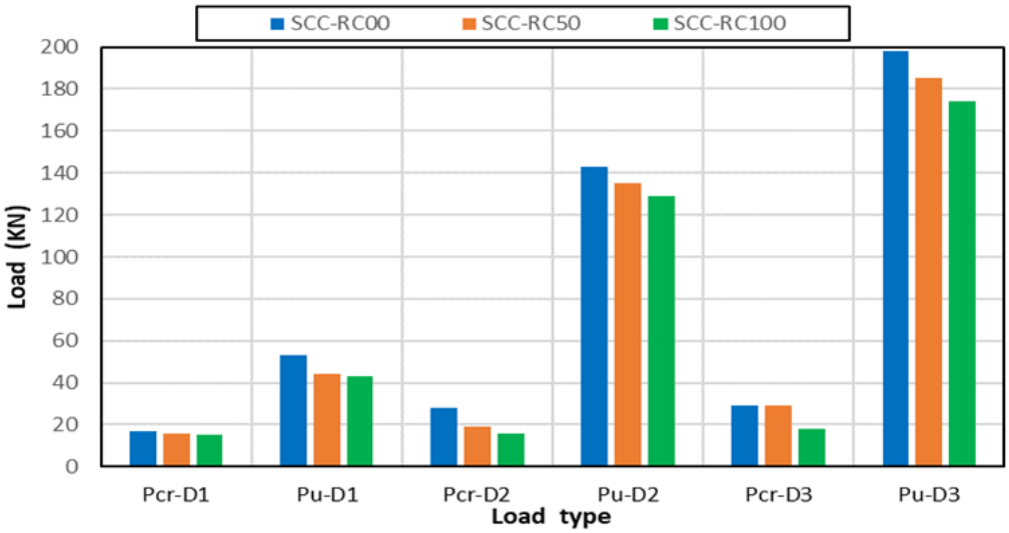

Fig. 4. Comparison between the first cracking load and the ultimate load of the T-beam specimens

3.3.2 Load-Deflection Curves

The flexural load test on the concrete T-beams was applied gradually until failure. At each loading stage, the deflection at the mid-span of the beam was recorded using LVDT, with the load being measured by an installed load cell. The load and deflection data were automatically saved on the computer in real-time. The study will examine the impact of different concrete types in the T-beam web and varying proportions of steel reinforcement on the load-deflection curves of each beam. In the graphs, the horizontal axis (X) represents deflection in millimeters (mm), while the vertical axis (Y) represents load in kilonewtons (kN).

3.3.2.1 Effect of Concrete Type

To investigate the effect of replacing natural coarse aggregate (NCA) with recycled coarse aggregate (RCA) in the concrete used for casting the web of T-beams, load-deflection curves were analyzed for each group. Figure 5 shows the load-deflection behavior of concrete beams with a reinforcement ratio of 0.45%, using different RCA replacement ratios (0%, 50%, 100%). The curves indicate that as the replacement ratio increases, the load-carrying capacity decreases with higher deflection, though all beams exhibited flexural behavior across the replacement ratios. In contrast, T-beams with a reinforcement ratio of 1.05% showed similar behavior regardless of whether NCA was replaced by RCA, with all beams maintaining flexural behavior, as depicted in Figure 6. For beams with a reinforcement ratio of 1.85%, shown in Figure 7, increasing the RCA replacement

ratio resulted in a shift from flexural to shear behavior. A full (100%) replacement of coarse aggregate weakened the concrete, altering the T-beam behavior from flexural to shear.

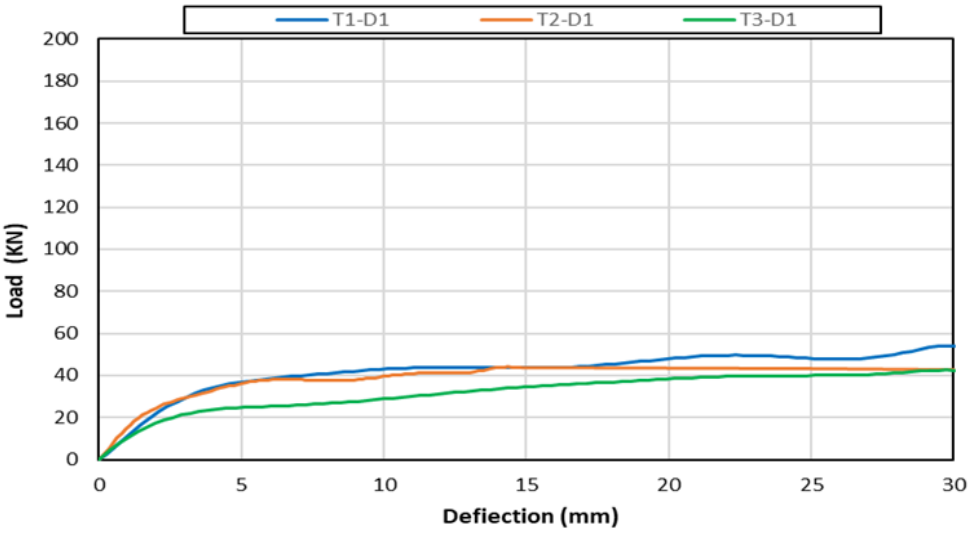

Fig. 5. Load-deflection curves for T-beams reinforced with steel bars of 8 mm

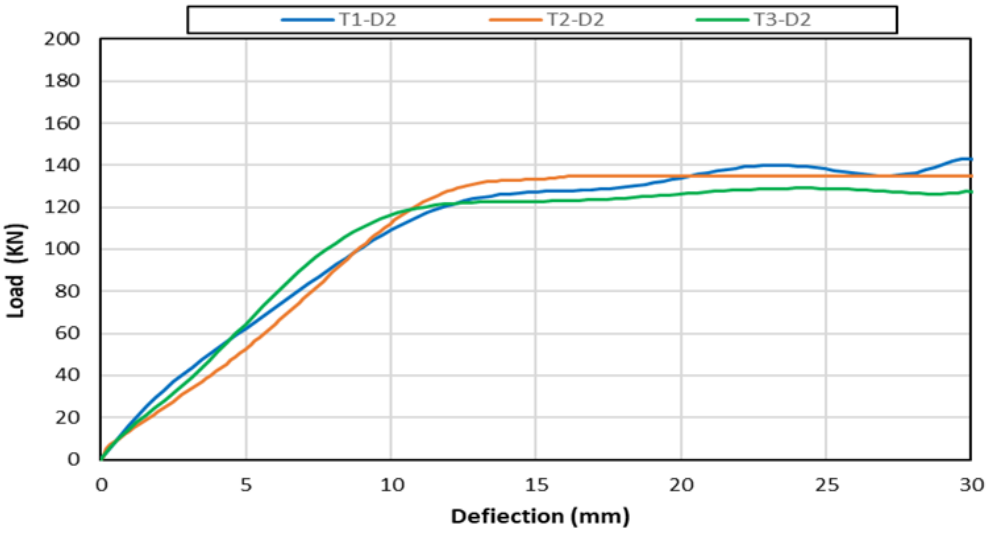

Fig. 6. Load-deflection curves for T-beams reinforced with steel bars of 12 mm

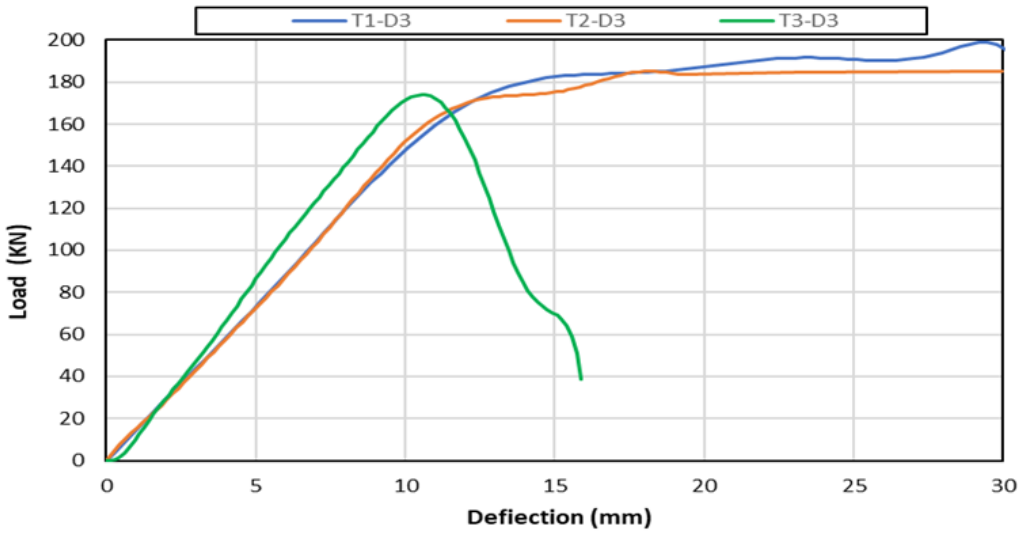

Fig. 7. Load-deflection curves for T-beams reinforced with steel bars of 16mm

3.3.2.2 Effect of Main Reinforcement

To investigate the impact of increasing the reinforcement ratio on the load-deflection behavior of concrete T-beams, Figure 8 illustrates the performance of T-beams made entirely with natural coarse aggregate (NCA) in both the flange and web, using three different reinforcement ratios (0.45%, 1.05%, and 1.85%).

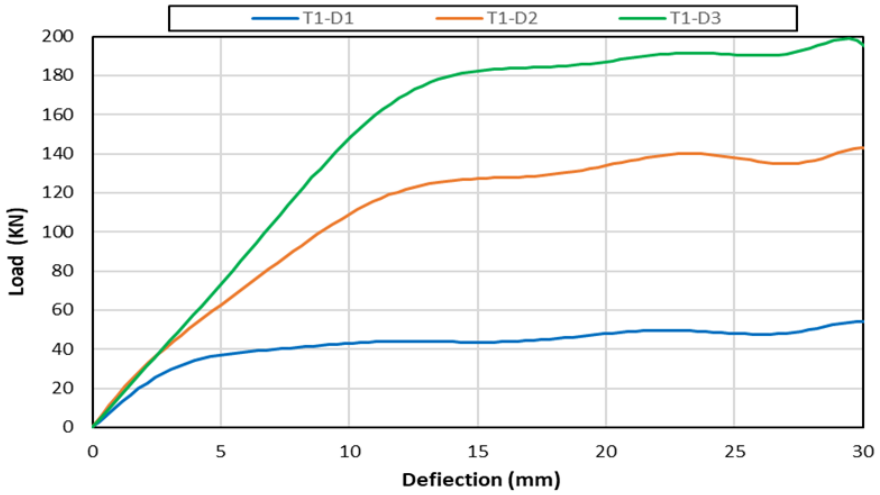

Fig. 8. Load-deflection curves for T-beams containing SCC-RC00 mixtures

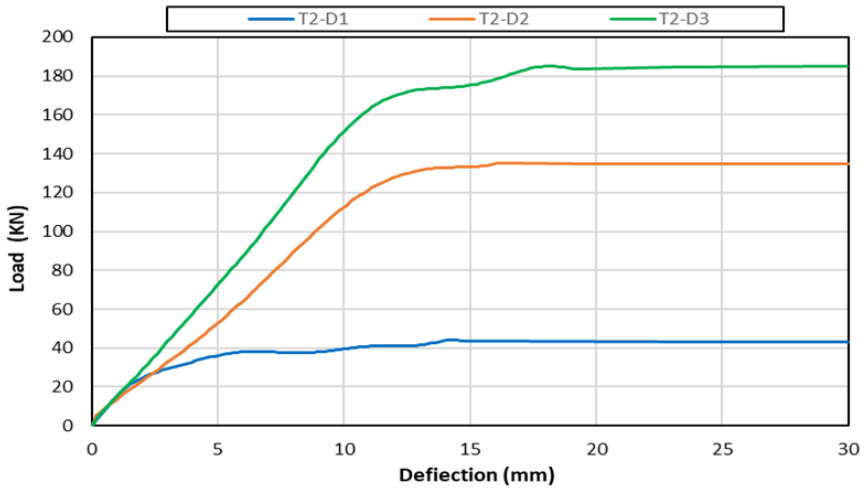

Fig. 9. Load-deflection curves for T-beams containing SCC-RC50 mixtures

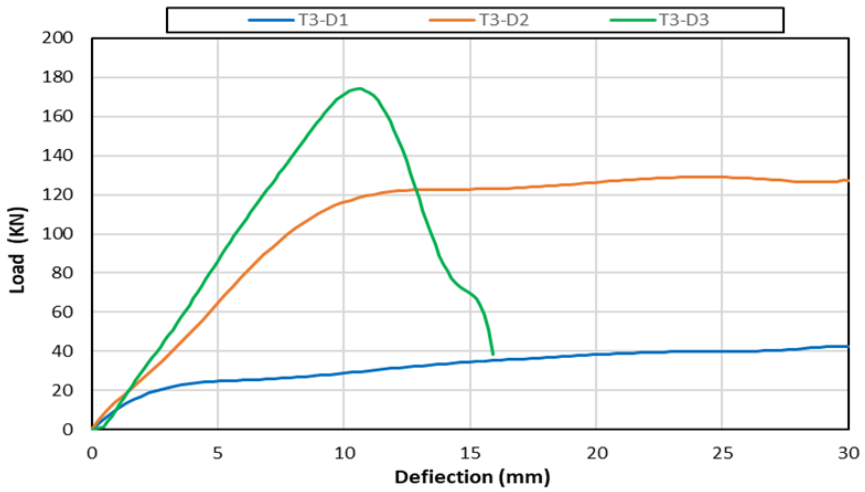

Fig. 10. Load-deflection curves for T-beams containing SCC-RC100 mixtures.

The use of NCA in the web's concrete helped preserve the flexural behavior of the T-beams, regardless of the steel reinforcement ratio. In contrast, replacing 50% of the natural aggregate with recycled coarse aggregate (RCA) partially maintains the flexural behavior of the beams, though the yield point is delayed as the reinforcement diameter increases, as shown in Figure 9. When 100% of the NCA in the web is replaced with RCA, the behavior of the T-beams gradually shifts from flexural to shear-dominant as the reinforcement ratio increases, as depicted in Figure 10.

3.3.3 Crack Patterns and Mod Failures

The failure patterns of concrete T-beams under loading are illustrated in Figures 11, 12, and 13. Vertical cracks initially develop from the middle of the beam's underside, resulting from a combination of flexural and shear failure. This effect becomes more pronounced as the percentage of recycled aggregate replacement increases. When using 16 mm diameter reinforcing steel, shear cracks appear alongside flexural cracks, and with higher aggregate replacement, shear cracks become more frequent until shear failure dominates, as shown in Figure 13.

Figure 11 highlights the failure modes of T-beams reinforced with 8 mm diameter bars, where flexural failure is predominant. Vertical cracks, concentrated in the beam's center, occur regardless of the aggregate replacement ratio. In contrast, Figure 12 shows the emergence of inclined cracks at a 45-degree angle in T-beams reinforced with 12 mm diameter bars. These inclined cracks appear alongside vertical cracks as the aggregate replacement ratio increases, resulting in a flexural-shear failure mode. As the main reinforcement ratio increases, the failure mode transitions from flexural-shear failure to pure shear failure, especially when coarse aggregate is fully replaced with recycled aggregate.

Fig. 11. Crack patterns and failure modes for T-beams reinforced with steel bar of 8 mm

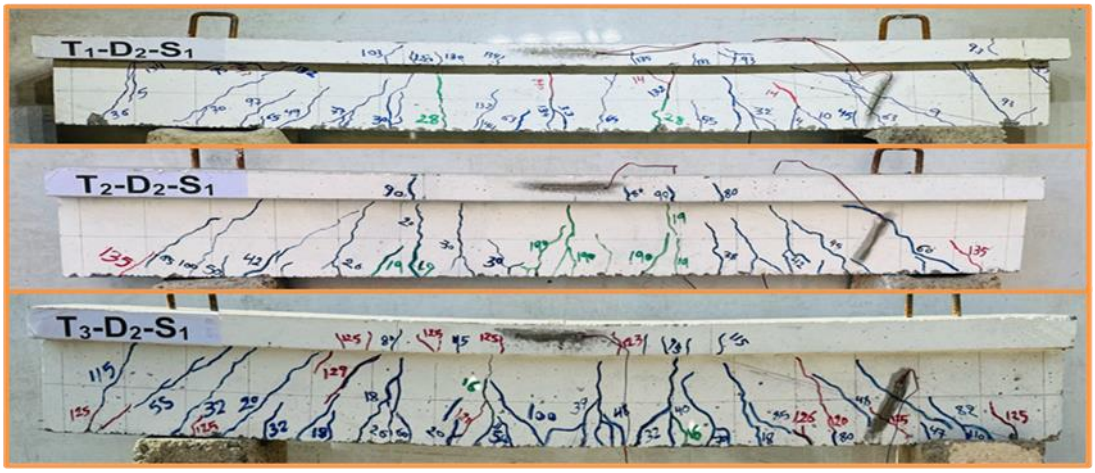

Fig. 12. Crack patterns and failure modes for T-beams reinforced with steel bar of 12 mm

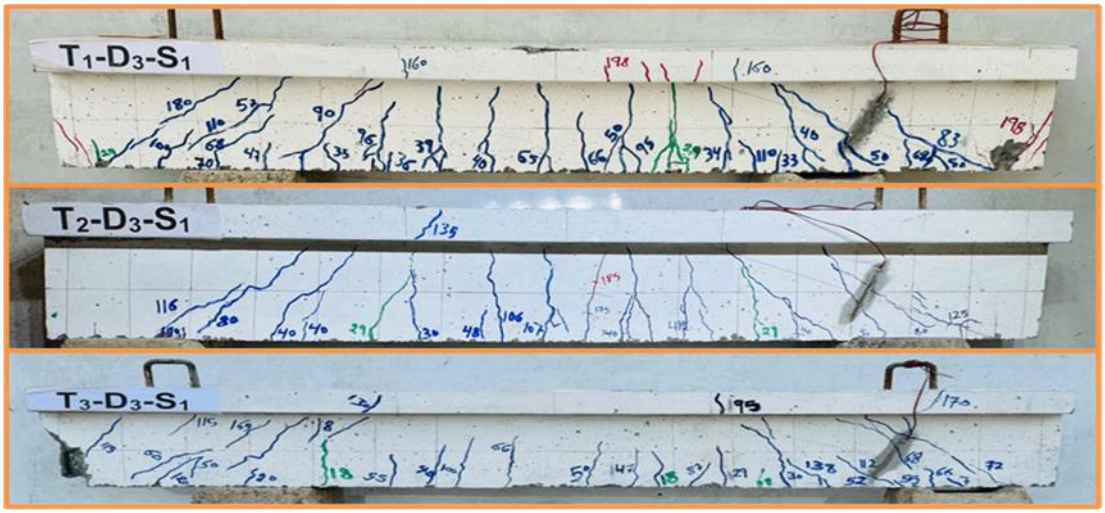

Fig. 13. Crack patterns and failure modes for T-beams reinforced with steel bar of 16 mm

3.3.4 Ductility Index

The ductility index measures a structural member's ability to withstand deformations without a substantial reduction in bending capacity. Several factors influence a member's deformability, such as the ratio of main reinforcement, the amount of secondary reinforcement, and the concrete strength [30]. The ductility index is expressed as the ratio of the deflection at ultimate load (Δu) to the deflection at yield point (Δy), as shown in Equation 1 [31]:

$$Ductility\ index\ =\ \Delta u/\Delta y \tag{1}$$

This equation was used to determine the ductility values of concrete beams by varying the ratios of the main reinforcement steel and the concrete strength. Generally, the ductility of concrete T-beams decreases as the steel reinforcement area increases, while the percentage of natural coarse aggregate (NCA) replacement remains constant. Additionally, increasing the replacement percentage of aggregates further reduces ductility, particularly in beams with a high reinforcement ratio.

3.3.5 Stiffness

Stiffness (K) quantifies an elastic body's resistance to deformation. The effective section stiffness is determined by the maximum bearing force and the corresponding deflection within the service load zone (elastic zone) [32]. This relationship can be expressed mathematically as follows:

$$K\ =\ Py/\Delta y \tag{2}$$

In general, the stiffness of concrete T-beams increases with a higher percentage of main steel reinforcement, regardless of the level of aggregate replacement [33]. When beams are reinforced with 16 mm diameter bars instead of 8 mm bars, the stiffness increases by 72%, 102%, and 238% for coarse aggregate replacement percentages of 0%, 50%, and 100%, respectively. This trend highlights how increased steel reinforcement enhances a structural member's resistance to bending and deformation caused by external loads. Additionally, the results presented in Table 10 indicate that increasing the percentage of coarse aggregate replacement with recycled aggregate improves the stiffness of concrete beams. This improvement may be due to the recycled aggregate's initial resistance to loads; however, this resistance diminishes rapidly as the loading increases [34].

4. Conclusions and Recommendations

The current study examines how varying proportions of recycled concrete aggregate (RCA) and the reinforcing steel ratio affect the flexural behavior of hybrid T-beams in self-compacting concrete (SCC). The main conclusions are as follows:

- Replacing natural aggregates with RCA affects the workability of SCC, but it remains within the acceptable range defined by EFNARC guidelines.
- Increasing RCA replacement from 0% to 100% leads to a reduction in compressive strength, from 67.0 MPa to 50.4 MPa, and in splitting tensile strength, from 5.93 MPa to 3.63 MPa.
- The load capacity of reinforced concrete T-beams decreases with higher RCA replacement ratios; however, this reduction is mitigated by increasing the reinforcement ratio. This suggests that using RCA in web concrete not only enhances load capacity but also provides economic and environmental benefits compared to natural coarse aggregate (NCA).
- Load-deflection curves indicate that as the reinforcement ratio increases, the T-beams transition from flexural to shear behavior with rising aggregate replacement ratios.
- Shear cracks develop and intensify as the percentage of main reinforcement increases. Nonetheless, replacing NCA with RCA contributes to the growth and expansion of shear cracks, ultimately leading to shear failure as the predominant failure mode.
- A higher aggregate replacement ratio correlates with decreased ductility, particularly in T-beams with a high reinforcement ratio.
- Conversely, the increase in aggregate replacement enhances the stiffness of concrete T-beams, especially those with significant reinforcement. This effect may be attributed to the initial load resistance offered by recycled aggregates, which diminishes with increased loading.

Future research should focus on optimizing RCA proportions in SCC to achieve a better balance between workability and strength. It is essential to investigate the long-term durability of these materials, including their resistance to sulfate and acid attacks, corrosion of steel reinforcement, and chloride ion penetration. Additionally, exploring the effects of RCA on other structural elements, such as slabs and columns, will be crucial for a comprehensive understanding.

Acknowledgment

The authors acknowledge that this study is supported by the University of Kirkuk and Al-Qalam University College, in Kirkuk, Iraq.

References

[1] Meko B, Ighalo JO, Ofuyatan OM. Enhancement of self-compatibility of fresh self-compacting concrete: A review. Cleaner Materials. 2021;1:100019. https://doi.org/10.1016/j.clema.2021.100019
[2] Mikhaltchouk I, Eklund J, Forsman M. Barriers and facilitators for usage of self-compacting concrete-An interview study. Inventions. 2024;9:50. https://doi.org/10.3390/inventions9030050
[3] Siddique R. Self-compacting concrete: materials, properties, and applications. Woodhead Publishing; 2019.
[4] Shawais ZA, Abdulhaleem KN, Ahmed SH, Hamada HM, Mohammed VR. Influence of recycled coarse aggregate and steel fiber on the workability and strength of self-compacting concrete. IOP Conf Ser Earth Environ Sci. 2024; p. 012084. https://doi.org/10.1088/1755-1315/1374/1/012084
[5] Mohammed VR, Abdulhaleem KN, Hamada HM, Humada AM, Majdi A. Effect of recycled aggregate concrete and steel fibers on the fresh properties of self-compacting concrete. E3S Web Conf. 2023; p. 02013. https://doi.org/10.1051/e3sconf/202342702013
[6] Xiao J, Xiao J. Recycled aggregate concrete. Springer; 2018. https://doi.org/10.1007/978-3-662-53987-3
[7] Sun C, Chen Q, Xiao J, Liu W. Utilization of waste concrete recycling materials in self-compacting concrete. Resour Conserv Recycl. 2020;161:104930. https://doi.org/10.1016/j.resconrec.2020.104930
[8] Xiao J, Li L, Tam VW, Li H. The state of the art regarding the long-term properties of recycled aggregate concrete. Struct Concr. 2014;15(1):3-12. https://doi.org/10.1002/suco.201300024
[9] Hamada HM, Jokhio GA, Al-Attar AA, Yahaya FM, Muthusamy K, Humada AM. The use of palm oil clinker as a sustainable construction material: A review. Cem Concr Compos. 2020;106:103447. https://doi.org/10.1016/j.cemconcomp.2019.103447
[10] Hamada HM, Al-Attar A, Abed F, Beddu S, Humada AM, Majdi A. Enhancing sustainability in concrete construction: A comprehensive review of plastic waste as an aggregate material. Sustain Mater Technol. 2024;40. https://doi.org/10.1016/j.susmat.2024.e00877
[11] Abed M, Nemes R, Tayeh BA. Properties of self-compacting high-strength concrete containing multiple uses of recycled aggregate. J King Saud Univ Eng Sci. 2020;32:108-14. https://doi.org/10.1016/j.jksues.2018.12.002

[12] Bonoli A, Zanni S, Serrano-Bernardo F. Sustainability in building and construction within the framework of circular cities and European new green deal: The contribution of concrete recycling. Sustainability. 2021;13:2139. https://doi.org/10.3390/su13042139
[13] Hamada HM, Shi J, Abed F, Humada AM, Majdi A. Recycling solid waste to produce eco-friendly foamed concrete: A comprehensive review of approaches. J Environ Chem Eng. 2023;11:111353. https://doi.org/10.1016/j.jece.2023.111353
[14] Abdulhaleem KN, Hamada HM, Majdi A, Yousif ST. Influence of palm oil fuel ash as agricultural waste on the environment and strength of geopolymer concrete. 2024.
[15] Sasanipour H, Aslani F. Durability properties evaluation of self-compacting concrete prepared with waste fine and coarse recycled concrete aggregates. Constr Build Mater. 2020;236:117540. https://doi.org/10.1016/j.conbuildmat.2019.117540
[16] Kapoor K, Singh S, Singh B, Singh P. Effect of recycled aggregates on fresh and hardened properties of self-compacting concrete. Mater Today Proc. 2020;32:600-7. https://doi.org/10.1016/j.matpr.2020.02.753
[17] Hason MM, Mussa MH, Abdulhadi AM. Flexural ductility performance of hybrid-recycled aggregate reinforced concrete T-beam. Mater Today Proc. 2021;46:682-8. https://doi.org/10.1016/j.matpr.2020.11.747
[18] You ZG, Wang XG, Liu GH, Chen HB, Li SX. Shear behavior of hybrid fiber-reinforced SCC T-beams. Mag Concr Res. 2017;69:919-38. https://doi.org/10.1680/jmacr.16.00470
[19] Khtara AK, Khudhaira JA. Flexural behavior of reinforced concrete T-beam cast with self-compacting concrete incorporating recycled concrete aggregate. Muthanna J Eng Technol (MJET). 2018;6. https://doi.org/10.18081/mjet/2018-6/210-221
[20] Fahmy MF, Idriss LK. Flexural behavior of large scale semi-precast reinforced concrete T-beams made of natural and recycled aggregate concrete. Eng Struct. 2019;198:109525. https://doi.org/10.1016/j.engstruct.2019.109525
[21] Lec A, Malik MM, Ali AY. Flexural and shear behavior of reinforced concrete T-section beams composed of hybrid concrete. 2015.
[22] Fang Z, Jiang H, Liu A, Feng J, Chen Y. Horizontal shear behaviors of normal weight and lightweight concrete composite T-beams. Int J Concr Struct Mater. 2018;12(1):1-21. https://doi.org/10.1186/s40069-018-0274-3
[23] Marzoq ZH, Borhan TM. The behavior of hybrid-reinforced concrete T-beams exposed to the flexural moment. Asian J Civ Eng. 2020;21:1005-12. https://doi.org/10.1007/s42107-020-00257-9
[24] ASTM C. 1084: Standard Test Method for Portland-cement content of hardened hydraulic-cement concrete. Philadelphia, USA; 1992.
[25] Bakhrakh BA, Solodov A, Larsen O, Naruts V, Aleksandrova O, Bulgakov B. SCC with a high volume of fly ash content. MATEC Web Conf. 2017; p. 03016. https://doi.org/10.1051/matecconf/201710603016
[26] Testing and Materials ASF. ASTM C136/C136M-19: Standard Test Method for Sieve Analysis of Fine and Coarse Aggregates. 2019.
[27] Bibm C, ERMCO EE, EFNARC. The European guidelines for self-compacting concrete: Specification, production, and use. SCC European Project Group, EFNARC; 2005.
[28] En B. 12390-3, Testing hardened concrete-Part 3: Compressive strength of test specimens. British Standards Institution. 2009; 22.
[29] ASTM C. Standard test method for splitting tensile strength of cylindrical concrete specimens. ASTM International C. 2011; 496.
[30] Rabi M, Shamass R, Cashell K. Structural performance of stainless steel reinforced concrete members: A review. Constr Build Mater. 2022;325:126673. https://doi.org/10.1016/j.conbuildmat.2022.126673
[31] Arslan G, Cihanli E. Curvature ductility prediction of reinforced high-strength concrete beam sections. J Civ Eng Manag. 2010;16:462-70. https://doi.org/10.3846/jcem.2010.52
[32] Rakhshanimehr M, Esfahani MR, Kianoush MR, Mohammadzadeh BA, Mousavi SR. Flexural ductility of reinforced concrete beams with lap-spliced bars. Can J Civ Eng. 2014;41:594-604. https://doi.org/10.1139/cjce-2013-0074
[33] Abdul-Razzaq KS, Abdul-Kareem MM. Innovative use of steel plates to strengthen flange openings in reinforced concrete T-beams. Structures. 2018;16:269-87. https://doi.org/10.1016/j.istruc.2018.10.005
[34] Etman EE, Afefy HM, Baraghith AT, Khedr SA. Improving the shear performance of reinforced concrete beams made of recycled coarse aggregate. Constr Build Mater. 2018;185:310-24. https://doi.org/10.1016/j.conbuildmat.2018.07.065

Research on Engineering Structures & Materials
www.jresm.org
Research Group

Research Article

Analytical modeling of fracture energy with cohesion effects based on experimental investigations

Amina Benguelil [*,1,a], Brahim Elkhalil Hachi [1,b], Mohamed Haboussi [2,c]

[1]*Laboratory of Development in Mechanics and Materials (LDMM), University of Djelfa, Algeria*
[2]*Process and Materials Sciences laboratory (LSPM) Sorbonne Paris Nord University, France*

Article Info

Article history:

Received 03 Sep 2024
Accepted 12 Nov 2024

Keywords:

Concrete;
Experimental investigation;
Fracture energy;
Analytical modeling;
Sand fines ratio;
Crack initial length

Abstract

The experimental characterization is the most exact method which describes and studies the material's real behavior and its response to different mechanical solicitations otherwise conducting experimental tests for every case is often impractical. This work presents an analytical model that describes the concrete fracture energy variation in function of the specimen's length, the crack initial length and the Sand fines ratio basing on experimental investigations. Three point bending tests were conducting on concrete specimens, using an MTS testing machine and according to the ASTM norms. The obtained experimental results were used to generate an analytical model based on ANOVA and experimental plan principles. The model was validated and adjusted. It has been found that the weakening of the studied specimens is majorly related to the increasing on the specimen's and crack initial lengths or by decreasing the sand fines ratio and the model shows in addition to that a clear parameter's classification, the sand fines ratio is the most influential factor and all the interactions including the sand fines ratio or the crack initial length present high effects. A high coherence between the model and the experimental values in term of fracture energy was noticed and that according to relative error that did not exceed the 28%. After adjustments, the error was highly ameliorated. The model helps in studying the concrete general behavior and offers a reliable tool contributing to the evaluation of the Fracture energy without going through experimental tests considered as costly in terms of time and price.

© 2025 MIM Research Group. All rights reserved.

1. Introduction

Understanding the relationships between the microstructural phenomena and the corresponding effects on macroscopic behavior is the main key to truly understanding the material general behavior and the principal way to the establishment of the predictive formulate models for large-scale structural performance and reliability [1]. This relation's complexity depends mainly on the material sensibility, the confounding effects of design, the imposed loads, and the climatic conditions relevant to the structures [2]. The general theory of material behavior develops systematic methods to represent material properties in a context of physical evidence and mathematical consistency [3]. The Fracture mechanics is a field that uses the fracture phenomena and parameters to develop predictive models. It is the discipline of mechanics that deals with the study of the cracks propagation in materials due to the extension of processing defects such as pores, inclusions, or even microscopic fissures. It uses analytical methods known as analytical solid mechanics to calculate the driving force on cracks and applies the experimental solid mechanics principals to characterize the material's resistance to fracture. The Materials

*Corresponding author: amina.benguelil@univ-djelfa.dz
[a]orcid.org/0009-0005-4588-1272; [b]orcid.org/ 0000-0002-6672-746X; [c]orcid.org/0000-0001-8901-6559
DOI: http://dx.doi.org/10.17515/resm2024.431me0903rs

fracture behavior can be classified in ductile and fragile, where the fragile behavior is considered hard to detect and to study for the raison that the fracture is brusque, happens in a very quick manner and the materials engendering these type of behavior are very sensitive to the smallest changes in the study parameters or in the testing procedures. Concrete is one of the most well-known and highly used materials engendering these quasi-brittle behavior and because of its importance as a construction material, its fracture and failure behavior has been the subject of extensive researches [4], theses researches has started in the 19th and the first half of the 20th where the demand for the concrete use has raised, these researches were focused on the concrete technology and its structural performances and lays majorly on the fracture and failure concrete behavior studies both experimental and numerical. The experimental investigations were divided on two main research axes, the investigations in term of concrete composition and nuances in a hand and on the material characterization and detection of their fracture parameters on the other one. To finally confuse these two axes in order to detected the optimum version of concrete to be used in different constructions sectors or to develop analytical predictive models that facilitate and helps in studying the concrete behavior without the need for experimental realizations. Focusing on the fracture energy predictive models based on experimental investigations were conducted such those presented by Bazant and Oh [5], proposing a model that links the said energy to the tensile strength, the aggregates diameter and the elasticity modulus, this model was simplified and reformulate later. Or the one developed by Hillerborg [6] based majorly on the area under the softening phase of the stress-strain curve obtained from bending test and takes also in consideration geometric parameters such as the crack length and the specimen's width. Meanwhile, the comite Euro International du béton [7] propose a simple empirical model defines the fracture energy in function of the aggregate maximum size and the cylinder compressive strength. This model was reformulated by Bazant et al. [8] and that by adding the water cement ratio. Years later, the Comite International du Béton [9] has proposed another model based on the mean value of the cylinder compressive strength. The JSCE [10] introduce as well a simplify model that contains only the aggregate maximum diameter and the cylinder compressive strength. Iman M.Nikbin et al. [11] propose a new model that takes in account the cylinder compressive strength, the concrete age and the water cement ratio. Others has proposed models based purely on numerical approaches and investigations such those conducted by Al-Saawani.M.A et al[12] who propose a model based on the Finite Element Modeling principals or even those based on cohesive approaches [13-17]. After analyzing the presented above models, it has been noticed that the generated models converge to the real behavior of concrete when more experimental parameters are taken into account. For that a lot of experimental works and researches highlighted the fracture parameters and their interchangeability with the specimen's size [18-27]. others present the concrete components impacts precisely the sand type and conclude that the sand grains shape, size and distribution can highly effect these fracture proprieties [28-32]. For our case, we are focused on three parameters which are the specimen's length, the crack initial length and the sand fines ratio considered as important and non-conventional factors. However, no model in literature (in our knowledge) has generated a relation between the fracture energy and these parameters in a hand neither define their interactions in the same model on the other one. Therefore, the present work came in the context of presenting a new analytical predictive model that defines the fracture energy in function of the mentioned above parameters and interaction's effect. It contains only experimental parameters. The model was elaborated based on experimental investigation results treated with on ANOVA and experimental Plan principles. The Database was extracted from three point bending testes done on concrete specimens through an MTS testing machine according to the ASTM norms. Studying and highlighting the effect of the specimen's length, the crack initial length and the sand classification was

extracted from the model and validated experimentally. By defining a relationship between the fracture energy and the experimental studied parameters, this works contribute on the concrete failure behavior studies as it can be used for numerical application.

2. Materials and Methods

2.1. Specimen's Geometry and Characteristics

The experimental approach of the present study is carried out in a context following the standard experimental procedures of engineering, such as those described in [33; 34]. We present here several parametric studies, where three different values for each factor were tested experimentally. All this configurations' sizes were realized according to the ASTM Norms particularly the ASTM C192/192M [35] dealing with the Standard Practice for Making and Curing Concrete Test Specimens in the Laboratory, the chosen specimens are all rectangular in shape and having the dimensions and characteristic recapitulated as follow:

2.1.1 The Specimen's Length

The tested specimen's length configurations are shown in Table 1.

Table 1. The tested specimen's lengths

The specimen's length	
S_l=160 mm	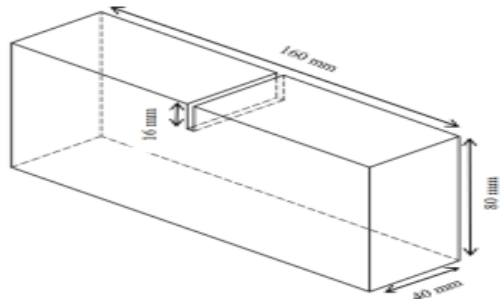
S_l=180 mm	
S_l=200 mm	

2.1.2 The Crack Initial Length

The tested crack initial length values are shown in the table below, and their size was kept as 160 x 80 x 40 mm:

Table 2. The crack initial lengths

The crack initial lengths	
C_l=1,6 mm	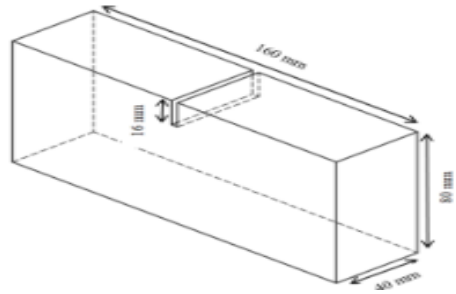
C_l=1,8 mm	
C_l=2 mm	

2.1.3 The Sand Type

This part deals with the Sand Class influence, where three different classes of sand were tested. Each class was firstly characterizing in term of chemical and granulometric composition. All the obtained tests are presented above:

- Site 01: From the Algerian center precisely the city of M'sila, the first class of samples was chosen.
- Site 02: from the Algerian East precisely the city of Khenchela, the second class of samples was chosen.
- Site 03: From the Algerian middle-south precisely the city of Djelfa, the third class of samples was chosen. The sand's type localization is presented on Table 3.

Table 3. The sand samples localization

Site 01	Site 02	Site 03

The sand samples chemical examinations have been done on laboratories specialized in sand characterization and engenders the results presenting in Table 4:

Table 4. The sand chemical compositions

Compositions (%)	Site 01	Site 02	Site 03
SiO2	92,52	94,26	89,17
Al2O3	0,54	2,04	1,21
Fe2O3	0,27	0,39	0,70
CaO	3,12	1,09	4,12
MgO	0,03	0,00	0,12
SO3	0,14	0,08	0,05

K2O	0,22	0,89	0,41
Na2O	0,01	0,23	0,01
P2O5	0,01	0,01	0,01
TiO2	0,11	0,06	0,15
MnO	0,01	0,01	0,01

For the Granulametric examinations have given the results presenting in Table 5:

Table 5. The Granulametric analysis results

Sand class	Sand Fines ratio	% Sieve /0,65µm
Site 01	1,44	1,2
Site 02	1,62	1,8
Site 03	1,86	2,6

2.2 Materials and Specimen Preparations

In this study, all specimens had been manufactured with a similar concrete mixture and procedure and that according to the ASTM C192/C192M. The main conditions imposed by this Norm and applied in our specimen's preparation can be recapitulated as follows:

- The components must be cleaned, sifted, dried and brought to a room with a temperature range of 68 to 86°F (20 to 30°C) and that even before mixing the concrete;
- The specimen molds must be installed on a rigid surface free from vibration or any other disturbances and as close as possible to the location where they will be stored for their first 24 hours. For Reusable molds, they shall be lightly coated with mineral oil or a suitable nonreactive release material before use;
- The Hand-mixed batches of concrete must be prepared in a manner that an amount of 10% will be remain as excess flow after filling the molds;
- Mix both fine and coarse aggregates with dry cement until they are thoroughly blended and the aggregates are uniformly distributed throughout the batches and that before adding the water;
- Adding water and mixing the mass until the concrete is homogeneous in appearance and has the desired consistency;
- Cover the mixed concrete in order to prevent evaporation during the specimen's full in procedure;
- Place the concrete in the molds using a scoop or a shovel; and genuinely tapping the mixture and highly vibrate the molds in order to release the extra water and to minimize as possible the air bulbs containing inside the specimen's
- The molds shall be left to dry at least for 24 Hours before getting storage.
- The specimens must be storage in a dry, free from humidity, clean from dust spaces and preferably in storage containers before carrying the tests (they must be stored at least for at least 28 days for flexural tests).

For the concrete tested mixture components and proportions, they are recapitulated in Table 6.

Table 6. Concrete component's proportions

Mixture	Values
Cement-Sand ratio (C/S)	1,11
Water-Cement ratio (W/C)	0,89

Cement (kg)	0.134
Fine aggregate 3-8 (kg)	0.515
Sand (kg)	0.429
Water (liter)	0.12

The specimen's preparation is recapitulated on the following steps:

- The specimens were realized via a normalized Wood Molds that ensures the fabrication of four specimens at time. The molds are lightly coated by a nonreactive burn oil before pouring the concrete mixture, as shown in Figures:

Fig. 1. The Wood Molds

- The components were cleaned, sifted and dried and measured according to the specimens' proportions, as shown in Figures:

Fig. 2. The components storage before mixing

- The measured components were mixed according to the ASTM C192/C192M, were the aggregates and the cement were well mixed before adding the sand and the water. The final mixture was also genuinely mixed and that in order to get an homogeneous concrete with the desired consistency, the obtained mix is shown in the picture below:

Fig. 3. The concrete mixture

- The concrete was pouring to the molds as required on the followed norm and the obtained specimens are shown in the Figure below:

Fig. 4. The specimen's concrete pouring

- The specimens were finely storage in a dry and free from dust and humidity space before transformed to the laboratory where they will be storage until the test curing.

Fig. 5. The specimen's storage

NB: it is to be mentioned that all the tests were applied on specimen's aging more than 28 days.

2.3 Experimental Procedures

The conducting experiments were a three point bending tests done according to the ASTM C293/C293M [36] and performed using an MTS testing machine one of the most efficient and well-known testing machine on the experimental fields. This testing machine uses a hydraulic system in the Crossbars displacement control the thing that offers a high stability during test, when applying small speeds, high loads or even while testing big specimens. The test curing can be controlled either manually through the control handle or automatically through the MPE software assistance. When choosing the automatically controlled tests, the MTS machine offers to users the possibility of generating their own procedure. The maximum loading can achieve a 100KN and the test can take even two hours of timing the thing that presents a high precision and detection of the smallest phenomenon that can appears during the tests. The results are also automatically generated through a data base acquisition system installed on the used software. Our tests were controlled by displacement and that for all specimens. Applying a constant displacement of 0.2 mm/min for almost an hour and fifteen (15) min ensure a high detection and precision of the obtained results. During the tests, the applied load and displacement were simultaneously recorded. Once the tests are finished, all the selected signals were outputted for treatment through a dynamic data acquisition system, the following Work chart presents the procedure applied during these tests:

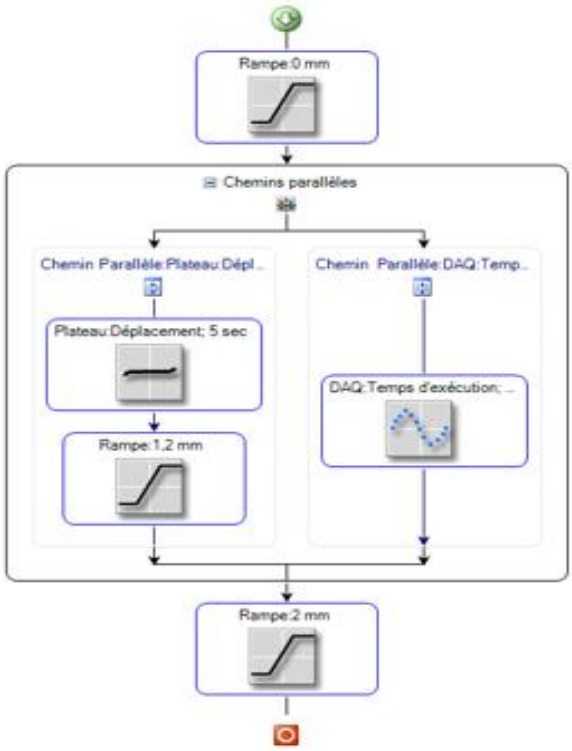

Fig. 6. The applied procedure

According to the presented above work chart, the procedure steps can be recapitulated as follow:

- Step 0: a Ramp that ensure the placement of lower Crossbars in an initial position of zero (0 mm) coordinate;

- Step 1: maintaining the lower Crossbars on obtained position from Step 0 for stabilizing the tested specimens.
- Step 2: Applying a constant Ramp to ensure a displacement from the stabilization position (0mm) to a - 1,2 mm (this position was determined after curing initial tests until defining the displacement generating the crack phenomenon and then using this value in the automatic procedure). The tests will be curing almost for an hour and fifteen min the thing that generate a tests speed equal to 0,2 mm/min (optimal speed for a stable and precise tests);
- Step 3: Releasing the cracked specimens by defining a Ramp displacement of 2 mm adequate for extracting the tested specimen.

For the testing specimen's set-up, it was done as clarified in the (ASTM C293/C293M) norms, knowing as "Standard Test Method for Flexural Strength of Concrete (Using Simple Beam with Center-Point Loading)". The tested specimens were installed on the MTS testing features according to the presented above installation norm and in accordance with the testing machine specifications, as shown in the Figure 8.

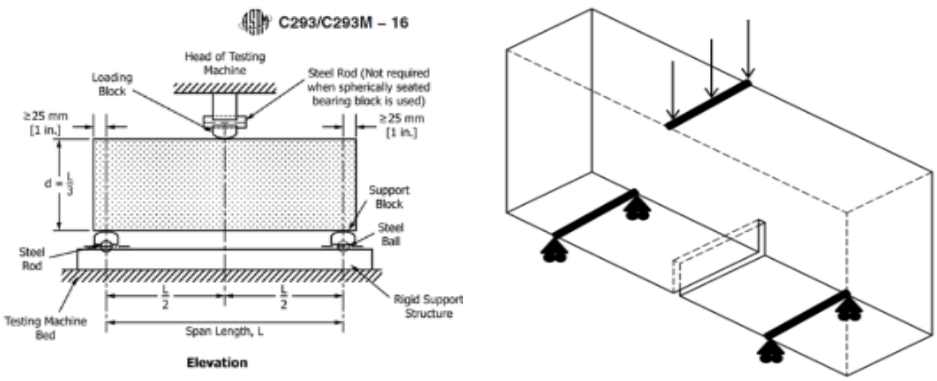

Fig. 7. The ASTMC293 three point bending tests set-up

Fig. 8. The ASTM C192 testing set-up

2.4 Experimental Results

This section includes all the obtained results, starting from the Load-Deflection curves, the parametric study results and the factors effects on the studied Fracture Energy.

- The Load-Deflection curves of the tested specimens are presented below:

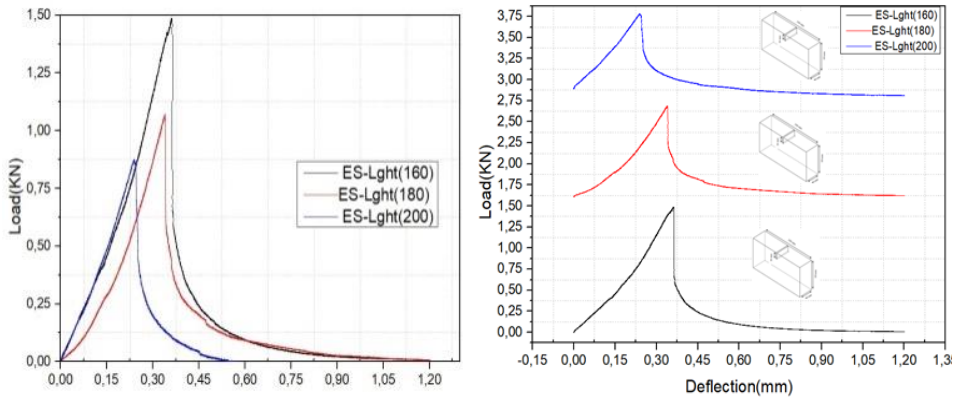

Fig. 9. Load-Deflection curve of the studied specimen's lengths

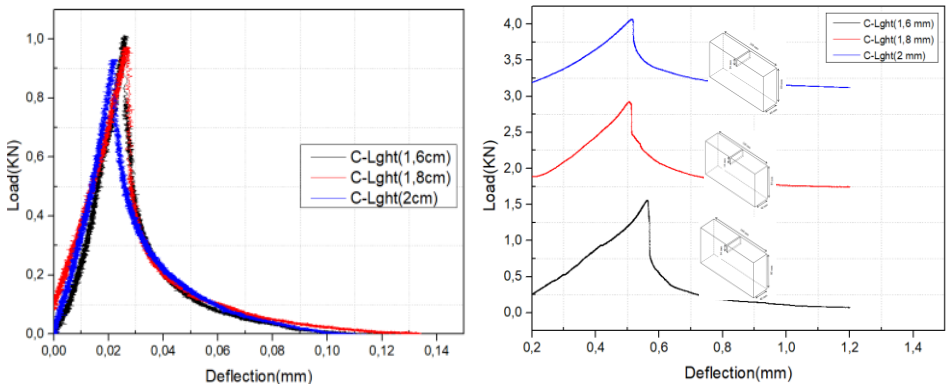

Fig. 10. Load-Deflection curve of the studied crack initial lengths

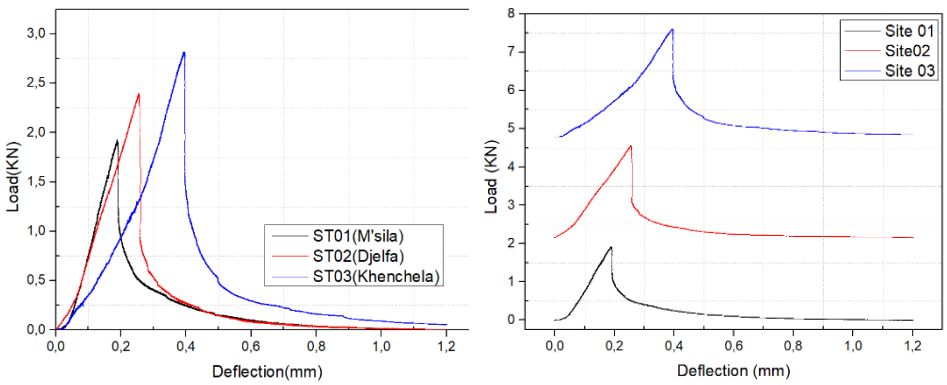

Fig. 11. Load-Deflection curve of the studied and classes

The Tables 7-9 recapitulates the fracture energies, the maximum deflections and the peak loadings for each factor and each configuration:

- The specimen's length effect on the fracture energy

The specimen's length effect on the fracture energy is presented on the Table 7:

Table 7. The specimen's length configurations

Factor	Values(mm)	P_l (KN)	$d_x\ 10^{-2}$ (mm)	G_f (GPA)
S_l	160	1,5	4,512	37,71
	180	1	4,051	32,03
	200	0,8	3,849	20,72

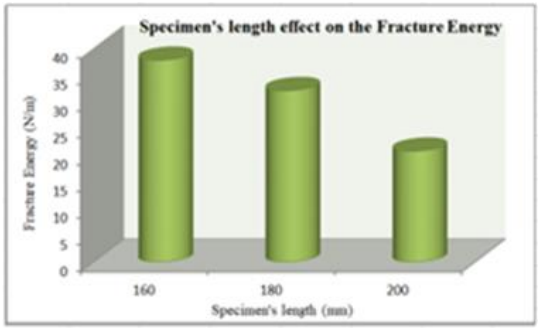

- The crack initial length effect on the fracture energy:

In Table 8, all the obtained results concerning the crack initial length effect on the fracture energy were presented:

Table 8. The Crack initial length configurations

Factor	Values	P_l (KN)	$d_x\ 10^{-2}$ (mm)	G_f (GPA)
C_l	1,6	1,013	2,228	30,64
	1,8	0,932	1,937	29,03
	2	0,875	2,308	22,71

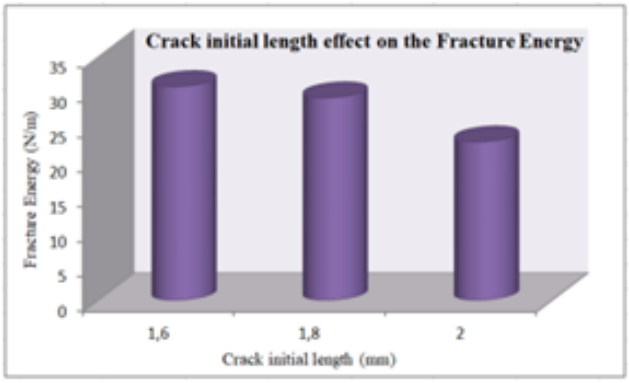

- The Sand Fines Ratio effect on the fracture energy:

The Table 9 shows the Sand fines Ratio effect on the fracture energy:

Table 9. The Sand fines ratio configuration

Factor	Values	P_l (KN)	$d_x\ 10^{-2}$ (mm)	G_f (GPA)
S_R	1,44	2	1,797	41,87
	1,62	2,4	2,480	45,59
	1,86	2,7	3,940	50,32

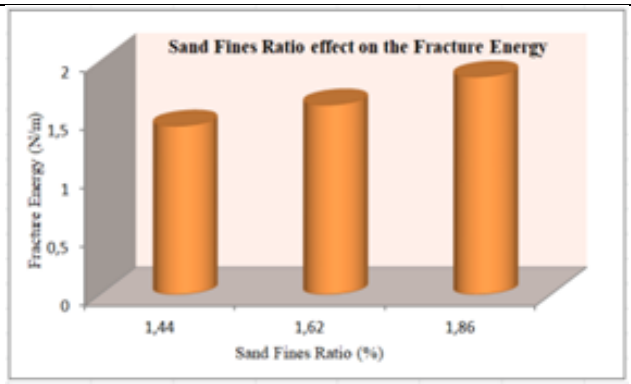

2.5 Results Discussion

For each studied parameter and configuration, the load-Deflection curves were plotted, the load maximum Deflection and the peak loading were extracted and the fracture energies were calculated. In a general contest, the presented curves were satisfying and representative; they reflect the reel behavior of concrete. The obtained results are recapitulated as follow:

- Specimen's length results: According to the presented curves and the recorded values, the fracture energies and peak loading increase while decreasing the specimen's lengths. Thus, we conclude that the augmentation on the specimen's length reduces the required energy to break it and the fracture phenomenon happens earlier.
- Crack initial length results: for this factor it has been noticed that the augmentation of the initial crack length engenders a considerable decreasing on the maximum deflection and on the fracture, energy required to generate the specimen's failure and that was clearly noticed on the fracture energy variation in function of the crack initial length. This means that the specimen's fragility depends on the crack initial length in a very considerable manner. During the bending tests a group of micro-fissures happens and their branching engenders the crack. The resultant fissure propagates where it dissipates the lower energy so it goes to the initial crack and more its initial length is bigger more it favors the specimen's failure.
- The Sand Fines Ratio results: For the sand classification and after presenting both chemical and Granulametric analysis, it has been noticed that the three samples differ majorly on their fines Ratio. This parameter has generated the results the most interesting and that because its impact was clearly appearing on both the maximum loading and the deflection causing the specimen's failure in a very considerable manner comparing to the two other parameters. The Load deflection curves show the high sensitivity of the concrete peak loading and maximum deflection to the smallest variation on the fine's ratio values. For the fracture energy histograms, the sand fines ratio augmentation engenders a considerable increase on the fracture values. This can be explained by the fact that the increasing on this Ratio increases also the mixture heterogeneity, so it makes the concrete mixture more consistent and augments its cohesion propriety.

3. Mathematical Modeling

The main objective through this section is the elaboration of an analytical model that illustrates and defines the variation of the fracture energy in term of specimen's length,

crack initial length and the send fines ratio. The model is elaborated based on experimental results and statistical methods [36]. In our case, we applied the ANOVA analysis combined with the experimental plan principles. The main steps of the model elaboration are presented below:

- Step I: before elaborating the model, it is necessary to extract experimental tests that illustrate all the possible cases and probabilities of the studied factors the thing that highlights in this case 27 tests recapitulated and presented in the Table 10:

Table 10. Experimental tests

Tests	S_R	S_l	C_l	G_f
ES-001	1,44	0,16	1,6	31,85
ES-002			1,8	28,23
ES-003			2	25,93
ES-004		0,18	1,6	27,35
ES-005			1,8	25,5
ES-006			2	24,73
ES-007		0,2	1,6	23,03
ES-008			1,8	22,53
ES-009			2	20,34
ES-001	1,62	0,16	1,6	61,17
ES-002			1,8	58,78
ES-003			2	57,69
ES-004		0,18	1,6	46,73
ES-005			1,8	46,46
ES-006			2	41,66
ES-007		0,2	1,6	38,54
ES-008			1,8	35,06
ES-009			2	34,15
ES-001	1,82	0,16	1,6	73,3
ES-002			1,8	73,3
ES-003			2	71,72
ES-004		0,18	1,6	67,91
ES-005			1,8	66,73
ES-006			2	64,67
ES-007		0,2	1,6	63,23
ES-008			1,8	62,45
ES-009			2	61,1

- Step II: the choice of the significant tests, some tests must be eliminated and that for increasing the model precision and eliminating the repetitions. The Table 11 recapitulates the chosen tests and their codification using ANOVA codes:

Table 11. The significant coded tests

Tests	S_R	S_l	C_l	$S_R * S_l$	$S_R * C_l$	$S_l * C_l$	$S_R * S_l * C_l$	G_f
ES-001	-1	-1	-1	1	1	1	-1	35,06
ES-002	-1	-1	1	1	-1	-1	1	38,54
ES-003	-1	1	-1	-1	1	-1	1	41,66
ES-004	-1	1	1	-1	-1	1	-1	50,15
ES-005	1	-1	-1	-1	-1	1	1	57,69
ES-006	1	-1	1	-1	1	-1	-1	61,1
ES-007	1	1	-1	1	-1	-1	-1	62,45

ES-008	1	1	1	1	1	1	1	64,67

It is to be clarified that the "-1" refers to the lowest value in the factors levels: the "1" refers to the highest one and the "0" code refers to the medium value.

- Step III: Finally, the model is obtained using the Rechtschaffner modeling method [38], as presented below:

$$G_f = a_0 + \sum a_i * X_i + \sum a_{ij} * X_i * X_j \quad (1)$$

After developing the Rechtschaffner approach we obtain the following equation:

$$G_f = a_0 + a_1 * X_1 + a_2 * X_2 + a_3 * X_3 + a_{12} * X_{12} + a_{13} * X_{13} + a_{23} * X_{23} + a_{123} * X_{123} + e \quad (2)$$

- Step IV: Using ANOVA calculation and the Rechtschaffner modeling method, the model coefficients, presented in Table 12:

Table 12. The model coefficients

Coefficients	a_0	a_1	a_2	a_3	a_{12}	a_{13}	a_{23}	a_{123}
Values	/	21 ,05	4,39	1,54	0,78	0,32	0,29	0,47

The final model is giving as the follows:

$$G_f = 21{,}05 * S_R - 4{,}39 * S_l - 1{,}54 * C_l - 0{,}78 * S_R * S_l + 0{,}32 * S_R * C_l + 0{,}29 * S_l * C_l - 0{,}47 * S_R * S_l * C_l + e \quad (3)$$

Where: G_f: the fracture energy, S_R; the sand fines ratio, S_l: specimen's length, C_l: crack initial length,

The proposed model shows the variation of the fracture energy in function of Sand fines ratio, the crack initial length and the specimen's length and their interactions. It is to be mentioned that the e is the global error recorded between the model and the experimental values used to adjust the proposed model. According to the models elaborated based on experimental investigation through AVOVA methods, the coefficients of each parameter and each interactions combination refers to its influence degree. The sand fines ratio is the most influential parameters because it represents the highest factor in the model formulation followed by the crack initial length and the specimen's length. For the specimen's length and the crack initial length, they present an inversely proportional relation due to their negative coefficients. The sand fines ratio engenders a proportional relation with the fracture energy variation and that because it has a positive coefficient on the model formulation. This can be explained physically by the fact that by increasing the fineness of the sand grains, the contact surfaces between these grains and the binder in concrete mixtures (in our case the cement) increase, which inevitably increases the cohesion and therefore the toughness of the material. The model shows also that the interactions between the sand ratio and the crack initial length engender a considerable impact comparing to the other combinations.

4. Validation Tests

In order to validate the proposed model supplement experiments were done and a comparison between the obtained experimental results and the model values was done in term of fracture energy, the Table 12 presents all the details:

Table 12. The validation tests

N	S_R	S_l	C_l	Exp G_f	Model G_f	R-Error
1	1,44	0,16	1,6	31,85	32,4956864	2,03%
2	1,44	0,16	1,8	28,23	32,8834976	16,48%
3	1,44	0,16	2	25,93	33,2713088	28,31%
4	1,44	0,18	1,6	27,35	32,3730992	18,37%
5	1,44	0,18	1,8	31,89	32,7593808	2,73%
6	1,44	0,18	2	33,68	33,1456624	1,59%
7	1,44	0,2	1,6	30,17	32,250512	6,90%
8	1,44	0,2	1,8	31,25	32,635264	4,43%
9	1,44	0,2	2	33,17	33,020016	0,45%
10	1,62	0,16	1,6	37,71	36,3283112	3,66%
11	1,62	0,16	1,8	37,29	36,7249568	1,52%
12	1,62	0,16	2	42,69	37,1216024	13,04%
13	1,62	0,18	1,6	46,73	36,2001836	22,53%
14	1,62	0,18	1,8	46,46	36,5949594	21,23%
15	1,62	0,18	2	41,66	36,9897352	11,21%
16	1,62	0,2	1,6	38,54	36,072056	6,40%
17	1,62	0,2	1,8	35,06	36,464962	4,01%
18	1,62	0,2	2	34,15	36,857868	7,93%
19	1,82	0,16	1,6	41,66	40,5867832	2,58%
21	1,82	0,16	2	45,59	41,3997064	9,19%
24	1,82	0,18	2	50,51	41,2609272	18,31%
25	1,82	0,2	1,6	46,16	40,318216	12,66%
26	1,82	0,2	1,8	40,23	40,720182	1,22%
27	1,82	0,2	2	38,41	41,122148	7,06%

For the validation tests, a comparison between the experimental fracture energy and the one calculated through the model was done and the relative errors between the two values were also calculated. It was found that for any value of the sand fines ratio, the specimen's length or the crack initial length, the fracture energies extracted and calculated were very close and presents a high coherence with the experimental results. The recorded Relative errors were very acceptable, where the smallest value was 0, 45% and the highest one was 28%, the thing that gives this model a high credibility and precession.

5. The Model Adjustment

After validating the model, we pass to the model adjustment using the error recorded during the validation. The error average is added to the proposed model and the new model will be compared once again to the experimental values. The new model became as follow:

$$G_f = 21{,}05 * S_R - 4{,}39 * S_l - 1{,}54 * C_l - 0{,}78 * S_R * S_l + 0{,}32 * S_R * C_l + 0{,}29 * S_l * C_l - 0{,}47 * S_R * S_l * C_l - 0{,}93 \quad (4)$$

The model adjustment results are presented in the Table 13:

Table 13. The validation tests

N	S_R	S_l	C_l	Exp G_f	Model G_f	R Error	New model	NR Error	Diff
1	1,44	0,16	1,6	31,85	32,4956864	2,03%	31,565686	0,89%	1,14%
2	1,44	0,16	1,8	28,23	32,8834976	16,48%	31,953498	13,19%	3,29%
3	1,44	0,16	2	25,93	33,2713088	28,31%	32,341309	24,73%	3,58%
4	1,44	0,18	1,6	27,35	32,3730992	18,37%	31,443099	14,97%	3,40%
5	1,44	0,18	1,8	31,89	32,7593808	2,73%	31,829381	0,19%	2,54%
6	1,44	0,18	2	33,68	33,1456624	1,59%	32,905662	2,30%	-0,71%
7	1,44	0,2	1,6	30,17	32,250512	6,90%	31,320512	3,81%	3,09%
8	1,44	0,2	1,8	31,25	32,635264	4,43%	31,705264	1,46%	2,97%
9	1,44	0,2	2	33,17	33,020016	0,45%	33,090016	0,24%	0,21%
10	1,62	0,16	1,6	37,71	36,3283112	3,66%	36,398311	3,48%	0,18%
11	1,62	0,16	1,8	37,29	36,7249568	1,52%	35,994957	3,47%	-1,95%
12	1,62	0,16	2	42,69	37,1216024	13,04%	36,191602	11,06%	1,98%
13	1,62	0,18	1,6	46,73	36,2001836	22,53%	36,270184	22,38%	0,15%
14	1,62	0,18	1,8	46,46	36,5949594	21,23%	35,664959	23,24%	-2,01%
15	1,62	0,18	2	41,66	36,9897352	11,21%	36,759735	11,76%	-0,55%
16	1,62	0,2	1,6	38,54	36,072056	6,40%	36,142056	6,22%	0,18%
17	1,62	0,2	1,8	35,06	36,464962	4,01%	35,534962	1,35%	2,66%
18	1,62	0,2	2	34,15	36,857868	7,93%	35,927868	5,21%	2,72%
19	1,82	0,16	1,6	41,66	40,5867832	2,58%	39,656783	4,81%	-2,23%
21	1,82	0,16	2	45,59	41,3997064	9,19%	41,163245	9,71%	-0,52%
24	1,82	0,18	2	50,51	41,2609272	18,31%	41,969706	16,91%	1,40%
25	1,82	0,2	1,6	46,16	40,318216	12,66%	41,922500	9,18%	3,48%
26	1,82	0,2	1,8	40,23	40,720182	1,22%	39,926713	0,75%	0,47%
27	1,82	0,2	2	38,41	41,122148	7,06%	40,330927	5,00%	2,06%

The model adjustment results show that by adding the average error to the elaborated model, the relative error has decrease considerably. The majority of the tested values had converged to the experimental ones and the new error did not exceed the 24%.

6. Conclusion

The main purpose through this work was the elaboration of an analytical model that defines the fracture energy in term of specimen's length, crack initial length and sand fines ratio and all their interaction probabilities based on experimental investigations. Based on three point bending tests through an MTS testing machine, ANOVA method and Experimental Plan principles the model was elaborated.

The experimental results can be recapitulated as follows:

- The specimen's length augmentation engenders a decrease on the fracture energy and the peak loading values.
- The crack initial length augmentation engenders a decrease on the fracture energy and the maximum deflection
- The augmentation of the sand fines ratio engenders a considerable increase on the fracture energy and presents a clear influence on both peak loading and maximum deflection point.

Concerning the modeling results, we can say that the elaborated model defines the fracture energy variation in function of the chosen parameters: the crack initial length, the specimen's length and sand fines ration and all their interaction probabilities. It shows according to ANOVA analysis that the sand fines ratio is the most influential factor and engender a proportional variation between the fracture energy and that because it has the highest coefficient in model formulation, followed by the crack initial length and finally the specimen's length. For the validation part, extra tests were done and that in order to compare the experimental fracture energy with the one calculated based on the elaborated model. A high coherence has been recorded between the two values and the recorded Relative Error doesn't exceed the 28%. These results give this model a high credibility and precession.

The elaboration of a mathematical model that engenders a relationship between the experimental parameters and the fracture energy is the main key to truly understand the concrete general behavior and a very efficient and precise manner to understand the corresponding effects engendering by the experimental or reel factors. This model is considered as the only model that relay the fracture energy to the specimen's length, the crack initial length and the sand fines Ratio with all their interaction probabilities.

Finally, it should be mentioned that the present study can offer a reliable tool contributing to the evaluation of the energy of concrete failure for researchers and graduate students wishing to use this parameter in their modelling (particularly numerical) without going through experimental tests which can be costly in terms of time and price.

References

[1] Aldahdooh MAA, Bunnori NM.Crack classification in reinforced concrete beams with varying thicknesses by mean of acoustic emission signal features. Construction and Builiding materials. 2013;45: 282-288. https://doi.org/10.1016/j.conbuildmat.2013.03.090

[2] Fronteddu L, Leger P, Tinawe R. The static and dynamic Static and Dynamic Behavior of Concrete Lift Joint Interfaces.Journal of structural Engineering.1998;124(12). https://doi.org/10.1061/(ASCE)0733-9445(1998)124:12(1418)

[3] Ibrahim M, Farhat M, Issa MA, Hass J. The Effect of Material Constituents on Mechanical and Fracture Mechanics Properties of Ultra-High-Performance Concrete. ACI Materials Journal.2017; 114(03): 453-465. https://doi.org/10.14359/51689717

[4] Landis EN.Micro-macro fracture relationships and acoustic emissions in concrete. Construction and Building Materials. 1999;13(1-2): 65-72. https://doi.org/10.1016/S0950-0618(99)00009-4

[5] Bazant ZP, Oh BH. Crack band theory for fracture of concrete. Materials and Structures. 1983;16(03):155-177. https://doi.org/10.1007/BF02486267

[6] Hillerborg A. The theoretical basis of a method to determine the fracture energy of concrete. Materials and Structure. 1985;18(4):291-296. https://doi.org/10.1007/BF02472919

[7] Comite Euro-International du Beton. CEB-FIB Model Code 1990. Thomas Telford: Lausanne,Switzerland. 1993.

[8] Bazan ZP. Concrete fracture models testing and practice. Engineering Fracture Mechanics. 2002;69(2):165-205. https://doi.org/10.1016/S0013-7944(01)00084-4

[9] Comite Euro-International du Beton. CEB-FIB Model Code 1994. Thomas Telford: Lausanne,Switzerland. 1994

[10] Japan Society of Civil Engineers. Standard Specifications for Concrete Structures 2007 ''Design". 2007; 15:1-503.

[11] Iman M, Nikbin SR, Allahyari H. A new empirical formula for prediction of fracture energy of concrete based on the artificial neural network. Engineering Fracture Mechanics. 2017;186 466-482. https://doi.org/10.1016/j.engfracmech.2017.11.010
[12] Al-Saawani MA, Al-Negheimish AI, El-Sayed AK, Alhozaimy AM.Finite Element Modeling of Debonding Failures in FRP-Strengthened Concrete Beams Using Cohesive Zone Model.Polymers.2022;14(9):1889. https://doi.org/10.3390/polym14091889
[13] Alexandridis A, Gardner NJ. The cohesion behavior development in relation with the concrete freshness. Cement and concrete Research. 1981;11(3): 323-339. https://doi.org/10.1016/0008-8846(81)90105-8
[14] Boyu C, Hongfa Y, Jinhua Z, Haiyan M, Fangming T. Effects of the embedding of cohesive zone model on the mesoscopic fracture behavior of Concrete: A case study of uniaxial tension and compression tests. Engineering failure analysis. 2022;142:106709. https://doi.org/10.1016/j.engfailanal.2022.106709
[15] De Maio U, Greco F, Leonetti L, Blasi P N, Pranno A. A cohesive fracture model for predicting crack spacing and crack width in reinforced concrete structures. Engineering Failure Analysis. 2022;139: 106452. https://doi.org/10.1016/j.engfailanal.2022.106452
[16] Haupt P.On the mathematical modeling of material behavior in continuum mechanics. Acta Mechanica.1993;100: 129-154. https://doi.org/10.1007/BF01174786
[17] Javanmardi MR, Maheri MR.Anisotropic Damage Plasticity Model for Concrete and Its Use in Plastic Hinge Relocation in RC Frames with FRP.Structures.2017; 12: 212-226. https://doi.org/10.1016/j.istruc.2017.09.009
[18] Ghasemi M, Ghasemi RM, Mousavi SR.The fracture parameters and size effect of steel fiber-reinforced self-compacting concrete.Construction and Building Materials. 2020; 201: 447-460. https://doi.org/10.1016/j.conbuildmat.2018.12.172
[19] Hua R, Wei D, Bensheng Z. Size effect on fracture properties of concrete after sustained loading.Materials and Structures. 2019; 52:16. https://doi.org/10.1617/s11527-019-1326-0
[20] Jirasek M, Rolshoven S, Grassl P.Size effect on fracture energy induced by non-locality.Numerical and analytical methods in Geomechanics.Special Issue: Computational Mechanics of Concrete and Concrete Structures. 2004;28: 653-670. https://doi.org/10.1002/nag.364
[21] Karagari A, Akhaveissy AH, Pietruszczak S .The Experimental and meso-scale investigation of size effect on fracture properties in three-point concrete beams (TPB).Theoretical and Applied Fracture Mechanics. 2023; 127: 104026. https://doi.org/10.1016/j.tafmec.2023.104026
[22] Ran Z, Syed YA, Loukili A.Experimental investigation on the correlation between the aggregate size effect and the structural size effect. Engineering Fracture Mechanics. 2020;234:107101. https://doi.org/10.1016/j.engfracmech.2020.107101
[23] Scorza D, Ronchei C, Vantadori S, Zanichli A.The Size-effect independence of hybrid fiber-reinforced roller-compacted concrete fracture toughness. Composites Part C: Open Access. 2022; 9: 100306. https://doi.org/10.1016/j.jcomc.2022.100306
[24] Yi C, Xiaozhi H. The interchangeability and selection of size effect and boundary effect experiments for characterization and prediction of quasi-brittle fracture of concrete.Theoretical and Applied Fracture Mechanics. 2020;122:103629. https://doi.org/10.1016/j.tafmec.2022.103629
[25] Kai D, Xiaozhi H, Wittmann FH. Size effect on specific fracture energy of concrete. Engineering Fracture Mechanics. 2007; 4: 87-96. https://doi.org/10.1016/j.engfracmech.2006.01.031
[26] Norashidah AR, Zainorizuan MJ, Zahir NNM.Fracture energy of foamed concrete by means of the three-point bending tests on notched beam specimens.ARPN Journal of Engineering and Applied Sciences. 2015;10(15):6562-6570.

[27] Dubey S, Ray S. Influence of heterogeneity on size effect models and fracture characteristics of plain concrete.Theoretical and Applied Fracture Mechanics.2023; 127: 103993. https://doi.org/10.1016/j.tafmec.2023.103993
[28] Belhadj B, Bederina M, Benguettach KH, Queneude M.Effect of the type of sand on the fracture and mechanical properties of sand concrete.Advances in Concrete Construction. 2014;2(1): 13-27. https://doi.org/10.12989/acc2014.2.1.013
[29] Hao Z, Zhe X, Yuying S, Lijuan L, Qiu Y, Xiaozhou Z, Bing C, Dongen C, Feng L,Yidong J.The Early mechanical performance of glass fiber-reinforced manufactured sand concret.Journal of Building Engineering. 2024;83:108440. https://doi.org/10.1016/j.jobe.2024.108440
[30] Konstantoni C, Paneda EM, Biscontin G, Flek NA.The Fracture of bio-cemented sands.Extreme Mechanics Letters. 2023;64:102086. https://doi.org/10.1016/j.eml.2023.102086
[31] Mingming Z, Jin XML, Xiapsa Y.The Influence of Stone Powder Content from Manufactured Sand Concrete on Shrinkage, Cracking, Compressive Strength. Buildings.2023; 13(7), 1833. https://doi.org/10.3390/buildings13071833
[32] Hashimoto R, Onoue K.The Crack Resistance of Concrete Using Granulated Blast Furnace Slag Sand under Flexural Stress. Proceeding in Civil Engineering. 21st ibausil International Conference on Building Materials, Ibausil, 825-832, 2023. https://doi.org/10.1002/cepa.2832
[33] Davim JP.Computational Methods and Production Engineering. Woodhead Publishing Reviews: Mechanical Engineering Series Elsevier,2017,I SBN 978-0-85709-481-0.
[34] Davim JP.Design of Experiments in Production Engineering. Springer, 2016,ISBN 978-3-319-23838-8.
[35] The ASTM C192/192M dealing with the Standard Practice for Making and Curing Concrete Test Specimens in the Laboratory
[36] The ASTM C293/C293M "Standards Test methods for flexural strength of Concrete (using simple beams with third point loading)".
[37] Davim JP.Statistical and Computational Techniques in Manufacturing. Springer,2012,ISBN 978-3-642-25859-6.
[38] Xianggui Q. Statistical properties of Rechtschaffner designs. Journal of Statistical Planning and Inference.2007; 137 (7): 2156 - 2164. https://doi.org/10.1016/j.jspi.2006.06.042

Blank Page

Research on Engineering Structures & Materials
www.jresm.org
Research Group

Research Article

Evaluation of CFRP confinement performance and predictive accuracy of design codes and stress-strain models for concrete

Abdellah Douadi [*,1,a], Riad Babba [2,b], Kamel Hebbache [1,c], Mourad Boutlikht [1,d], Nour El Houda Khitas [1,e], Abderraouf Messai [1,f], Redha Hammouche [3,g]

[1]*Civil Eng. Research Laboratory of Setif (LRGCS), Dept. of Civil Eng., Ferhat Abbas University of Setif 1, Algeria*
[2]*Faculty of Science and Technology, University of Tamanghasset, Algeria*
[3]*Materials and Durability of Construction Laboratory, Dept. of Civil Eng., Faculty of Science and Technology, Frères Mentouri University of Constantine 1, Algeria*

Article Info

Article history:

Received 06 Sep 2024
Accepted 05 Nov 2024

Keywords:

CFRP confinement;
Stress-strain models;
Design codes;
Concrete reinforcement

Abstract

This research investigates the effectiveness of different CFRP confinement types full, horizontal, and spiral and assesses the accuracy of various design codes and stress-strain models in predicting the performance of CFRP-confined concrete. Experimental results show that fully CFRP-confined specimens exhibit a significant increase in compressive strength by 89.36% compared to unconfined concrete, which had a compressive strength of 21.42 MPa, while horizontal CFRP strips with 30 mm spacing provide notable improvements in both strength (49.53% increase) and axial strain (610.78% increase). In contrast, spiral CFRP strips demonstrated lower effectiveness. Numerical evaluations revealed that the FIB model was accurate for horizontal confinements but overestimated compressive strength for spiral confinements. The ACI code offered reasonable predictions with deviations between -16% and 19%. Pellegrino et al and Wang et al. models performed well for horizontal CFRP strips but were less accurate for spiral configurations. The model proposed by Guo et al. overestimated the compressive strength for partially confined specimens. This study provides insights for optimizing CFRP confinement strategies and highlights the need for refinement in predictive models and design codes.

© 2025 MIM Research Group. All rights reserved.

1. Introduction

Civil engineers frequently confront the critical task of maintaining and rehabilitating existing concrete structures that have sustained damage due to material degradation, natural disasters, or inherent design deficiencies [1]. The need to enhance the durability and load-bearing capacity of such structures has led to the increasing adoption of fiber-reinforced polymers (FRPs) as reinforcement materials. FRPs, characterized by their exceptional strength-to-weight ratio, high corrosion resistance [2, 3], and outstanding ductility, have demonstrated significant potential in extending the service life of concrete structures, particularly under adverse environmental conditions and loadings [3, 4].

The damage caused by earthquakes, particularly in reinforced concrete structures, has further emphasized the urgent need for reinforcement, especially in buildings constructed with low-strength concrete [5, 6]. Earthquakes generate significant lateral and vertical forces that can severely compromise the structural integrity of these structures, leading to cracking, spalling, and even catastrophic collapses [7, 8]. The devastating 2023 Turkey-

[*]Corresponding author: abdellah.douadi@univ-setif.dz
[a]orcid.org/0000-0002-7761-8488; [b]orcid.org/0000-0001-8742-1403; [c]orcid.org/0000-0002-4409-3689; [d]orcid.org/0000-0003-0808-6438; [e]orcid.org/0009-0002-8854-4266; [f]orcid.org/0000-0002-5769-2218; [g]orcid.org/0009-0004-4458-8309
DOI: http://dx.doi.org/10.17515/resm2024.435me0906rs

Syria earthquake serves as a stark reminder of the consequences of inadequate reinforcement and the use of substandard materials, which contributed to widespread destruction and tragic loss of life [9]. Reinforcing low-strength concrete structures is essential for improving their ductility, energy dissipation, and overall resilience to seismic loads [10]. This need for reinforcement arises from concrete's inherent limitations, as it is strong in compression but weak in tension and shear. To overcome these weaknesses, various types of reinforcement have been developed and applied [11, 12].

Traditional steel reinforcement, such as rebar, has long been the standard in providing the tensile strength necessary to prevent cracking and improve the structural performance of concrete [13]. However, steel reinforcement is prone to corrosion, especially in aggressive environments, and its weight can pose challenges in some applications [14]. As a result, alternative reinforcement materials, such as fiber-reinforced polymers (FRPs), have gained prominence in recent years. FRPs, which include carbon fiber-reinforced polymers (CFRPs), glass fiber-reinforced polymers (GFRPs), and aramid fiber-reinforced polymers (AFRPs), offer several advantages over steel, including superior corrosion resistance [15, 16], a high strength-to-weight ratio, and ease of application in retrofitting projects. These materials are particularly effective in seismic retrofitting, where their ability to provide confinement and tensile reinforcement helps prevent premature failure, enhance ductility, and improve the overall earthquake resistance of structures [17]. Other types of reinforcement include textile-reinforced concrete (TRC), which integrates high-strength fibers into concrete matrices [18], and prestressed reinforcement, where steel or FRP tendons are tensioned to impart compressive stresses, further enhancing the structural capacity and reducing deflection. Together, these different types of reinforcement play a crucial role in improving the safety, durability, and performance of concrete structures, particularly in regions prone to seismic activity [19].

The foundational research on the application of FRPs in concrete confinement can be traced back to the pioneering work of Wolf and Miessler [20-22]. Their studies established the baseline understanding of how FRPs interact with concrete, providing the impetus for extensive subsequent research aimed at optimizing these interactions [23]. Over the past few decades, a substantial body of research has emerged, exploring the mechanical properties, durability, and effectiveness of various FRP materials, particularly carbon fiber-reinforced polymers (CFRPs), in strengthening concrete structures [4, 24]. The confinement provided by CFRP has been shown to significantly enhance both the compressive strength and ductility of concrete, primarily due to its ability to induce a three-dimensional compressive stress state within the concrete matrix [25, 26]. This confinement mechanism delays the onset of cracking and significantly mitigates the propagation of micro-cracks, thereby altering the failure mode of concrete from a brittle to a more ductile response [27, 28].

Extensive research efforts have focused predominantly on the effects of full FRP confinement, where the concrete column is entirely encased by the FRP material [29]. This method has been shown to yield significant improvements in key structural performance metrics, including load-carrying capacity, ductility, energy dissipation, and failure mode [30]. However, the practical application of full confinement is often limited by economic factors, access constraints, and architectural considerations [31]. Consequently, partial confinement methods have garnered increased attention as they offer a more resource-efficient alternative while still providing substantial performance benefits. Partial confinement typically involves the strategic application of FRP in discrete strips or bands, spaced at intervals along the length of the column, rather than a continuous wrap [32, 33]. This approach is particularly advantageous in scenarios where full wrapping is impractical or unnecessary.

Recent studies have investigated a variety of partial confinement configurations, such as horizontal strips, spiral bands, and grid patterns [34, 35]. These studies have provided valuable insights into how different confinement patterns and configurations influence the structural performance of concrete columns. Key findings indicate that the effectiveness of partial confinement is highly dependent on several factors, including the spacing of the FRP strips, the orientation of the fibers, and the overall geometry of the confinement pattern [36]. In particular, spiral confinement has shown promise in enhancing concrete's axial strength and ductility, with fewer issues related to debonding and void formation compared to other methods [37]. Nonetheless, while partial confinement methods offer notable advantages, the research remains relatively limited in scope, particularly when it comes to comparing their performance directly with full confinement techniques. Furthermore, existing design codes and stress-strain models have been primarily developed for fully confined concrete, with limited provisions or guidelines for partially confined structures. This gap in the current literature and design standards underscores the need for further research to develop and validate predictive models that accurately capture the behavior of partially confined concrete under various loading conditions.

The present study seeks to address these gaps by conducting a comprehensive investigation into the effects of partial CFRP confinement on concrete columns. Specifically, this research will examine two prevalent modes of partial confinement: horizontal strip confinement and spiral band confinement. The study will systematically compare the structural performance of columns subjected to these partial confinement methods with those of unconfined and fully confined columns. Key performance indicators, such as failure modes, stress-strain behavior, ultimate axial stress, and strain capacities, will be meticulously analyzed. The findings are expected to contribute to a deeper understanding of how partial CFRP confinement can be optimized to achieve maximum structural benefits while minimizing material usage and cost. Ultimately, the insights gained from this study will inform the development of more nuanced design guidelines and stress-strain models, thereby enhancing the practical application of FRP reinforcement in the retrofitting and strengthening of concrete columns in real-world scenarios.

2. Materials and Methods

The concrete mix was designed using the Dreux-Gorisse method, a well-established procedure in concrete mix design [38]. The particle size distribution of the aggregates, sands, and cement used in the mix was determined through particle size analysis tests, conducted in accordance with the NF EN 933-1 standard [39]. Table 1 provides a detailed overview of the mix design, including the proportions of each component, as well as the principal properties of the resulting concrete. This methodical approach ensures a well-graded mix that meets the specific requirements for both workability and strength.

Table 1. Mix proportions and characteristics of the concrete used

Component	Quantity
Cement (kg/m^3)	210
Water (kg/m^3)	115.5
Coarse aggregate 3/8 (kg/m^3)	218.68
Coarse aggregate 8/15 (kg/m^3)	977.06
Coarse Sand 0/3 (kg/m^3)	847.24
Water-to-Cement Ratio (W/C)	0.55
Compressive Strength, f_{co} (MPa)	21.42
Ultimate Strain, ε_{co} (%)	0.761

The mechanical properties of the carbon fiber-reinforced polymer (CFRP) composite, comprising both the fabric and the resin, were evaluated through standardized coupon testing.

Table 2. Properties of SikaWrap-230C/45 fabric

Property	Value
Tensile Strength (MPa)	4.300
Tensile Modulus (MPa)	234.000
Ultimate Elongation (%)	1.8
Fiber Density (g/cm^3)	1.76
Fabric Thickness (mm)	0.13

Table 3. Properties of Sika Dur 330 resin

Property	Value
Density (kg/l)	1.30
Tensile Strength (MPa)	> 30
Bond Strength to Concrete (MPa)	> 4
Elastic Modulus (MPa)	
- Flexural	3.800
- Tensile	4.50

Table 4. Mechanical properties of CFRP composite

Property	Value
Thickness of CFRP Composite t_f (per layer) (mm)	1
Elastic Modulus E_f (MPa)	34900
Tensile Strength f_{pr} (MPa)	480
Ultimate Strain ϵ_{fu}	2%

The results, detailed in Table 4, provide a comprehensive assessment of the composite's performance characteristics, including tensile strength, elasticity, and overall durability, crucial for understanding its behavior under various loading conditions. A total of cylindrical concrete specimens, each with a height of 320 mm and a diameter of 160 mm, were prepared and divided into eight distinct groups. Each configuration was tested three times to ensure statistical reliability. The confinement methods investigated included both full and partial confinement, employing horizontal and spiral bands. For partial confinement, the study evaluated parameters such as band spacing, the orientation of the bands relative to the horizontal, and the quantity of CFRP material used. In the experimental program, a consistent band width of 30 mm of unidirectional CFRP was used across all specimens, with the band spacing set at 30 mm, 45 mm, and 65 mm for both horizontal and spiral confinement methods. For specimens subjected to spiral partial confinement, additional reinforcement was applied at the specimen ends using a supplementary layer of unidirectional CFRP bands, each 20 mm wide, to improve end confinement and prevent premature failure. The labeling of the specimens followed a systematic convention: the first letter indicates the type of confinement (e.g., partial or

full), the second letter specifies the confinement method (horizontal or spiral), the third letter refers to the mode of confinement (e.g., uniform or partial), and the final numeral denotes the band spacing in millimeters. This standardized labeling ensured clear identification of each test configuration and its corresponding mechanical performance results.

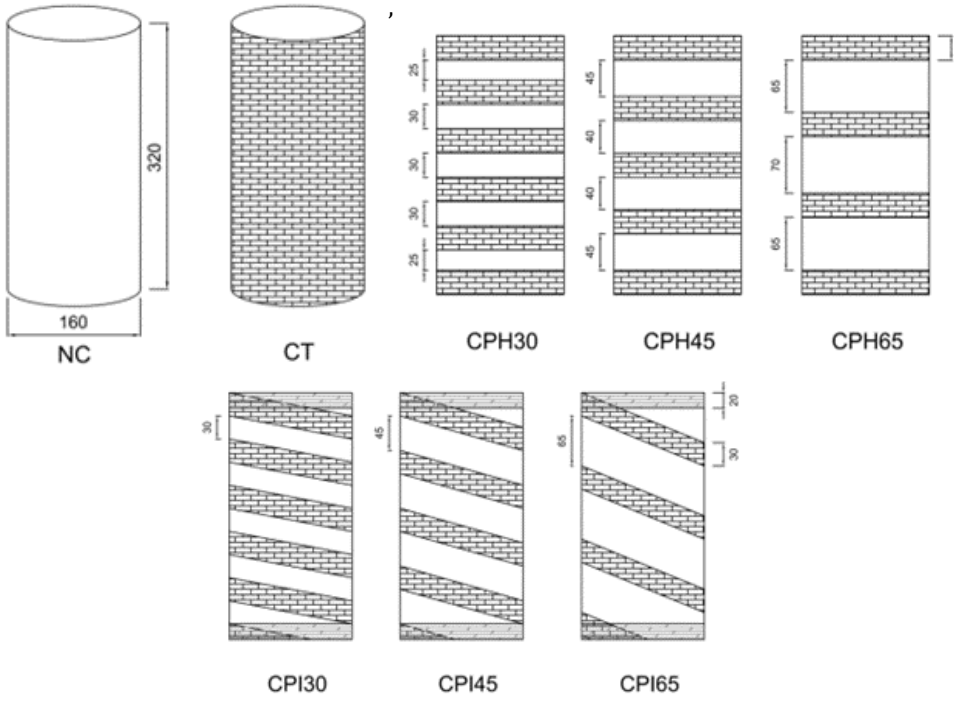

Fig. 1. Aspect of different confined configurations

For example, CPH45 denotes specimens partially confined with horizontal bands spaced 45 mm apart. Detailed confinement arrangements are illustrated in Figure 1. Compression tests were conducted using a universal testing machine (MCC8) with a capacity of 3000 kN, applying a controlled load increase rate of 0.5 MPa/s, as depicted in Figure 2. The positions of the bands on the specimens were marked using adhesive tape on the concrete surface (Figure 2). To ensure optimal contact between the load cell and the specimen, high-strength sulfur was used (Figure 2). Axial displacement measurements were recorded using three linear variable differential transformers (LVDTs) placed at mid-height (Figure 2). All confined specimens were overlapped by 150 mm according to the technical specifications of the SikaWrap-230C/45 fabric. They were cured at ambient laboratory conditions for 7 days to allow the epoxy resin to achieve full strength before testing. The abbreviations used to identify the specimen series are as follows:

- NC: Non-confined cylinders.
- CT: Cylinders fully confined with a single layer of CFRP.
- CP: Partially confined cylinders, where the second part of the code indicates either H for horizontal bands or I for spiral bands, and the third part specifies the spacing between bands (30 mm, 45 mm, or 65 mm). For instance, CPH45 refers to cylinders partially confined with horizontal bands spaced 45 mm apart.

Fig. 2. Methodology of CFRP application

3. Results and Discussion

3.1. Stress-Strain Behavior

Figure 3 presents the stress-strain behavior of all studied groups. Axial strains were determined using LVDTs, with the measurements obtained from three LVDTs placed at mid-height, as recommended by various researchers [40].

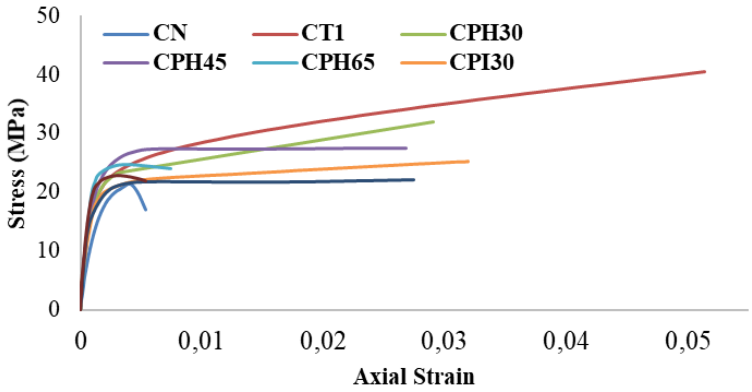

Fig. 3. Stress-Strain curves of all groups

Figure 3 displays the stress-strain curves for fully confined cylinders using CFRP composites. These curves reveal an initial ascending phase followed by a stress-softening branch. Conversely, the stress-strain behavior of partially confined concrete, shown in Figure 4, typically follows a bilinear pattern with hardening until failure (CFRP rupture). Initially, the curves exhibit linear behavior, dominated by the unconfined concrete's strength, indicating minimal activation of the CFRP confinement due to negligible lateral expansion. As the concrete experiences lateral expansion and increased axial strains, the response transitions to nonlinear. CFRP confinement becomes effective after the

unconfined concrete reaches its ultimate strength (fco= 21.42 MPa), resulting in additional cracking and a reduction in concrete stiffness.

For specimens with horizontal CFRP strips spaced 30 mm apart, the stress continued to rise linearly with a gradual slope until failure (f_{cc}= 32.03 MPa), as shown in Figure 4. At this point, the concrete was fully cracked, and CFRP confinement was fully engaged, leading to enhanced load capacity, increased compressive strength, and significantly improved ductility. Specimens partially confined with horizontal CFRP strips spaced 45 mm apart exhibited a bilinear stress-strain response with significant ductility, maintaining a consistent slope until failure at 27.4 MPa, as illustrated in Figure 4. The final stress at failure was substantially higher than the unconfined concrete strength, indicating effective confinement.

For specimens with strips spaced 65 mm apart (Figure 4), the stress-strain curves displayed a descending branch characterized by stress softening up to failure. The concrete sustained a portion of the axial load after reaching a peak strength of 24.71 MPa, but the strength gradually decreased until failure occurred at 23.84 MPa, slightly above the unconfined concrete strength (f_{co} = 21.42 MPa). Therefore, the confinement level was still deemed adequate.

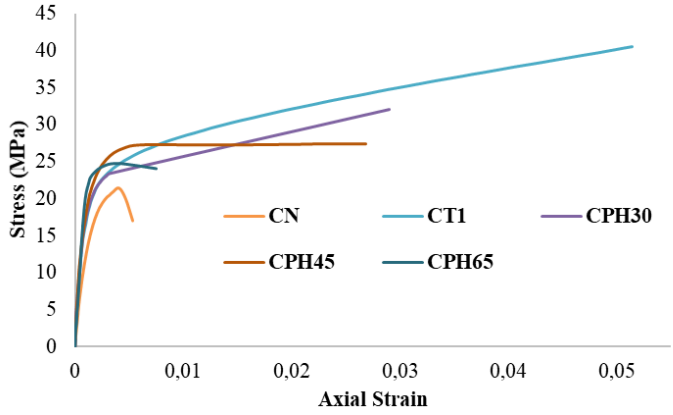

Fig. 4. Stress-Strain curves of horizontally confined groups

Figure 5 compares the stress-strain curves of partially confined cylinders with CFRP strips inclined at various angles to the horizontal. Each group has different spacings between the CFRP strips, resulting in different inclination angles, enabling a direct comparison between the series. As depicted in Figure 5, the stress-strain behavior of these specimens initially followed a linear path, similar to that of unconfined samples. For specimens with 30 mm and 45 mm spacings, the stress-strain curves exhibited a bilinear pattern with notable axial strain softening up to failure. The final stress at failure slightly exceeded the ultimate strength of the unconfined concrete.

For specimens with inclined CFRP strips spaced 65 mm apart (CPI65), the stress-strain curves displayed a short descending branch leading up to failure, with observable axial strain softening. These curves closely resemble those of specimens with horizontal CFRP strips spaced 65 mm apart (CPH65). Figures 3 to 5 demonstrate that the stress-strain curves for CFRP-confined concrete generally consist of two distinct segments, with the second segment either ascending or descending. In most specimens, the axial stresses increase monotonically until failure.

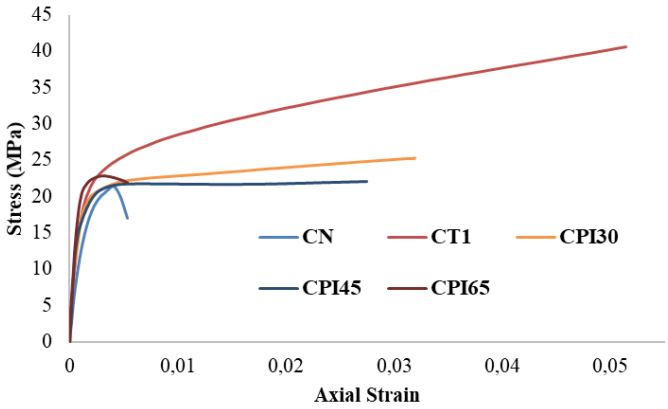

Fig. 5. Stress-Strain curves of spirally confined groups

However, only the stress-strain curves of the specimens with horizontal and inclined CFRP strips spaced 65 mm apart (CPH65 and CPI65) exhibit a descending branch. The relatively low volumetric ratios of CFRP applied in these two series are insufficient to produce a monotonically ascending stress-strain behavior. The volumetric ratio of CFRP is defined as:

$$\rho_f = \frac{A_f \pi D}{(\pi D^2/4)} = \frac{4 b_f n t_f}{DS} \quad (1)$$

Where: b_f, n_f, t_f represent the width of the FRP bands, the number of FRP layers, and the thickness of the FRP used for the confinement of the cylinder, respectively. D and S refers to the diameter and cross-sectional area of the column.

For specimens with a 65 mm spacing, the level of confinement approaches the threshold of inadequacy, leading to a reduced strength gain. In contrast, specimens with sufficient confinement, achieved through smaller spacings of 30 mm and 45 mm, exhibit significantly enhanced compressive strength and ultimate axial strain due to the more effective confinement.

3.2. Failure Mode

The groups exhibited distinct failure modes, as illustrated in Figure 6:

- Non-confined cylinders (NC): Failure initiation occurred through inclined cracking within the concrete, ultimately leading to concrete crushing as the primary failure mode (Figure 6-a).
- Fully confined cylinders (CT): The CFRP failed locally at mid-height due to concentrated lateral confinement, resulting in a sudden CFRP rupture accompanied by a significant explosion (Figure 6-b).
- Partially confined cylinders with 65 mm spacing (CPH65 and CPI65): These specimens predominantly failed through concrete crushing. Cracks formed between adjacent CFRP strips as the axial stress approached the strength of unconfined concrete, with the failure mode being characterized by diagonal shear cracking (Figures 6-c and 6-d).
- Partially confined cylinders with horizontal or spiral CFRP strips (CPH30, CPI30, CPH45, and CPI45): These specimens experienced CFRP strip rupture at mid-height due to tensile stress. The failure was marked by the disintegration of the concrete core, resulting in a conical cracking mode (Figures 6-e to 6-h).

- Cylinders subjected to compression: Failure occurred suddenly and explosively following CFRP composite rupture. The concrete adhered to the CFRP composite, indicating strong adhesion between the two materials (Figure 6). Post-explosion, intact CFRP strips were observed in several specimens.

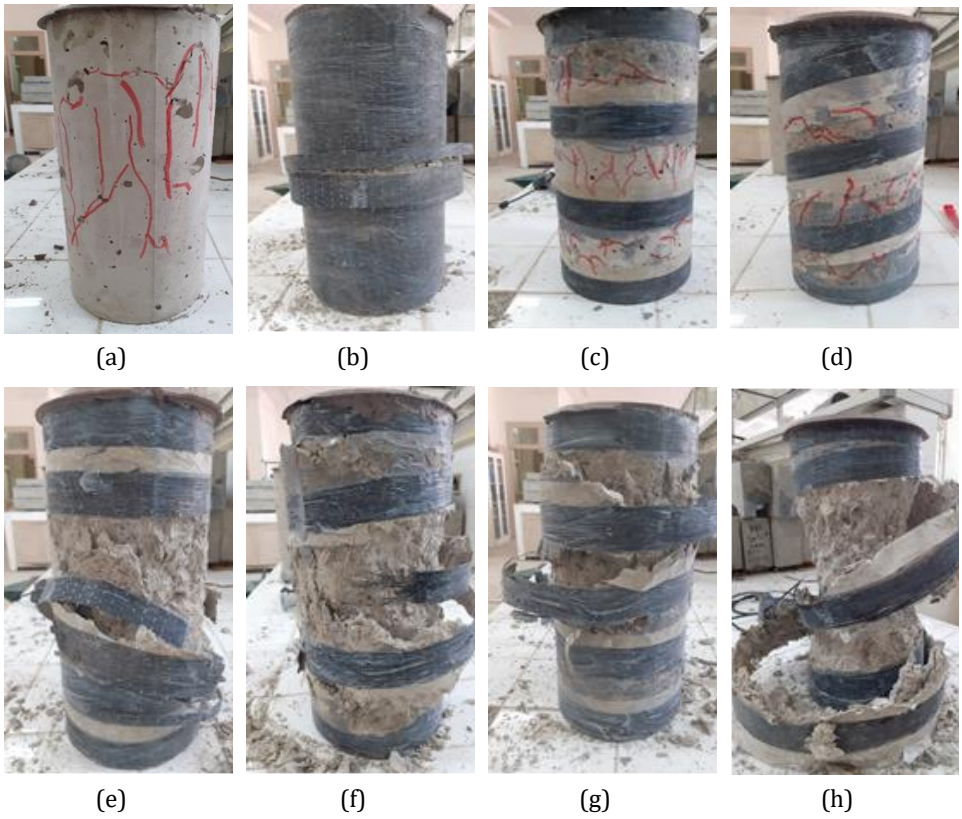

Fig. 6. Failure modes of specimens

Additionally, CFRP rupture did not occur at the cylinder ends due to the increased friction from the loading platens near both ends, as noted by Teng et al. (2015b). This expanded explanation provides a clearer understanding of the failure mechanisms across different confinement scenarios, highlighting the influence of CFRP strip spacing and orientation on the overall structural behavior. The observations underscore the critical role of adequate confinement in enhancing the load-bearing capacity and failure resistance of concrete cylinders.

3.3. Effect of Strip Spacing on Partial Confinement

Figure 7 provides a summary of the average compressive strength values and axial strains for all studied samples. It is evident that both partial and full CFRP confinement significantly enhance the ultimate compressive strength of the specimens compared to unconfined samples. The fully CFRP-confined cylinders demonstrated the highest strength improvement, with an increase of 89.36%. Among the partially confined specimens, those with horizontal CFRP strips spaced 30 mm apart showed the most substantial strength improvement, with a 49.53% increase over unconfined samples. This result indicates that the compressive strength of partially confined CFRP samples is approximately 21.03% lower than that of fully confined samples. However, this difference is relatively minor

considering the material savings achieved. Additionally, this configuration exhibited a 610.78% increase in axial strain compared to unconfined samples, although this is 43.56% lower than the axial strain observed in fully confined CFRP specimens. The effect of increased horizontal spacing on maximum axial strain was also apparent. Specimens with 45 mm and 65 mm spacing showed increases in displacement of approximately 556.48% and 106.40%, respectively.

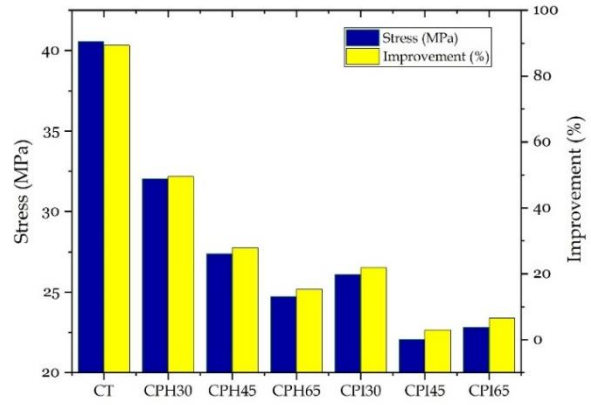

(a)

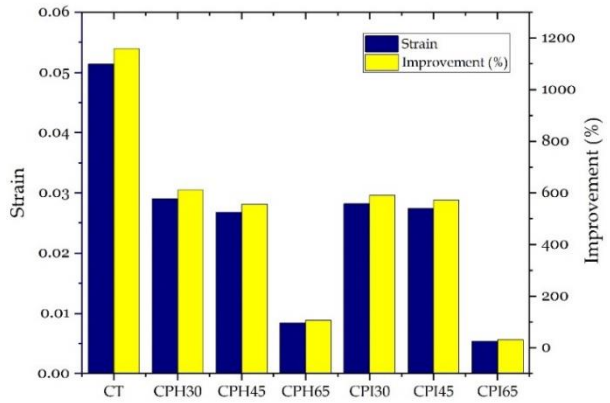

(b)

Fig. 7. Summary of experimental results compared to unconfined cylinders

For cylinders confined with spiral CFRP strips, the compressive strength results were more nuanced. The strength increased by 3.03% with 45 mm spacing and by 6.58% with 65 mm spacing. Although these values were lower compared to those with horizontal CFRP strips, a maximum strength increase of 21.90% over unconfined concrete was observed. The relationship between spiral spacing and ultimate axial strain was also evident, with displacement increasing as the spacing between spiral bands decreased. Specifically, axial strains increased by 591.42% at 30 mm spacing, 572.67% at 45 mm, and 30.47% at 65 mm spacing. Unconfined concrete had an axial strain of 0.00408, whereas the highest axial strains recorded were 0.0514 for fully confined specimens and 0.029 for all partial confinement configurations. This analysis underscores the significant impact of CFRP confinement on enhancing the compressive strength and axial strain capacity of concrete specimens, with the degree of improvement closely related to the confinement

configuration and the spacing of the CFRP strips. In addition to their impact on compressive strength, CFRP confinement techniques can also influence the bending and shear performance of concrete elements. Research has shown that CFRP reinforcement not only improves the flexural capacity of beams but also enhances shear strength, particularly in cases where transverse reinforcement is insufficient. These improvements are attributed to the ability of CFRPs to provide lateral confinement, reduce crack propagation, and enhance the overall ductility of concrete members. Thus, incorporating CFRP in both bending and shear applications presents a comprehensive solution for strengthening concrete structures.

3.4. Comparative Analysis of Strength Performance Between Full and Partial CFRP Confinement

Figure 8 presents a detailed comparison of the strength enhancements achieved through full versus partial CFRP confinement. The analysis reveals a strength differential of -21.03% between specimens confined with horizontal CFRP strips spaced at 30 mm and those fully confined with CFRP, where the composite material used in partial confinement represents less than half of the amount employed in full confinement. Despite the reduced material usage, the partially confined specimens exhibited a significant level of effectiveness in enhancing the compressive strength of the concrete cylinders.

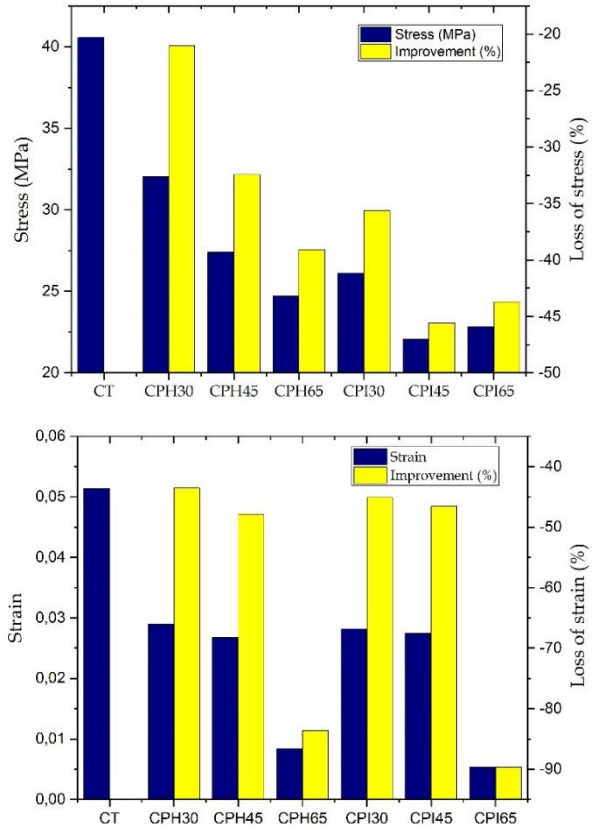

Fig. 8. Summary of experimental results relative to fully confined cylinders

The results indicate that the CPI45 specimen, with a strength improvement -45.59% lower than fully confined concrete, exhibited the least favorable performance among the partially confined samples. Notably, partial confinement using horizontal CFRP strips consistently outperformed spiral CFRP strip configurations in terms of strength enhancement. These findings underscore the efficacy of partial CFRP confinement, particularly with horizontal strips, in achieving substantial strength gains while optimizing material efficiency. The observed performance suggests that partial confinement can be a viable alternative to full confinement, offering a balance between structural enhancement and material economy.

3.5. Numerical Verification

Tables 5 and 6 present the ($\frac{\Delta f_{cc}}{f_{cc,exp}}$) between the theoretical maximum compressive strength $f_{cc,thé}$ and the experimental maximum compressive strength $f_{cc,exp}$for three design codes and three models of CFRP-confined concrete under axial compression ($\Delta f_{cc} = f_{cc,thé} - f_{cc,exp}$). Most predictions related to the compressive strength of CFRP-confined concrete appeared conservative compared to the experimental strength, with prediction results generally varying between 19% and -2% for horizontal partial confinement, though predictions for full confinement were somewhat less accurate. Despite these results, the models were still able to provide the best prediction for horizontal partial confinement, where the prediction values were closely aligned, ranging between -2% and 4%, with a maximum difference of 1 MPa. However, predictions for fully CFRP-confined concrete were overestimated by 20% when using the FIB model [41] .

Although the ACI code [42] does not account for partial confinement factors and fiber orientation reduction, the CFRP horizontal and spiral strip positions were considered using the k_e coefficient from the FIB model. The predicted confinement strength for most specimens remained within the range of -16% to 19%. Generally, the values predicted using the ACI code were very close to those of the CSA S806 code [43] and higher than those predicted by the FIB code for most samples. Nevertheless, the FIB model provided a more accurate prediction of confinement strength, particularly for partially CFRP-confined concrete, compared to the CSA S806 and ACI codes.

Table 5. Verification of design codes against experimental results

	b_f (mm)	s (mm)	Experimental	FIB Standard		CSA S806 standard		ACI Standard	
			$f_{cc,exp}$ (MPa)	$f_{cc,thé}$ (MPa)	$\frac{\Delta f_{cc}}{f_{cc,exp}}$	$f_{cc,thé}$ (MPa)	$\frac{\Delta f_{cc}}{f_{cc,exp}}$	$f_{cc,thé}$ (MPa)	$\frac{\Delta f_{cc}}{f_{cc,exp}}$
CT	/	/	40.56	48.83	20%	33.70	-17%	44.82	11%
CPH30	30	30	32.03	32.83	2%	31.36	-2%	40.64	27%
CPH45	30	45	27.4	28.50	4%	30.25	10%	38.70	41%
CPH65	30	65	24.71	24.23	-2%	28.83	17%	36.28	47%
CPI30	30	30	26.11	35.73	37%	33.65	29%	44.76	71%
CPI45	30	45	22.07	32.41	47%	33.65	52%	44.76	71%
CPI65	30	65	22.83	29.27	28%	33.65	47%	44.76	71%

The models proposed by Pellegrino et al [44] and Wang et al. [45] recommend using the k_e coefficient from FIB to account for the effect of strip spacing. These two models provide reasonable predictions for partially CFRP-confined concrete with horizontal strips, with the ratio between experimental and theoretical results ranging from 0% to 10% and 1% to 8%, respectively, with a maximum difference of 4 MPa and 2 MPa for the Pellegrino & Modena (2010) and Wang et al. [45] models, respectively. However, the stress-strain

model for CFRP-confined concrete by Guo et al. [46] did not yield accurate predictions except for the case of full confinement. This model significantly overestimated the ultimate compressive strength of partially CFRP-confined concrete compared to experimental data. Although FIB differentiates the k_e coefficient for horizontal and spiral CFRP strip confinement, the difference in values for spiral strips was too minor. Considering the spiral strip spacing, the calculated k_e coefficient remained approximately equal to 1 regardless of the strip spacing. Consequently, both the FIB and other codes and models have evidently overestimated the ultimate axial stress.

Table 6. Verification of stress-strain models against experimental results

	b_f (mm)	S (mm)	Experimental	Pellegrino et al.		Wang *et al.*,		Guo *et al.*	
			$f_{cc,exp}$ (MPa)	$f_{cc,the}$ (MPa)	$\frac{\Delta f_{cc}}{f_{cc,exp}}$	$f_{cc,the}$ (MPa)	$\frac{\Delta f_{cc}}{f_{cc,exp}}$	$f_{cc,the}$ (MPa)	$\frac{\Delta f_{cc}}{f_{cc,exp}}$
CT	/	/	40.56	54.16	34%	47.96	18%	38.45	-5%
CPH30	30	30	32.03	28.80	-10%	32.32	1%	35.11	10%
CPH45	30	45	27.4	26.47	-3%	29.26	7%	33.57	23%
CPH65	30	65	24.71	24.66	0%	26.74	8%	31.64	28%
CPI30	30	30	26.11	30.64	17%	34.64	33%	38.38	47%
CPI45	30	45	22.07	28.55	29%	32.00	45%	38.38	74%
CPI65	30	65	22.83	26.85	18%	29.77	30%	38.38	68%

In conclusion, while the safety benefits of CFRP confinement in enhancing the structural performance of concrete are well-documented, it is equally important to consider the economic aspect. The initial cost of CFRP materials is typically higher than that of conventional reinforcement methods. However, the long-term advantages associated with CFRP, such as reduced maintenance requirements, extended service life, and the ability to retrofit existing structures without significant downtime, can effectively offset these initial costs. Consequently, when evaluating CFRP as a strengthening solution, it is crucial to strike a careful balance between safety and cost-effectiveness. This comprehensive approach ensures optimized decision-making in practical applications, ultimately leading to more sustainable and resilient structural solutions. By acknowledging both the immediate financial implications and the broader benefits of using CFRP, stakeholders can make informed choices that enhance the overall integrity and longevity of concrete structures.

4. Conclusion

- This research undertook an in-depth examination of the performance and predictive accuracy of various design codes and stress-strain models for CFRP-confined concrete. By evaluating different types of CFRP confinement—full, horizontal, and spiral—along with assessing the effectiveness of multiple design codes and models, the study aimed to provide a clearer understanding of how these factors influence concrete strength and axial strain capacity. The findings result shows:
- Full CFRP Confinement: Demonstrated a substantial improvement in compressive strength, with an increase of 89.36% compared to unconfined concrete. This type of confinement provided the highest enhancement in concrete strength and axial strain capacity.
- Horizontal CFRP Strips: Particularly effective, with specimens featuring strips spaced 30 mm apart showing a 49.53% increase in compressive strength. This

configuration also exhibited a 610.78% increase in axial strain compared to unconfined samples, although this was 43.56% lower than fully confined specimens.

- Spiral CFRP Strips: Less effective compared to horizontal strips. While the compressive strength increased by 21.90% over unconfined concrete, the axial strain improvements were less pronounced, with an increase of 591.42% at 30 mm spacing, 572.67% at 45 mm, and 30.47% at 65 mm spacing.
- The FIB (2001) model was effective for horizontal CFRP confinements but overestimated stress for spiral confinements, while the ACI (2017) code provided reasonable predictions with deviations between -16% and 19%. Models by Pellegrino & Modena (2010) and Wang et al. (2018) accurately predicted horizontal CFRP strip performance, with deviations of up to 10%, but struggled with spiral confinements. The Guo et al. (2019) model significantly overestimated strength for partially CFRP-confined specimens, with discrepancies up to 45.59%.
- In conclusion, the findings from this study offer valuable insights for decision-makers in the field of structural engineering and construction. The demonstrated effectiveness of fully and horizontally CFRP-confined concrete, along with the varying performance of spiral configurations, provides a clear basis for selecting the most appropriate confinement strategy depending on the specific structural requirements. Furthermore, the analysis of predictive models and design codes, such as FIB (2001), ACI (2017), and models by Pellegrino et al., Wang et al., and Guo et al., underscores the need for refinements in these tools to improve accuracy. Decision-makers can use this research to enhance construction practices by adopting CFRP confinement strategies that optimize strength and strain improvements, while also aligning with reliable predictive models. This, in turn, will contribute to more efficient and resilient concrete structures, ensuring better performance and longevity in civil engineering projects.

This study opens new avenues for enhancing CFRP confinement techniques in concrete, suggesting that more accurate predictive models could be developed, particularly for partial confinements and spiral configurations. The findings also highlight the need to revise and refine current design codes to more accurately reflect the actual behavior of CFRP-confined concrete, especially in applications requiring high strength and durability. Future research could focus on exploring the interaction between different confinement types and optimizing the use of composite materials to maximize both structural efficiency and cost-effectiveness.

Acknowledgments

The authors acknowledge the support from the Directorate-General for Scientific Research and Technological Development (DGRSDT-Algeria). The authors are grateful to Merdas Abdelghani (Department of Civil Engineering, University of Ferhat Abbas, Sétif, Algeria) for their help to conduct the experimental program at Emerging Materials Research Unit (EMRU).

Appendix

Model	Stress	Strain
FIB standard [41]	$f_{cc} = f_{co}\left(0.2 + 3\sqrt{\frac{f_l}{f_{co}}}\right)$	$\varepsilon_{cu} = \varepsilon_{co}\left(2 + 1.25\frac{E_c}{f_{co}}\varepsilon_{fe}\sqrt{\frac{f_l}{f_{co}}}\right)$
CSA S806 Standard [43]	$f_{cc} = 0.85f_{co} + k_l k_c f_l$	/
ACI Standard [42]	$f_{cc} = f_{co} + 3.1\kappa_a f_l$	$\varepsilon_{cu} = \varepsilon_{co}\left[1.5 + 12\kappa_b\frac{f_l}{f_{co}}\left(\frac{\varepsilon_{fe}}{\varepsilon_{co}}\right)^{0.45}\right] \leq 0.01$
Pellegrino et al. [44]	$\frac{f_{cu}}{f_{co}} = 1 + k_1\frac{P_u}{f_{co}}$	$\frac{\varepsilon_{cu}}{\varepsilon_{co}} = 2 + B(\frac{P_u}{f_{co}})$
Wang et al., [45]	$\frac{f_{cc}}{f_{co}} = 1 + 3.3k_e\frac{f_l}{f_{co}}$	$\frac{\varepsilon_{cu}}{\varepsilon_{co}} = 1.75 + 12\left(\frac{f_l}{f_{co}}\right)\left(\frac{\varepsilon_{h,rup}}{\varepsilon_{co}}\right)^{0.45}$
Guo et al., [46]	$\frac{f_{cc}}{f_{co}} = 1 + 2(\rho_{Ke} - 0.01)\rho_\varepsilon$	$\frac{\varepsilon_{cu}}{\varepsilon_{co}} = 1.75 + 5.5\rho_{Ke}^{0.8}\rho_\varepsilon^{1.45}$

F_{cc}: Compressive strength of CFRP-confined concrete, F_{co}: Compressive strength of unconfined concrete, F_l: Lateral confinement stress provided by the CFRP, k_e Efficiency factor for the confinement type, *S:* Spacing between confinement bands, *D:* Diameter of the concrete cylinder, ϵ_{cu} : Ultimate strain of CFRP-confined concrete, ϵ_{co} : Ultimate strain of unconfined concrete, E_c *:* Modulus of elasticity of concrete, ϵ_{fl}: Effective strain in the CFRP material, *Kl*: Confinement factor related to the lateral confinement stress, *Kc*: Geometric factor for the section shape, *Kα*: Coefficient related to the axial confinement stress, *Kb*: Coefficient related to the deformation, $\boldsymbol{\rho\kappa e}$: Confinement stiffness ratio, $\boldsymbol{\rho\varepsilon}$: Confinement strain ratio, $\boldsymbol{\varepsilon h,rup}$: Ultimate strain of the CFRP jacket at rupture, $\boldsymbol{\varepsilon co}$: Strain of unconfined concrete under compression corresponding to $\boldsymbol{fc}$ or the applied compression load

References

[1] Hao H, Bi K, Chen W, Pham TM, Li J. Towards next generation design of sustainable, durable, multi-hazard resistant, resilient, and smart civil engineering structures. Eng Struct. 2023;277:115477. https://doi.org/10.1016/j.engstruct.2022.115477

[2] Singh P, Singh S, Ojha R, Tiwari P, Khan S, Kumar R, et al. Characterization of wear of FRP composites: A review. Mater Today Proc. 2022;64:1357-61. https://doi.org/10.1016/j.matpr.2022.04.236

[3] Siddika A, Al Mamun MA, Ferdous W, Alyousef R. Performances, challenges and opportunities in strengthening reinforced concrete structures by using FRPs-A state-of-the-art review. Eng Fail Anal. 2020;111:104480. https://doi.org/10.1016/j.engfailanal.2020.104480

[4] Ortiz JD, Khedmatgozar Dolati SS, Malla P, Nanni A, Mehrabi A. FRP-reinforced/strengthened concrete: State-of-the-art review on durability and mechanical effects. Materials. 2023;16(5):1990. https://doi.org/10.3390/ma16051990

[5] İnce O. Structural damage assessment of reinforced concrete buildings in Adıyaman after Kahramanmaraş (Türkiye) Earthquakes on 6 February 2023. Eng Fail Anal. 2024;156:107799. https://doi.org/10.1016/j.engfailanal.2023.107799

[6] Işık E, Avcil F, İzol R, Büyüksaraç A, Bilgin H, Harirchian E, et al. Field reconnaissance and earthquake vulnerability of the RC buildings in Adıyaman during 2023 Türkiye Earthquakes. Appl Sci. 2024;14(7):2860. https://doi.org/10.3390/app14072860
[7] Akar F, Işık E, Avcil F, Büyüksaraç A, Arkan E, İzol R. Geotechnical and structural damages caused by the 2023 Kahramanmaraş Earthquakes in Gölbaşı (Adıyaman). Appl Sci. 2024;14(5):2165. https://doi.org/10.3390/app14052165
[8] Ivanov ML, Chow W-K. Structural damage observed in reinforced concrete buildings in Adıyaman during the 2023 Türkiye Kahramanmaraş Earthquakes. Struct. 2023:105578. https://doi.org/10.1016/j.istruc.2023.105578
[9] Avcil F, Işık E, İzol R, Büyüksaraç A, Arkan E, Arslan MH, et al. Effects of the February 6, 2023, Kahramanmaraş earthquake on structures in Kahramanmaraş city. Nat Hazards. 2024;120(3):2953-91. https://doi.org/10.1007/s11069-023-06314-1
[10] Abdesselam A, Merdas A, Fiorio B, Chikh N-E. Experimental and numerical study on RC beams strengthened by NSM using CFRP reinforcements. Period Polytech Civ Eng. 2023;67(4):1214-33. https://doi.org/10.3311/PPci.21309
[11] Merdas A, Fiorio B, Chikh N-E. Study of the adhesion of composite strips and rods to concrete by bending (the beam test). C R Mec. 2011;339(12):796-804. https://doi.org/10.1016/j.crme.2011.10.002
[12] Merdas A, Fiorio B, Chikh N-E. Aspects of bond behavior for concrete beam strengthened with carbon fibers reinforced polymers-near surface mounted. J Reinf Plast Compos. 2015;34(6):463-78. https://doi.org/10.1177/0731684415573814
[13] Mesbah H-A, Benzaid R. Damage-based stress-strain model of RC cylinders wrapped with CFRP composites. Adv Constr Mater. 2017;5(5):539.
[14] Benzaid R, Chikh N-E, Mesbah H. Study of the compressive behavior of short concrete columns confined by fiber reinforced composite. Arab J Sci Eng. 2009;34(1B):15-26.
[15] Benzaid R, Mesbah H-A. The confinement of concrete in compression using CFRP composites-effective design equations. J Civ Eng Manag. 2014;20(5):632-48. https://doi.org/10.3846/13923730.2013.801911
[16] Mesbah H-A, Benzaid R, Benmokrane B. Evaluation of bond strength of FRP reinforcing rods in concrete and FE modelling. Int J Civ Eng Constr Sci. 2017;4(3):21-41.
[17] Benzaid R, Mesbah H, Chikh N-E. FRP-confined concrete cylinders: axial compression experiments and strength model. J Reinf Plast Compos. 2010;29(16):2469-88. https://doi.org/10.1177/0731684409355199
[18] Venigalla SG, Nabilah AB, Mohd Nasir NA, Safiee NA, Abd Aziz FNA. Textile-reinforced concrete as a structural member: a review. Buildings. 2022;12(4):474. https://doi.org/10.3390/buildings12040474
[19] Huang Y, Grünewald S, Schlangen E, Luković M. Strengthening of concrete structures with ultra high performance fiber reinforced concrete (UHPFRC): A critical review. Constr Build Mater. 2022;336:127398. https://doi.org/10.1016/j.conbuildmat.2022.127398
[20] Douadi A, Merdas A, Sadowski Ł. The bond of near-surface mounted reinforcement to low-strength concrete. J Adhes Sci Technol. 2019;33(12):1320-36. https://doi.org/10.1080/01694243.2019.1592944
[21] Boutlikht M, Lahbari N, Hebbache K, Tabchouche S. The assessment of strips arrangement effect on the performance of strengthened reinforced concrete beams. J Adhes Sci Technol. 2022;36(14):1510-27. https://doi.org/10.1080/01694243.2021.1977475
[22] Karouche A, Hebbache K, Belebchouche C, Lahbari N, Kessal O, Czarnecki S. External confined concrete cylinders behavior under axial compression using CFRP wrapping. Materials. 2022;15(22):8232. https://doi.org/10.3390/ma15228232
[23] Bisby LA. Fire behaviour of fibre-reinforced polymer (FRP) reinforced or confined concrete [dissertation]. Queen's University Kingston; 2003.

[24] Amran YM, Alyousef R, Rashid RS, Alabduljabbar H, Hung C-C. Properties and applications of FRP in strengthening RC structures: A review. Struct. 2018:208-38. https://doi.org/10.1016/j.istruc.2018.09.008
[25] Bai Y-L, Dai J-G, Teng J. Cyclic compressive behavior of concrete confined with large rupture strain FRP composites. J Compos Constr. 2014;18(1):04013025. https://doi.org/10.1061/(ASCE)CC.1943-5614.0000386
[26] Wang Y, Cai G, Larbi AS, Waldmann D, Tsavdaridis KD, Ran J. Monotonic axial compressive behaviour and confinement mechanism of square CFRP-steel tube confined concrete. Eng Struct. 2020;217:110802. https://doi.org/10.1016/j.engstruct.2020.110802
[27] Bains A. Numerical modelling of micro and macro cracking in plain and fibre-reinforced cementitious composites [dissertation]. Cardiff University; 2021.
[28] Le LA, Nguyen GD, Bui HH, Sheikh AH, Kotousov A. Incorporation of micro-cracking and fibre bridging mechanisms in constitutive modelling of fibre reinforced concrete. J Mech Phys Solids. 2019;133:103732. https://doi.org/10.1016/j.jmps.2019.103732
[29] Pham TM, Youssed J, Hadi MN, Tran TM. Effect of different FRP wrapping arrangements on the confinement mechanism. Procedia Eng. 2016;142:307-13. https://doi.org/10.1016/j.proeng.2016.02.051
[30] Magliaro J, Altenhof W, Alpas AT. A review of advanced materials, structures and deformation modes for adaptive energy dissipation and structural crashworthiness. Thin-Walled Struct. 2022;180:109808. https://doi.org/10.1016/j.tws.2022.109808
[31] Goel RK, Singh B, Zhao J. Underground infrastructures: planning, design, and construction. Butterworth-Heinemann; 2012. https://doi.org/10.1016/B978-0-12-397168-5.00007-9
[32] Kalfat R, Gadd J, Al-Mahaidi R, Smith ST. An efficiency framework for anchorage devices used to enhance the performance of FRP strengthened RC members. Constr Build Mater. 2018;191:354-75. https://doi.org/10.1016/j.conbuildmat.2018.10.022
[33] Lin S, Zhao Y-G, Li J. An improved wrapping scheme of axially loaded fiber-reinforced polymer confined concrete columns. Compos Struct. 2019;226:111242. https://doi.org/10.1016/j.compstruct.2019.111242
[34] Azhand A. Three-dimensional nonlinear waves under spatial confinement [dissertation]. 2016.
[35] Tejada ODT. Experimental assessment of FRP-confined concrete columns with damaged jackets [dissertation]. Queen's University; 2021.
[36] Liao J, Zeng J-J, Jiang C, Li J-X, Yuan J-S. Stress-strain behavior and design-oriented model for FRP spiral strip-confined concrete. Compos Struct. 2022;293:115747. https://doi.org/10.1016/j.compstruct.2022.115747
[37] Deogekar PS, Andrawes B. Hybrid confinement of high strength concrete using shape memory alloys and fiber-reinforced polymers. J Struct Integr Maint. 2018;3(1):22-32. https://doi.org/10.1080/24705314.2018.1426172
[38] Dreux G, Festa J. Nouveau guide du béton et de ses constitutants. Eyrolles; 1998.
[39] N.E. 933-1. Essais pour déterminer les caractéristiques géométriques des granulats - Partie 1 : détermination de la granularité - Analyse granulométrique par tamisage. 2012:19.
[40] Chen G, He Y, Jiang T, Lin CJ. Behavior of CFRP-confined recycled aggregate concrete under axial compression. Build Mater. 2016;111:85-97. https://doi.org/10.1016/j.conbuildmat.2016.01.054
[41] Triantafillou T, Matthys S, Audenaert K, Balázs G, Blaschko M, Blontrock H, et al. Externally bonded FRP reinforcement for RC structures. Int Fed Struct Concr. 2001. https://doi.org/10.35789/fib.BULL.0014
[42] Silva P, Kanitkar R. ACI 440.2 R and the new seismic strengthening guidelines using FRP. Spec Publ. 2018;327:20.1-20.16.

[43] Canadian Standards Association. Design and construction of building structures with fibre-reinforced polymers. 2012.
[44] Pellegrino C, Modena CJ. Analytical model for FRP confinement of concrete columns with and without internal steel reinforcement. J Compos Constr. 2010;14(6):693-705. https://doi.org/10.1061/(ASCE)CC.1943-5614.0000127
[45] Wang W, Martin PR, Sheikh MN, Hadi MNJ. Eccentrically loaded FRP confined concrete with different wrapping schemes. J Compos Constr. 2018;22(6):04018056. https://doi.org/10.1061/(ASCE)CC.1943-5614.0000898
[46] Guo Y-C, Gao W-Y, Zeng J-J, Duan Z-J, Ni X-Y, Peng KD. Compressive behavior of FRP ring-confined concrete in circular columns: Effects of specimen size and a new design-oriented stress-strain model. Constr Build Mater. 2019;201:350-68. https://doi.org/10.1016/j.conbuildmat.2018.12.183

Research on Engineering Structures & Materials
www.jresm.org
Research Group

Technical Note

The effect of increasing hidden layers on the performance of the deep neural network: Modelling, investigation, and evaluation

Abdel-Nasser Sharkawy *,[a]

Mechanical Eng. Dept., Faculty of Eng., South Valley University, Qena 83523, Egypt
Mechanical Eng. Dept., College of Eng., Fahad Bin Sultan University, Tabuk 47721, Saudi Arabia

Article Info

Article History:

Received 09 Sep 2024
Accepted 27 Nov 2024

Keywords:

Neural network performance;
Hidden layers;
Design and training processes;
Mean squared error;
Solar power station;
Investigation;
Assessment;
Comparison

Abstract

Neural networks have a profound impact on many real-life applications. In this paper, the influence of increasing the hidden layers of the neural network on its performance is investigated and presented. For this purpose, three structures of the neural network are designed. The first structure has only one hidden layer, the second structure has two hidden layers, and the third structure has three hidden layers. The inputs and the output of each neural network structure are the same. To design and train these structures, data are collected from a solar power station in Egypt. These data include the temperature of the solar photovoltaic module and the radiation which are the inputs of each neural network structure. In addition, the power of the photovoltaic module, which is the output of each neural network structure. The obtained data is 7200 samples and is divided into three different parts, the largest part for the structure train stage, part for the test stage, and the last part for the validating stage. The main aim of this division is to investigate the efficiency of the structure in different modes. The training of each structure is conducted by Levenberg-Marquardt technique. The mean squared error (MSE) value is the main parameter used to identify the completeness and the effectiveness of the train, test, and validating stages. In addition, the approximated error between the actual output and the predicted outputs by each neural network structure is calculated. Structures with four, five, and six hidden layers are also developed and investigated. The results show that the MSE value is decreasing with the increase of the hidden layers. The MSE values obtained using three, four, five, and six hidden layers are 0.01686, 0.01634, 0.01593, and 0.01586 respectively. Furthermore, the average value of the approximation error is very small and is 0.0396 using the three hidden layers. Therefore, the increase of the hidden layers of the neural network increases its accuracy and performance. The results of the proposed method are compared with previous related works from literature. The result of this comparison shows the superior accuracy of the proposed method.

© 2025 MIM Research Group. All rights reserved.

1. Introduction

Neural network is a powerful mathematical technique, and nowadays is widely used with many real applications such as in industry [1, 2], robotics [3], medicine [4], finance [5, 6], renewable energy [7, 8], and so on. It can be used with prediction or estimation problems, automatic control processes, and classifications or pattern recognitions, social media, and weather forecasting, [9]. Neural network has desirable advantages such as its effectiveness in any linear/nonlinear function approximation, adaptivity, and ability for generalization [10-12]. Different types of neural

*Corresponding author: abdelnassersharkawy@eng.svu.edu.eg
[a]https://orcid.org/0000-0001-9733-221X
DOI: http://dx.doi.org/10.17515/resm2024.442st0909tn

networks are found such as multilayer perceptron, feedforward, recurrent, cascaded forward, radial basis function, and NARX network, [12, 13]. In the current paper, we shed light on the estimation or prediction processes particularly the PV solar station output using the neural network.

Neural networks are widely used by previous researchers in the prediction or estimation of parameters in different fields. Neural networks are used for prediction of the power of wind turbine. Liu et al [14] structured a neural network for predicting and estimating the power of a wind plant. Their structure was built based on the speed and the direction of wind which were used as the neural network inputs. Their structure used only one hidden layer. For performance assessment, they used the value of root mean squared error which was in range between 14.99 to 17.086. In [15], Koroglu and Ekici developed a neural network to estimate the speed and power of the wind plant. Their structure was developed based on twelve inputs such as temperature, pressure, radiation, cloudiness, sunshine hours, and direction of wind. Their structure was implemented using only one hidden layer. For performance investigating, the value of mean squared error was used and was in the range of 0.3653 and 0.4721. Neural networks are used with heat exchangers. Kouidri et al. [16] developed a neural network to estimate the fouling resistance in a heat exchanger. Their structure was built based on six inputs such as the temperature and mass flux. They used only one hidden layer in their structure. For performance investigation, the normalized value of the mean squared error value was considered, and it was in the range of 0.032591 to 0.009694. Neural networks are used with the field of batteries. Teixeira et al. [17] structured a neural network for estimating the health state of batteries of lithium-ion. The structure was based on a vector of temperature, current, and voltage. For performance investigation, the mean squared error value is considered, and it was from 0.0376 to 0.1278.

Neural networks are used to predict the power of a solar PV station which is the related topic to our current paper. In [18], Barrera et al. developed a neural network to estimate the energy of a solar module. The inputs of their system were three factors based on radiation. Their neural network structure had only one hidden layer. For investigating their neural network performance, they depended on the mean squared error value which was 0.040. In [19], Gumar and Demir developed a neural network to estimate the power of solar module. Their structures used nine inputs such as date, time, humidity, pressure, temperature, and radiation. In their structure, they used only one hidden layer. For performance investigation, they used the mean squared error value which was 0.4607. Sharkawy et al. [20] structured three types of the neural network for estimating the power of solar module. Their structures were based on the radiation and the temperature of the solar module which were the inputs of the neural network structures. In their structures, they only used one hidden layer. For the performance investigation, they depended on the mean squared error values which are 0.275, 0.612, and 0.887. In [21], Azka et al. used a neural network with two hidden layers to estimate and model the power of a solar PV station. In their system, they used seven inputs which were temperature, pressure, humidity, precipitation, wind speed, cloud cover, and solar attitude. They also depended on the mean squared error value to evaluate their system which was a high value. Jinyeong Oh et al. [22] proposed a deep neural network to forecast the power of a solar PV station. Their method was implemented by using from two to ten hidden layers. They used 22 input variables based on stamps of time and conditions of weather such as temperature, humidity, the speed of wind, and so on. The best mean squared value that obtained with their approach was 0.0408. In [23], Sulaiman and Mustaffa developed a deep neural network-based approach for predicting the generation of the power of solar PV. In their approach, two hidden layers were used, and they used 11 inputs based on temperature, irradiation, and time. Their obtained best mean squared value was 0.3744. Amer et al. [24] developed a neural network with two hidden layers for the estimation of the output power of the solar plant. In the design of their system, they used 7 inputs based on features of irradiation, temperature, and the speed of wind. Their achieved mean squared error was 4.094. In [25], a neural network structure was proposed and trained with two different learning algorithms which were error back-propagation and Levenberg-Marquardt. They used this structure for estimation of the power of the solar PV by considering only hidden layer and two inputs which were the temperature and radiation. Their obtained mean squared error values were 0.0238 and 0.03482. Rushdi et al. [26] developed a

neural network with two hidden layers to estimate the power of solar-wind system. Their neural network was designed with many sets of features based on temperature, radiation, wind speed, and wind direction. The obtained mean squared error value was 0.01986.

From this discussion, the main challenge is to consider many hidden layers in the structure of the neural network to investigate its performance and accuracy. In addition, using the value of the mean squared error or the root mean squared error is recommended to assess the training and testing processes of the neural network. Using a few numbers of inputs can minimize the complexity of the neural network and the computations.

The main contribution and novelty of this paper can be presented in the following points:

- The effect of increasing the number of hidden layers in the structure of a neural network is investigated and analyzed.
- For this purpose, a neural network is designed with one hidden layer (NN1), two hidden layers (NN2), and three hidden layers (NN3). In addition, four, five, and six hidden layers were used. In each case, the performance and the accuracy of the neural network structure is determined and compared.
- For investigating the performance/accuracy of the neural network structure, the value of the mean squared error, and the approximation error are used. To reach very small values, many experiments and trials are conducted. Furthermore, very small size of inputs (two inputs) is considered.
- To design and train these structures, data are obtained from solar power plant in Egypt and these data are the temperature of the solar module and the radiation which are the inputs of each neural network structure. In addition, the power of the solar module, which is the output of each structure. The correlation between these variables is analyzed and drawn.
- For high investigation of the neural network performance and efficiency, the obtained data is divided into three parts: one part for the train case and the other two parts for the test and validating cases. After that, all these data are combined and used again to test the neural network structure.
- The process of training is conducted using the algorithm of Levenberg-Marquardt which is a very fast technique and achieves the desired performance easily.
- The experimental results reveal that increasing the number of hidden layers can effectively improve the performance and accuracy of neural networks. However, the time of training is increasing. For offline training, the time of training is not important.

The methodology conducted in the current paper is presented in Fig. 1. This methodology is discussed as follows:

- Six structures of neural networks are designed and developed by determining their inputs and output. Considering a plant of solar PV, the selected inputs are the temperature of the solar module and the radiation, whereas the output of each neural network structure is the output power.
- Data is collected from a solar PV plant in Egypt and the number of samples is 7200. These samples are divided into three parts. 5040 samples are used for the NN structure train, 1080 samples are used for the NN structure test, and 1080 samples which are used for the NN structure validating.
- In every stage, whether in training, testing, or validation, the mean squared error (MSE) is calculated. When the obtained MSE becomes very small value and close to zero, the training of the neural network structure is then finished.
- The MSE value of each NN structure is compared to determine which NN structure has the best performance and accuracy.
- Once the training process is completed, all data is combined again and the NN structure is tested, and the approximation error value is calculated. If this error is a very small value and close to zero, then the trained neural network structure is efficient in estimating the output correctly.
- The approximation error value resulted by each NN structure is also compared to determine the most preferable and accurate structure.

The rest parts of this paper are discussed as follows. Section 2 shows the design of the neural networks' structures using one, two, and three hidden layers. In section 3, the stages of the train, test, and validating are presented in detail. The mean squared error value for each stage and each structure is presented and compared. Section 4 shows a comparison between the actual output and the estimated outputs by the neural network structures. In addition, the approximated output is determined. Section 5 shows the use of four, five, and six hidden layers in brief. We do not concentrate on this part as their results are remarkably close to the neural network with three hidden layers. Section 6 compares the results from the current study with literature results. In section 7, the main keys of this paper are summarized and some recommendations for the future.

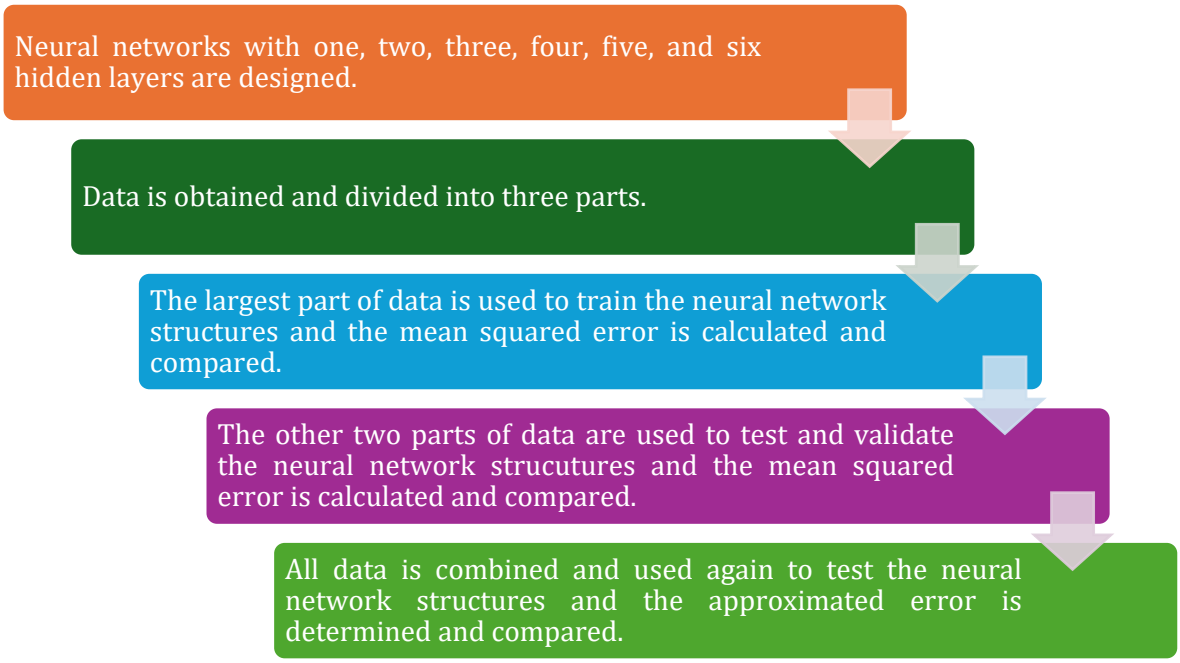

Fig. 1. The conducted methodology in the current paper

2. Structures' Design

In this section, the design of the proposed different structures of the NNs is discussed. To design and train and assess these structures, data from solar power station in Egypt is obtained. These data are obtained and available at the website [27]. This data is for Five days (7200 samples for 7200 minutes). These data are the temperature of the PV module and the radiation which are considered the inputs of the NN structure. In addition, the actual output power of the PV module, which is the output of the NN structure and used for the training process. This data is presented in Fig. 2. As shown, the signal of one day is close to the signal of another day because the data is collected from five consecutive days in summer and these days were approximately close together in conditions. Indeed, using different weather conditions is not important in our current study as we use the same data to train every neural network structure. In other meaning, the main aim of our study is to investigate the increase of hidden layers on the performance of the neural network. Therefore, it is recommended to use clear data without any outliers to show and clearly compare the performance of each structure.

Some analysis including the average, minimum, maximum, and standard deviation values about these data is presented in Table 1. The standard deviation is high whether for the input 1 (temperature), input 2 (radiation), or output (power). This means that the values are not close to each other. This is due to the fact that the measurements or the values of the variables during the day are different. This also can show the efficiency of the NN structures to work with different cases of data.

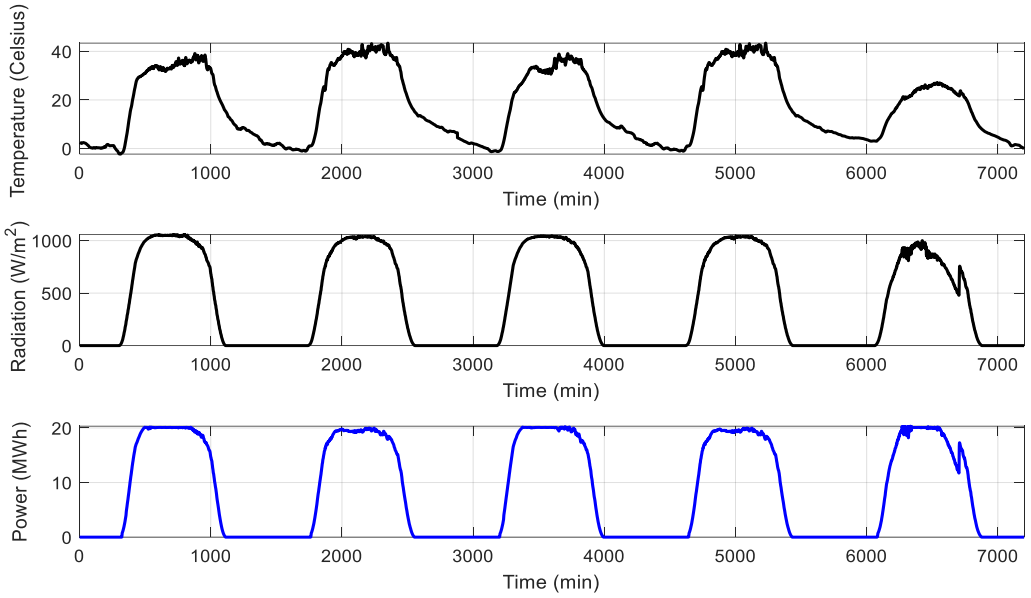

Fig. 2. The upper two diagrams are the inputs (temperature and radiation) for the designed NNs structures. The last diagram is the output (power) that is used for the train of the NNs structures

Table 1. Analysis for the inputs and the outputs used with the NN structures.

Parameter	Input 1 (Temperature - ℃)	Input 2 (Radiation - $\boldsymbol{W/m^2}$)	Output (Power - $\boldsymbol{MWh}$)
Average value	17.7191	418.1952	8.5044
Maximum Value	43.3975	1056.8	20.3270
Minimum Value	−2.2750	0	0
Standard deviation	14.3713	448.5777	8.9727

The temperature and radiation are selected to be the inputs of the neural network structure due to these variables are mainly in effecting the power of the solar PV as shown from the following equation [28, 29]:

$$Power = \eta_s \tau_g \alpha_s RA[1 - \mu_s(T_s - T_r)] \quad (1)$$

where, η_s is the reference solar cell efficiency, τ_g is the transmissivity of glass, α_s is the absorptivity of the cell, R is the radiation in W/m^2 unit, A is the whole cell area in m^2, μ_s is the thermal factor or coefficient of the cell efficiency in $\%/°C$, T_s is the temperature of the solar PV in ℃, and T_r is the referenced temperature in ℃. From this equation, the temperature and radiation are mainly factors that affect the power.

The correlation (heatmap) between the input variables (temperature and radiation) and the output variable (power) is analyzed and drawn using MATLAB as shown in Fig. 3. This Figure shows that high correlation and relationship between the temperature and radiation with the solar power. The temperature has a positive correlation with the power which is 0.9236. This means the increase in temperature leads to an increase in power. Furthermore, this correlation is remarkably close to 1 which means the temperature and the power are very related. The radiation also has a positive correlation with the power which is 0.9955. This also means the increase in radiation leads to an increase in power. In addition, this correlation is remarkably close to 1 which means that the radiation and power are very related. The inputs' variables are also very related since the correlation between temperature and radiation is 0.9348 which is remarkably close to 1.

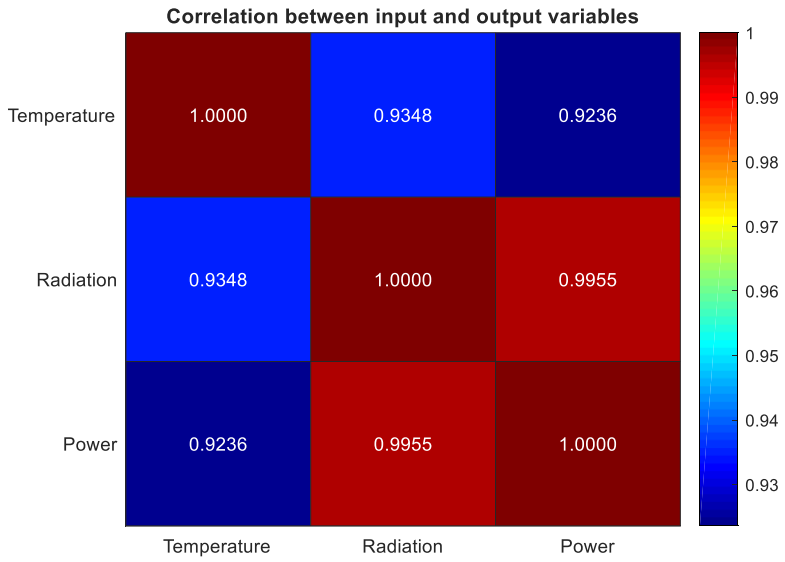

Fig. 3. The correlation (heatmap) between the input (temperature and radiation) and output (power) variables. This Figure is drawn using MATLAB

To investigate the effect of increasing the hidden layers of the NN architecture, three NN structures are designed: NN1(NN with one hidden layer), NN2 (NN with two hidden layers), and NN3 (NN with three hidden layers). The same inputs (temperature and radiation) and output (output power) are used with each NN structure. The specifications of each structure including the number of hidden layers, neurons for each layer, activation function for each layer, and inputs and outputs, are presented in Table 2.

Table 2. Comparison between the three structures of the NNs

Parameter	NN1	NN2	NN3
Number of inputs	Two (temperature and radiation)	Two (temperature and radiation)	Two (temperature and radiation)
Number of hidden layers	One	Two	Three
Number of hidden neurons	60	First hidden layer: 45 Second hidden layer: 45	First hidden layer: 65 Second hidden layer: 65 Third hidden layer: 65
Activation function	Hidden layer: Tanh Output layer: Linear	First hidden layer: Tanh Second hidden layer: Tanh Output layer: Linear	First hidden layer: Tanh Second hidden layer: Tanh Third hidden layer: Tanh Output layer: Linear
Number of outputs	One (Power)	One (Power)	One (Power)

In Table 2, the number of neurons for each hidden layer (hidden neurons) are obtained after many experiments (trails and errors) until the highest performance of the NN is reached. The highest performance of the NN is the obtaining of the smallest mean squared error value or value close to zero. In addition, as the hidden layers are increased from NN1 to NN3, the complexity is increased.

In Fig. 4, the shape of the designed structures is shown. These shapes are obtained from MATLAB software which is used in this work.

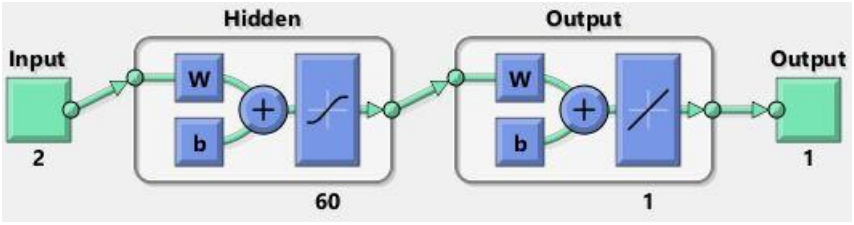

(a)

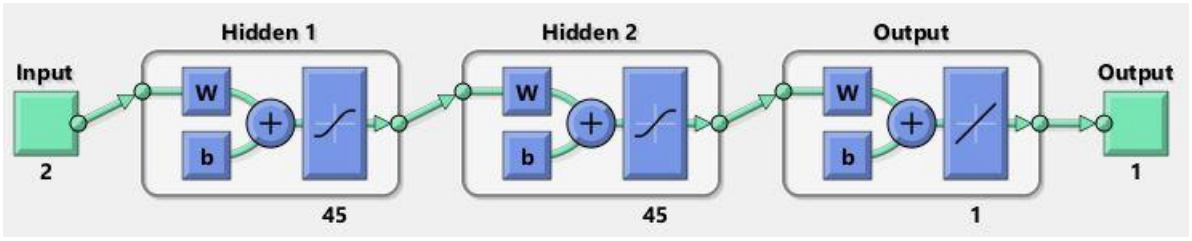

(b)

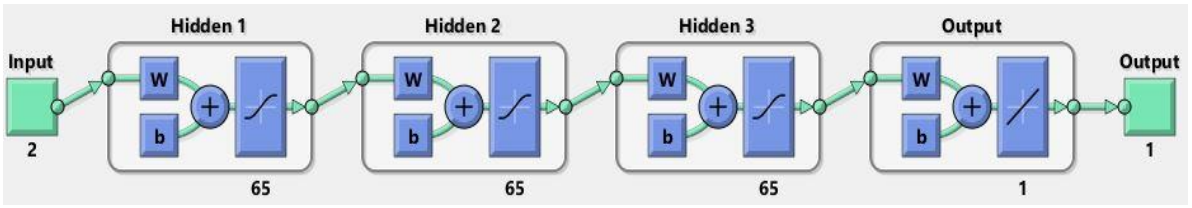

(c)

Fig. 4. The structure of the proposed NNs. (a) NN with one hidden-layer, (b) NN with two hidden-layers, and (c) NN with three-hidden layers

It should be noted that we use experimental (trial and error) methodology in determining the number of hidden layers. In other meaning, we use neural network structure with one, two, three, four, five, and six hidden layer and investigate the performance of each structure. The main aim of this methodology is to study the advantages and disadvantages of each structure to make it easy for future researchers to determine which structure can be used. The same methodology is followed for determining the number of neurons in each hidden layer. Many different neurons (from 2 to 120) are tried until the best performance of the structure is obtained. The best performance is achieving highest accuracy which is obtaining a very small value of mean squared error and approximation error. Indeed, this methodology is followed by previous researchers as seen in [30-35].

3. Structures' Training, Testing, and Validation

After the three NNs are structured, the second three stages are carried out which are the train and test and the validating. The obtained data mentioned in previous section is divided into three parts: the first part which is 5040 samples are used for the train, the second part is the 1080 samples which are used for the test, and the last part is the 1080 samples which are used for the validating.

Table 3. The division of the data for three stages (train, test, and validation) of the NNs structures.

Stage	Training	Testing	Validation	Total
Samples of Data	5040	1080	1080	7200

The division of these data is presented in Table 3. This division is also carried out randomly in MATLAB which is used in these stages. All these stages are conducted using processor of type

Intel(R) Core (TM) i5-8250U CPU @ 1.60GHz 1.80 GH and RAM of 8.00 GB. The crucial factor during these stages is obtaining the very small value of the mean squared error. The mean squared error value is calculated by the following equation:

$$Mean\ Squared\ Error\ Value = \sum_{i=1}^{n} \frac{(Actual\ output(i) - Predicted\ output(i))^2}{n} \quad (2)$$

where, n is the number of samples.

The training stage is carried out using the technique of Levenberg-Marquardt. This technique is a very fast and stable method and achieves the highest performance of the NN easily compared with other training algorithms, [36-38]. Many experiments which are trials and errors are executed to train the NN structures. These experiments include trying the use of many different hidden neurons and many different initializations of the weights until obtaining the very small value of the mean squared error. This methodology is followed by previous researchers as in ref. [32, 39]. The conducted methodology in the three stages (train, test, and validating) is shown in Fig. 5.

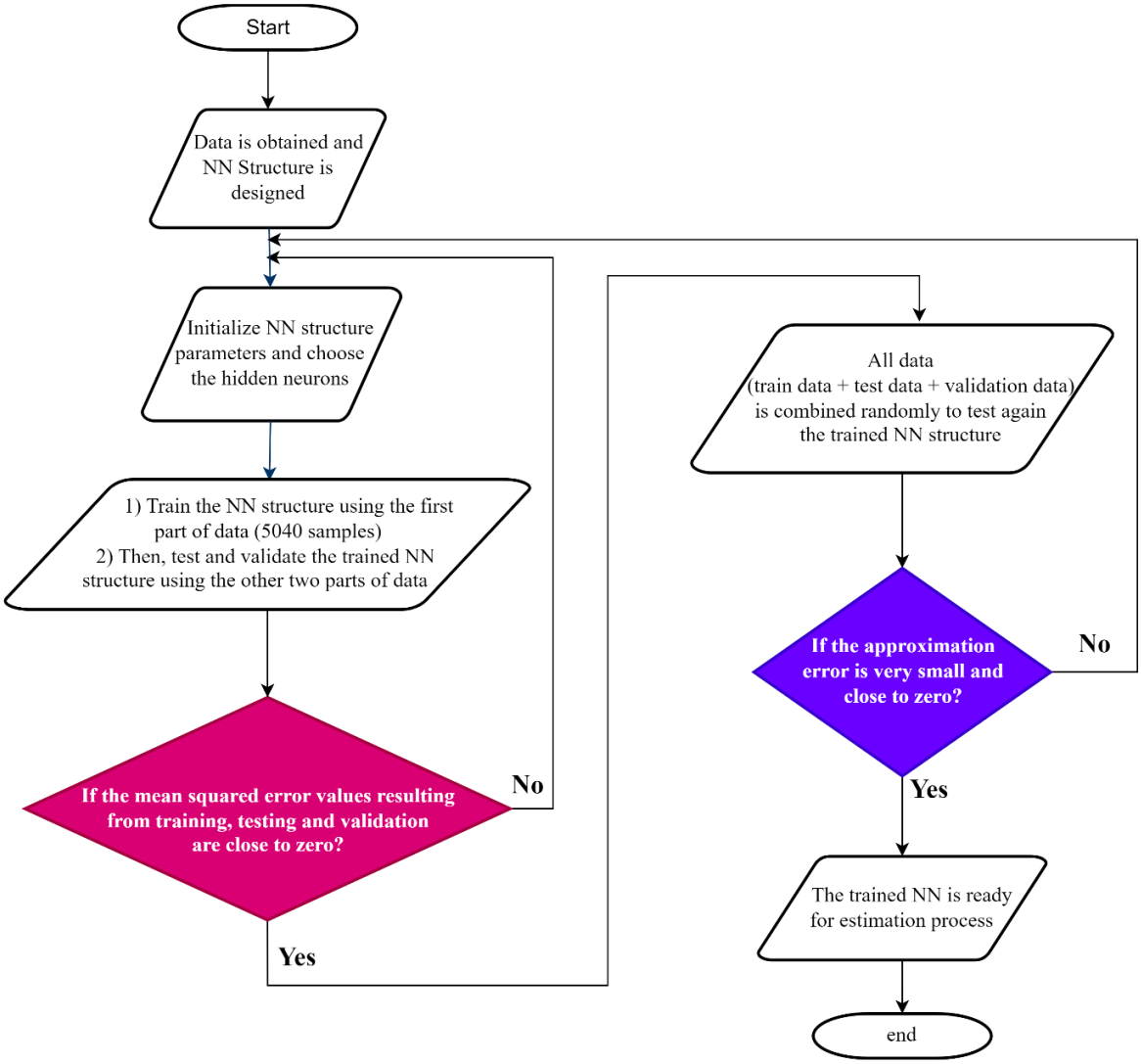

Fig. 5. A flowchart illustrating the conducted methodology for the train, test, and validating stages

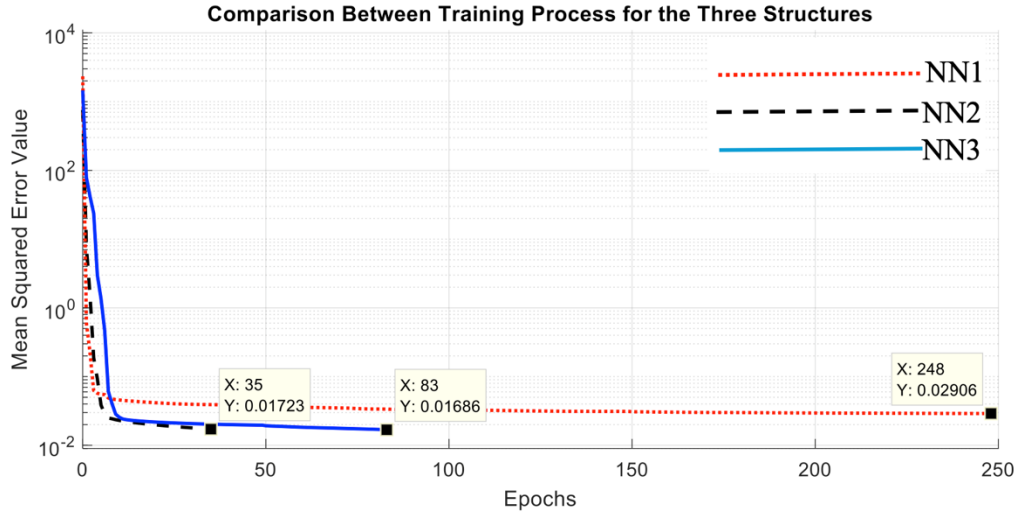

(a)

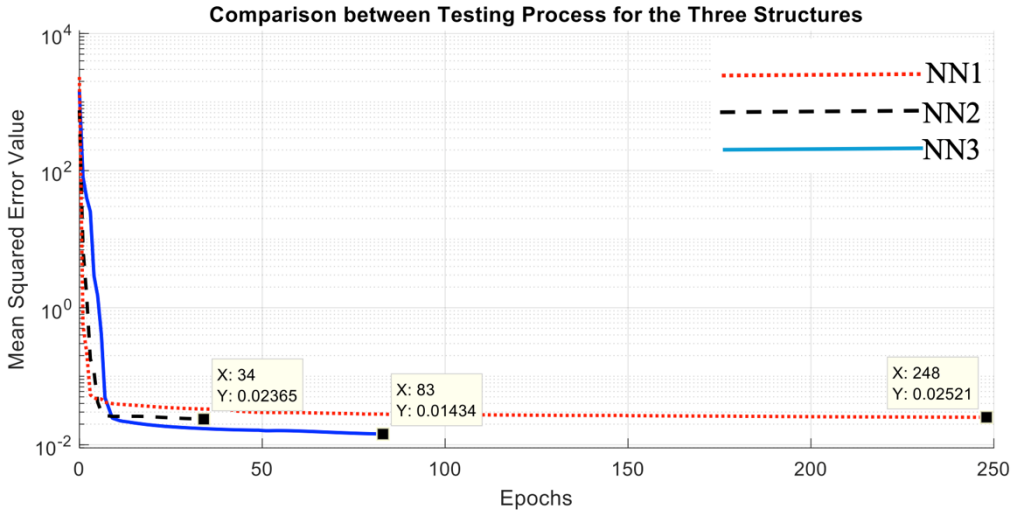

(b)

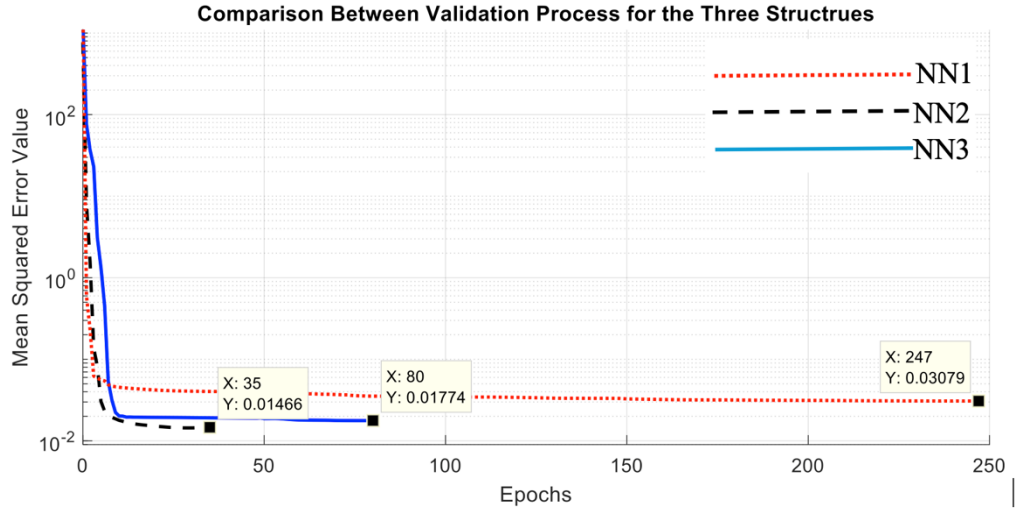

(c)

Fig. 6. Comparing the mean squared error value deduced by the three structures of NNs in case of (a) training, (b) testing, and (c) validation

The mean squared error values obtained from the three stages (training, testing, and validation) are shown in Fig. 6. The mean squared error resulting from training the three structures is presented in Fig. 6(a). As shown in this Figure, the mean square error from the NN3 is the smallest one compared with the other structures. This means that the error in the case of the NN3 is the lowest one and its accuracy is the highest. Other parameters during the stage of training are illustrated in Table 4 such as the used epochs, the time of training, and the regression. The regression resulting from NN3 is the best compared with the other structures. This also supports the fact that NN3 has the best accuracy. However, the time used for training the structure of NN3 is the highest. This means that there is a need for longer time to train the NN3 compared with other structures. Indeed, this is not particularly important if offline training is executed. In the case of online training, longer time for training is not desired. The number of epochs used with NN3 is between NN1 and NN2. We conclude that increasing the number of hidden layers improves the performance of the NN but increases the time of training and complexity

Table 4. The parameters obtained from training, test, and validating of the three different NNs structures

Parameter	NN1	NN2	NN3
Method of training	Levenberg-Marquardt technique		
MSE from training	0.02906	0.01723	0.01686
MSE from testing	0.02521	0.02365	0.01434
MSE from validation	0.03079	0.01466	0.01774
Used Epochs in training	248	35	83
Time used in training	31 seconds	3 minutes and 20 seconds	28 minutes and 5 seconds
Regression	0.9972	0.9981	0.9998

The testing and validating processes are conducted simultaneously with the training case. At each epoch/iteration, once a NN structure is trained, it is tested and validated, and the mean squared error value is calculated. This methodology is repeated until the smallest mean squared error value is reached in the three stages (train, test, and validation) simultaneously. As mentioned in previous section that the data used in test and validating stages are different from the training case. This is very useful to investigate and assess the effectiveness and the efficiency of the trained NN structures. The mean squared error values deduced from the test and the validating processes are shown in Fig. 6(b) and (c) and Table 4. The mean squared value deduced by the NN3 during the testing stage is the best/lowest compared with the other structures. In the validating stage, the mean squared error by the NN3 is located between the other structures. However, it is also very small value. From these results, we deduce that all the NN structures are trained in an exceptionally good way and the mean squared error values deduced by them are small and near to zero. In addition, the results are improved by increasing the hidden layers. This is clear as the results obtained by NN2 are better than the corresponding ones by NN1, and the results deduced by NN3 are the best compared with NN1 and NN2. On the other hand, the complexity and the time of training is increasing with NN3.

4. Output Estimation and Prediction

In this section, another stage of NN structure testing is conducted. All obtained data (train data + test data + validating data) are combined randomly in MATLAB to test the three designed structures. Then, the output of each NN structure is determined and compared with the actual output that is used for the training stage. Figure 7 shows a comparison between the actual output and the predicted ones using the trained NN1, NN2, and NN3. As shown in the Figure, the predicted outputs by NNs coincide with the actual output. This illustrates that all NN structures are trained in a very well and effective way. To show which NN structure is the most accurate compared with the others, a zoomed area from Fig. 7 is presented in Fig. 8.

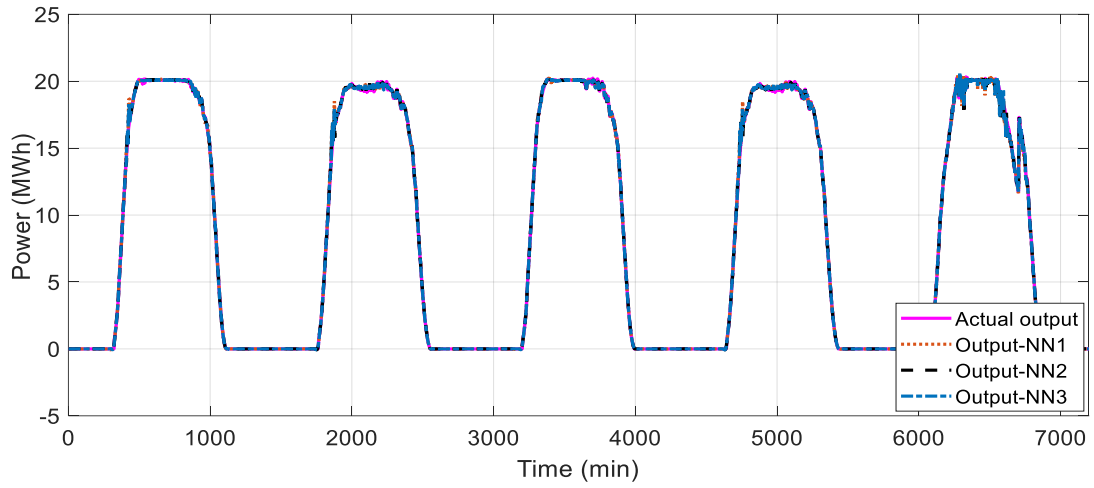

Fig. 7. The comparison between the actual output and the predicted outputs by NN1, NN2, and NN3. The colored curves are coinciding together

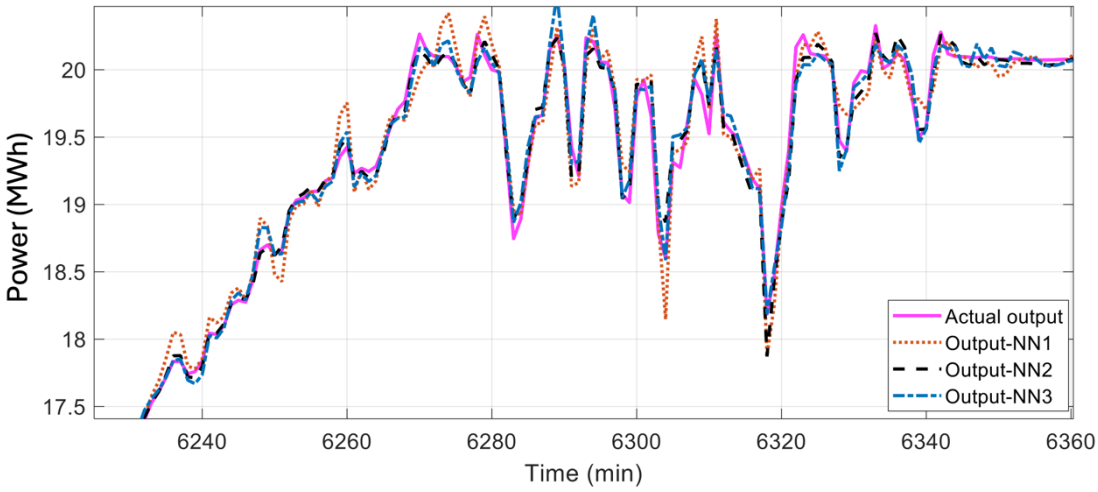

(a)

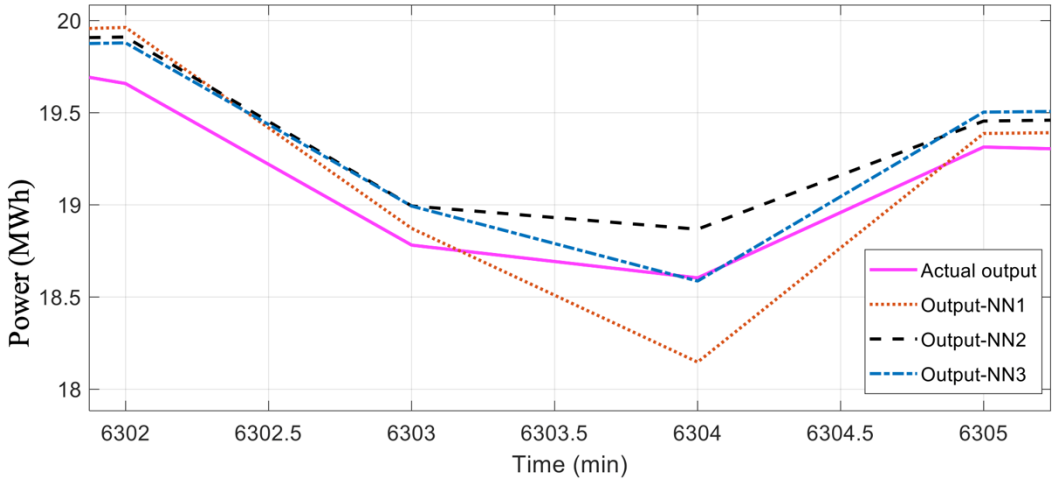

(b)

Fig. 8. Zoomed area from Fig. 7: the comparison between the actual output and the predicted outputs by NN1, NN2, and NN3. (a) Zoomed area during the 120 minutes between 6240 and 6360 minutes. (b) Zoomed area during the 3 minutes between 6302 and 6305 minutes

Zoomed area during 120 minutes between 6240 and 6360 minutes, as shown in Fig. 8(a) and zoomed area during 3 minutes between 6302 and 6305 minutes, as shown in Fig. 8(b). From Fig. 8, the estimated output by NN3 is the closest to the actual output and the estimated output by NN1 is the most distant to the actual output. This means that the NN3 is the most accurate compared with other structures and the NN1 is the lowest accurate. NN2's performance is better than NN1's performance and lower than NN3's performance. For more clarification, the error or the difference between the actual output and the predicted output by each structure is obtained. This error is calculated by the following equation:

$$Approximation\ Error = Actual\ output - Predicted\ output \tag{3}$$

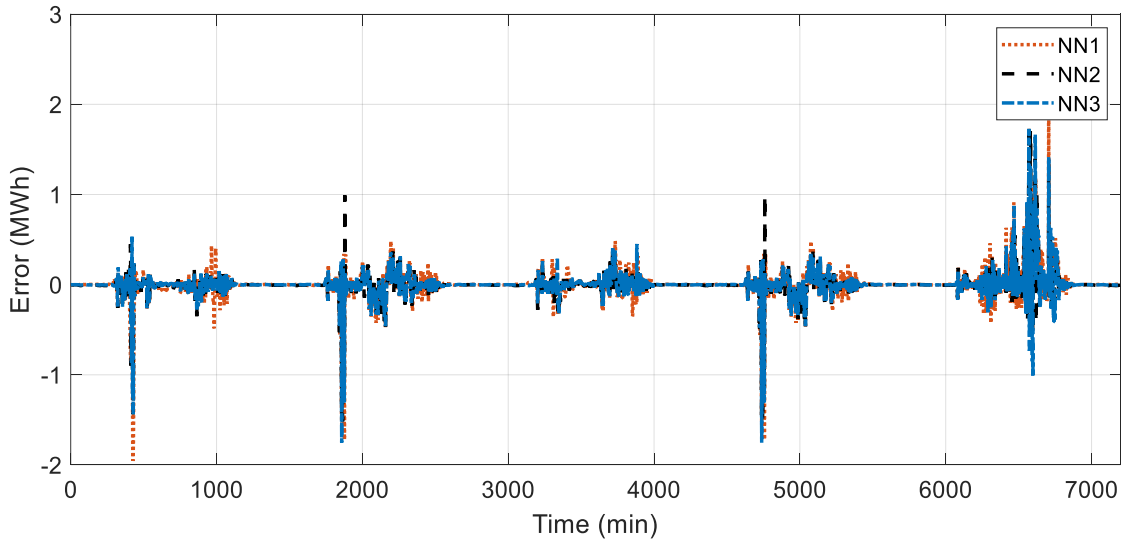

Fig. 9. The error or difference between the actual output and the predicted outputs by NN1, NN2, and NN3

Figure 9 shows the errors resulting from the three NN structures and Fig. 10 shows zoomed area from Fig. 9. From Fig. 9, the errors resulting from all structures are satisfactory and close to zero. This supports that the NN structures are effectively trained. From Fig. 10, the error resulting from NN3 is the smallest and the closest to zero compared to the corresponding ones by NN1 and NN2. The error obtained by NN1 is the worst case. This reveals that NN3 is the most accurate and NN1 is the least reliable. Analysis about these errors is presented in Table 5 such as the average value, minimum value, maximum value, and standard deviation. The maximum value of the error for each structure is small and this is good and supports that the structures are effectively trained. In addition, the standard deviation value is small for each structure which reveals that the deviation between the values is small. From this discussion, we conclude that increasing the hidden layers for the NN structure minimizes the error between the predicted and actual outputs. Therefore, the accuracy or the performance of the NN structure is increasing.

Table 5. Analysis of the error resulted by the developed NN1, NN2, and NN3.

Parameter	NN1	NN2	NN3
Average Value	0.0681	0.0474	0.0396
Maximum Value	2.3124	1.7753	1.7513
Minimum Value	3.8724e-06	4.4804e-07	2.5668e-06
Standard Deviation	0.1553	0.1212	0.1235

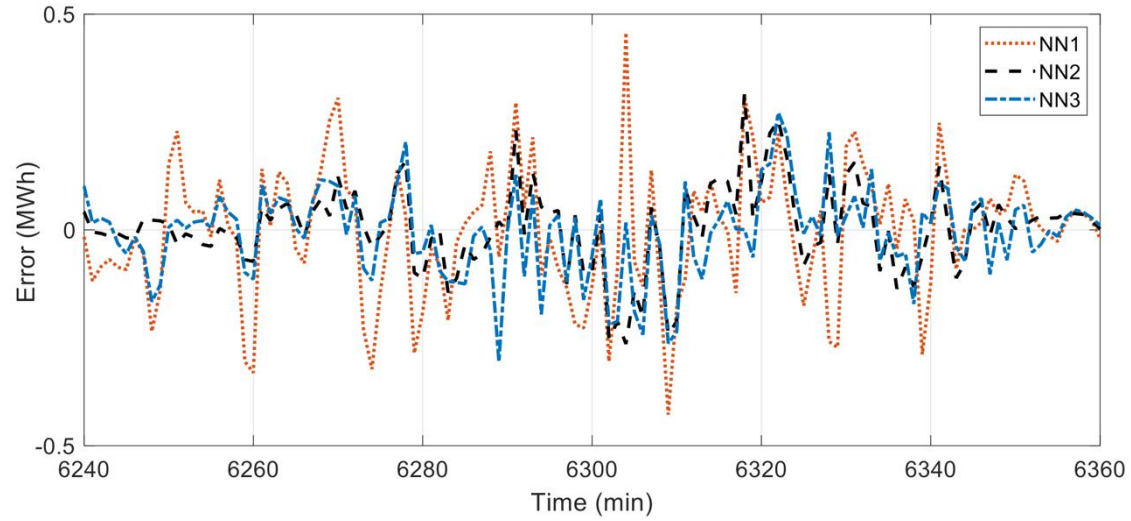

(a)

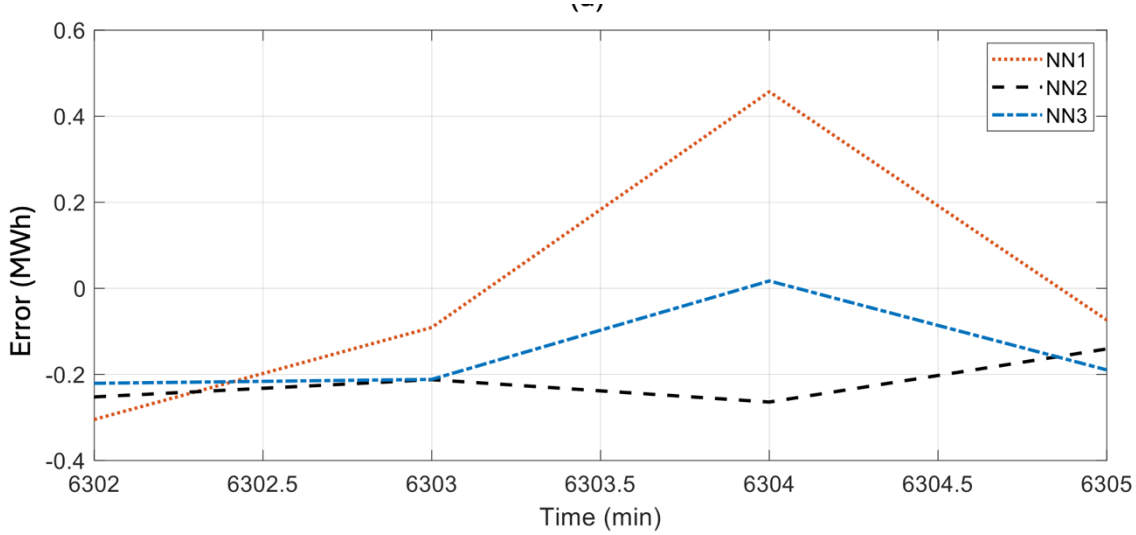

(b)

Fig. 10. Zoomed area from Fig. 9: the error or difference between the actual output and the predicted outputs by NN1, NN2, and NN3. (a) Zoomed area during the 120 minutes between 6240 and 6360 minutes. (b) Zoomed area during the 3 minutes between 6302 and 6305 minutes

5. Using More than Three Hidden Layers

In the previous sections, we presented in detail only neural networks structures using from one hidden layer up to three hidden layers. Using more than three hidden layers (see Fig. 11) is presented briefly in this section. Structures with four, five, and six hidden layers are also designed, and the same data is used to train, test, and validate these structures. To train these structures, few trials are conducted because these structures consume longer time compared with previous structures. The best results including the number of hidden neurons in each layer, the time of training, and the mean squared error value obtained from these structures are presented in Table 6. It should be noted that we do not use a remarkably high number of hidden neurons in each layer to avoid the longer time of training and the more complexity. In addition, we do not have a powerful computer or processor to do the calculations more easily and in a short time.

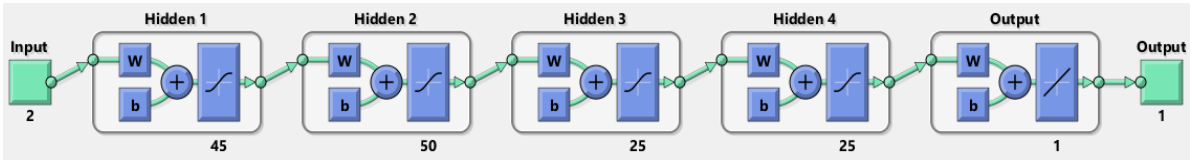

(a)

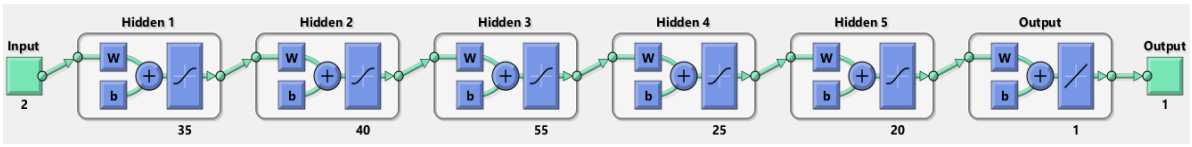

(b)

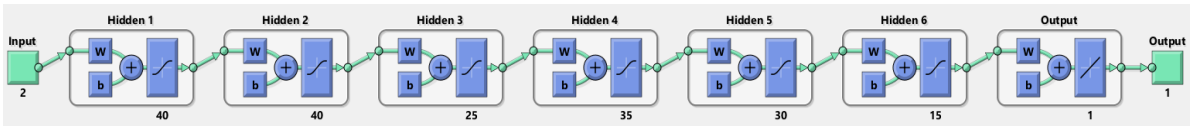

(c)

Fig. 11. The design of the NN with (a) four hidden layers, (b) five hidden layers, and (c) six hidden layers

Table 6. Results from neural networks structure using four, five, and six hidden layers.

Parameter	NN with four hidden layers	NN with five hidden layers	NN with six hidden layers
Number of hidden neurons in each layer	First hidden layer: 45 Second hidden layer: 50 Third hidden layer: 25 Fourth hidden layer: 25	First hidden layer: 35 Second hidden layer: 40 Third hidden layer: 55 Fourth hidden layer: 25 Fifth hidden layer: 20	First hidden layer: 40 Second hidden layer: 40 Third hidden layer: 25 Fourth hidden layer: 35 Fifth hidden layer: 30 Sixth hidden layer: 15
Mean squared error value	0.01634	0.01593	0.01586
Time of training	50 minutes and 15 seconds	1 hour and 20 minutes and 31 seconds	2 hours and 22 seconds

As shown in Table 6, the mean squared error values obtained from these structures is less than the corresponding ones obtained by NN3 (neural network with three hidden layers). The neural network structure with six hidden layers achieves the smallest MSE compared with other structures which is 0.01586 but with the highest computational time which is 2 hours and 22 seconds. This means that increasing the hidden layers of the neural network leads to minimizing the mean squared error and therefore increasing the accuracy and performance. However, the time of training and the complexity are higher compared with NN3. Therefore, we recommend using the neural network structure with six hidden layers or more if the high performance is the only factor that needs to be achieved regardless of the computational time and complexity. For who need to achieve high performance with less complexity and time, we recommend using the neural network structure with three hidden layers which is considered a trade-off between performance and complexity.

6. Comparison With Related Previous Works

This section compares the results of the presented study with other previous and closely related works which used the neural network approach in estimating solar PV power. The main parameters considered in this comparison are the MSE value, the number of inputs (input size), and the used number of hidden layers. The previous related works considered in this comparison are as follows: Barrera et al., 2020 [18], Gumar and Demir, 2022 [19], Sharkawy et al., 2023 [20], Jinyeong Oh et al., 2024 [22], Sulaiman and Mustaffa, 2024 [23], Rushdi et al., 2024 [26]. The results from this comparison are shown from Fig. 12 to Fig. 14. For this comparison, the proposed neural network structure using three hidden layers which makes trade-off between the high performance and the complexity and the neural network with six hidden layers which gives the best performance are included.

Figure 12 compares the number of hidden layers used by the proposed approach and other previous ones. From Fig. 12, previous researchers used different numbers of hidden layers from one hidden layer to ten hidden layers. This means that investigating the use of more than one hidden layer on the performance of the neural network is worth studying and analysis. The proposed neural network with six hidden layers and the previous approach of Jinyeong Oh et al., 2024 [22] have the highest number of hidden layers. Therefore, the complexity and the computational time of these approaches may be higher.

Increasing the number of inputs or the input size of the neural network structure can lead to increased complexity and calculations or computational time. Figure 13 shows a comparison between the number of inputs used by the proposed neural network structures and other approaches by previous researchers. From Fig. 13, the inputs used by our proposed approach particularly using three hidden layers and previous approaches of Sharkawy et al., 2023 [20] and Rushdi et al., 2024 [26] are only two inputs and less than the other approaches. Therefore, the complexity and the computational time of these approaches are lower.

The main important parameter that must be compared is the accuracy of the developed neural network. Achieving a highly accurate method is considered the main objective of any proposed method. The accuracy of the method can be investigated by comparing the mean squared error value (MSE). The method has less MSE value, has higher accuracy. A comparison between the MSE value of our proposed neural network structures and the pervious ones are presented in Fig. 14. From Fig. 14, our proposed neural structure, whether with three or six hidden layers, has the least MSE value compared with other previous structures. Therefore, the proposed neural network structures in this paper have the highest accuracy. From this comparison, the proposed neural network structure with three hidden layers has less complexity and error and higher accuracy compared to other neural network structures proposed by previous researchers.

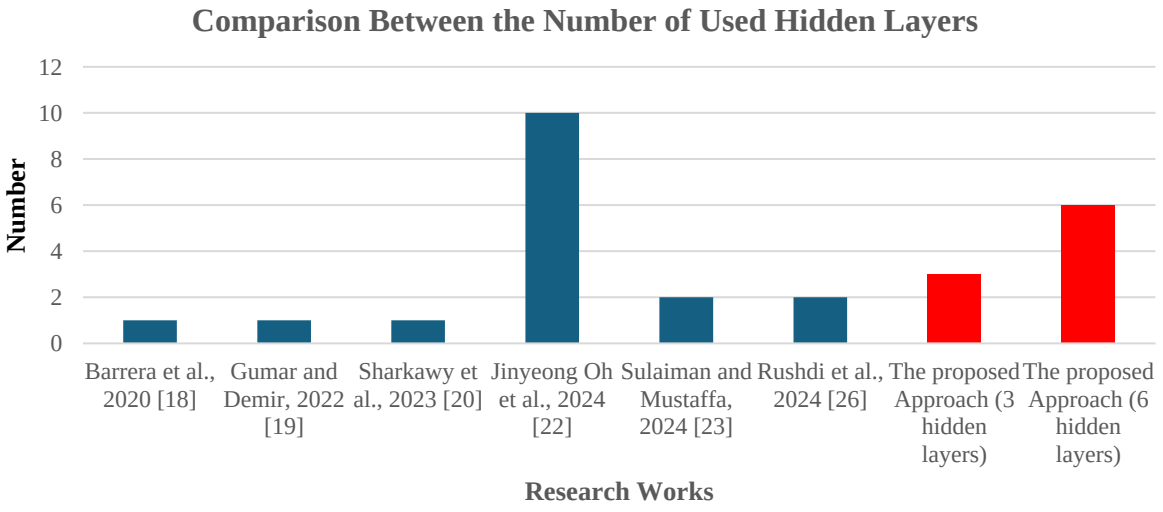

Fig. 12. Comparison between the number of hidden layers used by previous researchers

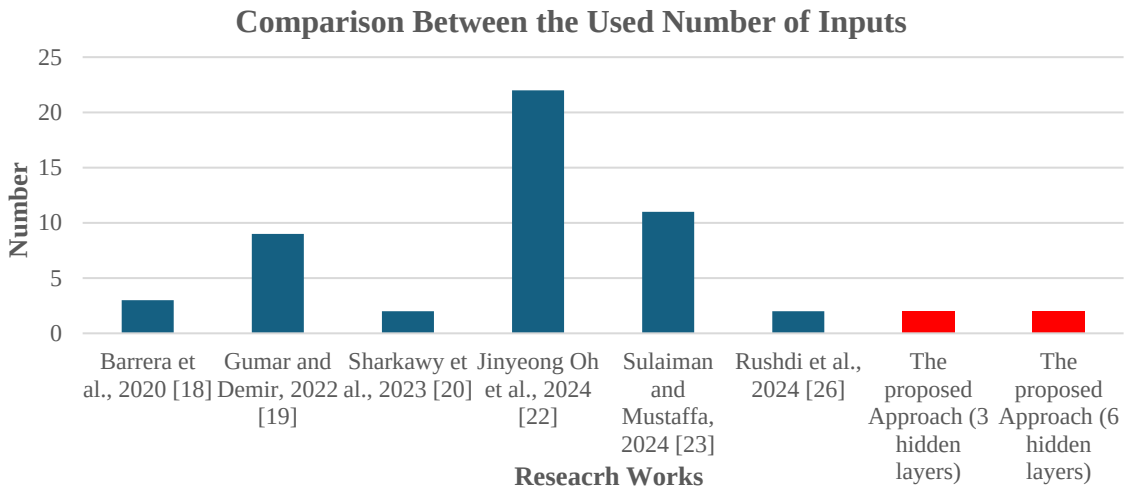

Fig. 13. Comparison between the number of inputs used by previous researchers

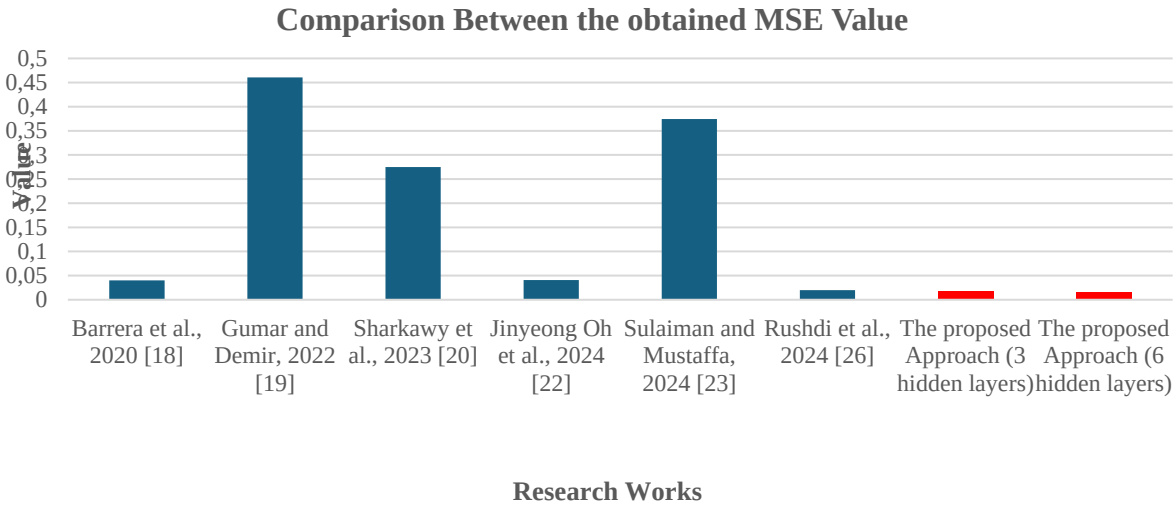

Fig. 14. Comparison between the obtained MSE value by previous researchers.

7. Conclusion and Future Work

In this paper, three neural networks structures are designed based on the principle of increasing the number of hidden layers to assess their accuracy and performance. The first structure has one hidden layer, the second structure has two hidden layers, and the last structure has three hidden layers. To complete the design of these structures, data is obtained from solar power station in Egypt. These data are the temperature of the photovoltaic module and the radiation which are used to be inputs to each NN structure. Also, the power of the photovoltaic module which is the output of each NN structure. The data is divided into three parts: one part for training and the other two parts for the test and validating. The mean squared error obtained by the neural network structure with three hidden layers is the smallest compared with other structures. However, the time used for the train and the complexity of the structure are highest. The mean squared error value by the neural network with one hidden layer is the highest, but the time used for the train and the complexity is the lowest. The training time and complexity of the neural network are not important if offline training is used. For more investigation, all data (train data + test data + validating data) are combined and used for again assessing each neural network structure and the approximated error between the actual output and the predicted output by each neural network structure is determined. The results reveal that the neural network with three hidden layers has the smallest error compared to other structures. The performance of using neural network structure with four,

five, and six hidden layers is also investigated and analysis. The results from this investigation show that the neural network with six hidden layers gives the best performance but with the highest computational time and complexity. In conclusion, increasing the hidden layers of the neural network structure increases its accuracy and performance but the computational time is increased. The results of the proposed approach are compared with other previous related works from literature. The result from this comparison reveals that the proposed method achieves the highest accuracy.

Some future works include investigation of the same methodology with other different data from different fields such as robotics, wind power plant, and agriculture, and so on. In addition, applying the same methodology with distinct types of neural networks is highly recommended. Using more samples with different conditions is worth investigating.

List of Abbreviations

Abbreviation	Meaning
NN	Neural network
NN1	Neural network with one hidden layer
NN2	Neural network with two hidden layers
NN3	Neural network with three hidden layers
MSE	Mean squared error
NARX	Nonlinear autoregressive with external input

References

[1] Zhang HC, Huang SH. Applications of neural networks in manufacturing: A state-of-the-art survey. Int J Prod Res. 2007;33(3):705-28. https://doi.org/10.1080/00207549508930175

[2] Lennox B, Montague GA, Frith AM, Gent C, Bevan V. Industrial application of neural networks-an investigation. J Process Control. 2001;11(5):497-507. https://doi.org/10.1016/S0959-1524(00)00027-5

[3] Jiang Y, Yang C, Na J, Li G, Li Y, Zhong J. A brief review of neural networks based learning and control and their applications for robots. Complexity. 2017;2017:14. https://doi.org/10.1155/2017/1895897

[4] Patel J, Goyal R. Applications of artificial neural networks in medical science. Curr Clin Pharmacol. 2008;2(3):217-26. https://doi.org/10.2174/157488407781668811

[5] Maniati M, Evangelos ES, Sklavos S. A neural network approach for integrating banks' decision in shipping finance. Cogent Econ Financ. 2022;10(1):1-20. https://doi.org/10.1080/23322039.2022.2150134

[6] Dube F, Nzimande N, Muzindutsi PF. Application of artificial neural networks in predicting financial distress in the JSE financial services and manufacturing companies. J Sustain Financ Invest. 2023;13(1):723-43. https://doi.org/10.1080/20430795.2021.2017257

[7] Kalogirou SA. Artificial neural networks in renewable energy systems applications: A review. Renew Sustain Energy Rev. 2000;5(4):373-401. https://doi.org/10.1016/S1364-0321(01)00006-5

[8] Iglesias-Sanfeliz Cubero ÍM, Meana-Fernández A, Ríos-Fernández JC, Ackermann T, Gutiérrez-Trashorras AJ. Analysis of neural networks used by artificial intelligence in the energy transition with renewable energies. Appl Sci. 2023;14(1):389. https://doi.org/10.3390/app14010389

[9] Kaushik V. 8 Applications of Neural Networks. Analytic Steps. Available from: https://www.analyticssteps.com/blogs/8-applications-neural-networks

[10] Haykin S. Neural Networks and Learning Machines. 3rd ed. Pearson; 2009. Available from: http://dai.fmph.uniba.sk/courses/NN/haykin.neural-networks.3ed.2009.pdf

[11] Nielsen MA. Neural Networks and Deep Learning. Determination Press; 2015. Available from: http://neuralnetworksanddeeplearning.com/

[12] Sharkawy AN. Principle of neural network and its main types: Review. J Adv Appl Comput Math. 2020;7:8-19. https://doi.org/10.15377/2409-5761.2020.07.2

[13] Pan Y. Different types of neural networks and applications: Evidence from feedforward, convolutional and recurrent neural networks. Highlights Sci Eng Technol. 2024;85:247-55. https://doi.org/10.54097/6rn1wd81

[14] Liu Z, Gao W, Wan YH, Muljadi E. Wind power plant prediction by using neural networks. In: 2012 IEEE Energy Conversion Congress and Exposition (ECCE). Raleigh, NC, USA: IEEE; 2012. p. 3154-60. https://doi.org/10.1109/ECCE.2012.6342351
[15] Koroglu T, Ekici E. A comparative study on the estimation of wind speed and wind power density using statistical distribution approaches and artificial neural network-based hybrid techniques in Çanakkale, Türkiye. Appl Sci. 2024;14(3):1267. https://doi.org/10.3390/app14031267
[16] Ikram K, Djilali K, Abdennasser D, Al-Sabur R, Ahmed B, Sharkawy AN. Comparative analysis of fouling resistance prediction in shell and tube heat exchangers using advanced machine learning techniques. Res Eng Struct Mater. 2024;10(1):253-70. http://dx.doi.org/10.17515/resm2023.858en0816
[17] Teixeira RSD, Calili RF, Almeida MF, Louzada DR. Recurrent neural networks for estimating the state of health of lithium-ion batteries. Batteries. 2024;10(3):1-28. https://doi.org/10.3390/batteries10030111
[18] Barrera JM, Reina A, Maté A, Trujillo JC. Solar energy prediction model based on artificial neural networks and open data. Sustain. 2020;12(17):1-21. https://doi.org/10.3390/su12176915
[19] Gumar AK, Demir F. Solar photovoltaic power estimation using meta-optimized neural networks. Energies. 2022;15(22):1-15. https://doi.org/10.3390/en15228669
[20] Sharkawy AN, Ali MM, Mousa HHH, Ali AS. Solar PV power estimation and upscaling forecast using different artificial neural networks types: Assessment, validation, and comparison. IEEE Access. 2023;11(February):19279-300. https://doi.org/10.1109/ACCESS.2023.3249108
[21] Azka R, Soefian W, Aryani DR, Jufri FH, Utomo AR. Modelling of photovoltaic system power prediction based on environmental conditions using neural network single and multiple hidden layers. IOP Conf Ser Earth Environ Sci. 2020;599(12032):1-7. https://doi.org/10.1088/1755-1315/599/1/012032
[22] Oh J, So D, Jo J, Kang N, Hwang E, Moon J. Two-stage neural network optimization for robust solar photovoltaic forecasting. Electron. 2024;13(9):1-30. https://doi.org/10.3390/electronics13091659
[23] Sulaiman MH, Mustaffa Z. Forecasting solar power generation using evolutionary mating algorithm-deep neural networks. Energy AI. 2024;16(April):100371. https://doi.org/10.1016/j.egyai.2024.100371
[24] Amer HN, Dahlan NY, Azmi AM, Latip MFA, Onn MS, Tumian A. Solar power prediction based on artificial neural network guided by feature selection for large-scale solar photovoltaic plant. Energy Reports. 2023;9(S12):262-6. https://doi.org/10.1016/j.egyr.2023.09.141
[25] Sharkawy A, Ali MM, Mousa HHH, Ali AS. Short-Term Solar PV Power Generation Day-Ahead Forecasting. International Journal of Robotics and Control Systems. 2022; 2(3):562–580. https://doi.org/10.31763/ijrcs.v2i3.780
[26] Rushdi MA, Yoshida S, Watanabe K, Ohya Y, Ismaiel A. Deep learning approaches for power prediction in wind-solar tower systems. Energies. 2024;17(15):1-23. https://doi.org/10.3390/en17153630
[27] NASA. POWER Data Access Viewer: Prediction of Worldwide Energy Resource. Available from: https://power.larc.nasa.gov/data-access-viewer/
[28] Nahar A, Hasanuzzaman M, Rahim NA. Numerical and experimental investigation on the performance of a photovoltaic thermal collector with parallel plate flow channel under different operating conditions in Malaysia. Sol Energy. 2017;144:517-28. https://doi.org/10.1016/j.solener.2017.01.041
[29] Nasrin R, Hasanuzzaman M, Rahim NA. Effect of high irradiation on photovoltaic power and energy. Int J Energy Res. 2018;42(3):1115-31. https://doi.org/10.1002/er.3907
[30] Mahdi BH, Yousif KM, Melhum AI. Application of artificial neural network to predict wind speed: Case study in Duhok City, Iraq. J Phys Conf Ser. 2021;1829(12002):1-8. https://doi.org/10.1088/1742-6596/1829/1/012002
[31] Rao KP, Babu TV, Anuradha G, Rao BVA. IDI diesel engine performance and exhaust emission analysis using biodiesel with an artificial neural network (ANN). Egypt J Pet. 2017;26(3):593-600. https://doi.org/10.1016/j.ejpe.2016.08.006
[32] Kwon S, Kim J. Real-time upper limb motion estimation from surface electromyography and joint angular velocities using an artificial neural network for human-machine cooperation. IEEE Trans Inf Technol Biomed. 2011;15(4):522-30. https://doi.org/10.1109/TITB.2011.2151869
[33] Zhang YF, Nee AYC, Fuh JYH, Neo KS, Loy HK. A neural network approach to determining optimal inspection sampling size for CMM. Comput Integr Manuf Syst. 1996;9(3):161-9. https://doi.org/10.1016/S0951-5240(96)00005-5
[34] Sharkawy AN, Ameen AG, Mohamed S, Abdel-Jaber GT, Hamdan I. Design, assessment, and modeling of multi-input single-output neural network types for the output power estimation in wind turbine farms. Automation. 2024;5(2):190-212. https://doi.org/10.3390/automation5020012
[35] Madhiarasan M, Deepa SN. Comparative analysis on hidden neurons estimation in multi-layer perceptron neural networks for wind speed forecasting. Artif Intell Rev. 2017;48(4):449-71. https://doi.org/10.1007/s10462-016-9506-6

[36] Du K, Swamy MNS. Neural Networks and Statistical Learning. Springer; 2014. https://doi.org/10.1007/978-1-4471-5571-3
[37] Marquardt DW. An algorithm for least-squares estimation of nonlinear parameters. J Soc Ind Appl Math. 1963;11(2):431-41. https://doi.org/10.1137/0111030
[38] Hagan MT, Menhaj MB. Training feedforward networks with the Marquardt algorithm. IEEE Trans Neural Netw. 1994;5(6):2-6. https://doi.org/10.1109/72.329697
[39] Sharkawy AN, Koustoumpardis PN, Aspragathos N. A neural network-based approach for variable admittance control in human-robot cooperation: Online adjustment of the virtual inertia. Intell Serv Robot. 2020;13:495-519. https://doi.org/10.1007/s11370-020-00337-4

Blank Page

Research on Engineering Structures & Materials
www.jresm.org
MIM Research Group

Research Article

Comparative analysis of R/SWIR, NIR/SWIR, and NDSI classification methods for determination of snow cover change on Erciyes Mountain, Türkiye using Landsat satellite images

Mustafa Hayri Kesikoglu [*,1,2,a]

[1]*Dept. of Civil Eng., Faculty of Engineering and Natural Sciences, Uşak University, Uşak, Türkiye*
[2]*Dept. of Urban and Regional Planning, Faculty of Architecture and Design, Uşak University, Uşak, Türkiye*

Article Info

Article History:

Received 10 Nov 2024

Accepted 11 Jan 2025

Keywords:

Change detection;
Classification;
Near-infrared/shortwave-infrared;
Normalized difference snow index;
Red/shortwave-infrared;
Remote sensing;
Snow cover

Abstract

Snow is a crucial factor impacting many areas, including freshwater resources, irrigation, floods, and avalanches. The study aims to compare the performances of unsupervised classification methods namely Normalized Difference Snow Index (NDSI), Red/Shortwave- infrared (R/SWIR), and Near-infrared/Shortwave-infrared (NIR/SWIR) band ratio methods in snow cover classification while determining the temporal change and trend in snow cover area during the past three decades on Erciyes Mountain. The study analyzed the snow cover on Erciyes Mountain from 1988 to 2020 using Landsat 5 TM and Landsat 8 OLI data with a spatial resolution of 30 meters. Three unsupervised classification methods were applied to atmospheric-corrected Landsat datasets to obtain snow cover maps. The results indicate a declining trend in snow cover on Erciyes Mountain due to global warming, with a significant reduction of about 87% over the past 32 years. Among the three classification methods, NDSI demonstrated the highest accuracy and Kappa coefficient, making it the most suitable approach for snow cover mapping in mountainous regions. The findings can supply valuable contributions to literature and assist in better use of accurate snow cover classification methods in high mountainous regions.

© 2025 MIM Research Group. All rights reserved.

1. Introduction

Snow is an important factor of the global water cycle [1]. As a significant precipitation type, it provides approximately one-sixth of the global population's water needs [2]. Its ability to store water in winter and release it in summer contributes to the regulation of water resources management and ecosystem health. Moreover, snow cover significantly influences local and regional climates, making its accurate monitoring essential for water management and climate modeling [3-5].

However, due to global warming and other climate change impacts, snow-cover areas are undergoing significant changes. These changes directly affect the seasonal distribution of water resources, hydrological cycles, and ecosystems, leading to issues such as water scarcity, flood risks, and biodiversity loss. Therefore, monitoring changes in snow cover areas and understanding the impacts of these changes is of paramount importance for sustainable water resource management and climate change adaptation efforts.

Given the rapidly increasing population and the impacts of global warming, snow cover monitoring and data extraction have become even more critical. Studies on snow cover

*Corresponding author: hayri.kesikoglu@usak.edu.tr; mkesikoglu@gmail.com
[a]orcid.org/0000-0001-5199-0815
DOI: http://dx.doi.org/10.17515/resm2025-524ml1110rs

areas can provide valuable insights into the global water and energy cycle, aiding in its better understanding and management.

Ground-based classical measurement methods can be used for snow cover monitoring, but these methods have some limitations. Therefore, measurements using remote sensing data offer an important alternative for fast and effective monitoring of large areas [6-8]. Remote sensing has become a critical tool for monitoring snow cover changes with the ability to make synchronous observations over large areas [4, 9]. Xi and Mei [10] note that remote sensing technology has become a fundamental approach for large-scale and high-precision snow monitoring, reinforcing the statement about the critical role of remote sensing in observing snow cover changes. Largeron, Dumont [11] emphasized that remote sensing is essential for detecting snow cover changes that cannot be effectively monitored through point measurements alone. Girotto, Musselman [12] highlighted the extensive coverage provided by remote sensing images, allowing for reliable seasonal snow monitoring in remote and complex mountainous regions. In addition, remote sensing data have the potential to overcome the limitations of terrestrial measurements by providing high resolution and consistency to monitor snow cover changes over large areas [9, 13]. Therefore, remote sensing stands out as an indispensable tool for snow cover monitoring and management.

Index and band ratio-based unsupervised classification methods for snow cover classification are used in remote sensing data analysis. These methods use combinations of various spectral bands to map snow cover accurately. Various index and band ratio-based unsupervised classification methods to determine snow cover using remote sensing images have been employed in some studies. Ambinakudige, Inamdar [14] analyze how NIR and SWIR band's spectral characteristics can be utilized to improve the accuracy of snow cover mapping, reinforcing the importance of using band ratios in remote sensing applications. Butt [15] calculated three band ratios (Band 2/Band 5, Band 4/Band 5, and Band 4/Band 7) using Landsat data for snow zoning mapping in the Hindukush, Karakoram, and Himalayan regions. He stated that the band ratios effectively minimized the shadow effect. Wang, Wang [16] proposed a spectral band ratio using near-infrared (NIR) and short-wave infrared (SWIR) bands to map snow cover in dense coniferous forests using Landsat 8 Operational Satellite Imager (OLI) data. Zhang, Wang [17] introduced a new index that optimizes the use of R/SWIR and NIR/SWIR band ratios to improve the mapping accuracy of debris-free glaciers. The authors compare the performance of these band ratios against traditional methods, demonstrating their effectiveness in reducing classification errors related to water and shadow. Andreadis and Lettenmaier [18] used a snow mapping algorithm based on two indices, namely the normalized difference vegetation index (NDVI) and NDSI, to integrate remotely sensed snow observations into a macroscale hydrology model. Sibandze, Mhangara [19] aimed to increase the snow cover mapping accuracy by combining Principal Component Analysis (PCA) with NDSI by proposing the Normalized Difference Principal Component Snow Index (NDPCSI) technique. They showed that the use of PCA along with NDSI can increase the accuracy of snow cover mapping. Kuter, Akyürek [20] used NDSI to create a conventional binary reference snow map that classifies the MODIS satellite image as snow or non-snow. This study highlights the importance of NDSI in snow cover classification. Similarly, Liu, Huang [21] used machine learning technologies and NDSI methods to map snow cover fractions using MODIS data. The study demonstrates the effectiveness of NDSI in snow cover classification. However, these methods also have some disadvantages. Such index and band ratio-based studies can sometimes make it difficult to classify mixed pixels correctly and affect the accuracy and precision in snow cover classification [22]. While these studies show that index and band ratio-based methods are used in snow cover

classification, they also highlight some limitations of these methods. Therefore, considering these disadvantages, this study investigates which of the R/SWIR, NIR/SWIR, and NDSI methods used for snow cover classification gives better results in snow cover classification at Erciyes Mountain.

Previous research has primarily concentrated on glacial changes at Erciyes Mountain [23-25]. It was stated that the glaciers melted over time and almost disappeared [25]. However, the change in the amount of snow cover was not examined. This study has two main aims. The first aim of the study is to determine the temporal change and trend in snow-cover areas. The study analyzes the temporal change and trend in snow cover on Erciyes Mountain, covering 32 years from 1988 to 2020, using 30-m spatial resolution Landsat 5 TM and Landsat 8 OLI data. While a large part of Erciyes Mountain is completely covered with snow in the winter season, a portion of this area is covered with snow in the summer months as well. Satellite images from the summer months were preferred to minimize the impact of high cloud cover at the summit. The second aim of the study is to compare the performance of unsupervised classification methods in snow cover classification. R/SWIR, NIR/SWIR, and NDSI methods were applied to the atmospherically corrected Landsat data sets to obtain snow cover maps. As a result of the assessments, the best unsupervised classification technique for snow-covered mountains similar to the Erciyes was determined.

2. Materials

2.1. Study area and data

Erciyes Mountain is a volcanic mountain located in Kayseri Province, Turkey, with an elevation of 3,917 meters [26]. This region provides an important natural area for studying snow cover dynamics. Erciyes Mountain significantly impacts water resources due to the heavy snowfall during the winter months and the melting of this snow cover during the summer months.

Landsat 4–5	Bands	Wavelength (micrometers)	Resolution (meters)
Thematic Mapper (TM)	Band 1 – Blue	0.45–0.52	30
	Band 2 – Green	0.52–0.60	30
	Band 3 – Red	0.63–0.69	30
	Band 4 – Near Infrared (NIR)	0.76–0.90	30
	Band 5 – Shortwave Infrared (SWIR) 1	1.55–1.75	30
	Band 6 – Thermal	10.40–12.50	120
	Band 7 – Shortwave Infrared (SWIR) 2	2.08–2.35	30
Landsat 8 Operational Land Imager (OLI) and Thermal Infrared Sensor (TIRS)	Band 1 – Ultra Blue (coastal/aerosol)	0.435–0.451	30
	Band 2 – Blue	0.452–0.512	30
	Band 3 – Green	0.533–0.590	30
	Band 4 – Red	0.636–0.673	30
	Band 5 – Near Infrared (NIR)	0.851–0.879	30
	Band 6 – Shortwave Infrared (SWIR) 1	1.566–1.651	30
	Band 7 – Shortwave Infrared (SWIR) 2	2.107–2.294	30
	Band 8 – Panchromatic	0.503–0.676	15
	Band 9 – Cirrus	1.363–1.384	30
	Band 10 – Thermal Infrared (TIRS) 1	10.60–11.19	100
	Band 11 – Thermal Infrared (TIRS) 2	11.50–12.51	100

Fig. 1. Features of Landsat 5 TM and Landsat 8 OLI/TIRS satellite images [28]

Temperature differences between day and night are intense and freeze-thaw cycles are effective most of the year. Therefore, it is of critical importance in terms of snow-cover monitoring and management. The wide coverage provided by remote sensing data offers significant advantages in terms of monitoring snow cover dynamics and producing results quickly [27]. In this study, Landsat 5 (August 1988, 2000, 2010) and Landsat 8 level 1A satellite images (August 2020) were used in the classification of snow cover and other areas. The data were downloaded from the United States Geological Survey (USGS) website freely. Fig. 1 describes the dataset in detail. The study area is divided into two main classes: snow cover and other areas. Fig. 2 shows the satellite images of the study area in RGB band combination.

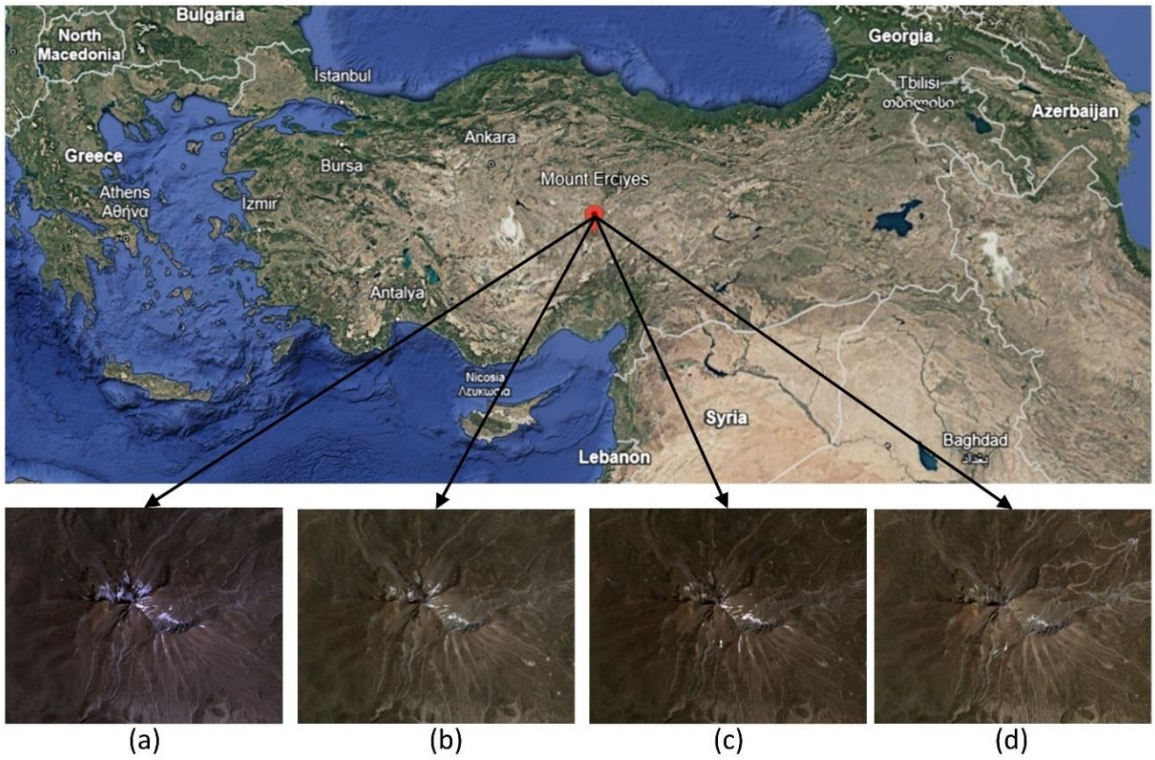

Fig. 2. Satellite images of Erciyes Mountain: (a) 1988, (b) 2000, (c) 2010, (d) 2020

3. Methodology

The classification and change detection approach used to determine snow cover changes with the aid of unsupervised classification methods is presented in Fig. 3. Firstly, Landsat satellite images were subjected to image preprocessing (geometric, radiometric, and atmospheric correction) processes according to the study flowchart. Then, atmospherically corrected Landsat satellite images were used to obtain snow cover areas using three different unsupervised classification methods (R/SWIR, NIR/SWIR, and NDSI). Finally, comparative analysis of the classification methods was performed and the snow cover area change was evaluated.

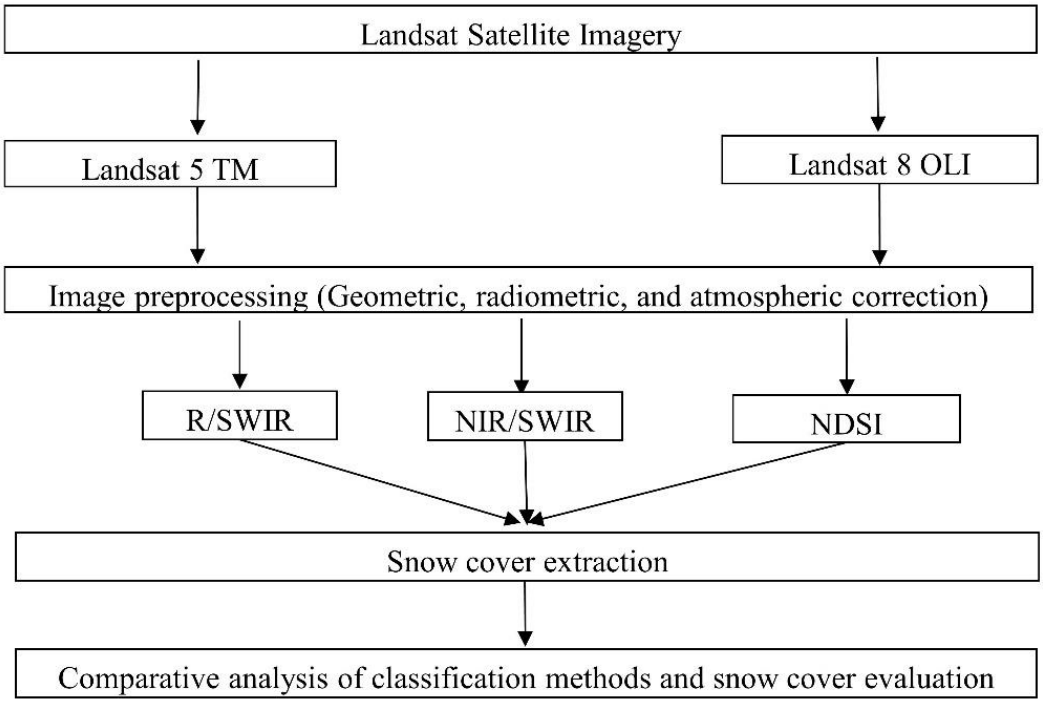

Fig. 3. Flowchart of study

3.1. Image Preprocessing

Initially, a study area was created from the peak to the mountain's slopes. The study area boundaries were used for all satellite data. Geometric correction, one of the image preprocessing stages, aims to align and rectify the image data to represent the geographic features and spatial relationships accurately. This process is carried out using ground control points (GCPs), which are known coordinates located at the same geographic position in both the reference image and the image to be transformed. These GCPs are evenly distributed across the image [29]. The geometric correction process resulted in a root mean square error (RMSE) value of 0.1 pixels in this study.

In change detection studies, it is significant to prefer satellite images with identical spatial and radiometric resolution to reduce errors caused by factors such as variations in sun angle, seasonal differences, or the satellite's position when using images from different years. Therefore, radiometric correction should be performed. This was achieved by transforming pixel brightness values of satellite images to spectral radiance values. Later, Spectral radiance values were processed using the FLAASH atmospheric correction in ENVI 5.3 software. This approach was implemented to effectively eradicate influences from reflected energy.

In this study, three different unsupervised image classification methods (R/SWIR, NIR/SWIR, and NDSI) were used to investigate which method would determine the snow cover most accurately.

3.2. Red/Shortwave Infrared Band Ratio

The Red / Shortwave infrared (R/SWIR) band ratio is an effective unsupervised classification method used to determine snow cover. This ratio is calculated by comparing the reflectance values of the red (R) and shortwave infrared (SWIR) bands. The formula is as Equation 1 follows [30]:

$$Band\ Ratio_1 = \frac{R}{SWIR} \tag{1}$$

The reflectance values in Landsat 5 TM bands 3 and 4 are denoted as R and SWIR. In Landsat 8 OLI, Band 4 and 5 correspond to R and SWIR because of the spectral bandwidth match. Snow shows high reflectance in the R band and low reflectance in the short-wave infrared. Therefore, this ratio is an effective tool for determining snow cover [30].

3.3. Near Infrared/Shortwave Infrared band ratio

The Near infrared / Shortwave infrared (NIR/SWIR) band ratio is another effective unsupervised classification method for determining snow cover. This ratio is calculated by comparing the reflectance values of the near-infrared (NIR) and short-wave infrared (SWIR) bands. The formula is as Equation 2 follows [30]:

$$Band\ Ratio_2 = \frac{NIR}{SWIR} \tag{2}$$

NIR and SWIR denote the reflectance values in Landsat 5 TM bands 4 and 5. Because of the spectral bandwidth match, the values for bands 5 and 6 correspond to NIR and SWIR in Landsat 8 OLI. Snow shows high reflectance in the NIR band and low reflectance in the SWIR band. This feature helps to distinguish snow cover from other surface types. Wang, Wang [16] used this method for snow cover mapping in dense coniferous forests. They emphasized that this method is one of the most effective methods used in snow cover mapping studies.

3.4. Normalized Difference Snow Index

Normalized Difference Snow Index (NDSI) is one of the important unsupervised classification methods used to determine snow cover areas thanks to the wide-area observations provided by remote sensing data. NDSI is calculated with the reflectance values of the green band (G) and SWIR bands. The formula is as Equation 3 follows [31]:

$$NDSI = \frac{(G - SWIR)}{(G + SWIR)} \tag{3}$$

The reflectance values in Landsat 5 TM bands 2 and 5 are denoted as G and SWIR. In Landsat 8 OLI, Bands 3 and 6 correspond to G and SWIR due to spectral bandwidth matching. NDSI values of 0.4 and above generally indicate the presence of snow cover [31]. Knowing the threshold value accelerates the snow cover monitoring and mapping processes, allowing researchers to obtain rapid results.

3.5. Snow Cover Extraction

The effectiveness of unsupervised classification methods (R/SWIR, NIR/SWIR, and NDSI) in snow cover extraction was analyzed in the current study. It was necessary to subject the classified images to a thresholding process to obtain the desired snow-covered areas using the classification methods employed in this study. Initially, Otsu's binary thresholding method [32, 33] was utilized to determine the threshold value. However, when the threshold values obtained using Otsu's method were applied, it was observed that the snow-covered areas could not be accurately detected in all three methods. Racoviteanu, Arnaud [34] suggested that the threshold value for classified images can be determined through careful visual inspection. Therefore, threshold values were determined using image histograms after visually analyzing the R/SWIR and NIR/SWIR classification images. For the NDSI classification images, the threshold value ≥ 0.4 was used as determined in previous studies [31, 35, 36]. Thus, places equal to or greater than the specified threshold value (NDSI ≥ 0.4) were determined as snow areas.

3.6. Performance Metrics

A confusion matrix is utilized to assess the performance of a classification model by comparing the predicted classifications to the actual classifications. It provides a wide summary of the classification results, allowing for the calculation of various performance metrics, including True Positives (TP), True Negatives (TN), False Positives (FP), and False Negatives (FN), as shown in Table 1 [37].

Table 1. Confusion matrix

Predicted Model	Ground Truth	
	Correct	Incorrect
Correct	TP	FP
Incorrect	FN	TN

In snow cover classification, TP refers to correctly identified snow-covered pixels, while TN denotes correctly identified non-snow-covered pixels. Conversely, FP represents non-snow-covered pixels incorrectly classified as snow-covered, and FN signifies snow-covered pixels mistakenly classified as non-snow-covered.

Performance metrics such as accuracy and Kappa statistic value can be obtained using confusion matrix parameters [38]. Accuracy is calculated as the proportion of the sum of true positive and true negative pixels to the total number of pixels within the images, representing the extent of correct classification. The Kappa statistic is employed to quantify the degree of concurrence between a classified image and reference data, serving as a valuable metric to assess the accuracy and consistency of the classification outcomes. The performance metrics' formulas are shown in Equation 4-7 [39].

$$Accuracy = \frac{TP + TN}{TP + TN + FP + FN} \tag{4}$$

$$P_O = \frac{TP + TN}{TP + TN + FP + FN} \tag{5}$$

$$P_E = \frac{(TP + FP)(TP + FN) + (TN + FP)(TN + FN)}{(TP + TN + FP + FN)^2} \tag{6}$$

$$Kappa = \frac{P_O - P_E}{1 - P_E} \tag{7}$$

Where P_O is the observed agreement, and P_E is the expected agreement by chance.

4. Results and Discussion

In the study, three unsupervised classification methods (R/SWIR, NIR/SWIR, and NDSI) were compared using ENVI 5.3 software to extract snow cover on Erciyes Mountain. Snow cover images derived from R/SWIR, NIR/SWIR, and NDSI are shown in Fig. 4.

A confusion matrix was used to evaluate the accuracy of the classified maps. 50 ground control points covering the study area were randomly generated using ArcGIS 10.8 software. The determination of these points as snow or other areas was determined with the help of Google Earth images. The accuracy and Kappa coefficient metrics were calculated to evaluate the performance of each classification method on Landsat satellite images of different years. Classification accuracies obtained by R/SWIR, NIR/SWIR, and NDSI are shown in Table 2.

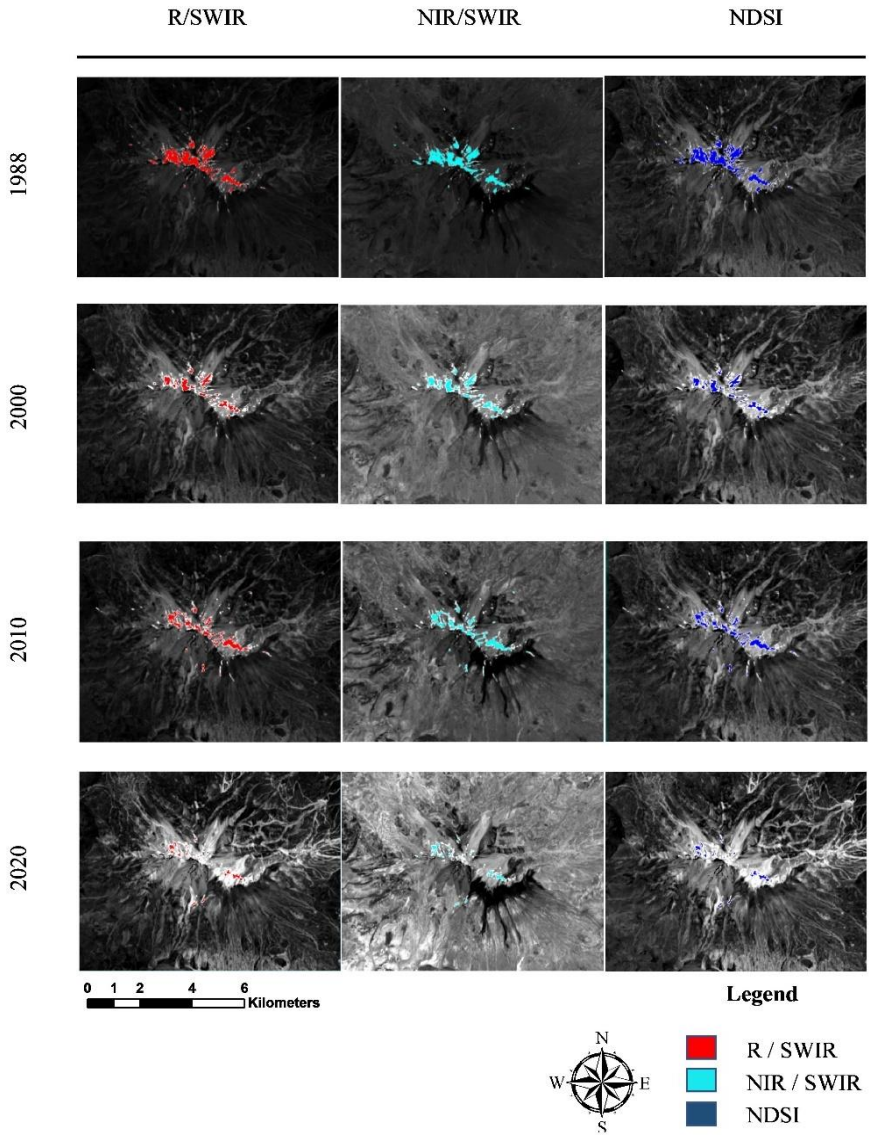

Fig. 4. Snow cover images derived from R/SWIR, NIR/SWIR, and NDSI

Table 2. Classification accuracies obtained by R/SWIR, NIR/SWIR, and NDSI

Method	R/SWIR		NIR/SWIR		NDSI	
Year	Accuracy	Kappa	Accuracy	Kappa	Accuracy	Kappa
1988	96%	86%	98%	93%	96%	86%
2000	94%	88%	90%	80%	96%	92%
2010	92%	84%	92%	84%	96%	92%
2020	92%	84%	96%	92%	98%	96%

The results reveal that the classification accuracies are generally high across the methods, with slight variations by year. For 1988, the highest accuracy (98%) and Kappa value (93%) were achieved with the NIR/SWIR method, while R/SWIR and NDSI methods showed slightly lower performance, each with 96% accuracy and an 86% Kappa value. In 2000, the NDSI method showed the best results, with 96% accuracy and 92% Kappa. The NIR/SWIR method, however, lagged behind with a 90% accuracy and 80% Kappa value. The R/SWIR method performed moderately well in 2000, achieving a 94% accuracy and an 88% Kappa. In 2010, the NDSI method continued to demonstrate superior performance,

with an accuracy of 96% and a Kappa value of 92%. Both the R/SWIR and NIR/SWIR methods achieved similar results for this year, each reaching 92% accuracy and an 84% Kappa value. Finally, for 2020, the NDSI method again yielded the highest accuracy (98%) and Kappa coefficient (96%). The NIR/SWIR method also performed well with 96% accuracy and a 92% Kappa value, while the R/SWIR method fell slightly behind, achieving 92% accuracy and an 84% Kappa value. Overall, the NDSI method consistently delivered the highest accuracy and Kappa values across different years, suggesting that it may offer more robust classification accuracy over time compared to R/SWIR and NIR/SWIR.

Table 3. Snow cover areas

Year	R/SWIR (Km^2)	NIR/SWIR (Km^2)	NDSI (Km^2)	Mean (Km^2)
1988	0.968	0.979	0.965	0.971
2000	0.414	0.437	0.404	0.418
2010	0.522	0.533	0.514	0.523
2020	0.128	0.133	0.127	0.129

An objective assessment was conducted by analyzing satellite images to account for snow cover changes from 1988-2020. Post classification comparison method was used to determine the snow cover change of the last 32 years in the study. The snow cover areas and change rates are reported in Tables 3 and 4 respectively.

Table 4. Snow cover changes according to the periods

Periods	R/SWIR Area (Km^2)	Rate (Km^2/ year)	NIR/SWIR Area (Km^2)	Rate (Km^2/ year)	NDSI Area (Km^2)	Rate (Km^2/ year)	Mean Area (Km^2)	Rate (Km^2/ year)
1988-2000	-0.55	-0.05	-0.54	-0.05	-0.56	-0.05	-0.55	0.05
1988-2010	-0.45	-0.02	-0.45	-0.02	-0.45	-0.02	-0.45	0.02
1988-2020	-0.84	-0.03	-0.85	-0.03	-0.84	-0.03	-0.84	0.03
2000-2010	0.11	0.01	0.10	0.01	0.11	0.01	0.11	0.01
2000-2020	-0.29	-0.01	-0.30	-0.01	-0.28	-0.01	-0.29	0.01
2010-2020	-0.39	-0.04	-0.40	-0.04	-0.39	-0.04	-0.39	0.04

Since the area values were close to each other, area evaluations were made by considering the average results obtained from the three methods. Table 3 shows that the highest snow covers mean value of almost 0.971 km^2 was detected in 1988 followed by the highest second value observed in 2010 with 0.523 km^2. The lowest snow cover mean value of 0.129 km^2 was observed in 2020. The lowest second value was observed in 2000 with 0.418 km^2.

In this study, the change detection approach was based on post-classification comparison [40, 41]. This method involves comparing classified images with each other to identify changes. The snow cover changes that occurred during the 32 years from 1988 to 2020 are seen in Table 4. Negative values show the total and average annual decrease in the amount of snow cover between certain periods, while positive values show the increment. According to the areas achieved from the average of results belonging to the three methods, the study showed that approximately 0.84 km^2 and 87 percent of the snow cover area had melted over the past three decades. The highest amount of snow melt was observed respectively in the periods of 1988-2000 and 2010-2020 with 0.55 km^2 and 0.39 km^2. However, there had been an increment in the snow cover area in the period of 2000-2010. This situation should be investigated further. The snow cover trend of about the past three decades can be seen in Fig. 6.

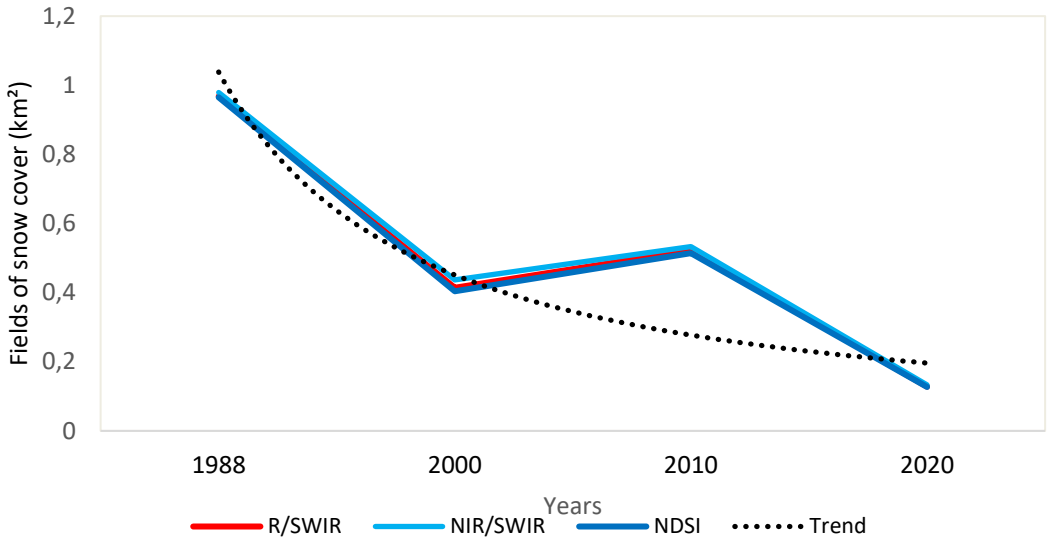

Fig. 6. Snow cover trend during the period 1988-2020

Fig. 6 indicates a significant decrease in snow cover areas between 1988 and 2020. The overall trend of snow cover change shows a decline during this period. It is investigated that the climatic conditions during the selected years to determine whether a dry climate may be responsible for the observed differences. The average temperatures and precipitations of each month over the last three decades can be seen in Fig. 7.

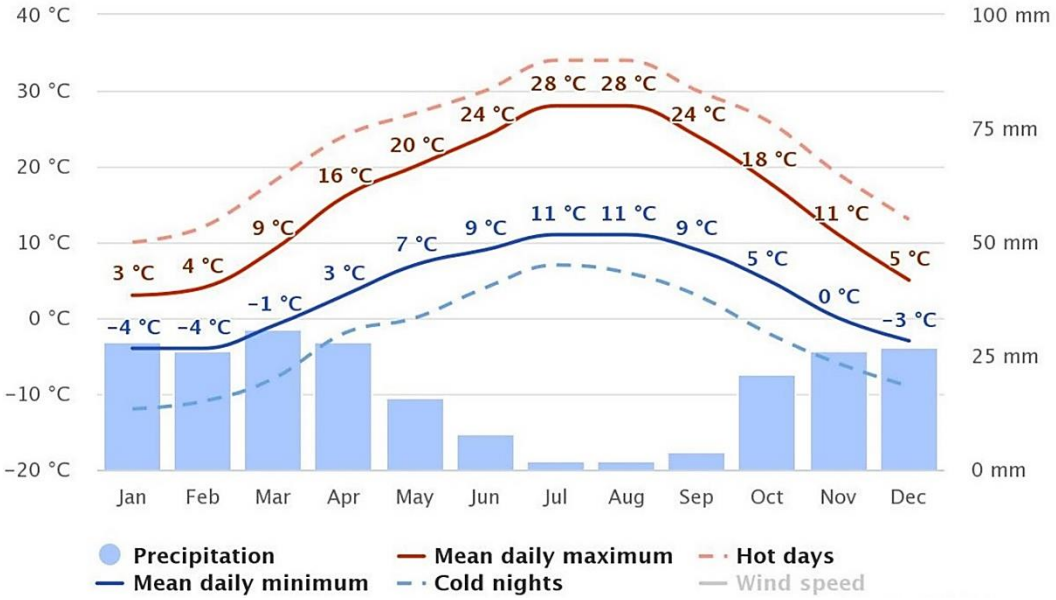

Fig. 7. Average temperatures and precipitations for Erciyes Mountain over the last three decades

As can be seen in Fig. 7, the "mean daily maximum" (represented by the solid red line) demonstrates the highest temperature recorded on an average day for each month on Erciyes Mountain. Likewise, the "mean daily minimum" (represented by the solid blue line) demonstrates the average lowest temperature recorded. The dashed red and blue lines correspond to the hottest day and coldest night, respectively, showcasing the monthly averages over the past three decades. The average temperatures on Erciyes Mountain have mostly been above 0 degrees Celsius (C°) and the precipitations below 30 mm. It is known

that high temperatures affect snowfall negatively. These data show us that global warming-based dry climate leads to a decrease in snow-covered areas in Erciyes mountain.

5. Conclusion

This study examined snow cover changes on Erciyes Mountain from 1988 to 2020, highlighting the importance of snow as crucial indicator of climate change. Changes in snow cover within mountainous regions are known to affect the continuity and sustainability of water resources significantly. By analyzing satellite imagery from different years, the study evaluated temporal trends and considered the links between these changes and the impacts of global warming. This research underscores the importance of conducting similar analyses across wider geographic areas to better understand regional trends.

The study compared the ratio-based R/SWIR and NIR/SWIR methods with the Normalized Difference Snow Index (NDSI) to determine the most effective classification method for snow cover detection. The results indicate that the NDSI method provides higher accuracy and Kappa coefficient than the other methods, establishing it as the most suitable classification approach for snow-covered mountainous areas. This suggests that the NDSI has a lower margin of error, yielding more reliable results in snow classification.

The findings show that the average snow cover area decreased from 0.971 km^2 in 1988 to 0.129 km^2 in 2020, representing an approximate 87% reduction. The most pronounced decline was observed during the periods of 1988-2000 and 2010-2020, linked to temperature increases and reduced precipitation due to climate change. However, a partial increase in snow cover was observed between 2000-2010, indicating that the complex effects of climate variations require further investigation. These findings highlight that snow cover trends offer significant insights into understanding the effects of global warming.

The study emphasizes the importance of accurate snow cover classification in mountainous regions, contributing valuable insights to future research. Improving classification accuracy enables more precise analysis of regional snow cover changes, which can inform local climate adaptation strategies. Therefore, further analysis of alternative classification methods for snow cover detection will be essential in advancing research on climate change impacts.

References

[1] Cho E, Vuyovich CM, Kumar SV, Wrzesien ML, Kim RS, Jacobs JM. Precipitation biases and snow physics limitations drive the uncertainties in macroscale modeled snow water equivalent. Hydrology and Earth System Sciences. 2022;26(22):5721-35. https://doi.org/10.5194/hess-26-5721-2022

[2] Liu Z, Wang T, Han J, Yang W, Yang H. Decreases in mean annual streamflow and interannual streamflow variability across snow-affected catchments under a warming climate. Geophysical Research Letters. 2022;49(3):e2021GL097442. https://doi.org/10.1029/2021GL097442

[3] Yu H, Zhang X, Liang T, Xie H, Wang X, Feng Q, et al. A New Approach of Dynamic Monitoring of 5-day Snow Cover Extent and Snow Depth Based on MODIS and AMSR-E Data From Northern Xinjiang Region. Hydrological Processes. 2012;26(20):3052-61. https://doi.org/10.1002/hyp.8253

[4] Ma Y, Zhang Y. Improved on Snow Cover Extraction in Mountainous Areas Based on Multi-Factor Ndsi Dynamic Threshold. The International Archives of the Photogrammetry Remote Sensing and Spatial Information Sciences. 2022;XLIII-B3-2022:771-8. https://doi.org/10.5194/isprs-archives-XLIII-B3-2022-771-2022

[5] Atasever Ü, Kesikoğlu M, Özkan C. EvaMapper: a novel MATLAB toolbox for evapotranspiration mapping. The International Archives of the Photogrammetry, Remote Sensing and Spatial Information Sciences. 2013;40:23-6. https://doi.org/10.5194/isprsarchives-XL-7-W2-23-2013
[6] Kesikoglu MH, Cicekli SY, Kaynak T, Ozkan C, editors. The determination of coastline changes using artificial neural networks in Yamula Dam Lake, Turkey. 2017 8th International Conference on Information Technology (ICIT); 2017 17-18 May 2017. https://doi.org/10.1109/ICITECH.2017.8079936
[7] Kesikoglu MH, Atasever UH, Ozkan C, Besdok E. THE USAGE OF RUSBOOST BOOSTING METHOD FOR CLASSIFICATION OF IMPERVIOUS SURFACES. Int Arch Photogramm Remote Sens Spatial Inf Sci. 2016;XLI-B7:981-5. https://doi.org/10.5194/isprs-archives-XLI-B7-981-2016
[8] Kesikoglu MH. Evaluating spatial resolution enhancement on impervious surface detection using support vector machine. Research & Design. 2024;1(1):33-42. https://doi.org/10.17515/rede2024-003bu1111rs
[9] Jin H, chen x. Spatio-Temporal Changes of Snow Cover and Its Relationship With Meteorological Factors on the Qinghai-Tibet Plateau, China. 2021. https://doi.org/10.21203/rs.3.rs-453378/v1
[10]Xi N, Mei G. Avalanche Susceptibility Mapping by Investigating Spatiotemporal Characteristics of Snow Cover Based on Remote Sensing Imagery Along the Pemo Highway-A Critical Transportation Road in Tibet, China. Water. 2023;15(15):2743. https://doi.org/10.3390/w15152743
[11]Largeron C, Dumont M, Morin S, Boone A, Lafaysse M, Metref S, et al. Toward Snow Cover Estimation in Mountainous Areas Using Modern Data Assimilation Methods: A Review. Frontiers in Earth Science. 2020;8. https://doi.org/10.3389/feart.2020.00325
[12]Girotto M, Musselman KN, Essery R. Data Assimilation Improves Estimates of Climate-Sensitive Seasonal Snow. Current Climate Change Reports. 2020;6(3):81-94. https://doi.org/10.1007/s40641-020-00159-7
[13]Gafurov A, Vorogushyn S, Farinotti D, Duethmann D, Merkushkin A, Merz B. Snow-Cover Reconstruction Methodology for Mountainous Regions Based on Historic in Situ Observations and Recent Remote Sensing Data. The Cryosphere. 2015;9(2):451-63. https://doi.org/10.5194/tc-9-451-2015
[14]Ambinakudige S, Inamdar P, Lotfata A. A Spectral Analysis of Snow in Mt. Rainier. Journal of Geography and Geology. 2018;10(3):20. https://doi.org/10.5539/jgg.v10n3p20
[15]Butt MJ. Exploitation of Landsat Data for Snow Zonation Mapping in the Hindukush, Karakoram and Himalaya (HKH) Region of Pakistan. Hydrological Sciences Journal. 2013;58(5):1088-96. https://doi.org/10.1080/02626667.2013.799774
[16]Wang X, Wang J, Jiang Z, Li H, Hao X. An Effective Method for Snow-Cover Mapping of Dense Coniferous Forests in the Upper Heihe River Basin Using Landsat Operational Land Imager Data. Remote Sensing. 2015;7(12):17246-57. https://doi.org/10.3390/rs71215882
[17]Zhang M, Wang X, Shi C, Yan D. Automated Glacier Extraction Index by Optimization of Red/Swir and NIR /SWIR Ratio Index for Glacier Mapping Using Landsat Imagery. Water. 2019;11(6):1223. https://doi.org/10.3390/w11061223
[18]Andreadis KM, Lettenmaier DP. Assimilating Remotely Sensed Snow Observations Into a Macroscale Hydrology Model. Advances in Water Resources. 2006;29(6):872-86. https://doi.org/10.1016/j.advwatres.2005.08.004
[19]Sibandze P, Mhangara P, Odindi J, Kganyago M. A Comparison of Normalised Difference Snow Index (NDSI) and Normalised Difference Principal Component Snow Index (NDPCSI) Techniques in Distinguishing Snow From Related Land Cover Types. South African Journal of Geomatics. 2014;3(2):197. https://doi.org/10.4314/sajg.v3i2.6
[20]Kuter S, Akyürek Z, Weber GW. Estimation of Subpixel Snow-Covered Area by Nonparametric Regression Splines. The International Archives of the Photogrammetry Remote Sensing and Spatial Information Sciences. 2016;XLII-2/W1:31-6. https://doi.org/10.5194/isprs-archives-XLII-2-W1-31-2016
[21]Liu C, Huang X, Li X, Liang T. MODIS Fractional Snow Cover Mapping Using Machine Learning Technology in a Mountainous Area. Remote Sensing. 2020. https://doi.org/10.3390/rs12060962

[22]Han T, Wang D, Jiang Y, Wang X. The Stepwise Discriminant Algorithm for Snow Cover Mapping Based on FY-3/MERSI Data. 2013. https://doi.org/10.1117/12.2031490
[23]Kurter A, Sungur K. Glaciers of Middle East and Africa-Glaciers of Turkey. Satellite image atlas of the world USGS professional paper. 1991;1386:1-30. https://doi.org/10.3133/pp1386G
[24]Sarıkaya M, Çiner A, Zreda M. Late Quaternary glacial deposits of the Erciyes Volcano. Yerbilimleri. 2003;27:59-74.
[25]Yavasli DD, Tucker CJ, Melocik KA. Change in the glacier extent in Turkey during the Landsat Era. Remote Sens Environ. 2015;163:32-41. https://doi.org/10.1016/j.rse.2015.03.002
[26]Aydar E, Şen E, Sarıkaya MA, Kuzucuoğlu C. In the Footsteps of Strabon: Mount Erciyes Volcano-The Roof of Central Anatolia and Sultansazliği Basin. Landscapes and Landforms of Turkey: Springer; 2019. p. 565-76. https://doi.org/10.1007/978-3-030-03515-0_33
[27]Yu F, Wang P, Liu L, Li H, Zhang Z. The Variability of Snow Cover and Its Contribution to Water Resources in the Chinese Altai Mountains From 2000 to 2022. Remote Sensing. 2023;15(24):5765. https://doi.org/10.3390/rs15245765
[28]Afrasinei GM, Melis MT, Arras C, Pistis M, Buttau C, Ghiglieri G. Spatiotemporal and spectral analysis of sand encroachment dynamics in southern Tunisia. European Journal of Remote Sensing. 2018;51(1):352-74. https://doi.org/10.1080/22797254.2018.1439343
[29]Dave CP, Joshi R, Srivastava S. A survey on geometric correction of satellite imagery. International Journal of Computer Applications. 2015;116(12). https://doi.org/10.5120/20389-2655
[30]Pellikka P, Rees WG. Remote sensing of glaciers: techniques for topographic, spatial and thematic mapping of glaciers: CRC press; 2009. https://doi.org/10.1201/b10155
[31]Butt MJ. Characteristics of Snow Cover in the Hindukush, Karakoram and Himalaya Region Using Landsat Satellite Data. Hydrological Processes. 2012;26(24):3689-98. https://doi.org/10.1002/hyp.8375
[32]Otsu N. A threshold selection method from gray-level histograms. IEEE transactions on systems, man, and cybernetics. 1979;9(1):62-6. https://doi.org/10.1109/TSMC.1979.4310076
[33]Kesikoglu MH, Ozkan C, Kaynak T. The impact of impervious surface, vegetation, and soil areas on land surface temperatures in a semi-arid region using Landsat satellite images enriched with Ndaisi method data. Environmental Monitoring and Assessment. 2021;193(3):143. https://doi.org/10.1007/s10661-021-08916-3
[34]Racoviteanu AE, Arnaud Y, Williams MW, Ordonez J. Decadal changes in glacier parameters in the Cordillera Blanca, Peru, derived from remote sensing. J Glaciol. 2008;54(186):499-510. https://doi.org/10.3189/002214308785836922
[35]Gaur MK, Goyal R, Saha D, Singh N, Shekhar S, Kumar A, et al. The Estimation of Snow Cover Distribution Using Satellite Data in the Cold Arid Leh Region Of Indian Himalaya. Polish Journal of Environmental Studies. 2021;31(1):63-73. https://doi.org/10.15244/pjoes/135606
[36]Hall DK, Benson CS, Field WO. Changes of Glaciers in Glacier Bay, Alaska, Using Ground and Satellite Measurements. Physical Geography. 1995;16(1):27-41. https://doi.org/10.1080/02723646.1995.10642541
[37]Günen MA. Fast building detection using new feature sets derived from a very high-resolution image, digital elevation and surface model. Int J Remote Sens. 2024;45(5):1477-97. https://doi.org/10.1080/01431161.2024.2313991
[38]Stehman S. Estimating the kappa coefficient and its variance under stratified random sampling. Photogrammetric engineering and remote sensing. 1996;62(4):401-7.
[39]Revuelto J, Alonso-González E, Gascoin S, Rodríguez-López G, López-Moreno JI. Spatial Downscaling of MODIS Snow Cover Observations Using Sentinel-2 Snow Products. Remote Sensing. 2021;13(22):4513. https://doi.org/10.3390/rs13224513
[40]Kesikoğlu MH, Cicekli SY, Kaynak T. The identification of seasonal coastline changes from landsat 8 satellite data using artificial neural networks and k-nearest neighbor. Turkish Journal of Engineering. 2020;4(1):47-56. https://doi.org/10.31127/tuje.599359
[41]Kesikoğlu MH, Kaynak T. Tracking seasonal coastal dynamics of Ağyatan wetland using object-based Classification and Regression Tree. Niğde Ömer Halisdemir Üniversitesi Mühendislik Bilimleri Dergisi. 2025;14(1):308-17. https://doi.org/10.28948/ngumuh.1559034

Blank Page

Research on Engineering Structures & Materials
www.jresm.org
Research Group

Research Article

Valorization of marine dredged sediments from Jebha Port as a sustainable alternative to dune sand in concrete manufacturing

Khadija Benhaddou [1,a], Ayoub Souileh [*,1,b], Latifa Ouadif [1,c], Achraf Mabrouk [2,d], Sabihi Abdelhak [3,e], Khadija Baba [4,f], Mustapha Rharouss [1,g]

[1]*Laboratory of Applied Geophysics, Geotechnics, Engineering Geology, and Environmental (L3GIE), Mohammadia Engineering School, Mohammed V University in Rabat, Morocco*
[2]*LAFH, Faculty of Sciences and Techniques, Hassan 1st University, Settat, Morocco*
[3]*Experimental Center for Major Works, Public Laboratory for Testing and Studies in Casablanca, Morocco*
[4]*Civil and Environmental Engineering Laboratory (LGCE), Mohammadia Engineering School, Mohammed V University in Rabat, Morocco*

Article Info

Article History:

Received 06 Feb 2025

Accepted 04 Apr 2025

Keywords:

Ecological alternative;
Dredged sediments;
Physico-chemical characterization;
Progressive incorporation;
Mechanical and rheological performance;
Concrete formulation

Abstract

The construction industry is facing increasing challenges due to the depletion of natural sand resources, making it essential to find sustainable alternatives. This study explores the potential of marine dredged sediments from Jebha Port, Morocco, as a substitute for dune sand in B30 concrete. By incorporating these sediments at different replacement levels (10% to 100%), the study evaluates their impact on the concrete's workability and strength. To start, a detailed physico-chemical analysis of the dredged sediments was carried out to understand their properties and how they might affect concrete performance. The sediments were then mixed into concrete at varying substitution rates, from small adjustments (10% and 25%) to complete replacement of dune sand (100%). The fresh-state properties showed that higher sediment content reduced workability, making the mix less fluid. However, with proper adjustments to the mix design, this issue could be managed. The study also examined the hardened-state performance, focusing on compressive and tensile strength. Results showed that replacing up to 25% of dune sand with marine sediments maintained acceptable strength, making the concrete suitable for non-structural applications. Beyond this level, mechanical performance declined, suggesting that total replacement may require further optimization. Overall, this research highlights those marine dredged sediments from Jebha Port can be a practical and eco-friendly alternative to natural dune sand. By reusing these sediments in construction, we can reduce environmental pressure on sand resources while promoting more sustainable building practices. This approach aligns with circular economy principles, turning what was once considered waste into a valuable material for the construction industry.

© 2025 MIM Research Group. All rights reserved.

1. Introduction

In Morocco, large quantities of materials must be dredged annually from seaports, rivers, and lakes to maintain maritime navigation safety, ensure port accessibility, facilitate port infrastructure operations, and optimize the use of extracted sediments. According to the National Ports Agency, around 3 million cubic meters of sediments are dredged annually, with over 70% comprising sand

*Corresponding author: ayoub.souileh@research.emi.ac.ma
[a]orcid.org/0009-0004-4216-5433; [b]orcid.org/ 0009-0001-7754-8109; [c]orcid.org/ 0000-0002-4613-1124; [d]orcid.org/ 0000-0002-4146-8211; 0000-0003-4603-4321; [g]orcid.org/ 0009-0003-2695-0426
DOI: http://dx.doi.org/10.17515/resm2025-665ma0206rs

- equivalent to more than 2 million cubic meters - mainly extracted from ports in Morocco's southern regions. [1] The issue of sediment accumulation is particularly prevalent in Atlantic coastal ports, especially in the central and southern sectors, spanning from Safi to Dakhla, where the highest dredging volumes are recorded.[2]

Currently, dredged sediments, particularly sand, are being investigated as a sustainable industrial alternative to conventional sand extraction. This approach aligns with public policies aimed at mitigating the challenges posed by the informal sector, which predominantly depends on the exploitation of beaches and dunes. [3] A key initiative in this context is the "Le Sable Vert" label, which fosters sustainability by incorporating environmental, social, and economic factors into the extraction and valorization of dredged materials. This shift has motivated professionals in the construction and public works (BTP) sector, both in Morocco and globally, to explore innovative solutions. As a result, there has been a growing body of research dedicated to the valorization of marine sediments as alternative construction materials, aiming to mitigate the depletion of natural resources, meet the rising demand for construction materials, and diversify supply sources.[4]

The incorporation of marine sediments into concrete has been widely explored in civil engineering, as concrete continues to be the most commonly used construction material globally. Research has primarily examined the substitution of conventional concrete components with dredged sediments, either as a replacement for cement or sand, and investigated the feasibility of replacing a portion of CEM I 52.5 cement with an equivalent volume of dried and ground dredged sediments from the Port of Dunkirk, France. Similarly, Hayek (2022)[5] investigated the valorization of marine sediments extracted from the ports of Pérols and Camargue, France, evaluating the partial replacement of sand with raw or pre-treated sediments in XS C30/37-class ordinary concrete formulations.

In this context, the present study investigates the effects of incorporating marine dredged sediments from the Port of Jebha on the mechanical and rheological properties of B30 concrete. To achieve this, dune sand in the reference mix was partially or fully replaced with dredged sediments at replacement rates ranging from 10% to 100%. A preliminary physico-chemical characterization of the sediments confirmed their suitability for use without the need for specific pre-treatment. The sediments were classified into two categories: C1 (cleaner sediments) and C2 (less clean sediments). Two concrete formulations incorporating these sediments were then tested to assess their impact on key properties, including workability (slump), compressive strength, and tensile strength.[6] Therefore, the valorization of dredged sediments represents a promising solution for concrete production, serving as a sustainable substitute for conventional sand. However, careful selection of processing methods and incorporation rates is essential to ensure adherence to regulatory standards and to preserve the optimal performance of the material.[7]

The use of dredged sediments as a substitute for dune sand offers an environmentally sustainable solution by decreasing dependence on natural dune ecosystems, which are vital for coastal preservation. This approach also tackles the challenge of managing dredged material waste by repurposing it for construction purposes, thus reducing the volume of materials either disposed of at sea or stored on land.[8]

This study evaluates the impact of marine dredged sediments from Jebha Port, Morocco, as partial or full replacements for dune sand in B30 concrete, focusing on their impact on workability and mechanical performance. By valorizing these materials, this study aligns with environmental policies aimed at lowering the ecological footprint of construction industries. It aligns with circular economy principles by reintegrating an industrial by-product into the lifecycle of construction materials. These initiatives contribute to the conservation of natural resources and help mitigate the environmental degradation associated with traditional sand extraction practices.[9]

1.1 Dredging Site

The sediments examined in this study were extracted from the port of Jebha, situated in northern Morocco, within the province of Chefchaouen in the Tanger-Tétouan-Al Hoceima region, as shown in Figure 1. The port of Jebha plays a crucial role in fishing activities and maritime trade. Located 162 km from Al Hoceima, it is accessible via the Mediterranean coastal road, which connects

Tétouan to Al Hoceima. Positioned between the limestone cliffs of Pointe des Pêcheurs and the Oued Misiaba, the port enjoys natural protection against ocean swells.[10]

This port is an essential economic driver for the region, facilitating the transport of goods and fishery products. Its approximate coordinates are 35°13'10" N and 4°40'45" W, giving it a strategic position along the Moroccan Mediterranean coastline.

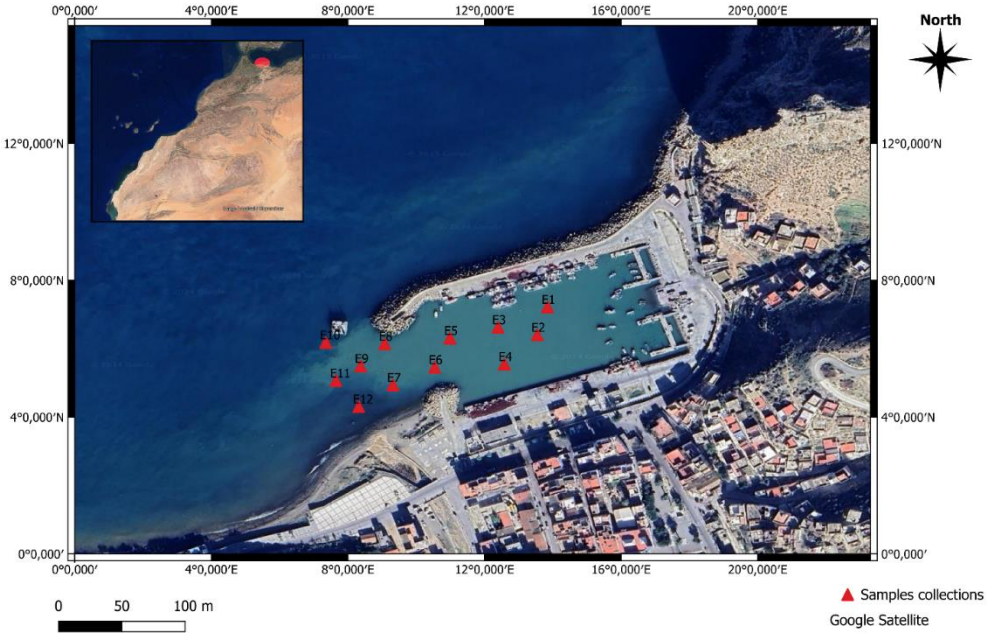

Fig. 1. Map showing the location of the dredging site at Jebha Port

2. Materials and Methods

Figure 2 illustrates the methodology employed in this study, outlining the key steps involved in evaluating the use of dredged sediments as a substitute for sand in concrete. These steps include sediment collection, physical, chemical, and mineralogical characterization, concrete formulation with varying substitution levels, and subsequent rheological and mechanical testing.

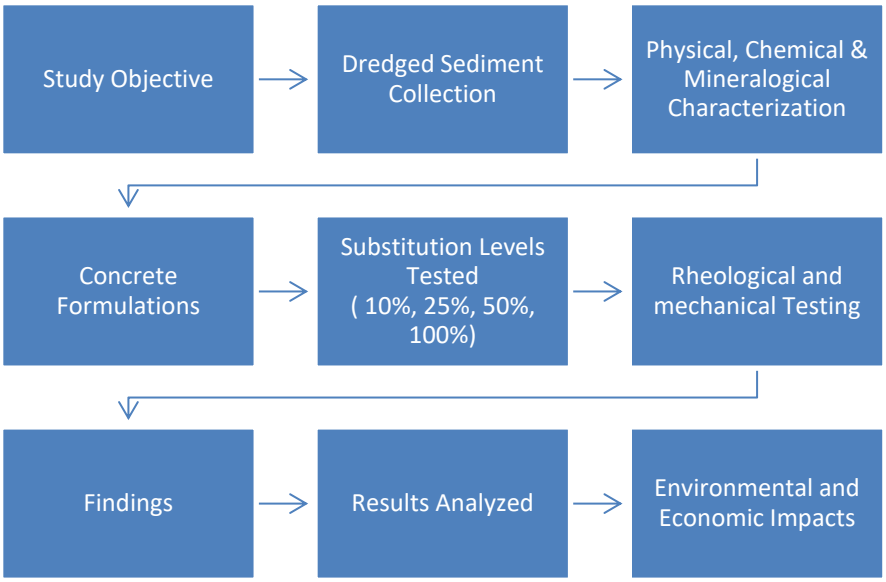

Fig. 2. The process of dredged sediment utilization in concrete production

Finally, the results are analysed to assess the performance of the material and evaluate its practical applications.[11,12]

2.1 Materials

The cement used in this study is a Portland cement, produced by grinding clinker that contains at least 65% clinker, with additional additives such as limestone or fly ash. This cement is sourced from the NOVACIM plant. The limestone aggregates, including crushed sand (0/4 mm), Gravel G0 (4/8 mm), and Gravel G1 (8/16 mm), are supplied by the Carritek quarry, located on the northern bank of the Oued Cherrate in the province of Skhirat, while the dune sand (0/1 mm) originates from the Souiria region. [13,14]

These granular fractions underwent identification tests in accordance with Moroccan standard NM 10.1813.[13] The crushed sand fraction (0-4 mm) and the dune sand fraction (0-1 mm) were subjected to physico-mechanical characterization tests. The dune sand demonstrates complementary properties when combined with coarse sand (0-4 mm). As such, their mixture (30% dune sand and 70% crushed sand) satisfies the requirements outlined in standard NM 10.1.813.[14] The identification characteristics of the dune sand are summarized in the following table;

Table 1. Results of identification tests for dune sand 0-1 mm

Designation	%< 0,25	%< 1	%< D= 1 mm	%< 1,4D= 1,25 mm	%< 2D= 2 mm	ES	MF	Soluble Sulfate in Acid (% SO_3)	Water-Soluble Chloride (% Cl^-)	Sulfide Content (S^{2-})
Result	63	99	99	100	100	74	1.32	0.019	0.001	0.022

The sediments used in this study were extracted from dredged materials at the port of Jebha. Twelve samples were collected from various points within the port. Initially in the form of sludge, these sediments were dried at 105°C in an oven to stabilize their mass, remove their water content, and prevent the need for subsequent mass corrections during incorporation into concrete. After drying, the samples were sieved at 2 mm to ensure a grain size comparable to that of the dune sands being substituted.[15]

(a) (b) (c)

Fig. 3. Stages of marine dredged sediment collection and processing: (a) excavator scooping dredged sediment from the water at the port, (b) sediment samples placed inside a drying oven for moisture removal, (c) weighing the dried sediment using a balance scale

2.2 Experimental Techniques

2.2.1 Sediment Characterization

The materials used in this study were thoroughly characterized using both physical and chemical methods. Particle size analysis was performed using two techniques: dry sieving after washing, in

accordance with the standard NM 00.8.082, and an additional method to ensure comprehensive analysis,[16] and sedimentation particle size analysis with a deflocculant, in compliance with standard NM 00.8.083.[17] Cleanliness tests were assessed through the measurement of the sand equivalent at 10% fines NM 10.1.732,[18] and the methylene blue test.

The organic fraction of the sediments was also determined according to standard XP P94-055,[19] and the total organic carbon content was measured in compliance with standard NM EN 13639.[20] Chemical analysis was performed using X-ray fluorescence spectrometry NM 10.1.005,[21] allowing for the determination of elemental concentrations. The carbonate content (% $CaCO_3$) was evaluated following NF 94-048,[22] the pH was measured according to NF ISO 10390,[23] and the loss on ignition at 1000°C was determined in accordance with NM 10.1.005.[21] Additionally, a mineralogical analysis of the JEBHA sediments was conducted using X-ray diffraction (XRD), The sediment samples for XRD analysis were collected from various depths, ranging from 0-10 cm to 30-40 cm, ensuring representative sampling for each sediment type. under standard conditions, as well as after two specific treatments: ethylene glycol saturation and heating at 550°C.[24] These analyses aimed to identify the mineralogical composition and the crystalline phases present. The identification was carried out using EMPYREAN (reflection-transmission Spinner configuration, MALVERN PANALYTICAL) and X'PERT PRO (reflection-transmission configuration, PANALYTICAL) instruments.[25]

2.2.2 Concrete Formulation

The study examined nine concrete formulations, including a reference mix, all designed using the Dreux-Gorisse method. In these formulations, the dune sand in the reference mix was replaced with untreated dredged sediments from the port of Jebha, used as granular correctors. The substitution rates for the dune sand were set at 10%, 25%, 50%, and 100%.[26]

Table 2. Components of 1 m^3 of concrete incorporating sediments from the port of Jebha at different substitution percentages

Sediment Percentage	RC 0%	10%	25%	50%	100%	10%	25%	50%	100%
		C1	C1	C1	C1	C2	C2	C2	C2
Element									
Gravel G1 (8/16)	530	530.53	530.53	530.53	530.53	530.53	530.53	530.53	530.53
Gravel G0 (4/8)	453	453.45	453.45	453.45	453.45	453.45	453.453	453.45	453.45
Crushed sand (0/4)	639	643.47	647.31	647.31	647.31	646.67	644.112	646.67	647.31
Dune sand	268	259.53	214.27	142.84	0	258.08	220.296	146.46	0
Sediment	0	26.80	67.00	134.00	268	26.80	67	134.00	268
Cement	360	360.00	360.00	360.00	360	360.00	360	360.00	360
Total water	159	135.21	136.44	140.87	159	133.465	133.609	137.89	159
Tempo 25 M admixture (1.9%)	6,84	6.84	6.84	6.84	6.84	6.84	6.84	6.84	6.84
W/C	0,4	0.4	0.4	0.4	0.4	0.4	0.4	0.4	0.4
S/G ratio	0,650	0.654	0.658	0.658	0.658	0.657	0.655	0.657	0.658
Density	2,43	2.43	2.43	2.43	2.42	2.45	2.43	2.44	2.42
Concrete temperature (°C)	24	19	21	18.7	18.7	22.5	20.8	21.2	18.5
Ambient temperature (°C)	21	17.6	18.5	18.9	16	18.5	19	21.7	17.2

Slump test by Abrams Cone (mm) at T15min	21	21	20	18	13	19	19	20	12

The formulations included the reference concrete (RC) with 0% substitution, as well as concretes in which dune sand was partially or fully replaced with sediments categorized as type 1 (C1) and type 2 (C2). For category 1, the substitutions were 10% C1, 25% C1, 50% C1, and 100% C1, while for category 2, the substitutions were 10% C2, 25% C2, 50% C2, and 100% C2. The categories C1 and C2 represent two different types of dredged sediments, while the percentages denote the proportion of dune sand replaced by these sediments.[27,28]

Ambient temperature and concrete temperature were measured, and the slump of the concrete was monitored over one hour. Slump values for the different mixes were determined using the Abrams cone test. The table below presents the details of the various formulations, including the quantities of each component in the concrete.[29] The reference concrete (CC) is classified as C30 and exhibits good workability, corresponding to slump class S4 (slump height between 16 and 21 cm). This was achieved using a water-to-cement ratio (W/C=0,4).[30]

2.2.3 Mechanical Strengths

The compression and tensile strength tests were conducted in accordance with Moroccan NM standards, ensuring reliable and standardized evaluation of concrete performance. These tests were carried out on cylindrical specimens (16 cm × 32 cm) to assess the mechanical behavior of concrete incorporating marine dredged sediments. After casting, the specimens were demolded after 24 hours and then stored in water for curing to allow full hydration. The compressive and tensile strength tests were performed at 7 and 28 days, following standard procedures to evaluate the development of mechanical properties over time. This standardized methodology ensures accurate and reproducible results, providing essential insights into the feasibility of using marine dredged sediments as a partial or total replacement for dune sand in concrete production.[31,32]

(a) (b) (c)

Fig. 4. Stages of compressive strength testing of concrete cylinders: (a) concrete cylinders before curing, showing the initial casting, (b) concrete cylinders submerged in water for curing to ensure hydration, (c) concrete cylinders being tested for compressive strength using a hydraulic press

3. Results and Comments

3.1. Sample Preparation

The raw sediments extracted from the port of Jebha underwent a thorough physico-chemical analysis to evaluate their quality and potential for use as a material in concrete. This study aims to investigate their feasibility as a partial or total substitute for dune sand in initial concrete formulations. Following this, an assessment of the mechanical properties of the resulting concrete was conducted to examine the impact of incorporating these sediments on the material's performance in both fresh and hardened states. To ensure granulometric consistency with dune

sand, the 12 sediment samples were heated at 100°C for 24 hours in an oven to eliminate excess water, then sieved through a 2 mm mesh. After identification tests, the samples were classified into two distinct categories based on their properties: Category C1 includes materials considered clean (VB index < 2), while Category C2 comprises those deemed less clean (VB index > 2).

3.2. Grain Size Distribution and Physical Properties

The analyzed sediments display a diverse granulometric distribution, ranging from coarse particles (> 20 mm) to fine particles (< 2 µm). Most samples exhibit a balanced particle size distribution, with a predominance of intermediate fractions (between 2 mm and 80 µm). However, certain samples, such as S10, contain a higher proportion of fine particles, whereas others, like S6 and S7, have a greater abundance of coarse particles.

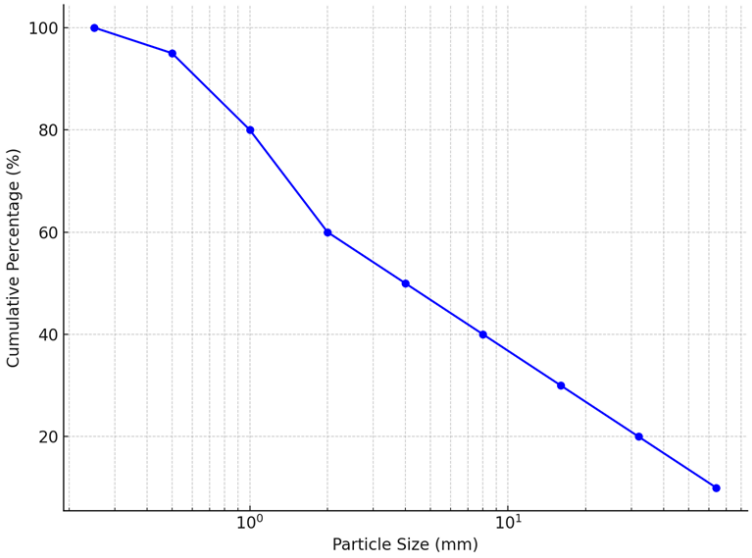

Fig. 5. Particle size distribution curve of dredged sediments from Jebha

3.3. Chemical and Mineralogical Composition

The chemical and mineralogical properties of the sediments were analyzed using X-ray fluorescence (XRF) and X-ray diffraction (XRD) techniques, as shown in Figures 7, 8, and 9. The sediments are primarily composed of silicon dioxide (SiO_2), with concentrations varying between 66.46% and 79.01%. Minor components include aluminum oxide (Al_2O_3), iron oxide (Fe_2O_3), and calcium oxide (CaO). The high quartz content reflects low chemical reactivity and excellent stability, making the sediments suitable as a sand substitute in construction applications.

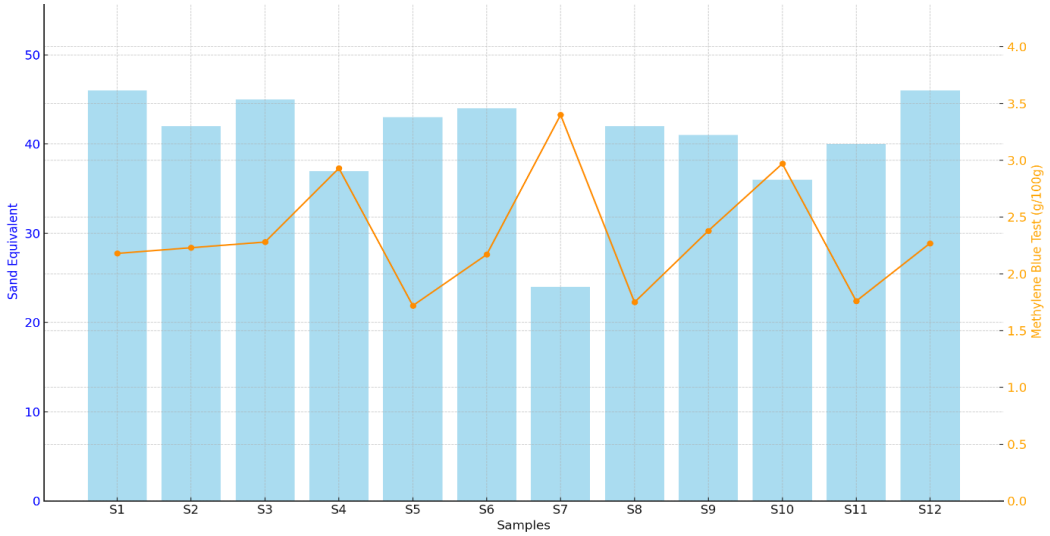

Fig. 6. Test Results for cleanliness: methylene blue value and sand equivalent

The methylene blue test values ranged from 1.72 to 3.40 g/100g, indicating the presence of fine particles that could influence the water demand of the mixtures. Additionally, the sediments exhibited alkaline pH levels, ranging from 8.60 to 9.16, suggesting a low potential for alkali-silica reactivity in concrete. The X-ray diffraction (XRD) analysis was used to characterize three powder samples, labeled XRD1, XRD2, and XRD3, extracted from the sediments of the port of Jebha. These samples were prepared using three different techniques: normal conditions, ethylene glycol saturation, and heating at 550°C.

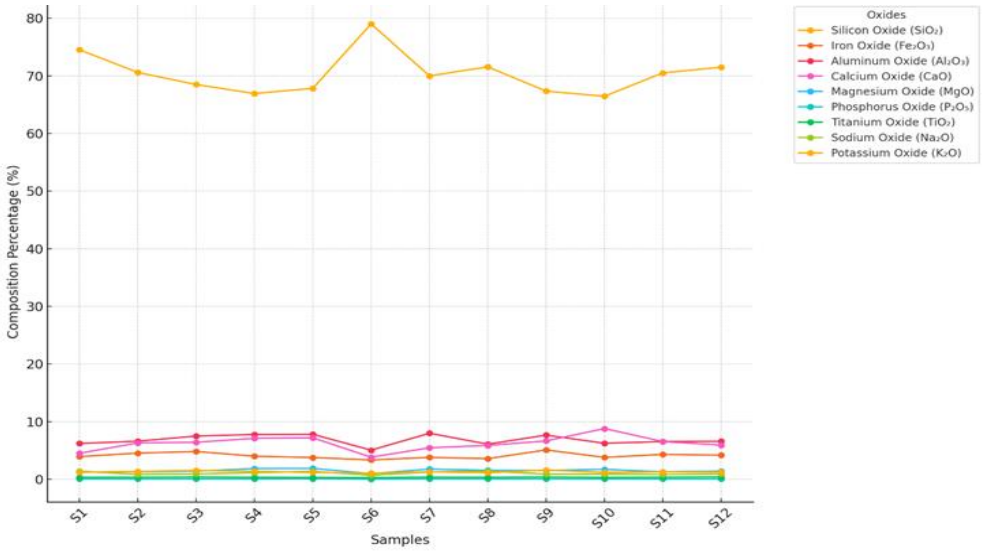

Fig. 7. X-ray fluorescence (XRF) analysis of dredged sediments

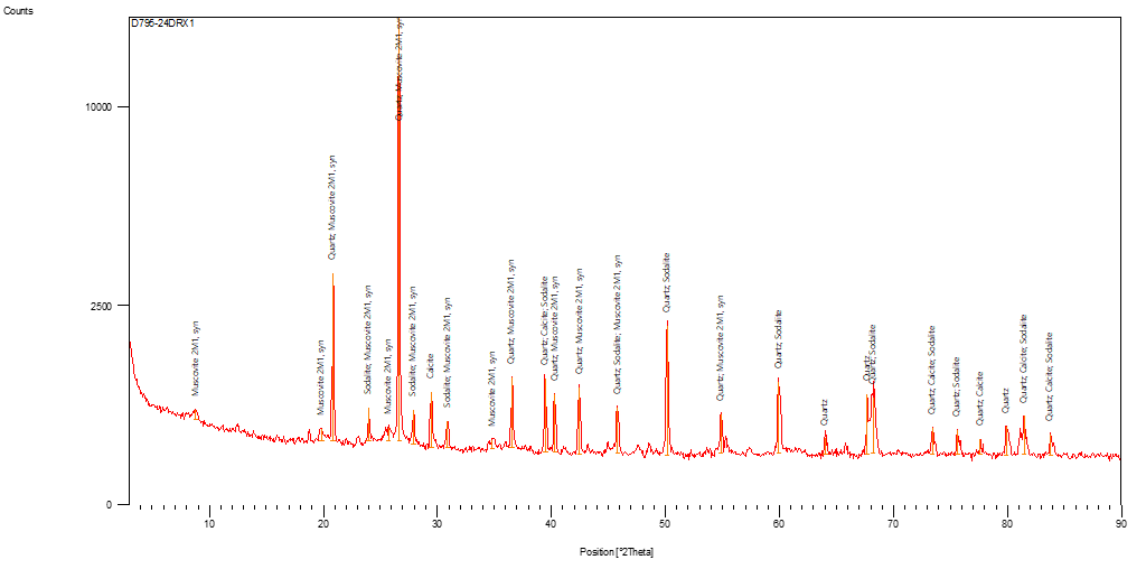

Fig. 8. Powder diffractogram of sample DRX1

The obtained results reveal a composition dominated by stable crystalline minerals, such as Quartz (SiO_2), Calcite ($CaCO_3$), Muscovite ($KAl_2Si_3AlO_{10}(OH)_2$), and, in some samples, Sodalite and Clinochlore. These minerals, recognized for their structural stability, showed no significant changes in the diffractograms after treatment, confirming the absence of expandable clay phases such as smectites. The observation of the crystalline phases presents in the sediments highlighted the stability of the minerals: the identified phases, particularly Muscovite and Clinochlore, retain unchanged interlayer distances (d = 10 Å) after ethylene glycol saturation and heating at 550 °C. This indicates a non-expandable structure resistant to thermal or chemical transformations. Quartz and Calcite: These minerals remain unchanged across the three preparation methods, reflecting their chemical inertia and high crystalline stability. The results confirm the absence of sensitive clay phases, such as smectites, which would have shown significant expansion under ethylene

glycol. Halite, identified in one sample (XRD3), may indicate an evaporitic origin or saline contamination.

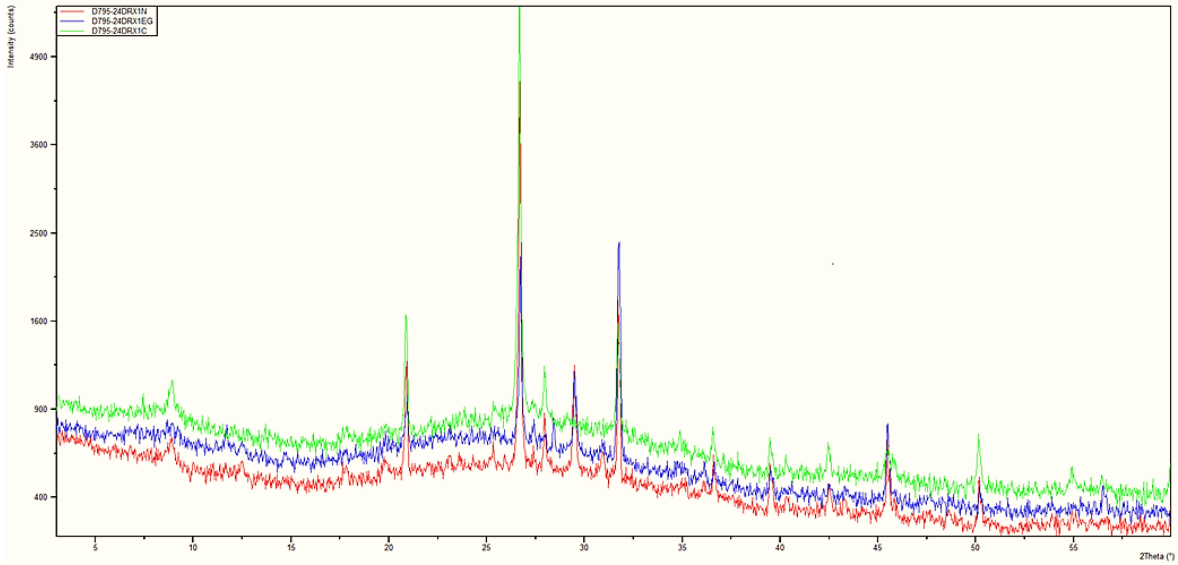

Fig. 9. Identification of clays on oriented slides

3.4. Rheological and Mechanical Properties

The results indicate a gradual decline in concrete slump as the substitution rate of dune sand with dredged sediments from the port of Jebha increases. This reduction is more pronounced for category C2, which has lower cleanliness compared to C1. For C1, the slump remains stable at 21 mm up to a 10% substitution, slightly decreases to 20 mm at 25%, then drops to 18 mm at 50%, and further declines to 13 mm at 100%, reflecting a progressive loss of workability due to the increasing presence of absorbent fines. For C2, the slump is already reduced to 19 mm at 10% and 25%, further decreases to 17 mm at 50%, and reaches 12 mm at 100%, highlighting a more significant impact on workability due to the higher content of fine particles and impurities.

3.5. Compressive Strength

For each test, five specimens were tested daily, and the average compressive strength values were calculated and illustrated in the respective figures. The analysis of the results reveals a gradual decline in compressive strength as the substitution rate of dune sand increases, both at 7 and 28 days. The compressive strength was measured using an average of three samples for each substitution ratio, and the mean values were calculated and represented in the graphs. The control samples (0% substitution) exhibited the highest strength, reaching 57.7 MPa at 28 days. In contrast, full substitution (100%) resulted in a significant reduction in compressive strength, with values of 48.2 MPa for C1 sediments and 48.0 MPa for C2 sediments. At lower substitution rates (10%–25%), the decrease in strength was moderate, indicating that these proportions could be suitable for non-structural applications where high mechanical performance is not a primary requirement.

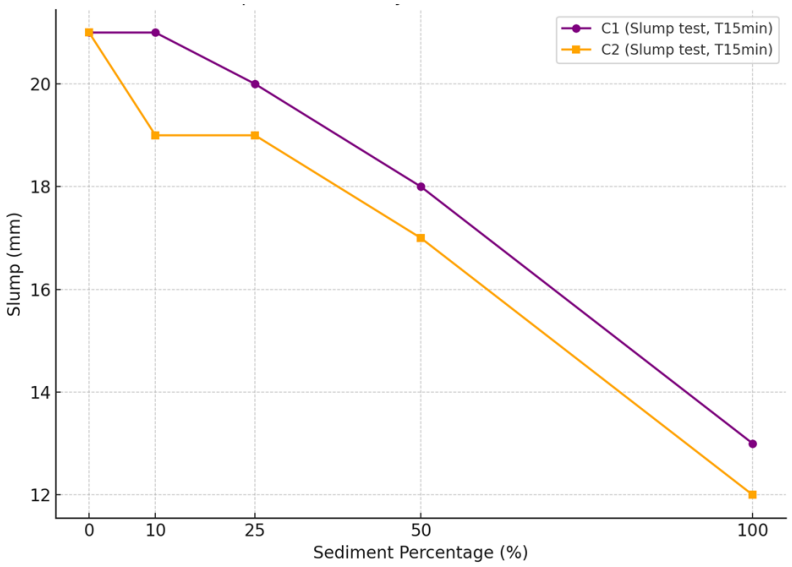

Fig. 10. Slump test result by Abrams Cone at T15 min of concrete with varying substitution ratios of dredged sediments C1 and C2

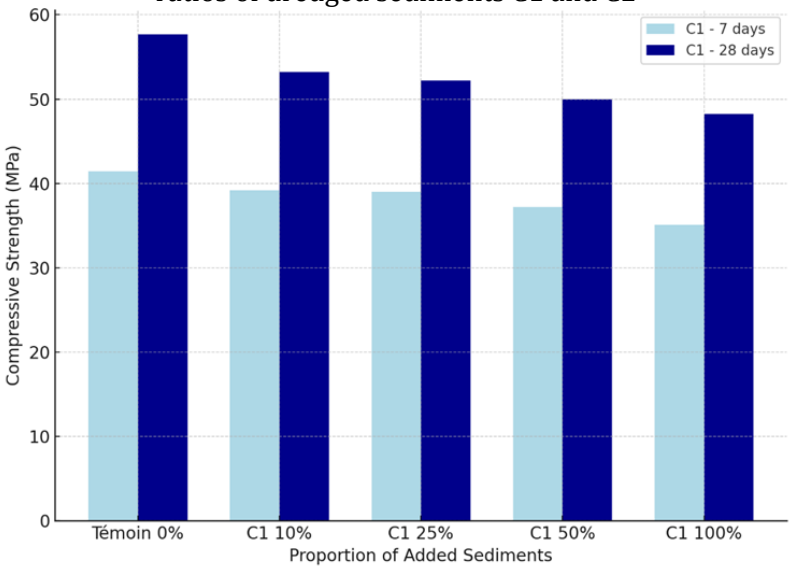

Fig. 11. Compressive strength of concrete with varying substitution ratios of dredged sediments C1

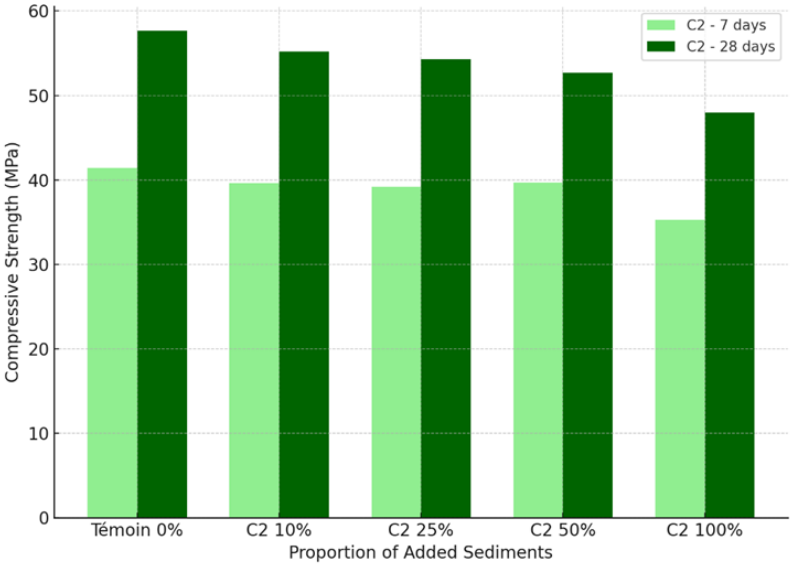

Fig. 12. Compressive strength of concrete with varying substitution ratios of dredged sediments C2

3.6 Tensile Strength

The results presented in Figure 13 indicate that the tensile strength of concrete is strongly influenced by the granulometry and cleanliness of the marine sediments. The granulometric analysis highlights a variable presence of fine particles (<2 µm), which negatively impact mechanical properties by increasing the specific surface area and disrupting the cement paste matrix. The sand equivalent test results confirm that C1 sediments, which are cleaner and contain fewer harmful fines, contribute to maintaining higher tensile strength. In contrast, C2 sediments, characterized by a higher impurity content, lead to a more pronounced reduction in mechanical performance.

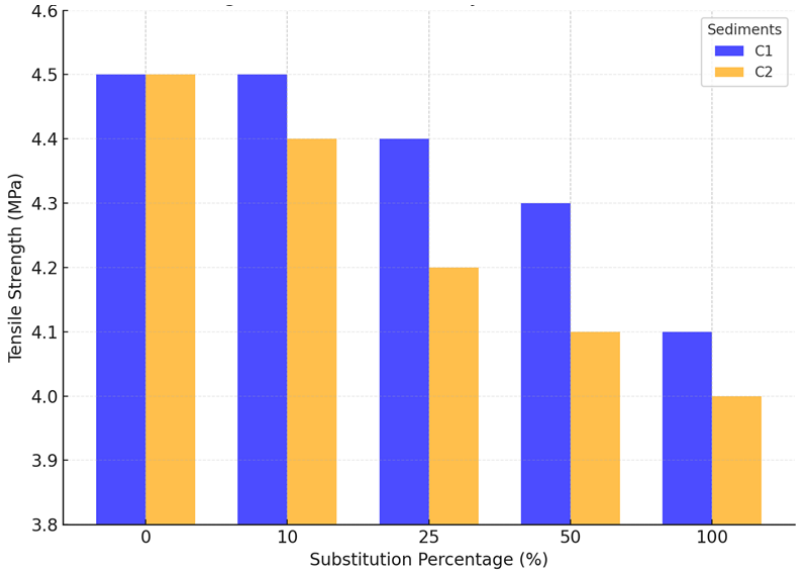

Fig. 13. Tensile strength of concrete at 28 days with varying substitution ratios of dredged sediments C1 and C2

4. Ecological Impact

Replacing dune sand with dredged sediments helps conserve natural sand resources, thereby protecting fragile ecosystems such as dunes and coastal environments. The compressive strength results (Figure 1) indicate that for substitution rates up to 25%, the concrete maintains adequate mechanical performance, making it suitable for non-structural applications.

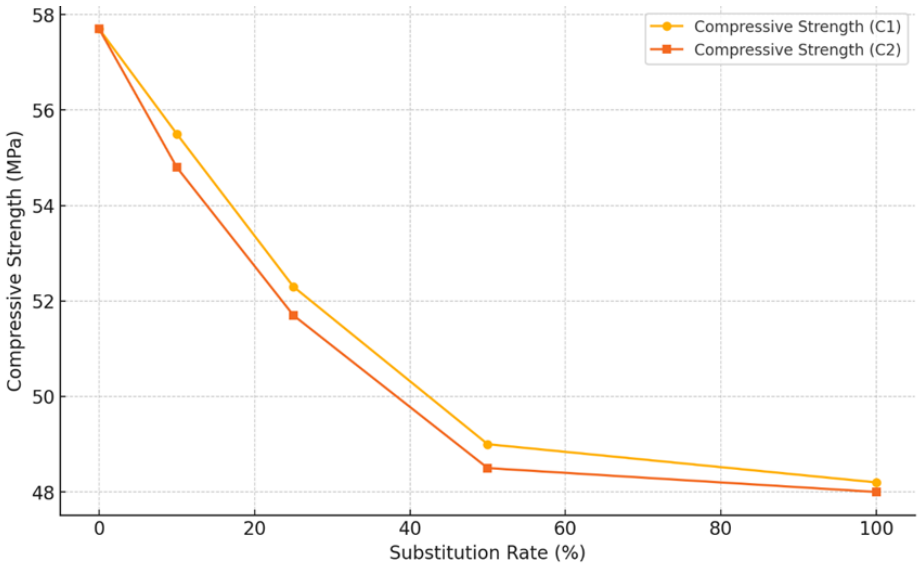

Fig. 14. The compressive strength of concrete at various substitution rates of dune sand with dredged sediments (C1 and C2 categories)

Figure 14 illustrates the relationship between the substitution rates of dune sand with dredged sediments (C1 and C2) and the compressive strength of concrete. The results show that as the substitution rate increases, the compressive strength gradually decreases. For C1 sediments, the 28-day compressive strength decreases from 57.7 MPa at 0% substitution to 48.2 MPa at 100% substitution. Similarly, for C2 sediments, the compressive strength decreases from 57.7 MPa to 48 MPa across the same substitution range. At lower substitution rates (10% and 25%), the impact on compressive strength is relatively minimal, with both C1 and C2 maintaining values above 50 MPa.

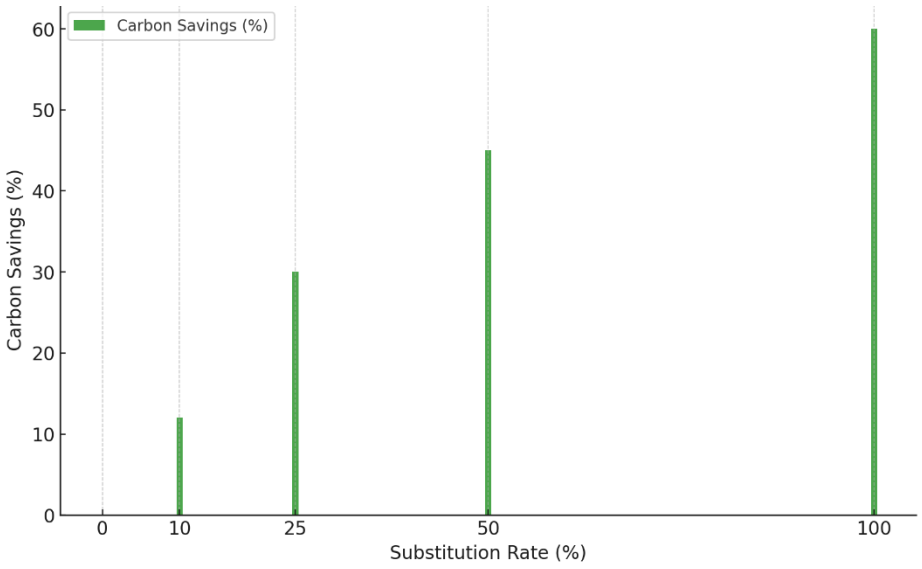

Fig. 15. Estimated percentage reduction in carbon emissions for different substitution rates of dune sand with dredged sediments

Figure 15 illustrates the carbon savings associated with replacing dune sand with dredged sediments in concrete production. The estimated savings increase progressively with the substitution rate, starting at 12% for a 10% substitution and reaching up to 60% for a complete replacement of dune sand.

5. Results and Discussion

The incorporation of dredged sediments from Jebha Port as a substitute for dune sand in concrete presents both advantages and challenges. This study highlights the impact of such substitution on the rheological and mechanical properties of concrete, emphasizing the need for optimization strategies to ensure material performance and sustainability. Recent studies have highlighted the use of marine dredged sediments as a sustainable alternative to dune sand in concrete [33]. The inclusion of such materials has been shown to reduce environmental impact and conserve natural resources [9].

One of the key observations in this study is the reduction in workability with increasing substitution rates. The slump test results indicate that workability remains acceptable at a 10% substitution level but declines significantly beyond 50%, particularly for C2 sediments. This decrease is primarily attributed to the higher presence of fine particles and active clay minerals, which increase water demand and disrupt the cohesion of the cementitious matrix [34]. To mitigate this effect, the use of a superplasticizer such as Tempo 25M or an alternative high-performance admixture is recommended [34].

Moreover, the cleanliness of sediments plays a crucial role in the overall workability of the mixture. Higher impurity content, particularly in C2 sediments, leads to a pronounced reduction in fluidity, which can be counteracted through a careful selection of additives and optimized mix designs. The incorporation of well-graded granular corrections may also improve the rheological behavior and limit excessive water demand, ensuring better cohesion and compaction of the mixture.

The compressive and tensile strengths of concrete decrease as the substitution percentage increases. At 28 days, the reference concrete exhibits a compressive strength of 57.7 MPa, while the fully substituted mix reaches 48.2 MPa for C1 sediments and 48 MPa for C2 sediments. At lower substitution levels (10%-25%), mechanical performance remains within acceptable limits, making these proportions suitable for non-structural applications [35]. However, at higher substitution rates, particularly at 50% and beyond, the presence of fines and impurities significantly affects the concrete's strength, underscoring the importance of controlling sediment quality [36].

Additionally, the results suggest that the presence of active clays in certain sediment samples, particularly in C2, contributes to a decline in adhesion and mechanical interlocking within the cementitious matrix. This phenomenon is confirmed by methylene blue test results, which indicate a higher adsorption capacity, signifying the presence of expansive clay minerals. To address this issue, supplementary treatments such as washing, thermal processing, or blending with coarser aggregates may be required to enhance the mechanical performance of the concrete. [37].

X-ray diffraction (XRD) analysis confirms that the sediments primarily consist of stable crystalline phases such as quartz and calcite, which contribute to their suitability as a construction material. However, the methylene blue test results reveal the presence of active clay minerals, especially in C2 sediments, which can weaken the adhesion within the cementitious matrix. This necessitates additional pre-treatment measures for sediments with high impurity levels before their incorporation into concrete [38].

Moreover, durability assessments indicate that moderate substitution rates do not significantly affect the long-term stability of the material. However, at higher incorporation levels, potential issues such as increased porosity and reduced resistance to aggressive environments must be considered. In particular, the susceptibility of certain samples to sulfate attack requires further study, and the addition of pozzolanic materials or supplementary cementitious binders may be necessary to enhance durability.

From an environmental perspective, replacing dune sand with dredged sediments offers a viable solution to reduce pressure on natural sand resources and mitigate the ecological consequences of uncontrolled sand extraction. Additionally, this approach significantly lowers the carbon footprint of concrete production by reducing transportation emissions and eliminating energy-intensive sand extraction processes. The estimated carbon savings range from 12% at a 10% substitution rate to approximately 60% at full replacement [39]. This approach aligns with circular economy principles, promoting the reuse of industrial by-products and reducing landfill disposal. Furthermore, the valorization of dredged sediments contributes to sustainable construction practices by integrating locally available materials, thus decreasing dependency on imported raw materials and fostering regional economic development [40].

For optimal use, it is recommended to limit substitution to moderate levels (≤25%) and incorporate chemical admixtures to counteract the negative effects of fines on workability. Furthermore, additional research should focus on the long-term durability of concrete containing dredged sediments, particularly under exposure to sulfate attack and freeze-thaw cycles. Investigating advanced processing techniques to improve sediment quality and assessing the economic feasibility of large-scale adoption will be crucial for integrating this sustainable practice into the construction industry. [41- 42]

Future studies should also explore the effects of sediment substitution on the thermal properties of concrete, particularly in applications requiring enhanced insulation performance. Additionally, life-cycle assessments and cost-benefit analyses will be essential to establish the broader economic and environmental viability of large-scale implementation.

6. Conclusion

This study highlights the promising potential of marine dredged sediments from Jebha Port as a sustainable alternative to traditional dune sand in B30 concrete. The results show that by replacing dune sand with marine dredged sediments up to 25%, the concrete retains an acceptable level of compressive strength, making it a good choice for non-structural applications where high strength

is not as critical. However, increasing the sediment content beyond this level can reduce the concrete's strength, emphasizing the need for a careful balance when using these sediments. The addition of marine dredged sediments does affect the workability of the concrete mix. As the proportion of sediments increases, the mix becomes stiffer and harder to work with. However, this challenge can be addressed through adjustments in the mix design, such as incorporating admixtures or optimizing the water content. These changes could help maintain the workability of the concrete without losing the environmental benefits of using dredged sediments.

One of the strongest arguments for using marine dredged sediments is the positive environmental impact. Substituting dredged sediments for dune sand reduces the demand for sand mining, which is known to cause environmental harm such as habitat destruction, waterway disruption, and the depletion of natural sand resources. By using dredged sediments, we help conserve precious natural resources and reduce the environmental footprint of sand extraction. Although the short-term performance of concrete with marine dredged sediments looks promising, further research is necessary to assess its long-term durability. Tests on carbonation, shrinkage, and resistance to aggressive environments will be crucial in determining whether this concrete will hold up over time. These additional studies will provide valuable insight into the durability and long-term viability of using dredged sediments in construction.

In terms of sustainability, this research contributes to a more sustainable approach to construction by supporting the reuse of waste materials. By turning marine dredged sediments into a valuable resource, this study aligns with circular economy principles, reducing waste and minimizing the need for virgin materials. This innovative approach offers a practical solution to the challenges of natural sand depletion and environmental impact.

In conclusion, marine dredged sediments from Jebha Port offer a promising, sustainable alternative to traditional dune sand in concrete production. With some adjustments to the mix design and further research into long-term durability, these sediments can be effectively used in non-structural concrete applications. Not only does this approach help conserve natural sand resources, but it also sets the stage for more sustainable and eco-friendly practices in the construction industry. With continued research, marine dredged sediments could become a key player in the future of sustainable building materials.

References

[1] Safhi AEM, Mejjad N, El FadilI H, Bortali M. Dredged materials in Morocco: Current practices, policies, and roadmap for sustainable management. Case Studies in Construction Materials 2024;20:e03045. https://doi.org/10.1016/j.cscm.2024.e03045

[2] Dauji S. Disposal of Sediments for Sustainability: A Review. IJEEE 2017;2:96. https://doi.org/10.11648/j.ijeee.20170206.12

[3] Bortali M, Rabouli M, Yessari M, Hajjaji A. Characterizing Harbor Dredged Sediment for Sustainable Reuse as Construction Material. Sustainability 2023;15:1834. https://doi.org/10.3390/su15031834

[4] Abderrahmane A. Extracting and trafficking Morocco's coastal sand,https://enact-africa.s3.amazonaws.com/site/uploads/2022-05-18-sand-extraction-in-morocco.pdf

[5] Hayek M, Soleimani T, Salgues M, Souche JC. Utilizing Fine Marine Sediment as a Partial Substitute for Sand in Self-Compacting Concrete Specially Designed for Application in Marine Environments. Sustainability 2024;16:2538. https://doi.org/10.3390/su16062538

[6] Safer O, Belas N, Belaribi O, Belguesmia K, Bouhamou NE, Mebrouki A. Valorization of Dredged Sediments as a Component of Vibrated Concrete: Durability of These Concretes Against Sulfuric Acid Attack. Int J Concr Struct Mater 2018;12:44. https://doi.org/10.1186/s40069-018-0270-7

[7] Kouali H, Chaouti A, Achtak H, Elkalay K, Dahbi A. Trace metal contents in the mussel Mytilus galloprovincialis from Atlantic coastal areas in northwestern Morocco: Levels of contamination and assessment of potential risks to human health. Marine Pollution Bulletin 2022;179:113680. https://doi.org/10.1016/j.marpolbul.2022.113680

[8] Bianchini A, Cento F, Guzzini A, Pellegrini M, Saccani C. Sediment management in coastal infrastructures: Techno-economic and environmental impact assessment of alternative technologies to dredging. Journal of Environmental Management 2019;248:109332. https://doi.org/10.1016/j.jenvman.2019.109332

[9] Soleimani T, Hayek M, Junqua G, Salgues M, Souche JC. Environmental, economic and experimental assessment of the valorization of dredged sediment through sand substitution in concrete. Science of The Total Environment 2023;858:159980. https://doi.org/10.1016/j.scitotenv.2022.159980

[10] Er-Ramy N, Nachite D, Anfuso G, Williams AT. Coastal Scenic Quality Assessment of Moroccan Mediterranean Beaches: A Tool for Proper Management. Water 2022;14:1837. https://doi.org/10.3390/w14121837
[11] Souileh A, Mabrouk A, Ouadif L, Hachmi DE. Analysis of the geotechnical and mineralogical characteristics of the Settat-Khouribga shale clay for potential civil engineering applications. Research On Engineering Structures And Materials. 2024, https://doi.org/10.17515/resm2024.408ma0824rs
[12] Souileh A, Ouadif L, Baba K, Doughmi K, Masrour I, Mabrouk A, Chrachmy M, Benhaddou, K. (Eco-performant mortar with clay shale from Settat, Morocco : Thermal, mechanical, and environmental analysis. Journal Of Ecological Engineering. 2025 26(3), 86-98. https://doi.org/10.12911/22998993/195975
[13] NM 10.1813: Moroccan Standard for determining the organic matter content in soils.
[14] NM 10.1.813: Moroccan Standard for determining the cation exchange capacity (CEC) of soils.
[15] Wilke BM. Determination of Chemical and Physical Soil Properties [Internet]. In: Monitoring and Assessing Soil Bioremediation. Berlin, Heidelberg: Springer Berlin Heidelberg; 2005: 47-95. https://doi.org/10.1007/3-540-28904-6_2
[16] NM 00.8.082: Moroccan Standard for determining the pH of soils.
[17] NM 00.8.083: Moroccan Standard for determining the electrical conductivity of soils.
[18] NM 10.1.732: Moroccan Standard for determining the total nitrogen content in soils.
[19] XP P94-055: AFNOR Standard. (1991). Soils: Investigation and tests - Determination of organic matter content - Calcination method. French Standards Association.
[20] NM EN 13639: Moroccan Standard equivalent to European Standard EN 13639, which specifies a method for determining the organic carbon content in mineral amendments.
[21] NM 10.1.005: Moroccan Standard for particle size distribution analysis of soils.
[22] NF P94-048: AFNOR Standard. (1996). Soils: Investigation and tests - Determination of organic matter content in soils - Sulfochromic oxidation method. French Standards Association.
[23] NF ISO 10390: AFNOR Standard. (2005). Soil quality - Determination of pH. French Standards Association.
[24] Yin K, Hong H, Churchman GJ, Li Z, Han W, Wang C. Characterisation of the hydroxy-interlayered vermiculite from the weathering of illite in Jiujiang red earth sediments. Soil Res. 2014;52:554. https://doi.org/10.1071/SR14014
[25] Ermrich M, Opper D. XRD for the analyst: getting acquainted with the principles. 2nd revised edition. Almelo: PANalytical; 2013.
[26] Hamza C, Bouchra S, Mostapha B, Mohamed B. Formulation of Ordinary Concrete using the Dreux-Gorisse Method. Procedia Structural Integrity 2020;28:430-9. https://doi.org/10.1016/j.prostr.2020.10.050
[27] Souileh A, Mabrouk A, Ouadif L, El Hachmi D, Chrachmy M, Benhaddou, K. Building earthquake resilience with clay shale : pioneering sustainable concrete solutions with eco-friendly materials. Research on Engineering Structures and Materials. 2024. https://doi.org/10.17515/resm2024.479ea1007rs
[28] Lynda Amel C, Kadri EH, Sebaibi Y, Soualhi H. Dune sand and pumice impact on mechanical and thermal lightweight concrete properties. Construction and Building Materials 2017;133:209-18. https://doi.org/10.1016/j.conbuildmat.2016.12.043
[29] Muttashar HL, Ariffin MAM, Hussein MN, Hussin MW, Ishaq SB. Self-compacting geopolymer concrete with spend garnet as sand replacement. Journal of Building Engineering 2018;15:85-94. https://doi.org/10.1016/j.jobe.2017.10.007
[30] Kapelko A. The possibility of adjusting concrete mixtures' fluidity by means of superplasticizer SNF.
[31] Li B, Jiang G, Hu J, Li Y, Wu F, Qin Z, et al. Specimen size effect on compressive and splitting tensile strengths of sustainable geopolymeric recycled aggregate concrete: Experimental and theoretical analysis. Journal of Cleaner Production 2024;434:140154. https://doi.org/10.1016/j.jclepro.2023.140154
[32] Prasad Acharya D, Raj Gyawali T. Investigation of the performance of natural molasses on physical and mechanical properties of cement mortar. Ain Shams Engineering Journal 2024;15:102355. https://doi.org/10.1016/j.asej.2023.102355
[33] Fořt J, Afolayan A, Kočí V, Scheinherrová L, Jan J, Borovec J, et al. Potential of water sediments in construction materials: Current approaches and critical consideration of future challenges. Heliyon 2025;11:e41121. https://doi.org/10.1016/j.heliyon.2024.e41121
[34] Zhao Z, Remond S, Damidot D, Xu W. Influence of fine recycled concrete aggregates on the properties of mortars. Construction and Building Materials 2015;81:179-86. https://doi.org/10.1016/j.conbuildmat.2015.02.037
[35] Mashaan NS, De Silva A. Review on Assessment and Performance Mechanism Evaluation of Non-Structural Concrete Incorporating Waste Materials. Applied Mechanics 2024;5:579-99. https://doi.org/10.3390/applmech5030033

[36] Titon B, Duchesne J, Fournier B, Rodrigues A. Concrete deterioration due to sulfide-bearing aggregates: Mineralogical and chemical characteristics of pyrrhotite in concrete aggregates from Trois-Rivières, Canada. Construction and Building Materials 2025;458:139670. https://doi.org/10.1016/j.conbuildmat.2024.139670
[37] Hayek, M., Soleimani, T., Salgues, M., Souche, J., & Garcia-Diaz, E. Valorization of uncontaminated dredged marine sediment through sand substitution in marine grade concrete. European Journal of Environmental and Civil Engineering, 2023;4008-4025. https://doi.org/10.1080/19648189.2023.2168765
[38] Heidari P, Rivard P, Wilson W. Multi-objective optimization of cement-based systems containing marine dredged sediment. Construction and Building Materials 2024;439:137228. https://doi.org/10.1016/j.conbuildmat.2024.137228
[39] Heidari P, Rivard P, Wilson W. Multi-objective optimization of cement-based systems containing marine dredged sediment. Construction and Building Materials 2024;439:137228. https://doi.org/10.1016/j.conbuildmat.2024.137228
[40] Tripathi D, Kumar R, Mehta P K, Singh A. A Sustainable Concrete with Manufactured Sand in Different Aggressive Environments. Dans Lecture notes in civil engineering. 2021: 3-10. https://doi.org/10.1007/978-981-33-6389-2_1
[41]Tripathi D, Kumar R, Mehta P K, Rawat V. An experimental study on the properties of SCC with manufactured sand. J. Indian Chem. Soc. 2020: 97(10a), 1673-1677.
[42] Tripathi D, Kumar R, Mehta P K, Singh A. (2022). Use of Mineral Admixtures and M-sand for Sustainable Concrete. Dans Lecture notes in civil engineering. 2022: 59- 64. https://doi.org/10.1007/978-981-16-8496-8_7

Research on Engineering Structures & Materials
www.jresm.org
MIM Research Group

Research Article

Sustainable stabilization of native subgrade soil for low-volume roads using copper slag and cementitious materials

Gunnam Sanijya [*,1, 2,a,b], Bala Murugan R [1,c], Samatha Chowdary P [2,d]

[1]*Annamalai University, Annamalai Nagar, Chidambaram 608002, India*
[2]*R V R & J C College of Engineering, Chowdavaram, Guntur 522019, Andhra Pradesh, India*

Article Info

Article History:

Received 14 Feb 2025
Accepted 20 May 2025

Keywords:

Soil stabilization;
Copper slag;
Expansive soils;
Low-volume roads;
Geotechnical properties;
Dynamic cone penetration test

Abstract

The efficacy and longevity of low-volume roads (LVRs) are contingent upon the stabilization of native subgrade soil. This study aims to investigate the viability of using copper slag as a stabilizer when mixed with cementitious materials comprising lime and Ordinary Portland cement (OPC). Varying copper slag concentrations (2–12%) and a set 8% of lime or OPC were applied to expansive soil samples. Laboratory tests—including the California bearing ratio (CBR), unconfined compressive strength (UCS), and free swell index (FSI)—were used to determine swelling behavior, bearing capacity, and strength enhancement. The in-situ strength was evaluated using the Dynamic Cone Penetration Test (DCPT). The findings indicate that the incorporation of copper slag substantially enhanced the properties of the soil. UCS increased from approximately 53 kPa (untreated) to over 660 kPa for cement-stabilized soil (with 10% slag) and ~619 kPa for lime-stabilized soil. CBR (soaked) nearly doubled from 8% (at 2% slag) to 16% (at 10% slag). The swell potential was significantly diminished, with a reduction of up to 70% in cement–slag mixtures and 65% in lime–slag mixes in terms of FSI. Beyond the ideal copper slag level of about 8–10%, marginal strength increases or slight losses were noted. Cement-stabilized combinations outperformed lime-stabilized mixes in wet-dry durability and strength. Microstructural study (SEM) confirmed the development of a calcium-silicate-hydrate (C-S-H) gel, which improved particle bonding. DCPT penetration (DPI) and CBR (R^2 = 0.90) were found to have an exponential empirical correlation, which enables the estimation of in-situ strength. This study contributes to the sustainable development of rural road infrastructure by providing a cost-effective and environmentally favorable method for enhancing expansive subgrades through the inclusion of an industrial by-product.

© 2025 MIM Research Group. All rights reserved.

1. Introduction

Serving as the foundation layer for all subsequent layers, the subgrade soil is a key component of the pavement construction. Particularly on low-volume roads (LVRs), which carry light traffic yet may struggle with limited resources and suboptimal construction conditions, its stability and strength are crucial for the lifetime and use of pavements [1]. Expansive soils, a troublesome subgrade material, provide major problems because of their high shrink-swell potential, which causes pavement heaving and cracking. Seasonal moisture changes can lead to major pavement damage in areas where expansive clays prevail, thereby requiring efficient stabilization strategies [2,3]. Recent research emphasizes the influence of expansive soils on infrastructure and the requirement of creative treatment; for example, waste-to-energy ash and other industrial byproducts have been tested to treat very expansive clays in road pavements [4-6].

*Corresponding author: gsanijya24@gmail.com
[a,b]orcid.org/0000-0002-4346-0985; [c]orcid.org/0009-0003-0352-6139; [d]orcid.org/0000-0001-6668-2460
DOI: http://dx.doi.org/10.17515/resm2025-682ma0214rs

Recent studies (2022–2025) show copper slag's promise in geotechnics. When mixed with lime or OPC, copper slag can significantly enhance the engineering qualities of expansive soils [7-10]. For instance, Jangid and Grover (2024) discovered that adding copper slag greatly strengthened and lowered the swell of an expansive clay, with around a 70% drop in free swell index at 30% slag concentration [11]. A mix of copper slag with hydrated lime and cement, according to Ekinci et al. (2022), improved the unconfined compressive strength of marine clay by as much as more pozzolanic processes and denser packing [12]. These investigations show the possibility of copper slag as a partial substitute for conventional stabilizers. Reflecting a more general movement toward sustainable binders, various industrial by-products such fly ash, ground-granulated blast furnace slag, and marble dust have also been studied for soil stabilization [13-17]. Combining copper slag with traditional binders can help to improve soil behavior specifically and usually at lower cost while also minimizing the environmental impact. Using copper slag in stabilization can help to balance some of the need for cement or lime, hence reducing energy consumption and CO_2 emissions linked with such binders [18-20].

Ensuring field performance and long-term durability is another facet of sustainable subgrade enhancement. Though they are vital, traditional lab tests—UCS, CBR, etc.—must be supplemented by field assessment methods [21]. Rapid evaluation of subgrade strength and compaction quality using the Dynamic Cone Penetration Test (DCPT) has proven to be a strong in-situ technique. Many recent research shows that pavement layer strength and CBR correspond strongly with DCPT findings, usually stated as Dynamic Penetration Index, DPI [22]. DCP can consistently reveal the strength of stabilized soils, according to Elias et al. (2023), hence it is a useful tool for field validation of laboratory findings [23]. Despite these developments, the literature still has gaps. Few studies have looked at copper slag with lime compared with cement on expansive soils in the setting of low-volume highways separately [24-26]. Furthermore, DCPT's application to assess such in situ stabilizations and development of region-specific correlations (DPI–CBR) remains. constrained.

2. Research Significance and Novelty

This study offers fresh insights and suggests a sustainable stabilization technique to fill noted gaps considering the stated before. Unlike previous studies that tend to emphasize one stabilizer or combination additives, this one looks at two distinct binary mixing systems: (i) copper slag + lime, and (ii) copper slag + OPC. This lets one directly compare their effectiveness in treating expansive subgrade soil, which is new for low-volume road uses. A field correlation between DCPT and CBR is also created especially for the treated soil, hence enhancing empirical formulas from literature that might not apply to all soil types. Including a straightforward statistical modeling approach helps us to confirm the impact of copper slag amount and binder type on strength increases, therefore supporting the results even more. Overall, the study's novelty lies in its integrated approach: combining sustainable materials (industrial waste + minimal cement/lime) with field validation and statistical analysis to ensure the findings are both practical and generalizable.

In summary, this research contributes to sustainable infrastructure development by demonstrating that copper slag, an industrial waste, can be effectively used with traditional binders to stabilize expansive soils. It provides much-needed data on the performance of slag-lime vs. slag-cement stabilization, introduces a field evaluation correlation for immediate use by engineers, and employs statistical modeling to reinforce the trends observed. The following sections detail the materials and methods, present the results with in-depth discussion and comparative insights, and finally draw conclusions highlighting the study's novel contributions and practical implications.

3. Materials and Methods

3.1 Mix Proportions and Materials

The components for this investigation include ordinary Portland cement (OPC), hydrated lime, copper slag, and an expansive subgrade soil. Locally called as black cotton soil, the expansive soil was gathered at a depth of 2.5 m at Narkulapaadu village, Amaravati (Guntur district, India). High plasticity and swell potential characterize this soil. Classifying it as high-plasticity clay (CH) under

the Indian Standard system, the liquid limit is 52% and plasticity index 28.7%. A high expansiveness is confirmed by the free swell index (FSI) of 120%, which creates notable concerns for pavement stability. The physical and index characteristics of the soil are summarized in Table 1. Especially, the natural UCS of this soil is only approximately 53 kN/m^2 (about 53 kPa), indicating very poor strength, and it has a significant clay component (~82% clay-sized particles).

Table 1. Physical and engineering properties of soil

S.No	Property	Value
1	Specific gravity	2.55
2	Particle size distribution	
	a) Sand (%)	16.8
	b) Gravel (%)	0.9
	c) Clay (%)	82.3
3	Liquid limit (%)	52
4	Plastic limit (%)	22.42
5	Shrinkage limit (%)	8.6
6	IS classification of soil	CH
7	Plasticity index	28.72
8	Optimum moisture content (%)	36.24
9	Maximum dry density (kN/m^3)	13.4
10	Unconfined Compression test (kN/m^2)	52.97
11	Differential free swell index (%)	120

A commercial OPC (53 grade) complying to IS 269:2015 [27] was the cement utilized. Among its main characteristics (Table 2) are a fineness of 325 m^2/kg, specific gravity of 3.04, initial setting time of 42 minutes, and 28-day compressive strength of about 59.4 MPa. A nearby supplier (Peduguralla Lime Factory) provided hydrated lime, a common high-calcium lime for soil stabilization.

Table 2. Physical properties of cement

Property	Value
Fineness (m^2/kg)	325
Specific Gravity	3.04
Initial Setting Time (minutes)	42
Compressive Strength (MPa)	59.4

The main sustainable component in this work is copper slag bought from Sterlite Industries in Tuticorin, India. A by-product of copper pyrometallurgy, copper slag is a black, glassy granular substance. The physical characteristics of the slag (Table 3) show that it is somewhat coarse (fineness modulus of 3.47, in the sand-sized range) and has a high specific gravity (3.5). Its bulk density (~1.91 g/cm^3) is greater than that of normal soils, and it has low water absorption (0.4%) and moisture content (0.25%). Copper slag's angular particles can enhance soil gradation and friction; its latent silica and alumina might interact with lime or cement to generate more cementitious materials.

Table 3. Physical properties of copper slag

Property	Value
Specific Gravity	3.5
Fineness Modulus	3.47
Bulk Density (g/cm^3)	1.91
Water Absorption (%)	0.40
Moisture Content (%)	0.25

Mix designs were selected for stabilization depending on preliminary research and literature. Both lime and cement were chosen with a cementitious binder content of 8% (by dry soil weight) since 6–8% is a generally useful range for treating very plastic clays. To isolate the impact of copper slag, this % was maintained constant. Incremental percentages of 0%, 2%, 4%, 6%, 8%, 10%, and 12% copper slag were added (by dry soil weight). Binder-alone stabilization is based on the 0% slag scenario (soil + 8% binder only). Considering reasonable replacement levels and to see whether too much slag could be harmful—as some research indicate lower performance beyond an optimum point—the top limit of 12% slag was selected. Binder kind and slag concentration define each combination; e.g., "Lime + 8% slag" or "Cement + 10% slag".

3.2 Sample Preparation

Following ASTM D6913 [28], expansive soil clods were air-dried, pulverized, and sieved through a 4.75 mm sieve to remove gravel and big clods. The needed amounts of dry soil, copper slag, and binder—lime or cement—were weighed for each batch and dry-mixed until a consistent combination resulted. Optimum moisture content (OMC ~36%) water was progressively added to the dry mix during mixing, constantly swirling and kneading the substance. Preliminary tests using normal Proctor compaction (ASTM D698 [29]) revealed the OMC. Mixing kept going until the workable, uniform soil-binder-slag mix showed.

To shape the test specimens, materials were compacted right after mixing. Consistency with subgrade field compaction was achieved by compacting the slurry into cylindrical molds (38 mm diameter x 76 mm height) using a Standard Proctor energy (ASTM D698 [29]) for UCS specimens. This meant putting the mix in three layers and using 25 blows of a 2.5 kg rammer dropped from 300 mm for each layer. Using altered Proctor effort according to ASTM D1557 [30], CBR test samples were made in CBR molds (152 mm diameter x 178 mm height) to guarantee a high degree of compaction reflective of field circumstances (energy ~2,700 kN-m/m^3). To prevent disruption, all specimens were meticulously extruded from molds following compression.

The compressed samples were cured in a humid atmosphere to gain strength. Stored in a curing chamber at about 27°C, each UCS sample was sealed in a plastic bag to stop moisture loss. Strength increases over time was evaluated using curing durations of 7, 14, and 28 days. This lets one see the pozzolanic reaction development, particularly for lime stabilization which is slower. Unless otherwise stated, specimens were soaked in water for approximately 4 hours to mimic worst-case field moisture conditions prior to testing. For CBR, designated samples were soaked for 96 hours to assess soaked CBR.

3.3 Testing Procedures

A suite of laboratory and field tests was performed to evaluate the stabilized soil's properties:

3.3.1 Unconfined Compressive Strength (UCS)

UCS tests were conducted in accordance with ASTM D2166/D2166M [31]. The cylindrical specimens were loaded axially at a strain rate of ~1% per minute until failure (Fig. 1 shows a schematic of the test setup). The peak load at failure was recorded, and UCS was computed as;

$$UCS = P/A \quad (1)$$

where P is the peak load and A is the cross-sectional area. UCS provides a measure of the soil's compressive strength without lateral confinement, indicating how well the stabilization improved the soil's load-bearing capacity. Cylindrical soil specimens (38 mm × 76 mm) are placed in a loading frame and compressed axially until failure. The maximum load is used to calculate the UCS.

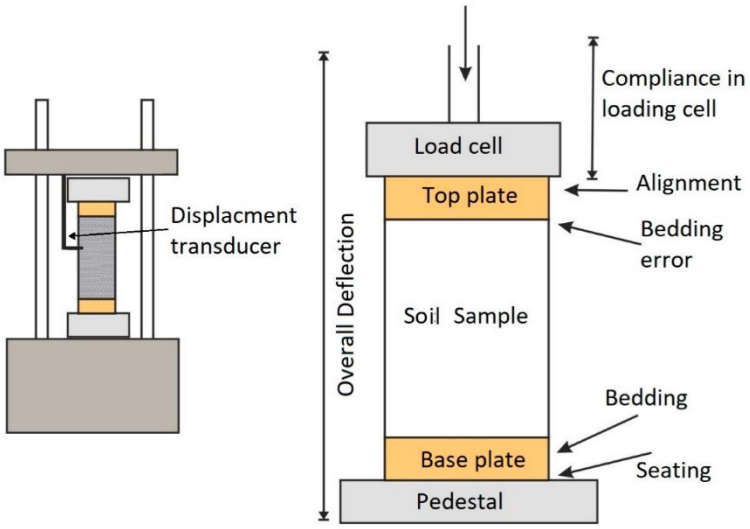

Fig. 1. UCS Test setup (schematic) [31]

3.3.2 California Bearing Ratio (CBR)

CBR tests were performed as per ASTM D1883 [32] to evaluate the stabilized soil's bearing capacity, which is critical for pavement design. Both unsoaked and soaked CBR were measured, but emphasis is on soaked CBR (96-hour soak) since subgrades often encounter wet conditions. After curing, samples in CBR molds were soaked (if required) and then penetrated with a standard piston (50 mm diameter) at 1.25 mm/min. The loads at 2.5 mm and 5.0 mm penetration were recorded. The CBR value is the ratio (in percentage) of the measured load to a standard load (1370 kg for 2.5 mm penetration. Fig. 2 shows the CBR test setup. Higher CBR indicates greater shearing resistance under a standard load, thus a more robust subgrade.

$$CBR\ Value = \frac{Measured\ Load}{Standard\ Load} \times 100 \tag{2}$$

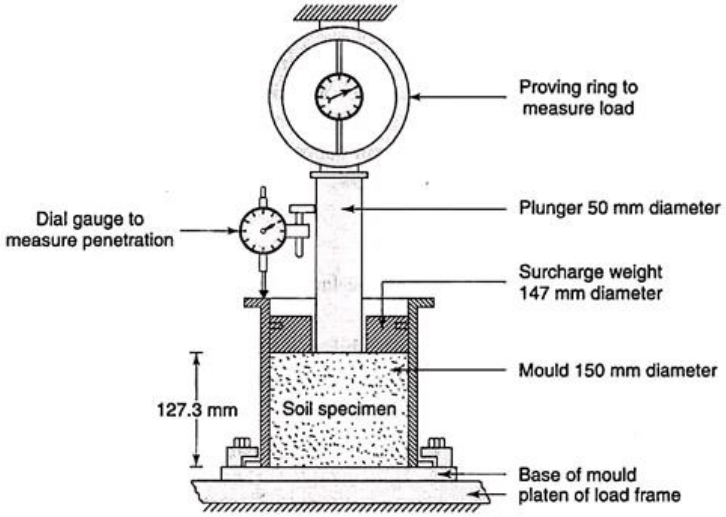

Fig 2. CBR Test Setup (schematic) [32]

3.3.3 Free Swell Index (FSI)

The free swell test (per ASTM D4829 [33]) quantifies the soil's swell potential when inundated. 10 g of oven-dry pulverized soil passing 425 μm sieve was used for each trial. The soil was poured into two graduated cylinders: one filled with distilled water and another with kerosene (non-polar liquid where clay doesn't swell). After 24 hours, the volumes in each cylinder were noted. FSI (%) was calculated as

$$FSI\ (\%) = \frac{V_w - V_k}{V_k} \times 100 \quad (3)$$

where V_w is the volume in water and V_k in kerosene. For stabilized soil, a reduction in FSI indicates that the treatment has inhibited the expansive clay minerals' ability to swell. Lower swell is desirable for subgrades to prevent pavement uplift. The test was done on powdered samples from cured and air-dried specimens for each mix to assess how stabilization reduced the inherent swell potential.

3.3.4 Dynamic Cone Penetration Test (DCPT)

The DCPT (also called DCP) was employed as a field test to assess in-situ strength of the stabilized soil layers. We followed ASTM D6951 [34] for test procedure. A pit (1 m × 1 m × 0.5 m) was prepared at the test site and backfilled with the stabilized soil mixture in layers, compacted to field density. The DCP apparatus consists of an 8 kg hammer dropping from 575 mm height onto an anvil that drives a 60° cone (20 mm base diameter) into the soil. The penetration after each blow (or set of blows) was recorded to calculate the Dynamic Penetration Index (DPI), typically reported in mm/blow. A higher DPI signifies softer ground (more penetration per blow), whereas a lower DPI indicates a stronger, more resistant soil. In our tests, DPI was recorded for each mix at the end of curing by performing DCP on the constructed test beds. The obtained DPI values were later used to estimate CBR via existing empirical correlations and to develop a project-specific correlation (see Section 4.4).

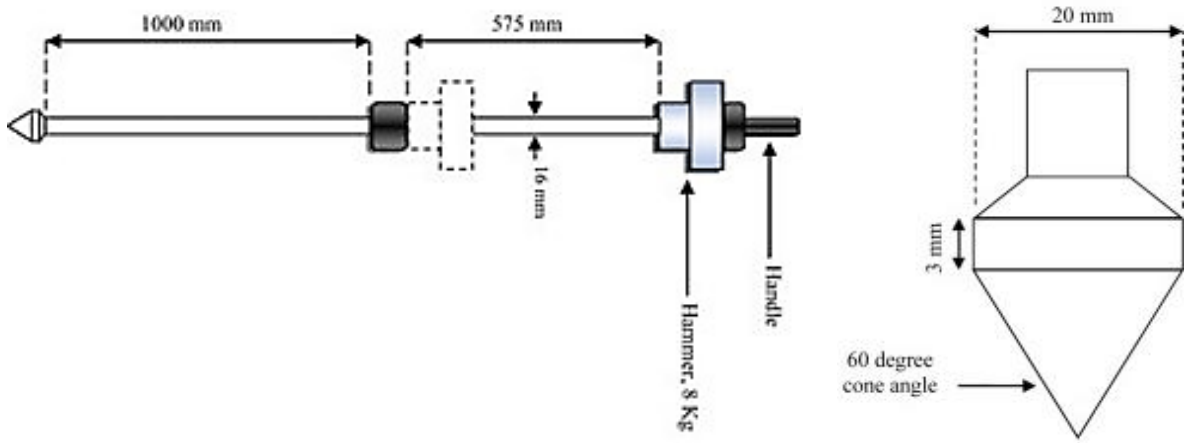

Fig. 3. Schematic of Dynamic Cone Penetration Test (DCPT) [34]

3.3.5 Durability (Wetting-Drying Cycles)

To evaluate the durability of stabilized soil under environmental stresses, wetting–drying (W-D) cycle tests were conducted (ASTM D559 [35]). Specimens stabilized with 8% binder and various slag contents were subjected to 12 cycles of alternate soaking (wetting) and oven-drying, simulating seasonal moisture fluctuations. Each cycle consisted of submerging the sample in water for 5 hours followed by oven drying at 60°C for 42 hours. After 12 cycles, the cumulative weight loss of each specimen was measured to assess material disintegration. In addition, UCS tests were performed after selected cycles (every 4 cycles) to see strength retention. This durability test indicates how well the stabilized soil can withstand repeated swelling and shrinkage—critical for long-term performance. Scanning Electron Microscopy (SEM) was also carried out on samples after 0, 4, 8, and 12 W-D cycles to observe microstructural changes (Section 4.5).

4. Results and Discussion

After curing and testing the various stabilized mixes, the results are presented and discussed in the following sub-sections. Unless stated otherwise, the discussed trends correspond to the 28-day cured samples, as they exhibited the highest strength and most stabilized behavior. All results for

lime-stabilized mixes (soil–lime–slag) are compared alongside those for cement-stabilized mixes (soil–OPC–slag) to highlight differences in performance. Wherever relevant, findings are contextualized with recent literature to underscore agreements or distinctions, thereby deepening the discussion.

4.1 Unconfined Compressive strength (UCS)

The UCS values of the stabilized soil showed a marked improvement with the addition of copper slag (Figure 4). The untreated soil had a UCS of only ~53 kPa (Table 1), which increased dramatically upon stabilization. With 8% binder alone (0% slag), the 28-day UCS reached around 380–420 kPa for lime and cement respectively (extrapolated from the 2% slag data trend). As copper slag content increased from 2% to 8%, UCS rose substantially for both binders. Cement-stabilized specimens exhibited higher strength gains compared to lime-stabilized ones at all equivalent slag contents. For instance, at the optimal 8% slag content, the UCS was about 600 kPa for the lime mix and 616–620 kPa for the cement mix. With 10% slag, UCS peaked at ~661 kPa for cement and ~619 kPa for lime (average values), reflecting roughly 50–65% strength gain over the 2% slag mixes (which were ~450 kPa and 400 kPa respectively). This indicates that copper slag provides additional strength beyond what the binder alone achieves, up to a point.

The initial rise in UCS with slag can be attributed to multiple factors. First, copper slag's high specific gravity and angular particles likely improved the packing density of the soil-binder matrix, thereby increasing the material's load-bearing capacity. Second, copper slag contains oxides of silicon, iron, and aluminum which, in the presence of lime or the calcium from cement hydration, can participate in secondary pozzolanic reactions. This leads to additional cementitious gel formation (such as C–S–H and C–A–H), binding soil particles more effectively. The microstructural analysis (Section 3.5) indeed confirmed the formation of C–S–H gels coating the particles in slag-amended mixes, especially at 8% slag where the structure was densest. Cement-based stabilization outperformed lime-based stabilization in UCS, particularly at early curing stages and lower slag contents, because OPC hydration provides an immediate supply of cementitious compounds (calcium hydroxide, calcium silicate hydrates) that strengthen the soil. Lime requires time to react with soil silica/alumina (a slower pozzolanic process), and thus lime-stabilized soils often gain strength more gradually. Kumar and Walia [16] have noted that lime's effect is time-dependent, improving plasticity and facilitating long-term strength, whereas cement yields more immediate strength gains.

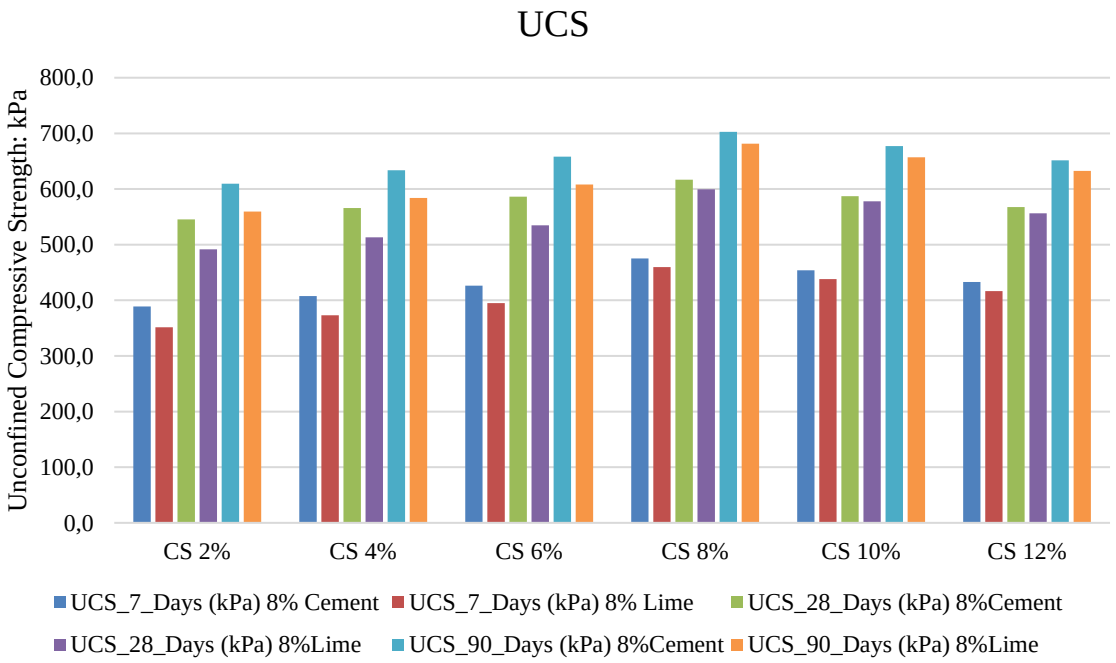

Fig. 4. UCS values for different proportions of copper slag and Cementitious materials

There appeared to be an optimum slag content around 8–10%. Beyond this, at 12% slag, the UCS did not increase further and in some cases showed a slight decrease (e.g., a marginal drop from 660 kPa at 10% slag to ~630 kPa at 12% slag for the cement mix, as inferred from Figure 4). This trend suggests that excessive slag might lead to diminishing or negative returns in strength. A plausible explanation is that at high slag content, not all slag particles can participate in bonding; instead, they may act as inert inclusions if insufficient binder is present to react with them. The surplus unreacted slag can create weak points or micro-voids in the matrix, slightly reducing strength. Similar findings were reported by Ekinci et al. (2022), who observed an optimal ratio of slag in a slag–lime–cement mix for peak strength, with too much slag causing a drop in UCS due to dilution of binder effectiveness. Therefore, while copper slag is beneficial, its content should be optimized relative to the binder amount. In our case, ~1 part binder to 1 part slag (8% each) was an optimal proportion for maximizing UCS.

4.2 California Bearing Ratio (CBR)

The CBR values of the stabilized soil followed trends similar to UCS, as expected, since both reflect soil strength. Figure 5 illustrates the soaked CBR for mixes with 8% binder (lime or cement) and varying slag. The native soil had a very low soaked CBR (<2%), typical of expansive clays that lose strength upon saturation. With stabilization, soaked CBR increased significantly. At 2% slag, the soil + 8% lime mix showed a CBR of about 4–5%, whereas soil + 8% cement showed around 6–8%. These base stabilized values (with minimal slag) were already improvements due to binder alone. As copper slag content increased to 8–10%, the CBR jumped markedly. The highest CBR recorded was about 16% for the cement-stabilized soil with 10% slag. The corresponding lime-stabilized mix had a CBR around 14–15% at 10% slag. In percentage terms, this is roughly a doubling of CBR from the low-slag cases (e.g., from ~8% at 2% slag to 16% at 10% slag in cemented mixes). Even 12% slag did not increase CBR further, indicating a leveling off. The unsoaked CBR (not shown in figure) were higher, as expected (roughly 1.5–2 times the soaked CBR), but since pavements are generally designed with soaked CBR for conservatism, our focus is on the soaked values.

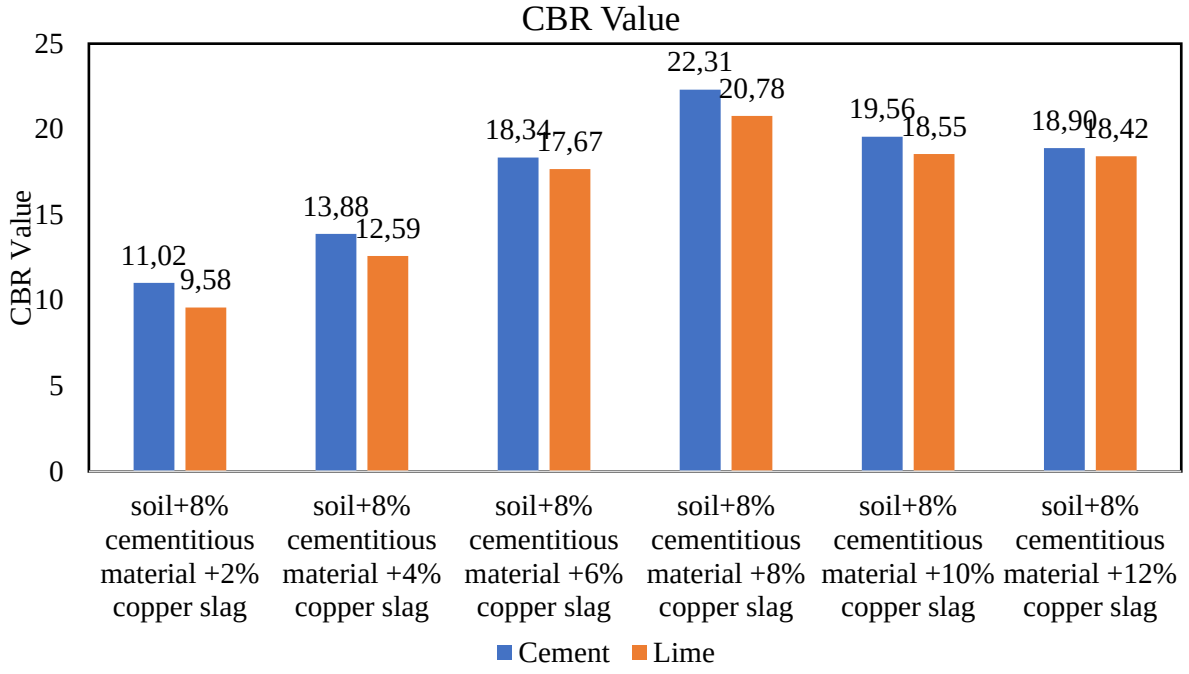

Fig. 5. CBR values of soil sample with optimum percentage of lime and cement and increasing percentage of copper slag

The enhancement in CBR with slag can be explained by improved particle interlock and shear resistance of the matrix. Copper slag particles act somewhat like a sand/gravel component in the soil, increasing the frictional stability under the penetrating piston. Moreover, the binding action of the cementitious products (from lime or cement reactions) with slag leads to a stiffer material that

resists penetration. It is noteworthy that cement+slag outperformed lime+slag in CBR as well, albeit modestly. At optimum slag, cement mix CBR was ~16% vs. lime mix ~14%. This aligns with the UCS results, since a higher UCS generally correlates with a higher CBR for a given soil type. Another observation is that beyond ~8–10% slag, the CBR did not substantially improve or may even decline slightly. This suggests an optimal point similar to UCS behavior. Additional slag beyond optimum may not contribute to bearing resistance proportionally and could even introduce excess fines that soften on soaking.

4.3 Free Swell Index (FSI)

The free swell index of the soil decreased dramatically upon stabilization (Table 4). The untreated soil's FSI was 120%, reflecting severe swelling potential. With the addition of 8% lime (no slag), the FSI dropped to around 50%, and with 8% cement (no slag) to about 40% (these can be inferred from the 2% slag entries in Table 5 as there is minimal slag effect at 2%). The inclusion of copper slag further suppressed the swelling. Each increment in slag content led to a lower FSI for both lime and cement mixes. At the optimum 8% slag, the FSI was reduced to 24% for the lime-stabilized soil and 19% for the cement-stabilized soil. These values represent an 80–85% reduction in swell potential compared to the original soil. Even at 12% slag, FSI went as low as ~15% with cement and ~20% with lime (meaning the expansive soil was practically converted to a non-expansive soil, as FSI < 20% is generally considered low expansiveness).

The greater efficacy of cement over lime in reducing FSI is evident but not as pronounced as in strength metrics. Both stabilizers achieved substantial swell reduction. Cement-stabilized soil's lower FSI can be attributed to the formation of cementitious compounds that bind clay particles and fill the voids, thereby restraining the soil from absorbing water and swelling. Lime also reduces swell by cation exchange and flocculation of clay particles (transforming them into more silt-like, non-expanding aggregates). However, lime's full impact on swell reduction can sometimes take longer to manifest, whereas our measurements were at 28 days. The addition of copper slag contributes to swell reduction in two ways: (1) Particle Replacement: slag particles (non-plastic) replace a portion of clay in the mix, directly reducing the amount of expansive clay present; (2) Pozzolanic Reaction: slag provides silica and alumina that, in presence of calcium (from lime or cement), form cementitious gels coating clay particles, which limits their expansion. The data indicates diminishing returns at higher slag contents (beyond ~8–10% slag, the FSI is already very low, so there's little swell left to eliminate). Notably, by 10–12% slag, the FSI values are nearly the same for both binders (~15–20%). This suggests a floor effect: once most clay is stabilized and excess voids are filled, the remaining slight swell might be due to pockets of untreated clay or micro-fissures on wetting, which neither additional slag nor a different binder can further reduce significantly. Achieving <20% FSI means the soil would pose minimal swelling problems in the field (comparable to an inert fill). This is a crucial outcome for the sustainability of pavements on such subgrades.

Table 4. Free Swell Index (FSI) of stabilized soil for varying copper slag content

Copper Slag (%)	FSI (%) with 8% Lime	FSI (%) with 8% Cement
0 (control)	50	40
2	30	25
4	28	23
6	26	21
8	24	19
10	22	17
12	20	15

Comparatively, Jangid and Grover observed ~70% reduction in swell with 30% copper slag alone [11]. Our study achieves a similar (~85%) reduction with a combination of lime/cement and much less slag, highlighting the efficiency of combined stabilization. Lime–fly ash mixtures in other studies also report significant swell reductions, reinforcing that proper admixtures can mitigate

expansive behavior [12-15]. The advantage of our copper slag approach is that it also contributes to strength, whereas some additives like only lime can reduce swell but not improve strength as much. Thus, the dual benefit of slag here is clear: it simultaneously increases strength and reduces swell, which is ideal for treating expansive subgrades.

4.4 Dynamic Cone Penetration (DCP) Test results

Field DCP tests were performed on both lime-stabilized and cement-stabilized pads with varying slag content. The results are summarized in Table 5 in terms of the Dynamic Penetration Index (DPI), which is the penetration per hammer blow (mm/blow). Lower DPI indicates a stronger (more resistant) soil. The general trend observed was that increasing copper slag content up to 8% reduced the DPI (thus improved the strength), while beyond 8%, the DPI slightly increased, especially for the lime-treated soil.

Table 5. Dynamic penetration index (DPI) for different mixes (after 28 days curing)

Copper Slag (%)	DPI (mm/blow) – Cement-stabilized	DPI (mm/blow) – Lime-stabilized
0 (8% binder only)	45.01	50.02
2	35.89	40.77
4	27.66	30.12
6	20.97	22.66
8	16.80	19.51
10	19.13	21.90
12	23.19	26.57

At 8% slag, the cement-stabilized pad achieved a DPI of 16.8 mm/blow, whereas the lime-stabilized pad had 19.5 mm/blow. These low DPI values correspond to a well-compacted, strong subgrade (for reference, a DPI <20 is usually associated with CBR well above 10% in many soils). The minimum DPI occurred at 8% slag for both binders, indicating peak strength, which aligns with the UCS/CBR optimum. When slag content was raised to 10% and 12%, DPI values increased (meaning penetration resistance dropped a bit). This again mirrors the slight drop in UCS/CBR at higher slag, showing consistency between lab and field indicators. Cement-treated soil consistently showed lower DPI (higher strength) than lime-treated soil at the same slag content, affirming the superior performance of cement noted earlier. To utilize the DCP results for practical evaluation, we compared the predicted CBR from existing empirical correlations with the actual CBR from lab tests. Several established equations relate DPI (or DCP penetration rate) to CBR; some examples are listed in Table 6. We applied these correlations to our DPI data (Table 7 shows an excerpt of predicted vs. experimental CBR for key mixes). It was found that existing correlations did not accurately predict our CBR values – predictions often deviated significantly, sometimes overestimating, or underestimating CBR especially for the lime-stabilized case. This is likely because those correlations were developed for different soil types or aggregate bases and may not directly apply to a stabilized expansive clay. For instance, Patel and Patel (2012) gave CBR = 24.903·(DPI)^(-1.331); using our DPI, this tended to over-predict CBR for low DPI (strong soils).

Table 6. Correlation equations developed for CBR and DPI by previous researchers

S. No.	Author/s	Material Type	Correlation equation
1.	Gabr et al. [36]	Mixture of fine-grained soil and granular material	Log CBR = 1.55 – 0.55 Log (DPI)
2.	Webster et al. [37]	Granular and cohesive materials	Log CBR = 2.465 – 1.12 Log (DPI)
3.	Mejias Santiago et al. [38]	High compressible clay	CBR = 442.92/(DPI)1.119
4.	Patel and Patel [39]	Clay soils and silty sands	CBR = 24.903(DPI)-1.331

Table 7. Predicting CBR values from DCP Index values using different empirical relations

Copper Slag (%)	Soil + Cement + Copper Slag						Soil + Lime + Copper Slag					
	Exp. CBR	Predicted CBR Values					Exp. CBR	Predicted CBR Values				
		[35]	[36]	[37]	[38]	[39]		[35]	[36]	[37]	[38]	[39]
2	11.02	5.29	4.95	1.82	8.06	0.21	9.58	4.59	4.62	2.13	6.99	0.18
4	13.88	7.09	5.71	1.31	10.79	0.30	12.59	6.44	5.45	1.46	9.81	0.27
6	18.34	9.66	6.65	0.93	14.70	0.43	17.67	8.86	6.38	1.02	13.48	0.39
8	22.31	12.39	7.52	0.70	18.85	0.58	20.78	10.48	6.92	0.85	15.94	0.48
10	19.56	10.71	7.00	0.83	16.30	0.49	18.55	9.21	6.50	0.98	14.01	0.41
12	18.90	8.63	6.30	1.05	13.14	0.38	18.42	7.41	5.84	1.25	11.28	0.32

Due to these discrepancies, we established a new empirical relationship tailored to our data. Figure 6 plots the experimentally measured CBR (soaked) against the corresponding DPI for all mixes. A clear inverse relationship is observed: as DPI decreases, CBR increases. We fitted various regression models (linear, power, exponential) to the data and found that an exponential model best described the CBR–DPI relationship for our stabilized soil. The correlation can be expressed as;

$$\mathrm{CBR} = 367.12\ \mathrm{DPI}^{-0.973} \tag{4}$$

The development of this site-specific correlation is a valuable outcome. It means that for similar soil and stabilization, one can quickly perform a DCP test in the field and estimate the subgrade's CBR using the above formula, without waiting for lab CBR tests. This is especially useful for quality assurance during construction of LVRs: if the DPI measured on compacted stabilized layers is below a threshold (e.g., 20 mm/blow), the correlation assures that the CBR (and hence subgrade support) is satisfactory (e.g., >13–15%). Our findings echo those of Lee et al. (2019), who emphasized that instrumented DCP can reliably assess subgrade strength in situ [23]. By refining the correlation for expansive soil stabilization, we contribute a practical tool for engineers dealing with such materials.

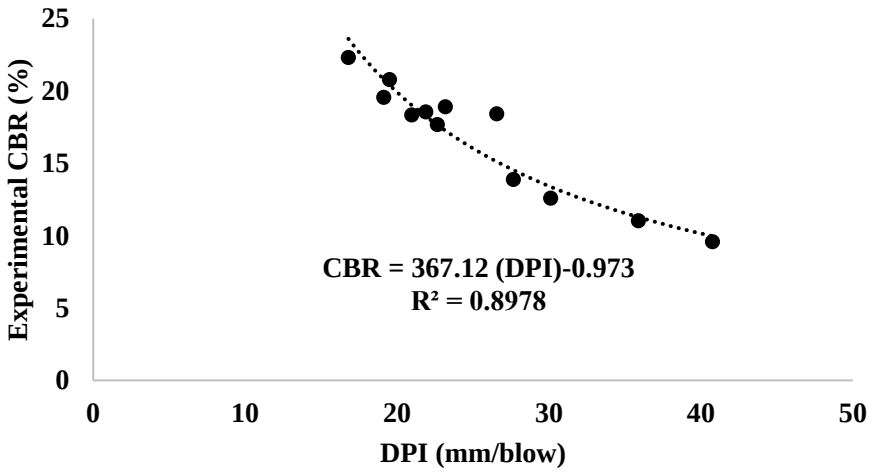

Fig 6. Correlation between DPI and experimental CBR

In summary, the DCPT results and the derived correlation reinforce the laboratory findings and add confidence that the improvements in soil properties (strength and stiffness) translate to field conditions. Cement-stabilized slag mixes show slightly better field performance than lime mixes, and the optimal slag content of ~8% is confirmed in the field by minimum DPI (maximum strength). The new DPI–CBR curve fills an important gap for field assessment, as previous generic correlations were unsuitable for our case. Future projects in similar soil environments can adopt this approach to verify stabilization effectiveness quickly on-site.

4.5 Microstructural Analysis (SEM)

Scanning Electron Microscopy was performed on selected stabilized soil samples to observe the micro-level changes due to the additives. Figure 7 (a–f) and Figure 8 (a–f) present secondary electron SEM images for soil mixed with 8% lime + various slag contents, and soil with 8% cement+various slag contents, respectively. The magnifications used (on the order of 1000–2000×) allowed us to identify particle bonding, fabric arrangement, and the presence of cementitious reaction products.

In the lime-stabilized series (Fig. 7), the untreated soil (not shown here) exhibited a loose fabric with clay platelets having a face-to-face orientation and significant inter-particle voids. With 2% slag + 8% lime (Fig. 7a), we start to see clay particles coated with thin reaction products and slag particles embedded in the matrix but not fully bonded. There are still considerable voids and a fragmented structure. By 8% slag + 8% lime (Fig. 7d), the micrograph reveals a much denser matrix: clay particles and slag are bonded by a web of cementitious gel (C–S–H and C–A–H). The structure is cohesive, with slag particles acting as nodes around which the gel has formed. This corresponds to the optimum mix where macroscopically we saw peak strength and lowest swell. At higher slag (Fig. 7f for 12% slag + lime), some unreacted slag particles are noticeable – appearing as dark, angular bodies not tightly covered by gel – and micro-cracks can be seen around them, indicating a point of potential weakness. This supports the idea that beyond optimum slag, the surplus may not integrate well into the matrix.

In the cement-stabilized series (Fig. 8), the images similarly show progressive densification up to an optimal slag content. 2% slag + 8% cement (Fig. 8a) already shows significant cementitious material binding the soil (since cement hydrates readily even without slag). The addition of slag introduces additional surfaces for C–S–H to form, and some slag appears partially hydrated (edges of particles slightly eroded, suggesting reaction). At 8% slag + 8% cement (Fig. 8d), the microstructure is very dense and uniform. The pores are filled with reaction products, and the slag particles are well bonded, effectively becoming part of a load-bearing skeleton. This image had the most tightly knit fabric among all, reflecting why this mix gave top performance. At 12% slag + 8% cement (Fig. 8f), similar to the lime case, a few voids and unreacted particle surfaces are apparent. The matrix is still solid, but one can discern areas where excessive slag led to pockets not fully cemented.

Overall, the SEM analysis confirms the mechanism of stabilization: the formation of cementitious gels (like C–S–H) from the reaction of calcium (from lime/cement) with silica/alumina (from soil and slag) is clearly evident. These gels are the binding agent that glue soil particles and slag together, transforming the soft clay into a firmer, aggregated structure. The optimal slag content (~8%) achieved a balance where enough slag was present to maximize these reactions and densify the matrix, but not so much as to leave unreacted excess. At this optimum, C–S–H crystals were observed abundantly, imparting rigidity and strength. The micrographs also explain the reduced FSI: in stabilized samples, clay particles are no longer free; they are encapsulated by or fused with cementitious products. This restrains the clay from swelling independently. We saw very few discrete clay platelets in the treated samples; most were part of larger cemented clusters.

The comparative microstructure between lime and cement mixes indicates that cement mixes had a slightly more coherent matrix at earlier stages (due to rapid hydration). Lime mixes, while eventually also forming substantial cementitious bonding (especially with slag's pozzolanic action), may have more heterogeneous distribution of products initially. This could be one reason the lime mixes needed more curing time to catch up in strength. Nonetheless, by 28 days and optimal mix, both showed a qualitatively similar dense structure. These microscopic observations strongly correlate with the macroscopic test results, lending confidence to our understanding of why and how copper slag and cementitious binders improved the soil.

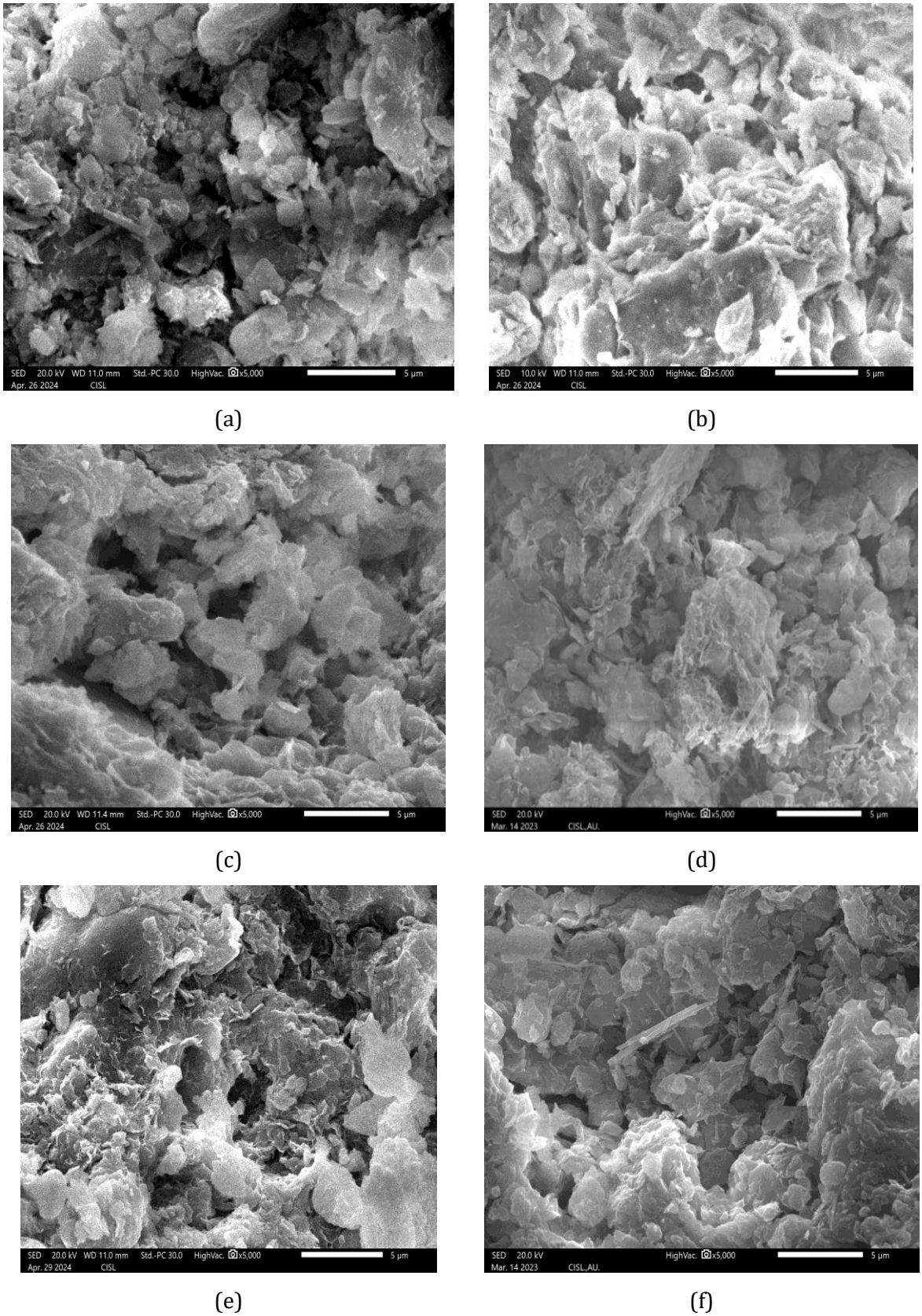

Fig. 7. Microstructural images (SEM) of soil samples stabilized with lime + copper slag (a) Soil + 8% lime with 2% slag, (b) Soil + 8% lime with 4% slag, (c) Soil + 8% lime with 6% slag Soil + 8% lime with 8% slag, (e) Soil + 8% lime with 10% slag and (f) Soil + 8% lime with 12% slag

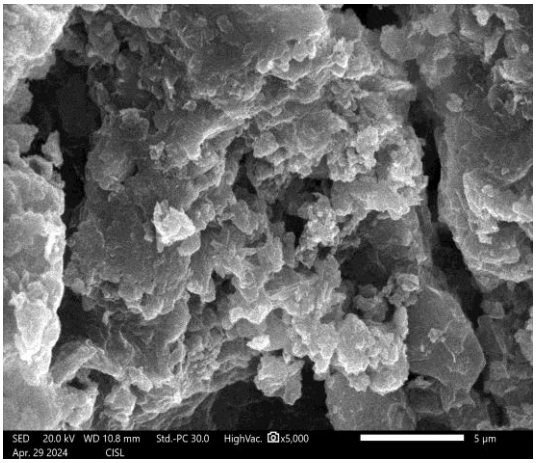

(a)

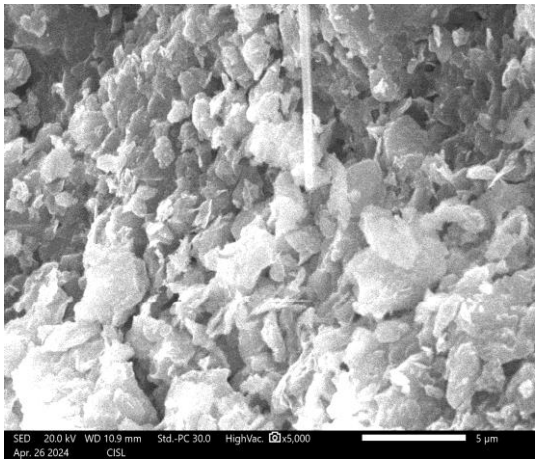

(b)

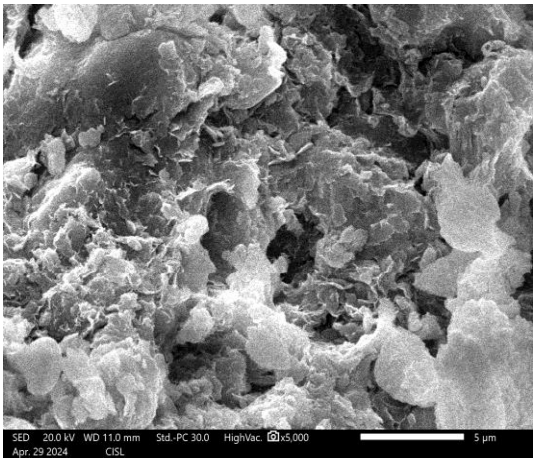

(c)

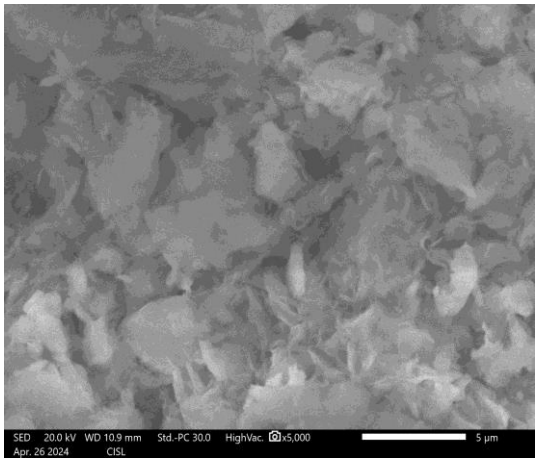

(d)

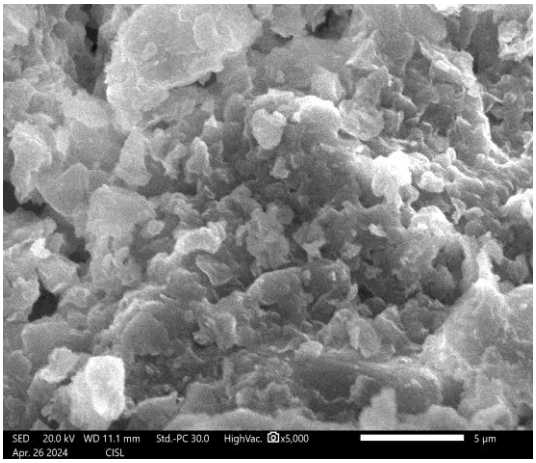

(e)

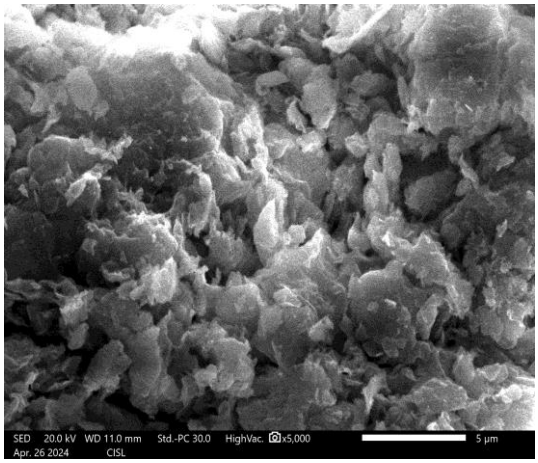

(f)

Fig. 8. Microstructural images (SEM) of soil samples stabilized with cement + copper slag(a) Soil + 8% Cement with 2% slag, (b) Soil + 8% Cement with 4% slag, (c) Soil + 8% Cement with 6% slag, (d) Soil + 8% Cement with 8% slag, (e) Soil + 8% Cement with 10% slag, and (f) Soil+ 8% Cement with 12% slag

4.6 Durability Under Wetting-Drying Cycles

One of the critical assessments for field applicability of stabilized soil is its durability against environmental loading. The wetting–drying (W-D) test results for samples with 8% binder and various slag contents are given in Table 8 (weight loss after 12 cycles) and Tables 9–10 (UCS after each cycle for cement and lime stabilized samples). After 12 W-D cycles, weight loss was observed in all samples due to erosion of particles and breakup of soil structure from repeated swelling-shrinkage. However, the magnitude of weight loss varied with slag content and binder type. As shown in Table 8, higher copper slag content led to lower weight loss, indicating better durability. For the cement-stabilized series, weight loss dropped from 8.2% at 2% slag to 5.7% at 10% slag. Beyond 10%, there was a slight uptick (5.9% at 12% slag), but 10% slag yielded the minimum weight loss. In the lime series, weight loss went from 10.5% at 2% slag down to 7.5% at 10% slag, then marginally up to 7.8% at 12%. This implies that 10% slag content provided the best resistance to W-D degradation, coinciding with what was noted in microstructural stability and earlier strength retention (indeed, earlier we saw optimum slag ~8% for peak strength; here 10% came out best for durability, suggesting a small trade-off where a tad more slag benefits durability slightly by filling voids even if strength doesn't further increase). Also, cement-stabilized samples consistently lost less weight than lime-stabilized ones for the same slag content (e.g., 10% slag: 5.7% loss cement vs 7.5% loss lime). This points to cement imparting better bonding that holds particles together under cyclic stress, whereas lime-stabilized soil, being a bit less strongly bonded, experienced more material detachment.

The strength retention over cycles was examined by measuring UCS after every cycle for some samples (Tables 9 and 10 list detailed UCS values cycle-by-cycle for cemented and limed samples at a representative slag content, presumably 8% or 10%). The general pattern observed was that UCS initially increased in the first few cycles, reached a peak around 6–8 cycles, and then decreased by cycle 12. For example, in the cement + 10% slag sample (from Table 9): the UCS started around 315 kPa after 1 cycle (which is lower than the 28-day initial UCS because the sample had been through a soak-dry already), then increased to ~661 kPa by cycle 10, and finally dropped to ~534 kPa by cycle 12. A similar trend happened in lime + 10% slag sample (Table 10): UCS rose from ~142 kPa at cycle 1 to ~619 kPa at cycle 8, then fell to ~152 kPa by cycle 12. The initial rise can be explained by continued pozzolanic reactions and pore consolidation: the wetting allows further lime/cement hydration and swelling presses particles tighter (which upon drying become denser), thus temporarily increasing strength in moderate cycles. However, repeated cycles eventually cause cumulative damage: micro-cracks form and widen, and some cementitious bonds break, leading to strength loss towards the end of the test. By 12 cycles, the lime-stabilized sample's UCS had dropped near to its 7-day strength level, whereas the cemented sample retained a higher UCS (still above 500 kPa, which is impressive given the abuse).

The SEM images after W-D cycles (Fig. 9 a–c) provide visual evidence of the damage progression described. After 4 cycles (Fig. 9a), micro-cracks initiate in the lime+slag sample, and some loose particles appear, although much of the structure is intact. By 8 cycles (Fig. 9b), cracks have expanded and more noticeable particle detachment is visible; the matrix is still holding but significantly stressed. After 12 cycles (Fig. 9c), the sample shows severe cracking and a disrupted matrix – essentially, the cumulative swelling and shrinkage have overcome the binding capacity in many spots, causing the soil structure to fragment. This correlates with the sharp drop in UCS from cycle 8 to 12. Notably, the cement-based samples showed finer cracks and less particle loss at equivalent cycles, corroborating why their strength remained higher and weight loss lower.

In practical terms, the durability tests indicate that the stabilized soil (especially with optimal slag ~8–10% and cement binder) has good resistance to seasonal moisture changes. The weight losses around 5–8% are relatively low, suggesting that the material does not significantly degrade or erode even after a year's worth of wet-dry cycles (12 cycles can be seen as an accelerated simulation of several seasons). The cement + slag mix with 10% slag performed best, making it the recommended formulation for field use where cyclic durability is a concern (e.g., in climates with pronounced wet and dry seasons). Lime + slag is slightly less durable but still substantially better than untreated soil, which would disintegrate under such testing.

These findings align with other studies on durability of stabilized soils. For instance, Ibrahim et al. (2022) found that adding industrial by-products improved the resistance of clayey soil to wet-dry cycles due to reduced moisture absorption and better cementation (though their materials differed) [40]. Our work specifically shows copper slag's contribution: by filling voids and participating in cementation, it lessens the internal volume changes and strengthens the soil against breakage. It is worth mentioning that while our lab W-D test is rigorous, actual field conditions may impose less extreme drying (the soil wouldn't typically oven-dry in the field). Thus, the performance in situ could be even better. Overall, the stabilized soil proved durable, satisfying an important criterion for sustainable application in road subgrades.

Table 8. Cumulative weight loss after 12 wet–dry cycles

Copper Slag (%)	Weight loss (%) – Lime mix	Weight loss (%) – Cement mix
0 (8% binder only)	12.0	9.0
2	10.5	8.2
4	9.8	7.6
6	8.9	6.8
8	8.1	6.2
10	7.5	5.7
12	7.8	5.9

Table 9. Variation of UCS values on wetting and drying of soil samples with Cement

Cycle no	UCS sample-1	UCS sample-2	Avg. UCS (kPa or kN/m^2)
1	315.43	315.49	315.46
2	408.67	408.72	408.70
3	443.88	443.96	443.92
4	486.68	486.95	486.82
5	516.99	517.22	517.11
6	556.69	557.01	556.85
7	587.03	587.62	587.33
8	609.20	609.39	609.30
9	626.63	626.79	626.71
10	660.45	661.30	660.88
11	556.73	557.10	556.92
12	533.73	533.85	533.79

Table 10. Variation of UCS values on wetting and drying of soil samples with Lime

Cycle no	UCS sample-1	UCS sample-2	Avg. UCS (kPa or kN/m^2)
1	141.68	141.73	141.71
2	177.35	177.65	177.50
3	247.36	247.37	247.37
4	355.25	355.35	355.30
5	441.44	441.63	472.72
6	510.51	510.51	510.51
7	592.33	592.39	592.36
8	618.56	618.75	618.65
9	520.88	520.90	520.89
10	400.87	401.53	401.20
11	201.96	201.80	201.88
12	151.97	151.90	151.93

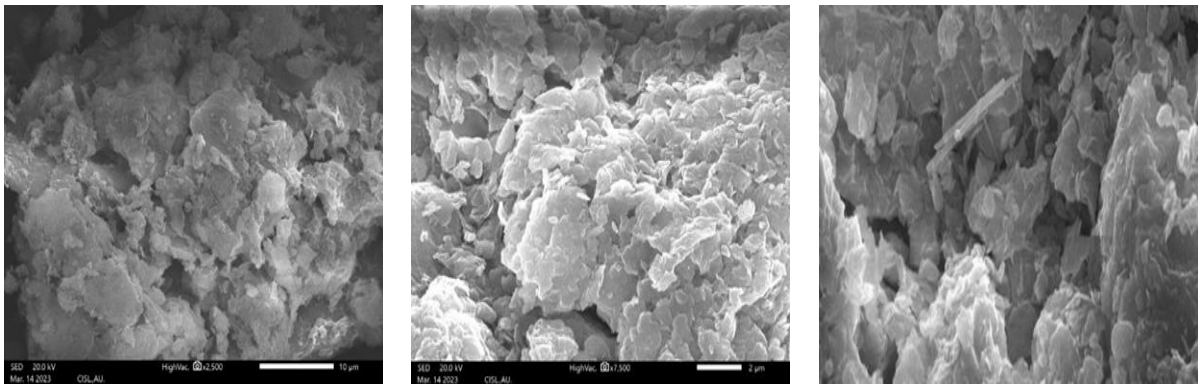

(a) (b) (c)

Fig. 9. SEM images after W-D cycles (a) SEM of 8% Lime with 8% slag at cycle 4 (W-D), (b) SEM of 8% Lime with 8% slag at cycle 8 (W-D), and (c) SEM of 8% Lime with 8% slag at cycle 12 (W-D)

4.7 Statistical Modeling of Strength Improvement

To further analyze the effects of copper slag content and binder type on the soil's strength, a simple statistical model was developed using the UCS data. A multiple linear regression (MLR) was performed with UCS as the dependent variable and two independent variables: (i) copper slag content (%) as a continuous variable, and (ii) a binder-type dummy variable (0 for lime, 1 for cement). This approach allows us to quantify the influence of each factor and their combined effect on UCS. Such statistical analysis of stabilization results has been advocated by recent researchers to validate experimental findings and enable predictions [41]. Using the 28-day UCS results for 0%, 2%, 4%, 6%, 8%, 10%, and 12% slag (with both binders), the regression yielded the following relationship:

$$UCS\ (kPa)=394+29\cdot B+21\cdot(slag\%) \quad (5)$$

Here, B is the binder dummy (B = 0 for lime, B = 1 for cement). The model has an R^2 =0.88, indicating that about 88% of the variance in UCS is explained by the linear combination of slag content and binder type. Both predictors are positively correlated with UCS, consistent with expectations: the coefficient 21 implies that, on average, each 1% increase in copper slag raises UCS by ~21 kPa (holding binder type constant), and the coefficient 29 means switching from lime to cement (with same slag%) adds about 29 kPa to UCS on average.

This statistical outcome reinforces the earlier discussion—copper slag content is a highly significant factor ($p < 0.001$ in the regression) in improving UCS, while the choice of binder (cement vs. lime) has a positive but relatively smaller effect. In fact, the regression suggests that roughly 75% of the strength gain (the part captured by the slag coefficient) is attributable to the copper slag itself (through densification and pozzolanic contribution), whereas the binder choice contributes the remaining difference. The interaction between slag and binder was also tested by adding a term (slag% × B) to the model, but it was not statistically significant. This implies that the rate of strength gain per % slag was similar for both binders in the range considered; cement simply provides an upward shift in strength across all slag contents.

The MLR model (Eq. 5) can be used to predict UCS for intermediate combinations or to interpolate/extrapolate within the tested range. For example, plugging slag = 5% and B = 1 (cement) yields UCS ≈ 394 + 29 + 21*5 = 528 kPa (which is reasonable based on our trend between 4% and 6% slag results). For slag = 8%, B = 1, UCS ≈ 394 + 29 + 168 = 591 kPa, close to the measured ~616 kPa (the slight underestimation is due to the non-linear nature at peak which the linear model smooths out). Nonetheless, the model is useful for a first approximation. It also highlights that even with no slag (0%), the model would predict ~394 kPa for lime and ~423 kPa for cement – representing the effect of 8% binder alone. This aligns with typical UCS of lime or cement treated high-plastic clays reported in literature.

Importantly, the statistical analysis confirms the significance of copper slag in the stabilization. The high R^2 and strong slag coefficient validate that the trends observed are systematic and not just experimental scatter. It provides an empirical evidence base to claim: *"Each percent of copper slag added (up to ~10%) contributes approximately 20–25 kPa of UCS improvement, regardless of whether lime or cement is used as the primary binder."* Meanwhile, using cement instead of lime yields on the order of 5–10% higher UCS in our case. These quantitative insights add credibility and clarity to the performance benefits of the proposed sustainable stabilization method.

The regression approach used here is relatively simple; more advanced models (non-linear regression, ANOVA, or even machine learning techniques) could capture the slight curvature in the slag-UCS relationship (peak at 8%). However, even in its simple form, our model's success suggests linear additivity of effects to a large extent. This aligns with the understanding that both binders ultimately produce similar reaction products (calcium-based gels), and slag acts largely as an independent contributor by improving the mixture's physical and chemical composition. Thus, the model is a convenient tool to estimate expected strength outcomes or to tailor mix proportions to reach a target strength. It also exemplifies how statistical modeling can be integrated with experimental studies to generalize findings – an approach increasingly seen in sustainable engineering research to ensure that empirical results can be translated into predictive frameworks [41,42].

In conclusion, the results obtained from laboratory tests, field DCPT, microstructural examination, and statistical analysis all converge on a consistent story: using copper slag in combination with a small amount of cement or lime can significantly enhance an expansive soil's performance. The optimum mixture (approximately 8% copper slag with 8% cement, in this study) yields the best balance of high strength, low swell, and good durability, making it highly suitable for improving low-volume road subgrades in problematic soil areas. The cement-based stabilization is somewhat superior to lime-based in all aspects except perhaps cost, but lime still provides a viable solution when cement is less accessible. The environmental benefits of incorporating an industrial waste like copper slag – reducing the need for cement/lime and repurposing a waste product – further accentuate the sustainability of this approach.

5. Conclusions

This study presents a sustainable and effective approach to stabilizing expansive subgrade soil by incorporating copper slag with conventional binders (cement and lime). A comprehensive suite of laboratory tests (UCS, CBR, FSI), field evaluation (DCPT), microstructural analysis (SEM), and statistical modeling was employed to assess performance.

- The inclusion of copper slag markedly enhanced soil strength. With 8% cement, UCS improved from ~450 kPa (2% slag) to 660 kPa (10% slag), and from ~400 to 619 kPa with lime. This is a 12-fold increase compared to untreated soil (~53 kPa). Cement-based mixes outperformed lime slightly, indicating greater efficiency in strength development. Optimal slag content was 8–10%.
- Soaked CBR values doubled with copper slag addition—rising to 16% (cement) and 14% (lime) at 10% slag—allowing for lighter pavement layers, ideal for low-volume roads. These results are on par with or better than other industrial waste stabilizations.
- Free swell index (FSI) fell drastically—by 65–70%—with cement–slag and lime–slag blends, transforming highly expansive soil into marginally expansive or non-expansive. This directly addresses pavement distress caused by swelling.
- A strong correlation ($R^2 \approx 0.90$) was established between DPI and CBR, enabling rapid field estimation of strength. The best performance (DPI ≈16.8 mm/blow) aligned with 8% slag content, confirming lab findings.
- SEM images revealed denser cementitious matrices with optimal slag content, dominated by C–S–H gel formation. These microstructures validated strength gains and explained why cement slightly outperformed lime.

- The best mix (8% cement + 10% slag) showed only 5.7% weight loss after 12 wet–dry cycles, retaining over 80% of peak strength. Lime-based mixes also showed good resilience, ensuring long-term field performance.

Finally, Copper slag, as a partial stabilizer, offers a cost-effective, eco-friendly solution for expansive soils. It boosts strength, reduces swell, and enhances durability, while promoting sustainable reuse of industrial waste. The findings support its practical application in rural and low-volume road construction, aligning with green infrastructure goals.

References

[1] Ardah A, Chen Q, Abu-Farsakh M. Evaluating the performance of very weak subgrade soils treated/stabilized with cementitious materials for sustainable pavements. Transp Geotech. 2017;11:107–19. https://doi.org/10.1016/j.trgeo.2017.05.002

[2] Zimar Z, et al. Waste-to-energy ash for treating highly expansive clays in road pavements. J Clean Prod. 2022;374:133854. https://doi.org/10.1016/j.jclepro.2022.133854

[3] Oppong F, Kolawole O. Reassessment of natural expansive materials and their impact on freeze-thaw cycles in geotechnical engineering: a review. Front Built Environ. 2024;10:1396542. https://doi.org/10.3389/fbuil.2024.1396542

[4] Hall MR, Najim KB, Keikhaei Dehdezi P. Soil stabilisation and earth construction: materials, properties and techniques. In: Modern Earth Buildings. Woodhead Publishing; 2012. p. 222–55. https://doi.org/10.1533/9780857096166.2.222

[5] Sambre T, Endait M, Patil S. Sustainable soil stabilization of expansive soil subgrades through lime-fly ash admixture. Discov Civ Eng. 2024;1(1):65. https://doi.org/10.1007/s44290-024-00063-1

[6] Mebarki M, Benyahia S, Dahmani S, Nhabih HT. Laboratory improvement of clay mineralogical and swelling properties using hydraulic binder treatment. Res Eng Struct Mater. 2025;11(2):933–55. http://dx.doi.org/10.17515/resm2025-752ma0313rs

[7] Pandey VK, Dhiman S, Bharti K. A review on the use of lime in soil stabilization. In: Latest Trends in Engineering and Technology. 2024. p. 414–21. https://doi.org/10.1201/9781032665443-59

[8] Dixit A, Das SK. Mechanical, microstructural, and durability assessment of cement slurry waste and coal combustion ash mixture as a sustainable subgrade construction material: experimental and mechanistic modeling approach. Constr Build Mater. 2025;458:139550. https://doi.org/10.1016/j.conbuildmat.2024.139550

[9] Abera YA. Sustainable building materials: a comprehensive study on eco-friendly alternatives for construction. Compos Adv Mater. 2024;33. https://doi.org/10.1177/26349833241255957

[10] Qureshi MA, Mistry HM, Patel VD. Improvement in soil properties of expansive soil by using copper slag. Int J Adv Res Eng Sci Technol. 2015;2(7):125–30.

[11] Jangid AK, Grover KS. Experimental investigation of mechanical properties of problematic expansive soil using copper slag and its statistical validation. Multiscale Multidiscip Model Exp Des. 2024;7(3):2147–61. https://doi.org/10.1007/s41939-023-00316-z

[12] Ekinci A, Filho HCS, Consoli NC. Copper slag–hydrated lime–Portland cement stabilised marine-deposited clay. Proc ICE Ground Improv. 2022;175(1):51–63. https://doi.org/10.1680/jgrim.18.00123

[13] Lavanya C, Kumar ND. Study on CBR of lime and cement stabilized copper slag cushion laid over expansive soil. In: Indian Geotechnical Conference 2019 (IGC-2019) Volume V. Springer; 2021. p. 129–39. https://doi.org/10.1007/978-981-33-6466-0_12

[14] Shi C, Meyer C, Behnood A. Utilization of copper slag in cement and concrete. Resour Conserv Recycl. 2008;52(10):1115–20. https://doi.org/10.1016/j.resconrec.2008.06.008

[15] Murari K, Siddique R, Jain KK. Use of waste copper slag, a sustainable material. J Mater Cycles Waste Manag. 2015;17:13–26. https://doi.org/10.1007/s10163-014-0254-x

[16] Bell FG. Lime stabilization of clay minerals and soils. Eng Geol. 1996;42(4):223–37. https://doi.org/10.1016/0013-7952(96)00028-2

[17] Kumar A, Walia BS, Bajaj A. Influence of fly ash, lime, and polyester fibers on compaction and strength properties of expansive soil. J Mater Civ Eng. 2007;19(3):242–8. https://doi.org/10.1061/(ASCE)0899-1561(2007)19:3(242)

[18] Al-Jabri KS, Al-Saidy AH, Taha R. Effect of copper slag as a fine aggregate on the properties of cement mortars and concrete. Constr Build Mater. 2011;25(2):933–8. https://doi.org/10.1016/j.conbuildmat.2010.06.090

[19] Mahedi M, Cetin B, White DJ. Performance evaluation of cement and slag stabilized expansive soils. Transp Res Rec. 2018;2672(52):164–73. https://doi.org/10.1177/0361198118757439

[20] Arulrajah A, et al. Recycled plastic granules and demolition wastes as construction materials: resilient moduli and strength characteristics. Constr Build Mater. 2017;147:639–47. https://doi.org/10.1016/j.conbuildmat.2017.04.178
[21] Sharma K, Kumar A. Geotechnical behaviour of copper slag mixed with different proportions of soil, lime, fly ash and cement—a review. In: Sustainable Environment and Infrastructure: Proceedings of EGRWSE 2019. Springer; 2021. p. 103–16. https://doi.org/10.1007/978-3-030-51354-2_10
[22] Aneke FI, Mostafa MMH. Performance assessment of pavement structure using dynamic cone penetrometer (DCP). Int J Pavement Res Technol. 2020;13:466–76. https://doi.org/10.1007/s42947-020-0249-z
[23] Elias HH, Shaban AM, Almuhanna RR. Assessing strength properties of stabilized soils using dynamic cone penetrometer test. Open Eng. 2023;13(1):20220489. https://doi.org/10.1515/eng-2022-0489
[24] Lee JS, et al. Assessing subgrade strength using an instrumented dynamic cone penetrometer. Soils Found. 2019;59(4):930–41. https://doi.org/10.1016/j.sandf.2019.03.005
[25] Garcia KE, et al. The role of dynamic cone penetrometer testing in assessing pavement subgrade strength: a literature review. Geomate J. 2024;26(117):132–42.
[26] Mohammadi SD, et al. Application of the dynamic cone penetrometer (DCP) for determination of the engineering parameters of sandy soils. Eng Geol. 2008;101(3–4):195–203. https://doi.org/10.1016/j.enggeo.2008.05.006
[27] Bureau of Indian Standards. BIS 269-2015 (Reaffirmed 2020): Ordinary Portland Cement – Specifications. New Delhi: BIS; 2020.
[28] ASTM International. ASTM D6913-2017: Standard Test Methods for Particle-Size Distribution (Gradation) of Soils Using Sieve Analysis. West Conshohocken, PA: ASTM; 2017.
[29] ASTM International. ASTM D698-2021: Standard Test Methods for Laboratory Compaction Characteristics of Soil Using Standard Effort. West Conshohocken, PA: ASTM; 2021.
[30] ASTM International. ASTM D1557-12e1 (2012): Standard Test Methods for Laboratory Compaction Characteristics of Soil Using Modified Effort. West Conshohocken, PA: ASTM; 2012.
[31] ASTM International. ASTM D2166/D2166M-2006: Standard Test Method for Unconfined Compressive Strength of Cohesive Soil. West Conshohocken, PA: ASTM; 2006.
[32] ASTM International. ASTM D1883-2021: Standard Test Method for California Bearing Ratio of Laboratory-Compacted Soils. West Conshohocken, PA: ASTM; 2021.
[33] ASTM International. ASTM D4829-2021: Standard Test Method for Expansion Index of Soils. West Conshohocken, PA: ASTM; 2021.
[34] ASTM International. ASTM D6951-2018: Standard Test Method for Use of the Dynamic Cone Penetrometer in Shallow Pavement Applications. West Conshohocken, PA: ASTM; 2018.
[35] ASTM International. ASTM D559-2015: Standard Test Methods for Wetting and Drying Compacted Soil-Cement Mixtures. West Conshohocken, PA: ASTM; 2015.
[36] Gabr MA, et al. DCP criteria for performance evaluation of pavement layers. J Perform Constr Facil. 2000;14(4):141–8. https://doi.org/10.1061/(ASCE)0887-3828(2000)14:4(141)
[37] Webster SL, Grau RH, Williams TP. Description and application of dual mass dynamic cone penetrometer. Vicksburg, MS: U.S. Army Corps of Engineers; 1992.
[38] Mejías-Santiago M, García L, Edwards L. Assessment of material strength using dynamic cone penetrometer test for pavement applications. In: Airfield and Highway Pavements 2015. ASCE; 2015. p. 837–48. https://doi.org/10.1061/9780784479216.074
[39] Patel MA, Patel HS. Experimental study to correlate the test results of PBT, UCS, and CBR with DCP on various soils in soaked condition. Int J Eng. 2012;6(5):244–9.
[40] Ibrahim M, et al. A review on utilization of industrial by-products in the production of controlled low strength materials and factors influencing the properties. Constr Build Mater. 2022;325:126704. https://doi.org/10.1016/j.conbuildmat.2022.126704
[41] Abdullah GMS, et al. Boosting-based ensemble machine learning models for predicting unconfined compressive strength of geopolymer stabilized clayey soil. Sci Rep. 2024;14(1):2323. https://doi.org/10.1038/s41598-024-52825-7
[42] Tuleun LZ, Wasiu J. Mechanical behavior of silty-clayey lateritic soil stabilized with recycled municipal solid waste ash. Res Eng Struct Mater. 2024. http://dx.doi.org/10.17515/resm2024.204me0303rs

Research on Engineering Structures & Materials
www.jresm.org
Research Group

Research Article

Mechanical performance of slurry-infiltrated fibrous concrete with varying ratios of scrap tire steel fibers and commercial steel fibers

Ravi Prasad Penda [*,1,2,a], I V Ramana Reddy [1,b]

[1]*Department of Civil Engineering, SVU College of Engineering, Sri Venkateswara University, Tirupati, Andhra Pradesh, India*
[2]*National Atmospheric Research Laboratory, Department of Space, Government of India, Gadanki, Andhra Pradesh, India*

Article Info

Article History:

Received 05 Mar 2025
Accepted 13 May 2025

Keywords:

Steel fibers;
Scrap tires;
Compressive strength;
Split tensile strength;
Commercial steel fibers;
Aspect ratio

Abstract

The limitation of using a high volume of fibers in concrete can be addressed with Slurry Infiltrated Fibrous Concrete (SIFCON), a high-performance fiber-reinforced concrete made by placing fibers in a mold and infiltrating them with cement slurry. Typically, commercially available steel fibers of various shapes and sizes are used in the production of SIFCON. This study explores the use of steel fibers extracted from scrap tires as a sustainable alternative to reduce energy consumption in fiber production. Compressive and split tensile strengths of SIFCON with 4% to 7% scrap tire steel fibers were tested and compared to SIFCON made with same volumes of commercially available steel fibers. The M20 design concrete mix and SIFCON slurry were prepared as reference mixes. Compressive and split tensile strengths of SIFCON and M20 concrete were tested using 100 mm and 150 mm cubes, and cylinders of 100×200 mm and 150×300 mm. Results showed that SIFCON with scrap tire fibers achieved about 80% of the compressive and 35% of the split tensile strength of SIFCON with commercial fibers, both significantly outperforming the reference mixes. Advanced techniques, like XRD and SEM were used to analyze SIFCON's internal structure, revealing details about its phase composition, morphology, and microstructure. Specimens were examined and compared to reference mixes, revealing a similar hydration phase in SIFCON. Experimental results show that randomly dispersed steel fibers from scrap tires and commercial sources enhance SIFCON's mechanical properties, making them suitable for its production.

© 2025 MIM Research Group. All rights reserved.

1. Introduction

In the current context, energy crises, as well as their impacts on our planet, are major global challenges. These problems are brought on by the growing population, the speed at which cities are being developed, and the production of large amounts of solid waste. Car and commercial vehicle manufacturing have increased dramatically due to rising demand, leading to a proportional increase in scrap tire production. The increasing use of automobiles in the modern world for the movement of people and goods has led to a problem regarding what to do with scrap tires when their usefulness has come to an end [1–3]. The high carbon content of scrap tires makes them a commonly used energy source in cement kilns [4].

High-strength steel fibers extracted from old tires can be reused as raw materials in steel manufacturing. Additionally, rubber from recycled tires serves as an energy source in various industries. To minimize the demand for commercially produced high-strength steel fibers, the focus

*Corresponding author: raviprasadvssc@gmail.com
[a]orcid.org/ 0009-0000-7323-2177; [b]orcid.org/ 0000-0002-4922-1782
DOI: http://dx.doi.org/10.17515/resm2025-721me0305rs

has been on recovering high-strength steel fibers from scrap tires as a means for the extraction of resources from waste. Scrap tires can be processed using pyrolysis, cryogenic, or mechanical techniques to recover steel fibers and rubber [5,6]. Steel fibers recovered from scrap tires, unlike manufactured commercial ones, may exhibit irregular shapes and inconsistent aspect ratios.

In the construction sector, steel fibers are utilized to produce steel fiber-reinforced concrete. Fiber-reinforced concrete with 1% coir or plastic fibers boosts durability, with coir enhancing tensile and flexural strength by 10% and 20%, and plastic fibers increasing them by 50% and 30%. It is a sustainable option for improving concrete strength and durability [7]. Experimental results showed a 13.6% increase in compressive strength for PPC with glass microfiber compared to control PPC. Adding glass microfiber to PPC reduced plastic shrinkage cracks and drying shrinkage while maintaining similar mechanical and durability properties. Glass microfiber showed no significant mechanical improvement in concrete at elevated temperatures [8]. Due to its higher fiber content, Slurry Infiltrated Fibrous Concrete (SIFCON) is considered an advanced form of Fiber-Reinforced Concrete (FRC). It enhances hardened properties such as strength, toughness, impact resistance, and modulus of rupture. In general, the fibers used to prepare SIFCON provide advantages equivalent to those of reinforced steel in RCC.

Higher fiber concentrations cannot be used to prepare fiber-reinforced concrete, though, because of the balling effect. Slurry Infiltrated Fibrous Concrete (SIFCON) is an advanced type of steel fiber-reinforced concrete, known for its high-performance, cementitious composition [9,10]. SIFCON is made differently from traditional fiber-reinforced concrete, which involves prepacking fibers into molds and allowing cement-mortar slurry to penetrate. The prepacking process allows the use of higher fiber content and a cementitious slurry with a lower water-to-cement ratio. This results in improved toughness and energy absorption compared to traditional steel fiber-reinforced concrete. Steel fibers from scrap tires are effectively used in SIFCON production, as they are manually arranged and infused with a cement mortar slurry matrix, preventing fiber balling. Available literature shows that few studies have explored the use of scrap steel fibers in SIFCON manufacturing. A higher fiber content in SIFCON improves homogeneity and enhances mechanical properties such as flexural strength, compressive strength, and energy absorption. Under blast loading, SIFCON incorporating waste steel fibers outperformed that made with industrial fibers, due to the hybrid nature of the fibers [11–15]. It has been found that the split tensile strength, compressive strength, and flexural strength of SIFCON are optimal at 9% fiber content. SIFCON's maximum flexural strength may be attained with fiber volumes and aspect ratios of 9% and 80, respectively [16]. It has been found that SIFCON has splendid quality in bond for all types of tests when cement is replaced with 15% of silica fume and 35% of volume of plain smooth steel fibers [17].

It has been shown that increasing the volume of hooked-end steel fibers in SIFCON mixes containing silica fume and fly ash enhances the impact energy-to-failure [18]. It has been demonstrated that the splitting tensile strength of SIFCON increased by increasing the fiber percentage in SIFCON [19]. SIFCON made with hooked-end steel fibers achieves maximum compressive and flexural strength when fiber volume is increased up to 10% [20]. Increasing the steel fiber content improves SIFCON's mechanical performance [21]. In comparison to plain cement and fiber-reinforced concrete slab specimens in flexure, SIFCON slab specimens exhibit superior stiffness, energy absorption, and load-carrying ability [22]. SIFCON's flexural and splitting strengths have increased due to its higher waste fiber content. However, compressive strength was unaffected by the use of discarded steel fibers. Waste steel fibers can be an attractive alternative in the creation of SIFCON, according to multi-objective optimization research [23]. Research has shown that incorporating SIFCON into regular concrete enhances strength properties while reducing the likelihood of crack propagation [24].

SIFCON has been successfully produced utilizing the two-layer method employing 6% fibers of steel from old tires. Furthermore, SIFCON with steel fibers from old tires matches the flexural strength of commercial fibers and surpasses reference mixes [25]. SIFCON with hooked-end fibers shows improved performance compared to crimped-end fibers, with a noticeable strength increase when 40% of the binder is replaced with GGBS. Microstructural analysis indicates that SIFCON exhibits

an equivalent level of hydration but at a faster pace compared to conventional concrete [26]. Incorporating scrap-steel fibers (SSFs) enhances the elastic modulus and splitting strength of scrap-steel fiber-reinforced concrete (SSFRC), while reducing linear shrinkage compared to concrete without SSFs [27]. Waste Recycled Tire Steel Fibers (WRTSFs) can enhance concrete's mechanical properties, but optimal results require careful control of fiber shape, aspect ratio, surface characteristics, quality, and dosage. The effectiveness of WRTSFs in concrete depends on their dispersion, orientation, distribution, and bond strength, with uniform dispersion significantly enhancing load-bearing capacity, toughness, and energy absorption [28].

This experimental study investigates the potential of using scrap tire steel fibers as an alternative to commercially available steel fibers in the production of SIFCON. The research focuses on evaluating the compressive and split tensile strengths of SIFCON reinforced with both scrap and commercial steel fibers. The study compares the mechanical performance of the variants, to show that scrap tire steel fibers are a viable, cost-effective option for structural and repair applications.

2. Experimental Program

2.1 Materials

2.1.1 Cement

43-grade OPC was utilized in the experimental program, complying with Indian standards [29]. Tables 1 and 2 present the physical characteristics and chemical composition of the cement, respectively.

Table 1. Physical properties of cement

Physical Characteristics	Test result
Specific gravity	3.13
Fineness	311.5 m^2/kg
Normal consistency	33 %
Setting time: Initial	47 min
Setting time: Final	252 min

Table 2. Chemical composition of cement

Type of oxide	Value (%)
CaO	61.81
SiO_2	20.65
Al_2O_3	5.67
Fe_2O_3	4.13
MgO	2.60
SO_3	2.79

2.1.2 Fine Aggregate

Throughout the experimental work, SIFCON specimens and the reference mix were prepared using natural sand that was collected from the riverbed. The maximum size of fine aggregate that can be utilized in the SIFCON slurry matrix is limited to 0.60 mm.

Table 3. Physical characteristics of fine aggregates

Physical Characteristics	Value
Fineness Modulus	2.80
Specific Gravity	2.65
Water Absorption	0.25 %
Bulk density	1650 kg/m^3

During the experimental work, the maximum particle size of the aggregate is maintained to produce SIFCON. Table 3 displays the fine aggregate's physical characteristics that were used in the experiment. The maximum size of the fine aggregate that can be utilized in M20 grade design mix concrete is 4.75 mm. The fine aggregate used in SIFCON and M20 grade concrete complies with the standards stipulated in IS: 383-1970 [36] and IS: 2386 (Part III)-1963 [37].

2.1.3 Coarse Aggregate

Throughout the experimental work, M20 grade concrete was prepared using natural granite stone, which was collected from the local quarry. The maximum size of coarse aggregate that can be utilized in M20 grade design mix concrete is 20 mm. Table 4 displays the coarse aggregate's physical characteristics that were used in the experiment which comply with the standards stipulated in IS: 383-1970 [36] and IS: 2386 (Part III)-1963 [37].

Table 4. Physical characteristics of Coarse Aggregates

Physical Characteristics	Value
Fineness Modulus	6.30
Specific Gravity	2.70
Water Absorption	0.40 %
Bulk density	1475 kg/m3

2.1.4 Mixing Water

Potable water available in the laboratory was used for producing the SIFCON specimens and reference mixes, as well as for their curing.

2.1.5 Chemical Admixture

A poly carboxylic ether superplasticizer with a high water-reducing range was used to achieve the required fresh properties of the SIFCON slurry mix, such as workability and flowability. Table 5 displays the characteristics of AURAMIX 450 from FOSROC Chemicals.

Table 5. Properties of superplasticizer

Color of appearance	Light yellow
Value of PH	Minimum 6.0
Volumetric mass	1.09–1.11
Content of chloride	Nil

2.1.6 Steel Fibers

2.1.6.1 Scrap Tire Steel Fibers

Steel fibers were collected from scrap tires through a survey. Recycling tires involves various technologies aimed at reclaiming valuable materials like rubber, steel, fiber etc., and converting them into useful products. Mechanical Processing, Pyrolysis, Devulcanization, Cryogenic Grinding and Biological Methods are the key technologies used in tire recycling. A scrap tire recycling facility was explored where a mechanical method is used to recover steel fibers from discarded tires, which were then used to prepare SIFCON specimens. Mechanical shredders at the recycling facility initially shred discarded tires into fragments. Next, the shreds undergo magnetic separation, where powerful magnets extract the steel fibers from the rubbery substance. By passing the remaining material through screens and filters, any residual steel fibers are further separated from the rubber fragments. The recycled steel fibers were manually cleaned to remove textiles and rubber before use in SIFCON fabrication. The collected steel fibers have irregular shapes. Figure 1 shows the steel fibers selected for testing from scrap tires. Table 6 presents the length and diameter of randomly selected scrap tire fibers.

Fig. 1. Scrap tire steel fibers

Table 6. Characteristics of scrap tire steel fibers

Fiber diameter (mm)	Fiber length (mm)	Aspect ratio (Average)	Fiber content by weight (%)
0.15 ± 0.01	26 ± 23	173	9.70
0.19 ± 0.01	13 ± 2	68	3.20
0.27 ± 0.02	37 ± 17	137	11.30
0.31 ± 0.01	45 ± 28	145	46.80
0.34 ± 0.01	30 ± 15	88	11.30
0.39 ± 0.03	46 ± 19	118	12.90
0.46 ± 0.01	68 ± 4	148	4.80

2.1.6.2 Commercial Steel Fibers

Additionally, the commercially available steel fibers used in the experimental work were round crimped steel fibers. The commercially available steel fibers selected for the study are displayed in Fig. 2. Table 7 displays the mechanical characteristics of the commercially available steel fibers.

Fig. 2. Commercially available steel fibers

Table 7. Mechanical characteristics of commercially available steel fibers

Fiber type	Crimped
Dia of fiber in mm	0.45
Length of fiber in mm	35
Aspect ratio of fiber (l/d)	77.77
Tensile Strength of fiber	1260 N/mm^2

2.2 Methodology

The concrete mix design for the M20 grade has been carried out in compliance with IS: 10262-2019 [30]. Table 8 lists the ingredient proportions used in M20 grade concrete. The cement utilized in the experiment underwent testing for multiple characteristics, such as consistency, fineness, specific gravity, and both initial as well as final setting times. In accordance with IS codes, tests were carried out on the aggregates for specific gravity, fineness modulus, bulk density, and water absorption. When choosing the chemical admixture and commercially available steel fibers for the study, data from the manufacturer was considered. The diameter, length, aspect ratio, and other properties of the steel fibers that were collected from the scrap tires used in the study were measured.

Table 8. Ingredients of M20 grade concrete mix

	Water	Cement	Aggregate	
			Fine	Coarse
Weight (kg)	160	320	667	1131
Volume (m^3)	0.50	1	2.08	3.53

As advised by EFNARC [31], a mini slump cone was used to conduct the flow test. The mini slump cone has internal dimensions of 70 mm at the top and 100 mm at the bottom, and it is 60 mm height. Figure 3 displays the apparatus used for flow testing in this investigation. After filling the mold with the SIFCON slurry and lifting it, the slurry mix's spread diameter was recorded. As per the guidelines specified in EFNARC [31], the slump flow was observed to be between 240 and 260 mm.

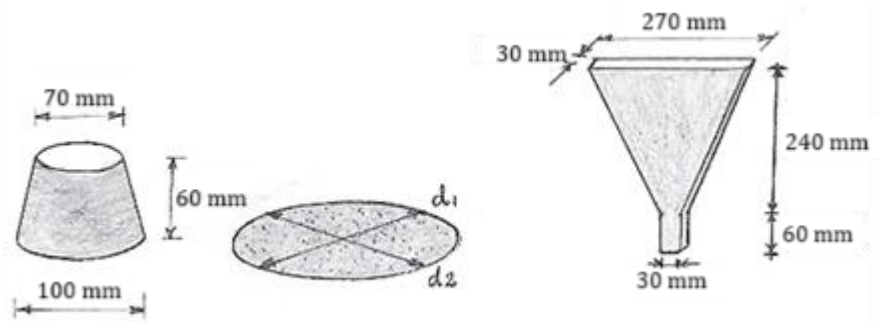

Fig. 3. Mini slump and V-funnel testing equipment

A mini-V-funnel test was also performed on the freshly prepared slurry mix of SIFCON. Figure 3 depicts the size and type of equipment used in this investigation. The test apparatus was filled with SIFCON slurry, and the amount of time needed to empty it was recorded. According to the requirements outlined in EFNARC [31], the test equipment had to be emptied between 7 and 11 seconds. As previously mentioned, fresh tests have been carried out with a 1:1 ratio of cement to fine aggregate. The water–cement ratio has been varied between 0.30 and 0.40 in 0.01 increments, as well as the superplasticizer between 0.50 and 2.00% by cement's weight in 0.1% increments. Figures 4 and 5 illustrate the steps for flow testing and the V-funnel test, respectively. The slurry mixes of SIFCON, with a 1:1 cement-to-sand ratio, was selected after extensive test trials, using a superplasticizer equal to 0.80% of the cement by weight and a water-to-cement ratio of 0.33. Table 9 gives the final proportion of the SIFCON slurry mix with the workability test results.

Table 9. Composition of SIFCON slurry mix

Cement	Fine Aggregate	Water to Cement ratio	Super plasticizer	Test results	
				Mini slump (mm)	Mini V-funnel (s)
1	1	0.33	0.80% of the cement weight	245	7.48

Upon finalizing SIFCON's slurry mix ratio, the production process is as follows: To make demolded specimens easier to remove, waste oil is applied to the molds used for specimen fabrication after the molds have been cleaned. Dry mixing must be done first using a 1:1 ratio of cement to fine aggregate. The dry mix must then be added with water and superplasticizer in accordance with the determined ratios. In order to ensure that the proper mixing of slurry mix, the entire slurry has to be mixed for at least two minutes.

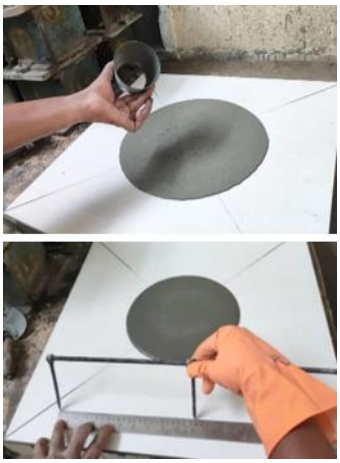

Fig. 4. Slump cone test

Fig. 5. V-funnel test

In order to ensure correct compaction and avoid honeycombing, the fibers in the molds are filled using a two-layer method. As a result, the initial layer of the mold is randomly hand-spread with 50% of the volume percentage of fibers. After the first layer is in place, the fiber bedding is filled with the produced SIFCON slurry mix and compacted using a table vibrator and hand tamping. Same procedure has been followed for second layer. The cast specimens remained at room temperature for a full day. The following day, the specimens are removed from their molds and subjected to the appropriate curing duration in a curing chamber. The irregular shapes and varying aspect ratios of the steel fibers from scrap tires, when randomly placed, caused difficulties in manufacturing specimens with a 6% fiber volume. Considering this, SIFCON specimens containing 7% steel fibers were produced using a three-layer technique, where they encountered difficulty in prepacking of final layer of fibers and compaction of the specimen. Figure 6 illustrates the steps in production of SIFCON specimens.

Fig. 6. Manufacturing of SIFCON

2.3 Compressive Strength Test

SIFCON cube specimens measuring 100x100x100mm, using different volume fractions of scrap tire steel fibers, commercially available steel fibers, and SIFCON reference specimens, were cast to determine compressive strength. SIFCON specimens contained fiber quantities of 314, 392.5, 471, and 549.5 kg/m^3, representing 4%, 5%, 6%, and 7% of volume of the concrete. However, M20 grade reference cube specimens were cast with a size of 150x150x150 mm. The specimen designations are shown in Table 10.

Table 10. Compressive strength specimen designations

Specimen	Size (mm)	Details of steel fiber		Quantity	Designation
		Source	Volume (%)		
M20 grade cube	150x150x150	----	----	9	RMCM20-1 to 9
SIFCON slurry cube	100x100x100	----	0	9	RMCF0-1 to 9
SIFCON cube	100x100x100	Steel fibers from scrap tires	4	9	S1CWF4-1 to 9
			5	9	S1CWF5-1 to 9
			6	9	S1CWF6-1 to 9
			7	9	S1CWF7-1 to 9
SIFCON cube	100x100x100	Commercially available steel fibers	4	9	S1CMF4-1 to 9
			5	9	S1CMF5-1 to 9
			6	9	S1CMF6-1 to 9
			7	9	S1CMF7-1 to 9

The specimen's compressive strength was tested with a universal testing machine. The test was conducted following the guidelines stipulated in IS: 516-1959 [32]. Figure 7 illustrates the arrangement for the compressive strength test. The specimens were tested after 3, 7, and 28 days of curing.

Fig. 7. Arrangement for compressive strength testing

2.4 Split Tensile Strength Test

SIFCON cylinders (100×200mm) were cast to assess split tensile strength. These specimens included various volume fractions of scrap tire steel fibers, commercially available steel fibers, and reference specimens. However, M20 grade reference cylinder specimens were cast with a size of 150mm in diameter and 300mm in height. Table 11 presents the specimen designations.

Table 11. Split tensile specimen designations

Type of specimen	Size (mm)	Details of steel fiber		Quantity	Designation
		Source	Volume (%)		
M20 grade cylinder	150 dia. & 300 high	----	----	9	RMCyM20-1 to 9
SIFCON slurry	100 dia. & 200 high	----	0	9	RMCyF0-1 to 9
SIFCON cylinder	100 dia. & 200 high	Steel fibers from scrap tires	4	9	S1CyWF4-1 to 9
			5	9	S1CyWF5-1 to 9
			6	9	S1CyWF6-1 to 9
			7	9	S1CyWF7-1 to 9
SIFCON cylinder	100 dia. & 200 high	Commercially available steel fibers	4	9	S1CyMF4-1 to 9
			5	9	S1CyMF5-1 to 9
			6	9	S1CyMF6-1 to 9
			7	9	S1CyMF7-1 to 9

The Specimens split tensile was tested with a universal testing machine. The test was conducted following the procedures stipulated in IS: 5816-1999 [33]. Figure 8 illustrates the setup for the split tensile strength test. Specimens were tested at 3, 7, and 28 days.

Fig. 8. Test setup of split tensile strength

2.5 Microstructural Analysis

This study analyzed the microstructural properties of SIFCON using XRD (X-Ray Diffraction) and SEM (Scanning Electron Microscopy) to understand its internal structure and characteristics. SIFCON with 6% scrap tire steel fibers was found to have enhanced mechanical properties. However, compaction was found to be challenging at this percentage of scrap tire steel fibers. Therefore, SEM and XRD analyses were conducted on SIFCON manufactured with 5% steel fibers from scrap tires. Further, SIFCON with 5% of commercially available steel fibers are also used for SEM and XRD. The samples were extracted from the tested specimens. Additionally, the analysis was carried out on reference samples for comparison.

3. Results and Discussion

3.1 Compressive Strength

Table 12 presents the compressive strength of SIFCON with different scrap tire steel fiber percentages, commercially available steel fibers, and reference specimens at 3, 7, and 28 days. Table 12 show compressive strengths of 16.69 and 36.46 N/mm^2 at 3 days, 22.12 and 41.54 N/mm^2 at 7 days, and 30.84 and 56.65 N/mm^2 at 28 days for the M20 mix and SIFCON slurry mix, respectively.

Table 12. Compressive strength of specimens

Sl. No	Type of Specimen	Steel Fibers		Specimen designation	Average Compressive strength (N/mm²)		
		Type	Percentage		3 days	7 days	28 days
1	M20 grade cube	----	----	RMCM20	16.69	22.12	30.84
2	SIFCON slurry cube	----	0	RM1CF0	36.46	41.54	56.65
3	SIFCON cube	Steel fibers from scrap tires	4	S1CWF4	39.97	44.84	59.60
4	SIFCON cube		5	S1CWF5	40.34	45.45	62.19
5	SIFCON cube		6	S1CWF6	42.86	46.15	63.36
6	SIFCON cube		7	S1CWF7	36.88	38.89	49.16
7	SIFCON cube	Commercially available steel fibers	4	S1CMF4	49.24	61.85	74.76
8	SIFCON cube		5	S1CMF5	49.76	68.60	81.13
9	SIFCON cube		6	S1CMF6	60.67	74.92	92.48
10	SIFCON cube		7	S1CMF7	59.09	73.33	86.50

Table 12 and Figure 9 present the 3-day compressive strengths of SIFCON containing 4% to 7% scrap tire steel fibers as 39.97, 40.34, 42.86, and 36.88 N/mm^2, respectively. These values are 139%, 142%, 157%, and 121% higher compared to the M20 mix, and 10%, 11%, 18%, and 1% higher compared to the SIFCON slurry mix. At 7 days, the corresponding values are 44.84, 45.45, 46.15, and 38.89 N/mm^2. These values are 103%, 105%, 109%, and 76% higher compared to the M20 mix, and 8%, 9%, 11%, and -6% higher compared to the SIFCON slurry mix. At 28 days, the compressive strengths for the same fiber percentages are 59.60, 62.19, 63.36, and 49.16 N/mm^2, respectively. These values are 93%, 102%, 105%, and 59% higher compared to the M20 mix, and 5%, 10%, 12%, and -13% higher compared to the SIFCON slurry mix.

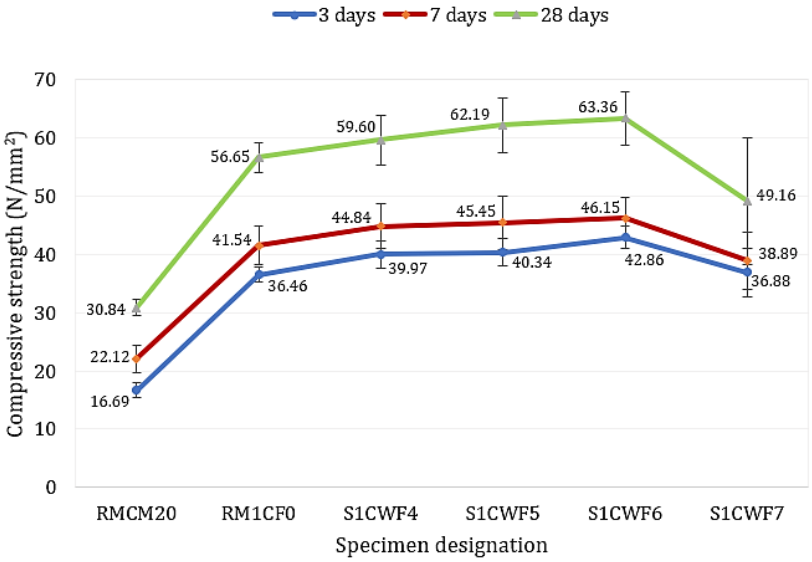

Fig. 9. Effect of scrap tire steel fiber content on compressive strength at 3, 7 and 28 days

According to Table 12 and Figure10, the 3-day compressive strength of SIFCON with 4% to 7% commercially available fibers is 49.24, 49.76, 60.67, and 59.09 N/mm^2, respectively. These values are 195%, 198%, 264%, and 254% higher compared to the M20 mix, and 35%, 36%, 66%, and 62% higher compared to the SIFCON slurry mix. At 7 days, the corresponding values are 61.85, 68.60, 74.92, and 73.33 N/mm^2. These values are 180%, 210%, 239%, and 232% higher compared to the M20 mix, and 49%, 65%, 80%, and 77% higher compared to the SIFCON slurry mix. Additionally, at 28 days, the compressive strengths for the same fiber percentages are 74.76, 81.13, 92.48, and 86.50 N/mm^2, respectively. These values are 142%, 163%, 200%, and 180% higher compared to the M20 mix, and 32%, 43%, 63%, and 53% higher compared to the SIFCON slurry mix.

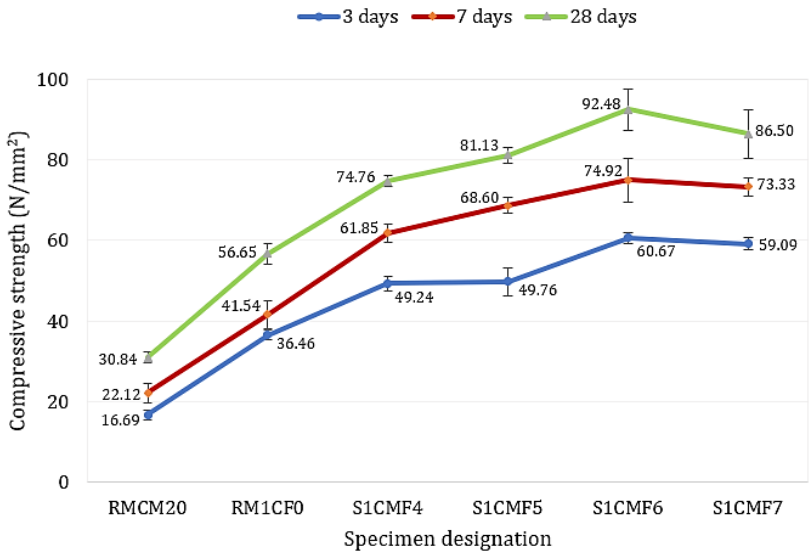

Fig. 10. Effect of commercial steel fiber content on compressive strength at 3, 7 and 28 days

Figure 11 shows the overall comparison of the compressive strengths of SIFCON and the reference mixes after curing periods of 3, 7, and 28 days. In summary, after 3 days of curing, increasing the amount of scrap tire and commercially available steel fibers in SIFCON from 4% to 7% resulted in a compressive strength improvement of up to 157% and 254% compared to M20 grade concrete, respectively. Additionally, the compressive strength increased by up to 18% and 66% compared to the SIFCON slurry mix, respectively. After 7 days of curing, increasing scrap tire and commercially available steel fibers in SIFCON from 4% to 7% boosted compressive strength by up to 109% and 239% over M20 grade concrete. Furthermore, the values increased by up to 11% and 77% compared to those of the SIFCON slurry mix, respectively.

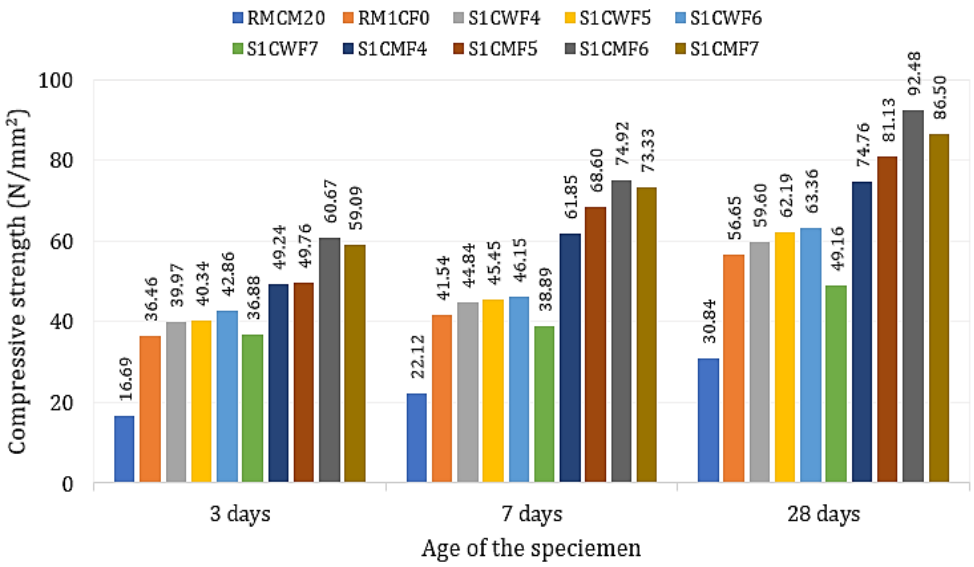

Fig. 11. Comparison of compressive strength between SIFCON and the reference mixes

After 28 days of curing, increasing the scrap tire and commercially available steel fibers in SIFCON from 4% to 7% boosted compressive strength by up to 105% and 200% over M20 grade concrete. Furthermore, the values increased by up to 12% and 63% compared to those of the SIFCON slurry mix, respectively. The results obtained were like those obtained in previous studies on SIFCON produced with waste steel fibers. SIFCON with 4% to 7% scrap tire steel fibers achieves 62% to 81%, 53% to 73%, and 57% to 80% of the compressive strength of SIFCON made with commercially available steel fibers at 3, 7, and 28 days, respectively.

These results are in good agreement with findings reported in previous studies on SIFCON incorporating waste steel fibers [23], where fiber inclusion was shown to substantially improve strength properties due to enhanced crack-bridging, improved fiber-matrix interaction, and increased energy dissipation. The current study further confirms that while scrap tire steel fibers are slightly less effective than their commercial counterparts, they still contribute significantly to compressive strength development. However, a limitation in the use of fiber volume was identified, as an increase beyond a certain point led to a reduction in strength. This aligns with the understanding that a higher fiber ratio can negatively impact mechanical properties by increasing void content [26]. This demonstrates the potential of using recycled fibers as a sustainable and cost-effective alternative without a substantial compromise in performance.

3.2 Split Tensile strength

Table 13 presents the split tensile strength of SIFCON with different scrap tire steel fiber percentages, commercially available steel fibers, and reference specimens at 3, 7, and 28 days.

Table 13. Split tensile strength of specimens

Sl. No	Type of Specimen	Steel Fibers		Specimen designation	Average Split tensile strength (N/mm²)		
		Type	Percentage		3 days	7 days	28 days
1	M20 grade cylinder	----	----	RMCyM20	1.61	2.12	2.71
2	SIFCON slurry cylinder	----	0	R1MCyF0	2.61	3.20	4.69
3	SIFCON cylinder	Steel fibers from scrap tires	4	S1CyWF4	2.88	3.84	4.96
4	SIFCON cylinder		5	S1CyWF5	3.23	4.08	5.98
5	SIFCON cylinder		6	S1CyWF6	4.49	4.80	7.88
6	SIFCON cylinder		7	S1CyWF7	4.55	5.82	7.29
7	SIFCON cylinder	Commercially available steel fibers	4	S1CyMF4	10.13	11.97	14.18
8	SIFCON cylinder		5	S1CyMF5	11.02	12.27	14.62
9	SIFCON cylinder		6	S1CyMF6	11.75	13.55	16.06
10	SIFCON cylinder		7	S1CyMF7	14.84	17.41	19.48

Table 13 show split tensile strengths of 1.61 and 2.61 N/mm^2 at 3 days, 2.12 and 3.20 N/mm^2 at 7 days, and 2.71 and 4.69 N/mm^2 at 28 days for the M20 mix and SIFCON slurry mix, respectively. Table 13 and Figure 12 show the 3-day split tensile strength of SIFCON with 4% to 7% scrap tire steel fibers as 2.88, 3.23, 4.49, and 4.55 N/mm^2, respectively. These values are 79%, 101%, 179%, and 183% higher compared to the M20 mix, and 10%, 24%, 72%, and 74% higher compared to the SIFCON slurry mix. At 7 days, the corresponding values are 3.84, 4.08, 4.80, and 5.82 N/mm^2. These values are 81%, 92%, 126%, and 175% higher compared to the M20 mix, and 20%, 28%, 50%, and 82% higher compared to the SIFCON slurry mix. At 28 days, the compressive strengths for the same fiber percentages are 4.96, 5.98, 7.88, and 7.29 N/mm^2, respectively. These values are 83%, 121%, 191%, and 169% higher compared to the M20 mix, and 6%, 28%, 68%, and 55% higher compared to the SIFCON slurry mix.

According to Table 13 and Figure 13, the 3-day compressive strength of SIFCON with 4% to 7% commercially available fibers is 10.13, 11.02, 11.75, and 14.84 N/mm^2, respectively. These values are 529%, 584%, 630%, and 822% higher compared to the M20 mix, and 288%, 322%, 350%, and 469% higher compared to the SIFCON slurry mix. At 7 days, the corresponding values are 11.97, 12.27, 13.55, and 17.41 N/mm^2. These values are 465%, 479%, 539%, and 721% higher compared to the M20 mix, and 274%, 283%, 323%, and 444% higher compared to the SIFCON slurry mix. Additionally, at 28 days, the compressive strengths for the same fiber percentages are 14.18, 14.62, 16.06, and 19.48 N/mm^2, respectively. These values are 423%, 439%, 493%, and 619% higher compared to the M20 mix, and 202%, 212%, 242%, and 315% higher compared to the SIFCON slurry mix.

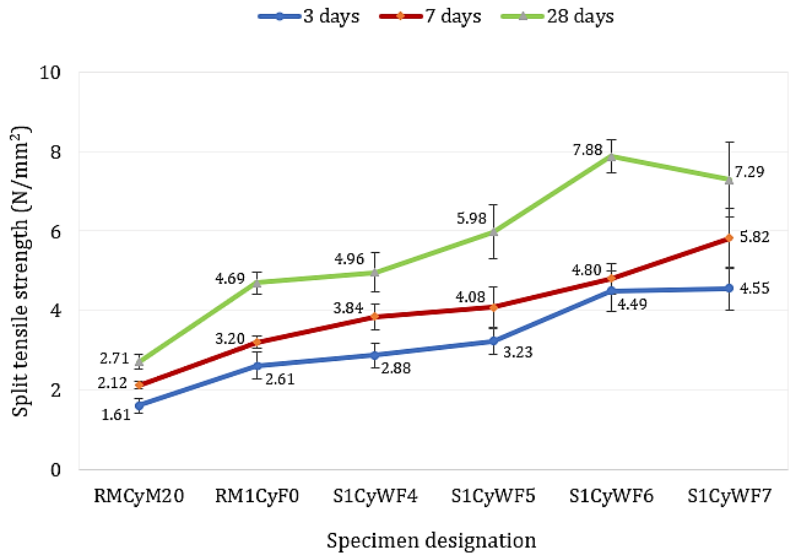

Fig. 12. Effect of scrap tire steel fiber content on split tensile strength at 3, 7 and 28 days

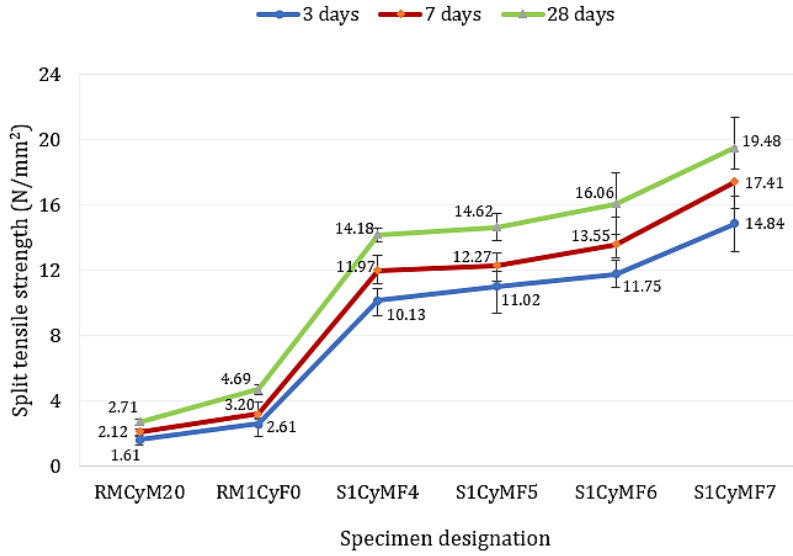

Fig. 13. Effect of commercial steel fiber content on split tensile strength at 3, 7 and 28 days

Figure 14 shows the overall comparison of the split tensile strengths of SIFCON and the reference mixes after curing periods of 3, 7, and 28 days. In summary, after 3 days of curing, increasing the amount of scrap tire and commercially available steel fibers in SIFCON from 4% to 7% boosted split tensile strength by up to 132% and 822%, respectively, compared to M20 grade concrete. Additionally, the values increased by up to 74% and 469% compared to the SIFCON slurry mix. After 7 days of curing, increasing scrap tire and commercially available steel fibers in SIFCON from 4% to 7% boosted split tensile strength by up to 175% and 721% over M20 grade concrete. Furthermore, the values increased by up to 82% and 444% compared to those of the SIFCON slurry mix, respectively. After 28 days of curing, increasing the scrap tire and commercially available steel fibers in SIFCON from 4% to 7% boosted split tensile strength by up to 191% and 619% over M20 grade concrete. Furthermore, the values increased by up to 68% and 315% compared to those of the SIFCON slurry mix, respectively. The results obtained were like those obtained in previous studies on SIFCON produced with commercial steel fibers. SIFCON with 4% to 7% scrap tire steel fibers achieves 28% to 38%, 32% to 35%, and 35% to 49% of the split tensile strength of SIFCON made with commercially available steel fibers at 3, 7, and 28 days, respectively.

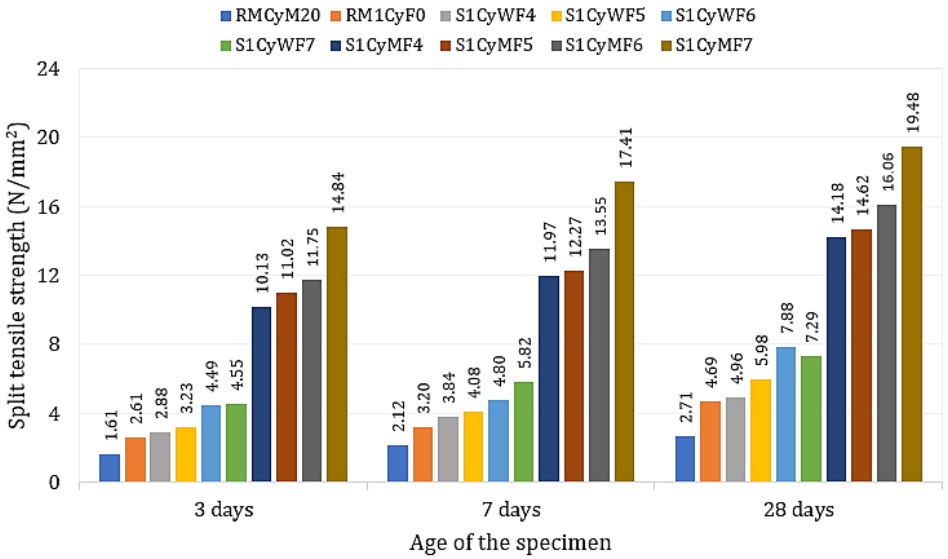

Fig. 14. Comparison of split tensile strength of SIFCON and reference mixes

These findings are consistent with previous studies on SIFCON produced using commercial steel fibers [23], which also reported significant improvements in tensile performance due to the bridging action of fibers and their ability to control crack propagation. The present study further reveals that although scrap tire steel fibers yield comparatively lower tensile strength than commercial fibers, they still contribute substantially to enhancing the performance of SIFCON. However, the fiber length of scrap tire steel fibers has been found to influence performance, aligning with the understanding that optimizing recycled steel fiber content for any mix requires careful consideration of dimensional factors, particularly fiber length [35]. These results support the viability of using recycled steel fibers as a sustainable reinforcement alternative, particularly where moderate tensile strength is acceptable.

3.3 Microstructural Analysis

Microstructural analysis was conducted on samples taken from specimens fractured during compression and split tensile testing. The microstructural analysis examined the Interfacial Transition Zone (ITZ) between the steel fibers and the cement paste to assess its hydration behavior [34]. The microscopic analysis of the specimens at 28 days was conducted at magnifications ranging from 2 to 500 µm. Samples of SIFCON containing 5% steel fibers from scrap tires, commercially available steel fibers, and reference mixes were used for SEM and XRD analyses. The results of XRD and SEM analyses are presented in Figures 15–19.

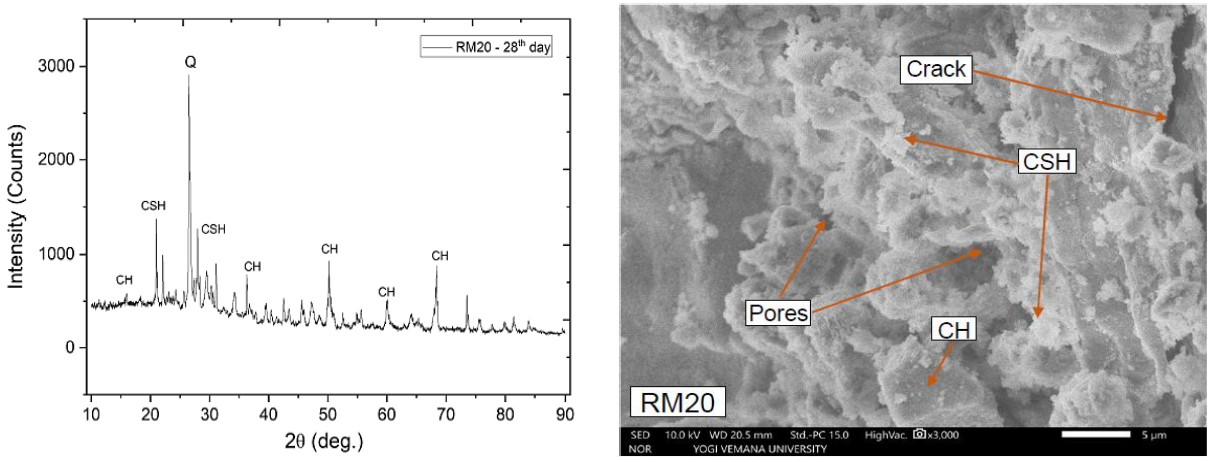

(a) (b)

Fig. 15. Images of reference M20 mix (RM20) (a) XRD (b) SEM

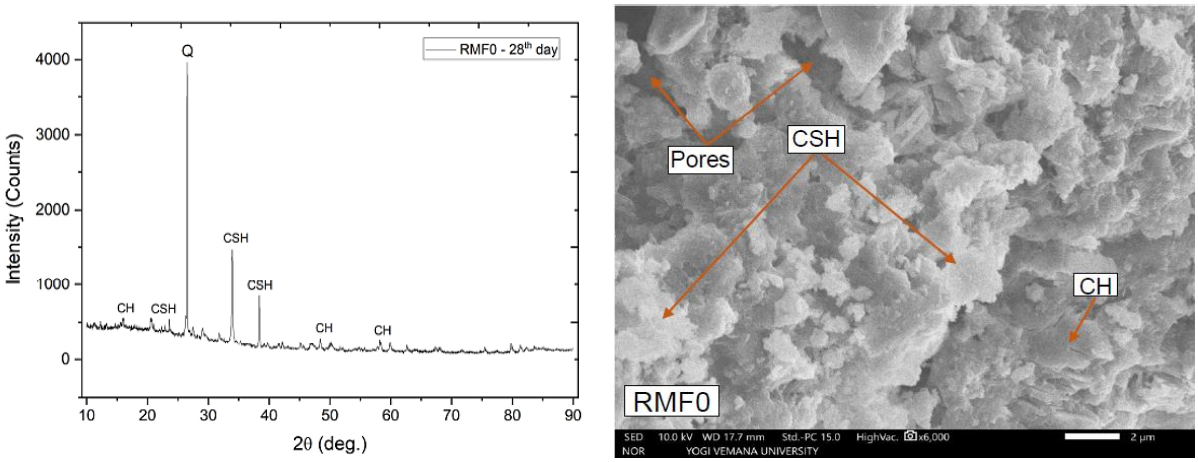

(a) (b)

Fig. 16. Images of reference SIFCON mix with 0% fibers (RMF0) (a) XRD (b) SEM

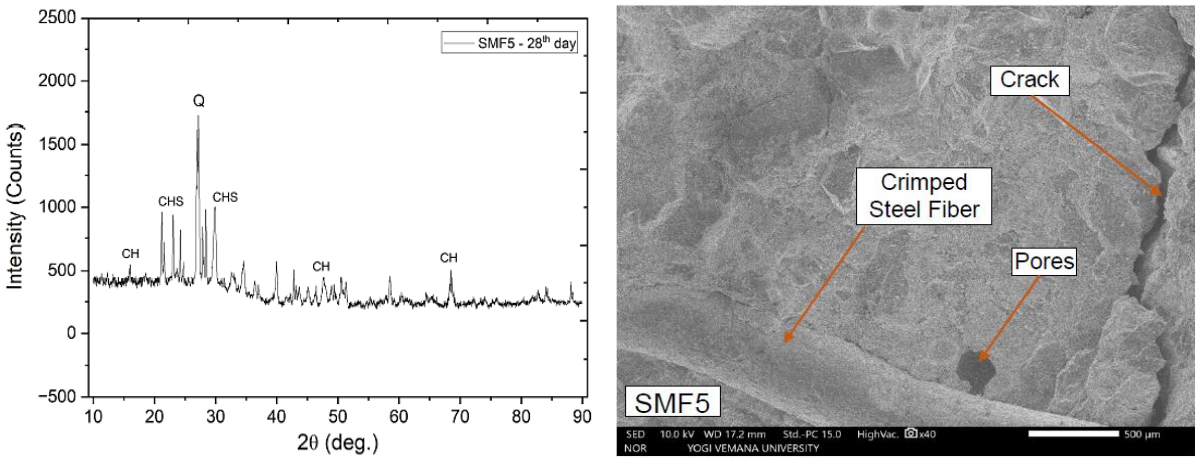

(a) (b)

Fig. 17. Images of SIFCON with 5% commercial steel fibers (SMF5) (a) XRD (b) SEM

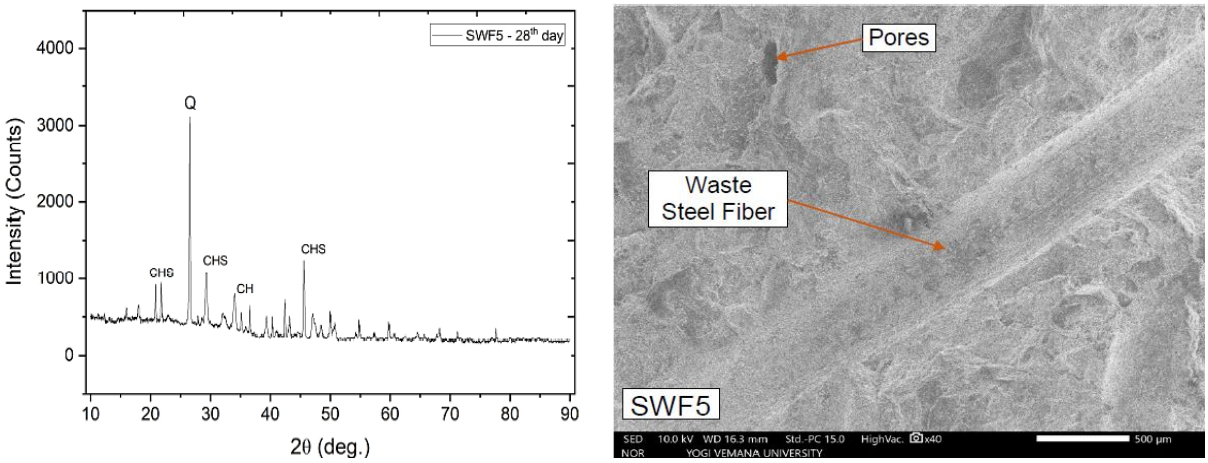

(a) (b)

Fig. 18. Images of SIFCON with 5% scrap tire steel fibers (SWF5) (a) XRD (b) SEM

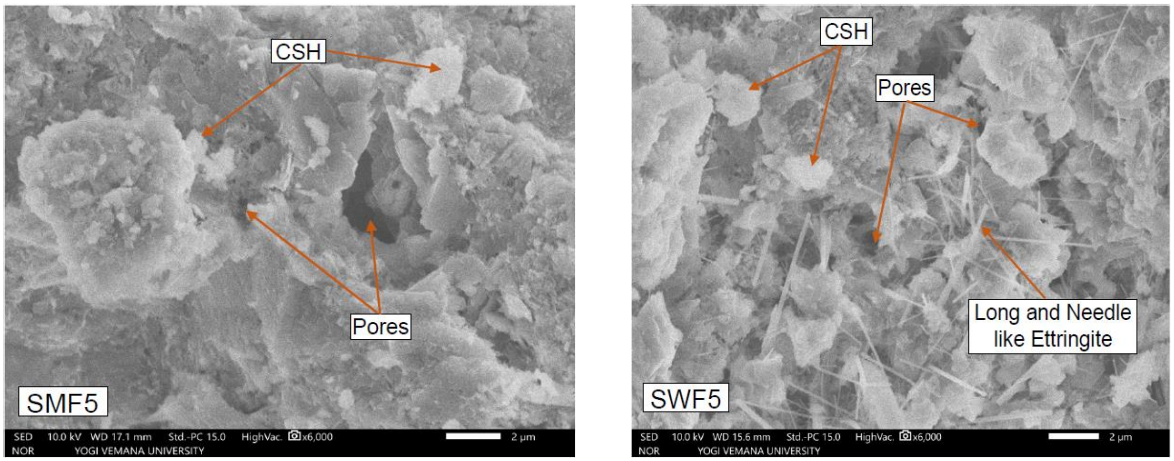

(a) (b)

Fig. 19. SEM images of SIFCON with 5% commercial and scrap tire steel fibers (a) SMF5 (b) SWF5

Figures 15(a)–18(a) illustrate the XRD analysis results for angles between 10° and 90°, demonstrating the presence of several hydrated phases, such as Calcium Silicate Hydrate (CSH), ettringite, and calcium hydroxide (CH). The major crystalline peaks observed represent the CSH phase, while ettringite appears with a lower peak. Figures 15(b)–18(b) and 19 depict bands of Calcium Silicate Hydrate (CSH), unreacted amorphous calcium hydroxide, and needle-shaped ettringite resulting from the hydration process.

4 Conclusions

Based on the evaluation of compressive and split tensile strengths of SIFCON reinforced with scrap tire and commercially available steel fibers, the following conclusions are drawn.

- The study shows that adding 4% to 7% of scrap tire and commercially available steel fibers significantly improves SIFCON's compressive strength at curing ages of 7, 14, and 28 days, with optimal performance observed at 6% fiber content. A slight drop at 7% is attributed to reduced workability of the mix and fiber clustering. SIFCON with both fiber types outperformed M20 concrete and plain SIFCON, emphasizing the importance of fiber content. While SIFCON with commercial steel fibers delivered higher strength, SIFCON with scrap tire steel fibers achieved 57–81% of that performance, demonstrating its potential as a sustainable and cost-effective alternative.
- Similarly, split tensile strength improved significantly with both scrap tire and commercially available steel fibers, steadily increasing from 4% to 7% fiber content across all curing ages. Commercial steel fibers provided the highest gains, but scrap tire steel fibers still outperformed M20 concrete and plain SIFCON, achieving 28–49% of the strength of commercial steel fibers. Nevertheless, they delivered significant improvements over M20 concrete and plain SIFCON, while serving as an eco-friendly and sustainable reinforcement alternative.
- SEM and XRD analyses revealed effective hydration and microstructural development in the Interfacial Transition Zone (ITZ) of SIFCON with both scrap tire and commercial steel fibers. The detection of C-S-H, ettringite, and unreacted CH at 28 days indicates continued hydration and strong fiber–matrix integration, aligning with the observed mechanical performance.
- This study highlights the effectiveness of recycled steel fibers, particularly from scrap tires, as a sustainable alternative to commercial steel fibers in SIFCON. Despite their irregular geometry, scrap tire steel fibers significantly enhanced compressive and split tensile strengths. Using up to 6% fiber content with a two-layer casting method yielded performance comparable to commercial fibers. These results demonstrate the potential of optimized scrap

tire fiber use as a cost-effective and eco-friendly reinforcement strategy for sustainable construction.

This study confirms that adding 4–7% steel fibers, especially 6%, significantly improves SIFCON's mechanical performance. Scrap tire fibers achieved up to 81% of the strength of commercial fibers and enhanced both compressive and tensile strengths, despite minor workability issues at higher doses. Microstructural analysis showed strong fiber–matrix bonding, highlighting recycled fibers as a viable, sustainable alternative for construction.

Acknowledgement

The authors thank Mr. K Naveen, Mr. G Malla Reddy and Ms. M Priyanka of S V University, Tirupati for their help in conducting the experiments. We also thank XRD and SEM Lab technicians of Physics department, Yogi Vemana University, Kadapa, Andhra Pradesh for conducting XRD and SEM analysis of the samples prepared for this study.

References

[1] UNEP. Revised technical guidelines for the environmentally sound management of used and waste pneumatic tyres, revised final version, Geneva, 2013:58p, UNEP/SBC/2013/2.
[2] Council of the European Union. Council Directive 1999/31/EC of 26 April 1999 on the landfill of waste, Official Journal of the European Union, 1999:182, Volume 42, 16 July 1999.
[3] NYSDEC. Waste Tire Management and Recycling Act, 2004:(518), 457-6400.
[4] Evans A, Evans E. Composition of a tyre: typical components, The Waste & Resources Action Programme, Banbury, 2006:5.
[5] Wojtowicz MA, Serio MA. Pyrolysis of scrap tires: can it be profitable?. Chemtech. 2006;48–53.
[6] Rani S, Agnihotri R. Recycling of scrap tyres. International Journal of Materials Science and Applications. 2014;3(5):164-167. https://doi.org/10.11648/j.ijmsa.20140305.16
[7] Vijay Babu K, Mallika Chowdary CH, Lingeshwaran N, Siva Kishore I. Structural application of fiber reinforced concrete. Research on Engineering Structures and Materials. 2024;x(x):1-34. http://dx.doi.org/10.17515/resm2024.305st0531rs
[8] Ojha PN, Singh A, Singh B, Patel V. Mechanical and durability properties of cement mortar and concrete reinforced with glass micro fibre. Res. Eng. Struct. Mater. 2022;8(2):265-281. http://dx.doi.org/10.17515/resm2021.350ma1007
[9] ACI Committee 544. ACI PRC-544.1R-96:Report on Fiber Reinforced Concrete. American Concrete Institute, 2002:66p, ISBN 9780870315282.
[10] Bentur A, Mindess S. Engineering & Technology. Fibre Reinforced Cementitious Composites, 2nd Edition, London, 2006:624, ISBN 9780429177293. https://doi.org/10.1201/9781482267747
[11] Tlemat H. Steel fibre from waste tyres to concrete; testing, modeling and design, PhD Thesis, University of Sheffield, South Yorkshire, England, 1-215, 2004.
[12] Zamanzadeh Z. Cement based materials reinforced with recycled steel fibres: mechanical, durability and structural performance, PhD Thesis, University of Minho, Portugal, 1-224, 2017.
[13] Drdlova M, Prachar V. The static and dynamic properties of slurry infiltrated fibre concrete with waste steel fibres from tires. International Journal of Structural and Civil Engineering Research. 2018;7(1):46–50. https://doi.org/10.18178/ijscer.7.1.46-50
[14] Lourenco L, Zamanzadeh Z, Barros JAO, Rezazadeh M. Shear strengthening of RC beams with thin panels of mortar reinforced with recycled steel fibres. Journal of Cleaner Production. 2018;194:112–126. https://doi.org/10.1016/j.jclepro.2018.05.096
[15] Drdlova M, Svitak O, Bibora P, Popovic M, Cechmanek R. Blast Resistance of Slurry Infiltrated Fibre Concrete with Waste Steel Fibres from Tires. MATEC Web of Conferences 149, 01060, 2018. https://doi.org/10.1051/matecconf/201814901060
[16] Sonone RG, Sharma S, Sharma HK. SIFCON-A High Performance Concrete - Experimental Investigations. International Journal of Innovative Technology and Exploring Engineering. 2020;10(2):109-112. https://doi.org/10.35940/ijitee.B8284.1210220
[17] Sampath P, Asha P. Strength and Durability Properties of SIFCON with Silica Fume and Waste Binding Wire. International Journal of Engineering and Advanced Technology. 2019;8(3S):917-923.
[18] Al-wahab Ali MA, Salih SA, Frayyeh QJ. Study the behaviour of Slurry infiltrated fibrous concrete (SIFCON) under impact loading, IOP Conf. Series: Materials Science and Engineering, 1-9, 2020. https://doi.org/10.1088/1757-899X/737/1/012069
[19] Abd-Ali MS, Essa AAA. Mechanical Properties of Slurry Infiltrated Fibrous Concrete (SIFCON) with Variation Steel Fiber Ratios and Silica Fume. Jour of Adv Research in Dynamical & Control Systems. 2019;11(01):1863-1872.

[20] Bajpai A, Chandak R. Experimental Studies on Slurry Infiltrated Fibrous Concrete (SIFCON). International Journal for Technological Research in Engineering. 2018;5(6):3180-3183.
[21] Vijayakumar M, Dinesh Kumar P. Study on Strength Properties of SIFCON. International Research Journal of Engineering and Technology. 2017;04(01):235-238.
[22] Sudarsana Rao H, Ramana NV, Gnaneswar K. Behaviour of restrained SIFCON two-way slabs part 1: flexure. Asian journal of civil engineering (building and housing). 2009;10(4):427-449.
[23] Ozkan Sengul. Mechanical properties of slurry infiltrated fiber concrete produced with waste steel fibers. Construction and Building Materials. 2018;186:1082-1091. https://doi.org/10.1016/j.conbuildmat.2018.08.042
[24] Renuka J, Rajasekhar K. Performance of Slurry Infiltrated Fibrous Concrete - A Comprehensive Review. Journal of Engineering Science and Technology Review. 2021;14(5):163-172. https://doi.org/10.25103/jestr.145.19
[25] Ravi Prasad Penda, Ramana Reddy IV. Experimental study on flexural strength of slurry infiltrated fibrous concrete (SIFCON) produced with various percentages of waste steel fibers recovered from used tires. E3S Web of Conferences, 529, 01026, 2024. https://doi.org/10.1051/e3sconf/202452901026
[26] Sindhu Nachiar S et al. Effect of steel fiber in SIFCON using GGBS as binder replacement. Materials Today: Proceedings. 2023;93:1-8. https://doi.org/10.1016/j.matpr.2023.07.281
[27] Asad Zia et al. Long-term performance of concrete reinforced with scrap tire steel fibers in hybrid and non-hybrid forms: Experimental behavior and practical applications. Construction and Building Materials. 2023;409:134011. https://doi.org/10.1016/j.conbuildmat.2023.134011
[28] Muhammad Nasir Amin et al. Application of waste recycle tire steel fibers as a construction material in concrete. Reviews on Advanced Materials Science. 2023;62:20220319. https://doi.org/10.1515/rams-2022-0319
[29] IS 8112: 2013, Ordinary Portland Cement, 43 grade-specification. Bureau of Indian Standards, New Delhi.
[30] IS 10262: 2019, Concrete Mix Proportioning-Guidelines. Bureau of Indian Standards, New Delhi.
[31] EFNARC 2005, Specification and guidelines for self-compacting concrete, European Federation for Specialist Construction Chemicals and Concrete Systems. Norfolk, UK.
[32] IS 516: 1959, Methods of test for strength of concrete. Bureau of Indian Standards, New Delhi.
[33] IS 5816: 1999, Splitting tensile strength of concrete – Method of test. Bureau of Indian Standards, New Delhi.
[34] Monteiro PJM, Mehta PK. Concrete: Microstructure, Properties and Materials, 3rd edition, Mc Graw Hill, 2006:ISBN 0071462899.
[35] Asad Zia et al. A Comprehensive Review of Incorporating Steel Fibers of Waste Tires in Cement Composites and Its Applications. Materials. 2022;15:7420. https://doi.org/10.3390/ma15217420
[36] IS 383: 1970, Specification for coarse and fine aggregates from natural sources for concrete. Bureau of Indian Standards, New Delhi.
[37] IS 2386 (P-III): 1963, Methods of test for Aggregates for concrete, Part-III specific gravity, density, voids, absorption and bulking. Bureau of Indian Standards, New Delhi.
[38] IS 456: 2000, Code of Practice for Plain and Reinforced Concrete. Bureau of Indian Standards, New Delhi.

Research on Engineering Structures & Materials
www.jresm.org
Research Group

Research Article

Physico-chemical characterization of fine gray clay with micrometric particle size

Yasser Oueld El Haj El Ghali [*,a], Abou-Bakr Cherki [b], Chouaib Benqlilou [c], Mohammed Khalil El Kouifat [d]

Higher National School of Mines of Rabat (ENSMR), Morocco

Article Info

Article History:

Received 06 Mar 2025

Accepted 13 May 2025

Keywords:

Clays;
Mechanical characterization;
Thermal characterization;
TGA;
DTA;
Hot plane method

Abstract

Clays are an interesting material used in several areas because of their abundance and natural ecological properties. Clay can be a building material either with rammed raw earth or fired clay bricks, also, it is used for the production of ceramics and pottery. In addition to that, absorbent clays are employed in soil remediation and water filtration, without forgetting the benefits of clays in health and wellness which allows them to be used in cosmetics, skincare, and hair products. In this study, thermophysical properties of a gray clay from the Gharb region of Morocco were investigated, to exploit its main assets and try to improve its weaknesses and limitations, so that this clay can be useful in different domains. Thus, this investigation will allow to control and to enhance this clay's properties to be used in different sectors in an optimal way. This clay is a very fine material, mainly composed of quartz, showing a thermal stability around 900°C and good mechanical strengths. In addition to that, this material has a thermal conductivity of 0.62 W $m^{-1}K^{-1}$ which proves that it is a good insulator.

© 2025 MIM Research Group. All rights reserved.

1. Introduction

Clay-based materials are used in different domains. Pottery production depend mainly on clay composition and its source of extraction [1-3], also since unsafe drinking water alone can cause many different illnesses, one of which is diarrhea and The World Health Organization (WHO) estimated that approximately 9.1% of the global burden of disease and 6.3% of all deaths worldwide could be prevented by improving water, sanitation and hygiene[4], it is important to consider nano clays as a natural solution for water treatment because of its effectiveness against contaminants and bacteria[5].

In addition to that, clay is introduced as an ecological material to minimize the use of concrete and reduce the embodied energy of the construction sector. Since clay was the most used across centuries, it was the main subject of numerous studies. Souileh et al. [6] investigated shale clay from Settat-Khouribga for potential civil engineering use. El Azhari et al. examined and compared the thermal performances of three types of unfired clay bricks from three different regions of Morocco [7] And also studied the influence of unfired clay use on the energy efficiency of buildings in south Morocco [8]. A similar study by Fgaier et al. [9] investigated the thermal behavior of North France's unfired clay bricks and examined the indoor temperature inside a building under real-life conditions. Atbir et al. [10] investigated natural white and red clay coming from the middle Atlas of Morocco and characterized this material mechanically and thermally. They also enhanced their properties and texture by adding sheep wool as ecological animal fibers. Generally, clay is incorporated with ecological

*Corresponding author: yasser.oueldelhajelghali@enim.ac.ma
[a]orcid.org/0009-0000-6994-1827; [b]orcid.org/0000-0002-2873-2727; [c]orcid.org/ 0000-0002-9303-6891;
[d]orcid.org/0000-0002-7130-6053
DOI: http://dx.doi.org/10.17515/resm2025-725ma0306rs

additives to enhance not only its thermal and acoustic properties but also its positive environmental impact, for example, grapevine shoots, psyllium seeds, rice husk, wood waste, granular cork [11-15]. However, mechanical strength is usually weakened, consequently, cement and lime can be added to restore them. El Wardi et al. [16] also enhanced Clayey soil from the Bensmim Region of Morocco with cork, which has caused a deterioration of mechanical properties. However, they created a sandwich material using cement mortar and plaster coating layers to improve thermal and mechanical properties, which has led to an ecological brick for construction. Moreover, Mountoumnjou et al. [17] proposed new low-cost ceramic microfiltration membranes composed of Kaolin, Bentonite, and limestone for bacteria removal, and Kassa et al. [18] conducted a series of cone index tests on clay treated with waste-based stabilizers to investigate the strength development based on their water absorption and retention capacities. This paper studies the thermophysical properties of local clay coming from the Gharb region of Morocco, with the perspective of identifying qualities to exploit and flaws to improve, therefore the various results of this study will provide insights into this clay's thermal insulation, ceramic manufacturing and sustainable construction with the aim to contribute to the development of optimized clay-based materials for various industrial applications, such as construction, water filtration and purification, pottery and production of ceramics.

2. Materials and Methods

2.1. Clay Material

The clay used for this study is gray clay taken from Khenichet, a small village in the Gharb region of Morocco (Figure 1). Knowing that many houses in this location were built using the rammed earth technique mixing this clayey soil with straw fibers.

Fig. 1. Khenichet - Sidi Kacem – Morocco

Fig. 2. Clay raw material

These houses prompted us to characterize this material and identify its thermal, mechanical, and chemical properties. This clay was collected in large quantities to realize different tests. The soil is rinsed with tap water and passed through a 100 µm sieve. Afterward, it is placed in a container and left in an oven at 105 °C until its mass becomes constant. The next step involves manually grinding the clay to reduce it to powder form ready for use (Figure 2).

Characterization Methods

2.2.1 X-Ray Diffraction

To determine the chemical composition of Khnichet's clay, a test of X-Ray Diffraction was performed. The PANalytical EMPYREAN diffractometer was used with a Copper (Cu) anode as a radiation source and wavelengths k- α1 (1,54060˚A) and K- α2 (1,54443˚A). It is a high-resolution test with a step size of 0.066 °2θ and a counting time per step of 113,2 seconds with a goniometer setup of a 240 mm radius and a divergence slit of 0.2177° width. The measurement was conducted in air at an ambient temperature of 25°C.

2.2.2 Particle Size Analysis

The particle size analysis was realized based on the sedimentometry method since the sieve analysis and the air separation method were inefficient and unable to differentiate between the small particles of this material. How- ever, the sedimentometry method can distinguish between particles with a diameter smaller than 80 µm. This test was performed following the specifications of the NF P94-057 standard. An 82,2g sample of Khenichet's clay was mixed with 440,2ml of distilled water, followed by the addition of 60 ml of a 5% sodium hexametaphosphate (SHMP) deflocculant solution. A mechanical stirrer mixes the whole mixture and the sedimentation speed determines the particle size.

2.2.3 Atterberg Limits

The Atterberg limits are conventional constants that define the threshold between:

- The transition of the soil from a liquid state to a plastic state (liquid limit: Wl)
- The transition of the soil from a plastic state to a solid state (plastic limit: Wp)

The value of these limits is the soil's water content at the considered transitional state, expressed as a percentage of the dry weight of the material. Therefore, the plasticity index Ip is defined, describing the range of plasticity being the difference between the two limits, Ip = Wl −Wp. The liquid limit is determined using the Casagrande device, while the plastic limit is identified using 3 mm diameter rolls.

2.2.4 Thermogravimetric Analysis and Differential Thermal Analysis

Differential Thermal Analysis (DTA) and Thermogravimetric Analysis (TGA) are the most commonly used techniques for studying the transformations that occur with energy consumption or release, whether or not associated with a loss of mass. DTA enables the identification of endothermic, exothermic, and invariant phenomena by measuring the temperature difference between the sample and a reference material over time or as a function of the sample's temperature, all under a controlled atmosphere. On the other hand, TGA permits tracking mass variations during heat treatment. It is useful for studying reactions involving volatilization, fixation of certain constituents, or interaction with a gas phase. The information obtained from TGA is mostly complementary to that of the DTA, and both tests were performed in N_2 atmosphere.

2.2.5 Mechanical Characterization

Compression strength is the most important characteristics of mechanical properties in the building sector. The uniaxial compression test for compression strength were conducted according to the standard EN 196-1 using a CONTROLS PILOT COMPACT-Line presented in Figure 3.

Fig. 3. Controls Pilot Compact-Line for compression strengths

2.2.6 Thermal Characterization

Thermal conductivity, thermal effusivity, and thermal capacity were analyzed for thermal characterization. The asymmetric hot plane method in steady-state was used to determine thermal conductivity [19], in fact, an experimental setup is constructed (Figure 4), consisting of a 40 Ω electric resistor powered by a 6V voltage, positioned beneath the sample, and on top of a 1 cm layer of polyethylene insulating foam. This assembly is placed between two 5 cm thick aluminum blocks. K-type thermocouples are strategically placed between the heating resistor and the insulating foam, between the foam and the lower aluminum block, and between the sample and the upper aluminum block. The thermocouple signals are captured using a data acquisition system and the temperature values in the steady-state permit a direct calculation of thermal conductivity.

Fig. 4. The asymmetric hot plane method in steady-state device

Fig. 5. The hot plane method in the transient regime

On the other hand, the hot plane method in the transient regime was for thermal effusivity and thermal capacity analysis (Figure 5) [19], where the electric resistor and the sample are positioned between two 5 cm thick polyurethane foam blocks, with the entire assembly placed between two 5 cm thick aluminum blocks.

A single thermocouple is situated between the resistor and the bottom layer of insulating foam. Temperature values were recorded using the data acquisition system, until stabilization is achieved after 45 minutes. During this transient phase, we analyze the change in temperature difference from the initial value in order to generate the experimental temperature thermogram. Subsequently, we determine the parameters that minimize the quadratic error between this experimental profile and the theoretical model of the hot plate method using a

MATLAB code of the Marquardt-Levenberg algorithm, which gives an estimated thermal effusivity and thermal capacity values.

2.3 Sample Preparation and Shrinkage Study

After getting the clay ready to use, mechanical and thermal samples are prepared by mixing it with water. This mixture appears to shrink more by increasing the water volume as shown in Figure 6. Making 256 cm³ samples by varying the water-clay ratio from 0,3 to 0,8 and letting them dry for 20 days at ambient temperature has caused a considerable volume diminution. The ratio of 0,3 reduced the original volume by 23,5% and the 0,8 ratio has caused a diminution of 59,4% as illustrated in Figure 7.

Fig. 6. Illustration of clay shrinkage

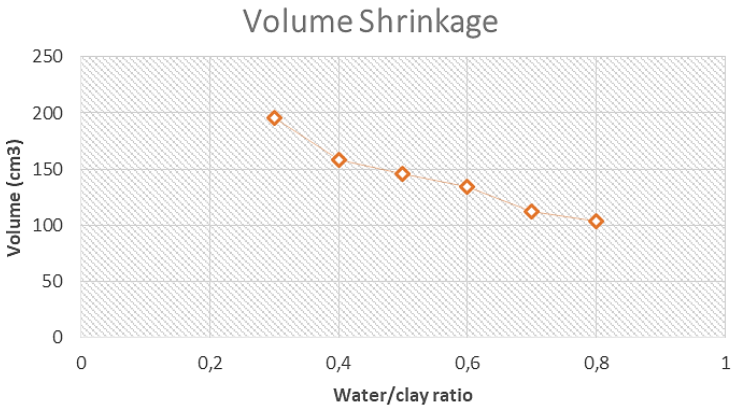

Fig. 7. Volume shrinkage as a function of water-clay ratio

The choice of water-clay ratio should minimize the shrinkage but also have a good texture and excellent workability, which leads us to the water-clay ratio of 0,5 since 0,3 and 0,4 didn't have a good texture and didn't take the shape of the molds. Therefore, 3 samples of 4×4×16 cm³ for mechanical tests (Figure 8) and 3 samples of 10×10×3 cm³ for thermal characterization (Figure 9) were made by mixing clay and water with a ratio of 0,5. Concerning the drying process, the samples were dried at ambient temperature for 10 days, and after unmolding the samples they were put in an oven at 40 °C for 24 hours. The mean density value of this material obtained from three samples is given in Table 1.

Fig. 8. Mechanical test samples

Fig. 9. Thermal test samples

Table 1. Density results

Sample	Clay	Relative error (%)
1	1,838	1,23
2	1,772	2,35
3	1,835	1,12
Mean Density Value ($g.cm^{-3}$)	1,815	

3. Results and Discussions

3.1 X-Ray Diffraction

The analysis of our material X-Ray diffraction pattern has given the results shown in Figure 10. There are four major spectra whose intensities are high and they present Quartz (SiO_2), Calcite ($Ca(CO_3)$), Muscovite ($KAl_2Si_3AlO_{10}(OH)_2$) and Kaolinite($Al_2Si_2O_5(OH)_4$). The percentages of these components according to XRD diffractograms are displayed in Table 2.

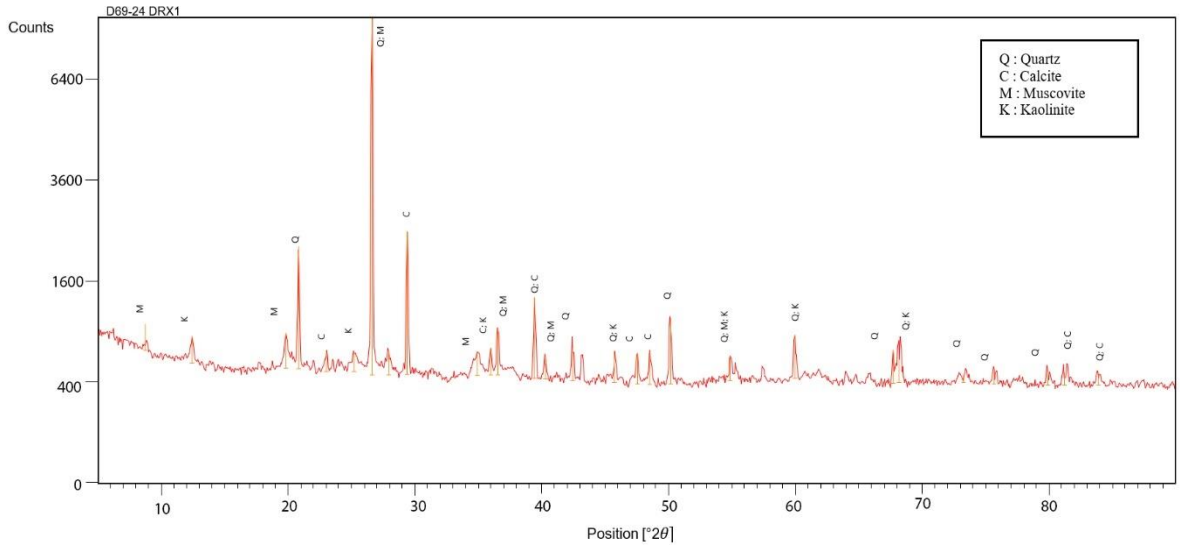

Fig. 10. X - Ray Diffraction pattern of Khenichet's clay

Table 2. Percentages of Khenichet's clay main components

Compound name	ICDD	Score	Scale factor	Chemical formula	Percentage (%)
Quartz	01-085-1054	76	0,986	SiO_2	74,936
Calcite	01-083-0578	57	0,300	$Ca(CO_3)$	17,1
Muscovite	00-007-0025	38	0,049	$KAl_2Si_3AlO_{10}(OH)_2$	1,862
Kaolinite	00-029-1488	31	0,025	$Al_2Si_2O_5(OH)_4$	0,775

This composition allows us to judge that this clay has a good compression strength since quartz is the most dominant component. Also, the high percentage of calcite proves a good resistance to high temperatures. Additionally, the low percentages of muscovite and kaolinite indicate that this clay should be enhanced with other materials to be used in pottery.

3.1 Particle Size Analysis

The Sedimentation method provided us with the granulometric curve shown in Figure 11. This curve, which resembles those of fine-grained materials, proves that this soil have micrometric-sized particle since more than 50% of the particle diameter does not exceed 20 µm and the biggest diameter of this material particle is 50 µm. Its fineness allows it to be a binder that can be mixed with other additives (palm seeds, hemp wool, bamboo fibers, wood waste...[14, 20, 21, 22] or a material useful for water filtration and purification at least from the big micrometric contaminants.

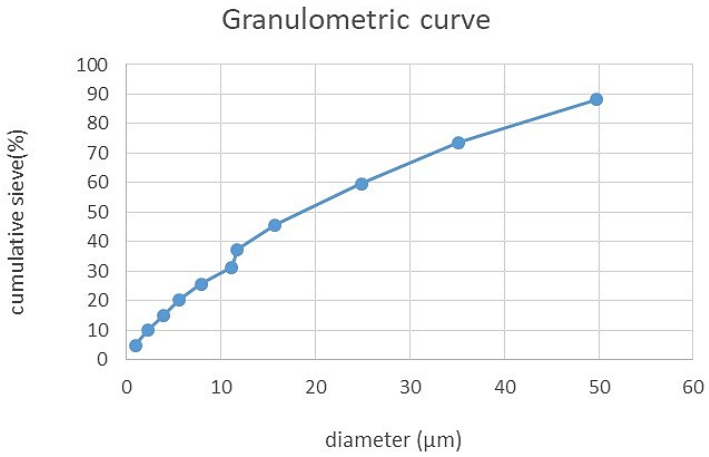

Fig. 11. Particle size analysis

3.2 Atterberg Limits

The plasticity analysis provided the Table 3 giving liquidity limit, plasticity limit, and plasticity index values. According to the Casagrande diagram (Figure 12), these values classify Khenichet's clay among materials of medium plasticity, which confirms that this clay should be enhanced by more kaolinite to be used in pottery.

Table 3. Atterberg limits results

Liquidity limit W_L (%)	Plasticity limit W_P (%)	Plasticity index I_P (%)
43.5	24.13	19.36

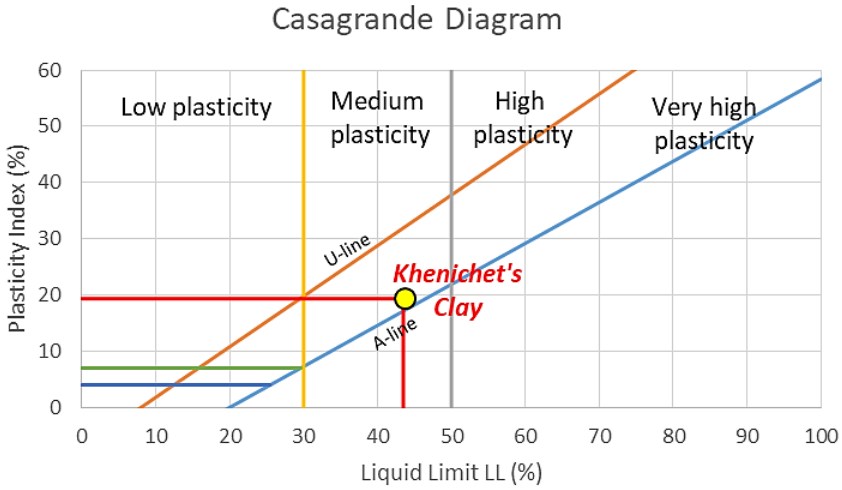

Fig. 12. Casagrande diagram for soil classification

3.3 Differential Thermal Analysis and Thermogravimetric Analysis

The behavior of Khenichet's clay after its exposure to temperature variation from ambient temperature to 1100°C is expressed in Figure 13.

The analysis of the analytical curves shows different zones:

- Zone 1: Around 100 °C, a first endothermic phenomenon is observed, coupled with a mass loss of approximately 1%, related to the release of physiosorbed water [23]

$$2\,FeOOH(s) \rightarrow Fe_2O_3(s) + H_2O\,(g) \quad (1)$$

- Zone 2: Between 300 °C and 480 °C, a second endothermic peak is observed, corresponding to the transformation of goethite into hematite, according to reaction (1). The associated mass loss is about 5%.
- Zone 3: Around 575 °C, an endothermic peak is observed, corresponding to the allotropic transformation of quartz (α → β).
- Zone 4: Between 700 °C and 850 °C, a strong endothermic transformation is recorded, associated with a mass loss of about 15%, which results from the decarbonation of calcite ($CaCO_3$) [24].

$$CaCO_3(s) \rightarrow CaO(s) + CO_2(g) \quad (1)$$

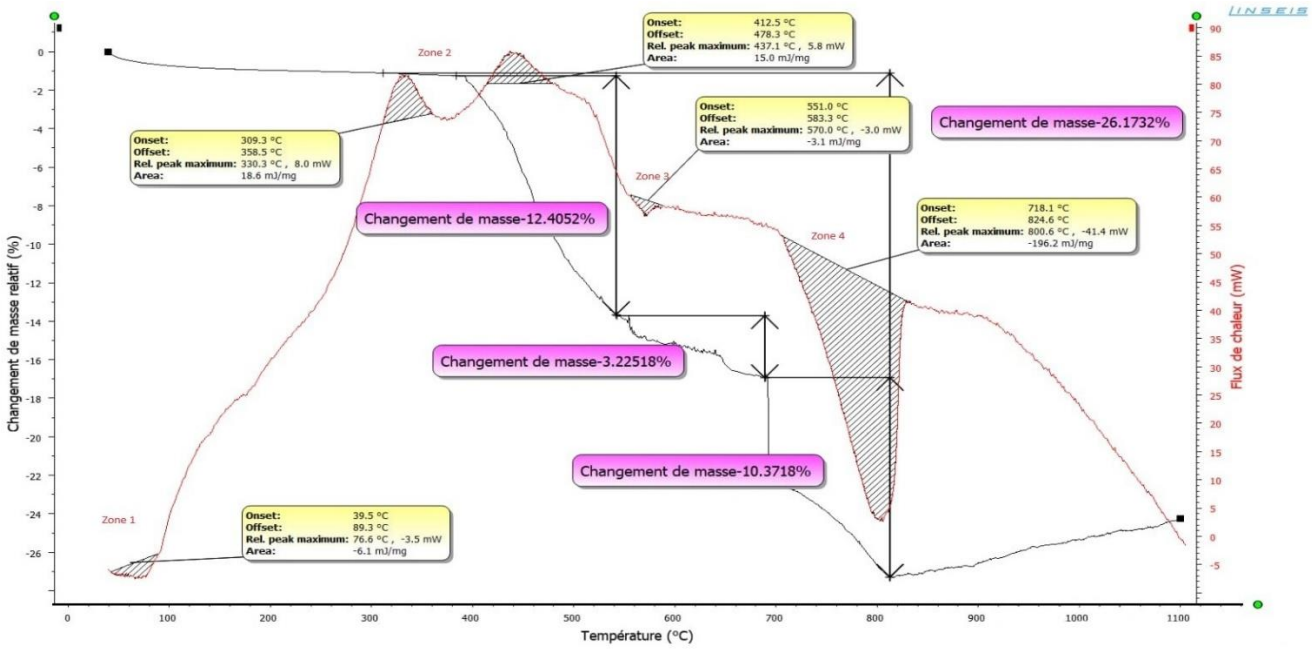

Fig. 13. DTA and TGA thermoanalytical curves

This analysis show that Khenichet's clay is losing a total mass of 26.17% before 850°C, but at 900°C this material become thermally stable, contrary to concrete material that attend stability between 1100°C and 1300°C.

3.4 Mechanical Characterization

Mean values of compression strength of Khenichet's clay are given in Table 4. The value of 4 MPa as compression strength is good since the average value of natural clay's compression strength falls within the 2 to 4.5 MPa range. The high percentage of quartz within this material explains this value since Michot et al. [25] showed that compression strength increases with the elevation of quartz percentage. Also, the fineness of this clayey soil reduces porosity and allows a good bonding between particles which strengthens the mechanical properties [11]. Atbir et al.[10] found a compression strength of 5,7 MPa and a flexural strength of 1,8 MPa for white clay and 4,4 MPa and 1,5 MPa respectively as compression and flexural strengths for red clay and these values were obtained after 90 days. Another work by Atbir et al. [26] investigated the compression behavior at 70 days of a clay material and found a value of 2,05 MPa. As for the clay used by Niyomukiza et al. [22], it has a compression strength of 3,3 MPa and this value was boosted to 4,4 MPa after the firing process. In line with this findings, agricultural wastes, as demonstrated by Kelani et al.[27], can improve the mechanical strength of concrete since the addition of sugar-cane bagasse ash, optimally (around 10%), has increased the compression strength by 12.6%.

Table 4. Khenichet's clay flexural and compression strength

Sample	Compression test			Relative Error (%)
	part 1	part 2	Mean value	Compression strength
1	4,18	4,13	4,155	4,8
2	3,58	3,62	3,6	9,2
3	4,72	3,55	4,135	4,3
Average Strength (MPa)			3,9633	

3.5 Thermal Characterization

This part presents the thermal conductivity, thermal diffusivity, and thermal capacity as three essential parameters in thermal characterization. Table 5 shows the results of thermal conductivity (λ). According to the results of table 5, this material is a moderate insulator with thermal conductivity of 0.62 $Wm^{-1}k^{-1}$ which is a good value falling within the typical range of building materials (0.1 to 2 $Wm^{-1}k^{-1}$)[28] and a better value than conventional concrete. This clay is mainly composed of quartz (75%) and Calcite (13%) with small quantities of Muscovite and Kaolinite, with this composition, it is natural for thermal conductivity to increase [25], in addition, the small particle size of this material decreases the porosity and increases the material's density. Therefore, the possibility of incorporating this clay with big particles of ecological additives will permit the creation of pores allowing more air space, which will cause the improvement of thermal properties.

Table 5. Thermal conductivity of Khenichet's clay samples

Material	Sample	Thermal conductivity (λ)	Sample mean λ value	Relative error	Material mean λ value
Clay	1_{clay}	0,66 0,66 0,57	0,63	0,01	0,62 $Wm^{-1}k^{-1}$
	2_{clay}	0,61 0,61 0,70	0,64	0,02	
	3_{clay}	0,60 0,65 0,60	0,61	0,01	

Generally, ecological additives improve the materials' thermal properties as proved in similar studies; thermal conductivity has decreased by 43% after the addition of granular cork to clay with a volume fraction of 45.6% [15], also the reduction attended 68% by filling the entire apparent volume with granular cork and the clay paste is added in such a way that the intergranular space between the cork granules is filled [16]. In addition to that, Atbir et al. [10] tried mixing red clay and white clay with sheep wool fibers which caused a reduction of thermal conductivity that reached 0.351 $Wm^{-1}k^{-1}$ for white clay and 0.382 $Wm^{-1}k^{-1}$ for red clay for 27g of fibers. Also, straw is very efficient as an ecological additive since it has reduced thermal conductivity from 0.504 $Wm^{-1}k^{-1}$ of a 100% clay sample to 0.263 $Wm^{-1}k^{-1}$ with only 4% of straw added [29]. There are a lot of studies in which a variety of ecological additives has been tested (wood waste, sisal fibers, palm seeds, bamboo fibers, hemp wool...[14, 30, 22, 21, 20]) always leading to the enhancement of thermal properties but with the difference that lies in the percentage of added ecological additives and the degree of thermal conductivity reduction, which indicates the insulating effectiveness of these additives.

As for the results of thermal effusivity, as a fitting parameter of the minimization of quadratic error between the theoretical and the experimental temperature thermograms of the hot plane method in the transient regime, they are presented in Table 6.

Table 6. Khenichet's clay Thermal effusivity (E)

Material	Sample	Thermal effusivity (E)	E sample average value	Relative error	E Material average value
Clay	1_{clay}	1155,79 1313,25 1202,18	1223,74	0,13	1081,32 $Wm^{-2}k^{-1}s^{1/2}$
	2_{clay}	953,19 825,84 1116,18	965,07	0,10	
	3_{clay}	1025,58 1156,50 983,42	1055,16	0,01	

The thermal effusivity of this material is equal to 1081.32 $Wm^{-2}K^{-1}s^{1/2}$, which is a normal value for clays that should be reduced by adding some additives. Atbir et al. [31] reduced thermal effusivity from 873 $Wm^{-2}K^{-1}s^{1/2}$ to 751 $Wm^{-2}K^{-1}s^{1/2}$just by adding 15 g of sheep wool fibers, and Laamrani et al. [32] reduced thermal effusivity by 49% when mixing clay with straw fibers going from 1001 to 510 $Wm^{-2}K^{-1}s^{1/2}$. Eventually thermal capacity ρc is estimated also using the method of the hot plane method in the transient regime and also obtained by minimizing the quadratic error between the theoretical and the experimental thermograms. Table 7 presents the results of this parameter and shows a mean value of 5516.44 $KJm^{-3}K^{-1}$.

Table 7. Thermal capacity results

Material	Sample	Thermal capacity (ρc)	ρc sample's mean value	Relative error	ρc material's mean value
Clay	1_{clay}	2591,68 3781,87 11331,71	5901,75	0,06	5516,44 $KJm^{-3}k^{-1}$
	2_{clay}	2779,69 5295,77 3077,05	3717,51	0,32	
	3_{clay}	2343,16 3580,08 14866,95	6930,07	0,25	

4. Conclusion

This work evaluated gray clay thermophysical properties sourced from the Gharb region of Morocco. Khenichet's clay is a fine material having particles not exceeding 50µm which exhibits considerable promise in purification and water potential. Also, the medium plasticity allows to take advantage of this clay in ceramic production. Additionally, it is composed mainly of Quartz and Calcite with fraction of Muscovite, and Kaolinite, therefore it should be mixed with other types of clay in order to have an enhanced structure in pottery and ceramics. However, the Quartz indicates a good compression strength of 4MPa and the Calcite caused the enhancement of thermal properties with a thermal conductivity of 0.6 $Wm^{-1}K^{-1}$, a thermal effusivity of 1081 $Wm^{-2}k^{-1}s^{1/2}$ and a thermal capacity of $KJm^{-3}K^{-1}$. Although, there is a possibility to improve mechanical properties using stabilization with cement or lime, the firing process at elevated temperatures-often exceeding 900°C- requiring a considerable amount of energy, or the compression techniques that involve high-pressure processing demanding mechanical energy and infrastructure that may not be readily accessible or sustainable, Hence,

these energy-consuming transformations will increase the embodied energy of this material's production process, causing more emissions of greenhouse gases and more pollution, which will make this material lose its natural and ecological aspect . On the other hand, thermal properties indicate a great insulating potential and this material can be improved by incorporating this clay with ecological additives (seeds, fibers, wastes, porous materials...), which introduce air-filled voids to reduce thermal conductivity and improve the overall thermal performance. Finally, the characterization of this clay demonstrated the great potential of the studied clay and allows us to have the perspective of enhancing its properties and utilize it as a sustainable construction, thermally efficient material, and potentially in water filtration. Its local availability, fine particle size, and favorable thermomechanical properties make it a viable eco-material.

References

[1] Gani NA, et al. Chemical composition of clays for pottery in Malaysia: a review. J Trop Resour Sustain Sci. 2015;3(1):144-53. https://doi.org/10.47253/jtrss.v3i1.549

[2] Glascock MD, Neff H, Vaughn KJ. Instrumental neutron activation analysis and multivariate statistics for pottery provenance. Hyperfine Interact. 2004;154:95-105. https://doi.org/10.1023/B:HYPE.0000032025.37390.41

[3] Hirshman AJ, Lovis WA, Pollard HP. Specialization of ceramic production: a sherd assemblage based analytic perspective. J Anthropol Archaeol. 2010;29(3):265-77. https://doi.org/10.1016/j.jaa.2010.03.003

[4] Prüss-Üstün A, et al. Safer water, better health: costs, benefits and sustainability of interventions to protect and promote health. Geneva: WHO; 2008.

[5] Annan E, et al. Application of clay ceramics and nanotechnology in water treatment: A review. Cogent Eng. 2018;5(1):1476017. https://doi.org/10.1080/23311916.2018.1476017

[6 Souileh A, Mabrouk A, Ouadif L, El Hachmi D. Analysis of the geotechnical and mineralogical characteristics of the Settat-Khouribga shale clay for potential civil engineering applications. Res. Eng. Struct. Mater., 2024; 10(4): 1699-1716. http://dx.doi.org/10.17515/resm2024.408ma0824rs

[7] Azhary K, Raefat S, Laaroussi N, Garoum M. Energy performance and thermal properties of three types of unfired clay bricks. Energy Procedia. 2018;147:495-502. https://doi.org/10.1016/j.egypro.2018.07.059

[8] El Azhary K, et al. The improving energy efficiency using unfired clay envelope of housing construction in the south Morocco. J Mater Environ Sci. 2017;8(10):3771-6.

[9] El Fgaier F, Lafhaj Z, Brachelet F, Antczak E, Chapiseau C. Thermal performance of unfired clay bricks used in construction in the north of France: Case study. Case Stud Constr Mater. 2015;3:102-11. https://doi.org/10.1016/j.cscm.2015.09.001

[10] Atbir A, et al. Physicochemical and thermomechanical performances study for Timahdite sheep wool fibers application in the building's insulation. Sci Rep. 2023;13(1):5038. https://doi.org/10.1038/s41598-023-31516-9

[11] Munoz P, Mendivil MA, Letelier V, Morales MP. Thermal and mechanical properties of fired clay bricks made by using grapevine shoots as pore forming agent. Constr Build Mater. 2019;224:639-58. https://doi.org/10.1016/j.conbuildmat.2019.07.066

[12] Balog AA, Cobîrzan N, Thalmaier G, Constantinescu H, Voinea M. Psyllium seeds used as pore forming agent in clay bricks. Procedia Manuf. 2019;32:242-7. https://doi.org/10.1016/j.promfg.2019.02.209

[13] More A, Tarade A, Anant A. Assessment of suitability of fly ash and rice husk ash burnt clay bricks. Int J Sci Res Publ. 2014;4(7):1-6.

[14] Er-rradi H, Idchabani R, Oubrek M, Bojji C, Boukhattem L, Doublali A, et al. Experimental study of composite materials based on ecological wastes. J Compos Mater. 2022;56(21):3295-306. https://doi.org/10.1177/00219983221113029

[15] Mounir S, Maalouf Y, Cherki A, El Khabbazi A. Thermal properties of the composite material clay/granular cork. Constr Build Mater. 2014;70:183-90. https://doi.org/10.1016/j.conbuildmat.2014.07.108

[16] El Wardi FZ, Khabbazi A, Cherki AB, Khaldoun A. Thermomechanical study of a sandwich material with ecological additives. Constr Build Mater. 2020;252:119093. https://doi.org/10.1016/j.conbuildmat.2020.119093

[17] Mountoumnjou O, Szymczyk A, Lyonga Mbambyah EE, Njoya D, Elimbi A. New low-cost ceramic microfiltration membranes for bacteria removal. Membranes. 2022;12(5):490. https://doi.org/10.3390/membranes12050490

[18] Kassa A, Raihan S, Hayano K, Phan BN, Yamauchi H, Mochizuki Y. Novel method for evaluating water absorption and retention of waste-based stabilizers using suction filtration. Soils Found. 2023;63(4):101334. https://doi.org/10.1016/j.sandf.2023.101334
[19] Laaroussi N, Lauriat G, Garoum M, Cherki A, Jannot Y. Measurement of thermal properties of brick materials based on clay mixtures. Constr Build Mater. 2014;70:351-61. https://doi.org/10.1016/j.conbuildmat.2014.07.104
[20] Dlmi M, et al. Experimental investigation on the thermal behavior of three different insulation materials: wood, polystyrene and hemp wool. Int J Eng Technol. 2017;9(5). https://doi.org/10.21817/ijet/2017/v9i5/170905037
[21] Karlinasari L, Hermawan D, Maddu A, Bagus M, Lucky IK, Nugroho N, et al. Acoustical properties of particleboards made from betung bamboo (Dendrocalamus asper) as building construction material. Bioresources. 2012;7(4):5700-9. https://doi.org/10.15376/biores.7.4.5700-5709
[22] Niyomukiza JB, Nabitaka KC, Kiwanuka M, Tiboti P, Akampulira J. Enhancing properties of unfired clay bricks using palm fronds and palm seeds. Results Eng. 2022;16:100632. https://doi.org/10.1016/j.rineng.2022.100632
[23] Balek V, Murat M. The emanation thermal analysis of kaolinite clay minerals. Thermochim Acta. 1996;282/283:385-97. https://doi.org/10.1016/0040-6031(96)02886-9
[24] Paama L, Pitkanen I, Peramaki P. Analysis of archaeological samples and local clays using ICP-AES, TGA-DTG and FTIR techniques. Talanta. 2000;51:349-57. https://doi.org/10.1016/S0039-9140(99)00281-7
[25] Michot A. Caractéristiques thermophysiques de matériaux à base d'argile : évolution avec des traitements thermiques jusqu'à 1400°C [thesis]. Limoges: University of Limoges; 2008.
[26] Atbir A, et al. Improvement of thermomechanical properties of porous plaster reinforced with a network of Morocco sheep wool skeletons for energy efficiency. Build Environ. 2023;234:110171. https://doi.org/10.1016/j.buildenv.2023.110171
[27] Kilani, A., Fapohunda, C., Adeleke, O., & Metiboba, C. (2022). Evaluating the effects of agricultural wastes on concrete and composite mechanical properties. Research on Engineering Structures and Materials, 8(2), 307-336. http://dx.doi.org/10.17515/resm2021.339st0912
[28] Franco A. An apparatus for the routine measurement of thermal conductivity of materials for building application based on a transient hot-wire method. Appl Therm Eng. 2007;27(14-15):2495-504. https://doi.org/10.1016/j.applthermaleng.2007.02.008
[29] El Azhary K, Chihab Y, Mansour M, Laaroussi N, Garoum M. Energy efficiency and thermal properties of the composite material clay-straw. Energy Procedia. 2017;141:160-4. https://doi.org/10.1016/j.egypro.2017.11.030
[30] Ouakarrouch M, El Azhary K, Mansour M, Laaroussi N, Garoum M. Thermal study of clay bricks reinforced by sisal-fibers used in construction in south of Morocco. Energy Rep. 2020;6:81-8. https://doi.org/10.1016/j.egyr.2019.11.045
[31] Atbir A, et al. Thermophysical study of a multi-layer brick of grids made of sheep's wool yarn and clay. AIP Conf Proc. 2019;2123(1). https://doi.org/10.1063/1.5117033
[32] Lamrani M, et al. Thermal study of clay bricks reinforced by three ecological materials in south of Morocco. Energy Procedia. 2019;156:273-7. https://doi.org/10.1016/j.egypro.2018.11.141

Research on Engineering Structures & Materials
www.jresm.org
Research Group

Research Article

Exploring the physical, mechanical, and thermal properties of oil palm trunk and ramie fiber hybrid bio composites as building insulation materials

Fakhriza [1,a], Muhd Haiyum [1,b], Nawawi Juhan [1,c], Jenne Syarif [1,d], Nurlaili [1,e], Ariefin [1,f], Bukhari Kasim [1,g], Indra Mawardi [1,h], Iskandar Hasanuddin [*,2,i], Muhammad [3,j], Faisal Abnisa [4,k]

[1]*Dept. of Mechanical Eng., Politeknik Negeri Lhokseumawe, Lhokseumawe, Indonesia*
[2]*Dept. of Mechanical and Industrial Eng., Faculty of Engineering, Universitas Syiah Kuala, Banda Aceh, Indonesia*
[3]*Dept. of Chemical Eng., Faculty of Engineering, Universitas Serambi Mekkah, Banda Aceh, Indonesia*
[4]*Dept. of Chemical and Materials Eng, Faculty of Engineering, King Abdulaziz University, Rabigh, Saudi Arabia*

Article Info

Article History:

Received 13 Mar 2025
Accepted 19 May 2025

Keywords:

Thermal insulation;
Hybrid bio composite ;
Oil palm trunk;
Ramie fiber;
Tapioca starch

Abstract

Agricultural waste has attracted the attention of researchers as a high potential reinforcement material for green thermal insulation. This study aimed to investigate the use of hybrid bio composites from oil palm trunks (OPTs) and ramie fibers as new raw materials for thermal insulation in buildings. In this paper, OPTs and ramie fibers were used as fillers in different particle sizes to fabricate hybrid bio composites using hot pressing, with tapioca starch biopolymer serving as a matrix. The bio composite was produced using a hot pressing machine at 9.8 MPa for 25 minutes, with pressing was conducted in two stages, namely 5 and 20 minutes. The physical, mechanical, and thermal properties of the OPTs and ramie fiber hybrid bio composites developed in this study and those of a pure OPTs bio composite as comparison were determined. The study found that the hybrid bio composites showed better performance and properties than the pure oil palm trunk bio composite. The results further showed that the HC200 hybrid bio composite sample had the lowest water absorption and thickness swelling (54.73 and 19.57, respectively), the HC40 hybrid bio composite sample had the highest moduli of rupture and elasticity (19.59 MPa and 2.95 GPa, respectively), and the HC20 hybrid bio composite sample had the lowest thermal conductivity coefficient (0.0807 W/mK). Thermogravimetric analysis showed that the hybrid bio composites had higher thermal stability at 309°C than the pure OPTs bio composite. From the research results, it can be concluded that the hybrid bio composites have the potential as thermal insulation materials for use in the construction sector.

© 2025 MIM Research Group. All rights reserved.

1. Introduction

Oil palm is one of the main commodities from the agricultural sector that has an essential role in Indonesia's economy. Indonesia produced 48.42 million tons of palm oil, with an oil palm plantation area of 14.59 million hectares and a growth rate in the range of 2–4% per year [1]. According to Abnisa, each palm oil tree produces approximately 10% palm oil, while the remaining

*Corresponding author: iskandarhasanuddin@usk.ac.id
[a]orcid.org/0009-0000-2028-5363; [b]orcid.org/0009-0006-4752-1470; [c]orcid.org/0009-0002-9277-4945; [d]orcid.org/0009-0005-6834-6387; [e]orcid.org/0009-0001-6665-3085; [f]orcid.org/0009-0005-5945-4490; [g]orcid.org/0009-0008-6298-6908; [h]orcid.org/0000-0001-6631-510X; [i]orcid.org/0000-0003-0899-7485; [j]orcid.org/0000-0001-5926-675X; [k]orcid.org/0000-0002-3017-1922
DOI: http://dx.doi.org/10.17515/resm2025-753me0313rs

90% becomes biomass waste. The waste generally is derived from the milling process and plantation activities. The milling process, in particular, mostly generates waste from empty fruit bunches, accounting for about 22% of all waste, followed by waste from mesocarp fibers (13.5%) and palm kernel shells (5.5%). Furthermore, the fronds and trunks are found as the primary biomass waste produced from plantations, constituting up to 70% and 20.5% of all biomass waste, respectively [2].

The volume of trunks is the main contributor to palm oil solid waste. Currently, only 25% of the trunks are utilized, while the remaining are still dumped as untreated waste. Oil palm trunks (OPTs) have the potential to be used as a bio composite board material for building panel structures. Some previous research has investigated their applications, including as particleboard, lumber, and laminated wood materials [3], [4], [5]. Most of the research mainly focused on the matrix selection and material strength, but none has investigated the thermal insulation property of bio composite boards produced from oil palm trunks. It is essential to examine this property as it can help improve the thermal insulation of the panels produced and increase their durability.

Generally, thermal insulation is provided by synthetic materials, such as glass wool, rock wool, styrofoam, fiberglass, extruded polystyrene, and expanded polystyrene. These materials have good thermal insulation, but their use brings harm to the environment, especially during processing and disposal in landfills [6]–[10]. Various innovations have been made to replace the synthetic with natural materials, including by using natural-fiber-based materials, such as wood [11], wheat and sunflower stalks [12], bamboo [13], oil palm empty fruit bunches [14], and corn cobs [15]. To bind reinforcement materials, thermosets such as polyester, epoxy, and urea-formaldehyde (UF) are normally used as resins. However, these types of resin are known to be non-environmentally friendly since they cannot be decomposed easily. Therefore, the use of natural resins will open up an opportunity to reduce the profuse use of synthetic materials, which also helps minimize environmental damage.

Many natural resins are available to be used as adhesives in the bio composite manufacturing process. A good resin must have a high starch content, which is an essential ingredient as an adhesive. The starch composition generally consists of amylose and amylopectin, which play different roles in the binding process; while amylopectin serves as an adhesive, amylose does as a hardener. Tapioca starch is acknowledged for its high amylopectin content, measuring 85%, compared to 72% in corn, 79% in potato, and 72% in wheat. However, the amylose content, which is basically responsible for slow recrystallization, brittleness improvement, and mechanical strength reduction, was found to be as low as 17% [16].

Besides thermal insulation, bio composites must also have high strength and low water absorption. The strength of a bio composite can be improved by adding a reinforcement mixture or additive materials. Using materials as a hybrid will increase their effectiveness because it can increase the cellulose content of the reinforcement and maximize the amount of waste utilized. High cellulose content can in turn improve the mechanical and physical properties of the bio composite board. Several researchers have previously reported the potential of oil palm trunks as an environmentally friendly insulation material [17]–[19]. These studies examined the thermal insulation properties of oil palm trunks by focusing on the characteristics of a single material, without integrating a hybrid bio composite approach. Combining oil palm trunks (OPTs) with other materials may enhance thermal and mechanical performance and expand its applications in environmentally friendly insulation. Ramlee et al. [20] produced bio composite boards of OPTs mixed with empty fruit bunches (EFBs). They reported that using solely OPTs tended to yield lower strength than when mixed with EFBs. Another study reported that the tensile property of pure sugarcane composite was improved by hybridizing with EFB fibers until 18.8% [20]. Furthermore, a bio composite board with low water absorption capacity is preferrable since it reduces the defect caused by natural moisture. High moisture absorption will lead to bio composite board swelling, matrix instability and cracking, and reduced mechanical properties [21].

This study aims to determine the physical, mechanical, thermal conductivity, and thermal stability characteristics of hybrid bio composites composed of OPTs and ramie fiber as thermal insulation materials. The effect of OPTs particle size and ramie fiber addition were evaluated. Bio composites

were produced using tapioca starch as the matrix and fabricated through hot pressing at a constant temperature and pressure. Various analyses were conducted, including water absorption, thickness swelling, flexural strength, tensile strength, thermal conductivity, and thermal stability.

2. Materials and Methods

2.1. Material

This study used oil palm trunks (OPTs) and ramie fibers as hybrid bio composite reinforcement materials. The oil palm trunks used in this study were collected from local oil palm plantations in Aceh, and the ramie fibers were obtained from ramie plantations in Yogyakarta, Indonesia (Fig. 1). Tapioca starch biopolymer bought from a local market was used as a matrix. This resin consisted of 15% amylose and 85% amylopectin [22]. The chemical compounds found in the oil palm trunks, ramie fibers, and tapioca starch are presented in Table 1. Furthermore, the mechanical and physical properties are listed in Table 2. In this study, physical and mechanical properties are reviewed because these two aspects determine the performance, reliability, and application of insulation materials. Physical properties affect thermal insulation capability and environmental resistance, while mechanical properties are important to ensure that the material is sufficiently strong and stable enough during installation and throughout its service life.

(a) (b)

Fig. 1. Materials (a) oil palm trunk and (b) ramie fiber

Table 1. The chemical compounds contained in OPTs, ramie fibers, and tapioca starch

Filler	Cellulose (wt%)	Holocellulose (wt%)	Hemicellulose (wt%)	Lignin (wt%)	Amylose (%)	Amylopetin (%)
OPTs	29-37	42-45	12-17	18-23	-	-
Ramie	68.6-76.2	-	13-16	0.6-0.7	-	-
Tapioca starch	-	-	-	-	15	85

Table 2. The mechanical and physical properties of OPTs and ramie fibers

Properties	OPTs [23] [17]	Ramie fiber [24]
Tensile strength (MPa	300-600	290-1060
Young Modulus (GPa)	8-45	5-128
Elongation (%)	5-25	1.2-4.6
Density (g/cm^3)	0.28	1.5-1.6
Thermal Conductivity (W/mK)	0.05-0.143	0.072-0.152

2.2. Preparation of OPTs and Ramie Fiber

OPTs ware cut into small pieces, dried, and milled using a ball mill (Planetary Mill, Fritsch, P6) using 20 mm diameter sintered corundum balls at 100 rpm to pass through 0.42–0.84 mm (20 mesh), 0.07–0.42 mm (40 mesh), and <0.07 mm (200 mesh) sieves. Variations in OPTs particle size and the addition of ramie fibers aim to produce bio composites with low thermal conductivity, improved mechanical strength, and enhanced structural stability. The ground OPTs were then boiled in water at a temperature of 100^{o}C for 30 minutes and dried in an oven at a temperature of

80°C for the next 24 h until reaching 10–15% moisture content. Pre-treatment of OPTs particles in hot water aims to remove starch granules from the parenchymatous tissue, which can enhance the mechanical properties and thermal stability of the bio composites [25]. Furthermore, ramie fibers were cut to a length of approximately 5 mm and subsequently treated with 5% NaOH (1000 g of water and 50 g of NaOH flake) for one hour. The fibers were then washed repeatedly to reach a neutral pH and dried in an oven at a temperature of 80°C for 24 h. NaOH treatment of OPTs fiber aims to reduce lignin and hemicellulose content. Previous studies have shown that soaking oil palm fiber in 5% NaOH for 1 hour can improve the mechanical properties of the bio composite. However, higher NaOH concentrations may lead to excessive lignin and hemicellulose, thereby diminishing fiber properties and the quality of the bio composite [26]. Fig. 2 depicts the preparation processes of OPTs and ramie fibers.

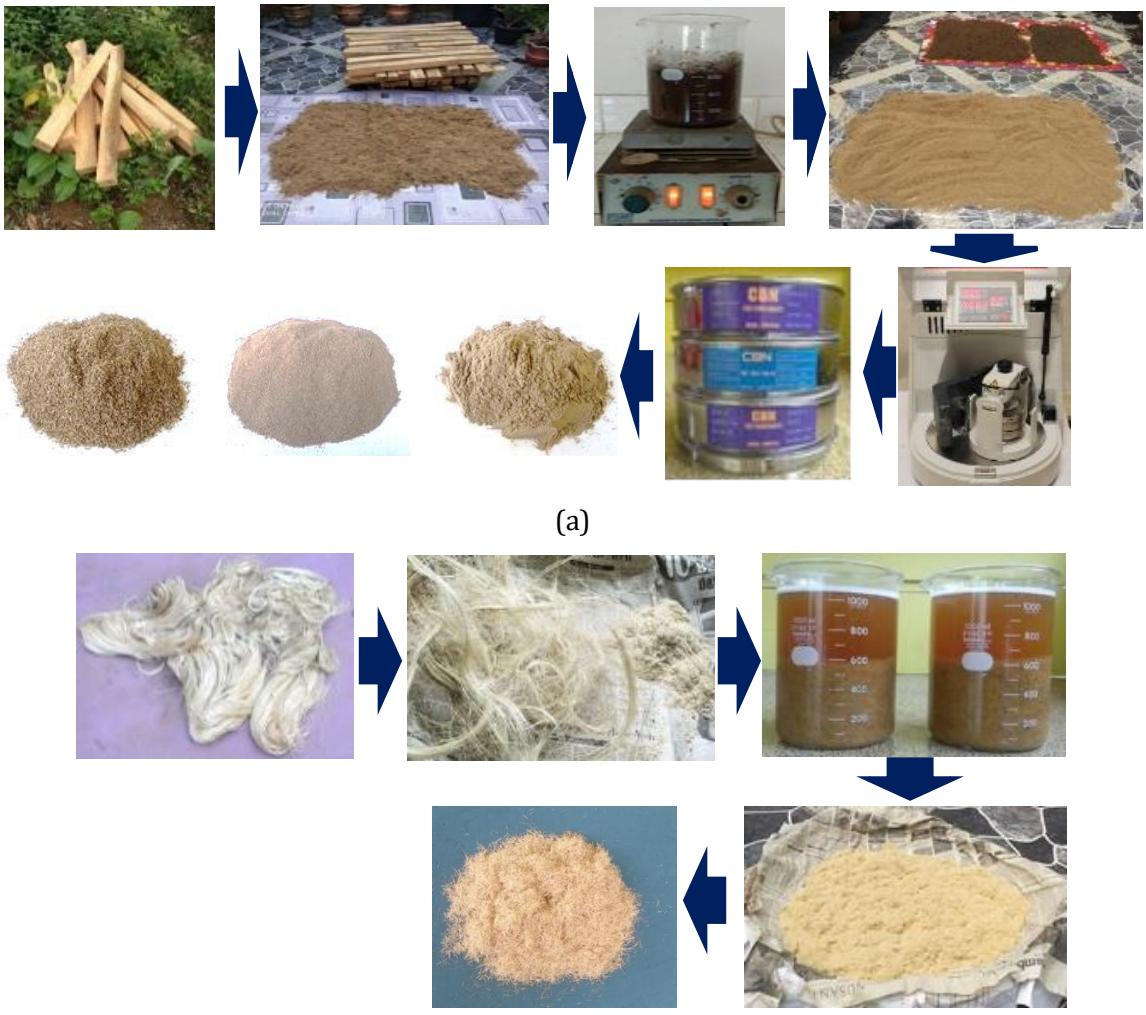

(a)

(b)

Fig. 2. The preparation processes of OPTs (a) and ramie fibers (b)

2.3. Fabrication of Hybrid Bio Composites

Hybrid bio composites were fabricated with the formulation as shown in Table 3 using hot pressing with a mold size of 150 mm × 150 mm × 30 mm and a target density of 0.70 g/cm^3. The target density of the bio composite was set at 0.7 g/cm^3 to balance lightness and structural integrity. This value also corresponds to the middle value of the JIS A 5908: 2003 standard [27] for particleboard, which is 0.4-0.9 g/cm^3. The density allows for the development of a material that is relatively lightweight yet sufficiently strong for various applications. Lower density tends to increase pore space, which can reduce thermal conductivity, but it may also compromise mechanical properties.

Table 3. Hybrid bio composite formulation

Bio Composite Type	Sample Code	Size of OPTs (mm)	OPTs particle (%)	Ramie fiber (%)
Bio Composite	BC20	0.42-0.84	70	0
	BC40	0.07-0.42	70	0
	BC200	<0.07	70	0
Hybrid Bio Composite	HC20	0.42-0.84	50	20
	HC40	0.07-0.42	50	20
	HC200	<0.07	50	20

In this study, pure OPTs bio composite was used as a comparison. Ramie fibers as fillers were mixed with tapioca starch, and 100 mL of hot water was then added to the mixture. Tapioca starch was used as a biopolymer matrix in an amount of 30% for all variations. The solution was stirred until completely mixed using a mechanical mixer (HM-620 Miyako, Indonesia) for 5 minutes at 200 rpm. The mixed solution was then poured into a mold and placed in a hot-press machine at a temperature of 150°C. To achieve a hybrid bio composite thickness of 10 mm, the hot-press machine was adjusted at 9.8 MPa for 25 min, and the pressing was performed in two stages: a temperature of 120°C was applied for 5 min in the first stage, and a temperature of 150°C was applied for 20 min in the second stage. After the hot-pressing process, the bio composite was kept in a dry room for seven days before use for testing. Figures 3 depict the different stages of the fabrication process of the hybrid bio composites.

Fig. 3. Stages of the fabrication process hybrid bio composites

2.4. Characterization of Hybrid Bio Composites

All the produced bio composite samples were characterized using physical tests (water absorption, thickness swelling, and scanning electron microscopy), mechanical tests (modulus of rupture, modulus of elasticity, tensile strength, and Young's modulus), and thermal analysis (thermal conductivity and thermogravimetric analysis).

2.4.1 Physical Test

For the water absorption and thickness swelling tests, three specimens were prepared with the size of 50 mm × 50 mm × 10 mm. Prior to the tests, the weight and thickness of the specimens were measured, followed by re-measurement after 24 h of an immersion process. Equation 1 was used to calculate the water adsorption capacity, and Equation 2 was used to determine the thickness swelling.

$$WA = \left(\frac{W_2 - W_1}{W_1}\right) x\ 100\ (\%) \quad (1)$$

$$TS = \left(\frac{t_2 - t_1}{t_1}\right) x\ 100\ (\%) \quad (2)$$

where W_1 is the initial mass of specimen before immersion in water, W_2 is the mass of specimen after immersion in water, t_1 is the initial thickness of specimen before immersion in water, and t_2 is the thickness of specimen after immersion in water.

2.4.2 Flexural Test

The modulus of rupture (MOR) and modulus of elasticity (MOE) were determined using the three-point bending approach. The tests involved five specimens measuring 150 mm × 20 mm × 10 mm, in accordance with the ASTM D790 standard [28], using the MTS EXCEED Model E43 universal testing machine with a crosshead speed of 2 mm/min and a load cell of 10 kN. The same setting of the machine was also applied to evaluate the tensile strength. The bending data obtained were used to determine the MOR and MOE using Equations 3 and 4.

$$MOR = \left(\frac{3PL}{2bh^2}\right)\ (MPa) \quad (3)$$

$$MOE = \frac{\Delta PL^3/4\Delta Ybh^3}{1000}\ (GPa) \quad (4)$$

where P is the maximum loading, L is the span, b is the width of specimen, h is the thickness of specimen, ΔY is the deflection, ΔP is the difference between the upper and lower loading.

2.4.3 Tensile Test

The tensile properties sample was cut into rectangular strips using the ASTM standard D3039 [29] with a dimension of 250 x 25 mm x actual thickness for each type of composite. Five samples were prepared for each variant, and the tests were conducted using an MTS EXCEED Model E43 (Japan) with a load cell of 10 kN and a crosshead speed of 2 mm/minute. The tensile properties data obtained were used to determine the tensile strength and modulus of elasticity using Equations 5 and 6.

$$\sigma = \frac{P}{A}\ (MPa) \quad (5)$$

$$E = \frac{\sigma}{\varepsilon}\ (MPa) \quad (6)$$

where P is the maximum loading, A is the cross-sectional area, σ is the stress, and ε is the strain.

The modulus of elasticity (E) is obtained from the linear (elastic) region of the load-displacement curve resulting from a tensile test. The slope ΔP/ΔY is used to calculate Δσ/Δε, considering the test specimen's dimensions.

2.4.4 Thermal Conductivity Test

The thermal conductivity test was conducted using an instrument from PHYWE Systeme GmbH (37070 Göttingen, Germany) in reference to the ASTM C177-97 standard [30]. The method was run in an insulated box equipped with a thermocouple in and out of the box. Thermal conductivity test specimens were prepared for each variation with dimensions of 150x150x10 mm. The test was conducted with the room temperature conditioned to 24°C. Measurements were started when the temperature inside the box reached 60°C, which was maintained for 30 minutes before data collection. The measurement data were then used to determine thermal conductivity values by applying Equation 7 below [31].

$$Q_{c,wall} = -kA\frac{T_1 - T_2}{\Delta x}\ (W) \quad (7)$$

where T_1 is the temperature of the inside surface, T_2 is the temperature of the outside surface, Δx is the distance between the two surfaces, and A is the surface area.

2.4.5 Thermogravimetric Analysis (TGA)

Thermogravimetric analysis (TGA) was carried out using the SHIMADZU model DTG 60 instrument. A sample weighing about 5 mg was scanned from room temperature to a temperature of 700°C with a heating rate of 40°C/min under nitrogen purging with a flow rate of 20 mL/min.

2.4.6 Scanning Electron Microscopy (SEM)

SEM was used to observe the surface morphology of the bio composites with an EVO MA10 model (ZEISS, Germany). Prior to SEM analysis, the samples were gold-coated with sputtering. The bio composites were characterized using the SEM EVO MA10 (ZEISS, Germany) with a working distance of 13-14 mm and a voltage of 20 kV during operation.

3. Results and Discussion

3.1. Water Absorption and Thickness Swelling

Water absorption test is an essential aspect in determining the quality of natural fiber composite materials. Table 4 and Figure 4 shows the percentage of water absorption and thickness swelling of the hybrid bio composites developed in this study after 24 h. The percentage of water absorption for all samples were found in the range of 54.73–74.40%. BC20 was found to absorb the highest amount of water (74.40%), which was similar to the percentage for HC20 (65.54%). Both samples were composed of OPTs with a particle size of 20 mesh. A larger particle size allows more water absorption compared to smaller particles. Large particles create open pores, enabling water to easily enter the material. Smaller particles tend to fill these open pores, reducing the pathway for water to enter. In addition, systems with narrower particle distribution (small particles) are more likely to form compact structures.

Table 4. Water absorption and thickness swelling value of hybrid bio composites

Bio composites sample	WA (%)	SD of WA	TS (%)	SD of TS
BC20	74.46	5.22	26	2.83
BC40	61.84	5.77	23.08	3.82
BC200	59.8	3.99	22.5	3.39
HC20	65.54	5.98	28.85	4.35
HC40	56.76	4.41	22.86	3.07
HC200	54.73	3.02	19.57	1.79

SD : standard deviation

Similar results were reported by previous research [32], which measured the water absorption of a particleboard made from palm oil wood. The study showed that the particleboard with a larger particle size (0.5–1 mm) had a water absorption capacity of 41.43%, compared to the 17.19% value for the particleboard with a particle size in the range of 0.1–0.5 mm. The same trend was also found for bio composite made from composite materials. Mawardi et al. noted that composite materials with larger particle sizes absorbed more water compared to materials with smaller particle sizes [33]. Hybridization with ramie fibers was expected to help reduce water absorption, which was proved by this study. It was found in this study that using OPTs and ramie fibers in a mixture resulted in a 5% reduction in water absorption. Ramlee et al. reported that the addition of co-reinforcement materials has the possibility to reduce water absorption due to compatible characteristics of mixed materials, which reduces void and porosity of the exposed surface area on

composites [20]. The phenomenon of decreased pore number due to the use of small particles and hybridization of ramie fibers, which increases density, is also illustrated by SEM scanning results (Fig. 12). Furthermore, reinforcement materials from natural fibers normally have a tendency to absorb more water due to their natural hydrophobic characteristic [23]. The absorbed water will in turn affect the thickness swelling of the hybrid bio composite s if it remains for a certain period of time. This study showed that after 24 hours of immersion, the highest thickness swelling was obtained where the thickness swelling was obtained at 29% when urea-formaldehyde (UF) was used to bind the natural reinforcement material (oil palm fronds). To improve the adhesive level, Pan et al. [34] tried to mix UF and polymethylene diphenyl isocyanate (PMDI), which is known as a common adhesive in the particleboard industry. However, their results showed that the thickness swelling of their produced hybrid bio composite was above 30%, which was higher compared to the result obtained from using tapioca starch as an adhesive in this experiment. UF and PMDI are the most commonly used binders in the particleboard industry, but they are known to cause health concerns and pose emission issues to the environment. The results of this study proved that tapioca starch can be an option to be used as an alternative natural adhesive to the widely used thermoset-based resins.

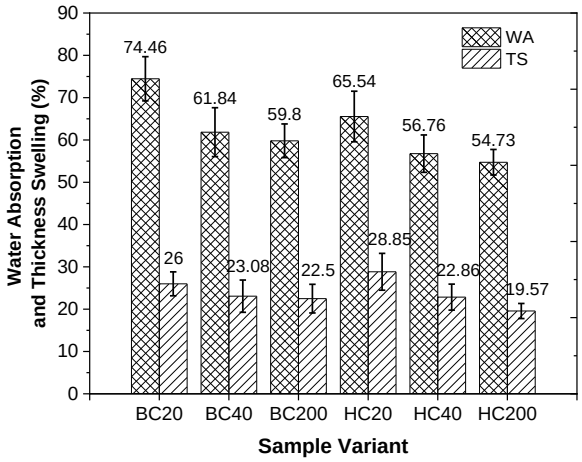

Fig. 4. Water absorption and thickness swelling of hybrid bio composites

3.2. Mechanical Properties of Hybrid Bio Composites

Figure 5 shows the load versus displacement curves for various bio composites: BC20, BC40, BC200, HC20, HC40, and HC200. The curves indicate that all specimens experience an increasing force until reaching a peak, after which the force gradually decreases, reflecting plasticity or flexural failure characteristics. The HC20 sample shows the highest flexural performance, while the BC200 sample shows the lowest flexural force value.

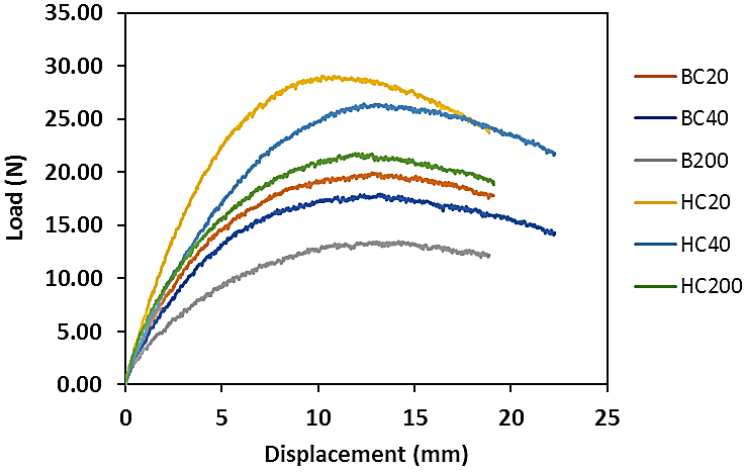

Fig. 5. Load vs displacement curves of hybrid bio composites' flexural properties

Figure 6 shows the results of the MOR and MOE tests for all the produced hybrid bio composite s, with decreasing MOR and MOE for smaller particle sizes. This finding was evident for both scenarios, with and without co-reinforcements. The single reinforcement was recorded to yield reduced MOR from 14.41 to 12.35 MPa, while the co-reinforcements used in the bio boards yielded a reduction in MOR from 18.89 to 16.65 MPa. Similar trends were also reported by several researchers, who used different reinforcement materials, such as wood, rice straws, and bamboo, with bio-resins used as binders [13], [15], [35] highlighting the role of such factors as particle size, porosity, density, and bending strength that might come into play (see Figure 7). Smaller particle sizes produce lower porosity [36], and low porosity in turn tends to increase the bio board density [15]. As density increases, the result of bending analysis will tend to drop, as revealed by MOR tests [13]. In this work, the density of the pure OPTs bio composite and the hybrid bio composite s ranged between 0.69 and 0.79 g/cm^3, as shown in Table 5.

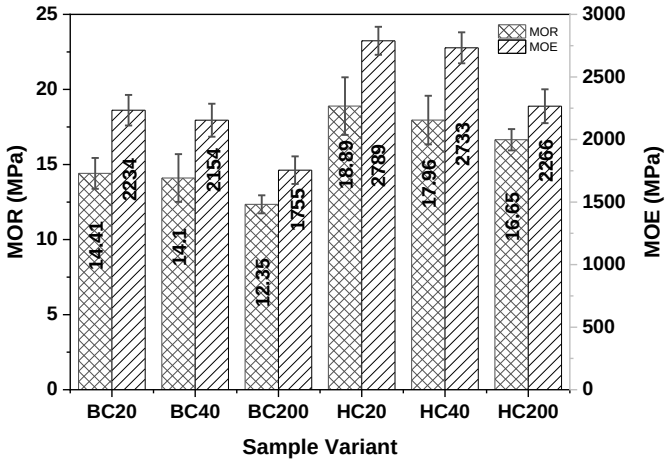

Fig. 6. MOR and MOE hybrid bio composites

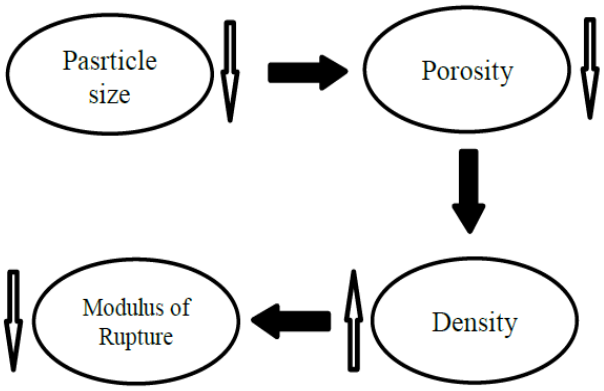

Fig. 7. Correlation of particle, porosity, density, and flexural strength

Figure 8 shows the tensile force versus displacement curve for bio composite variations: BC20, BC40, BC200, HC20, HC40, and HC200. In general, the curve shows an increase in tensile force with increasing displacement until reaching a peak, after which the force decreases sharply, indicating material failure. The HC200 sample showed the highest tensile performance, followed by HC40 and HC20, while BC20 showed the lowest performance. The results indicate that variations in the type and number of reinforcing materials significantly affect the mechanical characteristics, especially tensile strength and deformation resistance.

The tensile strength and modulus of elasticity of the hybrid bio composites are presented in Figure 9. As depicted in the figure, particle size and the addition of co-reinforcements had a positive effect on the tensile strength property. A smaller particle size with the addition of 20% ramie fibers yielded a higher tensile strength, increasing from 2.33 to 7.92 MPa, and a higher modulus of

elasticity, increasing from 55.68 to 157.20 MPa. In addition, the results of this study indicate that increased density is positively correlated with tensile strength. This is likely due to increased adhesion between the fiber and the matrix, which improves stress transfer efficiency from the matrix to the fiber. Conversely, at low density, numerous pores are formed, which act as sites for crack initiation and contribute to the decrease in bio composite strength.

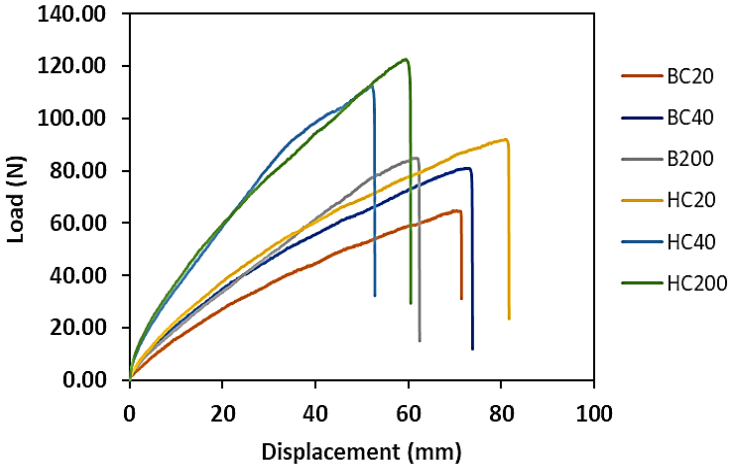

Fig. 8. Load vs displacement curves of hybrid bio composites' tensile properties

Mawardi et al. [37]) posited that the smaller particle size of a filler exhibits higher tensile strength because of better filler dispersion and filler-matrix interaction compared to fillers with larger particle sizes. This filler-matrix interaction is mainly influenced by the presence of lignocellulosic properties, where the presence of cellulose and hemicellulose will specifically improve the composite strength [38]. This study clearly showed that the addition of ramie fibers significantly improved the tensile strength, with a significantly greater amount of them (71.8 wt%) used than that of cellulose-containing OPTs (30.2 wt%) used. In this experiment, ramie fibers were incorporated into the hybrid samples (HC20, HC40, and HC200). The increasing trend of tensile strength linearly affected the modulus of elasticity, which was observed for all samples.

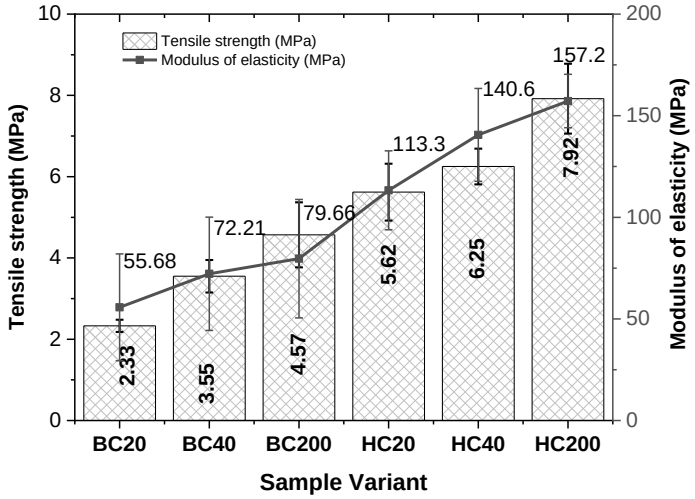

Fig. 9. Tensile properties of hybrid bio composites

3.3. Thermal Conductivity Coefficients

Thermal conductivity coefficients were used to determine the thermal insulation performance of the composites. As shown in Table 5, the highest coefficient was obtained by BC200. This indicates that the board was easy to transfer heat, which means it provided low insulation. According to Mati-Baouche, a bio board can be qualified as an insulator if its thermal conductivity measures 0.1 W/mK or lower [39]. Of the bio composite s produced in this study, BC20, HC20, and HC40 fell into the

category defined by Mati-Baouche. Thermal conductivity coefficients are an essential aspect to consider in choosing building materials for different weather conditions. Various factors affect the thermal insulation performance of a composite material, including fiber type, fiber-adhesive interface structure, density, particle size, and porosity. Of all the samples in this study, only BC200 and HC200 were observed to be out of the standard range, valued 0.18 and 0.17 W/mK, respectively (Table 5).

Table 5. Density and thermal conductivity of hybrid bio composites

Bio composite Type	Sample	Density (g/cm^3)	Thermal Conductivity (W/m.K)	Standard Deviation
Bio composite	BC20	0.69	0.0914	0.022
	BC40	0.75	0.1311	0.032
	BC200	0.77	0.1811	0.026
Hybrid Bio composite	HC20	0.71	0.0807	0.018
	HC40	0.77	0.0849	0.016
	HC200	0.79	0.1705	0.021

The thermal insulation values obtained in this study were better than not only those of vermiculite, sunflower stalks, and wheat stalks (0.063–0.334 W/mK) [12], but also that of corn cobs (0.101 W/mK) and they were comparable to the value for OPTs (0.055–0.091 W/mK) [6]. In addition, this study's thermal conductivity coefficients were relatively higher than those reported for wood waste [11] and synthetic fibers, such as glass and rock wool (0.032 to 0.045 W/mK) and polyester fabric (0.09 to 0.45 W/m K) [40]. Overall, the hybrid bio composites were better than the pure OPTs bio composite in terms of thermal conductivity coefficients. Hybridization with ramie fibers lowered the thermal conductivity value of the bio composites. This result is supported by a previous study [41], according to which thermal conductivity is influenced by fiber type and fiber structure.

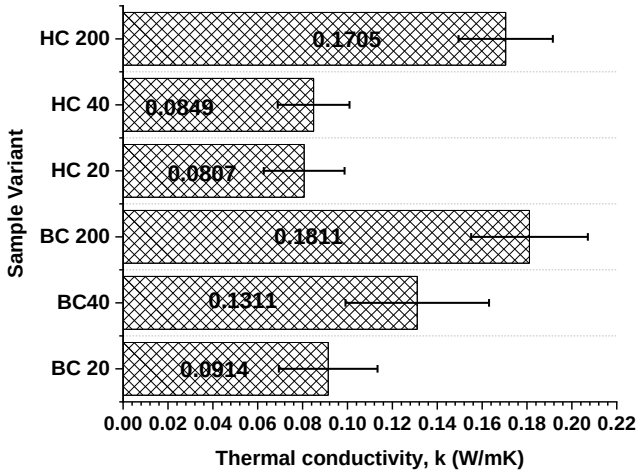

Fig. 10. Thermal conductivity of hybrid bio composites

Figure 10 depicts the effect of particle size on the thermal conductivity coefficient. HC20 and HC40 had thermal conductivity coefficients of 0.080 and 0.084 W/mK, respectively, making them suitable to be used as insulators. HC20 showed the lowest thermal conductivity coefficient (0.080 W/mK) among the bio composite samples. The thermal conductivity coefficient decreased with the increasing particle size, likely due to the higher density and reduced porosity of the bio composites. Pores within the bio composites contain gas, which hinders the flow of heat. This finding is supported by [37], who stated that porosity in wood composites serves as a burst center for phonons, thus reducing the thermal conductivity coefficient. A decrease in particle size within a specific range may decrease the thermal insulation property but not the mechanical properties.

3.4. Thermogravimetric Analysis

Figure 11 shows the thermogravimetric analysis (TGA) and derivative thermogravimetric analysis (DTGA) curves for the pure OPTs bio composite and hybrid bio composite samples. Overall, the TGA and DTGA curves for both types of bio composites have similar patterns, with three stages of degradation and weight loss (Fig. 11a). The first stage of degradation took place from 36 to 137°C and from 35 to 133°C for the pure OPTs bio composite and hybrid bio composite samples, respectively. The initial decreases of sample weight of up to 10% were due to evaporation of water from the samples. From 308 to 412°C and from 309 to 406°C, there was another major degradation, with weight losses reaching 65% and 59% for the pure OPTs bio composite and hybrid bio composite samples, respectively. This finding was relatively similar to that of a previous study [42], which reported decomposition of palm tree fibers at a temperature of 300°C by 50%. A final decomposition occurred within the temperature range of 391–600°C, with mass losses of up to 12%. The weight loss may happen due to the thermal decomposition of hemicellulose, carbon dioxide, water, and microfibrils.

The hybrid bio composite samples had higher initial degradation temperatures and lower weight losses compared to the pure OPTs bio composite sample. The initial degradation temperatures of the hybrid bio composites occurred at a minimum of 309°C and a maximum of 341°C (Fig. 11b). This results were better when compared to those for binderless particleboards from OPTs [43], and particleboards from OPTs added with ammonium dihydrogen phosphate (ADP) [19]. These findings showed that hybridization with ramie fibers improved the thermal stability of OPTs bio composites. The results of thermogravimetric analysis indicated that the hybrid bio composites have the potential to be used as thermal insulation materials.

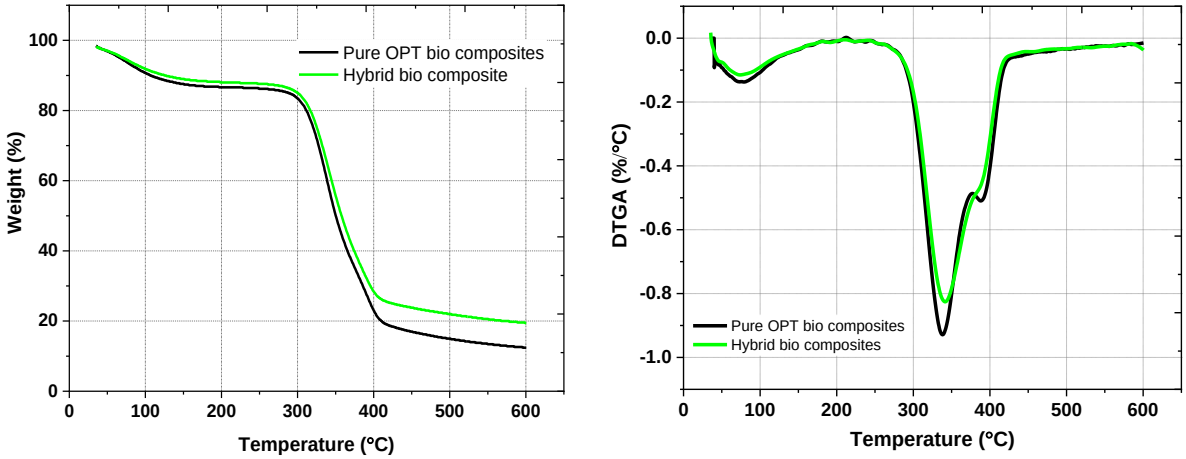

(a) (b)

Fig. 11. Thermal analysis of bio composites and hybrid bio composites (a) TGA and (b) DTGA

3.5. Analysis of Scanning Electron Microscopy (SEM)

Figure 12 shows the microscopic observations of the cross-sections of pure OPTs bio composite and hybrid bio composite samples under a scanning electron microscope (SEM). SEM micrographs of the pure OPTs bio composites and hybrid bio composite s are presented in Figure 12a and Figure 12b, respectively. Figure 12(a) shows that some fibers are well embedded in the matrix, while others show gaps or cavities around the fibers. The pure OPTs fibers are prone to detachment from the matrix, which impacts the composite's density, as higher void content results in lower density. The presence of voids in the bio composite indicates weak adhesion, which reduces the efficiency of stress transfer from the matrix to the fibers. This condition directly contributes to the decrease in the mechanical properties of the bio composite. The SEM image supports the results of the mechanical test, which shows low flexural and tensile strength. However, conversely, the voids serve as spaces for trapped air, which has low thermal conductivity. This phenomenon hinders heat flow through the material, as the air-filled pores act as insulators. In addition, the pores create

numerous interfaces between the solid and gas phases, each introducing thermal boundary resistance that further impedes heat flow.

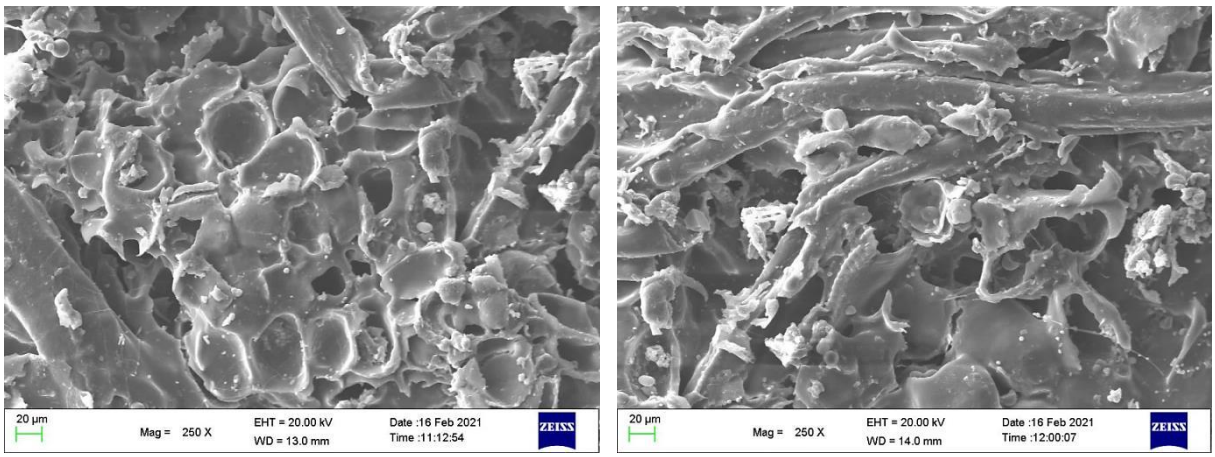

(a) (b)

Fig.12. SEM images of a cross section of composites (a) pure OPTs bio composite and (b) hybrid bio composite

Meanwhile, Figure 12b shows that additional ramie fibers produce a different morphology, where ramie fibers partially cover the parenchyma tissue. This tissue must be minimized due to its high water absorption capacity, which can reduce the mechanical properties of the bio composite . In some areas, ramie fibers appear well embedded in the matrix, while in other places, gaps between the fibers and the matrix indicate debonding. This debonding phenomenon has an impact on the decrease in the strength of the bio composite. However, overall, the presence of ramie fibre still positively contributes to increasing the elastic modulus and strengthening the structure, especially in composites with small particle sizes.

4. Conclusions

This study successfully developed a bio composite based on pure oil palm trunk and a hybrid bio composite combining oil palm trunk and ramie fiber. Overall, the results demonstrated that the addition of ramie fiber significantly improved the physical, mechanical, and thermal properties of the bio composite. Smaller oil palm trunk particle sizes improved water absorption resistance, thickness swelling, modulus of rupture (MOR), and modulus of elasticity (MOE), although not the thermal conductivity coefficient. The hybrid bio composite samples, especially types HC200, HC40, and HC20, exhibited good mechanical strength, water absorption resistance, dimensional stability, and thermal conductivity performance. The controlled water absorption and thickness swelling values, combined with adequate mechanical strength, indicate potential of this material for building insulation applications that require resistance to humidity fluctuations and light mechanical stress. In addition, the low thermal conductivity coefficient indicates the material capability to inhibit heat transfer, making it a strong candidate for energy savings by reducing indoor cooling or heating needs. The increased thermal stability with the presence of ramie fiber also expands the potential application of this material in higher-temperature environments.

Based on the results obtained, the hybrid bio composite of oil palm trunk and ramie fibers exhibits great potential for development as a renewable and environmentally friendly thermal insulation material. This result supports initiatives towards sustainable building materials and contributes to climate change mitigation through energy efficiency. Future research may explore several important directions. First, experiments with other types of natural fibers (such as kenaf, abaca, or bamboo fibers) or combinations with environmentally friendly synthetic fibers could further enhance the material's properties. Second, the use of various matrix materials, such as bio-based resins or natural polyurethanes, can be explored to improve the thermal and environmental performance. Third, long-term durability tests, including weathering, freeze-thaw cycles, and exposure to microorganisms, are important to validate the material's service life. Finally, a production cost analysis and a feasibility study for large-scale manufacturing should be conducted

to ensure the potential for widespread commercial application of this bio composite in the industrial sector.

Acknowledgments

The author thanks the Universitas Syiah Kuala and Politeknik Negeri Lhokseumawe, Aceh, Indonesia.

References

[1] Indonesia BS. Indonesian Oil Palm Statistic 2019. 2020; 9-17 ISBN 1978-9947
[2] Abnisa F, Arami-Niya A, Daud WMAW, Sahu JN, Noor IM. Utilization of oil palm tree residues to produce bio-oil and bio-char via pyrolysis. Energy Convers Manag. 2013;76:1073–82. https://doi.org/https://doi.org/10.1016/j.enconman.2013.08.038
[3] Saari N, Hashim R, Sulaiman O, Hiziroglu S, Sato M, Sugimoto T. Properties of steam treated binderless particleboard made from oil palm trunks. Compos Part B Eng. 2014;56:344–9. https://doi.org/https://doi.org/10.1016/j.compositesb.2013.08.062
[4] Selamat ME, Hashim R, Sulaiman O, Kassim MHM, Saharudin NI, Taiwo OFA. Comparative study of oil palm trunk and rice husk as fillers in gypsum composite for building material. Constr Build Mater. 2019;197:526–32. https://doi.org/10.1016/j.conbuildmat.2018.11.003
[5] Mawardi I, Nurdin N, Fakhriza F, Rizal S, Aprilia S, Faisal M, et al. Optimization of Particle Size and Ramie Fiber Ratio on Hybrid Bio Panel Production from Oil Palm Trunk as Thermal Insulation Materials. J Ecol Eng. 2023;24(2):39–49. https://doi.org/10.12911/22998993/156830
[6] Asdrubali F, D'Alessandro F, Schiavoni S. A review of unconventional sustainable building insulation materials. Sustain Mater Technol. 2015;4:1–17. https://doi.org/ 10.1016/j.susmat.2015.05.002
[7] Abu-Jdayil B, Mourad AH, Hittini W, Hassan M, Hameedi S. Traditional, state-of-the-art and renewable thermal building insulation materials: An overview. Constr Build Mater. 2019;214:709–35. https://doi.org/10.1016/j.conbuildmat.2019.04.102
[8] Ikubanni PP, Adeleke AA, Adekanye TA, Aladegboye OJ, Agboola OO, Ogunsemi BT. Particleboard from biomass wastes: A review of production techniques, properties, and future trends. R Res. Eng. Struct. Mater., 2025; 11(2): 713-740. http://doi.org/10.17515/resm2024.265ma0502rv
[9] Mehta PK, Kumarswamy A, Saraswat VK, Shekhar H. Manufacturing brick using waste rocket propellant: thermal insulation improvement through eco-friendly disposal. Res Eng Struct Mater. 2022;8(1):91–99. http://doi: 10.17515/resm2021.313st0615tn
[10] Kilani A, Fapohunda C, Adeleke O, Metiboba C. Evaluating the effects of agricultural wastes on concrete and composite mechanical properties. Res Eng Struct Mater. 2022;8(2):307–36. https://doi.org/10.17515/resm2021.339st0912
[11] Cetiner I, Shea AD. Wood waste as an alternative thermal insulation for buildings. Energy Build. 2018;168:374–84. https://doi.org/10.1016/j.enbuild.2018.03.019
[12] Binici H, Aksogan O, Dıncer A, Luga E, Eken M, Isikaltun O. The possibility of vermiculite, sunflower stalk and wheat stalk using for thermal insulation material production. Therm Sci Eng Prog. 2020;18:100567. https://doi.org/10.1016/j.tsep.2020.100567
[13] Nguyen DM, Grillet AC, Bui QB, Diep TMH, Woloszyn M. Building bio-insulation materials based on bamboo powder and bio-binders. Constr Build Mater. 2018;186:686–98. https://doi.org/10.1016/j.conbuildmat.2018.07.153
[14] Yaswan R, Kasim A, Nazir N, Malrianti Y, Ilyas RA. The Effect of Comparative Differences in Composition of Oil Palm Empty Fruit Bunches (OP-EFB) and HDPE Plastics: Physical and Mechanical Properties of Wood Plastic Composite (WPCs). J Fibers Polym Compos. 2025;4(1):56–67. https://doi.org/10.55043/jfpc.v4i1.248
[15] Viel M, Collet F, Lanos C. Development and characterization of thermal insulation materials from renewable resources. Constr Build Mater. 2019;214:685–97. https://doi.org/10.1016/j.conbuildmat.2019.04.139
[16] Chaudhary DS, Adhikari BP. Understanding polymeric amylose retrogradation in presence of additives. J Appl Polym Sci. 2010;115(5):2703–9. https://doi.org/10.1002/app.29906
[17] Mawardi I, Aprilia S, Faisal M, Rizal S. An investigation of thermal conductivity and sound absorption from binderless panels made of oil palm wood as bio-insulation materials. Results Eng. 2021;100319. https://doi.org/10.1016/j.rineng.2021.100319
[18] Elias NA, Othman SA. Preparation and Characterization of Oil Palm Tree for Insulation Material. Int J Sustain Constr Eng Technol. 2022;13(3):195–201. https://doi.org/10.30880/ijscet.2022.13.03.018
[19] Komariah RN, Miyamoto T, Tanaka S, Prasetiyo KW, Syamani FA, Umezawa T, et al. High-performance binderless particleboard from the inner part of oil palm trunk by addition of ammonium dihydrogen phosphate. Ind Crops Prod. 2019;141:111761. https://doi.org/10.1016/j.indcrop.2019.111761

[20] Ramlee NA, Jawaid M, Zainudin ES, Yamani SAK. Tensile, physical and morphological properties of oil palm empty fruit bunch/sugarcane bagasse fibre reinforced phenolic hybrid composites. J Mater Res Technol. 2019;8(4):3466–74. https://doi.org/10.1016/j.jmrt.2019.06.016
[21] Korkees F, Arnold C, Alston S. Water absorption and low-energy impact and their role in the failure of±45 carbon fibre composites. Polym Compos. 2018;39(8):2771–82. https://doi.org/10.1002/pc.24269
[22] Asrofi M, Sapuan SM, Ilyas RA, Ramesh M. Characteristic of composite bioplastics from tapioca starch and sugarcane bagasse fiber: Effect of time duration of ultrasonication (Bath-Type). Mater Today Proc. 2021;46:1626–30. https://doi.org/10.1016/j.matpr.2020.07.254
[23] Khalil HPSA, Dungani R, Hossain MS, Suraya NLM, Aprilia S, Astimar AA, et al. Mechanical properties of oil palm bio composite s enhanced with micro to nanobiofillers. In: Bio composite s. Elsevier; 2015. p. 401–35. https://doi.org/10.1016/B978-1-78242-373-7.00026-3
[24] Balla VK, Kate KH, Satyavolu J, Singh P, Tadimeti JGD. Additive manufacturing of natural fiber reinforced polymer composites: Processing and prospects. Compos Part B Eng. 2019;106956. https://doi.org/10.1016/j.compositesb.2019.106956
[25] Jumhuri N, Hashim R, Sulaiman O, Nadhari WNAW, Salleh KM, Khalid I, et al. Effect of treated particles on the properties of particleboard made from oil palm trunk. Mater Des. 2014;64:769–74. https://doi.org/10.1016/j.matdes.2014.08.053
[26] Shinoj S, Visvanathan R, Panigrahi S, Kochubabu M. Oil palm fiber (OPF) and its composites: A review. Ind Crops Prod. 2011;33(1):7–22. https://doi.org/10.1016/j.indcrop.2010.09.009
[27] A 5908. Japanese Industrial Standard: Particleboards. Tokyo, JSA: JIS Japan; 2003.
[28] D790 A. Standard Test Methods for Flexural Properties of Unreinforced and Reinforced Plastics and Electrical Insulating Materials. West Conshohocken, PA, USA: ASTM International; 2003.
[29] D3039 A. Standard Test Method for Tensile Properties of Polymer Matrix Composite Materials. West Conshohocken, PA, USA: ASTM International; 2014.
[30] C177-97. Standard Test Method for Steady-State Heat Flux Measurements and Thermal Transmission Properties by Means of the Guarded-Hot-Plate Apparatus. West Conshohocken, PA, USA: ASTM International; 1997.
[31] Limam A, Zerizer A, Quenard D, Sallee H, Chenak A. Experimental thermal characterization of bio-based materials (Aleppo Pine wood, cork and their composites) for building insulation. Energy Build. 2016;116:89–95. https://doi.org/10.1016/j.enbuild.2016.01.007
[32] Lamaming J, Hashim R, Sulaiman O, Sugimoto T, Sato M, Hiziroglu S. Measurement of some properties of binderless particleboards made from young and old oil palm trunks. Measurement. 2014;47:813–9. https://doi.org/10.1016/j.measurement.2013.10.007.
[33] Mawardi I, Nurdin N, Razak H, Amalia I, Sariyusda S, Aljufri A, et al. Development of Lightweight Engineered Wood Produced from Derived Sugarcane Bagasse and Coir Fiber: Evaluation of the Bending and Thermal Properties. J Korean Wood Sci Technol. 2025;53(1):1–13. https://doi.org/10.5658/WOOD.2025.53.1.1
[34] Pan Z, Zheng Y, Zhang R, Jenkins BM. Physical properties of thin particleboard made from saline eucalyptus. Ind Crops Prod. 2007;26(2):185–94. https://doi.org/10.1016/j.indcrop.2007.03.006
[35] Pham Van T, Schöpper C, Klüppel A, Mai C. Effect of wood and panel density on the properties of lightweight strand boards. Wood Mater Sci Eng. 2021;16(4):237–45. https://doi.org/10.1080/17480272.2019.1705906
[36] Wei K, Lv C, Chen M, Zhou X, Dai Z, Shen D. Development and performance evaluation of a new thermal insulation material from rice straw using high frequency hot-pressing. Energy Build. 2015;87:116–22. https://doi.org/10.1016/j.enbuild.2014.11.026
[37] Mawardi I, Aprilia S, Faisal M, Rizal S. Investigation of thermal conductivity and physical properties of oil palm trunks/ramie fiber reinforced biopolymer hybrid composites as building bio-insulation. Mater Today Proc. 2022. https://doi.org/10.1016/j.matpr.2022.01.249
[38] Mokhena TC, Mochane MJ, Motaung TE, Linganiso LZ, Thekisoe OM, Songca SP. Sugarcane bagasse and cellulose polymer composites. Sugarcane-Technology Res. 2018;225–40. http://doi.org/10.5772/intechopen.71497
[39] Mati-Baouche N, De Baynast H, Lebert A, Sun S, Lopez-Mingo CJS, Leclaire P, et al. Mechanical, thermal and acoustical characterizations of an insulating bio-based composite made from sunflower stalks particles and chitosan. Ind Crops Prod. 2014;58:244–50. https://doi.org/10.1016/j.indcrop.2014.04.022
[40] Patil SP, Bachhav BS, Markert B. Thermal conductivity of glass fiber-reinforced silica aerogels using molecular dynamics simulations. Ceram Int. 2022;48(2):2250–6. https://doi.org/10.1016/j.ceramint.2021.10.002
[41] Muthuraj R, Lacoste C, Lacroix P, Bergeret A. Sustainable thermal insulation bio composite s from rice husk, wheat husk, wood fibers and textile waste fibers: Elaboration and performances evaluation. Ind Crops Prod. 2019;135:238–45. https://doi.org/10.1016/j.indcrop.2019.04.053

[42] Ali ME, Alabdulkarem A. On thermal characteristics and microstructure of a new insulation material extracted from date palm trees surface fibers. Constr Build Mater. 2017;138:276–84. https://doi.org/10.1016/j.conbuildmat.2017.02.012

[43] Baskaran M, Hashim R, Said N, Raffi SM, Balakrishnan K, Sudesh K, et al. Properties of binderless particleboard from oil palm trunk with addition of polyhydroxyalkanoates. Compos Part B Eng. 2012;43(3):1109–16. https://doi.org/10.1016/j.compositesb.2011.10.008

Research on Engineering Structures & Materials
www.jresm.org
MIM Research Group

Research Article

Enhancement of mechanical properties and sulfuric acid resistance in slag-based geopolymer mortars via metakaolin incorporation

Zahraa Mohammed Kamil Al-Mayali [a], Mahmoud Ziada [*,b]

Department of Civil Engineering, Istanbul Aydin University, Istanbul, Türkiye

Article Info

Article History:

Received 08 May 2025

Accepted 02 Aug 2025

Keywords:

Metakaolin;
Slag;
Geopolymer;
Sulfuric acid;
Mechanical properties

Abstract

This study addresses the impact of metakaolin insertion on the mechanical features and resistance of sulfuric acid of geopolymer mortars composed primarily of ground-granulated blast furnace slag. Several mortar mixtures were created by partially substituting slag with different quantities of metakaolin (0–40%) and activated using a mixture of sodium hydroxide and sodium silicate solutions. Slump flow tests were conducted on the freshly created geopolymer mortar mixtures. After 28 days, capillary water absorption and the voids ratio were determined to assess the physical features of the geopolymer mortars. The mechanical performance of the mortars was measured using flexural strength, ultrasonic pulse velocity (UPV), and compressive strength tests at 28 days, while their durability was evaluated by submerging them in a 5% sulfuric acid solution for 28 days. Weight variations, mechanical assessments, and microstructural analyses were conducted on geopolymer mortars submerged in sulfuric acid to clarify the alterations in the geopolymer matrix. The findings indicated that a 30% substitution of metakaolin augmented flexural strength, compressive strength, and enhanced acid resistance by facilitating the development of a denser and chemically stable aluminosilicate gel. Following 28 days of exposure to sulfuric acid, the compressive strength of 30MK samples increased by 73.05% in comparison to the 0MK samples. This work demonstrates that the use of metakaolin enhances the balance between mechanical features and resistance of acid in slag-based geopolymer specimens, providing a sustainable and resilient alternative to traditional binders.

© 2025 MIM Research Group. All rights reserved.

1. Introduction

Geopolymer composites are binders created by amalgamating amorphous aluminosilicates and natural pozzolans, like red mud, metakaolin, and fly ash, using activators including sodium hydroxide (NaOH) and sodium silicate (Na_2SiO_3) [1,2]. The geopolymer structure comprises randomly interconnected silicon tetrahedra, with some silicon cations substituted by aluminum. Geopolymers exhibit superior mechanical properties compared to Portland cement, comprising improved thermal resistance, compressive strength, and diminished water absorption, along with beneficial chemical properties, including resistance to acids and the immobilization of hazardous substances [3,4]. Unlike cement, its production does not require sintering at high temperatures procedure, resulting in diminished CO_2 emissions [5].

Recently, geopolymers have garnered heightened interest for their possible application as building materials and eco-friendly binders that may partially substitute standard Portland cement (OPC) [6,7]. Studies demonstrate that geopolymers exhibit enhanced mechanical characteristics [8], including enhanced initial strength and reduced shrinkage [9,10]. Moreover, geopolymers can

*Corresponding author: mahmoudm.s.ziada@aydin.edu.tr
[a]orcid.org/0009-0008-1126-9992; [b]orcid.org/0000-0003-2986-6759
DOI: http://dx.doi.org/10.17515/resm2025-884me0508rs
Res. Eng. Struct. Mat. Vol. 11 Iss. 4 (2025) 1749-1765

serve as fireproof elements [11] owing to their intrinsic lightweight and thermal insulating characteristics [12,13]. Geopolymer composites can be manufactured using various sources, including byproducts. Metakaolin, slag, kaolin, and fly ash are the traditional basic substances utilized in the manufacture of geopolymer paste, mortar, and concrete [14].

Metakaolin, an exceptionally reactive pozzolanic substance, is a dehydroxylated variant of kaolinite [15]. Metakaolin functions as a valuable admixture, providing multiple benefits, including porosity, enhanced specific surface area, substantial absorbency, and robust coordinative bonding upon activation [16]. The initial response procedure and effectiveness of geopolymer based on metakaolin are impacted by the chemical makeup [17], dosing, and content of raw components [18–20], together with the curing parameters during the initial polymerization phase [21,22]. Xiao et al. [23] evaluated the synergistic effect of seawater and metakaolin on the efficacy of cementitious materials based on phosphogypsum as a sustainable substitute for Ordinary Portland Cement. Their results indicated that metakaolin improved long-term strength by facilitating the synthesis of N-A-S-H gel, providing both mechanical and environmental advantages. In addition, Guang Liang et al. [24] investigated the influence of coal-bearing metakaolin with varying specific surface areas on the sulfuric acid resistance of cement paste. Their results indicated that finer metakaolin markedly decreased porosity and deterioration while augmenting compressive strength and durability by boosting hydration product retention and restricting corrosion in acidic environments.

Alternative binders and additives have been investigated to enhance strength and durability in cementitious and various systems. Karimiazar et al. [25] revealed that the combined application of nano-silica and lime improved the strength and durability of sulfate-laden marl soil by facilitating secondary CSH gel formation and inhibiting ettringite formation. Teshnizi et al. [26] shown that cement kiln dust (CKD), an industrial by-product, enhanced the strength, stiffness, and durability of loess soil via particle aggregation and calcium-based gel formation, providing a sustainable alternative to conventional stabilizers. Karimiazar et al. [27] similarly observed that the treatment of reactive clay with 3% cement and 1% nano-silica or nano-alumina greatly enhanced the soaking CBR, improved the microstructure, and decreased swell potential, obtaining performance akin to greater cement concentrations. Mirzababaei et al. [28] discovered that the incorporation of 3% cement with nano-silica or nano-alumina improved the strength and water resistance of marl, allowing a reduction in cement consumption by augmenting CSH formation and decreasing porosity. Hashemi et al. [29] enhanced the stability of collapsing soils along the Sabzevar-Mashhad railway by using 5–10% lime and cement, noting an improvement in shear strength attributed to increased friction angles, with lime yielding superior compaction and less collapse potential compared to cement. Ezazi et al. [30] undertook experimental and computational investigations on the Chamshir tunnel lining, determining that segments reinforced with steel fibers and fiber-reinforced rebar exhibited superior strength and resistance to damage from TBM jack thrust compared to conventional rebar-reinforced concrete.

Additionally, geopolymers are employed as protective covering materials. Geopolymers offer benefits such as high strength, exceptional mechanical properties, and adjustable setting periods. In addition, geopolymers exhibit remarkable resistance to acid and alkali corrosion, as well as superior high-temperature endurance, characteristics typically lacking in traditional organic concrete protection methods. As a result, alkali-activated metakaolin-based geopolymers may possess considerable promise for applications in concrete surface protection [31,32]. Teshnizi et al. [33] examined the synergistic use of gypsum and rice husk ash for the stabilization of expanding clay soils on forest road subgrades. Their findings indicated enhanced strength, less flexibility and swelling, and the development of CSH and CAH gels, underscoring a sustainable approach to improving road stability in difficult soil conditions.

Portland cement-based materials frequently exhibit inadequate resistance to acid attack, resulting in a reduced service life for exposed structures. Structural deterioration results in various social, environmental, and physical consequences. The material obstacle can be established by placing barrier coatings on the composite surface to decrease the risk of chemical assault, thereby limiting acid infiltration into the concrete microstructure [34,35]. Nonetheless, these methods are costly

and laborious [36]. Although barrier coatings mitigate acid intrusion, they increase expenses and maintenance requirements. Geopolymers have inherent chemical resistance, providing a more cost-effective and resilient option. Recently, geopolymer binders have come to prominence as a feasible remedy to the effects of acid, owing to their microstructure. Extensive studies have been conducted on geopolymers due to their significant advantages in acid resistance. Geopolymers can produce acid-resistant materials appropriate for sewer pipelines, water tanks, and diverse applications in acidic environments. A previous study [37] investigated the acid deterioration process of fly-ash and showed a similar deteriorating using a geopolymer without of calcium. The sole distinction is that the dispersing SO_4^{2-} anions encounter the diffusing ions of calcium, resulting in the precipitation of crystals of gypsum within the infiltrating layer. Teshnizi et al. [38] assessed the impact of acid and temperature exposure on the compressive strength of geopolymer samples formulated from sustainable resources, including slag, zeolite, metakaolin, and Portland cement. The research indicated that slag-based mixes, especially those containing 8 M KOH, demonstrated enhanced resistivity and compressive strength under harsh circumstances, but alterations in alkaline activator concentration markedly affected durability. Shalan and Mohamed M. El-Gohary [39] investigated the influence of the chemical composition of geopolymers on the sulfuric acid resistance and mechanical features of the concrete. Their results indicated that elevated Al/Si and MgO concentrations, especially in conjunction with slag and metakaolin, facilitated the production of hydrotalcite and CASH, decreased porosity, and boosted resistance to acid assault. A further study [40] utilized metakaolin as an interim replacement for fly ash that is high in calcium in geopolymer materials and determined that the materials demonstrated enhanced the durability of acid impact compared to the singular material, attributable to the reduced calcium in the composites. Geopolymer compositions with various binders have varying sulfuric acid resistance, particularly for binders with and without calcium. Consequently, it is essential to evaluate the geopolymers' resistance, formulated with various binders, particularly slag and metakaolin, to sulfuric acid.

Despite increasing interest in alkali-activated materials that include slag and metakaolin, a comprehensive understanding of their performance under sulfuric acid exposure is still insufficient. The majority of the research done so far has only looked at geopolymers made from metakaolin or slag. However, there has been a dearth of research into how these two factors interact to improve mechanical performance, microstructural features, and chemical durability, especially when subjected to harsh environments like acid. Consequently, in this research, varying quantities of metakaolin were incorporated into slag at ambient temperature to construct a two-blend geopolymer mortar. The impact of metakaolin on the mechanical and microstructure characteristics of slag-based geopolymer mortar exposed to sulfuric acid was examined through various tests. Thus, this work focuses on improving the performance of slag-based geopolymers in adverse conditions by using metakaolin to create more durable composites. This fosters ecological and economic alternatives to conventional cement systems.

2. Materials and Experimental Methods

2.1. Materials Specification

This study utilized slag and metakaolin as binders, with their chemical compositions presented in Table 1. The specific gravities of slag and metakaolin were 2.9 and 2.4 g/cm^3, respectively. In addition, NaOH and Na_2SiO_3 served as activators in the geopolymer formulations, with their chemical properties presented in Tables 2 and 3. NaOH was used in the form of solid beads, while Na_2SiO_3 was provided as a commercially available solution. In addition, the fine aggregate utilized during this investigation was standard sand, according to the specifications of EN 196-1 [41]. This sand has a controlled particle size range between 0.08 mm and 2.00 mm. The fineness modulus is 2.70 and the sand was used in dry form to ensure correct mixing ratios. Moreover, sulfuric acid was employed as the acidic medium to examine the acid resistance of geopolymer mortar samples. Sulfuric acid was used at a concentration of 5% in this investigation.

Table 1. Chemical proportions of slag and metakaolin (%)

Materials	L.O.I.*	CaO	Fe_2O_3	MgO	SiO_2	Na_2O	Al_2O_3	K_2O	TiO_2
Slag	0.6	35.58	1.1	6.58	40.55	0.79	13.8	0.4	0.6
Metakaolin	1.17	0.19	0.85	0.16	56.1	0.24	40.23	0.51	0.55

*Loss of Ignition (L.O.I.)

Table 2. The chemical composition of the sodium silicate solution used (%)

SiO_2	Heavy metals	Na_2O	Fe	H_2O
27	≤ 0.005	8.2	≤ 0.005	64.8

Table 3. The chemical composition of sodium hydroxide (%)

Al (%)	Na_2CO_3	Cl (%)	NaOH	SO_4 (%)	Fe (%)
≤ 0.002	0.4	≤ 0.01	99.6	≤ 0.01	≤ 0.002

2.2. Proportions and Fabrication of Geopolymer Specimens

To make a 12M sodium hydroxide solution, 240g of sodium hydroxide was introduced to a 500 mL volumetric flask and was then filled up to the 500 mL mark with distilled water. Prior to formulating the slag-metakaolin geopolymer slurry used in the present study, a 12M sodium hydroxide solution was generated and permitted to cool at 20° C for one day. The sodium hydroxide was subsequently combined with the Na_2SiO_3 solution. Then, metakaolin was replaced with slag at rates of 0, 10, 20, 30, and 40% to form a dry binder mixture with sand. Then, the dry ingredients were mixed in a standard mortar mixer at 100 rpm for 2 min. Subsequently, the activator solution was added to this dry mixture and mixed at 150 rpm for 2 minutes to make it homogeneous. The mixtures were then placed in greased molds measuring 50×50×50mm and 40×40×160mm. The molds were then positioned on a vibrating table and compacted for 1 min at a frequency of 50 Hz to reduce trapped air and provide consistent density. The samples were subsequently extracted from the mold and preserved at 20 ± 2 °C for a duration of 28 days. Table 4 presents the quantities of the mixes utilized in this study.

Table 4. Design of geopolymer blends (kg/m^3)

Mixtures	NaOH	Na_2SiO_3	slag	aggregate	Metakaolin
0Mk	136.83	273.67	586.44	1267.69	0
10Mk	136.83	273.67	527.80	1256.94	58.64
20Mk	136.83	273.67	469.15	1246.19	117.28
30Mk	136.83	273.67	410.51	1236.42	175.93
40Mk	136.83	273.67	351.86	1223.71	234.57

2.3. Performed Tests

This study evaluated slump flow values, water absorption, UPV results, compressive strength, bending strength, mass changes, and visual assessment on geopolymer samples to evaluate the influence of metakaolin on the sulfuric acid resistance and mechanical characteristics of slag-based geopolymer mortars. In addition, scanning electron microscope (SEM) analysis was conducted to examine the microstructural properties of the samples. Slump flow values were evaluated for each mixture containing varying percentages of metakaolin to ascertain the mixture's consistency. The blends were arranged in 2 levels inside a cone apparatus on top, and the levels was tapped with hammer made of wood and copper as shown in Figure 1. After the installation process, the flat surface was thrown twenty-five times due to hand rotation. The cone was then elevated perpendicularly, then the spreading measurements in 2 distinct orientations were evaluated and averaged.

Fig. 1. Slump flow experiment conducted on fresh geopolymer mixtures

The compressive strength test was conducted by applying load to cube specimens of 50×50×50 mm using a pressing machine with a capacity of 250 kN and a loading rate of 0.6 MPa/sec in accordance with ASTM C109 [42] as illustrated in Figure 2 (a). Flexural strength tests were performed on 40 × 40 × 160 mm specimens with a loading rate of 0.469 MPa/sec to determine the flexural strength according to ASTM C348 [43] as presented in Figure 2 (b). These tests were first performed on geopolymer samples before immersion in a sulfuric acid solution. Moreover, a capillary water absorption experiment was carried out on geopolymer samples based on slag and metakaolin in accordance with ASTM C1585 [44]. Geopolymer samples consisting of slag and metakaolin prismatic specimens were subjected to drying for one day at 105°C. The samples' dry weight, subsequent to the application of Vaseline, excluding the surfaces in touch by water, was measured. Then, the dried samples were submerged in 5 mm depth of water. The samples were subsequently extracted from the water, and immersed sample weights (Ww) was recorded at different times. The findings were subsequently created, and the capillary water curves were conducted.

(a) (b)

Fig. 2. (a) Compressive strength and (b) flexural strength experiments conducted on hardened geopolymer samples

Furthermore, the sulfuric acid was diluted to a 5% concentration, and the specimens were replaced in the acid solution for 28 days at 20°C as illustrated in Figure 3. The solution was renewed every 7 days to maintain a constant concentration throughout the exposure period. This approach

ensured that the acidity level remained relatively stable. The compressive strength of the acid-exposed specimens was retested after 14 and 28 days. Similarly, flexural strength testing was performed on the geopolymer specimens after acid exposure at 14 and 28 days. In addition, mass change measurements were also performed on the cubic specimens, and a UPV test was performed on the cubic specimens before and after acid exposure after three, seven, fourteen, and twenty-eight days, following ASTM C597 [45] as presented in Figure 4.

(a) (b)

Fig. 3. Geopolymer samples immersed in sulfuric acid: (a) cubic, (b) prismatic specimens

Fig. 4. UPV experiment conducted on cubic geopolymer samples

Moreover, the specimens were categorized according to their metakaolin replacement ratio by weight to provide clarity in the presentation of the test findings. The sample codes used in the investigation are: 0Mk (0% metakaolin - 100% slag), 10Mk (10% metakaolin - 90% slag), 20Mk (20% metakaolin - 80% slag), 30Mk (30% metakaolin - 70% slag), and 40Mk (40% metakaolin - 60% slag).

3. Results

3.1. Slump Flow Values

Slump flow testing is the primary method and provides an exceptional assessment of workability. Despite their significant restrictions, workability evaluations are utilized for performance assurance and composite specifications. The creation of stable mixes with little slump flow has led to the adoption of flow testing [46]. Figure 5 depicts the median flow rates of metakaolin-substituted slag-based geopolymer mortar specimens. A peak flow of 166.7 mm was obtained from the 0MK geopolymer sample. Increasing the metakaolin concentration in geopolymer samples diminished the flow measurements of slag-based geopolymer mixes. The diameter diminishes were 0.69%, 1.08%, 1.44%, and 5.76% for 10MK, 20MK, 30MK, and 40MK, respectively, relative to the 0MK sample. The slump flow was probably reduced by the large surface area of metakaolin, which increased the water requirement, according to previous research [47,48].

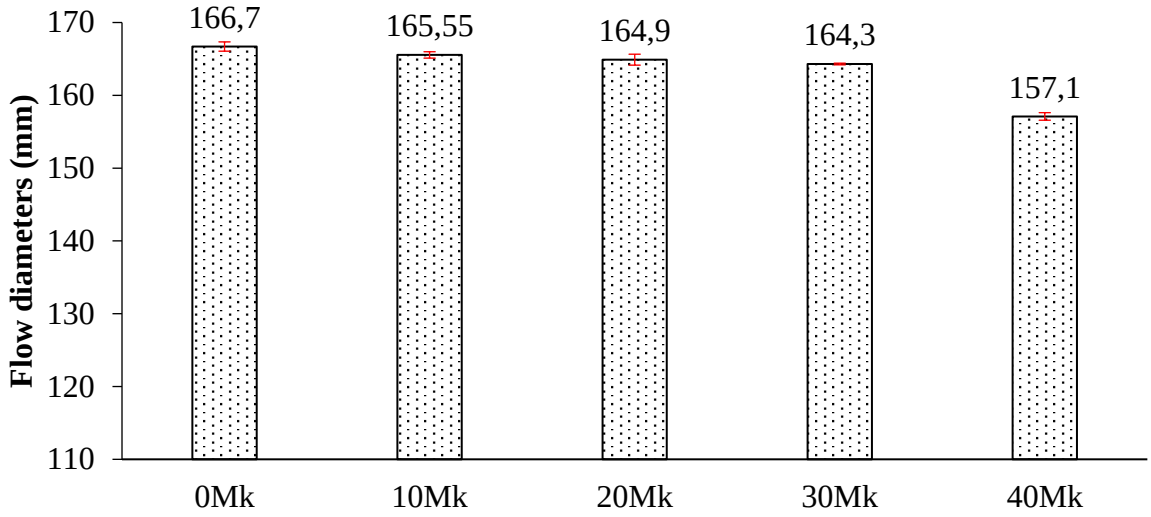

Fig. 5. Slump flow values of metakaolin substituted slag-based geopolymer mortar specimens

3.2. Water Absorption

Experiments for water absorption and capillary water absorption were conducted to evaluate the porosity of the geopolymer mortar specimens. Figure 6 depicts the void ratios and water absorption ratios. Figure 6 demonstrates that the sample containing 40Mk displayed the minimal void ratio, resulting in the smallest water absorption ratio relative to the remaining specimens. The sample void ratios decreased from 0Mk to 40Mk. The result reached is that the 40Mk sample demonstrated the greatest density. In addition, Figure 7 depicts the capillary water absorption curves of geopolymer samples with various metakaolin contents. The water absorption test produced consistent results, with 40Mk demonstrating the minimal water absorption relative to the remaining specimens. The capillary water absorption coefficients (kc) were calculated to enable a more efficient comparison, as seen in Figure 8. The number of voids in the samples decreased as the metakaolin content increased from 0Mk to 40Mk. 4.48%, 19.85%, 29.38%, and 32.63%. Metakaolin, possessing a much greater surface area than slag, improves particle packing and occupies interstitial spaces among bigger slag particles, leading to a denser microstructure and enhanced compactness [49].

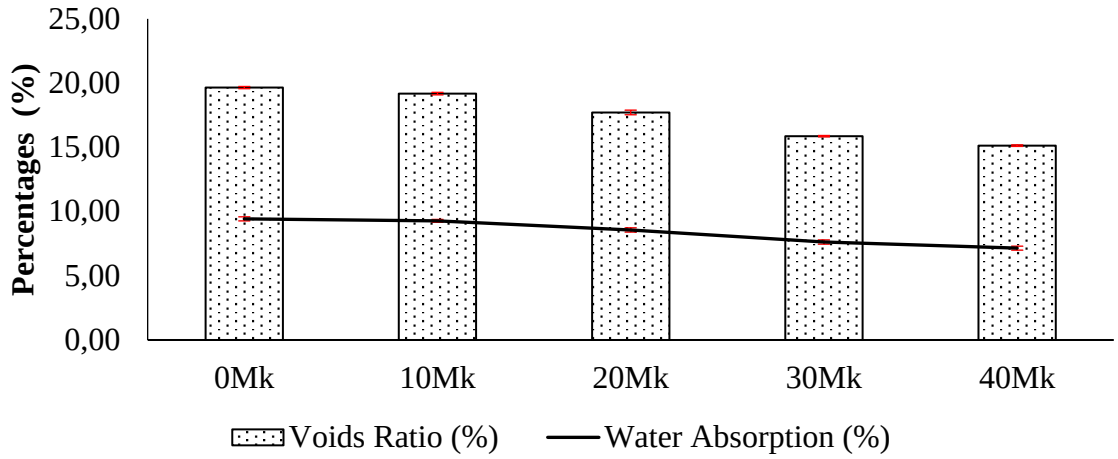

Fig.6. Water absorption and void ratios of slag-based geopolymer samples mixed with different proportions of metakaolin

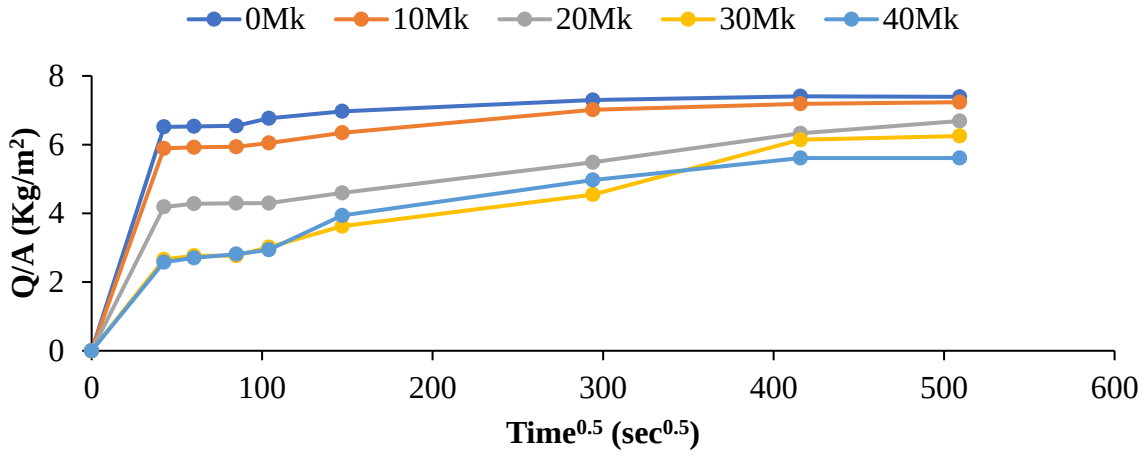

Fig. 7. The amount of water absorbed per square meter of slag-based geopolymer samples with varying metakaolin ratios

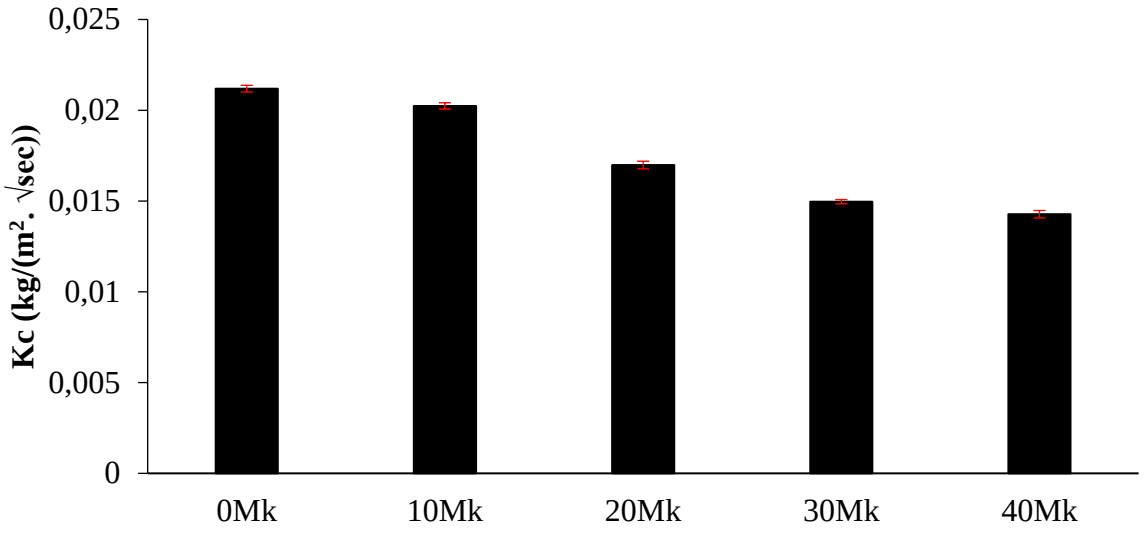

Fig. 8. Capillary water absorption coefficient of slag-based geopolymer cement with differing metakaolin ratios.

3.3. UPV Results

A UPV test was conducted on slag-based geopolymer samples with different proportions of metakaolin. This test sought to assess the impact of varied metakaolin concentrations on the specimens and to examine the consolidation of geopolymer following 28 days with differing metakaolin ratios. Figure 9 present the outcomes of the UPV experiment performed on the samples. A specimen matrix marked with a large number of voids requires a long permeation time, which reduces the permeation rate. The void ratio substantially influences the mechanical characteristics of geopolymer samples derived from slag and metakaolin. The study revealed that the highest UPV value in slag-based geopolymer samples was obtained at a concentration of 30MK after acid exposure. The UPV values of 30MK slag-based geopolymer samples increased by 30.91% compared to 0MK samples after 7 days of acid exposure. In addition, the UPV value of the 30MK sample exposed to acid until the 14th day increased by 18.29% compared to the 30MK sample that was not exposed to acid, while this percentage decreased to 16.06% after the 28th day of acid exposure. The increase in UPV values, especially in the first phase of acid exposure (7 and 14 days) observed in the 30MK samples, suggests that additional densification or filling of micro voids occurred in the geopolymer matrix. This can be explained by the fact that metakaolin forms a more chemically stable and dense aluminosilicate gel, and the N-A-S-H gel integrated with the slag-derived C-A-S-H gel forms a hybrid structure, which is less susceptible to acid-induced weathering and degradation. The 40MK samples had the greatest value prior to treatment with sulfuric acid. The void volume in the geopolymer structure exhibits an inverse correlation with the UPV values [50]. The enhancement is due to the smaller particle size and increased reactivity of metakaolin, which aids in the creation of a more chemically stable and denser aluminosilicate gel. Metakaolin facilitates the formation of N-A-S-H gel, which, when integrated with the C-A-S-H gel from slag, produces a hybrid gel structure that exhibits reduced vulnerability to acid-induced leaching and degradation [51,52]. This dual-gel technology has been shown to enhance durability and tolerance to harsh situations.

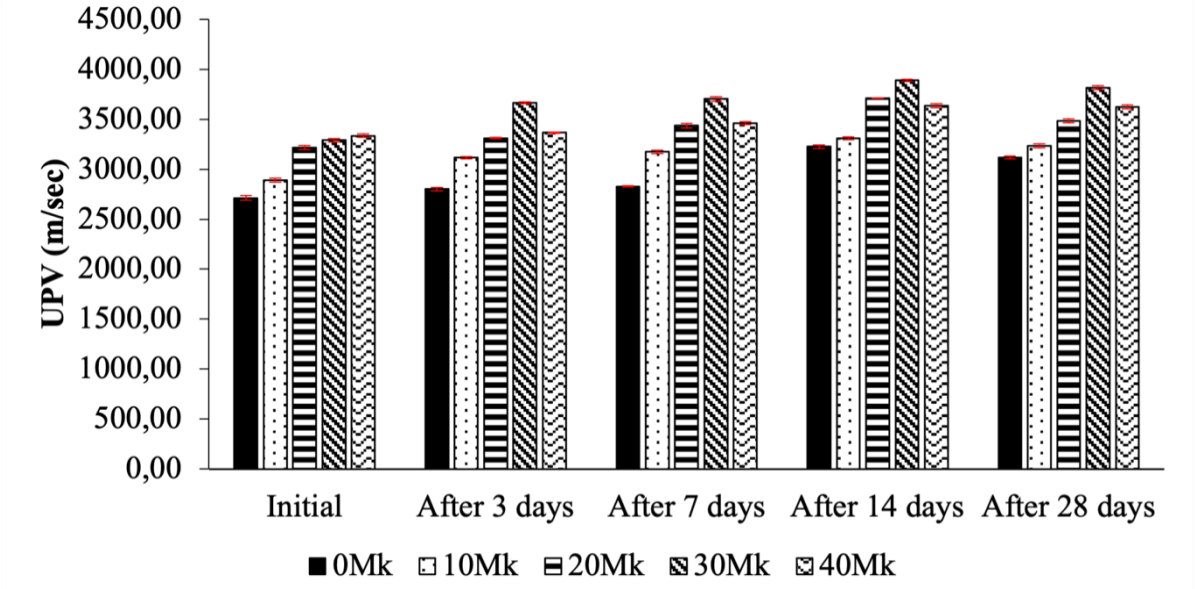

Fig. 9. UPV readings of geopolymer samples with different metakaolin ratios prior to and following exposure to sulfuric acid

3.4. Compressive Strength

This experiment aimed to investigate the mechanical properties of geopolymer samples with varying metakaolin concentrations. Three samples for each metakaolin concentration were examined prior to and following exposure to sulfuric acid for durations of 14 and 28 days. The obtained data were then averaged. Figure 10 shows the compressive strength results for geopolymer samples with varying metakaolin concentrations prior to and following fourteen and twenty-eight days of acid treatment. This work observed that the compressive strength of 40MK

exceeded the compressive strength of 0MK, 10MK, 20MK, and 30MK samples before acid exposure, while the compressive strength of 30MK exceeded the compressive strength of 0MK, 10MK, 20MK, and 40MK samples after 28 days of acid exposure. Despite the 40 MK combination demonstrating the greatest initial compressive strength, its performance declined following exposure to sulfuric acid in comparison to the 30 MK sample. This may result from the increased aluminosilicate content creating a denser gel, which improves initial mechanical strength but also adds more reactive sites susceptible to acid attack. Conversely, the 30 MK formulation seems to provide a superior equilibrium between chemical resilience and mechanical strength. Studies indicate that augmenting metakaolin concentration may elevate the Si/Al ratio; nevertheless, a larger Si/Al ratio does not always enhance acid resistance and may, in fact, diminish it owing to heightened gel depolymerization and dealumination in acidic environments [53]. In metakaolin-rich combinations, the abundant aluminosilicate structure is more vulnerable to sulfuric acid, resulting in increased strength degradation and observable deterioration relative to slag- or fly ash-based systems [54]. The data indicate that best acid resistance is attained not at maximum metakaolin concentration, but at intermediate levels when structural compactness and chemical resilience are more effectively matched.

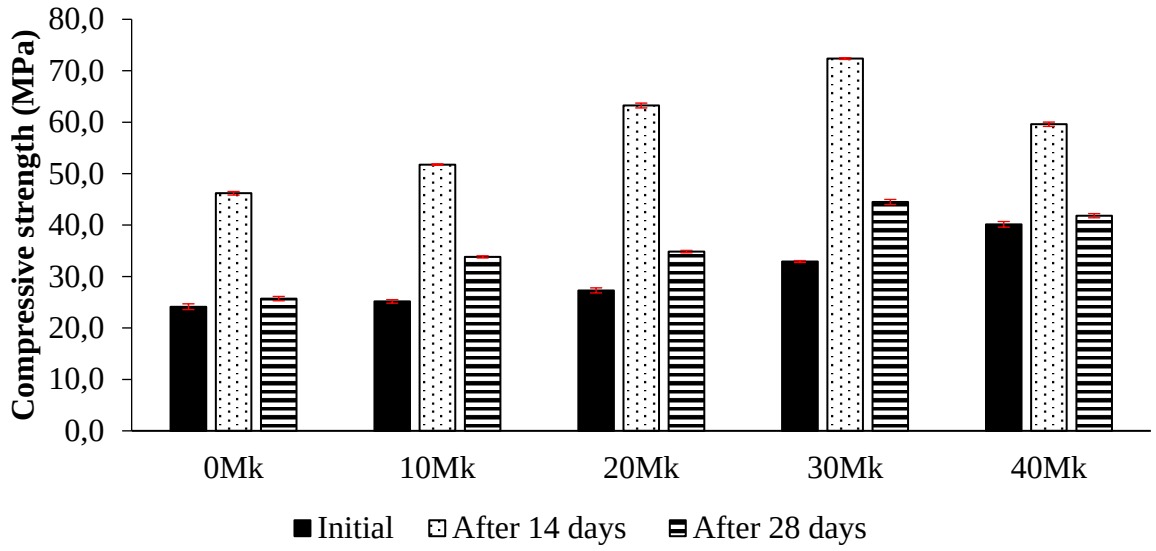

Fig. 10. Compressive strength findings of geopolymer samples with differing metakaolin proportions prior to and following 14 and 28 days of exposure to sulfuric acid

The compressive strength values of the metakaolin samples at 10MK, 20MK, 30MK, and 40MK increased compared to the samples without metakaolin before acid exposure by 4.29%, 13.12%, 36.43%, and 66.37%, respectively. This may be ascribed to the beneficial relationship between the alumina- and silica-rich metakaolin and calcium-rich slag. Metakaolin improves the polymerization process, creating C-A-S-H and N-A-S-H gels simultaneously, providing a denser and mechanically superior matrix [55]. The elevated reactivity and surface area of metakaolin promote a superior pore structure and enhanced particle packing, resulting in increased mechanical efficiency [56]. Following fourteen days of sulfuric acid treatment, the compressive strength values of the metakaolin samples at 10MK, 20MK, 30MK, and 40MK increased by 12.04%, 36.91%, 56.67%, and 29.05%, respectively, compared to the samples without metakaolin. In addition, subsequent to twenty-eight days of immersion in sulfuric acid, the compressive strength values of the 10MK, 20MK, 30MK, and 40MK samples increased by 31.51%, 35.52%, 73.05%, and 62.67%, respectively, compared with the 0MK samples. The reactive aluminosilicate properties of metakaolin form a three-dimensional geopolymer gel network (C-S-H and C-A-S-H), enhancing the density, strength, and mechanical properties [57]. After acid effect, the compression strength of the 30MK boosted by 119.82% following fourteen days compared to its initial strength before acid exposure. Also, after 28 days, the compressive strength of the 30Mk specimen reflected a 35.15% increase relative to strength before immersion in sulfuric acid. Thus, the compressive strength of the samples was

lower after 28 days of exposure to acid compared to the compressive strength after 14 days of exposure to acid. In cementitious concrete and geopolymers, sulfuric acid is believed to induce microstructural deterioration of geopolymer composites [58,59].

3.5. Flexural Strength

This experiment was conducted on geopolymer mortars. Flexural test sought to examine the mechanical properties of the mortar samples with various metakaolin concentrations. Average results were derived from the collected data. Figure 11 shows the strength results of mortar samples with various metakaolin concentrations subsequent to twenty-eight days of immersion in sulfuric acid. The research showed that the bending strength at 40MK concentration was superior to that of the metakaolin samples containing 0MK, 10MK, 20MK, and 30MK before acid exposure, while the flexural strength at 30MK concentration was superior to that of the metakaolin samples containing 0MK, 10MK, 20MK, and 40MK after acid exposure. As a result, the flexural strength enhancements of the 10MK, 20MK, 30MK, and 40MK geopolymer samples before acid treatment were 10.52%, 55.83%, 62.92%, and 90.03%, respectively, compared to the 0MK specimens. Subsequent to fourteen days of acid immersion, the flexural strength values of the 10MK, 20MK, 30MK, and 40MK geopolymer samples increased by 17.45%, 52.87%, 124.46%, and 115.71%, respectively, compared to the 0MK sample. After 28 days of exposure to sulfuric acid, the flexural strength values of geopolymer samples containing 10MK, 20MK, 30MK, and 40MK increased by 21.29%, 66.65%, 106.05%, and 103.18%, respectively, compared to the sample not exposed to 0MK. In addition, in comparison to the flexural strength of 30MK specimens that were not submersed in the acid solution, the flexural strength of 30MK specimens subjected to acid treatment for fourteen days boosted by 41.05%, while this increase decreased to 19.31% after 28 days. Thus, the flexural strength of mortar specimens submersed in sulfuric acid boosted after fourteen days, but this improvement declined significantly following twenty-eight days. This study demonstrated that metakaolin reacted with an alkaline solution to form geopolymer gels (e.g., C-S-H and C-A-S-H). Early exposure to sulfuric acid enhanced the interaction between the raw materials and the geopolymer gel, enhancing its strength for up to 14 days. Following 28 days of exposure to sulfuric acid, the geopolymer bonds began to degrade due to acid ions and the dissolution of silicates and aluminates, resulting in a decrease in their strength. Similar results were observed in a previous study, which indicated that sulfuric acid led to a decrease in strength, which is attributed to the dissolution of the aluminosilicate bonds [60].

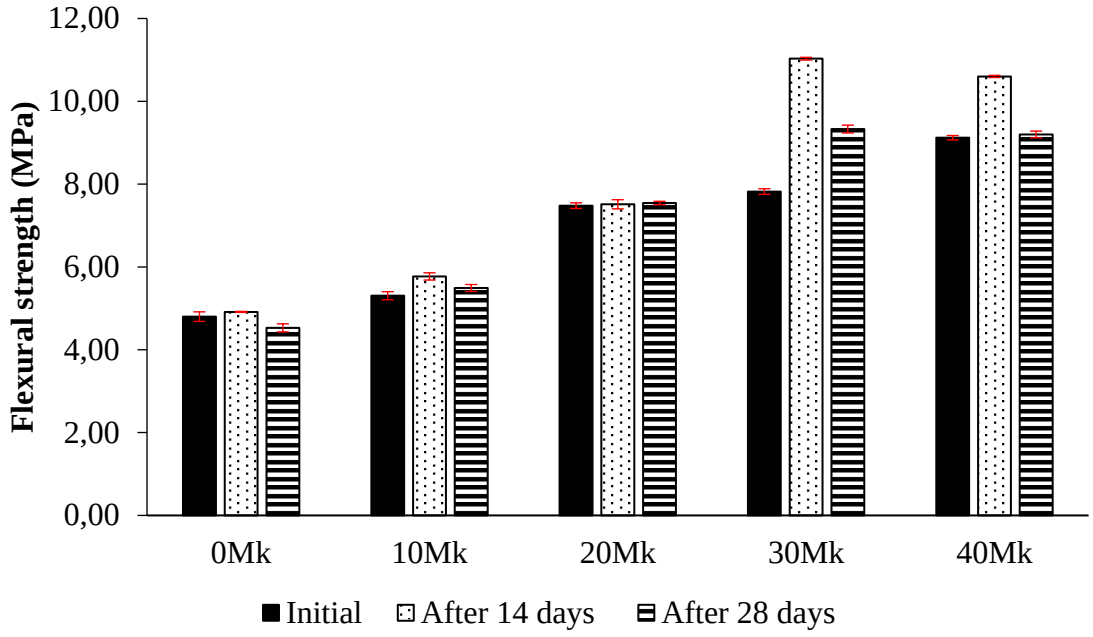

Fig. 11. Flexural strength measurements of geopolymer samples with various metakaolin fractions prior and following sulfuric acid effect

3.6. Mass Changes and Visual Assessment

A mass change test was conducted on materials immersed in 5% sulfuric acid. Figure 12 shows the increased mass change for geopolymer samples with varying metakaolin concentrations exposed to sulfuric acid over periods of 3, 7, 14, and 28 days. The mass of the 0MK geopolymer samples after 3, 7, 14, and 28 days of sulfuric acid exposure increased to 2.36%, 2.79%, 3.016%, and 1.037%, respectively, compared to the samples before exposure. Also, the increases for the 30MK sample were 4.064%, 4.617%, 5.099%, and 2.81% after 3, 7, 14, and 28 days of treatment with sulfuric acid, respectively. Furthermore, the interaction between metakaolin and calcium hydroxide produced calcium compounds that improved the density of the material and, hence, increased its mass [38]. Thus, when calcium compounds were produced, the mass of the samples increased. However, these increases reduced the mass increases of the samples containing metakaolin between 51.75%-105.37% from day 14 to day 28, while the decrease in the mass increase in the 0MK sample was 190.80%. The sharp decrease seen in the 0MK sample compared to the other samples can be attributed to the chemical reaction of sulfuric acid with the calcium content since the 0MK sample contains the highest amount of calcium [61]. Moreover, visual assessment was conducted on the geopolymer samples with varying metakaolin ratios immersed in sulfuric acid solution for 28 days, as illustrated in Figure 13. It was observed that more significant and visible damage occurred in all series after 28 days of acid treatment compared to the samples after 14 days of acid exposure.

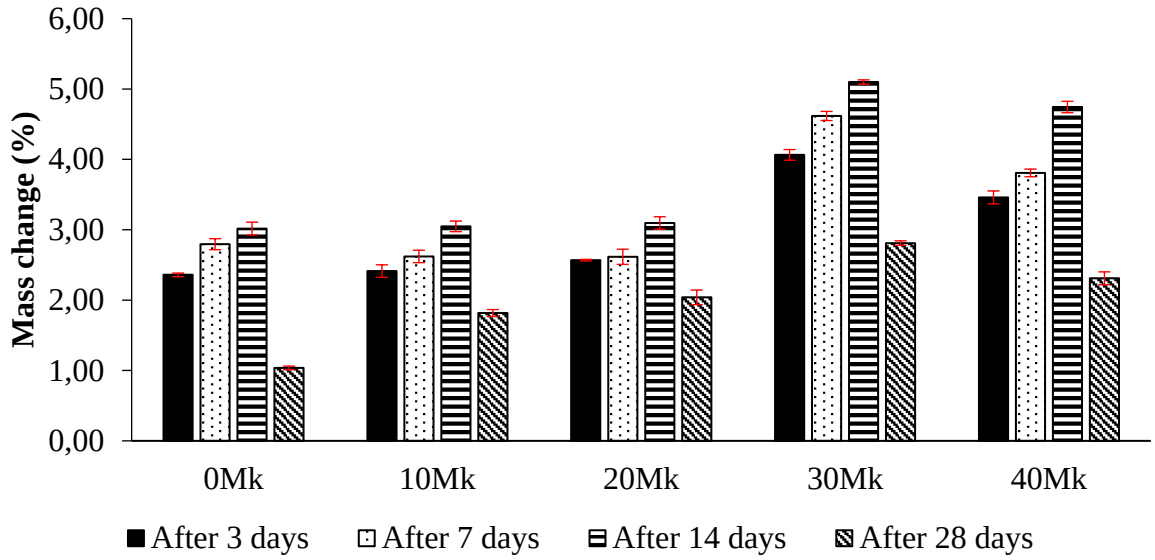

Fig.12. Mass increases of geopolymer samples with varying metakaolin specimens subjected to sulfuric acid for different durations

(a) (b) (c)

(d) (e) (f)

Fig.13. Visual assessment of (a) all series after 14 days of exposure to sulfuric acid, (b) 0MK, (c) 10MK (d) 20MK, (e) 30MK, and (f) 40MK, subsequent to 28 days of acid treatment

The outer shell of the samples exposed to acid for 28 days started to be damaged, and this damage caused changes in the cross-sectional dimensions of the samples and led to a decrease in their strength. In addition, it was observed that the damage was most severe in the 0MK sample, and this damage decreased with increasing metakaolin content. As the samples became more porous and absorbed more water, their strength decreased, indicating that the strength results correlate with the water absorption values [62].

3.7. Microstructural Investigation

The 0MK and 40MK samples were selected for SEM analysis because they had the lowest and highest strengths before acid exposure, respectively. Furthermore, to ensure accurate comparisons, the 0MK and 40MK samples exposed to acid for 28 days were also selected. This allowed a comparison of the samples exhibiting the lowest and greatest strengths before acid exposure with those from the same series after acid exposure. Figure 14 illustrates the SEM examination of the samples prior to and following 28 days of exposure to acid solution. As illustrated in Figure 14 (a), no calcium sulfate needle crystals and structural deterioration were observed in the 0MK samples before acid exposure. Subsequent to 28 days of exposure to acid, the emergence of calcium sulfate needle crystals was noted, as shown in Figure 14 (b), potentially resulting in considerable strength degradation. This is due to the exposure of sulfuric acid, which causes $HSO4^-$ ions to assault the microstructure and recrystallize the gypsum, leading to the deterioration of the aluminosilicate gel matrix [61]. In addition, Figure 14 (c) illustrates sample 40MK before acid exposure, exhibiting a relatively compact structure because of the differences between the surface areas of metakaolin and slag [49].

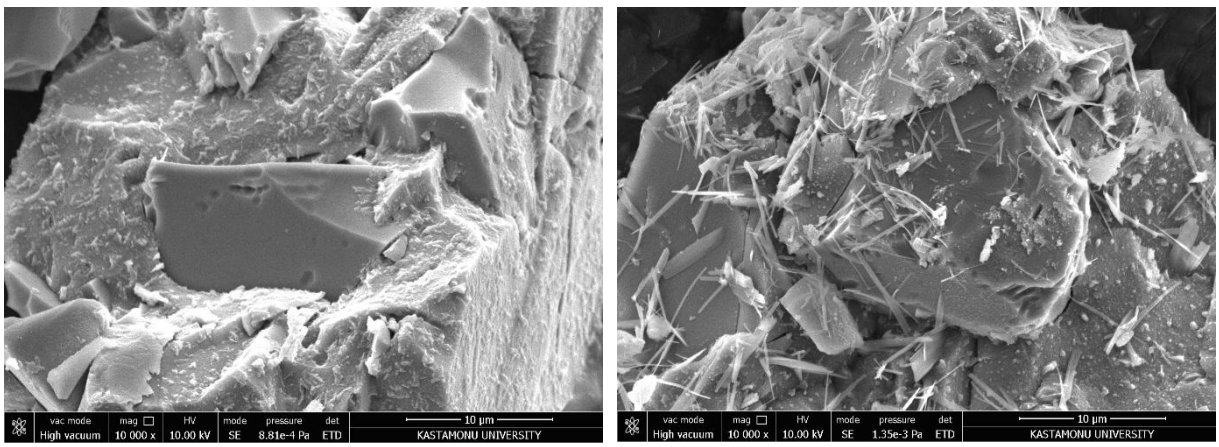

(a) (b)

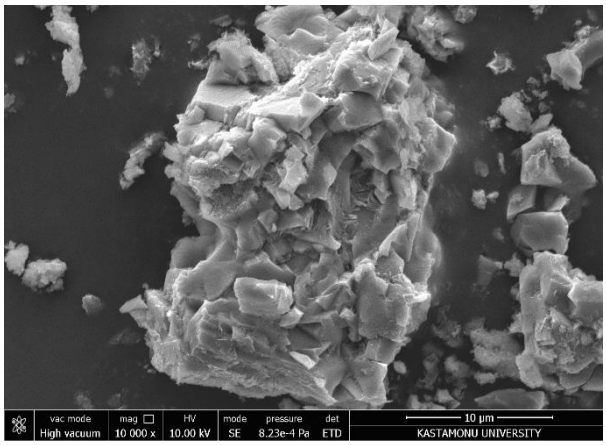

(c)

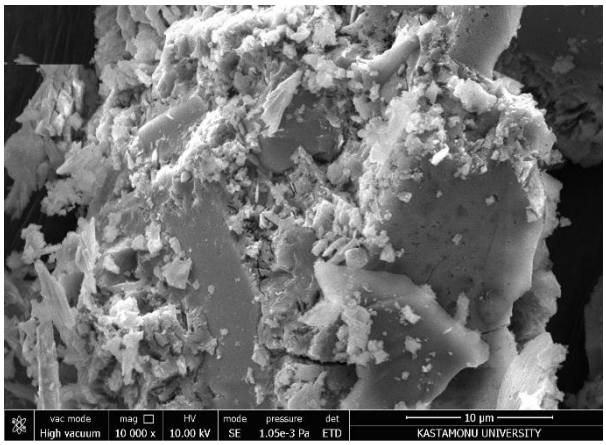

(d)

Fig.14. SEM microscopies of a) 0MK prior to sulfuric acid impact, b) 0MK following 28 days of sulfuric acid impact, (c) 40MK prior to sulfuric acid impact, and (d) 40MK subsequent to 28 days of exposure to acid treatment

Consequently, it was observed in Figure 14 (d) that sample 40MK had fewer calcium sulfate needle crystals than the 0MK sample following 28 days of acid treatment. This is due to metakaolin exhibiting superior resistance to acid corrosion, hence inhibiting the dissolution of ettringite-forming chemicals [63]. Djobo et al. [64] found that the sodium-rich gel in the sample enhances acid resistance, making permeability a determinant of the durability characteristics of geopolymer mortars.

4. Conclusions

- The flow test indicated that the geopolymer samples containing 40% metakaolin demonstrated the minimum flow value. Also, the augmenting of the metakaolin content decreased flow characteristics. This situation reveals the function of metakaolin in reducing workability. The reduced porosity and water absorption of samples containing elevated metakaolin content, specifically 30% and 40% MK, correlated with enhanced compressive strength. Samples exhibiting heightened porosity demonstrated diminished mechanical performance. The 30% MK geopolymer sample had the greatest UPV values, signifying superior cohesion and less porosity in the matrix. This highlights the significance of metakaolin in improving the density and stability of geopolymer structures.
- Samples with 30% and 40% metakaolin demonstrated superior compressive strength compared to those with lower proportions. Forty percent of metakaolin exhibited superior performance under initial conditions, whereas thirty percent of metakaolin demonstrated optimal performance following acid exposure. The optimal strength was linked to geopolymers due to the development of a three-dimensional geopolymer gel network (C-S-H and C-A-S-H). Strength augmented following 14 days of acid exposure, although diminished after 28 days. In addition, the flexural strength showed a decline following twenty-eight days of immersion in sulfuric acid. Moreover, immersion in sulfuric acid for 28 days led to the formation of calcium sulfate needle crystals inside the geopolymer matrix, resulting in crack propagation and a reduction in strength. Thus, 30% MK geopolymer sample was determined to be the ideal composition for acid-resistant geopolymer applications.
- This work significantly advances global sustainability objectives by demonstrating that slag-based geopolymer mortars, especially those enhanced with metakaolin, exhibit exceptional resistance to sulfuric acid while preserving robust mechanical properties. The results indicate that modifying metakaolin content improves chemical durability and facilitates more economical mix designs by minimizing excessive binder use. The use of industrial by-products like slag and metakaolin significantly reduces the carbon footprint relative to traditional Portland cement, hence enhancing the environmental benefits of geopolymer technology. Furthermore, the exhibited acid resistance establishes these materials as viable

options for enduring applications in infrastructure subjected to harsh conditions such as sewage systems, chemical storage facilities, and industrial plants where conventional protective measures are typically labor-intensive and expensive. The research emphasizes geopolymer mortars as a sustainable, durable, and cost-effective option, facilitating the development of environmentally friendly and durable building materials.

References

[1] Davidovits J. Geopolymers: inorganic polymeric new materials. J Therm Anal Calorim. 1991;37:1633-56. https://doi.org/10.1007/BF01912193

[2] Hardjito D, Rangan BV. Development and properties of low-calcium fly ash-based geopolymer concrete. 2005. https://doi.org/10.1080/13287982.2005.11464946

[3] Vickers L, Van Riessen A, Rickard WDA. Fire-resistant geopolymers: role of fibres and fillers to enhance thermal properties. Springer; 2015. https://doi.org/10.1007/978-981-287-311-8

[4] Ziada M. The Effect of Nano-TiO2 and Nano-Al2O3 on Mechanical, Microstructure Properties and High-Temperature Resistance of Geopolymer Mortars. Arab J Sci Eng. 2024. https://doi.org/10.1007/s13369-024-09570-w

[5] Provis JL, Van Deventer JSJ. Geopolymers: structures, processing, properties and industrial applications. Elsevier; 2009. https://doi.org/10.1533/9781845696382

[6] Duxson P, Provis JL, Lukey GC, van Deventer JSJ. The role of inorganic polymer technology in the development of 'green concrete'. Cem Concr Res. 2007;37:1590-7. https://doi.org/10.1016/j.cemconres.2007.08.018

[7] Rashad AM. Metakaolin as cementitious material: History, scours, production and composition-A comprehensive overview. Constr Build Mater. 2013;41:303-18. https://doi.org/10.1016/j.conbuildmat.2012.12.001

[8] Yan D, Chen S, Zeng Q, Xu S, Li H. Correlating the elastic properties of metakaolin-based geopolymer with its composition. Mater Des. 2016;95:306-18. https://doi.org/10.1016/j.matdes.2016.01.107

[9] Živica V, Balkovic S, Drabik M. Properties of metakaolin geopolymer hardened paste prepared by high-pressure compaction. Constr Build Mater. 2011;25:2206-13. https://doi.org/10.1016/j.conbuildmat.2010.11.004

[10] Martin A, Pastor JY, Palomo A, Jiménez AF. Mechanical behaviour at high temperature of alkali-activated aluminosilicates (geopolymers). Constr Build Mater. 2015;93:1188-96. https://doi.org/10.1016/j.conbuildmat.2015.04.044

[11] Temuujin J, Rickard W, Lee M, van Riessen A. Preparation and thermal properties of fire resistant metakaolin-based geopolymer-type coatings. J Non Cryst Solids. 2011;357:1399-404. https://doi.org/10.1016/j.jnoncrysol.2010.09.063

[12] Azimi EA, Al Bakri AMM, Liew YM, Heah CY, Hussin K, Aziz IH. Review of geopolymer materials for thermal insulating applications. Key Eng Mater. 2015;660:17-22. https://doi.org/10.4028/www.scientific.net/KEM.660.17

[13] Zhang Z, Provis JL, Reid A, Wang H. Mechanical, thermal insulation, thermal resistance and acoustic absorption properties of geopolymer foam concrete. Cem Concr Compos. 2015;62:97-105. https://doi.org/10.1016/j.cemconcomp.2015.03.013

[14] Fernández-Jiménez A, Monzó M, Vicent M, Barba A, Palomo A. Alkaline activation of metakaolin-fly ash mixtures: Obtain of Zeoceramics and Zeocements. Microporous Mesoporous Mater. 2008;108:41-9. https://doi.org/10.1016/j.micromeso.2007.03.024

[15] Duxson P, Lukey GC, van Deventer JS. Physical evolution of Na-geopolymer derived from metakaolin up to 1000°C. J Mater Sci. (n.d.).

[16] Cheng TW, Lee ML, Ko MS, Ueng TH, Yang SF. The heavy metal adsorption characteristics on metakaolin-based geopolymer. Appl Clay Sci. 2012;56:90-6. https://doi.org/10.1016/j.clay.2011.11.027

[17] Kong DLY, Sanjayan JG, Sagoe-Crentsil K. Factors affecting the performance of metakaolin geopolymers exposed to elevated temperatures. J Mater Sci. 2008;43:824-31. https://doi.org/10.1007/s10853-007-2205-6

[18] Duxson P, Provis JL, Lukey GC, Mallicoat SW, Kriven WM, van Deventer JSJ. Understanding the relationship between geopolymer composition, microstructure and mechanical properties. Colloids Surf A Physicochem Eng Asp. 2005;269:47-58. https://doi.org/10.1016/j.colsurfa.2005.06.060

[19] Roviello G, Menna C, Tarallo O, Ricciotti L, Ferone C, Colangelo F, et al. Preparation, structure and properties of hybrid materials based on geopolymers and polysiloxanes. Mater Des. 2015;87:82-94. https://doi.org/10.1016/j.matdes.2015.08.006

[20] Zhou W, Yan C, Duan P, Liu Y, Zhang Z, Qiu X, et al. A comparative study of high- and low-Al2O3 fly ash based-geopolymers: The role of mix proportion factors and curing temperature. Mater Des. 2016;95:63-74. https://doi.org/10.1016/j.matdes.2016.01.084

[21] Rieger D, Kovářík T, Říha J, Medlín R, Novotný P, Bělský P, et al. Effect of thermal treatment on reactivity and mechanical properties of alkali activated shale-slag binder. Constr Build Mater. 2015;83:26-33. https://doi.org/10.1016/j.conbuildmat.2015.02.024
[22] Muñiz-Villarreal MS, Manzano-Ramírez A, Sampieri-Bulbarela S, Gasca-Tirado JR, Reyes-Araiza JL, Rubio-Ávalos JC, et al. The effect of temperature on the geopolymerization process of a metakaolin-based geopolymer. Mater Lett. 2011;65:995-8. https://doi.org/10.1016/j.matlet.2010.12.049
[23] Xiao Y, Sun W, Tan Y, Sun D, Xing D, Wang D. Enhancement of phosphogypsum-based solid waste cementitious materials via seawater and metakaolin synergy: Strength, microstructure, and environmental benefits. Sustain Mater Technol. 2024;41:e01029. https://doi.org/10.1016/j.susmat.2024.e01029
[24] Guang L, Linhao W, Jinli W, Xiaoqiang D, Alfred A. Enhancing Sulfuric Acid Resistance of Cement Paste through Incorporation of CMK with Different Specific Surface Areas: An Analysis of Mechanical Properties and Durability. J Mater Civ Eng. 2025;37:4025113. https://doi.org/10.1061/JMCEE7.MTENG-18888
[25] Karimiazar J, Sharifi Teshnizi E, O'Kelly BC, Sadeghi S, Karimizad N, Yazdi A, et al. Effect of nano-silica on engineering properties of lime-treated marl soil. Transp Geotech. 2023;43:101123. https://doi.org/10.1016/j.trgeo.2023.101123
[26] Sharifi Teshnizi E, O'Kelly BC, Karimiazar J, Moosazadeh S, Arjmandzadeh R, Pani A. Effects of cement kiln dust on physicochemical and geomechanical properties of loess soil, Semnan Province, Iran. Arab J Geosci. 2022;15:1482. s12517-022-10751-w https://doi.org/10.1007/s12517-022-10751-w
[27] Jafar K, Ebrahim ST, Mehdi M, Masoud M, Reza A. California Bearing Ratio of a Reactive Clay Treated with Nano-Additives and Cement. J Mater Civ Eng. 2022;34:4021431. https://doi.org/10.1061/(ASCE)MT.1943-5533.0004028
[28] Mirzababaei M, Karimiazar J, Sharifi Teshnizi E, Arjmandzadeh R, Bahmani SH. Effect of Nano-Additives on the Strength and Durability Characteristics of Marl. Minerals. 2021;11. https://doi.org/10.3390/min11101119
[29] Hashemi H, Yazdi A, Teshnizi ES. Improvement of collapsing problematic soils on the Sabzevar-Mashhad railway route (northeast of Iran) using traditional additives. Nexo Rev Científica. 2023;36:383-403. https://doi.org/10.5377/nexo.v36i03.16461
[30] Ezazi M, Hossaini MF, Sheikhmali R, Khosrotash M, Sharifi Teshnizi E, O'Kelly BC. Assessment of steel-fiber-reinforced segmental lining of Chamshir water conveyance tunnel, Iran: Integrating laboratory experiments, field observations, and numerical analysis. Case Stud Constr Mater. 2024;20:e03144. https://doi.org/10.1016/j.cscm.2024.e03144
[31] Zarina Y, Al Bakri Abdullah MM, Kamarudin H, Khairul Nizar I, Abd Razak R. Reviews on the geopolymer materials for coating application. Adv Mater Res. 2013;626:958-62. https://doi.org/10.4028/www.scientific.net/AMR.626.958
[32] Wiyono D, Hardjito D. Improving the durability of pozzolan concrete using alkaline solution and geopolymer coating. Procedia Eng. 2015;125:747-53. https://doi.org/10.1016/j.proeng.2015.11.121
[33] Ebrahim ST, Mehdi M, Jafar K, Reza A, Kamran M. Gypsum and rice husk ash for sustainable stabilization of forest road subgrade. Q J Eng Geol Hydrogeol. 2024;57:qjegh2023-008. https://doi.org/10.1144/qjegh2023-008
[34] Aguiar JB, Camões A, Moreira PM. Coatings for concrete protection against aggressive environments. J Adv Concr Technol. 2008;6:243-50. https://doi.org/10.3151/jact.6.243
[35] Almusallam AA, Khan FM, Dulaijan SU, Al-Amoudi OSB. Effectiveness of surface coatings in improving concrete durability. Cem Concr Compos. 2003;25:473-81. https://doi.org/10.1016/S0958-9465(02)00087-2
[36] Tahri W, Abdollahnejad Z, Mendes J, Pacheco-Torgal F, De Aguiar JB. Cost efficiency and resistance to chemical attack of a fly ash geopolymeric mortar versus epoxy resin and acrylic paint coatings. Eur J Environ Civ Eng. 2017;21:555-71. https://doi.org/10.1080/19648189.2015.1134674
[37] Aiken TA, Kwasny J, Sha W, Soutsos MN. Effect of slag content and activator dosage on the resistance of fly ash geopolymer binders to sulfuric acid attack. Cem Concr Res. 2018;111:23-40. https://doi.org/10.1016/j.cemconres.2018.06.011
[38] Teshnizi ES, Karimiazar J, Baldovino JA. Effect of acid and thermo-mechanical attacks on compressive strength of geopolymer mortar with different eco-friendly materials. Sustainability. 2023;15. https://doi.org/10.3390/su151914407
[39] S.A. H, E.-G.M. M. Influence of sulfuric acid exposure on mechanical properties of alkali-activated concrete. Pract Period Struct Des Constr. 2024;29:4024041. https://doi.org/10.1061/PPSCFX.SCENG-1478
[40] Nuaklong P, Sata V, Chindaprasirt P. Properties of metakaolin-high calcium fly ash geopolymer concrete containing recycled aggregate from crushed concrete specimens. Constr Build Mater. 2018;161:365-73. https://doi.org/10.1016/j.conbuildmat.2017.11.152
[41] British Standards Institution. Methods of testing cement - Part 1: Determination of strength. 2009.

[42] ASTM C109/C109M-02. Standard test method for compressive strength of hydraulic cement mortars (using 2-in. or [50-mm] cube specimens). ASTM Int; 2020.
[43] ASTM C348. Standard test method for flexural strength of hydraulic-cement mortars. West Conshohocken, PA: ASTM Int; 2021.
[44] ASTM C1585-13. Standard test method for measurement of rate of absorption of water by hydraulic-cement concretes. ASTM Int; 2020.
[45] ASTM C597-09. Standard test method for pulse velocity through concrete. West Conshohocken, PA: ASTM Int; 2016.
[46] Domone P. The slump flow test for high-workability concrete. Cem Concr Res. 1998;28:177-82. https://doi.org/10.1016/S0008-8846(97)00224-X
[47] Sonebi M, Lachemi M, Hossain KMA. Optimisation of rheological parameters and mechanical properties of superplasticised cement grouts containing metakaolin and viscosity modifying admixture. Constr Build Mater. 2013;38:126-38. https://doi.org/10.1016/j.conbuildmat.2012.07.102
[48] Ferraris CF, Obla KH, Hill R. The influence of mineral admixtures on the rheology of cement paste and concrete. Cem Concr Res. 2001;31:245-55. https://doi.org/10.1016/S0008-8846(00)00454-3
[49] Zhu H, Liang G, Li H, Wu Q, Zhang C, Yin Z, et al. Insights to the sulfate resistance and microstructures of alkali-activated metakaolin/slag pastes. Appl Clay Sci. 2021;202:105968. https://doi.org/10.1016/j.clay.2020.105968
[50] Aksogan O. Durability of concrete made with natural granular granite, silica sand and powders of waste marble and basalt as fine aggregate. J Build Eng. 2018;19. https://doi.org/10.1016/j.jobe.2018.04.022
[51] Zhang Y, He Y, Cui X, Liu L. Enhancing freeze-thaw resistance of alkali-activated slag by metakaolin. ACS Omega. 2023;8:20869-80. https://doi.org/10.1021/acsomega.3c01600
[52] Bayrak B, Mostafa SA, Öz A, Tayeh BA, Kaplan G, Aydın AC. The effect of clinker aggregate on acid resistance in prepacked geopolymers containing metakaolin and quartz powder in the presence of ground blast furnace slag. J Build Eng. 2023;69:106290. https://doi.org/10.1016/j.jobe.2023.106290
[53] Bakharev T, Sanjayan JG, Cheng YB. Resistance of alkali-activated slag concrete to acid attack. Cem Concr Res. 2003;33:1607-11. https://doi.org/10.1016/S0008-8846(03)00125-X
[54] Yang W, Zhu P, Liu H, Wang X, Ge W, Hua M. Resistance to sulfuric acid corrosion of geopolymer concrete based on different binding materials and alkali concentrations. Materials (Basel). 2021;14. https://doi.org/10.3390/ma14237109
[55] Huseien GF, Mirza J, Ismail M, Ghoshal SK, Ariffin MAM. Effect of metakaolin replaced granulated blast furnace slag on fresh and early strength properties of geopolymer mortar. Ain Shams Eng J. 2018;9:1557-66. https://doi.org/10.1016/j.asej.2016.11.011
[56] Jaji MB, van Zijl GPAG, Babafemi AJ. Slag-modified metakaolin-based 3D printed geopolymer: Mechanical characterisation, microstructural properties, and nitrogen physisorption pore analysis. J Build Eng. 2024;81:108166. https://doi.org/10.1016/j.jobe.2023.108166
[57] Jindal BB, Alomayri T, Hasan A, Kaze CR. Geopolymer concrete with metakaolin for sustainability: a comprehensive review on raw material's properties, synthesis, performance, and potential application. Environ Sci Pollut Res. 2022;1-26. https://doi.org/10.1007/s11356-021-17849-w
[58] Vafaei M, Allahverdi A, Dong P, Bassim N, Mahinroosta M. Resistance of red clay brick waste/phosphorus slag-based geopolymer mortar to acid solutions of mild concentration. J Build Eng. 2021;34:102066. https://doi.org/10.1016/j.jobe.2020.102066
[59] Kwasny J, Aiken TA, Soutsos MN, McIntosh JA, Cleland DJ. Sulfate and acid resistance of lithomarge-based geopolymer mortars. Constr Build Mater. 2018;166:537-53. https://doi.org/10.1016/j.conbuildmat.2018.01.129
[60] Lezzerini M, Aquino A, Pagnotta S. Acid resistance of metakaolin-based geopolymers and geopolymeric mortars reinforced with coconut fibers. Fibers. 2024;12:40. https://doi.org/10.3390/fib12050040
[61] Javed U, Shaikh FUA, Sarker PK. Corrosive effect of HCl and H2SO4 exposure on the strength and microstructure of lithium slag geopolymer mortars. Constr Build Mater. 2024;411:134588. https://doi.org/10.1016/j.conbuildmat.2023.134588
[62] Ali I, Canpolat O, Doğruöz Güngör N, Yüzer N, Uysal M, Tanyıldızı H, et al. Comparison of bacterial healing performances of cave bacteria and Sporosarcina pasteurii in cement-based mortar. Processes. 2025;13. https://doi.org/10.3390/pr13030673
[63] Aygörmez Y, Canpolat O. Long-term sulfuric and hydrochloric acid resistance of silica fume and colemanite waste reinforced metakaolin-based geopolymers. Rev La Constr. 2021;20:291-307. https://doi.org/10.7764/RDLC.20.2.291
[64] Djobo JNY, Elimbi A, Tchakouté HK, Kumar S. Mechanical properties and durability of volcanic ash based geopolymer mortars. Constr Build Mater. 2016;124:606-14. https://doi.org/10.1016/j.conbuildmat.2016.07.141

Blank Page

Research on Engineering Structures & Materials
www.jresm.org
Research Group

Research Article

Optimizing indoor air quality in sustainable homes: A simulation-based evaluation of VOC emissions from bamboo-based materials

Sameh Fuqaha [*,a], Ahmad Zaki [b], Guntur Nugroho [c]

Department of Civil Engineering, Universitas Muhammadiyah Yogyakarta, Yogyakarta, Indonesia

Article Info

Article History:

Received 19 May 2025

Accepted 07 July 2025

Keywords:

Indoor air quality;
Volatile organic compounds;
Bamboo-based materials;
CONTAM simulation;
Sustainable building design

Abstract

This study presents a simulation-based assessment of indoor air quality (IAQ) in residential buildings using bamboo-based construction materials, with a focus on volatile organic compound (VOC) emissions. Nine case studies were modeled using CONTAM software, examining variations in material selection, adhesive type, ventilation rate, and indoor temperature. The baseline case, using oriented strand board (OSB) and cork flooring, produced peak total VOC (TVOC) levels of 3.775 mg/m^3 and formaldehyde concentrations up to 1.25 mg/m^3, exceeding recommended thresholds despite sufficient ventilation. Replacing OSB and cork with laminated bamboo panels and flooring bonded with soy-based adhesives resulted in a 70–80% reduction in VOC emissions, with TVOC levels dropping to 0.88 mg/m^3 and formaldehyde concentrations below 0.3 mg/m^3. In contrast, bamboo bonded with melamine urea formaldehyde (MUF) adhesives showed moderate improvements, with TVOC at 1.02 mg/m^3. Elevated indoor temperatures increased VOC levels by over 30%, while enhanced ventilation reduced them by 25–35%. Results from a mass balance analytical model aligned with simulation trends, supporting model validity. The findings demonstrate that combining low-emission bamboo materials with optimized ventilation offers a viable strategy for achieving healthier indoor environments, supporting sustainable and occupant-focused residential design.

© 2025 MIM Research Group. All rights reserved.

1. Introduction

Indoor air quality (IAQ) is a critical determinant of human health and comfort, especially in urban environments where individuals spend approximately 90% of their time indoors [1]. IAQ encompasses the quality of air within and around buildings and structures, directly affecting the health and comfort of occupants [2]. Poor IAQ is associated with a spectrum of health concerns, ranging from respiratory irritation and allergic reactions to more severe long-term impacts such as asthma, neurological disorders, and cancer [3]. Among the contributors to indoor air pollution, volatile organic compounds (VOCs) play a dominant role due to their ubiquitous presence in common building materials, furniture, adhesives, and coatings [4]. As global efforts toward sustainable building and low-carbon materials accelerate, there is growing interest in alternative building materials that minimize indoor emissions without compromising performance or aesthetic value [5].

Bamboo has gained traction as a promising renewable material in the construction industry due to its rapid growth cycle, high strength-to-weight ratio, and environmental benefits such as carbon sequestration and biodegradability [6]. Recent advancements in engineered bamboo products such as laminated bamboo panels and bamboo flooring have enabled their broader application in

*Corresponding author: sameh.h.psc24@mail.umy.ac.id
[a]orcid.org/0009-0000-6914-7148; [b]orcid.org/0000-0003-1166-5078; [c]orcid.org/ 0000-0002-7881-6451
DOI: http://dx.doi.org/10.17515/resm2025-910ma0519rs
Res. Eng. Struct. Mat. Vol. 11 Iss. 4 (2025) 1767-1786

interior architecture [7]. However, despite their ecological appeal, the impact of bamboo-based materials on IAQ remains underexplored, particularly in relation to VOC emissions under varying ventilation and thermal conditions [8]. Adhesives used in laminated bamboo, including melamine urea formaldehyde (MUF) and soy-based alternatives, can significantly influence VOC profiles, further complicating material selection for green design [9].

Traditional IAQ research has often focused on monitoring pollutant concentrations in existing buildings, but recent methodological shifts emphasize simulation-based modelling as a powerful tool for design-stage IAQ evaluation [10]. Models such as CONTAM, developed by the National Institute of Standards and Technology (NIST), allow for detailed assessment of airflow, contaminant dispersion, and thermal interactions across a variety of material and operational scenarios [11]. This tool supports early design-stage decisions by modelling how contaminants disperse indoors and predicting pollutant levels before a building is occupied. CONTAM can also estimate individual exposure by integrating occupancy schedules with predicted pollutant concentrations [12]. Its applications span infiltration studies [13,14], pollutant transport simulations [15], and occupant exposure analysis [16,17]. Despite its versatility, a known limitation is the assumption of uniform contaminant concentration within each zone [18]. By leveraging such simulations, researchers and designers can test the influence of material substitutions, ventilation strategies, and indoor environmental parameters without incurring the costs of physical experimentation.

This study addresses a critical research gap by systematically evaluating the effects of bamboo interior materials on IAQ using simulation-based modelling. The investigation is structured around multiple case studies, including configurations with and without bamboo elements, and further explores the role of adhesive type, flooring systems, mechanical ventilation rates, and indoor temperature conditions. The aim is to quantify how bamboo-based construction can contribute to reduced VOC emissions and improved IAQ performance in residential buildings. By bridging sustainable material science with IAQ simulation, this research contributes to the development of greener, healthier indoor environments in line with contemporary building performance goals.

2. Methodology

The methodology implemented in this research involved a simulation-based analysis to evaluate the impact of bamboo-based building materials on indoor air quality (IAQ), with a particular focus on the emission of volatile organic compounds (VOCs).

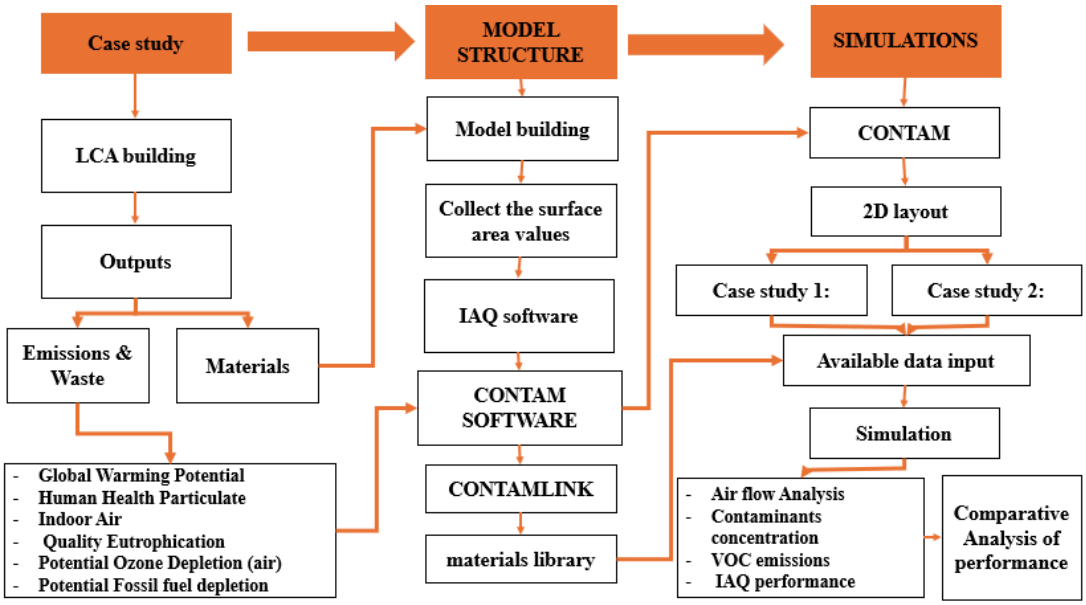

Fig. 1. Detailed simulation framework outlining data inputs, emission sources, material libraries, software integration, and analysis phases.

The study used CONTAM, a multizone indoor air quality and ventilation analysis software developed by the National Institute of Standards and Technology (NIST), as the primary simulation tool. The approach was structured into three main stages as in Fig. 1 and 2 present a case study selection, structural and IAQ model development, and simulation execution.

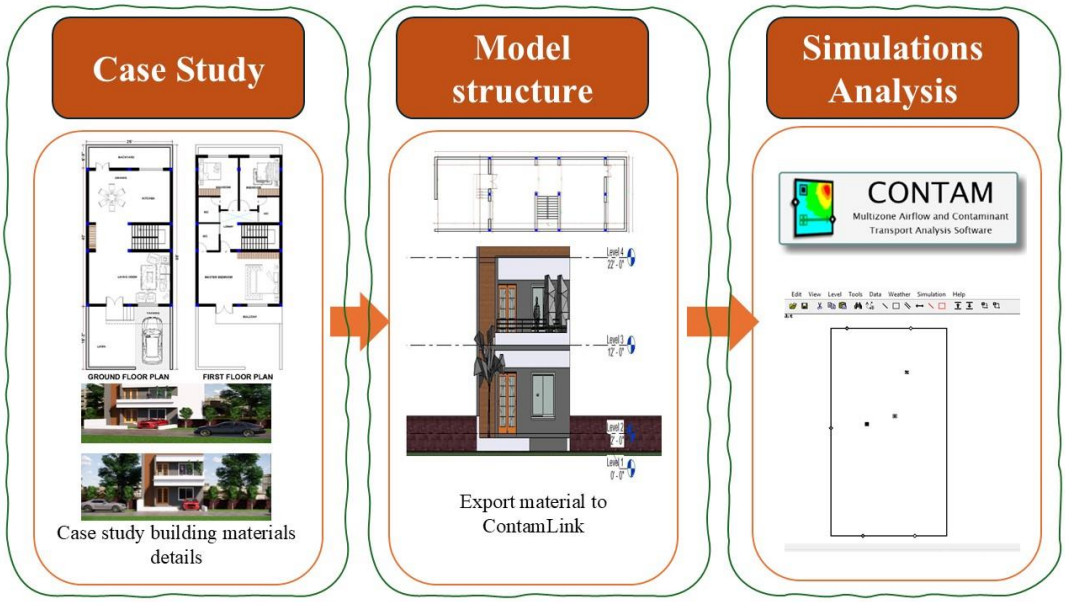

Fig. 2. Visual methodology workflow showing the transition from architectural modeling and material definition to IAQ simulation using CONTAM

In the first stage, a representative residential building was selected as a case study, including detailed architectural floor plans (ground and first floors) and exterior 3D renderings to establish the spatial and material configurations of the structure. Key materials used in the interior, such as bamboo-based panels and traditional timber, were documented for emission evaluation.

Table 1. Building and Simulation Setup Parameters in CONTAM

Parameter	Description/Value
Building Type	Residential, 2-story, timber frame (Jakarta proxy)
Total Floor Area	185 m^2
Indoor Volume (estimated)	518 m^3 (based on 2.8 m ceiling height)
Climate Zone	Temperate
Simulation Duration	8760 hours (full year)
Occupancy Schedule	6 a.m. – 10 p.m. (based on residential standards)
Ventilation System	Mechanical supply + natural infiltration
Ventilation Rate Range	30 – 138.3 L/s (based on simulation and SNI)
Modeling Software	Building: Autodesk Revit IAQ: CONTAM v3.4
Integration Tool	CONTAMLink v3.4
CONTAM Simulation Input	Multizone airflow + VOC emissions
Door Gap Flow Coefficient	0.001 (living–bedroom, always open)
Diffuser Flow Coefficient	0.005 (bedroom–corridor, night only)
Window Leakage Flow	0.002 (kitchen–outdoor, day only)

In the second stage, the architectural model was reconstructed in a CAD environment, where geometrical and structural information was integrated and prepared for export. The model was then converted using ContamLink, enabling the transfer of spatial and material data into the CONTAM environment. In the final stage, the model was imported into CONTAM software, a

multizone indoor air quality simulation tool, to assess airflow patterns and VOC emission behavior under different conditions. The simulation focused on contaminant transport across rooms, reflecting the influence of material choice on indoor air quality. The building was modeled after a two-story light-frame timber residence representative of tropical residential design. Its geometric and spatial configurations were developed in Autodesk Revit and exported to CONTAM via CONTAMLink. Environmental parameters such as climate zone (temperate), occupancy schedules, ventilation strategies, and infiltration paths were specified based on standardized input datasets as in Table 1. The simulation was executed over a full-year duration (8760 hours) using an hourly time step to capture seasonal variations in pollutant behavior.

CONTAM was selected for its proven multizone simulation capabilities, and its ability to efficiently assess VOC transport and ventilation dynamics across large timeframes (e.g., full-year simulations) with minimal computational demand. Its computational effectiveness and predictive accuracy have been substantiated through real-world applications and case studies [18–20]. Another prominent tool in the domain of fluid dynamics is Computational Fluid Dynamics (CFD), which offers a detailed numerical approach to modelling gas behaviour and flow interactions within complex environments. CFD has proven to be dependable in modelling pollutant dispersion and airflow in sensitive indoor areas, including healthcare facilities [21], food preparation spaces [22], and research laboratories [23]. However, when dealing with buildings that feature numerous rooms and architectural complexity, CFD simulations become resource-intensive and time-consuming. In contrast, CONTAM provides a more streamlined and resource-efficient option, enabling faster analysis with simplified input parameters [24]. Given these advantages, CONTAM is often the preferred solution for evaluating airflow dynamics, pressure distributions, and indoor contaminant pathways. While CFD models offer spatial resolution, CONTAM enables full-building analysis of contaminant movement and occupant exposure, making it suitable for early-stage material and IAQ evaluation [25,26].

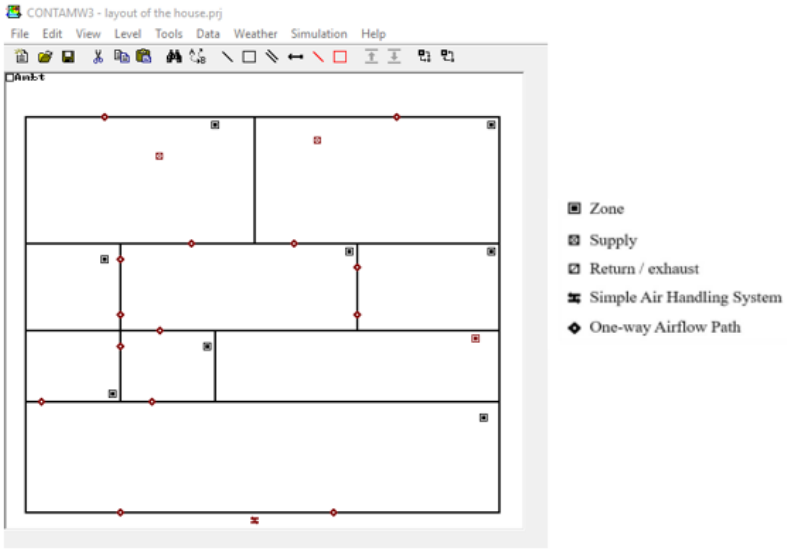

Fig. 3. Multizone layout of the case study house modeled in CONTAM for airflow and VOC simulation

The layout in CONTAM of the house, taken into consideration in this study, is shown in Fig. 3. The Figure presents the multizone layout of the residential case study building as modeled in CONTAM software. Each outlined rectangle represents a distinct indoor zone, such as bedrooms, living spaces, or service areas. The diagram includes key airflow components: supply vents (black squares), return/exhaust points (striped squares), a simple air handling system (fan icon), and one-way airflow paths (red diamonds), which simulate air movement between zones. This schematic serves as the foundation for simulating ventilation performance and VOC distribution throughout the house under various material and environmental scenarios. The simulation focused on comparing multiple case studies that varied in material configurations. The baseline case used

conventional materials like oriented strand board (OSB), gypsum wallboard, and cork flooring. Alternative scenarios incorporated laminated bamboo panels and bamboo flooring, bonded with either soy-based or melamine urea formaldehyde (MUF) adhesives. This allowed for a comparative analysis of emissions across both low-emission and standard material options.

The first case study was designed as the baseline configuration, where the building envelope and internal finishes reflected conventional construction practices. Wall assemblies consisted of oriented strand board (OSB) and gypsum board, while flooring materials included cork and gypsum-based products as in Fig. 4. This configuration provided a reference scenario against which alternative material strategies could be evaluated. All material data, including emission rates, were collected from manufacturers' specifications and peer-reviewed literature, ensuring consistency with industry standards.

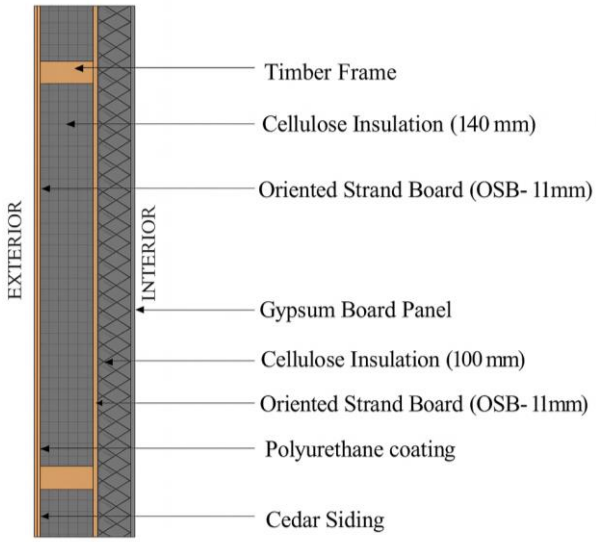

Fig. 4. Wall section of case study 1 (timber wall frame structure)

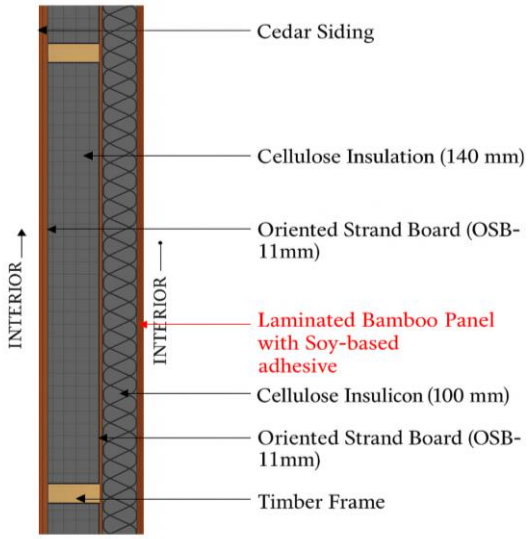

Fig. 5. Wall section of case study 2

In the second case study, the research introduced bamboo-based construction materials to replace conventional wall and floor components. Laminated bamboo panels and flooring were modelled in place of OSB and cork as in Fig 5, allowing for a comparative assessment of material influence on indoor air quality. This case study included several sub-scenarios that differed based on the type of adhesive used in the bamboo composites. These included melamine urea formaldehyde (MUF) adhesives, soy-based alternatives, and natural low-emission binders. Each sub-case retained the same architectural and volumetric parameters as the baseline model, ensuring that observed differences could be attributed solely to material substitutions.

The third case study extended the simulation analysis by varying key environmental parameters within the same building configuration. This phase explored the impact of modified ventilation rates and indoor temperatures on airflow and pollutant behaviour. Three environmental scenarios were modelled: one with reduced natural ventilation, another with increased indoor temperature, and a third with decreased temperature. These variations were intended to reflect realistic fluctuations in building operation and climate, and to assess how such conditions interact with material emissions. Table 2 presents the material configurations used across the different case studies in this research. It outlines the combinations of wall and floor materials, adhesive types, and known sources of volatile organic compounds (VOCs).

To accurately simulate inter-zonal air movement within the residential case study model, airflow connections were defined between key building spaces based on typical architectural layouts and ventilation behaviours. Airflow from the living room to the bedroom was modelled through a door gap with a flow coefficient of 0.001, and this pathway was assumed to be "always open," representing standard internal door conditions during occupancy hours. A second inter-zone connection was specified between the bedroom and corridor using a diffuser-type flow mechanism,

with a flow coefficient of 0.005. This connection operated under a "night only" schedule, reflecting mechanical system settings for enhanced nocturnal ventilation and thermal comfort. Additionally, a pathway was defined from the kitchen to the outdoor environment, simulating leakage through a window. This connection used a flow coefficient of 0.002 and was set to operate during the "day only" period, mimicking occupant behaviour of window opening for natural ventilation and door removal during cooking activities. These airflow configurations were incorporated into the CONTAM model to realistically capture pollutant transport dynamics across different building zones and enhance the fidelity of the IAQ simulation.

Table 2. Material configurations across case studies

Case Study	Wall Material	Floor Material	Adhesive Type	Known VOC Sources
CS1	OSB + Gypsum	Cork	–	OSB, cork
CS1.1	OSB + Gypsum	–	–	OSB
CS2.0	Bamboo + OSB	Partial Cork	Soy-based	Reduced
CS2.1	Bamboo + OSB	None	Soy-based	Minimal
CS2.2	Bamboo + OSB	–	MUF	Elevated
CS2.3	Full Bamboo	Bamboo	Soy-based	Lowest
CS3.0–3.2	Full Bamboo	Bamboo	MUF	Conditional on environment

Table 3 summarizes the zone-specific ventilation configurations used in the CONTAM model, including supply and exhaust pathways, as well as estimated air exchange rates for each room. These configurations reflect realistic residential ventilation behaviours, combining both mechanical and natural mechanisms. The values were selected based on common occupancy schedules and reflect performance ranges validated in literature and local building codes. Table 4 presents the emission characteristics of selected building materials used as input parameters for the CONTAM simulation. It includes total volatile organic compound (TVOC) and formaldehyde emission rates, expressed in $mg/m^2 \cdot h$, based on established literature sources. Emission rates for total VOCs and formaldehyde were based on literature values and material safety data sheets (MSDS). These values were assigned as emission factors in the CONTAM simulation environment and governed the mass transfer of pollutants from surfaces into the indoor environment.

Simulation scenarios were systematically structured to isolate the effects of materials and environmental controls as in Table 5. The primary control variables were indoor temperature and mechanical ventilation rate. While Case Study 1 simulated conventional material use, Case Study 2 explored bamboo integration, and Case Study 3 tested thermal and ventilation sensitivities. Environmental variations, including indoor temperature (25–30°C) and ventilation rates (59.8–138.3 L/s), were selected based on regional climate conditions (Jakarta proxy) and Indonesian SNI ventilation standards for residential buildings (SNI 03-6572-2001) [31]. This ensures that the simulation output reflects realistic residential environments in tropical regions

Table 3. Distribution of ventilation system by room and operation type

Description	Supply Inlet	Exhaust Outlet	Air Exchange Rate (1/h)
Living Room	Mechanical diffuser	Corridor return	0.5–0.7
Bedroom	Natural infiltration	Mechanical (night only)	0.4–0.6
Kitchen	Window (day only)	Mechanical vent hood	1.5–2.0
Bathroom	Mechanical vent grille	Mechanical fan	2.0–3.0
Corridor	Indirect via doors	Central return shaft	0.6–0.8

The simulation outputs included time-series data for average airflow rates and total VOC emissions (TVOC) over a one-year period. Data analysis was conducted by comparing average values across different scenarios and visually interpreting trends in air flow and emission rates using comparative graphs and box plots. The methodology provided a robust framework for assessing

the potential of bamboo materials in improving indoor air quality. It enabled the identification of both material-related and environmental factors influencing VOC emissions in residential buildings.

Table 4. Material emission factors (Input to CONTAM)

Material	TVOC Emission Rate (mg/m²·h)	Formaldehyde (mg/m²·h)	Source
OSB	0.5	0.2	[27]
Cork	0.6	0.3	[28]
Bamboo (Soy Adhesive)	0.1	0.03	[29]
Bamboo (MUF Adhesive)	0.3	0.1	[29]
Timber	0.4	0.15	[30]

Table 5. Simulation scenarios and control variables

Case Study	Temp. (°C)	Ventilation (L/s)	Duration	Purpose
CS1	25	59.8–126.5	1 year	Baseline reference
CS2.1	25	59.8–126.5	1 year	Material substitution
CS3.1	30	59.8–133.3	1 year	Temp stress test
CS3.2	25	87.3–138.3	1 year	Dilution strategy

To validate the simulation-based results generated by CONTAM, an analytical approach was adopted using a well-established indoor air quality model based on the principle of mass balance in a well-mixed zone. This method provides a simplified yet effective means to estimate time-dependent concentrations of volatile organic compounds (VOCs) within an enclosed indoor environment, given known emission and ventilation characteristics [32]. The well-mixed zone model assumes that indoor air is perfectly mixed and that pollutant concentrations are spatially uniform across the space[32,33]. The change in VOC concentration over time due to a continuous emission source is governed by the following mass balance as in Eq. (1).

$$C(t) = \frac{E}{Q}(1 - e^{\frac{-Q}{V}t}) \quad (1)$$

Where, C(t): the VOC concentration at time t (mg/m^3), E: the emission rate from indoor surfaces (mg/h), Q: the ventilation rate (m^3/h), V: the indoor air volume (m^3), t: the duration of accumulation (h).

For this study, the indoor volume (V) was estimated at 518 m^3, based on a two-story residential floor area of 185 m^2 and an average ceiling height of 2.8 meters. The ventilation rate (Q) was calculated using airflow rates extracted from simulation results, typically ranging from 455.4 to 497.9 m^3/h, depending on the case scenario. Emission rates (E) were estimated based on the dominant material configuration, varying from 12 mg/h for full bamboo with soy adhesives to 70 mg/h for conventional OSB and cork. The time frame (t) was set to 8 hours, simulating typical daily occupancy exposure. The results of the analytical estimates were then compared with the peak total VOC (TVOC) concentrations derived from the CONTAM simulations.

4. Results and Discussion

4.1 Case Study 1: Baseline Configuration

The analysis of Case Study 1, which utilized conventional building materials including OSB wallboards, gypsum panels, and cork flooring, revealed significant temporal variability in both airflow and VOC concentrations. The average airflow rate across the year ranged from 59.8 L/s in February to a peak of 126.5 L/s in May, with a clear upward trend from early spring to late summer, followed by a gradual decline toward the end of the year as in Fig. 6. These values are consistently above the SNI-based minimum threshold of 30 L/s for residential ventilation [34], indicating that

the mechanical system in this configuration delivers sufficient ventilation under standard operating conditions.

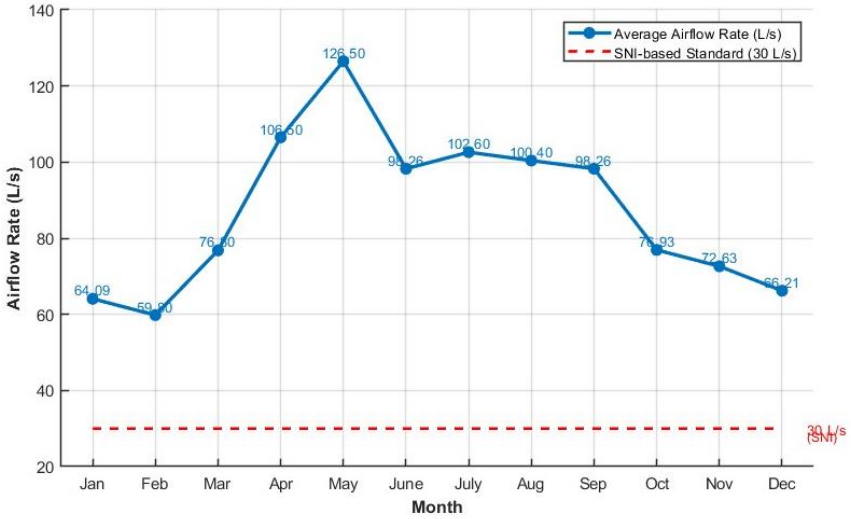

Fig. 6. Monthly average airflow rates for the baseline configuration, showing mechanical system performance across the year (Case Study 1)

Despite adequate ventilation rates, VOC concentrations in the case study remained above acceptable thresholds during most months. As shown in Fig. 7, total VOC (TVOC) levels from all materials peaked at 2.330 mg/m^3 in August, with the lowest level of 1.465 mg/m^3 recorded in December. These values significantly exceed the commonly cited benchmarks of 0.3 mg/m^3 for "Good" TVOC and 0.6 mg/m^3 for "Acceptable" TVOC, indicating persistent air quality concerns. Among individual materials, timber consistently exhibited the highest TVOC contribution, followed by OSB and gypsum, all of which remained above acceptable limits throughout the year. Although cork flooring contributed minimally to total TVOC, it remained the dominant source of formaldehyde, with relatively stable values across the months. These results highlight that even with compliant airflow design, pollutant levels can remain elevated due to material-based emissions, emphasizing the need to consider source control in addition to ventilation when aiming for healthier indoor environments.

4.2 Case Study 1.1: Impact of Cork Flooring Removal

In Case Study 1.1, cork flooring was excluded from the original material configuration to isolate its impact on indoor VOC levels, while the wall materials remained unchanged. As illustrated in Fig. 8, this material adjustment had no effect on the mechanical ventilation system's performance, as the average monthly airflow profile mirrored that of Case Study 1. The airflow rate peaked in May at 126.5 L/s and followed a consistent seasonal pattern, with values well above the SNI-based standard of 30 L/s throughout the year. This consistency confirms that changes in interior materials did not alter the ventilation dynamics, enabling a focused evaluation of VOC source reduction due solely to flooring modification.

However, Fig. 9 illustrates the VOC emission trends following the exclusion of cork flooring in Case Study 1.1. A notable improvement in indoor air quality was observed, with the annual peak of total VOC (TVOC) concentrations reduced from 3.775 mg/m^3 in the baseline scenario to 2.33 mg/m^3 in August. Formaldehyde levels—primarily linked to cork materials—also decreased significantly, peaking at 0.52 mg/m^3, which, while still exceeding the formal SNI limit, reflects a substantial drop from Case Study 1. The seasonal pattern of emissions remained consistent, suggesting the observed reductions were directly tied to material substitution rather than changes in airflow. Furthermore, the VOC contributions from timber, OSB, and gypsum remained nearly identical to the original case, reinforcing that the overall improvement was due to the elimination of cork-based emissions. This outcome highlights the critical role of strategic material selection in managing indoor pollutant levels. Although the reduction did not bring VOC concentrations below recommended thresholds,

it represents a meaningful step toward creating healthier indoor environments by targeting high-emission sources.

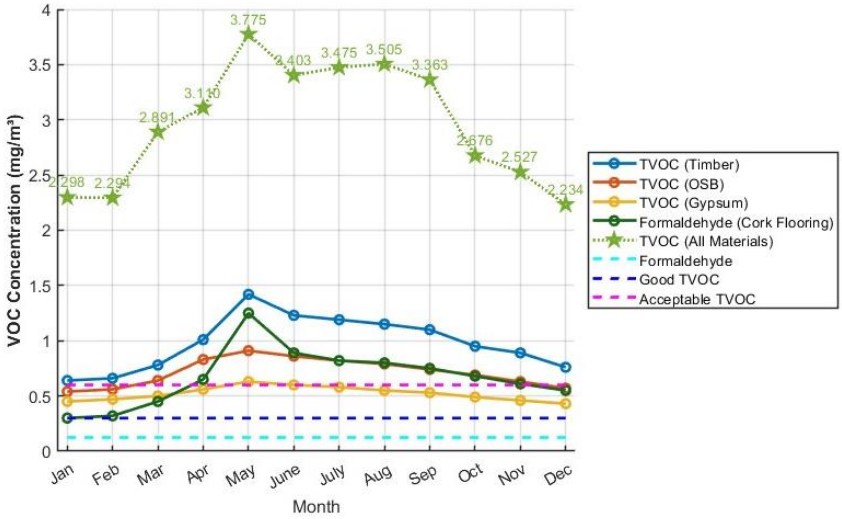

Fig. 7. VOC emission profile for the baseline case using OSB, gypsum, and cork flooring, highlighting monthly fluctuations in total VOC levels, Case Study 1

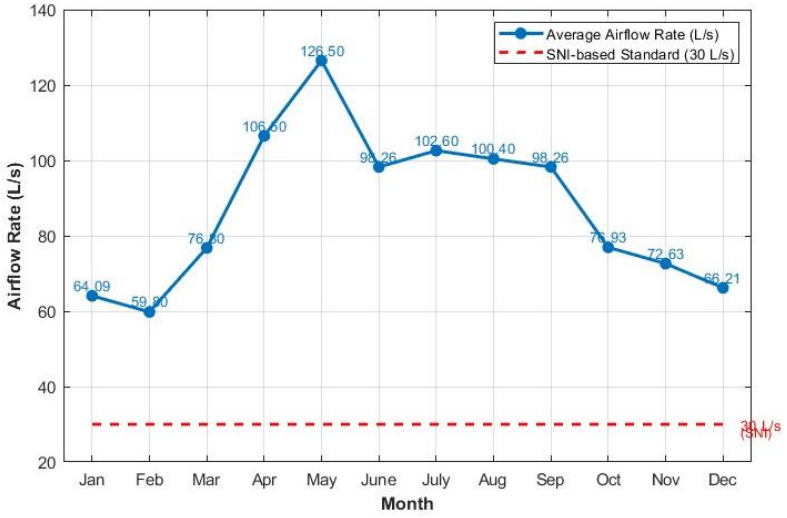

Fig. 8. Airflow rate trends following the removal of cork flooring, showing similar ventilation behavior to the baseline case (Case Study 1.1)

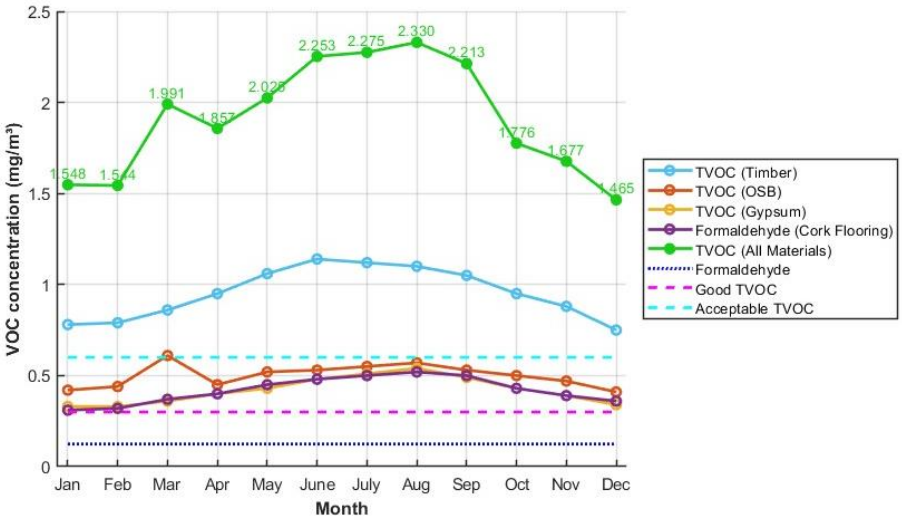

Fig. 9. VOC emission levels after removing cork flooring, demonstrating a significant reduction in total VOCs and formaldehyde concentrations (Case Study 1.1)

4.3 Case Study 2: Bamboo Material Substitution Scenarios

4.3.1 Case Study 2.0: Initial Bamboo Integration

In Case Study 2.0, laminated bamboo panels bonded with soy-based adhesives were introduced to replace conventional materials such as OSB boards and cork flooring. As shown in Fig. 10, the modification had no effect on the ventilation system, with monthly airflow rates mirroring those of previous case studies—ranging from 59.8 L/s in February to a peak of 126.5 L/s in May. Throughout the year, airflow remained well above the SNI standard of 30 L/s, confirming adequate ventilation performance.

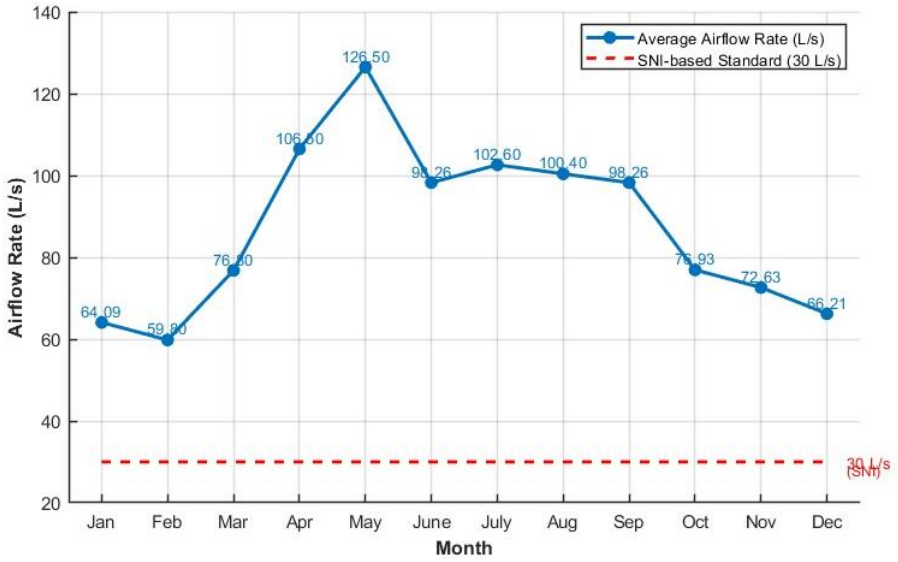

Fig. 10. Monthly average airflow rates for bamboo substitution scenarios, illustrating consistent ventilation performance across Cases 2.1–2.3.

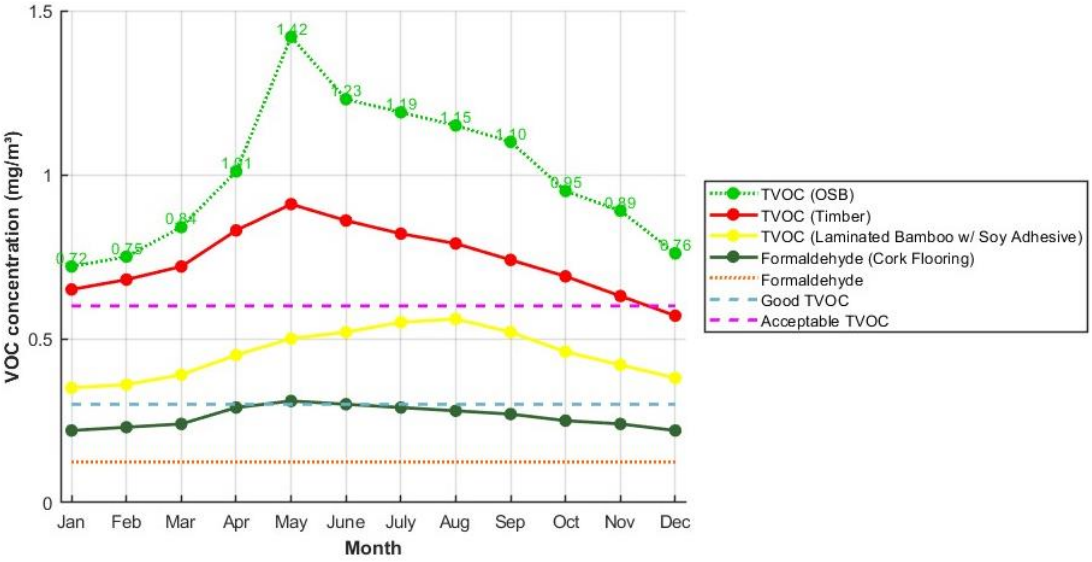

Fig. 11 VOC emission trends after partial integration of bamboo panels with soy-based adhesive, revealing improved IAQ over conventional materials (Case Study 2.0)

VOC emissions, illustrated in Fig. 11, showed a substantial reduction compared to the baseline. The peak TVOC level dropped to 1.23 mg/m^3 in May, significantly lower than the 3.775 mg/m^3 recorded in Case Study 1. Across all months, TVOC remained below 1.5 mg/m^3, with laminated bamboo panels emitting an average of 0.5 mg/m^3, demonstrating their low-emission profile. While OSB and timber still contributed to VOC levels, their impact was diminished. Additionally, formaldehyde emissions—previously elevated due to cork—were reduced as cork flooring was only partially

retained. These findings underscore the effectiveness of using soy-based adhesives in bamboo construction to improve indoor air quality without compromising airflow efficiency.

4.3.2 Case Study 2.1: Full Removal of Cork Flooring

In Case Study 2.1, cork flooring was eliminated to further reduce formaldehyde and VOC emissions. As shown in Fig. 12, laminated bamboo panels bonded with soy-based adhesives maintained consistently low emission levels throughout the year. Timber remained a moderate contributor to TVOC but did not exceed 1.0 mg/m^3 in any month. Notably, OSB emissions showed further decline, particularly during the cooler months, reinforcing the sensitivity of material emissions to seasonal temperature variations. The complete removal of cork—a primary source of formaldehyde—resulted in a significant improvement in overall indoor air quality, even during peak summer months. These findings confirm that replacing high-emission materials with lower-emission alternatives such as laminated bamboo can meaningfully reduce pollutant loads, supporting healthier indoor environments without compromising material performance.

4.3.3 Case Study 2.2: Bamboo Panel with MUF Adhesive

In Case Study 2.2, laminated bamboo flooring bonded with melamine-urea-formaldehyde (MUF) adhesive was assessed to understand the impact of synthetic binders on indoor VOC levels. As shown in Fig. 13, the emission profile of timber and OSB remained consistent with previous cases, while bamboo with MUF adhesive exhibited notably higher VOC concentrations, with values peaking near 0.96–1.02 mg/m^3 during warmer months. Although formaldehyde levels remained below critical limits, a slight increase was observed compared to soy-based adhesive scenarios, indicating that MUF-based products contribute more significantly to VOC burdens. The results underscore the importance of adhesive choice in sustainable material selection. While MUF adhesives offer structural reliability, they compromise indoor air quality when compared to bio-based alternatives. These findings reinforce the necessity of evaluating not just the base material but also binding agents when designing for low-emission environments.

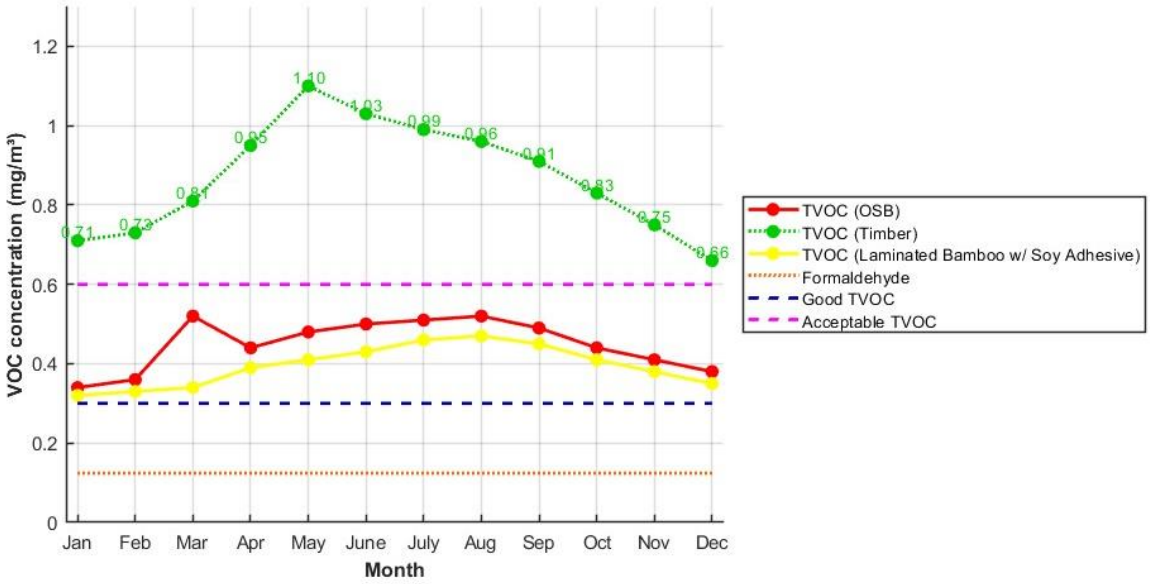

Fig. 12. VOC levels with complete replacement of cork flooring using laminated bamboo and soy adhesive, resulting in optimal IAQ performance (Case Study 2.1).

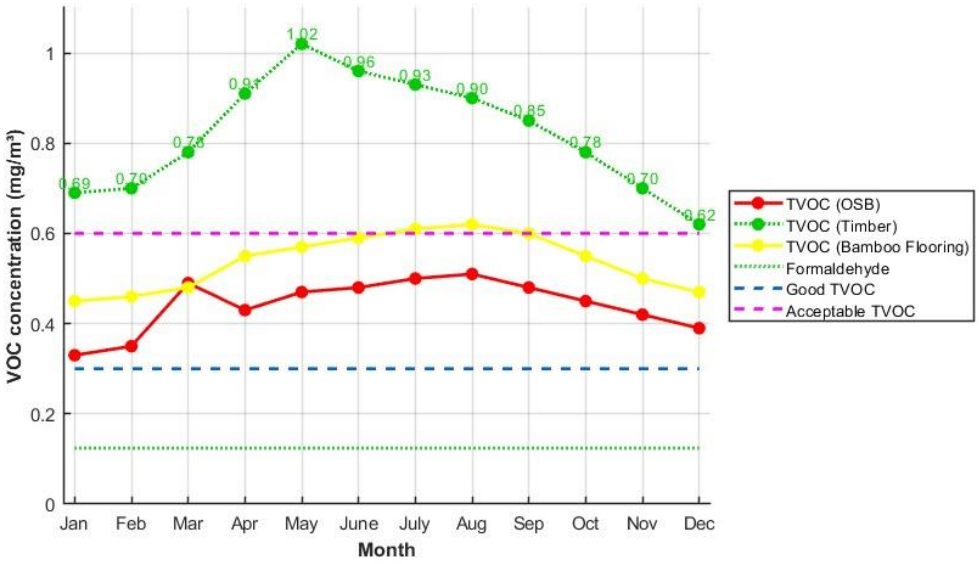

Fig. 13. VOC emission patterns with laminated bamboo using MUF adhesive, indicating higher pollutant levels compared to soy-based alternatives (Case Study 2.2)

4.3.4 Case Study 2.3: Bamboo Flooring Integration

In Case Study 2.3, laminated bamboo flooring was fully integrated alongside bamboo wall panels to assess the combined impact on indoor VOC emissions. As shown in Fig. 14, bamboo flooring consistently contributed lower TVOC levels than both OSB and timber across all months, with values remaining below 0.5 mg/m^3 throughout the year.

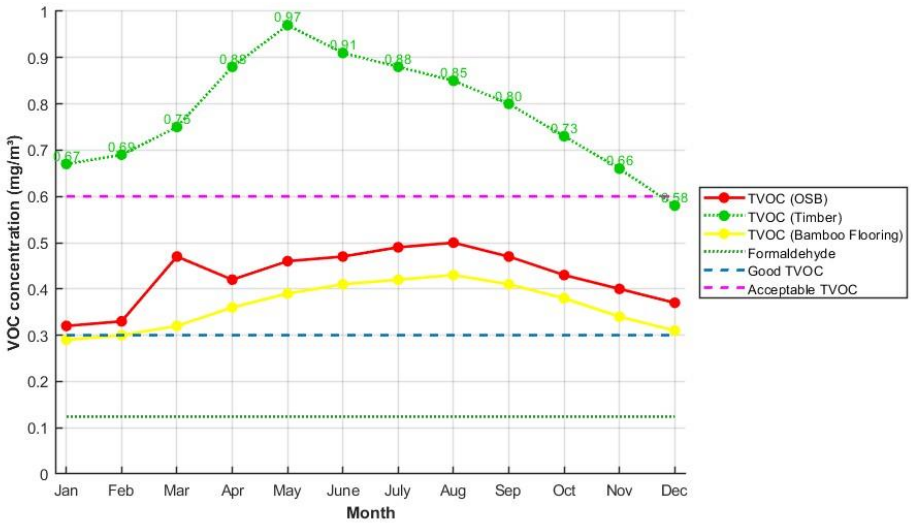

Fig. 14. Total VOC concentrations from full bamboo integration (walls and flooring), confirming cumulative emission reductions (Case Study 2.3)

These findings indicate that laminated bamboo, when used with low-emission adhesives, performs favorably as a sustainable interior finish. The combination of bamboo flooring and wall panels produced a cumulative reduction in pollutant emissions, highlighting the material's suitability for green building applications. This case reinforces the importance of pairing natural materials with optimized binders to achieve measurable improvements in indoor air quality. The results confirm that a holistic substitution strategy—targeting both surface and structural components—can yield superior environmental performance in residential interiors.

4.4 Case Study 3: Influence of Mechanical Ventilation and Temperature

4.4.1 Case Study 3.0: Bamboo Material with Standard Parameters

In Case Study 3.0, bamboo-based interior components, including laminated bamboo panels with melamine-urea-formaldehyde (MUF) adhesive and bamboo flooring—were analyzed under a fixed mechanical ventilation setting. As presented on Fig. 15, the monthly average airflow remained well above the SNI benchmark of 30 L/s, peaking at 138.3 L/s in May and reaching a minimum of 70.85 L/s in January, indicating stable mechanical system performance across seasonal variations.

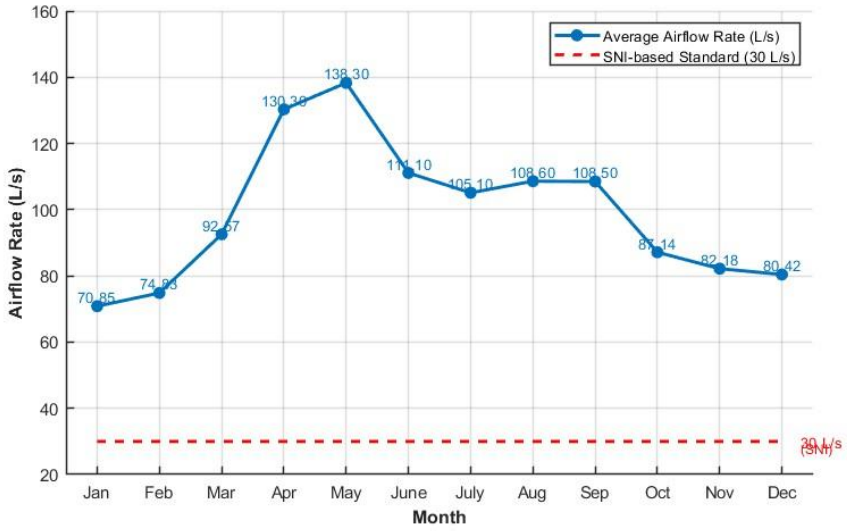

Fig. 15. Airflow behavior under standard environmental conditions for MUF-bonded bamboo configurations, reflecting seasonal ventilation performance (Case Study 3.0)

Despite adequate ventilation, VOC emissions varied by material, as shown on Fig. 16 Timber remained the highest contributor, peaking at 0.91 mg/m^3 in July before gradually declining. Laminated bamboo with MUF adhesive emitted moderate VOC levels ranging from 0.5 to 0.62 mg/m^3, with a maximum in August, slightly surpassing the "Acceptable" threshold of 0.6 mg/m^3. Meanwhile, bamboo flooring continued to perform favorably, maintaining VOC concentrations below 0.45 mg/m^3 throughout the year.

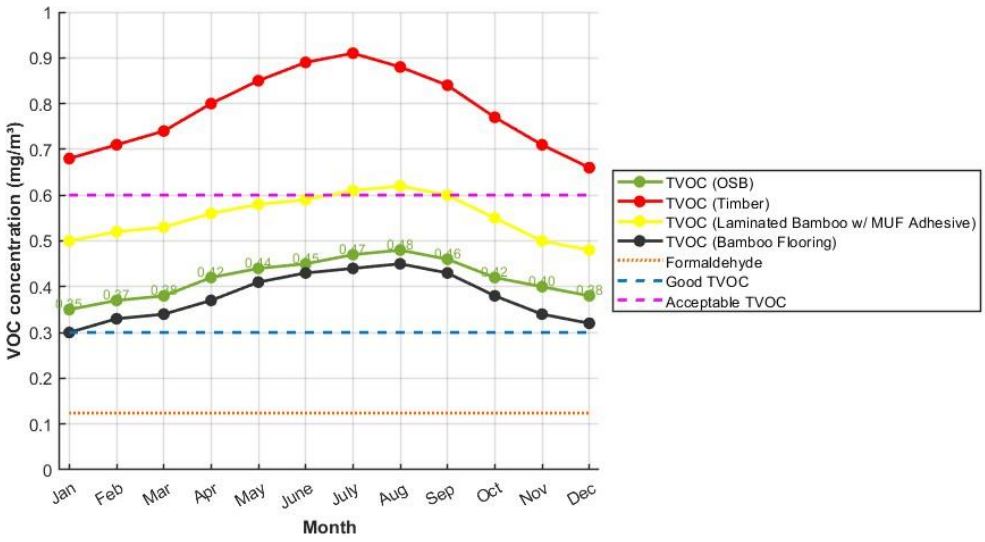

Fig. 16. VOC emission distribution from different material sources in a bamboo-based system under standard conditions (Case Study 3.0)

These outcomes suggest that although MUF-based adhesives enhance material durability, they also elevate indoor VOC emissions when compared to bio-based alternatives. The results reinforce the importance of selecting both sustainable base materials and low-emission binders to optimize indoor air quality while meeting structural performance goals. It is noted that VOC levels in certain configurations, including those using MUF adhesives or during high-temperature scenarios, still exceeded recommended IAQ thresholds. This suggests that material substitution alone is not sufficient, and must be complemented by thermal regulation and mechanical ventilation strategies to maintain optimal indoor air quality

4.4.2 Case Study 3.1: Increased Temperature Scenario

In Case Study 3.1, elevated indoor temperature conditions were simulated to evaluate their impact on VOC emissions, while maintaining the same mechanical ventilation setup as the baseline. As shown in Fig. 17, the airflow performance remained unchanged, peaking at 133.3 L/s in May, which confirms the stability of the system regardless of thermal variations.

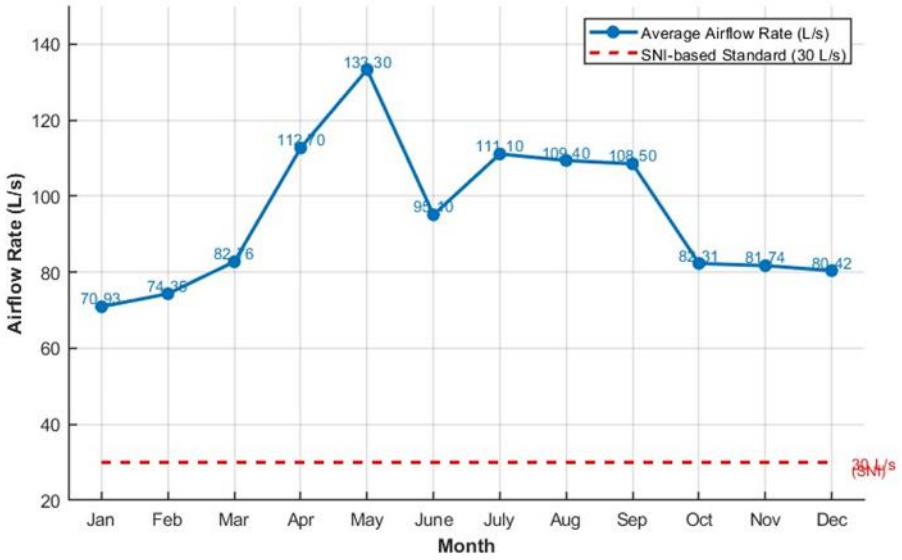

Fig. 17. Airflow rates during elevated temperature scenarios, showing consistent mechanical performance under thermal stress (Case Study 3.1)

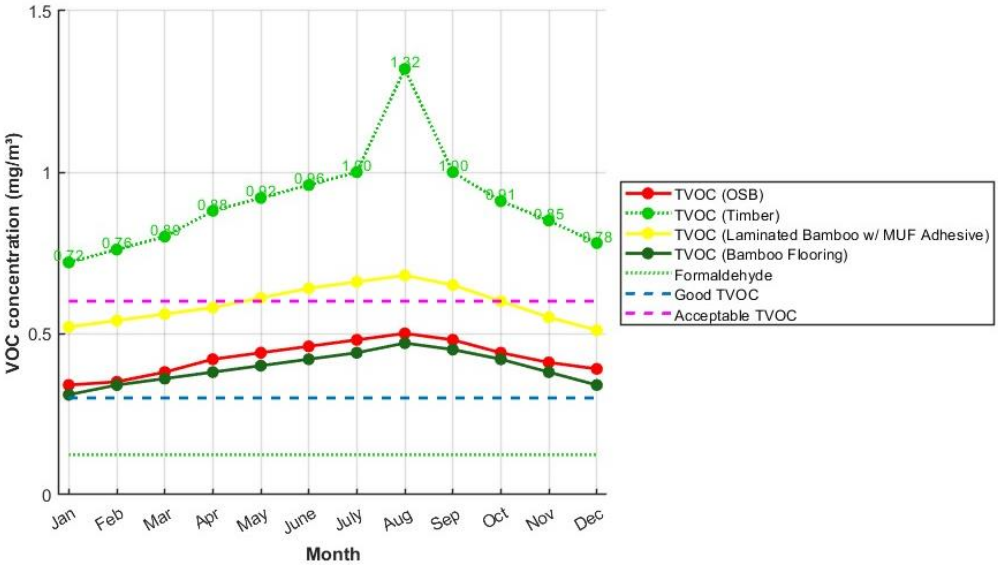

Fig. 18. VOC emissions under elevated temperatures, indicating a sharp increase in pollutant off-gassing from timber and MUF-bonded bamboo (Case Study 3.1)

However, VOC emissions exhibited clear temperature sensitivity. As illustrated in Figure 18, timber emissions peaked at 1.32 mg/m^3 in August, more than twice the peak level observed in Case Study 3.0. Likewise, laminated bamboo panels with MUF adhesive exceeded the acceptable limit, reaching 0.68 mg/m^3, while bamboo flooring saw increased emissions up to 0.47 mg/m^3 during the same month. These trends validate that VOC volatility intensifies with rising temperatures, as elevated heat accelerates off-gassing from building materials. While bamboo-based products remain environmentally promising, this case emphasizes that temperature conditions must be considered when evaluating long-term indoor air quality performance, particularly in thermally dynamic climates.

4.4.3 Case Study 3.2: Increased Ventilation Rate Scenario

In Case Study 3.2, the mechanical ventilation rate was elevated above baseline settings to evaluate the effectiveness of enhanced airflow in mitigating VOC concentrations. As shown on Fig. 19, the monthly average airflow exceeded 130 L/s during peak months and maintained higher values in cooler months, such as 87.34 L/s in November, compared to prior scenarios. This approach aimed to test whether dilution via airflow could offset emissions from high-VOC materials.

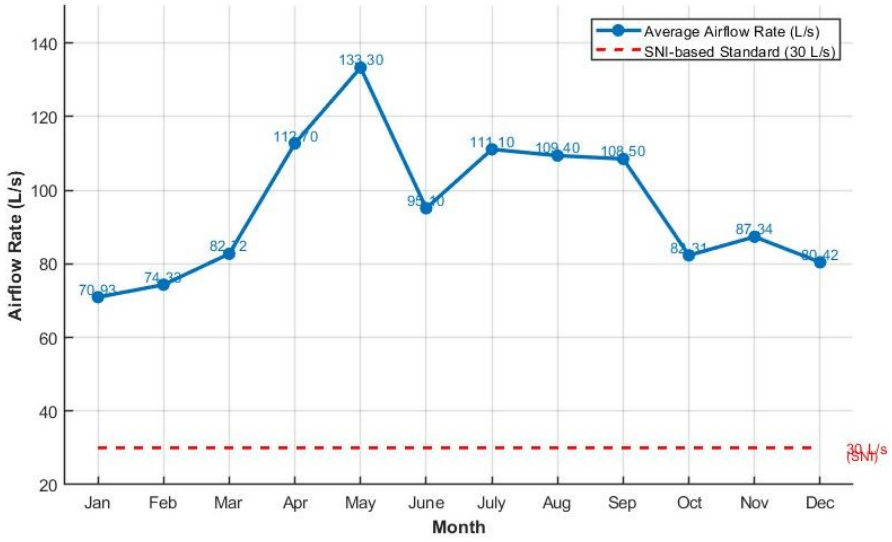

Fig. 19. Airflow patterns under enhanced ventilation conditions, demonstrating effective air dilution capacity in the system (Case Study 3.2)

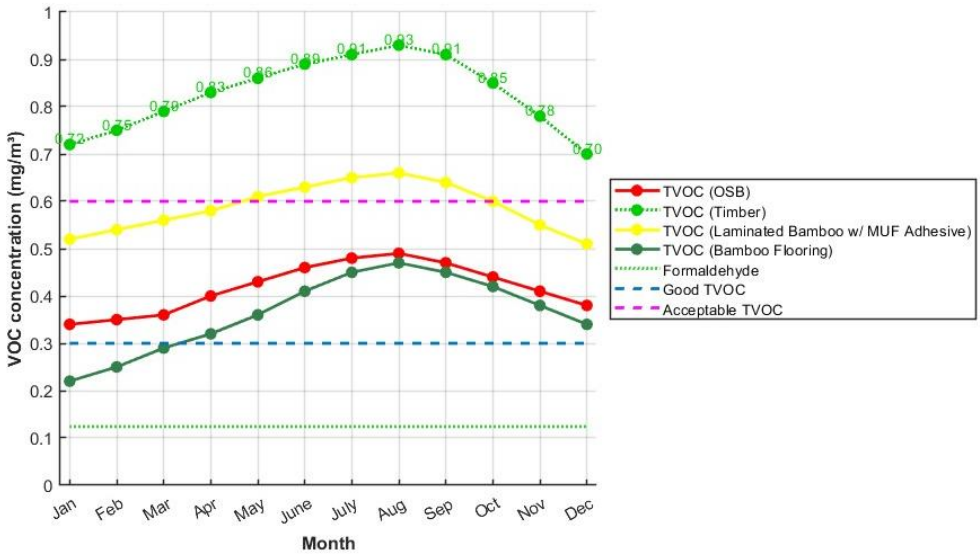

Fig. 20. VOC emission reduction achieved through increased mechanical ventilation, highlighting its effectiveness in pollutant dilution (Case Study 3.2)

The results, depicted on Fig. 20, indicate a measurable reduction in pollutant levels. Timber emissions dropped from a previous peak of 1.32 mg/m^3 (Case 3.1) to 0.93 mg/m^3, while bamboo flooring emissions decreased from 0.47 mg/m^3 to 0.34 mg/m^3 in December. Laminated bamboo with MUF adhesives also benefited, maintaining VOC concentrations near or just above the acceptable threshold throughout the year.

The simulation results across all nine case studies demonstrated that indoor air quality (IAQ) is highly sensitive to the choice of construction materials, adhesive types, and environmental conditions. In the baseline scenario (Case Study 1), the combination of OSB, gypsum, and cork flooring resulted in high indoor pollutant levels, with TVOC peaking at 3.775 mg/m^3 and formaldehyde at 1.25 mg/m^3, despite airflow rates exceeding the minimum SNI requirement. Removing cork in Case Study 1.1 improved IAQ, reducing TVOC to 2.33 mg/m^3 and formaldehyde to 0.52 mg/m^3. A detailed breakdown of these results is presented in Table 6, which compares the material configurations, emission peaks, airflow ranges, and overall IAQ performance for each case.

Significant improvements were observed in Case Studies 2.0 to 2.3, where laminated bamboo panels and bamboo flooring bonded with soy-based adhesives were introduced. These scenarios yielded the lowest emissions, especially in Case Study 2.1, where both cork and MUF adhesives were excluded—TVOC dropped to 1.10 mg/m^3, and formaldehyde was nearly undetectable. In contrast, Case Study 2.2, which used MUF adhesives, maintained acceptable but higher VOC levels, confirming that adhesive selection plays a key role in emission performance.

Environmental variables also influenced IAQ outcomes. In Case Study 3.1, increased indoor temperatures raised VOC emissions substantially, with timber TVOC reaching 1.32 mg/m^3. However, Case Study 3.2 showed that enhancing ventilation mitigated this effect, reducing TVOC to 0.93 mg/m^3, even when MUF adhesives were used. While the simulation framework focused on a single residential typology, the findings provide a generalized understanding applicable to similar urban housing typologies. Future extensions of this research could include multi-family units, school buildings, or commercial spaces to validate the material substitution strategy across broader building classes.

4.5 Comparison of Analytical and Simulated VOC Concentrations

The calculated analytical concentrations were then compared with the peak VOC values obtained from CONTAM for each case study. As shown in Table 7, while the analytical estimates were consistently lower in magnitude due to their idealized assumptions (e.g., perfect mixing), the relative trends closely matched the simulation outputs. High-emission cases (e.g., CS1 and CS1.1) yielded the highest VOC levels, while the bamboo-based systems (CS2.0–CS2.3) showed progressive reductions. Notably, Case Study 2.3, which employed full bamboo finishes with soy adhesives, achieved the lowest VOC values in both models. Additionally, environmental adjustments such as elevated temperature (CS3.1) and increased ventilation (CS3.2) reflected expected shifts in VOC behavior across both estimation methods.

The analytical values, while consistently lower in magnitude, exhibit the same relative trend as the simulation results. For instance, CS1, which employed high-emission materials such as OSB and cork, showed the highest values in both simulations (3.775 mg/m^3) and analytical estimates (0.154 mg/m^3). As lower-emission materials such as bamboo bonded with soy adhesives were introduced (CS2.0–CS2.3), the estimated VOC levels declined accordingly. Notably, CS2.3, which utilized full bamboo interior finishes, recorded the lowest simulated (0.88 mg/m^3) and analytical (0.026 mg/m^3) VOC concentrations.

Environmental variation scenarios further confirmed model reliability. In CS3.1, elevated temperature increased simulated VOC emissions (1.32 mg/m^3), mirrored by a higher analytical estimate (0.052 mg/m^3). Conversely, CS3.2 demonstrated the benefits of increased ventilation in reducing VOC levels, with both methods indicating decreased concentrations compared to CS3.1.

While absolute values differ due to idealized assumptions (e.g., perfect mixing), the directional agreement between the models validates the robustness of the CONTAM outputs. This consistency provides confidence in the simulation framework's capacity to predict indoor air quality trends resulting from material and environmental modifications. It also highlights the suitability of

bamboo with bio-based adhesives in delivering lower indoor VOC concentrations under realistic operating conditions.

Table 6. Summary of simulation results for all case studies

Case Study	Key Material Configuration	Peak TVOC (mg/m^3)	Peak Formaldehyde (mg/m^3)	Airflow Range (L/s)	IAQ Performance Summary
Case Study 1	OSB + Gypsum + Cork	3.775	1.25	59.8 – 126.5	Exceeded VOC limits despite good airflow
Case Study 1.1	OSB + Gypsum (Cork Removed)	2.33	0.52	59.8 – 126.5	Improved IAQ, still above threshold
Case Study 2.0	Bamboo (Soy Adhesive) + Partial Cork	1.23	<0.3	59.8 – 126.5	Major VOC reduction
Case Study 2.1	Bamboo (Soy Adhesive) + No Cork	1.10	Near-zero	59.8 – 126.5	Optimal IAQ performance
Case Study 2.2	Bamboo (MUF Adhesive)	1.02	~0.45	59.8 – 126.5	Acceptable, but higher than soy adhesive
Case Study 2.3	Full Bamboo Panels + Flooring (Soy)	0.88	<0.3	59.8 – 126.5	Consistently low emissions
Case Study 3.0	Bamboo + MUF Adhesive (Standard Ventilation)	0.91	~0.5	70.8 – 138.3	Acceptable IAQ, moderate emissions
Case Study 3.1	Bamboo + MUF + High Temperature	1.32	0.68	70.8 – 133.3	VOCs exceeded safe range
Case Study 3.2	Bamboo + MUF + Increased Ventilation	0.93	0.45	87.3 – 138.3	Effective VOC reduction via dilution

Table 7. Analytical and Simulated VOC Concentrations Across Case Studies

Case Study	Material Configuration	Emission Rate E (mg/h)	Ventilation Rate Q (m^3/h)	Indoor Volume V (m^3)	Duration t (h)	Analytical VOC C(t) (mg/m^3)	Simulated Peak TVOC (mg/m^3)
CS1	OSB + Gypsum + Cork	70	455.4	518	8	0.154	3.775
CS1.1	OSB + Gypsum (No Cork)	45	455.4	518	8	0.099	2.330
CS2.0	Bamboo (Soy) + Partial Cork	25	455.4	518	8	0.055	1.230
CS2.1	Bamboo (Soy) + No Cork	15	455.4	518	8	0.033	1.100
CS2.2	Bamboo (MUF Adhesive)	20	455.4	518	8	0.044	1.020
CS2.3	Full Bamboo (Soy Adhesive)	12	455.4	518	8	0.026	0.880
CS3.0	Bamboo (MUF), Standard Ventilation	18	497.9	518	8	0.036	0.910
CS3.1	Bamboo (MUF), High Temperature	25	479.9	518	8	0.052	1.320
CS3.2	Bamboo (MUF), Increased Ventilation	18	497.9	518	8	0.036	0.930

5. Limitations of the Study

This study relied on simulation-based modelling using CONTAM to assess the impact of bamboo materials on indoor air quality, which, while powerful, involves assumptions that may not fully capture real-world conditions. Material emission factors, particularly for VOCs and formaldehyde, were sourced from literature and manufacturer data, which may not reflect variability due to product aging, production differences, or in-situ environmental interactions. Moreover, the adhesive formulations used in bamboo composites were modelled based on ideal chemical compositions, without accounting for on-site factors such as curing variability or application inconsistencies that could affect emission behaviour.

Additionally, the analysis was limited to a single residential building typology within a temperate climate zone, which may restrict the generalizability of the findings to other building types or climatic conditions. Dynamic occupant behaviours, window use, furniture interactions, and potential HVAC system faults were not included in the simulations, potentially underestimating variability in indoor air quality. Furthermore, the focus was placed solely on VOCs and formaldehyde, excluding other indoor pollutants such as particulate matter and biological agents, which also influence occupant health. Future studies should integrate experimental validation and a broader pollutant scope to support more holistic IAQ assessment.

In addition, this study did not incorporate dynamic occupant behavior such as window operation, furniture interaction, or variable HVAC performance, all of which can influence IAQ outcomes. While the simulation assumed uniform zone concentrations and consistent airflow paths (e.g., door gaps, diffusers), real-world variability could lead to more complex pollutant distributions. Furthermore, although bamboo emission values were based on published data, experimental validation under local environmental conditions would enhance future model accuracy.

6. Conclusion

This study presents a comprehensive simulation-based investigation into the indoor air quality (IAQ) implications of using bamboo-based materials in residential construction, with a particular focus on volatile organic compound (VOC) emissions. Through nine detailed case studies modelled using CONTAM software, the research evaluated the effects of various interior material combinations, adhesive types, thermal conditions, and mechanical ventilation rates. The results consistently demonstrate that the integration of engineered bamboo bonded with soy-based adhesives substantially improves IAQ, with total VOC (TVOC) and formaldehyde levels significantly lower than those of conventional materials like OSB and cork.

Key findings reveal that even with sufficient ventilation, high-emission materials can cause pollutant concentrations to exceed acceptable limits, highlighting the importance of source control in achieving healthy indoor environments. Substituting these materials with bamboo-based alternatives especially when paired with bio-based adhesives resulted in up to a threefold reduction in TVOC, with values falling below 1.0 mg/m^3 in optimal cases. Environmental conditions were found to strongly influence emission behaviour. Elevated indoor temperatures intensified VOC off-gassing, particularly from timber and MUF-bonded bamboo products, while increased mechanical ventilation provided a partial mitigation strategy through pollutant dilution. These findings underline that material substitution alone is not sufficient; rather, IAQ optimization must be approached holistically, combining low-emission materials with climate-sensitive ventilation strategies.

To validate the simulation findings, an analytical estimation using the well-mixed zone model was conducted. Although simplified in assumptions, the analytical results closely mirrored the trends observed in CONTAM outputs, supporting the reliability and predictive value of CONTAM software in early-stage IAQ assessments. The alignment of both approaches reinforces confidence in the modelling framework and confirms its suitability for guiding low-emission material selection during the architectural design process.

Beyond technical outcomes, this research offers several practical implications for architects, designers, and policymakers. First, the findings advocate for the specification of bamboo-based

materials with soy-based adhesives in interior applications, especially in tropical and temperate climates. Second, given the influence of temperature and airflow, design strategies should integrate passive and active ventilation systems capable of responding to seasonal changes. Third, the framework can inform sustainable building codes and indoor air quality guidelines, promoting the adoption of bio-based materials in green certification systems.

Finally, although this study focused on a single residential building typology in a temperate proxy climate, the simulation approach is transferable to other building types, including schools, commercial spaces, and multi-family dwellings. Future research should extend this model to diverse climatic zones and incorporate experimental validations to further confirm emission behaviour under real-world conditions. Inclusion of economic analyses comparing bamboo-based systems with conventional materials would also enhance practical adoption. By demonstrating the material-environmental interplay in indoor pollutant control, this study contributes meaningful evidence to the growing discourse on health-centered, climate-resilient building design. It affirms that with appropriate material choices and system integration, sustainable construction can enhance both occupant health and environmental performance.

Acknowledgement

The authors acknowledge that this study is supported by the academic environment and facilities provided by Universitas Muhammadiyah Yogyakarta, which significantly contributed to the successful completion of this research.

References

[1] Singh S, Vishwakarma P, Gupta T. Review of Current and Future Indoor Air Purifying Technologies. ACS ES and T Engineering 2024;4:2607–30. https://doi.org/10.1021/acsestengg.4c00460
[2] Malhi K. IAQ versus IEQ: What's the difference? Consult Specif Eng 2021;58:6–14.
[3] Banerjee A, Melkania NP, Nain A. Indoor Air Quality (IAQ) in Green Buildings, a Pre-Requisite to Human Health and Well-Being. Digital Cities Roadmap: IoT-Based Architecture and Sustainable Buildings, 2021. https://doi.org/10.1002/9781119792079.ch9
[4] Pardo A, Israeli E. The Sick Building Syndrome as a Part of the Autoimmune (Autoinflammatory) Syndrome Induced by Adjuvant. 2024. https://doi.org/10.1002/9781119858430.ch15
[5] Bashir MT, Khan AB, Khan MMH, Rasheed K, Saad S, Farid F. Evaluating the Implementation of Green Building Materials in the Construction Sector of Developing Nations. Journal of Human, Earth, and Future 2024;5:528–42. https://doi.org/10.28991/HEF-2024-05-03-015
[6] Shu B, Xiao Z, Hong L, Zhang S, Li C, Fu N, et al. Review on the application of bamboo-based materials in construction engineering. J Renew Mater 2020;8. https://doi.org/10.32604/jrm.2020.011263
[7] Khajouei-Nezhad M, Semple K, Nasir V, Hu Y, Marggraf G, Hauptman J, et al. Advances in engineered bamboo processing: Material conversion and structure. Advances in Bamboo Science 2023;5. https://doi.org/10.1016/j.bamboo.2023.100045
[8] Shan B, Wang G, Lei P, Li T, Xiao Y, Qin S, et al. Experimental research on formaldehyde emission characteristics from glubam by climate chamber test. Sustainable Structures 2023;3. https://doi.org/10.54113/j.sust.2023.000027
[9] Pu H, Han K, Dai R, Shan Z. Semi-liquefied bamboo modified urea-formaldehyde resin to synthesize composite adhesives. Int J Adhes Adhes 2022;113. https://doi.org/10.1016/j.ijadhadh.2021.103061
[10] Jung C, Ismail MA, Arar M, AlQassimi N. Mitigating indoor air pollution in UAE's high-rise apartment buildings: a study on eco-friendly materials and adsorbents. Smart and Sustainable Built Environment 2024. https://doi.org/10.1108/SASBE-09-2023-0269
[11] Wang L, Dols WS, Chen Q. Using CFD capabilities of CONTAM 3.0 for simulating airflow and contaminant transport in and around buildings. HVAC and R Research 2010;16. https://doi.org/10.1080/10789669.2010.10390932
[12] Dols WS, Polidoro BJ. CONTAM User Guide and Program Documentation Version 3.4. National Institute of Standards and Technology 2020.
[13] Zhao FY, Cheng J, Liu B, Huang ZR, Li X. Indoor airflow and pollutant spread inside the cleanroom with micro-porous supplying panel and different ventilation schemes: Analytical, numerical and experimental investigations. Journal of Building Engineering 2020;31. https://doi.org/10.1016/j.jobe.2020.101405
[14] Lin W, Li L, Liu X, Zhang T. On-site measurement and numerical investigation of the airflow characteristics in an aquatics center. Journal of Building Engineering 2021;35. https://doi.org/10.1016/j.jobe.2020.101968

[15] Wang X, Cheng S, Zhou Y, Zhang H, Guan P, Zhang Z, et al. A review of the technology and applications of methods for evaluating the transport of air pollutants. J Environ Sci (China) 2023;123. https://doi.org/10.1016/j.jes.2022.06.022
[16] Argyropoulos CD, Hassan H, Kumar P, Kakosimos KE. Measurements and modelling of particulate matter building ingress during a severe dust storm event. Build Environ 2020;167. https://doi.org/10.1016/j.buildenv.2019.106441
[17] Fine JP, Gray J, Tian X, Touchie MF. An investigation of alternative methods for determining envelope airtightness from suite-based testing in multi-unit residential buildings. Energy Build 2020;214. https://doi.org/10.1016/j.enbuild.2020.109845
[18] Taylor J, Shrubsole C, Biddulph P, Jones B, Das P, Davies M. Simulation of pollution transport in buildings: The importance of taking into account dynamic thermal effects. Building Services Engineering Research and Technology 2014;35. https://doi.org/10.1177/0143624414528722
[19] García-Tobar J. A comparative study of indoor radon levels between two similar dwellings using CONTAM software. Environments - MDPI 2018;5. https://doi.org/10.3390/environments5050059
[20] Dols WS, Emmerich SJ, Polidoro BJ. Using coupled energy, airflow and indoor air quality software (TRNSYS/CONTAM) to evaluate building ventilation strategies. Building Services Engineering Research and Technology, vol. 37, 2016. https://doi.org/10.1177/0143624415619464
[21] Bhattacharyya S, Dey K, Paul AR, Biswas R. A novel CFD analysis to minimize the spread of COVID-19 virus in hospital isolation room. Chaos Solitons Fractals 2020;139. https://doi.org/10.1016/j.chaos.2020.110294
[22] Xie W, Gao J, Lv L, Hou Y, Cao C, Zeng L, et al. Parametrized design for the integration of range hood and air cleaner in the kitchen. Journal of Building Engineering 2021;43. https://doi.org/10.1016/j.jobe.2021.102878
[23] Liu W, Liu D, Gao N. CFD study on gaseous pollutant transmission characteristics under different ventilation strategies in a typical chemical laboratory. Build Environ 2017;126. https://doi.org/10.1016/j.buildenv.2017.09.033
[24] Dols WS, Milando CW, Ng L, Emmerich SJ, Teo J. On the benefits of whole-building IAQ, ventilation, infiltration, and energy analysis using co-simulation between CONTAM and EnergyPlus. J Phys Conf Ser, vol. 2069, 2021. https://doi.org/10.1088/1742-6596/2069/1/012183
[25] Du C, Chen J, McCarty D, Chen Q. Ventilation performance of induction displacement units in indoor spaces within cold regions. Sustain Cities Soc 2024;114. https://doi.org/10.1016/j.scs.2024.105755.
[26] Jahanbin A, Semprini G. Numerical study on indoor environmental quality in a room equipped with a combined hrv and radiator system. Sustainability (Switzerland) 2020;12:1–22. https://doi.org/10.3390/su122410576
[27] Makowski M, Ohlmeyer M, Meier D. Long-term development of VOC emissions from OSB after hot-pressing. Holzforschung 2005;59. https://doi.org/10.1515/HF.2005.086
[28] Silva GVA, Fernandes EDO. VOC emissions from cork materials. EPIC '98 2nd European Conference on Energy Performance and Indoor Climate in Buildings and 3rd International Conference on Indoor Air Quality, Ventilation and Energy Conservation in Buildings 1997:27–32.
[29] Yauk M, Stenson J, Donor M, Van Den Wymelenberg K. Evaluating volatile organic compound emissions from cross-laminated timber bonded with a soy-based adhesive. Buildings 2020;10. https://doi.org/10.3390/buildings10110191
[30] Salem MZM, Böhm M. Understanding of formaldehyde emissions from solid wood: An overview. Bioresources 2013;8. https://doi.org/10.15376/biores.8.3.4775-4790
[31] Indonesian National Standard (SNI). SNI 03-6572-2001Procedures for Designing Air Conditioning and Ventilation Systems in Buildings. Jakarta: 2001.
[32] Eickmann U, Liesche A, Wegscheider W. Harmonization and further development of models to calculate airborne contaminant concentrations at the workplace. Gefahrstoffe Reinhaltung Der Luft 2007;67.
[33] Rostami AA, Agyemang S, Pithawalla YB. A distributed computational model for estimating room air level of constituents due to aerosol emission from e-vapor product use. Food and Chemical Toxicology 2018;116. https://doi.org/10.1016/j.fct.2018.04.020
[34] Muslimsyah, Nizarli, Safwan, Edytia MHA, Huda K, Muftiadi. Analysis of ventilation conditions in the rumoh aceh exhibition museum. IOP Conf Ser Earth Environ Sci, vol. 1361, 2024. https://doi.org/10.1088/1755-1315/1361/1/012007

Research on Engineering Structures & Materials
www.jresm.org
Research Group

Research Article

Influence of calcium sources on strength and self-healing characteristics of bacterial concrete

Gouthami Patnaik Palter [*,1,a], Kanaka Durga Sambhana [1,b], Venkata Giridhar Poosarla [2,c], Potharaju Malasani [3,d]

[1]*Department of Civil Engineering, GITAM School of Technology, GITAM (Deemed to be University), Visakhapatnam, Andhra Pradesh, 530045, India*
[2]*Department of Life Sciences, GITAM School of Science, GITAM (Deemed to be University), Visakhapatnam, Andhra Pradesh, 530045, India*
[3]*Registrar, Apollo University, Chittoor, Andhra Pradesh, 517127, India*

Article Info

Article History:

Received 25 May 2025
Accepted 23 July 2025

Keywords:

Bio-mineralization;
Microbially induced calcium carbonate precipitation;
Calcium precursors;
Strength properties;
Microstructure analysis;
Induced pre-crack width healing

Abstract

Concrete cracking poses significant challenges for infrastructure longevity, leading to costly maintenance and structural weaknesses. This research investigates a sustainable solution using Microbially Induced Calcium Carbonate Precipitation (MICP) with *Bacillus subtilis*, a non-ureolytic bacterial agent, for autonomous crack repair. Alongside M20 grade concrete samples, bacterial concrete specimens were prepared in this study by incorporating three calcium-based precursors-calcium lactate, calcium nitrate, and calcium formate at varying dosages (1%, 2%, and 3% by weight of cement). These precursors stimulate the calcite formation during bio-calcification. Strength performance and self-healing behavior of induced pre-crack widths were evaluated over 91 days, with durability assessments including water absorption, porosity (28 days), and drying shrinkage over 91 days. Results showed that adding calcium precursors did not adversely affect strength. Notably, bacterial concrete with 1% calcium formate showed 31.1% strength increase, while 1% calcium lactate and 2% calcium nitrate achieved 18% and 28% improvements respectively, compared to conventional concrete specimens at 91 days. Samples with 3% calcium formate dosage achieved the lowest porosity (6.1%), which corresponded to the maximum compressive strength of 62MPa through effective pore filling. Remarkably, 1% calcium formate completely healed 2mm crack width by day 91. Scanning Electron Microscopy (SEM), Energy-Dispersive X-ray Spectroscopy (EDS), Fourier Transform Infrared spectroscopy (FTIR), and X-ray diffraction (XRD) analyses confirmed enhanced calcite precipitation and microstructural densification in optimal specimens, particularly with calcium formate. Non-ureolytic microbial systems enhance both strength and crack healing abilities establishing calcium formate at 1% dosage as the optimal precursor, providing a promising, resilient, self-sustaining construction material.

© 2025 MIM Research Group. All rights reserved.

1. Introduction

Despite its ubiquity and seeming simplicity, concrete's intrinsically diverse microstructure results in extremely complex mechanical behavior. At the core of this complexity are the development and spread of micro-crack networks, which are the primary causes of concrete structures' deterioration in strength [1]. Figuring out the impact of cracks reduces the need for expensive repairs and

*Corresponding author: 1260216403@gitam.in
[a]orcid.org/0000-0002-9491-2048; [b]orcid.org/0000-0002-4756-4191; [c]orcid.org/0000-0001-9827-6336; [d]orcid.org/0000-0001-6336-2103
DOI: http://dx.doi.org/10.17515/resm2025-926ma0525rs

replacements while maximizing the use of concrete. Inadequate understanding and treatment of cracks can jeopardize structural integrity and perhaps result in catastrophic failures. Investigations into the mechanisms of fracture propagation yield crucial information for early warning systems and safety assessment procedures. Through improved crack management, concrete service life can be extended to 100 years, which directly supports sustainability objectives by lowering replacement costs and the resulting carbon footprint [2]. In the United States alone, concrete infrastructure upkeep and repair currently cost more than $100 billion a year, with comparable proportionate expenses seen throughout the world. Treatments to remediate the crack using certain traditional methods were employed in the presence of human intervention, which requires incessant periodic investigation and application of external agents such as injecting, pasting techniques, and coatings on the concrete surfaces. However, these traditional remediation methods are limited because of the material's weak heat resistance, moisture sensitivity, labour-intensive and differential coefficient of thermal expansion [3-6]. The manufacture of cement, which is essential for these repairs, accounts for around 7% of carbon dioxide emissions worldwide. Compared to conventional manufacturing methods, bio-cementation reduces carbon emissions by 18–49.6% [7]. Moreover, chemical-based repair products frequently have compatibility problems and present health dangers, which makes maintenance tasks much more difficult [8, 9]. A revolutionary approach to infrastructure resilience is the self-healing concrete paradigm, in which the material is designed to utilize either of the two self-healing mechanisms, one being autonomous crack healing and the other being autogenous crack healing [10-12]. The autogenous healing technique is an organic process, and its healing capacity is possible when there is an addition of high binding mixtures and a delayed hydration process, confining to small cracks closure, i.e., 0.15-0.2 mm is achievable. Although its efficiency can be enhanced with additives like fibres, supplementary cementitious materials (SCMs), and curing agents, it is still inadequate for addressing larger cracks [13, 14]. An autonomous healing mechanism was explicated in order to combat the aforementioned problems by introducing certain intrinsic and extrinsic self-healing materials or agents into the concrete, which remain dormant lest activated by crack formation [15-20]. Cracks being healed with the aid of micro-organisms underlines the intrinsic treatment which relies on a novel technology of “Bio-mineralization” [21, 22], and other methods by incorporating polymers, carriers categorize extrinsic treatment which are of high cost [1, 23-26]. A promising subset of autonomous healing mechanisms involves the microbially induced calcium carbonate precipitation (MICP) technique for addressing the micro-crack networks in concrete structures. This innovative bio-chemical process converts organic substrates into inorganic compounds through the catalysis of bacteria, creating an alkaline environment that leads to calcium carbonate precipitation [27]. Calcium lactate, calcium nitrate, calcium formate, calcium acetate, calcium chloride, and calcium glutamate are such compounds that are supplemented as calcium precursors for undergoing the MICP process in self-healing concrete, either through metabolic conversion of organic compounds or ureolysis, or denitrification precipitation mechanism [21, 28-32]. Amongst which calcium lactate, calcium nitrate, and calcium formate are applicable at the field-scale level for the enhancement of concrete properties [33]. Calcium lactate is bio-compatible, low-cost, easily accessible, and can be directly added into the concrete matrix in mixing water [34-36]. Calcium nitrate is globally used in the admixture/agriculture industry scale. It acts as an accelerator; inhibits corrosion, is compatible with other additives, and is cost-effective [30, 37, 38]. Calcium formate is used in multiple roles in varied field-scale applications, especially in cement-based industries. It acts as an accelerator, anti-freezing agent, and is cost-effective [39, 40]. Calcium acetate and calcium chloride are also cost-effective, but calcium chloride alone may not be considered the optimal choice in MICP studies [41]. A study reported that MICP treatment exhibited a lifecycle cost decrease of roughly 98% when compared to conventional treatment approaches [7, 40, 41]. Most MICP studies have centered on ureolytic bacteria such as *Sporosarcina pasteuriia* and *Bacillus subtilis* species, which catalyze urea hydrolysis to produce carbonate ions. However, ureolytic pathways can result in ammonia by-products and are sensitive to pH and substrate conditions, limiting their scalability. Non-ureolytic bacteria like *B. subtilis* offer a biologically safer and chemically stable alternative, yet remain underexplored in MICP-based self-healing concrete. A study reported that recovery of compressive strength of the specimens was about 80% due to the MICP mechanism [42-44]. Certain study findings revealed a 32% enhancement in compressive

strength and a 37% enhancement in flexural strength attributed to the deposition of ($CaCO_3$), which filled micro voids and densified the concrete [42, 45-50]. Previous research demonstrated that MICP-treated concrete exhibited a 70% reduction in water permeability compared to untreated samples. The addition of calcium lactate alone directly would increase the strength in the concrete when used at up to 1 and 2% and potentially up to 3% by mass of cement [51]. The influence of the three self-healing agent's calcium lactate, calcium nitrate, and calcium formate on setting time, hydration kinetics, rheology, and compressive strength in the presence of spore-forming bacterial species was studied in the cement mortar. However, the ability of these self-healing agents in terms of strength and crack healing was not assessed, particularly in the context of non-ureolytic microbial systems [52]. This study addresses this gap by systematically evaluating the influence of three calcium precursors, i.e., calcium lactate, calcium nitrate, and calcium formate, on the mechanical properties and crack healing performance of *B. subtilis*-based microbial concrete. The precursors were incorporated at three dosage levels (1, 2, and 3 % by weight of cement (bwc)), and performance metrics included mechanical strength, porosity, water absorption, drying shrinkage, self-healing performance, and microstructural characterization.

2. Materials and Methods

2.1. Cement and Calcium Sources

The Ordinary Portland Cement (OPC) of 53 grade, complying with IS 12269: 2013, was used in this study. Potable water was utilized that complied with IS 456: 2000. The precursors incorporated in the study are Calcium lactate ($CaC_6H_{10}O_6.5H_2O$), (L), LR grade was from Triveni Interchem Pvt. Ltd., Gujarat; Calcium nitrate ($(CaNO_3)_2.4H_2O$), (N), LR grade was from locally made United Scientific Chemicals Pvt ltd., Visakhapatnam; Calcium formate ($Ca(HCOO)_2$),(F), 99% LR grade was from Future Lab, Bangalore. The physical properties of the cement, fine and coarse aggregates, including fineness of cement (R), specific gravity (G_s), water absorption (W_a), fineness modulus (FM), standard consistency (P), initial and final setting time according to the IS codes were tabulated in Table 1. The methodology adopted in this study is illustrated (Fig. 1).

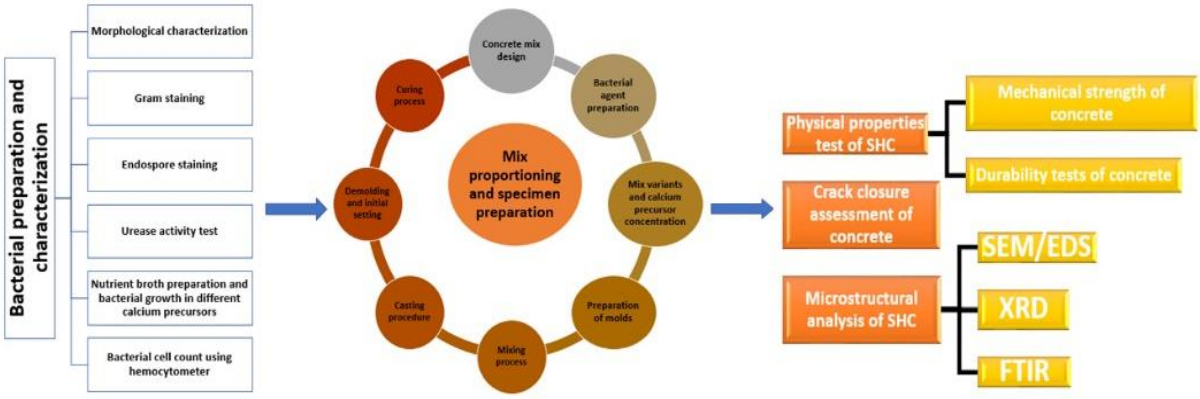

Fig. 1. Schematic flowchart of the methodology employed in the present study

Table 1. Physical properties of cement and aggregates

S.No	Materials	R	G_s	W_a	FM	P	Shape	Initial and Final setting time (min)	Referral codes
1	Cement	2.3%	3.1	-	-	33%	-	85 and 381	IS 4031 Part1:1996 IS 4031 Part4:1988 IS 4031 Part5:1988
2	Fine	-	2.6	0.5	2.2	-	-	-	IS 2386 Part1:1963 IS 383:2016
3	Coarse	-	2.7	0.55	6.0	-	Angular	-	

2.2 Bacterial Medium Preparation

In this study, *B. subtilis* was procured in the lyophilized form from Proprenz Biotech Pvt. Ltd., located in Hyderabad. The bacterium procured had undergone the microbiological investigations and examination in GITAM University, at Department of Microbiology, Visakhapatnam.

2.2.1 Identification of Bacteria

Nutrient broth (NB) was used for general cultivation of microorganism contains following ingredients: peptone (5 g/L), sodium chloride (5 g/L), HM peptone (1.50 g/L), and yeast extract (1.50 g/L). Utilizing nutritional agar media at pH-11 and 37 °C in an incubator, the bacterial spores were grown in a petri plate. Morphological examination was carried out using the Gram staining method and Endospore staining to determine bacterial structure and characteristics [53, 54]. Under the former method, to make a smear, a sterile inoculating loop was used to take a loopful of bacterial culture and spread it evenly throughout the surface. The smear was left to fully air dry. From a pure 18–24 h culture, the slant was infected with a strong diagonal streaking of the agar surface. For 24 h to 48 h, inoculated tubes were incubated at 35 to 37 °C with their caps unfastened. A microscope equipped with an immersion oil lens was used to study the coloured bacterial cells at a 100X magnification. In the latter method, the *B. subtilis s*pores were tested for their ability to form endospores by Schaeffer–Fulton endospore staining technique.

2.2.2 Urease Test

To identify bacteria capable of hydrolysing urea, the urease test was conducted using the urease enzyme. According to the conventional method, Christensen's urea agar slants were made using the following ingredients (per liter): urea (20.0 g), phenol red indicator (0.012 g), agar (20.0 g), sodium chloride (5.0 g), yeast extract (0.1 g), potassium dihydrogen phosphate (2.0 g), peptone (1.0 g), and dextrose (1.0 g). To avoid pressure build-up, the medium was distributed into test tubes and autoclaved for 15 minutes at 121°C with loose-fitting lids. To produce slanted surfaces, tubes were placed at an oblique angle during cooling after sterilization.

2.2.3 Culturing of the Bacterium

The bacterial strain was grown in commercial nutrient broth (HiMedia Laboratories, India) prepared by dissolving 6.5 g of powder in 1.5 L of distilled water, following the manufacturer's instructions. The exact composition of the broth reflects proprietary formulations including typical components such as peptone, sodium chloride, and yeast extract. Sterile HCl or NaOH was used as needed to bring the pH down to 7.0 ± 0.1.

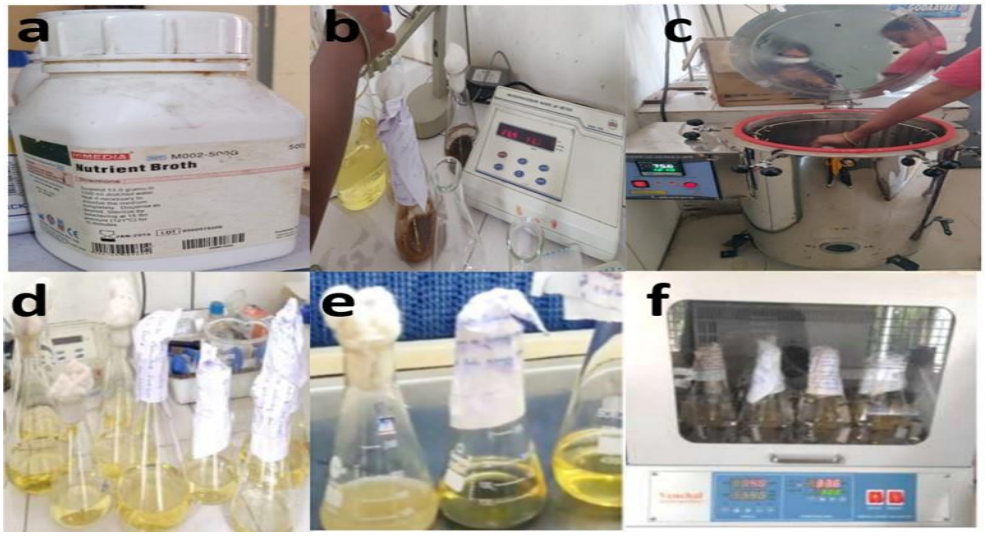

Fig. 2. Steps of media preparation. a. medium, b. pH setting, c. autoclaving at 121 °C for 15 min, d. broths after autoclave, e. inoculation using fresh pre-inoculum, and f. incubation in an orbital shaker for 24 h

To ensure sterility, the medium was poured into the proper containers, covered with aluminum foil and cotton plugs, and autoclaved for 15 minutes at 121 °C. A 2% (w/v) inoculum concentration was attained by aseptically transferring 5 g of bacterial biomass into 250 mL of sterile nutrient broth for inoculum preparation. This prepared inoculum was subsequently used to seed 1.5 L of nutrient broth in each experimental batch. For 24 hours, the infected broth was incubated at 30 °C with agitation at 148 rpm in an orbital shaker to guarantee proper aeration and mixing. The optical density (OD) at 600 nm was measured periodically to track growth, and a turbidity test was conducted to evaluate the impact of each calcium source on bacterial proliferation. The compatibility of the bacteria with different calcium sources, which are essential for the MICP process in self-healing concrete applications, was revealed by these studies. The bacterium medium preparation process is illustrated (Fig. 2).

2.2.4 Bacterial Cell Count Using Hemocytometer

Following a 24-hour incubation period, 0.1 µL of the bacterial culture was added to 1000 µL of diluent using a sterile pipette. This solution was serially diluted by a factor of 10 to achieve an appropriate dilution, with 10^{-1} identified as optimal. A cleaned hemocytometer featuring a grid with a volume of 0.1 mm^3 divided into five square blocks was filled with the diluted solution (Fig. 3). The spore count was observed under a microscope at 40X magnification, yielding a total count of live cells. Based on this data, the bacterial cell concentration was calculated using Eq. (1), and Eq. (2).

$$Average\ number\ of\ \ cells = \frac{Average\ of\ live\ cells}{Number\ of\ square\ blocks} \quad (1)$$

$$Bacterial\ cell\ concentration = Dilution\ factor\ X\ Average\ number\ of\ cells\ X\ 10^{-4} \quad (2)$$

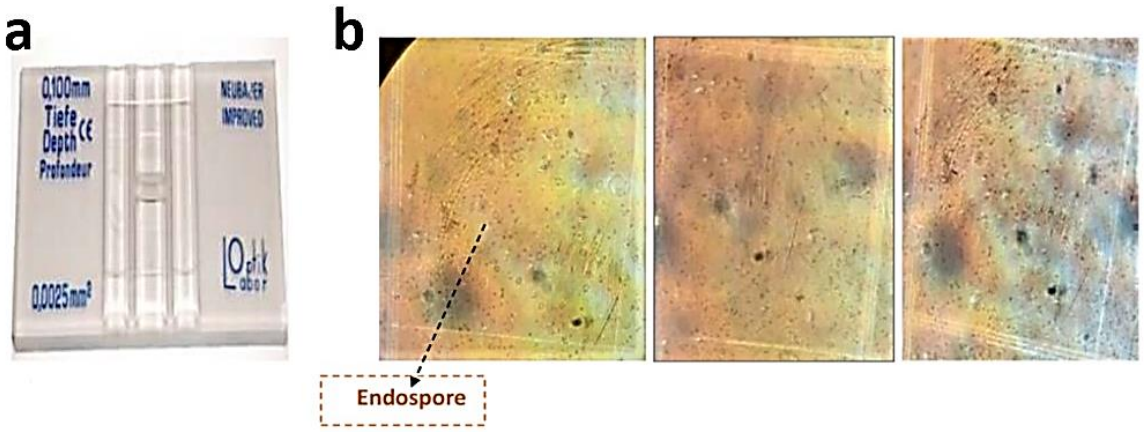

Fig. 3. Hemocytometer and b. square grids of hemocytometer

2.3 Concrete Mix Proportions

IS 10262:2019 was used to carry out the concrete mix design for M20 grade. This study compares the effects of nutrients in bacterial concrete (BC) on the strength and healing qualities of concrete. The conventional concrete (CC) with cement (350 Kg/m^3, fine aggregate 715.97 Kg/m^3, coarse aggregate 1207.84 Kg/m^3, and water 168 Kg/m^3) was designed. Nine different types of bacterial concrete mixes, split into three sets, inclusive of calcium lactate, calcium nitrate, and calcium formate precursors, were fabricated as shown in Table 2. Set A denoted bacterial specimens embedded with the required bacterial medium by incorporating: 1% dosage of calcium lactate as (1BC-L), 2% dosage of calcium lactate as (2BC-L), and 3% dosage of calcium lactate as (3BC-L). Set B denoted bacterial specimens embedded with the required bacterial medium by incorporating: 1% dosage of calcium nitrate as (1BC-N), 2% dosage of calcium nitrate as (2BC-N), and 3% dosage of calcium nitrate as (3BC-N). Set C denoted bacterial specimens embedded with the required bacterial medium by incorporating: 1% dosage of calcium formate as (1BC-F), 2% dosage of calcium formate as (2BC-F), and 3% dosage of calcium formate as (3BC-F).

Table 2. Mix proportions and dosages

Type of mix		Required bacterial medium (cells/mL)	Calcium lactate (bwc)	Calcium nitrate (bwc)	Calcium formate (bwc)
CC		-	-	-	-
1BC-L	Set A	10^5	1%	-	-
2BC-L		10^5	2%	-	-
3BC-L		10^5	3%	-	-
1BC-N	Set B	10^5	-	1%	-
2BC-N		10^5	-	2%	-
3BC-N		10^5	-	3%	-
1BC-F	Set C	10^5	-	-	1%
2BC-F		10^5	-	-	2%
3BC-F		10^5	-	-	3%

2.4 Concrete Specimen Preparation, Casting, and Curing

In the current investigation study, the concrete specimens were cast according to the specifications as per IS 516:1959, and outlined the protocols for preparation, casting, and curing of the concrete samples [55]. To thoroughly evaluate the mechanical performance and self-healing properties of the bacterial concrete, several specimen geometries were created. These included prismatic specimens with dimensions of (100 × 100 × 500 mm), cylindrical specimens with dimensions of (150 × 300 mm), and cubic specimens with dimensions of (100 × 100 × 100 mm). The concrete mixture was formulated in compliance with IS 10262:2019, the bacterial medium (containing *B. subtilis* with a required cell concentration of 10^5 cells/mL), and the calcium-based sources. The bacterial medium and calcium precursors were added directly to the mixing water to ensure even dispersion throughout the concrete matrix. The volume of the bacterial medium required for each specimen type was determined using the Eq. (3)[56] for the preparation of bacterial concrete, wherein the expression in the denominator represents the concentration of the prepared bacterial inoculum, experimentally estimated based on OD600 measurements and a standard calibration curve for *B. subtilis*. The casting process of the conventional and bacterial specimens is embellished (Fig. 4a) and (Fig. 4b).

$$Bacterial\ medium\ volume\ (mL) = \frac{Water\ (L) \times 1000\ \times 10^5}{Bacterial\ cell\ concentration\ (cells/mL)} \quad (3)$$

For 24 hours, the concrete examples were first set at room temperature, which was roughly 27 ± 2 °C. The specimens were carefully removed from their molds using techniques intended to avoid structural damage after the initial setting step was finished. Bacterial concrete specimens were demoulded with extra caution to maintain the integrated bacterial cells' survival and activity during the removal procedure. After demoulding, as per the guidelines, the specimens were immersed in a curing tank filled with potable water maintained at a constant temperature of 27 ± 2 °C. For bacterial concrete, the bacterial medium and calcium-based precursors were expected to react within the matrix during curing, facilitating self-healing mechanisms and enhancing the strength properties of the concrete.

(a)

Fig. 4a. Casting of traditional concrete specimens- cubes, beams, cylinders

(b)

Fig. 4. (a) Casting of traditional concrete specimens- cubes, beams, cylinders and (b) Casting of bacterial concrete specimens- cubes, beams, cylinders

2.5 Mechanical Strength Properties

The mechanical strength properties test includes flexural, split tensile, and compressive strength, performed according to IS 516 (Part 1): 2021 [57-59]. These were performed on the conventional concrete and three sets of bacterial concrete mixes for an age period of 3, 7, 14, 21, 28, 56, and 91 days. At the stipulated curing periods, specimens were removed from the curing tank, and any surface water was wiped off using a clean, dry cloth to ensure accurate measurements. The compressive strength test was performed on the cubical specimens by removing them from the curing tank at a specified age period and testing under a compressive testing machine (CTM)[57]. The load is applied at a controlled rate of 14 N/mm^2/min until the specimen can no longer sustain any additional load. The compressive strength (Fc) was calculated using the Eq. (4). Three-point bending test was conducted on prismatic specimens wherein the specimens were laid on the bed of the universal testing machine (UTM) on which two rollers were positioned [59]. The load was applied axially and symmetrically without causing torsional stress or constraints on the specimen. The rate of loading was maintained at 0.7 N/mm^2/min until failure. The failure pattern was analyzed as per the protocols mentioned in the codal provision. The flexural strength (F_b) was determined using the Eq. (5.1) and Eq. (5.2). The split tensile strength test was conducted on cylindrical specimens [58]. Within the CTM, the specimen was positioned horizontally between two loading wooden strips touching the top and bottom of the device. The split tensile strength (Fsp) was determined using an Eq. (6).

$$F_c\ (MPa) = \frac{F}{A_c} \tag{4}$$

Where F is the maximum load applied (in N) and Ac is the area of the specimen (in mm^2)

$$F_b(MPa) = \frac{P \times L}{B \times D^2}\,(For\ a\ failure\ within\ the\ middle\ third\ of\ the\ span) \tag{5.1}$$

$$F_b(MPa) = \frac{3P \times a}{B \times D^2} (For\ a\ failure\ outside\ the\ middle\ third) \quad (5.2)$$

Where P is the maximum load applied (in Newton), L is the effective span length (mm), B is the width (mm), D is the depth (mm), and a is the distance from the support to the failure point (mm).

$$F_{sp} = \frac{2P}{\pi ld} \quad (6)$$

Where P is the maximum load applied to the specimen (in Newton), l is the length of a cylinder (mm), and d is the cross-sectional dimension of the cylindrical specimen (mm).

2.6 Durability Tests of Concrete

2.6.1 Drying Shrinkage

In general, the parameters studied under the classification of durability are physical, chemical, mechanical, and microstructural. The long-term performance of a structure and its service life is mainly influenced by a critical durability parameter, i.e., drying shrinkage, wherein, due to the loss of moisture, there will be a reduction in concrete volume. This phenomenon plays a vital role in evaluating the dimensional stability and crack-resistance of concrete, especially in structures exposed to varying environmental conditions [20, 60]. The drying shrinkage test was conducted as per IS 4031 Part 10: 1988 [61, 62].

Fig. 5. (a) Reference rod and (b) testing specimen

Mortar beam mould specimens of size 25 mm x 25 mm x 285 mm were cast both for the cement paste with and without bacterial medium embedded with calcium sources. After 24 hours, specimens were demoulded and divided into two categories: one was moist, dry, and sun-dry conditions. Moist Drying: These specimens were exposed in a room at a controlled temperature of 27 ± 2 °C. Sun Drying: The specimens in this group were placed in an open environment under direct sunlight, simulating exposure to atmospheric drying. The length comparator apparatus was used to measure the length change in the specimens at regular intervals, (Fig. 5). The reference points on the specimen were aligned with the comparator pins for consistent measurement. The average difference in length of three specimens was the nearest 0.05 % of the effective gauge length, and this difference was reported as drying shrinkage (%) using Eq. (7).

$$\text{Drying shrinkage } (\%) = \frac{\Delta L}{L_0} \text{x } 100 \quad (7)$$

Where, ΔL is the difference in the measured length of the specimen (mm), L_0 is the reference rod gauge length (mm)

2.6.2 Water Absorption and Porosity

The second parameter under durability studies adopted is water absorption and porosity to assess the permeability and pore structure of the concrete. The water absorption test was conducted

following the guidelines provided in IS 2386 Part III: 1963 to evaluate the capacity of the concrete to absorb water under standard conditions [63]. The cubes of 100 mm x 100 mm x 100 mm were oven dried for 24 hours and then immersed in water for the next 24 hours. Dry and wet weights (M_{dry} and M_{sat}) were taken to compute the water absorption after 28 days of curing for each mix using Eq. (8). The porosity on the cubical specimens was measured as per code DIN 1048 so as to comprehend the process of water transport within the pore structure and to estimate the linked pore space after 28 days of curing of all the different specimens using Eq. (9).

$$\text{Water absorption (W)} = \frac{\text{Msat}-\text{Mdry}}{\text{Mdry}} \text{x100} \quad \text{(expressed in \%)} \tag{8}$$

$$\text{Porosity (P)} = \frac{\text{Msat}-\text{Mdry}}{\rho_w \text{ x V}} \text{x100 (expressed in \%)} \tag{9}$$

Where, M_{dry}=Oven dry weight of cubes (g); M_{sat}= after 24 hours wet weight of cubes (g)

2.7 Crack Healing Assessment

Concrete fissures play a crucial role in long-term performance in structural integrity and durability. Due to the self-healing mechanisms, there can be a reduction in the crack width; the crack can be sealed without any human intervention through an autonomous mechanism [6, 33, 64, 65]. In this study, crack closure assessment was conducted systematically to quantify the effect of bacterial agents and calcium-based nutrients on crack repair over time.

Fig. 6. Cracks inducing on the specimens using a CTM and b. Microscope used for the crack closure assessment

The crack healing quantification was performed by initially inducing the pre-crack by applying gradual loading (~100 kN) using CTM until the crack appeared on the surface of the concrete specimen after 28 days of water curing to ensure proper hydration [66, 67]. Care was taken to avoid overloading the specimens to ensure the cracks were well-defined but did not compromise the structural integrity of the concrete. To replicate real-world conditions, the induced cracks varied in width, ranging from approximately 0.1 mm to 4 mm. The microscope crack width detector with an optical magnification of X40 (manufactured by C&D Microsystem Limited, UK) (Fig. 6) was employed to precisely measure the initial crack widths. The specimens were further immersed in the curing tank for a period of 28 and 91 days. Each crack's width was measured at multiple points along its length to account for variability, and the maximum crack width closure was recorded on the aforementioned days of curing.

2.8 Microstructural Analysis of The Crack-Healed Sample

Microstructural analysis was conducted using SEM, XRD, and FTIR to understand bacterial concrete's microstructural changes and self-healing capabilities thoroughly at the microscale level to quantify the phase composition, crystal morphology, and chemical bond identification during the process of healing [28, 68-71]. SEM coupled with EDS was performed to capture high-resolution micrographs of the concrete's surface and the interfacial transition zones (ITZ). Samples were

fractured in order to expose fresh surfaces and allowed to dry. The SEM model named TESCAN MIRA S6123 comprises secondary electron mode (SE) was operated at an accelerating voltage of 15–20 kV, beam landing energy of 0.2 to 30 KeV and images were taken at magnifications ranging from 1000 to 5000X to provide detailed morphological observations, identifying the phases, and visualization of crack healing calcite precipitation. XRD analysis was conducted to identify the mineralogical phases in the bacterial concrete, specifically the polymorphs of calcium carbonate such as calcite, aragonite, and vaterite. The XRD instrument used was the Bruker D8 Advance Powder X-ray Diffractometer, which operates with Cu Kα radiation at a wavelength of 1.5418 Å. The finely powdered samples (particle size below 45 μm) were scanned over a 2θ range of 10° to 80° to generate diffraction patterns. FTIR was employed to identify and characterize the chemical bonds and functional groups present in the concrete samples, mainly focusing on bio-mineralization products such as calcium carbonate ($CaCO_3$). The analysis was conducted using the Bruker ALPHA-II ATR-FTIR Spectrophotometer. It is equipped with a zinc selenide (ZnSe) beam splitter and a high-resolution deuterated triglycine sulfate (DTGS) detector. The FTIR spectrum was recorded in the wavenumber range of 4000 cm^{-1} to 500 cm^{-1}, with an air-cooled IR source operating at 12V and 20W. Approximately 5 mg of the powdered sample was placed on the ATR crystal to ensure optimal surface contact, eliminating the need for additional sample preparation, such as pellet formation.

2.9 Statistical Analysis

The data were analyzed by analysis of variance (ANOVA) followed by Tukey's honestly significant difference (HSD) test to assess the significance of differences between the variances using Origin Pro 8.5 software. In each graph plotted, the error bars represent the standard deviation, and they remained less than 0.05 %. The data was found to be significantly different at $p<0.05$.

3. Results and Discussion

3.1 Bacterial Preparation and Characterization

The results obtained from the microbiological investigation of *B. subtilis* confirm its suitability for self-healing concrete applications. The bacterium's morphological, enzymatic, and growth characteristics were evaluated comprehensively, and its performance was analyzed in the context of its role in promoting calcium carbonate precipitation.

3.1.1 Morphological Characterization of Bacteria

The Gram staining analysis revealed the rod-shaped morphology of *B. subtilis* with purple staining, confirming its Gram-positive nature (Fig. 7a). The endospore staining revealed the presence of both vegetative cells and endospores in the *B. subtilis* culture. Under microscopic observation, the vegetative cells appeared pink. At the same time, the endospores were distinctly stained green (Fig. 7b), confirming the bacterium's ability to form endospores under the given conditions, demonstrating adaptability to conditions conducive to calcium carbonate precipitation.

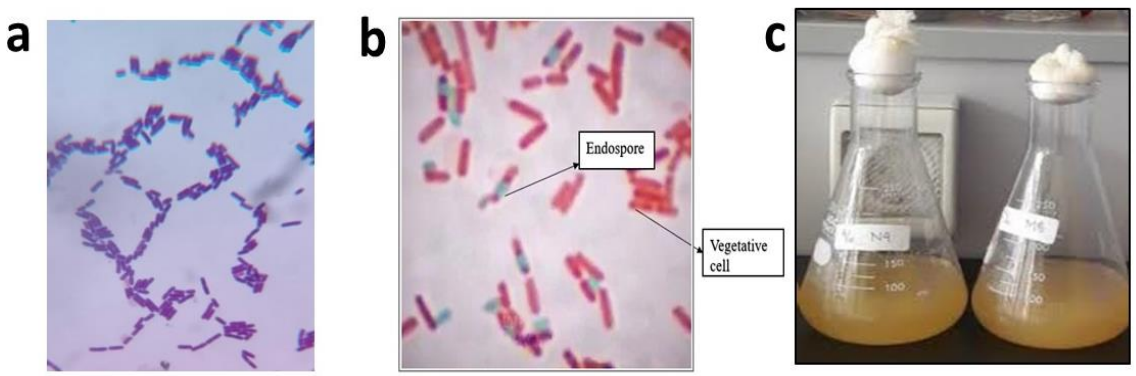

Fig. 7. (a) Microscopic image of *B. subtilis* (b) Endospores staining of *B. subtilis* and (c)Inoculated broth after 24 h incubation

The rod-shaped morphology of the bacterium, and in particular its ability to form endospores, supports its structural durability and survivability against harsh and alkaline environments in the concrete matrix. The bacterial spores thrived at 37 °C and pH 11 on nutritional agar media (Fig. 7c). Its ability to continue growing in these circumstances is essential to its self-healing concrete functioning. Its functionality in self-healing concrete depends on its capacity to sustain growth in these circumstances.

3.1.2 Urease Test

The urease activity test revealed that *B. subtilis* under the tested conditions, exhibited no hydrolysis of urea. This was evidenced by the absence of any color change within 6 hours, and no significant change was observed even after 24 h of incubation (Fig. 8). These results confirm that *B. subtilis* does not exhibit ureolytic activity, distinguishing it from traditional ureolytic bacteria, which rely on urea hydrolysis for calcium carbonate precipitation [68]. The lack of ureolytic activity positions *B. subtilis* as a non-ureolytic bacterium, making it an environmentally friendlier and potentially more sustainable option for self-healing concrete [1, 49, 72].

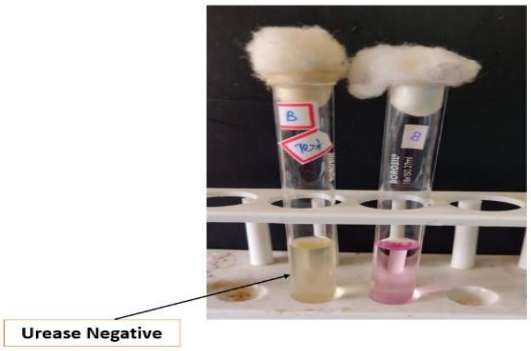

Fig. 8. Urease activity test of *B. subtilis* bacterium

3.1.3 Bacterial Growth Assessment

Robust bacterial growth was promoted by the nutritional broth made with peptone, sodium chloride, HM peptone, and yeast extract. In an orbital shaker incubator set to 30 °C and 148 rpm, the OD measurements, which showed 1.5 after 24 hours of incubation, showed exponential bacterial growth. Calcium formate demonstrated the most effective enhancement of bacterial growth. At 1 % calcium formate, OD peaked at 1.9 after 48 h, maintaining a notable level (1.3) even at 72 h (Fig. 9). This trend remained consistent at higher concentrations: at 2 % calcium formate, OD reached 2.1 (48 h), and at 3 %, it peaked at 2.0 (48 h). These findings demonstrate the metabolic compatibility of calcium formate with *B. subtilis*, which may be because formate is used as an auxiliary carbon source to promote cellular biosynthesis and energy production [73]. Calcium lactate supported a moderate growth at all the concentrations OD values peaked 1.5-1.9. This implies that while lactate might be a source of carbon, *B. subtilis* does not react metabolically to it in the same way that formate does [74, 75].

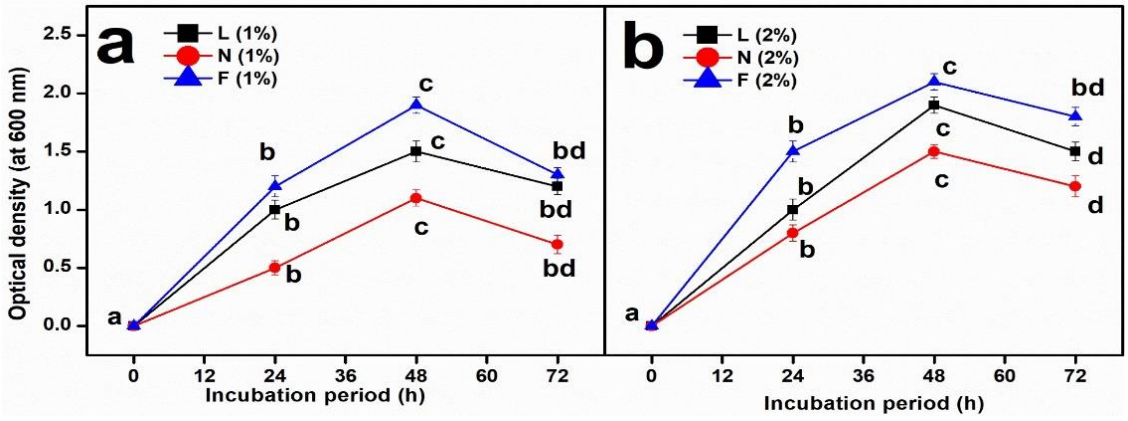

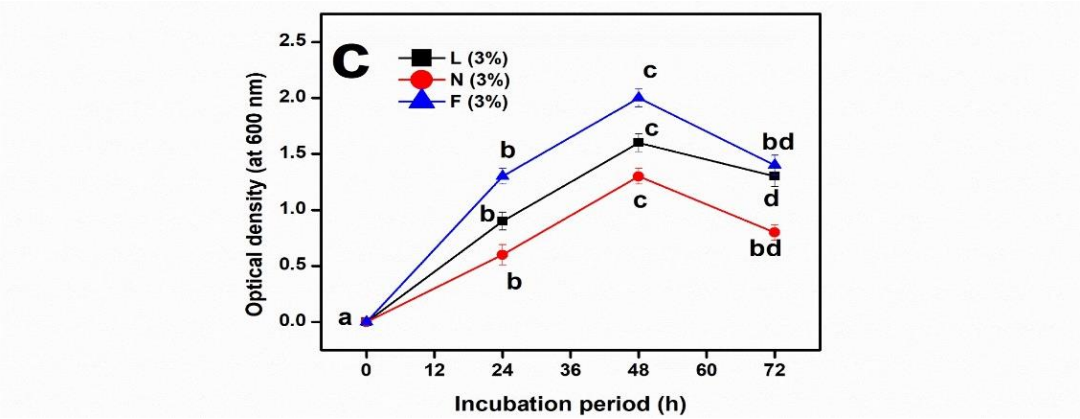

Fig. 9. *B. subtilis* growth with calcium precursors at (a) 1%, (b) 2%, and (c) 3% concentrations. L, lactate; N, nitrate; F, formate. SD < 0.05%; different letters indicate significance at $p < 0.05$ (Tukey's HSD)

In case of calcium nitrate alone, the OD values remained below 1.5 at all concentrations with a peak value of 1.5 at 48 hours at 2% dosage. This finding highlights that *B. subtilis* compatibility with calcium nitrate-based precursors is limited. These findings have been studied from previous studies reported on the implications of bacterial growth in presence of calcium-based precursors [27, 72, 73, 76, 77].

3.1.4 Bacterial Cell Concentration

Hemocytometer-based cell counting determined a spore concentration of 63 cells per 0.1 mm^3 at a dilution factor 10^{-1}. This corresponds to a viable bacterial cell density suitable for application in concrete. The Hemocytometer-based approach provided reliable quantification of bacterial cells, enabling precise incorporation into concrete mixtures. The concentration of bacterial cells in the suspension was determined to be 1.26×10^{-6} cells/mL, experimentally estimated based on OD600 measurements, and a standard calibration curve for *B. subtilis*. This measurement confirms the sufficient cell density for its intended use in MICP processes. The required bacterial medium concentration of 1 x 10^5 cells/mL was maintained in the samples.

3.2 Mechanical Strength: Long-Term Performance Analysis

3.2.1 Compressive Strength Test

As expected, the CC sample exhibited the lowest compressive strength among all mixes due to the absence of supplementary materials or chemical enhancements. At 3 days, the compressive strength was recorded as 14.97 MPa, steadily increasing to 18.27 MPa at 7 days, reaching 33.83 MPa at 28 days, and finally plateauing at 44.52 MPa at 91 days. The calcium lactate series demonstrated significantly enhanced compressive strength values compared to the CC mix. For instance, (1BC-L) mix achieved a strength of 33.27 MPa at 3 days, nearly doubling the value of CC mix (Fig. 10a). The increased strength is attributed to the presence of precursors that accelerate the hydration process and improve particle packing [78, 79]. A strength of 53.5 MPa was obtained by the (1BC-L) mix after 91 days, demonstrating sustained pozzolanic action. 2BC-L and 3BC-L also showed similar patterns, but with 3BC-L mix, somewhat lower values were depicted as the materials embedded in the cement matrix don't undergo proper hydration [21, 79-81]. The calcium nitrate series demonstrated superior performance, particularly at later curing ages. 2BC-N represented the highest strength amongst three dosages, achieving to 57.15 MPa at 91 days (Fig. 10b). The improvement is attributed to the crystalline admixture's ability to refine the pore structure, The microstructural densification from the crystalline material's self-healing capabilities contributed significantly to the improved mechanical properties [30, 82-84]. The development of compressive strength was found to be greatly impacted by the calcium formate series. The most pronounced enhancement became apparent at 3% dosage of calcium formate, achieving 37 MPa and a noteworthy of 62 MPa at 91 days (Fig. 10c). This improvement is attributed to the calcium formate ability to undergo crack control mechanism and compounded stress distribution evenly

within the matrix. These findings are in line with the studies that exhibited the efficiency of calcium formate in increasing the strength and effectiveness in crack mitigation [32, 85, 86].

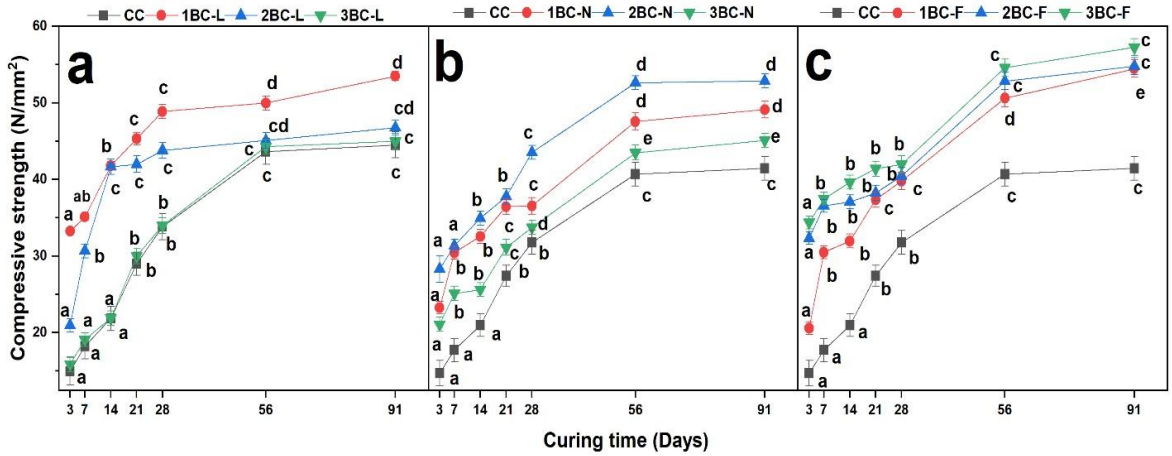

Fig. 10. Compressive strength of bacterial concrete with (a) calcium lactate, (b) calcium nitrate, and (c) calcium formate at 1%, 2%, and 3% dosages. CC: control; BC-L/N/F: bacterial concrete with respective precursors. SD < 0.05%; different letters indicate significance at $p < 0.05$ (Tukey's HSD)

3.2.2 Flexural Strength Test

A systematic evaluation of the impact of all three calcium sources on concrete's flexural strength was conducted. (1BC-L) mix, amongst the other two, exhibited the best performance across all curing ages. It achieved a flexural strength of 5.58 MPa at 91 days, significantly higher than that of the conventional concrete mix (CC, 4.5 MPa) (Fig. 11a). Additionally, it is attributed to the optimal performance as there is a balanced release of calcium ions, without causing excessive calcite formation or porosity. Similar findings were established from the earlier studies conducted [79, 87-91]. Calcium nitrate at 2% dosage (2BC-N) mix outperformed the other mixes for calcium nitrate-based systems, achieving a strength of 5.5 MPa at 91 days (Fig. 11b). This consistent improvement in flexural strength highlights the role of calcium nitrate as a hydration accelerator.

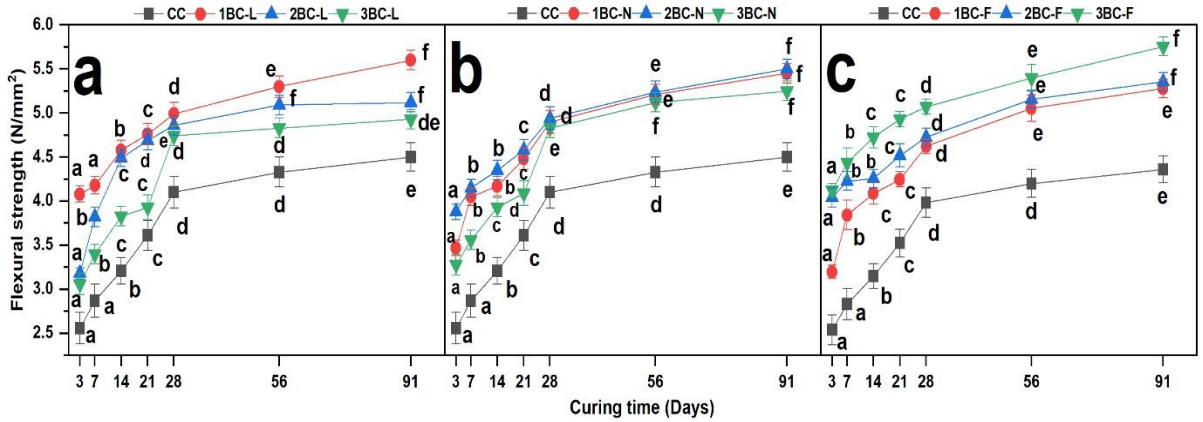

Fig. 11. Flexural strength of bacterial concrete with (a) calcium lactate, (b) calcium nitrate, and (c) calcium formate at 1%, 2%, and 3% dosages. CC: control; BC-L/N/F: bacterial concrete with respective precursors. SD < 0.05%; different letters indicate significance at $p < 0.05$ (Tukey's HSD)

However, both lower (1BC-N) mix and higher (3BC-N) mix concentrations showed relatively inferior results, with the (3BC-N) mix demonstrating a slight decline in long-term strength, potentially due to localized hydration reactions leading to uneven microstructural distribution [29, 92-94]. Mixes embedded with calcium formate displayed the most significant early-age strength gains. (3BC-F) mix achieved 4.25 MPa at 3 days and reached 5.99 MPa at 91 days (Fig. 11c), making

it the best-performing individual precursor across all curing ages. The high efficiency of the (3BC-F) mix is attributed to its dual role as a hydration accelerator and ITZ (interfacial transition zone) densifier. The presence of formate ions facilitated rapid calcium silicate hydrate (C-S-H) gel formation, which improved both early and long-term strength [32, 86, 95].

3.2.3 Split Tensile Strength

The effects of the three calcium sources on the split tensile strength of concrete were systematically assessed. Compared to all the mixes inclusive of calcium lactate, mix with 1% dosage of calcium lactate established an improvement at all curing periods (Fig.12a). At 91 days, (1BC-L) mix achieved a split tensile strength of 4 MPa, substantially higher than the control mix (CC), which registered 3 MPa. The balanced ionic release of calcium lactate in (1BC-L) mix likely contributed to uniform hydration and strength improvement. Higher concentrations, such as (3BC-L) mix, showed moderate increases in tensile strength (3.35 MPa at 91 days), potentially limited by residue build up and increased porosity caused by surplus ions. Several studies demonstrate similar findings to those shown in the current study [75, 79, 87, 88, 96]. Amongst the calcium nitrate-based mixes, (2BC-N) mix performance imputed acceleration properties of calcium nitrate, which facilitated matrix densification and enhanced bonding between aggregates and cement paste (Fig.12b). Conversely, (3BC-N) mix exhibited a slightly lower tensile strength of 3.75 MPa at 91 days due to over-acceleration of hydration. These findings were in line with the previous studies reported by the incorporation of calcium nitrate [92, 93, 97]. Bacterial concrete mix embedded with calcium formate substantial early-age strength enhancements, with (3BC-F) mix standing out as the best-performing individual precursor. At 91 days, (3BC-F) mix achieved a tensile strength of 4.11 MPa (Fig.12c), demonstrating its efficiency as a hydration accelerator and microstructure densifier [82, 85].

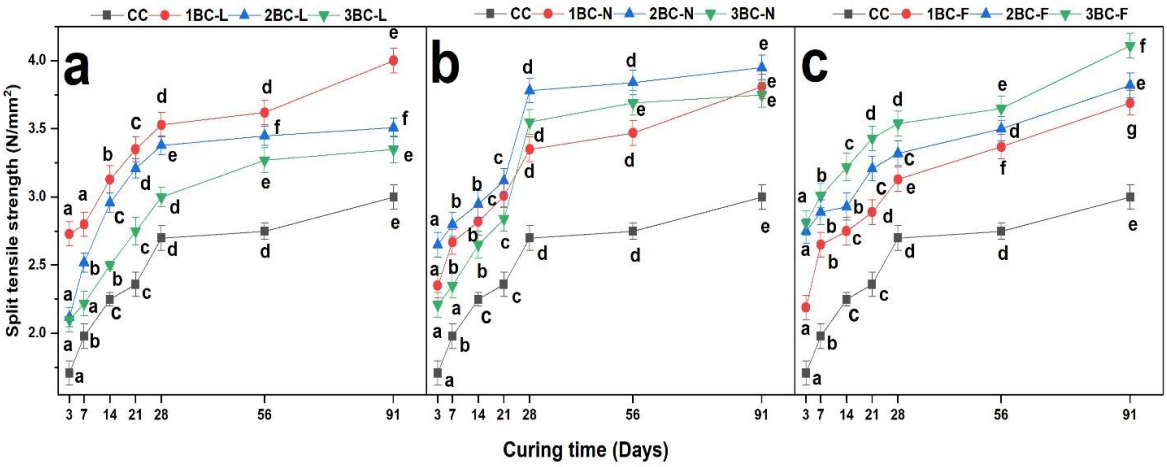

Fig. 12. Split tensile strength of bacterial concrete with (a) calcium lactate, (b) calcium nitrate, and (c) calcium formate at 1%, 2%, and 3% dosages. CC: control; BC-L/N/F: bacterial concrete with respective precursors. SD < 0.05%; different letters indicate significance at $p < 0.05$ (Tukey's HSD)

3.3 Durability Parameters

3.3.1 Drying Shrinkage

The drying shrinkage values for different concrete mixtures over 7, 35, and 91 days under sun-drying and moist-drying conditions give insight into how calcium-based precursors affect shrinkage performance, as shown in Table 3**.** Cement mortar mix showed relatively low drying shrinkage under both sun-drying (0.815 %) and moist-drying conditions (0.532 %). In the presence of mortar samples embedded with bacterium medium and calcium precursors exhibited an increase in shrinkage was observed at 7 days [55]. Bacterial mortar mixes such as (1BC-L) mix and (1BC-N) mix exhibited the highest shrinkage under sun-drying conditions at 1.363 % and 2.297 %, respectively. Under moist-drying conditions, the (1BC-N) mix displayed the highest shrinkage at

3.607 %. By 35 days, the trend showed significant shrinkage reductions across all mixes compared to the 7-day results. Mortar mix exhibited a shrinkage of 0.402 % (sun-dry) and 0.319 % (moist-dry). Bacterial mortar mix such as (3BC-L) and (2BC-N) achieved moderately lower shrinkage values under sun-drying (0.146 % and 0.471 %, respectively) compared to the earlier stages, indicating the mitigation of shrinkage effects with time, and these are aligning with the findings of [11, 98, 99]. At 91 days, drying shrinkage established stabilized values, casting minimal difference values under both drying conditions. Mortar mixes depicted values of 0.335 % (sun-dry) and 0.450 % (moist-dry), suggesting consistent behavior over time. Interestingly, bacterial mortar mixtures with higher calcium source dosages, such as (3BC-L), and (3BC-F) demonstrated minimal shrinkage values of about 0.079 % and 0.026 % and 0.103 % and 0.335 % under sun-dry and moist-dry conditions, respectively [32]. The results indicate that calcium-based nutrients significantly affect the drying shrinkage of concrete. The increase in 7-day observation is attributed to the high reactivity of the calcium precursors that accelerated more loss in moisture content due to enhanced hydration process, as supported by several research studies [32, 85, 89, 100]. The current study confirms that at an early age, shrinkage amplification necessitates careful consideration of dosage and curing conditions to balance performance outcomes. However, at higher concentrations, they mitigate the long-term shrinkage effect [101]. The standard deviation was less than 0.05 %. Means followed by letters are significantly different at $p < 0.05$ according to Tukey's HSD test.

Table 3. Drying shrinkage of conventional concrete and bacterial concrete using calcium precursors.

Mortar Mix Type	7th Day		35th Day		91st Day	
	Sun Dry	Moist Dry	Sun Dry	Moist Dry	Sun Dry	Moist Dry
Cement mortar	0.815^{a}	0.532^{a}	0.402^{a}	0.319^{a}	0.335^{a}	0.450^{a}
1BC-L	1.363^{b}	1.483^{b}	0.430^{a}	0.445^{b}	0.263^{a}	0.332^{a}
2BC-L	1.048^{c}	1.800^{c}	0.750^{b}	0.753^{c}	0.249^{a}	0.107^{b}
3BC-L	0.896^{a}	1.830^{c}	0.146^{c}	0.549^{b}	0.079^{b}	0.103^{b}
1BC-N	2.297^{d}	3.607^{d}	0.465^{a}	0.487^{b}	0.223^{a}	0.216^{c}
2BC-N	1.530^{e}	1.732^{c}	0.471^{a}	0.191^{d}	0.070^{b}	0.119^{b}
3BC-N	0.863^{a}	1.900^{c}	0.492^{a}	0.605^{e}	0.397^{a}	0.403^{a}
1BC-F	2.005^{f}	1.441^{b}	0.297^{d}	0.617^{e}	0.094^{b}	0.314^{a}
2BC-F	2.098^{f}	1.500^{b}	0.558^{a}	0.422^{b}	0.346^{a}	0.001^{b}
3BC-F	3.103^{g}	1.400^{b}	0.267^{d}	0.500^{b}	0.026^{b}	0.335^{a}

3.3.2 Water Absorption and Porosity

Two essential metrics for evaluating the durability and permeability qualities of concrete are water absorption and porosity. These properties directly affect the long-term structural performance and service life of concrete and control its vulnerability to environmental degradation [79, 102]. The conventional concrete mix (CC) exhibited a water absorption of 2.7 % and porosity of 7 %. These values represent the baseline for comparison with bacterial-based concrete mixes. (1BC-L) mix showed reduced water absorption (2.36 %) and porosity (6.3 %) compared to CC, indicating enhanced durability due to the densification of the microstructure [36]. (2BC-L) mix and (3BC-L) mix exhibited higher values of water absorption (3.34 % and 3.6 %, respectively) and porosity (8.52 % and 9.59 %), which may be attributed to the dosage of calcium lactate influencing hydration and void formation [103].

The results demonstrate that a controlled dosage of calcium lactate can reduce porosity and improve the water-tightness of concrete. (1BC-N) mix and (2BC-N) mix had moderate water absorption values (3.2 % and 2.96 %) and porosity (8.5 % and 7.4 %), suggesting slight improvements in durability compared to CC. (3BC-N) mix exhibited the highest water absorption (3.8 %) and porosity (10 %), likely due to increased voids or inconsistent hydration effects at higher calcium nitrate dosages. These results emphasize the need for optimization of calcium nitrate dosage to achieve a balanced microstructure with reduced porosity.

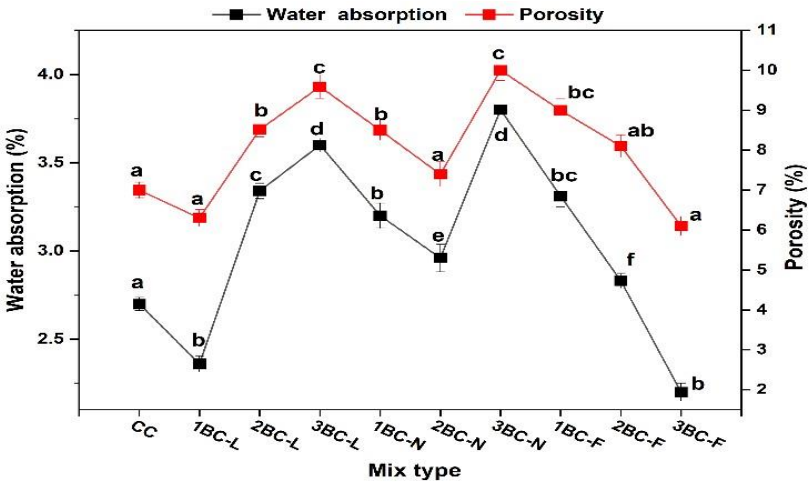

Fig. 13. Water absorption and porosity of conventional and bacterial concrete. SD < 0.05%; different letters indicate significance at p < 0.05 (Tukey's HSD).

The calcium formate mixes demonstrated good performance in terms of water absorption and porosity. (1BC-F) mix and (2BC-F) mix had slightly elevated water absorption values (3.31 % and 2.83 %, respectively) with 9 % and 8.1 % corresponding porosities. (3BC-F) mix exhibited the lowest water absorption (2.2 %) and porosity (6.1 %) among all calcium formate mixes (Fig.13) highlighting its potential for enhancing concrete durability. The performance of (3BC-F) mix indicates that calcium formate, when used in optimal amounts, effectively reduces voids and water ingress. Earlier research has demonstrated that calcium-based precursors such as calcium lactate, calcium nitrate and calcium formate significantly impact concrete's water absorption and porosity [32, 52, 94, 101, 104, 105].

3.4 Performance of Cracks' Self-Healing in Concrete

Cubical specimens (100 x 100 mm), one each of all mixes, including conventional concrete, were cast for examining the crack healing performance. (Fig.14) and (Fig.15) depicts the appearance of the induced pre-crack width and healing of the micro-cracks respectively due to the formation of calcite precipitation, which was observed using a Microscope crack width detector with optical magnification of 40X (C & D Microsystem Limited, UK). In a study performed on cement paste prismatic specimens where artificial cracks of about 1 mm were developed, the closure of a 0.8 mm crack width was reached after 20 days of repairing [106]. Calcium lactate at 1% dosage exhibited minimal induced pre-crack width compared to the other two dosages. Induced pre-crack width increased with an increase in dosage of calcium lactate. The complete healing of the induced pre-crack width was observed at 91 days at all dosages of calcium lactate. More amount of increased calcite formation with an increase in dosage was observed in case of calcium lactate as precursor. Although the higher dosages of calcium lactate enhance the calcite precipitation and aid in pore filling and healing of the crack width, excessively higher concentrations lead to a reduction in compressive strength, increasing the porosity of the concrete matrix before crack formation. Low concrete strength, with an increase in porosity, results in a more fragile matrix, which in turn leads to the development of wider induced pre-crack width under the application of gradual loading [81, 107]. Certain findings on crack healing depicted that in presence of calcium lactate 0.46 mm of crack closure using bacterium *B. alkalinitrilicus* [64]; with alkali resistant *B. subtilis* M9, bearing the calcium lactate medium and alcohol fibres 0.3 mm crack was created at bottom of the beam was evaluated with aid of SEM observation [108]. Both the mixes in the presence of spores and cultured form resulted in good healing of cracks in a finding [81, 109]. In a study conducted in the presence of *B. pasteurii* solution of 5 x 10^7 cells/mL and calcium lactate solution, when cured in sea-water, showed the maximum efficiency in healing of the crack [110]. The calcium nitrate at 2% dosage showed minimal induced pre-crack width compared to other two nutrients at the same dosages. The maximum induced pre-crack width was observed at 3% dosage and this is in juncture with the porosity developed at this dosage. In a study reported [67], with aid of Thermogravimetric analysis

the filling of the cracks due to $CaCO_3$ was evident in the specimens cast using ureolytic *B. sphaericus* in presence of calcium acetate, calcium nitrate and silica gel. A plain bacterium, either *B. sphaericus or D. nitroreducens,* with the inclusion of nutrients urea, yeast extract, 13.5g calcium nitrate and 9g calcium acetate added in the cement mortar resulted no major impact on the strength parameter [111]. The calcium formate series demonstrated excellent performance, with all mixes (1BC-F, 2BC-F, and 3BC-F) achieving complete closure by 91-day. Calcium formate has depicted a reduction in the induced pre-crack width (1.4 mm) along with the increase in the percentage dosage. This behaviour is attributed to their ability to provide sustained release of healing compounds, promoting continuous hydration and precipitation of calcium carbonate in cracks.

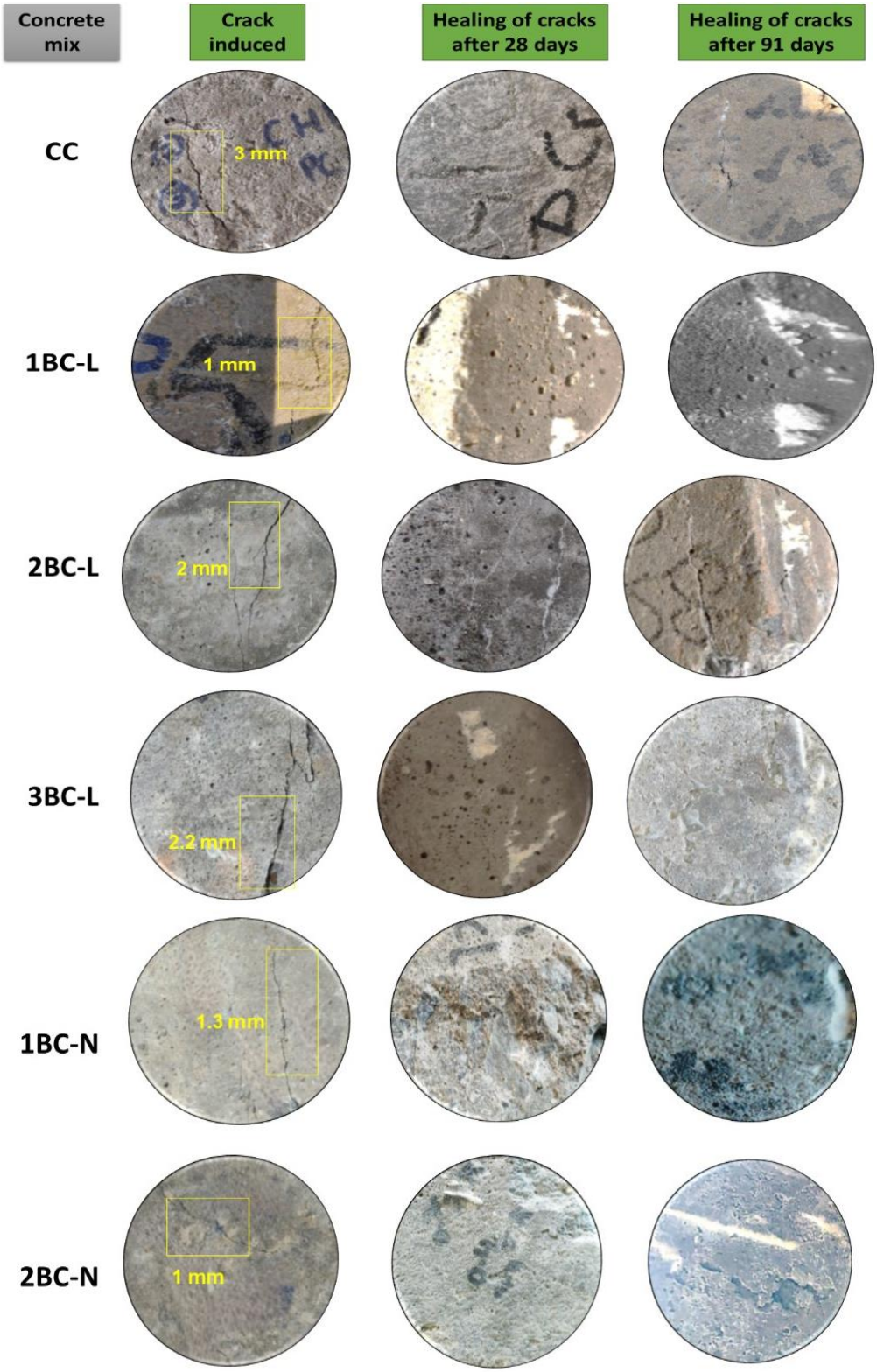

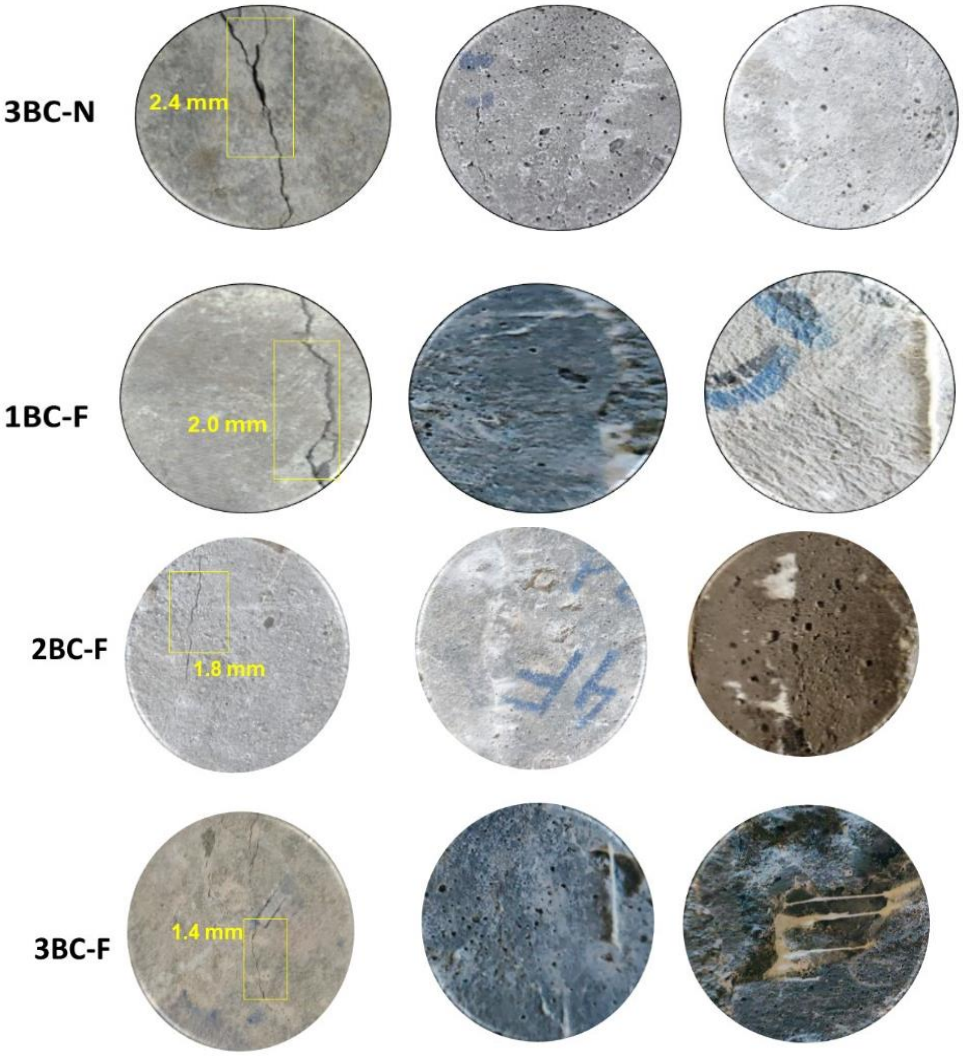

Fig. 14. Crack healing after 28 and 91 days. CC: control; BC-L/N/F: bacterial concrete with calcium lactate, nitrate, or formate at 1%, 2%, and 3% dosages.

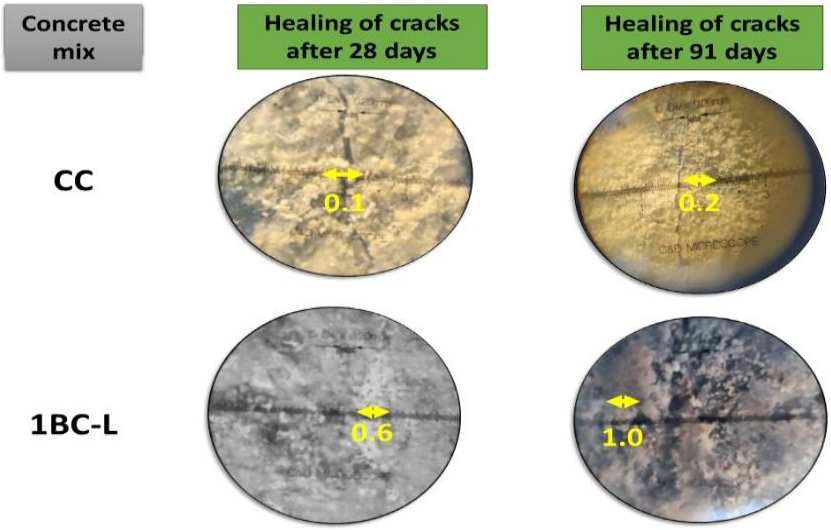

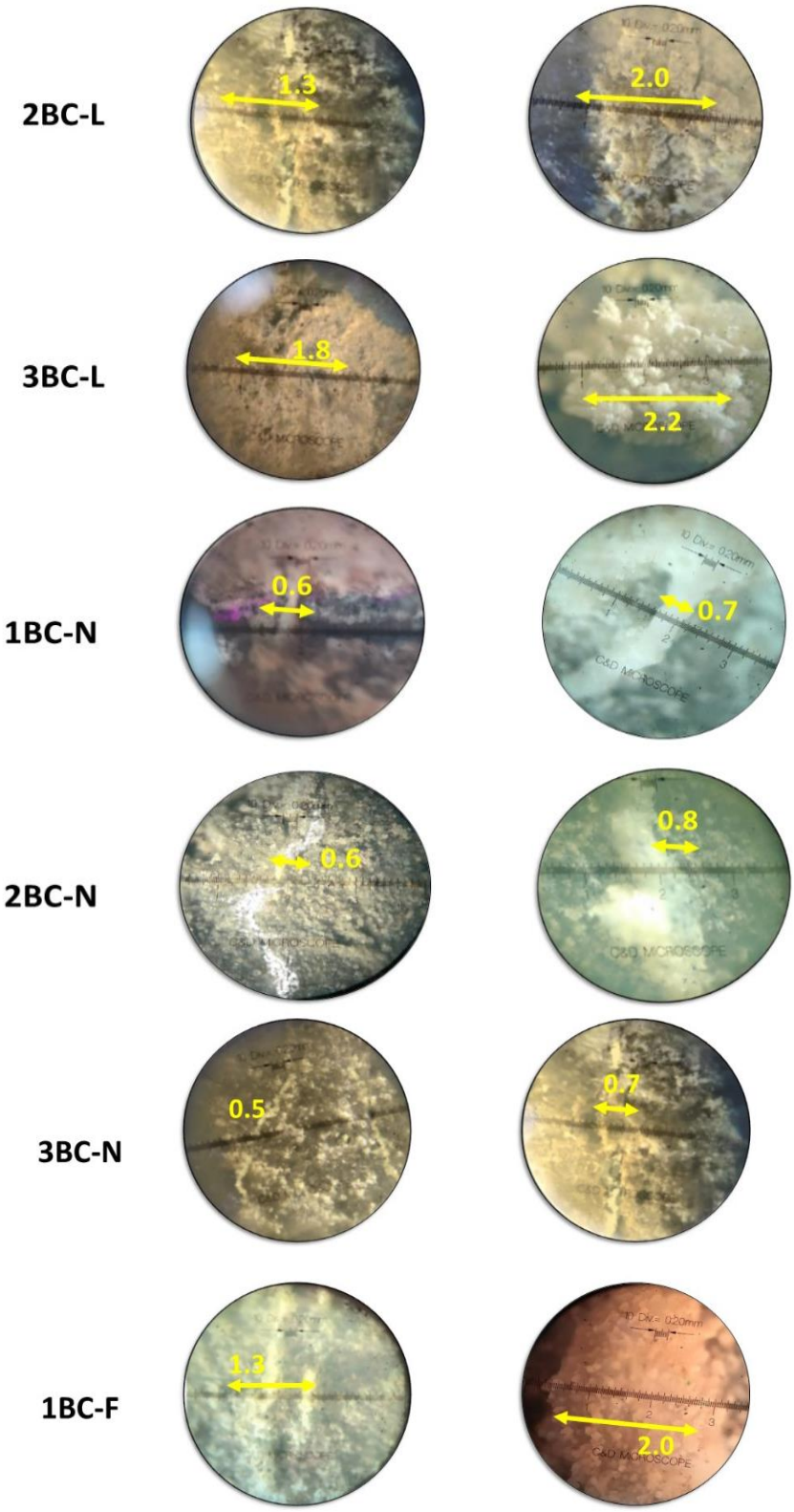
2BC-L
1.3
2.0
3BC-L
1.8
2.2
1BC-N
0.6
0.7
2BC-N
0.6
0.8
3BC-N
0.5
0.7
1BC-F
1.3
2.0

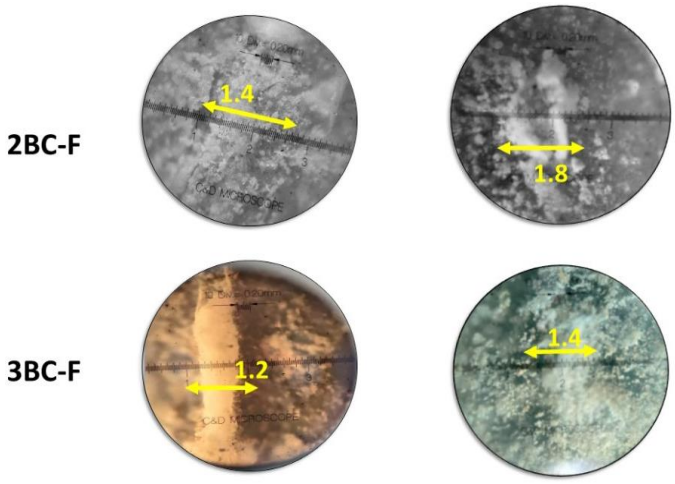

Fig. 15. Microscopic images of crack healing by calcite precipitation after 28 and 91 days. CC: control; BC-L/N/F: bacterial concrete with calcium lactate, nitrate, or formate at 1%, 2%, and 3% dosages.

3.5 Characterization of Materials

3.5.1 Scanning Electron Microscopy (SEM) Equipped with Energy Dispersive X-Ray Spectroscopy (EDS) Analysis

In a way to affirm the formation of MICP in the concrete matrix, SEM analysis was examined on the small size particles and powdered samples of cracked healed specimens after 91 days of healing period. To perform this analysis, conventional concrete (CC) sample specimen and also the bacteria incorporated samples maintaining a required cell concentration of 10^5 cells/mL, with 1% calcium lactate (1BC-L), 2% calcium nitrate (2BC-N), and 3% calcium formate (3BC-F) were preferred as they depicted highest compressive strength. The micrograph from SEM analysis of conventional concrete (CC) specimen revealed a minimal self-healing activity due to presence of limited calcite precipitation along the crack. Formation of the calcite occurred due to the carbonation process and also in presence of certain dispersed hydration products, examined to be small amounts of calcium silicate hydrate (C-S-H) which is the main binding phase appearing as fibrous structure; the by-product cubic C_3A appearing as hexagonal plate-like crystal; and the ettringite compound appearing as needle-like crystals (Fig. 16a). Although portlandite (CH) is present, the absence of substantial calcite deposition or ettringite suggests that the intrinsic healing potential of the conventional concrete is low. (Fig. 16b) represents an SEM image of the bacterial concrete at the required concentration of 10^5 cells/mL, supplemented with 1% dosage of calcium lactate (bwc) (1BC-L). The SEM image shows the formation of calcite($CaCO_3$) crystals along with rod-shaped structure of the *B. subtilis*, particularly along the crack surfaces, in association with bacteria indicated that the bacteria served as a nucleation site during the bio-mineralization process in the presence of precursors [112]. Increased quantities of C-S-H phases and ettringite are evident, suggesting enhanced hydration. Portlandite (CH) and C_3A crystals further corroborate the improved mineral precipitation and contribute to crack closure. (Fig. 16c) represents an SEM image of the bacterial concrete at the required concentration of 10^5 cells/mL, supplemented with 2% dosage of calcium nitrate (bwc) (2BC-N). A substantial growth in ($CaCO_3$) crystal growth and crack closure were apparent in the SEM images. Needle-like ettringite structures were prominently visible, playing a crucial role in sealing cracks and enhancing structural integrity [92]. (Fig. 16d) represents an SEM image of the bacterial concrete at the required concentration of 10^5 cells/mL, supplemented with 3% dosage of calcium formate (bwc) (3BC-F). The SEM analysis of 3BC-F highlights dense calcite formation and abundant C-S-H phases, which effectively fill and seal cracks. The presence of needle-like ettringite and microorganisms embedded within the concrete matrix indicated an active role of microbial activity in biochemical calcite precipitation. The overall microstructure appeared significantly denser compared to that of a conventional concrete specimen. These observations align with previous studies reporting that calcium precursors

improve mineral precipitation and hydration, thereby boosting the self-healing capability of concrete [8, 14, 64, 85, 96, 113-116].

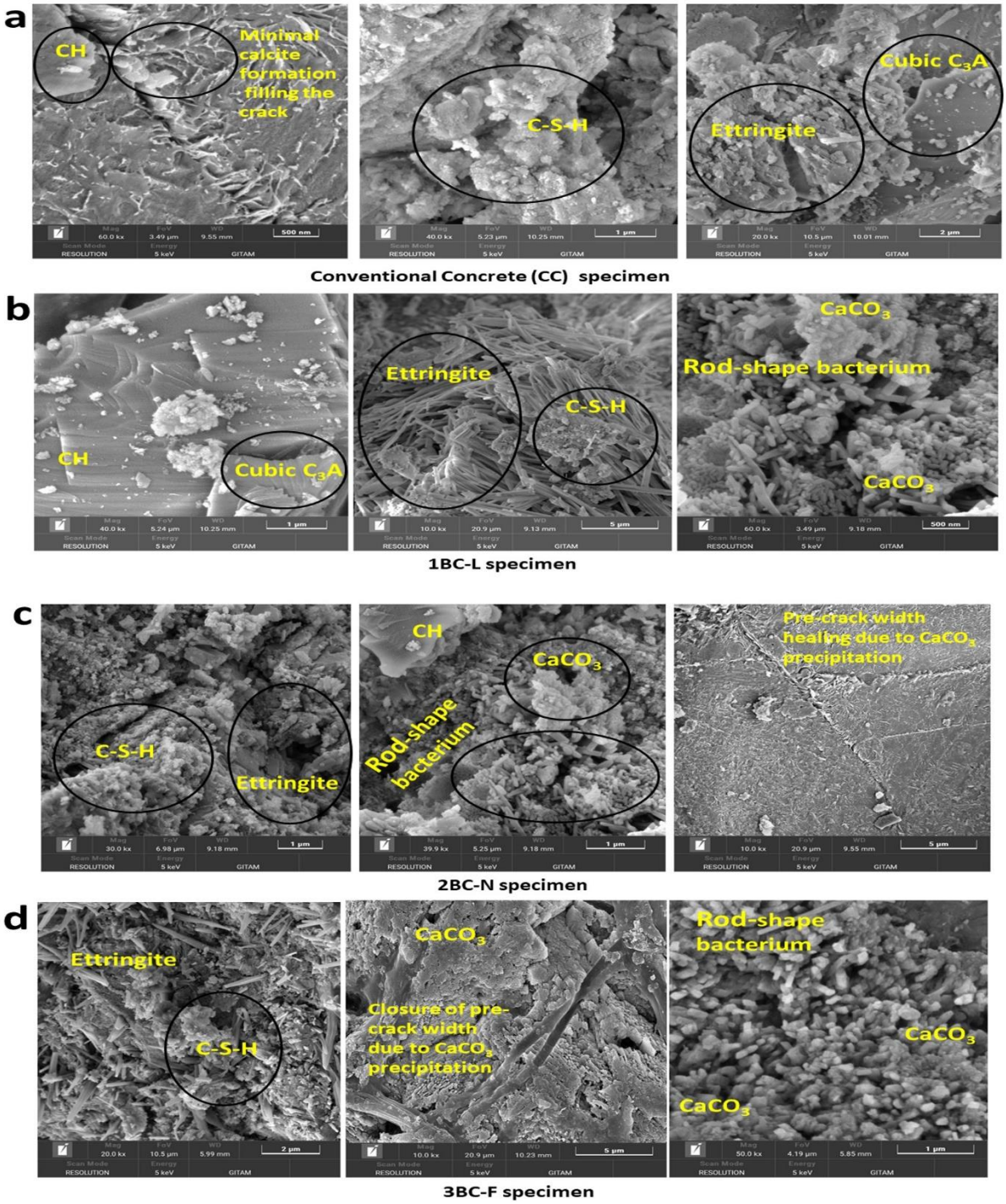

Fig. 16. SEM images of crack-healed concrete after 91 days: (a) CC: control, (b) 1BC-L: 1% calcium lactate, (c) 2BC-N: 2% calcium nitrate, (d) 3BC-F: 3% calcium formate.

Further, EDS provided detailed insights into the chemical constituents responsible for hydration, mineral precipitation, and crack healing. The results complement the microstructural observations from SEM analysis and offer a deeper understanding of the role of calcium-based additives. The EDS spectrum of CC (Fig. 17a) revealed considerable concentrations of oxygen (O, 40.77 wt%) and carbon (C, 25.22 wt%), with moderate levels of calcium (Ca, 18.02 wt%) and nitrogen (N, 4.80 wt%). The high carbon content indicated the limitation in ($CaCO_3$) precipitation, which explains the reduced self-healing potential observed in conventional concrete. (1BC-L) supplemented sample has shown a notable increase in oxygen (O, 44.18 wt %), calcium content (Ca, 30.72 wt %)

with a reduced carbon (C, 19.58 wt %) than CC sample, indicating a notable enhancement in mineral precipitation as shown in (Fig. 17b). The EDS spectrum of 2BC-N supplemented sample (Fig. 17c) has depicted a balanced levels of calcium (Ca, 21.72 wt %), carbon (C, 21.08 wt %), oxygen (O, 43.34 wt %), and nitrogen (N, 4.85 wt %). The increased nitrogen and oxygen levels reflect the beneficial effects of calcium nitrate on hydration and self-healing efficiency. The EDS spectrum of 3BC-F supplemented sample (Fig. 17d) revealed a substantial increase in calcium levels (Ca, 35.89 wt %), oxygen (O, 41.16 wt %), and carbon content (C, 14.96 wt %) is moderately lower than in the other samples, suggesting efficient carbon utilization and indicating robust calcite formation. *B. subtilis* is well-known for its role in calcite formation compared to plain concrete samples, which is similitude in the findings of research studies [5, 21, 24, 117]. These results indicate that calcium formate markedly strengthens the concrete matrix by promoting hydration and mineralization.

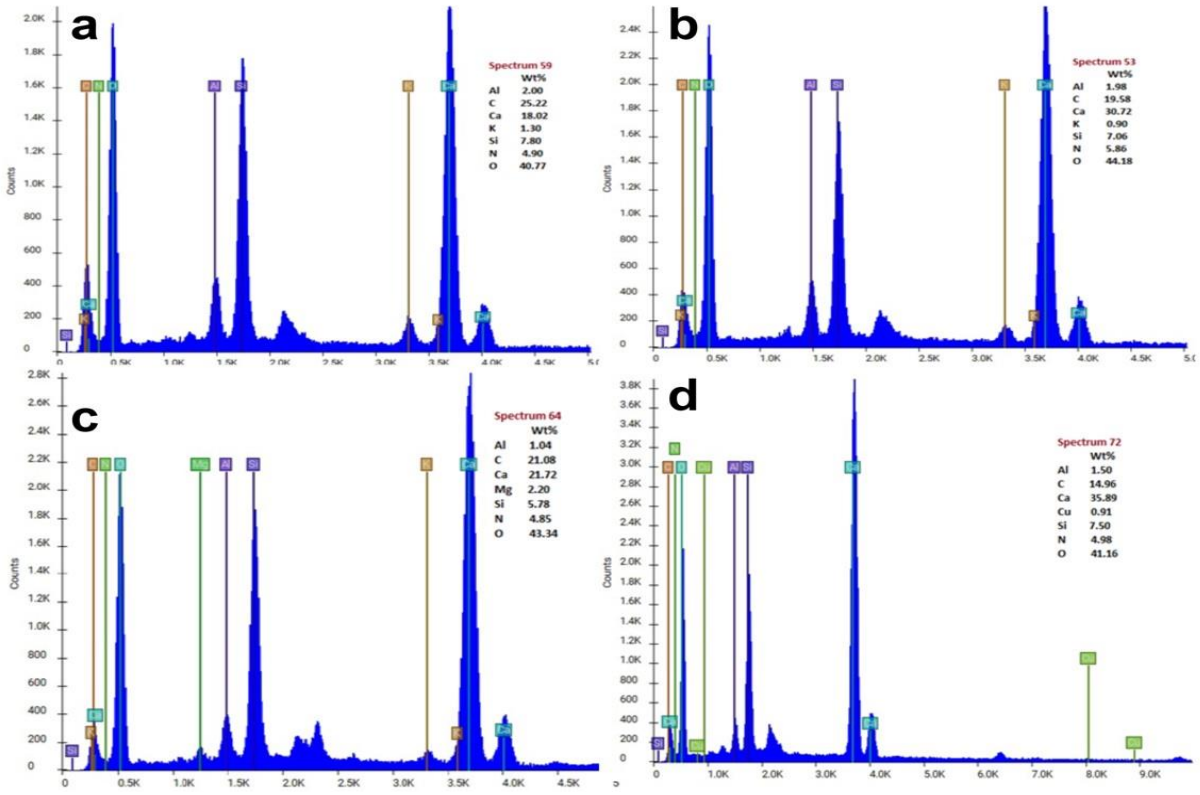

Fig. 17. EDS analysis of crack-healed concrete after 91 days: (a) CC: control, (b) 1BC-L: 1% calcium lactate, (c) 2BC-N: 2% calcium nitrate, (d) 3BC-F: 3% calcium formate.

3.5.2 Powder XRD Analysis of Concrete Samples

The powder X-ray diffraction analysis was performed on both the control and specific bacterial specimens considered for SEM/EDS to observe the cementitious and healing compounds formed in the crack 91 days after healing. The XRD pattern of the CC sample displayed (Fig. 18a) prominent peaks corresponding to calcium silicate hydrate (C-S-H), calcite (C), portlandite (P), and minor peaks of Alite (A) and Belite (B). The dominant peak position of 2Θ for (C) was obtained at 21.5°, indicating its primary role in providing strength to the matrix. Approximately, about (7-10%) the calcium carbonate polymorphs detected in the CC sample were in the form of calcite (C). In case of bacterial concrete samples, amongst the main mineral phases detected by XRD, calcite (C) was predominantly (up to 90%) observed in bacterial samples [118]. The incorporation of (1BC-L) supplemented sample has modified the crystalline profile of the material (Fig. 18b). The XRD pattern revealed an enhancement in calcite (C) formation, as evidenced by the increased intensity of the peak position 2θ at 28.6892°, which confirms its role in filling the pores. The XRD pattern of the sample supplemented with 2BC-N (Fig. 18c) demonstrates a moderate increase in the intensity of C-S-H and calcite (C) peaks. Peaks corresponding to Alite (A), Belite (B), and Portlandite (P) are also observed, but with reduced intensity, possibly due to the conversion of these phases into

secondary hydration products. Concerning the study for pure calcite [119], the highest peak position of 2Θ for calcite (C) was obtained at 26.02435°. The XRD analysis of the sample supplemented with 3BC-F (Fig. 18d) highlights the pronounced formation of calcite (C) and C-S-H. The peaks for secondary phases like Ferrite (F) and Ettringite (E) are more noticeable, suggesting a possible modification in the microstructure due to the formate addition [11]. The broader peaks of C-S-H indicate a possible amorphous nature, contributing to the improved flexibility and self-healing capacity of the matrix. However, the 3BC-F mix has identified the highest peak position of 2Θ for calcite (C) at 29.5°, indicating a pronounced crystallinity in its phase composition and thereby improving the self-healing properties of concrete. These observations align with previous studies indicating that calcium sources enhance mineral precipitation and hydration, thereby improving the self-healing properties of concrete [14, 116, 120, 121].

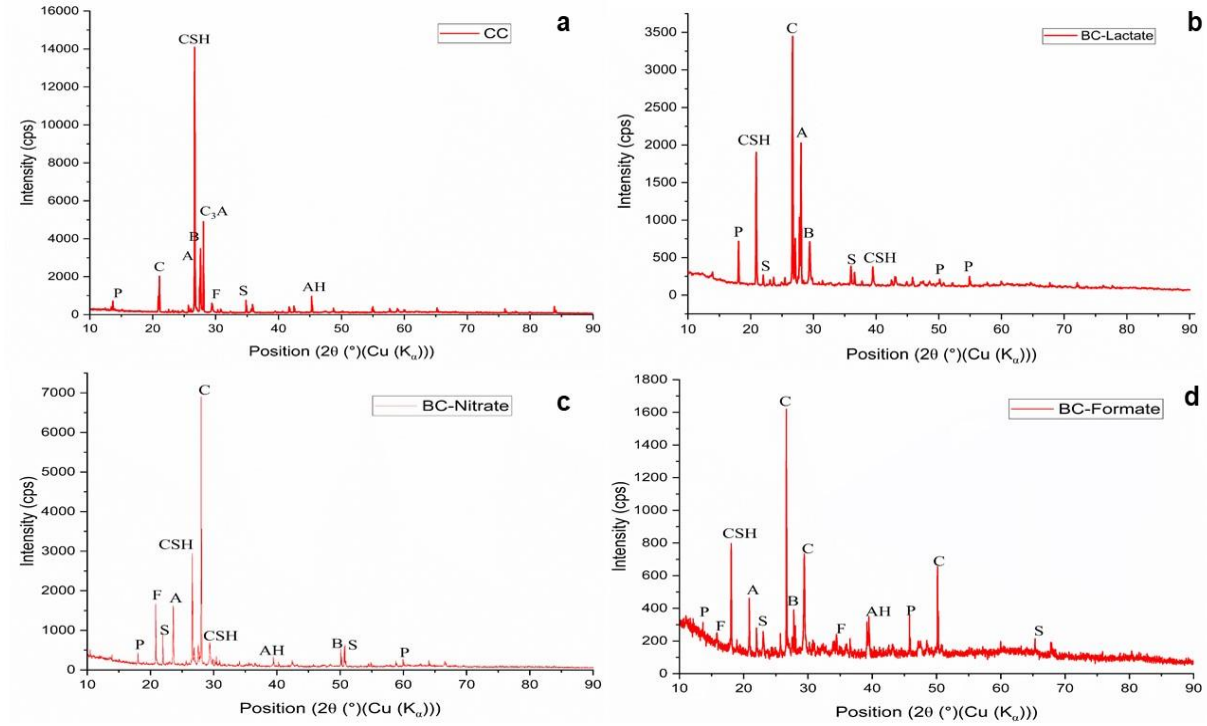

Fig. 18. XRD analysis of crack-healed concrete after 91 days: (a) CC: control, (b) 1BC-L: 1% calcium lactate, (c) 2BC-N: 2% calcium nitrate, (d) 3BC-F: 3% calcium formate.

3.5.3 Fourier Transform Infrared Spectroscopy (FTIR)

FTIR spectroscopy provides critical insights into the chemical interactions and hydration mechanisms in normal and self-healing concrete samples. The FTIR spectrum of conventional concrete (CC) exhibited peaks characteristic of hydration products (Fig.19a). A broad band around 3284 cm^{-1} corresponds to O-H stretching vibrations, signifying bound water in hydrated cement phases such as calcium silicate hydrate (C-S-H) and portlandite ($Ca(OH)_2$) [107, 122-124]. The peak at 1624 cm^{-1}, associated with H-O-H bending vibrations, confirms the presence of adsorbed water. Additionally, the sharp peak near 506–742 cm^{-1} is attributed to Si-O stretching vibrations, which indicate the formation of the primary strength-contributing C-S-H gel. Incorporating calcium lactate into concrete (1BC-L) moderately altered the FTIR spectrum. The O-H stretching band (3350 and 3777 cm^{-1}) intensified, indicating enhanced water retention, while a prominent peak near 1410 cm^{-1} confirmed the presence of carboxylate (COO^-) [123] groups from lactate ions (Fig.19b). The FTIR spectrum of concrete with 2BC-N revealed unique nitrate-associated peaks near 1409 cm^{-1}, indicative of NO_3^- group vibrations. The Si-O stretching band (505-1007 cm^{-1}) showed increased intensity compared to CC, suggesting that calcium nitrate effectively promotes the formation of C-S-H gel [123] (Fig.19c). Self-healing concrete with calcium formate (3BC-F) exhibited a distinct peak at 1408 cm^{-1}, corresponding to the stretching vibrations of formate ions ($HCOO^-$)[11, 123]. The enhancement of Si-O (508-963 cm^{-1}) peaks indicates that calcium formate significantly improves hydration and promotes C-S-H gel formation (Fig.19d).

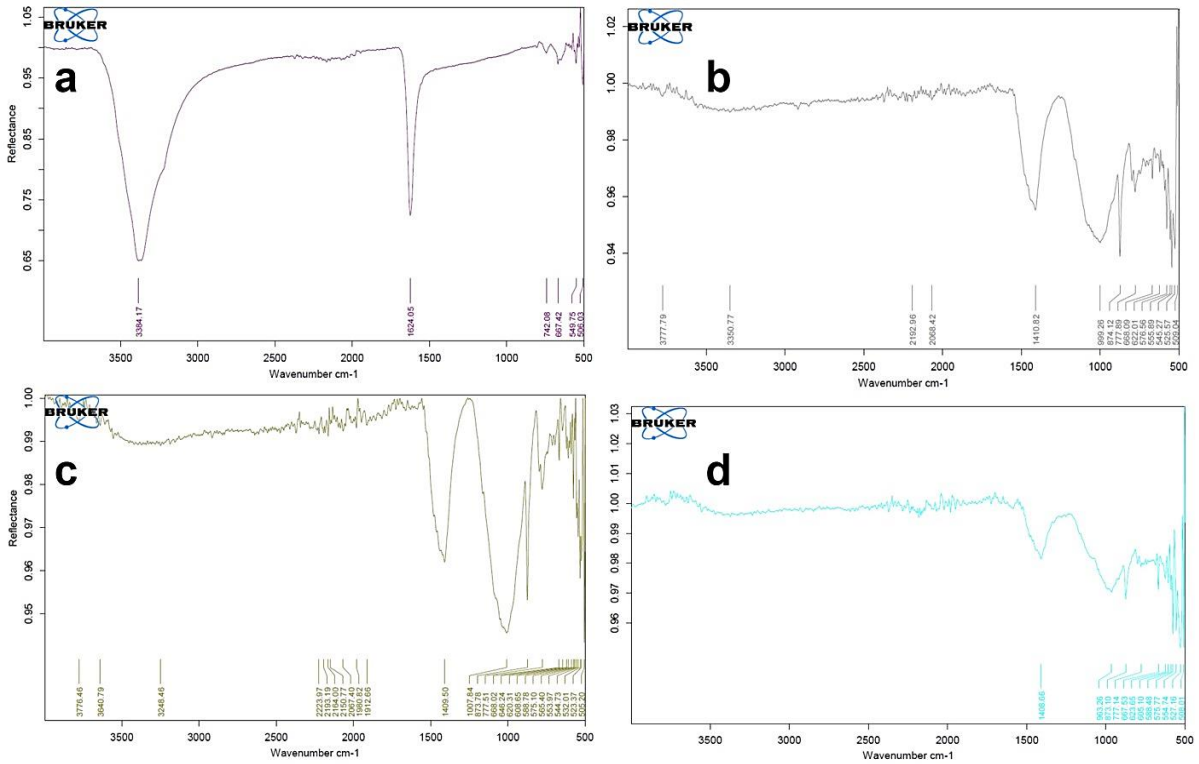

Fig. 19. FTIR analysis of crack-healed concrete after 91 days: (a) CC: control, (b) 1BC-L: 1% calcium lactate, (c) 2BC-N: 2% calcium nitrate, (d) 3BC-F: 3% calcium formate.

4. Conclusions

This current extensive research explains the crucial role of calcium-based precursors in enhancing the mechanical strength properties, durability tests, and autonomous self-healing mechanism of bacterial concrete through the Microbially induced calcium carbonate precipitation (MICP) technique. The experimental setup thoroughly evaluated three different precursors-calcium lactate, calcium nitrate, and calcium formate at varied dosages of (1%, 2%, and 3% by weight of cement) to determine how efficiently they perform in comparison to conventional M20 grade concrete in promoting strength and self-healing properties. The compressive strength evaluation demonstrated that all bacterial concrete formulations successfully retained the target mean strength of M20 grade conventional concrete, with calcium lactate at 1% dosage exhibiting a remarkable increase in strength both at early-age (3-day) and long-term (91-day) hydration periods. Calcium nitrate at 1% and 2% dosages exhibited better resistance characteristics, as it contributes to the densification of the concrete matrix. Conversely, calcium formate at 3% dosage consistently rendered the most substantial mechanical performance improvements, due to its potential in accelerating the C-S-H gel formation and subsequent matrix densification through enhanced bacterial activity. Material characterization techniques, including scanning electron microscopy (SEM) equipped with energy-dispersive X-ray spectroscopy (EDS), powdered X-ray diffraction (XRD), and Fourier-transform infrared spectroscopy (FTIR) rendered detailed insights into the chemical and crystalline phases responsible for self-healing and strength development, such as C-S-H and calcite. The pre-crack width healing evaluation demonstrated that each precursor exhibited distinct capabilities in promoting MICP-mediated healing across varying induced pre-crack widths. Calcium formate at 1% dosage exhibited maximum induced pre-crack width healing performance at both 28 and 91 days of healing period, demonstrating its exceptional capacity to facilitate bacterial proliferation and formation of calcite precipitation within crack interfaces. From the results, it can be concluded that calcium formate is the best nutrient, and it can be applied productively in bacterial concrete to promote and ameliorate the self-healing characteristics. Though in this current study effect of nutrients in the presence of bacteria on concrete parameters has been quantified, certain other factors need to be computed, such as

practical applications of self-healing concrete in real construction works, considering certain environmental conditions such as freeze-thaw cycles, marine exposure, and acidic attack. A detailed optimization study can be conducted for long-term durability effects in the presence of additional additives in order to identify various types of occurrences of cracks. In addition, the cost optimization can also be investigated through a thorough formulation of various calcium sources and their combinations for large-scale applications.

References

[1] Tan L, Xu J, Wei Y, Han J, Yao W. Aerobic non-ureolytic bacteria-based self-healing cementitious composites: a novel approach without added calcium precursor. Engineering Research Express. 2023;5(3):035006. https://doi.org/10.1088/2631-8695/ace298

[2] Roig-Flores M, Formagini S, Serna P. Self-healing concrete-what is it good for? Materiales de Construcción. 2021;71(341):e237-e. https://doi.org/10.3989/mc.2021.07320

[3] Seifan M, Samani AK, Berenjian A. Bioconcrete: next generation of self-healing concrete. Applied Microbiology and Biotechnology. 2016;100(6):2591-602. https://doi.org/10.1007/s00253-016-7316-z

[4] De Muynck W, Cox K, Belie ND, Verstraete W. Bacterial carbonate precipitation as an alternative surface treatment for concrete. Construction and Building Materials. 2008;22(5):875-85. https://doi.org/10.1016/j.conbuildmat.2006.12.011

[5] Qian C, Zheng T, Zhang X, Su Y. Application of microbial self-healing concrete: Case study. Construction and Building Materials. 2021;290:123-226. https://doi.org/10.1016/j.conbuildmat.2021.123226

[6] Wang J, Van Tittelboom K, De Belie N, Verstraete W. Use of silica gel or polyurethane immobilized bacteria for self-healing concrete. Construction and Building Materials. 2012;26(1):532-40. https://doi.org/10.1016/j.conbuildmat.2011.06.054

[7] Khoshtinat S. Advancements in Exploiting Sporosarcina pasteurii as Sustainable Construction Material: A Review. Sustainability. 2023;15(18):13869. https://doi.org/10.3390/su151813869

[8] De Muynck W, De Belie N, Verstraete W. Microbial carbonate precipitation in construction materials: a review. Ecological engineering. 2010;36(2):118-36. https://doi.org/10.1016/j.ecoleng.2009.02.006

[9] Worrell E, Price L, Martin N, Hendriks C, Meida LO. Carbon dioxide emissions from the global cement industry. Annual review of energy and the environment. 2001;26(1):303-29. https://doi.org/10.1146/annurev.energy.26.1.303

[10] Palter GP, Syeda M, Sambhana KD, Malasani P, Poosarla VG. A significant review on the performance of microbial concrete in comportment of diverse nutrients. Multidisciplinary Science Journal. 2023;5:2023ss0411. https://doi.org/10.31893/multiscience.2023ss0411

[11] Nodehi M, Ozbakkaloglu T, Gholampour A. A systematic review of bacteria-based self-healing concrete: Biomineralization, mechanical, and durability properties. Journal of Building Engineering. 2022;49:104038. https://doi.org/10.1016/j.jobe.2022.104038

[12] Zhang L, Zheng M, Zhao D, Feng Y. A review of novel self-healing concrete technologies. Journal of Building Engineering. 2024:109331. https://doi.org/10.1016/j.jobe.2024.109331

[13] Li VC, Yang E-H. Self healing materials: an alternative approach to 20 centuries of materials science. S Van Der Zwaag. 2007:161-93.

[14] Althoey F, Zaid O, Arbili MM, Martínez-García R, Alhamami A, Shah HA, et al. Physical, strength, durability and microstructural analysis of self-healing concrete: A systematic review. Case Studies in Construction Materials. 2023;18:e01730. https://doi.org/10.1016/j.cscm.2022.e01730

[15] Abo-El-Enein SA, Ali AH, Talkhan FN, Abdel-Gawwad HA. Application of microbial biocementation to improve the physico-mechanical properties of cement mortar. HBRC Journal. 2013;9(1):36-40. https://doi.org/10.1016/j.hbrcj.2012.10.004

[16] Achal V, Mukerjee A, Sudhakara Reddy M. Biogenic treatment improves the durability and remediates the cracks of concrete structures. Construction and Building Materials. 2013;48:1-5. https://doi.org/10.1016/j.conbuildmat.2013.06.061

[17] Tang Y, Xu J. Application of microbial precipitation in self-healing concrete: A review on the protection strategies for bacteria. Construction and Building Materials. 2021;306:1-11. https://doi.org/10.1016/j.conbuildmat.2021.124950

[18] Xu J, Wang X. Self-healing of concrete cracks by use of bacteria-containing low alkali cementitious material. Construction and Building Materials. 2018;167:1-14. https://doi.org/10.1016/j.conbuildmat.2018.02.020

[19] Xu J, Yao W. Multiscale mechanical quantification of self-healing concrete incorporating non-ureolytic bacteria-based healing agent. Cement and Concrete Research. 2014;64:1-10. https://doi.org/10.1016/j.cemconres.2014.06.003

[20] Wang J, Ersan YC, Boon N, De Belie N. Application of microorganisms in concrete: a promising sustainable strategy to improve concrete durability. Applied Microbiology and Biotechnology. 2016;100(7):2993-3007. https://doi.org/10.1007/s00253-016-7370-6
[21] Vijay K, Murmu M, editors. Experimental study on bacterial concrete using Bacillus subtilis micro-organism. Emerging Trends in Civil Engineering: Select Proceedings of ICETCE 2018; 2020: Springer. https://doi.org/10.1007/978-981-15-1404-3_20
[22] K. Mahmod A, A. Al-Jabbar L, M. Salman M. Bacteria Based Self-Healing Concrete :A Review. Journal of Engineering and Sustainable Development. 2021;25(Special):3-43-3-56. https://doi.org/10.31272/jeasd.conf.2.3.4
[23] Seshagiri R, Reddy VS, Sasikala C. Performance of microbial concrete developed using bacillus subtilis JC3. Journal of The Institution of Engineers (India): Series A. 2017;98(4):501-10. https://doi.org/10.1007/s40030-017-0227-x
[24] Vijay K, Murmu M. Effect of calcium lactate and Bacillus subtilis bacteria on properties of concrete and self-healing of cracks. International Journal of Structural Engineering. 2020;10(3):217-31. https://doi.org/10.1504/IJSTRUCTE.2020.108528
[25] Tobler DJ, Cuthbert MO, Greswell RB, Riley MS, Renshaw JC, Handley-Sidhu S, et al. Comparison of rates of ureolysis between Sporosarcina pasteurii and an indigenous groundwater community under conditions required to precipitate large volumes of calcite. Geochimica et Cosmochimica Acta. 2011;75(11):3290-301. https://doi.org/10.1016/j.gca.2011.03.023
[26] Vaezi M, SAZ, MJ. Recycled microbial mortar: Effects of bacterial concentration and calcium lactate content. Construction and Building Materials. 2020;234:1-11. https://doi.org/10.1016/j.conbuildmat.2019.117349
[27] Zhang Y, Pan Y, Ren T, Liang H, Zhang J, Zhang D. The Application of Calcium-Based Expansive Agents in High-Strength Concrete: A Review. Buildings. 2024;14(8):2369. https://doi.org/10.3390/buildings14082369
[28] Stanaszek-Tomal E. Bacterial concrete as a sustainable building material? Sustainability. 2020;12(2):696. https://doi.org/10.3390/su12020696
[29] Zhang Y, Guo HX, Cheng XH. Role of calcium sources in the strength and microstructure of microbial mortar. Construction and Building Materials. 2015;77:160-7. https://doi.org/10.1016/j.conbuildmat.2014.12.040
[30] Erşan YÇ, Verbruggen H, De Graeve I, Verstraete W, De Belie N, Boon N. Nitrate reducing CaCO3 precipitating bacteria survive in mortar and inhibit steel corrosion. Cement and Concrete Research. 2016;83:19-30. https://doi.org/10.1016/j.cemconres.2016.01.009
[31] Erşan YÇ, Belie Nd, Boon N. Microbially induced CaCO3 precipitation through denitrification: An optimization study in minimal nutrient environment. Biochemical Engineering Journal. 2015;101:108-18. https://doi.org/10.1016/j.bej.2015.05.006
[32] Heikal M. Effect of calcium formate as an accelerator on the physicochemical and mechanical properties of pozzolanic cement pastes. Cement and Concrete Research. 2004;34(6):1051-6. https://doi.org/10.1016/j.cemconres.2003.11.015
[33]Tziviloglou E, Van Tittelboom K, Palin D, Wang J, Sierra-Beltrán MG, Erşan YÇ, et al. Bio-Based Self-Healing Concrete: From Research to Field Application. 2016;273:345-85. https://doi.org/10.1007/12_2015_332
[34] Mors R, Jonkers H. Feasibility of lactate derivative based agent as additive for concrete for regain of crack water tightness by bacterial metabolism. Industrial crops and products. 2017;106:97-104. https://doi.org/10.1016/j.indcrop.2016.10.037
[35] Perrin A, Gagné R, Tran N, Petit L, Lors C. Large-scale apparatus for the quantitative evaluation of biorepair in a cracked concrete slab. Construction and Building Materials. 2024;448:138174. https://doi.org/10.1016/j.conbuildmat.2024.138174
[36] Chaerun SK, Syarif R, Wattimena RK. Bacteria incorporated with calcium lactate pentahydrate to improve the mortar properties and self-healing occurrence. Scientific reports. 2020;10(1):17873. https://doi.org/10.1038/s41598-020-74127-4
[37] Mokhtar N, Johari MAM, Tajarudin HA, Al-Gheethi AA, Algaifi HA. A sustainable enhancement of bio-cement using immobilised Bacillus sphaericus: Optimization, microstructural properties, and techno-economic analysis for a cleaner production of bio-cementitious mortars. Journal of Cleaner Production. 2021;318:128470. https://doi.org/10.1016/j.jclepro.2021.128470
[38] Ann KY, Jung HS, Kim HS, Kim SS, Moon HY. Effect of calcium nitrite-based corrosion inhibitor in preventing corrosion of embedded steel in concrete. Cement and Concrete Research. 2006;36(3):530-5. https://doi.org/10.1016/j.cemconres.2005.09.003
[39] Bandlamudi RK, Dutta JR, Kar A. Applications of microbial calcium carbonate precipitation in concrete through denitrification: a review. Innovative Infrastructure Solutions. 2023;8(4):113. https://doi.org/10.1007/s41062-023-01075-z

[40] Omoregie AI, Wong CS, Rajasekar A, Ling JH, Laiche AB, Basri HF, et al. Bio-Based Solutions for Concrete Infrastructure: A Review of Microbial-Induced Carbonate Precipitation in Crack Healing. Buildings. 2025;15(7):1052. https://doi.org/10.3390/buildings15071052
[41] Tao H, Jiang P, Qu J, Huang Y. The impact of various calcium ion sources on the curing efficacy of MICP. Scientific Reports. 2025;15(1):9149. https://doi.org/10.1038/s41598-025-94124-9
[42] El Enshasy H, Dailin DJ, Malek RA, Nordin NZ, Keat HC, Eyahmalay J, et al. Biocement: A Novel Approach in the Restoration of Construction Materials. In: Yadav AN, Rastegari AA, Gupta VK, Yadav N, editors. Microbial Biotechnology Approaches to Monuments of Cultural Heritage. Singapore: Springer; 2020. p. 177-98. https://doi.org/10.1007/978-981-15-3401-0_10
[43] Ali M, Mukhtar H, Dufossé L. Microbial calcite induction: a magic that fortifies and heals concrete. International Journal of Environmental Science and Technology. 2023;20(1):1113-34. https://doi.org/10.1007/s13762-022-03941-2
[44] Wang Y, Wang Y, Konstantinou C. Strength behavior of temperature-dependent MICP-treated soil. Journal of Geotechnical and Geoenvironmental Engineering. 2023;149(12):04023116. https://doi.org/10.1061/JGGEFK.GTENG-11526
[45] Algaifi HA, Bakar SA, Sam ARM, Ismail M, Abidin ARZ, Shahir S, et al. Insight into the role of microbial calcium carbonate and the factors involved in self-healing concrete. Construction and building materials. 2020;254:119258. https://doi.org/10.1016/j.conbuildmat.2020.119258
[46] Seifan M, Berenjian A. Microbially induced calcium carbonate precipitation: a widespread phenomenon in the biological world. Applied Microbiology and Biotechnology. 2019;103(12):4693-708. https://doi.org/10.1007/s00253-019-09861-5
[47] Chen H-J, Peng C-F, Tang C-W, Chen Y-T. Self-Healing Concrete by Biological Substrate. Materials. 2019;12(24). https://doi.org/10.3390/ma12244099
[48] Seifan M. Self-healing concrete: a novel nanobiotechnological approach to heal the concrete cracks: The University of Waikato; 2018.
[49] Justo-Reinoso I, Heath A, Gebhard S, Paine K. Aerobic non-ureolytic bacteria-based self-healing cementitious composites: A comprehensive review. Journal of Building Engineering. 2021;42:102834. https://doi.org/10.1016/j.jobe.2021.102834
[50] Wani S, Gęca MJ, Selvaraj T, Priya TS. Assessing the influence of Bacillus megaterium and Bacillus sphaericus in cementitious materials: Promoting sustainability towards strength, durability and crack repair. Ain Shams Engineering Journal. 2024;15(6):102748. https://doi.org/10.1016/j.asej.2024.102748
[51] Paine K, Alazhari M, Sharma T, Cooper R, Heath A, editors. Design and performance of bacteria-based self-healing concrete. The 9th International Concrete Conference 2016: Environment, Efficiency and Economic Challenges for Concrete; 2016.
[52] Luo M, Qian C. Influences of bacteria-based self-healing agents on cementitious materials hydration kinetics and compressive strength. Construction and Building Materials. 2016;121:659-63. https://doi.org/10.1016/j.conbuildmat.2016.06.075
[53] Coico R. Current protocols in microbiology: Wiley; 2006. https://doi.org/10.1002/9780471729259
[54] Sneath PH, Mair NS, Sharpe ME, Holt JG. Bergey's manual of systematic bacteriology. Volume 21986.
[55] Shruthi V, Tangadagi RB, Shwetha K, Nagendra R, Ranganath C, Ganesh B. Strength and drying shrinkage of high strength self-consolidating concrete. Recent Trends in Civil Engineering: Select Proceedings of ICRTICE 2019; 2021: Springer. https://doi.org/10.1007/978-981-15-5195-6_48
[56] Sk A, Rohit M, Sachin M, Babu R. Self-Healing Concrete Using Bacteria. 2020.
[57] Biswal US, Mishra M, Singh MK, Pasla D. Experimental investigation and comparative machine learning prediction of the compressive strength of recycled aggregate concrete incorporated with fly ash, GGBS, and metakaolin. Innovative Infrastructure Solutions. 2022;7(4):242. https://doi.org/10.1007/s41062-022-00844-6
[58] Kumar M, Kumar A, Solanki D, Mungule M. Low molarity geopolymer concrete: Effects on compressive strength, elastic modulus, sorptivity and chloride migration. Construction and Building Materials. 2023;409:134065. https://doi.org/10.1016/j.conbuildmat.2023.134065
[59] Neethu S, Tensing D, Vincent Sam Jebadurai S, Vincent S. Effect of sea sand in the behaviour of fresh concrete partially replaced with M-sand. Research on Engineering Structures and Materials. 2024;10(1):91-110.
[60] Vijay K, Murmu M, Deo SV. Bacteria based self- healing concrete - A review. Construction and Building Materials. 2017;152:1008-14. https://doi.org/10.1016/j.conbuildmat.2017.07.040
[61] Malathy R, Subramanian K. Drying shrinkage of cementitious composites with mineral admixtures. 2007.
[62] Joshi S, Goyal S, Mukherjee A, Reddy MS. Protection of concrete structures under sulfate environments by using calcifying bacteria. Construction and Building Materials. 2019;209:156-66. https://doi.org/10.1016/j.conbuildmat.2019.03.079
[63] Pitroda J. Assessment of sorptivity and water absorption of concrete with partial replacement of cement by fly ash and hypo sludge. IJARESM. 2015;1(2):33-42.

[64] Wiktor V, Jonkers HM. Quantification of crack-healing in novel bacteria-based self-healing concrete. Cement and Concrete Composites. 2011;33(7):763-70. https://doi.org/10.1016/j.cemconcomp.2011.03.012
[65] Wani S, Jan Gęca M, Selvaraj T, Shanmuga Priya T. Assessing the influence of Bacillus megaterium and Bacillus sphaericus in cementitious materials: Promoting sustainability towards strength, durability and crack repair. Ain Shams Engineering Journal. 2024;15(6):102748. https://doi.org/10.1016/j.asej.2024.102748
[66] Wang J, Soens H, Verstraete W, De Belie N. Self-healing concrete by use of microencapsulated bacterial spores. Cement and concrete research. 2014;56:139-52. https://doi.org/10.1016/j.cemconres.2013.11.009
[67] Van Tittelboom K, De Belie N, De Muynck W, Verstraete W. Use of bacteria to repair cracks in concrete. Cement and concrete research. 2010;40(1):157-66. https://doi.org/10.1016/j.cemconres.2009.08.025
[68] Stocks-Fischer S, Galinat JK, Bang SS. Microbiological precipitation of CaCO3. Soil Biology and Biochemistry. 1999;31(11):1563-71. https://doi.org/10.1016/S0038-0717(99)00082-6
[69] Das AK, Mallik M, Kalita P, Tag H. Optimization of Biogenic Calcium Carbonate Production Using Bamboo Dust as a Nutrient Source by Bacillus subtilis and Bacillus cereus for Enhanced Self-Healing Concrete. Journal of the Indian Chemical Society. 2025:101715. https://doi.org/10.1016/j.jics.2025.101715
[70] Nguyen MT, Fernandez CA, Haider MM, Chu KH, Jian G, Nassiri S, et al. Toward Self-Healing Concrete Infrastructure: Review of Experiments and Simulations across Scales. Chem Rev. 2023;123(18):10838-76. https://doi.org/10.1021/acs.chemrev.2c00709
[71] Shashank BS, Kumar.K P, Nagaraja PS. Fracture behavior study of self-healing bacterial concrete. Materials Today: Proceedings. 2022;60:267-74. https://doi.org/10.1016/j.matpr.2021.12.520
[72] Gat D, Tsesarsky M, Shamir D. Ureolytic calcium carbonate precipitation in the presence of non-ureolytic competing bacteria. Geo-Frontiers 2011: Advances in Geotechnical Engineering2011. p. 3966-74. https://doi.org/10.1061/41165(397)405
[73] Meng Q, Wang D, Fu X, Geng W, Zheng H, Bai W. Converting Bacillus subtilis 168 to a Synthetic Methylotroph by Combinatorial Metabolic Regulation Strategies. Journal of Agricultural and Food Chemistry. 2025. https://doi.org/10.1021/acs.jafc.4c09781
[74] Das AK, Mallik M, Kalita P, Tag H. Optimization of biogenic calcium carbonate production using bamboo dust as a nutrient source by Bacillus subtilis and Bacillus cereus for enhanced self-healing concrete. Journal of the Indian Chemical Society. 2025;102(6):101715. https://doi.org/10.1016/j.jics.2025.101715
[75] Qian S, Li J, Xu T, Diao E, Tang Y, Zhou X, et al. Calcium lactate efficiently induces production of bacillomycin D in Bacillus subtilis NS-174 and inhibition of spore germination of Aspergillus flavus in rice. International Journal of Food Science and Technology. 2023;58(2):824-30. https://doi.org/10.1111/ijfs.16241
[76] Hungria R, Mousa M, Hassan MM, Arce G, Omar O, Gavilanes A, et al. Self-Healing Efficiency of Cementitous Mortar Using Different Bacteria Protection Methods and Mineral Precursors. Journal of Materials in Civil Engineering. 2024;36(1):04023520. https://doi.org/10.1061/JMCEE7.MTENG-16130
[77] Zhu T, Dittrich M. Carbonate precipitation through microbial activities in natural environment, and their potential in biotechnology: a review. Frontiers in bioengineering and biotechnology. 2016;4:4. https://doi.org/10.3389/fbioe.2016.00004
[78] Liu J, Yu C, Shu X, Ran Q, Yang Y. Recent advance of chemical admixtures in concrete. Cement and Concrete Research. 2019;124:105834. https://doi.org/10.1016/j.cemconres.2019.105834
[79] Vaezi M, Zareei SA, Jahadi M. Recycled microbial mortar: Effects of bacterial concentration and calcium lactate content. Construction and Building Materials. 2020;234:117349. https://doi.org/10.1016/j.conbuildmat.2019.117349
[80] Irwan J, Anneza L, Othman N, Faisal Alshalif A. Compressive strength and water penetration of Concrete with Enterococcus Faecalis and calcium lactate. Key Engineering Materials. 2016;705:345-9. https://doi.org/10.4028/www.scientific.net/KEM.705.345
[81] Vijay K, Murmu M. Effect of calcium lactate on compressive strength and self-healing of cracks in microbial concrete. Frontiers of Structural and Civil Engineering. 2019;13:515-25. https://doi.org/10.1007/s11709-018-0494-2
[82] Ammar MA, Chegenizadeh A, Budihardjo MA, Nikraz H. The Effects of Crystalline Admixtures on Concrete Permeability and Compressive Strength: A Review. Buildings. 2024;14(9):3000. https://doi.org/10.3390/buildings14093000
[83] Erşan Y, Akin Y. Optimizing nutrient content of microbial self-healing concrete. 2018.
[84] Kardogan B, Sekercioglu K, Erşan YÇ. Compatibility and biomineralization oriented optimization of nutrient content in nitrate-reducing-biogranules-based microbial self-healing concrete. Sustainability. 2021;13(16):8990. https://doi.org/10.3390/su13168990

[85] Dong J, Wu H, Xie S, Shang X, Shi Z, Tu Z, et al. Impact of calcium formate and anhydrous sodium sulfate on the flowability, mechanical properties, and hydration characteristics of UHPC. Journal of Building Engineering. 2024;96:110534. https://doi.org/10.1016/j.jobe.2024.110534
[86] Chen L, Jiang L, Liu X, Xu P, Meng Y, Ben X, et al. Understanding the role of calcium formate towards hydration and deformation property of light-burned magnesia cement. Construction and Building Materials. 2021;289:122995. https://doi.org/10.1016/j.conbuildmat.2021.122995
[87] Abo Sabah SH, Anneza LH, Juki MI, Alabduljabbar H, Othman N, Al-Gheethi AA, et al. The Use of Calcium Lactate to Enhance the Durability and Engineering Properties of Bioconcrete. Sustainability. 2021;13(16):9269. https://doi.org/10.3390/su13169269
[88] Zanjad N, Pawar S, Nayak C. Experimental study on different properties of cenosphere based concrete using calcium lactate. Sigma Journal of Engineering and Natural Sciences. 2024;42(6):1786-96. https://doi.org/10.14744/sigma.2023.00132
[89] Irwan J, Anneza L, Othman N, Alshalif AF, Zamer M, Teddy T, editors. Calcium Lactate addition in Bioconcrete: Effect on Compressive strength and Water penetration. MATEC Web of Conferences; 2016: EDP Sciences. https://doi.org/10.1051/matecconf/20167801027
[90] Ducasse-Lapeyrusse J, Gagné R, Lors C, Damidot D. Effect of calcium gluconate, calcium lactate, and urea on the kinetics of self-healing in mortars. Construction and Building Materials. 2017;157:489-97. https://doi.org/10.1016/j.conbuildmat.2017.09.115
[91] Irwan JM, Anneza LH, Othman N, Alshalif AF, Zamer MM, Teddy T. Mechanical Properties of Concrete with Enterococcus Faecalis and Calcium Lactate. Procedia Engineering. 2017;171:592-7. https://doi.org/10.1016/j.proeng.2017.01.381
[92] Rusu MM, Faux D, Ardelean I. Monitoring the Effect of Calcium Nitrate on the Induction Period of Cement Hydration via Low-Field NMR Relaxometry. Molecules. 2023;28(2):476. https://doi.org/10.3390/molecules28020476
[93] Skripkiūnas G, Kičaitė A, Justnes H, Pundienė I. Effect of Calcium Nitrate on the Properties of Portland-Limestone Cement-Based Concrete Cured at Low Temperature. Materials. 2021;14(7):1611. https://doi.org/10.3390/ma14071611
[94] Erşan YÇ, Hernandez-Sanabria E, Boon N, de Belie N. Enhanced crack closure performance of microbial mortar through nitrate reduction. Cement and Concrete Composites. 2016;70:159-70. https://doi.org/10.1016/j.cemconcomp.2016.04.001
[95] Mirshahmohammad M, Rahmani H, Maleki-Kakelar M, Bahari A. Effect of sustained service loads on the self-healing and corrosion of bacterial concretes. Construction and Building Materials. 2022;322:126423. https://doi.org/10.1016/j.conbuildmat.2022.126423
[96] Bashaveni B, Pannem RMR. Case Studies in Construction Materials.
[97] Karagöl F, Demirboğa R, Kaygusuz MA, Yadollahi MM, Polat R. The influence of calcium nitrate as antifreeze admixture on the compressive strength of concrete exposed to low temperatures. Cold Regions Science and Technology. 2013;89:30-5. https://doi.org/10.1016/j.coldregions.2013.02.001
[98] Khan MNN, Kuri JC, Sarker PK. Effect of waste glass powder as a partial precursor in ambient cured alkali activated fly ash and fly ash-GGBFS mortars. Journal of Building Engineering. 2021;34:101934. https://doi.org/10.1016/j.jobe.2020.101934
[99] Muhammad S, Siddiqui HA, Abro MI, Usmani A, Mallick MAA. Bacillus subtilis as self-healing agent in cement mortar: Combined and the separate effect of bacteria and calcium lactate on self-healing behavior in cement mortar. Mehran University Research Journal Of Engineering & Technology. 2021;40(2):426-34. https://doi.org/10.22581/muet1982.2102.16
[100] Mammoliti L. Examination of the mechanism of corrosion inhibition by calcium nitrite and calcium nitrate-based admixtures in concrete. 2001.
[101] Huseien GF, Memon RP, Baghban MH, Faridmehr I, Wong LS. Effective microorganism solution-imbued sustainable self-curing concrete: Evaluation of sorptivity, drying shrinkage and expansion. Case Studies in Construction Materials. 2024;20:e03255. https://doi.org/10.1016/j.cscm.2024.e03255
[102] Pappupreethi K, Ammakunnoth R, Magudeaswaran P. Bacterial concrete: A review. International Journal of Civil Engineering and Technology. 2017;8(2):588-94.
[103] Mors R, Jonkers H. Effect on concrete surface water absorption upon addition of lactate derived agent. Coatings. 2017;7(4):51. https://doi.org/10.3390/coatings7040051
[104] De Belie N, Wang J, Bundur ZB, Paine K. Bacteria-based concrete. Eco-efficient repair and rehabilitation of concrete infrastructures: Elsevier; 2018. p. 531-67. https://doi.org/10.1016/B978-0-08-102181-1.00019-8
[105] Abo-El-Enein S, Ali A, Talkhan FN, Abdel-Gawwad H. Application of microbial biocementation to improve the physico-mechanical properties of cement mortar. Hbrc Journal. 2013;9(1):36-40. https://doi.org/10.1016/j.hbrcj.2012.10.004

[106] Luo M, Qian C-x, Li R-y. Factors affecting crack repairing capacity of bacteria-based self-healing concrete. Construction and Building Materials. 2015;87:1-7. https://doi.org/10.1016/j.conbuildmat.2015.03.117
[107] Luhar S, Luhar I, Shaikh FUA. A review on the performance evaluation of autonomous self-healing bacterial concrete: mechanisms, strength, durability, and microstructural properties. Journal of Composites Science. 2022;6(1):23. https://doi.org/10.3390/jcs6010023
[108] Feng J, Chen B, Sun W, Wang Y. Microbial induced calcium carbonate precipitation study using Bacillus subtilis with application to self-healing concrete preparation and characterization. Construction and Building Materials. 2021;280:122460. https://doi.org/10.1016/j.conbuildmat.2021.122460
[109] Vijay K, Murmu M. Experimental Study on Bacterial Concrete Using Bacillus Subtilis Micro-Organism. Emerging Trends in Civil Engineering: Springer; 2020. p. 245-52. https://doi.org/10.1007/978-981-15-1404-3_20
[110] Osman KM, Taher FM, Abd El-Tawab A, Faried AS. Role of different microorganisms on the mechanical characteristics, self-healing efficiency, and corrosion protection of concrete under different curing conditions. Journal of Building Engineering. 2021;41:102414. https://doi.org/10.1016/j.jobe.2021.102414
[111] Erşan YÇ, Da Silva FB, Boon N, Verstraete W, De Belie N. Screening of bacteria and concrete compatible protection materials. Construction and Building Materials. 2015;88:196-203. https://doi.org/10.1016/j.conbuildmat.2015.04.027
[112] Kanellopoulos A, Qureshi T, Al-Tabbaa A. Glass encapsulated minerals for self-healing in cement based composites. Construction and Building Materials. 2015;98:780-91. https://doi.org/10.1016/j.conbuildmat.2015.08.127
[113] De Muynck W, Debrouwer D, De Belie N, Verstraete W. Bacterial carbonate precipitation improves the durability of cementitious materials. Cement and Concrete Research. 2008;38(7):1005-14. https://doi.org/10.1016/j.cemconres.2008.03.005
[114] Chahal N, Siddique R, Rajor A. Influence of bacteria on the compressive strength, water absorption and rapid chloride permeability of concrete incorporating silica fume. Construction and Building Materials. 2012;37:645-51. https://doi.org/10.1016/j.conbuildmat.2012.07.029
[115] Joshi S, Goyal S, Mukherjee A, Reddy MS. Microbial healing of cracks in concrete: a review. Journal of Industrial Microbiology and Biotechnology. 2017;44(11):1511-25. https://doi.org/10.1007/s10295-017-1978-0
[116] Khan MBE, Shen L, Dias-da-Costa D. Self-healing behaviour of bio-concrete in submerged and tidal marine environments. Construction and Building Materials. 2021;277:122332. https://doi.org/10.1016/j.conbuildmat.2021.122332
[117] Mitra A, Sreedharan SM, Singh R. Concrete Crack Restoration Using Bacterially Induced Calcium Metabolism. Indian Journal of Microbiology. 2021;61(2):229-33. https://doi.org/10.1007/s12088-020-00916-0
[118] De Souza Oliveira A, Toledo Filho RD, Fairbairn EdMR, de Oliveira LFC, Gomes OdFM. Microstructural characterization of self-healing products in cementitious systems containing crystalline admixture in the short-and long-term. Cement and Concrete Composites. 2022;126:104369. https://doi.org/10.1016/j.cemconcomp.2021.104369
[119] Harrington EA. X-ray diffraction measurements on some of the pure compounds concerned in the study of Portland cement. American journal of science. 1927;13(78):467-79. https://doi.org/10.2475/ajs.s5-13.78.467
[120] Chen H, Qian C, Huang H. Self-healing cementitious materials based on bacteria and nutrients immobilized respectively. Construction and Building Materials. 2016;126:297-303. https://doi.org/10.1016/j.conbuildmat.2016.09.023
[121] Jiang L, Jia G, Jiang C, Li Z. Sugar-coated expanded perlite as a bacterial carrier for crack-healing concrete applications. Construction and Building Materials. 2020;232:117-222. https://doi.org/10.1016/j.conbuildmat.2019.117222
[122] Kadapure SA, Deshannavar UB, Katageri BG, Kadapure PS. A systematic review on MICP technique for developing sustainability in concrete. European Journal of Environmental and Civil Engineering. 2023;27(16):4581-97. https://doi.org/10.1080/19648189.2023.2194942
[123] Maurente-Silva DG, Borowski JVB, Cappellesso VG, Vainstein MH, Masuero AB, Dal Molin DCC. Effect of Exposure Environment and Calcium Source on the Biologically Induced Self-Healing Phenomenon in a Cement-Based Material. Buildings. 2024;14(12):3782. https://doi.org/10.3390/buildings14123782
[124] Pinto A, González-Fonteboa B, Seara-Paz S, Martínez-Abella F. Effects of bacteria-based self-healing nutrients on hydration and rheology of cement pastes. Construction and Building Materials. 2023;404:133142. https://doi.org/10.1016/j.conbuildmat.2023.133142

Research on Engineering Structures & Materials
www.jresm.org
MIM Research Group

Review Article

Artificial intelligence-assisted optimization of concrete mixes to enhance the durability of civil engineering structures in marine environments

Othmane Karrame [*,1,a], Mohammed Aqil [2,b], Mohammed Ammari [1,c], Laïla Ben Allal [1,d]

[1]*Research Team, Materials, Environment and Sustainable Development (MEDD), FST Tangier, Abdelmalek Essaadi University, Tetouan , Morocco*
[2]*3GIE laboratory, Mohammadia School of Enginnering, Mohamed V University, Rabat, Morocco*

Article Info

Article History:

Received 27 June 2025

Accepted 16 July 2025

Keywords:

Civil engineering;
Durability;
Aggressive media;
Artificial intelligence;
Concrete formulation additives

Abstract

The durability of concrete is a major concern for civil engineering professionals, a concern that is amplified by the considerable impact of climate change and environmental factors. This issue becomes critical for infrastructure located along maritime and river foreshores. These structures are constantly exposed to a series of aggressive agents, including chemical and mechanical actions, as well as variations in temperature and humidity. Therefore, to maintain the sustainability of these structures, a set of mineral additives and pozzolans is added to the concrete formulation to improve performance and extend the service life of concrete structures. With the emergence of Industry 4.0, the construction sector has undergone a profound transformation through the integration of various digital technologies throughout the entire project life cycle, from design to implementation. These technologies include BIM, modeling, artificial intelligence, automation, 3D printing, and optimization of concrete formulations. This technological shift has enabled significant advancements in material management and the enhancement of concrete durability. Leveraging alternative additives and AI technology, we can develop robust, environmentally friendly concrete that excels in challenging environments, delivering optimal results in terms of cost, time, and performance. The objective of this work is to demonstrate the potential of AI tools in optimizing concrete formulations by identifying the most effective combinations of additives, materials, and dosages to mitigate the effects of environmental aggressions on structures in maritime environments.

© 2025 MIM Research Group. All rights reserved.

1. Introduction

Concrete plays a structuring role in the development of territories. It has been adopted for building needs for decades in the four corners of the world. Indeed, this material has been fully privileged due to its proven quality characteristics, including strength, durability, thermal and acoustic performance. Moreover, it is known for its ability to meet different architectural and structural design needs. It is manifested in the majority of infrastructures: civil engineering structure, industrial or commercial equipment, road infrastructure, public facilities and housing. By its omnipresence, concrete has become a key component of urban modernization and the development of living spaces.

Moreover, although concrete combines key mechanical properties: rigidity, strength and durability, it is not immune to vulnerabilities and failures. Its durability can indeed be compromised when

*Corresponding author: othmane.karrame@etu.uae.ac.ma
[a]orcid.org/0009-0008-2530-5966; [b] orcid.org/0000-0001-6030-2287; [c]orcid.org/0000-0002-5664-7546;
[d]orcid.org/0000-0001-8801-5570
DOI: http://dx.doi.org/10.17515/resm2025-993ai0627rv

exposed to an aggressive environment characterized by chloride sulfate attack as well as thermal variations [1,2]. Seawater with an average salinity of 35 g/l, is dominated by NaCl, and also contains $MgCl_2$, $MgSO_4$, and $CaSO_4$, all of which react chemically with concrete [3]. In the Moroccan context, this phenomenon is very common, as structures built along the Atlantic and Mediterranean coasts are frequently subjected to these physical and chemical aggressions [4]. The consequences include series of cracks, surface dislocations and reinforcement corrosion. $MgCl_2$ dissolves portlandite ($Ca(OH)_2$), forms partially soluble $CaCl_2$, and develops expansive products such as Friedel's salt ($3CaO{\cdot}Al_2O_3{\cdot}CaCl_2{\cdot}10H_2O$) which induce cracking and increase porosity. Similarly, $MgSO_4$ produces gypsum ($CaSO_4{\cdot}2H_2O$) and brucite ($Mg(OH)_2$), which weaken the cementitious matrix. [6,7]. These reactions clearly demonstrate the limitations of traditional concrete formulation under marine environmental conditions.

To improve durability by limiting the penetration of aggressive agents and improving the mechanical performance of concrete, various materials and minerals were studied and incorporated into the concrete matrix. This approach indeed involves using additional cementitious materials such as fly ash (20–50% replacement) and silica fume (up to 10%), known for refining the pore structure and reducing permeability [32,33]. Recent advances also focus on nanomaterials such as nano-silica (1.5-2 wt%), nano-TiO and multi-wall carbon nanotubes that densify the microstructure, reduce chloride ion diffusion by up to 38%, and improve the interfacial transition area (ITZ) [21, 22]. Furthermore, the integration of treated loam and dredge products (used up to 20% substitution), PVC polymers and alternative binders such as ultra-fine palm oil ash (UPOFA, about 10% substitution), decreases porosity, enhances the compressive strength by up to 40% and resists sulfate attacks [24, 36, 40]. These approaches not only prolong the lifespan in marine environments, but also contribute to sustainability by integrating waste and reducing dependence on natural resources.

Furthermore, to better identify and optimize these innovative approaches aimed at strengthening concrete formulation, artificial intelligence, and more particularly machine learning, opens promising prospects. This technology based on neural networks and decision trees allows has become increasingly important in the optimization of concrete formulation. Unlike traditional models, AI can handle complex relationships between concrete composition, mechanical properties and environmental conditions, which is essential in aggressive environments with many influencing factors. ML models were used to predict compressive strength with errors less than 5%, optimize mixing designs and evaluate durability against chloride and sulfate attacks. [43, 45].

This work aims to design sustainable concrete for marine and river structures, by consolidating the results of scientific research carried out and optimized by artificial intelligence tools.

2. Aggressive Media and Pathologies of Concrete

2.1. Exposure Conditions and Aggressiveness of Marine Environments

The marine environment is one of the harshest and most aggressive environments for civil infrastructure, due to the combined effects of mechanical actions (such as swell, waves and tidal movements), chemical agents (including dissolved salts like chlorides and sulfates), climatic factors (including temperature fluctuations), and biological influences (such as microbial activity). Three exposure configurations can be distinguished for marine structures: the permanently submerged area which is generally less prone to degradation; the continuously emerged area, where concretes are partially affected by the transported chlorides, and the tidal zone, which is the most aggressive, subjected to alternating cycles of immersion and drying, which further promotes the accumulation and penetration of aggressive agents.

Salinity representing the determining factor which varies from a few g/L to more than 200 g/L, with an average of 35 g/L in the large oceans [3]. In Morocco, it is relatively stable on the Atlantic coast (about 35 g/L), but reaches up to 38-39 g/L on the Mediterranean coast, especially in areas with low water renewal [4, 5].

2.2. Mechanisms of Corrosion and Crack Propagation

Chloride ions, particularly $MgCl_2$, react with calcium hydroxide (portlandite) to form $CaCl_2$, which increases porosity, and also forms expansive salts such as ($3CaO\ Al_2O_3\ CaCl_2\ 10H_2O$), which are responsible for cracking. $MgSO_4$, in turn, causes the formation of secondary gypsum and brucite, which degrade cement hydrates and increase concrete porosity. These chemical reactions promote concrete cracking and reinforcement corrosion [6-8], as observed in several ports, where thickness losses due to chloride attack and carbonation have been reported [2].

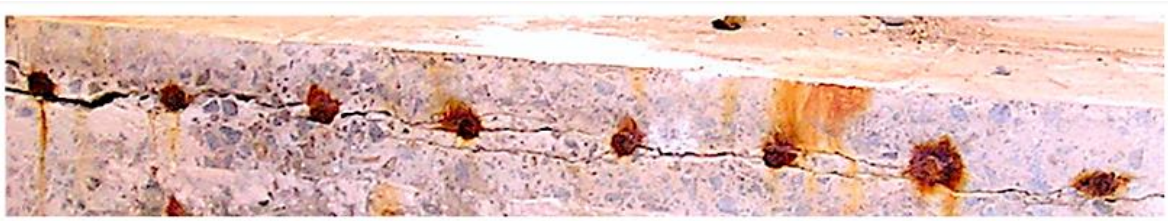

Fig. 1. Cut cross-section in 2009 of a 450 mm thick deck slab (cover 40 mm) exposed since the 1930s in the Newcastle Harbour marine atmosphere, showing delamination crack passing through the bottom of the 16 mm diameter bars. R.E. Melchers 2009 [2]

A study on a breakwater crown wall exposed in the marine environment revealed widespread corrosion of the reinforcements, confirmed by the appearance of concretions, internal damage (ultrasound) and strong chlorinated contamination (up to 150 mm deep). [9-11]. Corrosion rates exceeded 0.10µA/cm² in most of the structure, with 90% of values above 0.6µA/cm², which corresponds to a material loss greater than 0.070 mm/year. The calculated corrosion index classified the structure as very degraded, requiring immediate intervention [9-11]. In addition, another study [12] showed that chloride-induced corrosion in reinforced concrete beams subjected to flexural stresses progresses more rapidly in the presence of large deformations. Over a period of five years, five beams were exposed to a saline solution simulating a marine environment without artificial acceleration of corrosion. The results showed that bending cracks facilitated the entry of chlorides and oxygen, thus accelerating corrosion. The first signs appeared within the first 90 days.

Indeed, these beams, all with a width of 0.08 m, have variable heights (from 0.050 m to 0.104 m) in order to generate different levels of deflection in the middle under controlled loads, while maintaining the same initial stress in the reinforcements (210 MPa) [12]. This constant stress was essential for simulating the phenomenon of stress corrosion in conditions close to reality. The concrete used for all the beams had a homogeneous composition, with identical proportions. As a result, the bending cracks that appeared under the effect of the charges favored the penetration of chloride ions and oxygen, which led to an intensification of corrosion, especially in the central area in direct contact with the saline solution. The table below presents the geometric characteristics, reinforcement details and load and deflection parameters of the five beams tested:

Table 1. Characteristics of the tested beams [12]

Beam No.	Height (m)	Reinforcement	Concrete Cover (m)	Applied Load P (N)	Deflection (d) (m)	Slenderness Ratio (L/d)
1	0.050	2 × Ø8 mm (0.008 m) bars	0.025	2800	0.0100	200
2	0.070	2 × Ø8 mm (0.008 m) bars	0.025	1350	0.0067	300
3	0.082	2 × Ø8 mm (0.008 m) bars	0.025	1710	0.0050	400
4	0.094	2 × Ø8 mm (0.008 m) bars	0.025	2020	0.0040	500
5	0.104	2 × Ø8 mm (0.008 m) bars	0.025	2300	0.0033	600

The evolution of cracks was monitored throughout the duration of the test (1800 days), distinguishing between bending and corrosion cracks. The former is due to traction in the tense areas, while the latter result from the internal pressure exerted by the corrosion products. These two types of cracks interact and amplify each other, contributing to the degradation of the beam.

Table 2 below presents the observed linear trends for the total cracking area (sum of bending and corrosion cracks) as well as for the maximum width of the cracks, expressed by equations obtained via least squares method, with their determination coefficient R^2 indicating the quality of the fit. Consequently, this research highlights the crucial importance of crack and sag control to improve the durability of reinforced concrete structures in marine environments [12-14].

Table 2. Evolution of total cracking area and maximum crack width over time (up to 1800 days) [12]

Beam No.	Total Cracking Area ($m^2 \times 10^{-6}$) **x:** Time (in days) & **y:** Cracking area or crack width	R^2	Max Crack Width (m)	R^2
1	y=0.1282x+1.5998	0.97	y=0.0002x+0.1401	0.76
2	y=0.1084x−8.342	0.94	y=0.0001x+0.0475	0.89
3	y=0.0637x−0.9815	0.99	y=0.0002x−0.0018	0.87
4	y=0.0572x−10.697	0.91	y=0.00006x−0.0625	0.63
5	y=0.0574x−9.9234	0.97	y=0.00008x−0.0327	0.79

2.3. Effectiveness of Cementitious Binders and Resistance to Chemical Attacks

Three types of cementitious binders were evaluated in aggressive marine environments:

- OPC: Ordinary Portland cement,
- PBC: Pozzolanic cements, incorporating reactive mineral additions such as fly ash, silica fume or blast furnace slag,
- AAMs: Alkali-activated materials, high silica and alumina waste binders activated by alkaline solutions to generate N-A-S-H or C-A-S-H gels.

The analysis of this evaluation was directed towards their chemical interactions with abundant Cl^-, SO_4^{2-} and CO_2 ions in seawater, as well as their properties in the hardened state such as compressive strength, porosity, water absorption and chloride permeability. The results revealed that [15]:

- The OPC can lose between 15% and 25% of its mechanical strength after six months of exposure, compared to less than 10% for PBC, while AAAMs show stability due to the reduced portlandite content.
- The chloride permeability measured by the rapid migration test is significantly lower in PBC (1000-2000 C) and AAM (<1000 C) compared to that of OPC (>3000 C), reflecting a better resistance to penetration of aggressive agents.

Consequently, the combined marine conditions of wet-dry cycles, as well as high temperatures significantly increase the degradation of concrete, particularly OPC-based concretes [16,17]. Attacks on sulfates and acid aggressions are two major forms of concrete degradation in hostile environments. Sulphates present in soils or in certain industrial wastewater can react with the components of the cementitious matrix, leading to the formation of secondary ettringite. This process generates internal swelling that causes significant cracks to appear within the material [18,19]. In parallel, in industrial and agricultural environments, concrete is frequently exposed to acidic environments (pH < 5). This acidity induces a gradual dissolution of the cementitious paste, compromising the durability of the structure. Sulphuric and nitric acids, as well as some organic leachates, are particularly aggressive, causing significant mass losses and a strong deterioration of the mechanical strength of concrete [20]. Faced with these issues, several research studies have proposed the incorporation of pozzolanic materials such as silica fume or metakaolin. These additions densify the microstructure of the paste, thus reducing its permeability and improving its resistance to chemical attacks [35].

3. Conventional Methods for Improving Concrete Durability

3.1. Nanomaterials: Nano-silica, Nano-TiO_2, Carbon Nanotubes and Graphene

For several decades, engineers, researchers and professionals have been implementing a set of techniques and approaches incorporated into the concrete matrix in order to strengthen its

resistance to aggressive environments, thus providing a reference base in the field. The incorporation of nanofillers into concrete represents a significant advance to improve its durability without compromising its initial mechanical strength. Materials such as nano-silica (NS), nano-TiO (NT), multi-wall carbon nanotubes (MWCNTs) and multilayer graphene (MLG) densify the internal microstructure of concrete, reduce water absorption and limit chloride ion transport. Indeed, the incorporation of 1.5% by weight of nanosilica reduces the diffusion coefficient of chloride ions from 18.6×10^{-12} m^2/s (for the control concrete at 28 days) to 13.62×10^{-12} m^2/s at 84 days, representing a reduction of 26.8% [23].

These nanofillers also promote the formation of more compact C-S-H gels, modify the morphology of hydration products and improve cohesion between aggregates and the cementitious matrix by refining the interfacial transition zone (ITZ). For CO_2 emissions, the values increase from 463 kg/m^3 (for traditional high-strength concrete with a compressive strength of 88 MPa) to 360 kg/m^3 (for concrete with NS and 49 MPa), representing a reduction of 22.2% [22,23]. Similarly, the production cost decreases from USD 83/m^3 (88 MPa) to USD 60/m^3 (49 MPa with NS), which corresponds to a cost reduction of 27.8%. In terms of sustainability, the integration of nano-silica increases the durability indicator (kSB) by up to 16.6%, comparing with traditional concrete. Additionally, by combining 2 wt% of NS with 1 wt% of nano-calcium carbonate (NC) in ordinary and high-volume concrete of fly ash (HVFA), the performance is significantly improved. Sorptivity is reduced by 30% and chloride ion penetration is reduced by 38%. Microstructural analysis by MIP and DTA/TGA confirms a decrease in porosity and portlandite (CH), reflecting the higher efficiency of NS compared to NC, especially in 40% F-type HVFA concretes. [21-23]. This figure presents that incorporating 1.5 wt% nanofillers significantly improves the sustainability index of concrete by 11.7%–16.6%, without increasing cement content. It also shows the potential of low-cost, low-carbon, and durable nano-engineered concrete for marine engineering applications [23].

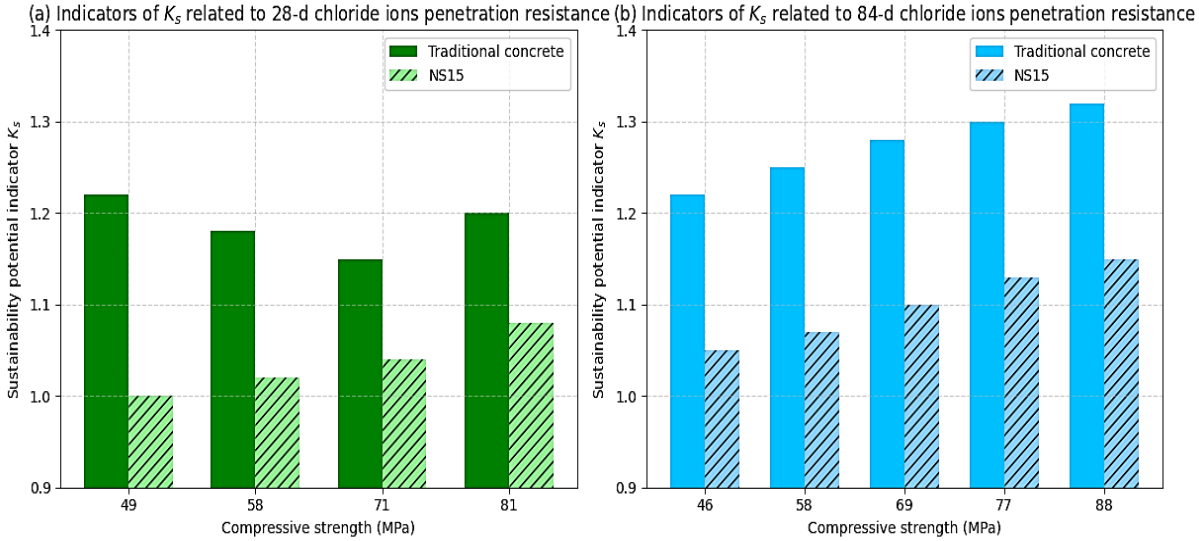

Fig. 2. Indicators of the sustainability potential indicator (kSB) related to 28-d and 84-d chloride ion penetration resistance [23]

3.2. UPOFA: Ultra-Fine Palm Oil Fuel Ash

The incorporation of alternative materials such as ultra-fine palm oil ash (UPOFA) significantly contributes to improving the compacity of concrete and reducing its porosity. 10% cement substitution with UPOFA reaches a compressive strength of 37.95 MPa at 28 days, which represents an increase of about 40% compared to control concrete without addition [24]. This improvement is also accompanied by better corrosion resistance and reduced chloride ion penetration. The RCPT (Rapid Chloride Penetration Test) and HCP (Half-Cell Potential) tests confirmed the good performance in terms of durability, while the high ultrasonic speeds measured by the UPV method (Ultrasonic Pulse Velocity) testify to a homogeneous and densified internal structure. [24], [25], [26].

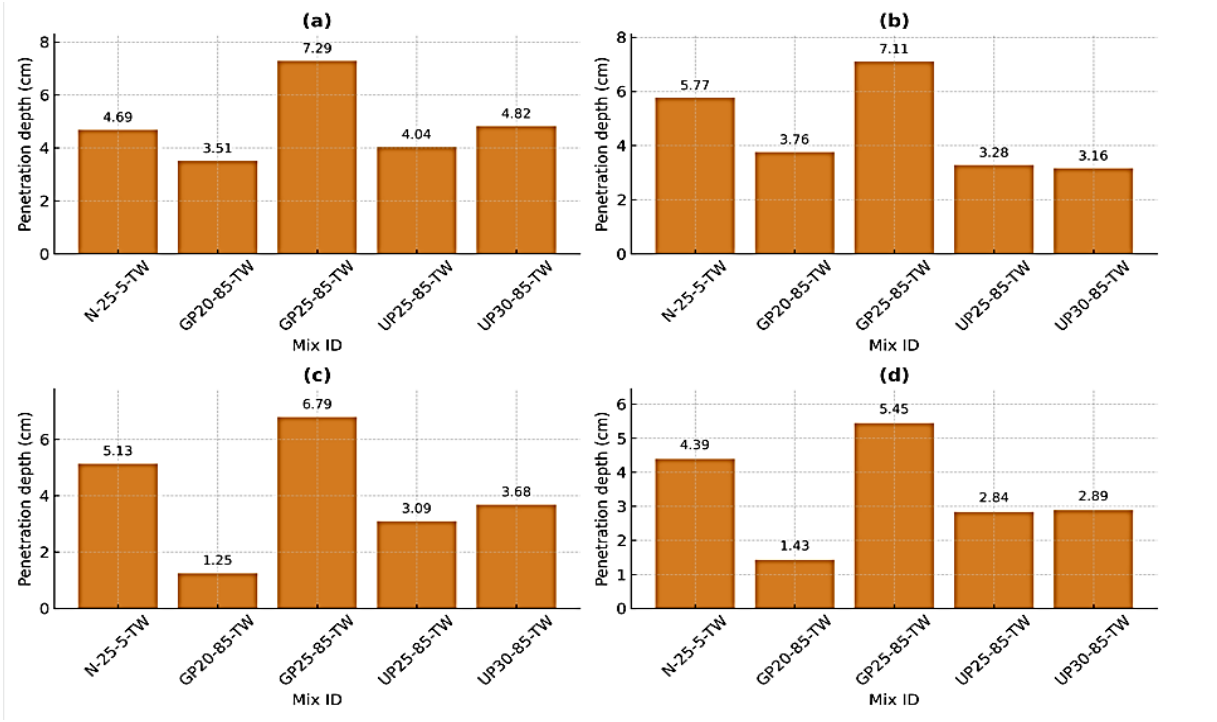

Fig. 3. Chloride-penetration depths of (a) RS-TW, (b) SS-TW, (c) RS-SW, and (d) SS-SW specimens [24]

This figure shows the chloride-penetration depths of the concrete disc specimens at 28 d. Specimens without POFA exhibited the following depths: N-RS-TW (4.69 cm), N-SS-TW (3.76 cm), N-RS-SW (5.13 cm), and N-SS-SW (1.43 cm). The highest penetration depth was observed in GP20-RS-TW, at 7.29 cm. Additionally, the penetration depth of the UPOFA samples tended to improve as the ratio of UPOFA increased. The tests [24] also revealed that a higher amount of UPOFA in cement decreases concrete compressive strength, particularly during the early curing period. Lower compressive strength indicates reduced density in the concrete matrix, primarily due to the presence of pores. Furthermore, concrete mixed with seawater and containing 10 % UPOFA showed a notable reduction in chloride-penetration depth. This improvement may be attributed to mineral admixtures like POFA, which effectively bind unbound chloride ions in seawater, thereby enhancing the concrete's durability [24].

3.3. Mineral Waste Additions: Crushed Glass, Marble, Silica Sand and Syenite Nephelin

The partial substitution of natural sands by mineral waste (syenite nephelin, marble, crushed glass, silica sand) also offers a sustainable solution, with a significant reduction in porosity, better compactness (increased UPV speed), and an improvement in mechanical and chemical properties. Crushed glass, rich in amorphous silica, promotes the formation of additional C-S-H via pouzzolanic reactions, reducing the Ca/Si ratio and increasing resistance to sulphate attacks (low mass loss and swelling at 90 days). Marble and syenite nephelin provide increased resistance to abrasion and shearing thanks to their fine grain size [27-29].

3.4. Fly Ash-Based Systems and Supplementary Cementitious Materials

Lv et al. [30,31] conducted a study on the addition of Crassostrea gigas (giant oyster) as a protective layer in concrete. They concluded that this layer further reduced the depth of neutralization of exposed concretes in the tidal zone. This protection is due to the ability of Crassostrea gigas to form a resistant barrier against chemical aggressions and limit the intrusion of chlorides and other aggressive ions. Simčič et al. [32,33] explored the effects of adding fly ash in concretes exposed to marine environments. Their study showed that partial replacement of cement with 20 to 50% fly ash appreciably reduces chloride penetration. Fly ash contributes to the formation of denser, more corrosion-resistant mineral phases in marine environments, which protects metal reinforcement

from premature degradation. Similarly, Zhang et al. [34] observed a palpable reduction in the chloride diffusion coefficient after 600 days of tidal exposure. The results designate that adding fly ash not only reduces chloride penetration, but also increases the durability of concrete exposed to moisture and salinity cycles. However, some research has shown that there are adverse effects of the excessive addition of silica fume (SF) in marine concretes. Indeed, Ganjian et al. [35] found that the incorporation of 7-10% SF, combined with 50% slag, resulted in an increase in water absorption from concretes exposed to the tidal zone and seawater. This could be due to a change in the porous structure of concrete, making the material more susceptible to water absorption and aggressive ion infiltration.

The study [35] has also revealed the impact of the marine environment on the properties of HVFA (High Volume Fly Ash) pastes, where 70% of cement is replaced by fly ash. Due to the low initial resistance of HVFA pastes, additions of 20% metakaolin (MK) and 10-20% quartz (Q-P) were made to compensate for this deficit. The samples were subjected to various hardening conditions in air, water, seawater and wetting/drying cycles, simulating tidal conditions over a period of 270 days. The results were analyzed using X-ray diffraction (XRD), thermogravimetry (TGA/DTG) and scanning electron microscopy (SEM), which allowed to show these mineralogical transformations at the level of the concrete paste.

3.5. Marine Silt and Dredged Sediments as Cement or Sand Substitutes

In the context of ports, silt which is abundant in marine environments and often considered a waste has great potential, particularly because of its fine grain size and its high content of silicates and aluminas. Research [36] has shown that after treatment (washing, drying, alkaline activation), it can be used as a partial substitution (10-20%) of cement or fines, without significant loss in mechanical performance and with reduced porosity. This recovery helps to limit the use of clinker and optimize the management of marine residues in the Moroccan coastal regions. [36]. Given that port and river dredging is essential to maintain the depths of navigation and create new operating basins, its planning and management represent a challenge for professionals given the large quantities of extracted sediments and the prohibitive costs of the operation. Therefore, the recovery and reuse of these materials, especially in the building sector, remains a promising solution.

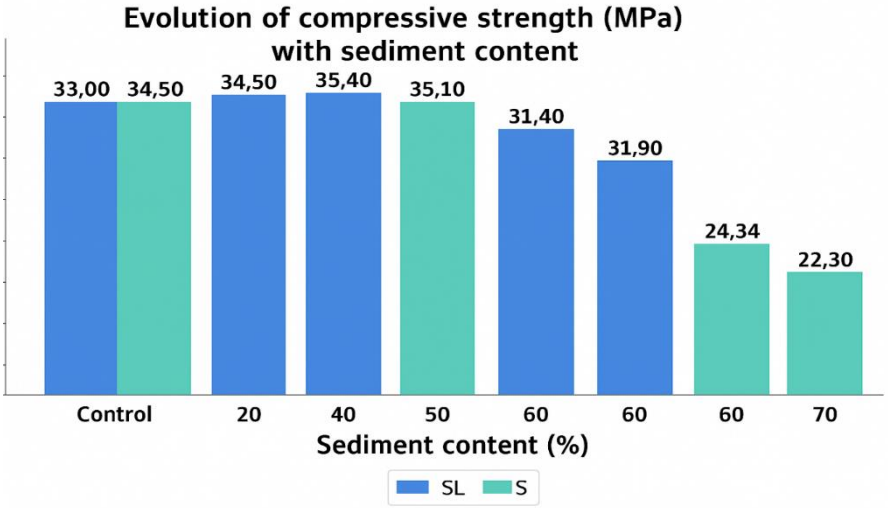

Fig. 4. Effect of Sediment Substitution Rate on the Compressive Strength of Fired Bricks [36].

A study [37] was carried out on the upgrading of sediments from the ports of Tangier and Larache by using them as a partial substitute for sand in cement mortars and in the manufacture of construction materials. The sediments, mainly composed of silt and fine sands, have a water content of 10.8% for those of Tangier and 12.5% for those of Larache. Chemical analyses show a low presence of heavy metals, but hydrocarbons are present in the sediments of Tangier at 0.2%. [36,37]. Results of mortar testing show that incorporation of up to 20% sand replacing sediment does not compromise resistance. with 10% and 20% sediment reached compression strengths of

33 MPa and 30 MPa respectively, meeting the standard for resistance in common applications [37]. In addition, durability tests, including resistance to freeze-thaw cycles, revealed that these mortars showed no degradation after 50 cycles. For the manufacture of construction materials, the addition of sediment has produced the materials with a compressive strength of 10 MPa for those containing 30% sediment and 8 MPa for those containing 70% [37]. These values are higher than the minimum strength required in the material.

The values in Figure 3 show that the Larache sediment allows to make a brick with better mechanical characteristics than those of the control for a rate substitution up to 50%. The 40% substitution rate gives resistance of 35.4 MPa higher than that of the control (7.3% increase) [36]. Thus on the same wavelength and in the context of optimizing clay substitution in the manufacture of terracotta building materials, the results showed that materials containing up to 50% of sediments from Larache have superior mechanical performances to the reference brick, with a compressive strength of 22 MPa, while those from Tangier, with 20% substitution, showed similar results to the control brick (strength of 25 MPa). However, above 60% substitution, the compressive strength drops to 15 MPa, which can be attributed to the increased presence of organic matter in sediments.

In conclusion for this study [36], the valorization of port sediments as building materials has a real interesting potential to reduce the volume of sediment to be disposed of while offering an ecological and economic alternative for the construction industry. This study [37] confirmed that these sediments can be used on a large scale without compromising the performance of the produced materials, paving the way for their use as local resources in construction.

3.6. PVC Grains and Polypropylene Fibers as Concrete-Enhancing Additives

In terms of durability, the study of shrinkage by a coupled experimentation-modeling approach showed that unidirectional drying induced moisture gradients responsible for internal stresses and cracks [39]. Control of relative humidity through internal cure, using PVC grains (partially substituting sand) and polypropylene fibers (partially replacing the binder), allows to modulate deformations and improve durability [38], [40]. PVC improves fluidity and reduces plastic shrinkage, while fibers increase compactness and limit delayed deformation. Poromechanic modeling, integrating moisture, stiffness and shrinkage, allowed to reproduce internal stresses and microcrack areas, confirming the efficiency of the fibers. However, the effect of temperature remains to be investigated, especially in construction conditions [41]. Validation of the model at full scale through durability testing (carbonation, sulphates, freeze-thaw cycles) is essential to confirm the applicability of formulations in aggressive environments [42].

The reinforcement of the concrete matrix by adding additives such as nanofillers, nano-silica, UPOFA (ultra-fine palm oil fuel ash), loam (treated loam), PVC grains and others further densify the microstructure, significantly reduces water absorption and chloride ion penetration and increases resistance to aggressive environments. Corollary, based on the results of the research presented in this chapter [21-42], these additives play an essential role in the longevity of concrete, particularly in maritime and port areas.

4. Contributions of Artificial Intelligence in Concrete Formulation

4.1. Modeling Concrete Complexity with AI in Aggressive Environments

Artificial intelligence (AI), and in particular artificial neural networks (RNAs), decision trees, or regression algorithms, have been increasingly used in the field of concrete formulation. These tools make it possible to model complex relationships between composition, mechanical properties and environmental conditions without requiring strict analytical laws [43].

In an aggressive environment, there are many parameters to consider (type of binder, porosity, resistance to chlorides, carbonation, etc.), which makes traditional models limited. AI provides an effective response to this complexity.

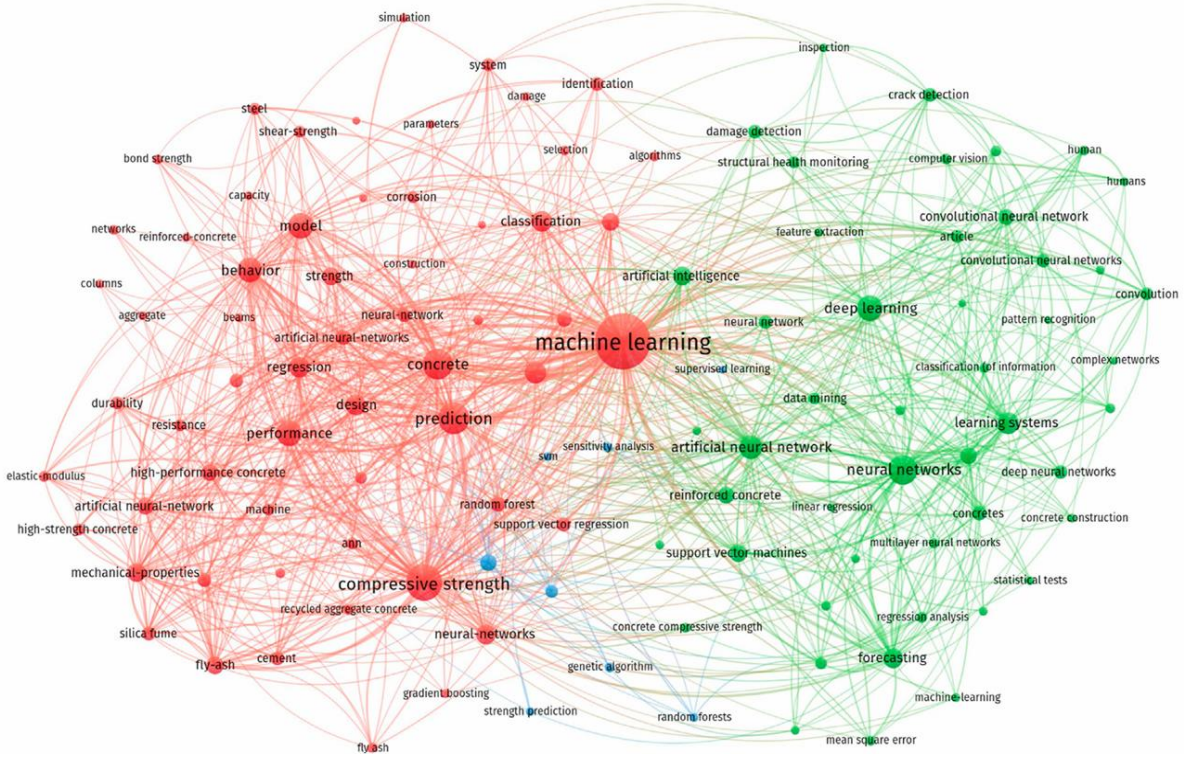

Fig. 5. Application of machine learning in concrete [44]

Figure 5 shows that ML has been used in different parts of concrete technology in different fields of studies. In Morocco [45], some laboratories are starting to develop local databases to integrate these e-learning techniques. Furthermore, the concept of Building 4.0 is directly inspired by Industry 4.0 and encompasses the digitalization of design, manufacturing and quality control processes in the construction sector. In this context, the concrete formulation becomes an integrated step in a global data-driven system. [44,45].

4.2. AI Driven Optimization and Predictive Modeling of Concrete Properties

Several recent studies [46] have used supervised learning models to optimize component dosing, predict marine sustainability or sulfates, and identify 'robust' formulations. For example, a neural network can predict compressive strength at 28 days with an error of less than 5%, based on input data such as E/C ratio, adjuvant content or sand type [46]. Indeed, the use of BIM (Building Information Modeling), combined with IoT sensors (Internet of Things), allows to collect real-time information on the performance in service and to adapt the formulations to the project requirements. All the more so as prototypes of automatic formulation systems based on multicriteria optimization algorithms (e.g. NSGA-II, genetic algorithms) are being tested in several laboratories [44]. They allow to simultaneously take into account mechanical resistance, cost, chemical durability and carbon footprint. [44, 46]

A recent study explored the effectiveness and relevance of machine learning algorithms, to accurately predict and classify concrete compressive strength taking into account formulation parameters and curing time [47]. The use of advanced analytical tools, such as SHAP (Shapley Additive Explanations) values and partial dependency graphs, allowed a detailed examination of the interactions between input variables and their impact on predictions. These results showed the potential of machine learning models to improve formulation optimization, quality assurance and compliance with engineering standards [47, 48]. The SHAP analysis, in particular, has allowed for a better understanding of the contributions of characteristics, both at the global and local scales, which has strengthened the interpretability of the model. In addition, the prediction of the mechanical characteristics of concrete such as its strength of concrete without the need for laboratory tests, undoubtedly allows to accelerate the design process by further reducing costs and time [48].

In this context, the studies conducted in this direction proposes an in-depth review of current applications of artificial intelligence, and more particularly machine learning (ML), in the field of concrete technology. The author highlights the increasing role of EL throughout the concrete life cycle, from raw material characterization to crack detection in in-service structures [44]. ML techniques make it possible to optimize the concrete formulation, predict its properties in fresh or hardened state and evaluate its durability against chemical or physical aggressions. They also offer non-destructive methods for early crack detection, including image analysis and convolutional neural networks. The study in question highlights the advantages of these approaches, including time savings, cost reduction and forecast accuracy [44, 49]. However, the author highlights the persistent challenges related to data quality, algorithm choice and understanding of these tools by civil engineers. In conclusion, the article recommends a better integration of machine learning into concrete engineering practices and university training, to facilitate the transition towards smarter and more sustainable construction [50]. Artificial intelligence (AI) has been used to predict the compressive strength of concrete, an advanced cementitious material known for its outstanding mechanical properties, high durability, very low permeability, as well as its ability to prefabricate and reinforce infrastructure works [50, 51].

In this study, an experimental database of over 200 fiber-reinforced ultra-high-performance concrete (UHSC) formulations was compiled from the scientific literature to predict flexural strength using artificial intelligence tools [52]. This base includes 15 input variables representing the characteristics of the constituent materials of the concrete: the contents of cement, fly ash, slag, silica fume, nano-silica, limestone powder, sand, aggregates, quartz powder, as well as the water contents, superplasticizer, rate of steel fibers, fiber diameter and length, and finally the curing time.

The target variable is the flexural strength, expressed in megapascals (MPa), whose values range from 5.6 to 41.5 MPa. The data was normalized and divided into two sets: 70% for model training and 30% for validation testing, with k-fold cross validation (k=10). The model performances were evaluated using standard statistical indicators: coefficient of determination (R^2), mean absolute error (MAE) and mean square error (RMSE). Among the ensemble techniques tested (Bagging, AdaBoost, Gradient Boosting, Extreme Gradient Boosting), the Bagging model showed the best performance with an R^2 of 0.95, a MAE of 2.05 MPa and a RMSE of 8.26 MPa, indicating very good prediction accuracy [52]. The SHAP analysis revealed that the variables having the most impact on flexural strength are the steel fiber ratio, curing time, superplasticizer amount, water content and active binders (cement, silica fume, quartz). This database thus constitutes a robust foundation for predictive modeling of the mechanical performance of UHSC using artificial intelligence approaches. [52, 53].

Several AI and machine learning models are commonly used in the field of concrete formulation and performance prediction, including: artificial neural networks (RNAs), decision trees, regression algorithms, as well as advanced models such as support vector regression (SVR), random forest, gradient boosting methods, LightGBM, XGBoost, and multi-layer perceptron (MLP). Each model has specific advantages depending on the characteristics of the problem to be solved [50-56]:

- Artificial neural networks (RNAs): particularly effective for modeling complex non-linear relationships between input variables (composition, environmental conditions) and mechanical properties or durability of concrete. Their ability to capture multiple interactions makes them suitable for complex formulations, but they require a large volume of data to avoid overfitting.
- Decision trees and random forest: these models are appreciated for their robustness and ability to manage heterogeneous data, as well as for their relative interpretability compared to neural networks. They are effective in identifying the most influential variables in the formulation and are less sensitive to noise in the data.
- Support Vector Regression (SVR): powerful for regression problems with moderate-sized datasets, SVR offers good generalization and an ability to model non-linear relationships via kernels. It is often used when the data are few but qualitative.

- Gradient Boosting Methods (Gradient Boosting, LightGBM, XGBoost): these ensemble techniques combine several weak models to improve predictive accuracy. They are very efficient in predicting complex properties such as durability or long-term resistance, while providing interpretability tools (e.g. SHAP) that help to understand the contributions of variables.
- Multilayer Perceptron (MLP): a type of simple but powerful neural network, often used for the prediction of mechanical properties when the data structure is not too complex.

In summary, the choice of model depends on the type and quantity of data available, the complexity of the relationships to be modeled, and the importance given to the interpretability of the results. For example, ensemble methods like XGBoost are preferred for their performance and interpretative ability in contexts where precision is crucial. Indeed, among the models tested, XGBoost demonstrated excellent performance with a determination coefficient (R^2) of 0.905 and a mean square error (MSE) of 69.48, thus highlighting its robustness and effectiveness in predicting concrete properties [50-56]. On the other hand, neural networks are better suited to very complex systems, while decision trees facilitate a more intuitive understanding of the factors influencing concrete durability.

4.3. SHAP-Based Interpretability in AI Models for Cementitious Material Performance Prediction

In order to overcome the "black box" nature inherent in many machine learning algorithms especially ensemble methods such as Gradient Boosting or hybrid models of explainable artificial intelligence (XAI) tools like SHAP (Shapley Additive Explanations) have become essential. These tools offer transparency in the model behavior by quantifying the contribution of each input characteristic to a given prediction. SHAP is based on cooperative game theory and assigns each feature an importance value for a particular prediction, in a manner analogous to how Shapley values allocate winnings to players based on their contributions to the total win in a cooperative game. As highlighted by Li et al. [54] in their study on fly ash concrete, the use of SHAP proved effective in identifying the most influential parameters for predicting compressive strength using both simple and hybrid machine learning models. This interpretability is essential not only for validating the robustness of predictive models but also for providing engineering insights that support the optimization of real-world concrete mixture designs. The study confirms that SHAP offers a consistent and mathematically rigorous approach to explaining complex interactions between variables such as fly ash content, water-to-binder ratio, and curing conditions. In particular, the water/binder ratio was found to have a decisive impact: its increase leads to a notable reduction in compressive strength, a finding corroborated by the works of Wang and Yu [56,57]. In another study [55], a SHAP analysis was also performed to interpret the model's predictions regarding flexural strength in ultra-high performance steel fiber reinforced concrete (UHPC). The results highlighted the dominant role of steel fibers, confirming their ability to delay both crack initiation and propagation. A positive contribution of fiber content to strength was observed, but only up to a certain optimal threshold, beyond which excess fiber content leads to saturation or segregation effects, negatively impacting.

Several previous studies have already demonstrated the effectiveness of artificial intelligence (AI) in modeling the mechanical behavior of special concretes, such as those incorporating fly ash or recycled aggregates [58]. The present work is part of this dynamic by highlighting the performance of advanced machine learning (ML) models coupled with an explicable approach (SHAP), not only to accurately predict concrete strength, but also to propose an innovative method, reliable and optimized formulation of mixtures. This method positions itself as an effective alternative to conventional empirical approaches, which are often time-consuming, costly and unreproducible [59-60]. In addition, AI and ML [59-60] contribute to the refinement and efficient optimization of concrete formulation by effectively solving the equation that links material composition, intrinsic properties of the constituents, and environmental conditions, especially under aggressive exposure scenarios: $P = f(C, M, E)$, where:

- P: Target mechanical properties of the final concrete (e.g., compressive or flexural strength)
- C: Concrete composition (e.g., binder content, water-to-cement ratio, additives)

- M: Mechanical and physical characteristics of individual raw materials (e.g., aggregate strength, fiber stiffness, binder reactivity)
- E: Environmental conditions (e.g., curing regime, temperature, chemical exposure)

This formulation reflects the interdependence between the input materials and conditions on the resulting concrete performance. By leveraging machine learning and explainable AI techniques such as SHAP, it becomes possible to model these interactions accurately and improve the formulation process beyond traditional empirical approaches. The integration of AI into construction 4.0 promotes better adaptation of formulations through real-time monitoring systems and the use of massive data.

5. Critical Discussion and Perspectives

The confrontation of data from academic theses, scientific articles and industrial feedback highlights that, despite the considerable advances in concrete technology, several major technological challenges remain. Common formulations struggle to adapt to complex environments such as marine, sulphate or acid environments. In addition to not taking into account the non-linear and dynamic effects related to the simultaneous combination of aggressive factors (temperature, humidity, chloride ions, sulfates, acidity), these formulations often involve rigid manufacturing processes, poorly optimized compositions, and require the addition of mineral additives and high-performance materials, as well as extended validation cycles. These requirements lead to additional costs, increased delays, and complexity of implementation in the field. This is also the case for certain alternatives such as dredging sludge or sediments, which although offering interesting performances on mechanical and environmental levels, pose additional difficulties: lack of performance standards, high characterization costs, high variability of materials, and lack of regulatory framework for their extraction. These barriers reduce the confidence of industrial actors, increase the perception of risk, and slow down their adoption on a large scale.

In this context, AI stands out for its ability to model complex and multivariate relationships, allowing the optimization of concrete formulation and anticipating its behavior in the medium and long term. Its effectiveness, however, depends on the existence of complete, structured and accessible databases. in addition, AI allows for the intelligent exploitation of local resources, by learning the properties of regional materials to precisely adjust dosages and formulate concretes adapted to specific constraints. This synergy between territorial valorization and advanced modeling gives birth to a new generation of concrete, more sustainable, resilient and adapted to aggressive contexts. To achieve these advances, targeted efforts are needed: development of appropriate international standards, creation of open data repositories, training of professionals in AI tools, and strengthening collaboration between engineers, materials researchers, data scientists and policy makers.

6.Conclusion

In conclusion, this study highlights the importance of an integrated approach to design sustainable and effective concretes, especially for structures exposed to aggressive environments such as marine, sulphate or acid environments. By combining the use of alternative materials as additives with AI tools, it becomes possible while optimizing costs and deadlines, to formulate a resistant concrete, ecological and adapted to environmental constraints. The results obtained highlight not only the technical and environmental advantages of these solutions, but also the current limitations in terms of standardization, available data and industrial applicability, which will need to be overcome in future work.

- The integration of alternative materials such as mud, silt, treated sediments, fly ash, ultrafine silica, polymer fibers and nanomaterials (nano-silica, graphene, nanotubes) significantly improve concrete's resistance to chemical and physical aggressions, while contributing to the reduction of CO emissions and the valorization of local waste; in particular, fly ash allows for a decrease in the heat of hydration and an increase in sustainability in sulphated or extreme environments.

- Conventional formulations remain limited by the rigidity of processes, high costs associated with the use of specialized additives, low adaptability to complex environmental conditions, and the lack of technical standards for non-conventional materials.
- Artificial intelligence tools, such as neural networks, SHAP and supervised learning algorithms, have made it possible to reliably predict the long-term performance of concrete and design optimized formulations based on exposure conditions.
- The AI approach allows a fine customization of compositions according to geological, climatic and functional constraints, by integrating multicriteria criteria such as resistance to compression, durability against sulfates or even energy footprint.
- The integration of the Construction 4.0 approach, based on advanced digital modeling and process digitalization, opens new perspectives for the design of smart, resilient and resource-efficient infrastructures.
- Despite the advances presented, several locks still need to be lifted: lack of standardization for alternative materials, absence of open databases, lack of training of actors in AI, and scarcity of large-scale experimental validations.
- The originality of this work lies in the synergy proposed between the exploitation of local resources, the valorization of waste, and the application of artificial intelligence to the formulation of sustainable concrete, an approach still little developed in the literature.
- Future perspectives should be oriented towards a more advanced multicriteria analysis (technical, economic, environmental), the development of structured data repositories, accelerated protocols for sustainability tests, and guidelines for normative integration on an industrial scale.

References

[1] Mehta PK. Durability of Concrete in Marine Environment - A Review. Int Concrete Abstr Portal. 1980;65:Symposium Paper.
[2] Melchers RE. Long-Term Durability of Marine Reinforced Concrete Structures. J Mar Sci Eng. 2020;8(4):290. https://doi.org/10.3390/jmse8040290
[31] Millero FJ. History of the Equation of State of Seawater. Oceanography. 2010;23(3):18-33. https://doi.org/10.5670/oceanog.2010.21
[4] Chouikh N, Janah H, Ouagajjou Y, Aghzar A. First record of Hesione sicula delle Chiaje, 1830 (Polychaeta: Hesionidae) for Mediterranean Moroccan coasts. J Mar Biol Assoc U K. 2024;104(1):e94. https://doi.org/10.1017/S0025315424000912
[5] Connah G. The Mediterranean frontier: North Africa. In: African Civilizations: An Archaeological Perspective. 1st ed. Cambridge: Cambridge University Press; 2015. p. 43-68. https://doi.org/10.1017/CBO9780511997617.004
[6] Neville A. Chloride attack of reinforced concrete: an overview. Mater Struct. 1995;28(2):63-70. https://doi.org/10.1007/BF02473172
[7] Verbeck GJ. Mechanisms of corrosion in concrete. In: Corrosion of Metals in Concrete, SP-49. Detroit: American Concrete Institute; 1975. p. 21-38.
[8] Al-Tayyib AJ, Khan MS, Allam IM, Al-Mana AI. Corrosion behavior of pre-rusted rebars after placement in concrete. Cem Concr Res. 1990;20:955-60. https://doi.org/10.1016/0008-8846(90)90059-7
[9] Torres Martín JE, Rebolledo Ramos N, Chinchón-Payá S, Helices Arcila I, Silva Toledo A, Sánchez Montero J, et al. Durability of a reinforced concrete structure exposed to marine environment at the Málaga dock. Case Stud Constr Mater. 2022;17:e01582. https://doi.org/10.1016/j.cscm.2022.e01582
[10] Otieno M, Ikotun J, Ballim Y. Experimental investigations on the influence of cover depth and concrete quality on time to cover cracking due to carbonation-induced corrosion of steel in RC structures in an urban, inland environment. Constr Build Mater. 2019;198:172-81. https://doi.org/10.1016/j.conbuildmat.2018.11.215
[11] Sohail MG, Salih M, Al Nuaimi N, Kahraman R. Corrosion performance of mild steel and epoxy coated rebar in concrete under simulated harsh environment. Int J Build Pathol Adapt. 2019;37(5):657-78. https://doi.org/10.1108/IJBPA-12-2018-0099
[12] Ortega NF, Moro JM, Meneses R. Corrosion in concrete structures with permanent deformation in marine environment. Open Constr Build Technol J. 2017;11(1):14-24. https://doi.org/10.2174/1874836801711010014
[13] Li Q, Yu H, Ma H, Chen S, Liu S. Test on durability of shield tunnel concrete segment under coupling multi-factors. Open Civil Eng J. 2014;8:451-7. https://doi.org/10.2174/1874149501408010451

[14] Su L, Cai J, Chen Q, Li G, Zhao J. Investigation on the flexural behavior of corroded concrete beams repaired by CFRP sheet under different corrosion levels. Open Civil Eng J. 2016;10:598-614. https://doi.org/10.2174/1874149501610010598
[15] Ting MZY, Yi Y. Durability of cementitious materials in seawater environment: A review on chemical interactions, hardened-state properties and environmental factors. Constr Build Mater. 2023;367:130224. https://doi.org/10.1016/j.conbuildmat.2022.130224
[16] Ketabchi H, Mahmoodzadeh D, Ataie-Ashtiani B, Simmons CT. Sea-level rise impacts on seawater intrusion in coastal aquifers: Review and integration. J Hydrol. 2016;535:235-55. https://doi.org/10.1016/j.jhydrol.2016.01.083
[17] Qu F, Li W, Dong W, Tam VWY, Yu T. Durability deterioration of concrete under marine environment from material to structure: A critical review. J Build Eng. 2021;35:102074. https://doi.org/10.1016/j.jobe.2020.102074
[18] Skalny JP, Marchand J, Odler I. Sulfate attack on concrete. In: Sulfate Attack on Concrete. 1st ed. CRC Press; 2001. p. 1-232. https://doi.org/10.4324/9780203301623
[19] Clifton JR, Frohnsdorff G, Ferraris C. Standards for evaluating the susceptibility of cement-based materials to external sulfate attack. In: Marchand J, Skalny J, editors. Materials Science of Concrete - Special Issue: Sulfate Attack Mechanisms. The American Ceramic Society; 1999. p. 337-56.
[20] Skalny JP, Marchand J, Odler I. Sulfate attack on concrete. In: Sulfate Attack on Concrete. 1st ed. Spon Press (Taylor & Francis Group); 2002. p. 1-232. https://doi.org/10.4324/9780203301623
[21] Shaikh FUA, Supit SWM. Chloride induced corrosion durability of high volume fly ash concretes containing nanoparticles. Constr Build Mater. 2015;99:208-25. https://doi.org/10.1016/j.conbuildmat.2015.09.030
[22] Bendapudi SCK. Contribution of fly ash to the properties of mortar and concrete. Int J Earth Sci Eng. 2011;4(6 SPL):1017-23.
[23] Sun T, Wang X, Ashour A, Ding S, Li L, Han B. High-durability, low-carbon, and low-cost nano-engineered concrete for marine concrete infrastructures. Cem Concr Compos. 2025;157:105877. https://doi.org/10.1016/j.cemconcomp.2024.105877
[24] Patah D, Dasar A, Nurdin A. Sustainable concrete using seawater, sea-sand, and ultrafine palm oil fuel ash: Mechanical properties and durability. Case Stud Constr Mater. 2025;22:e04129. https://doi.org/10.1016/j.cscm.2024.e04129
[25] Xiao J, Qiang C, Nanni A, Zhang K. Use of sea-sand and seawater in concrete construction: Current status and future opportunities. Constr Build Mater. 2017;155:1101-11. https://doi.org/10.1016/j.conbuildmat.2017.08.130
[26] Dhondy T, Remennikov A, Shiekh MN. Benefits of using sea sand and seawater in concrete: a comprehensive review. Aust J Struct Eng. 2019;20(4):280-9. https://doi.org/10.1080/13287982.2019.1659213
[27] Binici H, Aksogan O. Durability of concrete made with natural granular granite, silica sand and powders of waste marble and basalt as fine aggregate. J Build Eng. 2019;19:109-21. https://doi.org/10.1016/j.jobe.2018.04.022
[28] Singh M, Choudhary K. A study on environmental and economic impacts of using waste marble powder in concrete. J Build Eng. 2017;13:87-95. https://doi.org/10.1016/j.jobe.2017.07.009
[29] Binici H, Aksogan O, Kaplan H, Gorur EB, Bodur MN. Performance of ground blast furnace slag (GBS) and ground basaltic pumice (GBP) concrete against seawater attack. Constr Build Mater. 2008;22:1515-26. https://doi.org/10.1016/j.conbuildmat.2007.03.024
[30] Lv J, Cao Z, Hu X. Effect of biological coating (Crassostrea gigas) on marine concrete: Enhanced durability and mechanisms. Constr Build Mater. 2021;285:122914. https://doi.org/10.1016/j.conbuildmat.2021.122914
[31] Cai R, Han T, Liao W, Huang J, Li D, Kumar A, Ma H. Prediction of surface chloride concentration of marine concrete using ensemble machine learning. Cem Concr Res. 2020;136:106164. https://doi.org/10.1016/j.cemconres.2020.106164
[32] Simčič T, Pejovnik S, De Schutter G, Bokan Bosiljkov V. Chloride ion penetration into fly ash modified concrete during wetting-drying cycles. Constr Build Mater. 2015;93:1216-23. https://doi.org/10.1016/j.conbuildmat.2015.04.033
[33] Gao J, Liu C, Yang H, Wang Y, Zhang Z. Durability of concrete exposed to sulfate attack under flexural loading and drying-wetting cycles. Constr Build Mater. 2013;39:33-8. https://doi.org/10.1016/j.conbuildmat.2012.05.033
[34] Zhou Q, Lu C, Wang W, Wei S, Lu C, Hao M. Effect of fly ash and sustained uniaxial compressive loading on chloride diffusion in concrete. J Build Eng. 2020;32:101394. https://doi.org/10.1016/j.jobe.2020.101394

[35] Hamada HM, Abed F, Katman HYB, Humada AM, Al Jawahery MS, Majdi A, et al. Effect of silica fume on the properties of sustainable cement concrete. J Mater Res Technol. 2023;24:8887-908. https://doi.org/10.1016/j.jmrt.2023.05.147
[36] Ben Allal L, Ammari M, Frar I, Azmani A, Belmokhtar NE. Characterization and valorization of dredging sediments ports of Tangier and Larache (Morocco). Rev Paralia. 2011;4:5.1-13. https://doi.org/10.5150/revue-paralia.2011.005
[37] Bortali M, Raboutli M, Yessari M, Hajjaji A. Characterizing harbor dredged sediment for sustainable reuse as construction material. Sustainability. 2023;15(3):1834. https://doi.org/10.3390/su15031834
[38] Suiffi H, El Maliki A, Majid F, Cherkaoui O. The effect of using polypropylene fibers on the durability and fire resistance of concrete. Fract Struct Integr. 2021;15(58):296-307. https://doi.org/10.3221/IGF-ESIS.58.22
[39] Aqil M, Bahi L, Ouadif L, Amgaad S, Bouajaj A. The impact of the addition of plastic additives, polypropylene fibers and specimen shape on drying shrinkage and mass loss of high-performance sand concrete. Int J Civ Eng Technol. 2018;13(9):1617-32.
[40] Aqil M, Bahi L, Ouadif L, Amgaad S, Bouajaj A. Workability and durability of sand concrete based on cementitious matrix and plastic additives. Int J Civ Eng Technol. 2018;6(9):1617-32.
[41] Aqil M, Bahi L, Ouadif L, Belhaj S, Edderkaoui R. The influence of curing temperature, plastic additives and polypropylene fibers on the mechanical behaviour of cementitious materials. E3S Web Conf. 2020;150:02012. https://doi.org/10.1051/e3sconf/202015002012
[42] Kou S, Lee G, Poon C, Lai W. Properties of lightweight aggregate concrete prepared with PVC granules derived from scraped PVC pipes. Waste Manag. 2009;29(2):621-8. https://doi.org/10.1016/j.wasman.2008.06.014
[43] Xu J, Zhao X, Yu Y, Xie T, Yang G, Xue J. Parametric sensitivity analysis and modelling of mechanical properties of normal- and high-strength recycled aggregate concrete using grey theory, multiple nonlinear regression and artificial neural networks. Constr Build Mater. 2019;211:479-91. https://doi.org/10.1016/j.conbuildmat.2019.03.234
[44] Gamil Y. Machine learning in concrete technology: A review of current researches, trends, and applications. Front Built Environ. 2023;9:1145591. https://doi.org/10.3389/fbuil.2023.1145591
[45] El Kbiach MB, Bounab L, Tahiri A, Ezbakhe H, et al. An E-learning labs platform for Moroccan universities. In: Innovations in Smart Cities and Applications. Springer; 2018. p. 687–696. https://doi.org/10.1007/978-3-319-74500-8_63
[46] Nikoopayan Tak MS, Feng Y, Mahgoub M. Advanced machine learning techniques for predicting concrete compressive strength. Infrastructures. 2025;10(2):26. https://doi.org/10.3390/infrastructures10020026
[47] Li Z, Yoon J, Zhang R, et al. Machine learning in concrete science: applications, challenges, and best practices. NPJ Comput Mater. 2022;8:127. https://doi.org/10.1038/s41524-022-00810-x
[48] Alghrairi NS, Aziz FN, Rashid SA, Mohamed MZ, Ibrahim AM. Machine learning-based compressive strength estimation in nanomaterial-modified lightweight concrete. Eng. 2024; 14: 20220604. https://doi.org/10.1515/eng-2022-0604
[49] Abuodeh OR, Abdalla JA, Hawileh RA. Assessment of compressive strength of ultra-high performance concrete using deep machine learning techniques. Appl Soft Comput. 2020;95:106552. https://doi.org/10.1016/j.asoc.2020.106552
[50] Ahmad A, Ostrowski KA, Maślak M, Farooq F, Mehmood I, Nafees A. Comparative study of supervised machine learning algorithms for predicting the compressive strength of concrete at high temperature. Materials. 2021;14(15):4222. https://doi.org/10.3390/ma14154222
[51] Young BA, Hall A, Pilon L, Gupta P, Sant G. Can the compressive strength of concrete be estimated from knowledge of the mixture proportions? New insights from statistical analysis and machine learning methods. Cem Concr Res. 2019;115:379-88. https://doi.org/10.1016/j.cemconres.2018.09.006
[52] Wang Q, Hussain A, Farooqi MU, Deifalla AF. Artificial intelligence-based estimation of ultra-high-strength concrete's flexural property. Case Stud Constr Mater. 2022;17:e01243. https://doi.org/10.1016/j.cscm.2022.e01243
[53] Ben Chaabene W, Flah M, Nehdi ML. Machine learning prediction of mechanical properties of concrete: Critical review. Constr Build Mater. 2020;260:119889. https://doi.org/10.1016/j.conbuildmat.2020.119889
[54] Li H, Chung H, Li Z, Li W. Compressive strength prediction of fly ash based concrete using single and hybrid machine learning models. Buildings. 2024;14(10):3299. https://doi.org/10.3390/buildings14103299
[55] Khan K, Ahmad W, Amin MN, Ahmad A, Nazar S, Alabdullah AA. Compressive strength estimation of steel-fiber-reinforced concrete and raw material interactions using advanced algorithms. Polymers. 2022;14(15):3065. https://doi.org/10.3390/polym14153065

[56] Sekhar NS, Raghunath PN. Influence of water binder ratio on high performance concrete. Open Constr Build Technol J. 2014;8(1):18-21. https://doi.org/10.2174/1874836801408010018
[57] Yu R, Spiesz P, Brouwers HJH. Mix design and properties assessment of ultra-high performance fibre reinforced concrete (UHPFRC). Cem Concr Res. 2014;56:29-39. https://doi.org/10.1016/j.cemconres.2013.11.002
[58] Li H, Chung H, Li Z, Li W. Compressive strength prediction of fly ash-based concrete using single and hybrid machine learning models. Buildings. 2024;14(10):3299. https://doi.org/10.3390/buildings14103299
[59] Bhuva P, Bhogayata A. A review on the application of artificial intelligence in the mix design optimization and development of self-compacting concrete. Mater Today Proc. 2022;65(1):603-608. https://doi.org/10.1016/j.matpr.2022.03.194
[60] Chen B, Wang L, Feng Z, Liu Y, Wu X, Qin Y, Xia L. Optimization of high-performance concrete mix ratio design using machine learning. Eng Appl Artif Intell. 2023;122(C):106047. https://doi.org/10.1016/j.engappai.2023.106047

Research on Engineering Structures & Materials
www.jresm.org

Research Article

Comparing mechanical properties of concrete with recycled aggregates using different mixing methods

K. Pushpa [*1, a], S. Jayakumar [1, b], N. Pannirselvam [2, c]

[1]*Department of Civil Engineering, Sri Manakula Vinayagar Engineering College, Pondicherry University, Puducherry, India*
[2]*Department of Civil Engineering, College of Engineering and Technology, SRM Institute of Science and Technology, Kattankulathur, Tamil Nadu, India*

Article Info

Article History:

Received 09 July 2025

Accepted 04 Aug 2025

Keywords:

Construction and demolition waste;
Recycled aggregate;
Recycled aggregate concrete;
Mixing methods;
Sustainable concrete;
Two-stage mixing approach

Abstract

This study addresses the growing use of recycled coarse aggregate (RA) from construction and demolition waste (CDW) as a sustainable alternative in concrete production. It evaluates the influence of varying RA by 0%, 25%, 50%, 75% and 100% by natural coarse aggregate (NA) on the mechanical properties of M20 grade concrete. Additionally, the study compares four mixing methods: Normal Mixing Approach (NMA), Treated Aggregate Mixing Approach (TAMA), Two-Stage Mixing Approach (TSMA), and Mortar Mixing Approach (MMA). Results reveal that increasing RA content reduces the workability and strength of recycled aggregate concrete (RAC). The performance in workability, compressive strength, splitting tensile strength, and flexural strength of RAC by four mixing methods was compared. Among them, TSMA showed significant improvement of 27.27, 15.55, 9.3, and 12.22% compared to NMA for a 100% RA mix. TSMA enhances these properties by promoting better mortar coverage around aggregate particles, reducing pores and strengthening the interfacial transition zone. This study highlights that optimizing mixing techniques can improve RAC's performance, making it an environmentally responsible option for the construction industry.

© 2025 MIM Research Group. All rights reserved.

1. Introduction

India's rapid urbanization and infrastructure development, including construction, renovation, reconstruction, and highway expansion projects, significantly added to construction and demolition waste (CDW). As per the Centre for Science and Environment analysis, India produces approximately 150 million tons of CDW annually, yet only 1.3% of this waste is recycled [1, 2]. Most CDW is indiscriminately dumped in landfills, along roadsides, or in vacant plots, leading to environmental, ecological, and logistical challenges. These non-biodegradable materials occupy considerable space, pollute land, and cause long-term environmental degradation.

The construction sector's high demand for coarse aggregates, combined with the exhaustion of resources from natural and increased carbon dioxide emissions from producing virgin aggregates, underscores the need for sustainable alternatives. Recycled aggregates (RA), derived from CDW, offer a worthwhile solution by meeting the demand for coarse aggregates, preserving natural resources, reducing waste, and mitigating environmental pollution. Moreover, utilizing RA in construction promotes circular economy principles, which aim to reduce waste and encourage the continual use of resources, thereby aiding in achieving sustainability goals [3].

Despite these advantages, the adoption of RA in India faces several barriers, including insufficient CDW recycling facilities, high labour costs associated with segregation and processing, the absence

*Corresponding author: pushpajg@yahoo.com
[a]orcid.org/0009-0000-3268-8493 ; [b]orcid.org/0000-0003-3435-4301; [c]orcid.org/0000-0003-0776-0662
DOI: http://dx.doi.org/10.17515/resm2025-1018me0709rs
Res. Eng. Struct. Mat. Vol. 11 Iss. 4 (2025) 1833-1845

of standardized guidelines for recycled aggregates, and limited awareness among stakeholders [2]. Recycling CDW for use as aggregates in the construction sector presents a practical approach to reducing waste volumes and environmental impacts. The production of raw construction materials accounts for 80–90% of CO_2 emissions. In comparison, alternative materials like RA can reduce these emissions by up to 90%, offering a hopeful prospect for the environmental benefits of sustainable construction [4]. However, compared to regular concrete created from natural aggregates (NA), recycled aggregate concrete (RAC) is typically of lower quality, which increases the vulnerability of such structures [5]. The adhered hydrated cement on the surface of RA reduces its specific gravity, decreases its modulus of elasticity, and increases its porosity compared to NA, as demonstrated in various studies [6–8]. The heterogeneous nature of RA, adhered cement content, exposure conditions, crushing operations, and rheology further contribute to RAC's variability [3, 7–9]. Improving the quality of RA is vital for widespread applications of RAC [10, 11]. Among these quality enhancement methods, proper mixing techniques play a critical role in improving RAC properties and often offer an efficient option by reducing cost, time and energy consumption. This study specifically examines the impact of different mixing methods on optimizing the performance of RAC.

2. Literature Review

The use of RA in construction is a sustainable alternative and cost-effective than NA [4, 6, 12–14]. However, challenges such as reduced workability, mechanical performance and variability in the properties of RAC necessitate quality improvement measures [15]. Researchers have used several strategies to enhance RA quality and to optimize RAC performance. One widely adopted method for improving RA quality involves mechanical treatment, such as removing adhered cement content through abrasion techniques comparable to the Los Angeles abrasion method [16, 17]. Though effective, this process is energy-intensive and often results in surface cracks on the RA. Chemical treatment methods have also been investigated in previous research by presoaking RA in various acids, lime water, and sodium silicate to remove porous hydrated cement layers [18–22]. However, the disposal of used presoaking materials also causes environmental issues. Other innovative techniques utilized for enhancing RA include accelerated carbonation [23], incorporation of fine supplementary cementitious materials [6, 16, 24–27], and the use of admixtures or superplasticizers to reduce the water-cement ratio [10, 23]. Surface treatments, such as coating RA with cement slurry, have demonstrated improved micro-crack sealing and interfacial transition zone (ITZ) strength [22]. Additionally, using discrete fibres in RAC has been shown to improve ductility, toughness, and impact resistance while mitigating shrinkage cracking [28–31].

Experimental studies have focused on various aspects of RAC performance, including mechanical and durability properties [12, 14, 16, 32–34], shear strength [35, 36], leaching behavior [13], precast applications [37], and long-term deflection behavior [37]. These investigations underscore the potential of RA to meet construction standards when its quality is sufficiently improved. Among the quality enhancement methods, appropriate mixing techniques play a pivotal role in enhancing RAC properties [38–42]. These techniques not only improve the quality of RAC but also reduce costs, time, and energy consumption, making them an efficient choice for construction. Premixing techniques coat micro-cracks and pores on RA surfaces, stiffen aggregates, and improve ITZ, enhancing RAC performance [4, 38, 43, 44]. Although many methods to strengthen RA quality have been investigated in the literature, there are limited studies on the comprehensive and comparative effects of different mixing techniques on various mechanical properties (workability, compressive, splitting tensile and flexural strength) of RAC, especially evaluating these four methods (NMA, TAMA, MMA, and TSMA) together. This study aims to fill this gap and investigate the efficacy of different mixing processes as a quality enhancement method for concrete. Specifically, the effects of four distinct mixing techniques, Normal Mixing Approach (NMA), Treated Aggregate Mixing Approach (TAMA), Mortar Mixing Approach (MMA), and Two-Stage Mixing Approach (TSMA), on RAC's workability, compressive, splitting tensile, and flexural strength were analyzed. The goal was to identify an economical and sustainable approach to utilizing recycled aggregates derived from CDW.

3. Experimental Program

3.1. Materials and Their Properties

Portland Pozzolana Cement (PPC), which is fly ash-based and adheres to the Indian Standard IS: 1489-1 (1991) [45], was used as the binder for all mixes. The PPC has a specific gravity of 3.09, a normal consistency of 34%, and setting times of 42 minutes (initial) and 370 minutes (final) as shown in Table 1. Locally manufactured sand (M-Sand) served as the fine aggregate. It possesses a specific gravity of 2.46, a fineness modulus of 3.37, and falls within Zone II according to IS: 383-2016 [46]. Crushed granite rock with a nominal size of 20mm was sourced from local markets to function as the NA. This material exhibits a specific gravity of 2.68, water absorption of 0.75 % and a fineness modulus of 7.11. We collected CDW from nearby construction sites and landfills. The CDW was manually broken down, sieved, and segregated into coarse aggregates before use. The RA has a nominal size of 20mm, a specific gravity of 2.63, a water absorption of 4.44 %, and a fineness modulus of 7.01. IS: 2386-1963[47] guidelines were followed in conducting physical tests on aggregates. Table 1 enumerates the properties of the aggregates used.

Table 1. Physical properties of the constituents

Constituents	Materials Used	Specific Gravity	Consistency (%)	Water Absorption (%)	Setting Time (minutes)		Fineness Modulus
					Initial	Final	
Binder	PPC Cement	3.09	34	-	42	370	-
Fine Aggregate	M-Sand	2.46	-	0.93	-	-	3.37
Natural Aggregate	Crushed Gravel	2.68	-	0.75	-	-	7.11
Recycled Aggregate	Construction and demolition waste	2.63	-	4.44	-	-	7.01

3.2 Concrete Mix Proportion, Sample Preparation and Testing

Mix proportioning for the control concrete using NA for M20 grade concrete was prepared according to IS: 10262 (2019) [48], with a water-cement ratio of 0.5, and designated as NAC. The target compressive strength for this mix was 26.60 MPa. For the RAC, the natural coarse aggregate in the control mix was volumetrically replaced by 25, 50, 75, and 100% with RA. These mixes were designated 25RAC, 50RAC, 75RAC, and 100RAC, respectively. The mix proportion is given in Table 2.

Table 2. Mix proportions for M20 grade concrete

Mix Designation	Cement [kg/m^3]	M-Sand [kg/m^3]	RA Replacement [%]	NA [kg/m^3]	RA [kg/m^3]	Water [litres/m^3]
NAC	396	621	0	1169	0	198
25RAC	396	621	25	876.75	270.50	198
50RAC	396	621	50	584.50	541.00	198
75RAC	396	621	75	292.25	811.50	198
100RAC	396	621	100	0	1082	198

Workability of fresh concrete was assessed using slump cone tests, following IS: 456 (2000) [49] as in Fig. 1(a). The mixed concrete was arranged in roughly three layers within oiled cast iron moulds and compacted on a vibrating table. Three 150 mm cubes were fabricated for each mix type to test compressive strength using a 2000 kN compression testing machine (CTM) in Fig.1(b) of the model number AIM 317-E-DG-1. Furthermore, three cylinders with a diameter of 100 mm and a height of 200 mm for each mix type were cast to assess splitting tensile strength, as outlined in IS: 516 (2021) [50] using CTM as illustrated in Fig.2(c). Additionally, three prisms measuring 100 x 100 x 500 mm for each mix type were cast to assess flexural strength, utilizing a flexure

testing machine with 3-point loading of model number AIM331, following the guidelines of IS: 516 (2021) as in Fig. 2(d). Casted samples as in Fig. 1(a) were kept undisturbed for 24 hours, then demoulded, labelled, and immersed in a water-filled curing tank shown in Fig.1(b), at a nominal temperature of 30 °C and 60% relative humidity for 28 days.

(a) (b)

Fig. 1. (a)Casted samples and (b) Curing of samples in the curing tank

(a) (b) (c) (d)

Fig. 2. (a) Slump Cone Test (b) Compression Test (c) Splitting Tensile Test (d)Flexure Test

3.3 Mixing Methods

This study investigated four mixing techniques, namely: Normal Mixing Approach (NMA), Treated Aggregate Mixing Approach (TAMA), Mortar Mixing Approach (MMA), and Two-Stage Mixing Approach (TSMA), and their impact on the mechanical properties of RAC was evaluated [38–40, 42–44]. Five mixes of RAC were prepared for each mixing approach by substituting NA with RA at replacement levels of 0, 25, 50, 75, and 100% by volume. The mechanical strength of these samples was assessed after curing for 28 days. Schematic illustrations of each mixing method are presented in Figs. 3, 5, 6.

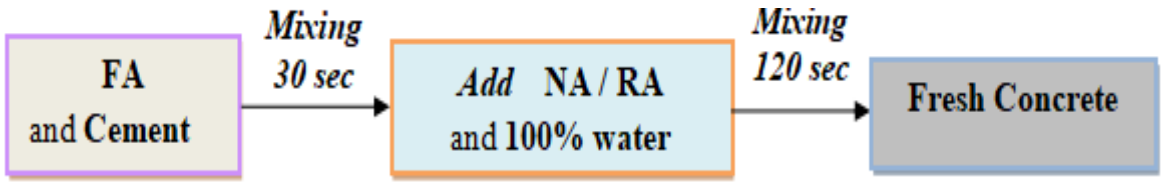

Fig. 3. Schematic illustration of NMA - Normal Mixing Approach [40]

In the NMA, fine aggregate (FA) and cement were added to the pan mixer and rotated for 30 seconds in a dry state. Subsequently, measured quantities of coarse aggregates NA and RA were added along

with the total amount of water, and the mixture was rotated for 120 seconds [38–40, 43], as illustrated in Figs. 3. In TAMA, treated aggregate (TA) is used instead of RA. The required quantity of RA was soaked for 24 hours in the cement slurry prepared by mixing 50% of the calculated cement content with water, as in Fig. 4(a). The soaked RA with cement coating was dried until a surface-dried aggregate coated with a cement layer was formed. TA, the surface-dried recycled aggregate, shown in Fig. 4(b), was used in casting concrete samples in the TAMA method following the mixing process similar to NMA as given in Fig. 3.

(a) (b)

Fig.4. (a) RA soaked in cement slurry and (b) Surface-dried RA (Treated Aggregates)

In MMA, cement and FA were dry mixed, and 75% of the total water was mixed thoroughly for 90 seconds. Subsequently, RA and NA were added with the remaining 25% water and mixed for 90 seconds [39]. This method is shown in Fig. 5. The TSMA, introduced by Tam et al. [40], splits the mixing process into two phases. In the first phase, only half the water is added; the remaining water is incorporated during the second phase. This method has significantly improved RAC strength, particularly at replacement ratios of up to 25% RA after 28 days of curing. Further enhancements have been achieved by incorporating silica fume or a cement-silica fume blend within the TSMA process [42]. The TSMA process is illustrated in Fig. 6.

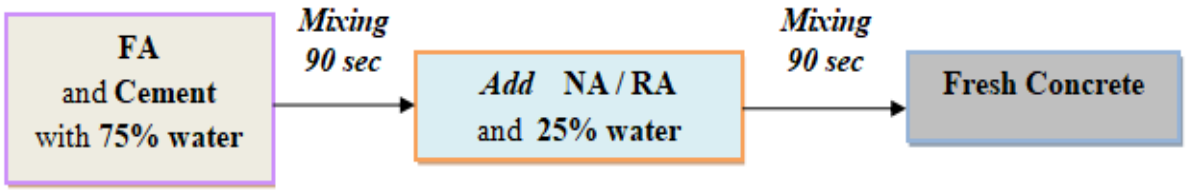

Fig. 5. Schematic illustration of MMA -Mortar Mixing Approach [39]

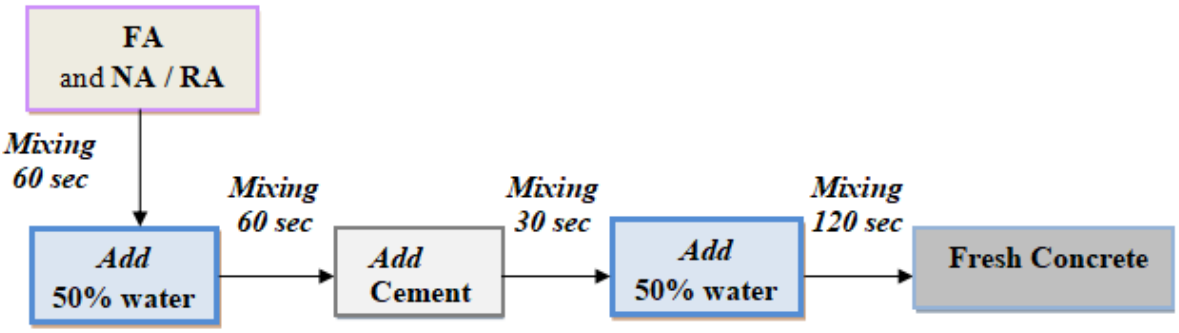

Fig. 6. Schematic illustration of TSMA - Two Stage Mixing Approach [40]

In NMA and TAMA, the total water required for mixing is added in a single stage along with all other ingredients in the mixer pan before rotation, as in Fig. 3. In contrast, in MMA and TSMA mixing processes, the required quantity of water is split proportionally into two parts and is added at different timings, as illustrated in Fig 5, 6.

4. Results and Discussions

4.1 Workability

A graphical plot of the average value of three trials in each mixture composition for slump results with different replacement levels of RA using NMA, TAMA, MMA, and TSMA is presented in Fig. 7. The concrete mix was designed to achieve a slump of 100 mm for M20-grade concrete as specified in IS 10262 (2019)[48]. For the control mix, NAC, mean slump values were 87mm, 93mm, 94mm, and 99 mm for NMA, TAMA, MMA, and TSMA, respectively. At a 25% RA replacement level, the average values of the slump test were 84mm, 87mm, 88mm, and 94mm for NMA, TAMA, MMA, and TSMA, respectively. The average slump values of 44mm, 49mm, 51mm, and 56mm for NMA, TAMA, MMA, and TSMA were observed for a 100% RA replacement level, and it was the lowest among all the mix types. These findings align with similar research reports [39, 51–53]. The decrease in workability is attributed to the presence of hydrated mortar adhered to the surface of RA, which exhibits a higher water absorption of 4.44% compared to 0.75% in NA, as shown in Table 1. This study's increasing order of mean slump values is NMA< TAMA<MMA< TSMA. Thus, it is evident that TSMA is more suitable than all other mixing methods for enhancing fresh concrete's workability.

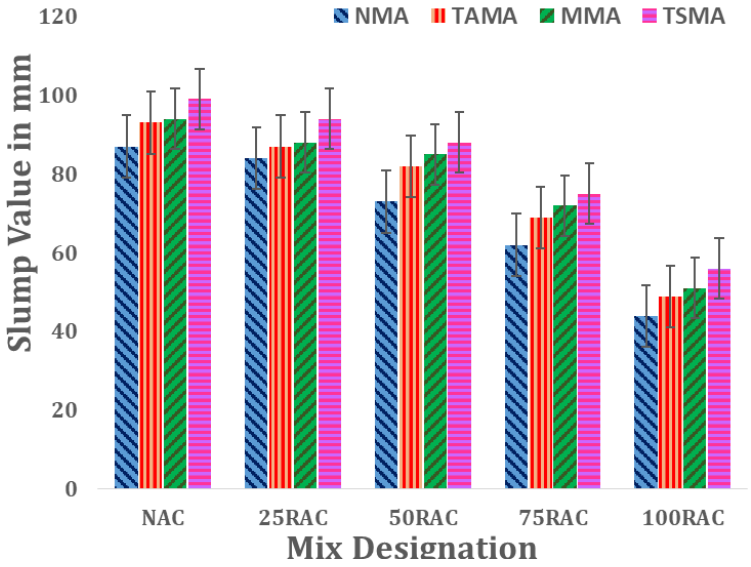

Fig. 7. Slump values in mm for four mixing approaches

4.2 Compressive Strength

This investigation involved conducting a compressive strength test on three 150mm concrete cubes for each mix after 28 days of curing as per IS: 516-2021[50]. The concrete compressive strength consistently diminished as the percentage of RA increased at replacement levels of NA. Previous researchers noted the same pattern in the results [40, 41, 43, 54–56]. The relationship between RA and ITZ significantly influences the compressive strength of RAC. The compressive strength primarily relies on the interconnections between cement paste and aggregate [39, 40].

The average compressive strength values of three samples tested after 28 days of curing ranged from 26.47 MPa to 17.17 MPa for NMA, 27.43 MPa to 17.62 MPa for TAMA, 27.86 MPa to 18.43 MPa for MMA, and 28.55 MPa to 19.84 MPa for TSMA, across varying RA replacement levels from 0% to 100%. Average values of 28-day compressive strength for various mixing approaches is represented in Fig. 8. Failure pattern of 100% RA cube samples for various mixing approaches is shown in Fig. 9. A 15.55 % improvement in compressive strength was observed for 100% RAC

using TSMA compared to increments of 2.62% and 7.34% observed in TAMA and MMA, respectively, relative to NMA. These findings align with similar trends described by other investigators [54, 55]. This study found TSMA to be more effective than other methods. The observed average compressive strength of 25% RA was 25.45 MPa (NMA), 26.58 MPa (TAMA), 26.95 MPa (MMA), and 27.25 MPa (TSMA). Among these, TAMA (26.58 MPa), MMA (26.95 MPa), and TSMA (27.25 MPa) values were agreeable with the M20 grade concrete target strength of 26.60 MPa.

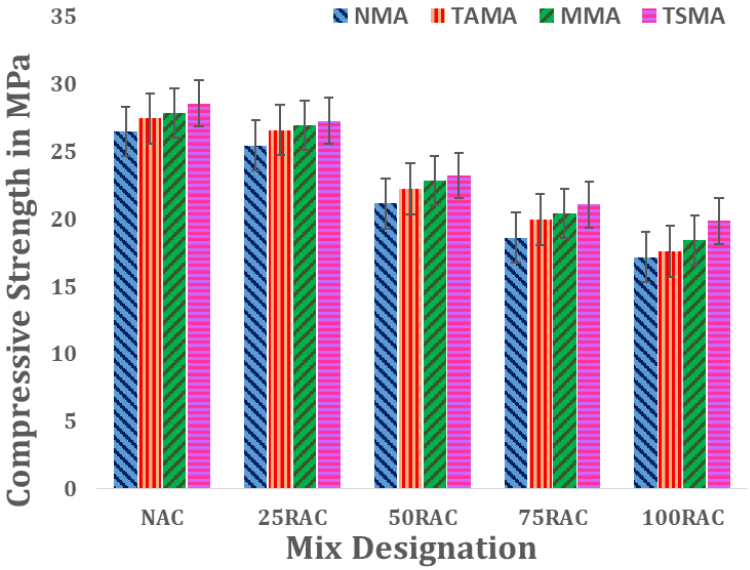

Fig. 8. Compressive strength of concrete for various mixing approaches

(a) (b) (c) (d)

Fig. 9. Damaged cube samples of 100 % RA mix for various mixing approaches(a) NMA (b) TAMA (c) MMA and (d) TSMA

4.3 Splitting Tensile Strength

The splitting tensile strength of concrete outlined in IS: 516-2021[50] was conducted on a cylinder sample with a diameter of 100 mm and height of 200 mm. Fig. 10 shows the graph of 28-day average splitting tensile strength of three cylinders for each concrete mix, where NA was replaced with RA by 0%, 25%, 50%, 75%, and 100% and by using four different mixing procedures, namely NMA, TAMA, MMA and TSMA. The average splitting tensile strength values ranged from 3.13 MPa to 2.15 MPa for NMA, 3.24MPa to 2.23 MPa for TAMA, 3.29MPa to 2.28 MPa for MMA, and 3.32 MPa to 2.35 MPa for TSMA. Fig.12 shows the damaged cylinder sample of 100% RA mix using the TSMA method. Among the four mixing approaches, TSMA showed the maximum improvement, ranging from 6.07% to 12.35%, followed by MMA with an increase of 4.97% to 9.56% and TAMA with a rise of 2.32% to 4.38%, compared to the NMA mixing approach. Based on the experimental results, TSMA and MMA were more effective than TAMA and NMA. The splitting tensile strength values

diminished as the replacement level of RA increased across all mixing procedures, as noted by several previous researchers [41, 43, 54, 55].

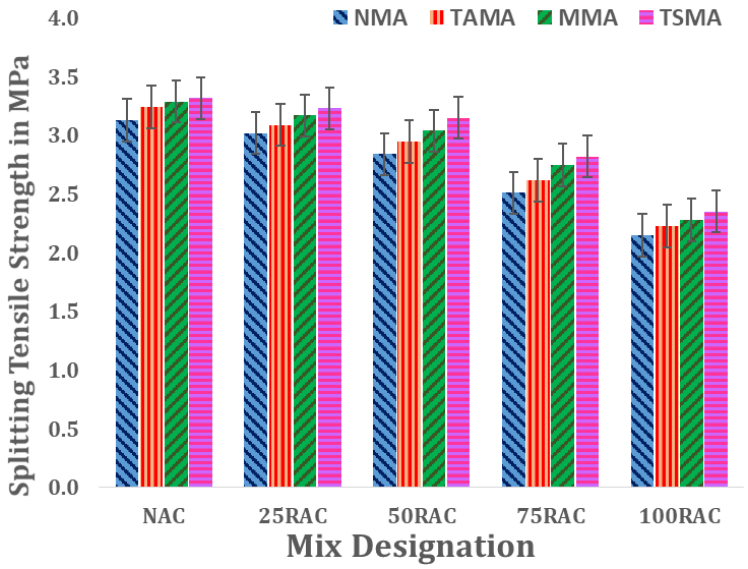

Fig. 10. Splitting tensile strength of concrete for various mixing approaches

4.4 Flexural Strength

The current study tested flexural strength on concrete beams measuring 100 mm x 100 mm x 500 mm, adhering to the guidelines outlined in IS: 516- 2021 [50]. Fig. 11 shows the variation in average flexural strength of three prism samples for 28 days of curing, with varying contents of RA and different mixing methods. Failure pattern of 100RAC beam samples using various mixing methods is shown in Fig.13. The flexural strength of RAC was observed to be lower than that of the control mix. This reduction is because of the poor quality of the adhering cement paste and the feeble interfacial bond between the old and new cement paste, as documented by prior researchers [53, 55, 56]. The mean flexural strength values ranged from 3.34 to 2.21 MPa for NMA, 3.47 to 2.25 MPa for TAMA, 3.52 to 2.32 MPa for MMA, and 3.75 to 2.48 MPa for TSMA. A 12.22 % improvement in flexural strength was observed for 100% RAC using TSMA compared to increments of 1.81% and 4.98% observed in TAMA and MMA, respectively, relative to NMA. Among all the mixing methods, the highest flexural strength was observed with the TSMA method, while the lowest was with the NMA method.

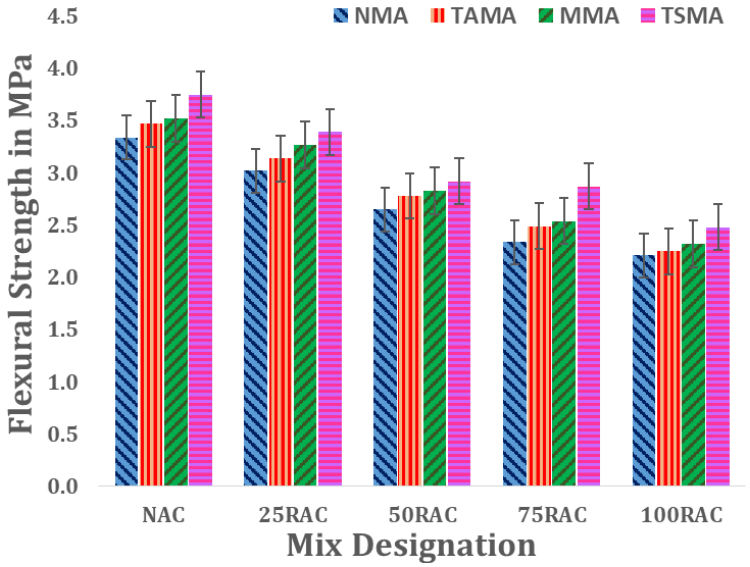

Fig. 11. Flexural strength of concrete for various mixing approaches

Fig. 12. Damaged NMA 100% RA cylinder

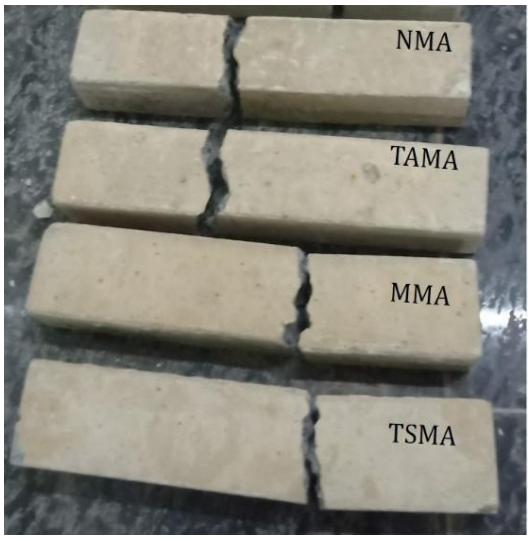

Fig. 13. Damaged 100% RA beam samples

4.5 Microscopic Analysis

Scanning Electron Microscopy (SEM) analysis was carried out for the control concrete, NAC with natural aggregate and 100RAC with recycled aggregate prepared by using TSMA mixing method at The Sophisticated Analytical Instruments Facility (SAIF) in IIT Madras, India, using FEI-Quanta FEG 200F, a versatile high resolution Scanning Electron Microscope to get a precise and accurate details. SEM analysis of Fig.14 (a, b) reveals that concrete with 100% RA exhibits a more porous, less dense and disconnected microstructure than NAC. The loose C-S-H gel, larger ettringite crystals and increased pore density of 100RAC indicate a weaker microstructure responsible for the reduced workability and mechanical strength. Despite this, both NAC and 100RAC still show active hydration, suggesting that performance has improved due to excess water for hydration in the TSMA mixing method as indicated by Tam et.al [40, 42].

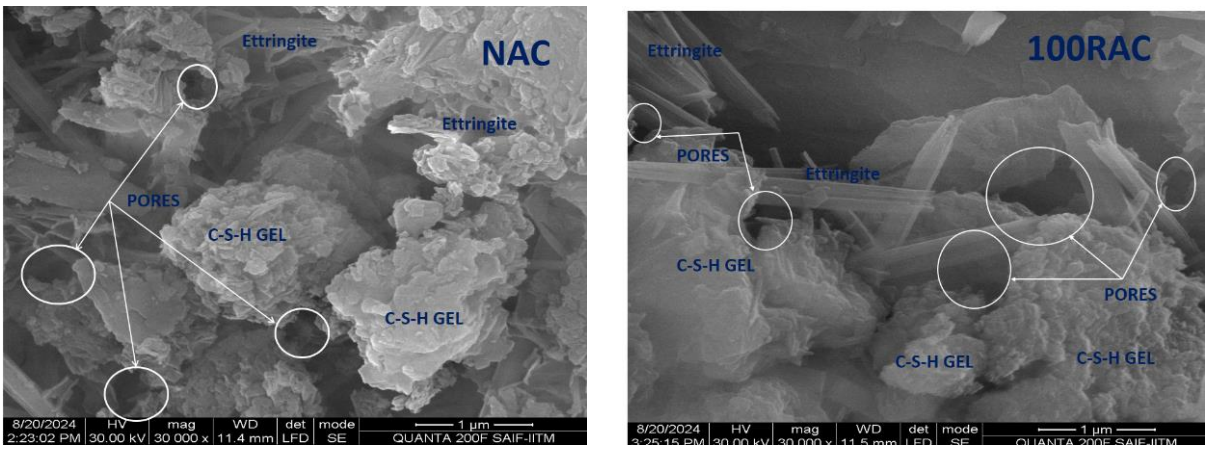

(a) (b)

Fig. 14. SEM image of (a) NAC and (b) 100% RA samples using TSMA

The adhered cement mortar at the ITZ of RA forms the weak portion in RAC. It is composed of many minute pores and cracks, which affect the ultimate strength of the RAC. These pores and cracks consume more water, reducing the water required for hydration at the ITZ of RAC. In TSMA, half the water added in the first stage creates a thin cement slurry that coats the recycled aggregates. This slurry penetrates the pores and cracks of the old mortar on the aggregates, filling them up. The remaining water is added in the second stage, which helps to complete the concrete mixing process. This process improves the bond between the recycled aggregate and the new cement paste, resulting in a stronger and more durable interfacial transition zone (ITZ) [40, 54, 55].

5. Conclusions

This investigation involved the preparation of five concrete mixtures by replacing NA with RA at volumetric substitution levels of 0, 25, 50, 75, and 100%. Four distinct mixing methodologies, specifically Normal Mixing Approach (NMA), Treated Aggregate Mixing Approach (TAMA), Mortar Mixing Approach (MMA), and Two-Stage Mixing Approach (TSMA), were utilised to ascertain the optimal replacement ratio of RA and the most appropriate mixing technique.

- The specific gravity and fineness modulus of RA were lower than those of NA; however, the water absorption of RA was higher. The presence of adhering cement on the surface of RA led to increased porosity and a compromised ITZ, reducing workability and mechanical properties in RA relative to NA.
- Workability, measured in terms of slump value, decreased with increasing levels of RA substitution across all concrete mixes. Maximum reduction was observed for 100% RA substitution. The higher water absorption property of RA is likely responsible for this decrease. Among the mixing methods, TSMA yielded the highest slump values, ranging from 99 mm to 56 mm for different RA mixes, followed by MMA, TAMA and NMA. The observed slump of 94 mm in TSMA for 25% RA substitution is closer to the designed slump value of 100mm.
- Compressive strength of the mixes reduced with an increment in the replacement levels of RA. For 25% RA substitution, compressive strengths were 25.45, 26.58, 26.95, and 27.25 MPa for NMA, TAMA, MMA and TSMA, respectively. The TAMA, MMA, and TSMA values were consistent with the target strength of 26.60 MPa for M20 grade concrete. TSMA and MMA showed improvements of 7.07% and 5.89% over NMA.
- Splitting tensile strength ranged from 2.15 MPa to 3.32 MPa and decreased with increasing RA replacement levels across all the mix types. For 25% RA substitution, splitting tensile strengths were 3.02 MPa (NMA), 3.09 MPa (TAMA), 3.17 MPa (MMA), and 3.23 MPa (TSMA).
- Flexural strength also decreased with increasing levels of RA substitution across all mix types using various mixing methods. Values ranged from 2.21 MPa to 3.75 MPa. Flexural strength values for 25% RA substitution were 3.02 MPa, 3.14 MPa, 3.27 MPa, and 3.39 MPa for NMA, TAMA, MMA and TSMA, respectively. Among these methods, TSMA yielded the highest flexural strength value (12.25%), followed by MMA (8.28%), concerning NMA.

Based on the above observations, it can be concluded that NA can be replaced by up to 25% of RA without affecting the workability and mechanical properties of normal-strength concrete. Among the four mixing approaches studied, TSMA gives the best result, followed by MMA. The two-stage mixing method is significant because it specifically targets and mitigates the main limitation of recycled aggregate concrete—the weak ITZ—by ensuring better mortar coverage around aggregate particles, pore reduction, better hydration and bonding at the aggregate-cement interface. This not only improves the strength and durability of RAC but also broadens its practical applications in construction.

The economic and environmental evaluation of the four mixing methods—Normal Mixing Approach (NMA), Treated Aggregate Mixing Approach (TAMA), Mortar Mixing Approach (MMA), and Two-Stage Mixing Approach (TSMA)—reveals significant differences in sustainability, cost-effectiveness, and practical application. NMA, the most conventional method, and TAMA involve mixing all components with full water content simultaneously. While operationally simple and cost-efficient in the short term, it often results in poor bonding with recycled aggregates, reducing strength and durability, and may require higher cement content, thus increasing environmental impact through elevated CO_2 emissions. MMA improves upon this by pre-mixing cement and fine aggregate with 75% water, enhancing hydration and particle distribution. This staged mixing moderately improves workability and strength, better balancing performance and resource efficiency. TSMA, the most advanced method, divides water and introduces materials in stages, significantly enhancing the coating of recycled aggregates and the overall microstructure of the concrete. This leads to superior compressive strength, durability, and water efficiency, reducing cement usage and reducing carbon emissions. Although TSMA requires more time and energy due

to multiple mixing steps, its long-term benefits in sustainability and structural performance outweigh the initial operational costs. Therefore, TSMA stands out as the most sustainable and cost-effective approach for projects prioritizing durability and environmental responsibility. At the same time, MMA serves as a practical alternative when simplicity and moderate improvements are desired over traditional NMA.

This research underscores the potential of RA as a sustainable material in concrete production while emphasising the importance of optimizing mixing techniques to enhance RAC performance. The findings highlight the role of mixing approaches like TSMA in promoting sustainable construction practices and advancing the use of recycled materials in industry. Future studies should investigate long-term durability, economic feasibility, and environmental impact to further validate the practical applications of RAC with RA in different construction scenarios.

Acknowledgements

The authors thank the management, principal, and HoD of Civil Engineering, Sri Manakula Vinayagar Engineering College, Madagadipet, Puducherry, for providing research facilities in the institution. The authors are immensely pleased to sincerely thank all who contributed directly or indirectly to bringing this project to a publishing platform.

References

[1] HaitherAli H, G A. Sustainable urban development: Evaluating the potential of mineral-based construction and demolition waste recycling in emerging economies. Sustain Futur. 2024;7:100179. https://doi.org/10.1016/j.sftr.2024.100179

[2] Malladi RC, Ajayan SA, Chandran G, Selvaraj T. Upcycling of construction and demolition waste: Recovery and reuse of binder and fine aggregate in cement applications to achieve circular economy. Clean Eng Technol. 2025;24:100864. https://doi.org/10.1016/j.clet.2024.100864

[3] Marvila M, de Matos P, Rodríguez E, Monteiro SN, de Azevedo ARG. Recycled Aggregate: A Viable Solution for Sustainable Concrete Production. Materials (Basel). 2022;15(15):5276. https://doi.org/10.3390/ma15155276

[4] Sizirici B, Fseha Y, Cho CS, Yildiz I, Byon YJ. A review of carbon footprint reduction in construction industry, from design to operation. Materials (Basel). 2021;14(20):6094. https://doi.org/10.3390/ma14206094

[5] Ozmen HB, Inel M. Effect of concrete strength and detailing properties on seismic damage for RC structures. Res Eng Des. 2024;1(1):1-11. https://doi.org/10.17515/rede2024-005en1124rs

[6] Al Martini S, Khartabil A, Saboumi AR. Sustainable concrete using recycled aggregate and supplementary cementitious materials. In: 6th International Conference on Engineering Mechanics and Materials; 2017. Vol. 2.

[7] Pacheco J, de Brito J, Chastre C, Evangelista L. Experimental investigation on the variability of the main mechanical properties of concrete produced with coarse recycled concrete aggregates. Constr Build Mater. 2019;201:110-20. https://doi.org/10.1016/j.conbuildmat.2018.12.200

[8] Paglia C, Antonietti S, Mosca C. Preliminary exploration of recycling cementitious aggregates in the building field. 2021.

[9] Pani L, Francesconi L, Rombi J, Mistretta F, Sassu M, Stochino F. Effect of parent concrete on the performance of recycled aggregate concrete. Sustainability. 2020;12(23):9399. https://doi.org/10.3390/su12229399

[10] Oikonomou ND. Recycled concrete aggregates. Cem Concr Compos. 2005;27(2):315-8. https://doi.org/10.1016/j.cemconcomp.2004.02.020

[11] Seddik Meddah M. Recycled aggregates in concrete production: engineering properties and environmental impact. MATEC Web Conf. 2017;101:05021. https://doi.org/10.1051/matecconf/201710105021

[12] Oikonomopoulou K, Ioannou S, Savva P, Spanou M, Nicolaides D, Petrou MF. Effect of mechanically treated recycled aggregates on the long term mechanical properties and durability of concrete. Materials (Basel). 2022;15(8):2871. https://doi.org/10.3390/ma15082871

[13] Sani D, Moriconi G, Fava G, Corinaldesi V. Leaching and mechanical behaviour of concrete manufactured with recycled aggregates. Waste Manag. 2005;25(2):177-82. https://doi.org/10.1016/j.wasman.2004.12.006

[14] Scrivener KL, John VM, Gartner EM. Eco-efficient cements: Potential economically viable solutions for a low-CO_2 cement-based materials industry. Cem Concr Res. 2018;114:2-26. https://doi.org/10.1016/j.cemconres.2018.03.015

[15] Kaabeche S, Belaoura M. The effects of the quality of recycled aggregates on the mechanical properties of roller compacted concrete. Res Eng Struct Mater. 2025;11(2):587-605.
[16] Guo H, Shi C, Guan X, Zhu J, Ding Y, Ling TC, et al. Durability of recycled aggregate concrete - A review. Cem Concr Compos. 2018;89:251-9. https://doi.org/10.1016/j.cemconcomp.2018.03.008
[17] Oikonomopoulou K, Savva P, Ioannou S, Nicolaides D, Petrou MF. Production of recycled aggregate concrete using construction and demolition waste. In: RILEM Bookseries. Vol. 34. 2022. https://doi.org/10.1007/978-3-030-76465-4_24
[18] Al-Waked Q, Bai J, Kinuthia J, Davies P. Enhancing the aggregate impact value and water absorption of demolition waste coarse aggregates with various treatment methods. Case Stud Constr Mater. 2022;17:e01267. https://doi.org/10.1016/j.cscm.2022.e01267
[19] Joseph M, Boehme L, Cornelly C, Anseeuw I, Declercq W, Vandenwalle L. Recycled concrete in weak acidic environments. Key Eng Mater. 2016;677:224-32. https://doi.org/10.4028/www.scientific.net/KEM.677.224
[20] Kumar NN, Kathirvel P, G M, Raja Mohan Kaliyaperumal S. Strength properties of recycled aggregate concrete treated with low concentration acetic acid. Int J Eng Technol. 2018;7(3.12):403. https://doi.org/10.14419/ijet.v7i3.12.16115
[21] Li P, Zhang D, Wei D, Xiong J, Li J. Effect of chemical enhancing-technology on the properties of recycled aggregate. Adv Civ Eng. 2020;2020:8875348. https://doi.org/10.1155/2020/8875348
[22] Tanta A, Kanoungo A, Singh S, Kanoungo S. The effects of surface treatment methods on properties of recycled concrete aggregates. Mater Today Proc. 2022;50:1848-52. https://doi.org/10.1016/j.matpr.2021.09.223
[23] Liu K, Xu W, Sun D, Tang J, Wang A, Chen D. Carbonation of recycled aggregate and its effect on properties of recycled aggregate concrete: A review. Mater Express. 2021;11(9):1439-52. https://doi.org/10.1166/mex.2021.2045
[24] Dabhade AN, Chaudari SR, Gajbhaye AR. Effect of flyash on recycle coarse aggregate concrete. 2014;5.
[25] Guo MZ, Ling TC, Poon CS. Photocatalytic NOx degradation of concrete surface layers intermixed and spray-coated with nano-TiO_2: Influence of experimental factors. Cem Concr Compos. 2017;83:279-89. https://doi.org/10.1016/j.cemconcomp.2017.07.022
[26] Jalilifar H, Sajedi F, Razavi Toosi V. Evaluating the durability of recycled concrete made of coarse recycled aggregate concrete containing silica-fume and natural zeolite. Rev Constr. 2020;19(3):457-73. https://doi.org/10.7764/rdlc.19.3.457-473
[27] Yao Y, Wu B, Zhang W, Fu Y, Kong X. Experimental investigation on the impact properties and microstructure of recycled steel fiber and silica fume reinforced recycled aggregate concrete. Case Stud Constr Mater. 2023;18:e02213. https://doi.org/10.1016/j.cscm.2023.e02213
[28] Ahmadi M, Farzin S, Hassani A, Motamedi M. Mechanical properties of the concrete containing recycled fibers and aggregates. Constr Build Mater. 2017;144:392-8. https://doi.org/10.1016/j.conbuildmat.2017.03.215
[29] Bai G, Zhu C, Liu C, Liu B. An evaluation of the recycled aggregate characteristics and the recycled aggregate concrete mechanical properties. Constr Build Mater. 2020;240:117978. https://doi.org/10.1016/j.conbuildmat.2019.117978
[30] Marinković S, Josa I, Braymand S, Tošić N. Sustainability assessment of recycled aggregate concrete structures: A critical view on the current state-of-knowledge and practice. Struct Concr. 2023;24(2):846-61. https://doi.org/10.1002/suco.202201245
[31] Kachouh N, El-Maaddawy T, El-Hassan H, El-Ariss B. Shear behavior of steel-fiber-reinforced recycled aggregate concrete deep beams. Buildings. 2021;11(9):423. https://doi.org/10.3390/buildings11090423
[32] Rahal KN, Al-Khaleefi AL. Shear-friction behavior of recycled and natural aggregate concrete-An experimental investigation. ACI Struct J. 2015;112(3):315-24. https://doi.org/10.14359/51687748
[33] Tošić N, Marinković S, Pecić N, Ignjatović I, Dragaš J. Long-term behaviour of reinforced beams made with natural or recycled aggregate concrete and high-volume fly ash concrete. Constr Build Mater. 2018;176:344-58. https://doi.org/10.1016/j.conbuildmat.2018.05.002
[34] Haider M, Sharma A. Comparison of concrete made through TSMA using metakaolin and GGBS vs normal concrete made through NMA. Int Res J Eng Technol. 2021;8(9):1680-7.
[35] Jagan S, Neelakantan TR, Saravanakumar P. Mechanical properties of recycled aggregate concrete treated by variation in mixing approaches. Rev Construction. 2021;20(2):236-48. https://doi.org/10.7764/RDLC.20.2.236
[36] Tam VWY, Gao XF, Tam CM. Microstructural analysis of recycled aggregate concrete produced from two-stage mixing approach. Cem Concr Res. 2005;35(6):1195-203. https://doi.org/10.1016/j.cemconres.2004.10.025

[37] Tam VWY, Soomro M, Evangelista ACJ, Haddad A. Deformation and permeability of recycled aggregate concrete - A comprehensive review. J Build Eng. 2021;44:103393. https://doi.org/10.1016/j.jobe.2021.103393
[38] Tam VWY, Tam CM. Diversifying two-stage mixing approach (TSMA) for recycled aggregate concrete: TSMAs and TSMAsc. Constr Build Mater. 2008;22(9):2068-77. https://doi.org/10.1016/j.conbuildmat.2007.07.024
[39] Kumar S, Pandey V. Experimental investigation of recycled aggregate concrete using pre-soaked slurry two stage mixing approach. Int J Civ Eng Technol. 2017;8(3):89-97.
[40] Liang Y, Ye Z, Vernerey F, Xi Y. Development of processing methods to improve strength of concrete with 100% recycled coarse aggregate. J Mater Civ Eng. 2015;27(5):04014171. https://doi.org/10.1061/(ASCE)MT.1943-5533.0000909
[41] Bureau of Indian Standards. IS 1489-1 (1991): Specification for Portland pozzolana cement, Part 1: Flyash based. New Delhi: BIS; 1991.
[42] Bureau of Indian Standards. IS 383:2016 - Coarse and fine aggregate for concrete - Specification (Third Revision). New Delhi: BIS; 2016.
[43] Bureau of Indian Standards. IS 2386-1 (1963): Methods of test for aggregates for concrete, Part I: Particle size and shape. New Delhi: BIS; 1963.
[44] Bureau of Indian Standards. IS 10262:2019 - Concrete mix proportioning - Guidelines (Second Revision). New Delhi: BIS; 2019.
[45] Bureau of Indian Standards. IS 456:2000 - Plain and reinforced concrete - Code of practice (Fourth Revision). New Delhi: BIS; 2000.
[46] Bureau of Indian Standards. IS 516 (Part 1/Sec 1):2021 - Compressive, flexural and split tensile strength. New Delhi: BIS; 2021.
[47] Verma A, Babu VS, A S. Influence of modified two-stage mixing approaches on recycled aggregate treated with a hybrid method of treatment. Aust J Struct Eng. 2022;23(3):230-53. https://doi.org/10.1080/13287982.2022.2048479
[48] Silva RV, de Brito J, Dhir RK. Use of recycled aggregates arising from construction and demolition waste in new construction applications. J Clean Prod. 2019;236:117629. https://doi.org/10.1016/j.jclepro.2019.117629
[49] Li Z, Bian Y, Zhao J, Wang Y, Qiu X, Liu Q. Sustainable building materials-recycled aggregate and concrete: a systematic review of properties, modification techniques, and environmental impacts. Environ Sci Pollut Res Int. 2024;31(18):20814-52. https://doi.org/10.1007/s11356-024-32397-9
[50] Li W, Xiao J, Sun Z, Kawashima S, Shah SP. Interfacial transition zones in recycled aggregate concrete with different mixing approaches. Constr Build Mater. 2012;35:1045-55. https://doi.org/10.1016/j.conbuildmat.2012.06.022
[51] Kong D, Lei T, Zheng J, Ma C, Jiang J. Effect and mechanism of surface-coating pozzolanic materials around aggregate on properties and ITZ microstructure of recycled aggregate concrete. Constr Build Mater. 2010;24(5):701-8. https://doi.org/10.1016/j.conbuildmat.2009.10.038
[52] Limbachiya M, Meddah MS, Ouchagour Y. Use of recycled concrete aggregate in fly-ash concrete. Constr Build Mater. 2012;27(1):439-49. https://doi.org/10.1016/j.conbuildmat.2011.07.023 https://doi.org/10.1016/j.conbuildmat.2011.07.023
[53] Nicoara AI, Stoica AE, Vrabec M, Rogan NŠ, Sturm S, Ow-Yang C, et al. End-of-life materials used as supplementary cementitious materials in the concrete industry. Materials (Basel). 2020;13(8):1954. https://doi.org/10.3390/ma13081954
[54] Agarwal M, Choudhary MC, Aggarwal VR. An experimental study on properties of concrete with recycled aggregates and synthetic fibres - A literature review. Int J Earth Sci Eng. 2017;10(4):442-9. https://doi.org/10.21276/ijee.2017.10.0247
[55] Ali B, Fahad M, Mohammed AS, Ahmed H, Elhag AB, Azab M. Improving the performance of recycled aggregate concrete using nylon waste fibers. Case Stud Constr Mater. 2022;17:e01468. https://doi.org/10.1016/j.cscm.2022.e01468
[56] Paluri Y, Mogili S, Mudavath H, Noolu V. Effect of fibres on the strength and toughness characteristics of recycled aggregate concrete. Mater Today Proc. 2021;38:2537-40. https://doi.org/10.1016/j.matpr.2020.07.555

Blank Page

Research on Engineering Structures & Materials
www.jresm.org
Research Group

Research Article

Impact of industrial waste fillers in self-compacting mortars: A comparative analysis of mechanical performance

Ahmed Messaoud Djebara [*,1,2,a], Mohamed Mouli [1,b], Karim Belmokretar [1,c], Ramdane Chihaoui [1,d], Yassine Senhadji [1,3,e], Ahmed Soufiane Benosman [1,4,f], Mehdi Seghiri [5,g]

[1]*Department of Civil Engineering, National Polytechnic School of Oran, Laboratory of Materials LABMAT, Algeria*
[2]*Department of Architecture, University of Algiers 1, Algeria*
[3]*Department of Civil Engineering, University of Mascara, Algeria*
[4]*Ecole Supérieure en Sciences Appliquées de Tlemcen, Algeria*
[5]*Faculty of Sciences and Technology, University of Tamanghasset, Algeria*

Article Info

Article History:

Received 18 June 2025
Accepted 20 Aug 2025

Keywords:

Industrial waste;
Glass;
Brick;
Ceramic;
Self- compacting mortars;
Hydration heat;
Mechanical performance

Abstract

This study investigates the viability of utilizing non-biodegradable industrial waste streams specifically ground glass, crushed brick, and sanitary ceramics as alternative fillers in self-compacting mortars (SCMs). A conventional SCM mixture incorporating traditional limestone filler served as the control benchmark. The research assessed the influence of substituting conventional fillers with waste-derived materials, varying their proportions while maintaining a constant cement content. The experimental results showed that the inclusion of alternative fillers enabled the target slump flow values to be achieved with a lower water-cement ratio, thus reducing water demand. However, the mortars with brick and ceramic fillers had longer mini-V- funnel flow times. Analysis of the hydration heat revealed that brick and ceramic fillers accelerated early hydration reactions, whereas glass fillers exhibited a delayed reactivity. Mortars containing these alternative fillers showed significant mechanical strength increases over time; compressive strength and dynamic modulus of elasticity increased significantly. After 365 days of curing, compressive strength values increased by 34% and 37% for mortars containing brick and ceramic fillers, respectively, and by 31% for those incorporating glass fillers, relative to the control mortar. These findings highlight the promising potential of valorizing industrial waste materials as efficient, economical, and environmentally sustainable alternatives to conventional limestone fillers in SCMs.

© 2025 MIM Research Group. All rights reserved.

1. Introduction

The construction industry represents one of largest consumers of raw materials globally and is a significant contributor to environmental degradation. Notably, cement production a fundamental component of concrete is responsible for approximately 8% of worldwide carbon dioxide emissions [1]. Concurrently, the accumulation and disposal of non-biodegradable industrial waste, such as glass, brick, and sanitary ceramic residues, present formidable environmental challenges across numerous regions. These materials occupy valuable landfill space and pose long-term ecological threats.

*Corresponding author: a.messaouddjebara@univ-alger.dz
[a]orcid.org/0009-0001-4506-6391; [b]orcid.org/0000-0001-7199-4928; [c]orcid.org/0000-0001-8184-9898; [d]orcid.org/0000-0002-6507-1446; [e]orcid.org/0000-0003-0678-3424; [f]orcid.org/0000-0002-0344-020X; [g]orcid.org/0000-0001-5332-4840.
DOI: http://dx.doi.org/10.17515/resm2025-978me0718rs

Self-compacting mortars (SCMs), derived from the technological advances of self-compacting concrete (SCC), represent a significant innovation within construction material science [2]. Characterized by exceptional flowability, homogeneity, and stability, SCMs possess the ability to spread and consolidate solely under gravitational forces, obviating the need for mechanical vibration. Their carefully regulated viscosity enables them to efficiently fill formwork and envelop reinforcing elements without inducing segregation, blocking, or bleeding phenomena [3]. Achieving these functional properties necessitates a high content of fine materials (cement and fillers), elevated dosages of chemical admixtures, and a relatively low water-to-binder ratio [4].

In SCM formulations, fillers play a vital role in enhancing rheological performance, optimizing fresh-state workability, controlling cement dosage, and regulating the heat generated during hydration, thereby reducing the risk of cracking in the hardened mortar. Conventionally, limestone fillers are preferred due to their ability to densify the granular skeleton, enhance cohesion, and limit particle segregation [5]. However, limestone fillers present certain limitations, such as geographically constrained availability, high transportation costs, and the absence of pozzolanic activity, which restricts their capacity to enhance the long-term mechanical properties of the mortar. In response to these shortcomings, extensive research has focused on identifying alternative filler materials. Various natural pozzolans and mineral additions, including natural pozzolan [6], dolomite [7], fly ash [8], silica fume [4], and metakaolin [9], among other industrial by-products, have been investigated.

Among these alternatives, waste glass, brick, and ceramic materials are attracting increasing attention due to their favorable chemical compositions and inherent pozzolanic activity. Glass waste, composed predominantly of silica (73%), sodium oxide (13%), and lime (10%), demonstrates significant pozzolanic reactivity, beneficial for mortar and concrete applications [10]. Previous investigations into the incorporation of glass powder into SCC have yielded divergent results. Some studies reported reductions in slump flow and compressive and flexural strengths when glass powder was added at dosages of 5%, 10%, and 15% [11], while others found a significantly enhanced flexural strength by up to 6.85% [12].

Brick and ceramic waste materials are generated primarily from production defects (ranging from 15% to 30% of manufactured products) or demolition activities. Composed mainly of silica (SiO_2) and alumina (Al_2O_3), these materials exhibit notable pozzolanic activity. Prior research demonstrated that the partial replacement of cement with brick powder in SCM formulations could yield compressive strengths comparable to or even exceeding those of traditional mixes [13]. Additional studies observed that brick powder improved both compressive and flexural strength, albeit with an increase in viscosity without significantly impairing workability [14].

It is important to highlight that while previous investigations predominantly focused on utilizing such waste-derived materials as partial cement replacements, relatively few studies have explored their use as fillers. In this context, Zengfeng Zhao and al. [15] evaluated the substitution of limestone fillers with brick powder in SCMs and noted an initial reduction in compressive strength at 7 days, subsequently offset by pozzolanic reactions leading to strength recovery after 28 days.

Our study pioneers the use of industrial waste as fillers (< 200 μm) rather than cement substitutes (< 80 μm), enabling substantially higher waste incorporation: 150 kg/m^3 of fillers versus just 90-135 kg/m^3 in typical cement substitution (20-30%). This dual-benefit approach achieves 30-40% grinding energy savings due to less demanding particle size requirements, and remarkable mechanical enhancements. These gains stem from the synergistic interplay between granular packing effects and the waste materials' latent pozzolanic activity, which collaboratively refine the matrix microstructure into a denser, more resilient composite.

The primary objective of the presen4.t study is to assess the feasibility of employing ground glass, brick, and ceramic waste as alternative fillers in self-compacting mortar formulations. The originality of this work lies in the specific application of these materials as fillers, rather than as cement substitutes, coupled with a comprehensive evaluation of their influence on both early-age and long-term performance properties. The specific objectives pursued are as follows:

- To characterize the physicochemical properties of the alternative fillers derived from industrial waste.
- To investigate the effects of these fillers on the rheological behavior of fresh SCMs.
- To evaluate their influence on hydration heat evolution.
- To monitor the development of mechanical properties, including compressive and tensile strength, and dynamic modulus of elasticity, over a period extending to 365 days.

By valorizing industrial waste within high-performance construction materials, this study supports the advancement of circular economy principles, contributing both to environmental sustainability and the enhancement of material performance

2. Experimental Program

2.1 Materials

2.1.1 Cement

The cement utilized in this study was a Portland cement classified as CEM I 52.5 R, conforming to Algerian standard NA 442, which is harmonized with European standard EN 197-1 [16]. This cement grade was selected due to its high early strength development and purity (≥95% clinker) to clearly isolate the effects of industrial waste fillers on high-performance mortars, while reflecting regional construction practices where this cement class dominates demanding structural applications. The chemical composition, detailed in Table 1, indicates a significant presence of calcium oxide (CaO, 63.25%) and silicon dioxide (SiO_2, 25.35%), these components are primarily responsible for the mechanical strength development through the formation of calcium silicate hydrate (C-S-H) gel as a result of hydration reactions.

2.1.2 Fillers

The fillers investigated were derived from various types of recovered industrial waste:

- Glass Fillers (Gl): Sourced from discarded green glass bottles collected from uncontrolled disposal sites. The bottles were subjected to cleaning, crushing, and fine grinding to achieve an appropriate particle size distribution.
- Brick Fillers (Br): Obtained from defective products rejected by a brick manufacturing facility due to non-conformity with quality standards.
- Ceramic Fillers (Cr): Retrieved from sanitary ceramic production waste, processed similarly to the brick fillers.
- Limestone Fillers (LS): Employed as the reference filler, representing the material most frequently employed in production processes of mortars and self-compacting concrete

Glass (Gl) Brick (Br) Ceramic (Cr)

Fig. 1. Various types of waste materials

All waste-derived materials underwent preliminary cleaning and crushing using a hammer mill. Subsequently, they were oven-dried at 105°C for 24 hours and finely ground in a ball mill to achieve a particle size below 200 µm. The grinding duration was adjusted individually for each filler type to achieve a fineness comparable to that of the limestone filler. Notably, brick fillers required extended grinding times, while glass fillers, constrained by the available equipment, were processed to the highest achievable fineness. Figure 1 presents the appearance of the waste materials before and after processing. The chemical and physical characteristics of fillers and cement are presented in Tables 1 and 2, respectively. Scanning Electron Microscopy (SEM), combined with Energy Dispersive X-ray Spectroscopy (EDS), was employed to investigate the morphology and elemental composition of the fillers (Figure 2).

Table 1. Chemical composition of the fillers and cement (%)

(%)	LS	Gl	Br	Cr	CEMI
$CaCO_3$	94.5	-	-	-	-
CaO	-	7.40	9,20	9.61	63.26
SiO_2	2.95	74.52	49.26	54.32	25.36
Al_2O_3	1.46	5.5	29.41	27.67	5.77
Fe_2O_3	0,02	0.4	2.50	1.2	0.30
MgO	0,15	0.55	2.26	0.37	1.76
Na_2O	0,3	11.02	0.75	1.64	0.05
TiO_2	0,023	0.09	0.59	0.37	0.124
P_2O_5	0,026	0,04	0.17	0.12	0.078
Cl	0.05	0,003	0.011	0.005	0.03
K_2O	0,08	0,45	1.66	0.87	0.45
Mn_2O_3	13ppm	39ppm	0.01	0.02	38ppm
Cr_2O	10ppm	19ppm	0.04	0.01	5ppm
SO_3	-	0.04	0.11	0.04	2.83
L.O.I	43,2	1.28	2.48	1.46	2.97
(SiO_2+Al_2O_3+ Fe_2O_3)	-	80	81.14	83.4	-

Table 1 provides a comprehensive analysis of the chemical composition (% mass) of the conventional limestone filler (LS), alternative waste-derived fillers (glass-GI, brick-Br, ceramic-Cr), and Portland cement (CEM I 52.5 R). These data reveal critical insights into the intrinsic properties governing filler performance in self-compacting mortars (SCMs): Dominant Oxides and Reactivity:

- Limestone Filler (LS): Comprises 94.5% $CaCO_3$ (inert carbonate phase), with negligible reactive oxides (SiO_2 + Al_2O_3 + Fe_2O_3 = 4.43%). This confirms its role as a physically functional but chemically inert filler, primarily enhancing particle packing without contributing to pozzolanic reactions.
- Glass (GI): High SiO_2 (74.52%) and Na_2O (11.02%) content aligns with typical soda-lime glass. The combined pozzolanic oxides (SiO_2 + Al_2O_3 + Fe_2O_3 = 80%) signify latent reactivity, though low CaO (7.40%) and Al_2O_3 (5.5%) limit early gel formation.
- Brick (Br): Rich in SiO_2 (49.26%) and Al_2O_3 (29.41%), yielding high pozzolanic oxide content (81.14%). Elevated Al_2O_3 promotes C-A-H/C-A-S-H gel formation, accelerating strength development.
- Ceramic (Cr): Highest pozzolanic oxide fraction (83.4%), with balanced SiO_2 (54.32%) and Al_2O_3 (27.67%). This optimal composition explains its superior pozzolanic indices (I_{28}=0.87, I_{90}=0.99, Table 2).

Spectroscopy (EDS) for the alternate fillers glass, brick, and ceramic, as well as the reference filler limestone. These analyses yield vital understanding of:

- iMorphology and Physical Structure:
- Glass Filler (Gl): Particles with angular and smooth surfaces (red arrow) explain low interparticle friction as enhancing workability. Their limited surface area slows down the pozzolanic reaction.

- Brick and Ceramic Filler (Br): Depicted particles and irregular porous microstructure (blue arrow) improve specific surface area, aiding nucleation in early hydration. This chemically enhances the pozzolanic index and structurally contributes to micro-defect-rich C-A-S-H gel formation.
- Limestone (LS): No arrows indicate the rounded and compact morphology which suggests its inert nature. This explains the filler's role as a rheologically-active filler without pozzolanic activity.
- Mineralogical Composition (EDS): EDS mappings validate Table 1 data:
- High silica (Si) in Gl (74.52%) and aluminosilicates (Al/Si) in Br/Cr drive differential pozzolanic reactivity. Elevated alumina (Al) in Br/Cr (29.41%/27.67%) promotes C-A-H/C-A-S-H gel formation, enabling microstructural densification

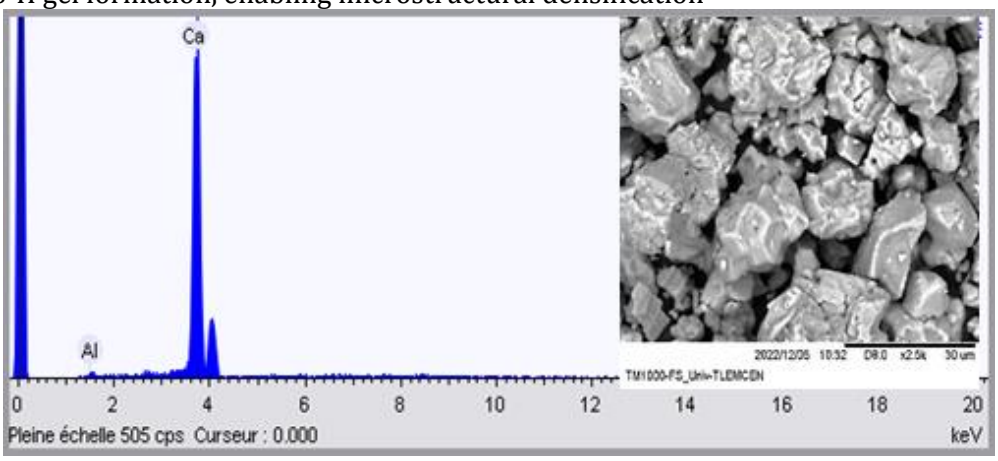

Lime Stone

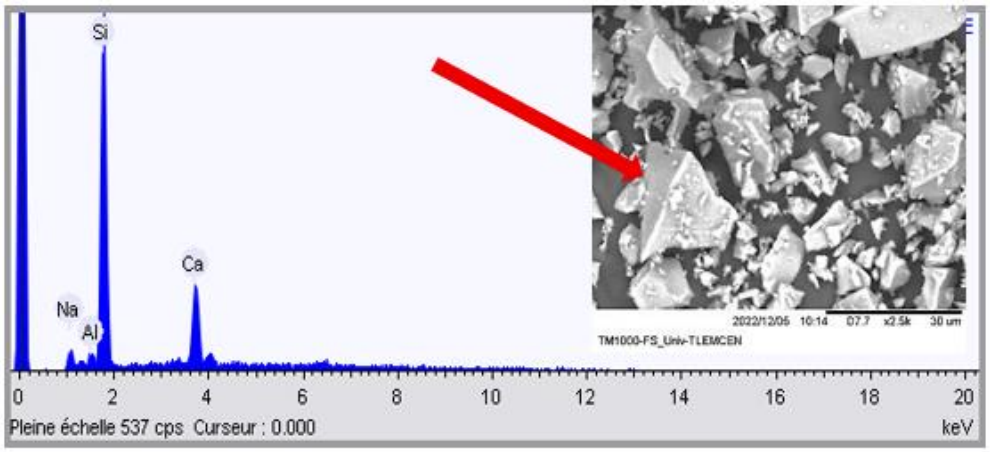

Glass

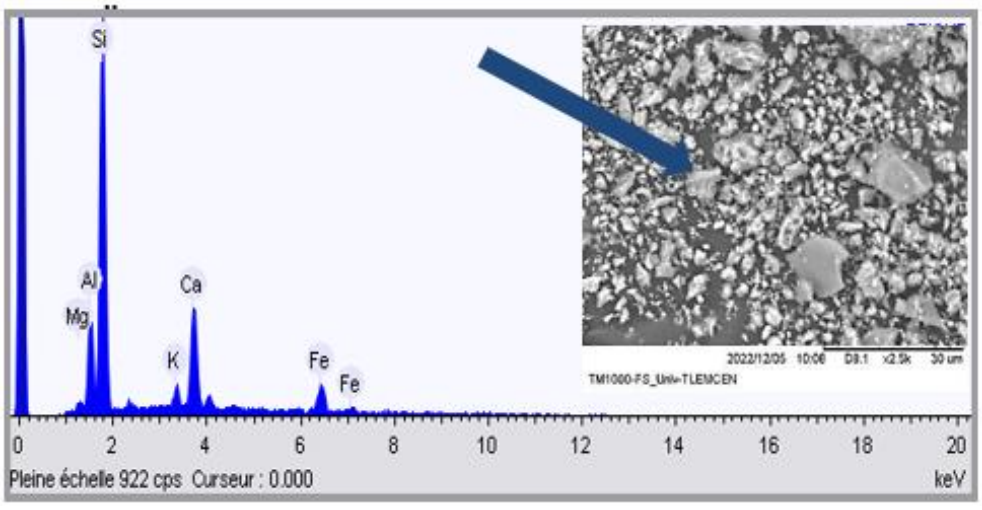

Brick

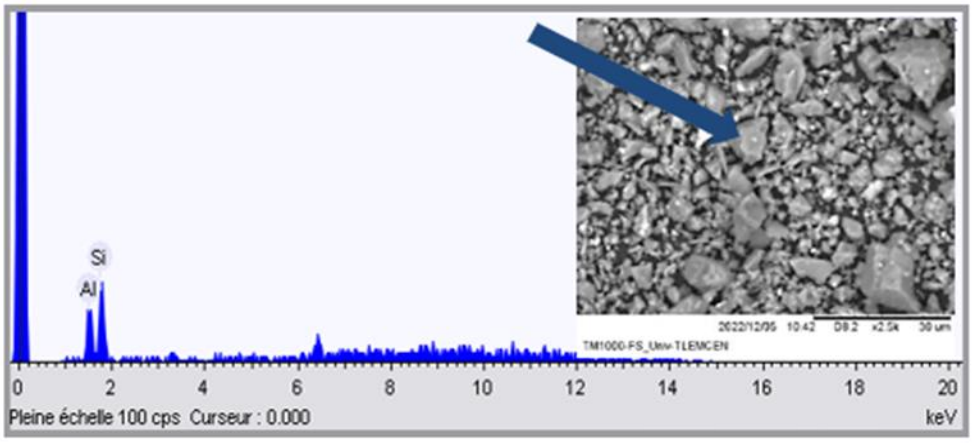

Ceramic

Fig. 2. Results of SEM and EDS analyses of the filler materials

Table 2. Physical properties of fillers and cement

Physical character.	Color	Specific gravity	Refusal 45 µm%	i_{28}	i_{90}
LS	White	2,62	28	-	-
Gl	White	2,51	32,2	0,73	0,78
Br	Red	2,56	22,5	0,83	0,93
Cr	White	2,53	17	0,87	0,99
CEMI	White	3,1	-	-	-

Furthermore, the pozzolanic activity indices (i_{28} and i_{90}) corroborated the reactivity of these fillers, particularly for ceramics, where values of 0.87 and 0.99 were observed at 28 and 90 days, respectively.

2.1.3 Sands and admixtures

Two types of sand were combined for mortar preparation: fine siliceous sand and coarse calcareous sand. A blend of fine sand and coarse sand was selected to achieve optimal spreadability and fluidity necessary for self-compacting mortar characteristics. The sands exhibited the following physical properties: Fineness Modulus of 2.2; Apparent Density of 1305 kg/m^3; Absolute Density of 2500 kg/m^3; and Sand Equivalent (SE) of 88. A third-generation polycarboxylate-based superplasticizer, compliant with the NF EN 934-2 standard [17], was used at a saturation dosage corresponding to approximately 5% of the cement weight. This elevated dosage aimed to minimize water content while enhancing long-term mechanical performance. All mortar mixtures were prepared using distilled water.

2.2 Formulation of Mortars

Each filler type (brick, ceramic, limestone, and glass) was incorporated into separate self-compacting mortar formulations. The quantity of water added to each mix was adjusted to maintain a target slump flow diameter within the range of 24 to 26 cm (specifically, 250 ± 10 mm), as specified in the test methodology. Table 3 provides a summary of the mortar compositions utilized.

Table 3. Different formulations of self-compacting mortars (g)

SCM	LS	Gl	Br	Cr
Cement		450		
Filler	150	150	150	150
Water	180	168.75	157.5	157.5
F Sand		720		
C Sand		480		
SP		22.5		

2.3 Test Methods

2.3.1 Fresh State Properties

The fresh-state behavior of the mortars was evaluated following the EFNARC guidelines [18] to quantify workability adjustments required for alternative fillers. Immediately after mixing, the slump flow was measured using a mini-cone, and flow time was determined using a mini-V-funnel apparatus. In order to ensure comparable slump flows (targeted at 250 ± 10 mm) across different formulations, the water-to-cement (W/C) ratio was adjusted for each mortar while maintaining a constant superplasticizer dosage.

(a) (b)

Fig. 3. Rheological property measurement: (a) Mini-slump cone; (b) Mini V-funnel apparatus

2.3.2 Fresh Density

The fresh (or bulk) density of the self-compacting mortars was determined in accordance with NF EN 1015-6 [19] as a critical indicator of volumetric efficiency, especially given the lower specific gravity of waste fillers (Table 2). For each formulation, a cylindrical container with a known volume of 1 litre was filled with fresh mortar without the application of compaction or vibration, then weighed. The apparent density was determined by dividing the mass of the mortar by the volume of the container. For each mixture, three measurements were conducted, and the average value was recorded.

Fig. 4. Fresh density measurement using a calibrated cylindrical container

2.3.3 Heat of Hydration

The evolution of hydration heat was assessed in accordance with standard NF EN 196-9 [20] using a semi-adiabatic Langavant calorimeter to identify acceleration/delay effects induced by waste fillers reactivity. A mortar sample weighing 1500 g was placed into a calibrated cell coated with a

thin oil film to prevent external moisture exchange. Temperature measurements were recorded every 10 minutes over a period of 72 hours.

Fig. 5. Semi-adiabatic hydration heat monitoring using a Langavant calorimeter

2.3.4 Mechanical Strength

Mechanical properties of the mortars, including compressive and flexural strength, were characterized using prismatic specimens measuring 4 × 4 × 16 cm^3, prepared according to NF EN 196-1 [21] to evaluate long-term performance gains from pozzolanic reactions. Tests were conducted after curing periods of 2, 7, 28, 90, 270, and 365 days. Specimens were cured in lime-saturated water at a constant temperature of 20°C until testing. Testing at 2 days, a key stage of primary hydration, assesses the early strength development of CEM I 52.5 R cement and fillers reaction (nucleation), essential for validating rapid-cycle applications like accelerated formwork removal or precast concrete production.

Fig. 6. Mechanical strength testing on prismatic specimens (4×4×16 cm^3)

2.3.5 Dynamic Modulus of Elasticity

The dynamic modulus of elasticity (Ed) was evaluated non-destructively using the Ultrasonic Pulse Velocity (UPV) method, in accordance with ASTM C597[22] to assess microstructural densification resulting from filler interactions, complementing mechanical strength data. This technique has been widely recognized as an effective non-destructive method for assessing the elastic properties and quality of cementitious materials, as documented by Malhotra and Carino [16]. Measurements were conducted on the same prismatic specimens (4×4×16 cm^3) used for compressive strength testing, at both 28 and 365 days of curing, prior to mechanical failure testing.

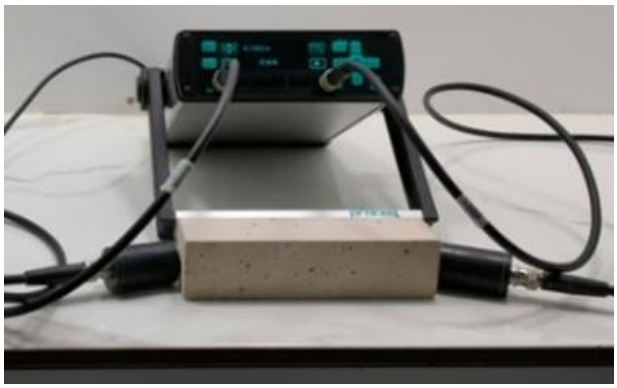

Fig. 7. Non-destructive measurement of dynamic modulus of elasticity (Ed) via ultrasonic pulse velocity

3. Results and Discussion

3.1 Fresh Properties Fresh Density

The mini-slump spread is widely regarded as the most indicative parameter for evaluating the flowability of self-compacting mortars. As shown in Table 4, all SCM mixtures achieved slump flow diameters within the acceptable range of 24 to 26 cm, conforming to EFNARC recommendations [18].

It was observed that mortars incorporating brick and ceramic fillers required a lower water content (approximately 35% relative to the mass of cement) compared to mortars utilizing limestone fillers, which necessitated about 40%. This reduction in water demand for waste-derived fillers is a significant finding. However, as this inherently alters the water-cement (w/c) ratio, it is expected to directly influence key mechanical properties. Consequently, comparisons between filler types must consider that observed differences in strength (compressive, flexural) and durability are likely attributable both to the filler characteristics and the resulting w/c ratio difference. This underscores the importance of reporting mix design parameters when evaluating filler effects in SCMs. It is noteworthy that Corinaldesi and Moriconi [23] reported contrasting results, indicating an increase in water demand with higher levels of filler substitution. Such discrepancies are likely attributable to differences in filler fineness and morphological characteristics between their study and the current work. In general, a reduction in water demand is associated with improved mechanical performance.

Regarding flow time measurements using the mini-V-funnel, mortars containing limestone fillers exhibited optimal flow (9 s), while brick and ceramic fillers showed extended flow times (20 s and 14 s, respectively) exceeding EFNARC's strict recommended range of (7–11 s) for self-compacting mortars. This deviation, particularly critical for brick filler (+82% above limit), indicates reduced flowability attributed to higher surface adhesion of these waste materials. This reduced flowability stems from the inherently higher surface adhesion tendencies of brick and ceramic fillers, attributed to three key factors:

- *Particle Morphology:* Angular shard-like structures (Fig. 2) increase interparticle friction and physical water trapping [24].
- *Surface Roughness*: Microscale asperities enhance capillary forces and binder adsorption [25].
- *Chemical Reactivity*: Surface hydroxyl groups (-OH) from Al_2O_3/SiO_2-rich compositions (Table 1) exhibit hydrophilic behavior, competing with superplasticizer molecules for water interaction [26]. In contrast, glass fillers (despite angularity) demonstrate smoother surfaces and lower chemical affinity, resulting in closer-to-limit flow times (12 s).

Table 4. Fresh state properties of self-compacting mortars incorporating different fillers

SCMs	LS	Gl	Br	Cr
W/C	0.40	0.375	0.35	0.35
Spreading (cm)	24.2	25.6	25.4	25.6
Mini V-funnel (s)	9	12	20	14
Fresh density (g/cm^3)	2.35	2.31	2.33	2.32

3.2 Fresh Density

The lower fresh density observed in mortars containing glass fillers is attributed to the inherently lower specific gravity of glass (2.51 g/cm^3) compared to that of limestone filler (2.62 g/cm^3). Although this density difference is modest, it can nonetheless influence key hardened- state properties such as thermal conductivity and acoustic insulation performance.

These results align with those reported by Felekoğlu et al [27], who documented a reduction in the fresh density of self-compacting mortars upon the incorporation of pozzolanic materials with densities lower than that of cement. Similarly, Uysal and Sumer [28] noted that the use of alternative fillers in self-compacting concrete led to a marginal reduction in fresh density an outcome potentially beneficial for applications where reduced weight is advantageous.

3.3 Heat of Hydration and Heat Flow

Figures 8 and 9 present the temperature and cumulative heat evolution curves during hydration process, while Table 5 summarizes key parameters including early activation metrics (Q_{10h}, T_{10h}), peak hydration parameters (T_m, t, Q_m), and percentage increases relative to control.

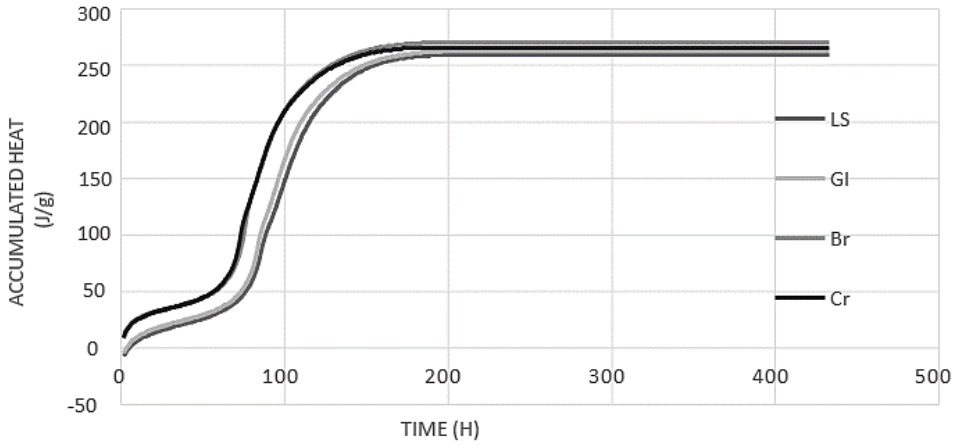

Fig. 8. Accumulated heat

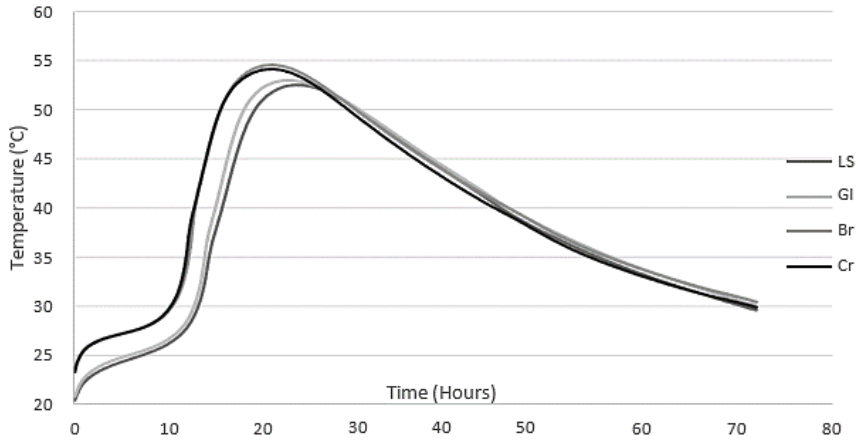

Fig. 9. Released heat

The results indicate that mortars incorporating brick and ceramic waste experienced significantly accelerated heat release within the first 10 hours of hydration, as quantitatively demonstrated by:

- Cumulative heat at 10 hours: Brick-filled mortar (Br) released of 55 J/g, ceramic-filled mortar (Cr) of 56 J/g , 67-70% higher than limestone control (LS of 33 J/g) and glass-filled mortar (Gl of 36 J/g).
- Temperature differential at 10 hours, Br and Cr mortars reached 29.82°C and 29.63°C respectively, exceeding LS (26.24°C) by 3.39-3.58°C (Fig. 9).

This acceleration stems from a nucleation effect: the fine, reactive particles (d < 200 µm) provide abundant preferential sites for nucleation of C-S-H phases. Specifically:

- Surface Area Amplification: High specific surface area (17and 22.5%< 45 µm, Table 2) creates nucleation substrates [29].
- Template Effect: Al/Fe-rich surfaces (Table 1: 27.6 and 29.4% Al_2O_3) align Ca^{2+} and silicate ions, accelerating early gel growth [30].

This early acceleration culminated in peak temperatures of 54.6°C (Br) and 54.1°C (Cr) at 20.8 hours markedly higher and earlier than LS (52.5°C at 23.4 hours). The nucleation effect of fine, reactive particles (SiO_2+Al_2O_3 >80%, Table 1) promoted rapid C-S-H formation, while glass fillers exhibited delayed reactivity due to their smoother, less reactive surfaces. Conversely, mortars containing glass fillers exhibited delayed hydration kinetics and lower early heat release. Despite these initial differences, the cumulative heat output of all mortar formulations converged after 72 hours. Furthermore, mortars containing ceramic and brick fillers reached their peak temperatures approximately at 21 hours, whereas mortars with limestone and glass fillers attained peak temperatures at around 22.5 hours.

Table 5. Characteristics of Hydration for the various self-compacting mortars

SCM	LS	Gl	Br	Cr
Q_{10h} (j/g)	33	36	55	56
% Q_{10h}	-	9.1	66.66	69.7
T° 10h (°C)	26.24	26.7	29.82	29.63
Qm (j/g)	260	263	270	265
% Qm	-	1.15	3.85	1.92
T°m (°C)	52.52	52.99	54.56	54.13
tT°m (h)	23.35	22.51	20.84	20.85

These observations are attributed to the nucleation effects provided by fine brick and ceramic particles, which enhance early-stage cement hydration. It is well established that nucleation phenomena are influenced by filler fineness and their affinity with hydration products [30].

Wild et al. [31] reported that partial replacement of cement with metakaolin accelerates the hydration process due to the rapid formation of pozzolanic products. Similarly, Kadri et al. [32] and Berodier and Scrivener [33] highlighted the significant role of particle fineness and mineral composition in promoting early hydration.

The present findings suggest that oxides present in the brick and ceramic fillers actively interacted with calcium hydroxide (CH) generated during hydration, accelerating the formation of calcium silicate hydrate (C-S-H) and calcium aluminate hydrate (C-A-H) gels, thereby contributing to the enhanced initial heat release

3.4 Evolution of Mechanical Properties

Compressive strength is a critical indicator of mortar performance, influenced by variables such as water-to-cement (W/C) ratio, cement content, sand properties, and filler characteristics. Mechanical strength tests aimed to validate the trends observed in hydration heat behavior. Previous investigations involving brick [13,14], ceramic [34,35], and glass [12,36,37] as cement substitutes have demonstrated their pozzolanic potential.

As illustrated in Figure 10, compressive strength values for all mortar formulations consistently increased over time, with no strength reductions observed at any curing age. Mortars containing brick and ceramic fillers exhibited higher early-age strengths at 2 and 7 days, indicating accelerated strength development.

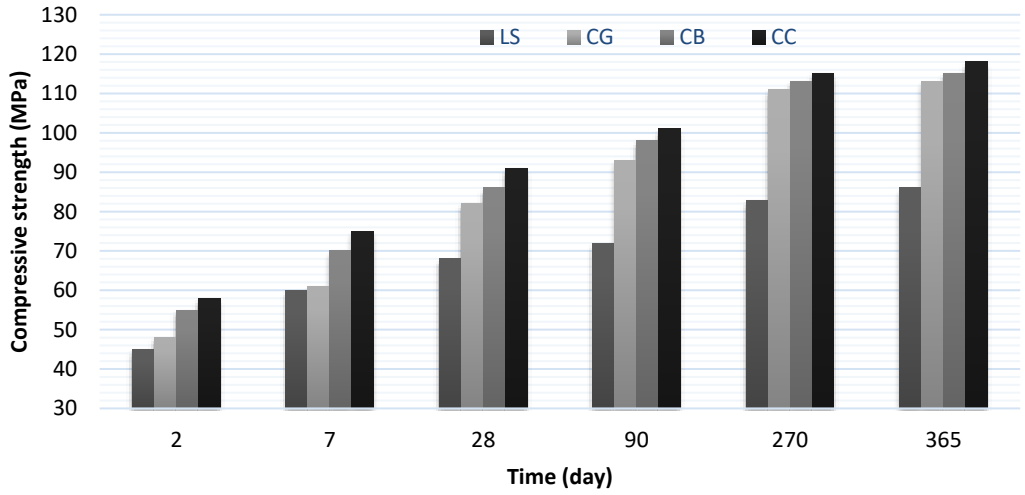

Fig. 10. Compressive strength of SCMs

At later stages, particularly after 365 days of curing, mortars incorporating brick and ceramic fillers achieved compressive strengths 34% and 37% higher, respectively, than the control mortar. Similarly, mortars incorporating glass fillers exhibited a 31% strength increase compared to the control. It is important to note that the pozzolanic reactions associated with brick and ceramic fillers were activated at early ages, affirming their nucleation effects. In contrast, glass fillers demonstrated delayed pozzolanic activity, with significant contributions to strength development observed primarily after 28 days of curing.

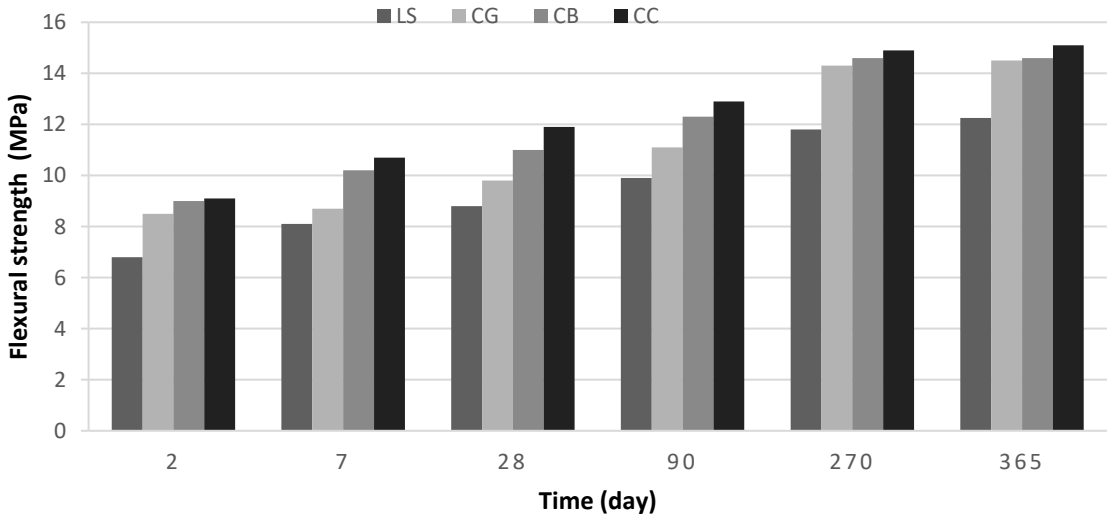

Fig. 11. Flexural strength of SCMs

The mechanical performance hierarchy (ceramic: +37% > brick: +34% > glass: +31% at 365 days) stems from differential chemical reactivity: Ceramic (Al_2O_3 of 27.7%) and brick (Al_2O_3 of 29.4% and Fe_2O_3 of 2.5%) fillers catalyze early C-A-S/H and C-A-F/H gel formation through aluminous sites, yielding +20% higher 7-day strength versus glass. Conversely, glass filler (SiO_2 of 74.5%) exhibits delayed alkaline dissolution (>28 days) restricted to homogeneous C-S-H gels, compounded by unfavorable particle size (32.2% retained at 45µm) and smooth vitreous surfaces that limit pozzolanic reactivity (i_{90} of 0.78 vs. 0.99 for ceramic). Figure 11. Presents the evolution

of flexural strength which mirrored the trends observed for compressive strength, thus reinforcing the reliability of the results.

The superior long-term performance of mortars containing brick and ceramic fillers can be attributed to the lower W/C ratios, enhanced microstructural densification, and pozzolanic reactions leading to formation of C-A-H and C-A-S-H gels, especially due to high alumina content [14,19]. On the other hand, glass fillers, characterized by low alumina content, primarily facilitated the delayed generation of secondary C-S-H gels after prolonged curing periods. Notably, all mortars incorporating industrial waste-derived fillers achieved compressive strengths exceeding 80 MPa at 28 days. According to the ACI 363R-10 report [38], these mortars qualify as high-performance mortars (HPMs), given that the threshold for high-strength classification typically starts at 55 MPa and may vary regionally. In contexts where conventional concretes routinely reach 62 MPa, mortars achieving strengths in the range of 83–103 MPa are considered high-performance. Accordingly, the mortars produced in this investigation demonstrate mechanical performance consistent with HPM standards

3.5 Dynamic Modulus of Elasticity

The dynamic modulus of elasticity (Ed), determined via the UPV technique, measures the propagation speed of ultrasonic waves through the material, where faster wave passage reflects denser and stiffer microstructures, resulting in higher Ed values. As noted by Neville [39], this non-destructive technique offers valuable information about the internal structure and mechanical properties of cementitious materials. The evolution of Ed over time for various SCM formulations is presented in Table 6.

Table 6. Dynamic Modulus of Elasticity (Ed, GPa) of SCMs

SCM	LS	Gl	Br	Cr
28days	46.4	47.0	50.8	49.2
365days	50.5	53.3	56.1	55.1

Consistent with compressive strength trends, Ed increased progressively across all formulations up to 365 days of curing, reflecting continued hydration and pozzolanic reactions that enhance matrix densification. This time-dependent evolution aligns with findings by Benaicha et al. [40], who observed similar patterns in self-compacting concrete incorporating various mineral additions. At all ages, mortars incorporating alternative fillers demonstrated notably higher Ed values than the reference mortar (SCM LS). At 28 days, relative increases in Ed were recorded as +1.24% for SCM Gl, +9.44% for SCM Br, and +5.86% for SCM Cr. These enhancements became more pronounced at 365 days, reaching +5.59%, +11.11%, and +9.16%, respectively. These results are consistent with research by Kou and Poon [41], who reported enhanced elastic properties in concrete containing recycled glass powder.

The superior Ed values observed in mortars with waste-based fillers can be ascribed to the development of a denser and more refined microstructure, attributed to both the physical filler effect and the pozzolanic reactivity of glass, brick, and ceramic powders. According to Mehta and Monteiro [42] the generation of additional calcium silicate hydrate (C-S-H) and calcium aluminosilicate hydrate (C-A-S-H) gels leads to a stiffer matrix with reduced porosity, thereby facilitating faster ultrasonic pulse propagation and resulting in higher calculated Ed values. This microstructural refinement has been confirmed by Yusuf et al. [43] using scanning electron microscopy on mortars containing pozzolanic materials.

The ranking of mortars based on dynamic modulus (SCM Br > SCM Cr > SCM Gl > SCM LS) closely parallels that observed for compressive strength, reinforcing the well-established correlation between these two properties in cementitious systems. This strong correlation between Ed and compressive strength is well-established for cementitious materials, as demonstrated by Popovics [44] and Trtnik et al. [45], who found that both properties are fundamentally linked to the quality and density of the hydrated paste and the interfacial transition zone.

The results confirm that the incorporation of industrial waste fillers not only enhances the mechanical performance but also significantly improves the stiffness of self-compacting mortars—an outcome particularly beneficial for structural applications where high rigidity and minimal deformation as emphasized by Breysse [46] in his comprehensive review on non- destructive assessment of concrete structures. Enhancements in Ed of up to 11.11% were recorded at 365 days for mortars incorporating brick-based filler.

4. Conclusion

This study systematically investigated the potential for valorizing industrial waste streams namely ground glass, sanitary ceramic, and brick waste as alternative fillers in self-compacting mortar (SCM) formulations. Based on the experimental results obtained, the following key conclusions are drawn:

- For the target slump flow (250 ± 10 mm), mortars with brick/ceramic fillers achieved comparable fluidity at reduced water-cement ratios (0.35 vs. 0.40 for limestone filler), indicating lower water demand. However, these mixes exhibited V-Funnel flow times exceeding EFNARC limits (20 s and 14 s vs. 9 s for control), revealing higher viscosity. Optimization of superplasticizer dosage or particle gradation is recommended.
- Mortars with waste-derived fillers showed marginally lower fresh densities (2.31 to 2.33 g/cm^3) compared to limestone-based mixes (2.35 g/cm^3), attributable to the lower specific gravity of glass (2.51), brick (2.56), and ceramic (2.53) versus limestone (2.62). This reduction, while modest (<2%), may benefit weight-sensitive applications.
- The use of brick and ceramic fillers accelerated the early hydration process, as evidenced by peak temperature measurements occurring at 21 hours, in contrast to 22.5 hours for mortars containing limestone and glass fillers.
- Mortars formulated with alternative fillers exhibited significant long-term improvements in mechanical strength. After 356 days of curing, compressive strengths increased by 37% and 34% for brick and ceramic fillers, respectively, and by 31% for glass fillers, relative to the reference mortar.
- The incorporation of waste-derived fillers led to a marked enhancement in the dynamic modulus of elasticity, indicative of the formation of a denser and stiffer microstructural framework. Notably, brick-filled mortars exhibited the highest improvement, with Ed values increasing by up to 11.11% at 365 days.
- Among the fillers evaluated, ceramic fillers demonstrated superior performance across most criteria, attributable to their high fineness and favorable chemical composition, which promoted pozzolanic activity.

Overall, the findings underscore the considerable potential of valorizing industrial waste materials as efficient and sustainable alternatives to traditional fillers in SCMs. The integration of these materials not only mitigates environmental impacts associated with waste disposal and resource extraction but also enhances the mechanical properties of mortars to a level consistent with high-performance standards.

Future research should aim to optimize filler dosage levels and explore the synergistic effects of combining multiple waste-derived fillers to further enhance performance and broaden the applicability of SCM technologies.

References

[1] Andrew RM. Global CO2 emissions from cement production. Earth Syst Sci Data. 2018;10(1):195-217. https://doi.org/10.5194/essd-10-195-2018

[2] Okamura H, Ouchi M. Self-compacting concrete. J Adv Concr Technol. 2003;1(1):5-15. https://doi.org/10.3151/jact.1.5

[3] Elemam WE, Abdelraheem AH, Mahdy MG, Tahwia AM. Optimizing fresh properties and compressive strength of self-consolidating concrete. Constr Build Mater. 2020;249:118781. https://doi.org/10.1016/j.conbuildmat.2020.118781

[4] Choudhary R, Gupta R, Nagar R. Impact on fresh, mechanical, and microstructural properties of high strength self-compacting concrete by marble cutting slurry waste, fly ash, and silica fume. Constr Build Mater. 2020;239:117888. https://doi.org/10.1016/j.conbuildmat.2019.117888
[5] Esping O. Effect of limestone filler BET(H2O)-area on the fresh and hardened properties of self-compacting concrete. Cem Concr Res. 2008;38(7):938-44. https://doi.org/10.1016/j.cemconres.2008.03.010
[6] Khoman RK, Owaid HM. Development of sustainable high performance self-compacting concrete incorporating natural and waste pozzolanic materials. Res Eng Struct Mater. 2025 Jul. http://dx.doi.org/10.17515/resm2025-912ma0520rs
[7] Kumar RV, Prabaghar A. Evaluation of strength of self-compacting concrete having dolomite powder as partial replacement for cement. Res Eng Struct Mater. 2023;10(2):445-59. http://dx.doi.org/10.17515/resm2023.48ma0725rs
[8] NAA, Muthusamy N, Natarajan B, PR. Optimization of high performance concrete composites by using nano materials. Res Eng Struct Mater. 2023;9(3):843-59. http://dx.doi.org/10.17515/resm2022.602ma1213
[9] Akinpelu MA, Amao AO, Salman A-SM, Gabriel DS. Sustainable self-compacting concrete: A study on the combined effects of waste glass powder and metakaolin as cement replacements. Res Eng Struct Mater. 2025 Mar. http://dx.doi.org/10.17515/resm2025-610ma0105rs
[10] Dahamma EK, Hama SM, AL-Jumaily IA. Effect of nano-sized clay and waste glass powder on rheological and hardened properties of self-compacting concrete. Res Eng Struct Mater. 2023;9(3):743-61. https://doi.org/10.17515/resm2022.563ma1026
[11] Vanjare MB, Mahure SH. Experimental investigation on self-compacting concrete using glass powder. Int J Eng Res Appl. 2012;2(3).
[12] Safi HU, Behsoodi MM, Sharifi MN. A comparative analysis of compressive and flexural strength in concrete with partial cement replacement using waste glass powder. Indones J Mater Res. 2024;2(1):1. https://doi.org/10.26554/ijmr.20242120
[13] Si-Ahmed M, Kenai S. Behavior of self-compacting mortars based on waste brick powder. Curr Mater Sci. 2020;13(1):39-44. https://doi.org/10.2174/2666145413666200219091459
[14] Karatas M, Turk K, Açıkgenç Ulaş M, Ulucan Z. Effect of Elazig region waste brick powder on strength and viscosity properties of self-compacting mortar. 9th International Congress on Advances in Civil Engineering, ACE'10, Karadeniz Technical UniversityAt: Trabzon, Turkey. 2010.
[15] Zhao Z, Grellier A, El Karim Bouarroudj M, Michel F, Bulteel D, Courard L. Substitution of limestone filler by waste brick powder in self-compacting mortars: Properties and durability. J Build Eng. 2021;43:102898. https://doi.org/10.1016/j.jobe.2021.102898
[16] EN 197-1:2011. Cement - Part 1: Composition, specifications and conformity criteria for common cements.
[17] EN 934-2:2009. Admixtures for concrete, mortar and grout - Part 2: Concrete admixtures.
[18] EFNARC. Specification and guidelines for self-compacting concrete. European Federation of Producers and Applicators of Specialist Products for Structures; 2002.
[19] EN 1015-6:1998. Methods of test for mortar for masonry - Part 6: Determination of bulk density.
[20] NF EN 196-9. Methods of testing cement - Part 9: Heat of hydration - Semi-adiabatic method.
[21] EN 196-1:2016. Methods of testing cement - Part 1: Determination of strength.
[22] ASTM C597-22. Standard test method for ultrasonic pulse velocity through concrete.
[23] Corinaldesi V, Moriconi G. Characterization of self-compacting concretes prepared with different fibers and mineral additions. Cem Concr Compos. 2011;33(5):596-601. https://doi.org/10.1016/j.cemconcomp.2011.03.007
[24] He X, Fang Y, Peng Y, Shen W, Qiao D, Wang M. Mortar's rheological property and workability investigation based on morphology impact factor for graded sand particles. Constr Build Mater. 2022;328:126987. https://doi.org/10.1016/j.conbuildmat.2022.126987
[25] Ge W, et al. Study on the workability, mechanical property and water absorption of reactive powder concrete. Case Stud Constr Mater. 2023;18:e01777. https://doi.org/10.1016/j.cscm.2022.e01777
[26] Li Y, et al. Effect of clay minerals on polycarboxylate superplasticizer and methods to improve the performance of concrete containing clay: a review. J Mater Sci. 2023;58(39):15294-313. https://doi.org/10.1007/s10853-023-08989-0
[27] Felekoğlu B, Tosun K, Baradan B, Altun A, Uyulgan B. The effect of fly ash and limestone fillers on the viscosity and compressive strength of self-compacting repair mortars. Cem Concr Res. 2006;36(9):1719-26. https://doi.org/10.1016/j.cemconres.2006.04.002
[28] Uysal M, Sumer M. Performance of self-compacting concrete containing different mineral admixtures. Constr Build Mater. 2011;25(11):4112-20. https://doi.org/10.1016/j.conbuildmat.2011.04.032
[29] Pang L, Liu Z, Wang D, An M. Review on the application of supplementary cementitious materials in self-compacting concrete. Crystals. 2022;12(2):180. https://doi.org/10.3390/cryst12020180

[30] Lawrence P, Cyr M, Ringot E. Mineral admixtures in mortars: Effect of inert materials on short-term hydration. Cem Concr Res. 2003;33(12):1939-47. https://doi.org/10.1016/S0008-8846(03)00183-2
[31] Wild S, Khatib JM, Jones A. Relative strength, pozzolanic activity and cement hydration in superplasticised metakaolin concrete. Cem Concr Res. 1996;26(10):1537-44. https://doi.org/10.1016/0008-8846(96)00148-2
[32] Kadri EH, Aggoun S, De Schutter G, Ezziane K. Combined effect of chemical nature and fineness of mineral powders on Portland cement hydration. Mater Struct. 2010;43(5):665-73. https://doi.org/10.1617/s11527-009-9519-6
[33] Berodier E, Scrivener K. Understanding the Filler Effect on the Nucleation and Growth of C-S-H. J Am Ceram Soc. 2014 Dec;97(12):3764-73. https://doi.org/10.1111/jace.13177
[34] Ahmad S, Khan RA, Shamim S, Chandra U. Effect of waste ceramic sanitary ware as partial replacement of aggregates and cement in concrete. Innov Infrastruct Solut. 2023;8(8):205. https://doi.org/10.1007/s41062-023-01166-x
[35] Zhang P, Zhang P, Wu J, Guo Z, Zhang Y, Zheng Y. Mechanical properties and durability of sustainable concrete manufactured using ceramic waste: A review. J Renew Mater. 2023;11(2):937-74. https://doi.org/10.32604/jrm.2022.023290
[36] Bouleghebar Y, Bentchikou M, Boukendakdji O, El-Hadj K, Debieb F, Maisarah A. The effect of brick and glass powder on the mechanical properties and porosity of self-compacting mortar. J Appl Eng Sci. 2023;13(1):39-52. https://doi.org/10.2478/jaes-2023-0006
[37] Shi C, Wu Y, Riefler C, Wang H. Characteristics and pozzolanic reactivity of glass powders. Cem Concr Res. 2005;35(5):987-93. https://doi.org/10.1016/j.cemconres.2004.05.015
[38] Ghosh SK, American Concrete Institute, editors. Report on structural design and detailing for high-strength concrete in moderate to high seismic applications. 1st ed. Farmington Hills, MI: American Concrete Institute; 2007.
[39] Neville AM. Properties of concrete. Essex: Pearson Education Limited; 2011.
[40] Benaicha M, Hafidi Alaoui A, Jalbaud O, Burtschell Y. Dosage effect of superplasticizer on self-compacting concrete: Correlation between rheology and strength. J Mater Res Technol. 2019;8(2):2063-9. https://doi.org/10.1016/j.jmrt.2019.01.015
[41] Kou SC, Poon CS. Properties of self-compacting concrete prepared with recycled glass aggregate. Cem Concr Compos. 2009;31(2):107-13. https://doi.org/10.1016/j.cemconcomp.2008.12.002
[42] Mehta PK, Monteiro PJM. Concrete: Microstructure, properties, and materials. New York: McGraw-Hill; 2006.
[43] Yusuf MO, et al. Microstructural characteristics, modeling of mechanical strength and thermal performance of industrial waste glass blended concrete. Appl Sci. 2022;12(17):8600. https://doi.org/10.3390/app12178600
[44] Analysis of the concrete strength versus ultrasonic pulse velocity relationship. Semantic Scholar.
[45] Trtnik G, Kavčič F, Turk G. Prediction of concrete strength using ultrasonic pulse velocity and artificial neural networks. Ultrasonics. 2009;49(1):53-60. https://doi.org/10.1016/j.ultras.2008.05.001
[46] Breysse, D. Nondestructive evaluation of concrete strength: An historical review and a new perspective by combining NDT methods. Construction and Building Materials. 2012;33,139-163. https://doi.org/10.1016/j.conbuildmat.2011.12.103

Research on Engineering Structures & Materials
www.jresm.org
MIM Research Group

Research Article

Enhancing the performance of cold bitumen emulsion mixtures with coir and glass fibres: Experimental and numerical analysis

Fatimah Fahem Al-Khafaji *,a

Environmental Engineering Dept., Faculty of Engineering, University of Babylon, Babylon, Iraq

Article Info

Article History:

Received 27 Mar 2025

Accepted 25 June 2025

Keywords:

Cold bitumen emulsion mixtures;
Hot mix asphalt;
Natural waste coir fibres;
Synthetic glass fibres;
Finite element analysis;
ABAQUS

Abstract

Cold bitumen emulsion mixtures (CBEMs) offer significant benefits over hot mix asphalt (HMA), including sustainable energy consumption, eco-friendliness, and cost-effectiveness. However, their adoption is limited due to prolonged curing times and low early-life strength. This study examines the reinforcing process of CBEMs with both coir fibres as eco-friendly waste additives and glass fibres as synthetic additive to enhance crack resistance and prolong pavement life. The developed CBEMs are evaluated in terms of tensile strength, creep behavior, fracture toughness, and rutting resistance, using an optimal fibre length of 15 mm and a content of 0.4% by the aggregate weight. Employing both coir and glass fibre reinforcement within CBEMs led to increase the tensile strength by 47% and 87%, respectively. Creep strain was reduced by 33.3% and 56.7% at 60° C after 4000 seconds, while at 40° C, the reductions reached 10% and 66.7%. Fracture toughness increased by 52% and 85%, and rutting depth decreased by 43% and 56%, respectively. The best results were achieved by the glass fibre-reinforced CBEM, which exhibited the highest structural performance, durability, and moisture resistance. The implemented finite element modelling (FEM) using ABAQUS software strongly aligns with experimental results in terms of performance behavior. The adopted statistical analysis confirmed considerable alignment between experimental and numerical results regarding fracture toughness and crack length, thereby validating the reliability and accuracy of the FEM approach.

© 2025 MIM Research Group. All rights reserved.

1. Introduction

CBEMs have proven to be an efficient substitute for conventional HMA, as their production requires less energy due to processing at lower temperatures [1]. CBEMs produce fewer emissions while consuming less fuel, thereby contributing to cost reduction [2]. The longer curing time and initial weakness in such mixtures limited their large-scale application in road paving projects. In order to address these matters, some new researches have tried to enhance the mechanical properties of CBEMs by adding reinforcing material in the form of coir fibres (natural additives) and glass fibres (synthetic additives) [3]. Coir fibers are actually obtained from coconut husk (one of the residues from agriculture) and glass fibers are generated from silica glass with excellent strength in addition to light weight [4]. The incorporation of these reinforcements greatly improves the tensile strength, rutting resistance, stiffness, and cracking resistance of CBEMs, providing a more effective alternative to conventional HMA.

The semi-circular bending (SCB) test has emerged as a reliable method for assessing the fracture characteristics of asphalt mixtures offering valuable insights into how cracks develop and

*Corresponding author: mat.fatimah.fahem@uobabylon.edu.iq
[a]orcid.org/0009-0004-3050-846X
DOI: http://dx.doi.org/10.17515/resm2025-786ma0327rs

propagate under load [5]. In addition, indirect tensile stiffness modulus (ITSM) test, creep test, and Hamburg wheel-track test (HWTT) are commonly used to evaluate the performance of CBEMs. Finite Element Modeling (FEM) in pavement engineering enables a comprehensive evaluation of material responses under diverse loading scenarios [6]. The extended finite element method (XFEM), in particular, excels at simulating crack propagation without the need for remeshing, making it a valuable technique for assessing the performance of fiber-reinforced materials [7]. A statistical approach has been included in this study to confirm the alignment between the experimental and numerical results.

1.1 Literature Review

The literature on CBEMs highlights several studies that have explored various methods for improving their performance. Wu S et al. [8], reviewed various fibres in asphalt pavements, highlighting their performance and test methods. Basalt, polyester, cellulose, steel, glass, lignin, and polypropylene fibres were found to improve properties such as rutting resistance, tensile strength, fatigue life, and moisture resistance, with tests like Marshall stability, indirect tensile strength, and fatigue life tests used for evaluation. This summary provided a foundation for identifying the novelty of the current study. Solak H et al. [9] examined the use of synthetic fibers in asphalt pavements, highlighting improvements in tensile strength, fatigue resistance, rutting, and moisture damage. The study summarized the effectiveness of polypropylene and polyester fibers and presented common evaluation methods, including the Marshall stability test, indirect tensile strength test, and wheel tracking test. This review provided a clear foundation for optimizing fiber-reinforced asphalt mixtures. Addae DT et al. [10] conducted a comprehensive review of cold mix asphalt (CMA) mixtures, examining the effects of modifiers, curing conditions, and compaction methods on their mechanical, functional, and long-term performance. The study highlighted improvements in stiffness, rutting resistance, moisture susceptibility, and aging durability, providing a foundation for developing sustainable and durable CMA mixtures. Jain S et al. [11] provided an overview of CMA technology, discussing its materials, design procedures, field applications, and performance characteristics. They emphasized CMA's cost-effectiveness, lower energy consumption, and environmental benefits compared to hot mix asphalt. The study also addressed challenges such as lower early strength and longer curing times, highlighting the need for further research to enhance CMA's mechanical properties and broaden its applications.

Guo Q et al. [12] explored the effects of various fibres, including glass, basalt, and steel, on asphalt mixtures, specifically their impact on low-temperature properties and cracking resistance. The study reveals that fibre-reinforced asphalt concrete (FRAC) demonstrates greater fracture energy (FE) and dissipated creep strain energy (DCSE) than the control concrete. This research contributed to the development of more durable asphalt pavements in cold climates.

Li Z et al. [13] analyzed the characteristics of bagasse fibers and their impact on asphalt mixtures. The study focused on surface modifications to improve fiber compatibility with asphalt, enhancing high-temperature deformation resistance and water stability, though slightly reducing low-temperature performance. The findings suggested that with proper treatment, bagasse fibers could effectively reinforce asphalt pavements. In addition, Malik et al. [14], carried out a laboratory-driven investigation into the performance of CBEMs incorporating waste glass as a partial replacement for fine aggregates. The study aimed to evaluate the mechanical properties and durability of these modified mixtures. Key findings indicated that the inclusion of waste glass enhanced the stiffness and rutting resistance of the CBEMs, while maintaining acceptable levels of moisture susceptibility. These results suggest that utilizing waste glass in CBEMs can be a sustainable approach to improving pavement performance while addressing environmental concerns related to glass waste disposal. Moreover, Briceño-Balza et al. [15], performed a study on the indirect tensile strength and stability of fiber-reinforced cold asphalt mixes, incorporating synthetic microfibers. The results showed that adding 0.05% and 0.10% microfiber slightly weakened the mixtures, while 0.15% improved performance.

The study, prepared by Hubbard-field method with ITS tests, revealed the potential of microfibers to improve the properties of cold asphalt. Overall, the literature underscores the potential of fibre-

reinforced CBEMs as a sustainable alternative to HMA, with FEM providing a robust framework for analyzing and predicting their performance under real-world conditions.

1.2 Research Novelty

The novelty of this study is to exploit natural and synthetic fibres to improve the mechanical properties of cold asphalt mix in terms of crack resistance, tensile strength, rutting and creep resistance. The integration of FEM in ABAQUS to simulate fibre reinforcement effects is a novel approach, offering a detailed understanding of material performance and validating the superior performance of the adopted fibres through both experimental and numerical methods. Conducting a statistical analysis to confirm the alignment between the experimental and the conducted FAM results in terms of efficiency and structural integrity.

1.3 Research Main Objectives

- To investigate the influence of natural and synthetic fibres in boosting the crack resistance, tensile strength, rutting and creep resistance of cold asphalt mixture.
- To use of FEA with ABAQUS to simulate the effects of fibre reinforcement on CMA.
- To compare the performance of different fibres, identifying the most effective reinforcement method for enhancing the longevity and durability of pavements.
- To confirm the alignment between the experimental and the simulated FAM results using statistical approach.

2. Materials and Testing

2.1 Materials

The research focused on selecting a suitable cold bituminous emulsion mixture (CBEM) based on material availability and full-scale testing. Crushed granite was used as the aggregate, with its gradation and physical properties detailed in Tables (1) and (2). The aggregates were prepared in accordance with BS EN 933-1 standards [16]. A cationic slow-setting bituminous emulsion (C50B3) with a 40-60 penetration grade was chosen for its strong bonding properties. Limestone dust, comprising approximately 6% of the aggregate's weight, was used as a filler. The used additives are selected from two origins as follow:

- Coir fibres, as natural additives, are extracted from the husk of coconuts, which are considered waste materials, as shown in Figure (1). Their utilization not only reduces environmental waste but also promotes sustainable resource management by repurposing discarded materials. They are strong, durable, and biodegradable, making them an eco-friendly material [17].
- Glass fibres, as synthetic additives, are thin, strong, and lightweight fibres made from silica-based glass as shown in Figure (2), commonly used as reinforcement in composite materials [18]. They are produced by melting glass and drawing it into fine strands, offering high strength, durability, and resistance to heat and chemicals.

Table 1. Maximum aggregate size of 14 mm [19]

Size of the sieve (mm)	14	10	6.3	2	1	0.063
Passing precents (standard limits)	100	77 – 83	52 – 58	25 – 31	14 – 26	6
Passing precents (approved gradation)	100	80	55	28	20	6

Table 2. Physical properties of aggregate

Physical properties	Coarse Agg.	Fine Agg.
Bulk density by (g/cm^3) [20]	2.87	2.76
Apparent density by (g/cm^3) [20]	2.93	2.83
Water absorption by (%) [20]	0.7	1.6

Fig. 1. Coir fibres

Fig. 2. Glass fibres

2.2 Optimization of Fibres as Reinforcement Material

Glass fibers were selected to optimize and enhance the stiffness of CBEM. Laboratory tests assessed the effects of different fiber lengths (10 mm, 15 mm, and 20 mm) and contents (0.3%, 0.4%, and 0.5% of the aggregate's total weight). The results identified the optimal fiber content and length as 0.4% and 15 mm, respectively, as shown in Figure (3). For the record, the same optimum fibre content and length were adopted for the coir fibres on order to conduct a suitable comparison between both additives within CBEMs, acknowledging that their effectiveness differ due to the distinct properties for each fibre type. The addition of coir and glass fibres to CBEMs can reduce workability by increasing internal friction and viscosity, affecting mixing and construction feasibility. Although, the conducted dosage of fiber content for both types was selected at 0.4% by weight of aggregate as the optimum dosage based on multiple trials to ensure a balanced blend. This level provided improved mechanical performance with minimal impact on workability and compaction, maintaining practical constructability for both coir and glass fibre-reinforced CBEMs.

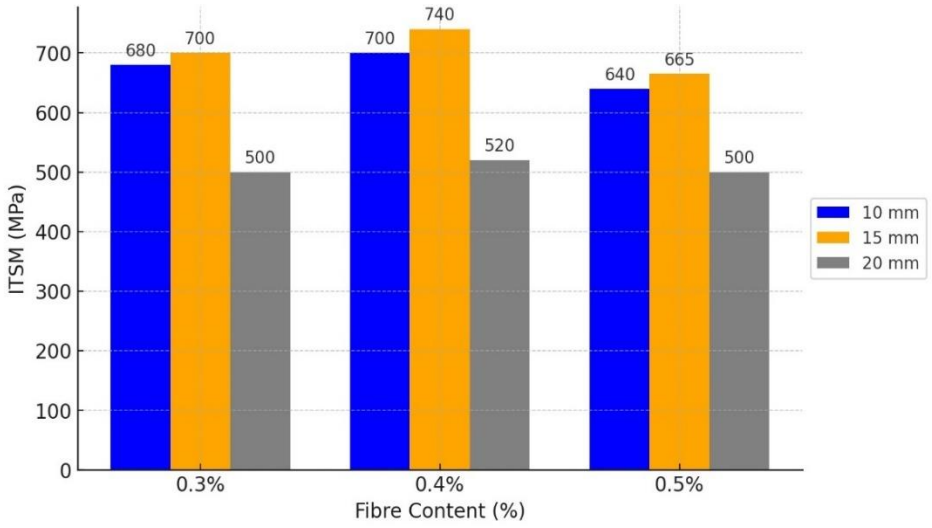

Fig. 3. Optimization of glass fibres

2.3 Mix Design

The Cold bitumen emulsion mixtures (CBEM) mix design was developed following the Asphalt Institute's MS-14 methodology [21], incorporating pre-mixing water contents ranging from 3% to 6% by aggregate mass. Using equations (1) and (2), the Initial Emulsion Content (IEC) was calculated as 6.16%. After several trials, it was conducted that a 3% pre-moisture content ensured proper coverage for CBEM preparation.

$$P = 0.7 \times (0.5C + 0.05A + 0.1B) \quad (1)$$

Where: P: Initial content of the bituminous residual (% of total dry weight of aggregate); C: The passed weight of aggregate from sieve 0.075 mm; A: The retained weight of aggregate on sieve 2.36 mm; B: The retained weight of aggregate on sieve 0.075 mm and passed sieve 2.36 mm.

$$I.E.C = \frac{P}{X} \quad (2)$$

Where: $I.E.C$: Initial emulsion content (% of total mixture mass); X: Bituminous emulsion content. The calculated initial emulsion content was 12.35% of aggregate weight. CBEM samples were prepared using a mixer as in Figure (4), combining water, filler and aggregate for 1 minute at low rapidity. The emulation of bitumen was gradually introduced after 30 seconds, while mixing was maintained for an additional 1.5 minutes.

Fig. 4. Mixer machine

2.4 Testing Procedures

After determining the optimal mixtures, the next step was studying the importance of crack propagation on the engineering and material characteristics of CBEMs for the cold course of surface. This was achieved via a sequence of experimental tests, including indirect tensile stiffness modulus test (ITSM), semi-circular bending test (SCB), and creep test. These assessments measured the modules of stiffness and the ability of CMA to resist propagation of crack.

2.4.1 Crack Propagation Test (Semi-Circular Bending - SCB)

The fracture toughness or tensile strength of bituminous mixtures was measured using the bending test (SCB), following BS EN 12697-44 [22]. CBEM mixtures, prepared as described in section 2.3, were compacted into half-cylinder specimens measuring 150 mm in diameter and 50 mm in thickness. A notch, 2 mm in wide and 10 mm in deep, was made at the center of each specimen to evaluate crack growth, in accordance with the standard [23], as shown in Figure (5).

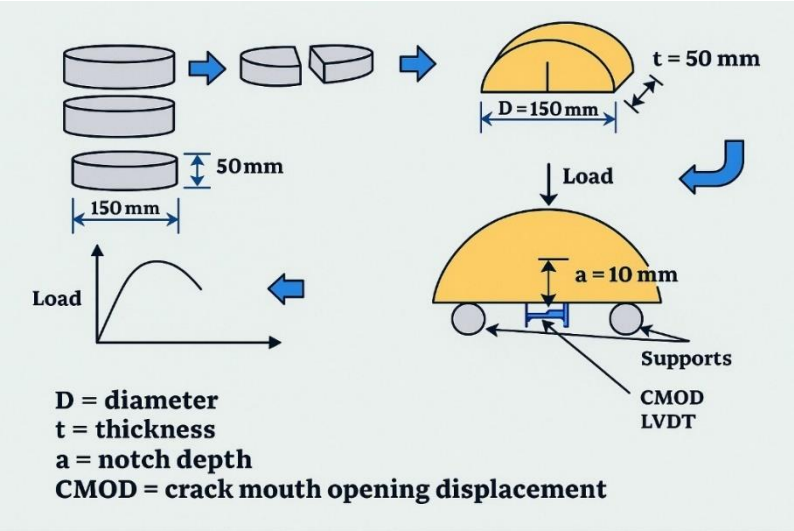

Fig. 5. The diagram of semi-circle bending samples preparation and test procedure

The bottom of each semi-circular sample experienced tensile stress by applying a load from the top with a three-point bending system at 5° C, as illustrated in Figure (5). In accordance with BS EN 12697-44 [22], the test was performed at a constant deformation rate of 5 mm/min, gradually increasing the load until the maximum force (F max) was achieved. This force is directly related to the specimen's resistance to crack propagation (fracture toughness). Figures (6) and (7) illustrate a demonstration of semi-circle bending evaluation. Through the test, the maximum load prior to the failure being recorded [23]. By means of BS EN 12697-44 [22], the concentrated stress at failure (σ_{max}) and toughness of fracture (Kic) were considered using the following equations:

$$\sigma_{max} = \frac{4.263 \times F_{max}}{D \times t^2} \tag{3}$$

Where: *D*: Specimen diameter by (mm); *t*: Specimen thickness by (mm); *F max*: Maximum force by (N); *σ max*: Maximum level of stress at failure by (N/mm²).

$$Kic = \sigma_{max} \times f\left(\frac{a}{w}\right) \tag{4}$$

Where: *W*: Specimen height by (mm); *A*: Specimen notch depth by (mm); *σ max*: Maximum stress at failure by (N/mm²); *f (a/W)*: Specimen geometric factor = 5.956 at 9 < a < 11 (mm) and 70 < W < 75 (mm).

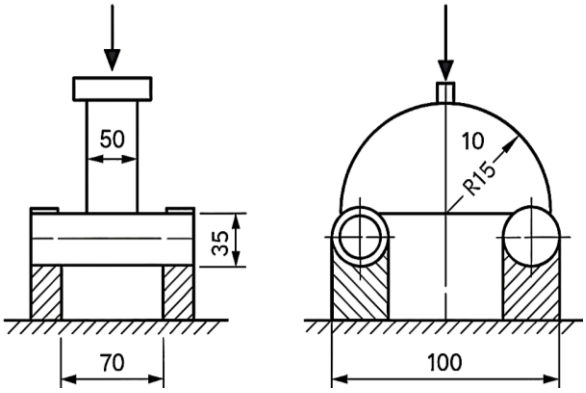

Fig. 6. The specimen of semi- circle plan

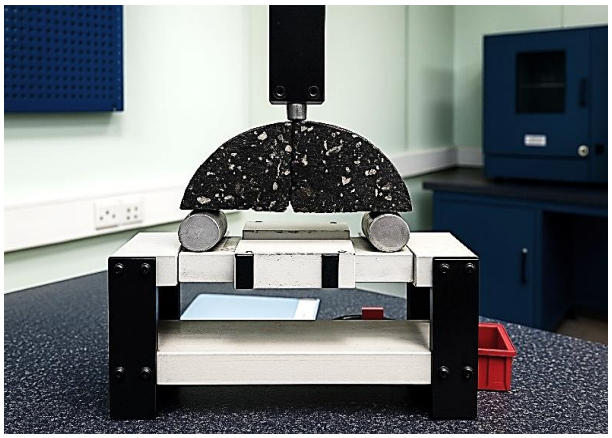

Fig. 7. The semi-circle specimens in laboratory

2.4.2 Indirect Tensile Stiffness Modulus (ITSM) Test

The ITSM test, conducted in accordance with BS EN 12697-26 [24], evaluates the stiffness modulus of cold mix asphalt (CMA) samples under varying curing times and temperatures. This test operates by applying a repeated compressive load along the vertical diametrical plane of a cylindrical specimen, generating indirect tensile stress within the material. The corresponding horizontal deformation is measured to determine the stiffness modulus, which represents the asphalt mixture's ability to resist deformation under loading conditions. Figure (8) illustrates the ITSM testing apparatus.

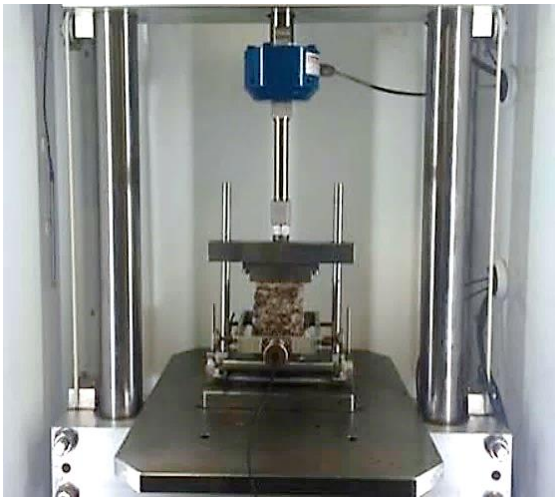

Fig. 8. Apparatus for indirect tensile test

2.4.3 Creep Test

The test of creep, focused in conformity of BS EN 12697-25 [25], evaluated the viscoelastic properties of CBEMs under sustained loading, comparing reinforced and unreinforced samples. In this test, a static load is exerted on a cylindrical asphalt sample at a specified temperature for a defined period. The resulting time-dependent deformation (creep) is measured to evaluate the mixture's ability to resist rutting and long-lasting deformation under continuous traffic loads [25]. Figure (9), depicts the creep test configuration.

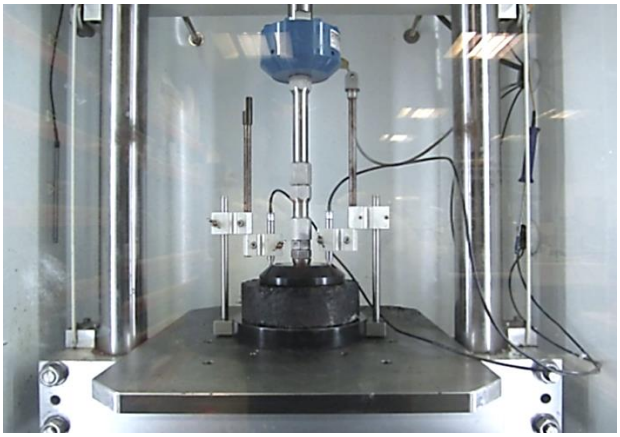

Fig. 9. Creep test configuration

2.4.4 Humburg Wheel Track Test

The HWTT, which is described by EN 12697-22 [26], is European standard to assess rutting resistance and moisture susceptibility of asphalt mixes under simulated traffic loading. A standard load of 705 ± 10 N is applied by a steel or rubber wheel that applies repeatedly over the surface of the sample, which is brought to raised temperature (usually 50° C) and positioned underwater as

shown below in Figure (10). The test measures rut depth over time and runs for a maximum of 20,000-wheel repetitions or when a target rut depth is achieved, and gives insight into how resistant an asphalt mixture is to permanent deformation and moisture damage, especially for surface courses under climatically sensitive conditions. Test samples prepared for the Hamburg wheel-track test are normally about 320 mm long, 260 mm wide, and 60 mm thick, as presented in Figure (11). These slabs are compacted within a specified mold by using a lab pneumatic roller compactor, as shown in Figure (12) according to EN 12697-33 and ASTM D8079 [26].

Fig. 10. The apparatus of Hamburg wheel-track

Fig. 11. Hamburg wheel-track sample

Fig. 12. Lab pneumatic roller compactor

3. Finite Element Modelling FEM

Finite element analysis in ABAQUS involved splitting the model to tiny elements, which were linked by shared nodes. The integrating of elements and nodes created a mesh, with mesh density determined by the number of elements. Loads and boundary conditions were applied to the nodes, and stress analysis was performed to assess strain, displacement and stresses in every component [27]. The extended finite element analysis (XFEA) was used for crack growth modeling, differing from conventional FEM by introducing special displacement functions based on the partition of unity theory. This approach prevents discontinuities within elements and allows crack growth simulation without remeshing [27].

The fracture progression in the SCB test was analyzed using XFEM, as illustrated in Figure (13), which depicts crack growth prediction for a CBEM specimen with a 10 mm notch depth. Additionally, Figure (14), presents the maximum load and displacement of a typical cold mix asphalt sample at 97 second of step time, which is the best period for evaluating the material's

performance. In addition, ABAQUS software was used to simulate the experimental rut behavior, enabling accurate prediction of rut depth progression under repeated loading.

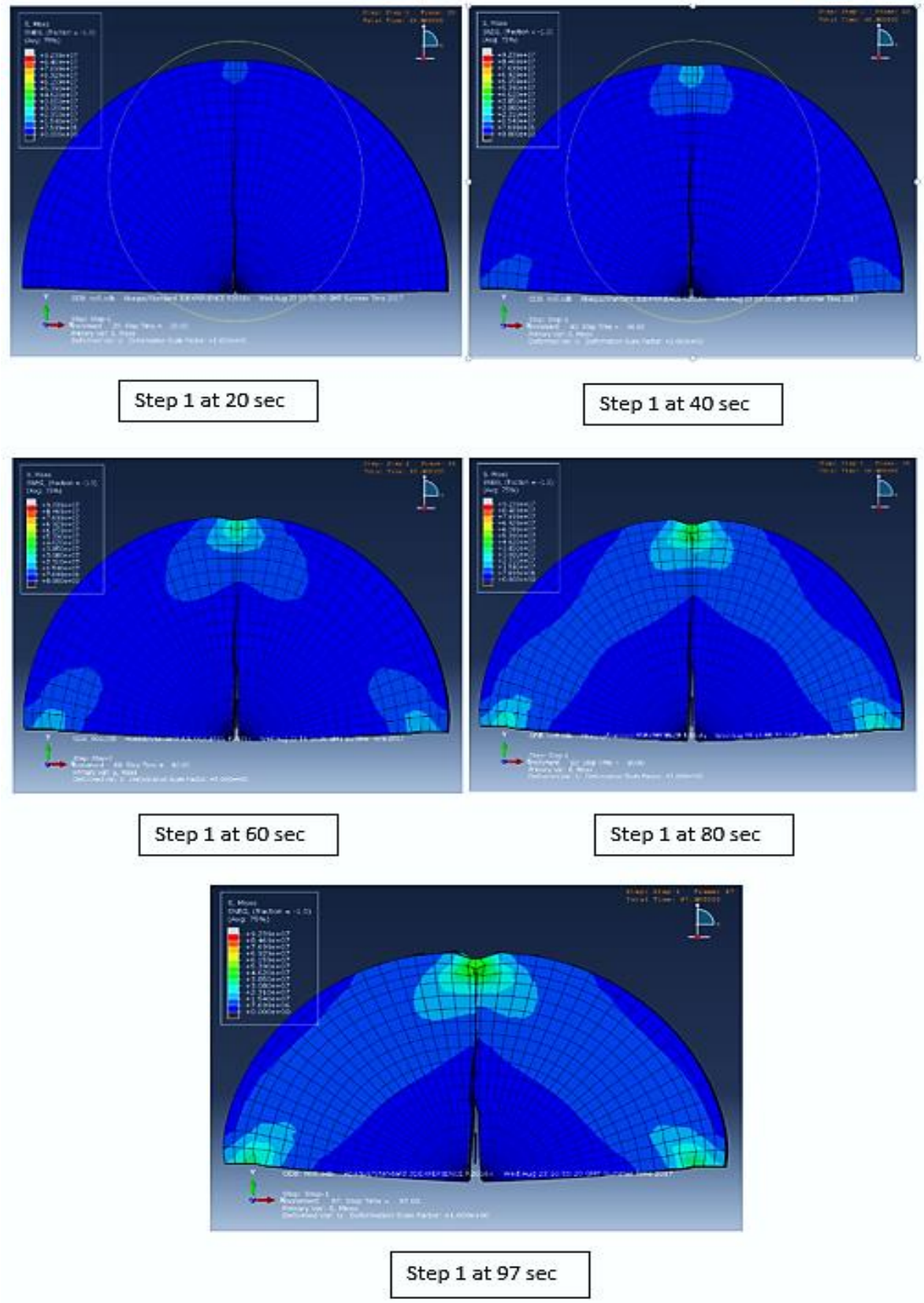

Fig. 13. Propagation of crack for conventional semi-circle specimen

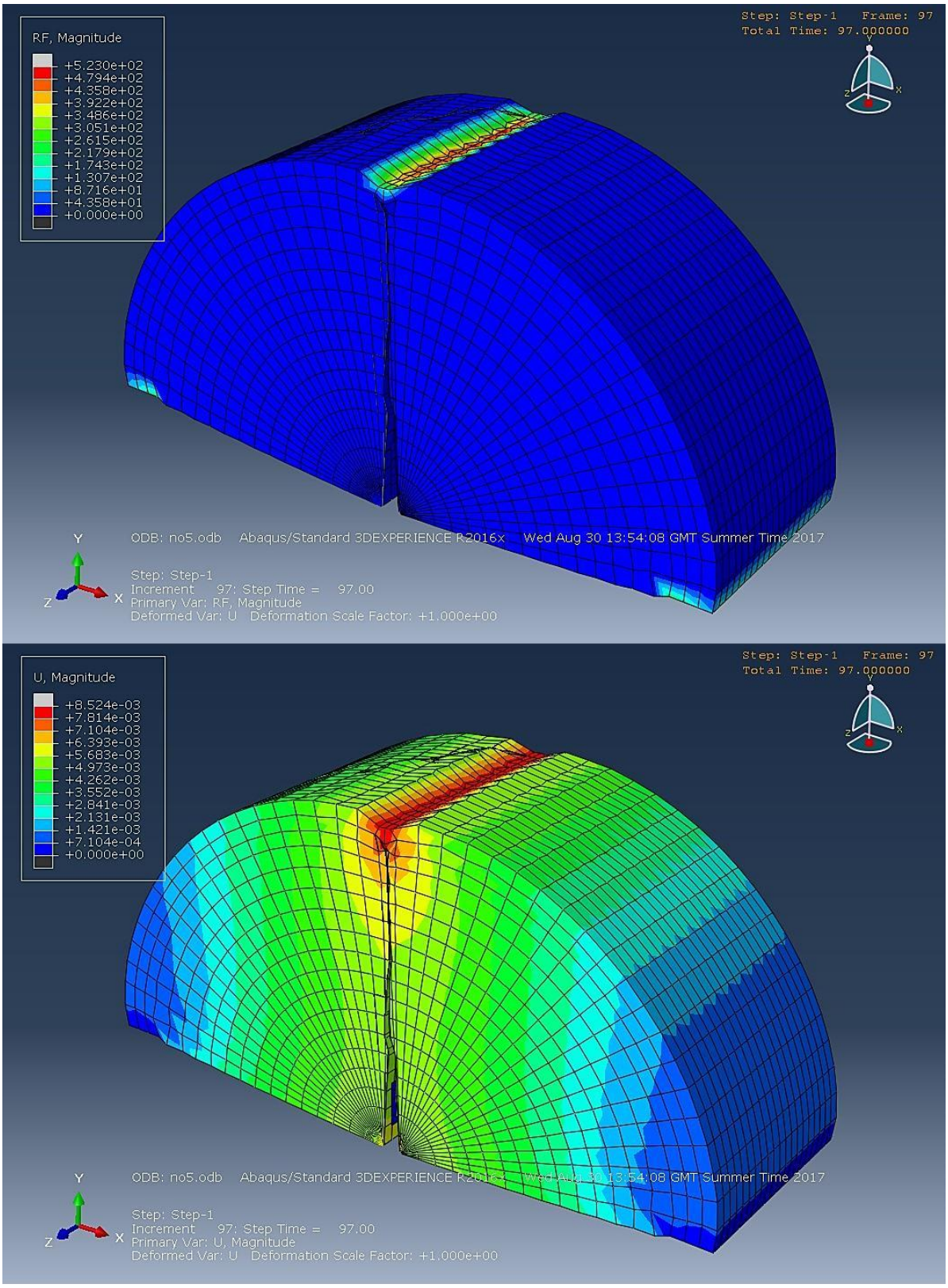

Fig. 14. Level of reaction force and movement of conventional cold mix asphalt model at the second of 97 as a step time

A flow chart revealed the methodology of research in the Figure 15.

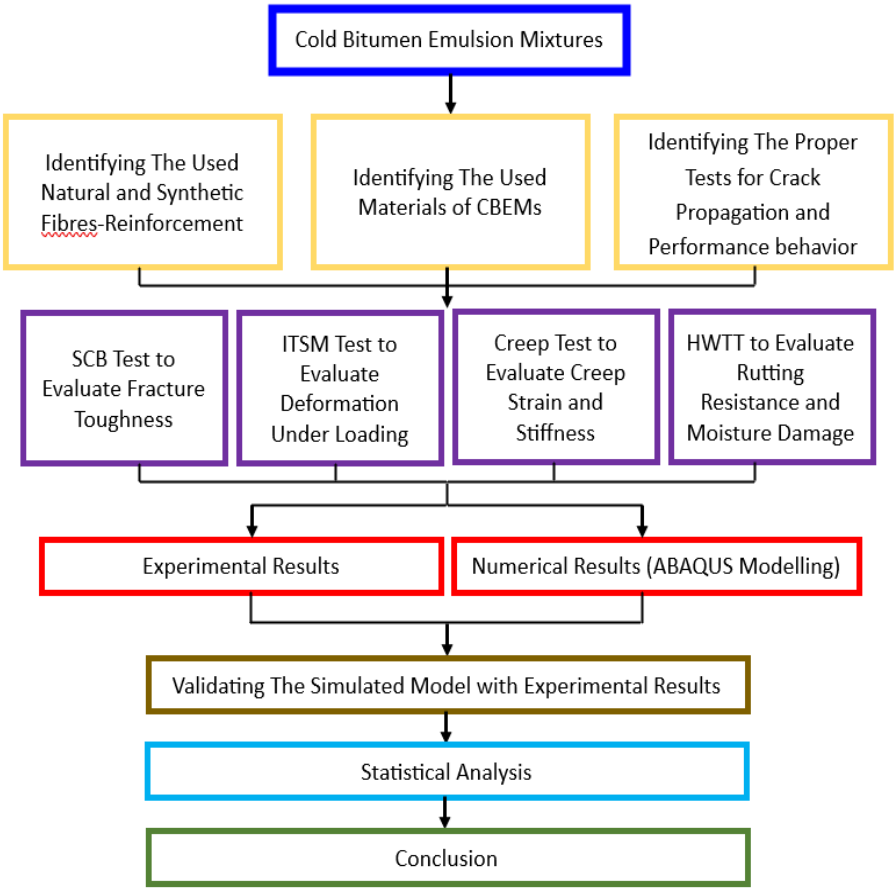

Fig. 15. Approach of research

4. Results and Discussion

4.1 SCB Test Results

This research focuses on evaluating the maximum load capacity of CBEM specimens at failure, as derived from their peak displacement. The corresponding maximum stress is then calculated to conduct the fracture toughness, which is directly related to this stress. Fracture toughness was evaluated using monotonic semi-circular bending (SCB) tests, analyzing the load-displacement behavior across three CBEM types: conventional cold bituminous emulsion mixture, natural reinforcement of CBEM (coir fibre), and synthetic reinforcement CBEM (glass fibre). Among these, glass fibre-reinforced CBEMs achieved the highest fracture toughness and maximum stress due to the high strength, stiffness, and energy absorption capacity of glass fibres, which enhance resistance to crack initiation and propagation. The ultimate stress at failure (σ_{max}) of all cold bituminous emulsion mixtures was calculated using Eq. (3), as described previously and presented in Table (3), below:

Table 3. Failure stress at maximum level (experimentally)

σ_{max} of conventional CBEM	σ_{max} of CBEM modified with coir fibre	σ_{max} of CBEM modified with glass fibre
1.455 (N/mm^2)	2.211 (N/mm^2)	2.688 (N/mm^2)

The results showed that incorporating coir fibre increased the ultimate stress (σ_{max}) by 52%, at the same time glass fibre reinforcement led to increase the ultimate stress by 85% in comparison to conventional CBEM. The enhancement in the ultimate stress of the modified CBEMs with coir fibres is basically owing to natural lignocellulosic composition of these fibres, which contribute in a

moderate tensile strength and flexibility. These kinds of fibres aid in bridging the micro-cracks and improving the distribution of stress with CBEMs. Although, such improving process is limited owing to the effects of coir fibres within CBEMs in lowering the stiffness and decreasing the interfacial bonding. Meanwhile, the glass fibres contribute in increasing the ultimate stress due to their effects within CBEMs in rising the levels of tensile strength, stiffness and strengthening the interfacial bonding with the CBEM matrix, allowing for more efficient load transfer and better resistance to crack propagation.

Rasheed A. [28], examine a resistance of cold mix asphalt samples to crack and deformation with as well as without reinforcement of glass fibre to enhance mixture performance in road maintenance. Rasheed A.'s study showed improvements in tensile strength reaching 15% at maximum load failure and 33% at ultimate failure in comparison to control micro asphalt, based on three-point bending tests. However, the current study represents a significant advancement in the field, offering superior mechanical performance and paving the way for future innovations in fibre-reinforced CBEMs, ensuring greater durability, resilience, and environmental sustainability in pavement engineering. Figure (16), shows the load-displacement behavior of CBEMs during SCB tests.

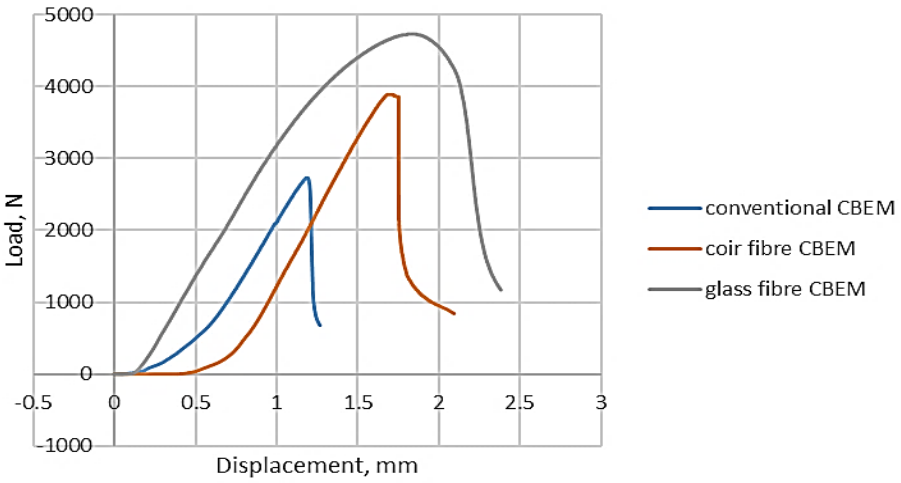

Fig. 16. Load-displacement behavior of CBEMs in SCB tests

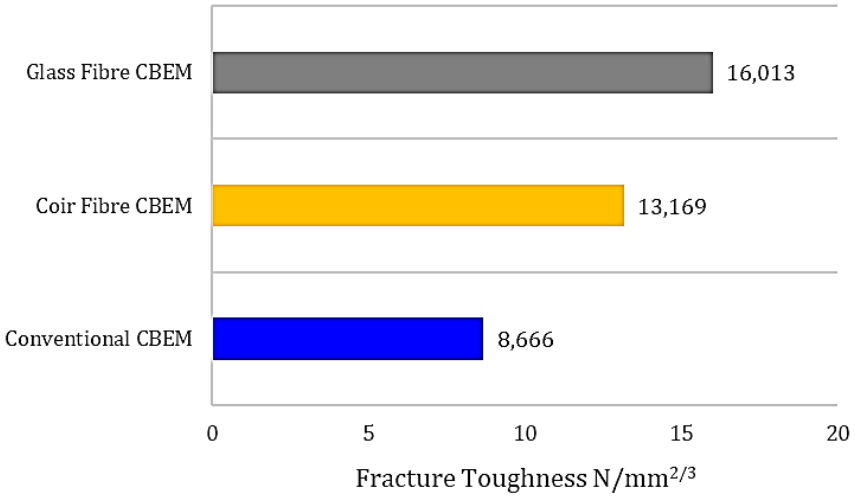

Fig. 17. Fracture toughness of the adopted types of CBEMs

Subsequently, the fracture toughness of the conventional samples of CBEM, as well as the modified CBEM with coir fibre and glass fibre, was calculated based on the concentrated stress obtained from the monotonic semi-circular bending test and by applying Eq. (4), as described previously. The intended toughness of fracture consequences is presented in Figure (17).

The results showed that fracture toughness increased by 52% with coir fibre and by 85% with glass fibre, compared to the conventional CBEM. The adopted glass fibres reveal a superior performance due to their mechanical properties and stronger interaction with the CBEM. The natural and more ductile coir fibres provide a remarkable boost in toughness; however, coir fibres contribute to lower stiffness and exhibit weaker bonding within CBEMs. Zhao S., et al. [29], investigated the fracture properties of cement emulsified asphalt mortar (CEAM), by optimizing the binder and emulsion content in order to enhance the performance. Their achieved result in term of the fracture toughness was 10.0 N/mm$^{2/3}$, which is lower than the conducted results in the current study. On the other hand, the ongoing study has offered new techniques in the field of CBEMs industry by using both natural and synthetic fibers to enhance the mix performance.

4.2 Indirect Tensile Stiffness Modulus (ITSM) Results

The tested fibre reinforced CBEMs in this study showed considerably higher ITSM than conventional CBEMs and most superior performance at 0.4% fibre rate and 15 mm in length. CBEMs reinforced with coir and glass fibres achieved 4400 and 5600 MPa, respectively after 28 days of curing in terms of ITSM, while conventional CBEMs achieved 3000 MPa. This represents an increase of 47% for coir fibres and 87% for glass fibres in comparison with the conventional mix. These improvements are directly related to the particular physical and mechanical properties of each type of fibre:

- Coir fibers are natural lignocellulosic fibers with good tensile strengths but high ductility and superior energy-absorbing ability. Incorporating of these fibres within the matrix of CBEMs leads to form a network that bridges microcracks, delaying their propagation and improving the mixture's resistance to deformation. The nature of their rough surface texture works to enhance the bonding power with the bitumen leading to increase the stiffness of CBEMs. However, these kinds of fibres have common issues related to high absorbent and low stiffness in comparison to synthetic fibres, therefore development process of ITSM remains in moderate level.
- Glass fibers are synthetic fibers with extremely high tensile stress, high stiffness, and chemically stable. Incorporating these fibres within the CBEMs leads to increase the efficiency of load transfer, high resistance to deformation, and creating an internal reinforcing grid to constrains the developed cracks under stress. As a result of thin diameter and strong bonding characteristics of these fibres, it allows stress to be redistributed more effectively, leading to improved ITSM levels. In addition, glass fibres maintain their structural integrity during mixing and curing, resulting in superior mechanical performance.

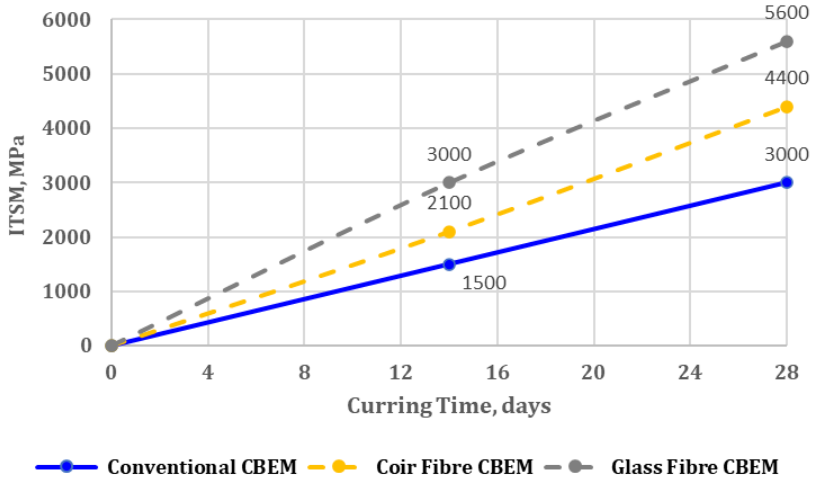

Fig. 18. ITSM Results for Conventional and Reinforced CBEMs

Furthermore, the ITSM of CBEMs increases over time as moisture evaporates and the binder hardens. Initially low due to high water or solvent content, the modulus rises as the mixture gains strength and cohesion, continuing to increase until stabilization. Compared to Du S. [30], who

investigated the mechanical performance of cold mix asphalt reinforced with natural and manufactured fibres, including polyester, polypropylene, polyacrylonitrile, lignin, and basalt. The results of the previous study showed improvements in ITSM by 35% with polyester fibres, 30% with polypropylene fibres, 25% with polyacrylonitrile fibres, 20% with lignin fibres, and 30% with basalt fibres. Even though these fibres contributed in the enhancement process of ITSM levels, their improvements were generally lower than those observed with coir and glass fibres in the current study. Figure (18) presents the ITSM results for various CBEMs.

4.3 Creep Test Results

The creep test results at 1000 to 4000 second period, showed that the conventional CBEM, particularly at 60° C, had a consistent rise in strain to 3.0% at 4000s, showing low stiffness and high deformability under heat. Adding coir fibres moderately enhanced the performance by reducing the strain level to 2.0% at 60° C and 1.8% at 40° C after 4000 seconds, showing a little higher stiffness than the conventional CBEMs. The observed improvement in the stiffness due to the influence of coir fibres is attributed to the natural structure of these fibres which provides moderate tensile strength and limits the grown deformation under load. Even though, the irregular surface texture and lower elastic modulus of these fibres contribute in reducing their overall reinforcing efficiency. On the contrary, the glass fibre-reinforced CBEM showed the lowest values of strain (1.2 - 1.3%), which equate to the highest stiffness, showing superior resistance to deformed shape and optimum structural stability at all the temperature regimes and time intervals. The behavior of glass fibres within CBEMs is mainly related to their high tensile strength and stiffness, as well as better interfacial bonding with the CBEM matrix, leading to enhance the load transfer and restrict the development of strain. As a result, the generated CBEMs exhibit lower strain, high stiffness, and better overall structural integrity. Guo Y. et al. [31] examined the effects of different fibre types on the mechanical properties of cold asphalt mixtures and their role in enhancing durability. On the basis of the trends in performance highlighted in their study, the reduction levels of creep strains at 60° C after 4000 seconds of testing was reported as 55% for glass fibers, 45% for polypropylene, 40% for polyester, 30% for basalt, and 20% for cellulose. Comparatively, the ongoing work provides clear and efficient results, with glass fibre-reinforced CBEMs showing a 56.7% improvement in creep resistance, while coir fibre reinforcement resulted in a 33.3% improvement. Consequently, the recent study builds upon previous work by conducting additional performance tests to provide a more comprehensive understanding of fibre reinforcement's impact on CBEM properties. Figure (19) illustrates the creep strain versus time for different CBEMs.

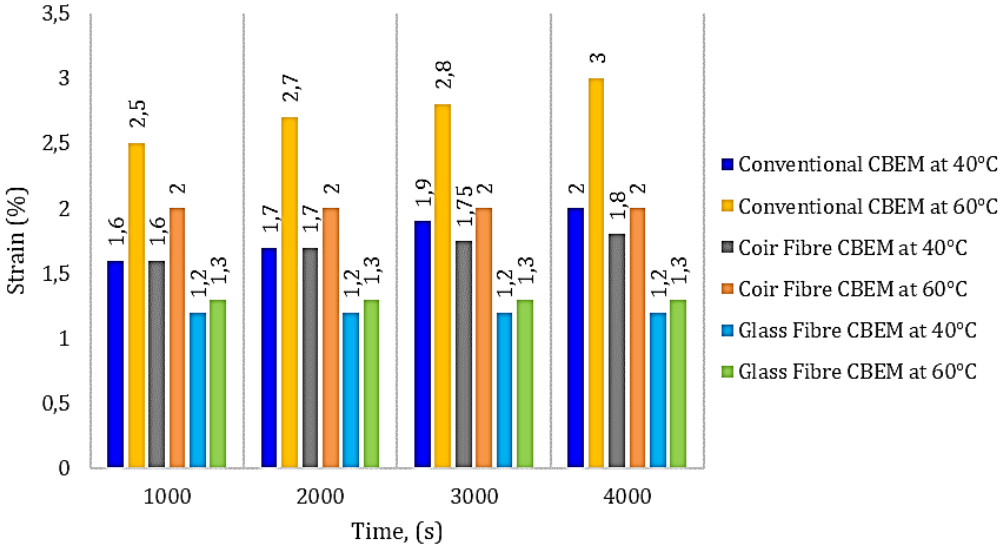

Fig. 19. Creep Strain vs. Time for CBEMs at Different Temperature

4.4 Hamburg Wheel-Track Test Results

The result of Hamburg test revealed an effective improvement in the rutting resistance and moisture sensitivity for both coir and glass modified CEAMs in comparison to conventional mix. After 20000 passes in the wheel-track test, the developed rut depth in the conventional CBEM reached 10.8 mm, indicating poor resistance to permanent deformation and high vulnerability to moisture damage under repeated loading. The incorporation of coir fibres within CBEMs reduced the ruth depth to 6.2 mm, achieving a 43% reduction compared to conventional CBEM. Furthermore, the glass fibre-modified CBEM achieved the lowest rut depth of 4.8 mm, corresponding to a 56% reduction. These improvements are contributed to the ability of the adopted fibres to strengthen the internal matrix of CBEM, effectively control the growth of microcracks, and distribute the applied stresses more efficiently within the mixture. Basically, glass fibers contribute to greater stiffness and tensile strength, strengthening the mixture's structure and improving its rutting and resistance to moisture at advanced stages of loading. Table (4), represent the results of wheel-track test. Amal R et al. [32], investigated the reinforcing process of cold bituminous mixtures using natural coir fibres (20 mm length at 0.25%, 0.5%, and 0.75% by weight of mix). In their study, the optimum fibre dosage (0.5%) resulted in a rut depth of approximately 8.4 mm. On the other hand, the ongoing study demonstrated that coir fibre-modified CBEM achieved a rut depth of 6.2 mm, under the same number of load passes, while glass fibre-modified CBEM exhibited even better performance, with a rut depth of 4.8 mm. Overall, the findings of the current study confirm the superior performance of fibre reinforcement method, specifically with glass fibres, in enhancing rutting resistance and moisture sensitivity under the applied traffic loading.

Table 4. Rut depth for the developed CBEMs (experimentally)

CBEM type / No. of passes	Rut depth in (mm) for the conventional CBEM	Rut depth in (mm) for the coir fibre CBEM	Rut depth in (mm) for the glass fibre CBEM
5000	4.2	2.6	1.8
10000	7.3	4.3	3.1
15000	9.5	5.5	4.2
20000	10.8	6.2	4.8

4.4 Finite Element Modelling (FEM) Results

4.4.1 In Terms of Load-Displacement Behavior

Each cold asphalt mixture specimen exhibited peak force and the corresponding displacement, as shown in Figure (20), which represents the load–displacement of the three CBEM types. CBEMs reinforced with glass and coir fibres outperform conventional CBEMs in terms of load resistance behavior.

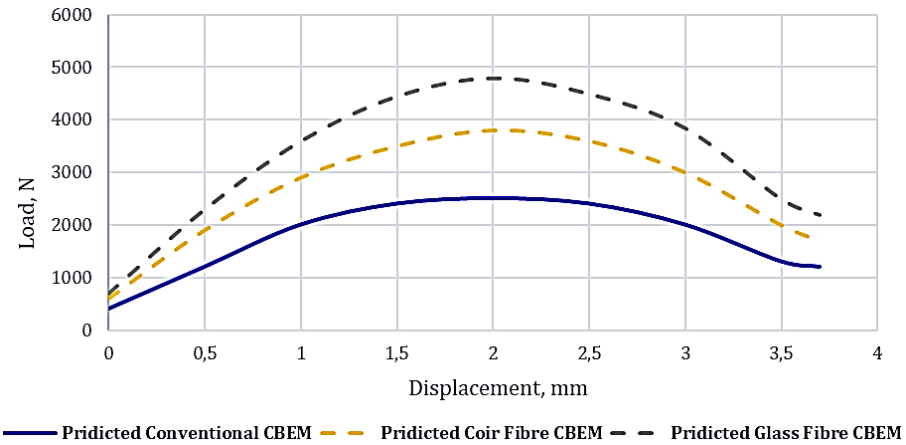

Fig. 20. Load- displacement behavior of cold bituminous emulsion mixture models

The glass fibre-reinforced CBEM achieved the highest load resistance, approximately 4800 N, followed by the coir fibre-reinforced CBEM at around 3750 N, while the conventional CBEM reached 2500 N.

4.4.2 In Terms of Ultimate Stresses at Failure (Stiffness)

The ultimate stress at failure (σ_{max}) of all cold bituminous emulsion mixtures specimens was calculated depending on Eq. (3), as previously described, and the results presented in Table (5), below. As shown in Table (5) above, glass fibre-reinforced CBEM exhibited the highest stiffness, followed by the coir fibre-reinforced CBEM, then the conventional mix.

Table 5. Failure stress at maximum level (modelling)

σ_{max} of conventional CBEM	σ_{max} of CBEM modified with coir fibre	σ_{max} of CBEM modified with glass fibre
1.446 (N/mm^2)	2.129 (N/mm^2)	2.701 (N/mm^2)

4.4.3 In Terms of Fracture Toughness

All three models of cold bituminous emulsion (conventional model, reinforced coir fibre model, and reinforced glass fibre model) were assessed via toughness of fracture (crack growth resistant) based on the determined values of stress demonstrated in Table (5) above, and calculated using Eq. (4), as previously described. Figure (21), shows the fracture toughness of the numerical models of cold mix asphalt specimens.

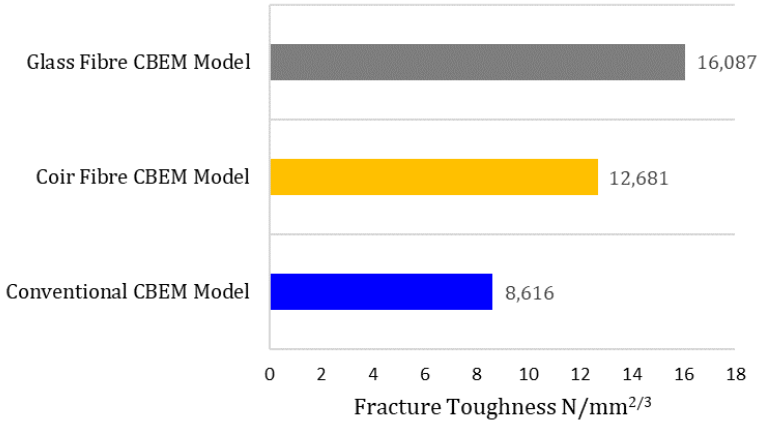

Fig. 21. Fracture toughness of the adopted types of CBEMs models

Figure (21), clearly shows that the glass fibre-reinforced CBEM recorded the highest fracture toughness, followed by the coir fibre-reinforced CBEM. Furthermore, the conventional cold mix asphalt revealed the lowest resistance to crack growth.

4.4.4 In Terms of Performance Behavior

The FEM, conducted through ABAQUS software, successfully simulated the experimental rut behavior, enabling accurate prediction of rut depth progression under repeated loading. The glass fibre-reinforced CBEM exhibited the lowest rut depths, followed by the coir fibre-reinforced CBEM, while the conventional CBEM recorded the highest rut depths, as shown in Table (6), below.

Table 6. Rut depth for the developed CBEMs (modelling)

CBEM type / No. of passes	Rut depth in (mm) for the conventional CBEM	Rut depth in (mm) for the coir fibre CBEM	Rut depth in (mm) for the glass fibre CBEM
5000	4.4	2.7	1.9
10000	7.6	4.5	3.3
15000	9.8	5.8	4.4
20000	11.2	6.5	5.1

4.5 FEM Validation

4.5.1 Comparison Approach

The results of finite element modelling (FEM) closely matched the experimental findings, confirming the model's reliability in simulating crack propagation and performance behavior of CBEMs under loading conditions, as shown in Figures 22 and 23.

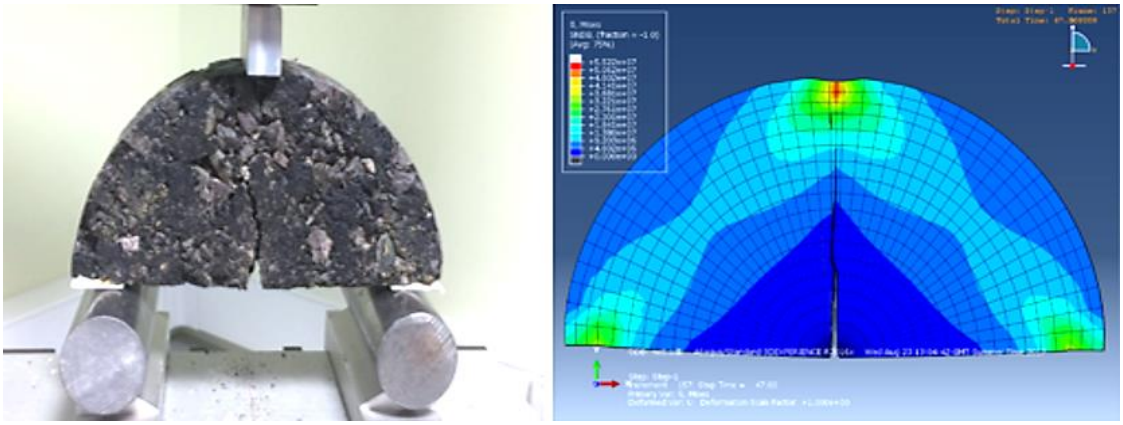

Fig. 22. Validation of experimental and numerical results for crack propagation in CBEM

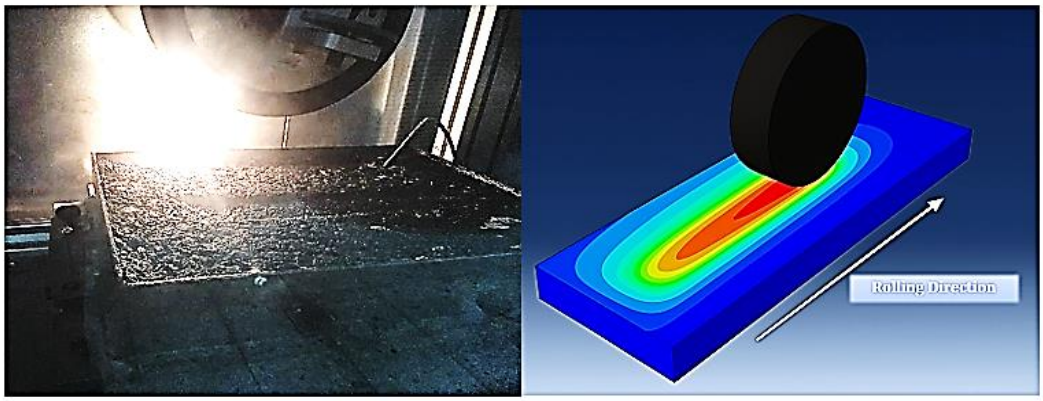

Fig. 23. Validation of experimental and numerical results for performance behavior in CBEM

Figure (24), presents the findings from laboratory SCB tests and FEM simulations for a 10 mm crack notch in conventional CBEM. The FEM accurately replicates the load-displacement curve when compared to the experimental data. Both the experimental and FEMs recorded reaction forces of approximately 2500 N, then the experimental load-displacement curve begins to decline gradually in comparison to FEM curve, approximately at a displacement of 1.3 mm. Figure (25), presents the FEM alongside the laboratory SCB test results for CBEM reinforced with coir fiber. The FEM provides a reasonable estimation in comparison to the experimental data, with both exhibiting similar load-displacement behavior. However, the experimental load-displacement curve begins to decline earlier than the FEM curve, approximately at a displacement of 1.6 mm. The greatest alignment between the load-displacement curves of the FEM and the experimental work is observed in the CBEM reinforced with glass fiber, as illustrated in Figure (26). The figure shows that the maximum load required to reach peak displacement is nearly identical in both the experimental SCB test and the FEM simulation, with a peak load of approximately 4900 N and a displacement of 1.9 mm.

Figure (27), clearly demonstrates that the fracture toughness values from the FEM analysis closely align with those from the experimental SCB tests for all three types of CBEM. The FEM, performed using ABAQUS software, effectively captured the experimental results, enabling accurate prediction of crack growth behavior through both experimental and numerical methods. Figure (28), reveals perfect alignment between the experimental rut depth behavior and the simulated FEM of ABAQUS for all the types of CBEMs, under all the applied wheel-track passes.

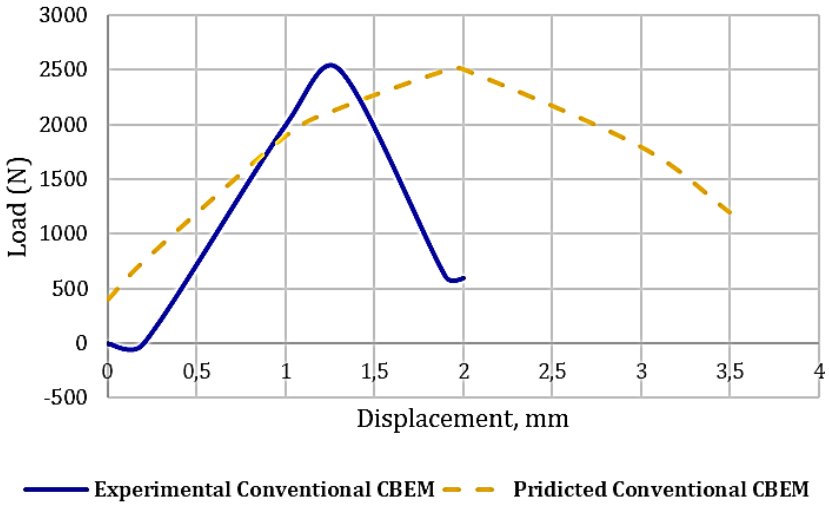

Fig. 24. Comparison of experimental work with FEM load-displacement curves for conventional CBEM

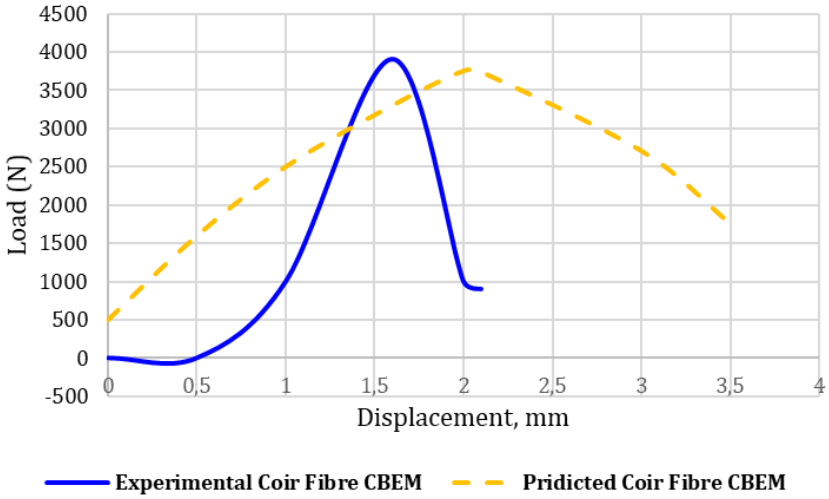

Fig. 25. Comparison of experimental work with FEM load-displacement curves of CBEM reinforced with coir fibre

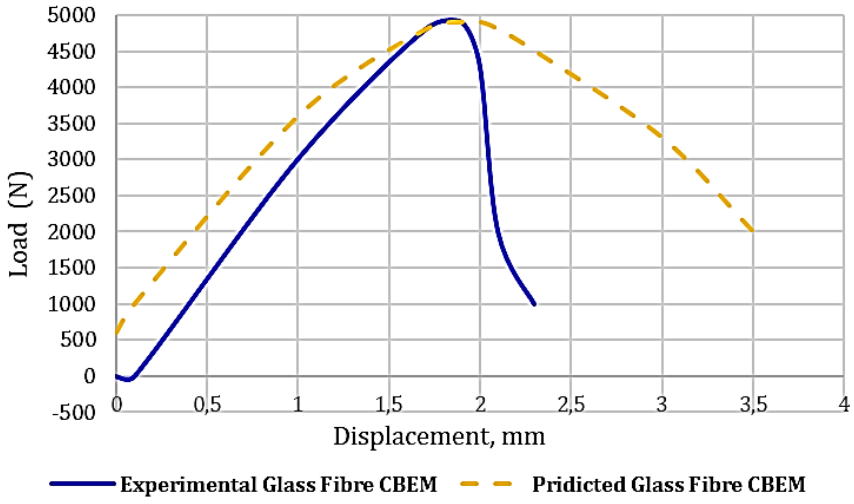

Fig. 26. Comparison of experimental work with FEM load-displacement curves of CBEM reinforced with glass fibre

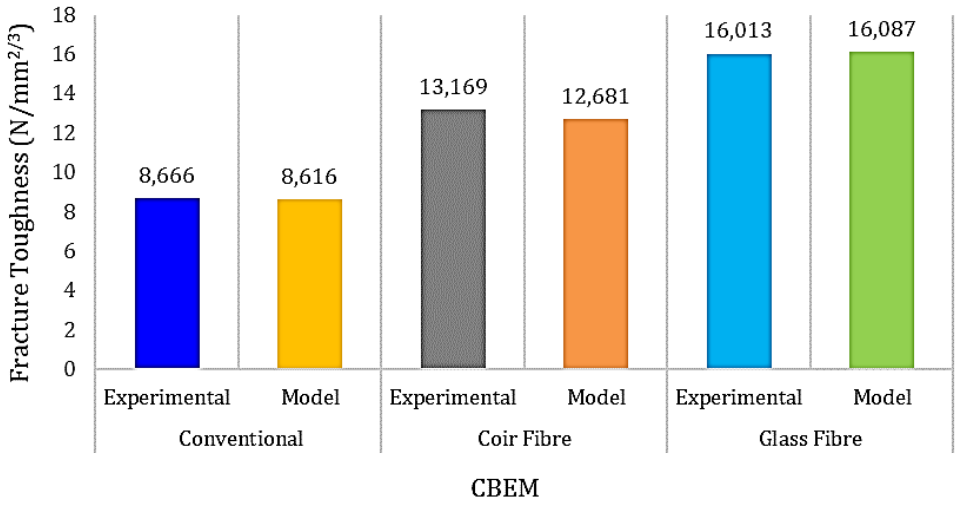

Fig. 27. Fracture toughness results from both the experimental method and the FEM method

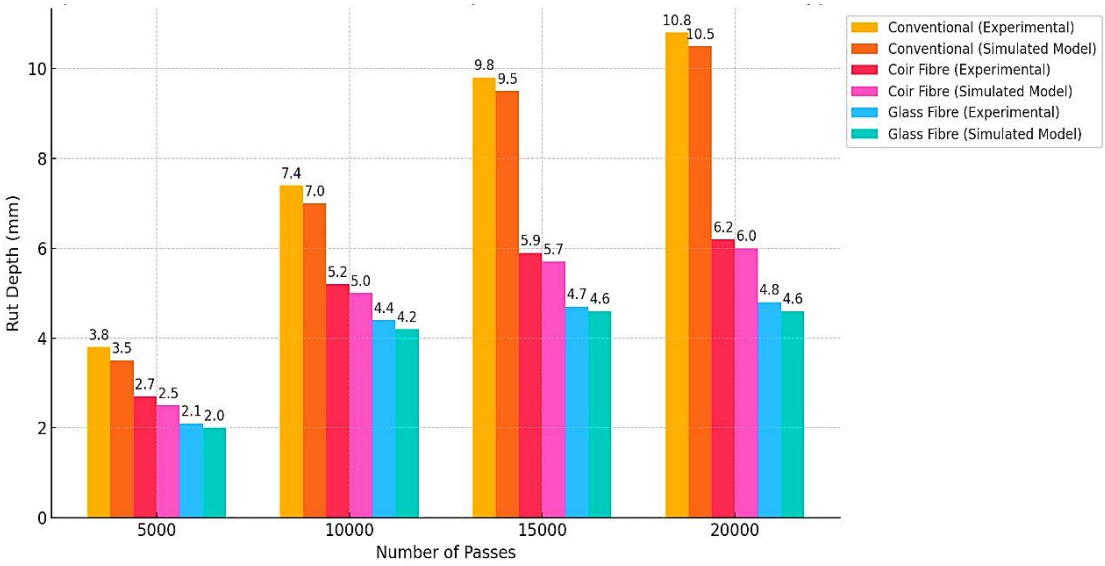

Fig. 28. Experimental vs. simulated FEM rut depth for all the types of CBEMs

4.5.2 Statistical Validation

To support the reliability and credibility of the achieved fracture toughness results for both experimental and numerical data of CBEMs, standard deviation and one-way ANOVA analysis were implemented to confirm the significance of differences between CBEM types, as shown below:

4.5.2.1 Part 1: Standard deviation of differences

The differences between experimental and numerical data for fracture toughness results are concluded from the previous Figure (27), as shown below in Table (7).

Table 7. The difference values between experimental and numerical results of fracture toughness for CBEMs

CBEM type	Fracture toughness experimental values / N/mm$^{2/3}$	Fracture toughness numerical values / N/mm$^{2/3}$	The difference values
Conventional	8.666	8.616	0.050
Coir fibres	13.169	12.681	0.488
Glass fibres	16.013	16.087	-0.074

- 1- Mean of differences (D), as in Eq. (5).

$$D = \frac{0.050 + 0.488 + (-0.074)}{3} = 0.1547 \quad (5)$$

- 2- Squared Deviations from the Mean, as in Eq. (6).

$$\sum (D_i - D)^2 = 0.01097 + 0.1111 + 0.0523 = 0.17437 \quad (6)$$

D_i: The difference between the experimental and numerical data

- 3- Variance (S^2), as is Eq. (7).

$$S^2 = \frac{\sum (D_i - D)^2}{n - 1} = \frac{0.17437}{2} = 0.0872 \quad (7)$$

n: The number of pairs

- 4- Standard Deviation (S), as in Eq. (8).

$$S = \sqrt{S^2} = \sqrt{0.0872} = 0.2953 \quad (8)$$

4.5.2.2 Part 2: One-Way ANOVA

- 1- Grand mean (GM), as in Eq. (9).

$$GM = \frac{8.666 + 13.169 + 16.013 + 8.616 + 12.681 + 16.087}{6} = 12.5387 \quad (9)$$

- 2- Sum of squares between experimental and numerical groups (SSB), as in Eq. (10).

$$SSB = n\,(x_1^- - GM)^2 + n\,(x_2^- - GM)^2$$
$$SSB = 3 \times (0.0060) + 3 \times (0.0061) = 0.0364 \quad (10)$$

x_1^-: 12.616 (mean of experimental); x_2^-: 12.461 (mean of numerical); n: 3 (values per group)

- 3- Sum of squares within experimental and numerical groups (SSW), as in Eq. (11).

$$SSW = 27.4519 + 27.9855 = 55.4374$$

$$SSW_{Experimental} = (8.666 - 12.616)^2 + (13.169 - 12.616)^2 + (16.013 - 12.616)^2 = 27.4519 \quad (11)$$

$$SSW_{Numerical} = (8.616 - 12.461)^2 + (12.681 - 12.461)^2 + (16.087 - 12.461)^2 = 27.9855$$

- 4- Degrees of freedom (df), as in Eq. (12), and Eq. (13).

$$df_1 = k - 1 = 2 - 1 = 1 \quad (12)$$

$$df_2 = N - k = 6 - 2 = 4 \quad (13)$$

df_1: degree of freedom between experimental and numerical groups; df_2: degree of freedom within experimental and numerical groups; *k:* 2 (number of groups); *N:* 6 (total observations: 3 experimental + 3 numerical)

- 5- Mean squares (MS), as in Eq. (14), and Eq. (15).

$$MS_{between} = \frac{SSB}{df_1} = \frac{0.0364}{1} = 0.0364 \quad (14)$$

$$MS_{within} = \frac{SSW}{df_2} = \frac{55.4374}{4} = 13.8593 \quad (15)$$

- 6- F-statistic, as in Eq. (16).

$$F = \frac{MS_{between}}{MS_{within}} = \frac{0.0364}{13.8593} = 0.0026 \quad (16)$$

- 7- p-Value

$p = 0.9619 \cong 96\%$

The statistical validation conducted using standard deviation and one-way ANOVA confirmed that there is no significant difference between the experimental and numerical fracture toughness values. The low standard deviation (0.2953 N/mm^{2}/^{3}) and high p-value (0.9619) indicate strong agreement, thereby validating the reliability and accuracy of the numerical model in simulating the fracture behavior of the adopted CBEMs.

4.6 STATUSXFEM

XFEM is a scheme available in ABAQUS software was employed to Effectively predict crack propagation in CBEMs. A crucial output variable in XFEM is STATUSXFEM ("status of the enriched element"), which signifies the condition of present cracks. The sample is fully cracked when its STATUSXFEM value reaches 1.0, whereas a STATUSXFEM of 0.0 indicates an entirely intact sample with no cracks. If the STATUSXFEM value falls between 0.0 and 1.0, the element is partially cracked, reflecting progressive damage [33]. As shown in Figure (29), the sample becomes fully fractured when time of step reaches 47 seconds, as indicated by the scheme of extended finite element value reaching 1.0.

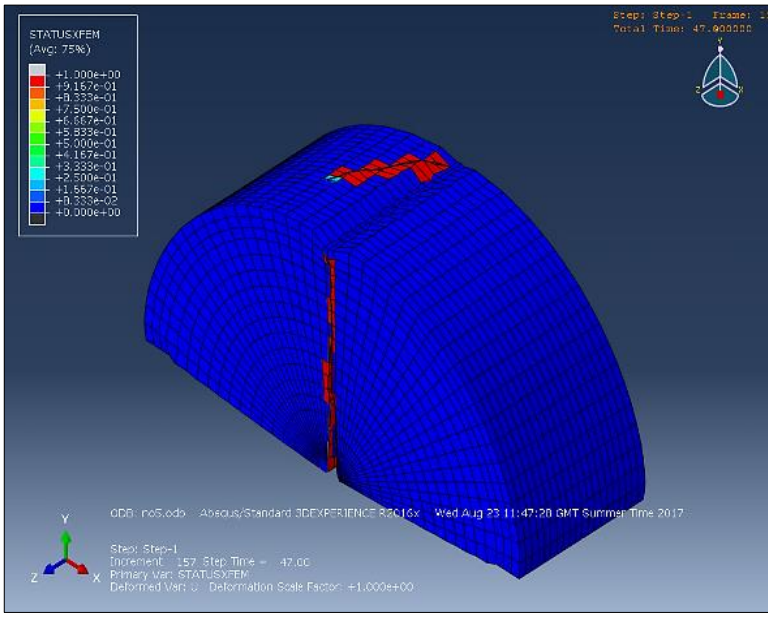

Fig. 29. The extended finite element scheme for three types of cold mix asphalt samples

Fig. 30. Crack length recording under three-point bending test

To conduct a more explicit comparison between the experimental and numerical results, the recorded crack length of the generated CBEMs during the SCB test was employed for this purpose. Here, the test specimen is fixed at the ends with a center load imposed up to the point of failure as shown below in Figure (30). The crack length at a specific time period of 47 second (the same duration of XFEM scheme), was calculated by analyzing crack and fracture behavior during loading though a connected digital dial gauge. The conducted comparison between the experimental and numerical data are illustrated in Table (8), in terms of the generated crack length under loading.

Table 8. CBEMs crack length for both experimental and numerical generated data

CBEM type	Experimental crack length (mm)	XFEM crack length (mm)
Conventional CBEM	1.300	1.235
Coir fibres CBEM	0.855	0.812
Glass fibres CBEM	0.704	0.669

Both experimental and the XFEM numerical results are considerably combined, revealing a strong agreement in crack length predictions at the 47-second time mark. To support this alignment in results, the coefficient of correlation (R^2), mean absolute error (MAE), and root mean squared error (RMSE) are additionally calculated as show below:

- Step 1: Compute the mean of experimental crack lengths (y^-), as in Eq. (17).

$$y^- = \frac{1.300 + 0.855 + 0.704}{3} = 0.953\ mm \tag{17}$$

- Step 2: Compute the errors

$|y_i - \hat{y_i}| = 0.065$ for convensional, 0.043 for coir fibres, 0.035 for glass fibres ;

$(y_i - \hat{y_i})^2 = 0.0042$ for convensional, 0.0018 for coir fibres, 0.0012 for glass fibres

$y_i - \hat{y_i} = 0.065$ for convensional, 0.043 for coir fibres, 0.035 for glass fibres

yi: Experimental crack length for each CBEM type

yi^: XFEM-predicted crack length for each CBEM type

- Step 3: Calculate the error metrics, as in Eq. (18), Eq. (19), and Eq. (20).

$$Mean\ Absolute\ Error\ MAE = \frac{\sum|y_i - \hat{y_i}|}{n} = \frac{0.065 + 0.043 + 0.035}{3} = 0.0477mm \tag{18}$$

$$Root\ Mean\ Squared\ Error\ RMSE = \sqrt{\frac{\sum(y_i - \hat{y_i})^2}{n}} = \sqrt{\frac{0.0042 + 0.0018 + 0.0012}{3}} = 0.0493mm \tag{19}$$

$$Coefficient\ of\ Corrilation\ (R^2) = 1 - \frac{\sum(y_i - \hat{y_i})^2}{\sum(y_i - y^-)^2} = 1 - \frac{0.0042 + 0.0018 + 0.0012}{0.1204 + 0.0096 + 0.0620} = 0.962 \cong 96\% \tag{20}$$

5. Conclusion

Integrating natural and synthetic fibres into CMA effectively enhances its mechanical properties. These fibres strengthen the asphalt matrix, improving resistance to cracking and resulting in greater durability. Natural fibres offer a sustainable, cost-effective option, whereas synthetic fibres provide greater strength and long-term stability. The objective of this research was to carry out in-depth analysis of the semi-circular bending (SCB) test to evaluate the cracking resistance of fibre reinforced cold mix asphalt.

Furthermore, the rutting performance was analyzed by performing the Hamburg wheel-track test (HWTT) to assess the mixtures' resistance to permanent deformation and sensitivity to moisture under repeated traffic. Moreover, a 3D model of finite element was utilized to validate experimental SCB and the wheel- track results, providing a detailed analysis of the failure mechanism, and the mixtures' performance under repeated loading. Besides that, a statistical approach has been employed in terms of fracture toughness and crack length to validate both the experimental and numerical results. The outcomes concluded from this investigation are: -

- The optimal ITSM results are achieved when the fibre is 15 mm in length and the content of fibre is 0.4%.

- Reinforcing the conventional CBEM with coir and glass fibres significantly increased the tensile strength by 47% and 87%, respectively, resulting in notable improvements in the ITSM.
- Employing both coir and glass fibres within CBEMs, led to decrease the creep strain by 33.3% and 56.7%, respectively, compared to the conventional mix at 60° C after 4000 seconds of testing. Likewise, at 40° C and after 4000 seconds, the creep strain decreased by 10% and 66.7%, respectively, in comparison to conventional mix.
- Incorporating both coir and glass fibres within CBEMs led to a substantial increase in creep stiffness compared to the conventional CBEM, across different temperatures.
- Integrating both both coir and glass fibres within CBEMs led to increase the fracture toughness by 52% and 85%, respectively, compared to the conventional CBEM, revealing a superior performance of glass fibres.
- Utilizing both coir and glass fibres within CBEMs led to decrease the rutting depth by 43% and 56%, respectively, in comparison to conventional CBEM. This demonstrates the effectiveness of using such fibres to enhance CBEM performance in terms of rutting resistance and moisture susceptibility.
- The conducted FEMs in terms of load-displacement behavior, ultimate stresses at failure (stiffness), fracture toughness, and performance behavior under repeated loading, achieved considerable alignment with the experimental results, confirming the model's reliability and efficiency.
- The adopted statistical approach in terms of fracture toughness confirmed that there was no significant difference between the experimental and numerical values, thereby validating the reliability and accuracy of the numerical model in simulating the fracture behavior of the adopted CBEMs.
- The used statistical analysis between the experimental and the XFEM numerical results revealed a strong agreement in crack length predictions, achieving a coefficient of correlation (R^2) of 96%.

This study has purposes of investigating the impact of natural and synthetic fibres on the crack resistance of CMA, tensile strength of CMA, strain resistance, rutting resistance, and to simulate these effects using FEA with ABAQUS. However, a key limitation of this research is the absence of additional service tests, for example the long-term durability testing, aging effects, and the test of asphalt pavement analyzer (APA) for assessing fatigue cracking. In addition, a detailed cost–benefit and lifecycle assessment for the developed CBEMs is acknowledged as one of the study's limitations. To enhance this research, future studies should focus on addressing these limitations.

References

[1] Rogo KU. Performance of fine dense-graded cold mix asphalt incorporating spent garnet and palm oil fuel ash (Doctoral dissertation, Universiti Teknologi Malaysia).
[2] Kim C, Lawson K, Rajan J, Tan A. 2020 CBEMS Design Project.
[3] Deb P, Lakshman Singh K. Mix design, durability and strength enhancement of cold mix asphalt: a state-of-the-art review. Innovative Infrastructure Solutions. 2022 Feb;7:1-22. https://doi.org/10.1007/s41062-021-00600-2
[4] Gunarathne DS, Udugama IA, Jayawardena S, Gernaey KV, Mansouri SS, Narayana M. Resource recovery from bio-based production processes in developing Asia. Sustainable Production and Consumption. 2019 Jan 1;17:196-214. https://doi.org/10.1016/j.spc.2018.11.008
[5] Safazadeh F, Romero P, Mohammad Asib AS, VanFrank K. Methods to evaluate intermediate temperature properties of asphalt mixtures by the semi-circular bending (SCB) test. Road Materials and Pavement Design. 2022 Jul 3;23(7):1694-706. https://doi.org/10.1080/14680629.2021.1911831
[6] Liu Z, Gu X, Ren H, Zhou Z, Wang X, Tang S. Analysis of the dynamic responses of asphalt pavement based on full-scale accelerated testing and finite element simulation. Construction and Building Materials. 2022 Mar 28;325:126429. https://doi.org/10.1016/j.conbuildmat.2022.126429
[7] Sedmak A. Fatigue crack growth simulation by extended finite element method: A review of case studies. Fatigue & Fracture of Engineering Materials & Structures. 2024 Jun;47(6):1819-55. https://doi.org/10.1111/ffe.14277

[8] Wu S, Haji A, Adkins I. State of art review on the incorporation of fibres in asphalt pavements. Road Materials and Pavement Design. 2023 Jun 3;24(6):1559-94. https://doi.org/10.1080/14680629.2022.2092022
[9] Solak H, İskender E, Aksoy A, İskender C. Use of Synthetic Fibers in Asphalt Pavements-Mini Review. InInternational Conference on Advances in Civil Engineering 2023 Sep 6 (pp. 415-423). Singapore: Springer Nature Singapore. https://doi.org/10.1007/978-981-97-1781-1_38
[10] Addae DT, Rahman M, Abed A. State of art literature review on the mechanical, functional and long-term performance of cold mix asphalt mixtures. Construction and Building Materials. 2023 Oct 12;400:132759. https://doi.org/10.1016/j.conbuildmat.2023.132759
[11] Jain S, Singh B. Cold mix asphalt: An overview. Journal of cleaner production. 2021 Jan 20;280:124378. https://doi.org/10.1016/j.jclepro.2020.124378
[12] Guo Q, Wang H, Gao Y, Jiao Y, Liu F, Dong Z. Investigation of the low-temperature properties and cracking resistance of fiber-reinforced asphalt concrete using the DIC technique. Engineering Fracture Mechanics. 2020 Apr 15;229:106951. https://doi.org/10.1016/j.engfracmech.2020.106951
[13] Li Z, Zhang X, Fa C, Zhang Y, Xiong J, Chen H. Investigation on characteristics and properties of bagasse fibers: Performances of asphalt mixtures with bagasse fibers. Construction and Building Materials. 2020 Jul 10;248:118648. https://doi.org/10.1016/j.conbuildmat.2020.118648
[14] Malik MI, Mir MS, Mohanty B. Cold Bitumen Emulsion Mixtures with Waste Glass: A Laboratory-Driven Investigation into Performance. Journal of Materials in Civil Engineering. 2025 Jan 1;37(1):04024438. https://doi.org/10.1061/JMCEE7.MTENG-17875
[15] Briceño-Balza JE, Castillo-Pernía LJ, Mercado-Marquez M. Evaluation of indirect tensile strength and stability of fiber-reinforced cold asphalt mixes. Revista Ciencia e Ingeniería. Vol. 2025 Dec;46(1).
[16] Jones MR, Halliday JE, Csetenyi L, Zheng L, Strompinis N. Utilising fine and coarse recycled aggregates from the Gulf Region in concrete. InProceedings of the TMS Middle East-Mediterranean Materials Congress on Energy and Infrastructure Systems (MEMA 2015) 2016 (pp. 13-23). Springer International Publishing. https://doi.org/10.1002/9781119090427.ch2
[17] Naamandadin NA, Rosdi MS, Mustafa WA, Aman MN, Saidi SA. Mechanical behaviour on concrete of coconut coir fiber as additive. InIOP Conference Series: Materials Science and Engineering 2020; 932(1): 012098). IOP Publishing. https://doi.org/10.1088/1757-899X/932/1/012098
[18] Kamath SS, Chandrappa RK. Additives used in natural fibre reinforced polymer composites-a review. Materials Today: Proceedings. 2022 Jan 1;50:1417-24. https://doi.org/10.1016/j.matpr.2021.08.331
[19] Zhang Y, Sun L, Cheng H. Effects of nominal maximum aggregate size and compaction effort on the mechanical properties of hot-mix asphalt (HMA). Construction and Building Materials. 2022 Mar 21;324:126715. https://doi.org/10.1016/j.conbuildmat.2022.126715
[20] Shubbar A, Nasr MS, Kadhim A, Hashim TM, Sadique M. Performance Comparison of 45° and 90° Herringboned Permeable Interlocking Concrete Pavement. Infrastructures. 2023 May 22;8(5):97. https://doi.org/10.3390/infrastructures8050097
[21] Al-Jumaili MA, Issmael OD. Sustainability of Cold Recycled Mixture with High Reclaimed Asphalt Pavement Percentages. Appl. Res. J. 2016;2:344-52.
[22] Wright M, James D, Sanchez D, Wayman M, D'Angelo G, Parajuli U, Airey G, Hadley A, Brough C. Laboratory Evaluation of the Performance of Bio-Binders in Conjunction with WMA & RA. InThe International Workshop on the Use of Biomaterials in Pavements 2024 Sep 20 (pp. 24-34). Cham: Springer Nature Switzerland. https://doi.org/10.1007/978-3-031-72134-2_3
[23] Meng Y, Kong W, Gou C, Deng S, Hu Y, Chen J, Fan L. A review on evaluation of crack resistance of asphalt mixture by semi-circular bending test. Journal of Road Engineering. 2023 Mar 1;3(1):87-97. https://doi.org/10.1016/j.jreng.2022.07.003
[24] Aljuboryl A, Airey GD, Grenfell JR. Laboratory evaluation of stiffness and fatigue susceptibility of asphalt paving materials incorporating environmental factors. InBearing capacity of roads, railways and airfields 2017 Jul 20 (pp. 223-230). CRC Press. https://doi.org/10.1201/9781315100333-29
[25] Hashim TM, Abbas GH, Al-Khafaji FF, Alwash AA, Al-Mulali MZ, Ali YA. Using papyrus fiber ash as a sustainable filler modifier in preparing low moisture sensitivity HMA mixtures. Journal of the Mechanical Behavior of Materials. 2022 Aug 29;31(1):649-55. https://doi.org/10.1515/jmbm-2022-0072
[26] Wasilewska M, Grzyb D, Gardziejczyk W. Preliminary assessment of the properties of composite layers based on porous asphalt and coloured mortar. InMATEC Web of Conferences 2024 (Vol. 396, p. 02005). EDP Sciences. https://doi.org/10.1051/matecconf/202439602005
[27] Sukumar N, Moës N, Moran B, Belytschko T. Extended finite element method for three-dimensional crack modelling. International journal for numerical methods in engineering. 2000 Aug 20;48(11):1549-70. https://doi.org/10.1002/1097-0207(20000820)48:11<1549::AID-NME955>3.0.CO;2-A
[28] Rasheed A. Development of a New Environmentally Friendly Glass Fibre Reinforced Cold Mix Microasphalt with High Resistance to Cracking and Deformation. Liverpool John Moores University (United Kingdom); 2018.

[29] Zhao S, Ouyang J, Yang W. Research on fracture properties of cement emulsified asphalt mortar based on viscoelastic fracture mechanics. Construction and Building Materials. 2025 Apr 4;470:140664. https://doi.org/10.1016/j.conbuildmat.2025.140664
[30] Du S. Effect of different fibres on the performance properties of cold recycled mixture with asphalt emulsion. International Journal of Pavement Engineering. 2022 Aug 24;23(10):3444-53. https://doi.org/10.1080/10298436.2021.1901100
[31] Guo Y, Tataranni P, Sangiorgi C. The use of fibres in asphalt mixtures: A state of the art review. Construction and Building Materials. 2023 Aug 1;390:131754. https://doi.org/10.1016/j.conbuildmat.2023.131754
[32] Amal R, Narendra J, Sivakumar M, Anjaneyulu MV. Performance Evaluation of Cold Bituminous Mix Reinforced with Coir Fibre. AIJR Proceedings. 2021 Apr 11:559-68. https://doi.org/10.21467/proceedings.112.67
[33] Liu Z, Zhang Y, Liu H, Liu X, Liang J, Shao Z. Fatigue Characteristics Analysis of Carbon Fiber Laminates with Multiple Initial Cracks. Applied Sciences. 2024 Sep 23;14(18):8572. https://doi.org/10.3390/app14188572

www.jresm.org

Research on Engineering Structures and Materials

Compendex on Engineering Village

Scopus

DRJI

TÜBİTAK ULAKBİM

ProQuest

crossref

Google Scholar

Universal Impact Factor
Scientifically derived Journal Impact Factor

SIS Scientific Indexing Services

Journal Seeker Research Bible

CiteFactor
Academic Scientific Journals

EZB Elektronische Zeitschriftenbibliothek

Open Academic Journals Index

GIF
GLOBAL IMPACT FACTOR

ASOS indeks

Cosmos

Publication Forum

INFOBASE INDEX

ROOTINDEXING
JOURNAL ABSTRACTING AND INDEXING SERVICE

Scope Database
Journal Indexing & Citation Analysis

Research Group
https://mimrg.net/